

Innovative Load Testing Systems

Prepared for:
National Cooperative Highway Research Program

TRANSPORTATION RESEARCH BOARD
OF THE NATIONAL ACADEMIES

Submitted by:
Samuel G. Paikowsky

March 2006

ACKNOWLEDGMENT

This work was sponsored by the American Association of State Highway and Transportation Officials (AASHTO), in cooperation with the Federal Highway Administration, and was conducted in the National Cooperative Highway Research Program (NCHRP), which is administered by the Transportation Research Board (TRB) of the National Academies.

COPYRIGHT PERMISSION

Authors herein are responsible for the authenticity of their materials and for obtaining written permissions from publishers or persons who own the copyright to any previously published or copyrighted material used herein.

Cooperative Research Programs (CRP) grants permission to reproduce material in this publication for classroom and not-for-profit purposes. Permission is given with the understanding that none of the material will be used to imply TRB, AASHTO, FAA, FHWA, FMCSA, FTA, or Transit Development Corporation endorsement of a particular product, method, or practice. It is expected that those reproducing the material in this document for educational and not-for-profit uses will give appropriate acknowledgment of the source of any reprinted or reproduced material. For other uses of the material, request permission from CRP.

DISCLAIMER

The opinion and conclusions expressed or implied in the report are those of the research agency. They are not necessarily those of the TRB, the National Research Council, AASHTO, or the U.S. Government.

This report has not been edited by TRB.

THE NATIONAL ACADEMIES

Advisers to the Nation on Science, Engineering, and Medicine

The **National Academy of Sciences** is a private, nonprofit, self-perpetuating society of distinguished scholars engaged in scientific and engineering research, dedicated to the furtherance of science and technology and to their use for the general welfare. On the authority of the charter granted to it by the Congress in 1863, the Academy has a mandate that requires it to advise the federal government on scientific and technical matters. Dr. Ralph J. Cicerone is president of the National Academy of Sciences.

The **National Academy of Engineering** was established in 1964, under the charter of the National Academy of Sciences, as a parallel organization of outstanding engineers. It is autonomous in its administration and in the selection of its members, sharing with the National Academy of Sciences the responsibility for advising the federal government. The National Academy of Engineering also sponsors engineering programs aimed at meeting national needs, encourages education and research, and recognizes the superior achievements of engineers. Dr. William A. Wulf is president of the National Academy of Engineering.

The **Institute of Medicine** was established in 1970 by the National Academy of Sciences to secure the services of eminent members of appropriate professions in the examination of policy matters pertaining to the health of the public. The Institute acts under the responsibility given to the National Academy of Sciences by its congressional charter to be an adviser to the federal government and, on its own initiative, to identify issues of medical care, research, and education. Dr. Harvey V. Fineberg is president of the Institute of Medicine.

The **National Research Council** was organized by the National Academy of Sciences in 1916 to associate the broad community of science and technology with the Academy's purposes of furthering knowledge and advising the federal government. Functioning in accordance with general policies determined by the Academy, the Council has become the principal operating agency of both the National Academy of Sciences and the National Academy of Engineering in providing services to the government, the public, and the scientific and engineering communities. The Council is administered jointly by both the Academies and the Institute of Medicine. Dr. Ralph J. Cicerone and Dr. William A. Wulf are chair and vice chair, respectively, of the National Research Council.

The **Transportation Research Board** is a division of the National Research Council, which serves the National Academy of Sciences and the National Academy of Engineering. The Board's mission is to promote innovation and progress in transportation through research. In an objective and interdisciplinary setting, the Board facilitates the sharing of information on transportation practice and policy by researchers and practitioners; stimulates research and offers research management services that promote technical excellence; provides expert advice on transportation policy and programs; and disseminates research results broadly and encourages their implementation. The Board's varied activities annually engage more than 5,000 engineers, scientists, and other transportation researchers and practitioners from the public and private sectors and academia, all of whom contribute their expertise in the public interest. The program is supported by state transportation departments, federal agencies including the component administrations of the U.S. Department of Transportation, and other organizations and individuals interested in the development of transportation.
www.TRB.org

www.national-academies.org

TABLE OF CONTENTS

LIST OF FIGURES	viii
LIST OF TABLES	xix
ACKNOWLEDGEMENTS	xxi
SUMMARY OF FINDINGS	1
CHAPTER 1 Introduction, Research Approach and Principles.....	4
1.1 Introduction	
1.1.1 Background	
1.1.2 Research Objectives	
1.2 Research Approach	
1.3 Principles	
1.3.1 Outlook	
1.3.2 Load Application and Force Incident	
1.3.2.1 Impact Analysis	
1.3.2.2 Relative Wavelength and Pulse Propagation	
1.3.2.3 Pulse Duration, Relative Wavelength and Pile Testing	
1.3.2.4 Intermediate Conclusions	
1.4 Classification of Pile Testing	
1.5 Testing Methods	
CHAPTER 2 Findings – Testing Methods – Critical Review	11
2.1 Overview	
2.2 The Drop Weight System	
2.2.1 General	
2.2.2 Dynamic Measurements During Pile Driving and their Analyses	
2.2.3 Background and Use	
2.2.3.1 General	
2.2.3.2 Advantages	
2.2.3.3 Disadvantages	
2.2.4 Review of Available Systems	
2.2.4.1 General	
2.2.4.2 System DW-A	
2.2.4.3 System DW-B	
2.2.4.4 System DW-C	
2.2.4.5 System DW-D	
2.2.4.6 System DW-E	
2.2.4.7 System DW-F	
2.2.4.8 System DW-G	
2.2.4.9 System DW-H	
2.2.4.10 System DW-I	
2.2.4.11 Discussion and Summary	

- 2.2.5 Dynamic Measurements of Impacted In-Place Constructed Deep Foundations
 - 2.2.5.1 In-Place Constructed Deep Foundations
 - 2.2.5.2 Dynamic Measurements
 - 2.2.5.3 Difficulties Associated with the Impact of a Drilled Shaft
 - 2.2.5.4 Case History
- 2.2.6 Existing Codes and Guidelines
 - 2.2.6.1 Overview
 - 2.2.6.2 The Chinese Code
- 2.3 Statnamic Testing
 - 2.3.1 General
 - 2.3.2 Active Research and Usage
 - 2.3.3 Device Component
 - 2.3.4 Instrumentation
 - 2.3.4.1 General
 - 2.3.4.2 Accelerometers
 - 2.3.4.3 Displacements
 - 2.3.4.4 Force and Strain
 - 2.3.4.5 Data Acquisition System (DAS)
 - 2.3.5 Methods of Analysis
 - 2.3.5.1 Overview
 - 2.3.5.2 Signal Matching
 - 2.3.5.3 Unloading Point Method
 - 2.3.5.4 Modified Unloading Point Method
 - 2.3.5.5 Segmental Unloading Point Method
 - 2.3.6 Critical Evaluation
- 2.4 The Static Testing Methods
 - 2.4.1 Overview
 - 2.4.2 Static Cyclic Testing
- 2.5 Osterberg Cell Load Testing
 - 2.5.1 Introduction
 - 2.5.2 O-Cell Load Testing Method and Application
 - 2.5.2.1 Review
 - 2.5.2.2 State DOT Use
 - 2.5.3 Comparison Between O-Cell (bottom up) and Traditional (top-down) Compression Load Test
 - 2.5.3.1 General
 - 2.5.3.2 Hong Kong Railway
 - 2.5.3.3 Downtown Hong Kong
 - 2.5.3.4 New Mexico
 - 2.5.3.5 Singapore
 - 2.5.3.6 Osaka, Japan
 - 2.5.3.7 Tests in Florida Limestone
 - 2.5.3.8 Summary and Discussion
 - 2.5.4 Finite Element Analysis
 - 2.5.4.1 Introduction
 - 2.5.4.2 Previous Work

2.5.4.3	Model Description	
2.5.4.4	Comparison with Field Tests	
2.5.4.5	Summary of the Soil Model Study	
2.5.4.6	Summary of the Rock Model Study	
2.5.5	A Simplified Analytical Solution for the consideration of Poisson's Effect in a Pile	
2.5.5.1	Overview	
2.5.5.2	Model Description and Derivation of Solution	
2.5.5.3	Stress Coefficient K_r	
2.5.5.4	Comparison of Top Down and O-Cell Loading	
2.5.5.5	Field Test Comparison	
2.5.5.6	Parametric Study	
2.5.5.7	Intermediate Summary	
2.5.6	Summary and Conclusion	
2.6	The Simbat Method	
2.6.1	General	
2.6.2	Theoretical Background	
2.6.3	Methodology	
2.6.4	Dynamic to Static Conversion	
2.6.5	Analysis of Results	
2.6.6	Case Histories	
2.6.6.1	National Geotechnical Experimentation Site at Texas A&M University	
2.6.6.2	Ship Street, Dublin, Ireland	
2.6.7	Database	
2.6.8	Summary and Conclusions	
2.7	The Fundex Method	
2.7.1	General	
2.7.2	Theoretical Background	
2.7.3	Testing Procedures and Interpretation	
2.7.4	Case Histories	
2.7.5	Conclusions	
2.8	The Smartpile Method	
2.8.1	General	
2.8.2	Testing Procedure	
2.8.3	Theoretical Background	
2.8.4	Case Histories	
2.8.5	Summary and Conclusions	
2.9	The Smartcoil System	
2.9.1	Background and Use	
2.9.2	Advantages	
2.9.3	Limitations	
2.9.4	Need for Research	

CHAPTER 3 Findings – Databases and Interpretations	84
3.1 Overview	

- 3.2 Deep Foundations Nominal Strength
 - 3.2.1 Overview
 - 3.2.2 Databases
 - 3.2.3 Failure Criterion for Statically Loaded Driven Piles
 - 3.2.4 Load Test Procedure for Statically Loaded Driven Piles
 - 3.2.5 Failure Criterion for Statically Loaded Drilled Shafts
- 3.3 Drop Weight Databases Analysis
 - 3.3.1 General
 - 3.3.2 General Drop-Weight System Evaluation
 - 3.3.2.1 General Relationship
 - 3.3.2.2 Drop Weight System Requirements
 - 3.3.3 Drilled Shafts Static Capacity
 - 3.3.3.1 Database DW/LT 2000
 - 3.3.3.2 Static Capacity
 - 3.3.4 Static Shaft Capacity vs. Drop Weight Dynamic Predictions
 - 3.3.5 Evaluation of Results
 - 3.3.5.1 Overview
 - 3.3.5.2 Static Capacity vs. Dynamic Predictions for Driven Piles
 - 3.3.5.3 Intermediate Conclusions
 - 3.3.6 Ram Requirements
- 3.4 Statnamic Database Analysis
 - 3.4.1 Overview
 - 3.4.2 Background
 - 3.4.3 Sources of Data
 - 3.4.4 Analysis Procedure
 - 3.4.5 Results
 - 3.4.5.1 General
 - 3.4.5.2 Rock
 - 3.4.5.3 Sand
 - 3.4.5.4 Silt
 - 3.4.5.5 Clay
 - 3.4.6 Summary of Database Analysis
 - 3.4.7 Development of the Rate Effect Factor
 - 3.4.8 Conclusions and Recommendations

CHAPTER 4 Findings – Models.....101

- 4.1 Overview
- 4.2 Simplified Fundamental model
 - 4.2.1 Overview
 - 4.2.2 Model Description
 - 4.2.3 Model Evaluation
 - 4.2.3.1 Overview
 - 4.2.3.2 Underdamped System ($\zeta < 1$)
 - 4.2.3.3 Critically Damped ($\zeta = 1$)
 - 4.2.3.4 Overdamped ($\zeta > 1$)
 - 4.2.3.5 Impact without Capblock

- 4.2.4 Model Performance
- 4.2.5 The Influence of a Load Testing System
- 4.2.6 Case Histories
- 4.3 Simulation of a Ram Impact with a Deep Foundation
 - 4.3.1 Overview
 - 4.3.2 Analysis Procedure – Stage I
 - 4.3.2.1 Overview
 - 4.3.2.2 Model Geometry
 - 4.3.2.3 Constraints
 - 4.3.2.4 Material Models
 - 4.3.3 Parametric Studies
 - 4.3.3.1 General
 - 4.3.3.2 Models Generated to Study the Effect of Drop Height
 - 4.3.3.3 Models Generated to Study the Effect of Ram Diameter
 - 4.3.3.4 Models Generated to Study the Effect of Offset (Uneven) Impact
 - 4.3.4 Format for the Presentation of the Results from Stage I
 - 4.3.4.1 Stress Propagation Images
 - 4.3.4.2 Detailed Force and Velocity
 - 4.3.4.3 Animations
 - 4.3.5 Results from Stage I
 - 4.3.5.1 Overview
 - 4.3.5.2 Baseline Model
 - 4.3.5.3 Smaller Diameter Ram
 - 4.3.5.4 Uneven Impact (Tilted Ram)
 - 4.3.6 Discussion of Results – Stage I
 - 4.3.6.1 Baseline Model
 - 4.3.6.2 Smaller Diameter Ram
 - 4.3.6.3 Uneven Impact (Tilted Ram)
 - 4.3.6.4 Operational Conclusions
 - 4.3.7 Analysis Procedure – Stage II
 - 4.3.7.1 Overview
 - 4.3.7.2 Model Geometry, Constraints, and Material Properties
 - 4.3.8 Baseline Model Results
 - 4.3.8.1 Surface Conditions
 - 4.3.8.2 One Meter Below the Surface
 - 4.3.9 Uneven Impact (Tilted Ram)
 - 4.3.9.1 Surface Conditions
 - 4.3.9.2 One Meter Below the Surface
 - 4.3.9.3 Two Meters Below the Surface
 - 4.3.9.4 Three and Four Meters Below the Surface
 - 4.3.10 The Use of a Soft Cushion to Mitigate Uneven Impact (Tilted Ram)
 - 4.3.11 Intermediate Conclusions
- 4.4 Rheological Model of Pile Behavior Under Loading
 - 4.4.1 Overview
 - 4.4.2 Model Description
 - 4.4.2.1 Overview

- 4.4.2.2 Stage 1 ($P \leq T^*0$)
- 4.4.2.3 Stage 2 ($T^*0 < P < T^*1 + T^*0$)
- 4.4.2.4 Stage 3 ($T^*0 + T^*1 < P < T^*1 + T^*2 + T^*0$ and $P_a > T^*1$)
- 4.4.2.5 Stage 4 ($T^*1 + T^*2 + T^*0 < P < T3$)
- 4.4.2.6 Stage 5 ($T3 < P < T4$)
- 4.4.2.7 Stage 6 ($P > T4$)
- 4.4.2.8 Condition of Model Operation ($E2 T^*1 < E1 T^*2$)
- 4.5 Model Evaluation Using Newbury Test Pile #2
 - 4.5.1 Overview
 - 4.5.2 Parameters
 - 4.5.3 Static Load-Displacement Relationship Based on Statnamic Test Results
- 4.6 Conclusions

CHAPTER 5 Summary, Codes, Conclusions, Recommendations and Suggested Research.....125

- 5.1 Summary
 - 5.1.1 Summary Tables
 - 5.1.2 Summary of Study
- 5.2 Codes
 - 5.2.1 Overview
 - 5.2.2 Chinese Code
 - 5.2.3 Japanese Code
 - 5.2.4 American Standard
- 5.3 Observations, Conclusions and Recommendations
 - 5.3.1 General
 - 5.3.2 Principles
 - 5.3.3 Testing Methods
 - 5.3.3.1 General
 - 5.3.3.2 Drop Weight System
 - 5.3.3.3 Statnamic Tests
 - 5.3.3.4 Osterberg Cell
 - 5.3.3.5 The Secondary Testing Methods
- 5.4 Suggested Research
 - 5.4.1 Overview
 - 5.4.2 Drop Weight Systems
 - 5.4.2.1 Status
 - 5.4.2.2 Proposed Title for Research Statement
 - 5.4.2.3 Development
 - 5.4.2.4 Databases
 - 5.4.2.5 Models
 - 5.4.2.6 Tests
 - 5.4.2.7 Guidelines
 - 5.4.2.8 Priority
 - 5.4.2.9 Budget
 - 5.4.3 Statnamic Testing
 - 5.4.3.1 Status

- 5.4.3.2 Proposed Title for Research Statement
- 5.4.3.3 Development
- 5.4.3.4 Databases
- 5.4.3.5 Models
- 5.4.3.6 Tests
- 5.4.3.7 Guidelines
- 5.4.3.8 Priority
- 5.4.3.9 Budget
- 5.4.4 Osterberg Cell
 - 5.4.4.1 Status
 - 5.4.4.2 Proposed Title for Research Statement
 - 5.4.4.3 Development
 - 5.4.4.4 Databases
 - 5.4.4.5 Models
 - 5.4.4.6 Tests
 - 5.4.4.7 Guidelines
 - 5.4.4.8 Priority
 - 5.4.4.9 Budget
- 5.4.5 Research Statement
 - 5.4.5.1 Overview

REFERENCES139

APPENDIX A (Part A, B, and C) – Details of Osterberg Cell Finite Element Analysis

APPENDIX B (Part A, B, and C) – Details of Databases

APPENDIX C (Part A and B) – Codes

FIGURES

TABLES

LIST OF FIGURES

- Figure 1: Stress Propagation in a Fixed End Bar Struck by a Moving Mass (after Timoshenko and Goodier, 1934)
- Figure 2: Stress Wave Magnitude and Duration (Graphical Representation of Functions S_0 and S_1) as a Function of the Ratio Between the Masses of the Pile and the Striking Body (Paikowsky 1982)
- Figure 3: Physical and Mechanical Representation of a Mass Impacting Infinite Long Pile
- Figure 4: Non-Dimensional Force Pulses in a Pile as a Function of Time and the Ratio of Cushioning Element to Pile Stiffness (Holeyman 1992, see also Parola, 1970)
- Figure 5: Typical Load Testing Values for Pile Acceleration vs. (a) Relative Wavelength and (b) Force Duration (after Holeymann, 1992)
- Figure 6: Wave Propagation through a Pile with Free Ends; (a) As a Result of Sudden Applied Force R_i Located at X_i , (b) As a Result of Activation of R_i by a Traveling Compression Wave, (c) Velocity Effect at Pile Top Caused by a Resistance Step Force R_i at Location X_i
- Figure 7: Typical Loading Durations for Various Tests Performed on Test Pile #3 by the Geotechnical Engineering Research Laboratory of the University of Massachusetts Lowell, at the Newbury Test Site
- Figure 8: Notations Used for Model of Pile and Soil in TEPWAP Analysis (Paikowsky, 1982)
- Figure 9: Flow Chart Describing the Analysis Process Using TEPWAP (Paikowsky, 1982)
- Figure 10: Drop Weight System DW-A (Li, 1993); (a) General View, and (b) Lowering the System in an Excavation Above a Drilled Shaft
- Figure 11: Drop Weight System DW-B (Li, 2000); (a) General View, and (b) Close View with Dynamic Measurements Taken by Zengxuan (Frank) Li
- Figure 12: Drop Weight System DW-C (Weibing, 2000) From TL to BR; (a) General View, Hanging Ram without a Guiding System and the Data Acquisition System, (b) Transducer Attachment under the Hanging Ram, (c) Ram and Cushion, Close up View with Pipes Keeping the Ram above the Pile, (d) Impact
- Figure 13: Israeli Drop Weight System DW-D (GTR, 1997); (a) Photograph, and (b) Schematic
- Figure 14: Isotop Drop Weight Device DW-E (Sokolovsky et al., 1998)
- Figure 15: GRL Newton's Apple System DW-F; (a) General View, (b) Details of Instrumented Ram Impacting a Drilled Shaft (Robinson and Rausche, 2000)
- Figure 16: Drop Weight System DW-G (Briaud et al. 2000)
- Figure 17: Drop Weight System DW-H (Townsend et al. 1991)
- Figure 18: Drop Weight System DW-I (Longgen et al. 1999)
- Figure 19: Individual Force and Velocity Records of Four Strain and Acceleration Gauges Used During Impact No. 3 on Shaft-A (GTR, 1997)
- Figure 20: Individual Force and Velocity Records of Four Strain and Acceleration Gauges Used During Impact No. 4 on Shaft-A (GTR, 1997)
- Figure 21: Average Force and Velocity Measurements for Impact No. 3 on Shaft-A (GTR, 1997)
- Figure 22: Average Force and Velocity Measurements for Impact No. 4 on Shaft-A (GTR, 1997)

- Figure 23: Signal Match Analysis (CAPWAP) Results for Impact No. 3 on Shaft-A (GTR, 1997)
- Figure 24: Signal Match Analysis (CAPWAP) Results for Impact No. 4 on Shaft-A (GTR, 1997)
- Figure 25: Schematic of the Statnamic Testing Device
- Figure 26: Statnamic Piston (16 MN)
- Figure 27: Statnamic Cylinder (4 MN)
- Figure 28: (a) 4MN Reaction Mass Utilizing Gravel and Water in a Rectangular Steel Shell
(b) 16 MN Reaction Masses Utilizing Concrete in a Steel Shell
- Figure 29: (a) 30MN Gravel Catch System (b) Mechanical Catch System Utilizing Submerged, Water-filled Reaction Masses
- Figure 30: (a) 0.6 MN Device and (b) 4 MN Device Utilizing Mechanical and Hydraulic Catch Mechanisms Respectively
- Figure 31: Piezoelectric Accelerometer Diagram (Courtesy of PCB Piezotronics)
- Figure 32: Capacitive Accelerometer Diagram
- Figure 33: Wheatstone Bridge (Courtesy of Optim Electronics)
- Figure 34: MEGADAC Computer System (Courtesy of Optim Electronics)
- Figure 35: MEGADAC Daisy-Chain
- Figure 36: K-V Model (After DAS 1994)
- Figure 37: UPM Time Window for C Determination
- Figure 38: Variation in C Between Times (1) and (2)
- Figure 39: Selection Criteria (After Middendorp 1998)
- Figure 40: The effects of Mass Ratio on Statnamic Load Duration
- Figure 41: Statistics Screen Available in Statnamic Analysis Software
- Figure 42: Schematic of Segments and Strain Gauge Levels
- Figure 43: SUP Software Screen Capture (Gage Level Information Input Screen)
- Figure 44: SUP Segmental Analyzer Module
- Figure 45: Static Pile Load Testing Procedure According to ASTM in Comparison with the Static-Cyclic Loading Procedure (Paikowsky et al., 1999)
- Figure 46: Various Static and Statnamic Test Results, Test Pile #2 in Newbury MA (Hajduk et al., 1998)
- Figure 47: Static-Cyclic Test Plots of Displacement vs. Time and Load vs. Displacement (a) Slow Maintained (b) Short Duration (c) Static-Cyclic
- Figure 48: Schematic Diagram of O-cell Testing
- Figure 49: O-cell Testing Results for the Kowloon-Canton Railway, Hong Kong (Littlechild et al., 2000)
- Figure 50: Schematic Diagram of Axi-symmetric FE Model
- Figure 51: Drucker-Prager Model Yield Surface in Meridian Plane
- Figure 52: Pile-Soil and Pile-Rock Interface Model
- Figure 53: Dimensions and Instrumentation of Test Shaft, Henderson Case
- Figure 54: Comparison of Load vs. Displacement Curve, O-cell Test, Henderson Case
- Figure 55: Comparison of Load Transfer Curve, O-cell Test, Henderson Case
- Figure 56: Comparison of Load vs. Displacement Curve, Top Down Test, Henderson Case
- Figure 57: Dimensions and Instrumentation of Test Shaft, Wilsonville Case
- Figure 58: Comparison of Load vs. Displacement Curve, O-cell Test, Wilsonville Case
- Figure 59: Comparison of Load Transfer Curves, O-cell Test, Wilsonville Case

- Figure 60: Comparison of Load vs. Displacement Curve, Top Down Test, Wilsonville Case
- Figure 61: Dimensions and Instrumentation of Test Shaft, Denver Case
- Figure 62: Comparison of Load vs. Displacement Curve, O-cell Test, Denver Case
- Figure 63: Comparison of Load Transfer Curves, O-cell Test, Denver Case
- Figure 64: Comparison of Load vs. Displacement Curve, Top Down Test, Denver Case
- Figure 65: Top Down vs. O-cell Computed Load-Deflection for Soils
- Figure 66: Computed Tip Resistance and Side Shear for $K_0=1$, $\delta=31^\circ$
- Figure 67: Stress Path at Points Along the Shaft/Soil Interface
- Figure 68: Comparison of Side Shear vs. Displacement for Rock Models
- Figure 69: Computed Rock Socket Shear Stresses
- Figure 70: Effect of E_{rock} on Load vs. Displacement Curve, Top Down Test
- Figure 71: Effect of E_{rock} on Side Load vs. Displacement and Tip Load vs. Displacement Curve, Top Down Test
- Figure 72: Effect of E_{rock} on Load vs. Displacement Curve, O-cell Test
- Figure 73: Side Load vs. Displacement Comparison for Different Effect of E_{rock} Values
- Figure 74: Effect of ϕ_i on Load vs. Displacement Curve, Top Down Test
- Figure 75: Effect of ϕ_i on Side Load vs. Displacement and Tip Load vs. Displacement Curve, Top Down Test
- Figure 76: Effect of ϕ_i on Load vs. Displacement Curve, O-cell Test
- Figure 77: Side Load vs. Displacement Comparison for Different ϕ_i Values
- Figure 78: Effect of E_{rock} and ϕ_i on the Difference Between Two Testing Methods (top down vs. O-Cell)
- Figure 79: Shear Stress Distribution Comparison for Different E_{rock} Values
- Figure 80: Shear Stress Distribution Comparison for Different ϕ_i Values (z =depth below rock, L_{socket} =socket length)
- Figure 81: Simplified Model of Rock-Socketed Pile
- Figure 82: The Effect of E_p / E_s and V_p on Stress Coefficient K_r
- Figure 83: Free Body Diagram for a Segment of Pile
- Figure 84: Load Distribution, Example
- Figure 85: Comparison of Side Shear Distribution
- Figure 86: Load Distribution using the Simplified Model for the Wilsonville, AL Case; (a) O-cell Test, (b) Top Down Loading
- Figure 87: Side Shear Distribution for Wilsonville (a) Case I, (b) Case II, and (c) Case III
- Figure 88: Load Distribution, O-cell Test, Denver Case
- Figure 89: Side Shear Distribution, Denver Case
- Figure 90: Side Shear Distribution for Different E_p / E_s
- Figure 91: Side Shear Distribution for Different ϕ_i
- Figure 92: Side Shear Distribution for Different c_1
- Figure 93: General Arrangement of the Simbat system (Testconsult Website)
- Figure 94: The Components of the Simbat System (Testconsult Website)
- Figure 95: Dynamic Testing at Varying Strain Rates (Testconsult Website)
- Figure 96: Simbat Pile/Soil Model (Testconsult Website)
- Figure 97: Digital/Optical Theodolite used in the Simbat Test (Testconsult Website)
- Figure 98: Raw Curves from a Single Impact (Testconsult Website)
- Figure 99: Separation of Forces, Calculated $R_{dynamic}$ (Testconsult Website)
- Figure 100: Predicted Load/Settlement Curves (Testconsult Website)

- Figure 101: Simbat Dynamic to Static Correction Procedure (Testconsult Website)
- Figure 102: Correction of Velocity Using Theodolite Measurement (Testconsult Website)
- Figure 103: Computer Matching of Velocity (Testconsult Website)
- Figure 104: Computer Matching of Displacement (Testconsult Website)
- Figure 105: Comparison between Static and Dynamic Load Tests (Testconsult Website)
- Figure 106: Final Static Load Settlement Plot from Simbat (Testconsult Website)
- Figure 107: Bored Piles at NGES-TASU Sites (Briaud et al., 2000)
- Figure 108: Complete Load-Settlement History for All Test on Pile No.2 (Briaud et al., 2000)
- Figure 109: Comparison between Predicted and Measured Static Capacities (Briaud et al., 2000)
- Figure 110: Comparison of Simbat and Static Testing Results (Long, 2001)
- Figure 111: Piles in Rock – Loading to SWL / 1.5SWL (Long, 2001)
- Figure 112: Piles in Sand and Gravel Loading to SWL TO 1.5SWL (Long, 2001)
- Figure 113: All piles Loading to SWL / 1.5SWL (Long, 2001)
- Figure 114: Influence of Pile Diameter/Length to Diameter Ratio (Long, 2001)
- Figure 115: Mobilized Safety Factor (Long, 2001)
- Figure 116: Case History of Identification of Failed Pile (Long, 2001)
- Figure 117: The Fundex Field Testing System (Americanpiledriving Website)
- Figure 118: Force Pulses Acting on a Given Pile’s Head under Different Size Impacting Mass and a constant Stroke Height of 1.5m
- Figure 119: The Load Settlement Curves Calculated for a Dynamic, a Fundex and a Static Load Test (Schellingerhort, 1996)
- Figure 120: Illustration of a Pseudo Static Pile Load Tester (Schellingerhort, 1996, Coe.Berkeley Website)
- Figure 121: Maximum Force as a Function of Drop Height (Schellingerhort, 1996)
- Figure 122: The Force at the Pile Top as a Function of Time for Different Drop Heights (Schellingerhort, 1996)
- Figure 123: The Measured Force and Displacement Under a Single Impact by PSPLT (Schellingerhort, 1996)
- Figure 124: Load Displacement Curve Generated by Four Consecutive Drop Heights (Schellingerhort, 1996)
- Figure 125: Case 1, Comparison of a Static Load Test and Fundex Measurements (Schellingerhort, 1996)
- Figure 126: Case 2, Comparison of a Static Load Test and Fundex Measurements (Americanpiledriving Website)
- Figure 127: Case 3, Comparison of a Static Load Test and Fundex Measurements (Iwanowski et al., 1984)
- Figure 128: Case 4, Comparison of a Static Load Test and Fundex Measurements (Iwanowski et al., 1984)
- Figure 129: Smartpile Test Set-up (Ooi and Frederick, 2003)
- Figure 130: Force Sensor (a) Elevation View (b) Plan View (Ooi and Frederick, 2003)
- Figure 131: Smartpile Sensor Installation Photographs (Geotechnical Engineering Research Laboratory, University of Massachusetts Lowell, Newbury Site TP#3)
- Figure 132: Typical Force Versus Time Plots from Smartpile Test: (a) with a Peak between F_{sd} and F_{ds} , and (b) with a Trough between F_{sd} and F_{ds} . (Ooi and Frederick, 2003)

- Figure 133: The Smartpile Testing Field Measurements using Top and Tip Sensors (Haley & Aldrich, 1995)
- Figure 134: The Smartpile Testing Field Measurements using Top Measurements Alone (Haley & Aldrich, 1995)
- Figure 135: The Smartpile Measurements for TP#1 (Ooi and Frederick, 2003)
- Figure 136: The Static Testing Result for TP#1 (Ooi and Frederick, 2003)
- Figure 137: The Smartpile Measurements for TP#1 (Ooi and Frederick, 2003)
- Figure 138: The Static Testing Result for TP#1 (Ooi and Frederick, 2003)
- Figure 139: Illustration of Smartpile results for Courthouse Project Frederick Engineering Co. (Haley & Aldrich, 1995)
- Figure 140: Comparison of PDA Prediction and Smartpile Measurements (Tests were done by Haley & Aldrich, Cambridge, MA, May 1995)
- Figure 141: Typical Smart Coil System (SCS) Setup (after Frederick, 1999)
- Figure 142: Histogram and frequency distributions of KSD for 186 PD/LT2000 pile-cases in all type of soils (Paikowsky and Stenerson 2000)
- Figure 143: Comparison between pile capacity based on Davisson's criterion for slow maintained load tests and static cyclic load test capacity for 75 piles (Paikowsky et al., 1999)
- Figure 144: CAPWAP Drilled Shaft Capacity vs. Transferred Energy
- Figure 145: The Ratio of CAPWAP Drilled Shaft Capacity to Transferred Energy vs. Transferred Energy (No. of Cases=167, Mean=196, S.D.=174)
- Figure 146: CAPWAP Drilled Shaft Capacity vs. Transferred Energy for Capacity to Energy Ratio < Mean+1.5(S.D.)
- Figure 147: Transferred Energy vs. Nominal Energy
- Figure 148: Drilled Shaft Static Load Test Results (Representative Capacity) vs. Drop Weight CAPWAP Analysis for All Cases
- Figure 149: Drilled Shaft Static Load Test Results (Davisson's Failure Criterion) vs. Drop Weight CAPWAP Analysis for All Cases
- Figure 150: Drilled Shaft Static Load Test Results (FHWA Failure Criterion) vs. Drop Weight CAPWAP Analysis for All Cases
- Figure 151: Drilled Shaft Static Load Test Results (DeBeer Failure Criterion) vs. Drop Weight CAPWAP Analysis for All Cases
- Figure 152: Drilled Shaft Static Load Test to Failure Results (Representative Capacity) vs. Drop Weight CAPWAP Analysis
- Figure 153: Drilled Shaft Static Load Test to Failure Results (Davisson's Failure Criterion) vs. Drop Weight CAPWAP Analysis
- Figure 154: Drilled Shaft Static Load Test to Failure Results (FHWA Failure Criterion) vs. Drop Weight CAPWAP Analysis
- Figure 155: Drilled Shaft Static Load Test to Failure Results (DeBeer Failure Criterion) vs. Drop Weight CAPWAP Analysis
- Figure 156: Drilled Shaft Static Extrapolated Load Test Results (Representative Capacity) vs. Drop Weight CAPWAP Analysis
- Figure 157: Drilled Shaft Extrapolated Static Load Test Results (Davisson Failure Criterion) vs. Drop Weight CAPWAP Analysis
- Figure 158: Drilled Shaft Extrapolated Static Load Test Results (FHWA Failure Criterion) vs. Drop Weight CAPWAP Analysis

- Figure 159: Drilled Shaft Extrapolated Static Load Test Results (DeBeer Failure Criterion) vs. Drop Weight CAPWAP Analysis
- Figure 160: Static L.T. Capacity Over CAPWAP Prediction vs. Ram Weight Over Static L.T. Capacity: (a) Using the Representative Static Capacity, (b) Using the FHWA Failure Criterion
- Figure 161: Measured Static Capacity (FHWA Failure Criterion) vs. Ram Weight Using Database DW/LT 2000 for All Load Test Cases
- Figure 162: Relationship Between the Ratio of Ram Weight to Drop Weight Capacity (FHWA Failure Criterion) vs. Ram Weight Based on Database DW/LT 2000
- Figure 163: Load Test Program Parameters used to Uniquely Define Comparisons
- Figure 164: TFC-241 Pre
- Figure 165: TFC-241 Post
- Figure 166: TFC 532 Pre
- Figure 167: TFC 532 Post
- Figure 168: FLLS TP-1/2 Pre
- Figure 169: FLLS TP-1/2 Post
- Figure 170: FLLS TP-3/4 Pre
- Figure 171: FLLS TP-3/4 Post
- Figure 172: JFK OMSF P-10 Pre
- Figure 173: JFK OMSF P-10 Post
- Figure 174: NNO T1 Pre
- Figure 175: NNO T1 Post
- Figure 176: STG LT-1 Pre
- Figure 177: STG LT-1 Post
- Figure 178: BC Pier 15 Pre
- Figure 179: BC Pier 15 Post
- Figure 180: BC Pier 10 Pre
- Figure 181: BC Pier 10 Post
- Figure 182: BC Pier 5 Pre
- Figure 183: BC Pier 5 Post
- Figure 184: Ohito TEST Pre
- Figure 185: Ohito TEST Post
- Figure 186: BQE SA 1&8 Pre
- Figure 187: BQE SA 1&8 Post
- Figure 188: STG LT-5 Pre
- Figure 189: STG LT-5 Post
- Figure 190: SHONAN T6 Pre
- Figure 191: SHONAN T6 Post
- Figure 192: SHONAN T5 Pre
- Figure 193: SHONAN T5 Post
- Figure 194: SHONAN T2 Pre
- Figure 195: SHONAN T2 Post
- Figure 196: SHONAN T2 Post
- Figure 197: SHONAN T1 Post
- Figure 198: Aub 2 Pre
- Figure 199: Aub 1 Post

Figure 200: Aub 10 Pre
 Figure 201: Aub 10 Post
 Figure 202: Aub 8 Pre
 Figure 203: Aub 8 Post
 Figure 204: Aub 7 Pre
 Figure 205: Aub 7 Post
 Figure 206: Aub 5 Pre
 Figure 207: Aub 5 Post
 Figure 208: Aub 3 Pre
 Figure 209: Aub 3 Post
 Figure 210: Aub 2 Pre
 Figure 211: Aub 2 Post
 Figure 212: NIA TP-1&2a Pre
 Figure 213: NIA TP-1&2a Post
 Figure 214: NIA TP-1&2b Pre
 Figure 215: NIA TP-1&2b Post
 Figure 216: NIA TP-1&3a Pre
 Figure 217: NIA TP-1&3a Post
 Figure 218: NIA TP-1&3b Pre
 Figure 219: NIA TP-1&3b Post
 Figure 220: NIA TP-9&10a Pre
 Figure 221: NIA TP-9&10a Post
 Figure 222: NIA TP-9&10b Pre
 Figure 223: NIA TP-9&10a Post
 Figure 224: NIA TP-5&6b Pre
 Figure 225: NIA TP-5&6b Post
 Figure 226: NIA TP-5&6a Pre
 Figure 227: NIA TP-5&6a Post
 Figure 228: LC T-114.5 Pre
 Figure 229: LC T-114.5 Post
 Figure 230: LC X-123 Pre
 Figure 231: LX C-123 Post
 Figure 232: Safety and Resistance Factors vs. Rate Effect Factor
 Figure 233: Predicted (SLD) vs. Actual (SLT) for Rock
 Figure 234: Predicted (SLD) vs. Actual (SLT) for Silt
 Figure 235: Predicted (SLD) vs. Actual (SLT) for Sand
 Figure 236: Predicted (SLD) vs. Actual (SLT) for All Soils
 Figure 237: Predicted (SLD) vs. Actual (SLT)
 Figure 238: (a) Definition Diagram for Pile Driving Equations, (b) Equilibrium of Ram, (c) Equilibrium at Capblock-pile Interface, (d) Definition Diagrams for Pile Force (Irvine, 1986)
 Figure 239: Equivalent Model for Pile System (Irvine, 1986)
 Figure 240: Force Pulse on Pile Head ($\zeta < 1$)
 Figure 241: Non-dimensional Force Pulse on Pile Head ($\zeta < 1$)
 Figure 242: Force Pulse on Pile Head ($\zeta = 1$)
 Figure 243: Non-dimensionally Force Pulse on Pile Head ($\zeta = 1$)

- Figure 244: Limiting Cases for Dynamic Loads in Piles (a) Rigid Capblock, and (b) Rigid Pile (Irvine, 1986)
- Figure 245: Dimensional Force Pulse on Pile Head ($\zeta > 1$)
- Figure 246: Non-Dimensional Force Pulse on Pile Head ($\zeta > 1$)
- Figure 247: Force Pulse on Pile Head
- Figure 248: Non-dimensional Force Pulse on Pile Head
- Figure 249: Force Pulses on Pile Head ($\zeta < 1$)
- Figure 250: Non-dimensional Force Pulses on Pile Head ($\zeta < 1$)
- Figure 251: Force Pulse on Pile Head ($\zeta < 1$)
- Figure 252: Non-dimensional Force Pulse on Pile Head ($\zeta < 1$)
- Figure 253: Force Pulses on pile Head ($\zeta < 1$)
- Figure 254: Non- dimensional Force Pulses on pile Head ($\zeta < 1$)
- Figure 255: Force Pulses on Pile Head ($\zeta > 1$)
- Figure 256: Non- dimensional Force Pulse on Pile Head ($\zeta > 1$)
- Figure 257: Force Pulses on Pile Head ($\zeta > 1$)
- Figure 258: Non- dimensional Force Pulse on Pile Head ($\zeta > 1$)
- Figure 259: Force Pulses on Pile Head ($\zeta > 1$)
- Figure 260: Non- dimensional Force Pulse on Pile Head ($\zeta > 1$)
- Figure 261: Force pulses on the Pile Head with Same R Value
- Figure 262: Force Pulses on Pile Head ($\zeta < 1$) $M=50\text{kN}$, $H=1.5\text{m}$,
 $K=(2.0,1.5,1.0,0.5,0.25*1000\text{KN/mm})$
- Figure 263: Force Pulses on Pile Head ($\zeta < 1$) $M=420\text{kN}$, $H=0.5\text{m}$,
 $K=(2.0,1.5,1.0,0.5,0.25*1000\text{KN/mm})$
- Figure 264: Capblock Stiffness K vs. Force Pulse Duration T_p ($0.0596 < \zeta < 0.9985$)
- Figure 265: Force Pulses on Pile Head ($\zeta > 1$) $M=150\text{kN}$, $H=0.5\text{m}$,
 $K=(15,10,5,2.5,1,0.5*1000\text{KN/mm})$
- Figure 266: Force Pulses on pile Head ($\zeta > 1$) $M=1500\text{kN}$, $H=0.1\text{m}$,
 $K=(0.5,0.4,0.3,0.2,0.1,0.05 *1000\text{KN/mm})$
- Figure 267: Time Histories of Force Pulses on Pile Head ($\zeta < 1$) (Same Energy)
- Figure 268: Force Pulses on Pile Head ($\zeta < 1$)
- Figure 269: Force Pulse on Pile Head Same M and H , Different I
- Figure 270: Non- Dimensional Force Pulse on Pile Head Same M and H , different I
- Figure 271: Force Pulse on Pile Head (Same K , H and I , Different M)
- Figure 272: The Influence of a load Testing System
- Figure 273: Force Pulse on pile Head (Newbury Test Pile No.2)
- Figure 274: Force Pulse on pile Head (Newbury Test Pile No.3)
- Figure 275: Schematic of Pile and Impact System in LSDYNA Modeling
- Figure 276: Isometric View of Pile and Ram
- Figure 277: Top View of Pile
- Figure 278: Top View of Ram
- Figure 279: Half-Symmetry Constraint Schematic for Ram and Pile
- Figure 280: Constraint Schematic for the Pile's Tip
- Figure 281: Isometric View of System with a Rotated Ram for an Offset (Uneven) Impact
- Figure 282: (a) Depiction of Nodes and Elements on the Concrete Pile Chosen for the Detailed Presentation of the Results (b) Depiction of Nodes Chosen for

Calculating Velocity and Elements Chosen for Calculating Normal Stress for the Non-symmetric (Uneven impact) Analysis

- Figure 283: Calculated Normal Stress for Elements on Concrete Surface in Baseline FE Model
- Figure 284: Calculated Velocity (V*I) for Nodes on Concrete Surface in Baseline FE Model
- Figure 285: Calculated Normal Stress for Elements ~1m Below Surface in Baseline FE Model
- Figure 286: Calculated Velocity (V*I) for Nodes ~1m Below Surface in Baseline FE Model
- Figure 287: Calculated Normal Stress for Elements ~2m Below Surface in Baseline Model
- Figure 288: Calculated Velocity (V*I) for Nodes ~2m Below Surface in Baseline FE Model
- Figure 289: Calculated Normal Stress for Elements ~3m Below Surface in Baseline Model
- Figure 290: Calculated Velocity (V*I) for Nodes ~3m Below Surface in Baseline FE Model
- Figure 291: Calculated Normal Stress for Elements on Concrete Surface in FE Model with Ram Diameter = 0.2m for 0ms – 20ms
- Figure 292: Calculated Velocity (V*I) for Nodes on Concrete Surface in FE Model with Ram Diameter = 0.2m for 0ms – 20ms
- Figure 293: Calculated Normal Stress for Elements ~1m Below Surface in FE Model with Ram Diameter = 0.2m for 0ms – 20ms
- Figure 294: Calculated Velocity (V*I) for Nodes ~1m Below Surface in FE Model with Ram Diameter = 0.2m for 0ms – 20ms
- Figure 295: Calculated Normal Stress for Elements ~2m Below Surface in FE Model with Ram Diameter = 0.2m for 0ms – 20ms
- Figure 296: Calculated Velocity (V*I) for Nodes ~2m Below Surface in FE Model with Ram Diameter = 0.2m for 0ms – 20ms
- Figure 297: Calculated Normal Stress for Elements ~3m Below Surface in FE Model with Ram Diameter = 0.2m for 0ms – 20ms
- Figure 298: Calculated Velocity (V*I) for Nodes ~3m Below Surface in FE Model with Ram Diameter = 0.2m for 0ms – 20ms
- Figure 299: Calculated Normal Stress for Elements on Concrete Surface in FE Model with Ram Diameter = 1.0m and Tilt Angle = 1° for 0ms – 16ms
- Figure 300: Calculated Velocity (V*I) for Nodes on Concrete Surface in FE Model with Ram Diameter = 1.0m and Tilt Angle = 1° for 0ms – 16ms
- Figure 301: Calculated Normal Stress for Elements ~1 m Below Surface in FE Model with Ram Diameter = 1.0m and Tilt Angle = 1° for 0ms – 16ms
- Figure 302: Calculated Velocity (V*I) for Nodes ~1m Below Surface in FE Model with Ram Diameter = 1.0m and Tilt Angle = 1° for 0ms – 16ms
- Figure 303: Calculated Normal Stress for Elements ~2 m Below Surface in FE Model with Ram Diameter = 1.0m and Tilt Angle = 1° for 0ms – 16ms
- Figure 304: Calculated Velocity (V*I) for Nodes ~2 m Below Surface in FE Model with Ram Diameter = 1.0m and Tilt Angle = 1° for 0ms – 16ms
- Figure 305: Calculated Normal Stress for Elements ~3m Below Surface in FE Model with Ram Diameter = 1.0m and Tilt Angle = 1° for 0ms – 16ms
- Figure 306: Calculated Velocity (V*I) for Nodes ~3m Below Surface in FE Model with Ram Diameter = 1.0m and Tilt Angle = 1° for 0ms – 16ms
- Figure 307: Calculated Normal Stress for Elements on Concrete Surface in FE Model with Ram Diameter = 1.0 and Tilt angle = 0° for Time = 0ms – 40ms

- Figure 308: Calculated Velocity for Nodes on Concrete Surface in FE Model with Ram Diameter = 1.0 and Tilt angle = 0° for Time = 0ms – 40ms
- Figure 309: Calculated Normal Stress for Elements on Concrete Surface in FE Model with Ram Diameter = 1.0 and Tilt angle = 0° for Time = 0ms – 10ms
- Figure 310: Calculated Velocity for Nodes on Concrete Surface in FE Model with Ram Diameter = 1.0 and Tilt angle = 0° for Time = 0ms – 10ms
- Figure 311: Calculated Normal Stress for Elements on Concrete Surface in FE Model with Ram Diameter = 1.0 and Tilt angle = 0° for d = -0.5 to 0.5m
- Figure 312: Calculated Normal Stress for Elements on the Concrete Surface in the FE Model with Ram Diameter = 1.0m and Tilt Angle = 0° for Time Equal to; (a) 1.8ms, (b) 2.0ms, (c) 2.5ms, (d) 3.0ms, (e) 3.5ms, (f) 4.0ms, (g) 4.5ms, (h) 5.0ms, (i) 6.0ms, (j) 7.0ms, (k) 8.0ms, and (l) 9.0ms
- Figure 313: Calculated Normal Stress for Elements 1m Below the Concrete Surface in the FE Model with Ram Diameter = 1.0m and Tilt Angle = 0° for Time equal to; (a) 1.8ms, (b) 2.0ms, (c) 2.5ms, (d) 3.0ms, (e) 3.5ms, (f) 4.0ms (g) 4.5ms, (h) 5.0ms, (i) 6.0ms, (j) 7.0ms, (k) 8.0ms, and (l) 9.0ms
- Figure 314: Calculated Normal Stress for Elements on the Concrete Surface in the FE Model with Ram Diameter = 1.0m and Tilt Angle = 1° for Time = 0ms – 40ms
- Figure 315: Calculated Velocity for Nodes on the Concrete Surface in the FE Model with Ram Diameter = 1.0m and Tilt Angle = 1° for Time = 0ms – 40ms
- Figure 316: Calculated Normal Stress for Elements on the Concrete Surface in the FE Model with Ram Diameter = 1.0m and Tilt Angle = 1° for Time = 0ms – 10ms
- Figure 317: Calculated Velocity for Nodes on the Concrete Surface in the FE Model with Ram Diameter = 1.0m and Tilt Angle = 1° for Time = 0ms – 10ms
- Figure 318: Calculated Normal Stress for Elements on the Concrete Surface in the FE Model with Ram Diameter = 1.0m and Tilt Angle = 1° for d = -0.5 to 0.5m and time equal to (a) 1.8 to 2.2ms, and (b) 2.0 to 4.5ms
- Figure 319: Calculated Normal Stress for Elements on the Concrete Surface in the FE Model with Ram Diameter = 1.0m and Tilt Angle = 1° for Time Equal to; (a) 2.0ms, (b) 2.5ms, (c) 3.0ms, (d) 3.5ms, (e) 4.0ms, (f) 5.0ms, (g) 6.0ms, (h) 7.0ms, (i) 8.0ms, (j) 9.0ms, and (k) 10.0ms
- Figure 320: Calculated Normal Stress for Elements 1m Below Concrete Surface in FE Model with Ram Diameter = 1.0m and Tilt Angle = 1° for Time equal to; (a) 2.0ms, (b) 2.5ms, (c) 3.0ms, (d) 3.5ms, (e) 4.0ms, (f) 4.5ms, (g) 5.0ms (h) 6.0ms, (i) 7.0ms, (j) 8.0ms, (k) 9.0ms, and (l) 10.0ms
- Figure 321: Calculated Normal Stress for Elements 2m Below the Concrete Surface in the FE Model with Ram Diameter = 1.0m and Tilt Angle = 1° for Time equal to; (a) 2.0ms, (b) 3.0ms, (c) 4.0ms, (d) 5.0ms, (e) 6.0ms, (f) 7.0ms, (g) 8.0ms, (h) 9.0ms, (i) 10.0ms, (j) 11.0ms, and (k) 12.0ms
- Figure 322: Calculated Normal Stress for Elements 3m Below the Concrete Surface in the FE Model with Ram Diameter = 1.0m and Tilt Angle = 1° for Time Equal to (a) 6.0ms, (b) 7.0ms, (c) 8.0ms, and (d) 9.0ms
- Figure 323: Calculated Normal Stress for Elements 4m Below the Concrete Surface in the FE Model with Ram Diameter = 1.0m and Tilt Angle = 1° for Time Equal to (a) 6.0ms, (b) 7.0ms, (c) 8.0ms and (d) 9.0ms

- Figure 324: Calculated Normal Stress for Elements 2m Below the concrete Surface in the FE Model with Ram Diameter = 1.0m and Tilt Angle = 1° with a Soft Cushion for Time Equal to (a) 3ms, (b) 6ms, (c) 8ms, (d) 10ms, (e) 12ms, and (f) 14ms
- Figure 325: Average Forces with Time Across the Shaft at the Top (Surface) and One and Two Diameters Below the Surface (1m, 2m Respectively) for Representative and “Soft” Wood Cushions
- Figure 326: The Rheological Model Component for the Description of Pile-Soil Interaction
- Figure 327: Load Displacement Relations for Element T
- Figure 328: Load Displacement Relations for Element T*
- Figure 329: Time –Settlement Relations Under a Constant Load Step P_j
- Figure 330: Load-Displacement Relations for a Compression Express static-Cyclic Test with Defined Controlling Loads, the Maximum Elastic Load (P_c), the Bearing Capacity (P_k), the Failure Load (P_f) and the Maximum Applied Load (P_{max})
- Figure 331: Comparison of Load-Displacement Relations for a Static Slow Maintained Load Test Measured and Calculated by the Rheological Model Based on a Statnamic Test No. 3 on Newbury Test Pile No. 2 (TP#2-3)
- Figure 332: Comparison of Load-Displacement Relations for a Static Slow Maintained Load Test Measured and Calculated by the Rheological Model Based on a Statnamic Test No. 4 on Newbury Test Pile No. 2 (TP#2-4)

LIST OF TABLES

- Table 1: Typical Key Attributes of Different Types of Pile Tests (Holeyman, 1992)
- Table 2: Summary of Innovative Load Testing Methods and Analyses
- Table 3: Summary of Drop Weight Systems
- Table 4: Sources for Possible Difficulties of Dynamic Measurements on In-Place Constructed Deep Foundations
- Table 5: Listing of Statnamic Devices and Capacities
- Table 6: Summary of Static Load Test Procedures (after Paikowsky et al., 1999)
- Table 7: Comparison of the Maximum Mobilized Unit Shaft Resistance, Henderson Case
- Table 8: Comparison of the Unit Shaft Resistance Between Field Test Results and Model Results, Wilsonville Case
- Table 9: Comparison of the Maximum Mobilized Unit Shaft Resistance, Wilsonville Case
- Table 10: Comparison of Side Shear at Gage Intervals Between Field Test Results and Model Results, Denver Case
- Table 11: Comparison of the Maximum Mobilized Unit Shaft Resistance, Denver Case
- Table 12: Effect of the Different Factors on Pile Response and Difference Between Two Testing Methods
- Table 13: Detailed Results for Different E_p / E_s
- Table 14: Detailed Results for Different ϕ_I
- Table 15: Detailed Results for Different c_i
- Table 16: Comparison of Pile Capacities from Smartpile and Static Load Test (Ooi and Frederick, 2003)
- Table 17: Testing Results Summary for US Courthouse Pile Foundation (Ooi and Frederick, 2003)
- Table 18: Evaluation of Failure Criteria for Statically Loaded Drilled Shafts
- Table 19: Recommended Relations Between Tested Shaft Capacity and Drop Weight System Requirements for $0.5m < H < 2.5m$
- Table 20: Statistical Summary of Drop-Weight Dynamic Analysis Predictions for Drilled Shafts
- Table 21: Statistical Summary of Dynamic Methods for Capacity Prediction of Driven Piles (Paikowsky and Stenersen, 2000)
- Table 22: A Statistical Summary of the Performance of the FHWA Drilled Shaft Static Analysis Method (Based on Paikowsky, 2004)
- Table 23: Statnamic Database Summary
- Table 24: Pile Specific Bias (λ) Values
- Table 25: Summary of Safety Factors without Using Rate Effect Corrections
- Table 26: Summary of Rate Effect Factors and Associated Values
- Table 27: Summary of Rate Effect Factors and Design Values
- Table 28: Data Details for an Under-Damped System ($\zeta < 1$)
- Table 29: Data Details for an Over-Damped System ($\zeta > 1$)
- Table 30: Secant Modulus of Elasticity for Common Capblock and Pile Cushion Materials
- Table 31: Data Details for the Analyses with the Same M, H, and K, and a Different I
- Table 32: The Influence of a Load Testing System (Data Details for Figure 272)
- Table 33: Details of Newbury Test Pile No. 2, Figure 273 (a,b,c)
- Table 34: Details of Newbury Test Pile No. 3, Figure 274 (a,b,c)

- Table 35: Model Statistics
- Table 36: Material Properties
- Table 37: Component Geometry for Baseline Model
- Table 38: Drop Height and Corresponding Impact Velocity
- Table 39: Ram Diameter and Corresponding Density
- Table 40: Ram Impact Angle
- Table 41: Summary of Attributes for Modeled Ram
- Table 42: Summary of Model Parameters Obtained from the Statnamic and Static Tests of TP#2
- Table 43: Summary Table for the Attributes, Status and Future Work of the Primary Investigated Load Testing Systems
- Table 44: Summary Table for the Attributes, Status and Future Work of the Secondary Investigated Load Testing Systems

ACKNOWLEDGEMENTS

The presented research was sponsored by the American Association of State Highway and Transportation Officials (AASHTO), under project 21-08. The panel of the research project is acknowledged for their comments and suggestions. The support and encouragement of Mr. Timothy Hess of the NCHRP is appreciated. Dr. Dan Brown and Ms. Lijun Shi of the University of Auburn researched the Osterberg cell testing method and contributed to Chapter 6 and section 2.5. Dr. Lora Operstein of the Israel Institute of Technology (Technion) investigated the development of the rheological model presented in Chapter 4. Dr. Gray Mullins of the University of South Florida contributed to Chapter 6 and sections 2.3, 3.4. Mr. Frank Li and Ms. Erin Griffin of the Geotechnical Engineering Research Laboratory at the University of Massachusetts, Lowell, researched the performance of the drop weight systems as part of their graduate studies. Mr. Li is also acknowledged for his contributions to data collected from tests carried out in China as well as the translation of Chinese codes. Mr. Timothy Mustone, Ms. Jennifer Gorczyca and in particular Ms. Ching-Pei Liang of the Mechanical engineering department of the University of Massachusetts, Lowell performed the FEM analysis LS DYNA under the direction of the PI and Prof. James Sherwood. Mr. Les Chernauskas of GTR Inc. assisted in the development of the Israeli drop weight testing system, the dynamic measurements and the analyses. Dr. Frank Rausche and Mr. Brent Robinson of GRL Inc. are acknowledged for their help in collecting case histories for the drop weight database. The help of Ms. Laural Stokes and in particular the contributions of Ms. Mary Canniff in the preparation of the manuscript are appreciated.

SUMMARY OF FINDINGS

A traditional static axial deep foundation load test is performed by a slow application of a force produced against an independent reaction, imitating structural loading. It is the most reliable method to determine the pile's performance as commonly required under typical service conditions. The major limitations of this testing are: (i) high cost associated with set-up, test duration, interpretation and construction delays, and (ii) inability to obtain information about the pile-soil interaction along the pile without additional testing means (e.g., tell tales, strain gauges, etc.). These limitations are acute when high capacity foundations are involved.

Alternative methods to the standard static load testing have been developed in two principal avenues: (i) Static loading by methods that either do not require independent, external reaction for load application (e.g. Osterberg cell; Osterberg, 1989), or short duration, pseudo-static loading procedures (e.g. Static-Cyclic Testing; Paikowsky et al., 1999) and, (ii) Dynamic testing in which the pile is exposed to dynamic efforts (i.e. a force or stress is generated within or at the boundary of the pile through the intervention of mass and acceleration). These testing methods include the generation of low and high strain waves as well as impacts that produce long relative wavelengths most appropriately termed kinetic testing or fast penetration testing.

Both avenues of alternative testing methods (static and dynamic) are researched in the presented study. Simplified models along with a relative wavelength concept are utilized for pile testing classifications. The different innovative testing methods are reviewed, concentrating on three primary (widely used) and four secondary pile test types, namely: Drop Weight System, Statnamic test and Osterberg Load Cell technology being the primary and Simbat, Fundex, Smartpile and SmartCoil being the secondary. The static load test procedures including the relatively fast static-cyclic testing method are summarized and used as a benchmark.

Following a review of the systems and testing procedure, the different testing methods were researched according to the available data, need for investigation and perceived difficulties.

The drop weight system was investigated via two databases. One of dynamic measurements and the associated predicted capacity (DW2000), and the other including drilled shafts for which static load tests had been carried out in addition to the dynamic measurements of the drop weight testing (DW/LT2000). Database DW2000 was used to examine the typical performance of a drop weight system (e.g. energy transfer), and to develop generic recommendations for the required ram weight and stroke height for a given capacity (ultimate or needed). Database DW/LT2000 was used for evaluating the developed recommendations and refining them based on the tested foundation; differentiating between the major sources of resistance (end bearing vs. frictional), and associating the recommendations to the permanent displacement of the deep foundation. The predicted capacities in database DW/LT2000 were compared to the capacities measured in the static load tests using various interpretation methods and differentiating between static load tests to failure and non-failed extrapolated static loading. The results were compared to the performance of the same dynamic prediction methods when utilized for driven piles for which large databases are available, as well as the performance of static capacity prediction methods. Specific difficulties associated with the ram-pile impact were investigated using the impact specific FE code LS-DYNA. Realistic three-dimensional simulation of a ram impact with a pile were performed for the first time allowing identification of the major source of dynamic measurement difficulties when conducting drop weight testing (i.e. uneven impact), and examining various remedies (e.g. soft cushion) and test recommendations (e.g. instrumentation at-

tachment location away from impact). The above analyses and available reviewed codes had led to the following major conclusions:

The ram weight should be larger than 1% of the expected mobilized capacity in the case of frictional shafts or shafts for which more than 2mm permanent set (under the analyzed blow) can be achieved. For end bearing shafts, the ram weight should be larger than 1.5% of the expected mobilized capacity. A distance of two diameters or more should be maintained between the impact and the strain measurements, which should be carried out at least at four locations around the perimeter. The accuracy of the tests is as reliable as those carried out for driven piles under restrike, subjected to the limitations of the available case histories of database DW/LT2000.

The Statnamic testing method was investigated via a database of case histories comparing predicted capacity to that measured by static load-tests. Sub-categorization and past experience suggested large capacity overpredictions when using the method in deep foundations constructed in cohesive soils (i.e. silts and clays). Attempt was made to introduce a rate effect factor based on soil type and testing performance (e.g. $\eta = 0.69$ in silt and $\eta = 0.65$ in clays). The use of these “correction factors” suggest improved performance of the method in all testing conditions. These factors are based on currently available small database (e.g. 13 cases in silt and 4 in clay). The approach presented is practical for the immediate testing needs and allows the great benefits associated with the Statnamic testing method (mobility of very high impacts). It is not based however on a fundamental solution that addresses the mechanics behind the problem. This was addressed via a rheological model that was developed in the research that seems to have the potential of addressing kinetic testing for which one-dimensional wave mechanics is not applicable.

The investigation of the Osterberg cell (O-cell) testing method concentrated on a Finite Element Method (FEM) study addressing the major issues encountered during O-cell tests in soil or rock and researching the controlling factors. The study targeted the issue of underlying differences between deep foundation interfacial shear resistance when being loaded from top down (conventional use and static testing) versus from down up (O-cell testing). A sample analytical model to examine the same issues was developed as well. A limited number of detailed case histories was used to examine the analyses. The available data were found to be extremely difficult to use due to their scarcity, the influence of the tests themselves on the measured results (e.g. shear of concrete-rock interface in static test and then comparing the results to O-cell test on the already sheared interface), and spatial variability when running two tests on two adjacent foundations. The best comparative tests in soft soil appear to indicate relatively good correlation between side shear resistance in O-cell and top down loading. Overall, the presented research suggests that the differences in mobilized base resistance from an O-cell loading and top down loading are relatively minor for shafts in soil or rock. The differences in mobilized side shearing resistance from an O-cell loading and top down loading are relatively minor in soil with most instances having measured values of unit side shear from an O-cell to be slightly conservative relative to top-down loading. For shafts in rock, the unit side shear values mobilized during O-cell tests tend to be conservative relative to unit side shear values which may be mobilized from top down loading. The differences increase as the modulus of the rock mass approaches 10% or higher than the modulus of the shaft’s concrete.

The four secondary testing methods were reviewed to the extent of available data and/or possible examination via models.

The Simbat method is essentially a drop-weight testing with improved displacement measurements, and a different interpretation procedure than the standard signal matching analysis. Comparisons on the basis of ultimate static capacity seem to show difficulties for piles in clay and overall prediction accuracy lower compared to the standard dynamic method procedures. Comparisons be-

tween predicted to measured values on the basis of settlement alone (especially within the working loads) are available for a large number of cases but are of limited significance in the context of capacity evaluation, being appropriate for proof testing.

The Fundex load testing system extends the time period of an impact via springs. The resulting long stress waves cannot be analyzed via wave propagation analyses but require addressing the resulting dynamic effects. The simple model used by the method for test result interpretation is not effective in doing so. The limited information available for comparing testing results to static load tests along with the theoretically questionable basis makes the method less attractive for ultimate capacity prediction purpose at the present.

The Smartpile method employs effective technology to directly measure forces in the pile during impact testing mostly of driven piles. The interpretation methods of the test results (under the limited available data and when comparing the predictions to static load-test results) point to the inability of the method to address the complex soil-pile interaction during driving.

The Smartcoil method appears to be a novel, interesting concept, but no information is available of its actual implementation, let alone effectiveness.

Several models were developed and utilized to assist the study. A simple model is used to investigate the behavior of piles under impact and categorize the testing methods, and is demonstrated through a detailed case history. The second model represents a change in the approach of testing interpretation. A rheological model is developed for analyzing the deep foundation response under different testing methods. The model, while applicative to all testing methods, seems to be particularly attractive for addressing the deficiencies of kinetic testing (e.g. Statnamic tests).

CHAPTER 1

INTRODUCTION, RESEARCH APPROACH AND PRINCIPLES

1.1 INTRODUCTION

1.1.1 Background

Traditional static axial load test is performed by a slow application of a force produced against independent reaction, imitating structural loading. It is the most reliable method to determine the pile's performance as commonly required under typical service conditions. The major limitations of this testing are: (i) high cost associated with set-up, test duration, interpretation and construction delays, and (ii) inability to obtain information about the pile-soil interaction along the pile without additional testing means (e.g. tell tales, strain gauges, etc.). These limitations are acute when high capacity foundations are involved.

Alternative methods to the standard static load testing have been developed in two avenues:

- (i) Static loading by methods that either do not require independent, external reaction for load application (e.g. Osterberg cells – Osterberg, 1989), or short duration, pseudo-static loading procedures (e.g. Static-Cyclic Testing; Paikowsky et al., 1999).
- (ii) Dynamic testing in which the pile is exposed to dynamic effects i.e., a force or stress is generated within or at the boundary of the pile through the intervention of mass and acceleration.

These testing methods include the generation of low and high strain waves as well as impacts that produce long relative wavelengths most appropriately termed kinetic testing. (Holeyman, 1992) or fast penetration testing.

1.1.2 Research Objectives

1. Evaluate the innovative load testing methods for deep foundations and recommend interim procedures for use and interpretation.
2. Present a plan for additional research, testing, and analysis needed to provide guidelines for use of innovative load testing methods.

1.2 RESEARCH APPROACH

Both avenues of the alternative methods (i.e. static and dynamic) are included in the present research project.

To attain the above objectives, one must first and foremost develop a clear understanding of the principles behind the testing methods. Such understanding allows: (i) testing methods categorization, (ii) examination of possible methods of analysis, and (iii) clear understanding of the scope of each method's performance under given conditions.

The research goals were therefore obtained in the outlined stages:

1. Review of the underlying principles of pile testing methods – in order to gain insight and classify the methods based on principles of operation.

2. Identification of primary and secondary available testing methods – in order to prioritize the research efforts.
Stage 1 and 2 are presented in Chapter 1.
3. Detailed review and relevant analyses of the three primary testing methods:
 - a. Drop Weight
 - b. Statnamic
 - c. Osterberg Cell
4. Review of available analyses and database for the four secondary testing methods:
 - a. Simbat
 - b. Fundex
 - c. Smartpile
 - d. Smartcoil.
 Stages 3 and 4 are presented in Chapter 2. For the Osterberg cell method limited database was used and hence the entire investigation is presented in Chapter 2.
5. Build up and review analysis of databases for two of the major testing methods:
 - a. Static Analyses (Summary)
 - b. Drop Weight
 - c. Statnamic
 Stage 5 is presented in Chapter 3.
6. Investigation of three fundamental models dealing with:
 - a. Simplified pile-impact body modeling – in order to grasp the controlling parameters for the method employing pile impact.
 - b. Detailed impact analysis – in order to study the effect of the impact detail on the stresses in the pile and hence the relations between the measurements taken on the pile, the assumptions made and the analyses.
 - c. Alternative modeling – exploring the difficulty of existing models through the investigation of alternative model of different principles and its implementation for different testing methods.
 Stage 6 is presented in Chapter 4.
7. Review of existing codes and/or proposals falling under the categories of the investigated methods and final recommendations of the methods are presented in Chapter 5.
8. Final conclusions summarizing the findings and proposing future efforts are also presented in Chapter 5.

1.3 PRINCIPLES

1.3.1 Outlook

The following section outlines the basic methodology for understanding the underlying principles of the testing methods. This leads to the testing categorization (section 1.4) and the description and the analyses of the tests themselves (chapters 2 and 3).

1.3.2 Load Application and Force Incident

1.3.2.1 Impact Analysis

A realistic analysis of a mass impacting a fixed end rod was discussed by several authors with the final solution given by Boussinesq (1883) (see Timoshenko and Goodier, 1934). The following section is based on Paikowsky (1982) in which a use of the analysis was made. Figure 1 presents the stress propagation in a fixed end bar struck by a moving mass, M

In a relatively simple analysis based on the conservation of the momentum and the relationship between force and velocity under elastic wave propagation, one can derive the following relations: (for development details see Timoshenko and Goodier, 1934).

$$\sigma_o = v_o \sqrt{E\rho} \quad (1)$$

$$s_o = \sigma_o e^{-\left(\frac{2\alpha t}{T}\right)} \quad (2)$$

$$s_1(t) = s_o + \sigma_o e^{-2\alpha\left[\left(\frac{t}{T}\right)-1\right]} \left[1 + 4\alpha\left(1 - \frac{t}{T}\right)\right] \quad (3)$$

for which:

- σ_o = the front stress of the compressive wave pulse
- v_o = impact velocity of the striking mass, M
- E, ρ = modulus of elasticity and mass density of the pile
- S_o = the compressive wave at time interval $0 < t < T$
- T = stress pulse travel time to tip and back $T = 2L/c$
- L = Pile length
- C = speed of wave propagation in the pile
- α = M_p/M ratio of mass of pile to impacting mass
- s_1 = the compressive wave at time $T < t < 2T$

A graphical representation of the functions S_o and S_1 for various values of α (the ratio between the mass of the rod to the mass of the impacting body) is presented in Figure 2. The relationship of Figure 2 suggests that with the decreasing of the size of the hammer (impacting mass) relative to the pile, a sharper pulse of a shorter duration is achieved. For hammers twice the mass of the pile the produced stress wavelength is significantly longer than the time required for the wave to travel down and up the pile.

The model and relationship of Figures 1 and 2 and equations 1 to 3 can be directly applied to impact driving. Further details of impact representation can be obtained via numerical modeling (e.g. Smith 1960), but it is easier in the framework of generic application of bodies in contact (as in this research) to resort to simplified relations based on frequencies. The following review was assisted mostly by Holeyman (1992), with appropriate referencing to other relevant publications.

When external mass, M, interacts under impact velocity, v_i , with the head of an half infinite long pile, the physical system and its mechanical representation can be described as shown in Figure 3 (Parola, 1970 and Van Kotten, 1977). The system includes the impacting mass, the cushioning element in the impact, and the representation of the pile as a dashpot with a damping factor equal to the pile impedance, suitable for short waves dynamic events. This representation allows for easy devel-

opment of conceptual analytical relationships between the impacting mass size and velocity, the cushioning element, and the pile's impedance in the shape of non-dimensional force pulses in the pile.

In developing the graphs shown in Figure 4, the following relationship has been used:

- M, v_0 = mass and velocity of impacting body
- k = equivalent spring coefficient of cushioning element
- I = pile impedance
- where $I = \rho c A$
- ρ, A = the pile's specific mass (density) and cross-section
- c = one dimensional longitudinal wave speed of the pile's material

where
$$c = \sqrt{\frac{E}{\rho}} \quad (4)$$

E the pile's material Young's modulus

The force pulse in the pile as presented in Figure 4 is normalized in relation to the pile's impedance and impact velocity. The developed pulses are calculated as a function of the natural frequency, ω_n , for different ratios between the cushioning element and the pile's stiffness:

$$\omega_n = \sqrt{\frac{k}{m}}, \quad \gamma = \frac{k}{2I}, \quad \frac{\omega_n}{\gamma} = 2I\sqrt{kM} \quad (5)$$

The relationships in Figure 4 clearly demonstrate the effect of the cushioning element in relation to the pile's stiffness on the time length of the force pulse developed in the pile, and the magnitude of that force as the function of the impact velocity.

The non-dimensional peak amplitude F_{\max}/Iv_0 decreases as $2I/\sqrt{kM}$ increases, whereas the duration of the impact decreases proportionally with $\sqrt{k/M}$. For example, in dynamic pile driving of direct impact of steel over steel, a very sharp, short duration pulse force (on the order of 5 milliseconds) will develop in the pile. The pulse wavelength will increase when introducing cushion in the system, and further increased when using a system like Statnamic all the way to systems of coiled springs under a falling mass, as the tests conducted by "Dynatest" (Gonin et al., 1984) or Fundex (Schellinghout and Revoort, 1996), resulting in a wave length of over 400 milliseconds. For waves of very long duration, the representation of the pile in Figure 3 needs to be complemented with a spring in parallel to the dashpot that acts practically alone under static loading. Such system is presented and analyzed in section 4.2.

1.3.2.2 Relative Wavelength and Pulse Propagation

While Figure 4 provides the relationship between the testing mechanism and the developed wavelength, one next must examine the relationship between the produced wave length and the ability to analyze the pile-soil system. Such a measure can be done through the explicit relationship of distance to time as presented in Figure 2, or the relationship between the wavelength and the pile length, introducing the relative wavelength Λ .

$$\Lambda = \text{Length of the force pulse} / \text{double length of the pile (2L)} \quad (6)$$

The relationship between pile acceleration, force duration, and relative wavelength (which represents the sharpness and duration of the force pulse) for different pile tests is presented in Figure 5. To better understand the concept of the relative wavelength, one needs to follow the propagation of a force pulse through a pile realizing the importance of the pulse sharpness and its length relative to the pile's length.

When a compressive force pulse propagates down the pile, it will be reflected whenever there is a change in the pile impedance (e.g. change in cross-section) or as a result of external forces (i.e. friction), generating two waves, as presented in Figure 6, a compressive wave up and a tension wave down, which combines with the initial pulse. Upon reaching the pile toe (under easy or normal driving conditions, say less than 4 BPI – Blows Per Inch) the resulting downward compressive wave is reflected upward and reversed (compression becomes tension) with a compressive offset corresponding to the mobilized toe resistance. On its way up toward the pile head, the wave interacts again with (and activates) the shaft resistance, and impedance changes, arriving back to the pile top after time $t = 2L/c$ in which L is the pile's length and c speed of wave propagation. This depiction of wave mechanism results in the understanding that:

- (i) A shorter pulse duration enables higher resolution of the propagating waves and the combined reflections,
- (ii) The number and complexity of the waves depends on the changes of the cross-section of the pile, and
- (iii) The reflecting wave is affected by the interaction of the pile with the soil (shaft and end resistances) allowing the interpretation of the soils resistance along the shaft.

1.3.2.3 Pulse Duration, Relative Wavelength and Pile Testing

Following the above, one can examine the different dynamic testing in light of the produced relative wavelength and possible interpretation. Integrity testing that utilizes reflection techniques (for a state-of-the-art review see Paikowsky and Chernauskas 2003, Chernauskas and Paikowsky 1999) uses a small hammer to introduce low strain, short duration pulse that is typically characterized by a relative wave length of 0.1, which provides for maximum depth resolution. Dynamic testing during driving is typically characterized by a relative wavelength of 1, associated with force duration of 5 to 20 milliseconds. These relations allow for depth resolution for typical piles while providing high strain testing. Further enhancement of the depth resolution is possible with additional internal measurement near the pile's tip (e.g. Smart Pile System; Frederick, 1999 or McVay et al., 2004). Dynamic Fast Penetration (or Kinetic Testing) such as Statnamic (Berminghamer and Janes, 1990), as well as Dynatest or Fundex, are characterized by a relative wave length Λ of 10 or higher and, therefore, do not allow for depth resolution. The produced pulse duration is about 50 to 200 milliseconds (about an order of magnitude larger than that of impact dynamic testing), and practically the front of the wave's reflection from the tip arrives back to the top before the main portion of the wave propagates through the pile.

Although these tests resort to inertial actions on masses to generate their extended force pulse, they can be referred to as "Kinetic Tests" or "Dynamic Fast Penetration" as the inertial forces within the pile are small compared to the force being applied. As a result of their high relative wave length, the interpretation of these tests cannot make use of the wave equation form of analysis, hence, different from tests which can be categorized as Dynamic Wave Action tests (e.g. Drop Weight). This fact does not affect the ability to determine the total capacity/resistance of shafts from kinetic tests using

other techniques or diminishes their distinctive advantages such as mobility and the ability to produce high energy impacts to mobilize the resistance of very high capacity shafts.

1.3.2.4 *Intermediate Conclusions*

The above presented approach allows for the development of a framework that can obtain the required objectives and assess in an unbiased way, the claims (often misleading) of the different testing promoters.

1.4 CLASSIFICATION OF PILE TESTING

The approach presented in previous sections lead to the categorization of pile testing based on the nature of the loading and its duration relative to the pile itself. The relative wave length (Λ) explains the relationship between the loading, the transfer of the loading in the pile, the importance of dynamic effects, and the ability to analyze the pile-soil interaction as a result of measurements recorded at the pile's top.

Table 1 outlines the different tests based on this categorization and their relevant method of analysis. A discussion of the possible methods of analysis is presented as part of section 4.5. A summary of the range of possible pile testing and the associated characteristics is presented in Table 2. As an illustration of actual testing results, Figure 7 presents data obtained from a research test pile cluster at a bridge reconstruction site in Newbury, Massachusetts. The research at the site was conducted by the Geotechnical Engineering Research Laboratory at the University of Massachusetts Lowell, guided by the author as part of a long-term research sponsored by the Massachusetts Highway Department (see e.g. Paikowsky and Chen, 1998, and Paikowsky and Hajduk, 1999).

Figure 7 presents magnitudes and durations of load measurements during some of the testing conducted on a 14-inch square, 80 foot long pre-stressed, pre-cast concrete pile. The pile was instrumented and subjected to various testing over a long period of time; relevant information is provided by Paikowsky and Hajduk (2004), Hajduk et al. (2000), and Hajduk et al. (1998). The data in Figure 7 demonstrates the principles previously discussed. The driving system produced an impact of about 5 milliseconds in wave length, the Statnamic test produced a wave length of about 60 milliseconds, a Static-Cyclic load test was carried out at about 15 minutes while a short duration static testing was about 8 hours. A slow maintained load test that was carried out at the site was not included in Figure 7, as it adversely affected the time scale. The data in Figure 7 clearly demonstrates by measurement the different time ranges phenomena associated with the different tests, and its ramifications will be further discussed in the following sections.

1.5 TESTING METHODS

The innovative testing methods examined in this research include dynamic tests; both high-strain wave action and kinetic-fast penetration as well as static tests. Table 2 presents a summary of the methods under the above general categorization. A background regarding the fundamental differences between the methods and their categorization was presented in section 1.4. A detailed review of the methods is presented based primarily on the extent use of the methods. The primary three methods used worldwide, namely drop weight, Statnamic and Osterberg Load Cell, received most attention while four secondary methods were reviewed to a different level of detail as available.

CHAPTER 2

FINDINGS – TESTING METHODS – CRITICAL REVIEW

2.1 OVERVIEW

Chapter 2 describes the three primary and four secondary testing methods. The tests are critically reviewed, methods of analysis are presented and specific analyses are carried out when relevant. Database analysis and evaluation relevant to the reviewed methods are presented in the following chapters.

2.2 THE DROP WEIGHT SYSTEM

2.2.1 General

High strain dynamic testing can be applied to any pile type not necessarily during driving. The application of dynamic testing specifically to in-place constructed deep foundations is done by dropping a weight on the pile top, producing a dynamic stress-wave through an impact. The test results are then being analyzed using the conventional dynamic methods of analysis though often those are restricted by the special conditions of the in-place constructed deep foundations and the drop weight testing. The first use of high strain dynamic testing of in-place constructed foundations was made in 1975 on a project in Charleston, West Virginia (Goble et al., 1993). The following sections provide basic information regarding the routine dynamic measurements and their analysis followed by a review of the drop weight systems.

2.2.2 Dynamic Measurements During Pile Driving and their Analyses

The standard "Pile Dynamics" methods used during pile driving operation are outside the scope of the present research. The techniques and the instrumentation are utilized however by the "Drop Weight" method presented in the following section. A review summarizing the dynamic methods and their analyses is presented therefore to accommodate the understanding of the drop weight technique. The following section is based mostly on Paikowsky (1995), Paikowsky et al. (1994) and Paikowsky et al. (1996).

Dynamic analyses of piles are methods that predict pile capacity based on the pile behavior during driving. Evaluation of static capacity from pile driving is based upon the concept that the driving operation induces failure in the pile-soil system; in other words, a very fast load test is carried out under each blow. There are basically two methods of estimating the ultimate capacity of piles on the basis of dynamic driving resistance: pile driving formulae (i.e., dynamic equations) and Wave Equation (W.E.) analysis.

Dynamic equations can be categorized into three groups: theoretical equations, empirical equations and those that consist of a combination of the two. The theoretical equations are formulated around analyses that evaluate the total resistance of the pile, based on the work done by the pile during penetration. While being conceived as a low quality method, the fundamental principle of the work-energy conservation is valid and when used with dynamic measurements (i.e. the Energy Approach, Paikowsky et al., 1994, Paikowsky and Stenersen, 2000) it results in the most accurate method to predict the long-term pile's capacity out of dynamic measurements during driving.

The theoretical formulations assume elasto-plastic force-displacement relations for which the total work is:

$$W = R_u \left(S + \frac{Q}{2} \right) \quad (7)$$

where R_u is the yield resistance (capacity), Q is the quake denoting the combined elastic deformation of the pile and the soil, and S is the set, denoting the plastic deformation (permanent displacement) under each blow.

When the work of the resisting forces, W , is equated to the energy delivered to the pile, i.e., $W = E_d$, we can extract the basic familiar elements of the dynamic equations:

$$R_u = \frac{Ed}{\left(S + \frac{Q}{2} \right)} \quad (8)$$

The Wave Equation (W.E.) relates to the phenomenon of stress propagation in a pile during driving that can be described by the following equation of motion:

$$E_p \frac{\partial^2 u}{\partial x^2} - \frac{S_p}{A_p} \bullet f_s = \rho_p \frac{\partial^2 u}{\partial t^2} \quad (9)$$

where:

- $u(x,t)$ = longitudinal displacement of infinitesimal pile segment
- A_p, S_p = pile area and circumference, respectively
- E_p, ρ_p = modulus of elasticity and unit density of the pile material.

The friction stresses (f_s) are activated by the pile movement, and under free wave motion ($f_s = 0$), the above equation becomes the familiar 1-D W.E. (One-Dimensional Wave Equation) of an elastic wave propagating in a slender homogenous body with a uniform cross-section. The friction stresses are traditionally represented by a soil model suggested by Smith (1960). The static soil resistance-displacement relationship is assumed to be elasto-plastic and is represented by a spring in series with a slider. The dynamic resistance (R_d) is assumed to be viscous (soil type related) and, therefore, velocity dependent, represented by a dashpot parallel to the spring. The resisting soil force (R_t) is a combination of the two as shown in Figure 8. The different parameters included at the bottom of Figure 8 (e.g., J, Q, UR, QR) are the parameters used to specify the assumed behavior of the soil-pile interaction for each pile element.

The wave equation formulation is used in two ways:

- (a) Pre-driving analysis, where the entire system is modeled, including the pile, hammer and driving system, as was first suggested in a comprehensive practical approach by Smith (1960) and further improved to include different hammers, splices, etc. (e.g., GRL, 1995).
- (b) Post driving analysis, utilizing dynamic measurements obtained near the pile head during driving.

Post-driving signal matching analyses utilize the measured force signal (calculated from strain readings) and the measured velocity signal (integrated with time from acceleration readings) obtained near

the pile top during driving. These analyses model the pile-soil system, in a continuous or discrete form, as shown at the upper section of Figure 8, with the element denoted as (I-1) representing the point of measurement. The velocity signal is used as a boundary condition at that point while varying the parameters describing the soil resistance in order to solve the above wave equation and match the calculated and measured force signals.

The soil parameters, describing a simple elastoviscoplastic material as previously mentioned, include the side and tip quake, side and tip damping, and the pile shaft and tip ultimate resistances. The tip model is identical to that of the shaft without the upward resistance ($U_R = 0$, refer to Figure 8). Additional parameters may be used to describe soil resistance and rebound ratio for unloading different from that of loading. Further improvements are possible through a better modeling of the physical phenomena, e.g., considering the inertia of the displaced soil mass as indicated by Paikowsky et al. (1994), Paikowsky and Chernauskas (1996), and Hajduk et al. (2000). Other improvements of the soil model itself are restricted due to: (a) the limited available information from dynamic acceleration and strain response at one point of measurement and (b) the poor ability to simulate soil following the complex loading sequences it undergoes during driving, set-up and static loading.

The signal matching process is described in the form of a flow chart in Figure 9. The subscripts *msd.* and *cal.* denotes measured and calculated values, respectively. Iterations are performed by changing the soil model variables for each pile element in contact with the soil until the best match between the force signals (calculated and measured) is obtained. The results of these analyses are assumed to represent the actual distribution of the ultimate static capacity along the pile. This procedure was first suggested by Goble, Likins and Rausche (1970), utilizing the computer program CAPWAP. Similar analyses were developed by others (see Paikowsky, 1982 and Paikowsky and Whitman, 1990) utilizing the program code TEPWAP and (see Middendorp and van Weel, 1986) using TNOWAVE.

2.2.3 Background and Use

2.2.3.1 General

Drop weight systems are increasingly being used to dynamically test cast-in-place piles; i.e., drilled shafts, caissons and pressure injected footings, or even to test old driven piles for re-use. These tests are especially important for high capacity piles (say design load over 2.5MN) for which static load test is either very expensive or physically difficult to conduct (e.g., over water). Conventional pile driving hammers may be inadequate to test these deep foundation types since (i) they typically cannot deliver enough energy to mobilize the ultimate bearing capacity, (ii) the size and location of the foundation member can present problems in adequately delivering the energy from the ram to the pile, and (iii) they are expensive to use. Simple drop weight systems have therefore been developed that overcome the limitations of conventional hammers and allow for a relatively inexpensive dynamic testing of these deep foundations.

A typical drop weight system consists of four components: a frame and/or a guide for the drop weight (ram), the ram, a trip mechanism to release the ram, and a striker plate with or without a cushion. Strain gages and accelerometers are placed along the pile top to obtain stresswave measurements utilizing available PDA's (Pile Driving Analyzers). Details of available systems are described in Section 2.2.4. The advantages and disadvantages of the system are listed below.

2.2.3.2 Advantages

The advantages when compared to static load testing methods are similar to those of standard dynamic pile testing:

- a. Rapid testing time.
- b. The ability to deliver high energy to test high capacity and physically large deep foundations including old foundations at locations with limited accessibility.
- c. The ability to use transducers and data acquisition systems for monitoring driven piles (such as the Pile Driving Analyzer of Pile Dynamics and TNO Foundation Pile Diagnostic System).
- d. The test provides a means to conduct integrity testing concurrent with capacity determination, which is particularly important for in-place constructed deep foundations.
- e. Low test cost relative to standard static load test.
- f. Current techniques of analysis include field methods (such as the Case Method (Goble et al., 1975) and the Energy Approach (Paikowsky, 1982, Paikowsky et al., 1994, Paikowsky 2004)) and signal matching e.g. CAPWAP (Rausche, 1970).

2.2.3.3 *Disadvantages*

- a. The selected mass and drop height must be of sufficient energy to mobilize the resistance of the deep foundation in order to obtain adequate capacity measurements.
- b. The installation of in-place constructed deep foundations (drilled shafts, caissons, etc.) can cause irregularities in pile geometry (shape) and homogeneity that can dramatically affect current measurement techniques and analysis methods.
- c. For increased quality of the obtained force measurements, the gauges need to be away from the impact and as high as possible above the ground. This results in the need to create either “extensions” of cast in-place shafts or excavations around the shaft, and the use of multiple gauge systems.
- d. Although several studies have already been conducted comparing dynamic and static measurements of cast in-place deep foundations (Rausche and Seidel, 1984, Jianren and Sihong, 1992, Townsend et al., 1991), a comprehensive comparison study which incorporates significant number of case histories other relevant information (such as installation records) is not yet available.

2.2.4 **Review of Available Systems**

2.2.4.1 *General*

The testing entails the impact of a mass with the pile top. As such, large variation of possibilities exist ranging from a non-guided drop of a mass by a crane to a well designed guided system of varying ram weight and stroke, including a driving system (capblock, striking plate, cushion) at the pile’s top. Naturally these systems are locally developed and at times are site specific. Table 3 presents a summary of various available systems and the following section presents each system individually.

2.2.4.2 *System DW-A*

System DW-A was developed in Zhanjing, Guangdong province, P.R. of China and is described by Li (1993). This drop weight system includes a four-sided frame and a guide system made of angle iron, as shown in Figure 10. Three independent steel hammers weighing 30kN, 50kN, and 80kN can be used. The trip mechanism to release the hammer consists of two pulleys and a hook. This drop weight system can provide a maximum potential energy of 320kN•m with the 80kN ram falling 4m. A crane is required for the field testing.

2.2.4.3 *System DW-B*

System DW-B was developed in Shanghai, P.R. of China and is described by Li (2000). This drop weight system has a portable triangular frame (tripod) and a 60kN steel ram, as presented in Figure 11. The trip mechanism to release the hammer is a “smart” hook that can be opened by a manual pull resulting in a free falling ram. The rope and pulley system is used manually in the field and substitutes the need for a crane. This drop weight system can provide a maximum energy of 150kN•m with the 60kN hammer falling 2.5m.

2.2.4.4 *System DW-C*

System DW-C was developed in Shanghai, P.R.China and is described by Weibing (2000). This is the most simple version of a drop weight system which includes the aforementioned smart manual hook, a steel ram and a crane without the use of a frame or a guide system, as presented in Figure 12. To ensure an impact, the ram is held in place above the piles by pushing rods against the ram from various directions (Figure 12c). The maximum potential energy depends on the crane’s capacity and the weight of the ram. In fact, any kind of ram can be used with this system. The ram described in Figure 12 consists of steel plates stacked on each other and held together by four bolts. Such arrangements allow variation of the weight but usually results with a ram having a larger cross-section than that of the shaft.

2.2.4.5 *System DW-D*

System DW-D was developed by Geodynamica and GTR, (GTR, 1997) to test in-place constructed deep foundations in Israel and is presented in Figure 13. This device is similar in principle to other drop weight systems presently in use with the distinction of modularity in ram weight as well as uniqueness in trip mechanism. The Israeli Drop Weight Impact Device uses modular weights that can be arranged into ram weight combinations of 20, 40, 50, 70, or 90kN and has an adjustable drop height of up to 4 meters thereby allowing for potential energy of up to 360kN•m. Typically, a pile cushion is used below the striking plate to even pile impact stresses across the pile’s top. Additional long hammer was developed for the production of short duration waves and better integrity capabilities

2.2.4.6 *System DW-E*

System DW-E was developed in Israel by Isotop and is described by Sokolovski et al., (1998). The system is similar in concept to the SPT “donut” shape hammer, as shown in Figure 14. The device rests on the shaft’s top and the ram slides over the guiding central column.

2.2.4.7 *System DW-F*

System DW-F is called Newton’s Apple and was developed by GRL Inc. of Cleveland, Ohio, and presented by Robinson and Rausche (2000), and Hussein et al. (2004); see Figure 15. Newton’s apple includes a new concept in the data acquisition for drop weight systems. The ram is modular and its weight can be varied between 50 and 200kN. With these ram weights, and utilizing free release drop heights of up to 2.7m, a maximum energy of 540kN•m can be applied.

The guide frame has a 1.8 x 1.8m footprint and a height of 6m. After the ram is lifted by the crane to its top position, a pin is inserted through the ram lifting bar into the guide frame to transfer the ram weight to the frame. Hydraulic cutter then cuts the cables holding the ram and cause it to fall.

The loading systems termed “Newton’s Apple” is also instrumented for measuring the pile’s top force utilizing an accelometer attached to the ram. If accurate, this principle reduces substantially the need for pile excavations or extension for strain sensor attachment. It also has the potential to be more accurate than the calculation of force from strain measurement alone when the concrete quality is questionable. Comparison between measured ram force and the force computed from pile strain measurement yields a very close agreement according to Robinson and Rausche (2000), and Hussein et al. (2004).

2.2.4.8 *System DW-G*

System DW-G was used by Texas A&M University (Briaud et al., 2000) and is presented in Figure 16. A drop hammer is used with swinging leads arrangement and operated with a crane. The hammer has a ram weighing about 90kN and the reported falling height was varied from 0.3 to 5m. An electronic theodolite was placed (by ESSI-Testconsult, see section 2.6.3 and Figure 97) about 15m away from the pile together with a target on the pile to continuously record the dynamic displacement of the pile associated with each blow. The cushion on the pile top (detailed in Figure 16) consisted of 200mm (8in) of plywood overlay with a 75mm (3in) thick striker plate that protects well the pile, but substantially decreases the energy delivered to the pile’s head to be only about 20% of the free fall potential energy of the ram.

2.2.4.9 *System DW-H*

System DW-H is essentially a drop hammer provided by Pileco of Houston. The system having swinging leads is described by Townsend et al. (1991) and is presented in Figure 17. The system is similar to System DW-G and was operated with a small crane.

The ram of 75kN was lifted with a crane to the specified drop heights. After transferring the ram's weight to the leads system, a hydraulic cutter was used to cut a cable holding the ram in place, dropping it in a free fall. The shaft cushion consisted of 200mm (8in) of plywood overlay with a 75mm (3in) thick steel striker plate. The permanent shaft displacement was measured using a stationary laser beam.

2.2.4.10 System DW-I

System DW-I was used for high strain dynamic testing by Tongji University in Shanghai and is described by Longgen et al. (1999). Depicted in Figure 18, the system is self sufficient with a guiding system and electric winch for lifting the ram as well as a manual triggering for a free fall at the desired height.

2.2.4.11 Discussion and Summary

(a) Discussion

The different drop weight systems described in sections 2.2.4.2 to 2.2.4.10 present a wide range of possibilities for applying an impact to a pile's top. The systems can be categorized based on their complexity, flexibility (modularity), energy level, and so on. A discussion based on such categorization alone does not relate to issues of greater significance, namely the influence of the drop weight system type on the impact shape, and that in return on the dynamic analysis. Section 2.2.2 described the dynamic measurements and their analyses. The following section (2.2.5) discusses the difficulties encountered by dynamic measurements of in-place constructed deep foundations. In light of the issues described in section 2.2.5, it is important to note that systems, which do not provide evenly distributed impact due to inability or difficulties in ram alignments (e.g. systems DW-B and DW-E), result in uneven stress distribution leading to incorrect force calculation based on local strain measurements at the outer boundary. The use of a cushion greatly increases the even distribution of stresses across the shaft, but elongates the time and reduces the peak of the produced stress wave. As a result, the signal matching analysis is more difficult and the energy transferred to the pile head is smaller, therefore requires the application of a higher energy to examine a shaft of a given capacity. The Newton apple system tries to overcome this problem by measuring the acceleration of the ram, and by knowing the ram's mass the impact force can be calculated. This direct method overcomes the problem of uneven stress distribution and/or poor quality of concrete, especially in the pile's circumference, where the strain gauges are attached. The limitation of the system is, however, by the fact that it measures the impact force, but not the force that transfers to the pile itself. For that reason, energy loss in the impact and the use of a soft cushion desirable for even stress distribution would result in differences between the force measured through the ram and that actually experienced by the pile.

(b) Summary

A wide range of drop weight systems is available to provide an impact. In addition to the geometrical features of the system, namely guiding system, ram mass, and dropping height (i.e. energy), the system's effectiveness is greatly affected by the quality of the impact. A detailed impact Finite Element Method (FEM) analysis was carried out, able to model the significance of each parameter and its influence on the recorded dynamic values, this analysis is presented in Chapter 4.

2.2.5 Dynamic Measurements of Impacted In-Place Constructed Deep Foundations

2.2.5.1 In-Place Constructed Deep Foundations

In place constructed deep foundations (IPCDF), or drilled deep foundations (known as drilled shafts, bored piles, cast in place piles, caissons, piers, auger cast piles, continuous flight auger piles, etc.) are commonly used worldwide where they are more suitable or cost effective than driven piles

and/or alternatively for carrying large loads, replacing pile groups. A variety of construction methods and installation equipment are available (e.g. O'Neill and Reese, 1999). Due to the nature of their construction, however, limited quality control is possible and the structural integrity and the geotechnical capacity of these foundations remain highly variable and uncertain. The quality of the foundation depends upon the construction method (Camp et al., 2002, Paikowsky, 2004, Paikowsky et al., 2004), the subsurface conditions, the quality of the materials (grout, cement, concrete, slurry, etc.), and the quality of the contractor (i.e. workmanship). As such, the use of drilled deep foundations particularly confronts the limitations of the traditional static load tests.

2.2.5.2 *Dynamic Measurements*

Typical dynamic measurements include the attachment of a pair of accelerometers and a pair of strain gauges to the pile (ASTM D4945-00). The acceleration (a_{cc}) is integrated to provide the velocity signal at the point of measurements with time ($v(t) = \int_0^t a_{cc}(t) dt$) and the strain (ϵ_t) is measured between two fixed points (typically 76.2mm (3 inches) apart) allowing to calculate the force signal with time ($F(t) = \epsilon(t) \bullet A_p \bullet E_p$) at the point of measurement. This calculation assumes uniformity of strain (ϵ_t), and hence stresses across the pile's section as well as knowledge of the cross sectional area (A_p), and the pile's material modulus of elasticity, E_p .

2.2.5.3 *Difficulties Associated with the Impact of a Drilled Shaft*

Four fundamental sources of difficulties are associated with the dynamic measurements of drilled shafts:

- a. Sources related to construction
- b. Sources related to the ram's impact
- c. Sources related to the point of measurement
- d. Sources related to the shaft's resistance

Table 4 presents a summary of sources, their effect, and possible remedy. These sources of difficulties affect the aforementioned assumptions made for conducting and analyzing dynamic force measurements. For example, construction procedures affecting the top of the drilled shaft, cause irregular geometrical shape, non-homogeneous cross-section, and often non-uniform concrete. All of these factors affect the calculated forces. The stresses can be assumed as uniform when measured some distance away from the impact location. Non-uniform impact, in particular impact at one point of contact (rotated ram), will cause uneven stresses across the shaft at a large distance from the point of impact. The force measurements remain, therefore, problematic under such conditions. Additional difficulty, more common with the impact of drilled shafts than driven piles, is the high frictional resistance that develops close to the ground surface. This condition creates early high signal reflections upwards that invalidate the proportionality of the force and velocity measurements, hence, do not allow independent assessment of the measurements, and often create difficulties in signal match analyses. The uneven impact stress distribution and early reflections both call for (i) the use of multiple gauges around the shafts' perimeter, and (ii) the establishment of a measurement point at a cross-section further from the pile top and ground surface as much as possible. This last requirement typically contradicts the normal mode of shafts design and construction, and requires either extension be-

yond the ground elevation (see for example Figure 13) or excavation next to the shaft (see for example Figures 12 and 16).

2.2.5.4 Case History

Five tests were conducted on drilled shafts for researching and optimizing the effect of rock-socket depth on the drilled shaft performance in a given site (GTR, 1997).

Shaft A was 60cm in diameter and 13m long, including a 2 m rock socket. A 2m extension was built above ground surface, and 4 pairs of gauges were used around the pile (see Figure 13). Drop weight system DW-D, described in section 2.2.4.5, was used to apply impact, and a 75mm thick plywood cushion was used. Figures 19 and 20 present the individual four force and velocity signals that were recorded for blows no. 3 and 4 respectively. The numbers next to the individual gauge readings refer to the full scale of the graph (in kN for F and m/sec for V). Blow no. 3 was the result of a 90.7kN ram with a 1.5m stroke, and blow no. 4 was obtained using the same ram with a stroke of 1.75m. The information presented in Figures 19 and 20 suggests the following:

- a. In both measurements (blow 3 and 4) the accelerometers readings were practically identical for all four instruments, unaffected by the ram or the drilled shaft.
- b. Uneven forces were calculated at the different points of measurements around the shaft in both cases in spite of the advanced guided impact device, the cushion, and the distance between the impact to the point of measurements (about 3 pile diameters).
- c. A “symmetric” uneven impact was recorded for blow 3, such that gauges diagonally to each other recorded similar forces, namely F1 and F3 recorded similar force, as did F2 and F4.
- d. A completely uneven distributed impact was recorded for blow 4 as depicted in Figure 20. Each of the strain gauges measured a different force at the respective point of measurement. Some of the measurements show signs of concrete cracking at the area in which the gauge was mounted (e.g. F1), resulting in a permanent force reading (plastic deformation) following the impact.
- e. The use of multiple points of measurement allowed, however, to obtain reliable and consistent data that were used for a signal match analysis as presented in Figures 21 and 22 for impact numbers 3 and 4 respectively. An average of all gauges was used as the representative force and velocity signals for impact number 3. F1 gauge’s record of blow no. 4 was excluded for the average measured force signal, which was achieved by utilizing the other three measurements (F2, F3 and F4).
- f. Figures 23 and 24 present the summary of the signal match analysis (CAPWAP) for impacts no. 3 and 4 respectively. A good match was obtained between the measured and calculated forces for both analyzed impacts.
- g. Figures 21 and 22 clearly show the smaller peak velocity measurements (presented in force units when multiplying the velocity by the pile impedance) compared to the force measurements. These behaviors are a result of a high friction between the soil and the pile at the upper portion of the pile close to the ground surface. Verification for this observation is obtained from the signal match analyses presented in Figures 23 and 24, showing a force distribution along the pile with high frictional resistance forces close to the ground surface.

2.2.6 Existing Codes and Guidelines

2.2.6.1 Overview

While being popular worldwide, very limited references are available to the drop weight method in codes and regulations. One such code is the Chinese specifications for high strain dynamic testing. Chapter 5 presents a translation of the Chinese code. The present section refers to the relevant parts related to the drop weight system specifications of size and shape as previously discussed.

2.2.6.2 The Chinese Code

The drop weight system is the main method authorized for capacity evaluation in the Chinese national and some of the provincial codes for high strain dynamic testing of piles. There are two reasons that can explain this issue; (i) cast-in-place piles are commonly used in China as they are more cost effective than driven piles, and (ii) pile capacities based on dynamic test results are permitted to be used only after a significant set-up period following the end of driving. For example, the duration required for piles driven in sands (!) is 7 to 14 days for the Chinese and Shanghai codes, respectively. As a result, drop weight becomes an economical alternative to a costly crane and pile driving hammer mobilization.

The significance of the Chinese code in relation to the drop weight systems is summarized as following:

- a. The code fully recognizes the drop weight system with the major parts being applicable for both tests (dynamic tests on driven piles and cast-in-place piles).
- b. The tests are recognized also for pile/shaft integrity purpose.
- c. Some provisions refer specifically to cast-in-place shafts e.g. 5.1.2.3, 5.1.3.3, 5.1.4.2, 6.1.6, 7.1.2.2 and 7.3.1.3 in JGJ106-97.
- d. The set-up duration between the end of driving and dynamic/drop-weight testing is prescribed clearly based on soil type
- e. The drop weight system used for high strain pile dynamic testing requires providing sufficient energy with ensured impact eccentricity. No detailed drop weight system specifications, (such as hammer type, trip mechanism and frame), are provided except the requirement that the hammer weight and shape need to stand by general requirements as given in the following two examples:

Chinese Code (Specification for High Strain Dynamic Testing of Piles, JGJ106-97, section 4.0.3): The hammer should be a homogeneous mass with a symmetric shape, preferably made of steel. The bottom of the hammer should be smooth. For a free falling ram, the weight of the ram need to be greater than 1% of the estimated bearing capacity of the pile.

Shanghai Foundation design code (DGJ-11-1999, section 14.5.3): The hammer is required to assure 2mm set (net settlement) under a single blow and the ram weight should be between 0.8% to ~1.5% of the estimated bearing capacity of the pile.

2.3 STATNAMIC TESTING

2.3.1 General

One method of high-strain, rapid load testing that is used to predict the capacity of both shallow and deep foundations is the Statnamic load test. Developed by Berminghammer Foundation Equipment, Canada, and The Netherlands Organization (TNO), Netherlands, the Statnamic load test is based on Newton's second and third laws of motion. Using these two principles, the Statnamic test is able to apply a relatively large load to the foundation without the need for massive equipment. This is accomplished by launching a reaction mass upward off of the foundation at up to 20 times the acceleration due to gravity (20 g's). Since Newton's second law states that force is proportional to acceleration, a large applied load is generated from a small mass. This mass is initially in direct contact with the foundation, so the force associated with the launching of this mass acts equally and oppositely down onto the foundation, according to Newton's third law.

Statnamic tests have been conducted on many types of foundations including:

- a. drilled shafts,
- b. auger cast-in-situ piles,
- c. driven H-piles,
- d. pipe piles,
- e. prestressed square concrete piles (voided and unvoided),
- f. spun cast cylinder piles (post tensioned),
- g. prestressed cylinder piles
- h. FRP composite piles
- i. cast-in-place concrete footings
- j. precast concrete footings
- k. temporary built-up steel plate footings

The preponderance of these tests were conducted on foundations constructed in primarily granular soils. The rationale for its use is largely due to the close agreement reported to date for these soil types and the economy of the test method.

Universities, federal and state agencies, have conducted Statnamic research worldwide.

2.3.2 Active Research and Usage`

Presently research is being conducted in as much as seven countries worldwide. The various researchers and general areas of interest are listed below:

- a. United States
 - Auburn University* Dan Brown, axial and lateral analysis of drilled shafts
 - Brigham Young University* Kyle Rollins, lateral analysis and pile groups
 - Johns Hopkins University* Rajah Anandanarajah, cyclic lateral analysis, Statnamic earthquake simulator
 - Texas A&M* Jean Louis Briaud, comparison testing
 - University of Massachusetts (Lowell)* Samuel Paikowsky, rate of loading in clay and rheological modeling
 - University of South Florida* Gray Mullins, segmental unloading point method, model pile testing in frustum confining vessel
- b. Canada

- University of Western Ontario* M. Hesham El Naggar, axial analysis using signal matching, lateral analysis
McMaster University Robert Horvath and Dieter Stolle, rate of loading, model pile in frustum confining vessel
- c. Indonesia
Petra Christian University S. Prawono, axial and lateral testing
- d. Japan
Tokyo Institute of Technology O. Kusakabe, standardization and building codes
Kyusyu Kyoritsu University Y. Maeda, axial analysis methods, including wave analysis
Kanazawa University Tatsunori Matsumoto, analysis methods and field testing
Yamaguchi University T. Aso and T. Aida, signal matching techniques
Nippon Institute of Technology H. Kubota and F. Kuwabara, loading rate
Kyoto University M. Kimura, model pile testing using air-pressure device
- e. Korea
Seoul University M.M. Kim, axial testing, analysis methods
- f. England
Sheffield University Adrian Hyde, rate of loading in clay, model pile testing in clay consolidation chamber
- g. Australia
University of Western Australia Mark Randolph, model pile testing using soil anchors as reaction

Other Statnamic research in Taiwan, Singapore, and the Netherlands is also ongoing but the areas of focus are yet unknown. Some of the research at the above Universities has been funded, or partially funded, by Berminghammer Foundation Equipment and/or TNO Profound; but much has been funded by state or federal agencies such as the FHWA in the United States, the Japanese Geotechnical Society, Committee for Rapid Load Test Methods, as well as numerous research institutes associated with large Japanese companies.

Statnamic have been used by nine companies and conducted in nineteen different countries.

2.3.3 Device Component

A Statnamic test device is comprised of three key components as shown schematically in Figure 25. These are a piston (Figure 26) containing a combustion chamber, a cylinder (Figure 27), and a reaction mass (Figure 28). The Statnamic process involves placing the piston onto the foundation and loading it with a combustible fuel, installing the cylinder assembly over the piston, securing the reaction mass to the cylinder, and then igniting the fuel. Quickly forming gas pressure from combustion accelerates the reaction mass causing an equal and opposite force to be generated into the foundation. This pressure is ultimately vented in a controlled manner as the piston and cylinder separate. Numerous devices are available that are capable of achieving various magnitudes of loading. The overall capacity of a device is determined by the cross-sectional area of its piston, designed as a pressure vessel limited to 103MPa (15,000psi).

There are several Statnamic devices available which allow tests to be performed from 0.45kN to 33MN. By varying reaction mass combinations and fuel charges the load produced by each device can be varied. The maximum capacity of a device is dictated by the cross-sectional area of the piston or cylinder, which can experience up to 104MPa before damaging equipment. Presently 10 different size devices are available. The device sizes and practical load ranges are listed in Table 5.

As the Statnamic testing produces large forces from accelerating reaction masses upward, an associated logistical consideration arises in catching the airborne mass. Several mechanistic systems have been successfully implemented. These systems include: a gravel catching mechanism, a hydraulic catching mechanism, and a mechanical catching mechanism.

The gravel catching system is a crude but effective method of catching the silencer/reaction mass assembly after the test. The system involves placing “a gravel structure” around the Statnamic device forming an annular cavity, which is then filled with gravel. As the masses achieve flight, the gravel flows down to fill the void created by the displacing mass, eliminating the return pathway, thus catching the reaction mass. The gravel should be uniform (poorly graded) and angular to perform correctly. Round gravels flows too easily and can often displace upon reentry of mass, which can cause significant damage to equipment. Well graded gravels tend to compact tightly and make disassembly of gravelly structure extremely difficult. This type of system can be used with all size devices and was the first truly effective catching method. Due to the advent of mechanical and hydraulic catching systems for smaller devices, gravel catch systems are typically used for devices larger than 4MN. Shown in Figure 29 is a 30MN gravel catch structure (a) and a mechanical catch device (b) that utilizes submerged, water-filled reaction masses.

The introduction of hydraulic and mechanical catching systems practically eliminated the use of gravel structure systems for tests of 4MN and below. The hydraulic catch mechanisms consist of a large alignment frame equipped with long hydraulic catching rams in each of the four corners of the frame. These rams are actuated with nitrogen/hydraulic accumulators (gas over oil chambers), which use 1 MPa nitrogen pressure to force hydraulic fluid into the rams via one-way valves (one for each ram). The silencer/reaction mass assembly simply rests on the rams prior to the test, which confines the nitrogen gas and oil within the accumulators. As the masses accelerate upwards, the nitrogen gas confinement is removed and the gas expands forcing the rams to chase the masses to the apex of their flight. Downward movement is restricted by the one-way fluid flow through the valves. Upon completion of the test, the reaction masses are easily lowered by re-routing the fluid in the ram back to the accumulators. Figure 30 displays the 0.6MN and 4MN catch mechanisms. This system is very efficient when multiple tests are performed; and due the deletion of gravel has become more attractive to many contractors. Once assembled the system can be moved fully assembled from pile to pile with an 80-ton crane such that in one day as many as 20 tests on multiple foundations can be conducted with a well trained crew.

2.3.4 Instrumentation

2.3.4.1 General

When first introduced in the late 1980's, Statnamic testing was performed while monitoring only the applied load and resulting displacement at the top of the foundation. Later, to aid in data regression, it became commonplace to also monitor the associated acceleration directly, and more recently, both top and toe accelerations are recorded for excessively long deep foundations such as drilled shafts or driven piles. This provides some level of redundancy in the data because having both acceleration and displacement as a function of time allows the motion of the foundation to be independently defined by either numerical integration or differentiation.

2.3.4.2 Accelerometers

Although there are many types of accelerometers, two primary types are used in Statnamic testing; piezoelectric, and capacitive. A piezoelectric accelerometer utilizes the piezoelectric property of quartz or ceramic crystals. These crystals produce an accumulation of oppositely charged particles on their surface when they are deformed. This charge is proportional to the amount of strain, and therefore the stress, to which the crystal is subjected. A firmly affixed mass is used to cause a deflection in the crystal (Figure 31). The magnitude of this deflection is proportional to the magnitude of the applied force, which is in turn proportional to the acceleration (PCB Piezotronics, 1999). The corresponding voltage that develops across the crystal is conditioned and then returned through signal leads to the acquisition system. There it is converted to acceleration using a calibration constant supplied by the manufacturer of the device (e.g. 100 mV/g).

Capacitive type accelerometers operate in a similar fashion in which an accelerating mass responds to an externally applied force. In this type of accelerometer there are two conductive plates separated by an air gap (Figure 32). This air gap serves as the dielectric, and within it is a proof mass supported by a flexible armature. This forms a pair of capacitors between the plates and the mass. When the device is subjected to an acceleration, the proof mass is displaced and this creates a capacitance change. The change in capacitance is measured and converted to acceleration, again using a calibration constant supplied by the manufacturer (PCB Piezotronics, 1999).

Each type of device has a useful frequency range over which it can operate. This is much less than the natural frequency of the internal components of the accelerometer, and is determined by the construction of the device. It can also be affected by the manner in which the device is mounted. Experience with both piezoelectric and capacitive devices has demonstrated that for top-of-shaft Statnamic testing, the capacitive units produce a cleaner signal and are less likely to be affected by transient vibrations in the system. If the piezoelectric models are used instead, they must be mounted as securely as possible to prevent over-excitation (ringing) of the internal electronics.

2.3.4.3 *Displacements*

Along with acceleration, the displacement of the foundation during the test is also measured. Statnamic pistons are equipped with photovoltaic displacement transducers mounted in the center of the piston assembly. These transducers are located behind a special mirror that reflects back a portion of the light that is directed to its surface from a stationary reference laser. The remainder of the light is used to excite the photocells. When activated they produce an output voltage that is proportional to vertical position. This voltage is measured by the acquisition system and converted to displacement again using a calibration constant.

2.3.4.4 *Force and Strain*

The Statnamic force applied to the foundation is measured using a resistance-type load cell, which is also integral to the piston assembly. The load cell is essentially a strain gage-instrumented steel cylinder, the gages being configured as a Wheatstone Bridge (Figure 33). When the load is applied to the cylinder it causes a resistance change in the bonded, resistance-type strain gages.

Knowing the properties of the cell material stress is calculated, and then when multiplied by the cross-sectional area (of the cell), force is obtained. Using a load cell directly has an advantage over pile strain measurements since it is independently calibrated by the manufacturer, converting the measured output voltage of the cell into force based on the magnitude of the excitation voltage (e.g. 2.07×10^{-7} mV/V/kN). Referring to Figure 33, the excitation voltage is applied across terminals (V) and

(R), and the measured output is read across terminals (+) and (-). When the bridge is fully balanced (initial condition) the voltage differential between (+) and (-) is zero. When the bridge is shifted out of the balanced condition (load applied) the voltage differential between these terminals is nonzero, and can be equated to the applied load.

In addition to acceleration, displacement, and applied load, strain within the foundation is also measured during some Statnamic tests. To do this, a resistive strain gage is mounted to a specially prepared length of rebar. A lead wire is attached to the gage, and then several layers of protective coatings are applied. This protects the strain gage from the harsh environment in which it will operate. The final instrumented rebar, referred to as a *sister bar*, is secured at the desired elevation within the foundation. For a reinforced, drilled shaft, the sister bar is usually mounted to the reinforcing cage before it is lowered into the hole. For precast, prestressed driven piles, the sister bars are installed at the precast yard before concrete for the piles is poured. For unreinforced drilled shaft foundations, a small void is left along the length of the shaft during pouring. Later, the sister bar is lowered into this void to the proper elevation, and then grout is used to set it into position and fill the remainder of the void.

Sister bar-mounted strain gages are typically used in groups of two or three per gage elevation. This is done for two reasons. First, having more than one gage at a particular level provides redundancy in the event of a device failure. Second, by placing multiple gages around the diameter of a shaft, any eccentricities in the applied loading can be measured and accounted for in the data regression. Being able to measure and record the strain at various levels along a foundation offers many advantages if the data can be properly regressed.

2.3.4.5 Data Acquisition System (DAS)

The use of a high-speed microcomputer is required to collect data during a Statnamic test. A typical test duration is 120 milliseconds, during which time nearly 1000 readings of load, displacement, and acceleration are made. Additional data both before and after the test is also recorded to confirm the steady state (static) response. A sampling rate of 5000 recordings per second is used to ensure the collection of an adequate number of data points to fully describe the event. Such a sampling rate demands a powerful acquisition system. The two most commonly used devices to date are discussed.

One acquisition system often employed is the *Foundation Pile Diagnostic System* (FPDS) that is optional equipment with each new Statnamic device. Developed by The Netherlands Organization (TNO), it is comprised of a specialized junction box/signal conditioner and laptop computer combination to which the load cell, accelerometer, and laser are connected. FPDS software has the ability to perform the data acquisition and data reduction for top-of-shaft information. Currently it cannot monitor embedded strain gages, and its reduction technique is pre-defined and cannot be changed.

Another data acquisition system often used is the MEGADAC computer available from Optim Electronics (Figure 34). This is a highly flexible data acquisition tool that can accept multiple input cards to which the transducers are connected. Shown in Figure 35, multiple MEGADAC devices can be daisy-chained such that literally hundreds of channels can be monitored during a test. The MEGADAC and associated Test Control System (TCS) can be configured to perform the data acquisition tasks for virtually any application. TCS will not handle any of the data regression but it exports all recorded data in a standard ASCII format. This makes it convenient to import the data into a spreadsheet application for analysis.

2.3.5 Methods of Analysis

2.3.5.1 Overview

Several methods of analysis are available for the Statnamic test data. A rather crude mechanism of analysis involves a stress wave capacity factor, which correlates Statnamically applied loads to the actual static capacity via the quotient of the measured values. This method requires side-by-side static and Statnamic testing and provides little to no adjustments for inertial or viscous damping effects. The forces associated with time dependent effects are dependent on the acceleration and velocity experienced by the foundation and should be more closely linked to these values. Several test programs in the United States have been conducted using this method for cohesive soil types in conjunction with inertial correction.

2.3.5.2 Signal Matching

A second method of analysis is aimed at determining the static capacity of a Statnamically loaded deep foundation is signal matching. This method uses the same approach as dynamic testing whereby the measured response of the top of the pile/shaft is compared to the model-predicted values from wave-equation solutions. The results are dependent on a number of user-defined variables and derives its solution from the model's ability to match the field conditions. At present no commercial testing firms are using this method on a regular basis. For more details and the difficulties associated with the application of the method to stress waves produced by Statnamic testing, see sections 1.3 and 1.4.

2.3.5.3 Unloading Point Method

The first widely accepted method of analyzing Statnamic data was the Unloading Point Method (UPM). The UPM is a simple method, which allows the equivalent static resistance to be derived from the measured Statnamic force (Middendorp, 1993). Therein a simple Kelvin-Voigt model is used to represent the foundation/soil system as a rigid body supported by a non-linear spring and a linear dashpot in parallel (see Figure 36). The spring represents the static soil response (F_{Static}). This includes the elastic response of the foundation as well as both the foundation/soil interface and surrounding soil response. The dashpot is used to represent the dynamic resistance, which depends on the rate of pile penetration.

The UPM makes two primary assumptions in its determination of the damping coefficient "c". The first is the static capacity of the pile is constant once it plunges as a rigid body. The second is that the damping coefficient is constant throughout the test. By doing so a window is defined in which to calculate the damping coefficient. Referring to Figure 37 showing a typical Statnamic load-displacement curve, the first point of interest (1) is that of maximum Statnamic force. At this point the static resistance is assumed to have become steady state. Thus, any extra resistance is attributed to that of the dynamic forces (ma and cv). The next point of interest (2) is that of zero velocity which has been termed the "Unloading Point." At this point the foundation is no longer moving and the resistance due to damping is zero. The static resistance from point (1) to (2) can then be calculated by the following equation:

$$F_{Static\ UP} = F_{Statnamic} - (ma)_{Foundation} \quad (10)$$

where, $F_{Statnamic}$, m , and a are all known parameters; $F_{Static UP}$ is the static force calculated at (2) and assumed constant from (1) to (2).

Next, the damping coefficient can be calculated throughout this range, from maximum force (1) to zero velocity (2). The following equation is used to calculate c :

$$c = [F_{Statnamic} - F_{Static UP} - (ma)_{Foundation}] / v \quad (11)$$

Damping values over this range should be fairly constant. Often the average value is taken as the damping constant, but the most constant value should be used (see Figure 38). Note that as v approaches zero, point (2), values of c can be different from that of the most representative value and therefore the entire trend should be reviewed. Finally the derived static response can be calculated as follows:

$$F_{static} = F_{Statnamic} - (ma)_{Foundation} - (cv)_{Foundation} \quad (12)$$

The UPM has proven to be a valuable tool in predicting damping values, when the foundation acts as a rigid body. However, as the pile length becomes long an appreciable delay can be introduced between the movement of the pile top and toe, hence negating the rigid body assumption. This occurrence also becomes prevalent when an end bearing condition exists; in this case the lower portion of the foundation is prevented from moving jointly with the top of the foundation.

Middendorp (1998) uses a term denoted as the “Stress Wave Number” (N_w) to quantify the applicability of the UPM. The wave number is calculated by dividing the wave length (D) by the foundation depth (L). D is obtained by multiplying the wave speed c in length per second by the load duration (T) in seconds. Thus, the wave number is calculated by the following equation:

$$N_w = \frac{D}{L} = \frac{cT}{L} \quad (13)$$

Through empirical studies Middendorp determined that the UPM would accurately predict static capacity, from Statnamic data, if the wave number was greater than 12. Using wave speeds of 5000m/s and 4000m/s for steel and concrete respectively and a typical Statnamic load duration, the UPM is limited to piles shorter than 40 m (steel) and 32 m (concrete). Note the relative wavelength Λ of equation 6 is half N_w ($\Lambda = 0.5N_w$) and the material presented in sections 1.3.2.2 and 1.4 is directly relevant.

Based on load duration, foundation length, and material properties, a foundation may require various analysis methods. Figure 39 is a flow chart that can be used as a guide to determining the correct method for analyzing load test data. DLT and SLT, are used as acronyms for Dynamic and Static Load Tests, respectively. N_w is the wave number as calculated above. From Figure 39 it is seen that if the stress wave number is lower than 6 then the test should be evaluated using dynamic procedures. For tests with stress wave numbers of 1000 or greater static load-displacement behavior can be expected. It is also noted that for stress wave numbers less than 12 stress wave phenomena can be expected, and for those greater than 12, no stress wave corrections are necessary.

Statnamic tests cannot always produce wave numbers greater than 12, and as such there have been several methods suggested to reduce stress wave phenomena in Statnamicly tested long piles: (1) lengthen the load duration, (2) use a “stress wave capacity factor,” and (3) use a signal matching algorithm.

Although mildly affected by the venting mechanism, the load duration is primarily influenced by the mass to force ratio. As the amount of mass used for testing approaches 100% the test duration approaches that of a S.L.T. Figure 40 shows the effect of mass ratio on Statnamic load durations; this was observed by maintaining a constant mass and varying the Statnamic force (expressed as percent of device capacity). High mass to force ratios are plausible, but could negate some of the savings associated with small equipment mobilization. However, if mobilization costs can be minimized while maintaining high mass ratios, stress wave phenomena can be negated. Further, the recent advent of the submerged reaction mass option means that large mass to force ratios are attainable that permit longer duration loading and high machine utilization.

Free software that performs the UPM analysis (developed for the Federal Highway Administration) is available at <http://www.eng.usf.edu/~gmullins/>. In addition to automating the UPM calculations, the software conveniently executes all required numerical integration and differentiation of the collected data. Further, key statistics from the damping coefficient analysis are recorded and displayed in a user-friendly interface (Figure 41) as well as many other options.

Given the shortcomings of the UPM, users of Statnamic testing have developed a remedy for the problematic condition that arises most commonly. The scenario involves relatively short piles ($N_w > 12$) that do not exhibit rigid body motion, but rather elastically shorten within the same magnitude as the permanent set. This is typical of rock-socketed drilled shafts or piles driven to dense bearing strata that are not fully mobilized during testing. The consequence is that the top of pile response (i.e. acceleration, velocity, and displacement) is significantly different from that of the toe. The most drastic subset of these test results show zero movement at the toe while the top of pile elastically displaces in excess of the surficial soil quake (e.g. upwards of 25 mm). Whereas with plunging piles (rigid body motion) the difference in movement (top to toe) is minimal and the average acceleration is essentially the same as the top of pile acceleration; tip restrained piles will exhibit an inertial term that is double than when using top of pile movement measurements to represent the entire pile.

2.3.5.4 *Modified Unloading Point Method*

The Modified Unloading Point Method (MUP) makes use of an additional toe accelerometer that defines the toe response. The entire pile is still assumed to be a single mass, m , but the acceleration of the mass is now defined by the average of the top and toe movements. A standard UPM is then conducted using the applied top of pile Statnamic force and the average accelerations and velocities. The derived static force is then plotted against top of pile displacement as before. This simple extension of the UPM has successfully overcome most problematic data sets. Plunging piles instrumented with both top and toe accelerometers have shown little analytical difference between the UPM and the MUP. However, MUP analyses are now recommended whenever both top and toe information is available.

Although the MUP solved most of the problems associated with unmet UPM conditions, there still exists a scenario where Statnamic data cannot be analyzed without signal matching or wave equation analyses. This is when the wave number is less than twelve (relatively long piles). In these cases the pile may still only experience compression (no tension waves) but the delay between top and toe movements causes a phase lag. Hence an average of top and toe movements does not adequately represent the pile.

2.3.5.5 *Segmental Unloading Point Method*

The Segmental Unloading Point Method (SUP) was developed to analyze foundations that would not satisfy the conditions for UPM or MUP analyses. Specifically, when the wave number is less than 12, the assumption of rigid body motion is not reasonable; in these conditions, appreciable compression waves have been observed in Statnamic data sets. The overall effect is that the top and toe response of the pile experience an out-of-phase condition and wave type analyses are best suited. A second aspect addressed by SUP, but less noted by designers, is the mechanism by which a long pile develops capacity irrespective of the test type or duration (static or Statnamic). Due to strain incompatibility, a long pile cannot develop its ultimate capacity simultaneously from all soil strata; but rather will develop from top down depending on the stiffness of the strata and the relative displacements caused by elastic compression. This is contrary to classical pile capacity calculations, which simply sum the predicted ultimate skin friction contributions from various layers. This method, denoted as SUP, discretizes a foundation into shorter lengths (called segments) that each meet the criteria of the UPM and hence move more like a rigid body. This allows the standard UPM to be applied to each segment using the fundamental equation of motion. Then the total derived static response can be calculated as the sum of the derived static response from the individual segments with respect to time. In that the peak segmental capacities may not occur at the same time or top of pile displacement, this summation is not simply the sum of the peak segmental capacities, but rather the summation of capacities with respect to the top of pile displacement. This method requires the use of strain gages at various levels along the length of the foundation. Thereby, soil load and displacement distributions are measured and not assumed or modeled (Lewis, 1999; Mullins et al., 2002).

The fundamental concept of the SUP is that the acceleration, velocity, displacement, and force on each segment can be determined from strain gage measurements. The individual segment displacements are determined using the relative displacement with respect to the top of pile movement from the cumulative elastic compression as measured from strain gages. The velocity and acceleration of each segment are then determined by numerically differentiating the displacement with respect to time. The segmental forces are determined from the difference in force from strain gages at the levels bounding the segment.

The maximum number of segments is dependent on the available number of strain gage layers. However, strain gage placement does not necessitate assignment of segmental boundaries; as long as the wave number of a given segment is greater than 12, the segment can include several strain gage levels within its boundaries. The number and the elevation of strain gage levels are usually determined based on soil stratification; as such, it is useful to conduct an individual segmental analysis to produce the shear strength parameters for each soil strata. A reasonable upper limit on the number of segments should be adopted because of the large number of mathematical computations required to complete each analysis. Figure 42 is a sketch of the SUP pile discretization.

The notation used for the general SUP case defines the pile as having m levels of strain gages and $m+1$ segments. Strain gage locations are labeled using positive integers starting from 1 and continuing through m . The first gage level below the top of the foundation is denoted as GL^1 where the superscript defines the gage level. Although there are no strain gages at the top of foundation, this elevation is denoted as GL^0 . Segments are numbered using positive integers from 1 to $m+1$, where segment 1 is bounded by the top of foundation (GL^0) and GL^1 . Any general segment is denoted as segment n and lies between GL^{n-1} and GL^n . Finally, the bottom segment is denoted as segment $m+1$ and lies between GL^m and the foundation toe.

The SUP analysis defines an average acceleration, velocity, and displacement traces that are specific to each segment. To do this strain data and a boundary displacement are needed. The bound-

ary displacement may come from the Statnamic laser reference system (top), top of pile acceleration data, or from embedded toe accelerometer data.

The displacement is calculated at each gage level using the change in recorded strain with respect to an initial time zero using Equations 14 through 17. Because a linearly-varying strain distribution is assumed between gage levels, the average strain is used to calculate the elastic shortening in each segment. Equations 14 and 16 are specific to gage level 1; whereas Equation 15 and 17 are general for all subsequent levels.

level one displacement

$$x_1 = x_{\text{laser}} - [(\Delta\varepsilon_{\text{GL}}^0 + \Delta\varepsilon_{\text{GL}}^1)L_{\text{seg}}^1]/2 \quad (14)$$

subsequent level displacements

$$x_n = x_{n-1} - \Delta\varepsilon_{\text{average seg } n} L_{\text{seg } n} \quad (15)$$

where

$$\Delta\varepsilon_{\text{GL}}^0 = \Delta F_{\text{Statnamic}} / AE \quad (16)$$

$$\Delta\varepsilon_{\text{average seg } n} = (\Delta\varepsilon_{\text{GL}}^{n-1} + \Delta\varepsilon_{\text{GL}}^n)/2 \quad (17)$$

and

x_{laser}	=	the top-of-pile displacement
x_n	=	the displacement at the nth gage level
$\Delta\varepsilon_{\text{average seg } n}$	=	the average change in strain in segment n
$L_{\text{seg } n}$	=	the length of the nth segment
$\Delta\varepsilon_{\text{GL}}^n$	=	the change in strain in the nth strain gage level
$\Delta F_{\text{Statnamic}}$	=	the change in measured Statnamic force with
AE	=	foundation area and elastic modulus

To perform an unloading point analysis, only the top-of-segment motion needs to be defined. However, the MUP analysis, which is now recommended, requires both top and bottom parameters. The SUP lends itself naturally to providing this information. Therefore, the average segment movement is used rather than the top-of-segment; hence, the SUP actually performs multiple MUP analyses rather than standard UPM. The segmental displacement is then determined using the average of the gage level displacements from each end of the segment as shown in the following equation:

$$x_{\text{seg } n} = (x_{n-1} + x_n) / 2 \quad (18)$$

where $x_{\text{seg } n}$ is the average displacement consistent with that of the segment centroid.

The velocity and acceleration, as required for MUP, are then determined from the average displacement trace through numerical differentiation using Equations 19 and 20, respectively:

$$v_n = (x_{n,t} - x_{n,t+1}) / \Delta t \quad (19)$$

$$a_n = (v_{n,t} - v_{n,t+1}) / \Delta t \quad (20)$$

where

$$\begin{aligned}
 v_n &= \text{the velocity of segment } n \\
 a_n &= \text{the acceleration of segment } n \\
 \Delta t &= \text{the time step from time } t \text{ to } t+1
 \end{aligned}$$

It should be noted that all measured values of laser displacement, strain, and force are time dependent parameters that are field recorded using high-speed data acquisition computers. Hence the time step, t , used to calculate velocity and acceleration is a uniform value that can be as small as 0.0002 seconds.

The average motion parameters (x , v , and a) for segment $m+1$ cannot be ascertained from measured data, but the displacement at GL^m can be differentiated directly providing the velocity and acceleration. Therefore, the toe segment is evaluated using the standard UPM. These segments typically are extremely short (1 - 2 m) producing little to no differential movement along its length.

Each segment in the shaft is subjected to a forcing event which causes movement and reaction forces. This segmental force is calculated by subtracting the force at the top of the segment from the force at the bottom. The difference is due to side friction, inertia, and damping for all segments except the bottom segment. This segment has only one forcing function from GL^m and the side friction is couple with the tip-bearing component. The force on segment l is defined as:

$$S_l = S_{\text{statnamic}} - E_l A_l \varepsilon_l \quad (21)$$

On subsequent segments

$$S_m = E_m A_m \varepsilon_m \quad (22)$$

And on the toe segment

$$S_n = A_{(n-1)} E_{(n-1)} \varepsilon_{(n-1)} - A_n E_n \varepsilon_n \quad (23)$$

where

$$\begin{aligned}
 S_n &= \text{the applied segment force from strain measurements} \\
 E_n &= \text{the composite elastic modulus at level } n \\
 A_n &= \text{The cross-sectional area at level } n \\
 \varepsilon_n &= \text{The measured strain at level } n
 \end{aligned}$$

Once the motion and forces are defined along the length of the pile, an unloading point analysis on each segment is conducted. The segment force defined above is now used in place of the Statnamic force as used by the UPM. Equation 24 redefines the fundamental equation of motion for a segment analysis:

$$S_n = m_n a_n + c_n v_n + S_n \text{ Static} \quad (24)$$

where

$$\begin{aligned}
 S_n \text{ Static} &= \text{The derive static response of segment } n \\
 m_n &= \text{The calculated mass of segment } n \\
 c_n &= \text{The damping constant in segment } n
 \end{aligned}$$

The damping constant (in Equation 25) and the derived static response of the segment are computed (Equation 26) consistent with standard UPM analyses:

$$C_n = (S_n - S_n \text{ static})/v_n \quad (25)$$

$$S_{n \text{ static}} = S_n - m_n a_n - c_n v_n \quad (26)$$

Finally the top-of-pile derived static response can be calculated by summing the derived static response of the individual segments as displayed in the following equation:

$$F_{\text{static}} = \sum_{n=1}^{m+1} S_{n \text{ static}} \quad (27)$$

By providing both the derived static and displacement from each segment, the SUP method can provide the T-Z response of each segment. By design, these segments typically correspond to each of the various layers of interest to the designer.

Due to the large number of computations and organization associated with this method of analysis, an analysis software designed specifically for SUP analyses is presently undergoing alpha testing and will be freely available within the year (Figures 43 and 44). For updated information visit <http://www.eng.usf.edu/~gmullins>.

2.3.6 Critical Evaluation

As a dynamic impact application method, the Statnamic testing is evaluated on the basis of comparisons between the Static Load Derived (SLT), i.e. the capacity and load displacement as obtained via analysis of the measured data, in comparison with the pile behavior under static loading. A database presenting and analyzing such cases is presented in Chapter 3.

2.4 THE STATIC TESTING METHODS

2.4.1 Overview

Although static testing is not an integral part of innovative load testing systems it remains relevant in three ways:

- a. Part of innovation in testing comes by the alteration of the traditional static testing, (see section 1.1.1). Methods as the Osterberg load cell (to be discussed in detail in section 2.5) or static-cyclic procedures become, therefore, part of the researched scope.
- b. As traditional up-down static load test and in particular slow maintained (standard) load test is the most reliable method to determine the pile's performance, it remains a benchmark for the examination of any other method.
- c. One of the major difficulties in fast rate testing is the prediction of the pile's behavior under static loading; in particular constant maintained loading, i.e. creep effects. These predictions via practical simplified models are best developed when one tries to predict creep behavior from short duration pseudo-static loading rather than, for example, from dynamic measurement during driving for which the main difficulty remains the separation between static to dynamic components. One of the presented models in Chapter 4 is aimed to address these difficulties with initial expansions to enable predictions from faster loading (e.g. Statnamic Testing).

Table 6 presents a summary of the main attributes of static load test procedures. Figure 45 provides a graphical representation of some of the static load testing procedures showing the percent of design load, as a function of the duration of load application. Details description and analyses of

the Osterberg Cell method are provided in section 2.5. The following section briefly describes the static cycle testing as it relates to the presented research in the following way:

- a. It allows to examine “fast-static” loading compared to dynamic (see section 1.4).
- b. It allows to examine the influence of load rate and testing method on the benchmark static capacity (to be presented in Chapter 3).
- c. It allows to develop models to be tested through different loading rate starting with “fast-static” and moving to fast penetration and dynamic.

2.4.2 Static Cyclic Testing

A new method for carrying out a static load test and interpreting the results is described by Paikowsky et al. (1999). This approach is based on a methodology developed by Dr. Valery Operstein during her work as the Chief Engineer at Ukrspetsstroiproekt, a soils and foundations research design institute in Dniepropetvorsk, Ukraine. A pile is loaded to failure by applying a load at a high constant rate of approximately 150kN/min (15 t/min) and then unloaded at a fast rate of approximately 300kN/min (30 t/min). Typically a series of three load-unload cycles is performed within a time period of less than one hour. The method enables the unique determination of the ultimate pile capacity based on the load-settlement relations in the load-unload cycle, which is closely related to the fundamental physical mechanism of soil/pile interaction.

The method was investigated using four approaches: (i) the study of an instrumented laboratory model pile (44.5mm (1¾ inch) diameter, 610mm (24in) long), (ii) a field model pile (76.2mm (3in) diameter, 3.05m (10ft) long, driven and loaded via drilling rods), (iii) a full-scale instrumented pile cluster (two 324mm (12¾ inch), 31.39m (103ft) and 24.38m (80ft) long pipe piles, and one 356mm-square (14-inch-square), 24.38m (80ft) long, pre-cast concrete pile), and (iv) analysis of a database obtained from the Ukraine comparing slow-maintained and static cyclic testing on a large number of full-scale case histories.

The extensive investigation by Paikowsky et al. (1999) has proved the validity of the method when compared to tests that require a period of at least 10 times longer to perform. The available extensive data gathered during this research enables to investigate load rate effect within the 'static' zone in the closest possible range to kinetic testing. Figure 46 presents the load displacement relations comparing various static (maintained load test – MNT, and short duration – SD), static-cyclic (SC), and Statnatics (STN) load-testing procedure carried out on a 24.38m (80ft) long 323.85mm (12¾ inch) diameter closed ended pipe pile. The pile was part of a testing program carried out by the PI at Newbury, Massachusetts with the support of the Massachusetts Highway Department to the Geotechnical Engineering Research Laboratory at the University of Massachusetts Lowell.

Figure 47 presents details of the loading rate and associated pile movements for the load testing procedures (slow maintained, short duration and static-cyclic). In spite of the significant differences between the load rate application procedures, all static tests resulted in a similar capacity assessment, while the Statnamic test resulted in a significantly different assessment. These facts will be further examined in Chapter 3 where the load-displacement relations of the different static tests and failure criteria are examined.

2.5 OSTERBERG CELL LOAD TESTING

2.5.1 Introduction

This section presents a critical assessment of the Osterberg Cell (O-cell) load testing technology. The study has been concentrated on a basic Finite Element study and key case histories. As such, it is presented as one unit in section 2.5 with the details provided in Appendix A. Named for its inventor, Dr. Jorj Osterberg, the O-cell load testing method involves the use of an embedded expendable jack, which is cast within the test foundation. Although the method has occasionally been used with driven piles, the primary use of the technology is for drilled shaft foundations. As shown on Figure 48, this embedded jack is used to load one part of the shaft against the other so as to conduct a loading test without the need for independent reaction. In many cases (and increasingly in recent years), cells have been placed at multiple levels within the shaft in order to conduct loading tests of different isolated portions of the test shaft.

The most compelling advantage of utilizing the O-cell technique is the fact that field measurements of load transfer can be made on very high capacity drilled shafts (including rock sockets). These are constructed under realistic conditions at full scale, and thus provide measurement data which are impractical or prohibitively expensive to obtain in any other way. O-cell testing has in many ways revolutionized the design and use of high capacity drilled shafts by giving engineers a practical way to validate design load transfer values and reduce the extreme conservatism that has existed for years in the design of these foundations. The greatest concern about utilizing the O-cell technique is the fact that the shaft is loaded from the bottom up rather than from the top down, deviating from the way in which the structure will load the shaft. There is a need, therefore, to examine the O-cell test in order to assess potential differences in unit load transfer, which could be related to test conditions, hence assist engineers interpreting and utilizing the results of this test with confidence.

This study is thus focused on the interpretation O-cell load testing results. Comparisons between O-cell testing and conventional top-down loading are examined, with emphasis on the interpretation of O-cell test results for use in design for conventional loading conditions. O-cell test results have traditionally been used to measure unit side shear and unit end bearing resistance values and these measured unit values are assumed to apply directly for design for typical top-down axial load application. This research has examined the comparison between unit load transfer values from O-cell and top-down loading conditions in three ways:

- a. Review the state of practice of the O-cell testing technology and available field load test data which might allow direct comparisons of O-cell and conventional top-down loading tests (sections 2.5.2 and 2.5.3).
- b. Compare conventional top down testing and O-cell testing using finite element models. This technique has the potential for examining the state of stress in the near field soils around a test shaft and in aiding understanding of behavior (section 2.5.4).
- c. Compare conventional top-down loading and O-cell testing using simple analytical solutions that could aid in identifying any variations between bottom-up and top-down loading and improve interpretation of the O-cell test method (section 2.5.5).

2.5.2 O-Cell Load Testing Method and Application

2.5.2.1 Review

A review of the O-cell testing method and technology is provided by Osterberg (1995), which describes the test method and equipment. The use of O-cell testing for drilled shafts for highway bridges is also summarized by O'Neill and Reese (1999). The cell itself is composed of a large diameter pressure cell, which contains a pressurized fluid (usually water or oil). The large diameter of the

cell compared to conventional hydraulic jacks allows relatively large forces to be generated for a given pressure. Typical pressures of up to 69 MPa (10,000 psi) are used although devices are now reportedly capable of up to 103 MPa (15,000 psi). Standard sizes are typically up to 81 cm (32 inches) diameter, and these may be used in parallel within a large diameter shaft (a cloverleaf arrangement of 4 cells at a given elevation is possible) to generate very large forces. The cell(s) are typically attached to the base of the rebar cage and tack-welded to hold the cell together until testing (at which time an initial loading to break the tack welds is required). With the multi-level approach, it is necessary to weld the upper cell(s) sufficiently to support the cage below to the lower cell level during installation. It is also necessary to provide a tremie bypass line so that concrete placement between and around the cells can be accomplished.

Embedded LVDT's are used to measure the relative displacement across the cell and have largely replaced the earlier practice of using telltales extending to the surface. Strain gauges are also commonly used to interpret the distribution of resistance along the shaft. Vibrating-wire type instrumentation is generally used for O-cell testing, with monitoring by a computer-based data logger.

In the current practice in the United States, O-cell load testing is performed exclusively by Loadtest, Inc. as a turnkey operation. For highway projects, the actual location of cells, magnitudes of anticipated loads, and many other details of the load test setup are commonly specified by state DOT's or their consultants. Loadtest may sometimes provide input into the details of the test setup, but often their input is either not sought or is very limited. Loadtest, Inc. is usually subcontracted as a specialty sub to the general contractor on the project.

One of the compelling reasons for using O-cell testing is for the possibility of examining behavior of full size drilled shafts which have been constructed under realistic construction conditions and loaded to large unit side shear and end bearing stresses. On a number of projects, O-cell load testing has provided data that demonstrate the influence of construction techniques on performance, especially in rock socket shafts (Osterberg and Hayes, 1999; Osterberg, 2001). Examples include the effect of bottom hole cleanliness and disturbance on the base resistance of drilled shafts, the influence of lateral fluid concrete pressure on side shearing resistance in rock sockets, the effect of sidewall roughness on side shearing resistance in rock sockets, and the influence of drilling fluid contamination on side shearing resistance.

2.5.2.2 State DOT Use

A number of interviews were conducted with geotechnical professionals employed with state DOT agencies in order to develop a general sense of the use of O-cell load testing technology. Not every state was contacted, but emphasis was placed on those states where the technology is known to be employed. The most widespread use appears to be in the southeastern states. Of these, Mississippi notably appears to be the largest user with O-cell testing routinely on perhaps 50 or more projects in the last 10 years. Most other southeastern (e.g., FL, GA, KY, NC, SC, VA) states have used O-cell testing on select larger projects involving drilled shafts. Several states (AL, NM, MN, CO, NV, CA, MA, RI, CT) have used O-cell testing occasionally or only on a very few projects and do not consider its use routine. Only a few states have used O-cells in production shafts. A number of state geotechnical engineers perceive the use of O-cells for rock-socket drilled shafts to be an important use in light of the difficulty in quantifying the performance of such shafts. However, most tests have actually been performed on sites in coastal deposits where large bridge projects and heavily loaded foundations are more common.

Most state geotechnical engineers who have utilized O-cell testing have tended to accept the measurements as indicative of axial performance of drilled shafts in conventional top down loading. Almost no comparative tests have been performed. New Mexico performed comparative tests on two shafts at a single location in dense sands; these test results will be discussed subsequently. Florida has and is currently sponsoring a research study at the University of Florida relating to O-cell and other test methods, but this research has generated no new comparative tests of O-cell and conventional top down static testing (there are some tests involving O-cell and Statnamic measurements).

2.5.3 Comparison Between O-Cell (bottom-up) and Traditional (top-down) Compression Load Test

2.5.3.1 General

There are numerous references to O-cell testing in the technical literature, most of the type that describe the technology as an innovative new method for testing with a subsequent case history of use on a project. Some researchers (Gorczyca et al. 1999, Horvath et al. 1980, Chua et al. 1994) have reported compressive and uplift load test results or O-cell test results, but they didn't tend to compare the side shear resistance derived from a top down test and a bottom up test. The emphasis of this research was to search for published cases where comparative test data are available between O-cell testing and conventional testing, or where other critical examinations of the O-cell testing method have been described. Very few such papers exist, although several of interests are described below.

2.5.3.2 Hong Kong Railway

Littlechild, et al. (2000) describe a load test of shafts in Hong Kong which were socketed into rock as a part of a large scale load testing program on the Kowloon-Canton Railway. Five of these tests combined a kentledge (dead weight) top down test of a shaft with an embedded O-cell (stage 1), followed by loading via the O-cell at the toe with the kentledge removed (stage 2), followed by loading via the O-cell plus the kentledge (stage 3) to fully engage the end bearing.

Two of these five shafts fully mobilized the side shear of the socket during stage 2, and one of these two had also fully mobilized the side shear of the socket during stage 1 prior to the stage 2 loading. Shaft TWW1 had a 2m long socket within a highly fractured and weathered granodiorite (RQD = 0). Stage 1 loading via kentledge mobilized 800kPa (about 8.4tsf) of unit side shear at a displacement of approximately 50 mm after which a stage 2 loading upward from the O-cell mobilized a unit side shear of 1000kPa (about 10.4tsf) at a displacement of approximately 90mm. The kentledge was then engaged to perform the stage 3 loading. Shaft TSW1 had a 1.5m socket into a moderately strong, moderately to slightly weathered metasandstone (RQD = 35-74%). Stage 1 loading via kentledge mobilized 4200kPa (about 44tsf) of unit side shear at a displacement of only 8mm; this was not considered to have produced yielding at the pile/soil interface. The stage 2 loading via O-cell mobilized 6000kPa (about 63tsf) of side resistance at a displacement of 10mm and was observed to fail the socket as the resistance dropped dramatically to only about 2000kPa (about 21tsf) at a displacement of 18mm. The authors attributed the strain softening behavior to breakout of a fractured rock cone around the socket due to the uplift loading. None of the other test shafts fully mobilized the side shear resistance.

In end bearing, only shaft TWW1 mobilized large displacements at the shaft base for both kentledge and O-cell loadings. The stage 1 kentledge loading of this shaft mobilized a base resistance

of 12.9MPa (about 135tsf) at a displacement of 62mm (5% of the shaft diameter), and stage 3 O-cell loading mobilized a maximum base resistance of 16MPa (about 167tsf) at a displacement of 86mm (7% of the shaft diameter). The 86mm displacement appears to have been measured with respect to the start of the stage 3 test, as a plot of the total movement (Figure 49) suggests that the load vs. deflection response at the shaft base from the stage 3 loading provided an extension of the load vs. deflection response from the stage 1 loading.

2.5.3.3 *Downtown Hong Kong*

Ng et al. (2001) report the results of tests in Hong Kong for some downtown buildings founded on weathered igneous and granitic rocks in which side shear values are measured and reported. Several of these load tests included both top down loading and O-cell loading.

One test in decomposed granite is reported in which a 1.5m diameter shaft was loaded from the top down to mobilize large downward side shear, after which an embedded O-cell was expanded to mobilize side shear of the same shaft in the opposite direction. For the completely decomposed granite (avg N SPT = 75b/f), 60kPa side shear (0.6tsf) was mobilized during the downward loading at a displacement of around 6 mm. The O-cell loading mobilized approximately 105kPa (1.1tsf) at a similar absolute displacement upward, about 80% higher. However, the downward loading resulted in a permanent set in the shaft and if the displacement in the O-cell loading is considered with respect to the zero position at the start of the O-cell test rather than the absolute zero, then the O-cell loading mobilized a similar side shear at a similar displacement. The same is true for the lower portion of the shaft in the somewhat less highly decomposed granite (avg N SPT > 200b/f), at somewhat higher values of mobilized unit side shear. The side shearing resistance of this shaft did not exhibit strain softening behavior.

Four shafts were tested using both top down and O-cell loading in weathered rocks. Only two of these shafts (both in granitic rock) achieved displacements in side shear exceeding 10mm in both directions. Of the four shafts, three were loaded first by top down loading followed by O-cell, the fourth was loaded first by O-cell followed by top down. In each case, the second loading stage appeared to have been influenced by the first, in which the stiffness and stress-strain behavior differed from the initial loading. The authors concluded that the initial loading in these weathered rocks caused a loss of bond in the socket and the breaking off of asperities at the shaft/socket wall interface. The loss of bonding produced a hysteresis-induced softening related to the cyclic loading.

Ng et al. (2001) conclude that for the drilled shaft in granitic soil, the stiffness and mobilized side shear at the first and second stage loading is similar. However, for the drilled shafts in weathered rocks, both the stiffness and mobilized side shear is substantially lower during the second stage of a two-stage test due to the loss of bond produced during the initial stage of loading. These data suggest that direct comparisons of O-cell and top down loading from multi-directional tests on a single shaft can be problematic.

2.5.3.4 *New Mexico*

The unpublished results of loading tests on two shafts for a bridge in New Mexico are reported by Meyer (1996), and include top down loading followed by O-cell loading in the opposite direction. These two tests are at a single site and part of a study to compare drilling fluids (bentonite vs. polymer). Each shaft was 762mm (30 inch) diameter and 13.7m (45ft) deep and was constructed in the very dense saturated alluvium of the Rio Grande channel (sand/gravel/cobble). Standard penetra-

tion test values averaged around $N_{SPT} \approx 50b/6''$ over most of the length of the shafts. In each shaft the O-cell was placed at approximately the 2/3-depth point of the shaft. The testing sequence in each case was to conduct a top down loading to a displacement of at least 38mm (1.5 inches) (5% of the shaft diameter), unload, perform a second top down loading to a total displacement of about 76.2mm (3 inches), unload, perform the O-cell loading. In both cases the O-cell produced failure of the upper 2/3 of the shaft in side shear with very small downward movement of the bottom 1/3 of the shaft (less than 12.7mm (½ inch)). The O-cell was pumped to achieve an upward movement of the shaft of around 152.4mm (6 inches) in each case.

Based on the interpreted strain gauge data, the top down loading of the upper shaft segment (upper 2/3 of the shaft) produced a maximum load transfer in side shear of around 4.4MN (440 tons) and 5.5MN (550 tons) in the bentonite and polymer shafts, respectively. The side shear vs. displacement response was very nonlinear after about 12.7mm (½ inch) of movement but was observed to increase in a strain-hardening manner to the maximum downward displacement at between 38mm (1.5 inches) and 51mm (2 inches).

The O-cell loading in the upward direction indicated much lower maximum values of side shear, with totals of around 2MN (200 tons) and 2.7MN (270 tons) in the bentonite and polymer shafts, respectively. Values at displacements of between 38mm (1.5 inches) and 51mm (2 inches) were even lower; however, the load deflection curves clearly demonstrated the effect of the loading history as each curve exhibited an “S” shape with a local peak at around 12.7mm (½ inch) of upward movement followed by additional hardening at 51mm (2 inches) to 102mm (4 inches) of upward movement as the earlier downward displacements were recovered. This behavior suggests that the top down loading history had a substantial effect on the response of the shaft to the upward directed loading.

2.5.3.5 *Singapore*

An unpublished project report prepared by Molnit and Lee (1998) has been provided by Loadtest, Inc. in support of this research. This report provides a comparison between two 1.2m diameter by 38m long test shafts in a deep deposit of silty clay/clayey silt soil. The majority of capacity of these shafts is derived from side shear. One of these shafts was loaded to failure using a kentledge (dead weight) loading from the top down and the other was loaded via a multi-stage O-cell system. The load settlement response for this test was developed using load increments of approximately 10% of the maximum load and 1 hour hold periods at each load increment. Several increments were held for longer periods and the maximum load was maintained for 24 hours. The O-cell testing was performed using the normal procedure in which each of many smaller load increments are held for a period of 4 minutes. Thus, there is a potential for the kentledge test to exhibit somewhat softer response due to creep in the clayey bearing soils.

The kentledge system loaded shaft PTP15 to a total load of approximately 28MN and developed a displacement at the top of the shaft of around 120mm (10% of shaft diameter). The O-cell test produced a failure of the upper 27m (above the upper O-cell level) and of the tip resistance (at the 38m depth), but not of the lower portion of the shaft between the two O-cell levels between the depths of 27m and 38m. Assuming that this lower section of shaft was at a state of incipient failure, the projected top-down response from the O-cell testing reportedly indicates a displacement of around 100mm at a total equivalent load of 28MN. Even if this lower portion of the shaft were able to support some additional load (which seems likely), it appears that the two tests produce reasonably similar results. Equivalent top-down load settlement curves were very similar, both showing the onset of large

deformations at a load of around 20MN and a displacement of around 25mm. A portion of the increased settlement from the kentledge loading test is undoubtedly due to the longer sustained loading in these clay soils.

In spite of the differences relating to soil creep and possible lack of fully developing a small portion of the shaft resistance in the O-cell test, the Singapore tests probably provide the most direct comparison data available between the top-down and O-cell method. For this soft soil site, it appears reasonable to conclude that any differences between the two test methods (top-down vs O-cell) are likely to be less than 10% and this magnitude of difference between two different shafts can easily be attributed to site variability.

2.5.3.6 *Osaka, Japan*

Comparative tests at another deep soft soil site are reported by Kishida, Tsubakihara, and Ogura (1992) (unpublished report). These tests are on shafts of 1.2m diameter and 38.5m length, almost identical in size to the Singapore data. The soils are interbedded silts and clays in the upper 29m, with significant dense sand layers interbedded with clay below that depth. One test shaft was subjected to vertical compression loading (top-down), and had a “friction-cut” within the top 17m. This appears to have been performed using an oversized hole with a casing inside, but some small amount of load transfer was still mobilized within this zone. A total top-down load of approximately 20MN was applied to this shaft, producing a downward displacement of around 150mm. Interpretation of strain gauge instrumentation suggests that the pile tip mobilized just over 6 MPa of unit end bearing at a tip displacement of around 75mm (6% of the shaft diameter).

Two shafts were tested using an embedded O-cell placed very near the shaft base. One of these shafts had the “friction cut” in the upper 17m as per the top-down test shaft and the other had no reduction in side shear. Both of the O-cell tests failed in end bearing without fully mobilizing the side shear capacity of these shafts. The two O-cell tip resistances were similar, and matched very closely with the interpreted response of the base of the top-down test (approximately 5.5 and 6.2MPa at a displacement equal to 7% of the shaft diameter). Unfortunately, the O-cell tests mobilized only 2 to 3mm of displacement in side shear; unit side shear at these small displacements was in general agreement with the side shear at very small displacements in the top-down test, but full side resistance cannot be compared.

In summary, the Osaka tests suggest that the tip resistance mobilized during two O-cell tests in soil compare closely with that interpreted from a conventional top-down test of a similar shaft.

2.5.3.7 *Tests in Florida Limestone*

Knight, et al (1995). of the Florida DOT describe two projects in Florida in which both O-cell tests and top-down rapid loading tests are performed. All of the top-down tests were performed using the Statnamic device. Conventional static loading tests are not described in this paper. Tests were performed at a site near Tampa and another site in the Florida Panhandle. All of the shafts described are in Florida limestone, a notoriously variable bearing material that has solution cavities and extremely variable strength properties over small distances. Most of the tests described in this paper have complicating factors that preclude a direct comparison of results. In some cases the O-cell test failed the side shear of the socket without mobilizing full end bearing, in others the end bearing failed without mobilizing side shear. Only one of the rapid top-down loading tests fully mobilized the ultimate shaft capacity (which would require mobilizing both end bearing and side shear, since these are developed

simultaneously in a top down test). The authors described the highly variable nature of the limestone conditions in Florida, which suggests that even two shafts constructed very nearby are likely to have significantly different behavior. Side shear response in the limestone was also observed to yield in a very brittle fashion in some of the O-cell tests, an observation which suggests that multiple tests of a single test shaft in such material would be affected by load history.

The one test in which the Statnamic loading appeared to fully mobilize the shaft capacity was at the Gandy Bridge site near Tampa. This shaft was 1.2m (48 inches) in diameter with a socket extending about 4.6m (15ft) into limerock. The rapid loading of this shaft achieved over 25mm (1 inch) of peak displacement with a permanent set of around 7.6mm (0.3 inch) at the top of the shaft. Interpretation of strain gauge instrumentation suggests that an ultimate side shear resistance of around 1 MPa (11tons/ft²) was mobilized. An O-cell test was performed on a similar 1.2-meter (48-inch) diameter shaft about 3.7m (12ft) away. The O-cell test shaft encountered a layer of soft clayey soil within the intended “socket” and was interpreted to have an effective rock socket length of 3.2m (10.6ft). Tilting of the cell was noted during the test, suggesting an uneven resistance of either the socket or the base or both. The O-cell test indicated a maximum side shear of approximately 1MPa (11tons/ft²) at an upward movement of the socket of around 25mm (1 inch).

These results would appear to be in reasonably good agreement. However, caution should be exercised, as comparisons are difficult under such variable subsurface and construction conditions.

2.5.3.8 *Summary and Discussion*

Comparative large-scale field tests where top-down loading tests and O-cell loading tests to failure are extremely rare. Comparisons of top-down and O-cell loading from multiple tests on a single shaft by loading in opposite direction can potentially be misleading because of the influence of loading history; the initial loading influences subsequent loadings. Comparative tests from O-cell and top-down on identical test shafts are extremely rare and potentially influenced by spatial variability in subsurface conditions. Especially in variable geotechnical conditions such as those in Florida limestone, it is difficult if not impossible to isolate the influence of test methodology from other factors. For the limited data, which are available as described in the previous sections, it can be concluded that no compelling evidence exists that the O-cell test method results in systematic errors of a substantial magnitude.

Small details relating to construction appear to have the potential to influence capacity relating to direction of loading. For instance, a drilled shaft socketed into rock is commonly constructed using a temporary casing extending to the top of rock, followed by a change of tools and/or change of diameter in the as-built dimensions of the shaft. A top-down loading would be influenced by the bearing stress on this “shoulder” resulting from the change in diameter, whereas a bottom-up loading would lift the shoulder off of the rock surface. Common overbreak near the top of a hard stratum could produce a tapered geometry that would likewise result in greater axial load resistance from a top-down loading.

A rough sidewall within a rock socket could conceivably produce direction-dependent side shearing resistance. Some difference in the shape of a tool-induced groove within a rock socket could potentially result in a differing slope of the top side of the groove from that of the bottom side with a resulting difference in interface behavior. The author is aware of no such measure of small scale measurements of the actual interface structure, but the work of Hassan and O’Neill (1997) indicate the importance of the shape of asperities and interface geometry on the performance of rock sockets. It is also conceivable that any contamination that might be trapped within the recessed grooves of the side-

wall during concrete placement could result in a difference in contact bond strength or friction between the upper and lower surfaces of asperities at the rock/concrete sidewall.

A potentially significant consideration for drilled shaft rock sockets is the “Poisson’s Ratio Effect” in which the lateral strains resulting from compression in the shaft result in increased lateral stress at the shaft/rock interface and potentially may affect the bond stress at the interface. A top-down loading will produce greater axial compressive stress in the shaft as the base resistance is engaged, and the compressive stresses in the shaft will be greater in the upper portion of the socket. The bottom-up loading from the O-cell test will produce a lower overall axial stress in the shaft and this stress will be greatest at the bottom diminishing to near zero at the top. Thus, the “bulging” in the shaft due to the “Poisson’s Effect” will be less significant for the O-cell loading than will occur when an axial load is imposed from the top. This subject is addressed in the analytical portion of the report (see following sections), but has not been investigated through comparative field loading tests. Finally, it must be acknowledged that for cases of high capacity rock socket shafts, top down loading tests are extremely difficult and expensive to perform and this lack of conventional test data greatly restricts the opportunities for comparing such test results with those of O-cell tests.

The above discussion of potential differences between bottom up and top down loading is largely speculative, given the lack of systematic direct field comparisons between the two. Given the difficulties cited above in comparing the results of full scale field loading tests, there is a need for comparative field tests on test shafts which are carefully constructed at a site with relatively uniform conditions and a very thorough geotechnical site characterization. Ideally a site of weak rock or hard soil would be most suitable for such a study; the limited field data suggest that soft soil sites are less likely to have significant variations relating to direction of loading and drilled foundations are less likely to be utilized or subjected to large loading conditions in weak soil. Drilled shafts constructed on or within hard rock are likely to be controlled by structural considerations rather than axial capacity at the shaft/rock interface.

2.5.4 Finite Element Analysis

2.5.4.1 Introduction

A significant part of the Osterberg Load Cell research was directed toward a comprehensive model of the O-cell using the finite element technique. This effort was taken for the following, (i) to provide insight into the fundamental aspects of any potential differences between loading using the O-cell method and a conventional top down load, and (ii) to allow a parametric study of selected variables that may influence the testing results. The following sections provide a summary of the modeling work, with some of the details provided in Appendix A.

The current research utilizes the general purpose code ABAQUS for analysis. This code is widely used in many fields of engineering and is particularly powerful for nonlinear problems. MSC/Patran is used as a pre- and post-processor for generating the mesh and presenting results graphically. The finite element analysis involves modeling piles embedded in both soil and rock. A detailed parametric study was conducted on both models with a focus on the influence of each factor on the difference of the top down test and the O-cell test. Some field tests are included to verify the finite element model.

2.5.4.2 Previous Work

Many researches have utilized the finite element method for modeling the pile response; some of the relevant studies are reviewed in this section.

Osterberg and Gill (1973) reported a study of the load transfer mechanism for socketed pile in hard soils or rocks. A finite element model was built in a finite domain, where both pile and bearing medium were assumed to linear elastic. Both elastic and elasto-plastic analyses were performed. The bond between pile and bedrock was considered perfect in elastic analysis. While in elasto-plastic analysis, the interface was assumed to follow Mohr-Coulomb model. The author stated that the behavior of materials up to the normal working load was within the elastic range. A large part of the applied load was carried by the side shear in the top part of the shaft. The soft layer at the base of the pile had a little effect on load transferred by side shear. It was then concluded that the conventional design assumption regarding load transfer above the base of a socketed shaft was overly conservative.

Donald et al. (1980) presented a finite element analysis of rock socketed piles in Melbourne mudstone with an ultimate compressive strength of 3.0-10.0MPa. Both elastic and elasto-plastic analyses were conducted. However, the authors mainly discussed the parametric study for elasto-plastic solutions with three different rock models: $\phi = 0$ model, $c - \phi$ model and $c - \phi$ model with interface joint model.

In $\phi = 0$ model, yield started at the top and bottom of the shaft, followed by the yield of all the rock adjacent to the shaft. The rock below the pile tip yielded at last, leading to the difficulty of convergence. While in $c - \phi$ model, yield zone appeared at a larger stress compared to $\phi = 0$ case and developed continuously in rock around and below the pile without reaching the ultimate load capacity. But when the interface joint was considered in the analysis, the joint slipping began at a lower stress and increased steadily with the increase of the applied load. The authors also found different shear distribution along the pile for different rock models. The shear distribution in $\phi = 0$ case was relatively uniform with a higher value at both ends, which may be errors indicated by the authors. For $c - \phi$ model, the shear distribution was uniform at low applied stress, which was also true for $c - \phi$ model with interface joint. But at large stress level, the shear stress was much larger at the top of the pile for $c - \phi$ model, while it was still uniform when interface joint was added.

Rowe and Pells (1980) conducted a finite element method theoretical study of pile-rock socket behavior to analyze the factors affecting the response of an isolated socket. The finite element program ROSOC involved in the study allows strain-softening interface behavior. Therefore, the pile-rock interface behavior was modeled using Mohr-Coulomb failure criterion, but with a residual adhesion after slipping occurs, which was assumed to be zero in the study.

A series parametric study led the authors to a conclusion that the response of a socketed pile was dependent on L/D and stiffness ratio E_c / E_r . The authors presented that piles with a high stiffness ratio or low L/D exhibited a brittle response, as did the smooth sockets. For the typical degree of roughness, the response ranged from slightly brittle to plastic with some strain-hardening. It was also shown that 20-60% of the applied load was carried in end bearing for typical short piles with L/D=1 to 2.

Leong and Randolph (1994) presented the results of finite element analyses of the response of rock-socketed piles. The finite element model involved a mapped infinite element based on the inverse method to represent the unbounded domain. The pile-rock interface was modeled using six-node Goodman type joint elements. Both Mohr-Coulomb model and Leong and Randolph model were used to represent pile-rock interface behavior. Compared with Mohr-Coulomb model, Leong and Randolph model allowed gradual mobilization of peak friction and dilation. It also included

strain-softening behavior. The rock mass was considered to obey Mohr-Coulomb criterion with a shear strength and zero dilation.

The authors analyzed shaft response with and without intimate base contact. For side shear only sockets, a soft layer of elements with a modulus of $E_{soft} = 0.1E_m$ was placed right below the pile tip. It was found that in socketed piles with side shear only, the response showed strain-softening behavior. The average shear stresses were dependent on the embedded ratio L/D , the diameter of the pile D , and the ratio of concrete modulus to rock mass modulus E_c / E_m . The maximum mobilized average shear stress decreased with the increase of L/D and D . However, the pile-rock interface showed differing behavior for the Mohr-Coulomb and Leong and Randolph models. The Mohr-Coulomb model showed the same increased rate of normal stress and shear stress with slip, which is unrealistic. For Leong and Randolph model, the normal stress increased past the peak shear displacement, while the shear stress decreased after the peak shear displacement and reached a residual shear stress. In the sockets with both side shear and end bearing, the overall load response showed a strain-hardening behavior. However, the side shear component still displayed a strain-softening response with more plasticity because of the interaction of side shear and end bearing.

Hassan et al. (1997) performed an investigation of the side load transfer mechanisms of IGM (cohesive intermediate geomaterial) from elastic-plastic finite element analyses using the finite element code ABAQUS, which is the finite element program used in this study. The concrete shaft was assumed isotropic, homogeneous and elastic. An elastic-plastic model was used to model the IGM mass, and a nonassociate flow rule was employed for dilation. The IGM-concrete interface was modeled using Coulomb friction model.

The author investigated the side load transfer mechanisms of rough, smooth and smear IGM sockets respectively. For the rough IGM socket, the interface was idealized by sequential reverse curvilinear segments to form a sinusoidal profile of a long wavelength. The study showed that the initial normal interface stress has a significant influence on the behavior of both rough and smooth sockets. For rough sockets, the elastic phase of response extends as the normal stress increases. The maximum side shear f_{max} of smooth sockets increases with the increase of normal stress. The authors also drew a conclusion that the interface dilation has only a relatively small effect on the socket behavior.

It was suggested that failure be defined based on settlement for rough, long wavelength IGM sockets since large settlements tend to be associated with side shear failure. A relationship between f_{max} and IGM compressive strength q_u was also derived from parametric study. f_{max} increases with the increase of q_u and E_m because of the Poisson's effect in concrete. However, f_{max} is not influenced by the internal friction angle of IGM, which resulted in the direct relationship between f_{max} and q_u , making it possible to use a conventional α -factor approach for design.

Chua et al. (2000) performed a finite element analysis of drilled shafts in stiff soils using the program GEOT2D. A load test in Albuquerque, NM was evaluated using the finite element model to match the field measurement. In the analysis, the stress-strain response of soils was modeled by a hyperbolic stress-strain curve, which follows the following equation

$$\sigma_1 - \sigma_3 = \frac{\varepsilon}{\frac{1}{E_i} + \frac{\varepsilon}{(\sigma_1 - \sigma_3)_{ult}}} \quad (28)$$

where σ_1 and $\sigma_3 =$ the major and minor principal stress,
 $(\sigma_1 - \sigma_3)_{ult} =$ ultimate compressive strength,
 $\varepsilon =$ axial strain, and,
 $E_i =$ initial tangent modulus.

For the interface elements between the shaft and soil, the ultimate shear stress was expressed as $\tau_{ult} = c + \sigma_n \tan \phi$, and the shear stiffness was also a hyperbola that was related to the normal stress and the shear stress.

Based on the analyses, Chua and his co-workers proposed a design procedure that was especially suitable for stiff soils, for which case FWHA guideline was believed to be overly conservative. In this procedure, the ultimate shaft resistance was proportional to the effective overburden pressure, $f_{ult} = \beta \sigma_{ovr}$, where β was a function of internal friction angle of surrounding soil and depth. The ultimate end bearing pressure was defined corresponding to a top displacement of 5% of the shaft diameter, which was given by $q = K_b K_l \sigma_{ovr} |_{z=L}$, where $K_b = 10 - 0.07 D_R$ and $K_l = K_0 + (K_p - K_0)(1 + z)^{-0.5}$, and D_R is the relative density of the soil at the base of the shaft, K_0 and K_p are at-rest earth pressure coefficient and passive earth pressure coefficient respectively. It was shown that the design equation was consistent with the predictions using FWHA equations when the relative density was assumed to be about 35%.

Fellenius et al (1999) reported the use of FE analysis to model an O-cell test of a rectangularly shaped, 2.4m² cross section by 28m long barrette in a deep deposit of residual soil. This analysis was performed using an elastic-plastic soil with a thin (0.1m thick) layer of soil at the barrette/soil interface used in an attempt to model a slurry film at the interface. The FE model was back-calibrated to the results of the O-cell test (also utilizing some strain gauge data) in order to back fit effective-stress soil properties. Pore water pressures were taken as zero over most of the length of the foundation, as groundwater levels were at a depth of 26m. The FE model was then used to simulate a conventional top down test of the barrette. The authors conclude that there was generally very little difference between the computed unit side shear values for the two types of tests and no appreciable difference between the two methods of loading in the soils below the barrette.

McVay, Huang, and Casper (2001) have performed numerical simulations of O-cell and conventional static axial load testing in Florida limestone. These simulations include the use of a finite element code developed by the authors to model Florida limestone using an elastic-plastic constitutive model with a capped yielding (Drucker-Prager) surface and a tension cutoff. The FE model is an axisymmetric model with the shaft bound to the limestone without the use of a contact surface. Thus failure at the shaft/rock interface is exclusively modeled as failure of the rock material itself, a characteristic the authors thought to be representative of shafts in this rough limestone material.

Comparisons of this model between a top down loading and an O-cell loading lead the authors to conclude that the limiting side shear in the limestone was similar where failure occurs at the shaft/rock interface. Near the top of the rock socket in the upward loading case, a cone breakout failure was observed in which the failure propagated away from the shaft/rock interface to produce tensile failure in the surrounding rock. This condition results in lower "measured" side resistance from the O-cell loading compared to a conventional top down loading, but is always on the conservative side. The authors conclude that this condition is most influential for relatively short sockets with length/diameter ratios on the order of 1.75 or less.

2.5.4.3 Model Description

Schematic Figure 50 illustrates the brief diagram of the finite element model for both top down test and O-cell test. The geometry shown is used for all of the results presented in this report. The details of the model are described below.

Geometry and Element Type A two dimensional axi-symmetric model was used for both top down and O-cell load tests, which reduced the problem size thus the computing time significantly. A Fully integrated 4 nodes (first-order) quadrilateral axis-symmetric element type was used for both soil and pile.

As to the boundary conditions, a symmetric boundary condition was applied to the symmetric boundary, and only vertical displacement is permitted. At far side of the model (boundary far away from the shaft), horizontal pressure boundary condition was used. Horizontal pressure that is proportional to depth was applied to this boundary. By doing this, the in-situ ratio of horizontal to vertical stress may be controlled. At the bottom of the model, a rough contact surface was used. On this surface, friction can develop and no relative displacement will occur. This is used to prevent horizontal displacement of the bottom boundary.

Constitutive Model

1. Soil

An elastic-plastic (Drucker-Prager) constitutive model was used to simulate soil properties, which has Von Mises yield surface as its yielding criteria. The yield surface can be expressed as

$$F = t - p \tan \beta - d = 0 \quad (29)$$

where

d = cohesion;

β = friction angle;

$$t = \text{Octahedral shear stress, } t = \sqrt{\frac{1}{3}[(\sigma_1 - \sigma_2)^2 + (\sigma_2 - \sigma_3)^2 + (\sigma_3 - \sigma_1)^2]}; \quad (30)$$

$$p = \text{Octahedral normal stress, } p = \frac{1}{3}(\sigma_1 + \sigma_2 + \sigma_3). \quad (31)$$

Figure 51 shows the failure envelope in p-t plane. In this model, there is a regime of purely elastic response, after which some of the material deformation is not recoverable and can be idealized as being plastic. Plastic deformation within the soil mass has been modeled using an associative flow rule, which implies that dilation occurs during plastic yield. Note that these parameters are for a Drucker-Prager yield surface; they represent the angle of the shear surface and intercept of the octahedral shear stress with respect to the mean principal stress rather than the conventional Mohr-Coulomb relations (which work poorly for a three dimensional stress state).

2. Rock

Rock is modeled similarly to soil, but with a much higher stiffness. In general, the rock stiffness has important influence on the behavior of the rock/shaft interface with the strength properties of the rock mass of lesser importance. Both linearly elastic and Drucker-Prager models have been employed to simulate the behavior of the rock mass. Compared to the soil model, Drucker-Prager properties include much higher cohesion intercepts and stiffness.

3. Concrete Shaft

Concrete shaft was modeled as linear elastic material, with no plastic yielding of the concrete material.

Pile-Soil and Pile-Rock Interface The interaction surface between the pile and the soil was modeled as a frictional contact surface, which allows slip. When the shear stress on that surface exceeds some value, soil and pile will not stick with each other and slip will occur. Coulomb friction theory is used in the model so that maximum frictional shear stress on the interaction surface is proportional to the normal pressure by a friction coefficient. The failure envelope is shown in Figure 52a, where δ is the friction angle and the friction coefficient is $\mu = \tan \delta$. Once the shear stress exceeds the maximum frictional shear stress, slip will occur. For this friction model, an interface stiffness is applied to allow small relative deformation prior to slip, so the contact stiffness is not infinity even if slip is not developing. Note that there is no dilation associated with slip of the contact surface.

For the interface model between the shaft and rock, it is possible that the interface will include some adhesion bond as well as a greater roughness than a shaft/soil interface. A modified frictional model with cohesion, shown in Figure 52b, was applied to the interface between the pile and the rock. The maximum shear stress can be written as $\tau_{\max} = c_i + \sigma_{\text{contact}} \tan \phi_i$. A FORTRAN program was written to interact with ABAQUS, with two input parameters c_i and ϕ_i used to define the interface behavior.

Top Down Load Test In the top down test, load is applied to the top of the pile as a pressure load. The whole test was divided into three steps, which are described as follows.

Step 1: Apply gravity force, and at the same time, apply horizontal pressure on far side boundary with $K_0 = 0.43$ (normal consolidated);

Step 2: Add additional horizontal pressure for over-consolidated case, skip this step for normal consolidated case;

Step 3: Apply external load to the top of the pile.

In order to avoid residual stresses, the contact surface between soil and pile was modeled as frictionless in the first two steps so that the pile can settle down without any obstruction. In step 3, friction coefficient was changed to the desired value to provide side shear. In all cases, the end of step 2 is the base state of step 3, so this base state was deducted from the final results to get the response under the external load.

O-cell Load Test In the O-cell load test, O-cell was embedded close to the base of the shaft as a contact surface without thickness. O-cell pressure will generate forces with the same magnitude in opposite directions. The interaction between two parts of shaft was modeled as contact surface so that the load can be transferred between two parts of pile when gravity force was applied. Similar to the top down load test, there are three steps during calculation.

Step 1: Apply gravity force, and at the same time, apply horizontal pressure on far side boundary with $K_0 = 0.43$ (normal consolidated);

Step 2: Add additional horizontal pressure for over-consolidated case, skip this step for normal consolidated case;

Step 3: Apply O-cell pressure.

Similar to the top down load test, the friction coefficient of contact surface between soil and shaft is zero in the first two steps and changed to the desired value in the last step. Since the upper part of pile will move upward without any constraint after contact surface between soil and pile fails, soft springs were added to the top of the pile to allow a convergent solution as the load approaches and

exceeds the shaft uplift capacity. When dealing with the results, this soft spring force is deducted from the total load.

2.5.4.4 Comparison with Field Tests

In order to verify the finite element model, three well-documented field tests were simulated using the finite element model. The model results were compared with the field test results. Three test cases were collected from different states, including piles embedded in both soils and rocks. Each of the three cases involves an O-cell test. Accordingly, the O-cell finite element model was built for each case, and the corresponding top down test was simulated. The detailed description of each case can be found in Appendix A.

Henderson, NV Case (Loadtest, Inc., 1999) The test site mainly consists of very stiff sandy lean clay with gravel, with several silty sand layers. The test shaft was 1.5m (60in) in diameter and 12.2m (40ft) long, and the top of the shaft was 13.7m (45ft) below the ground surface. A detailed dimension and shaft instrumentation is shown in Figure 53. The O-cell was placed at 7.7m (25.2ft) below the top of the shaft, with the other 4.5m (14.8ft) shaft carrying the downward load.

During the test, the maximum applied O-cell pressure was 52.4MPa (7600psi), resulting in a load of 9.71MN (1980kips). The maximum mobilized upward and downward displacement was 22.9mm (0.9in) and 124.5mm (4.9in) respectively. The unit shaft resistance could be derived from the strain gage data, which was calculated as 51.7kPa (1.08ksf) from the top of the shaft to strain gage level 130kPa (2.72ksf) from strain gage level 3 to strain gage level 422kPa (8.83 ksf) from strain gage level 2 to O-cell, and 288kPa (6.02ksf) from O-cell to strain gage level 1.

A finite element model was built up to simulate the field test. The 13.7m (45ft) sand and clay layer above the top of the shaft was omitted in the modeling, but the overburden pressure was applied on the top of the mesh. Two different sets of interface properties were employed to the pile-soil interface. The following is a list of parameters used in the model.

Soil properties:

Young's modulus $E = 69MPa$ (10ksi)

Cohesion $c = 552kPa$ (80psi)

Friction angle $\phi = 0$

Pile-Soil interface properties:

Upper part shaft: Cohesion $c_i = 0kPa$

Friction angle $\phi_i = 27^\circ$

Lower part shaft: Cohesion $c_i = 0kPa$

Friction angle $\phi_i = 18.5^\circ$

The comparison of the load vs. displacement curve from measurement and the numerical model is shown in Figure 54. For the downward movement curve, the finite element model exhibits a somewhat stiffer behavior, apparently due to some compression of debris on the base during the actual field test. Both the finite element model and measurement have a similar average side resistance, although the measured side shear is somewhat stiffer.

The load transfer curve can be calculated from the strain gage data, which is shown in Figure 55. At the lower load level, the load transfer curve from both results match fairly well. The measured data indicate that somewhat more load is carried by the middle of the shaft (4.6m (15ft) to 7.6m (25ft) depth range) at large load levels than for the FE model.

With both measured results and model results, a comparison can be made regarding the maximum mobilized side shear at different depth intervals, as shown in Table 7. Also shown on this table are computed side shear values from the model using a top down loading instead of the o-cell bottom up loading. At the interval from gage 1 to O-cell and O-cell to gage 2, measured results have the largest value, which is 288kPa (6.02ksf) and 422kPa (8.83ksf) respectively. At the interval from gage 2 to gage 3 and gage 3 to the pile top, the top down test exhibit the largest value, 240kPa (5.03ksf) and 310kPa (6.49ksf) respectively. The distribution of maximum side shear resistance is altered by the direction of loading.

Figure 56 presents top down load vs. displacement relations derived from the O'cell test, and calculated by the numerical analysis. The results of this comparison demonstrate the ability of the finite element model used in this study with regards to capturing the main features of the o-cell load test performance.

Wilsonville, AL Case (Loadtest, Inc., 1994) The test shaft involved was 81.3cm (32in) in diameter and 5.6m (18.5ft) long. The test site consists of the approximately 0.3m (1ft) of fill, underlain by shale, which has a maximum compressive strength of 9.0MPa (1300psi). Groundwater was not encountered in the shaft. The detailed dimension and instrumentation is shown in Figure 57.

The load test was conducted on Feb. 9, 1994, about 26 hours after the placement of the concrete. The maximum applied O-cell load was 4.75MN (534tons) with an upward displacement of 16.8mm (0.66in) and a downward displacement of 60.6mm (2.38in). The maximum mobilized side shear was 747kPa (7.8tsf) from O-cell to gage 1, 412kPa (4.3tsf) from gage 1 to gage 2, 364kPa (3.8tsf) from gage 2 to gage 3, and 125kPa (1.3tsf) from gage 3 to gage 4 respectively.

The finite element model was built with the following properties.

Rock properties:

Young's modulus $E_{rock} = 414 \text{ MPa}$ (60 ksi)

Cohesion $c_{rock} = 1 \text{ MPa}$ (200 psi)

Friction angle $\phi_{rock} = 14^\circ$

Pile-rock interface properties:

Cohesion $c_i = 207 \text{ kPa}$ (30 psi)

Friction angle $\phi_i = 50^\circ$

Figure 58 shows the load-displacement curve from both field test and model calculation. The computed and measured downward displacements match fairly well. For the upward displacement, the finite element model yields at a slightly lower maximum shear stress and appears more brittle; this could be because dilatancy was not included in the model of the pile-rock interface. However, the failure load is about the same at which the side resistance was failed.

The comparisons of the derived load transfer curve at different load levels are presented in Figure 59. Note the load was calculated from the vertical strain data as been done in the field test. The two curves match well at low load level, but at large load level, the finite element model exhibits lower side shear close to the bottom of the shaft. This can also be observed from the comparison of the unit shaft resistance at gage intervals, as shown in Table 8. This reduction in side shear at failure in the model appears to be related to opening of the contact nodes at the end of the socket adjacent to the o-cell.

With both measured results and model results, a comparison can be made regarding the maximum mobilized side shear at different depth intervals, as shown in Table 9. At the interval from the O-cell to gage 1, measured results have the largest value, which is 747kPa (7.8tsf). While at the interval from gage 1 to gage 2 and gage 2 to gage 3, there is no much difference among three results, with

an approximate value of 383kPa (4.0tsf). However, at the interval of gage 3 to gage 4 (the top part of the shaft), the top down test exhibit the largest value 431kPa (4.5tsf) as expected. Figure 60 presents top down load vs. displacement relations derived from the O-cell test and calculated by the numerical analysis.

Denver, CO Case (Loadtest, Inc., 1998) The test site consists of a layer of 3.0m (10ft) sandy lean clay, overlying weathered clystone with silty sand and fined grained seams. The detailed shaft information and instrumentation is show in Figure 61. The nominal shaft diameter was 106.7cm (42in). The top 1.37m (4.5ft) of the test shaft was in the clay layer, and the socket length was 5.26m (17.25ft).

The test was carried out on Jan 14, 2002, with a maximum load of 2.5MN (559kips). At this load level, the total upward movement was 40.1mm (1.58in), and the downward movement was 58.4mm (2.30in). The unit side shear was calculated as 52kPa (1.08ksf) from the top of the shaft to strain gage 126kPa (2.63ksf) from strain gage 2 to strain gage 1, and 168kPa (3.51ksf) from strain gage 1 to the O-cell level.

It should be noticed that 1.4m (4.5ft) of the test shaft was in the clay soil layer. Therefore, in the finite element model, the interface properties used for at the pile-clay interface are different from those at the pile-rock interface, which is much weaker. The pile-clay interface was assumed to have 34kPa (5psi) resistance. The 1.8m (6ft) deep clay above the top of the shaft was neglected in the finite element mesh, but its influence on the overburden pressure was considered. In the finite element model, 30.2kPa (4.375psi) vertical pressure was applied on the top of mesh. The following is a list of parameters used in the model.

Rock properties:

Young's modulus $E_{rock} = 276MPa$ (40ksi)

Cohesion $c_{rock} = 345kPa$ (50psi)

Friction angle $\phi_{rock} = 10^\circ$

Pile-rock interface properties:

Cohesion $c_i = 66.2kPa$ (9.6psi)

Friction angle $\phi_i = 31^\circ$

Pile-clay interface properties:

Cohesion $c_i = 34.5kPa$ (5.0psi)

Friction angle $\phi_i = 0$

The comparison of the load vs. displacement curved from both field test and finite element model is shown in Figure 62. It is again shown that the two downward movement curves fit very well, but the finite element model appears stiffer in uplift than the field test although the failure load is about the same for both cases.

Similar to the real test, the strain information can be used to calculate the side load transfer and then estimate the unit shaft resistance. Figure 63 shows the load transfer curves at different load levels. Similar to Wilsonville case, the two side load transfer curves match well. However, when the applied load increases, the difference between field test and finite element model is becoming larger. The derived unit shaft resistance was summarized in Table 10. Again the finite element models shows a lower unit side shear at large load level because some contact nodes became open and could not contribute to the side resistance.

Figure 64 presents top-down load vs. displacement relations derived from the O-cell test and calculated by the numerical analysis. Presented in Table 11 is a comparison of the mobilized side shear from the measurement, finite element O-cell test model and top down test model. For the O-cell

test, the maximum mobilized side shear occurs at the bottom of the shaft from both measurement and model results. For the top down test, the maximum side shear occurs at the top of the rock socket since the overlying clay layer has weaker interface properties.

Summary Three field tests were compared with the finite element model. Generally, the downward displacement curves and the maximum side shear in uplift can match the measured results fairly well. For the upward displacement curve differences in stiffness were sometimes observed, even when the maximum values of unit side shear were close. These differences may be related to dilatancy of the pile-rock interface, which is not captured in the finite element model.

2.5.4.5 *Summary of the Soil Model Study*

This section summarizes the significant findings of the soil model. The detailed soil model results are presented in Appendix A. Various cases regarding different in-situ horizontal stress ratio were performed, and the difference between the top down test and the O-cell test was analyzed.

Properties Common to All In the soil model, the concrete shaft is 0.9 m (3 ft) in diameter and 9.1 m (30 ft) long. For the O-cell load test, the Osterberg load cell is embedded 0.9 m (3 ft) above the bottom of the shaft with zero thickness. The following is a list of properties used in the analysis if not specified.

Concrete shaft: $E = 34,473 \text{ MPa}$ (5,000 ksi), $\nu = 0.3$;

Soil: $E = 97 \text{ MPa}$ (14 ksi), $\nu = 0.3$, $\beta = 31^\circ$, $d = 55 \text{ kPa}$ (8 psi);

Rock: $E = 9,653 \text{ MPa}$ (1400 ksi), $\nu = 0.3$;

Pile-Soil Interface: $\delta = 31^\circ$.

In calculation, soil was modeled as fully associated, which means the dilation angle equals the friction angle.

Results for Soil Models Presented on Figure 65 are the computed load vs. deflection comparisons for the four cases analyzed involving shafts embedded within soil. Note that this soil is representative of a fairly competent material with significant cohesion such as a cemented sand or stiff silty clay. Figures 65a-c illustrate cases with an extreme range of in-situ horizontal stress ratios ranging from $K_o = 0.43$ to 2.0; case (b) with $K_o = 1$ is likely to be more representative of typical conditions in stiff or dense soil. These data suggest that the O-cell method tends to produce excellent comparisons for the cases where K_o was relatively low and tends to be increasingly conservative as K_o becomes large. Note that for these cases, failure tended to be at the frictional interface between the shaft and soil. Figure 65d illustrates the case for $K_o = 1$ but with a much increased interface friction so that the failure tended to be in the adjacent soil elements over much of the length of the shaft. This case indicated a somewhat closer agreement than the similar case (b) with a smaller interface friction angle although still slightly conservative.

An examination of the differences in behavior is instructive, and will be focused on the $K_o = 1$ case for purposes of this discussion; details of all of the other runs are provided in Appendix A. Presented on Figure 66 are comparisons of the load vs. deflection for tip resistance and side shear for the case of $K_o = 1$, interface friction $\delta = 31^\circ$. The tip resistance from the two loading conditions is seen to be nearly identical, with the O-cell loading somewhat conservative in the side shear with respect to the top down loading. Thus, almost all of the differences between the top down and O-cell loading is attributed to differences in side shear from pushing up vs. pushing down.

The differences related to load direction appear to be related to differences in the normal stresses on the shaft/soil interface related to direction of loading. Presented on Figure 67 are plots of the stress history at selected nodes along the interface for the two cases with $K_o = 1$; Figure 67a pre-

sents the results for interface friction $\delta = 31^\circ$, Figure 67b presents the results for $\delta = 50^\circ$. The normal stresses at the interface are seen to decrease slightly for the upward directed (O-cell) loading, while normal stresses tended to remain almost constant or increase slightly for the top down loading. The result of these differences in normal stress is most notable for the $\delta = 31^\circ$ case, where the initial contact with the yield surface is shifted slightly to the right and thus mobilizes a higher shear stress at yield. Note that the yield surface in this case is clearly represented by the $\delta = 31^\circ$ line, indicating failure at the frictional interface. For the $\delta = 50^\circ$ case, the differences are much smaller and the yield surface at failure corresponds to the shear strength properties of the soil rather than the interface for all except the most shallow depth. Note the indication of cohesion by the points tracking on the yield surface. Only the 1.5m (5ft) depth for the O-cell loading appears to contact the $\delta = 50^\circ$ line. Thus the failure in the soil is indicated and the cohesive nature of the soil makes differences in normal stress at the interface much less significant.

Preliminary Results for Linear Rock Model with Frictional Interface The model used for the rock case uses the same mesh as described previously with the upper 4.6m (15ft) composed of soil as in previous models ($K_o = 1$, $\phi_i = 31^\circ$) and the material below the 4.6m (15ft) depth composed of rock. With the O-cell placed at 0.9m (3ft) above the base, the effective socket length tested is therefore 3.7m (12ft), with a length/diameter ratio of 4. The rock includes a frictional interface with a relatively high friction angle between the shaft and rock of $\phi_i = 50^\circ$, with the rock considered to be a sufficiently strong material to force failure at the interface. Thus, this model includes no provisions for “cone breakout” as was the case in the models analyzed by McVay et al. (2001). For the top down loading, a “soft base” was constructed by defining a row of elements immediately below the tip of the shaft to have a very low modulus. This approach is considered similar to that which would be used to conduct a full-scale physical test in the field in which a compressible material might be placed into the base of the shaft excavation. For both the top down and O-cell loading case models, only failure in side shear is observed.

Presented on Figure 68 is a plot of the load in side shear vs. displacement for the top down and O-cell loadings of the rock-socketed drilled shaft. Note that the O-cell loading is seen to be relatively conservative for this condition in terms of overall side shear capacity. More insight into the behavior in these FE models is available from the shear stress data plotted vs. depth along the shaft on Figure 69. Normal stresses follow an identical pattern. These data suggest that the relative distribution of side shear along the shaft is quite dramatically different between the two loading cases, even though the average might be reasonably similar. In each case the highest shear stresses coincide with the highest normal stresses, which in turn are biased towards the end of the rock socket, which is feeling the most intense axial load in the shaft. The magnitude of this effect is related to the Poisson’s ratio in the shaft and rock; in soil the modulus of the soil is so much lower that the Poisson’s effect is insignificant. In this case the modulus of the rock was around 28% of the shaft concrete modulus and the effect is quite dramatic.

It is thought that there are a number of case histories of O-cell loading in which strain gauges indicate a strong bias of higher unit side shear in the portion of the socket nearest the O-cell. This pattern is consistent with the behavior observed in this model. More investigation of such case histories is warranted.

Note that this pattern of shear stress in a rock socket is associated with a frictional shaft/rock interface. If the failure mode of the socket in side shear is better represented by a shearing failure through a material which is considered to have strength that is independent of the confining stress, the pattern of maximum side shear stress would tend to be more uniform at failure. Further investigation

of this behavior is warranted, although it is considered by the writer that the confining stress plays a strong role in the maximum shear stress, which can be developed (even concrete strength is strongly influenced by confining stress).

Summary The FE analysis of a limited range of conditions suggests that the O-cell method of load testing is likely to be conservative in estimating shaft capacity under most instances with respect to conventional top down load testing techniques. The most significant differences relate to the side shear response of the shaft to upward directed loading in lieu of downward directed loading. The relative difference is small in instances where side shear is dominated by cohesion in the soil or where the ratio of horizontal to vertical stress (K_0) in the soil around the shaft is small. Relative differences are more significant in cases where K_0 is high and in rock sockets where the rock modulus is of the same order of magnitude as the concrete modulus and the side shearing resistance is influenced by the normal stress at the shaft/rock interface.

2.5.4.6 *Summary of the Rock Model Study*

This section of the report describes the detailed FE parametric study regarding several factors believed to have significant influence on the behavior of shafts embedded in rock. The ratio of the average mobilized side shear from a top down loading and from the O-cell loading is examined in order to evaluate potential differences between the two testing methods. The effect of different geometric and material parameters on this ratio is examined and summarized in this section, with details provided in Appendix A.

Properties Common to All In the rock socket pile model, the shaft is identical to that used in the soil model described previously. Analyses are performed with a 4.6m (15ft) thick dense sand layer overlying the rock layer of interest. The O-cell is placed at the tip of the pile to load the base resistance against the side shear. Unless otherwise specified, the properties for soil, rock, concrete pile and the interface are listed as below.

Concrete shaft: $E = 34,473\text{MPa}$ (5000ksi), $\nu=0.3$;

Soil: $E = 97\text{MPa}$ (14ksi), $\nu=0.3$, $\beta = 31^\circ$, $d = 55\text{kPa}$ (8psi);

Rock: $E_{rock} = 483\text{MPa}$ (70ksi), $\nu=0.3$, $\phi_{rock} = 20^\circ$, $c_{rock} = 1,379\text{kPa}$ (200psi);

Pile-Soil Interface: $\delta = 31^\circ$;

Pile-Rock Interface: $\phi_i = 31^\circ$, $c_i = 138\text{kPa}$ (20 psi).

Rock Model Results Several parameters are believed to have significant influence on the pile response. The influences of seven factors were examined in the analysis, including embedded ratio L_{socket} / D , rock modulus E_{rock} , rock cohesion c_{rock} , dilation angle of rock mass ψ_{rock} , interface friction angle ϕ_i , interface cohesion c_i , and in-situ horizontal stress ratio K_0 . The difference between the top down test and the O-cell test is represented by a ratio of the average mobilized side shears in both tests, $(f_{rock})_{td} / (f_{rock})_{oc}$.

The dilation angle of rock was observed to have almost no effect on the pile response, primarily because failure of the socket in side shear was generally dominated by interface properties. Two different cases were performed, one with fully associated flow rule (the dilation angle equals to the friction angle), the other with non-associated flow rule (the dilation angle is zero). Almost no difference was found for side resistance, with small difference for end bearing; the model with dilation shows a little stronger behavior of the end bearing. The two cases result in the side shear ratio $(f_{rock})_{td} / (f_{rock})_{oc}$ of 1.29 for non-associated flow rule and 1.30 for associated flow rule.

Presented on Table 12 is a summary of the average mobilized side shears in both tests and the difference between the two testing methods for the influence of interface friction angle ϕ_i , rock modulus E_{rock} , interface cohesion c_i , rock cohesion c_{rock} , length to diameter ratio L_{socket}/D , and K_o . The effect of each factor on the average mobilized side shear and the difference between two testing methods is presented. In general, the O-cell testing results are conservative compared with the top down test results for all cases since the mobilized side shear in the O-cell test is always smaller than in the top down test.

It is observed from Table 12 that all six factors have significant influence on the pile response. The mobilized side shears from both the top down testing and the O-cell testing increases with the increase of E_{rock} , c_{rock} , ϕ_i , c_i and K_o . But E_{rock} and ϕ_i exhibit the most significant influence. For instance, for $\phi_i = 31^\circ$ case, the average side shear increases 71% for the top down test and 18% for the O-cell test respectively when E_{rock} increases from 483MPa (70ksi) to 4,826MPa (700ksi). When $E_{rock} = 783\text{MPa}$ (70ksi), the average side shear increases 47% for the top down test and 33% for the O-cell test respectively when ϕ_i increases from 31° to 50° . The effect of c_i appears to be uniform. The difference between two adjacent cases is close to 69kPa (10psi) (the difference of c_i), but with a lower value for the O-cell test. It should be noticed that the influence of c_{rock} is not very substantial. The increase of the average side shear is only about 8% for the top down test and 20% for the O-cell test when the rock was considered as elastic (corresponding to a c_{rock} of infinity) instead of using Drucker-Prager model with $c_{rock} = 1.38\text{MPa}$ (200psi). The influence of K_o is significant since it can change the contact pressure at the pile-rock interface, which will then result in the change of the maximum side shear. However, for the embedded ratio L_{socket}/D , although it can improve the pile capacity, the unit side shear doesn't change very much for the top down test unless it is large enough. But for the O-cell test, there's no much difference in the average side shear with a little decrease for larger L_{socket}/D case. For example, when L_{socket}/D increases from 5 to 10 for $\phi_i = 50^\circ$ case, the side shear from the top down test increases approximately 15%, but no significant change was found for the side shear from the O-cell test.

Figure 70 illustrates the effect of E_{rock} on the load vs. displacement behavior from the top down test. It is shown that the increase of rock modulus can greatly improve the pile response. For instance, to mobilize 7.6mm (0.3in) displacement, the required load for $E_{rock} = 483\text{MPa}$ (70ksi) case is about 5.8MN (1300kips), while for $E_{rock} = 4,826\text{MPa}$ (700ksi) and $E_{rock} = 48,263\text{MPa}$ (7000ksi) case, it is up to 10.7MN and 20.0MN (2400kips and 4500kips) respectively. Note $E_{rock} = 48,263\text{MPa}$ (7000ksi) case is not very realistic because the rock modulus is even greater than the modulus of the concrete, which will cause some dramatic behavior. It is also indicated that the mobilized displacement for $E_{rock} = 48,263\text{MPa}$ (7000ksi) case is very small, part of which is induced by the compression of the concrete pile.

Presented in Figure 71 is the effect of E_{rock} on side load vs. displacement curve and tip load vs. displacement curve derived from the top down test. For $E_{rock} = 4,826\text{MPa}$ (700ksi) and $E_{rock} = 48,263\text{MPa}$ (7000ksi) case, the side load vs. displacement curve does not show a peak value like $E_{rock} = 483\text{MPa}$ (70ksi) case, but exhibiting a strain-hardening behavior. Therefore, it's quite difficult to estimate the side load at yielding or failure. It was found that the maximum side load occurs at a displacement of 5.1-7.6mm (0.2-0.3in) for most of the cases performed in which the peak side load exists, so it's reasonable to choose the side load at which a 5.1-7.6mm (0.2-0.3in) displacement is mobilized as the failure side load. Figure 71(b) shows that the rock modulus has a significant effect on the tip load vs. displacement curve. Much stronger end bearing behavior was observed for $E_{rock} = 48,263\text{MPa}$ (7000ksi) case. The maximum tip load was found about 10.2MN (2300kips) with a mobilized displacement of only less than 3.8mm (0.15in). Comparing Figure 71(b) and Figure 70 indicates

that for $E_{rock} = 48,263\text{MPa}$ (7000ksi) case, most of the displacement at the pile top is induced by the compression of the concrete pile.

The same trend can also be found from the O-cell testing results, as shown in Figure 72. Both side resistance and end bearing resistance can be improved a lot with the increase of the rock modulus, especially when the rock modulus increases from 4,826MPa to 48,263MPa (700ksi to 7000ksi). The maximum applied O-cell pressure for three cases is 4,688kPa, 4,826kPa and 6,550kPa (680psi, 700psi and 950psi) respectively. But no significant downward movement was mobilized except for $E_{rock} = 483\text{MPa}$ (70ksi) case.

The comparison of the side load vs. displacement curve between two testing methods for three cases is shown in Figure 73. The $E_{rock} = 4,826\text{MPa}$ (700ksi) case and $E_{rock} = 48,263\text{MPa}$ (7000ksi) case are very similar in the side load vs. displacement curves from both tests except that less displacement has been mobilized for $E_{rock} = 48,263\text{MPa}$ (7000ksi) case. For these two cases, the two curves match well before yielding, but the O-cell test gives a much lower side resistance as observed before. While for $E_{rock} = 483\text{MPa}$ (70ksi) case, the O-cell test appears stiffer before failure, but it still results in a lower side resistance. The average side shear mobilized at the pile-rock interface can be then calculated as shown in Table 12.

Similar study has been done with regard to the influence of ϕ_i . Shown in Figure 74 is the comparison of the load-displacement curves from top down test. It is obvious that larger friction angle results in stronger pile-rock system. More insight into the effect of the frictional on the top down testing method can be found from side load vs. displacement curve and tip load vs. displacement curve, as presented in Figure 75. Figure 75(b) indicates that there's little difference in tip load vs. displacement curve, but the difference in side load vs. displacement curve is significant as shown in Figure 75(a). The maximum side forces are 10,149MPa, 6,991MPa, and 5,102MPa (1472kips, 1014kips, and 740kips) for $\phi_i = 50^\circ$, $\phi_i = 31^\circ$, and $\phi_i = 14^\circ$, respectively. The three cases show the same pattern of side shear response. A maximum side force is obtained at a displacement of between 5.1-7.6mm (0.2-0.3in), after which the side force decreases somewhat to a residual value showing a strain-softening behavior.

The comparison of the load vs. displacement curve from O-cell test is shown in Figure 76. Similar to the top down test, there's almost no difference in O-cell load vs. downward displacement curve. However the difference in O-cell vs. upward displacement curve is significant. The maximum applied O-cell pressure for three cases is 7,584kPa, 5,860kPa and 4,688kPa (1100psi, 850psi and 680psi), respectively. It is again concluded that the friction angle at pile-rock interface has almost no influence on end bearing, but has substantial effect on side resistance.

Figure 77 presents the comparison of side load vs. displacement curve for three cases. All three cases show the similar behavior, with O-cell testing results conservative comparing with the top down testing results. But before failure, the O-cell test gives a stronger behavior than the top down test. The comparison of the difference between the top down testing and the O-cell testing can be derived as shown in Table 12.

Difference Between Top Down Test and O-cell Test It was found that the most important factors that affect the difference between the two testing methods, are E_{rock} and ϕ_i . The influences of the other factors on the difference of the two testing methods are not very significant compared with E_{rock} and ϕ_i .

The influences of E_{rock} and ϕ_i are presented in Figure 78. It is shown that the increase of E_{rock} or ϕ_i will result in the higher $(f_{rock})_{td}/(f_{rock})_{oc}$ ratio. Therefore, for cases with hard rock with a very rough surface, judgment should be made when using the O-cell test results for foundation design. It

was also found that the effect of ϕ_i is more considerable if Young's modulus of rock is larger. Similarly the effect of the rock modulus is more significant if rock surface is rougher.

Side Shear Distribution More insight regarding the side shear distribution can be found from Figure 79 and Figure 80. Note that z is the depth below the top of the socket (15ft deep) and L_{socket} is the socket length, which is 4.6m (15ft). The shear stress distribution is represented by the ratio of the shear stress at any depth to the average shear stress, which was calculated from the procedure described in Appendix A.

Figure 79 shows the difference of the shear stress distribution along the pile length between the top down test and the O-cell test for $E_{rock} = 483\text{MPa}$ (70ksi) and $E_{rock} = 4,826\text{MPa}$ (700ksi). It appears that the shear stress distribution is more uniform with a lower rock modulus especially for the top down test. The result from the top down test for $E_{rock} = 483\text{MPa}$ (70ksi) case shows that the ratio of the shear stress to the average shear stress is very close to 1.0 at the depth with a z/L_{rock} of 0.2 to 0.9. While for $E_{rock} = 4,826\text{MPa}$ (700ksi) case, the distribution is more varied. It is shown again the difference of shear stress distribution between the two testing methods. For the top down test, the maximum shear stress occurs at the top of the socket, but for the O-cell test, the maximum side shear occurs close to the O-cell.

Shear stress distribution for different ϕ_i values is shown in Figure 80. It is again indicated that the shear stress has a larger value at the top of the socket for top down test, but for O-cell test, the shear stress has a larger value close to the O-cell. The contact nodes at the bottom tend to be open for both tests. The comparison of the three sets of curves indicates that for a lower interface friction angle case, the shear stress distribution is more uniform for both top down test and O-cell test. However, for larger interface friction angle case, for example $\phi_i = 50^\circ$, the distribution is more diverse. The ratio of the shear stress at the top of the socket to the average shear stress is about 4.0, which is only about 1.7 for $\phi_i = 14^\circ$ case.

Summary and Conclusions For the top down load test, the pile response suggests that side resistance is mobilized before the end bearing, and the side load vs. displacement tends to exhibit a strain-softening behavior with a peak value occurring at a displacement of 5.1-7.6 mm (0.2-0.3 in) for most cases. The end bearing is mobilized after the failure of the side shear. But for some strong cases, such as large rock modulus case, the side load response shows a strain-hardening behavior, which is due to the larger contact pressure developed at the pile-soil interface.

It has been found that little difference can be induced by different dilation angle of the rock Ψ_{rock} . But other six factors, including pile-rock interface friction angle ϕ_i and cohesion c_i , Young's modulus of rock E_{rock} , cohesion of rock c_{rock} , embedded ratio L_{socket}/D , and the stress ratio K_o , have considerable influence on the pile response in both top down test and O-cell test. However, E_{rock} and ϕ_i were found to have most significant influence.

The results of these analyses suggest that there may be inherent differences between loading from the bottom up in the O-cell test and loading from the top down due to differing normal stress conditions at the interface. These differences are amplified at increasing values of rock modulus E_{rock} and interface friction ϕ_i .

High values of rock modulus tend to produce greater increases in normal stress at the interface. These must be due to Poisson's ratio effects in the shaft, since dilation at the interface was zero in the model. At high values of E_{rock} , the rock socket offers greater resistance to this bulging in the shaft. The Poisson's ratio effect is more significant for a top down loading than for an O-cell loading because the base resistance is engaged during the top down and thus the average vertical stress in the shaft (which produces the bulging effect) is higher in this case. Note that the O-cell loading tends to

underpredict maximum side shear in this case and is thus conservative when used to indicate side shear capacity of a rock socket.

The effects described above only matter if the interface is treated as a frictional surface where the shearing resistance is influenced by normal stresses. Thus, the interface friction ϕ also is of significant influence. With higher values of interface friction, the effect of higher normal stresses in a top down loading vs. an O-cell loading are more significant. Again, the O-cell loading is seen to be conservative and underestimate side shear as interface friction is a more significant contributor to side shear resistance.

2.5.5 A Simplified Analytical Solution for the consideration of Poisson's Effect in a Pile

2.5.5.1 Overview

In order to evaluate the relative effect of the “bulging” of an axially loaded shaft on the side shear capacity at the interface (see section 2.5.3), a simplified analytical solution has been derived. The derivation of this model is described, followed by an examination of the potential effect on the axial response and those conditions for which this effect might be important.

2.5.5.2 Model Description and Derivation of Solution

A simplified closed form equation is derived based on the Hooke's law for a cylindrical column of elastic material (the shaft) and cavity expansion theory for the surrounding rock.

As illustrated in Figure 81, for purposes of relating radial strains to radial interface stress the soil or rock is represented by a linear elastic, isotropic, and homogeneous mass which can be characterized by two parameters, Young's modulus E_s and Poisson's ratio ν_s . The concrete pile is represented as an elastic cylinder with a Young's modulus E_p and Poisson's ratio ν_p . The interface between the shaft and rock is modeled as a contact surface, which may have both cohesion (bond strength independent of normal stress) and friction, in accordance with the familiar Mohr-Coulomb model,

$$f_{\max} = c_i + \sigma_r \tan \phi_i \quad (32)$$

where c_i = cohesion of the interface; and ϕ_i = internal friction angle.

The radial stress σ_r is computed as follows:

$$\sigma_r = K_0 \sigma_v + K_r \sigma_z \quad (33)$$

where K_0 is the ratio of horizontal stress to vertical stress at rest (prior to axial loading), σ_r is the overburden pressure, σ_z is the applied vertical stress in the shaft due to the axial loading, and K_r represents the ratio of the radial stress at the interface to the applied vertical stress in the pile. The latter terms represent the Poisson's ratio effect in which the vertical stress changes in the shaft produce radial strains in the socket and thus radial stress at the interface. Note also that $K_0 \sigma_v$ represents the starting condition of interface stress and may be controlled by the fluid concrete pressures during concrete placement (as is assumed in some of the FHWA design procedures, O'Neill and Reese, 1999).

The relation between radial strain in the rock socket and radial stress can be described using the well established theory for expansion of a cylindrical cavity, as is commonly used for interpretation of pressuremeter tests (Baguelin, 1978). The radial stress at the wall of the cavity can be written as;

$$\sigma_r = \sigma_{r0} + 2G\varepsilon_r \quad (34)$$

where

- σ_{r0} = initial radial stress,
- G = shear modulus of soil,
- ε_r = radial strain.

The incremental radial stress is proportional to the incremental radial strain, $\Delta\sigma_r = 2G\Delta\varepsilon_r$. Rewriting this equation in terms of incremental radial strain leads to

$$(\Delta\varepsilon_r)_s = \frac{\Delta\sigma_r}{2G_s} = \frac{\Delta\sigma_r(1 + \nu_s)}{E_s} \quad (35)$$

The radial strains in the pile can be described according to Hooke's law, as

$$(\Delta\varepsilon_r)_p = \frac{1}{E_p}[\Delta\sigma_r - \nu_p(\Delta\sigma_z + \Delta\sigma_\theta)] \quad (36)$$

For this axi-symmetric problem (similar to a triaxial test specimen), the stresses in the r and θ direction are the same. So Equation (36) becomes

$$(\Delta\varepsilon_r)_p = \frac{1}{E_p}[(1 - \nu_p)\Delta\sigma_r - \nu_p\Delta\sigma_z] \quad (37)$$

The radial strains in the pile and soil must be equal in quantity, but with the opposite sign. Therefore,

$$-(\Delta\varepsilon_r)_s = (\Delta\varepsilon_r)_p \quad (38)$$

$$-\frac{\Delta\sigma_r(1 + \nu_s)}{E_s} = \frac{1}{E_p}[(1 - \nu_p)\Delta\sigma_r - \nu_p\Delta\sigma_z] \quad (39)$$

Equation (39) results in a relationship between the change of the radial stress and the vertical stress, which can be represented as the following equation,

$$\Delta\sigma_r = \frac{E_s\nu_p}{E_p(1 + \nu_s) + E_s(1 - \nu_p)}\Delta\sigma_z = \frac{\nu_p/(1 - \nu_p)}{1 + (E_p/E_s)(\frac{1 + \nu_s}{1 - \nu_p})}\Delta\sigma_z \quad (40)$$

So the ratio of the radial stress at the interface to the applied vertical stress in the pile, K_r is obtained from Equation (40) as $\Delta\sigma_r/\Delta\sigma_z$

$$K_r = \frac{\nu_p/(1 - \nu_p)}{1 + (E_p/E_s)(\frac{1 + \nu_s}{1 - \nu_p})} \quad (41)$$

Note that K_r is dependent on the properties of both pile and surrounding soil. The maximum shear stress can now be expressed as

$$f_{\max} = c_i + (K_0\sigma_v + K_r\sigma_z)\tan\phi_i \quad (42)$$

2.5.5.3 Stress Coefficient K_r

The simple analytical model described above provides a means of comparing the effect of Poisson's ratio in the pile on the side shearing resistance of a frictional interface. This is obviously a simplified model, and does not include any effect of dilatancy at the interface as side shear is fully engaged. Nevertheless, the model is useful in identifying those conditions for which the Poisson's ratio effect might be significant.

The effect of the pile/soil modulus ratio E_p/E_s appears to be the most significant factor influencing the parameter K_r . The relative influence of modulus ratio on K_r is illustrated on Figure 82 for two different values of ν_p . Poisson's ratio for soil is $\nu_s = 0.3$ for both cases, although ν_s has relatively little effect. For a typical value ν_p of 0.2, this equation suggests that as the soil or rock modulus exceeds 1/10 that of concrete (modulus ratio of 10), K_r becomes significant. For these cases, the applied vertical pressure contributes significantly to the radial stress resulting in an important increase of side shear resistance. For a relatively high modulus ratio typical of soil, $E_p/E_s = 1000$ indicates $K_r = 0.00023$; this low value suggests that the Poisson's effect in the shaft is negligible for such conditions. These results are consistent with the results from the finite element analysis where cases with a high E_p/E_s computed greater difference between the O-cell testing method and the top down testing method than cases with a low E_p/E_s .

2.5.5.4 Comparison of Top Down and O-Cell Loading

A simple spreadsheet is useful to model the behavior of a rock socket using the equations derived above. A shaft is subdivided into short segments and incremental calculations are performed on each segment as indicated in Figure 83.

For the O-cell loading at maximum load, the mobilized base resistance is input as the load in the bottom segment of the shaft. The load on each subsequent segment above the bottom is calculated from

$$Q_{i+1} = Q_i - W - f \cdot (\pi D \Delta z) \quad (43)$$

where W is the self weight of the pile segment, f is the unit load transfer, πD is the circumference and Δz is the length of the segment. The unit load transfer f is computed using equation (42) with the radial stress at the shaft/rock interface determined from the axial stress in the shaft, σ_v and K_r determined from the modulus ratio according to equation (41). The interface strength parameters, c_i and ϕ_i are adjusted so as to back-match a test condition where the load at the top of the socket would be zero (or equal to the dead weight above the socket or a known load condition determined from instrumentation). Note that for a given test condition, the interface strength parameters back-calculated in this manner represent mobilized strength properties at the input O-cell loading. Since two parameters are fitted to the test data in this manner, the solution is not unique; however, strain gauge data may be utilized to provide constraints on the back-match to a test condition. Note also that the practice of reporting a single value of unit load transfer along a shaft is tantamount to assuming $\phi_i = 0$ and effectively removes any effect of radial stress at the interface.

After back-analysis of the O-cell loading, the top down loading condition is modeled similarly except that the load is calculated from the top of the pile downward to the bottom. Interface strength parameters, c_i and ϕ_i are as determined from the O-cell loading. A load value is input at the top of the shaft, segment load transfer computed from top to bottom, and a residual value of base resistance computed. The input top load is varied until the computed base resistance is equal to the mobilized O-cell base resistance; this condition is taken as representative of a top down loading condition which mobilizes an equivalent base resistance to that of the O-cell condition. In most instances, the displacements required to mobilize a substantial base resistance are sufficiently large to fully mobilize the side shear. For purposes of this discussion, interface strength parameters are not assumed to vary after yield at the interface is achieved (i.e., no strain softening or strain hardening yield surface is as-

sumed). Post-yield changes in side shear load transfer occur only as a result of changes in interface normal stresses.

As an example, a hypothetical rock socket shaft is analyzed using this approach. The example is a 0.9m (3ft) diameter by 4.6m (15ft) deep shaft embedded into a rock material with a modulus of 10% of that of the concrete ($E_p/E_s=10$). Strength properties at the shaft/rock interface are cohesion, $c_i = 138\text{kPa}$ (20psi) and interface friction, $\phi_i = 31^\circ$. To achieve yield at this interface for an O-cell bottom-up loading, a mobilized base resistance of 2.46MN (553kips) is computed; this value provides a computed axial load of zero at the top of the shaft as shown on Figure 84. Also shown on Figure 84 are the results of computations with the same model with a top down loading, with the load at the top for a mobilized base resistance of 2.46 MN (553 kips). The load applied on the top of the pile in this case is adjusted (to a magnitude of 5.20 MN (1170 kips)) until the load at the bottom equals to the O-cell load. The unit load transfer for the O-cell test and top down loadings in this example are illustrated on Figure 85. Although the interface strength properties are identical for both loadings, this plot reveals that the unit load transfer in side shear in the top down test is larger than that from the O-cell test. The differences are due to the Poisson's effect, which increases the normal stress on the interface in the upper portions of the shaft for the top down loading case relative to an O-cell bottom up loading.

2.5.5.5 *Field Test Comparison*

The analytical model described above is compared with the results of two field loading tests of drilled shafts in weak rock. O-cell test data with reasonably good instrumentation are examined from a case in moderately strong shale from Wilsonville, Alabama, and from a test of a socket in a weak claystone near Denver, Colorado.

Wilsonville, AL The Wilsonville, AL case was modeled using the spreadsheet implementation of the analysis method described above. The project information for this rock-socket shaft was presented earlier in this report and will only be briefly described. The shaft was 813mm (32in) in diameter and extended approximately 5.6m (18ft) into shale of moderate strength (unconfined compressive strength from cores was around 8,963kPa (1300psi)). Based on estimates of elastic modulus for shale with strengths in this range, the stiffness ratio (E_{pile}/E_{rock}) was estimated to be approximately 65. At an O-cell load of 4.41MN (992kips) the settlement of the base was approximately 38.1mm (1.5in) and upward displacements of the socket were nearly 12.7mm (0.5in).

Presented on Figure 86a is a plot of load vs. depth for the O-cell test and three models of the test result. The measured points are interpreted from strain gauge measurements. The plots from the three models are as follows:

- Case I: this model uses a completely frictional interface at the shaft/rock boundary, with $c_i = 0$ and $\phi_i = 75^\circ$. The interface friction was back calculated to provide 4.41MN (992kips) of side shear resistance for the O-cell loading.
- Case II: this model uses a load transfer model for side shear that includes both interface friction and cohesion. The interface friction was taken as $\phi_i = 50^\circ$, and the interface cohesion was assumed to vary linearly with depth from a value $c_i = 0$ at the top of the socket to $c_i = 400\text{kPa}$ (58psi) at the base. The unit side shear at the base of the socket was back calculated to provide 4.41MN (992kips) of side shear resistance for the O-cell loading.
- Case III: this model uses a load transfer model for side shear that does not include friction. In order to match the patten of load distribution observed in the measurements, the unit side shear was assumed to vary linearly with depth from a value $c_i = 0$ at the top of the

socket to $c_i = 586\text{kPa}$ (85psi) at the base; $\phi_i = 0^\circ$. The unit side shear at the base of the socket was back calculated to provide 4.41MN (992kips) of side shear resistance for the O-cell loading.

The three models described above and shown on Figure 86a are intended to span the range of possible models for interface behavior of this rock socket. The plots on Figure 86a indicate that a reasonably good match can be obtained with all three of the models described above. The Case II model which includes both cohesion and interface friction is likely the most plausible model of the true behavior as it includes elements of both friction and bond strength which is independent of friction (cohesion).

The load distribution curves for top down loading to mobilize 4.41MN (992kips) of base resistance are presented on Figure 86b for each of the three models. The top down load resistance for this mobilized base resistance ranges from 8.229MN (1850kips) for Case III (precisely 2 times the mobilized O-cell load minus the weight of the shaft) to 8.674MN (1950kips) for Case II to 9.786MN (2200kips) for Case I. These differences represent the increased mobilized side shearing resistance due to the Poisson's effect. The mobilized unit side distribution for each model is shown along with measured values (from differences in strain measurements) in Figures 87a,b,c. For the Case II condition with $\phi_i = 50^\circ$ and $c_i = 0$ to 400 kPa (0 to 58 psi), the differences between the O-cell mobilized side shear and the top down loading are relatively small, with the O-cell indicated unit side shear values slightly conservative (by about 10%).

Denver, CO The Denver, CO case shaft was 107cm (42in) in diameter and extended through 1.4m (4.5ft) of clay overburden to socket approximately 2.3m (7.5ft) into a weak claystone. $E_{\text{pile}}/E_{\text{rock}}$ was estimated to be approximately 100 for this example. At an O-cell load of 2.49MN (559kips) the settlement of the base was approximately 50.8mm (2in) and upward displacements of the socket were around 38.1mm (1.5in).

Presented on Figure 88 is a plot of load vs. depth for the O-cell test and the model of the test result. The measured points are interpreted from strain gauge measurements. The model uses a load transfer model for side shear that includes both interface friction and cohesion. The interface cohesion was taken as $c_i = 34\text{kPa}$ (5psi) in the clay above the rock and throughout the rock layer. The interface friction was back calculated to $\phi_i = 41.6^\circ$ to provide 2.49MN (559kips) of side shear resistance (less the weight of the shaft) for the O-cell loading.

The mobilized unit side distribution for this model is shown along with measured values (from differences in strain measurements) in Figure 89. The differences between the O-cell mobilized side shear and the top down loading are relatively small, with the O-cell indicated unit side shear values slightly conservative.

2.5.5.6 Parametric Study

Overview The analyses described previously and the two example cases in weak rock appear to suggest that the use of measured unit load transfer in side shear from O-cell tests directly for design for top down loading might be quite reliable in low modulus soils, and slightly conservative in weak rock. It is instructive to examine a range of hypothetical test conditions to identify conditions where differences between top down loading and the O-cell test might be more significant. For this study, a model composed of a 0.9m (3ft) diameter shaft embedded 4.6m (15ft) into a rock or soil layer is examined with a range of differing elastic modulus for the layer and interface properties.

Stiffness Ratio E_p/E_s The modulus ratio, E_p/E_s has been shown to significantly influence the coefficient K_r . For the two test cases of Wilsonville, Alabama and Denver, Colorado, these values

were in the limited range of 65 to 100. For the hypothetical test case described above, the influence of K_r is examined for a range of E_p/E_s from 1 to 100. Analyses were performed for the 0.9m (3ft) diameter by 4.6m (15ft) long socket with interface properties of $c_i = 138\text{kPa}$ (20psi) and $\phi_i = 31^\circ$ in each case. The base resistance mobilized in the O-cell test was that required to overcome the side shear using these interface strength parameters. Because of the Poisson's effect near the bottom of the socket in the O-cell test for the stiffer layer ($E_p/E_s = 1$), this condition was able to mobilize significantly greater base resistance. The comparisons of the mobilized side shear between the top down test and the O-cell test for $E_p/E_s = 1$, $E_p/E_s = 10$, and $E_p/E_s = 100$ are shown in Figure 90 and summarized in Table 13. Also shown in Table 13 are the values of the average mobilized side shear over the entire socket and the ratio of side shear from a top down loading to a bottom up loading, f_{td}/f_{oc} .

For the $E_p/E_s = 1$ case in which the rock material has a modulus equal to that of the shaft, the resultant O-cell load is 6.895MN (1550kips), and the top load to generate this base load is 53.4MN (12,000kips); this is not really a realistic condition since the compressive stress in the pile is large enough to damage the concrete. In such a case, geotechnical failure of the pile is not in question as the base resistance is sufficient to support the entire load on the shaft and structural limitations will govern. However, this case is included to illustrate the extreme of the effect of the stiffness ratio. The case of $E_p/E_s = 10$ represents a condition, which may be encountered in relatively competent rock and is used for additional evaluation of variables.

Interface Friction Angle ϕ_i The influence of the interface friction angle is examined for the case of $E_p/E_s = 10$ and using a consistent interface cohesion of 138kPa (20psi). Presented on Figure 91 are comparisons of the shear stress distribution for three cases ranging from $\phi_i = 14^\circ$ to $\phi_i = 50^\circ$. The detailed results are summarized in Table 14. Note that the intermediate case is the same as the intermediate case for stiffness ratio.

These results demonstrate the influence of interface friction on the Poisson's effect for O-cell and top down loading for shafts in rock with a rock modulus approaching 10% of that of concrete. As the interface friction is higher, the measured unit side shear from an O-cell test tends to be more conservative with respect to the unit side shear which may be mobilized from a top down loading.

Interface Cohesion c_i For the intermediate rock socket case of $\phi_i = 31^\circ$ and $E_p/E_s = 10$, the effect of interface cohesion is examined. Analyses for a range of c_i values of 69kPa, 138kPa and 276kPa (10psi, 20psi and 40psi) are presented in Figure 92 and summarized in Table 15.

Although the interface cohesion influences the magnitude of base resistance which might be mobilized during an O-cell test (more side shear against which to react), the relative effect on the ratio of mobilized side shear from the top down loading vs. the O-cell loading is minor.

2.5.5.7 *Intermediate Summary*

In this section, a simplified analytical solution was derived to evaluate the Poisson's ratio effect in which the axial stress in the shaft is seen to influence the normal stress at the shaft/rock interface. The solution is based on compatibility between stresses in the rock derived from cavity expansion theory and stresses in the shaft derived from Hooke's law. A simple spreadsheet implementation of the model was developed to simulate the O-cell test and top down loading and examine some field load test cases and to perform a parametric study to examine the effect of several variables. The results of this study suggest that the unit side shear values mobilized during an O-cell test will be somewhat conservative relative to those values mobilized during a top down loading for conditions in which:

- The rock mass has a modulus approaching 1/10 that of the concrete, and

- The shaft/rock interface includes a significant frictional component

Both of these factors are significant, and the results from this study indicate trends similar to those of the finite element analyses described previously.

2.5.6 Summary and Conclusions

An investigation of the O-cell test has been performed, including an examination of available field test data, finite element analyses, and a simple analytical model developed as a part of this study and implemented using spreadsheet computations. The emphasis is on a critical examination of the method of loading a pile from the bottom up and utilizing the measured values of base resistance and unit side shearing resistance to design for top down loading conditions. This approach is most often used with drilled shaft foundations.

The O-cell testing methodology is seen to be a very powerful tool and is commonly used by many state DOT's for bridge foundation project. Several states use the test routinely (several projects each year) and most states use it occasionally. The test is popular for drilled shafts embedded into rock or hard bearing strata and the interpretation of the test methods is generally to use unit load transfer values of base and side resistance (derived from strain gauge measurements or multiple level O-cells) directly for design. The most compelling advantage of the test is that it allows direct measurement of the load resistance of full-scale test shafts to extremely large loads. No other method is as practical or cost effective for load resistance values of several thousand kips.

Direct comparisons of field loading tests of identical shafts from top down and O-cell loadings are virtually nonexistent. A very few tests are described which allow some comparisons to be made, and these indicate no major differences between observed behavior. The best comparative tests are in soft soil and appear to indicate relatively good correlation between side shear resistance in O-cell and top down loading. One significant test case in cemented sands was described with two shafts subjected to top down and O-cell loading which appeared to indicate a major difference; however, the difference was attributed to the fact that the same test shaft was subjected to multiple loadings in opposite directions, and the load history probably affected the results. A problem with several comparative tests relates to failure to fully mobilize resistance in one or both portions of base and side resistance. Very careful preparation and conduct of a series of loading tests is required in order to isolate the variable of test method from the many other variables that can affect individual test results. Some other factors are identified which can affect comparison results, including spatial variability in the bearing formation (e.g., Florida limerock) and construction details such as a "step down" in diameter on the top of the rock formation. There is a compelling need for carefully conducted comparative tests between O-cell and top down loadings on full scale field tests.

A simple analytical model is developed and used along with nonlinear finite element models, to investigate the O-cell test method. Previous finite element studies are also described. The simple analytical model provides a means of interpreting test results with the inclusion of interface friction and the Poisson's ratio effect in which axial stresses in the shaft will influence the normal stress at the interface and thus the mobilized unit side shear resistance. The results of these analytical studies suggest the following:

- The differences in mobilized base resistance from an O-cell loading and a top down loading are relatively minor for shafts in soil or rock.
- The differences in mobilized side shearing resistance from an O-cell loading and a top down loading are relatively minor in soil in which the modulus of the soil is several orders of magnitude less than that of the concrete. In most instances the measured values of unit

side shear from an O-cell test will tend to be slightly conservative relative to a top down loading. The distribution of unit side shear will tend to have higher values at greater depth for the O-cell loading relative to the top down loading. The in-situ stresses are seen to have some influence, with greater differences noted for very high values of K_o (ratio of horizontal to vertical in-situ stress).

- For shafts in rock, the unit side shear values mobilized during O-cell tests tend to be conservative relative to unit side shear values which may be mobilized from top down loading. The differences are relatively minor if the modulus of the rock mass is on the order of 1/100 of that of the concrete or less. The differences can be significant if the rock mass modulus approaches 1/10 that of the concrete or more. The differences are strongly influenced by the friction coefficient at the shaft/rock interface. Current practice of describing the bond strength in side shear as a constant that is related to the unconfined compressive strength does not account directly for interface friction. The effect is attributed to a Poisson's ratio effect in the shaft, in which the axial stress in the shaft itself influences the normal stress on the shaft/rock interface. The axial stress is higher in a shaft, which is subjected to top down loading and is engaging base resistance than is the case in an O-cell test. In the top down loading the axial load in the shaft varies from a maximum at the top to a minimum equal to the mobilized end bearing at the shaft base; in the O-cell test the axial load in the shaft varies from a maximum at the mobilized base resistance to near zero at the top of the shaft.

Even with shafts in rock, it must be noted that the variability between O-cell testing and top down loading observed in this research tends to suggest that the O-cell test is conservative. Given that most O-cell tests are likely to indicate that existing geotechnical practice has been even more conservative, it is unlikely that the use of O-cell testing in practice has led to excessive conservatism in design. Rather, the research described in this report suggests that there is a need to better understand the fundamental behavior of drilled foundations socketed into rock and the O-cell test method is an instrumental tool for improving this understanding.

There is a need for additional research on the behavior of drilled foundations socketed into rock. This research should consist of carefully controlled and instrumented loading tests using both top down and O-cell methods, along with a thorough investigation of in-situ rock properties. Reliable measurements of rock mass modulus and interface properties are important, and it is desirable to conduct tests for a range of rock materials and in rock strata, which have relatively consistent properties (minimize spatial variability so that other variables can be evaluated). A better understanding of the results of O-cell tests has the potential to significantly improve the reliability and cost-effectiveness of drilled foundations in rock.

2.6 THE SIMBAT METHOD

2.6.1 General

The latest method for pile bearing capacity testing to be introduced in 1998 is known as Simbat and was developed by the CEBTP (Center Experimental De Recherches Et D'études Du Batiment Et Des Travaux Publics) in France and is currently offered by Testconsult of Cheshire, UK. The objective of this method is to predict the static behavior of a pile from dynamic measurements. Very few end users would admit to a full understanding of either how this method works or what are its limitations.

In 1979 the CEBTP (France) was sponsored by the FNTP (Federation National des Travaux Publics) to undertake research into existing classical methods of pile testing and to develop a test that would be equally applicable to cast in place piles. The result of this research program is a methodology known as Simbat, which was included in a series of class A prediction trials in Belgium in 1987.

In general, the methodology is similar in concept to that described and researched as the Drop Weight System (see Figure 93). The Simbat™ methodology consists of applying a number of impacts to the pile, typically ten. The mass is dropped from a range of heights so that the pile/soil system is subjected to varying strain rates. The bigger the drop height, the bigger the impact velocity and the higher the strain rate is. For each impact, the magnitude of the soil reaction, $R_{dynamic}$, is calculated using classical wave equations. The upwards and downwards waves, which were generated by the impact, are separated. It is the upward waves that quantify the soil reaction and it is that which determines the behavior of the pile under load.

The soil reactions measured in this way are total including dynamic forces and must be separated to evaluate the static resistance. The Simbat™ system has a procedure that automatically generates its own dynamic to static correction. Unlike other techniques, there is no requirement to make assumptions concerning soil damping factors and the like. Different procedures are used for cohesive and non-cohesive soils.

The system comprises of the following main components (refer to Figure 94):

1. Data collection unit, for capture of strain, acceleration and displacement
2. Site computer
3. Optical theodolite to measure dynamic displacement of pile
4. Accelerometers and strain gauges
5. Software for signal acquisition and data processing

2.6.2 Theoretical Background

The method is based on the propagation of waves in long elastic cylinders. When the pile top is struck with the falling weight the pile section is deformed (enlarged) and this enlargement travels down the pile to the toe where it is reflected back up. In a free, un-damped pile, the particle velocity of the return wave would be identical to the original wave.

When the pile is surrounded and restrained by soil, part of the wave is reflected back up at each and every external restraint, the remainder of the wave continues downwards. So at any one time there are both upwards and downwards forces and velocities in the pile.

The Simbat technique makes use of a separation formulation for the upwards and downwards forces, F_{up} and F_{down} and calculate dynamic soil reaction, $R_{dynamic}$, as the difference between the up-

wards force in a free pile and the real upwards force measured. The conversion of dynamic to static reaction is carried out by expressing $R_{dynamic}$ as:

$$R_{dynamic} = R_{static} + (K * e_{penetration})^a \quad (44)$$

where:

- $e_{penetration}$ = permanent penetration, (set).
- K = a parameter which is a function of the pile and the sequence of the blow.
- a = a parameter which is a function of the soil.

K is obtained by means of impacting a number of hammer blows to the pile, which causes the pile to move at different strain rates. A regression analysis of dynamic reaction versus strain rate is then carried out and equivalent static reaction is determined by extrapolating backwards to the point corresponding to zero strain rate (see Figure 95).

An additional procedure often used is a numerical simulation whereby experimental signals are introduced into a computer program and compared with theoretically generated signals. The choice of a realistic pile/soil model is of great importance. The soil model used by Simbat is shown in Figure 96.

Classical numerical simulations are based on assuming elastic / perfectly plastic soil reaction together with viscous damping (J) and simulation between the movement of the soil and that of the pile. This technique, though used routinely by all dynamic methods seems to draw more upon empirical consideration than physical characteristics, (Paikowsky et al. 1996).

In the Simbat model, (see Figure 96), the displacement of the pile and that of the soil are clearly differentiated. The difference between these displacements is $e_{penetration}$. The reaction in the spring and dashpot are linked to the displacement of the pile. Slippage between the pile and soil is obtained from the stresses generated by the radial component. Simbat assumes the pile body is an elastic continuum, with forces being concentrated on a number of discrete points for the purpose of calculation. The static test prediction is obtained by adding the elastic pile deflection to the permanent deflections.

2.6.3 Methodology

Before performing the field testing, a pile 'cap' is built, 2.5 times the pile diameter in height, and well reinforced to prevent bursting under the drop weight impact. As this cap is to serve as a dynamometer it must be smooth with the same cross section as the testing pile and of good quality of homogeneous concrete. As such, the generated stresses become uniform over the section; with a small time interval before the upward wave from the first soil layer arrives.

Very similar to the traditional dynamic testing method, two strain gauges and two accelerometers are used along with an electronic theodolite. A target is mounted on the side of the cap, two diameters from the top. All the instruments are connected to a single dedicated data acquisition system.

A drop weight of sufficient mass to mobilize the pile is used to generate the input force. A cushion is placed on the top of the pile cap both to protect the concrete and to increase the duration of the impact. In practice a coiled nylon rope cushion has been found to be most suitable. The height of drop of the falling mass is progressively increased until a small permanent penetration is recorded.

The drop height is then successively increased or decreased to achieve differing strain rates as described earlier. A full load settlement plot requires typically 10-15 blows.

During many years of site experience, it has been found that a direct measure of pile deflection during impact is essential for the correct interpretation of data. It is only by making such measurements that the pile top velocity can be correctly inferred from the acceleration data. This measurement also provides a second independent check to the magnitude of the pile movement during the impact.

Testconsult Limited (Warrington, United Kingdom) developed a special digital, optical theodolite that measures the entire deflection cycle of the pile during impact as well as the permanent deflection caused by the blow (see Figure 97). The device focuses on a small target attached to the pile, through a 500mm lens and operates at 10,000 data points per second. The resolution is 0.14mm at a distance of 5m from the pile.

The theodolite mounts conveniently on a standard surveyors' tripod and can be positioned at up to 10 m from the pile. The target is lit by a small halogen lamp attached to the side of the enclosure. A laser pointer, incorporated inside the enclosure facilitates setting up the theodolite and aiming it correctly at the target. A LED display aids the correct focussing of the lens. The unit operates from any 12-volt supply, making it safe for site use

A series of impacts are made with the hammer drop height being progressively increased or decreased (refer to Figure 93). All data, (i.e. acceleration, strain and displacement), are stored on a disk for subsequent processing. Typical raw data is shown in Figure 98.

Signal processing of each test follows the following stages:

1. Correction of acceleration and velocity using the direct theodolite displacement;
2. Separation of forces F_{up} and F_{down} ; (Figure 99)
3. Calculation of dynamic soil reaction $R_{dynamic}$;
4. Regression analysis to obtain $f(V_{penetration})$ and thus K ,
5. The dynamic to static factor;
6. Calculation of elastic shaft compression;
7. Plot of total settlement/load. (Figure 100)

Finally, a series of computer simulations are carried out in order to verify the measured signals and to calculate the distribution of soil resistance down the shaft and at the pile toe.

The processing and reporting software is inevitably quite complex and detailed. It has, however, been designed to be clear, user friendly and powerful. The main functions are:

1. Creation of a table of files for each pile.
2. Correction of acceleration data using the theodolite displacement.
3. Separation of forces allowing the calculations of the dynamic and total reaction of the pile, for each blow.
4. Determination of the dynamic/static correction and plotting of predicted load/settlement graph.
5. Signal matching analysis to get the soil resistance distribution and pseudo-static load-displacement curve.

Site data is downloaded into the PC, and for each pile, a table is created while information regarding the hammer drop height, file name, and permanent penetration is provided. The data for each blow is then called up simply by clicking on the file name. The acceleration/velocity is then corrected using the theodolite data and the up and down forces and velocities separated in the normal way to give $R_{dynamic}$, the total or dynamic reaction for each blow. These values are automatically placed in the table and a predicted static load settlement plot is produced.

The last stage is the predicted static load/ settlement plot for each pile. This is done using algorithms that do not need any assumptions concerning soil damping factors. The separation and distribution of soil resistance along the shaft and at the base are determined by the signal matching analysis.

The latest version of the Simbat™ program leads the operator through a logical sequence of operations and prompts the operator for inputs, invalid entries etc. Written in a low level language the software is extremely fast. Special printouts for rapid reporting have been incorporated.

Computer simulation is not always done. A load / settlement curve, with maximum load related to the maximum applied energy in the test, is only generated. No direct estimation of the ultimate capacity is made. Also no account is taken of the influence of different soil layers or of the possibility of a very stiff layer at the pile base.

The soil / pile interaction does not account for many of the characteristics of true soil behavior such as non-linear stiffness characteristics, yielding, strain softening / hardening, stress history, plasticity, anisotropy etc.

2.6.4 Dynamic to Static Conversion

Assuming that a certain pile in clay has an ultimate static capacity of 400kN, the resistance of the same pile under dynamic loading would be considerably higher, possibly by a factor of 2, so that the dynamic reaction could be 800kN. This is because of the time-dependent visco-elastic nature that most soils exhibit. The faster the strain rate, the bigger the soil resistance will be. This effect is apparent even at relatively slow strain rates - a constant rate of penetration test (CRP) on a pile will produce a higher ultimate capacity than a slow maintained load test. It is therefore necessary to find a method of correcting the dynamic reaction to a static value and there are several approaches, (Testconsult website).

The first method, and the one used by the early researchers in this field, was to establish a large database of correlations based on actual results of dynamic and static tests being carried out on the same piles. In this way, soil 'damping' factors slowly evolved for different soil types. The soil damping factor (J) ranged from just over 1 for highly cohesive clays to less than 0.1 for non-cohesive sands and gravels. The static reaction was then calculated by firstly estimating an appropriate J factor based on knowledge of the soil conditions. The measured (or dynamic) reaction was then reduced by an amount proportional to the J factor and the pile top velocity to give a static value. This method is still in use today and is an extremely rapid and useful indicator although its accuracy does depend on a correct assumption of J.

Simbat avoids the necessity to assume a J factor. But it requires that a large number, typically ten or more, separate hammer blows are applied to the pile and the dynamic reaction is measured for each one of them. The impacts are arranged so that a wide range of soil strain rates are achieved, all within the range considered as high strain rates, (in comparison to static load), however some of the blows achieve higher strain rates than others. In practice, this is easily achieved simply by varying the drop height of the mass. Figure 95 shows the principle of the operation.

By projecting the dynamic measurements back to a zero strain rate or zero penetration velocity, the static reaction is obtained. In fact, the projection is not necessarily a straight line as shown in Figure 95.

One of the advantages of this method is that, coupled with an accurate measurement of the pile's top displacement for each blow, a complete load/settlement plot can be produced. It also avoids, as mentioned previously, the need to assume a soil damping factor which may or may not be appro-

priate for the particular soils. The technique is different to the previously mentioned one in that pile penetration velocity is used as an adjuster and not pile top velocity - these two values are quite different. Finally it also avoids the need to refer to the ultimate capacity of the pile, a quantity that has been defined in many different ways and is not necessarily the true sum of all the soil reactions. An example of this correction procedure is given in Figure 101.

2.6.5 Analysis of Results

Velocity is not measured directly but derived from the integral of the acceleration. To confirm the quality of this data the acceleration is integrated twice and compared with the displacement record obtained by the theodolite. Corrections can be made by applying either parabolic or linear functions (see Figure 102). The data verification through two independent measuring systems is very important and one of that is often neglected in the separation of forces.

The first stage of the analysis, (which is often carried out on site), is to determine the dynamic soil reaction for each blow using classical principles. A complete separation of forces diagram is shown in Figure 99. This procedure is undertaken on all blows, and tabulated together with the permanent penetration for each blow (Figure 101).

There are two reasons for carrying out computer simulations: (a) to verify that the dynamic reaction calculated using classical Case principles is equal to the sum of the individual limit reaction; (b) to determine the distribution of soil resistances along the shaft and at the pile toe.

The Simbat model was described earlier. Essentially the procedure consists of splitting the pile into 13 discrete elements and assigning soil and pile parameters for each of these elements. The soil properties are entered as elastic and viscous components and the ultimate or limit reaction. These parameters are then adjusted until the model responds in the same way as the pile, both in terms of velocity and displacement (see Figures 103 and 104). If the Case principles are shown to be applicable for each blow then the dynamic reactions previously determined can be accepted. If not, then the total reaction of the model must be used in the final stage of analysis.

The results shown in Figure 101 are soil reactions plotted against pile head penetration. It is therefore necessary to add to this plot the shaft's elastic compressibility. The most reliable and accurate method of determining this value is by direct use of the theodolite (displacement) and force measurements. It is not strictly accurate to simply divide the displacement by the force and instead the integrals of these two measurements are used. This shaft compressibility has been added to the toe penetration and two final static/load settlement plots are given in Figures 105 and 106.

2.6.6 Case Histories

2.6.6.1 National Geotechnical Experimentation Site at Texas A&M University

To evaluate the ability of large-strain dynamic testing methods, (namely the drop weight method (PDA), Statnamic method and the Simbat method), to predict the static capacity of cast-in-place piles, three cast-in-place piles were constructed at the National Geotechnical Experimentation Sites at Texas A&M University (Figure 107). Various companies were then invited to perform large-strain dynamic testing and make class "A" predictions of the static capacity of these three piles. The static capacity was measured using conventional static load tests.

The Texas A&M University National Geotechnical Experimentation Site includes two sites of primarily sand and clay. The top layers, 12.5m at the sand site and 6.5m at the clay site, are both

100,000-year-old river deposits, while the hard clay underlying both sites is a 45,000,000-year-old marine shale that was deposited by a series of transgressions and regressions of the Gulf of Mexico. The sand is medium-dense silty sand. Details of the soil properties are in Briaud (1997) and Simon and Briaud (1996). Pile #2 and #4 were installed at the sand site and pile #7 in the clay site (Figure 107).

Figure 108 provides a detailed comparison between the actual static load test results to the Simbat test results for pile No.2. Figure 109 presents the comparison for all tested piles and methods of analyses. The Simbat test results on these three piles were in the range of $\pm 50\%$ of the static test results, with one of the tests (#7) accurately predicting and the other two ranging from +50% to -50%.

2.6.6.2 Ship Street, Dublin, Ireland.

A pile 0.3 m in diameter, 8.2 m long with a rock socket of 3 m, CFA pile was tested. Comparison of static load test results and Simbat test results is shown in Figure 110. It can be seen that the comparison of the two provides a very good agreement with the static pile test showing a slightly stiffer behavior. Simbat tends to overestimate the residual settlement at the end of the test.

2.6.7 Database

A database comprised of 46 static pile tests from 32 sites around Ireland has been assembled by Professor Michale Long from University College Dublin (Long, 2001, see Appendix B). Cases were obtained from four different piling contractors, thus ensuring that the study is not confined to one single piling technique. For many of the sites, the number of dynamic tests exceeded the number of static tests.

Test results have been sub-divided into three categories based on soil type, piles in rock, sand and gravel. A good spread in the data exists in terms of rock type, location of sites around Ireland, pile diameter and pile length. Very few of the test pairs were carried out on the same pile, i.e., most of the data for which static behavior is compared to Simbat test results, relates to two different piles at the same site. It should be pointed out that this database was compiled in Ireland, where the maximum load applied in a static load testing is usually 1.5 times the specified working load (SWL).

Both the measurements in the static tests and the predictions from Simbat, at SWL and 1.5 SWL, have been given as well as the Maximum $R_{dynamic}(=R_{static})$ value.

Inspection of the data shows that for a particular site, the prediction made by the dynamic test is nearly always the same for all of the tests at the specific site. Therefore in order to simplify the plots, data are plotted in terms of the static test result versus the average of all the dynamic test results for that site.

Comparisons between the actual measured settlements versus the predicted settlement, for the piles in rock, at SWL and 1.5 SWL, are shown on Figure 111. The data compare reasonably well. They generally are clustered near the $X=Y$ line (Simbat prediction = static load test result), with a majority of the points falling above the line. The coefficient of correlation (r) can be used as a statistical measure of the reliability of the data. This is a statistical test for significance of a two variable linear relationship. If $r=0$, no linearity exists whereas if $r=1$, perfectly linearity exists. In this case $r=0.63$ and 0.69 for loading to SWL and 1.5 SWL respectively, suggesting moderate linearity exists. It is interesting that r is higher for loading to 1.5 SWL.

Data for the piles in sand and gravel are shown in Figure 112. Again, the data are clustered near the $X=Y$ line with an approximately equal number of points falling on either side. In this case

$r=0.69$ and 0.80 for loading to SWL and 1.5 SWL respectively. It is possible that the piles in sand and gravel show best correlation because the actual situation of a pile in a layer of uniform sand and gravel comes closest to the theoretical model assumed in the Simbat process.

Insufficient data exists for piles in clay to provide a meaningful plot. However these data are included in Figure 113 for all piles. When all the information is included, the comparison appears slightly poorer. Again it tends to be more points above rather than below the $X=Y$ line, suggesting that Simbat overestimates settlement. For all test results, $r=0.38$ and 0.4 for loading to SWL and 1.5 SWL respectively, suggesting moderate to poor correlation.

Lines representing a 100% overestimation and a 50% underestimation of the static test result by Simbat are included in Figure 113. These lines seem to encompass most of the data points. This suggests that if a Simbat dynamic test is used to estimate the results of a static test, on a similar pile on the same site, then the result is likely to be in the range of +100% and -50% of the true one. To put this into context, taking a typical test result where Simbat predicts a settlement of 4mm at SWL, then the likely true result will lie in the range of 2mm to 8mm. It is suggested that these differences are small and are likely to be acceptable in many circumstances.

A plot of the ratio of measured settlement in static tests to predicted settlement in the dynamic tests against pile diameter is given in Figure 114 left. The results show a tendency for an approximate linear increase in the ratio with increase pile diameter. This suggests that Simbat will increasingly underestimate the results for piles of increasing diameter and is possibly due to insufficient energy being imparted to these piles. However a lack of data for the large diameter piles makes it difficult to make any definitive conclusions but this topic warrants further study with more data.

The same ratio is plotted against pile length / diameter ratio on Figure 114 right. For short “stiff” piles, Simbat will underestimate the static settlement but as the ratio of length / diameter increases, the dynamic technique will increasingly overestimate the pile settlement. This again suggests that more dynamic energy would be required for the “stiff” piles in order to mobilize true movement.

A plot of the ratio of the maximum equivalent static load mobilized in the Simbat test to the SWL is given in Figure 115. This value could be considered to be the mobilized factor of safety. The values range between 1.55 and 2.35, with an average of about 1.75. Typically static tests on working piles are taken to 1.5 SWL and therefore these values seem reasonable.

A concern of most owners would be whether the Simbat test was capable of identifying problematic at piles on site. Experience has been positive in this regard and in a number of circumstances the findings of the dynamic test have been ratified by a conventional test.

An example of this is a site in the Irish Midlands. A 300mm diameter bored cast-in-place pile was constructed through about 5m of very soft silts / clay and peats and was founded 2.5m into a medium dense glacial gravel stratum. The pile was a preliminary trial pile and was designed to have a SWL of 600kN. A Simbat test was carried out and yielded the results shown on Figure 116. It can be seen that the test suggests that the pile would have failed at about 920kN and hence had a safety factor of about 1.5, which was deemed to be inadequate.

Subsequently a static test was carried out. The results are again shown in Figure 116 and they ratify the results of the Simbat test. It can be seen that beyond a load of about 900kN the pile begins to settle significantly, suggesting ultimate capacity has been reached.

Examination of the grouting records showed that significant loss had occurred in the very soft deposits. The process was modified and the piling proceeded satisfactorily.

2.6.8 Summary And Conclusions

1. The Simbat is not a common method. Theoretical and practical research is required to further examine its performance.
2. The Simbat method is described with the following characteristics:
 - selecting a falling mass as a force generator;
 - use of selected section measurement;
 - use of an electronic theodolite for displacement measurement;
 - pile-soil interaction revisited, which take into account the radiation impedance of the soil;
 - use of numerous tests with variable force to obtain the correlation between static and dynamic resistance, and use of the penetration velocity as parameter.
3. Comparison between predicted to measured values on the basis of settlement alone is of limited significance. These values are usually quite accurate within the pile working loads, mostly in the elastic zone of interaction (Paikowsky et al., 1994). These comparisons are meaningless for failure conditions and hence the method's ability to predict the pile's capacity is not examined through the presented relations. The comparison of settlement predicted by Simbat to that measured in the static test however reasonable correlation according to the following.
 - Correlation for piles in sand and gravel ($r = 0.75$) seem to be quite well, however for piles in rock ($r = 0.66$) and piles in clay ($r = 0.26$ with very limited database), the results are not very good.
 - There is little difference between the correlation at SWL and 1.5 SWL.
 - If a Simbat test is used to estimate the results of a static test, on a similar pile on the same site, the result is likely to be in the range of +100 and -50% of the true one.
 - Simbat seems to underestimate settlement for short, relatively large diameter piles suggesting that there is insufficient energy imparted to these piles in the dynamic test process.
4. In general, the Simbat process seems to mobilize sufficient load to give an adequate factor of safety and the Simbat test appears to be useful for identifying problem piles.
5. The error provided for the actual capacity comparisons for the Simbat tests ranges from – 50 to 50 percent, which is larger than the typical error obtained by the common dynamic testing.
6. Considering the vast data and experience accumulated for dynamic pile testing (PDA), the advantages of Simbat may need substantial accumulation of experience and testing.

2.7 THE FUNDEX METHOD

2.7.1 General

The Fundex method, jointly developed by Funderingstechnieken Verstraeten BV (Fundex) (Oostburg, The Netherlands) and Ifco Foundation Expertise BV (Waddinxveen, The Netherlands), is a pseudo static pile load testing method. The equipment shown in Figure 117 allows for a fast and cost effective load testing method which greatly decreases the damping and inertial effects. Similar to Statnamic, the Fundex method extends the loading period, but it achieves it in a different manner.

2.7.2 Theoretical Background

The applied load in the Fundex method can be described by a simple model: a mass m , with a spring k , is dropped from a height h onto a rigid base.

During dynamic load testing, the applied force on the pile is directly correlated to the change of momentum. Its relation is presented by:

$$\vec{P} = \int \vec{F} dt = mv_{pre} - mv_{post} \quad (45)$$

where, m is the mass used for the test and v_{pre} & v_{post} are the velocities of the mass before and after the interaction with the pile.

Referring to equation (45), it is assumed that: $F_{action} = F_{reaction}$. The action force is exercised on the pile and the reaction force on the drop-mass. Equation (45) is simplified by neglecting gravity, since it is very small relative to the impact force. The velocity of the drop-mass is given by:

$$v = \sqrt{2gh} \quad (46)$$

in which, g is the acceleration of gravity; and h is the height of the stroke.

During a dynamic load test the magnitude of the exerted force is comparable to the ultimate pile bearing capacity. Equation (45) shows the relation of the load duration with the change of momentum on the pile. Extending the load time requires increasing mass or velocity (height of the stroke). Figure 118 was developed for completeness of the presentation using a model presented in section 4.2 with undamped system (section 4.2.3.2). Figure 118 shows the force pulses acting on a given pile's head under different mass sizes impacting with the same stroke height of 1.5m. The time indicates the duration of the load transfer, or how "static" the load is. A definition of this time is the duration of which the load is above a certain percentage of the maximum load. This percentage is usually 50%, ($t_{50\%}$). When different systems are to be compared, identical time scales must be used.

The curves presented in Figure 118 refer to a steel tube pile with a cross section $A = 0.2m^2$, the density of the pile $\rho = 7850kg/m^3$ and the Yongs modulus $E = 2 \cdot 10^{11} N/m^2$. The spring stiffness k is $10^9 N/m$. The stroke height kept constant as 1.5m and the striking velocity Δ_0 is 5.42m/s.

The duration, $t_{50\%}$, of a load test performed can be calculated using equation (45) and (46). It is advised to use a mass of 5-10% of the pile's ultimate bearing capacity, velocity $v_{pre} = 0$, assuming that the mass reaches a height of 1.5 m, and that the force as a function of time has a simplified triangular shape. The duration of the load is as follows:

$$t_{50\%} = \frac{m\sqrt{2gh}}{F_{ultimate}} = \frac{0.1F_{ultimate}\sqrt{2gh}}{F_{ultimate}} = 0.1\sqrt{\frac{2h}{g}} \approx 50ms \quad (47)$$

in which, $t_{50\%}$ is the duration where the force exceeds 50% of the maximum force; $F_{ultimate}$ is the ultimate pile bearing capacity.

The force pulse acting on the pile head during the impact generates a shock wave in the pile. The traveling time of the wave from the pile head to the bottom and back causes a delay in the response to the reaction forces of the subsoil. This is why for loads of relatively short duration only the

velocity of the pile head is used for the analysis instead of displacement. The duration of the load should be compared with the wave travel time. A load becomes quasi-static when:

$$t_{50\%} \gg \frac{2L}{c} \quad (48)$$

in which, L is the pile length and c is the stress wave velocity in the pile as previously discussed conceptually in section 1.3 (relative wavelength) and for Statnamic testing in section 2.3.5 (wave number).

Figure 119 shows calculation results of the load-settlement relationship for a dynamic testing, a Fundex testing and a static load testing. The parameters used in the calculations for the examples in Figure 119 are: Soil Stiffness=0.28GN/m, Soil damping=1.3MN/m, Wave Velocity=4180m/s, Pile Length=16.4m, Pile Cross Section=0.4m x 0.4m and the Youngs Modulus=42GN/m². The force as a function of time is (1-cos(t)). The $t_{50\%}$ is 4ms for the dynamic test and 40ms for the Fundex test. The curves in Figure 119 calculated by assuming: (a) the pile toe reaction force is generated by a pure elastic spring and (b) the pile has no side friction. From Figure 119, it can also be seen that the quasi-static test method matches very well with the elastic load-settlement curve. The shape of the looped curve is caused by the time delay between load and settlement and does not relate to the shaft friction, since that is lacking in this simple model.

2.7.3 Testing Procedures and Interpretation

The field testing is performed by special equipment: Pseudo Static Pile Load Tester (PSPLT) (see Figure 120). The PSPLT was especially designed to execute Fundex load testing. The procedures of the test are as follows.

The PSPLT is brought to the test site by a low-loader. It moves on its tracks to the test pile, which the pile head has previously been prepared. When the rig is positioned and the measuring devices are attached the test can start.

Field testing starts by dropping a mass on the top of a pile. A heavy coiled spring system has been attached to the bottom side of the mass in order to soften the impact and spread the transmitted energy over a longer period (compared to the impact time of a normal dynamic test using a drop weight).

The mass m and the coiled spring system elastic coefficient k are respectively 25,000kg and 8MN/m, the drop height h is equal to zero when the spring touches the base. The maximum force is then represented as:

$$F_{\max} = mg \left(\sqrt{\frac{2kh}{mg} + 1} + 1 \right) \approx \sqrt{2mgkh} \quad (49)$$

Figure 121 is a graphical representation of equation 49 with the parameters of the PSPLT. The duration of the load is between:

$$175ms \approx \pi \sqrt{\frac{m}{k}} > t_{50\%} > \frac{2\pi}{3} \sqrt{\frac{m}{k}} \approx 117ms \quad (50)$$

In this way a slow-rising, long lasting impact is introduced to the pile, without causing the typical wave propagation effects. The dynamic effects which are present during Dynamic Load Testing, and which hamper the interpretation enormously are avoided by spreading the impact wave over a longer period of time (up to 400 milliseconds total and effectively up to 200 milliseconds). At the completion of the downward movement, the mass (with springs) hits an anvil, which rests on the head of the test pile and the transmitted energy to the test pile. The coiled springs distribute that energy as a function of time as stated above. On completion of the upward stroke as a result of the “bounce”, the mass is caught in its highest position, by hydraulic clamps, to avoid a direct second blow.

Figure 122 shows the force at the pile’s head as a function of time. The force pulse duration acting on the pile’s head has a very small dependence on the drop height. The above described model is a good approximation of the force exerted by the PSPLT as a function of time. An error is introduced by the assumption that the coil springs are massless. The assumption of a rigid base is justified, because the displacement of the pile during loading is far less than the compression of the coiled springs.

Both the force-time and the velocity-time signals are registered by a computer, which plots the analysis results as a load-displacement curve. By repeating the test with different drop heights (see Figure 122), several points in the load-settlement curve are obtained, through which the curve is constructed by the software program. Figure 123 shows the measurements of one single drop. The load-settlement curve is obtained by directly measuring the forces and settlements throughout the whole testing process (see Figure 124). The force introduced in the pile during the impact is measured by means of a calibrated (dynamic) load cell. The maximum force introduced in the pile can be checked by measuring independently the elastic compression of the springs underneath the mass. The absolute displacement of the pile during the blow is measured by using an optical system, which was developed by Ifco. The optical system includes a transmitter attached to the side of the tested pile and a receiver, which is placed at a distance of 15 to 20m away from the test pile. This optical measuring system has accuracy better than 0.1mm in both horizontal and vertical direction. The distance between the pile and the optical receiver is sufficient to ensure minimal ground vibrations.

2.7.4 Case Histories

The Fundex method has been used to predict the pile bearing capacity at various sites in the Netherlands, Belgium, USA and Germany. Four case histories were gathered and presented in Figures 125 to 128. The first one is from Schellingerhort et al. (1996), the second was provided by American Piledriving, Inc website, Case 3 and Case 4 were carried out at two sites in France (Iwanowski and Berglars, 1984).

As illustrated in Figures 125 to 128, all the piles were not tested to failure by the Fundex method and as such the ultimate bearing capacity cannot be obtained. However, within the range of the tested load, the load- displacement curve provided by the Fundex method matches fairly well that obtained from the static method, suggesting that the allowable bearing capacity may be obtained using the Fundex method.

Further investigations are necessary to find a better relationship between the results of the pseudo static test and those of the common static test. The lack of adequate and useful comparison tests is the reason that such a match has not yet been well defined.

2.7.5 Conclusions

The Fundex load testing system is extending the time period of an impact via springs attached to the impacting mass. The general notion of a longer loading duration being more “static like” has the limitations of creating a long stress wave which on one hand does not allow the use of wave propagation analysis based on the wave equation (see section 1.3), and on the other hand does not eliminate the dynamic effects. As a result, the testing method requires independent means of evaluation to consider the dynamic effects of the loading. The simple model used for test result interpretation (mass m , spring k , drop h onto a rigid base) does not consider the dynamic loading effect and seems not to provide a satisfactory solution.

From the data available it seems that comparisons between the Fundex method of interpretation and static load tests are very limited in the number of cases available and the range of the loading (of either the fundex or the static tests). At present, the Fundex testing method can be viewed and examined as a convenient and economic quality control method and should not be substituting static load testing.

2.8 THE SMARTPILE METHOD

2.8.1 General

An innovative method of load testing piles was presented by Frederick Engineering Co. of Whippany, New Jersey. The method, called Smartpile, is aimed at providing the ultimate bearing capacity of the pile and information about pile integrity as well as the hammer transfer efficiency.

By means of installing a force transducer within the pile head and collecting signals by a set of equipment called Smartpad, a force-time curve under the impact force can be obtained. If another transducer is installed in the pile tip, the end bearing capacity is also obtained and hence the side friction force.

Figure 129 shows a typical setup for the Smartpile testing. Two impulse force sensors are placed internally within the pile (the bottom one is not necessary if the toe bearing capacity or side friction is not desired). Details of the force sensor set-up and its implementation by the Geotechnical Engineering Research Laboratory at UMass Lowell are presented in Figures 130 and 131, respectively. The top sensor is about 50mm (2in) below the pile head, and the other is about 50mm (2in) above the pile tip. The Smartpile measures force directly (not via strain) and the force sensors are located centrally along the line of impulse of the hammer. The sensors, however, cannot be retrieved after the test and hence considered disposable.

2.8.2 Testing Procedure

The Smartpile test set-up is shown in Figure 129. In concrete piles and shafts, the force sensors are installed at the head and tip of the pile prior to pouring the concrete, with wires extending from the sensors to near the top of the pile. These wires come out from the side near the top of the pile. They are then connected to the data acquisition system when the pile is ready for driving. The data acquisition system consists of a converter amplifier, an oscilloscope and a plotter.

The force sensors are durable and can withstand the impact force of most pile driving hammers or drop weights in the case of drilled shafts. The force sensor is a mechano-electrical sensor consisting of a piezo-film sandwiched between two plates for protection (Figures 130 and 131). When an impact force is applied to the sensor, an electrical signal is generated. The strength of this signal is proportional to the resistance offered by the pile. The electron flow from the sensor is converted to a voltage using a multi-channel converter. This signal is amplified, directed to an oscilloscope and plotted. The force sensors are factory-calibrated prior to driving.

Values of bearing capacity of production piles can be estimated using an ancillary component of the Smartpile testing equipment. Known as Smartpad, it consists of two layers of 19mm (0.75inch) thick plywood with a force sensor sandwiched between. The Smartpad is sized and shaped equal to the pile cross-section. When the pile is close to its final penetration depth, the Smartpad is placed on the pile head, connected to the data acquisition system and struck only for about four or five blows. Smartpad provides the pile capacity based on the information recorded at the pile head only. The bearing capacity of the pile toe is not recorded. Unlike the pre-placed force sensors in concrete pile elements, the pad must be removed and replaced when further driving is necessary to minimize degradation of the plywood, which can lead ultimately to the damage of the sensors.

To test steel pipe or H-piles, circular and rectangular metal plates, respectively, are welded to the top of the pile. Smartpad is then placed on the metal plate prior to testing. The metal plate can also be used when testing hollow precast concrete piles. Timber piles can be load tested by securing the Smartpad directly on the pile head.

The Smartpile instrumentation can be transported in two carry-on cases, each measuring 0.52m (20.5in) x 0.43m (16.8in) x 0.22m (8.5in) and each weighing approximately 18 kilograms (40 pounds). One case holds approximately 90m (300ft) of cable, a reel and a collapsible stand. The second case houses the data acquisition hardware and software.

Using the very sensitive force sensor that is placed at the pile and that is linked electronically to a data acquisition system, force-time curves can be generated for each hammer blow. From the force-time curve, the ultimate bearing capacity of the pile can be determined directly as outlined in the following section. When similar sensors are placed at the pile toe (to measure the end bearing), the difference between the total and tip capacities is the side resistance. This method can also be used to provide an indication of the pile integrity during driving as well as to estimate the hammer transfer efficiency.

2.8.3 Theoretical Background

The Smartpile method is a high strain dynamic testing method, which consists of applying an impact to the pile's head and measuring the response similar to PDA, TNO and Simbat.

Typical force versus time plot obtained from Smartpile tests are illustrated in Figure 130. Exactly based on these force-time plots, information on the pile bearing capacity, pile integrity and hammer transfer efficiency can then be estimated.

Based on Ooi and Frederick (2003), at time corresponding to T_1 , the force is assumed to be large enough to overcome the sum of the side and tip resistances of the pile. The force corresponding to this time is called F_{sd} , after which the pile begins to depart from the soil, and therefore, F_{sd} is believed to correlate well with the ultimate pile bearing capacity.

After the time T_1 , the pile begins to move relative to the soil. The penetration continues until the force in the pile falls below the resisting force offered by the soil, at which time, the soil re-adheres to the pile and will move up with the pile during elastic rebound. When this occurs at time T_3 , the force in the pile head is denoted by F_{ds} . F_{ds} is the side friction between the soil and the pile plus the end bearing that is just large enough to prevent movement of the pile with respect to the soil.

Between times T_1 and T_3 , the force-time curve is generalized to either form a peak or a trough. A peak force will develop if the rate of flow of energy from the ram is faster than the pile can absorb. This is characteristic of a pile with relatively low impedance. A trough will occur if the pile head moves readily away from the ram. This corresponds to a pile having a value of impedance that is relatively large. The time when the maximum peak force or minimum trough force (F_p) occurs is T_2 . The occurrence of a peak force between times T_1 and T_3 is shown in Figure 132. F_p marks the maximum force in the pile at which the force in the pile starts to decline thereby causing the pile shaft to elastically rebound. The pile rebounds due to elastic unloading of the pile and of the soil below the tip. Usually, the upper portion of the pile springs back elastically more than the lower part of the pile, which tends to resist the upward pile movement and which in turn causes the pile to reach a state of static equilibrium. In the case where the force-time curve forms a trough (Figure 132), the force at the pile head increases so much when the pile shaft springs back elastically that it causes an increase in the force at the pile head sensor.

Time T_4 indicates the end of the impact event. If recorded long enough, the force usually diminishes to zero.

When placed at the pile toe, a force sensor can also yield the tip capacity. Thus, knowing the total pile capacity from the pile head sensors and the tip capacity, the side resistance can be determined.

Excessive pile driving stresses can lead to pile damage. Using the measured forces in the pile, the driving stresses can be determined in the field. Therefore, the structural integrity of the pile can be easily maintained by limiting the driving stress to be below allowable values during driving.

If pile damage is suspected during driving, the pile integrity can be determined by viewing the force-time curves on an oscilloscope, which forms part of the data acquisition system. Possible indications of pile damage include an abrupt change in the force-time curve for the pile head coupled with a diminution of the force-time curve for the pile toe. However, the latter can also occur when the pile tip penetrates from a firm stratum to a weaker stratum. Therefore, consideration of the force-time curves for both pile head and toe coupled with judgment based on observations during driving (e.g., sound of the hammer impacting the pile and blow counts) are necessary to assess pile integrity.

The hammer transfer efficiency, η , is the percentage of the total hammer energy that is effective in causing the pile to move. It can be estimated as follows:

$$\eta = \frac{E_m}{E_t} \quad (51)$$

where E_m is the component of dynamic energy within the force-time curve that causes the pile to move and E_t is the total energy of the ram. For single acting and drop hammers, E_t is equal to the

product of the weight of the ram and the stroke. Neglecting the effects of the energy due to pile inertia, E_m can be approximated as follows:

$$E_m = SF_{ave} \quad (52)$$

where S is the pile set and F_{ave} is the average force between times T_1 and T_3 . F_{ave} is obtained by dividing the integral of the force-time curve between times T_1 and T_3 by $(T_3 - T_1)$. At or near refusal, the pile set and therefore, the hammer transfer efficiency approaches zero. As a result of the small set, the impact energy readily rebounds from the pile back into the ram. When the pile is far from refusal, consistently low values of hammer transfer efficiency could be an indication of the use of an inadequate hammer.

Two Smartpile measurements in the field are shown in Figures 133 and 134. The records in Figure 133 have both pile head and bottom measurements and the records in Figure 134 have the head measurement alone.

The static bearing capacity can be obtained directly from the field measurement. For testing pile shown in Figure 133, the predicted total static bearing capacity is $F_{sd} = 3,896\text{kN}$ (438tons) with the end bearing capacity $F_t = 1,939\text{kN}$ (218tons) and side friction capacity $F_s = 1,957\text{kN}$ (220tons). For the testing pile shown in Figure 134, the total predicted static bearing capacity is $F_{sd} = 2,224\text{kN}$ (250tons)

2.8.4 Case Histories

Two cases presented by Ooi and Frederick (2003) and several testing results in Cambridge, MA reported by Haley & Aldrich (1995) are provided and discussed herein.

The results of Smartpile tests conducted during the installation of two 305mm (12in) square pre-cast and pre-stressed concrete piles are compared to the results of static load tests on the same piles. These piles were constructed to support a bridge along Route 315 over Farmington River near Simbury, Connecticut. The design engineer for this project was Fay, Spofford and Thorndike and the piling contractor was Mohawk Northeast, Inc.

The subsurface soils consist of a sand and silt layer that is at least 24.4m to 25.9m (80 to 85 feet) thick. Based on blow counts of about 3 blows/25mm (blows/inch) during final driving, the two test piles did not appear to be end bearing in a very hard stratum. The piles were driven using an Uddcomb H6H external combustion hammer.

For simplicity, the piles are denoted as test piles 1 and 2. Test pile 1 was 24.1m (79ft) long driven at Pier 2 on April 7, 1992. Based on the force-time plot from the pile head sensor (Figure 135), the ultimate bearing capacity was estimated to be about 868kN (98tons) using Smartpile. The tip capacity of the pile is fairly negligible (7.5kN or 0.84tons). This is consistent with the soil profile and with the low blow counts during driving. The results of a static load test performed on April 10 and 11, 1992 (3 to 4 days after Smartpile testing) are presented in Figure 136. The ultimate pile capacity was estimated using the following methods: Davisson's (1972) limit load criterion, DeBeer's (1967) method, Chin's (1970 & 1971) method and Brinch-Hansen's (1963) 80% criterion. The results of these load test interpretation methods are summarized in Table 16. The ultimate capacity of test pile 1 varies from a low of 543kN (61tons) using DeBeer's method to a high of 1,050kN (118tons) using Chin's method. The ultimate capacity of 868kN obtained via Smartpile interpretation seem to fall at the very high end of the static applied load and substantially higher than the capacity obtained via the

Davisson's criterion of 560kN (63tons). The settlement required to mobilize the ultimate capacity in test pile 1 is about 12mm (0.46inches).

Test pile 2, 28m (92ft) long, was driven at the east abutment of the aforementioned bridge on May 16, 1992. Based on the records shown in Figure 137, the ultimate bearing capacity of this pile was estimated to be about 1,080kN (121tons) using Smartpile. The tip capacity was not measured. A static load test was performed on May 27 and 28, 1992, 11 to 12 days after Smartpile testing. Based on the load-settlement curve shown in Figure 138, the static ultimate pile capacity was estimated using the same procedures as for test pile 1. A summary of the load test interpretation methods is also shown in Table 16.

The ultimate capacity of test pile 2 varies from a low of 712kN (80tons) using DeBeer's method to a high of 1,210kN (136tons) using Chin's method. The ultimate capacity of 1,080 kN using Smartpile again coincides with the maximum statically possible applied load and substantially higher than that obtained by Davisson's Criterion. The settlement required to mobilize the ultimate capacity in test pile 2 is about 15mm (0.6 inches). Compared to test pile 1, the higher capacity in test pile 2 is due to the increased pile length and therefore, larger side resistance.

Based on the results of static load tests on two 305mm (12-inch) square precast, prestressed concrete piles, compared to the capacities derived using Smartpile, the latter are close to the upper bound of possible static loads. Values of pile capacity using Smartpile are higher than those predicted using Davisson's method by about 55% for test pile 1 and 26% for test pile 2. Values of pile capacity using Smartpile are very similar to those predicted using Brinch-Hansen's 80% criterion.

Typical Smartpile records for a pile foundation project in Cambridge, MA are presented in Figure 139. Comparison between predictions by standard dynamic testing (PDA) using the Case method and the Smartpile predictions are summarized in Table 17 and presented in Figure 140. The results suggest the Smartpile predictions to be consistently higher (excluding one case) in comparison to the Case method predictions.

2.8.5 Summary And Conclusions

The Smartpile method is not a commonly used method and theoretical and experimental research requires its in-depth examination. The results of static load tests on two friction piles were compared to the results of Smartpile testing. When compared to the commonly used Davisson's pile load test interpretation method, Smartpile was found to over-predict the pile capacity having very similar values to those obtained via the Brinch Hansen's 80% load test interpretation criterion. These limited observations may indicate on the inability of the interpretation method to account for the dynamic effects as well as load and resistance progression along the pile (in contrast to the rigid body assumption made). Lack of field testing makes it difficult to derive general conclusions. The following conclusions are based, therefore, on the evaluation of the theoretical basis against the limited testing results.

Advantages of the Smartpile method are:

1. Similarly to routine dynamic testing during driving, the test is non-destructive and the test piles can be used as production piles.
2. The ultimate bearing capacity of the pile is obtained directly without use of any empirically derived calibration constants or factors and without the need to estimate the dynamic resistance of the pile. As a result, the pile bearing capacity can be obtained immediately in the field. No office analysis is required.

3. The tip capacity of the pile can also be directly measured. Thus, the side resistance can be calculated by subtracting the tip capacity from the total ultimate pile capacity.
4. Correlation of the bearing capacity of production piles to those of the test piles can be achieved using ancillary equipment.
5. The test equipment including data acquisition system, software and cables are portable.
6. Information on pile integrity can be obtained during driving.
7. The hammer transfer efficiency, which is a measure of the energy required to advance the pile in relation to the total energy delivered by the hammer, can be estimated.
8. The test can be performed on both driven piles and bored piles (drilled shafts). To test drilled shafts, a drop hammer is required to provide the impact on the test shaft.

Some of the disadvantages of this method (especially those that lie in it theoretical assumptions) are:

1. The method assumes the pile to be a rigid body, which may be applicable in some theories (e.g. total work done by penetration). It seems however that the Smartpile method used this assumption to conclude that the soil resistance at the side and the tip of the pile is mobilized at the same time or reaches its maximum value at the same time. This may be true only for very stiff piles primarily in soft soils. The real pile-soil interaction mechanism during penetration under dynamic forces is far more complex.
2. The Smartpile method assumes no difference between the dynamic resistance and the static resistance of the soil when F_{sd} was thought as the ultimate bearing capacity. This again may not be reasonable in many cases in which either large soil displacements take place and/or the soil is highly viscous.
3. The transducers installed in the pile cannot be retrieved after the test. This results in extra cost due to time (e.g. installation during casting of precast piles) and materials. In addition when considering pile monitoring during construction there is a need to randomly select the tested pile.
4. Professional experience with dynamic pile driving monitoring suggest that the force signals in many cases could not be so easily categorized into the two cases as assumed by the method. No substantiation to this assumption was provided by the method.
5. Limited information on Smartpile system is available and more tests need to be performed.

2.9 THE SMARTCOIL SYSTEM

2.9.1 Background and Use

The Smart Coil System (SCS) is a proprietary load testing method being developed by Leonard Frederick of Frederick Engineering Company of Whippany, New Jersey. The SCS consists of magnetic flux sensor, which is wrapped around the pile during driving, and an accompanying data acquisition system. A typical SCS setup is shown in Figure 141.

The SCS is based on the principle of magnetostriction. When a stress is applied to a magnetostrictive material, such as steel, there is a corresponding change in the magnetization. This accompanying change is known as the Valleri Effect. When a stresswave is induced into the pile during driving or restrike, a magnetic flux sensor coiled around the pile develops an electrical current. The developer of this method claims that this electric current is proportional to the resistance of the pile be-

ing driven. Since any magnetostrictive material produces this current, this system can be used on any pile that contains steel, such as steel pipe piles and reinforced concrete piles.

2.9.2 Advantages

The main perceived advantage for the SPS is the convenience of use. The system can be placed around any pile containing steel that is driven or installed in such a way that produces stress within the pile (e.g. jacking).

It is unknown at the present time whether the system is comparable in price to conventional static load tests.

2.9.3 Limitations

There are several disadvantages and/or limitations related with the SCS. The most severe of these limitations is that lack of a simplistic method of determining bearing capacity. According to the developer, the system is calibrated during the driving of one pile, after which it can be used for additional piles of the same type. However, it is unclear as to whether this calibration is based on corresponding static load test results or other means. Additional limitations include:

- a. **Pile Accessibility:** A portion of the pile must be uncovered in order for the system to work, thereby preventing driving to ground level.
- b. **The SCS does not work on non- magnetostrictive material,** such as timber piles.
- c. **Sensitivity:** It is uncertain if the system is sensitive to accompanying magnetic fields, such as those produced by power equipment and power lines.
- d. **Lack of Relevant Literature:** At the present time, the developer has not published details about the SCS in any geotechnical engineering publication.

2.9.4 Need for Research

The Smart Coil System is a unique and attractive load testing method for driven piles. The lack of relevant literature and accompanying peer review of the system, coupled with no known comparison of SPS test results to static load tests, illustrates the need for the system to be evaluated. The primary focus of the proposed research will be to critically review of the testing and analysis methods based on relevant theory and correlate these to future static load tests.

CHAPTER 3

FINDINGS – DATABASES AND INTERPRETATIONS

3.1 OVERVIEW

The performance of an analysis and/or a testing method can be examined when compared to a reference (benchmark) measurement. The results of a static load test serve as such reference and hence are important when evaluating a method of analysis (Paikowsky 2002) or a testing method (see section 2.4). The key stages of using static load test results for the evaluation of other test results are:

- (a) Evaluation of the static testing methods and the establishment of a nominal strength.
- (b) Development of databases that compare the examined method and/or analyses to the established strength.

The first part of this chapter (sections 3.2) is based primarily on relevant findings of Paikowsky (2002). Other sections in this chapter are related to the databases developed specifically for the current study. The chapter focuses on the methods for which significant data were accumulated and does not include limited databases that are used as part of the critical assessment (e.g., section 2.5 and Appendix A for the Osterberg Cell technology and section 2.6 for the Simbat Method). The details of the relevant databases are provided in Appendix B.

3.2 DEEP FOUNDATIONS NOMINAL STRENGTH

3.2.1 Overview

Probabilistic calibration of resistance factors for any predictive method utilizing a database is possible when the nominal geotechnical pile strength (i.e. static pile capacity) is defined and compared to the outcome of the calibrated prediction method. The definition of ultimate static capacity given static load test results (load-displacement relations) is not unique, and the use of the term reference static capacity for calibration (may include judgment) is more appropriate than nominal strength. The static load test results depend on the load testing procedures and the applied interpretation method, often being subjective. The following sections examine each of these factors and its influence on the reference static capacity, concluding with a recommended unique procedure to be followed in the calibration.

3.2.2 Databases

Three major databases were developed by Paikowsky (2004) for the primary statistical evaluation of resistance factors for the design and construction of driven piles and drilled shafts. Six additional peripheral databases were assembled and/or used for the investigation of specific aspects as needed. The features of the major databases are described below. Detailed cases are presented in Appendix B (dynamic) and Appendix C (static) of Paikowsky (2004).

The drilled shaft database consists of 256 drilled shaft cases and was developed at the University of Florida mostly as an integration of databases gathered by the Florida Department of Transportation (FDOT), the Federal Highway Administration (FHWA) and by O'Neill et al. (1976). The driven pile static analysis database consists of 338 driven piles. The database was

developed at the University of Florida mostly as an integration of databases gathered by the University of Florida (UOF), FHWA, and the University of Massachusetts Lowell (UML) (see e.g. Paikowsky et al., 1994), and the Louisiana Transportation Research Center (LTRC). The driven pile dynamic analysis database PD/LT2000 contains information related to 210 driven piles that have been statically load tested to failure and dynamically monitored during driving and/or re-strike (403 analyzed measurements). PD/LT 2000 is comprised of the integration of databases PD/LT (Paikowsky et al. 1994) and PD/LT2 (Paikowsky and Labelle, 1994) with expansion by an additional 57 pile cases as described by Paikowsky and Stenerson (2000).

3.2.3 Failure Criterion for Statically Loaded Driven Piles

Past work related to driven piles (Paikowsky et al. 1994) have resorted to a “representative” static pile capacity based on the assessment of five interpretation methods; Davisson’s Criterion (Davisson, 1972), Shape of Curve (similar to the procedure proposed by Butler and Hoy, 1977), Limiting Total Settlement to 25.4 mm and to 0.1B (Terzaghi, 1942), and the DeBeer log-log method (DeBeer, 1970). A single representative capacity value was then calculated for the analyzed case as the average of the methods considered relevant (i.e. provided reasonable value). The evaluation of a new testing method or the development of LRFD calibration in a framework suitable for future modifications (Paikowsky 2004) requires that the evaluated resistances are based on an objective, reproducible procedure. In order to do so, the static capacity of each pile in database PD/LT2000 was evaluated utilizing all five aforementioned criteria and a representative capacity was assigned for each pile. A statistical analysis was then carried out by determining the mean and standard deviations of the ratio of the representative pile capacity to the method being evaluated. Details of the analyses and their results are presented by Paikowsky and Stenerson (2000). Figure 142 shows the histogram and calculated distributions (normal and lognormal) for Davisson’s failure criterion in which k_{SD} is the ratio of the designated static capacity to that defined by Davisson’s failure criterion. Davisson’s criterion was found to perform the best overall and was therefore chosen as the single method to be used when analyzing load-displacement curves. The method provides an objective failure criterion and was also found to perform well for piles exceeding a diameter of 610mm (examined through 30 pile cases). The data presented in Figure 142 demonstrates, however, that: (i) though small, a bias exists in the static capacity used as a reference for the evaluation of predictive methods for capacity evaluation of driven piles, and (ii) this bias (and other considerations) needs to be accounted for when evaluating the interpretation results of a specific field static load tests.

3.2.4 Load Test Procedure for Statically Loaded Driven Piles

An additional factor to examine is the influence of the static load testing procedure (loading rate within the ‘static’ range) on the designated pile capacity. This influence was examined in two ways. Two detailed case histories from a research site in Newburyport, Massachusetts, were evaluated. A pipe and pre-stressed concrete heavily instrumented friction piles were tested over a lengthy period of time at a bridge reconstruction site. Both piles were tested using three types of static load testing procedures: slow maintained (testing duration of about 45 hrs), short duration (testing duration of about 6-8 hrs), and static cyclic (testing duration of about 15 min.). Details about the piles and the testing are presented by Paikowsky and Hajduk (1999, 2000) and Paikowsky et al. (1999), the load-settlement results for the concrete pile were presented in Figure

46. The interpretation of the load-displacement relationships in both cases suggested that the ‘static’ test type had an insignificant influence on the pile capacity, (referring to a failure criterion irrespective of the displacement).

The effect of the test type was further investigated utilizing a database containing information related to 75 piles tested under slow maintained and static-cyclic load testing procedures. In the static-cyclic procedure, the piles were loaded to failure using a high loading rate and then unloaded. The process was repeated for four cycles. The testing procedure and its interpretation method are presented by Paikowsky et al. (1999). A comparison between the pile capacity based on Davisson’s failure criterion for the slow maintained tests and the static-cyclic capacity is presented in Figure 143. The obtained relations and the associated statistical information suggest that there is no significant influence on the static pile capacity based on the applied static load rate. The static cyclic load test results were also compared to the representative static pile capacity (based on the aforementioned five methods) resulting in a mean K_{SC} of 1.023 and a standard deviation of 0.057.

These evaluations led to the conclusions that Davisson’s pile failure criterion can be used as a method to determine the reference pile capacity for driven piles irrespective of the pile’s diameter and the static load-testing procedure.

3.2.5 Failure Criterion for Statically Loaded Drilled Shaft

Static load tests of small to medium capacity drilled shafts (say up to 5 MN) are similar to that of driven piles. It is common, however, to design and build high capacity drilled shafts (10 MN and more) often as an alternative to a large group of small capacity driven piles (e.g. in the Northeast region of the USA). As part of the current project, the static load-test results of drilled shafts were gathered for the drop weight database. These tests were examined utilizing the failure criteria previously described for driven piles, and the FHWA criterion for drilled shafts (O’Neil and Reese, 1999). This criterion establishes the failure load as that associated with a displacement of five percent of the diameter at the shaft (0.05B), if plunging of the shaft cannot be achieved. The results of this study are presented in Table 18, suggesting that the use of the FHWA criterion provides a reliable and a simple failure interpretation for statically loaded drilled shafts.

3.3 DROP WEIGHT DATABASES ANALYSIS

3.3.1 General

The DW/LT 2000 Database has been built up focusing on the research of cast-in-place pile testing using the drop weight system. A concentrated effort was made to obtain case histories where both, static load test and dynamic measurements of the drop weight system are available. Two hundred and fifty-four (254) cases were identified as potentially viable for the drop weight system analysis. The task of actually obtaining reliable static pile load-test results with dynamic measurements was found to be more difficult than first anticipated. While 167 cases were analyzed for dynamic measurement, only 39 cases of the statically loaded drilled shafts (the only type of in-place constructed deep foundation used) met the FHWA failure criterion. The databases were separated and renamed therefore as DW2000 for all cases and DW/LT 2000 for the cases containing static and dynamic data, presented in Appendix B. The results of the data-

bases analyses are presented and discussed in the following sections. These analyses allow us to examine the requirements of the drop weight driving system and carrying out a significant analysis of the method's accuracy.

3.3.2 General Drop-Weight System Evaluation

3.3.2.1 General Relationship

The general DW 2000 Database was evaluated to examine levels of delivered energy vs. evaluated capacity. Figures 144 to 146 present the relationship between static capacities based on a signal match prediction (using CAPWAP) vs. the maximum measured transferred energy. Figure 144 shows all available cases (167), while Figure 145 presents the same data using the ratio of predicted capacity over the measured transferred energy vs. the transferred energy. Figure 145 also presents the zones, which limit data around the mean of the ratio between the calculated capacity and the transferred energy. These zoning allows to identify “outliers” and chose reasonable data, excluding data points beyond one and a half standard deviation (1.5 S.D.) around the mean. Figure 146 examines the cases for which both extremes of high capacity with low energy or low capacity with high energy were omitted (9 cases only). Figure 147 presents the relationship between the nominal energy (potential energy of the ram based on it's mass and the drop height) and the transferred energy calculated by the dynamic measurements (integration of the velocity times the force with time). The mean of the data (38.8%) reasonably agrees with the slope of the best-fit line through the data.

3.3.2.2 Drop Weight System Requirements

The observed relationship in Figure 147 together with the average transferred energy efficiency of 154 cases, ($\eta=39\%$) were translated to the dimensions of drop weight system vs. capacity combination (with $\eta=40\%$ for simplicity). These initial recommended relationships are tabulated in Table 19 and were used as a preliminary recommendation to guide the study.

3.3.3 Drilled Shafts Static Capacity

3.3.3.1 Database DW/LT 2000

Two tables in Appendix B summarize all the cases for which details of static load test results (load-displacement relations) could be obtained along with dynamic measurements and signal matching capacity predictions. The first table (p.1-p.8) provides details regarding the shaft's geometry and construction as well as the static capacity, and the second table (p.9-p.14) provides details regarding the dynamic measurements and the prediction ratio. A total of 68 cases were gathered out of which 44 cases were for drilled shafts in which the load test was carried out to failure and 24 cases are for shafts for which failure was not obtained. As not all 44 shafts satisfy all failure criteria, or they are irregular (e.g. CFA shaft) some are excluded from the various analyses. It should be noted that at times even if clear failure was not obtained, the test was carried out to satisfy one of the failure criteria. The number of cases therefore does not match between one interpretation analysis to the other.

3.3.3.2 *Static Capacity*

The shafts for which the load-test was not carried out to failure were analyzed for load-test extrapolation based on the procedure proposed by Paikowsky and Tolosko (1999). All cases were analyzed using Davisson's failure Criterion (Davisson, 1972), DeBeer's Criterion (DeBeer, 1970), shape of curve similar to the method proposed by Butler and Hoy (1977) and the FHWA drilled shafts capacity criterion (absolute displacement equal to 5% of the shaft's diameter). Details of the methods are provided by Paikowsky et al. (1994) and Paikowsky and Tolosko (1999). A representative capacity value is achieved by averaging the "acceptable" capacities of the different methods.

3.3.4 **Static Shaft Capacity vs. Drop Weight Dynamic Predictions**

A set of 12 graphs were prepared examining the relationships between the predicted capacity based on dynamic measurements and signal matching analysis (CAPWAP) vs. static capacity. The different relationships are based on four different capacity evaluation methods (representative, Davisson, FHWA, and DeBeer) and three states of data (all data, only shafts loaded to failure, and only non-failure static load tests with extrapolated load displacement relations). The graphs are presented in Figures 148-159. A summary of the obtained results including the number of the related figure is provided in Table 20.

The presented data and the statistical analysis suggest the following:

- a. The dynamic prediction for the cases in which the drilled shafts were loaded statically to failure are very accurate with overall prediction ratio varying between 0.85 to 1.05 and standard deviations between 0.12 to 0.19 with very small over prediction, (on the unsafe side). These cases are limited to a maximum shaft capacity of 17MN.
- b. The predictions are particularly impressive when referring to the 'adopted' static failure criterion, i.e. the FHWA method (0.05B) for which the bias for the 39 analyzed cases is 1.05 and the standard deviation is 0.12, hence having a COV of 0.114.
- c. The cases for which extrapolation was required, result in substantially overall less accurate prediction and a high scatter. These included however five drilled shaft cases in the capacity range of 20 to 33MN and most likely dynamic loading could not mobilize the shaft's capacity.
- d. The obtained results are promising regarding the accuracy of the method and need to be further evaluated in relation to the accuracy of the dynamic predictions as obtained for driven piles and static analysis predictions for drilled shafts.

3.3.5 **Evaluation of Results**

3.3.5.1 *Overview*

The obtained results are backed by a good size database, and hence, affirms the performance of the drop weight system. As the method of data acquisition and analysis is similar to that used for dynamic testing of driven piles, an assessment of the results is achieved via comparison to statistical analyses for driven piles. A perspective is also gained by examining the accuracy of static analysis methods commonly used in the design of drilled shafts.

3.3.5.2 *Static Capacity vs. Dynamic Predictions for Driven Piles*

Time of driving, driving resistance, and area ratio proved to be controlling parameters for the dynamic method's performance for driven piles (Paikowsky, 2004, Paikowsky and Stenersen, 2000). Table 21 present the data relevant to the drilled shafts dynamic analyses. By and large, the dynamic impact of drilled shafts is not associated with large soil displacements and often is accompanied by what could be termed for driven piles as 'refusal' --high driving resistance. The relevant cases are therefore the signal matching (CAPWAP) analyses of driven piles during re-strike (marked by BOR in Table 21). For these cases, very little effect was found to the driving resistance (blow count) and overall the signal matching technique of the dynamic measurements was proven as a very accurate method. The results presented in Table 20 for the tests to failure should therefore be compared to the results presented in Table 21 for the BOR cases. As Table 21 refers to static analysis that was defined by Davisson's failure criterion, a direct comparison can be done with the relevant analysis in Table 20. Overall, a fairly reasonable accuracy was obtained in both databases, COV= 0.224 for the drilled shafts and COV = 0.339 for the driven piles. While the bias of the driven piles suggests a small under prediction (1.158) the bias of the drilled shafts suggest an over prediction (0.85).

3.3.5.3 *Static Capacity vs. Static Analysis Predictions for Drilled Shafts*

Paikowsky (2004) examined the performance of the drilled shaft's static analysis methods depending on the soil type, design method, and construction method. The static analysis methods predicted the drilled shafts capacities in ratios varying between 0.83 to 2.27 (measured over predicted) with coefficients of variation varying between 0.25 to 0.74. Table 22 presents a statistical summary of the FHWA drilled shaft design method (Reese and O'Neill, 1988) when applied to drilled shafts in sand, clay, mixed soil and rock (IGM method see O'Neill et al., 1996, O'Neill and Reese, 1999) for varied construction methods.

The overall results suggest that the static analyses are by and large over predictive (on the unsafe side) except when the drilled shafts are constructed in clay, and overall the uncertainty of the prediction is high compared to the drop weight testing performance.

3.3.5.4 *Intermediate Conclusions*

A very high accuracy in prediction was obtained using the drop weight system for drilled shafts. The data related to the driven piles affirms the statistical analysis that was obtained for the drilled shafts when related to cases of restricked piles and relatively small displacements. While it is expected that the drop weight tests under the examined conditions would result with predictions more accurate than static analyses, the accuracy presented in the results of Table 20 remain surprisingly good. One possibility is the lack of knowledge regarding 'class A' predictions for which the dynamic analyses were carried out without the knowledge of the static load-test results. The conclusion regarding the effectiveness and high accuracy of the method remains overall with the emphasized need for additional data of high quality testing.

3.3.6 Ram Requirements

The previously developed guidelines (section 3.3.2.2) can now be evaluated based on actual performance. Figure 160 presents the relationship between the accuracy of the prediction (ratio of static capacity over dynamic) versus ram weight over the static capacity (Figure 160a utilizing the representative capacity and 160b utilizing the FHWA failure criterion) for all cases. The overall trend of the data suggests that when the ram's weight is below 1% of the capacity, there is mostly under prediction, as apparently the capacity could not have been mobilized. In an attempt to further shed light on the observed behavior, the pile cases were categorized according to end bearing piles and friction piles both for cases in which the load test was carried out to failure and extrapolated cases. This categorization was based on two examinations (i) shape of curve (general failure was assumed to be related to friction piles) and (ii) soil type at the tip (see Appendix B for details). Examination of the data in Figure 160 (a and b) based on this categorization suggests the following conclusions:

- a. End bearing shafts most likely require larger ram to capacity ratio for possible mobilization of the capacity. A ratio of over 1.5% seems as appropriate.
- b. The capacity of shafts utilizing mostly friction resistance can be mobilized with ram weight of over 1% of the expected capacity.
- c. It is reasonable to assume that the extrapolated cases were such that both static and dynamic testing did not succeed to mobilize the capacity.
- d. More data are required to confirm the above conclusions.

Further examination of the ram and capacity relations is carried out in the data analysis presented in Figures 161 and 162. Figure 161 was developed using the data for static load test capacity based on FHWA criterion for all cases (failure and extrapolation) providing the relationship between the shaft capacity and the weight of the ram used in the test. The obtained relationship (though a trendline of limited correlation as indicated by the coefficient of variation) is used to develop Figure 162. The relationships of both curves support those presented in Figure 160. It also suggests that smaller rams can mobilize relatively smaller capacities and the use of a ram weight as 1% of the expected capacity requires a ram heavier than a certain minimum. Additional two lower and upper data encompassing trendlines were added to Figures 161 and 162. These lines suggest that no ram weight less than 0.5% of the measured capacity should be used and a ram weight of 2.5% of the capacity should not encounter any difficulty in the mobilization of the capacity under any given conditions (excluding the structural limits of the piles). The relations in Figures 161 and 162 are supplemental only and are limited to the available data at the present time.

3.4 STATNAMIC DATABASE ANALYSIS

3.4.1 Overview

A comprehensive database was assembled from 34 deep foundations load test sites where both Static (SLT) and Statnamic (STN) testing were conducted. Table 23 provides a summary for the statnamic database. The deep foundations studied include cast-in-place and driven concrete piles, as well as driven steel pipe and H-piles. Six of these comparisons were in Japan, two in Taiwan, while the remainder were installed and tested in the United States. The main bearing soil strata of each pile was determined from boring logs and divided broadly into four subgroups:

rock, sand, silt, and clay. As the Statnamic testing induces loading rate effects, the effects were considered based on soil types. A rate effect factor (η) was introduced to unify the reliability and statistical probability of failure as outlined by FHWA (1998) for Load and Resistance Factor Design.

3.4.2 Background

Since its inception in the late 1980s, Statnamic (STN) testing has been studied and evaluated to provide Static Load Derived (SLD) capacity. The Unloading Point Method (UPM) is the most widely used and accepted means of regressing Statnamic data (see section 2.3.5.3). The UPM subtracts two components from the original STN load-displacement curve to produce the SLD curve. These two components are an inertial effect, due to the acceleration of the foundation, and a viscous damping effect due to the velocity of the foundation. Both of these components affect the true Static capacity of the foundation, and therefore must be determined during STN data regression. The UPM is subdivided into three analysis categories: (1) Basic UPM using only top of pile measurements, (2) Modified Unloading Point (MUP) which uses the basic UPM measurements as well as toe acceleration measurements, and (3) Segmental Unloading Point (SUP) which uses top and toe measurements (as in MUP analyses) as well as strain measurements along the length of the foundation. The appropriateness of each analysis method is largely dependent of the foundation length and material. As such, when meeting the requirements of these methods, the analysis of the foundation is reliable.

Numerous researchers and industry leaders have previously conducted studies involving the comparison of SLT and STN testing on the same or nearby foundations to physically compare test results. A comprehensive review of all available literature on these studies and their data had yet to be done to investigate a universal effectiveness of the SLD-predicted capacity as compared to an SLT capacity. However, with the continued use of STN testing worldwide and the growing number of data sets becoming available, this study is immensely important in its goal of developing a unified STN analysis method for foundations in each soil subgroup.

3.4.3 Sources of Data

To gather appropriate information for a diversified database, several sources were utilized consisting of testing consultants, published literature, university researchers, Federal organizations, and equipment manufactures. Applied Foundation Testing, Inc. contributed data from many projects involving various types of piles and soils tested commercially in the United States. The soil data for the test piles from Japan were extracted from earlier publications showing comparisons between regressed STN data and SLT data (Inamura, et al., 1995; Sakimoto, et al., 1995; Nagaoka, et al., 1995; Matsumoto, et al., 1995). Electronic raw data sets were also made available by the respective authors. Auburn University contributed the raw data collected during a testing program which included STN and SLT testing of drilled shafts in silt at the NGES in Opelika, Alabama. The Federal Highway Administration (FHWA) contributed data from tests of H-piles in their test pit. Berminghammer, Inc. of Hamilton, Ontario also contributed data from two test piles that had been tested in Taiwan. A unique name was generated for each test pile and data set in the database which contained the pile type, bearing strata soil type, whether both test were conducted on the same pile or adjacent piles, the order of testing, the comparison method used, the SLT method, and identification information. For simplicity, a coding scheme was de-

veloped for each parameter of the unique name that would enable further analysis and sorting capabilities as more data became available. Figure 163 illustrates the definition of the codes used to sort the load test information. Table 23 is a summary of the analyzed test programs.

3.4.4 Analysis Procedure

The raw STN data for each pile was analyzed using SAW R4, a macro-driven spreadsheet developed by the University of South Florida (USF) for STN data regression using the UPM, MUP, or SUP. SLD curves were generated from SAW R4 and transferred to a separate workbook developed for this study to compare the SLD and SLT curves of each pile side by side. These workbooks were used to develop a database that could be further analyzed to determine the load rate effects on each pile systematically. Data was collected from the researchers pertaining to the geotechnical site conditions in the form of SPT and CPT evaluations. Based on these site evaluations each comparison data set was subdivided into a soil subgroup dependent on the soil type of the bearing layer. The four subgroups were: sand, silt, clay and rock. The geotechnical differences amongst these soil types warranted investigation of each individually, rather than as a whole. Thereby the effects of differing soil types on the SLD curves could be analyzed accordingly.

Four methods were employed to determine the appropriate capacities for comparison purposes from the unadjusted SLD and SLT curves. These included the Davisson, Projected Davisson, Smallest Displacement, and Projected Envelope. All of the piles used for this study were evaluated using either the Smallest Displacement or the Projected Envelope method. The Smallest Displacement method determined the lesser maximum displacement of either the SLD or SLT curve at which displacement the load of the both tests could be compared. Capacities of each curve at this displacement were then recorded in the database. The Projected Envelope method was used to determine the capacity of a pile after the soil had been yielded during a previous test and a load-displacement curve had been fully developed. This involved the calculation of a failure envelope and its equation was used to predict a capacity to which the other test could be compared at a maximum displacement. The Davisson and Projected Davisson comparison methods utilize the Davisson failure capacities as prescribed by the FHWA, and remain as options as the database is expanded in the future.

The database was developed to automatically link and update the curves in each soil subgroup through a master workbook. The bias factor (λ) of each pile could be calculated upon the selection of a soil specific η . The bias factor is a measure of the precision with which the SLD capacity predicts the SLT capacity, and is calculated by equation 53:

$$\lambda = \frac{SLT}{\eta SLD} \quad (53)$$

From this equation it can be seen that a λ value less than 1.0 would signify an over prediction by the SLD capacity, and a value of λ greater than 1.0 would signify an under prediction by the SLD capacity. Soil specific η values were determined that unified the average λ value for all soil types. Therein, a different η value was determined for each of the four soil types. The average and standard deviation of each soil subgroup λ value was used to determine a resistance factor for STN testing. Though presented in some of the tables, the calculated resistance factor

using FORM (First Order Second Moment) are beyond the scope of the present study.

3.4.5 Results

3.4.5.1 General

Examination of the SLD curves before and after application of the η_{soil} can be compared to show the effectiveness of this analysis method. The results of this study are presented in the following sections. Each section represents those piles founded in one of the four soil subgroups and includes a brief summary of the test site and parameters. Each set of graphs depicts an unadjusted data set (Pre) and η_{soil} adjusted data set (Post). The final section includes a summary of the results of each soil subgroup and defines the appropriate η values, which were determined from the analyses presented herein.

3.4.5.2 Rock

The first set of graphs show the data collected from piles installed and tested in Taiwan in 1999. These piles were founded in a weathered shale rock. The first set of load-displacement curves represent tests conducted on TFC 241, the second set on TFC 532. A SLT followed by a STN were conducted on TFC 241, whereas a STN followed by a SLT was performed on TFC 532. Both piles were 1.5 m diameter, approximately 75 m long drilled shafts. Figure 164 shows the load-displacement curves of TFC 241. These curves, based on the raw test data, already exhibit relatively similar load-displacement responses.

Figure 165 shows the same SLT curve, although an η_{rock} of 0.96 has been applied to the SLD loads to produce a slightly different SLD curve. The new SLD capacity used for comparison to the SLT capacity is taken at a displacement of -0.0172m. The SLD and SLT capacity at this displacement is -23387kN and -23544kN, respectively. Using equation 53, the bias factor (λ) for this particular comparison is 1.01, which indicates a slight under prediction of the SLT capacity by the SLD capacity with the η_{rock} applied. This is an example of the Smallest Displacement method used for this as well as other specimen piles.

Figure 166 shows the load-displacement response of the raw data collected from pile TFC 532, while Figure 167 shows the load-displacement response after applying η_{rock} . This pile was analyzed using the Smallest Displacement Method at a displacement of -0.0157m. The SLT and SLD capacities recorded at this displacement were 25,084kN and 24,548kN, respectively. Therefore λ for this pile was equivalent to 1.02. Although introduction of the η value makes the result conservative, the η value was determined based on the overall average performance of this test method in rock and was therefore applied to all such tests.

The second site at which piles were founded into rock was located in Florida, where the bearing layer consisted of both weak (N=23) and hard (N>50) weathered limestone. Both sets of data represent tests conducted on similar piles within close proximity to each other. The static load test configuration utilized an anchored reaction beam and conformed to the Quick Method. Figures 168 and 169 represent a comparison between two 1.0m diameter, 7.8m long drilled shafts. These shafts were compared using the Smallest Displacement Method at a displacement of -0.026m. The SLT and SLD capacities recorded at this displacement were 6,957kN and 6,587kN, respectively. Figures 170 and 171 show a comparison between two 1.0m diameter, 13.70m long drilled shafts. These shafts were also compared using the Smallest Displacement

Method at a value of -0.022m. The SLT and SLD capacities recorded at this displacement were 4,733kN and 5,164kN, respectively. The application of η_{rock} to both sets of data yielded λ values of 1.06 and 0.92.

The next site consisted of data recorded from a static and statnamic load test on the same pile that had been installed for a light rail system at JFK Airport in Queens, New York. The pile tested, known as Tapertube Pile, was a non-uniform polygon (12 sided) steel pile with 457mm (18in) top diameter and 203mm (8in) bottom diameter. The pile was 16m long and filled with concrete after driving. Kentledge (dead weight) static tests were performed with 1-hour holds for incremental loading and a 24-hour hold at maximum load. The static and statnamic data sets were compared using the Smallest Displacement Method at a value of -0.011m. The SLT and SLD capacities recorded were 3,509kN and 3,289kN, respectively, yielding a λ value of 1.07 (see Figures 172, 173).

Figures 174 and 175 show the results from a 0.8m diameter, 11m long steel pipe pile. This pile was installed at a test site in Noto Peninsula, Japan. The pile was driven through a soft rock known as Wakura Diatomaceous Mudstone (N=15). Statnamic testing was carried out 14 months after a cyclic static load test was conducted. This data set was evaluated the Projected Envelope Method. The SLT curve demonstrated a shear failure load of 4,440kN. After application of the η_{rock} the SLD capacity was 4,987kN. A λ value of 0.89 was determined for this pile.

The St. George Island Bridge site consisted of 6 concrete cylinder test piles, of which LT-1 was driven into a rock bearing layer. This pile was tested both statically and statnamicly. A static load test was performed first followed by three cycles of Statnamic testing. The three cycles of Statnamic testing were conducted seven days after the static load test. The 8 to 12 hour static load tests utilized a kentledge system rather than an anchored reaction system. LT-1 had an outer diameter of 1.37m, a wall thickness of 0.20m, and a length of 24.4m. Assessment of the data recorded for this pile concluded that the SLT and SLD capacities were 9,608kN and 9,316kN, respectively (see Figures 176, 177). The λ value for this analysis was equal to 1.03.

The average λ of the seven piles founded in rock used in this study was equal to 0.999, with a standard deviation of 0.068 after an η_{rock} value of 0.96 had been applied to the SLD loads.

3.4.5.3 Sand

The first three data sets founded in sand were collected from piles installed at the Bayou Chico Bridge site located in Pensacola, Florida. These piles were driven and tested in 1997. Figures 178 and 179 show the load-displacement curves generated from a cyclic static load test and a subsequent statnamic load test two months later of the same pile at Pier 15. This was a 610mm (24 in) square prestressed concrete pile, with a length of 10.5m. This pile was compared using the Projected Envelope method. The load-displacement curves generated from the 3 cycles of static load testing exhibit a failure envelope that has been plotted as the dotted line with constant slope. The slope of this line was determined from the maximum loads of each static load cycle and the corresponding displacements. Based on this analysis, the SLT and SLD capacities were 5,612kN and 5,387kN, respectively. After application of the η_{sand} the resulting λ value for this pile was 1.04.

Figures 180 and 181 show the load-displacement curves generated from a cyclic static load test and a subsequent statnamic load test two months later of the same pile at Pier 10. This was a 610mm (24in) square prestressed concrete pile, with a length of 13.4m. The data was evaluated using the Smallest Displacement method at a displacement of -0.013m. Based on this

analysis, the SLT and SLD capacities were 3,382kN and 3,175kN, respectively. After application of the η_{sand} the resulting λ value for this pile was 1.07.

Figures 182 and 183 show the load-displacement curves generated from a cyclic static load test and a subsequent statnamic load test two months later of the same pile at Pier 5. This was a 24" square prestressed concrete pile, with a length of 13.4m. The data was evaluated using the Projected Envelope method. Based on this analysis, the SLT and SLD capacities were 4,309 kN and 4,740kN, respectively. After application of the η_{sand} the resulting λ value for this pile was 0.91.

The next data set was collected from the Ohito Bridge site in Shizouka, Japan. A 1.5m diameter, 11m long Cast-In-Place Concrete Pile (drilled shaft) embedded 10.5m mainly in sandy gravel with boulders and an intermediate layer of low blow count ($N = 3$ to 5 blows) silt and silty sand. The bearing layer was dense sandy gravel with boulders having blow counts in excess of 50 blow counts. The static load test was performed four weeks after pile installation. The SLT consisted of five loading cycles to a maximum load of 24MN. The statnamic testing commenced ten days after the full release of the SLT load. A target Statnamic load of 12MN was desired for the test. Figures 184 and 185 show the load-displacement curves of the two tests prior to and after application of η_{sand} . The SLT capacity was recorded as 10,747kN, and the SLD capacity was 10,523kN. The SLD capacity was based on the Smallest Displacement method at a value of -0.096m. The λ value was equal to 1.02, which was a slight under prediction of the SLT capacity by the adjusted η_{sand} SLD capacity.

Figures 186 and 187 are load-displacement curves generated from testing of foundations for the Brooklyn Queens Expressway in Queens, New York. Two separate but similar shafts within close proximity to each other were independently tested and compared. The shafts had an outer diameter of 1.52m, and a length of 18.29m. The SLT capacity was recorded as 7,606kN, and the SLD capacity was 8,019kN. The SLD capacity was based on the Smallest Displacement method at a value of -0.008m. The λ value was equal to 0.95, which was a minimal over prediction of the SLT capacity by the adjusted η_{sand} SLD capacity.

The St. George Island Bridge site consisted of 6 concrete cylinder test piles, of which LT-5 was driven into a sand bearing layer. This pile was tested both statically and statnamicly. A static load test was performed first followed by Statnamic testing. The Statnamic testing was conducted three days after the static load test. The 8 to 12 hour static load tests utilized a kentledge system rather than an anchored reaction system. LT-5 had an outer diameter of 1.37m, a wall thickness of 0.20m, and a length of 24.3m. A Projected Envelope analysis of data recorded for this pile concluded that the SLT and SLD capacities were 12,575kN and 10,683kN, respectively (see Figures 188, 189). The λ value for this analysis was equal to 1.18.

The Shonan Test Site in Ciba Prefecture, Japan consisted of six test piles (5 concrete and 1 steel). All were statnamicly loaded but only four of the six were tested with both static and statnamic devices (Piles T1, T2, T5, and T6). Pile T6 was a driven steel pipe pile 13 m long, 400 mm outer diameter, and a 9 mm wall thickness. The pile was subjected to three Statnamic tests four weeks after installation, with the second and third tests being conducted two weeks after the initial Statnamic test. Figures 190 and 191 show the load-displacement response of these tests before and after application of η_{sand} . The SLT was performed two weeks thereafter. The Smallest Displacement method was used to analyze the data and determine SLT and SLD capacities of 1,028kN and 1,056kN, respectively. These capacities yielded a λ of 0.97.

Pile T5 was a PHC Pile that had been placed into a 5m deep bored hole and then driven an additional 2m. The bearing layer was composed of sand. This pile was 7 m long, had an outer di-

iameter of 400 mm and a wall thickness of 60mm. The report did not mention whether this pile was grouted as was piles T1 and T2. Pile T5 was subjected to three SLT cycles prior to a single Statnamic cycle. Figures 192 and 193 show the load-displacement response of these tests before and after application of η_{sand} . The SLT was performed two weeks thereafter. The Projected Envelope method was used to analyze the data and determine SLT and SLD capacities of 476kN and 509kN, respectively. These capacities yielded a λ of 0.94.

Piles T1 and T2 were PHC piles, 7m long, 400mm outer diameter, with a wall thickness of 60mm bored into a soil consisting of humus, loam, and clay for the first 6.5m and into a fine sand strata the remaining 0.5m. While extracting the auger the lower portion of the hole was injected with a lower water/cement ratio and higher compressive strength grout (35MPa), while the rest of the hole was injected with a higher water/cement ratio and lower compressive strength (20MPa) cement grout. Once fully grouted, the precast pile was placed into the freshly grouted excavation. Pile T2 was Statnamicly tested followed by three cycles of SLT. Pile T1 was subjected to two cycles of SLT, followed by two Statnamic tests 2 to 3 days after the SLTs.

Figures 194 and 195 show the load-displacement response Pile T2 before and after application of η_{sand} . The SLT was performed two weeks thereafter. The Smallest Displacement method was used to analyze the data and determine SLT and SLD capacities of 415kN and 451kN, respectively. These capacities yielded a λ of 0.92.

Figures 196 and 197 show the load-displacement response of Pile T1 before and after application of η_{sand} . The SLT was performed two weeks thereafter. The Smallest Displacement method was used to analyze the data and determine SLT and SLD capacities of 478kN and 505kN, respectively. These capacities yielded a λ of 0.95.

Ten piles that had been founded in sand were included in this study. The analysis of these piles provided an average λ of 0.994, with a standard deviation of 0.083 after the REF of 0.91 had been applied to each SLD data set.

3.4.5.4 *Silt*

The third soil subgroup included those piles bearing in silts. Figure 198 shows the load-displacement curves generated from a standard static load test and a subsequent statnamic load test two weeks later of the same pile. This pile was one of many installed in Opelika, Alabama by Auburn University during a testing series conducted in 1997. This pile was a 0.92m diameter, 11.54m long drilled shaft. Again, this pile was compared using the Projected Envelope method. Figure 36 shows the load-displacement curves from both tests prior to application of any REF. The load-displacement curve generated from the Static load testing exhibits a shear failure envelope that has been plotted as the dotted line with a vertical slope. By examination the SLD capacity over predicts the capacity that could be expected with regards to the shear failure envelope of the static load test. Figure 199 shows the same load-displacement curves, although the loads used for plotting of the SLD curve have been adjusted by the REF determined for silt as 0.69. By examination the SLD curve now slightly under predicts the pile's capacity at the maximum displacement achieved during the statnamic testing. The bias factor for the REF applied data was equal to 1.01, which confirms the slight under prediction of the static capacity by the SLD curve. The SLT and SLD loads used for this comparison are -2302kN and -2275kN, respectively.

Figures 200 thru 211 consist of results from identical piles as Aub 1 included in the Auburn testing series. These piles were founded in similar soil conditions as the previous set. The

SLD and SLT loads used for comparison of pile Aub 10 were 2069kN and 1647kN, respectively, yielding a λ of 0.80. The SLD and SLT loads used for comparison of pile Aub 8 were 1894 kN and 1672kN, respectively, yielding a λ of 0.88. The SLD and SLT loads used for comparison of pile Aub 7 were 2549kN and 2429kN, respectively, yielding a λ of 0.95. The SLD and SLT loads used for comparison of pile Aub 5 were 2496kN and 2703kN, respectively, yielding a λ of 1.08. The SLD and SLT loads used for comparison of pile Aub 3 were 1248kN and 1194kN, respectively, yielding a λ of 0.96. The SLD and SLT loads used for comparison of pile Aub 2 were 2304kN and 2397kN, respectively, yielding a λ of 1.04.

The remaining set of piles included in the Silt subgroup were installed and tested as part of a construction project for the Newark International Airport. These piles were closed end steel piles having a outer diameter of 0.32m, a wall thickness of 0.02 m and a length of 27.52m. After these piles were driven the inner cavity was filled with concrete. Each set of piles compared were separate piles installed within close proximity of the other. In all 5 piles were tested using SLT and 5 identical piles in similar soil conditions were tested using STN. The first set of piles were NIA TP 1&2a and were compared using the Smallest Displacement method and yielded capacities of 1511 kN and 1287kN for the SLT and SLD, respectively. The second set of piles (NIA TP 1&2b) was also evaluated using the Smallest Displacement method, which resulted in capacities of 2669kN and 2496kN for the SLT and SLD, respectively. The Smallest Displacement method was again used to analyze the third set of piles, being NIA TP 1&3a. This analysis resulted in a SLT capacity of 1576kN and a SLD capacity of 1397kN. The next set of piles (NIA TP 1&3b) were evaluated using the Projected Envelope method with which a SLT capacity of 2238kN and a SLD capacity of 2018kN. The next set of piles (NIA TP 9&10a) was again compared using the Smallest Displacement method, which yielded a SLT capacity of 2425kN and a SLD capacity of 2058kN. The sixth and final set included from this construction site were designated NIA TP 9&10b. The results of evaluating these piles using the Smallest Displacement method were a SLT capacity of 3371kN and an SLD capacity of 2947kN. The λ values for these six sets of piles range from 1.07 to 1.18. The following Figures 212 thru 223 show the SLT and SLD results both prior to and after the application of the Silt REF for the previously mentioned six pile sets.

Eleven piles that had been founded in silt were included in this study. The analysis of these piles provided an average λ of 1.041, with a standard deviation of 0.116 after the REF of 0.69 had been applied to each SLD data set.

3.4.5.5 Clay

Finally the last soil subgroup in which the piles were founded was clay. Figure 224 shows the load-displacement curves generated from a standard static load test and a subsequent static load test on two sets of nearby piles. These piles were installed in Newark, New Jersey. These piles were closed end steel pipe piles with an outer diameter of 0.32m, an inner diameter of 0.30m, and a length of 27.52m. Again, these piles were compared using the Smallest Displacement method. Figure 224 shows the load-displacement curves from both tests prior to application of any REF. The load-displacement curve generated from the static testing exhibits a marked difference from that generated by the static testing of the nearby pile. By examination the SLD capacity over predicts the capacity that could be expected with regards to the maximum displacement achieved during the static testing. Figure 225 shows the same load-displacement curves although the loads used for plotting of the SLD curve have been adjusted by the REF determined for clay as 0.65. By examination the SLD curve now slightly under predicts

the pile's capacity at the maximum displacement achieved during the statnamic testing and yielding a λ value of 1.04. Figures 226 and 227 are load-displacement curves for piles with identical dimensions and which were installed on the same site in Newark as those just described. Similar analysis of this second set resulted in an SLT capacity of 2189kN and an SLD capacity of 1942kN. Again the SLD capacity now under predicts the SLT capacity with a λ value of 1.13.

The second site from which piles were included in the clay soil subgroup was Contraband Bayou in Lake Charles, Louisiana. The first pile included herein was designated T-114.5. Figures 228 and 229 show the results of STN and SLT testing on this pile before and after application of the REF analysis method of a 455 mm diameter prestressed concrete pile that was 12.95m long. A SLT was performed first via a reaction beam system followed by a STN 12 hours later. After application of the clay REF this set of curves was analyzed using the Smallest Displacement method with which a SLT capacity of 2293kN, a SLD capacity of 2070kN and a λ value of 1.11 was determined. The second pile from this test site was designated X-123 and was a 455 mm diameter, 17.67m long prestressed concrete pile. Four cycles of STN testing were performed on this pile prior to SLT testing via a reaction beam system. It was noted that the reaction piles for the SLT reaction beam system were installed prior to STN testing. Based on a Smallest Displacement analysis of the REF applied load-displacement curves SLT and SLD capacities of 2306kN and 2664kN, respectively, were determined. The λ value for this analysis was equal to 0.87. Figures 230 and 231 show the raw SLD and SLT curves and the REF applied SLD and SLT curves, respectively.

Four piles or pile sets that had been founded in clay were included in this study. The analysis of these piles provided an average λ of 1.035, with a standard deviation of 0.119 after the REF of 0.65 had been applied to each SLD data set. Therefore, after application of the REF the SLD capacity tended to under predict the SLT capacity by approximately 4%.

3.4.6 Summary of Database Analysis

Table 24 summarizes the bias values, λ , for each soil subgroup previously presented. Soil Type 1, 2, 3 and 4 are assigned to rock, sand, silt and clay, respectively. Also included are the Site ID and Pile ID for each data set.

3.4.7 Development of the Rate Effect Factor

A new factor was introduced that would account for over-predictions associated with the rapid loading caused by Statnamic tests. The rationale for its inclusion was based on simplifying design procedures by recommending a uniform safety factor or resistance factor regardless of soil type. Further, it would eliminate the advent of over-predictions and maintain a reasonable probability of failure. As such, the ratio of the static capacity to the predicted capacity (bias) was used to evaluate the effects of such a factor. The rate effect factor, denoted with the Greek letter $\tilde{\eta}$, is simply a soil type-dependent constant multiplier used to reduce the load capacity predicted by analyses when using Unloading Point Methods. Such methods include UPM, MUP, and SUP as discussed in section 2.3.5. Therefore the derived static capacity would then equal the rate effect factor times the Unloading Point Method-derived static capacity ($SLD = \tilde{\eta}$ UPM Capacity).

The ratios of static load test capacity to UPM-predicted capacity (herein simply referred to as λ) for rock, sand, silt, and clay were evaluated for the 34 load tests critically evaluated for this study. Therein, rock showed the least over prediction with $\lambda = 0.96$, and clay showed the

highest over prediction with $\lambda = 0.67$. Likewise, the reproducibility of the prediction is important to the probability of failure and is represented by the standard deviation of the bias factor. In this regard subjected to the limited presented data, the Statnamic test method is uniform from soil type to type as is evidenced by the small variation in the standard deviation shown in Table 25. Also listed are the safety factors and resistance values that would be associated with various soil types should no rate effect factor be introduced.

Using these values for the evaluation of Statnamic tests results would be cumbersome and not in line with common design practice. Therefore rate effect factors were selected for each soil such that the same safety factor or resistance factor could be used for all soils. These factors were selected by (1) determining what factor would produce no average over-prediction in rock, (2) determining the associated safety factor or resistance factor for that condition, and (3) finding the rate effect factor for each soil that would produce the same safety factor or resistance factor. To this end, the safety factor and resistance factor (S.F. and ϕ) were calculated for each soil as a function of $\tilde{\eta}$. Figure 232 shows the graphical relationship between S.F., ϕ and $\tilde{\eta}$ for each soil. Therein, it is shown that resistance factors greater than one are generated when gross under-predictions are encountered. Although resistance factors higher than 1.0 (or S.F. < 1.0) are atypical, these trends are not surprising in that these curves are generated to maintain a given probability of failure (in this case 1% with $\beta = 2.5$), (FHWA, 1998). Note that if a needlessly low rate effect factor were imposed on the predicted capacity, a similarly unusually low S.F. would then be required such that the probability of failure is maintained. These values are in agreement with common practice where Statnamic tested rock bearing strata (which have little to no rate effects) would require a F.S. of 2 with almost no correction. Further, as the cost of testing increases drastically with higher loads, it is advantageous to minimize under predictions associated with needlessly high safety factors. Hence, the largest possible rate effect factors were selected which would provide a balance between proven capacity and safety while imposing a uniform resistance factor.

Starting with the value for rock, $\tilde{\eta}_{\text{rock}} = 0.96$ was selected to produce a unity bias factor and resulted in a resistance factor of 0.73. Using this resistance factor value for each soil, the $\tilde{\eta}$ values for sand, silt, and clay were calculated to be 0.91, 0.69, and 0.65, respectively. Table 26 summarizes the recommended values of $\tilde{\eta}$, ϕ , and S.F. to be used in the analysis of Statnamic data when analyzed by the UPM and the associated values used to produce them. Figures 233 to 236 show the distribution of the predicted load capacity using the rate effect factors versus the actual static capacity for the various soil types.

3.4.8 Conclusions and Recommendations

The Statnamic load test method is a relatively new technology that has gained worldwide appeal to many designers based on its ability to economically test high capacity foundations and produce a detailed load-displacement response. The latter has great significance due to the many forms of failure criteria used in practice throughout the world. The economy of the method is afforded via minimal interruptions to construction time-lines due to the absence of reaction anchors or beams. However, the limitation of the test method (as well as with dynamic load methods) is the short duration of the loading. Therein, all materials, geotechnical and structural alike, exhibit a stiffer response to rapidly applied loads than more slowly applied loads. Rock and sand are only mildly affected by this phenomenon, whereas the effects in silts and clay are more pronounced. It is the responsibility of the design engineer to determine the duration of the anti-

pated loading event on the structure or foundation and appropriately choose a test methodology and/or analysis method to produce the desired effect. When using the Statnamic test method to determine the dynamic response of a foundation, little to no interpretation may be necessary. However, when using Statnamic testing to predict the static response of a foundation, a suitable analysis procedure should be selected. The analysis methods most commonly used worldwide involve inertia and viscous damping correction. This study has shown that these methods can be readily used in the design of statically loaded structures if a rate effect factors is incorporated in the analysis. With the inclusion of these factors, a single safety factor or resistance factor can be employed regardless of soil type.

Rate effect factors were developed to calibrate the UP-predicted load response to the measured static response while developing a recommended safety factors. The values presented in Table 27 should be applied to Unloading Point (UPM) analyses to predict the static response and design foundations using Statnamic test results. Statnamic testing firms in the American continents have adopted the use of the rate effect factors listed herein. Therefore, designers will only rarely have the need for those factors that were determined without $\tilde{\eta}$.

The three analysis methods recommended for use with the above rate effect factors are the Unloading Point Method (UPM), the Modified Unloading Point Method (MUP), and the Segmental Unloading Point Method (SUP). These methods are identical in concept but vary in the required field data collection and should be selected based on pile length and/or performance. The UPM should be limited to relatively short foundations (wave number, $N_w > 12$) that exhibit a plunging response (i.e. measurable permanent set). The required field data should include top of pile measurements of load, acceleration, displacement (optional), and time.

The MUP method is also limited to the same length piles ($N_w > 12$) but can be used when the foundation exhibits an elastic response (i.e. minimal permanent set). In those instances the top and toe displacement must be recorded independently for the MUP analysis. This method therefore requires field measurements of load, top of pile acceleration, toe of pile acceleration and time.

The SUP method can be used for much longer piles ($N_w > 6$) but must have strain gage instrumentation located along the length of the foundation defining shorter segments with $N_w > 12$. Field measurements should include top of pile load, acceleration, displacement and time measurements as well as those from appropriately spaced embedded strain gages and toe acceleration. All field measurements from each of these methods should be sampled at a sufficient rate to minimize discretization errors (greater than 4000 Hz).

Two public domain software packages have been developed that perform Unloading Point analyses: SAWR4 and SUPERSAW which can be downloaded from <http://www.eng.usf.edu/~gmullins/>. As a result of this study, these packages have been updated to include the rate effect factor when predicting the static equivalent response. Therein, the derived static load is defined as:

$$SLD = \eta UP \text{ Capacity} \quad (54)$$

From which the design capacity can be expressed as:

$$P_n = \phi SLD, \text{ (LRFD)} \quad P_{usable} = SLD/SF, \text{ (ASD)} \quad (55)$$

where $\phi = 0.7$, or S.F. = 2.

CHAPTER 4

FINDINGS – MODELS

4.1 OVERVIEW

The different testing methods (while investigated individually in detail) need to be examined from a comprehensive viewpoint regarding principles and interpretation. Section 1.3 presented the principles allowing to categorize the methods based on the loading duration. The present chapter reviews the testing methods through three approaches. One; presenting and investigating in detail a simplified/fundamental model allowing (similarly to the material presented in section 1.3) to examine the different methods and their mechanisms. The second; advanced FEM analysis is used to study in detail the impact between a ram (impacting body) and a pile, common to most of the testing methods. The use of this relatively new analysis allows to investigate the effect of the impact on the stresses developed at the top of a pile and hence on the measurement and interpretation techniques when using any impact testing (e.g. drop weight and statnamic). The third; relates to an attempt to develop a model with a different approach than the traditional analyses, addressing the pile response to various load rates via rheological models.

4.2 SIMPLIFIED FUNDAMENTAL MODEL

4.2.1 Overview

A fundamental model allows examination of the testing methods in an absolute and relative form as discussed in Chapter 1. All pile testing methods can be principally described as a Mass M acting on the end of a slender bar (pile head) with an impact velocity v_i . One simplified fundamental model of impact and/or dynamic behavior was presented in section 1.3.2.1 (referenced to Holeyman 1992 and originally attributed to Parola 1970 and Van Kotten, 1977) and was used for testing classification in sections 1.3.2.3 and 1.4. While being effective for this purpose, the attempt to utilize the same model with more realistic parameters raised difficulties.

An alternative model utilizing the Kelvin-Voigt rheological model was examined. This model was independently used by Dr. Gray Mullins to examine Statnamic test results (section 2.3.5.3).

4.2.2 Model Description

The Kelvin-Voigt model was proven to be very effective for simulating pile driving (Irvine, 1986) and hence appealing to the needs of this research. The model, presented in Figure 238 consists of a spring in parallel to a dashpot subjected to a mass. In the more generic case of our research, the spring represents the stiffness of the entire system including the pile and the driving system set-up. The viscous damping dashpot provides the dynamic resistance developed during penetration but its representation includes other direct and indirect factors such as the soil inertia, soil damping and depending on the type of test (e.g. driving vs. static) and the amount of soil that participates in the process (Paikowsky and Chernauskas, 1996, Hajduk et al. 2000). The mass represents the applied force from a ram in pile driving to the equivalent of a pressure in Statnamic test and a jack force in a static load test.

Irving (1986) treats the pile as a wave-guide radiating energy away from its upper face in a similar way to tensile stress wave propagation in cables with the obvious difference being that at least the initial wave in the pile is compressive, (and it remains to be compressive in 'hard' driving). In this treatment, reflections will not be considered. However, elasto-plastic behavior at the pile head is considered later. The definition diagram and schematic shown in Figures 238 and 239 provide the necessary details.

Following Irving (1986) and referring to Figure 238, the equation governing the deceleration of the ram with a mass M is:

$$M\Delta_1 + K(\Delta_1 - \Delta_2) = 0 \quad (56)$$

where Δ_1 is the absolute displacement of the ram after contact is made with the capblock, which is of compressive stiffness K . The displacement Δ_2 is the absolute displacement of the upper end of the pile at its junction with the capblock. Note that the weight of the ram has been left out of the above equation because it is generally insignificant when compared to the inertia force $M\Delta_1$ - after all the ram falls through a significant height and is stopped suddenly.

The other equation relevant to pile driving is a force balance between the capblock and the pile head. In order to determine the force in the pile head we need analyze the stresses in the pile itself. This analysis (referring to Figure 238) follows the traditional one-dimensional wave equation formulation (1-D W.E) (see e.g., Graff, 1975) and hence is abbreviated.

Let x measure distance from the pile head, and let $u(x,t)$ be the axial displacement of the pile. Equilibrium of an element of the pile, of length dx , is:

$$F + \partial F - F + \rho A \frac{\partial^2 u}{\partial t^2} dx = 0 \quad (57)$$

or

$$\frac{\partial F}{\partial x} + \rho A \frac{\partial^2 u}{\partial t^2} = 0 \quad (58)$$

where ρ is the density of the pile and A its cross-sectional area.

Using elastic relations:

$$\rho A \frac{\partial^2 u}{\partial t^2} - EA \frac{\partial^2 u}{\partial x^2} = 0 \quad (59)$$

where E is the modulus of elasticity of the pile material.

Following the traditional differential equation solution for a disturbance traveling in infinity long bar, leads to the force at some point of the pile being:

$$F = -EA \frac{\partial u}{\partial x} \quad (1.3.15) \quad (60)$$

and the alternative expression for the force in the pile being:

$$F(x,t) = \frac{EA}{V_d} \frac{\partial u}{\partial t} = \rho AV_d \frac{\partial u}{\partial t} \quad (61)$$

Therefore, at the pile head, where $u \equiv \Delta_2$, we have the result

$$F(0,t) = \rho AV_d \dot{\Delta}_2 \quad (62)$$

Thus, the force balance at the capblock-pile interface is

$$K(\Delta_1 - \Delta_2) = \rho AV_d \dot{\Delta}_2 \quad (63)$$

Linking the two equations we obtain

$$M \ddot{\Delta}_1 = -\rho AV_d \dot{\Delta}_2 \quad (64)$$

which may be integrated directly to

$$M \dot{\Delta}_1 = -\rho AV_d \Delta_2 + \text{constant} \quad (65)$$

The constant may be evaluated once we have established the initial conditions. The height that the ram falls allows its striking velocity to be calculated, say, Δ_0 , thus:

$$\dot{\Delta}_1(0) = \dot{\Delta}_0 \quad (66)$$

and, as the pile head has no initial displacement (i.e. $\Delta_2(0) = 0$) so

$$M \dot{\Delta}_1 = M \dot{\Delta}_0 - \rho AV_d \Delta_2 \quad (67)$$

Substituting for Δ_2 then gives the equation of motion for the ram-capblock system,

$$M \ddot{\Delta}_1 + \frac{KM}{\rho AV_d} \dot{\Delta}_1 + K\Delta_1 = \frac{KM}{\rho AV_d} \dot{\Delta}_0 \quad (68)$$

with initial conditions of $\Delta_1(0) = \Delta_0$ and $\dot{\Delta}_1(0) = 0$. This equation exhibits pure viscous damping due to the radiation of energy away from the capblock by the pile, which can be quantified. Written in a standard form the equation is

$$\ddot{\Delta}_1 + 2\zeta\omega \dot{\Delta}_1 + \omega^2 \Delta_1 = 2\zeta\omega \dot{\Delta}_0 \quad (69)$$

where $\zeta = \sqrt{kM}/2\rho AV_d$. The forcing term is constant; hence it is possible to use the earlier solutions.

4.2.3 Model Evaluation

4.2.3.1 Overview

The model is first investigated using the limiting stages of the parameters, following Irvine (1986) and presenting examples.

4.2.3.2 Underdamped System ($\zeta < 1$)

Many of the pile tests are proof-tests--non-failed load testing in which the displacement of the pile and the soil is limited, e.g. dynamic testing during hard driving or often drop weight tests. As such, the resistance forces occurring at the interface of the pile and the soil do not reach slippage. In this case; the testing is generally to check the pile capacity for meeting a certain safety factor.

The force pulse on the pile's head is:

$$F_p = \frac{M\omega \dot{\Delta}_0}{\sqrt{1-\zeta^2}} e^{-\zeta\omega t} \sin \omega_d t \quad (70)$$

or

$$F_p = K \left(\frac{\dot{\Delta}_0}{\omega_d} e^{-\zeta\omega t} \sin \omega_d t \right) \quad (71)$$

The displacement of the pile head is found to be:

$$\Delta_2(t) = \frac{2\zeta \dot{\Delta}_0}{\omega} \left[1 - e^{-\zeta\omega t} \left(\cos \omega_d t + \frac{\zeta}{\sqrt{1-\zeta^2}} \sin \omega_d t \right) \right] \quad (72)$$

Peak values of pile force and pile displacement are:

$$F_{p,\max} = K \dot{\Delta}_0 / \omega_d \quad (73)$$

$$\Delta_{2,\max} = 4\zeta \dot{\Delta}_0 / \omega \quad (74)$$

where: $\zeta = \sqrt{kM}/2\rho AV_d$
 $\omega_d = \omega\sqrt{1-\zeta^2}$

$$V_d = (E/\rho)^{\frac{1}{2}}$$

$$\omega = \sqrt{k/M}$$

A = pile's cross section

ρ = density of the pile

E = material Yong's modulus of pile

Δ_0 = striking velocity= $\sqrt{2gh}$, h =drop height.

An example had been studied for which the force pulses developed at the pile's head are shown in Figures 240 and 241 for an underdamped system in an absolute and normalized fashion, respectively. The pile is a steel pipe with $E=2 \times 10^{11}$ Pa and an outside diameter of 1100mm, wall thickness of 35mm and a length of 28m. It is driven by a single acting hammer with a ram weight of 50kN and energy of 75kNm (i.e. the ram falls 1.5 m). The capblock material is softwood, with a rated spring constant in compression of 1000kN/mm.

4.2.3.3 Critically Damped system ($\zeta = 1$)

When $\zeta \rightarrow 1$, $\omega_d = \omega\sqrt{1-\zeta^2} \rightarrow 0$. The force in the pile then becomes:

$$F_p = K \dot{\Delta}_0 t e^{-\omega t} \quad (\zeta = 1) \quad (75)$$

The pile-head displacement is:

$$\Delta_2(t) = \frac{2\dot{\Delta}_0}{\omega} [1 - e^{-\omega t} (1 + \omega t)] \quad (\zeta = 1) \quad (76)$$

The peak pile force occurs when $t = 1/\omega$ and is:

$$F_{P,max} = \frac{K \dot{\Delta}_0}{\omega} e^{-1} \quad (77)$$

Note that $F_{P,max}$ will not occur before the reflected wave returns to the pile head if $\omega < V_d/2L$.

An example had been studied for the critically damped system case and the force pulses acting at the pile's head are shown in Figures 242 and 243. The pile is a steel tube with $E=2 \times 10^{11}$ Pa and outside diameter of 500mm, wall thickness of 20mm and length 28m. It is driven by a single acting hammer ram weight of 50kN and energy of 75kNm (i.e. the ram falls 1.5m). The capblock material is softwood, with a rated spring constant in compression of 1100kN/mm.

4.2.3.4 Overdamped ($\zeta > 1$)

Overdamped cases can be considered when a relatively large displacement takes place between the pile and the soil interface, (i.e. easy driving), where the impact and the traveling wave overcome the pile resistance. The solution can be written as:

$$F_p = K \left(\frac{\dot{\Delta}_0}{\omega \sqrt{\zeta^2 - 1}} e^{-\zeta \omega t} \sinh[\omega t \sqrt{\zeta^2 - 1}] \right) \quad \zeta > 1 \quad (78)$$

and

$$\Delta_2(t) = \frac{2\zeta \dot{\Delta}_0}{\omega} \left[1 - e^{-\zeta \omega t} \left(\cosh[\omega t \sqrt{\zeta^2 - 1}] + \frac{\zeta}{\sqrt{\zeta^2 - 1}} \sinh[\omega t \sqrt{\zeta^2 - 1}] \right) \right] \quad \zeta > 1 \quad (79)$$

The damping parameter ζ represents one way to measure the stiffness of the capblock relative to the pile. For example, when the capblock stiffness is very large, $\zeta \gg 1$, and in this situation the peak pile force is:

$$F_{p,\max} \rightarrow K \dot{\Delta}_0 / 2\omega\zeta \quad \text{or} \quad F_{p,\max} \rightarrow \rho A V_d \dot{\Delta}_0 \quad (80)$$

This is a classical result (considering some of the original stress wave studies by the 19th century physicist, Hopkinson) obtained when the capblock is infinitely stiff.

In the other extreme, when $\zeta \ll 1$ we have a capblock that is flexible compared to the pile and the result is:

$$F_{p,\max} \rightarrow K \dot{\Delta}_0 / \omega \quad (81)$$

In this situation the pile may be considered rigid and $F_{p,\max}$ is simply the reaction to a mass falling and resting on a spring (the capblock) of stiffness K . The fundamentally different forms for the time history of axial force in the pile head are shown schematically in Figure 244.

One worked example had been examined to demonstrate the responses in the situation of over-damped system (see Figures 245 and 246). A prestressed concrete pile of 450mm diameter and a length of 20m, with a density of 2,350 kg/m³ and $E=2.5 \times 10^{10}$ Pa, the pile is driven by a single acting hammer with a ram weight of 150kN falling a distance of 1.3m. The capblock material is softwood, with a rated spring constant in compression of 1500kN/mm.

4.2.3.5 Impact without Capblock

In static load testing and some of the high strain dynamic testing (e.g. steel pile driving) no capblock is used. In these cases, the equations govern response of a mass and a dashpot.

We can write:

$$F_p = \rho A V_d \dot{\Delta} = \rho A V_d \dot{\Delta}_0 \exp[-(\rho A V_d t) / M] \quad (82)$$

The peak value of which occurs at the start and is

$$F_{p.\max} = \rho A V_d \dot{\Delta}_0 \quad (83)$$

leading to a peak axial stress of:

$$\sigma_{\max} = F_{p.\max} / A = \rho V_d \dot{\Delta}_0 \quad (84)$$

The worked example with the following details had been studied and shown in Figures 247 and 248. The pile is a steel ($E=2 \times 10^{11}$ Pa) pipe with an outside diameter of 1,100mm, a wall thickness of 35mm and a length of 28m. It is driven by a single acting hammer with a ramweight of 50kN and energy 75kJ (i.e. the ram falls 1.5m). No capblock was present.

4.2.4 Model Performance

A parametric study for an under-damped system is detailed in Table 28 for ten various cases, where G is the ram weight, H is the free falling height, K is the cushion stiffness and I is the pile impedance. The results are presented in a dimensional form in Figure 249 and in a non-dimensional form in Figure 250. Cases 1 to 5 are the same in both figures because they have the same R & K. When presenting the same forces in a non-dimensional format, all the cases of a constant K & R result in an identical normalized force, hence the non-dimensional presentation has only six graphs in it with cases one through five overlapping.

Figures 251 and 252 further illustrate the above concept by changing the falling height of ram while the duration of the force pulse remains constant if the R remains constant. In other words, with the same drop weight system for the same pile, the changing of the ram's falling height results in a different peak force pulse but does not affect the pulse duration. Another observation can be made from these two figures; keeping the same ram weight G for the same pile impedance I, the duration of the force pulse will increase as the value of R increases. For the aforementioned reason, just four curves are presented in the normalized relations presented in Figure 252. Cases 1 to 5 have identical R value (3.352) and cases 7, 9 and 10 also have identical R value (4.740). Cases 1 to 5 have however the same duration of force pulse and same non-dimensional force pulse curves, while cases 7, 9 and 10 have different duration of force pulse and different non-dimensional force pulse curves (see Figures 253 and 254). The value of G, K and I controls this difference. Cases 1 to 5 have the same G, K and I; while cases 7, 9 and 10 have the same I and different G and K. Same R value depends on the increasing of G and the decreasing of K.

A parametric study for an over-damped system is detailed in Table 29 for nine various cases. The results of all the cases are presented in a dimensional format in Figure 255, and in a non-dimensional format in Figure 256. Also, the cases of a constant K & R resulting in an identical normalized force, hence the non-dimensional presentation has only six graphs in it with cases one through four overlapping.

Figures 257 and 258 clearly demonstrate that with just a change in the falling height of the ram, the duration of the force pulse remains the same as long as the R is kept constant. That is to say, with the same drop weight system, and the same pile, a change in the ram's falling

height changes the peak of the force pulse but does not affect the duration of it (similarly to what is shown in Figures 251 and 252). Keeping the same ram weight G , and pile impedance I , the duration of the force pulse increases as the value of R increases.

Cases 1 to 4 have the same R value (0.279) and cases 6, 8 and 9 have the same R value (0.683). Cases 1 to 4 however have the same duration of force pulse and same non-dimensional force pulse curves, while cases 6, 8 and 9 have different duration of a force pulse and different non-dimensional force pulse curves (see Figures 259 and 260). The values of G , K and I control this difference. Cases 1 to 4 have the same G , K and I ; while cases 6, 8 and 9 have the same I and different G and K values. Identical R -values depend on the increasing of G and the decreasing of K . In distinction from the under-damped cases, the duration of the force pulse in the over damped cases depend more on the weight of the ram. The capblock spring constant does not affect the duration.

Defining t_1 as the duration from $F_p=0$ to $F_p=F_{p,max}$, and t_2 as the duration of the force pulse, when increasing the value of ζ , the ratio of the duration t_1 to t decreases quickly. The same happens in both cases, i.e., under-damped and over-damped systems.

The values of K , M and I affect the duration of the force pulse. The duration increases when the value of K decreases and the value of M increases. The duration decreases when the value of I is increased for the same M , K , I , (i.e. same testing system, ζ and $R = \omega_n / \alpha$ are constant), the change in H only can change the value of $F_{p,max}$ but does not bring changes in the force pulse duration.

For a given loading system under a specific condition of operation (M , $\dot{\Delta}_0$), the impact force is a function primarily of the pile geometry and the damping of the system, controlled by K and I . This is illustrated by the parameters of Table 30 and the force pulses depicted in Figure 261 showing the variation of the impact (magnitude and duration) for the same impact (constant G, H) with the same R but different I and K combinations: $I_2 = 2I_1$, $K_2 = 4K_1$ and $I_3 = 3I_1$, $K_3 = 9K_1$, such that all result with a constant R . Figures 262 and 263 illustrate that as the spring/system becomes stiffer, the force duration decreases and its magnitude increases. The hammer for the cases in Figure 262 is very heavy and its weight is up to 420kN. The R values of cases 1 and 2 in Figure 263 are 0.99853 and 0.864752 respectively and the shapes of these two curves have the characteristics of the curves of an over-damped system.

Figure 264 further illustrates the influence of the capblock stiffness (spring/system) K on the force pulse duration under the situation of under-damped system. The duration of the force pulse decreases as the value of K increases when the value of K is less than 15000 kN/mm. The duration of the force pulse decreases more quickly when the value of K is smaller than 15,000 kN/mm. For a reference comparison, Table 30 provides values of modulus of elasticity E for several materials of capblock and pile cushion. The value of spring constant can be computed as $K=AE/L$.

Figures 265 and 266 present the force pulses as a function of the capblock (spring/system) stiffness K vs. for an over-damped system. The change in the value of K has little influence on the final force pulse duration. The peak of the force pulse attenuates more quickly when the value of K is larger. The hammer weight significantly affects the force pulse duration as it increases when the weight of the hammer increases. The duration of the force pulse is approximately 80ms when the hammer weighs 150kN, and is approximately 600ms when the hammer weighs 1500kN.

The shapes of the force pulses obtained by the model vary substantially when different M and H are used even if the energies of the stroke are identical (see Figure 267). When M is

increased and H is decreased, the duration increases quickly and F_{\max} decreases very fast. When applied to high strain dynamic testing of piles the use of an oversized M and a small H may not only cause damage to the pile top but the larger duration reduces the quality of the acquired data and its interpretation.

Getting same $F_{P,\max}$ by different M and H, we find that the energies of the stroke of the hammer increase as the M increase and H decrease (see Figure 268) even when using the same value of K. It means that for the same energy (same stroke), and the same rate of energy transferred, we do not the the same $F_{P,\max}$.

Table 31, Figures 269 and 270 present the variation of the force pulses developed at the pile head while using the same drop weight system for different piles. In general, the peak force increases and the duration of the force pulse decreases with an increase in the pile impedance for a given drop weight system (same M, H and K). The peak of the force pulse rises earlier as the duration of the force pulses increases. However, this phenomenon is reduced with the increase in the pile impedance. The durations is kept constant and the peaks of the force pulses increases slowly when the pile impedance is larger than 8,000 kN/m/s while the value of R is larger than 5.930 in these two figures.

Figure 271 illustrates the variation of the force pulses at the pile head when rams of different weights are applied to the same pile. The peak force and the duration of the force pulses increase with the increase of the hammer weight.

The presented material, thus illustrates that by using the presented simplified model it is possible to simulate the force pulses developed at the head of a pile as generated by different loading methods

4.2.5 The Influence of a Load Testing System

An analysis is carried out to demonstrate the impact developed at a pile head under different testing systems. Table 32 details the model parameters used for this purpose. Figure 272 presents the force pulse developed at the pile head for the different testing systems acting on a prestressed concrete pile, 450mm in diameter and with a length of 18m. The density of the pile is 2,350kg/m³ with E=25,000MPa.

The four force pulses at the pile head are related to the different pile testing methods simulating in this example namely; the drop weight, Statnamic, Fundex and a static loading systems changing the hammer weight and falling height to simulate the load applied to the pile head, changing the value of K to simulate the different systems (include pile, soil, cushion, hammer, falling height and stiffness, see Table 32), the model shows a good performance for demonstrating the influence of test type on the force developing at the pile's top.

4.2.6 Case Histories

Test Pile No. 2 and No. 3 of Newbury, Massachusetts (Hajduk et al., 1998) were used in order to compare the applicability of the presented simplified model to an actual case history. Tables 33 and 34 provide the parameters that were extracted from the actual pile behavior during dynamic driving, Statnamic and Static load testing. Part (a) of Tables 33 and 34 outlines the exact parameters with the ram weight and height being established as equivalent to the measured energy and force. The results of applying these parameters to the model are presented in Figures 273a and 274a. While the overall force magnitudes are reasonable, the pulse duration is

represented very well for the dynamic driving only with the Statnamic and static testing resulting in pulses of a substantial shorter duration compared to the actual observed (see Figure 7) behavior. This results from two reasons: (a) the need to represent static and, Statnamic loading by an impact mass, i.e. to 'equivalent' presentation and (b) the fact that during static and Statnamic tests, the wave length is so much longer relative to the pile's length (the concept of relative wave length was presented in chapter 1; Λ = length of the force pulse / double length of the pile) that much more soil participates in the process and the stiffness of the system and the pile's impedance (I) is therefore much different than that related to the geometry of the pile itself.

Parts (b) and (c) in Tables 33 and 34 and the corresponding results in Figures 273(b, c) and 274 (b, c) demonstrate the changes required in the model to match the actual behavior. Note the different time scales in parts a, b, and c of the figures.

Pile impedance I needed to be increased in order to get the reasonable result with this model for the analyzed cases. In general, the effect of soil around the pile on the increase of the value of I should be relatively small.

4.3 SIMULATION OF A RAM IMPACT WITH A DEEP FOUNDATION

4.3.1 Overview

LS-DYNA is an advanced software program for dynamic Finite Element Method (FEM) analysis developed by Livermore Software Technology Corporation. LS-DYNA is commonly used by the automotive industry for impact analysis and hence serves as an ideal tool for investigating the impact of a ram with a concrete pile. The ultimate goal of modeling such impact is to determine the stress wave distribution across and along the pile as a function of time after impact for different controlling parameters such as the ratio of ram diameter to pile diameter, the drop height, impact angle, and the use of a plywood cushion. The models under investigation were created using the HyperMesh pre-processor and exported in LS-DYNA explicit finite element analysis code format. Post-processing was completed using LS-DYNA Post.

The analysis was carried out in two stages; first, a broad investigation into the aforementioned factors using a relatively simpler modeling, e.g. not modeling the striking plate and the cushion as detached units. In the second stage, a detailed analysis was carried out focusing on what was found to be of the most important factor in the first stage, i.e. the uneven impact of the ram. This analysis was examining the stresses across the pile at the surface and at different distances below the pile's top as well as the effect of a softer cushion on the uneven impact.

4.3.2 Analysis Procedure – Stage I

4.3.2.1 Overview

A 3-D half-symmetry baseline model was initially generated. The baseline model consists of four components, a steel ram, a steel striker plate, a plywood cushion and a 40m long concrete pile. The diameter of the pile and the ram is 1m. A schematic of the model is shown in Figure 275. The analysis simulates a 2m drop of the ram by prescribing an initial velocity for the ram,

locating it 0.1m above the striker plate. Table 35 summarizes the major parameters of the baseline model, which was then altered for each subsequent analysis case.

4.3.2.2 *Model Geometry*

Figure 276 shows an isometric view of the entire system, with an enlarged view of the region of interest. The different shades (colors in original) in Figure 276 represent the different components, from top down; the ram is shown in red, the striker plate in green, the plywood cushion in blue and the concrete pile in yellow. Figures 277 and 278 show the top view of the pile and ram respectively.

The node and element summary for the baseline model is provided in Table 36. Linear elastic material properties were used for each component in the model and they are listed in Table 37, where as dimensions for the components are listed in Table 38. To prescribe the contact between the ram component and striker plate component, the part option was used with the *CONTACT_AUTOMATIC_SURFACE_TO_SURFACE definition card in LS-DYNA. For this type of definition a master component (the ram) and a slave component (the striker plate) are defined. The slave component deforms in response to the impact of the master component. Coincident nodes were prescribed between the striker plate and the plywood cushion, and between the plywood cushion and the concrete pile because these sets of components were assumed to be moving completely in alignment with one another.

4.3.2.3 *Constraints*

To generate the baseline half-symmetry model, constraints were added along the flat portion of each component in the modeled ram-pile system. Essentially, this edge was placed on rollers (Figure 279). The rollers allowed motion in the y-direction from the impact and in the x-direction due to the Poisson effect. Translation and rotation was not allowed in the z-direction along the centerline edge due to symmetry.

The pile's tip was modeled so that the pile could not translate in the y-direction (vertical). In addition, all rotational degrees of freedom were constrained. Again, schematically, this set of boundary conditions is analogous to placing the pile on top of rollers as shown in Figure 280.

4.3.2.4 *Material Models*

For the present study, all materials were modeled with LS-Dyna's *MAT_ELASTIC definition. This definition assumes that the material is linear elastic and isotropic. It determines the material response based upon the Cauchy Stress tensor.

$$S_{ij}^{\nabla^{n+1/2}} = 2G \dot{\epsilon}_{ij}^{\prime n+1/2} \quad (85)$$

With the pressure calculated according to

$$p^{n+1} = -K \cdot \ln V^{n+1} \quad (86)$$

In equations (85) and (86), G is the shear modulus, K is the bulk modulus and V is the ratio of the current volume to the original volume.

In future studies, to further refine this model, it is recommended that an investigation be conducted into the applicability of other LS-Dyna material models developed specifically for the behavior of concrete (pile) and plywood (cushion). Also, in advanced FE investigations into the response of the pile to the impact of the ram, it may be more appropriate to model the steel ram and striker plate with an elastic-plastic material model to take into account damage and/or permanent deformations of those components.

4.3.3 Parametric Studies

4.3.3.1 General

Once the baseline model was completed, parametric studies were performed. These parametric studies were designed to study the effects of ram diameter, drop height and impact angle on the system. Each of these altered models was generated directly from the baseline model to reduce the possibility of errors. The creation of these models is discussed in more detail in the paragraphs that follow.

4.3.3.2 Models Generated to Study Effect of Drop Height

The baseline model was altered to account for a variation in drop height. This change was incorporated into the baseline model by altering the impact velocity using Eq. 87.

$$v^2 = 2g_o(x - x_o) + v_o^2 \quad (87)$$

where v is the impact velocity, g_o is the acceleration due to gravity, $(x-x_o)$ is the drop height and v_o is the initial velocity of the ram. In this case, g_o is 9.81 m/s^2 , and v_o is zero because the ram is dropped from rest. Table 39 shows the parameters that were altered to generate the models for the drop height study.

4.3.3.3 Models Generated to Study the Effect of Ram Diameter

When altering the ram diameter, it was necessary to keep the amount of energy of the impact equal to that in the baseline model. For simplicity of stage I analysis, the density of the ram was altered so that the weight of the ram would be kept constant in each of these studies while the volume changed due to the changes in the ram's diameter. Table 40 shows the values that were altered to generate models with different ram diameters.

4.3.3.4 Models Generated to the Study Effect of an Offset (Uneven) Impact

To examine the instance when the ram may not impact the striker plate squarely and the effect of this type of occurrence on the propagating wave, models were generated from the baseline model with a ram diameter of 1m and the ram impacting the striker plate at 3 offsets. To produce the offset, the elements that compose the ram were rotated about a point on the outer edge as shown in Figure 281.

4.3.4 Format For The Presentation of the Results from Stage I

4.3.4.1 Stress Propagation Images

A series of screen captures was generated showing the propagation of the stress wave through the concrete pile. The first image in each series shows the pile in the unstressed state. The second image shows the pile at the time step when impact first occurs. The seven following images depict the stress at equal intervals until approximately 0.005s. It was insured that the plots would show states of stress for the pile exceeding the time of wave travel to pile tip and back. These images were observed and analyzed aiding in the following presentation.

4.3.4.2 Detailed Force and Velocity

Sets of stress/force and velocity/force plots have also been generated which show the results for each FE model. The first figure in the set shows stress versus time and the equivalent force (for the local stress multiplied by the cross-section area) at three different distances from the center of the pile, (Figure 282a). The second figure in the set shows the change in velocity (as velocity on one axis and multiplied by the impedance to be expressed in force units in the other axis) versus time for the same locations. It is important to examine the stress distribution at a distance from the top of the pile because following St. Venant principle; the stress wave is expected to become uniform across the pile at some distance away from the impact. Traditionally this distance is believed to be at twice the value of the diameter, or 2m for the analyzed case. Two additional distances, above and below 2m (1m and 3m) were also chosen for this analysis to provide additional values for comparison with the stress developed at the impacted surface. The detailed stresses and velocities were therefore presented at four positions along the length of the pile, making it 12 points all together, (three locations at four cross sections).

4.3.4.3 Animations

A series of animations have been generated showing the stress-wave propagation along the pile. These images clearly present the zones of stress variation and the way the controlling parameters affect the stress distribution and as a result the force measurements at the pile's surface.

4.3.5 Results from Stage I

4.3.5.1 Overview

The preliminary results include detailed stresses/forces and velocity plots for three cases; the baseline case, a 0.2m ram diameter, and the baseline for an uneven impact (tilted ram). The presented results explore the stress and velocity variations for each case, and their influence on the traditional dynamic measurements. In transferring from stress to force, one should note that the local calculated stress was multiplied by the pile's cross sectional area, hence only under uniform stress distribution the force is correctly calculated. The term Equivalent Force is used to describe the values of the forces obtained this way.

The meaning of the results, and their operational conclusions are provided in the sections following the presentation of the preliminary results.

4.3.5.2 *Baseline Model*

The baseline model (ram diameter = pile diameter = 1m, drop height = 2.0m, perfectly even blow, see Tables 39, 40, and 41) set of results are depicted in Figures 283 through 290.

4.3.5.3 *Smaller Diameter Ram*

An even impact of a 0.2m ram diameter (see Table 40) having the same energy as the baseline ram was analyzed as a representative case for the smaller ram impact. The obtained stresses/forces and velocities are presented in Figures 291 through 298.

4.3.5.4 *Uneven Impact (Tilted Ram)*

The baseline model was analyzed for a marginal uneven impact of 1° , translated to 17.5mm gap between ram and pile at one side of the perimeter. Figures 299 through 306 present the detailed stresses/forces and velocities associated with this analysis. In contrast to the even impact, which creates axisymmetric stress conditions, the uneven blow creates uneven stresses not in an axisymmetric arrangement. These can be analyzed in the half symmetry model used, but the presentation of the results was modified to include nodes in equal distances (half radius and perimeter) along the diameter (refer to Figure 282b) on the opposite side to the nodes for which the stresses are presented for the even impact models.

4.3.6 **Discussion of Results – Stage I**

4.3.6.1 *Baseline Model*

The baseline model analysis suggests that assuming a perfectly even impact over a soft cushion with a round ram (equal to the pile's diameter), results as expected with almost a perfectly even stress wave across the pile section. The match between the velocity multiplied by the impedance and the force calculated based on the local stress, reaffirms the results of an evenly distributed stress wave that continues to propagate in this way along the pile (Figures 283 through 290). Detailed examination show that some stress unevenness exists at the top of the pile (close to the impacted surface, see Figure 283) to be further investigated in the following section. This relatively small stress unevenness does not affect the velocity (Figure 284), and completely disappears within one diameter away from the pile's surface (Figure 285).

4.3.6.2 *Smaller Diameter Ram*

The smaller diameter ram creates a high stress concentration at the zone of impact such that a very high stress exists under the center of the ram (Figure 291), diminishing in magnitude towards a zone outside the impact area. In all cases, however, the velocity remains mostly unaffected (Figure 292) and the uneven stress becomes mostly uniform within one pile diameter (Figure 293). The creation of a high stress short duration wave using such ram can be beneficial

for integrity analysis purpose allowing sharp reflection of waves from zones of low quality and/or discontinuity.

4.3.6.3 *Uneven Impact (Tilted Ram)*

A relatively slight uneven impact creates a large stress variation between one side of the shaft to the other (Figure 299). In spite of a sizeable soft cushion, these uneven stresses continue to exist until three diameters away from the impact surface (Figures 301 and 303). In all cases uniform velocity exists across the pile in all sections indicating the reliability of these measurements when available.

4.3.6.4 *Operational Conclusions*

1. Pile velocity can easily be measured by one or two accelerometers, as even velocities exist throughout the pile surfaces and at locations down the exposed shaft.
2. The use of a ram smaller in diameter relative to the shaft it is impacting upon, creates a high stress short duration wave, which can be beneficial for defect detection even under conditions in which the shaft capacity is not fully mobilized.
3. Most significant stress variations exist under uneven impacts when the ram is not parallel to the impacted shaft. This commonly occurring condition takes place due to uneven shaft top surface, non-vertical pile, and in almost all impact systems having difficulties in producing a ram that is perfectly aligned with the shaft's axis. The large variation in stresses exists in the analyzed model in spite of a sizeable soft cushion and, hence, calls for the following actions:
 - a. The use of a sizeable cushion when testing drilled shafts. This conclusion affects the energy of the required system as a larger cushion translates to a higher loss of energy, requiring a larger impact system.
 - b. Multiple force point measurements around the shaft.
 - c. Measuring dynamic forces at a distance as large as possible away from the impact, in the case of uneven impact this distance can be three pile diameters and more.

4.3.7 **Analysis Procedure – Stage II**

4.3.7.1 *Overview*

As the most significant effect on the uniformity of the stress distribution seem to originate from an uneven impact due to a tilted ram, this case was examined in detail in comparison to the baseline.

4.3.7.2 *Model Geometry, Constraints, and Material Properties*

The details of the analyzed driving system (ram) are summarized in Table 41. The segmental modeling was changed by having the striking plate and the cushion (refer to Figure 276) modeled as free standing bodies (i.e. can separate from each other). The surfaces between the striking plate and the cushion and between the cushion and the pile were modeled using the contact formulation as used between the ram and the striking plate in stage I, described in section

4.3.2.2. The material properties used are those presented in Table 37 only differing by the selected wood modulus of $7.0E+09\text{Pa}$ being a more realistic value in relation to the soft cushion used in stage I of the analysis.

4.3.8 Baseline Model Results

4.3.8.1 Surface Conditions

The stress and velocity with time at eight points across the pile's surface (refer to Figure 282b) are presented in Figures 307 and 308, with further details on a smaller time scale presented in Figures 309 and 310. A complementary graph presents the stresses as a function of the location at the pile's surface for various times, and is presented in Figure 311. The obtained results suggest large variation in contact stress across the impact location with velocities overall similar at each point.

To obtain a better feel for this variation, isometric 3-D images were prepared, detailing the contact stresses at the pile's surface with time and are presented in Figure 312 (a to l). The obtained images show high stresses around the external rim of the contact between the ram, striking plate, wood and the pile's top.

4.3.8.2 One Meter Below the Surface

Figure 313 (a to l) describes the normal stresses across the pile at a location 1.0m (0.5 diameter) below the surface, for various times of the stress passing along the pile. The obtained images clearly show a well-distributed stress across the pile's section. It should be noted that the stress is uniform and what seem to be a stress increase at the circumference is only a result of the isometric presentation of the data. Additional presentation of the stress at the depth of 2m (1 diameter) from the surface had shown similar results shifted only in time.

4.3.9 Uneven Impact (Tilted Ram)

4.3.9.1 Surface Conditions

The stress and velocity with time at eight points across the pile's surface (see Figure 282) are presented in Figures 314 and 315 with further details on a smaller time scale presented in Figures 316 and 317 respectively.

A complementary graph describes the stress as a function of the location at the pile's surface for various times, and is presented in Figure 318. The obtained results suggest a very large variation in the normal stresses and velocities across the surface of the pile and moreover this variation seem to last for a significant time length in relation to the time required for the stress wave to travel to the pile's tip and back (see Figure 314). A detailed investigation is, therefore, required in order to assess the significance of an inclined impact, even though such an incline is considered in most cases very small (1°).

Isometric 3-D images of the normal stress at the pile's surface with time are presented in Figure 319 (a to k). The images clearly show a stress concentration at the point of initial contact between the ram-striking plate-wood and pile. This concentration remains high throughout the time of impact

4.3.9.2 *One Meter Below the Surface*

Figure 3200 describes the normal stresses across the pile at a location 1.0m (1 diameter) below the surface, for various times of the stress passing along the pile. Within the distance of half a diameter, the sharp stress peaks that appear at the surface are muted but a large variation exists between the stresses at one side of the cross-section to the other.

4.3.9.3 *Two Meters Below the Surface*

Figure 321 describes the normal stresses across the pile at a location 2.0m (2 diameters) below the surface, for various times of the stress passing along the pile. The stresses remain markedly uneven across the section throughout the passing of the wave.

4.3.9.4 *Three and Four Meters Below the Surface*

Further attempts to elucidate the changes in the normal stress distribution across the pile at a large distance from the surface are presented in Figure 322 and 323 for distances of 3m and 4m (3 and 4 diameters) from the pile top, respectively. Both figures show a more evenly stress distribution with increase in the distance from the impact, but even at four diameters away from the pile top the stresses seem to be highly uneven across the pile.

4.3.10 **The Use of a Soft Cushion to Mitigate Uneven Impact (Tilted Ram)**

The analyzed cases presented in the previous section suggest a troublesome situation in which a ram impact in a small inclination will result with uneven stress distribution across a shaft for a large distance (over four diameters) away from the surface of the shaft. In an attempt to examine mitigating solution, an analysis has been carried out for which the cushion was assumed to be two order of magnitude “softer” than the realistic value used in stage II of the analysis ($E=7 \times 10^7 \text{Pa}$ vs. $7 \times 10^9 \text{Pa}$). The results of this analysis, describing the normal stress distribution across the shaft at a distance 2m (two diameters) away from the shaft’s surface are depicted in Figure 324.

The obtained results clearly show improved stress distribution across the shaft in comparison with the one with a more realistic “harder” cushion presented in Figure 321. However, the duration of the stress wave had significantly increased (in time) and decreased in magnitude. So while an improvement is made in the distribution of the stress, its quality for analysis in signal match or in amount of energy arriving to the shaft had significantly diminished.

Figure 325 illustrates the difference between the two cases. The average force across the shaft’s section at the surface, 1m and 2m below the surface are plotted against time for the two cushions discussed above. The “softer” cushion is clearly seen to reduce the peak average force/stress by about half while doubling the wave duration.

4.3.11 **Intermediate Conclusions**

The advanced modeling of an impact between a ram and a drilled shaft as presented in this section, leads to the following conclusions:

1. Realistic impact analysis is obtained using the FEM analysis LS-DYNA
2. An even impact of a ram with a drilled shaft results with various local stress concentrations at the surface. These variations become irrelevant within a short distance of 0.5m from the shaft's top.
3. A relatively small tilt in the ram (1°) during impact, results with significant uneven stress distribution across the shaft's surface and away at a relatively large distance (four diameters) along the pile's shaft.
4. The use of a soft cushion mitigates the problem of a large stress variation across the shaft, but diminishes significantly in the quality of the stress wave for use in signal match analysis and reduces the energy transfer to the shaft.

4.4 RHEOLOGICAL MODEL OF PILE BEHAVIOR UNDER LOADING

4.4.1 Overview

The proposed rheological model is aimed at achieving a robust yet simple model allowing the simulation of the pile's load-displacement behavior under Static (Standard), Express Static-Cyclic, Statnamic and Dynamic Load tests. Initial promising results are presented in this manuscript while further research is required.

4.4.2 Model Description

4.4.2.1 Overview

Referring to Figure 326, the rheological model consists of traditional spring elements (E), dashpots η , two-directional sliders activated in compression and tension T (see Figure 327), and elements T^* , which are one-directional sliders, active in compression only (Figure 328).

The five main units of the model are labeled as "a", "b", "c", "d", and "e" marked in Figure 326. Elements "a" and "b" are two Kelvin elements in parallel subjected to sliders T_1^* and T_2^* . Element "c" above "a" and "b" control the elastic pile/soil system and has a slider T_0^* in parallel to units "a" and "b". Elements "d" and "e" are two additional Kelvin elements in sequence with "a", "b", and "c".

Upon loading, the soil/pile system response undergoes a transition from elastic to elasto-plastic and finally to a plastic state. For Statnamic test, the fast loading is continuous, in Express Static-Cyclic the loading is continuous but at a reduced velocity (comparable to Statnamics) and for the static test, in each stage the loading is increased in several steps maintaining a constant load in each step.

4.4.2.2 Stage I ($P \leq T_0^*$)

During the initial loading, when the load $P < T_0^*$ (elastic stage) the displacements are only in the element E_0 and are directly related to the applied load P:

$$S_1 = \frac{P}{E_0} \quad (88)$$

where $S_1 =$ pile settlement during the first loading stage [L]
 $E_0 =$ the spring constant [F/L]

4.4.2.3 Stage 2 ($T^*0 < P < T^*1 + T^*0$)

At the next stage of loading (Visco-elastic), the displacements are absent in elements T^*_1 , T^*_2 , T_3 and T_4 , (assuming that $T_3 < T_4$). This stage ends when the force in unit “a” achieves the limit value, T^*_1 , i.e. $P_a = T^*_1$. The differential equation for each loading step during this stage of the load-displacement relations is as follows:

$$(\eta_1 + \eta_2) \frac{dS_{2j}}{dt} = \Delta P - S_{2j}(E_1 + E_2) \quad (89)$$

The solution of this equation with the initial condition $t = 0$, $S_{2j} = 0$ is:

$$S_{2j}^{cr} = \frac{\Delta P}{E_1 + E_2} (1 - e^{-\alpha_1 t}) \quad (90)$$

where : S_{2j}^{cr} - creep settlement for the time the load is kept constant during the loading step. The corresponding relationship of settlement and time are presented in Figure 329 where α_1 is a constant:

$$\alpha_1 = \frac{E_1 + E_2}{\eta_1 + \eta_2} \quad [1/T] \quad (91)$$

where $\Delta P =$ the analyzed (additional) load step [F]
 $t =$ time associated with each loading (and settlement) step [T]
 $E_1 + E_2 =$ spring constants one and two in parallel [F/L]
 $\eta_1 + \eta_2 =$ dashpot one and two in parallel [F/V = FT/L]

The incremental settlement of the pile for each step during the 2nd stage is:

$$S_{2j} = S_{2j}^{im} + S_{2j}^{cr} \quad (92)$$

where : S_{2j}^{im} - immediate settlement.

$$S_{2j}^{im} = \frac{\Delta P}{E_0} + \frac{\Delta P}{E_{0,1}} \quad (93)$$

hence:

$$S_{2j} = \frac{\Delta P}{E_0} + \frac{\Delta P}{E_{0,1}} + \frac{\Delta P}{E_1 + E_2} * (1 - e^{-\alpha_1 t}) \quad (94)$$

If $t \rightarrow \infty$, the stabilized settlement for the load P at the j-step of the second stage, S_{2j}^{st} is (using equation 90):

$$S_{2j}^{st} = \frac{\Delta P}{E_1 + E_2} \quad (94a)$$

hence;

$$S_{2j} = \frac{\Delta P}{E_0} + \frac{\Delta P}{E_{0,1}} + S_{2j}^{st} (1 - e^{-\alpha_1 t}) \quad (95)$$

and the final settlement of step j in the second stage is:

$$S_{2j} = \frac{\Delta P}{E_0} + \frac{\Delta P}{E_{0,1}} + \frac{\Delta P}{E_1 + E_2} \quad (96)$$

$E_{0,1}$ - spring constant, defined using equation 93 as:

$$E_{0,1} = \frac{\Delta P}{S_{2j}^{im} - \frac{\Delta P}{E_0}} \quad (97)$$

4.4.2.4 Stage 3 ($T0^* + T1^* < P < T^*1 + T^*2 + T^*0$ and $Pa > T^*1$)

The load in this stage is smaller than the bearing capacity of the pile ($Pk = T^*_1 + T^*_2 + T^*_0$ - see Figure 330). The differential equation describing the load settlement relations for each load step during the third stage is:

$$\eta_2 \frac{dS_{3j}}{dt} = \Delta P - S_{3j} \cdot E_2 \quad (98)$$

The solution of this equation with the initial condition $t = 0$, $S_{3j} = 0$ is:

$$S_{3j}^{cr} = \frac{\Delta P}{E_2} (1 - e^{-\alpha t}) \quad (99)$$

where: $\alpha_2 = \frac{E_2}{\eta_2} \quad [1/T] \quad (100)$

and $E_2 =$ spring constant $[F/L]$
 $\eta_2 =$ dashpot $[F T/L]$

Similar to the response during the second stage, the settlements at each step during the third stage are:

$$S_{3j} = S_{3j}^{im} + S_{3j}^{cr} \quad (101)$$

where the immediate settlement:

$$S_{3j}^{im} = \frac{\Delta P}{E_0} + \frac{\Delta P}{E_{0,1}} \quad (102)$$

where S_{3j}^{im} and S_{3j}^{cr} are the immediate and creep settlement under the j-step in the third stage, respectively. If $t \rightarrow \infty$, the stabilized settlement of step-j in the third stage is:

$$S_{3j}^{st} = \frac{\Delta P}{E_2} \quad (103)$$

hence

$$S_{3j} = \frac{\Delta P}{E_0} + \frac{\Delta P}{E_{0,1}} + S_{3j}^{st} (1 - e^{-\alpha_2 t}) \quad (104)$$

The final (stabilized) settlement of step-j in the third stage is:

$$S_{3j}^{st} = \frac{\Delta P}{E_0} + \frac{\Delta P}{E_{0,1}} + \frac{\Delta P}{E_2} \quad (105)$$

4.4.2.5 Stage 4 ($T^*1 + T^*2 + T^*0 < P < T3$)

When $P > T^*_1 + T^*_2 + T^*_0$ the bearing capacity of the pile is exceeded and a permanent (non-reversible) movement of the pile takes place. The velocity of the settlement is however limited.

During the loading of the fourth stage a prescribed settlement value is obtained but settlement stabilization cannot be reached. T_3 is the failure load, (P_f of Figure 330 to be discussed in section 3) beyond which the velocity of the settlement rises sharply.

The velocity of the settlement in the fourth stage is:

$$\frac{dS_{4j}}{dt} = \frac{P - (T^*_1 + T^*_2 + T^*_0)}{\eta_2} \quad (106)$$

$$S_{4j}^{cr} = \frac{P - (T^*_1 + T^*_2 + T^*_0)}{\eta_2} * t \quad (107)$$

The settlement for each loading step is:

$$S_{4j} = S_{4j}^{im} + S_{4j}^{cr} \quad (108)$$

$$S_{4j}^{im} = \frac{\Delta P}{E_0} + \frac{\Delta P}{E_{0,1}} \quad (109)$$

where S_{4j}^{im} and S_{4j}^{cr} are the immediate and creep settlements under the j-step in the fourth stage, respectively.

$$S_{4j} = \frac{\Delta P}{E_0} + \frac{\Delta P}{E_{0,1}} + \frac{P - (T_1^* + T_2^* + T_0^*)}{\eta_2} * t \quad (110)$$

4.4.2.6 Stage 5 ($T_3 < P < T_4$)

When the load exceeds the failure load but is below the maximum applied static load (P_f and P_{max} of Figure 330, respectively). At this stage the velocity of the settlement rises sharply.

T_3 – failure load during the static test (P_f)

T_4 - maximum force that can be applied during the static tests. $T_4 = P_{max}$

The settlement during each loading step during the fifth stage is:

$$S_{5j} = S_{5j}^{im} + S_{5j}^{cr} \quad (111)$$

where S_{5j}^{im} is the immediate settlement in the system and S_{5j}^{cr} is the creep settlement.

$$S_{5j}^{im} = \frac{\Delta P}{E_0} + \frac{\Delta P}{E_{0,1}} \quad (112)$$

$$S_{5j}^{cr} = \frac{P - (T_1^* + T_2^* + T_0^*)}{\eta_2} * t + \frac{P - T_3}{\eta_3} * t \quad (113)$$

$$S_{5j} = \frac{\Delta P}{E_0} + \frac{\Delta P}{E_{0,1}} + \frac{P - (T_1^* + T_2^* + T_0^*)}{\eta_2} * t + \frac{P - T_3}{\eta_3} * t \quad (114)$$

t – time associated with each individual load step-j of the fifth stage

4.4.2.7 Stage 6 ($P > T_4$)

This stage exists only in tests in which the applied load exceeds the maximum static load (P_{max} of Figure 330) due to dynamic or other effects (e.g. during Statnamic tests).

The incremental settlement for each loading step in stage 6 is:

$$S_{6j} = S_{6j}^{im} + S_{6j}^{cr} \quad (115)$$

$$S_{6j}^{im} = \frac{\Delta P}{E_0} + \frac{\Delta P}{E_{0,1}} \quad (116)$$

$$S_{6j}^{cr} = \frac{P - (T_1^* + T_2^* + T_0^*)}{\eta_2} * t + \frac{P - T_3}{\eta_3} * t + \frac{P - T_4}{\eta_4} * t \quad (117)$$

$$S_{6j} = \frac{\Delta P}{E_0} + \frac{\Delta P}{E_{0,1}} + \frac{P - (T_1^* + T_2^* + T_0^*)}{\eta_2} * t + \frac{P - T_3}{\eta_3} * t + \frac{P - T_4}{\eta_4} * t \quad (118)$$

t - time associated with each individual load step - j of the sixth stage.

4.4.2.8 Condition for Model Operation ($E_2 T^*1 < E_1 T^*2$)

Assuming that a movement in element T_1^* is initiated before a movement in element T_2^* takes place. As such, the force in unit “a” achieves T_1^* and the movement in unit “a” begins ($P_a = T_1^*$), while no movement takes place in unit “b” for which $P_b < T_2^*$. If $t \rightarrow \infty$, the movements (settlements) in elements “a” and “b” are equal:

$$S_a^{st} = S_b^{st} \quad (119)$$

$$S_a^{st} = \frac{T_1^*}{E_1} \quad (120)$$

The force in the element “b” is therefore equal to:

$$P_b = E_2 * S_b^{st} = E_2 * \frac{T_1^*}{E_1} < T^*2 \quad (121)$$

Hence, the condition for the model operation is:

$$E_2 * T_1^* < E_1 * T_2^* \quad (122)$$

This condition is examined during the numerical solution of the model. If shown otherwise the obtained values are reexamined.

4.5 MODEL EVALUATION USING NEWBURY TEST PILE #2

4.5.1 Overview

Extensive site investigation, dynamic, static, static cyclic and Statnamic tests were carried out by the Geotechnical Engineering Research laboratory of the University of Massachusetts Lowell. The Statnamic test results compared to the static test results for two test piles are presented by Hajduk et al. (1998). The presented rheological model was evaluated using these two test piles following the above outlined procedures. The results of two Statnamic tests on Test Pile-2 were used to calculate the 'static' load displacement relations and are compared to the measured results.

4.5.2 Parameters

Table 42 presents a summary of the model parameters as obtained from the Statnamic tests impact #3 and impact #4. For comparison, the parameters were also determined for the static load-test results. The following comments can be made regarding the obtained parameters:

- (1) The detailed recorded initial load displacement relations affect the calculated E_0 . The large variation between one Statnamic test to the other is due to delay in the displacement response after load application. This however has no significant effect on the evaluated capacity.
- (2) As anticipated η_4 is four or five orders of magnitude smaller than η_1 and η_2 and hence the only active dashpot during the Statnamic test.

4.5.3 Static Load-Displacement Relationship Based on Statnamic Test Results

The calculated relationships based on the STATNAMIC tests TP#2-3 and TP#2-4 (for slow #3 and #4, respectively), are presented in Figures 331 and 332, respectively.

As seen, the calculated results based on both statnamic tests are in close agreement with the load-displacement relations measured in the slow maintained Static Test for pile TP#2.

These results can be further evaluated by observing the information presented in Figure 46 showing that the measured statnamic force-displacement relations (Figure 46a) and the derived static force-displacement by the UPM method of Figure 46b (see section 2.3.5.3) substantially over predict the static measured capacity. However utilizing the recommended rate effect factor presented in this research for piles in clay, $\eta=0.65$ (see Table 26), would result with a close agreement to the measured static capacity.

4.6 CONCLUSIONS

The presented model provides a basis for the simulation of pile-soil interaction under various load rates. The successful implementation of the model for controlled cases in which static, static-cyclic and Statnamic tests have been carried out is the first stage for the model verification. To the best of our knowledge it is the first time that such model is developed and implemented for high rate testing. Further examination of the model need to be carried out, followed by a parametric evaluation of the Statnamic test results under various soil conditions.

CHAPTER 5

SUMMARY, CODES, CONCLUSIONS, RECOMMENDATIONS AND SUGGESTED RESEARCH

5.1 SUMMARY

5.1.1 Summary Tables

Tables 43 and 44 summarize the major attributes, status and proposed future work for the primary and secondary investigated load testing systems.

5.1.2 Summary of Study

A traditional static axial deep foundation load test is performed by a slow application of a force produced against an independent reaction, imitating structural loading. It is the most reliable method to determine the pile's performance as commonly required under typical service conditions. The major limitations of this testing are: (i) high cost associated with set-up, test duration, interpretation and construction delays, and (ii) inability to obtain information about the pile-soil interaction along the pile without additional testing means (e.g., tell tales, strain gauges, etc.). These limitations are acute when high capacity foundations are involved.

Alternative methods to the standard static load testing have been developed in two principal avenues: (i) Static loading by methods that either do not require independent, external reaction for load application (e.g. Osterberg cell; Osterberg, 1989), or short duration, pseudo-static loading procedures (e.g. Static-Cyclic Testing; Paikowsky et al., 1999) and, (ii) Dynamic testing in which the pile is exposed to dynamic efforts (i.e. a force or stress is generated within or at the boundary of the pile through the intervention of mass and acceleration). These testing methods include the generation of low and high strain waves as well as impacts that produce long relative wavelengths most appropriately termed kinetic testing or fast penetration testing.

Both avenues of alternative testing methods (static and dynamic) are researched in the presented study. Simplified models along with a relative wavelength concept are utilized for pile testing classifications. The different innovative testing methods are reviewed, concentrating on three primary (widely used) and four secondary pile test types, namely: Drop Weight System, Statnamic test and Osterberg Load Cell technology being the primary and Simbat, Fundex, Smartpile and SmartCoil being the secondary. The static load test procedures including the relatively fast static-cyclic testing method are summarized and used as a benchmark.

Following a review of the systems and testing procedure, the different testing methods were researched according to the available data, need for investigation and perceived difficulties.

The drop weight system was investigated via two databases. One of dynamic measurements and the associated predicted capacity (DW2000), and the other including drilled shafts for which static load tests had been carried out in addition to the dynamic measurements of the drop weight testing (DW/LT2000). Database DW2000 was used to examine the typical performance of a drop weight system (e.g. energy transfer), and to develop generic recommendations for the required ram weight and stroke height for a given capacity (ultimate or needed). Database DW/LT2000 was used for evaluating the developed recommendations and refining them based on the tested foundation; differentiating between the major sources of

resistance (end bearing vs. frictional), and associating the recommendations to the permanent displacement of the deep foundation. The predicted capacities in database DW/LT2000 were compared to the capacities measured in the static load tests using various interpretation methods and differentiating between static load tests to failure and non-failed extrapolated static loading. The results were compared to the performance of the same dynamic prediction methods when utilized for driven piles for which large databases are available, as well as the performance of static capacity prediction methods. Specific difficulties associated with the ram-pile impact were investigated using the impact specific FE code LS-DYNA. Realistic three-dimensional simulation of a ram impact with a pile were performed for the first time allowing identification of the major source of dynamic measurement difficulties when conducting drop weight testing (i.e. uneven impact), and examining various remedies (e.g. soft cushion) and test recommendations (e.g. instrumentation attachment location away from impact). The above analyses and available reviewed codes had led to the following major conclusions:

The ram weight should be larger than 1% of the expected mobilized capacity in the case of frictional shafts or shafts for which more than 2mm permanent set (under the analyzed blow) can be achieved. For end bearing shafts, the ram weight should be larger than 1.5% of the expected mobilized capacity. A distance of two diameters or more should be maintained between the impact and the strain measurements, which should be carried out at least at four locations around the perimeter. The accuracy of the tests is as reliable as those carried out for driven piles under restrike, subjected to the limitations of the available case histories of database DW/LT2000.

The Statnamic testing method was investigated via a database of case histories comparing predicted capacity to that measured by static load-tests. Sub-categorization and past experience suggested large capacity overpredictions when using the method in deep foundations constructed in cohesive soils (i.e. silts and clays). Attempt was made to introduce a rate effect factor based on soil type and testing performance (e.g. $\eta = 0.69$ in silt and $\eta = 0.65$ in clays). The use of these “correction factors” suggest improved performance of the method in all testing conditions. These factors are based on currently available small database (e.g. 13 cases in silt and 4 in clay). The approach presented is practical for the immediate testing needs and allows the great benefits associated with the Statnamic testing method (mobility of very high impacts). It is not based however on a fundamental solution that addresses the mechanics behind the problem. This was addressed via a rheological model that was developed in the research that seems to have the potential of addressing kinetic testing for which one-dimensional wave mechanics is not applicable.

The investigation of the Osterberg cell (O-cell) testing method concentrated on a Finite Element Method (FEM) study addressing the major issues encountered during O-cell tests in soil or rock and researching the controlling factors. The study targeted the issue of underlying differences between deep foundation interfacial shear resistance when being loaded from top down (conventional use and static testing) versus from down up (O-cell testing). A sample analytical model to examine the same issues was developed as well. A limited number of detailed case histories was used to examine the analyses. The available data were found to be extremely difficult to use due to their scarcity, the influence of the tests themselves on the measured results (e.g. shear of concrete-rock interface in static test and then comparing the results to O-cell test on the already sheared interface), and spatial variability when running two tests on two adjacent foundations. The best comparative tests in soft soil appear to indicate relatively good correlation between side shear resistance in O-cell and top down loading. Overall, the presented research suggests that the differences in mobilized base resistance from an

O-cell loading and top down loading are relatively minor for shafts in soil or rock. The differences in mobilized side shearing resistance from an O-cell loading and top down loading are relatively minor in soil with most instances having measured values of unit side shear from an O-cell to be slightly conservative relative to top-down loading. For shafts in rock, the unit side shear values mobilized during O-cell tests tend to be conservative relative to unit side shear values which may be mobilized from top down loading. The differences increase as the modulus of the rock mass approaches 10% or higher than the modulus of the shaft's concrete.

The four secondary testing methods were reviewed to the extent of available data and/or possible examination via models.

The Simbat method is essentially a drop-weight testing with improved displacement measurements, and a different interpretation procedure than the standard signal matching analysis. Comparisons on the basis of ultimate static capacity seem to show difficulties for piles in clay and overall prediction accuracy lower compared to the standard dynamic method procedures. Comparisons between predicted to measured values on the basis of settlement alone (especially within the working loads) are available for a large number of cases but are of limited significance in the context of capacity evaluation, being appropriate for proof testing.

The Fundex load testing system extends the time period of an impact via springs. The resulting long stress waves cannot be analyzed via wave propagation analyses but require addressing the resulting dynamic effects. The simple model used by the method for test result interpretation is not effective in doing so. The limited information available for comparing testing results to static load tests along with the theoretically questionable basis makes the method less attractive for ultimate capacity prediction purpose at the present.

The Smartpile method employs effective technology to directly measure forces in the pile during impact testing mostly of driven piles. The interpretation methods of the test results (under the limited available data and when comparing the predictions to static load-test results) point to the inability of the method to address the complex soil-pile interaction during driving.

The Smartcoil method appears to be a novel, interesting concept, but no information is available of its actual implementation, let alone effectiveness.

Several models were developed and utilized to assist the study. A simple model is used to investigate the behavior of piles under impact and categorize the testing methods, and is demonstrated through a detailed case history. The second model represents a change in the approach of testing interpretation. A rheological model is developed for analyzing the deep foundation response under different testing methods. The model, while applicative to all testing methods, seems to be particularly attractive for addressing the deficiencies of kinetic testing (e.g. Statnamic tests).

5.2 CODES

5.2.1 Overview

While being popular worldwide, the innovative load testing systems have limited available references in codes and regulations. One such code is the Chinese specification for high strain dynamic testing that specifically includes the drop weight testing.

5.2.2 Chinese Code

Mr. Frank Li, of the research team, had worked previously in China in high strain drop weight dynamic testing. To examine the practice there, and recognizing the fact that it is the only known code to include drop weight testing, an effort was made to translate this code to English. The results of this effort are presented in Appendix C. It is emphasized that this translation is not intended for any other purpose other than the above and hence the research team is not responsible for the accuracy of the translation and/or for any other use made of this translation.

In reference to the attached translation, please note the following:

1. The code fully recognizes the drop weight system with the major parts applicable for both tests (dynamic tests on driven piles and drop weight on in-place constructed deep foundations).
2. The tests are recognized for integrity purpose also.
3. Some provisions refer explicitly to in-place constructed deep foundations e.g. 5.1.2.3, 5.1.3.3, 5.1.4.2, 6.1.1.2, 6.1.4, 7.3.1.3 and others.
4. Additional relevant table from the Shanghai Foundation Code (of time delay for testing) was added at the end of the document.
5. Some sections of the codes, while instructing the user in a reasonable way, lack specifics which detracts from its meaning.

5.2.3 Japanese Code

A draft for a Japanese code for rapid load test of single pile is available and is provided in Appendix C (Part B). Though not specifically mentioning a testing system, the suggested loading duration and name implies the use of kinetic testing such as the Statnamic test (see Figures 5, 7 and Table 1 of this report).

5.2.4 American Standard

Subcommittee D18.11 of Committee D18 on Soil and Rock of the ASTM have examined a proposed standard testing method for piles under rapid axial compression, namely the Statnamic test. As the standard has not yet been approved and published no reference is provided.

5.3 OBSERVATIONS, CONCLUSIONS AND RECOMMENDATIONS

5.3.1 General

This section summarized the observations and conclusions derived at the study. Suggested *relevant recommendations are marked by bold italics text* along the relevant observations and conclusions.

5.3.2 Principles

1. The classification of pile testing on the basis of relative wave length (Λ , which represents the duration of the force pulse relative to the pile's length) was found to be

- effective. This classification explains the relationship between loading, the transfer of the loading in the pile, the importance of dynamic effects and the ability to employ wave mechanics principles in analyses evaluating the pile-soil interaction when utilizing measurements recorded at the pile top. Such classification prevents misconception about the duration of the loading and its relationship to static loading.
2. The use of simplified models enables to gain insight to the mechanical principles of the various testing methods to the point of obtaining reasonable practical representation of field measurements. Their use should be encouraged as a mean to evaluate and demonstrate the relationships between the impacting body and the pile for the different testing methods.
 3. ***Advanced new modeling (e.g. LS-DYNA) enables to simulate dynamic interactions (e.g. ram-pile impact) in a realistic way, previously not available. The use of such analyses is recommended to identify problems, limits and solutions for various drop weight systems and foundations. Such study will provide guidance for effective utilization of the impact application and measuring systems, (as was demonstrated) and hence allow the development of better guidelines.***
 4. ***The use of a rheological model for the purpose of impact analysis based on evaluating a test result under one rate of loading (e.g. static) from another rate of loading (e.g. kinetic) have proven to be very successful and promising. Further effort is required for the examination of the model under a wide range of testing methods and conditions.***

5.3.3 Testing Methods

5.3.3.1 General

Sizeable databases (relative to the state of the art) were accumulated for the evaluation of two of the testing methods; drop weight and Statnamic tests. The results of the databases analyses and relevant other information lead to the following conclusions and ***recommendations (highlighted in bold italics):***

5.3.3.2 Drop Weight System

1. The construction methods of drilled deep foundations allow for limited quality control, and hence the structural integrity and the geotechnical capacity are highly variable and uncertain.
2. Dynamic testing is an attractive alternative solution for static load-testing of in-place constructed deep foundations (IPCDF). These need however, to provide wave resolution with depth in order to enable meaningful structural integrity evaluation and soil-pile interaction interpretation based on wave mechanics.
3. The preferable stress wave for drilled foundations dynamic testing consists of high stress peak short duration signal with a small as possible relative wavelength ($\Lambda < 1$). These are obtained by high velocity impact of longer and narrower rams.
4. Drop-weight systems consist of simple mechanical elements allowing dropping a weight on the top of a deep foundation. Various drop weight set-ups exist with systems of

- choice encompassing modular weights, variable drop height and better control of ram alignment.
5. Dynamic measurements consist of acceleration and strain measurements on the circumference of the deep foundation element and possible acceleration measurement of the ram. The measurement of the ram's acceleration provides the impact force experienced by the ram, which is accurate for representing the pile top as long as the impact is even and strain measurements are taken at the pile top. The calculation of the force signal from the strain measurement assumes the knowledge of the drilled shaft's modulus and cross section as well as uniform stress distribution.
 6. Sources for possible difficulties of dynamic measurements on in-place constructed deep foundations (see Table 4) include:
 - a. Construction problems – non-uniform cross-section, uneven shaft surface and poor quality of concrete in the exterior sections.
 - b. Testing problems – low energy and/or low velocity impact, uneven ram impact.
 - c. Reaction problems – the development of high friction at the top part of the shaft.
 7. ***The problems associated with the quality and geometry of the foundation can be controlled by the appropriate construction of the shaft's top. The construction of a vertical, uniform and level head shaft extension (possibly in a sleeve) of two-diameter long can also be achieved by an excavation around the shaft.***
 8. Even ram impact on a striking plate and a cushion creates a symmetric, non-uniform contact stresses at the surface (Figure 312). These stresses become however uniform within a short distance of about one radius from the pile's top (Figure 313). Uneven impacts due to a tilted ram (even with a small inclination of 1°) creates uneven stress wave at the surface that remains uneven at a great distance (of over four diameters) from the pile's top (Figures 319-320). The use of a soft cushion system attains a more uniform stress distribution with the price of energy loss and a signal of smaller peak stress and higher duration (Figures 324-325). ***This difficulty in dynamic measurements can only be solved with the attachment of multi strain gauges (minimum four) around the perimeter at a distance of at least two-diameters from the shaft's top.***
 9. The use of a ram of a smaller diameter than the shaft itself creates uneven stresses at the surface that become uniform across the shaft within a short distance from the shaft's top (within one diameter) (Figures 291-294).
 10. High reaction forces (friction) close to the shaft's top create early reflection waves, which invalidate the proportionality between the measurements of force and velocity (multiplied by the shaft's impedance). This creates two problems: (a) inability to examine independently the force measurements affected by many sources of difficulties, and (b) the need to conduct a very careful signal matching analysis.
 11. ***The ram weight should be larger than 1% of the expected mobilized capacity in the case of frictional shafts or shafts for which more than 2mm permanent set (under the analyzed blow) can be achieved. For end bearing shafts, the ram weight should be larger than 1.5% of the expected mobilized capacity (Figure 160).***
 12. ***Drop weight tests to failure (either structural or geotechnical) are best conducted by applying multiple impacts with a gradual increase of the impact energy (height and/or weight). Three to five impacts were experienced to be adequate with the higher number relevant to initial tests in a specific project and the lower number applied to subsequent tests under similar conditions.***

13. The comparison between capacity predictions of drilled deep foundations based on dynamic measurements and signal matching analysis and static load tests had resulted in excellent agreement. The ratio of measured to calculated capacity (based on the FHWA failure criterion) was found to be 1.05 ± 0.12 (1 S.D.) for 39 cases (Figure 154, Table 20). This ratio can be compared to that obtained for driven piles in restrike analyzed by signal matching analysis. For 162 piles, this ratio was found to be 1.16 ± 0.39 (1 S.D.). Both ratios well exceed the typical accuracy of static analyses of drilled shafts, which varies between 0.90 to 1.71 and coefficients of variation between 0.30 to 0.60.

5.3.3.3 *Statnamic Tests*

1. State of the practice review of the testing method including equipment procedures and analysis methods is presented. As the tests involve the creation of a long force wave, it results with relative wavelength (Λ) greater than 10, not suited for analysis employing wave mechanics.
2. The analysis methods most commonly used worldwide for the interpretation of Statnamic tests make use of simplified mechanical principles employing inertia and viscous damping correction. ***The accuracy of these interpretation methods when utilized for deep foundations in cohesive soil subsurface conditions was found to be unsafe when compared to static load test results (bias-static to prediction ratio of about 0.7 for 20 cases in silt and clay, see Table 25).***
3. A simple and practical improvement is suggested in this study by incorporating a rate effect factor. With the inclusion of these factors, a single safety factor or resistance factor can be employed regardless of soil type.
4. ***Rate effect factors were developed to calibrate the Unloading Point (UP) predicted load response to the measured static response while developing a recommended safety factors. The values presented in Table 26 should be applied to UP analyses to predict the static response and design foundations using Statnamic test results. Statnamic testing firms in the American continents have adopted the use of the rate effect factors listed herein. Therefore, designers will only rarely be exposed to un-factored predictions.***
5. The three analysis methods recommended for use with the above rate effect factors are the Unloading Point Method (UPM), the Modified Unloading Point Method (MUP), and the Segmental Unloading Point Method (SUP). ***These methods*** (identical in concept but vary in the required field data collection) ***should be selected based on pile length and/or performance.***
 - a. ***The UPM should be limited to relatively short foundations (wave number, $N_w > 12$) that exhibit a plunging response (i.e. measurable permanent set). The required field data should include top of pile measurements of load, acceleration, displacement (optional), and time.***
 - b. ***The MUP method is also limited to the same length piles ($N_w > 12$) but can be used when the foundation exhibits an elastic response (i.e. minimal permanent set). In those instances the top and toe displacement must be recorded independently for the MUP analysis. This method therefore requires field measurements of load, top of pile acceleration, toe of pile acceleration and time.***

- c. ***The SUP method can be used for much longer piles ($N_w > 6$) but must have strain gage instrumentation located along the length of the foundation defining shorter segments with $N_w > 12$. Field measurements should include top of pile load, acceleration, displacement and time.***
- 6. Two public domain software packages have been developed that perform Unloading Point analyses: SAWR4 and SUPERSAW which can be downloaded from <http://www.eng.usf.edu/~gmullins/>. As a result of this study, these packages have been updated to include the rate effect factor when predicting the static equivalent response.

5.3.3.4 Osterberg Cell

Detailed FE analyses and comparisons to data from case histories lead to the development of the following recommendations:

1. No specific changes in the practice of O-cell testing for drilled shafts in soil are suggested at the moment. However, it is advisable that the sole source provider of the tests (Loadtest, Inc.) be consulted in the planning process so that the location of the cell(s) are placed in the optimum location so that measurements of side shear and base resistance are obtained.
2. Recently completed, detailed, full scale testing comparing up-down to down-up loading on identical instrumented 1.5m diameter rock socketed drilled shafts is presented by Kwon et al. (2005), (not reviewed earlier in this study). This detailed study suggests that improvements are needed to the method currently used for the equivalent top-down curves derived from the down-up curves.
3. ***The average unit side shear measured during an O-cell test on a drilled shaft socket into rock is expected to be conservative and the distribution of maximum side shear resistance (interpreted from strain gauges) is expected to be biased toward higher values nearest the O-cell. It is suggested that designers either use average values of maximum unit side shear or at least temper the measured unit side shear values with judgment in regards to distribution with respect to depth.***
4. ***It is recommended that O-cell testing be performed in test shafts, which will not function as production shafts. Strain-softening of the maximum side shearing resistance has been noted with shafts which have been loaded to failure with full load reversal, and this degradation in side shearing resistance would potentially reduce the top-down load capacity of a shaft which has been loaded to side shear failure from a bottom-up loading.***
5. In view of the widespread use of the O-cell test for drilled shafts in rock and the lack of direct field comparisons between O-cell tests and top-down tests under such conditions, there is a compelling need for research to conduct such tests. It is recommended that a few major bridge projects for which O-cell tests are to be employed in rock sockets be selected as candidate projects for comparative tests to be performed. A comparative load test program would then need to be carefully designed to attempt to isolate the test method as a single variable; tested rock sockets would need to be constructed under identical conditions in rock conditions which must be relatively uniform. The results of such tests would be extremely valuable not

only in evaluating test methods, but in developing a better understanding of drilled shaft behavior in rock.

5.3.3.5 *The Secondary Testing Methods*

Secondary additional less widely used innovative testing methods have been reviewed and evaluated. The Simbat method is essentially a type of a drop weight system with some advantages gained from additional high quality independent measurements and some limitation due to the restricted analysis methods. A larger database and possibly examination of various other analysis methods will most likely proven the concept promising. The other examined methods suffer either from a theoretically deficient concept (Fundex) or a theoretical deficient interpretation method (Smartpile). Section 5.1.2 and Table 44 present best the comments relevant to these methods.

5.4 SUGGESTED RESEARCH

5.4.1 Overview

Tables 43 and 44 provide a summary of the reviewed methods attributes, current status and proposed future work. In the previous sections of Chapter 5 and throughout the manuscript, references are made to required research. The following are general suggestions with details to follow:

1. All testing methods suffer from two issues: (a) lack of clear identification of the conditions in which the methods operate best or are not reliable and the degree of uncertainty, and (b) lack of good quality data associated with highly controlled testing environment.
2. In spite of the fact that two of the methods were evaluated with a relatively sizeable database, many questions remain regarding the quality of the data (drop weight system) or the robustness and consistency of the interpretation (Statnamic).
3. New analytical tools like the impact analysis provide information that is valuable for testing evaluation, guidance and the development of testing procedures.
4. New interpretation concepts (e.g. the presented rheological model) which are not 'locked' in the entrenched analysis methods (e.g. wave mechanics or oversimplified Kelvin-Voigt models) seem to have the ability to better address the needs of testing which are faster than static tests but slower than dynamic (i.e. kinetic). Their potential requires a relatively limited effort and has the potential for a high return.

Three possible research statements (or their combination), each related to the three major testing methods are proposed. The following section addresses each of the primary researched methods and following a status statement provides suggested future research categorized into five areas namely; Development, Database, Models, Tests and Guidelines.

5.4.2 Drop Weight System

5.4.2.1 *Status*

This is a mature testing method that enjoys the flexibility of locally developed drop weight equipment and data acquisition systems. Though the market of equipment for dynamic monitoring of pile driving in the US is controlled by a single commercial entity, alternative equipment is readily available and current technology can be utilized for the same purpose as well. These facts contributed to the method's relatively low cost and common use worldwide. The major deficiencies are associated with clear identification of limitations and solutions so guidelines can be developed for its successful use, addressing issues of equipment requirements, testing procedures and data collection as well as interpretation method and its application in construction. Due to the mature nature of the method, LRFD AASHTO specifications can be prepared as part of the project.

5.4.2.2 *Proposed Title for Research Statement*

Title: Load and Resistance Factor Design (LRFD) Specification for Drop Weight System Testing

5.4.2.3 *Development*

1. Testing equipment – technically analyzing the equipment requirements to address specific needs – e.g. even impact, modular ram, controlled drop height, etc.
2. Measuring equipment – the needs here can be addressed in two ways; (i) developing alternative simple and generic measuring equipment that can be obtained in a fraction of the cost compared to the commercially available proven equipment used for dynamic measurements of driven piles, and (ii) incorporating tools and ideas used in other testing methods to complement the available system (with or without (i) above). For example, independent measurement of displacement as commonly used by Statnamic or Fundex and/or independent measurement of force instead of strain as commonly used by the Smartpile system (not necessarily the same components), and via the ram acceleration as used by Newton's Apple.

5.4.2.4 *Databases*

DW/LT 2000 is a reasonable size database; however, it is limited in the number of cases of good quality. The quality of a database is compromised when the number of tests is limited and an effort is made to make use of any possible available case history. More data is currently available worldwide and, hence, the database can be significantly expanded with the proper resources. Such development is essential for the establishment of the method as demonstrated in the present research (section 3.3.). The developed databases can be used to develop performance based resistance factors as part of LRFD AASHTO specifications.

5.4.2.5 *Models*

As the signal matching analysis was proven to be a powerful tool for the cases in which a short wavelength exists ($\Lambda < 1$), alternative methods do not seem necessary at the time. Simulation models of the impact between the ram and the deep foundation are an excellent tool to investigate problems, limitations and possible solutions. The study presented in this research is only preliminary in the possibilities of its use, but provides an excellent demonstration to such powerful modeling in recognizing the critical shortcomings of the testing system and addressing solutions. Extensive more realistic study to the one presented (e.g. including essential non-elastic behavior of the cushion) and non-uniform shafts can help immensely in the investigation of the limitation of the method, possible solutions and development of guidelines.

5.4.2.6 *Tests*

Benchmark high quality testing is required as many of the case histories used in the database are of limited quality. The testing should be carried out for drop weight and conventional top-down axial static loading on instrumented in-place constructed deep foundations, and need to specifically address; reliability of total capacity prediction including the ability to obtain repeatable predictions out of sequential impacts, accuracy of soil-structure interaction predictions and the effects of testing and shafts problems (e.g. uneven impact, low quality foundations, etc.) on the test results.

Such tests would be better conducted after above stages are completed (development, database, models) so they can be guided by the results of the studies as well as the implementation of additional/new equipment as suggested in section 5.4.2.3.

5.4.2.7 *Guidelines*

1. Impact equipment technical details – e.g. guarantee of even impact, free fall, etc.
2. Deep foundation preparation – e.g. sleeve with free extensions above or below ground, smooth and level top, etc.
3. Testing – ratio of impact mass to tested capacity, reliability, maximum wavelength.
4. Data acquisition – type and number of gauges and their location.
5. Procedure – number of drops, height of fall, quality of data, independent measurement.

5.4.2.8 *Priority*

1. Ram-pile impact modeling
2. Database
3. Guidelines
4. Development
5. Tests

5.4.2.9 *Budget*

\$650,000 – including three dedicated field tests

5.4.3 Statnamic Testing

5.4.3.1 Status

Due to its unique advantages providing high mobility and enormous capacity in difficult to reach places, the method is applied under relevant conditions worldwide. While technically competent in performance and measurements, the method's use is hampered by its low reliability when applied in cohesive subsurface conditions. It seems that the key impediment lies in developing reliable methods of interpretation.

5.4.3.2 Proposed Title for Research Statement

Title: Modeling, Testing and Guidelines Development for Statnamic Testing

5.4.3.3 Development

1. Testing equipment seems to be continuously developing and provides reliable performance so no direct research should be conducted here.
2. Measuring equipment is well conceived and reliable. Effort can be made in improving the ability to obtain multipoint force measurements along the pile to address the modified and segmental unloading point methods (MUP and SUP).

5.4.3.4 Databases

Expansion of databases is a consistent need and should be part of an ongoing effort. As far as the major limitation of the method lies in its performance in cohesive soils, the effort of testing, modeling and database building should concentrate in that direction. Reliable resistance factors according to LRFD methodology can be obtained at least for the cases for which sufficient data are available (e.g. tests in granular soils). Additional factors can be evaluated for other conditions utilizing available data and professional expertise.

5.4.3.5 Models

As the use of wave mechanics based analysis is inadequate for addressing the needs of interpreting Statnamic load-test results, other models were developed. The current models seem to be limited in their ability to correctly address the pile-soil interaction when Statnamic testing deep foundations in cohesive soils. The rate effect factors developed and proposed in this research are by no means a fundamental solution, but practically address current needs. It is suggested to concentrate the efforts therefore, in an alternative model and method of analysis capable of addressing the Statnamic test results in all subsurface conditions. The model developed and presented in this research can serve as a good starting point of such effort.

5.4.3.6 *Tests*

Well designed tests under specific conditions can enhance tremendously our ability to use the method under all subsurface conditions. Such tests should be carried out following the development of promising models, most likely in cohesive subsurface conditions and in well instrumented deep foundations so all possible methods of analysis can be examined. Statnamic and static load tests will need to be carried out with careful regard to the test timing and time effects on the capacity.

5.4.3.7 *Guidelines*

A concentrated need exists in classifying the limitation of the method with a clear distinction between reliable and unreliable conditions for application.

5.4.3.8 *Priority*

1. Development of a model for test results interpretation
2. Development
3. Database
4. Tests
5. Guidelines

5.4.3.9 *Budget*

\$650,000 – including three dedicated field tests and industry cooperation

5.4.4 Osterberg Cell

5.4.4.1 *Status*

The O-cell is a proprietary method marketed by a single vendor. In principle, the method was used in a different variation (as a flat jack test) for many years prior to its establishment and patent in the USA (as a mature and well-conceived technology). Its high capacity and static load application are clear advantages, while its high cost, load direction and reliability are a deterrent from a much larger use.

5.4.4.2 *Proposed Title for Research Statement*

Title Examination, Testing and Guidelines Development for Osterberg Cell Testing Method

5.4.4.3 *Development*

Alternative, simple and low cost technical development can be done based on long used technology like the flat jack. Such development can provide a simple testing procedure at a fraction of the presently marketed O-cell technology.

5.4.4.4 *Databases*

Well-documented, high quality case histories are difficult to obtain due to cost, effect of reverse loading on the test results (hence the need for two independent foundations), multiple factors which affect the test results (hence isolation of cause and effect are difficult) and more. While additional cases emerge around the world (e.g. Kwon et al., 2005), the systematic large scale load testing does not seem practical. It is recommended though to keep up an ongoing effort of database buildup while focusing on well-conceived new high quality testing, possibly as part of bridge construction.

5.4.4.5 *Models*

Two types of efforts relevant to the O-cell are required to be addressed:

- (i) A study addressing the factors affecting top-down and down-up interfacial shear and force displacement curves. Example of such study is presented in this research but other considerations are difficult to obtain via the FE modeling.
- (ii) The accuracy and effectiveness of the equivalent top-down curves obtained from the down-up test results.

5.4.4.6 *Tests*

Well-conceived instrumented tests on two “identical” foundations loaded up-down and down-up are needed. Isolation of material and segmental testing is required.

5.4.4.7 *Guidelines*

As a proprietary testing method, guidelines should be developed for optimal conditions of use, limitations and reliability under variable testing conditions.

5.4.4.8 *Priority*

1. Modeling
2. Guidelines
3. Databases
4. Tests

5.4.4.9 *Budget*

\$650,000 – including two double field tests and industry cooperation

REFERENCES

1. AASHTO, (1994). *LRFD Highway Bridge Design Specifications*. SI Units, 1st Edition, American Association of State Highway and Transportation Officials, Washington, DC.
2. ASTM D4945-00, (2000). "Standard Test Method for High-Strain Dynamic Testing of Piles," *Annual Book of Standards, Section Four Construction*. ASTM, Vol. 04.08, West Conshohocken, PA.
3. ASTM (1999). "Standard Test Method for Piles Under Rapid Axial Compressive Load." (Submitted – Unpublished)
4. ASTM, (1996). *Annual Book of Standards. Volume 04.08, Soil and Rock (I): D420-D4914*, American Society for Testing and Materials, West Conshohocken, PA.
5. Baker, C.N., Drumright, E.E., Briaud J.-L., Mensah, F D., and Parikh, G. (1993). *Drilled Shafts for Bridge Foundations*, Publication No. FHWA-RD-92-004, Federal Highway Administration, Washington DC, pp. 336
6. Birmingham, P. and Janes, M. (1990). "Statnamic test. An innovative method for testing deep foundations", *Proceedings of the Annual Conference and the First Biennial Environmental Speciality Conference*, May 16-18, Hamilton, Ontario, Canada, vol. 2, part 2, Canadian Society for Civil Engineering, Montreal, Quebec, Canada, p. 590.
7. Bielefeld, M.W., Middendorp, P., (1995). "Statnamic Simulation." *Proceedings, First International Statnamic Seminar*, Vancouver, BC, Canada, September 27-30.
8. Boussinesq, J. (1883). *Compt. Rend.*, Paris, p. 154
9. Bowles, J.E. (1996). *Foundation Analysis and Design*, The McGraw-Hill Companies, Inc., New York, USA.
10. Briaud, J.L. (1997). *The National Geotechnical Experimentation Sites at Texas A&M University: Clay and Sand—a Summary*, Rep. NGES-TAMU-007, Civil Engineering, Texas A&M University, College Station, Texas.
11. Briaud J.L., Ballouz M., and Nasr G. (2000), "Static Capacity Prediction by Dynamic Methods for Three Bored Piles", ASCE, *Journal of Geotechnical and Geoenvironmental Engineering*, Vol. 126, No.7, July, 2000, pp.640-649.
12. Brusey W.G. (2000). "JFKIA-Post Grouted Drilled Shafts and Driven Piles-Update", *Proceedings, 25th Annual Meeting and 8th International Conference and Exposition*, Deep Foundations Institute, New York, October 5-7, pp.169-179.
13. Butler, H.D. and Hoy, H.E. (1977). *Users Manual for the Texas Quick-Load Method for Foundation Load Testing*, Report No. FHWA-IP-77-8. Federal Highway Administration, Washington, DC, pp. 59.
14. Camp, W.M., Brown, D.A., and Mayne, P.W. (2002). "Construction Method Effects on Axial Drilled Shaft Performance", ASCE *Geotechnical Special Publication*, no. 116, vol. I, pp. 193-208.
15. Cannon, J.G. (2000). "Case study on the application of high strain dynamic pile testing", *Proceedings, Sixth International Conference on the Application of Stress-Wave Theory to Piles*, S. Niyama, and J. Beim eds, September 11-13, São Paulo, Brazil, Balkema, Rotterdam-the Netherlands, pp.399-402.
16. Chenghua, L. (2001). "Nanchang Mingshi Garden Foundation Testing Report", Jiangxi Huachang Civil Engineering Testing Center (20000602).
17. Chua K.M., Aspar W.A.N., Meyers R. (1994). "Testing and Predicting the Movement of a Drilled Shaft in New Mexico", *Proceedings of Settlement '94 Vertical and Horizontal Deformations of Foundation and Embankment*, College Station, Texas, June 16-18,

- ASCE Geotechnical Special Publication No.40, pp. 279-290.
18. Chua K.M., Meyers R., Samtani N.C. (2000). "Evaluation of a Load Test and Finite Element Analysis of Drilled Shafts in Stiff Soils", *Proceedings of the Conference Geo-Denver 2000 New Technological and Design Developments in Deep Foundations*, Aug 5-8, Denver, Colorado, ASCE, Geotechnical Special Publication No. 100, pp. 269-283.
 19. Coyle, H.M., and Reese, L.C. (1966). "Load Transfer of Axially Loaded Piles in Clay." *ASCE Journal of the Soil Mechanics and Foundation Division Proceedings*, 92 (SM 2), pp. 1-26.
 20. Das, B.M. (1993). *Principles of Soil Dynamics*. PWS-Kent Publishing Company, Boston, MA.
 21. Davisson, M.T. (1972). "High Capacity Piles," *Proceedings of the Soil Mechanics Lecture Series on Innovations in Foundation Construction*, American Society of Civil Engineers, Illinois Section, Chicago, March 22, pp. 81-112.
 22. DeBeer, E.E. (1970). Proefondervindelijke bridrage tot de studie van het grandsdraagvermogen van zand onder funderinger op staal. (Experimental Determination of the Shape Factors and the Bearing Capacity Factors of Sand) English version, *Geotechnique*, Vol. 20, No. 4, pp. 387-411.
 23. DiMillio, A. (1998), *A Quarter Century of Geotechnical Research*, FHWA-RD-98-13X, Disseminated by Federal Highway Administration (FHWA) Research, and Technology U.S. Department of Transportation.
 24. Donald I.B., and Chiu, H.K. (1980). "Theoretical analysis of rock socketed piles", *Proceedings International Conference on Structural Foundations on Rock*, Sydney, Australia, Vol. 1, A.A. Balkema, Rotterdam-the Netherlands, pp. 303-315.
 25. Dunncliff, J. (1988). *Geotechnical Instrumentation for Monitoring Field Performance*. John Wiley and Sons, Inc., New York, NY.
 26. Fellenius, B.H., Altaee, A., Kulesza, R., and Hayes, J. (1999). "O-Cell Testing and FE Analysis of 28-m-Deep Barrette in Manila, Philippines," *Journal of Geotechnical & Geoenvironmental Engineering*, ASCE, v 125 n 7, pp. 566-575.
 27. FHWA. (1998). *Load and Resistance Factor Design (LRFD) for Highway Bridge Substructures*, National Highway Institute, FHWA HI-98-032, Washington, DC.
 28. Frederick, L. (1999). *SMART COIL System Promotional Material*, Frederick Engineering, Whippany, New Jersey.
 29. Frederick, L. (1999). *SMARTPILE System Promotional Material*, Frederick Engineering, Whippany, New Jersey.
 30. Garbin, E. (1999). *Data Interpretation for Axial Statnamic Testing And The Development Of The Statnamic Analysis Workbook*. Master's Thesis, University of South Florida, Tampa, Florida.
 31. Getz, K., and Gilbert, M. (1997). *VBA Developer's Handbook*. SYBEX, Inc., Alameda, CA, USA.
 32. Goble, G.G., Likins, G., and Rausche, F. (1970). *Dynamic Studies on the Bearing Capacity of Piles Phase III*, Report No. 48, Division of Solid Mechanics, Structures and Mechanical Design, Case Western Reserve University.
 33. Goble, G.G., Scanlan, and Tomko, J.J. (1967). *Dynamic Studies on the Bearing Capacity of Piles, Phase II, Volume I and II*, Case Western Reserve University.
 34. Goodwin, J.W. (1993). "Bi-directional load testing of shafts to 6000 tons." *Design and Performance of Deep Foundations: Piles and Piers in Soil and Soft Rock*, ASCE

- Geotechnical Special Publication No. 38: pp. 204-217.
35. Gonin, H., Coelus, G., and Leonard, M.S.M. (1984). "Theory and performance of a new dynamic method of pile testing", *Proceedings, Second International Conference on the Application of Stress-Wave Theory to Piles*, G. Holm, H. Bredenberg, and C-J. Gravare eds, Stockholm, Sweden, May 27-30, A.A. Balkema, Rotterdam the Netherlands, pp. 403-410.
 36. Gorczyca M.E., Difini J.T., Chadbourne W.A., and Lambrechts J.R. (1999), "Load Testing on Deep Rock-Socketed Drilled Shafts", *Proceedings of Sessions of Geo-Congress 98 Special Geotechnical Testing: Central Artery/Tunnel Project in Boston, Massachusetts*. ASCE, Geotechnical Special Publication, No. 91, pp. 100-115.
 37. Graff, K.F. (1975). *Wave Motion in Elastic Solids*, Ohio State University Press, Columbus, Ohio.
 38. GRL (1995). *GRLWEAP Program, Wave Equation Analysis of Pile Driving*. GRL Engineers, Inc., Cleveland, Ohio.
 39. GTR (1997) "Dynamic Pile Testing Report - Israel Electric Company, Haifa, Israel", Final Report, Project 97.118, Geosciences Testing and Research, North Chelmsford, Massachusetts.
 40. Guoxi Z., Zhuchang Ch., and Jinli L. (1995). *Pile Foundation Engineering*, Beijing, China. September.
 41. Hajduk, E.L., Paikowsky, S.P., Mullins, A.G., Ealy, C.D., Lewis, C. and Hourani, N.M. (1998). "The Behavior of Piles in Clay during Statnamic and Different Static Load Testing Procedures", *Proceedings, 2nd International Statnamic Seminar*, Tokyo, Japan, October 28-30.
 42. Hajduk, E., Paikowsky, S., Holscher, P., and Barends, F. (2000). Accelerations of a Driven Pile and the Surrounding Soil. *Proceedings, 6th International Conference on the Applications of Stress-Wave Theory to Piles*, September 11-13, 2000. São Paulo City, Brazil, Balkema, Rotterdam-the Netherlands, pp. 541-548.
 43. Hanwu Z. (1995). "Wuhan Jianfa Hotel Foundation Testing Report", Material from Rock & Sea, Inc.
 44. Hassan, K. M. and O'Neill, M.W. (1997). "Side load-transfer mechanisms in drilled shafts in soft argillaceous rock." *ASCE Journal of Geotechnical Engineering*, 123(2): pp. 145-151.
 45. Hussein, M., Robinson, B., and Likins, G. (2004). "Applications of a Simplified Dynamic Load Testing Method for Cast-In-Place Piles", *GeoSupport 2004 Drilled Shafts, Micropiling, Deep Mixing, Remedial Methods, and Specialty Foundation Systems*, J.P. Turner and P.W. Mayne eds., ASCE Geotechnical Special Publication No. 124, pp. 110-121.
 46. Highway Research Board. (1967). *Bridges and Structure*, Highway Research Record No. 167, Washington, D.C.
 47. Holeyman, A.E. (1992). "Technology of Pile Dynamic Testing", *Proceedings, Fourth International Conference on the Application of Stress-Wave Theory to Piles*, F.B.J. Barends ed., The Hague, the Netherlands, September 21-24, Balkema, Rotterdam the Netherlands, pp.195-215.
 48. Horvath, R.G. (1995). "Influence of Loading Rate on the Capacity of a Model Pile in Clay." *Canadian Geotechnical Journal* Vol. 32, National Research Council, Canada, pp. 364-368.

49. Horvath, R.G., and Trow, W.A. (1980). "Results of Tests to Determine Shaft Resistance of Rock-Socketed Drilled Pilers", *Proceedings, International Conference on Structural Foundations on Rock*, Sydney, Australia, Vol. 1, A.A. Balkema, Rotterdam-the Netherlands, pp. 349-361.
50. Irving, M. (1986). *Structural Dynamics, for Practicing Engineers*, Allen & Unwin, Ltd., London.
51. Iskander, M., Kelley, S., and Ealy, C. (2001). "Load Tests on Drilled Shafts with Planned Defects in Varved Clay", *TRB 80th Annual Meeting 2001 Session on Drilled Shafts & Other Foundation Issues*, January 7-11, Washington, DC.
52. Iwanowski, T., and Berglars B. (1984). "Pre-stressed Disk Spring Cap – Influence of Parameters on Shape of Stress Pulse in Pile", *Proceedings Second International Application of Stress-Wave Theory on Piles*, G. Holm, H. Bredenberg, and C-J. Gravare eds, Stockholm, Sweden, May 27-30, A.A. Balkema, Rotterdam the Netherlands, pp. 411-420.
53. Janes, M. (1995). "Statnamic Load Testing of Strain Instrumented Large Diameter Bored Shafts," *Proceedings 1st International Statnamic Seminar*, Vancouver, BC, Canada, September 27-30.
54. Jedele, L.P., and Bedenis, T.H. (1993). "Drilled pier load capacity of Detroit area hardpan using an Osterberg load cell." *Proceedings 3rd International Conference on Case Histories in Geotechnical Engineering*, University of Missouri-Rolla, 3(2), pp. 1213-1220.
55. Jianping Y. (2001). "Cuihu Garden Foundation testing Report", Jiangxi Huachang Civil Engineering Testing Center (991204).
56. Jianren, D., and Shihong, Z. (1992). "The appraisal of results from PDA high strain dynamic tests on large and long drilled piles." *Proceedings, Fourth International Conference on the Application of Stress-Wave Theory to Piles*, F.B.J. Barends ed., The Hague, the Netherlands, September 21-24, Balkema, Rotterdam the Netherlands, pp.271-278.
57. Justason, M.D., Mullins, G., Robertson, D.T., and Knight, W.F. (1998). "A comparison of static and Statnamic load tests in sand: a case study of the Bayou Chico bridge in Pensacola, Florida" *Proceedings Second International Statnamic Seminar*, Tokyo, Japan, October 28-30.
58. Keisar I. (1998). "Israel Route#10 Har-Yona Bridge" *Dilled Shafts Testing Report* for the Office of Development, Israel.
59. Keisar I. (2000). "Israel Ralnot Jenusalem" *Dilled Shafts Testing Report* for the Office of Development, Israel.
60. Keisar I. (2001). "Israel Maa'leh Ha'domim" *Dilled Shafts Testing Report* for the Office of Development, Israel.
61. Kishida, H., Tsubakihara, Y., and Ogura, H. (1992). "Pile Loading Tests at Osaka Amenity Park Project," unpublished report to Mitsubishi Corp.
62. Knight, W.F., Puckett, T.N., Bennett, K.D., Robertson, D.T., and Spears, L.D. (1995). "A Comparison of Statnamic and Osterberg Field Tests in Florida Limestone," *Proc. of the Symposium on Geology and Geotechnical Engineering*, March, v31, pp 390-404.
63. Kwon, O.S., Choi, Y., Kwon, O., and Kim, M.M. (2005). "Comparison of the Bi-directional Load Test with the Top-down Load Test," to be published in the *Proceedings of the 84th TRB Annual Meeting*, January, Washington, DC.

64. Leong, E.C., and Randolph, M.F. (1994). "Finite element modeling of rock-socketed piles", *International Journal for Numerical and Analytical Methods in Geomechanics*, Vol. 18, pp. 25-47.
65. Lewis, C. (1999). *Analysis Of Axial Statnamic Testing Using The Segmental Unloading Point Method*. Master's Thesis, University of South Florida, Tampa, Florida.
66. Li, Z.(Frank). (2000). Personal Communication, Hongqi Huayuan Foundation Testing Project, Shanghai Civil Engineering Quality Testing Center, Shanghai, P.R., China (System DW-B).
67. Li, Z.(Frank). (1993). Personal Communication, Baiyuan Plaza Foundation Testing Project. Zhanjiang Civil Engineering Quality Testing Station, Zhanjiang, Guangdong Province, P.R. China, (System DW-A).
68. Liang X. (2000). "Analyzing the bearing capacity mechanism of large diameter diving casing cast-in-situ concrete piles by using high strain dynamic testing", *Proceedings, 6th International Conference on the Application of Stress-Wave Theory to Piles*, September 11-13, São Paulo City, Brazil, Balkema, Rotterdam-the Netherlands, pp.369-373.
69. Littlechild, B.D., Hill, S.J., Plumbridge, G.D., and Lee, S.C. (2000). "Load Capacity of Foundations on Rock," *Proceedings of the Conference Geo-Denver 2000 New Technological and Design Developments in Deep Foundations*, Aug 5- 8, Denver, Colorado, ASCE, Geotechnical Special Publication No. 100, pp. 140-157.
70. Loadtest, Inc. (1994). *Report on Osterberg Cell Load Testing*, Loadtest, Inc., project No. LT-163, Feb. 15, 1994.
71. Loadtest, Inc. (1998). *Report on Osterberg Cell Load Testing*, Loadtest, Inc., project No. LT-8402.
72. Loadtest, Inc. (1999). "Report on Osterberg Cell Load Testing", Loadtest, Inc., project No. LT-8352.
73. Long, M (2001). "Assessment of SIMBAT dynamic pile tests". *Foundations & Ground Improvement Proceedings of Specialty Conference 2001 A Geo Odyssey*. Blacksburg, Virginia, June 9-13, ASCE, Geotechnical Special Publication no. 113, pp.539-553.
74. Longgen, Z., Liu, L., and Geng, N. (1999). *New Technology of Soil and Foundation Engineering Testing*, Beijing, Mechanical Industry Press (in Chinese), China.
75. Mann, A.T. (1997). *Visual Basic 5 Developer's Guide*. Sam's Publishing, Indianapolis, Indiana, USA.
76. Meyer, R. (1996). "A Comparison of Two Shafts between Polymer and Bentonite Slurry Construction and between Conventional and Osterberg Cell Load Testing," presentation given at the SW Transportation Geotechnical Engineers Conference, Little Rock, AR, unpublished.
77. McVay, M., Huang, S. and Casper, R. (2001). "Numerical Simulation of Drilled Shafts for Osterberg, Pullout, and Axial Compression Loading in Florida Limestone," Internal University of Florida Report.
78. McVay, M.C., Putcha, S., Consolazio, G., and Alvarez, V. (2004) "Development of a Wireless Monitoring System for Pile Driving", presentation at the 83rd Annual TRB Meeting, January 11-15, TRB, Washington, DC, paper ID 04-3478, 19pgs.
79. Michigan State Highway Commission. (1965). *A Performance Investigation of Pile Driving Hammers and Piles*. Lansing, Michigan.
80. Middendorp, P., van Foecken, R.J. (1998). "When to apply Dynamic Load Testing and Statnamic Testing," *Proceedings Second International Statnamic Seminar*, Tokyo, Japan,

- October 28-30.
81. Middendorp, P., Berminham, P., and Kuiper, B. (1992). "Statnamic Load Testing Of Foundation Piles" *Proceedings, Fourth International Conference On Application Of Stress-Wave Theory To Piles*, F.B.J. Barends ed., The Hague, the Netherlands, September 21-24, Balkema, Rotterdam the Netherlands, pp. 581-588.
 82. Middendorp, P., and van Weel, P.J. (1986). "Application of Characteristic Stress Wave Method in Offshore Practice." *Proceedings, 3rd International Conference on Numerical Methods in Offshore Piling*. Nantes, France, May 21-22, Editions Technip, Paris.
 83. Molnit, T., and Lee, J.S. (1998). "Comparison Report, Osterberg Cell Test Method (PTP14) versus Kentledge Test Method (PTP15), MRT C701, Singapore," Loadtest, Inc., report to Hyundai Construction, April, 1998.
 84. Mukaddam M. A., and Iskandarani W. M. (1996). "High Strain Dynamic Testing of Cast in -Situ Piles in the UAE", *Proceedings, Fifth International Conference on the Application of Stress-Wave Theory to Piles*, F.C. Townsend, M. Hussein, and M. McVay eds, Orlando, Florida, September 11-13, pp.805-809.
 85. Mullins, G., Garbin, E.J., Lewis, C., and Ealy, C. (1998). "Statnamic Testing: University of South Florida Research," *Proceedings Second International Statnamic Seminar*, 1998, Canadian Embassy of Japan, Tokyo, Japan, October 28-30.
 86. Nayak N. V., Kanhere D. K., and Vaidya R. (2000). "Static and High Strain Dynamic Test Co-Relation Studies on Cast-in-Situ Concrete Bored Piles" *Proceedings, 25th Annual Meeting and Eighth International Conference and Exhibition*, New York, NY, October 5-7, Deep Foundations Institute, New Jersey, pp.245-252.
 87. Ng, C.W.W., Rigby, D.B., Li, J.H.M., Yau, T.L.Y. and Tang, W.H. (2001). "Side Shear of Large Diameter Drilled Shafts in Weathered Geomaterials," *Foundations & Ground Improvement Proceedings of Specialty Conference 2001 A Geo Odyssey*. Blacksburg, Virginia, June 9-13, ASCE, Geotechnical Special Publication no. 113, pp. 758-772.
 88. Nishimura, S., and Matsumoto, T. (1998). "Wave Propagation Analysis During Statnamic Loading of a Steel Pipe Pile," *Proceedings Second International Statnamic Seminar*, Canadian Embassy of Japan, Tokyo, Japan, October 28-30.
 89. Ohio Department of Transportation. (1975). *Bearing Capacity of Piles from Dynamic Measurements*, Research Report OHIO-DOT-05-75, Final Report.
 90. O'Neill, M.W., and Reese, L.C. (1999). *Drilled Shafts: Construction Procedures and Design Methods*. Report No. FHWA-IF-99-025, Federal Highway Administration, August, 758 p.
 91. Ooi, P.S.K., and Frederick, L.L. (2003). "An Innovative Method of Load Testing Deep Foundations", *Geotechnical Testing Journal*, ASTM, West Conshohocken, PA, Vol. 26, no. 2, pp. 210-218.
 92. Osterberg, J.O., and Gill, S.A. (1973). "Load Transfer Mechanism for Piers Socketed in Hard Soils or Rock", *Proceedings 9th Canadian Rock Mechanics Symposium*, December 13-15, Montreal, Quebec Canada, Ottawa, Mines Branch, pp. 235-262.
 93. Osterberg, J.O. (1995). *The Osterberg Cell for Load Testing Drilled Shafts and Driven Piles*. Report No. FHWA-SA-94-035, Federal Highway Administration, February, pp. 92.
 94. Osterberg, J., and Hayes, J. (1999). "Clean Bottoms," presentation at ADSC Annual meeting, Vail, CO, July.
 95. Osterberg, J. (2001). "Load Testing High Capacity Piles; What Have We Learned?"

- Proceedings, 5th International Conference on Deep Foundation Practice.* April 4-6, Singapore, CI-Premier Pte Ltd.
96. Osterberg, J. (1989). "New device for load testing driven piles and drilled shafts separates friction and end bearing." *Proceedings, Third International Conference on Piling and Deep Foundations*, J. Mitchell and J. Burland eds., London, Deep Foundations Institute, New Jersey, pp. 421- 427.
 97. Paikowsky, S.G. (1982). *Use of Dynamic Measurements to Predict Pile Capacity Under Local Conditions*. M.Sc. Thesis, Department of Civil Engineering, Technion-Israel Institute of Technology.
 98. Paikowsky, S.G. (1995). Using Dynamic Measurements for the Capacity Evaluation of Driven Piles. *Civil Engineering Practice*, Journal of the Boston Society of Civil Engineers Section/ASCE. Vol. 10, No. 2, pp. 61-76.
 99. Paikowsky, S.G. (2004). *Load and Resistance Factor Design (LRFD) for Deep Foundations* with contributions by Birgission G., McVay M., Nguyen T., Kuo C., Baecher G., Ayyub B., Stenerson K., O'Mally K., Chernauskas L., and O'Neill M., NCHRP Report 507, National Cooperative Highway Research Program report for Project NCHRP 24-17, pp. 134 (not including Appendices).
 100. Paikowsky S.G., and Chen Y.L. (1998). "Field and Laboratory Study of the Physical Characteristics and Engineering Parameters of the Subsurface in the Newbury Bridge Site". Research Report submitted to the Massachusetts Highway Department, January.
 101. Paikowsky, S.G., and Chernauskas, L.R. (2003). "Review of Deep Foundations Integrity Testing - Methods And Case Histories" 2003 BSCES-Geo-Institute Deep Foundation Seminar, Boston November 15, pp30.
 102. Paikowsky, S.G., and Chernauskas, L.R. (1992). "Energy Approach for Capacity Evaluation of Driven Piles", *Proceedings Fourth International Conference on the Application of Stress-Wave Theory to Piles*. F.B.J. Barends ed., The Hague, the Netherlands, September 21-24, Balkema, Rotterdam the Netherlands, pp. 595-601.
 103. Paikowsky, S.G., and Chernauskas, L.R. (1996). "Soil Inertia and the Use of Pseudo Viscous Damping Parameters", *Proceedings Fifth International Conference on the Application of Stress-Wave Theory to Piles*, F.C. Townsend, M. Hussein, and M. McVay eds, Orlando, Florida, September 11-13, pp. 203-216.
 104. Paikowsky, S.G., and Hajduk, E.L. (1999). "Design and Construction of an Instrumented Test Pile Cluster", Research Report submitted to the Massachusetts Highway Department, Geotechnical Research Laboratory, University of Massachusetts-Lowell, Lowell, Massachusetts.
 105. Paikowsky, S.G., and Hajduk, E.L. (2004). "Design and Construction of Three Instrumented Test Piles to Examine Time Dependent Pile Capacity Gain", to be published in ASTM Geotechnical Testing Journal, November 2004.
 106. Paikowsky, S.G., Klar, I., and Chernauskas, L.R. (2004). "Performance Evaluation of CFA vs. Bentonite Slurry Drilled Shafts Utilizing Drop Weight Testing", ASCE Geotechnical Special Publication no. 124, *Geo-Support 2004: Drilled Shafts, Micropiling, Deep Mixing, Remedial Methods, and Specialty Foundation Systems*, eds. J.P. Turner and P.W. Mayne, Orlando, Florida, January 29-31, 2004, pp. 637-652.
 107. Paikowsky, S.G., and LaBelle V.A. (1994). "Examination of the Energy Approach for Capacity Evaluation of Driven Piles", *Proceedings International Conference on Design and Construction of Deep Foundations*. Orlando, Florida, December 6-8, FHWA, Vol. II

- pp. 1133-1149.
108. Paikowsky, S., LaBelle, V., and Hourani, N. (1996). "Dynamic Analyses and Time Dependent Pile Capacity", *Proceedings 5th International Conference on the Application of Stress-Wave Theory to Piles*. F.C. Townsend, M. Hussein, and M. McVay eds, Orlando, Florida, September 11-13, pp. 325-339.
 109. Paikowsky, S.G., LaBelle, V. A., and Mynampaty, R. N. (1995). *Static and Dynamic Time Dependent Pile Behavior*. Research Report submitted to the Massachusetts Highway Department-Geotechnical Section, Geotechnical Research Laboratory, University of Massachusetts-Lowell, Lowell, Massachusetts.
 110. Paikowsky, S.G., LaBelle, V.A., Regan, J.E., and Chernauskas, L.R. (1994). "Pile Settlement Based on Dynamic Measurements", *Proceedings of Settlement '94 Vertical and Horizontal Deformations of Foundation and Embankment*, College Station, Texas, June 16-18, ASCE Geotechnical Special Publication No.40, pp.269-278.
 111. Paikowsky, S.G., Operstein, V., and Bachand, M. (1999). *Express Method of Pile Testing by Static-Cyclic Load*. Research Report submitted to the Massachusetts Highway Department, Geotechnical Research Laboratory, University of Massachusetts-Lowell, Lowell, Massachusetts.
 112. Paikowsky, S.G., Regan, J.E., and McDonnell, J.J. (1994). *A Simplified Field Method for Capacity Evaluation of Driven Piles*. FHWA, report no. FHWA-RD-94-042, Washington, DC.
 113. Paikowsky, S.G., and Stenersen, K.L. (2000). "The Performance of the Dynamic Methods, their Controlling Parameters and Deep Foundation Specifications", Key-Note lecture, *Proceedings of the 6th International Conference on the Application of Stress-Wave Theory to Piles*, S. Niyama and J. Beim eds, September 11-13, São Paulo, Brazil, Balkema, Rotterdam-the Netherlands, pp. 281-304.
 114. Paikowsky, S.G., Tolosko, T.A. (1999). *Extrapolation of Pile Capacity from Non-failed Load Test*. FHWA publication number FHWA-RD-99-170, December, 169 pp (HNR publication).
 115. Paikowsky, S.G., and Whitman, R.V. (1990). "The Effects of Plugging on Pile Performance and Design", *Canadian Geotechnical Journal*, August, Vol. 27, No. 4, pp. 429-440.
 116. Parola, J. F. (1970). *Mechanics of Impact Pile Driving*, Ph.D. Dissertation, University of Illinois at Urbana-Champaign, 252 pp.
 117. PCB Electronics, (1999). Technical Support Website. <http://www.pcb.com/tech-accel.html>
 118. PCB Electronics, (1999). Capacitive Accelerometer 3701 Operating Manual.
 119. Person, R., (1997). *Using Microsoft Excel 97*. Que Corporation, Indianapolis, IN, USA.
 120. Pile Dynamics Inc. (1995). *PDA - Pile Driving Analyzer, PAK Users Manual*, March Pile Dynamic, Inc., Cleveland, OH.
 121. Pile Dynamics, Inc., (1996). *PDA Pak Users Manual*. Pile Dynamic, Inc., Cleveland, OH, pages A-1 to A-29.
 122. Poulos, H.G., Davis, E.H. (1980). *Pile Foundation Analysis and Design*. John Wiley and Sons, Inc., New York.
 123. Prebahapan, N., Broms, B., and Yu, R. (1990). "Dynamic Testing of Bored Piles", *Proceedings, Tenth Southeast Asian Geotechnical Conference*, Taipei, Taiwan, April 16-20, p.373-378.
 124. Qiangyang, C. (2001). "Comparison of the Dynamic tests and Static tests results on 8 drilled shafts ", *Pile Dynamic Tests Technology*, China Building Material Industrial

- Press.
125. Rausche, F. (1970). "Soil Response from Dynamic Analysis and Measurements on Piles", Ph.D. Dissertation, Division of Solid Mechanics, Structures and Mechanical Design, Case Institute of Technology (Case Western Reserve University), Cleveland, Ohio.
 126. Rausche, F., and Seidel, J. (1984). "Design and performance of dynamic tests of large diameter drilled shafts", *Proceedings, Second International Conference on the Application of Stress-Wave Theory to Piles*, G. Holm, H. Bredenberg, and C-J. Gravare eds, Stockholm, Sweden, May 27-30, A.A. Balkema, Rotterdam the Netherlands, pp. 9-16.
 127. Robinson, B., and Rausche, F. (2000). "Dynamic Pile Load Test and Crosshole Sonic Logging Results", Reports submitted by GRL to the FHWA, November 2000, see also GRL Newsletter No. 38, December, 2000.
 128. Rowe, R.K., and Pells, P.J.N. (1980). "A Theoretical Study of Pile-Rock Socket Behavior", *Proceedings International Conference on Structural Foundations on Rock*. Sydney, Australia, Vo.1, No.1, A.A. Balkema, Rotterdam-the Netherlands, pp. 253-264.
 129. Schellingerhout, A.J.G., and Revoort, E. (1996). "Pseudo Static Load Tester", *Proceedings, Fifth International Conference on the Application of Stress-Wave Theory to Piles*, F.C. Townsend, M. Hussein, and M. McVay eds, Orlando, Florida, September 11-13, pp. 1031-1037.
 130. Schmertmann, J.H., and Crapps, D.K. (1994). "Past, present and future practice in deep foundations, with Florida emphasis." *Proceedings, International Conference on Design and Construction of Deep Foundations*. Orlando, Florida, December 6-8, FHWA, pp. 188-208.
 131. Seidel J., and Rausche, F. (1985). "Correlation of Static Dynamic Tests on Large Diameter Drilled Shafts", *Proceedings, Second International Conference on the Application of Stress-Wave Theory to Piles*, G. Holm, H. Bredenberg, and C-J. Gravare eds, Stockholm, Sweden, May 27-30, A.A. Balkema, Rotterdam the Netherlands, pp.313-318.
 132. Seitz, J.M. (1984). "Dynamic testing of bored piles in non-cohesive soils" *Proceedings, Second International Conference on the Application of Stress-Wave Theory to Piles*, G. Holm, H. Bredenberg, and C-J. Gravare eds, Stockholm, Sweden, May 27-30, A.A. Balkema, Rotterdam the Netherlands, pp.201-209.
 133. Serway, R. A. (1992). *Physics For Scientists And Engineers*. 3rd Edition, Volume 1, Harcourt Brace and Company, Florida.
 134. Simon, P., and Briaud, J.L. (1996). *The National Geotechnical Experimentation Sties at Texas A&M University: Clay and Sand—Soil Data in Electronic From 1995-1996*. Research Report NGES-TAMU-006, Civil Engineering, Texas A&M University, College Station, Texas.
 135. Smith, E.A.L. (1960). "Pile-Driving Analysis by the Wave Equation", *Journal of Soil Mechanics and Foundations*. American Society of Civil Engineers, August 1960, pp. 35-61.
 136. Sokolovski, M., Keisar, I., and Cohen, S. (1998). "Load Testing of Piles on Road No. 10 in Yona Mountain", Summary Engineering Report Ministry of Urban Development, Department of Engineering Design, Foundations Section, Israel, November 1988 (in Hebrew).

137. Stotzer, E., Beyer, M., and Schwank, S. (1991). "Drilling equipment for large diameter bored piles," *Proceedings 4th International Conference on Piling and Deep Foundations*. Stresa, Italy, April 7-12, Vol. 1, A.A. Baklema, Rotterdam the Netherlands, pp. 503-516.
138. Texas Highway Department. (1973). *Bearing Capacity for Axially Loaded Piles*. Research Report 125-8-F Sept. 1967 - Aug. 1973, pp. 134.
139. Timonshenko, S.P., and Goodier, J.N. (1934). *Theory of Elasticity*, McGraw -Hill Book Company, Inc., New York.
140. Townsend, F., Theos, J.F., and Sheilds, M.D. (1991), "Dynamic Load Testing of Drilled Shaft - Final Report." University of Florida, Department of Civil Engineering, Gainesville, Florida.
141. Van Kotten, (1977). *Dynamic Pile Testing*. Inst. TNO for Building Materials and Building Structures, Report, January, the Netherlands.
142. Weibing, X. (2000) Personal Communication, Ouyang Garden Foundation Testing Project, Tongji University, Shanghai, P.R. China, (System DW-C).
143. Website of American Piledriving, Inc.
http://www.americanpiledriving.com/new_page_1.htm
<http://www.americanpiledriving.com/compaction.htm>
144. Website of IFCO Foundation Expertise BV (Waddinxveen, The Netherlands)
<http://www.ifco.nl>
145. Website of Funderingstechnieken Verstraeten BV (FUNDEX) (Oostburg, The Netherlands)
<http://www.nijgh.nl/bouwwereld/verstraeten/pindex.html>
146. Website of Berkeley Seismic Review Committee (SRC) in University of California at Berkeley.
<http://www.coe.berkeley.edu/EPA/forefront/sp02/seismic.html>
147. Website of TESTCONSULT, Inc. "SIMBAT - A Dynamic Load Test for Bored Piles"
<http://www.testconsult.co.uk/services/technical/index.html>
148. Website of TESTCONSULT, Inc. "An Improved Method for the Prediction of Pile Bearing Capacity from Dynamic Testing".
<http://www.testconsult.co.uk/services/technical/index.html>
149. Website of TESTCONSULT, Inc. "SIMBAT-Large Scale Dynamic Pile Testing".
<http://www.testconsult.co.uk/services/index.html>
150. Website of TESTCONSULT, Inc. "SIMBAT- Pile Dynamic Testing".
<http://www.testconsult.co.uk/services/equipment/corrmet.html>
151. Xuefeng W., Shiming W. (2001), "The New Technology on Pile Tests", Science Press, p.173-175.
152. Yong, Q. (2000). "Hongcheng Hotel Pile Foundation Testing Report", Jiangxi Institute of Architecture Design.
153. Zhangling, L. (2001). "Nanchang Xintianzhou 2# Building Pile Foundation Tests Report", Jiangxi Youse Inc. Civil Engineering Testing Center.

22-2/1 COPY NO.

NCHRP 21-08

INNOVATIVE LOAD TESTING SYSTEMS

APPENDIX A

Details of Osterberg Cell Finite Element Analyses

Prepared for
National Cooperative Highway Research Program
Transportation Research Board
National Research Council

By
Dan A. Brown and Lijun Shi
Department of Civil Engineering
University of Auburn
Auburn, AL

Samuel G. Paikowsky, P.I
Geosciences Testing and Research Inc. (GTR)
55 Middlesex St., Suite 225
N. Chelmsford, MA. 01863

August 2002

TABLE OF CONTENTS

Part A – Study of a soil Model	A-1, A-81
Part B – Parametric Study of Rock Socketed Pile	B-1, B-89
Part C – Comparison with Field Tests	C-1, C-39

Part A

STUDY OF A SOIL MODEL

INTRODUCTION

This portion of the research describes the development of a finite element model for the Osterberg load test. In the Osterberg (O-cell) load test, an Osterberg load cell is embedded at the bottom of the test shaft. When it is pressurized, a pair of forces in the opposite direction will be generated. The downward force from the bottom of the cell is resisted by the bearing stratum while the upward force from the top of the cell is resisted by the weight of the pier and by the skin friction along the sides of the shaft. The O-cell load test can therefore directly separate end bearing and side friction. In order to compare the Osterberg load test with conventional load tests, the topdown test is also simulated using finite element method. In topdown test, load is applied to the top of the pile so that pile and the surrounding soil will settle, which will be resisted by both end bearing and side friction.

The finite element model allows a parametric study to be conducted by changing some properties to analyze the influence of these properties on the final capacity and load transfer, etc. For example, soil over-consolidation ratio, soil properties and roughness of soil surface play an important roll in pile capacity. In this project, several cases with different properties mentioned above were calculated and results were compared with respect to topdown test versus O-cell test and different cases.

FINITE ELEMENT CODE—ABAQUS & MSC/PATRAN

ABAQUS was used to perform the finite element analysis since it provides a large number of capabilities for analyzing different problems, including many nonstructural applications. And it is also powerful to model material properties, including some models particularly for soil, such as Drucker-Prager model used in this project, which are very common in geotechnical engineering. ABAQUS is used throughout the world for stress, heat transfer, and other types of analysis in mechanical, structural, civil, and related engineering applications.

It can deal with general analysis including

- Static stress/displacement analysis
- Viscoelastic/viscoplastic response
- Transient dynamic stress/displacement analysis
- Transient or steady-state heat transfer analysis
- Transient or steady-state mass diffusion analysis
- Steady-state transport analysis
- Coupled problems

and linear perturbation analysis which includes

- Static stress/displacement analysis
- Dynamic stress/displacement analysis

Model for material includes metals, cast iron, rubber, plastics, composites, resilient and crushable foam, concrete, sand, clay, and jointed rock. The material response for each of these models may be highly nonlinear. General elastic, elastic-plastic, and elastic-viscoplastic behaviors are provided. Both isotropic and anisotropic

behavior can be modeled. User-defined materials can also be created with a subroutine interface.

MSC/PATRAN is used as preprocessor and postprocessor in this project, which is compatible with ABAQUS. Finite element model and mesh can be generated easily by drawing and PATRAN will generate the input file for ABAQUS automatically. After running ABAQUS, results may be read by PATRAN, so displacements and stresses can be presented very clearly so that the critical point or element can be located very quickly by just looking at the displacement and stress fringe results. Different useful kinds of graphs can be plotted in PATRAN such as load-displacement curve.

MODEL DESCRIPTION

The brief diagram of models for topdown test and O-cell test are shown in Figure A-1 and Figure A-2 respectively. The details of finite element modeling are described as follows.

Geometry, Element Type and Boundary of Mesh

A two dimensional axis-symmetric model was used for both topdown and O-cell load tests, which reduced the problem size thus the computing time significantly. ABAQUS includes both first-order and second-order elements with fully and reduced integration method. In this axis-symmetric model, fully integrated 4 nodes (first-order) quadrilateral axis-symmetric elements were used for both soil and pile.

Figure A-3 shows the finite element mesh, the dimension of which is 60ft deep by 45ft radial. Soil below the pile tip is 10 times of the pile diameter and the width of the mesh is 15 times of the pile diameter. As shown in Figure A-3, finite element is finer near the pile than that far away from the pile.

Boundary conditions are very important in the modeling. The model used in this project was simulated as close to the real case as possible. On the symmetric boundary (left side of the mesh), symmetric boundary condition was applied, which means only vertical displacement is permitted and horizontal displacement is constrained. At far side of the model (boundary far away from the shaft or right side of the mesh), horizontal pressure boundary condition was used. Horizontal pressure that is proportional to depth was applied to this boundary. By doing this, the in-situ ratio of horizontal to vertical stress may be controlled. At the bottom of the model, a rough contact surface was used. On this surface, friction can develop and no relative displacement will occur. This is used to prevent horizontal displacement of the bottom boundary.

Constitutive Model

Soil

An elastic-plastic (Drucker-Prager) constitutive model was used to simulate soil properties, which has Von Mises yield surface as its yielding criteria. The yield surface can be expressed as

$$F = t - p \tan \beta - d = 0$$

where

d=cohesion;

β =friction angle;

t=Octahedral shear stress, $t = \sqrt{\frac{1}{3}[(\sigma_1 - \sigma_2)^2 + (\sigma_2 - \sigma_3)^2 + (\sigma_3 - \sigma_1)^2]}$;

p=Octahedral normal stress, $p = \frac{1}{3}(\sigma_1 + \sigma_2 + \sigma_3)$.

Figure A-4 shows the failure envelope in p-t plane. In this model, there is a regime of purely elastic response, after which some of the material deformation is not recoverable and can be idealized as being plastic. Plastic deformation has been modeled using an associative flow rule, which implies that dilation occurs during plastic yield. Such behavior is thought to be appropriate for dense granular soils.

Rock

Rock has a much higher stiffness than soil, so its deformation is relatively small and it's difficult to fail the rock. Therefore, for the research performed to date, rock was simply modeled as linear elastic material.

Concrete Shaft

Concrete shaft was modeled as linear elastic material and its stiffness is much higher than that of soil.

Contact Surface Between Soil and Pile

The interaction surface between the pile and soil is described as a frictional contact surface, which allows slip. When the shear stress on that surface exceeds some value, soil and pile will not stick with each other and slip will occur. Coulomb friction theory is used in the model so that maximum frictional shear stress on the interaction surface is proportional to the normal pressure by a friction coefficient. The failure envelope is shown in Figure A-5, where δ is the friction angle and the friction coefficient is $\mu = \tan \delta$. Once the shear stress exceeds the maximum frictional shear stress, slip will occur. For this friction model, an interface stiffness is applied to allow small relative deformation prior to slip, so the contact stiffness is not infinity even if slip is not developing.

Topdown Load Test

In topdown test, load is applied to the top of the pile as a pressure load. The whole test was divided into three steps which are described as follows.

Step 1: Apply gravity force, and at the same time, apply horizontal pressure on far side boundary with $K_0 = 0.43$ (normal consolidated);

Step 2: Add additional horizontal pressure for over-consolidated case, skip this step for normal consolidated case;

Step 3: Apply external load to the top of the pile.

In order to avoid residual stresses, the contact surface between soil and pile was modeled as frictionless in the first two steps so that the pile can settle down without any obstruction. In step 3, friction coefficient was changed to the desired value to provide side shear. In all cases, the end of step 2 is the base state of step 3, so this base state was deducted from the final results to get the response under the external load.

O-cell Load Test

In O-cell load test, O-cell was embedded 3ft above the base of the shaft as a contact surface without thickness. O-cell pressure will generate forces with same magnitude in opposite direction. The interaction between two parts of shaft was modeled as contact surface so that the load can be transferred between two parts of pile when gravity force was applied. Similar to the topdown load test, there are three steps during calculation.

Step 1: Apply gravity force, and at the same time, apply horizontal pressure on far side boundary with $K_0 = 0.43$ (normal consolidated);

Step 2: Add additional horizontal pressure for over-consolidated case, skip this step for normal consolidated case;

Step 3: Apply O-cell pressure.

As in topdown load test, the friction coefficient of contact surface between soil and shaft is zero in the first two steps and changed to the desired value in the last step. Since the upper part of pile will move upward without any constraint after contact surface between soil and pile fails, soft springs were added to the top of the pile to allow a convergent solution as the load approaches and exceeds the shaft uplift capacity. When dealing with the results, this soft spring force is deducted from the total load.

In order to compare the results from topdown load test and O-cell load test, an equivalent topdown load versus settlement curve was generated from O-cell load test using the method described as follows. On O-cell test load-displacement curve, select a specified movement and then find the corresponding side load and ending bearing load. Adding these two loads will give the equivalent topdown load corresponding to the movement. Refer to “Construction of the Equivalent Top-Loaded Load-Settlement Curve from the Results of an O-cell” for details. When doing this, elastic shortening of the shaft was also considered although the magnitude of this elastic shortening was very small relative to the total settlement.

PROPERTIES COMMON TO ALL

In all cases for both Osterberg load test and topdown test, 3ft diameter concrete shaft was used, which is 30ft deep. For O-cell load test, Osterberg load cell is embedded

3ft above the bottom of the shaft with zero thickness. The following are properties and each material.

Concrete shaft: $E = 5000ksi, \nu = 0.3;$

Soil: $E = 14ksi, \nu = 0.3, \beta = 31^\circ, d = 8psi;$

Rock: $E = 1400ksi, \nu = 0.3;$

In calculation, soil was modeled as fully associated, which means the dilation angle equals the friction angle.

CASES ANALYZED

Several cases in terms of different over-consolidation ratio and friction coefficient of soil-pile interface were calculated for both topdown load test and O-cell load test. The following presents results case by case and also compares results of topdown load test and O-cell load test. For the following, μ refers to the friction coefficient of the contact surface between soil and pile and δ refers to the corresponding friction angle. K_0 is the ratio of horizontal stress to vertical stress.

Case I: All Soil, $K_0 = 0.43$, (Normal Consolidated), $\mu = 0.6$ ($\delta = 31^\circ$)

In this case, all soil is normal consolidated with the properties described before. Figure A-6 and A-7 show the load-displacement curve for topdown test and O-cell test respectively. As shown in the plots, stiffness decreases with the increase of the applied load. For topdown test, the whole system failed at about 170kips of applied load, after which the stiffness decreases rapidly. In Figure A-7, node 2378 represents the upper part of the shaft and node 2502 represents the lower part of the shaft. For the O-cell test, the load for the upper part of the pile has been adjusted for the soft spring force at the top of the pile, which enables the downward force to mobilize additional end bearing. It's

obvious that side shear failed first at about 130kips applied load. At the beginning of applying O-cell pressure, there's almost no movement because there's initial stress in the system due to the self weight of soil and pile, and this stress needs to be overcome before significant displacement occurs. Note that the "end bearing" includes side shear on the 3ft shaft below the O-cell, which is also true for following cases.

The equivalent topdown load vs displacement generated from O-cell test is shown in Figure A-8, comparing with the result from topdown test. It is indicated that the two curves match well for this case and the O-cell slightly underestimates the capacity. Figure A-9 and Figure A-10 show the tip load vs displacement curve and side load vs displacement curve for both tests respectively. For topdown test, the tip load was calculated from the vertical stress at O-cell level and side load was calculated by subtracting tip load from total load. Comparing these two figures, it can be concluded that most of the applied load is resisted by end bearing, which can also be seen from the load-displacement curve for O-cell test shown in Figure A-7. As shown in figures, tip load vs displacement curve and the first part of side load vs displacement curve for two tests match well. But the topdown test shows more strain softening than the O-cell test.

Figure A-11 is the comparison of stress path (shear stress vs normal stress) at different nodes along the contact surface between soil and pile from the topdown test and the O-cell test. At the beginning of the test, deeper node was at a higher stress than the lower node due to the overburden pressure. The initial stress state at the same node is the same for topdown and O-cell tests, and the shear stress for all nodes starts from zero because the contact surface is frictionless before top loads or O-cell pressures are applied. The stress paths for the topdown test and the O-cell test are somewhat different, with

more significant differences at shallow depths. As the applied load is increasing, slip will occur after overcoming the surface frictional stress. This can be seen from the sudden change of the slope of each curve. After slip occurs, stress path follows the contact surface property defined, i.e. $\mu = 0.6$. Connecting the failure envelope will result in a straight line with a slope of 0.6. These plots suggest that the failure occurred at the contact rather than within the soil. As a general trend, the normal stresses along the interface tended to decrease during O-cell loading and increase slightly for topdown loading.

Figure A-12 and Figure A-13 are normal stress and shear stress at different loads on soil-pile interface changing with the depth in topdown test respectively. As shown in the figures, normal stress and shear stress curves are very similar in shape. Normal stress and shear stress increase with the depth at the beginning of the test, but with the increase of the applied load, both normal stress and shear stress curves become totally different. It's indicated in Figure A-12 that at some depths normal stress decreases with the increase of the applied load, this is because the contact surface tends to open. Similarly, normal stress and shear stress versus depth curves at different loads in O-cell test are shown in Figure A-14 and Figure A-15. The maximum normal stress is not at the bottom of the shaft, but at a depth of from about 27.5ft at load=54kips to 22.5ft at load=204kips. Similar to the topdown test, the shear stress curve is very similar to normal stress curve except at depth around O-cell where the contact nodes tends to open which result in zero normal stress and shear stress.

Figure A-16 and Figure A-17 show comparison of stress path (octahedral shear stress vs octahedral normal stress) of different soil elements below the pile toe. Element

1062 in topdown test and 62 in O-cell test are at the same location, as are element 1065 and 65. The soil almost failed from the beginning of applied due to initial stress state because of large deviatoric stress in this normally consolidated condition, and the straight line corresponds to soil yield surface envelope. It is also shown that the stress path in topdown test and O-cell test is almost same.

For this case, it's obvious that side friction is easier to fail than end bearing and end bearing provides most of the resistance to the applied load. This holds true for both topdown and O-cell load test. Results from topdown and O-cell test are consistent and match fairly well, but O-cell test tends to overestimate pile capacity a little. Also, soil is easy to fail because the horizontal pressure is small which leads to high deviatoric or shear stress.

Case II: All Soil, $K_0 = 1$, $\mu = 0.6$ ($\delta = 31^\circ$)

For the same soil and other conditions, over-consolidated cases were calculated with a higher ratio of in-situ horizontal to vertical stress (K_0). This case is probably more representative of typical soil conditions for drilled shafts. For $K_0 = 1$, Figure A-18 and Figure A-19 show the load vs displacement curve for topdown and O-cell test respectively. It is obvious that the capacity was much higher compared to normal consolidated case for both tests. In the O-cell test, it's hard to tell whether side shear or end bearing failed first as shown in Figure A-19. But it is clear that the contact surface between soil and pile failed at a load of about 350 kips. Similar to normal consolidated case, there's very small movement at the beginning of the O-cell test due to the self weight of the upper part of the shaft, and side shear is mobilized at less than ¼ inch of displacement.

Figure A-20 shows the match between the load vs displacement curve of topdown test and equivalent topdown load vs displacement curve generated from O-cell test. It is indicated that the O-cell test is conservative compared with the topdown test. For instance, at 1in displacement, the corresponding load from the topdown test is about 580kips, while load from the O-cell test is around 500kips. This can be also concluded from the side load vs displacement curve shown in Figure A-22. Figure A-21 is the plot of tip load vs displacement curve for both the topdown test and the O-cell test, which shows that the results of two tests match well. Comparing Figure A-21 and Figure A-22, it can be found that side load is a little higher than tip load, indicating that end bearing and side friction almost have same capacity.

Similar to normal consolidated case, shear stress vs normal stress curves at different nodes along the interface between soil and pile were plotted in Figure A-23 for both topdown test and O-cell test. There's no difference between topdown test and O-cell test at the beginning of the test, but the upward directed O-cell loading tends to reduce the effective normal stress compared to the topdown loading. After slip, all nodes tended towards slight strain-softening along the yield surface that defines the contact surface properties.

Figure A-24 to Figure A-27 show normal stress and shear stress changing with along the length of the pile for topdown and O-cell test respectively. The maximum value for both normal stress and shear stress is not at the bottom of the shaft, which reflects the shadowing effect of the mobilization of end bearing. For both the topdown test and O-cell test, normal stress decreases with the increase of the applied load. While shear stress increases first and then decreases with the increase of the applied load in topdown test,

but increases in O-cell test. This corresponds to the different stress path which is shown in Figure A-23.

Figure A-28 to Figure A-29 are plots showing the comparison of stress path of different soil elements below the pile toe for both the topdown test and O-cell test. For each element, the stress path is almost same for topdown and O-cell test, starting from a low Octahedral shear stress with both shear stress and normal stress increasing until reaching the failure envelope or yielding. After yielding, all nodes followed the path specified for the soil properties.

Case III: All Soil, $K_0 = 2$, $\mu = 0.6$ ($\delta = 31^\circ$)

This case represents a heavily consolidated soil with large locked-in horizontal stresses, $K_0 = 2$. The results in terms of load vs displacement curve, stress path for soil-pile interface and soil elements, etc, are presented as follows.

Figure A-30 shows the load vs displacement curve for topdown load test. With the capacity increasing as compared to $K_0 = 1$ case, pile began to yield at a load of approximately 1000kips. For the O-cell test, the load vs displacement curves are plotted on Figure A-31, showing that end bearing failed before the failure of side shear. Note that a relatively large movement was required to mobilize side shear.

The equivalent topdown load vs displacement curve generated from O-cell test is shown in Figure A-32 comparing the load vs displacement curve from the topdown test. It can be seen easily that O-cell test is relatively conservative. For example, it will require a load of 1000kips to produce 0.5in displacement for the topdown test as compared to about 700kips for the O-cell test. Figure A-33 and Figure A-34 present tip load vs displacement curve and side vs displacement curve respectively. For topdown test, no

more than 30% of the applied load was transferred to pile tip and most was resisted by the side shear. Comparing the results from topdown and O-cell test, it's not difficult to find that O-cell test is conservative which is also shown in Figure A-32.

As before, Figure A-35 shows shear stress vs normal stress curves at different nodes along the soil-pile interface for both topdown test and O-cell test. Again, shear stress started from zero for all nodes and initial stress states for topdown test and O-cell test are same. Each node follows its own stress path for different test until reaching failure envelope. At a depth of 15ft, normal stress increases after failure in topdown test but decreases in O-cell test. At depths of 5ft and 10ft, normal stress decreases after slip occurs. But at a depth of 20ft, normal stress increases after slip occurs. So different nodes have different stress path and post failure behavior.

Normal stress and shear stress changing along the depth of the pile for topdown test and O-cell test are shown in Figure A-36 through Figure A-39 respectively. Similar to the above two cases, different nodes have different stress path, so it's hard to tell how normal stress and shear stress change with the applied load as a whole.

Figure A-40 and Figure A-41 compare the stress path of different soil elements below the pile toe for the topdown test and O-cell test. For this case, all four elements start with a state close to the failure envelope, with horizontal stress greater than vertical stress. However, with the increasing of the applied load (or vertical stress), the difference between the vertical stress and horizontal stress decreases, which leads the shear stress to decrease. But the average normal stress (or Octahedral normal stress) increases. After reaching some point, vertical stress becomes the first principal stress. Then with the increase of the applied load, shear stress increases until failure.

For this case, pile capacity increases compared with Case II, so does side friction. It can be seen that end bearing fails first for this case and most of the applied load is resisted by side friction. Comparing topdown and O-cell tests shows that the O-cell test tends to be conservative for these conditions of high lateral stress. Another important point is stress path of soil element, which is different from the previous two cases. This is because horizontal stress is greater than the vertical stress at the beginning of the test, thus horizontal stress is the first principal stress. But vertical stress becomes the first principal stress with the increasing of applied load. This results in shear stress decreasing first and then increasing.

Case IV: All Soil, $K_0 = 1$, $\mu = 1.2$ ($\delta = 50^\circ$)

Roughness of soil-pile interface can affect side resistance directly, so it's necessary to analyze how friction coefficient of soil-pile interface influence the results in topdown and O-cell test. This case can be compared with Case II with same conditions except twice of friction coefficient was used to define a very rough soil-pile interface.

Load-displacement curve for topdown test was plotted in Figure A-42. Compared to Case II, capacity increases greatly. For this case, about 1160kips applied load is required to produce 1in settlement, while in Case II, only about 580kips is needed to have 1in displacement occur. This is also shown in load vs displacement curve for O-cell test plotted in Figure A-43. For Case II, side shear failed at an O-cell load of about 350kips, but side shear did not fail even at around 700kips O-cell load for this case. Note also that larger displacement is required to mobilize side shear. It is also apparent that the rough base and differing stress conditions mobilize greater end bearing than for case II.

However, note that this “end bearing” includes side shear on the lower 3ft socket below the O-cell.

Figure A-44 shows the equivalent topdown load vs displacement curve generated from the O-cell test as compared with load vs displacement curve from the topdown test. The two curves match fairly well and the O-cell test tends to underestimate the capacity slightly for this case. Tip load vs displacement and side load vs displacement curve are shown in Figure A-45 and Figure A-46 respectively. Similar to Case III, most of the applied load goes to side shear indicating end bearing is weak compared with side shear, which can be seen from the load vs displacement curve shown in Figure A-43. This is due to the high friction coefficient of the soil-pile interface. For tip load, O-cell test overestimates the capacity while underestimating capacity for side load.

Figure A-47 is a stress path plot for different nodes along soil-pile interface for topdown and O-cell test as before. Since the contact surface friction coefficient is very high, surrounding soil yielded before the contact surface. This can be seen from the envelope of stress path at depths of 10ft, 15ft and 20ft, which is close to the soil failure envelope. It's also shown that soil at all depths tends to dilate because normal stress increases with the increase of applied load.

As before, Figure A-48 to Figure A-51 are plots of normal stress and shear stress versus depth curves at different loads for topdown test and O-cell test. For this case, in topdown test, both normal stress and shear stress increase with the increasing of the applied load, and from the magnitude of the shear stress as compared to the normal stress, the contact won't fail. In O-cell test, shear stress increases with the increase of the applied load, but normal stress does not.

Stress path of different soil elements below the pile toe are plotted in Figure A-52 and Figure A-53. Similar to other cases, stress path is almost same for topdown test and O-cell test. Each element followed specific stress path until soil yielding.

For this case, side friction improves greatly as compared to Case II indicating that roughness of soil surface is important for pile capacity. Therefore, the total pile capacity improves significantly. Because of high friction coefficient, it's hard to fail the contact surface resulting in the failure of the surrounding soil. This can be seen from the stress path curves at different nodes along the soil-pile interface.

Case V: Soil Over Rock, $K_0 = 1$, $\mu = 1.2$ For Rock And $\mu = 0.6$ For Soil

In this case, soil deposit is composed of two layers: 15ft soil over rock. Different contact surface friction coefficients were used, 1.2 for rock-pile interface and 0.6 for soil-pile interface. For the topdown test, in order to fail the side shear, a false base was used under the pile tip as might be done with a physical test in rock. This false base is thin layer with a very low Young's modulus (1.4ksi) and zero Poisson's ratio.

Figure A-54 shows load-displacement curve for the topdown test, which is similar to other cases but with a much higher capacity. As shown in the figure, pile failed at a load of about 1400kips after which displacement increases rapidly. The generated tip load vs displacement curve and side load vs displacement curve are shown in Figure A-55 and Figure A-56 respectively. Obviously, only a very small part of the applied load goes to pile tip because of low stiffness of the false base. Figure A-56 also compares the result from the topdown test and the O-cell test, showing that the O-cell test is conservative in this case. Figure A-57 is the load-displacement curve for the O-cell test. As shown in

figure, the downward displacement of pile tip is almost nothing due to the high stiffness of rock. Side shear failed at about 1000kips O-cell load.

Figure A-58 and Figure A-59 show the stress path at different nodes along contact surface in soil and rock respectively. Comparing these two figures, it can be seen that stresses in rock are much higher than in soil because of different stiffness. And they have different failure envelope with a slope of 0.6 and 1.2 respectively. Soil tends to dilate (normal stress increase) at all depth. In the O-cell test, it's very difficult to fail the contact surface at depth of 28ft as shown in Figure A-59 that the stress path at that depth is far from the failure envelope.

Figure A-60 to Figure A-63 show the change of normal stress and shear stress along the length of pile for topdown and O-cell tests respectively. As shown in figures, both normal stress and shear stress in the topdown test and the O-cell test increase with the increase of the applied load. Normal stress curves are similar shear stress curves. It is also shown that stress in rock is much high than in soil which is also concluded from Figure A-58 and Figure A-59, and this is because rock has a much higher stiffness than soil.

For this case, pile capacity increases greatly due to the high stiffness of rock deposit. Because of its high stiffness, it's very difficult to fail the end bearing, which can be found from the load-displacement curve of the O-cell test. Furthermore, rock accounts for most of the side shear as shown in the plot of shear stress vs depth. The O-cell test is conservative in estimating side friction for this case.

SUMMARY

Finite element models for both topdown test and O-cell test were built up using ABAQUS and MSC/PATRAN. Different boundary conditions were applied to simulate the real situation in the load test. Several cases were calculated and results were analyzed and compared between the topdown test and the O-cell test. From the above analysis, several conclusions can be drawn described as follows.

- 1) In general, the O-cell test seems to underestimate pile capacity more or less;
- 2) The ratio of in-situ horizontal to vertical stress affects capacity significantly.
With the increase of K_0 , pile capacity improves;
- 3) Roughness of the soil surface plays an important roll in improving pile capacity. The increase of friction coefficient will improve side resistance directly.
- 4) Rock improves capacity in both end bearing and side friction;
- 5) Stress path for soil element is almost same for the topdown test and the O-cell test, but the stress path for contact surface is different for the topdown test and the O-cell test although they start from the same stress state.
- 6) From the normal stress and shear versus depth curves, it is indicated that the maximum normal stress or shear stress is not always at the bottom of the pile. There's no a simple relation between the curves and the applied load which is because every node has a different stress path.

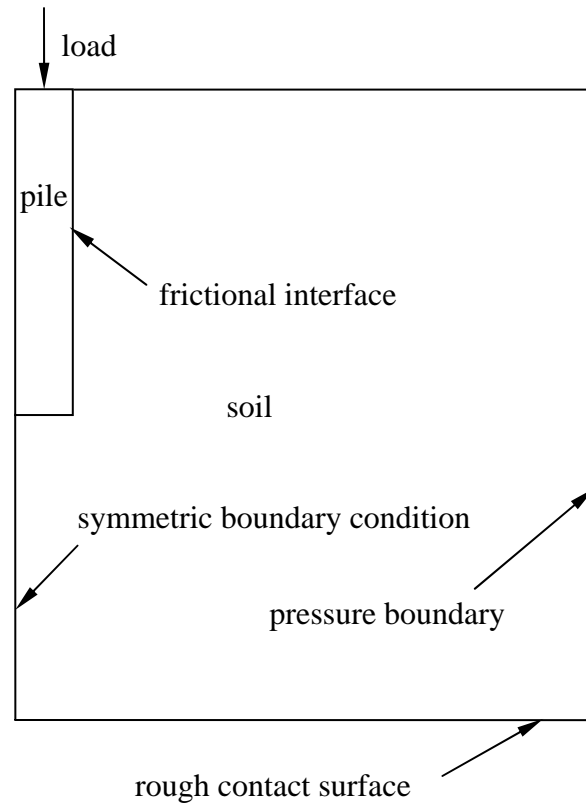


Figure A-1 Topdown Load Test Model

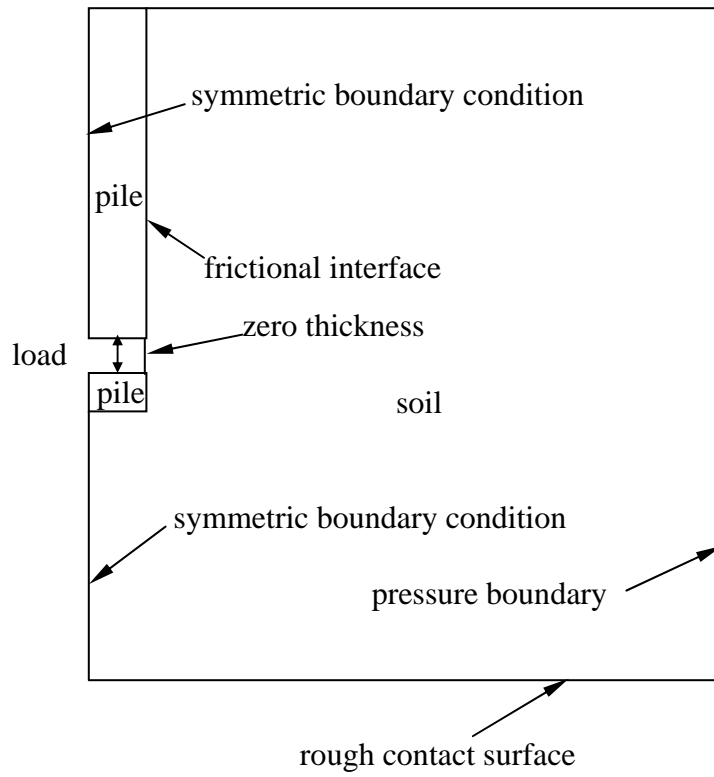


Figure A-2 O-cell Load Test Model

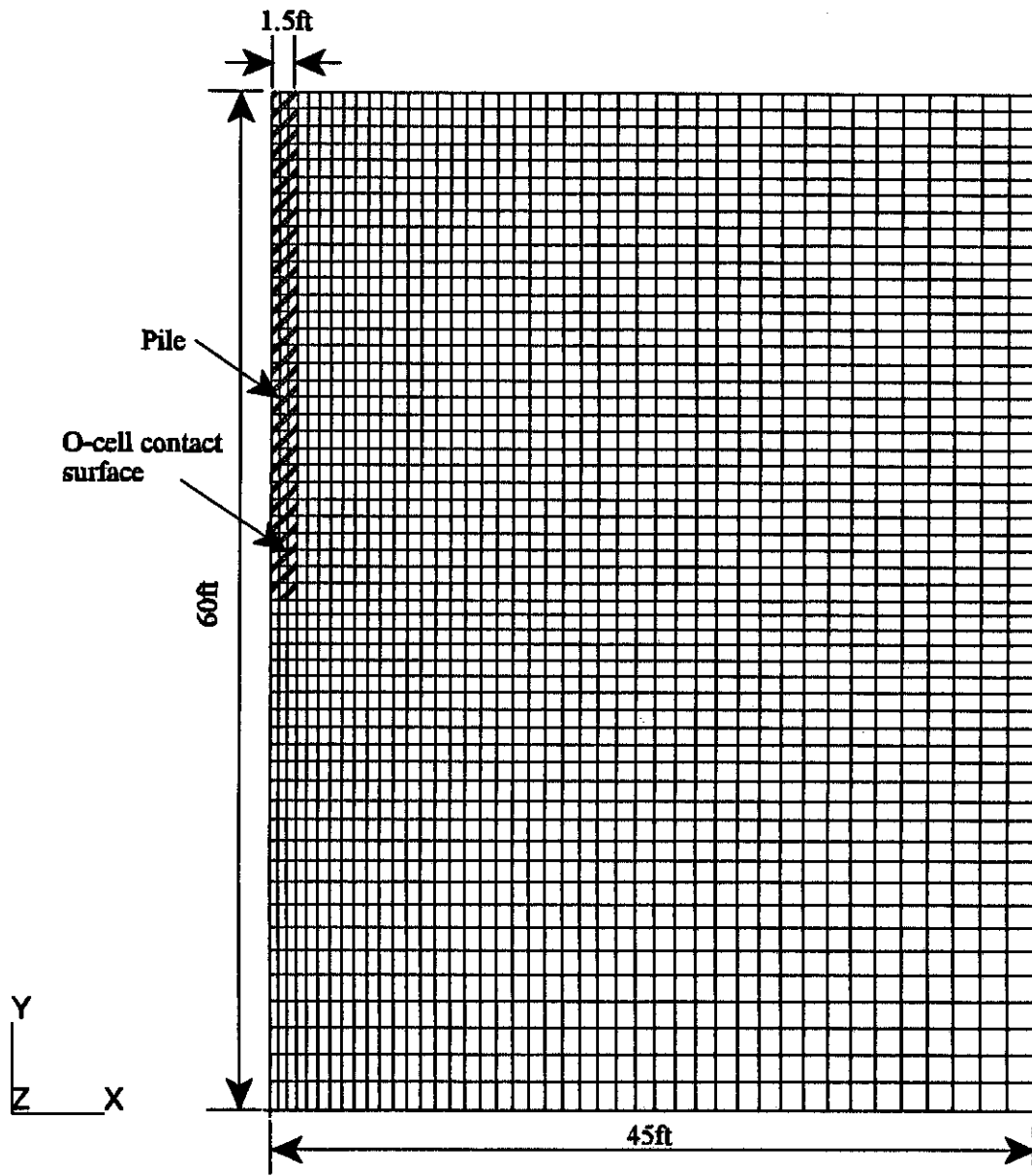


Figure A-3 Finite Element Mesh

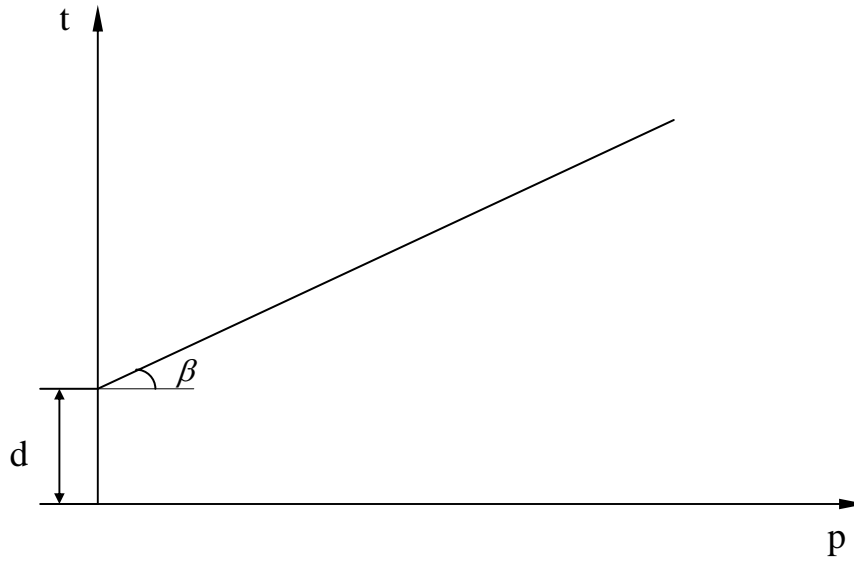


Figure A-4 Linear Drucker-Prager Model

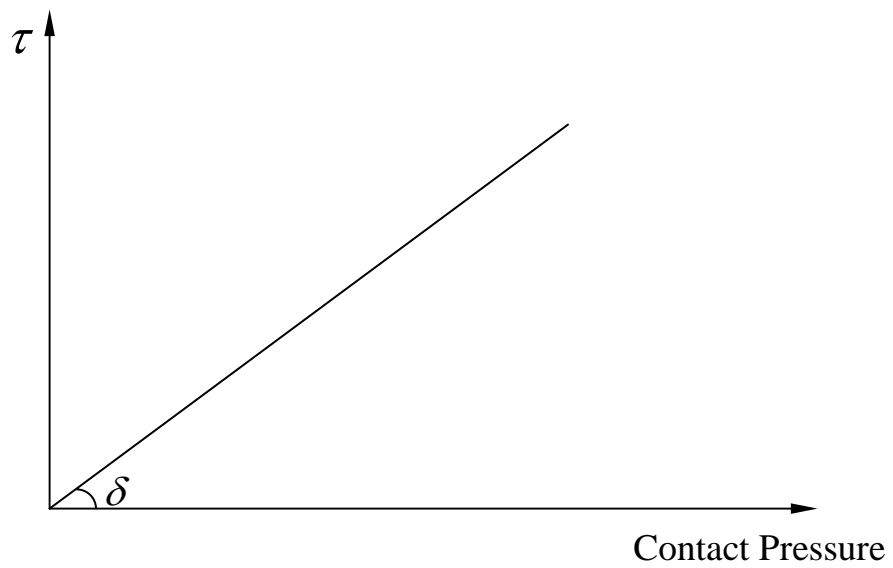


Figure A-5 Frictional Contact Surface

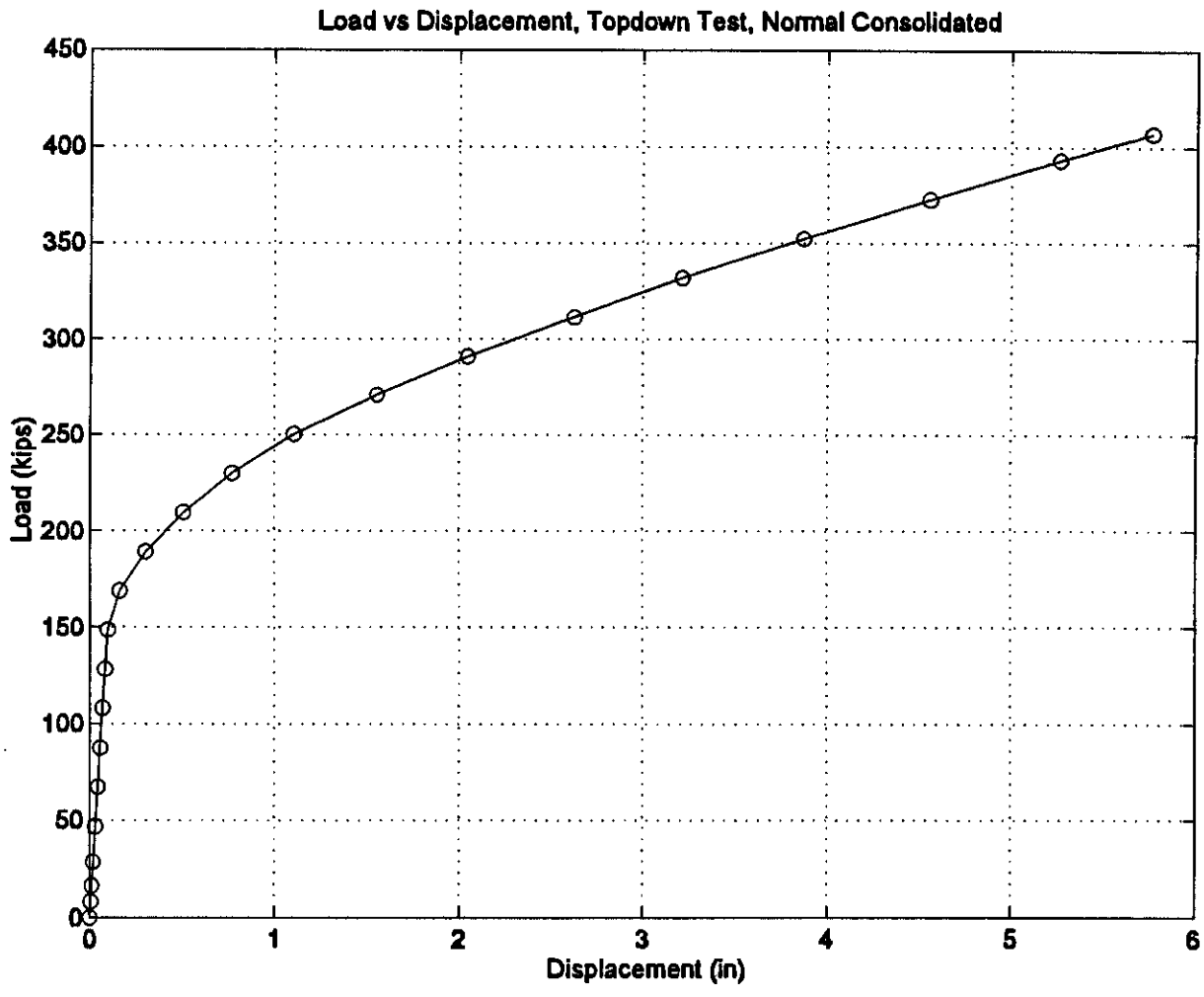


Figure A-6 Load-Displacement Curve, Topdown Test, Normal Consolidated

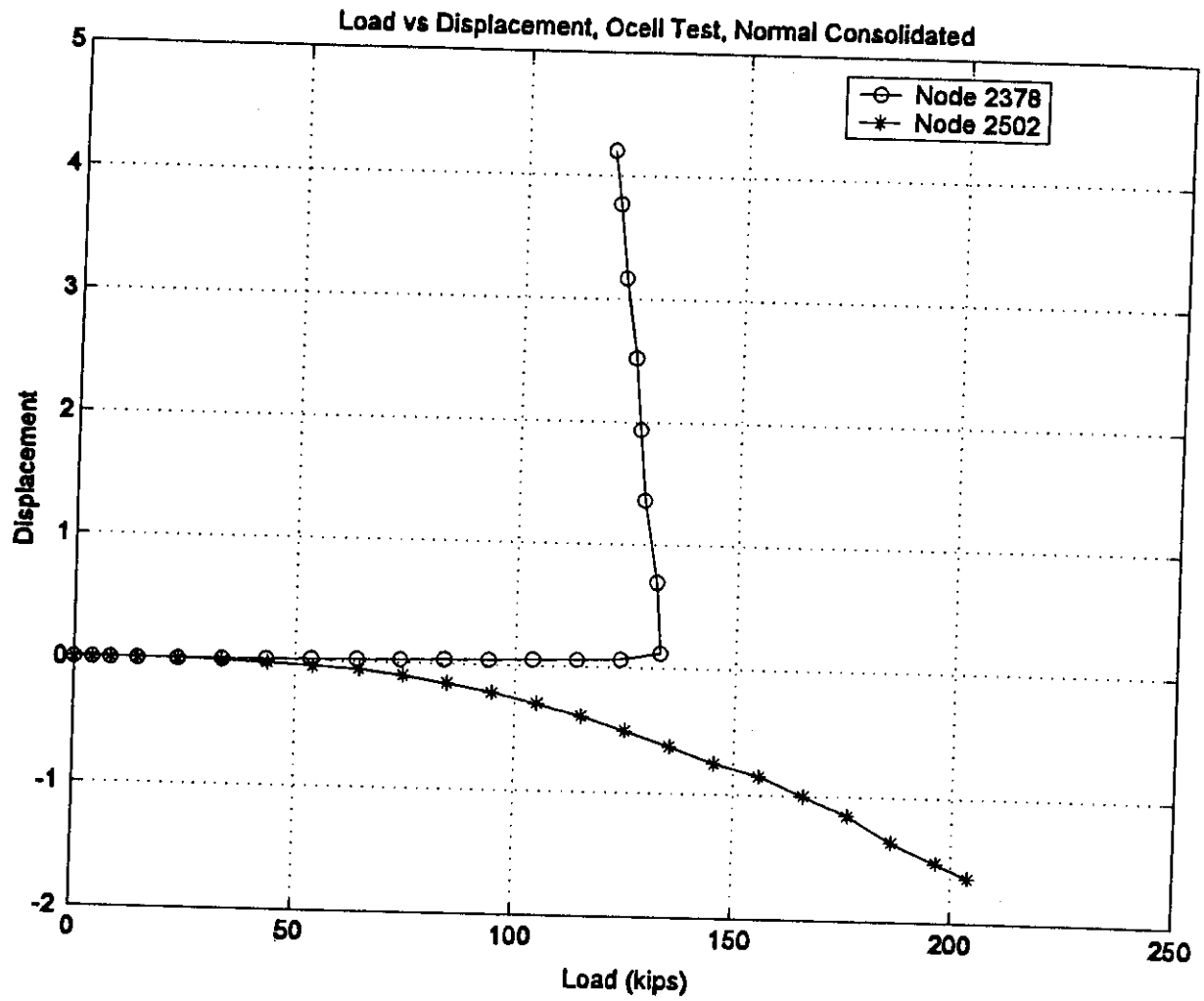


Figure A-7 Load-Displacement Curve, O-cell Test, Normal Consolidated

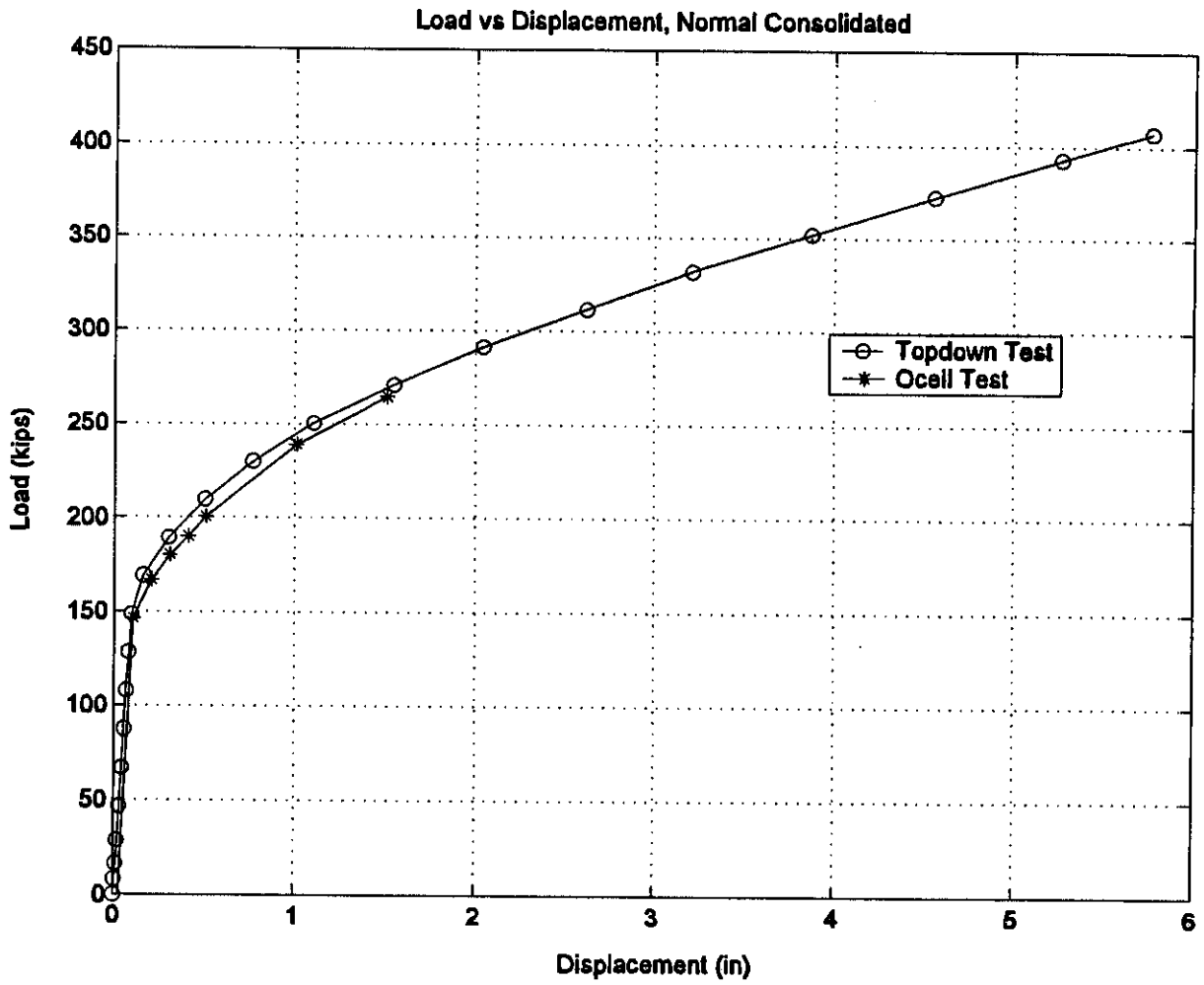


Figure A-8 Comparison of Topdown Test and O-cell Test, Normal Consolidated

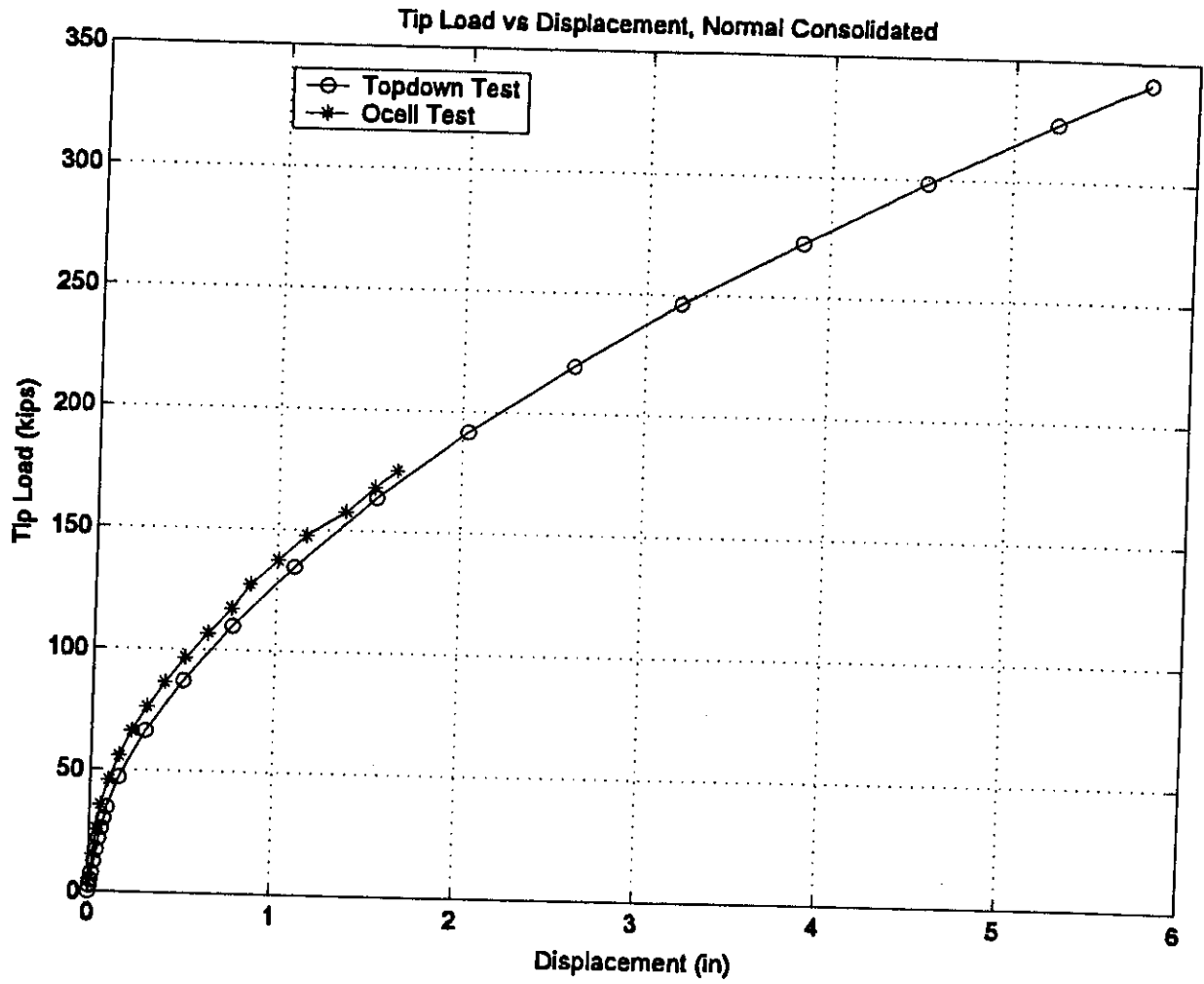


Figure A-9 Tip Load vs Displacement Curve, Normal Consolidated

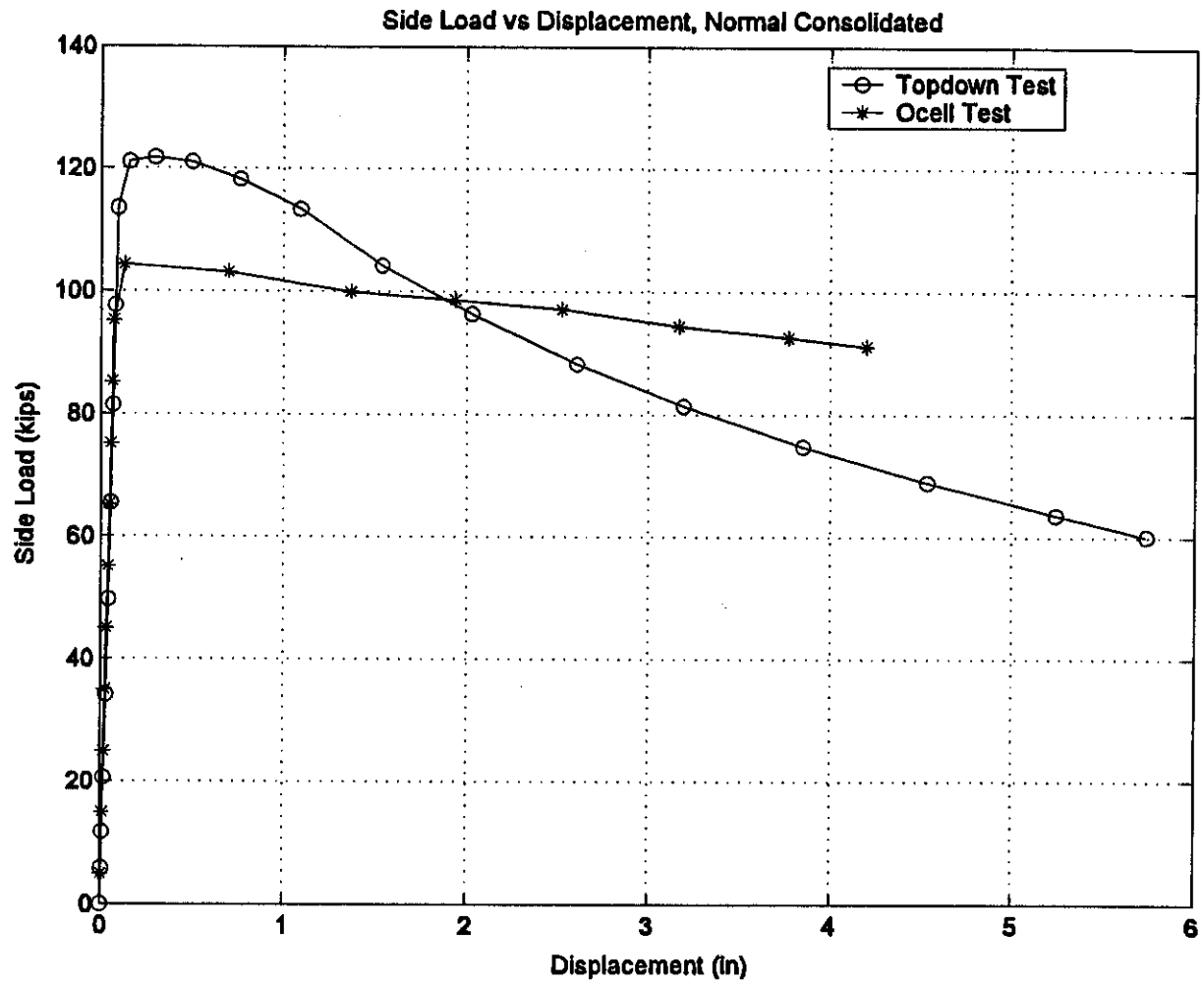
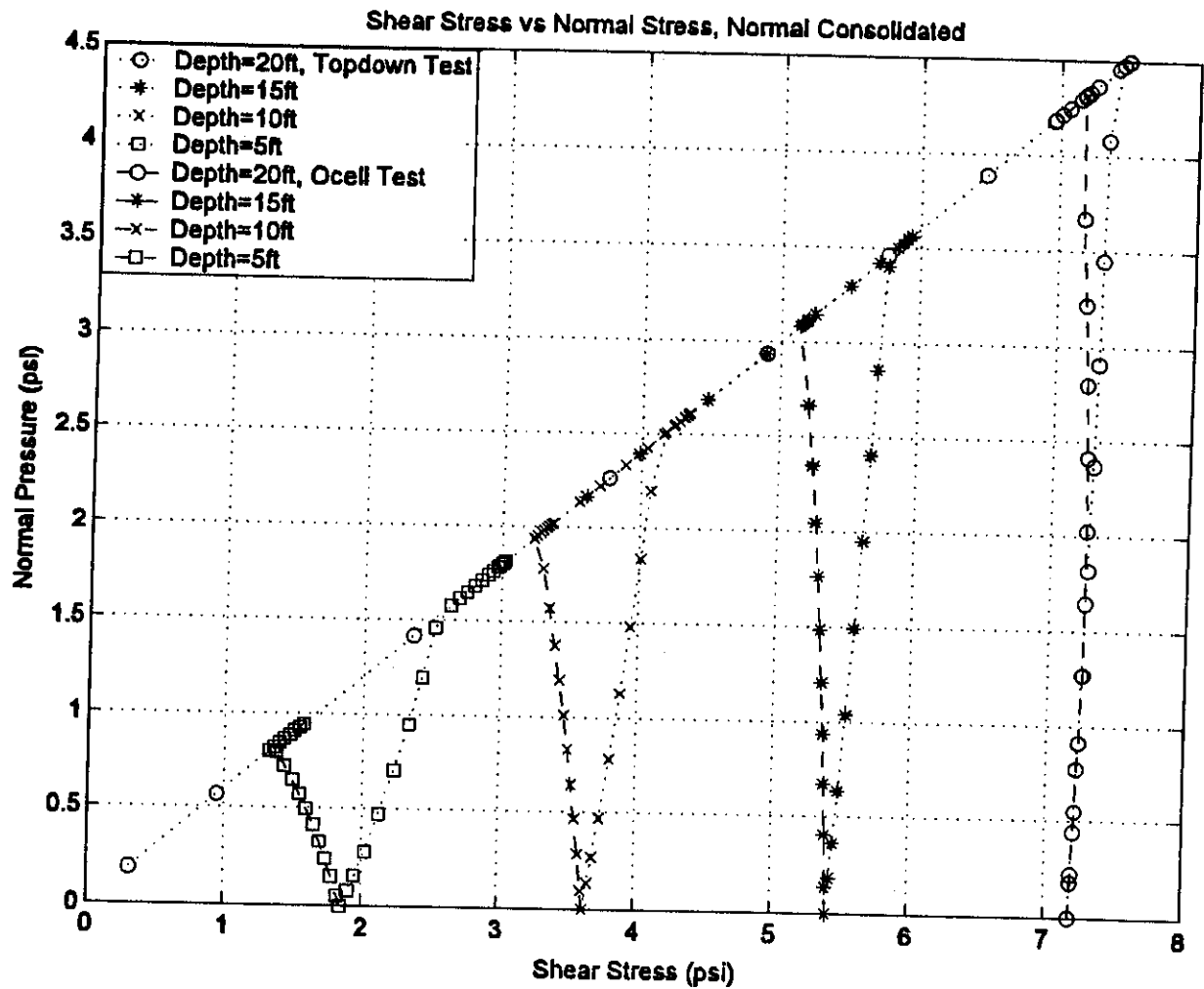


Figure A-10 Side Load vs Displacement Curve, Normal Consolidated



*Figure A-11 Stress Path at Different Nodes on Soil-Pile Interface,
Normal Consolidated*

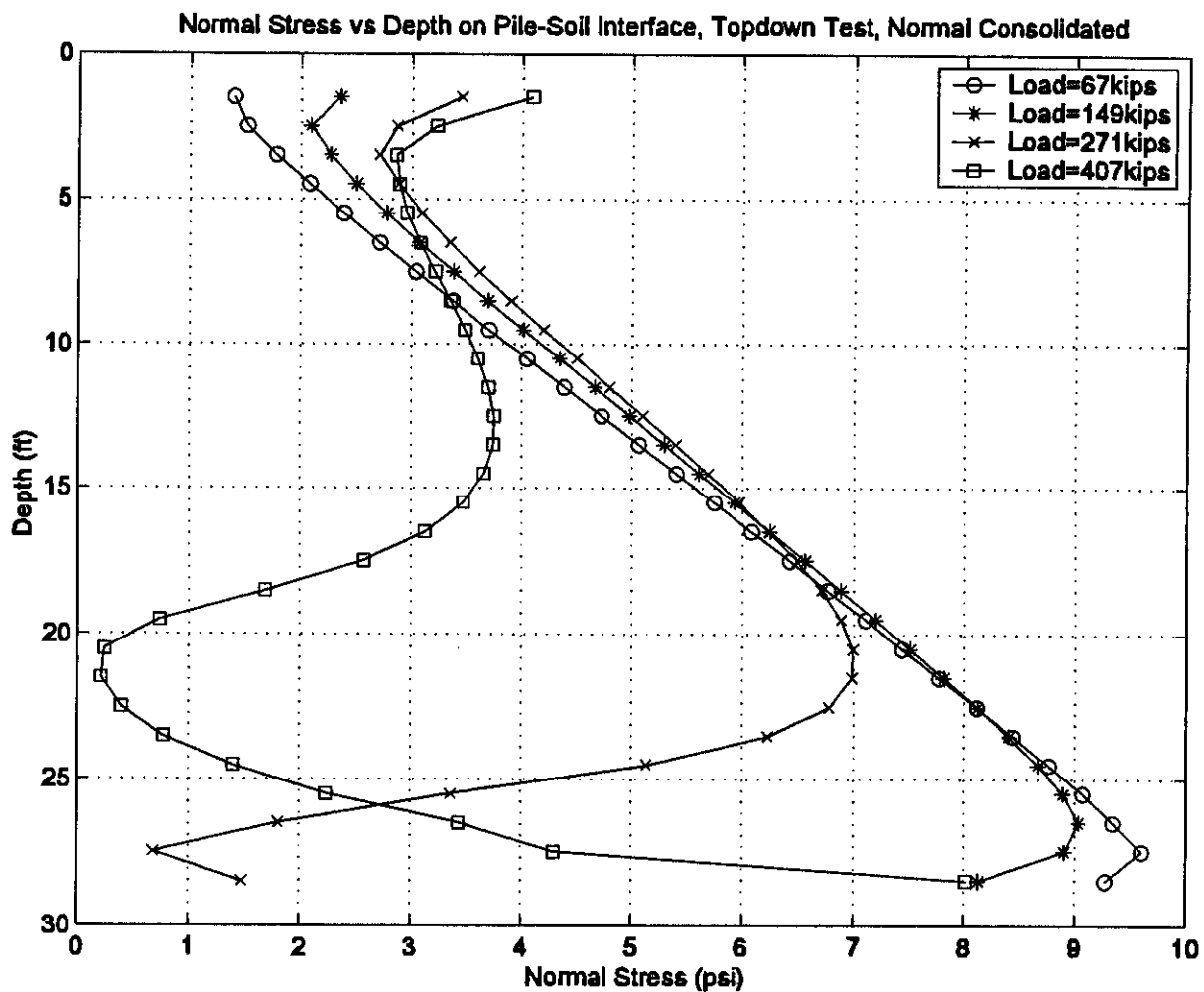


Figure A-12 Normal Stress vs Depth Curve, Topdown Test, Normal Consolidated

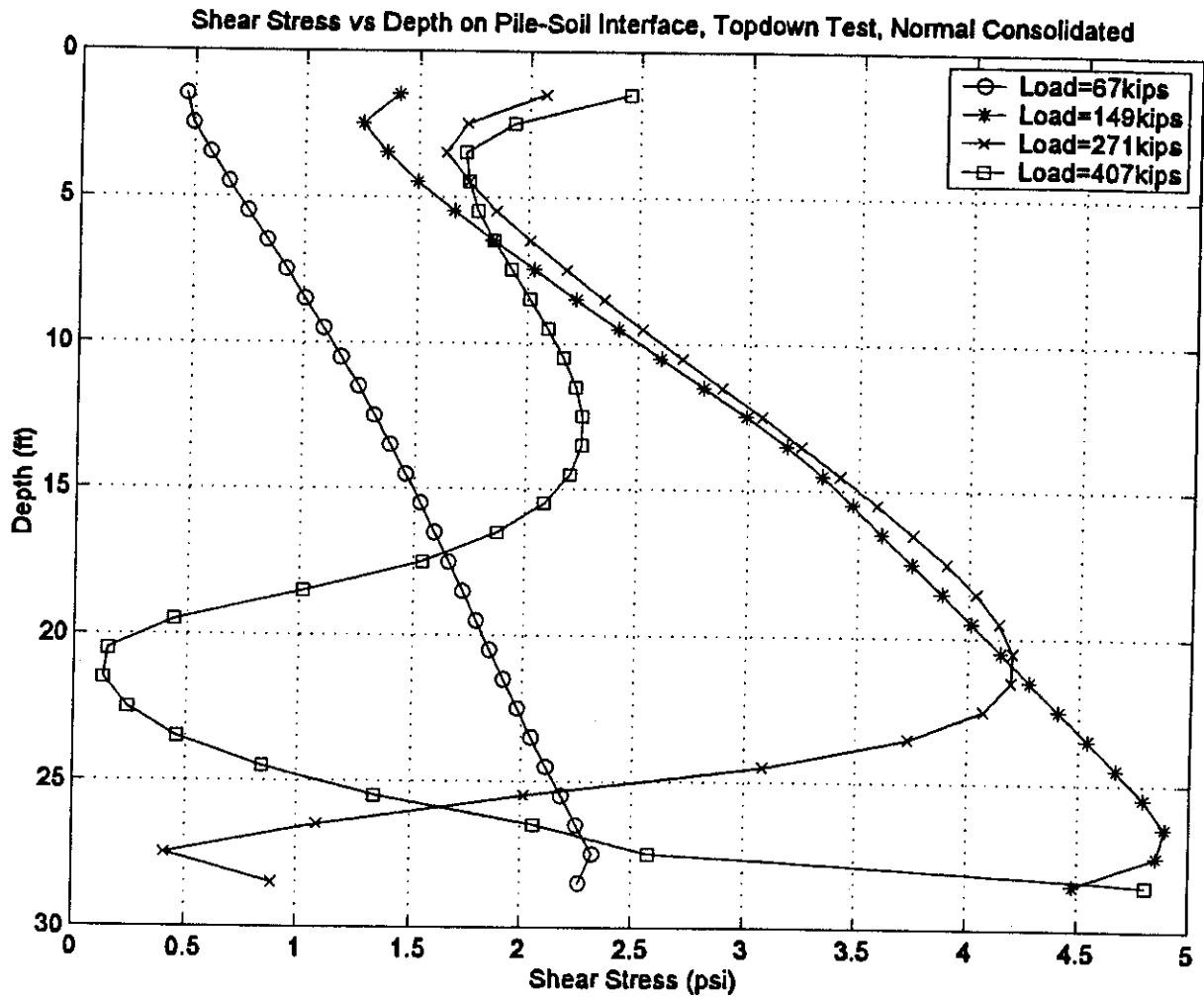
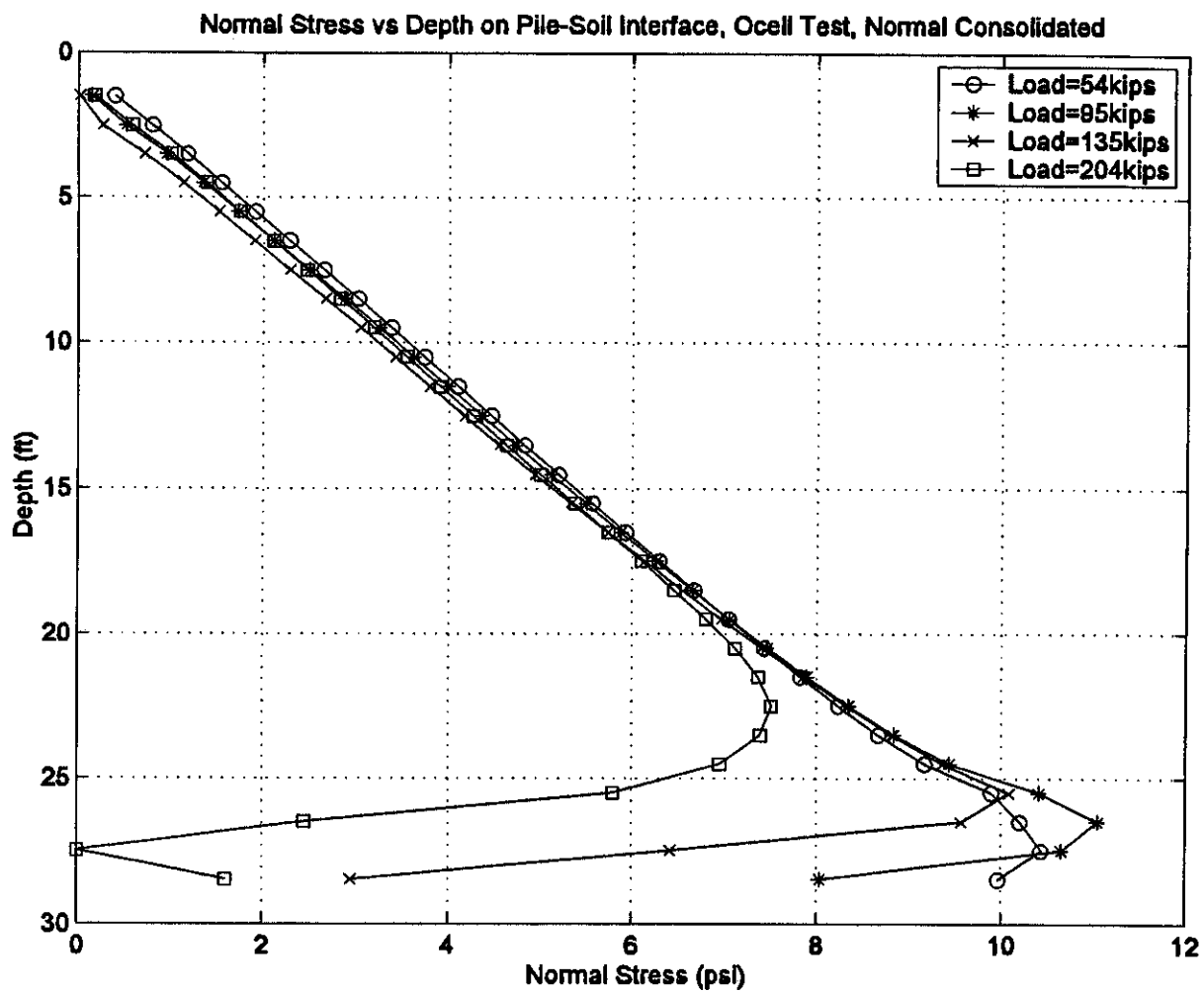


Figure A-13 Shear Stress vs Depth Curve, Topdown Test, Normal Consolidated



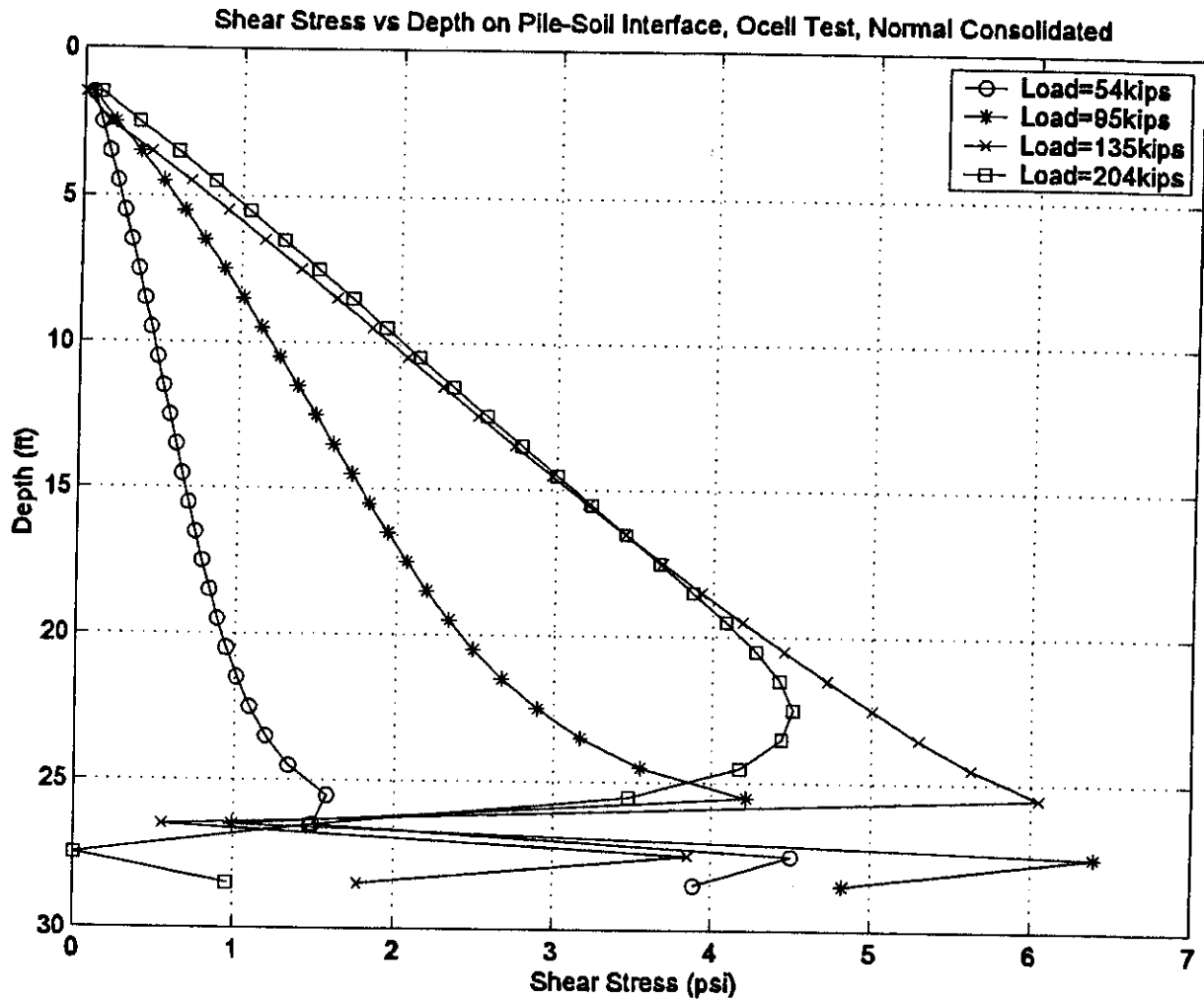


Figure A-15 Shear Stress vs Depth Curve, O-cell Test, Normal Consolidated

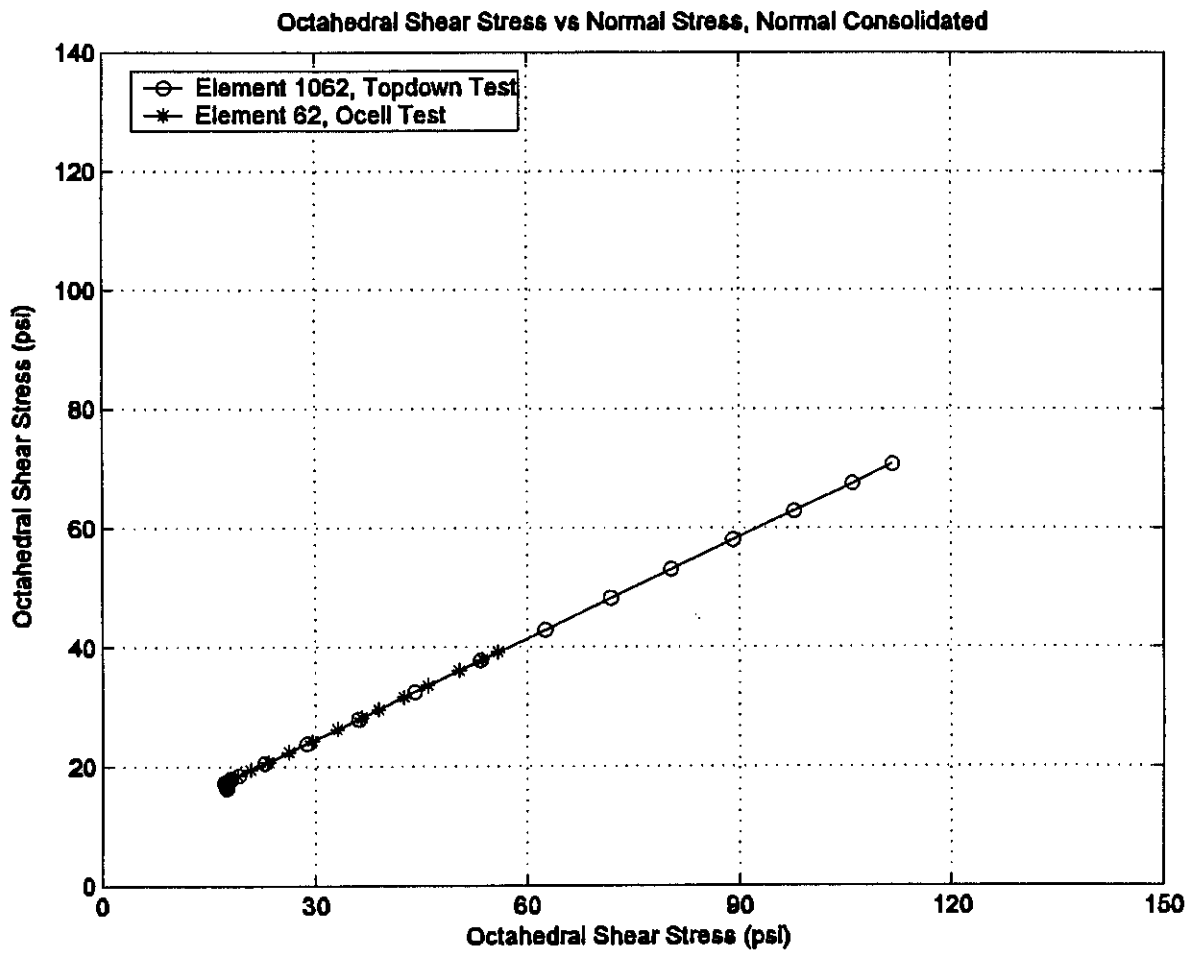


Figure A-16 Stress Path of Soil Element, Normal Consolidated

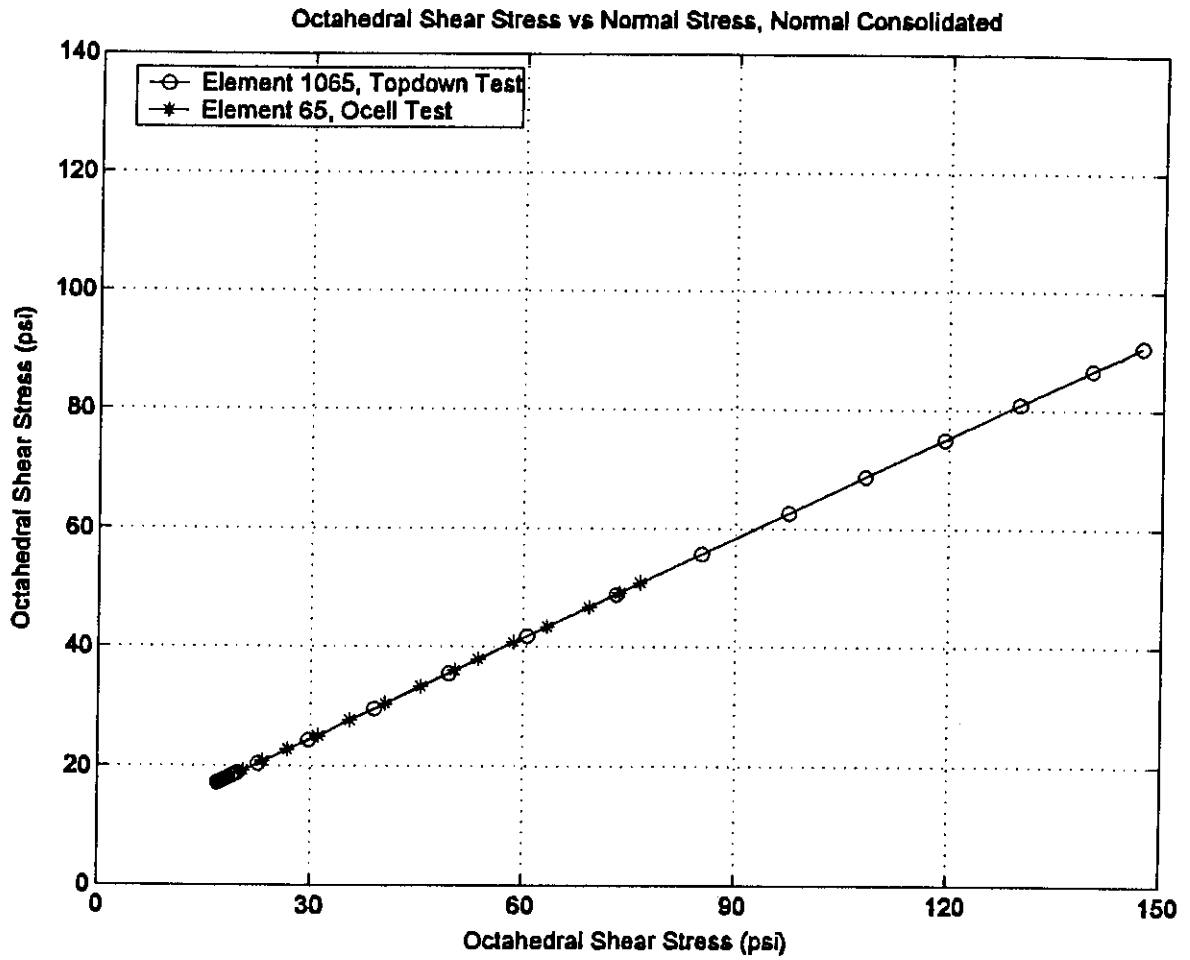


Figure A-17 Stress Path of Soil Element, Normal Consolidated

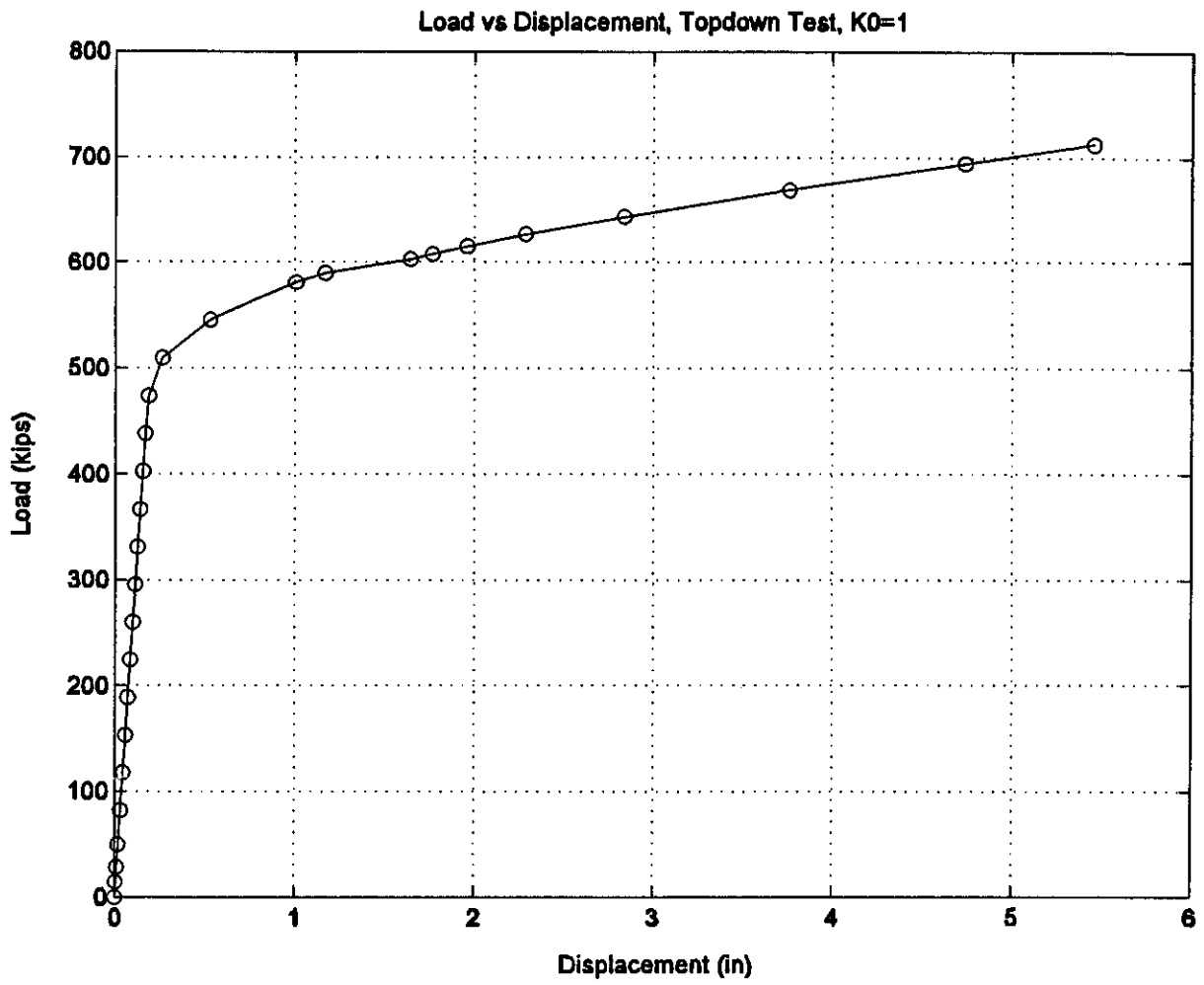


Figure A-18 Load-Displacement Curve, Topdown Test, $K_0=1$

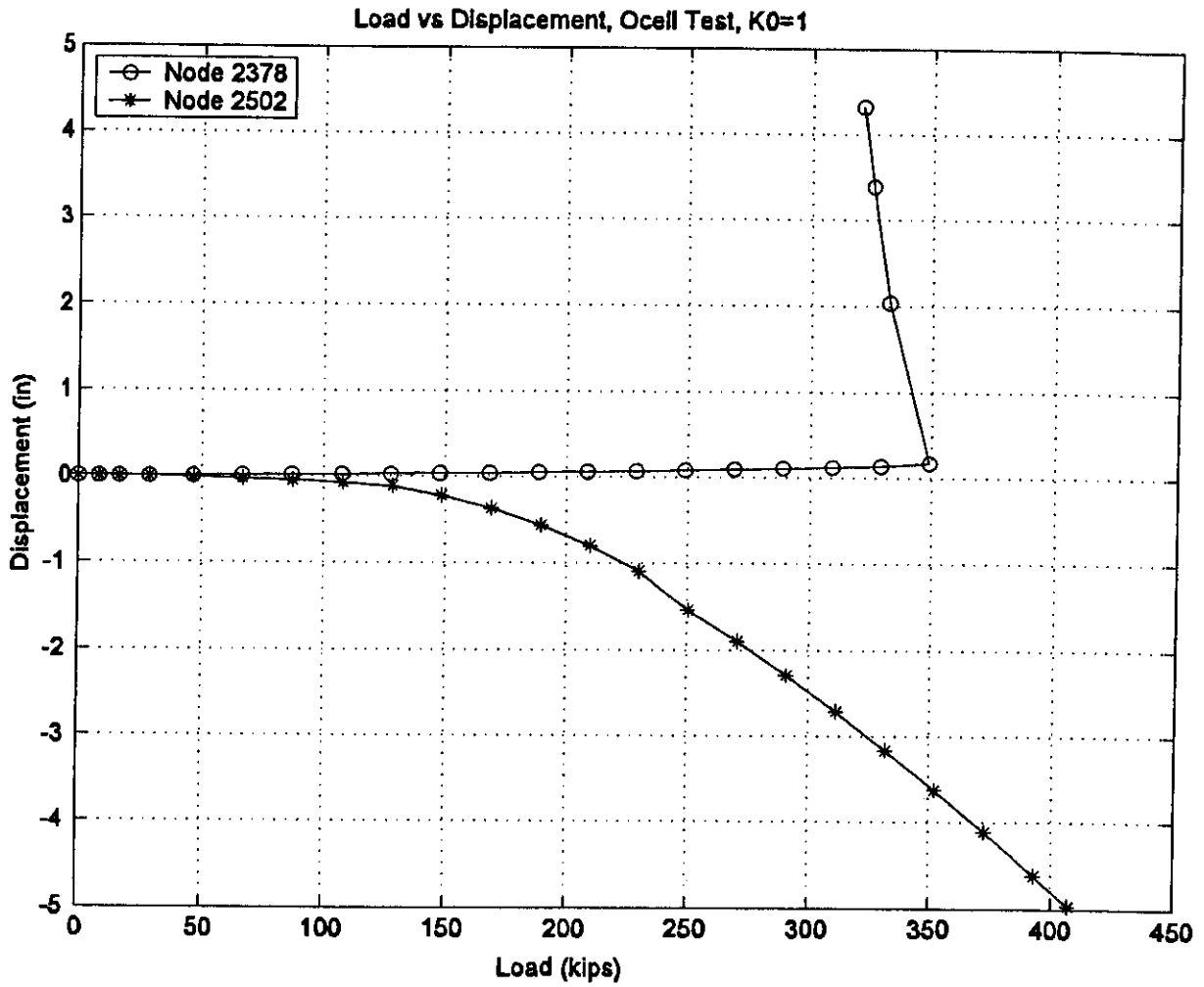


Figure A-19 Load-Displacement Curve, O-cell Test, $K_0=1$

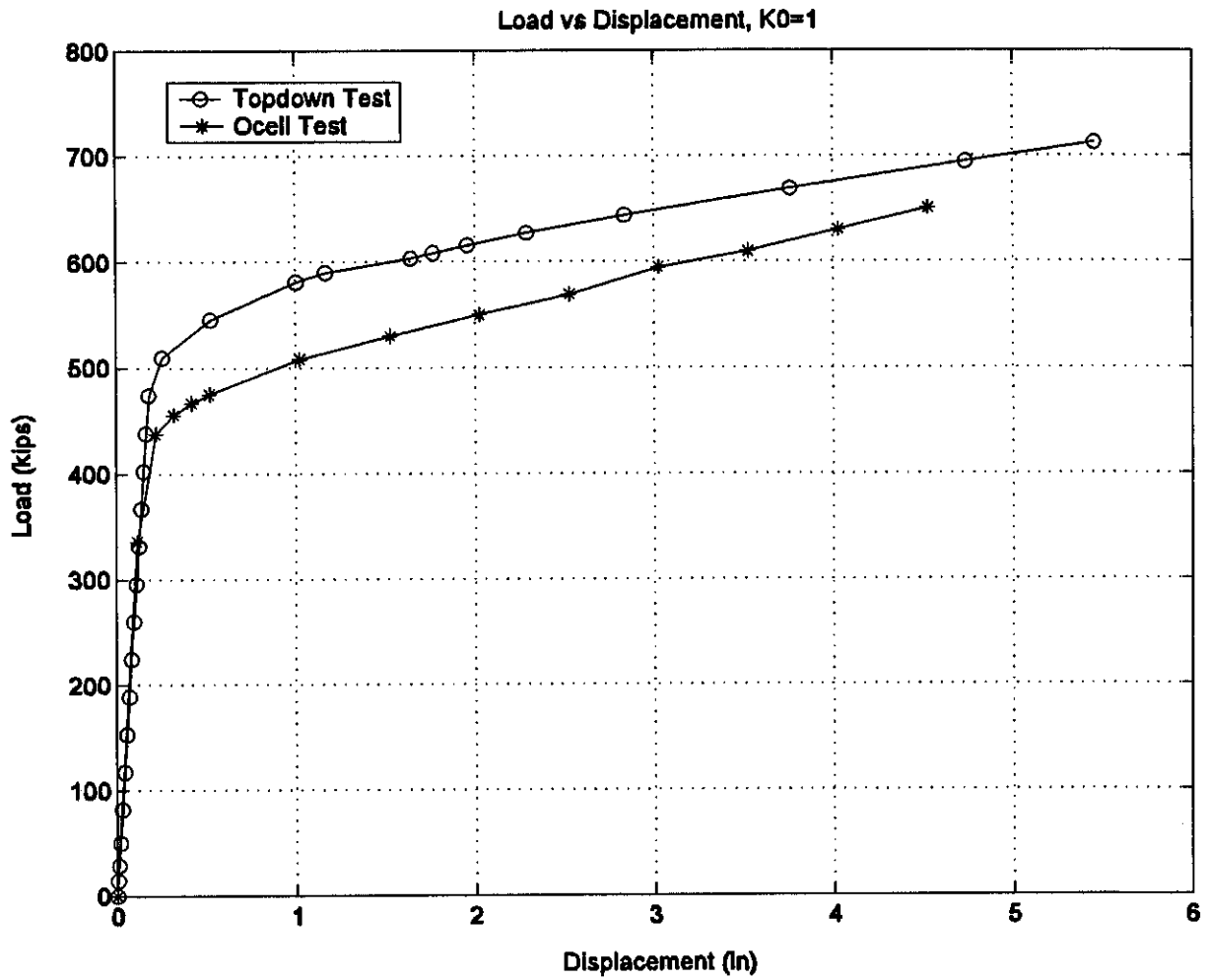


Figure A-20 Comparison of Topdown Test and O-cell Test, $K_0=1$

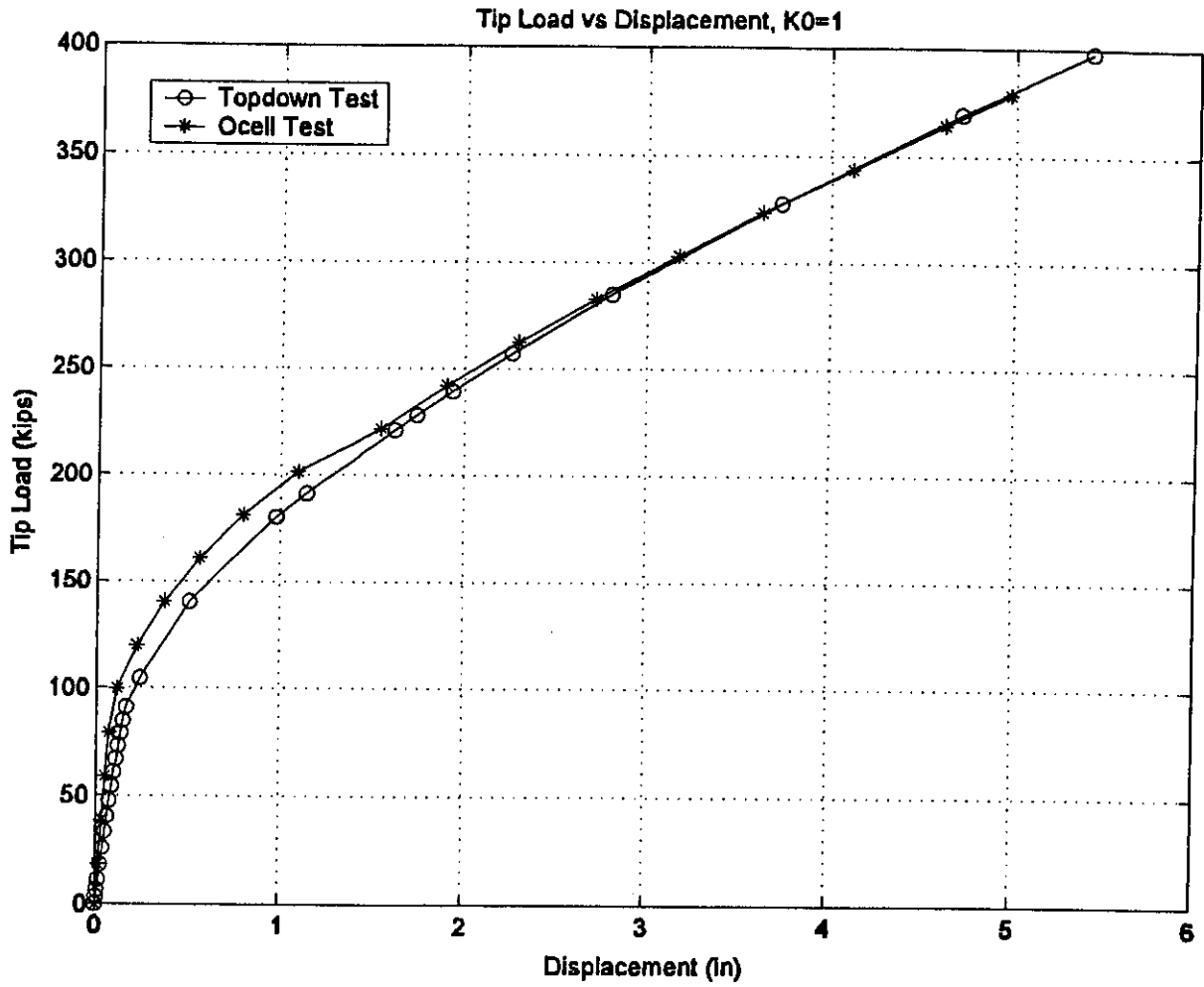


Figure A-21 Tip Load vs Displacement Curve, $K_0=1$

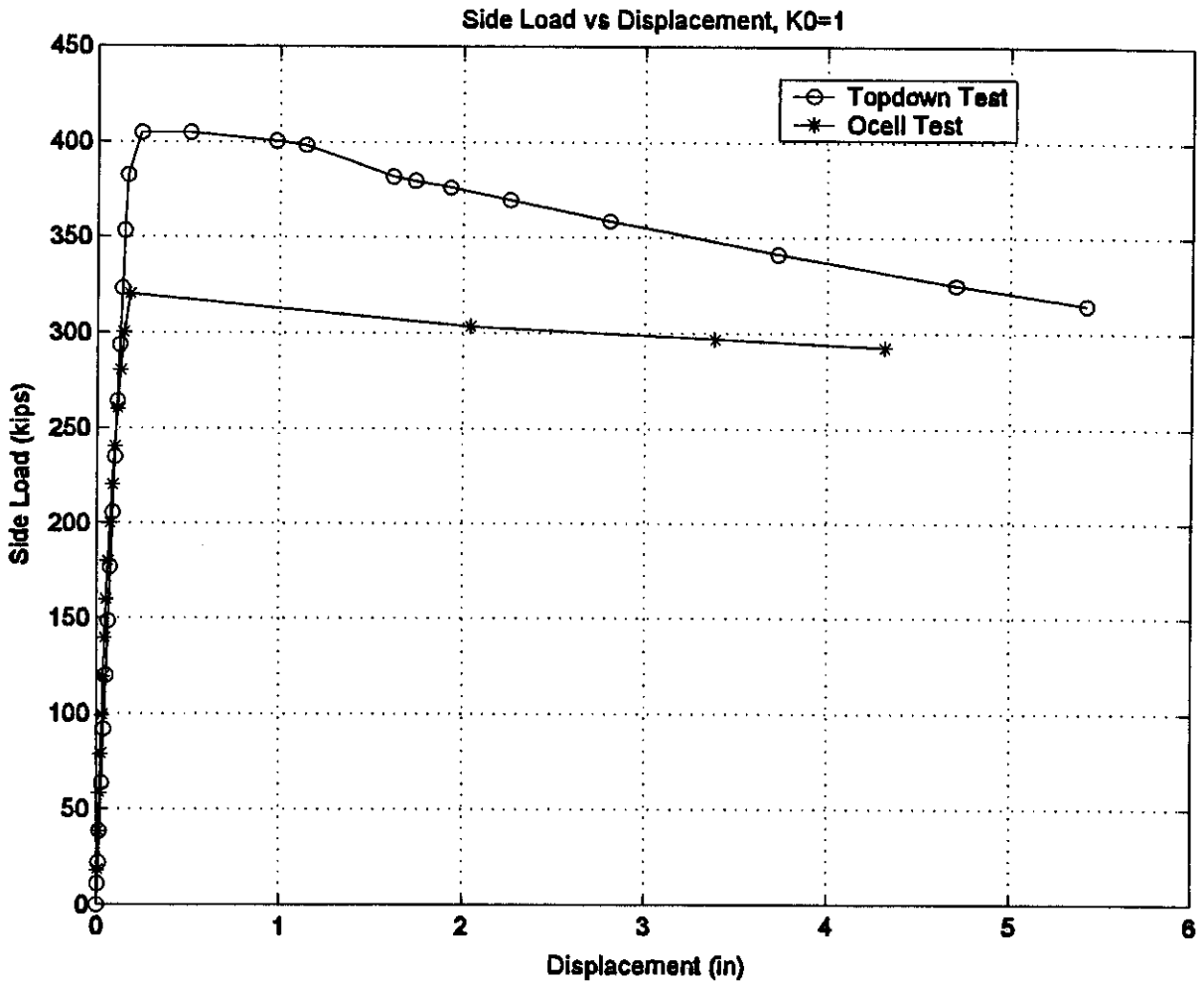


Figure A-22 Side Load vs Displacement Curve, $K_0=1$

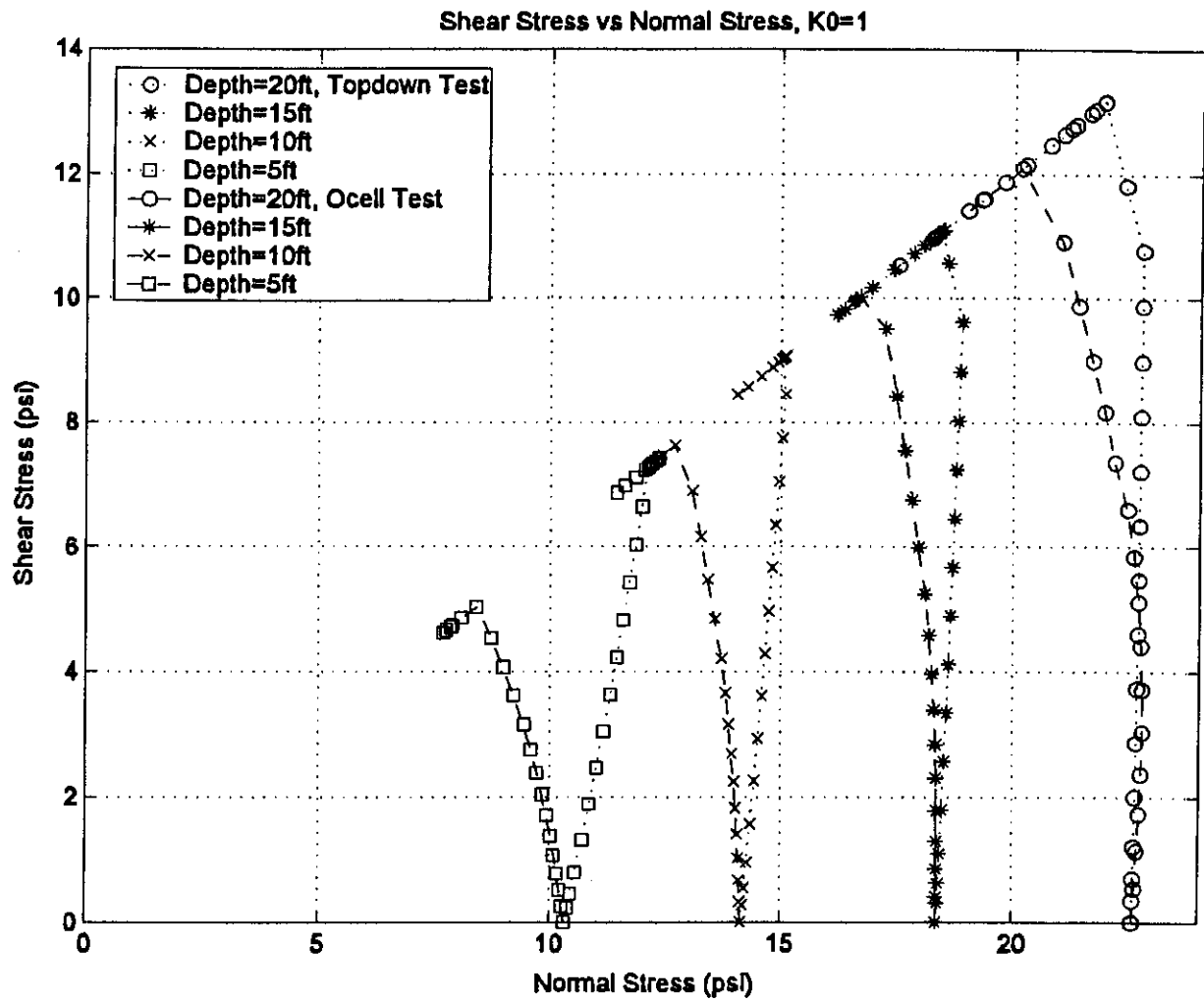


Figure A-23 Stress Path at Different Nodes on Soil-Pile Interface, $K_0=1$

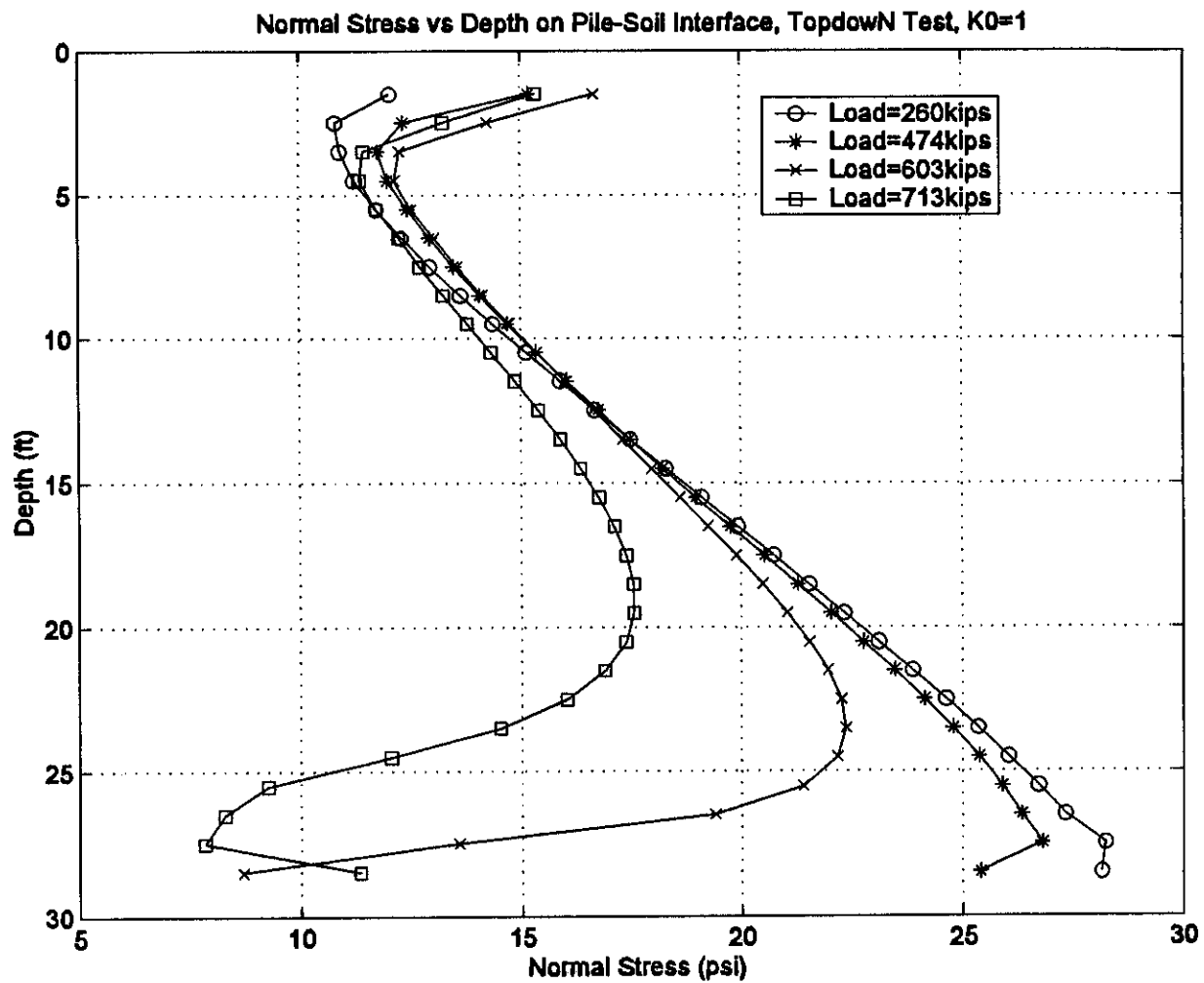


Figure A-24 Normal Stress vs Depth Curve, Topdown Test, $K_0=1$

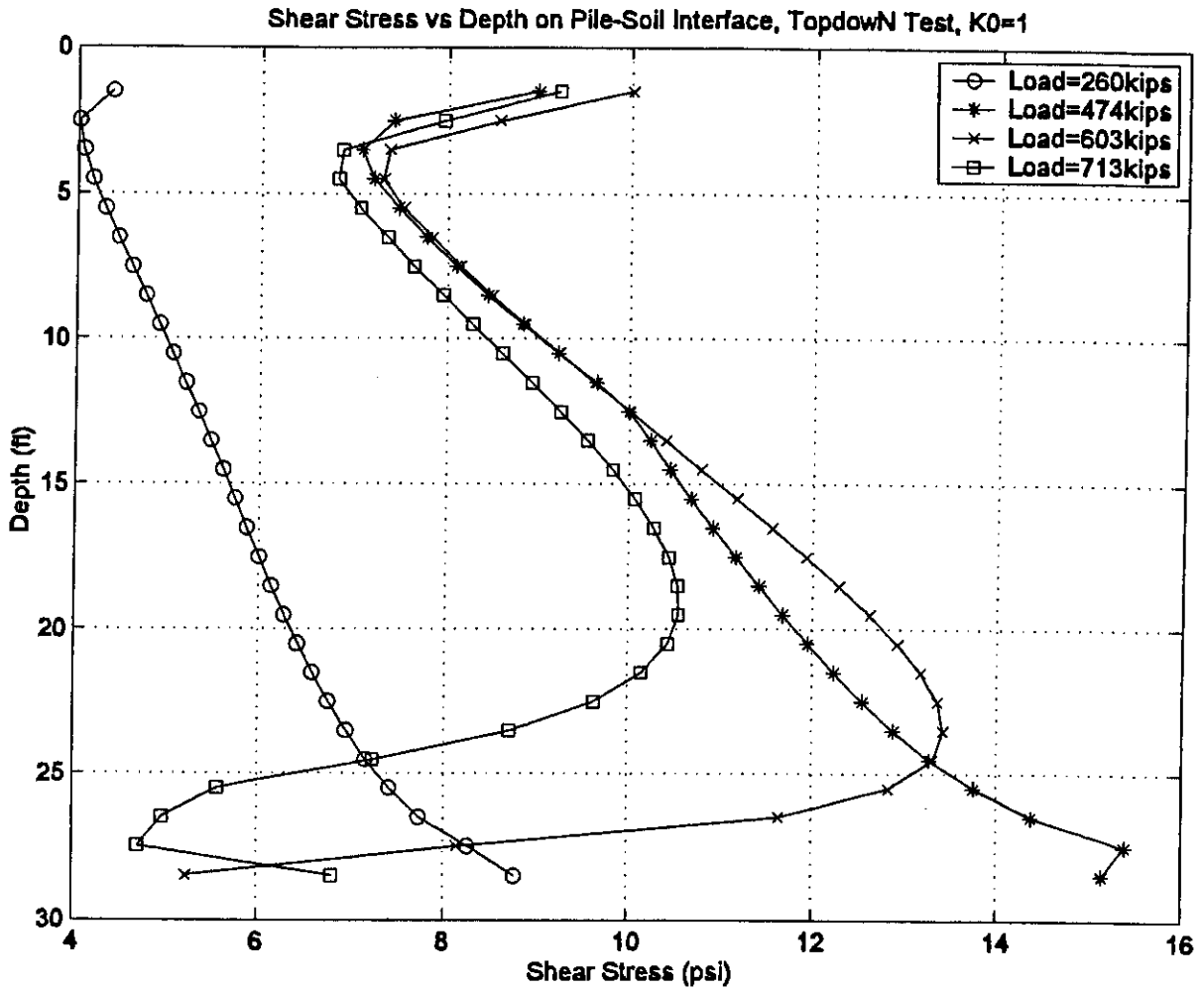


Figure A-25 Shear Stress vs Depth Curve, Topdown Test, $K_0=1$

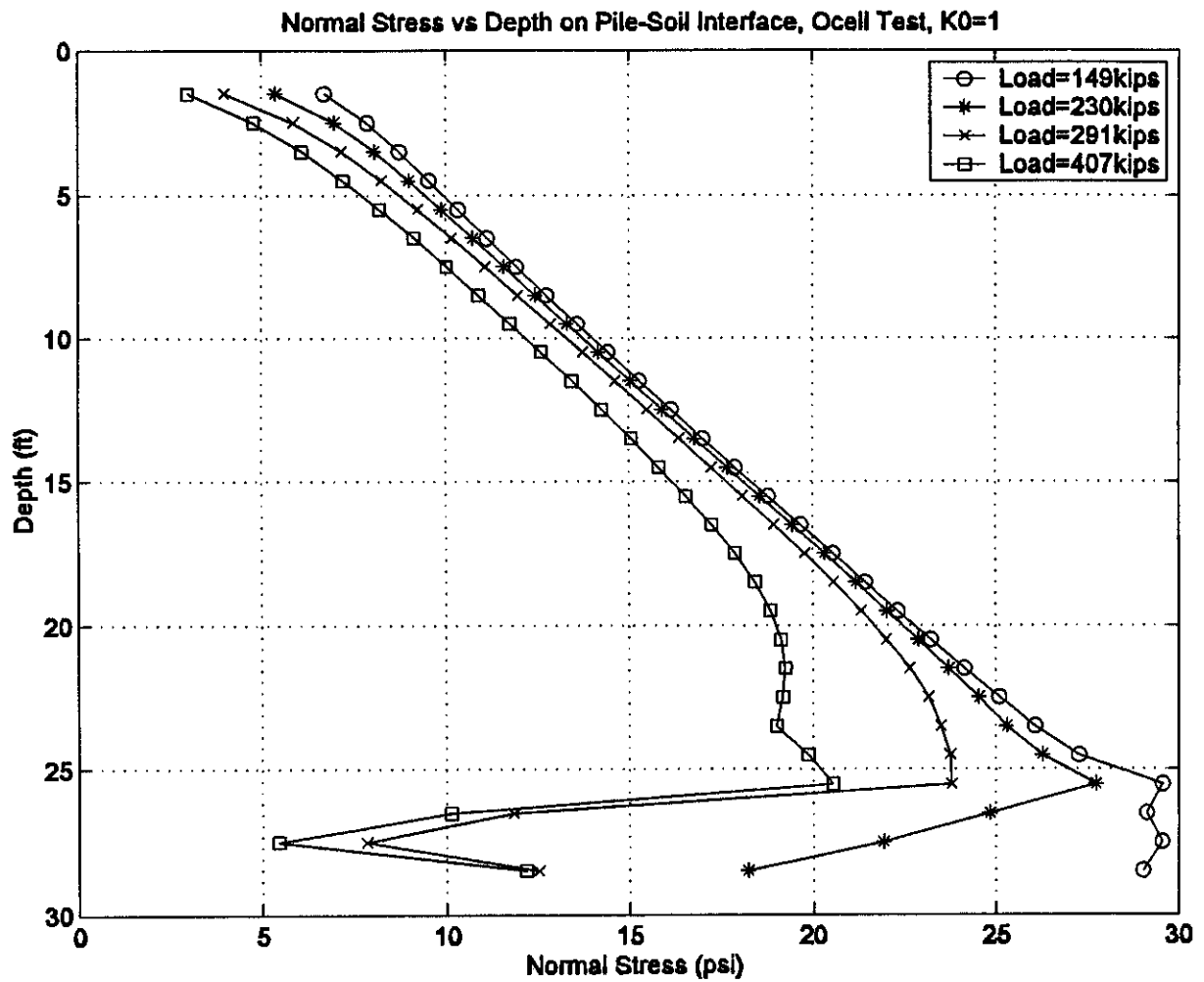


Figure A-26 Normal Stress vs Depth Curve, O-cell Test, $K_0=1$

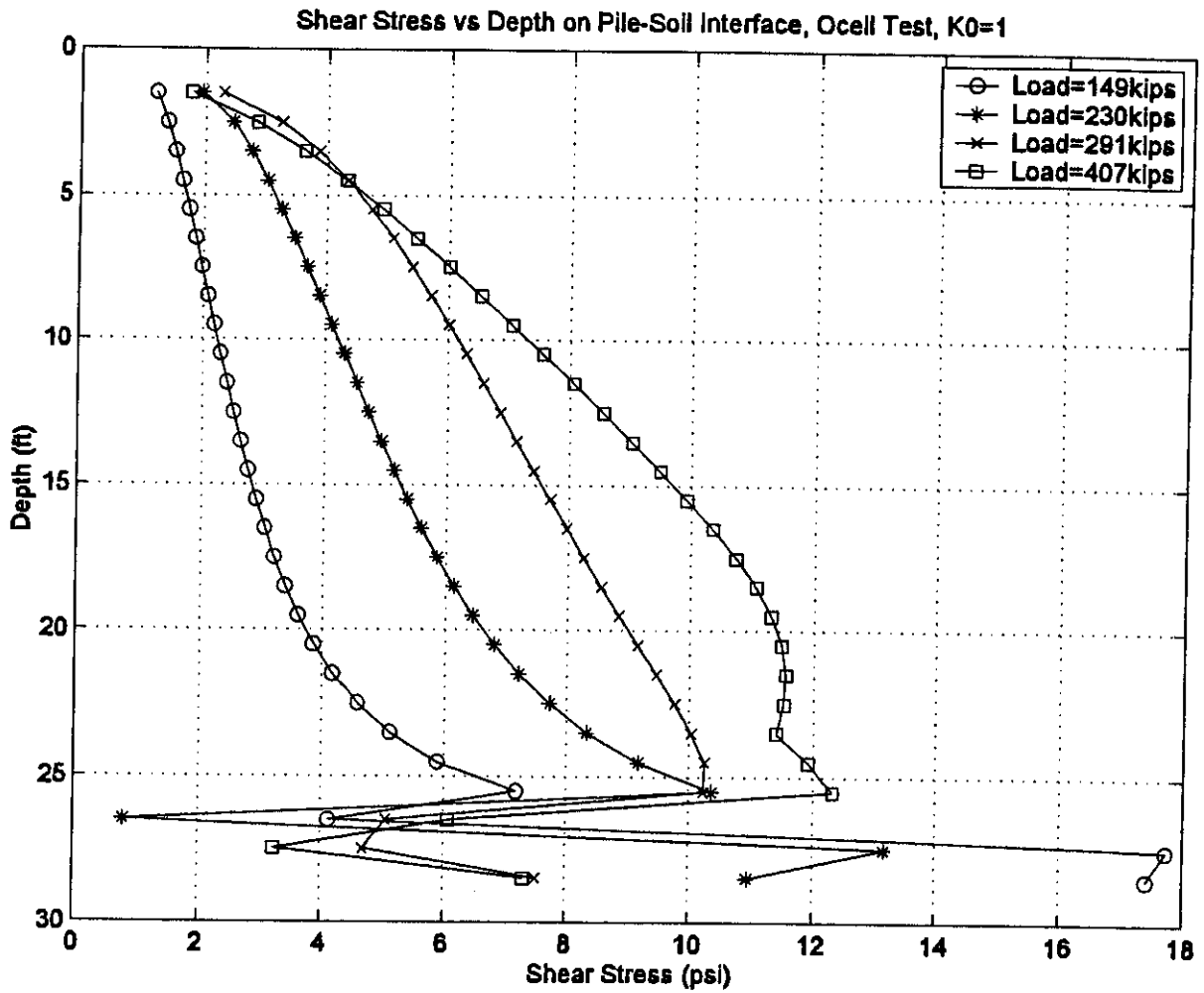


Figure A-27 Shear Stress vs Depth Curve, O-cell Test, $K_0=1$

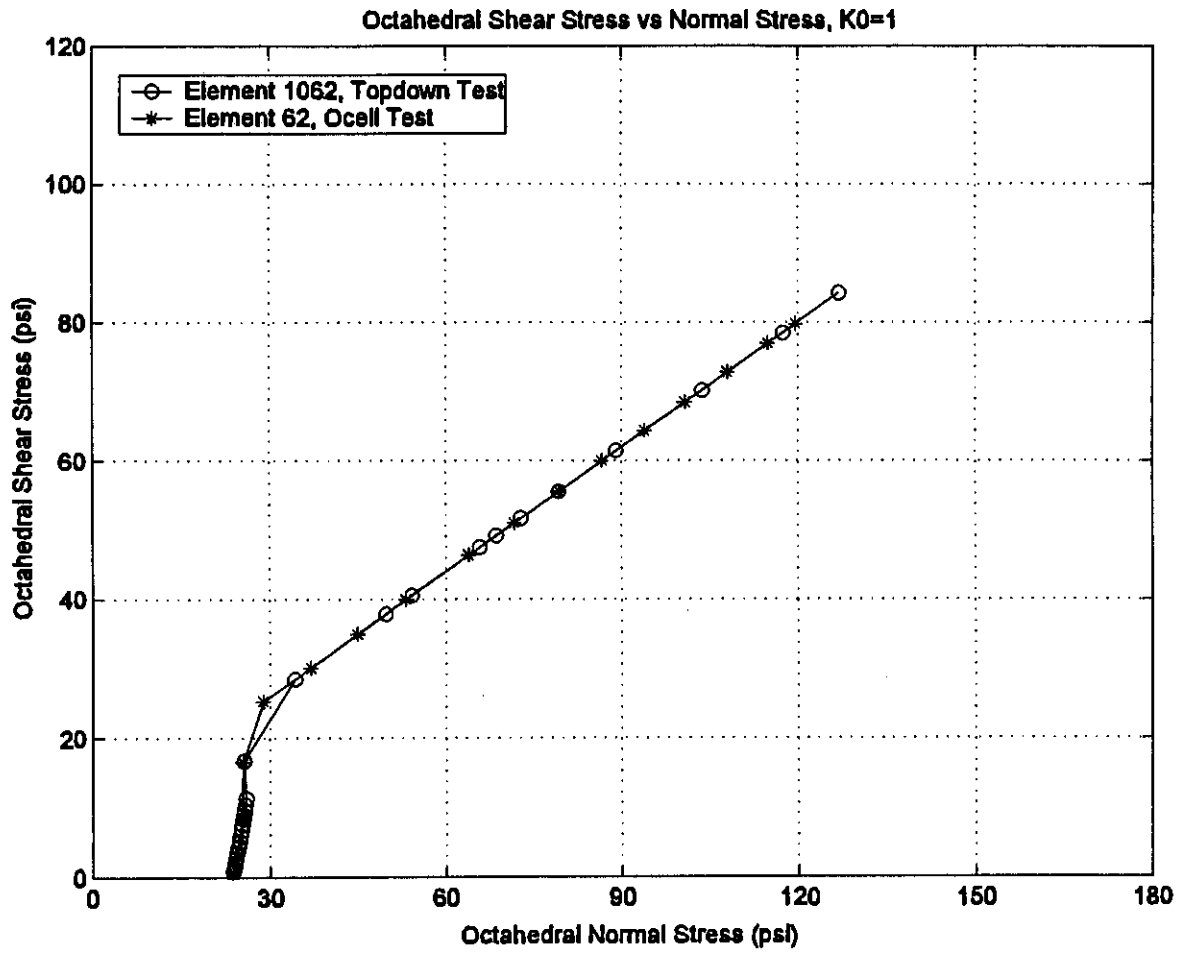


Figure A-28 Stress Path of Soil Element, $K_0=1$

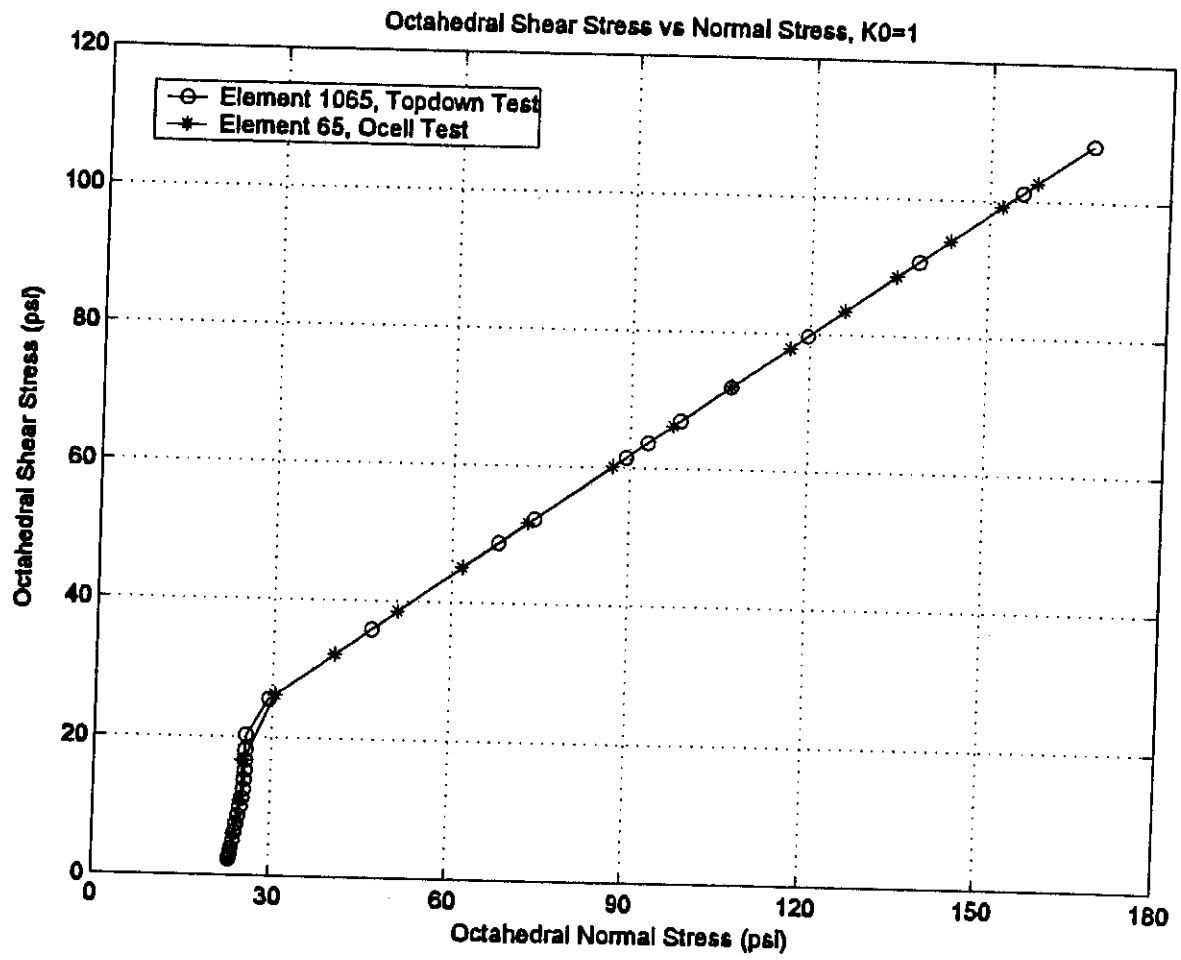


Figure A-29 Stress Path of Soil Element, $K_0=1$

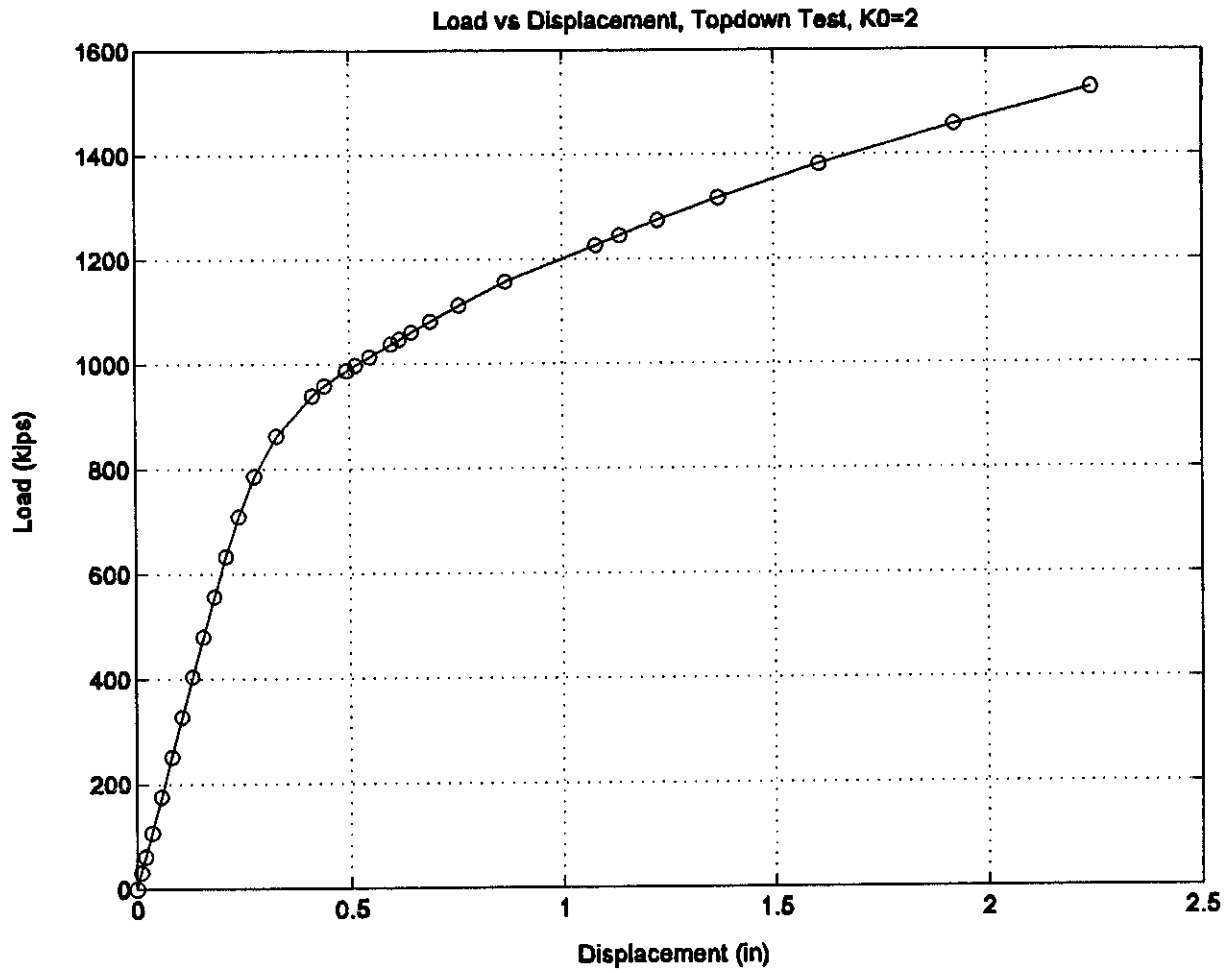


Figure A-30 Load-Displacement Curve, Topdown Test, $K_0=2$

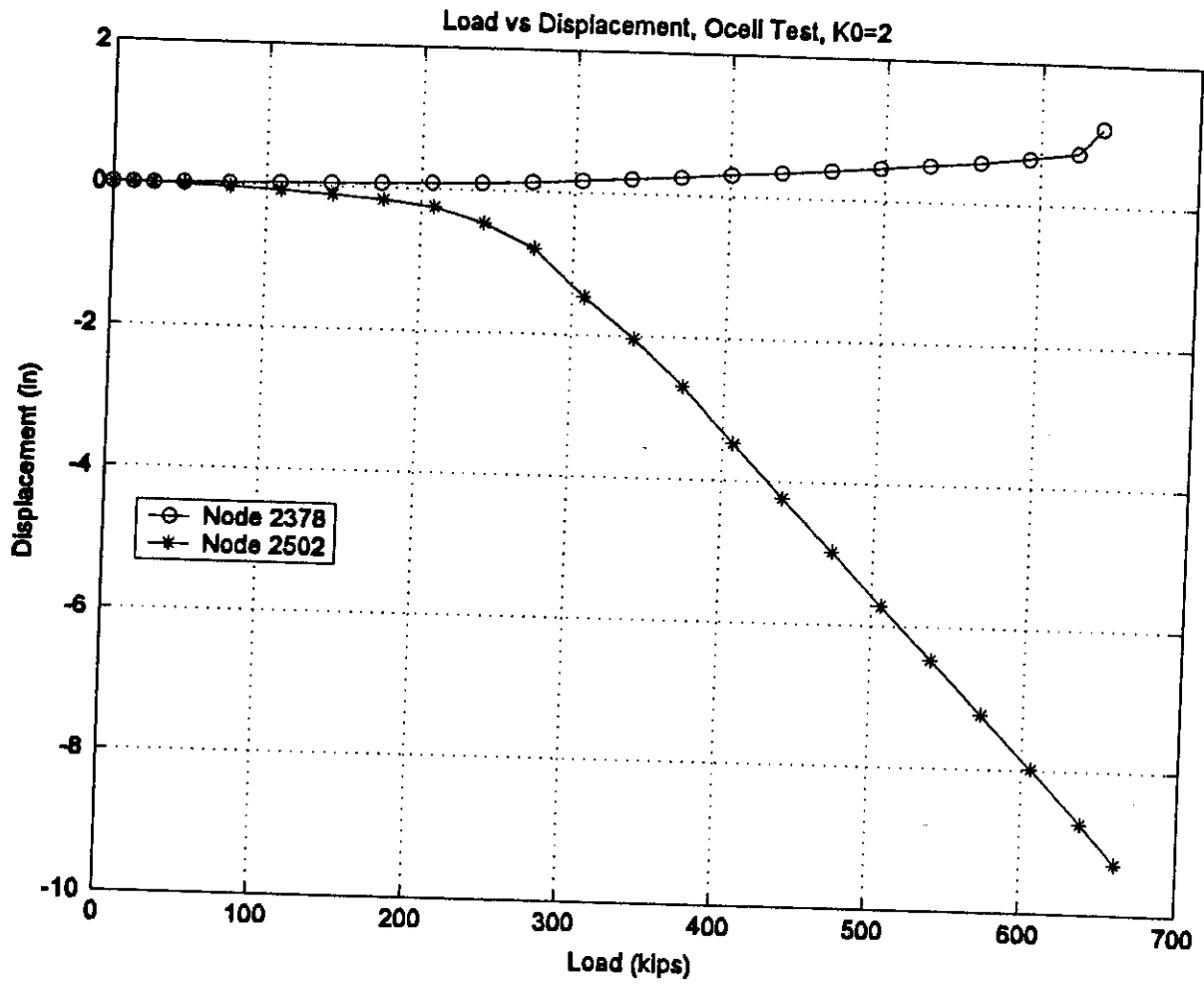


Figure A-31 Load-Displacement Curve, O-cell Test, $K_0=2$

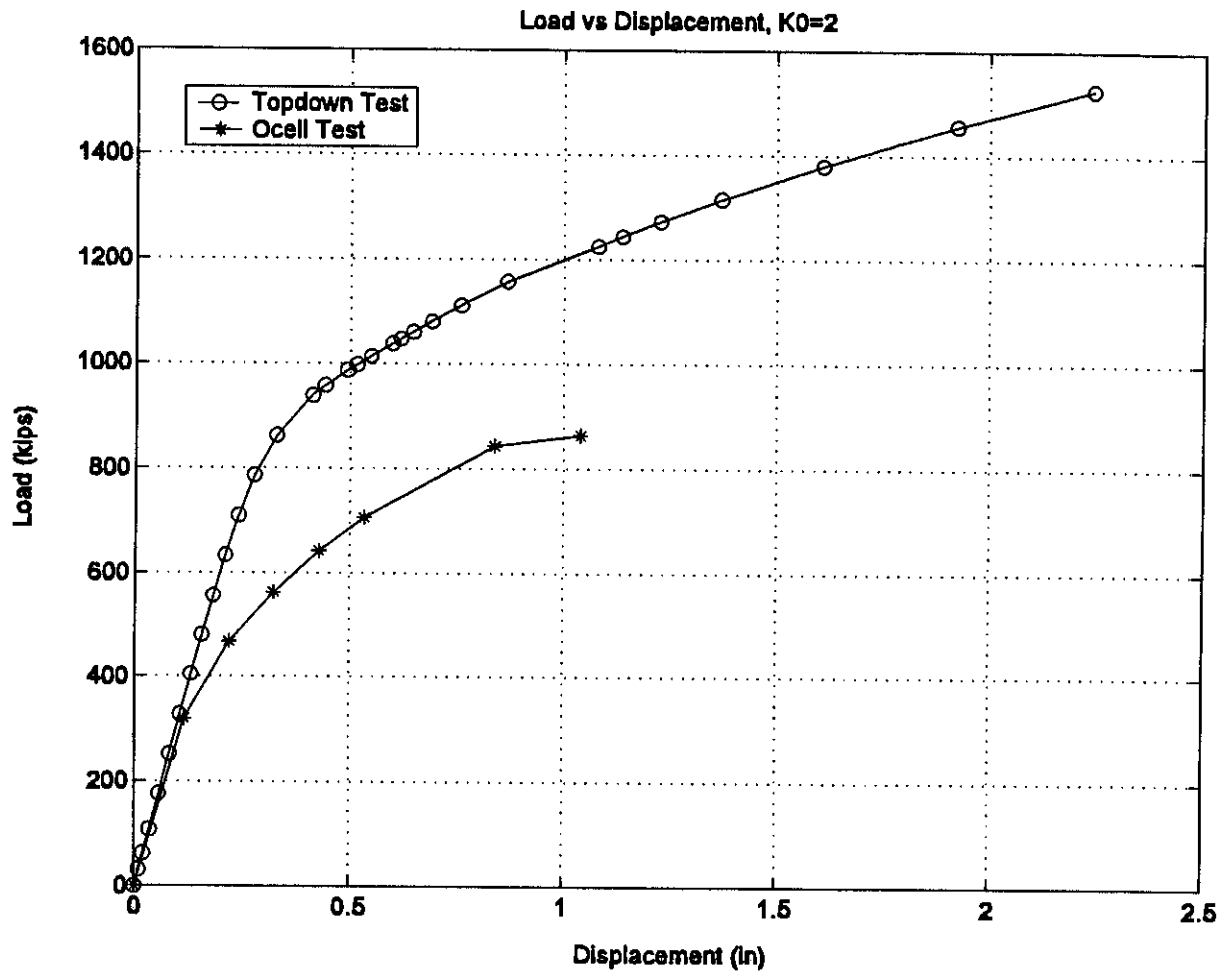


Figure A-32 Comparison of Topdown Test and O-cell Test, $K_0=2$

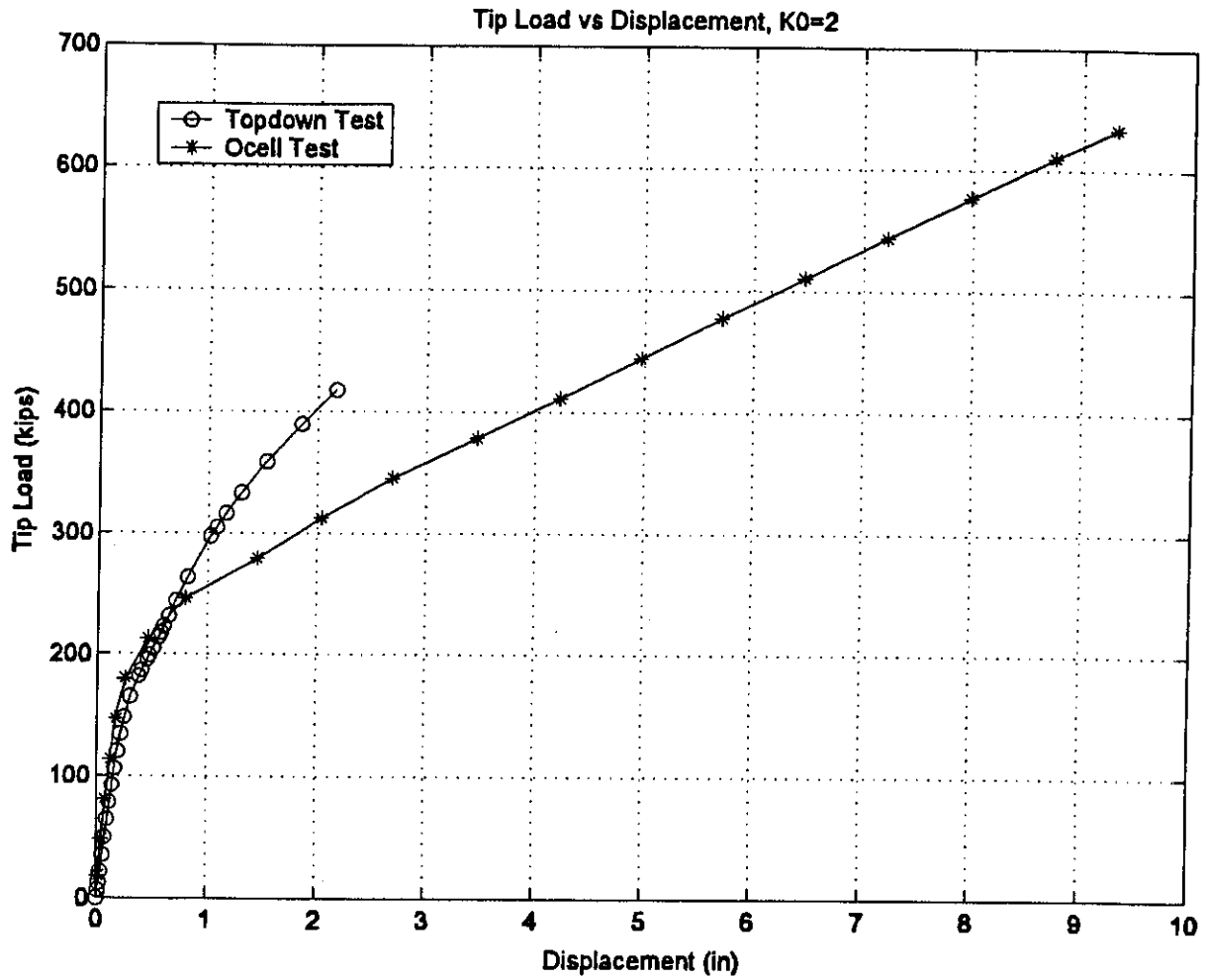


Figure A-33 Tip Load vs Displacement Curve, $K_0=2$

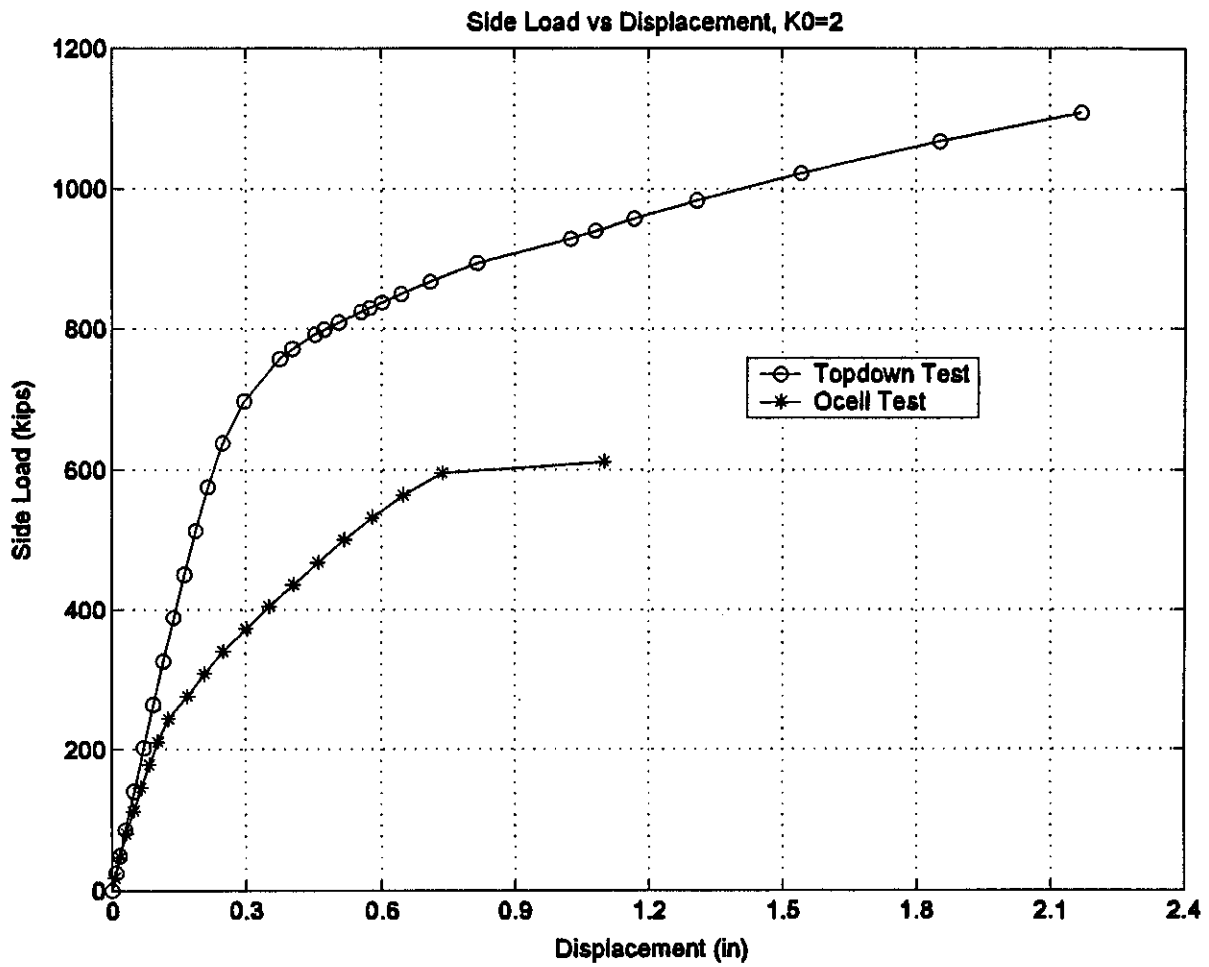


Figure A-34 Side Load vs Displacement Curve, $K_0=2$

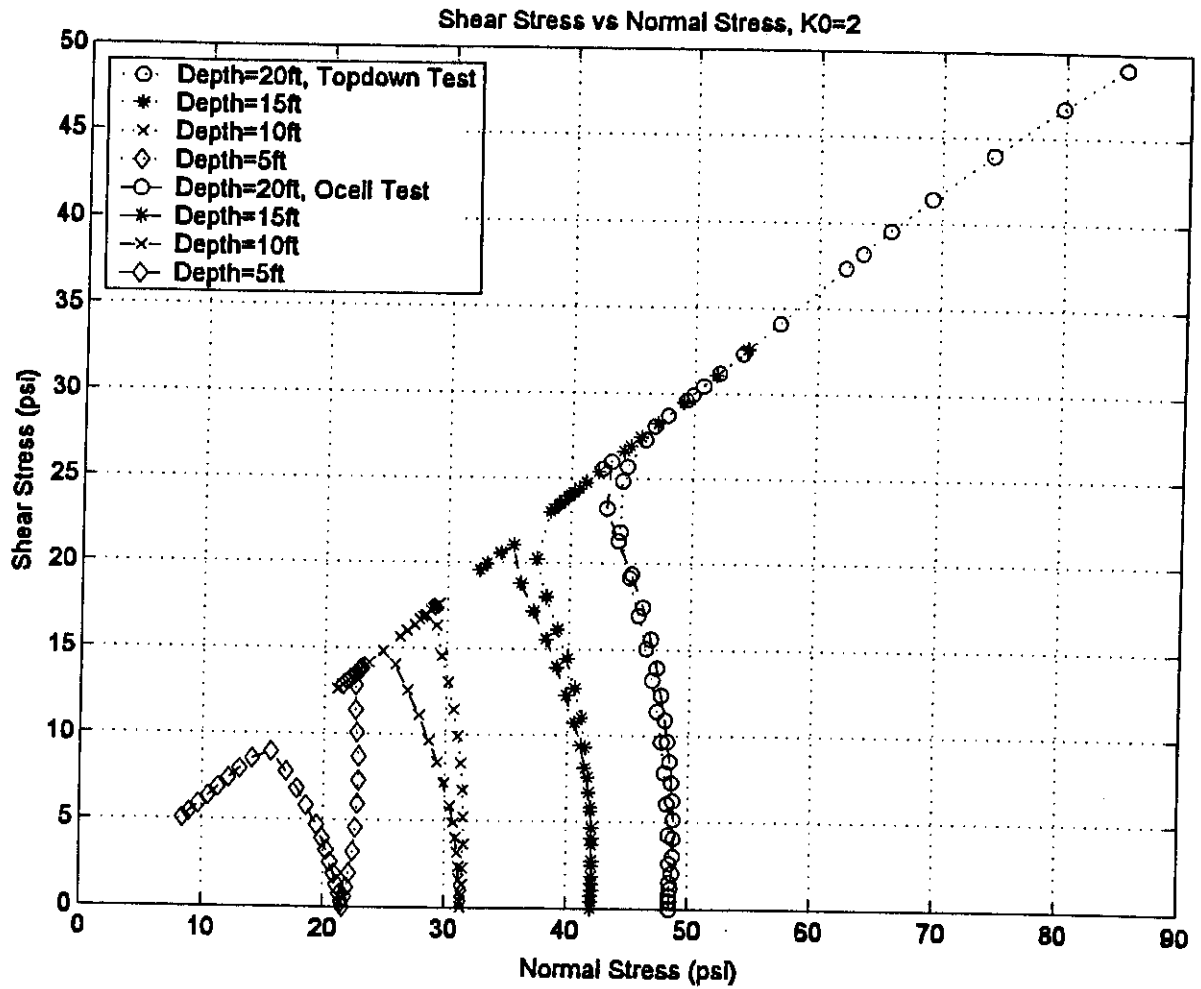


Figure A-35 Stress Path at Different Nodes on Soil-Pile Interface, $K_0=2$

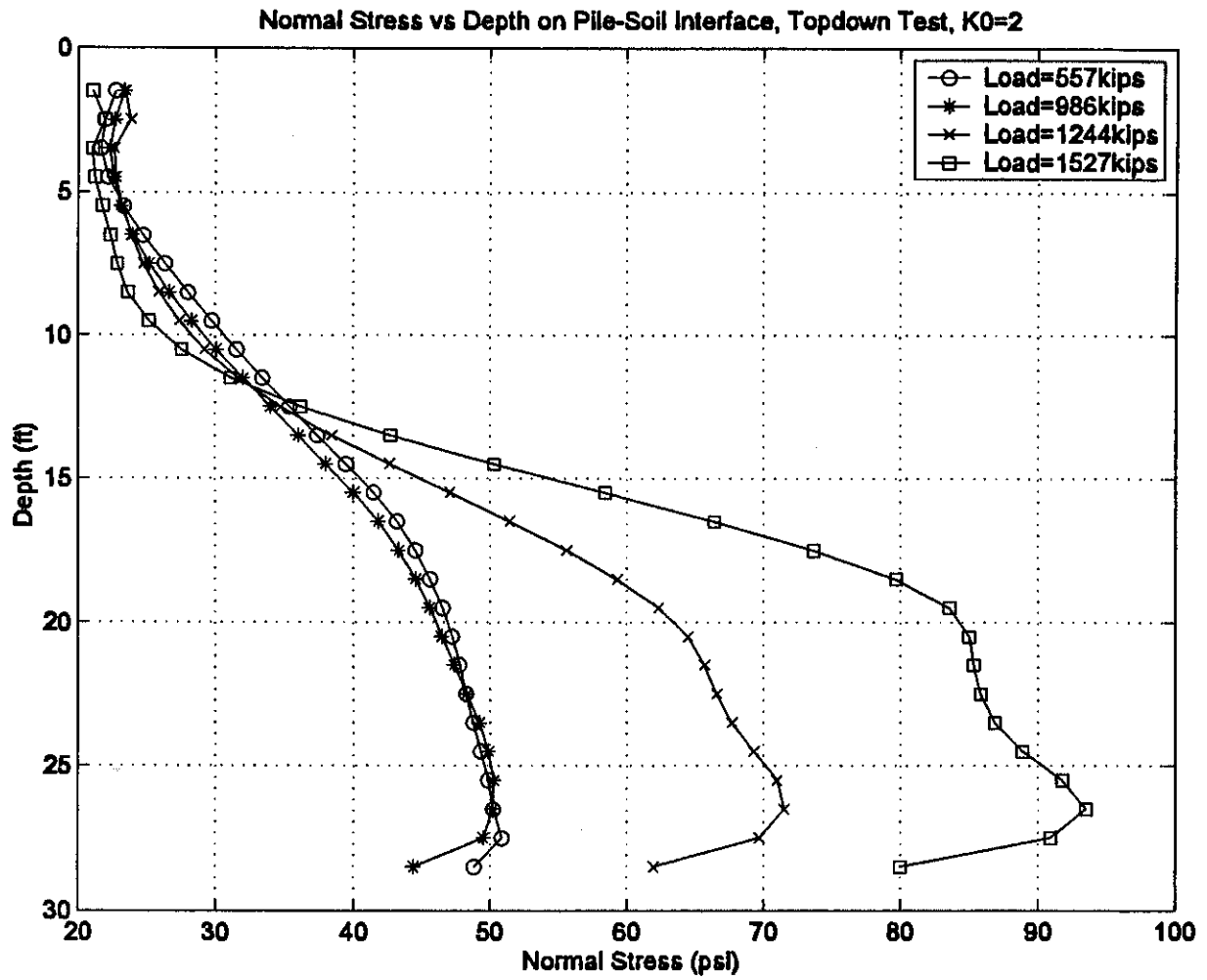


Figure A-36 Normal Stress vs Depth Curve, Topdown Test, $K_0=2$

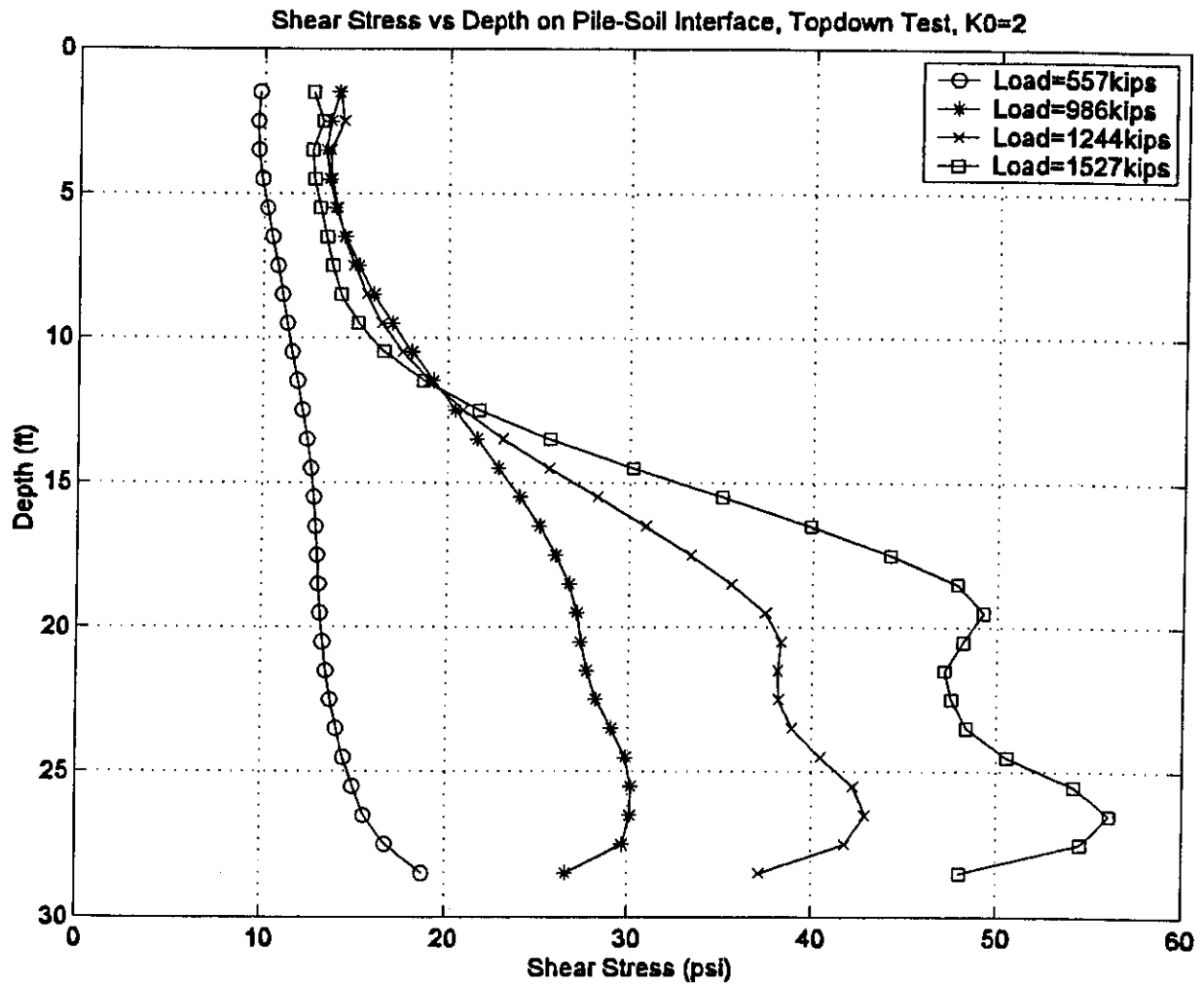


Figure A-37 Shear Stress vs Depth Curve, Topdown Test, $K_0=2$

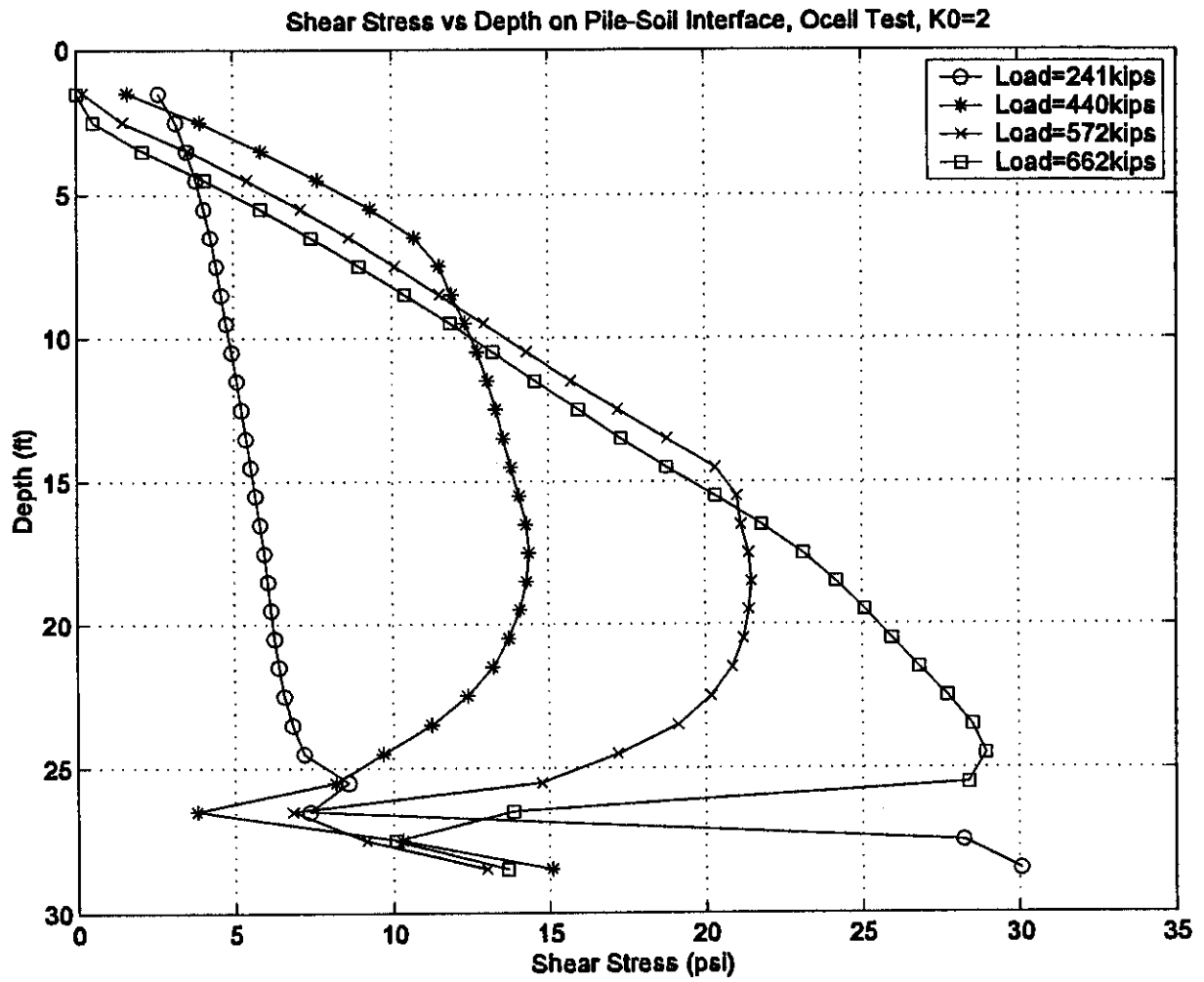


Figure A-39 Shear Stress vs Depth Curve, O-cell Test, $K_0=2$

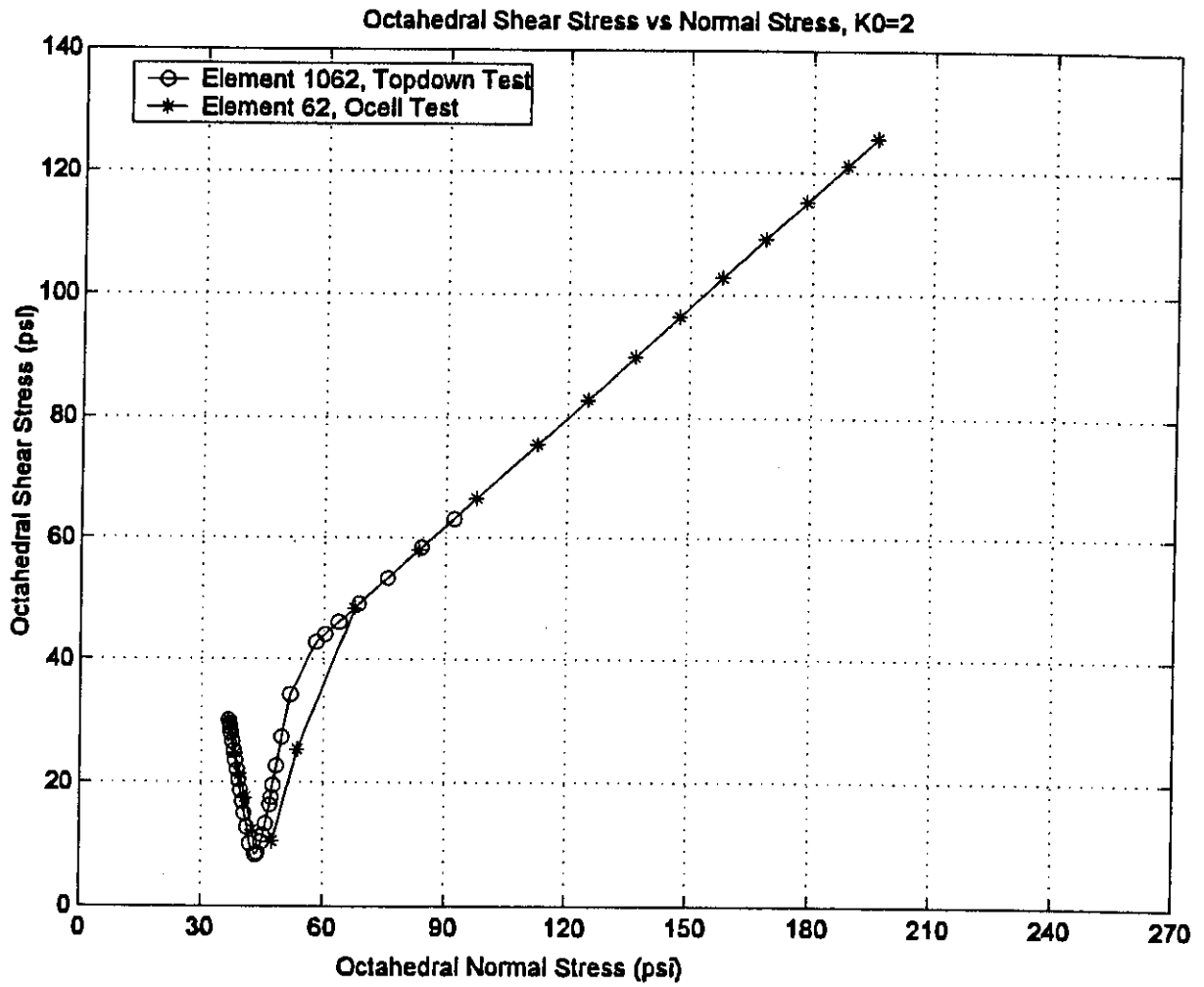


Figure A-40 Stress Path of Soil Element, $K_0=2$

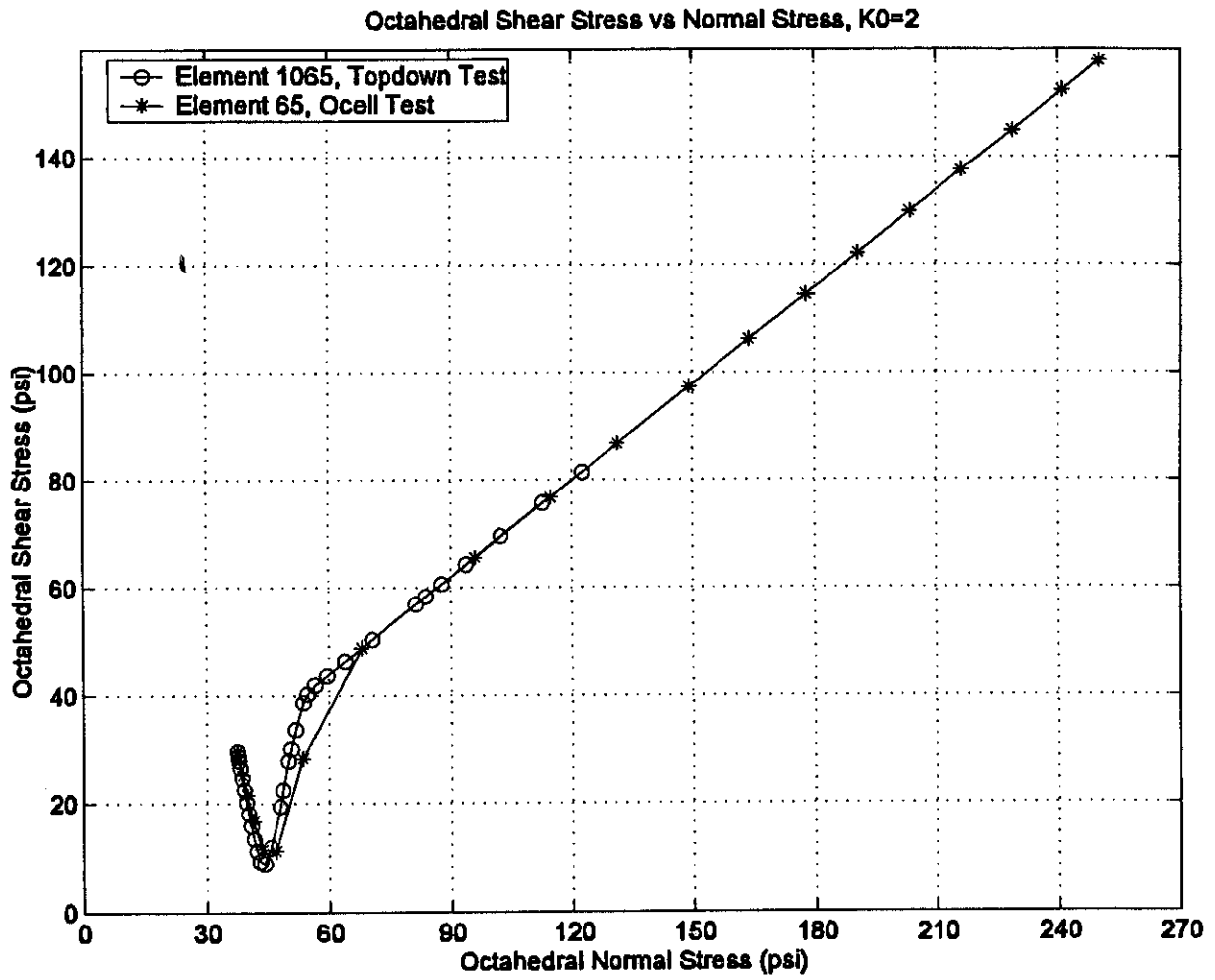


Figure A-41 Stress Path of Soil Element, $K_0=2$

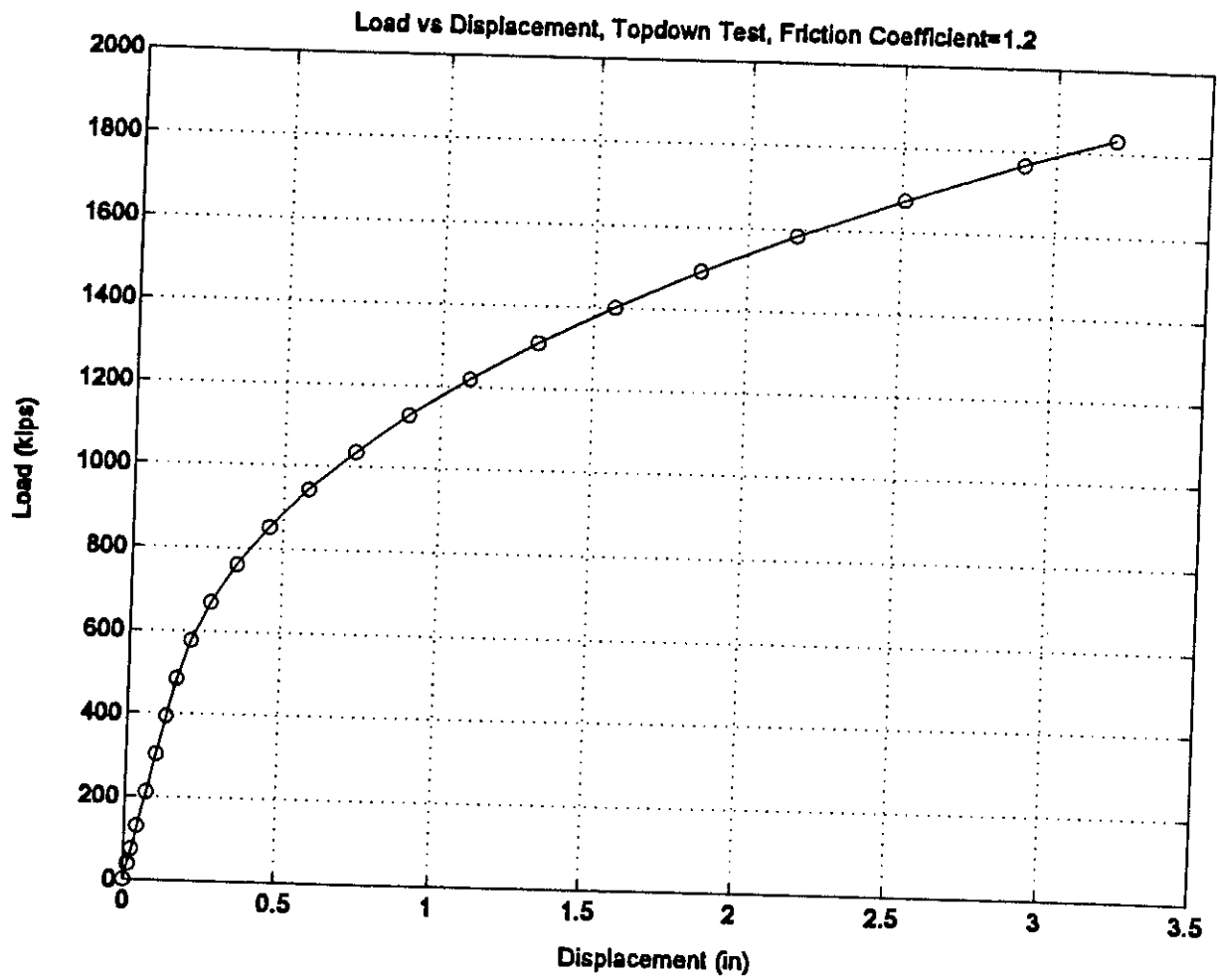


Figure A-42 Load-Displacement Curve, Topdown Test, $\mu=1.2$

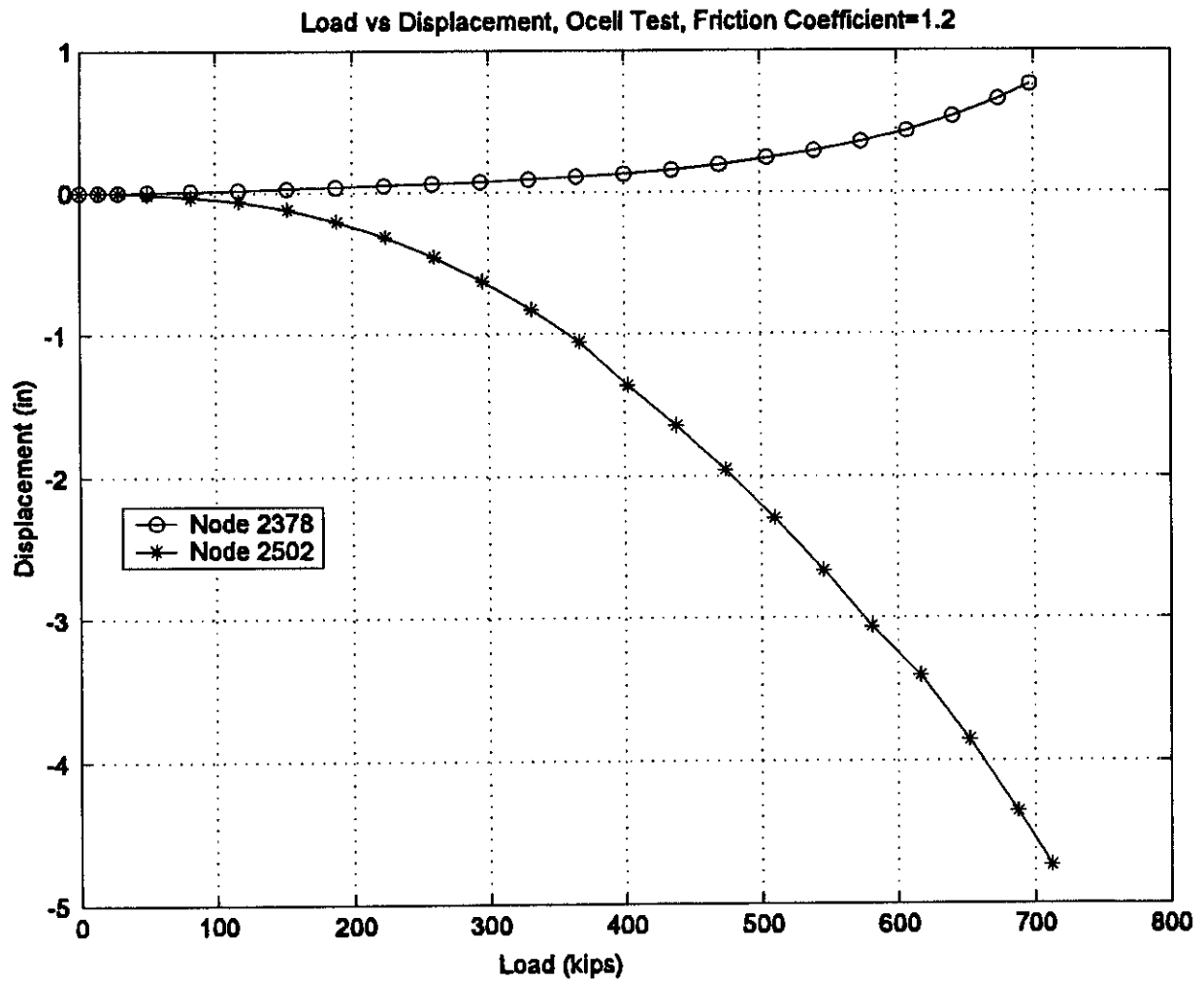


Figure A-43 Load-Displacement Curve, O-cell Test, $\mu=1.2$

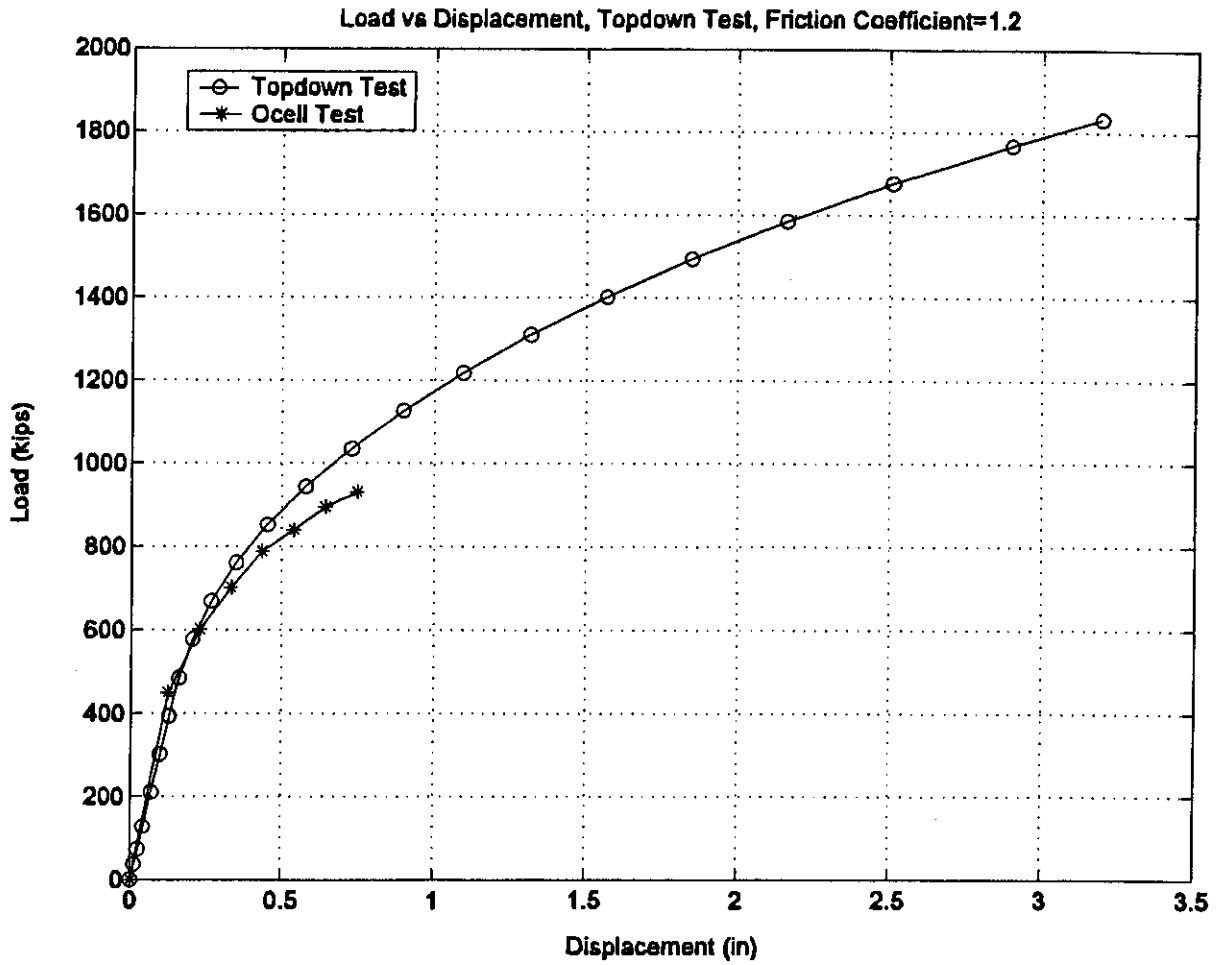


Figure A-44 Comparison of Topdown Test and O-cell Test, $\mu=1.2$

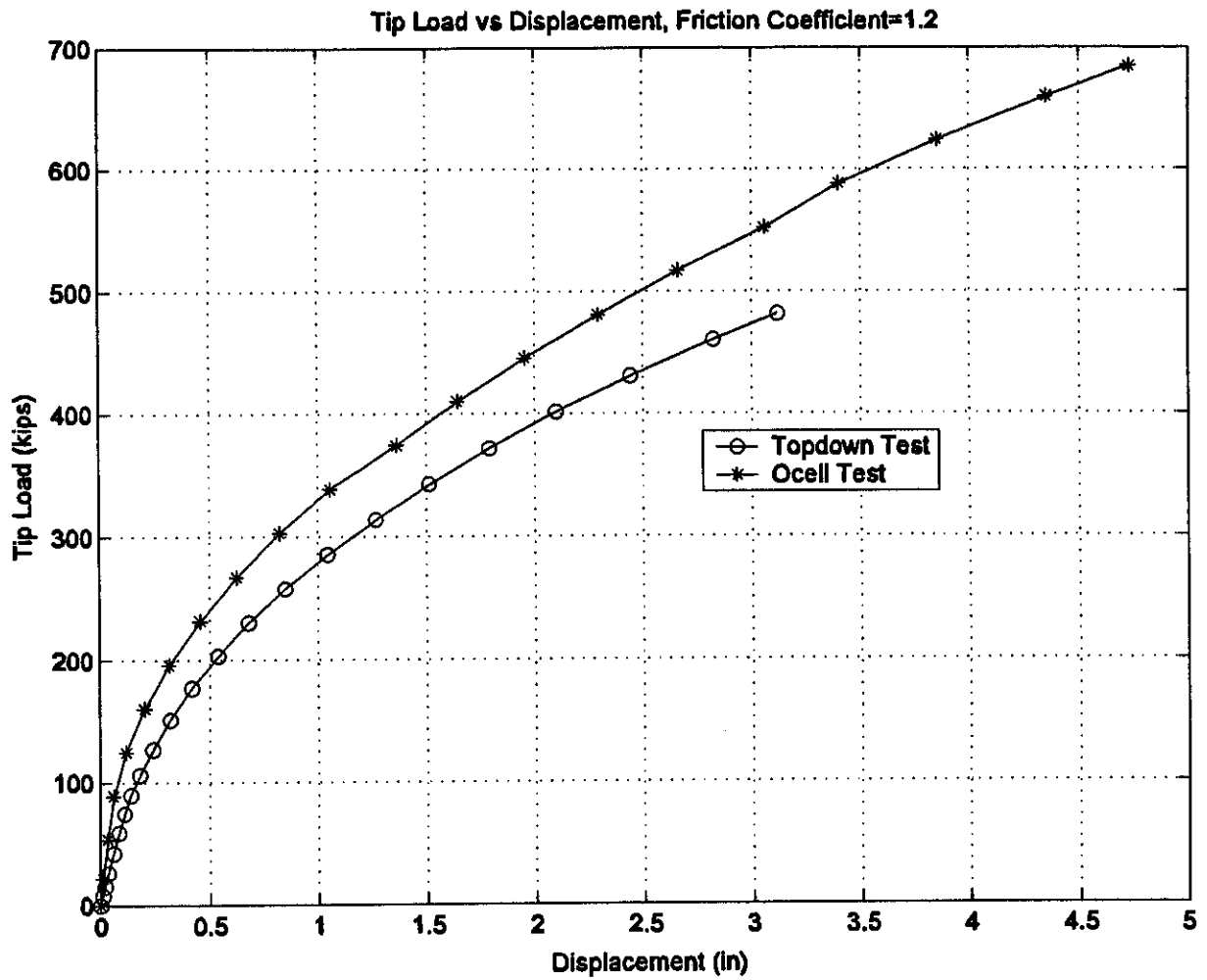


Figure A-45 Tip Load vs Displacement Curve, $\mu=1.2$

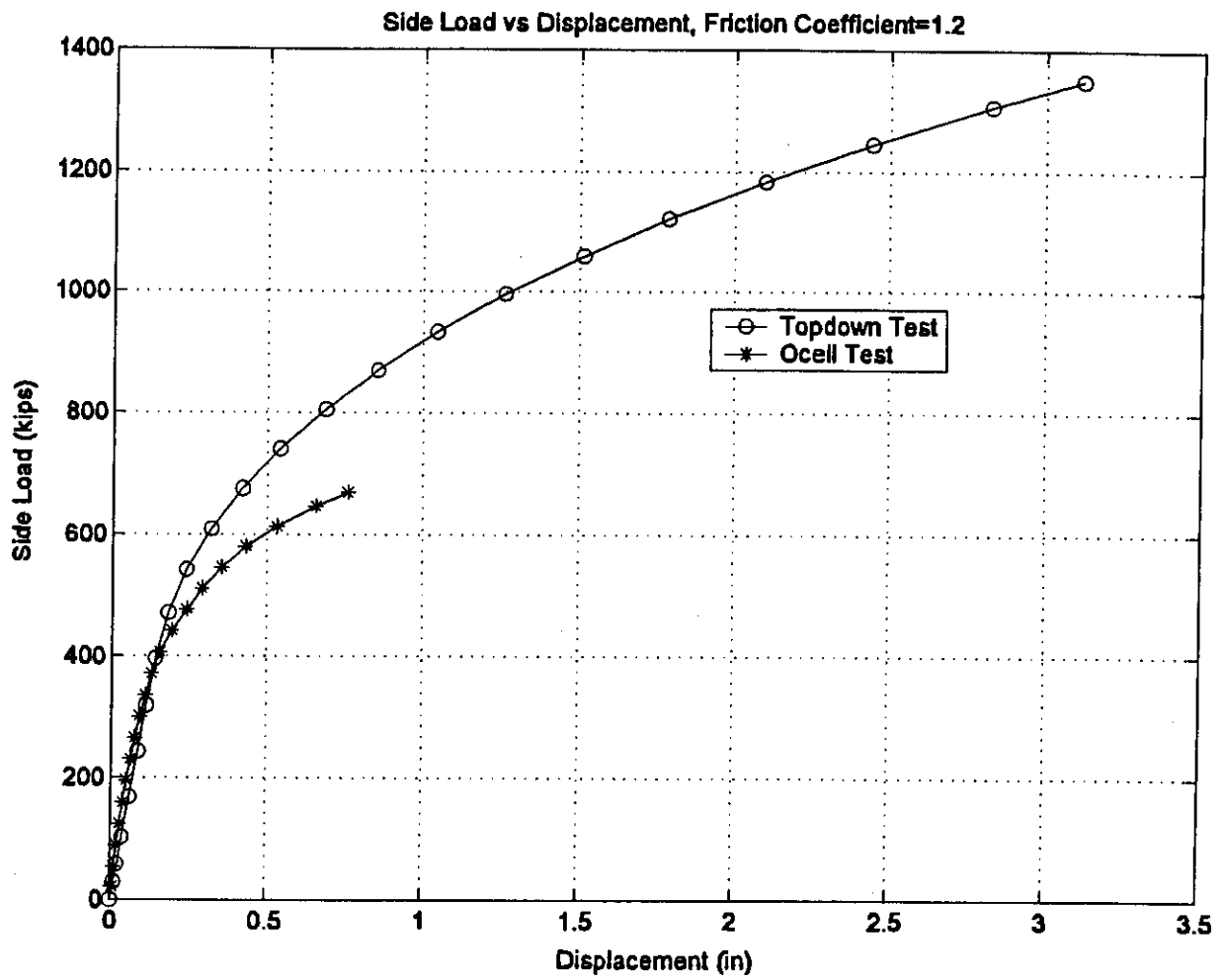


Figure A-46 Side Load vs Displacement Curve, $\mu=1.2$

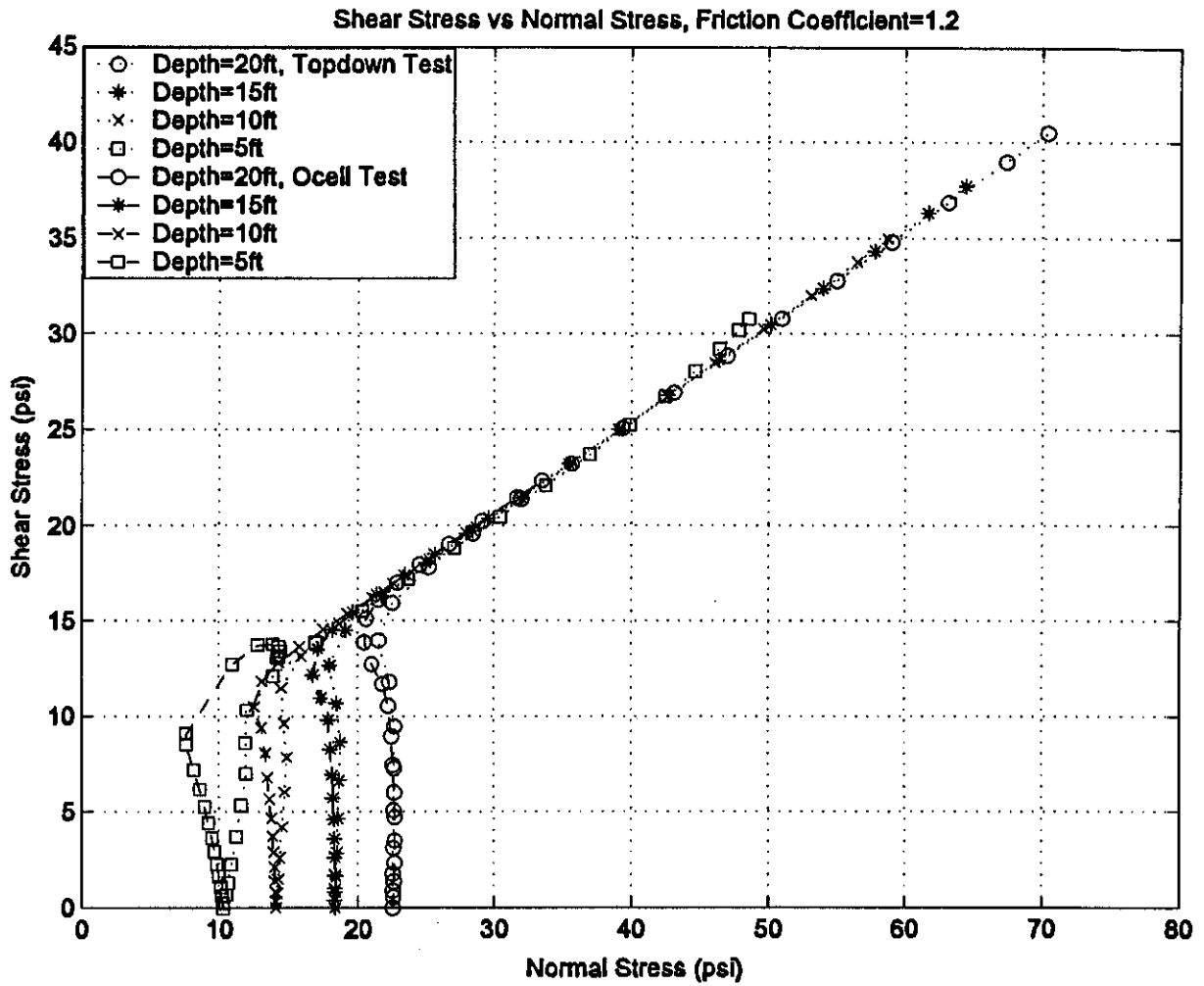


Figure A-47 Stress Path at Different Nodes on Soil-Pile Interface, $\mu = 1.2$

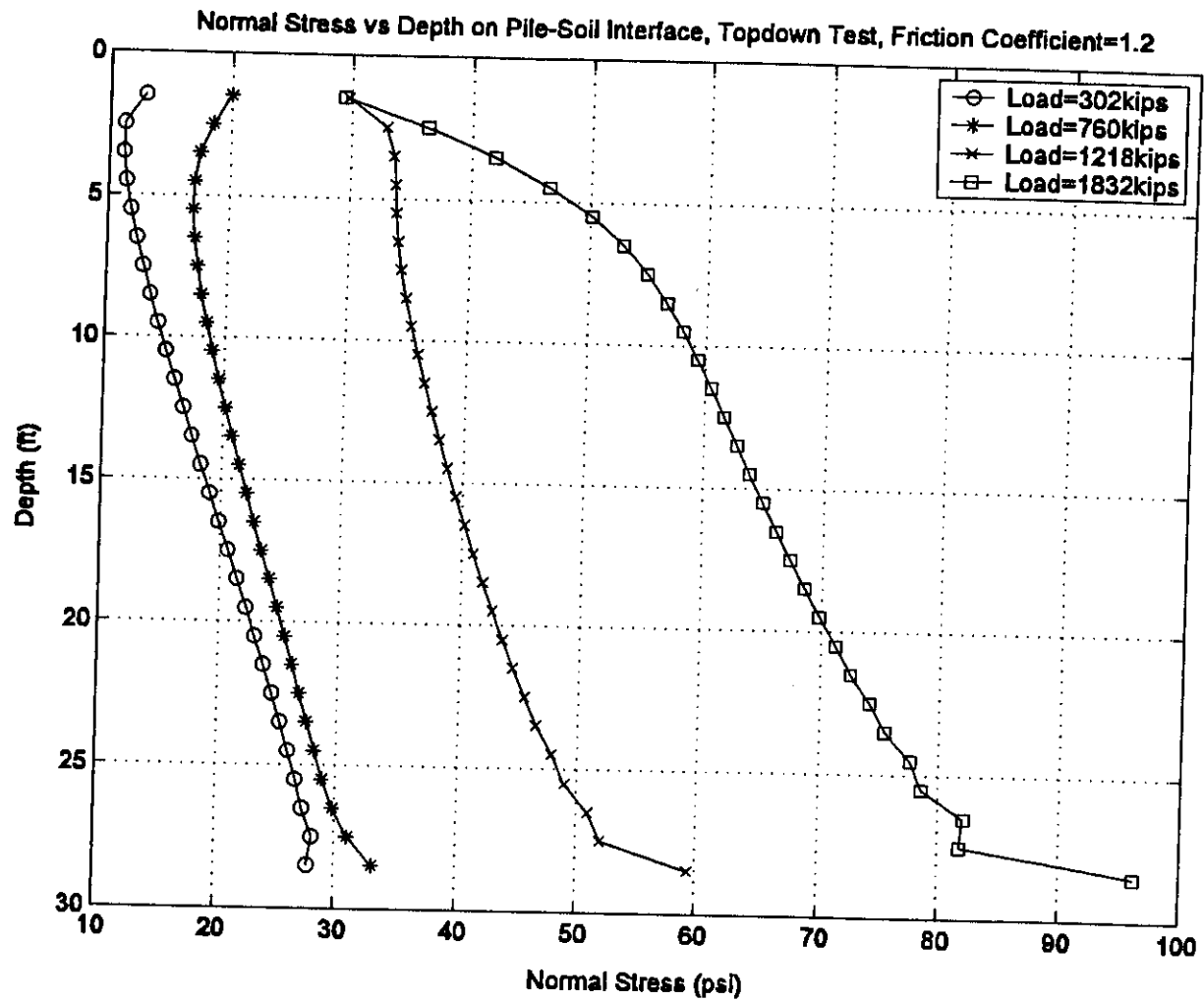


Figure A-48 Normal Stress vs Depth Curve, Topdown Test, $\mu=1.2$

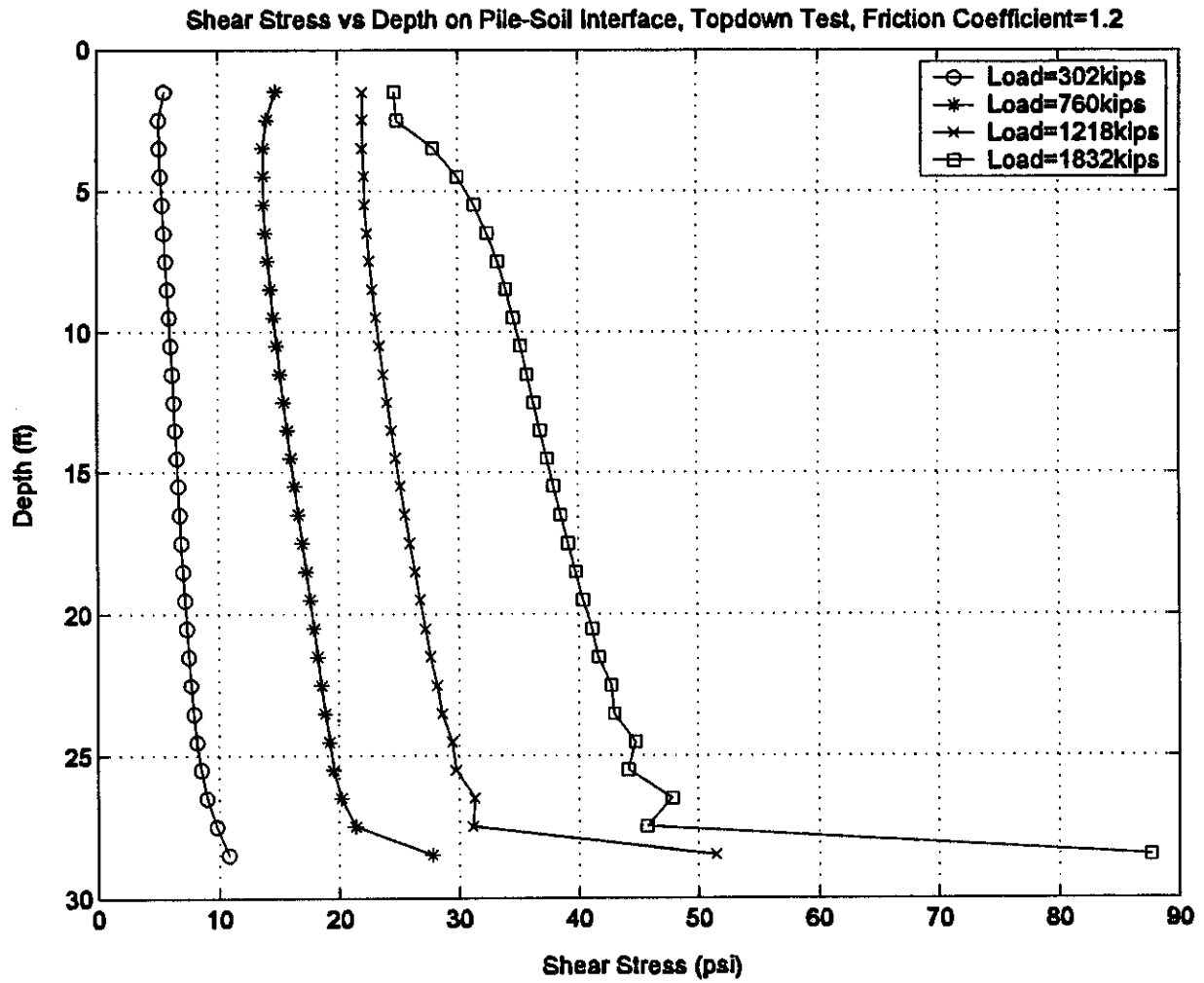


Figure A-49 Shear Stress vs Depth Curve, Topdown Test, $\mu=1.2$

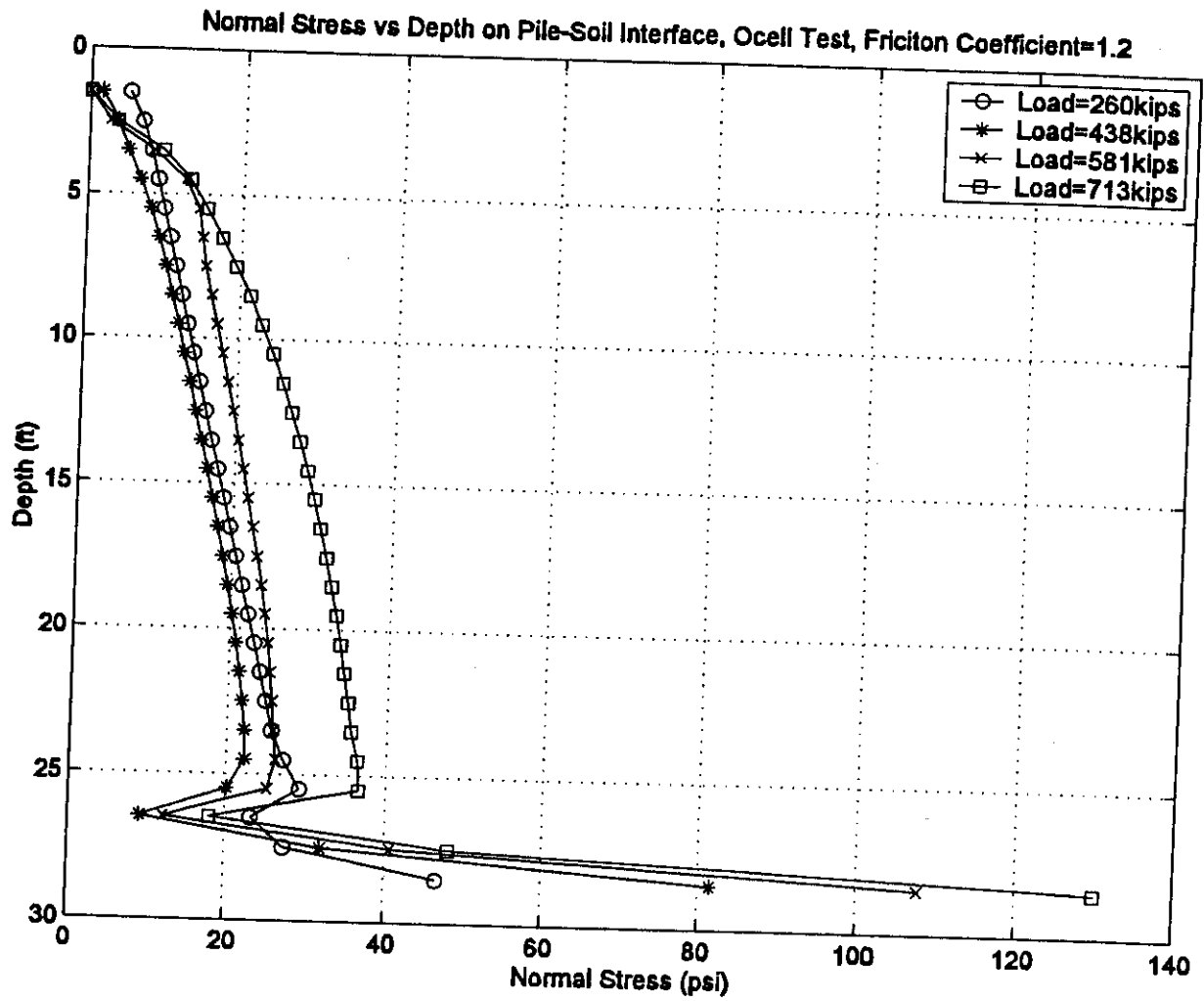


Figure A-50 Normal Stress vs Depth Curve, O-cell Test, $\mu=1.2$

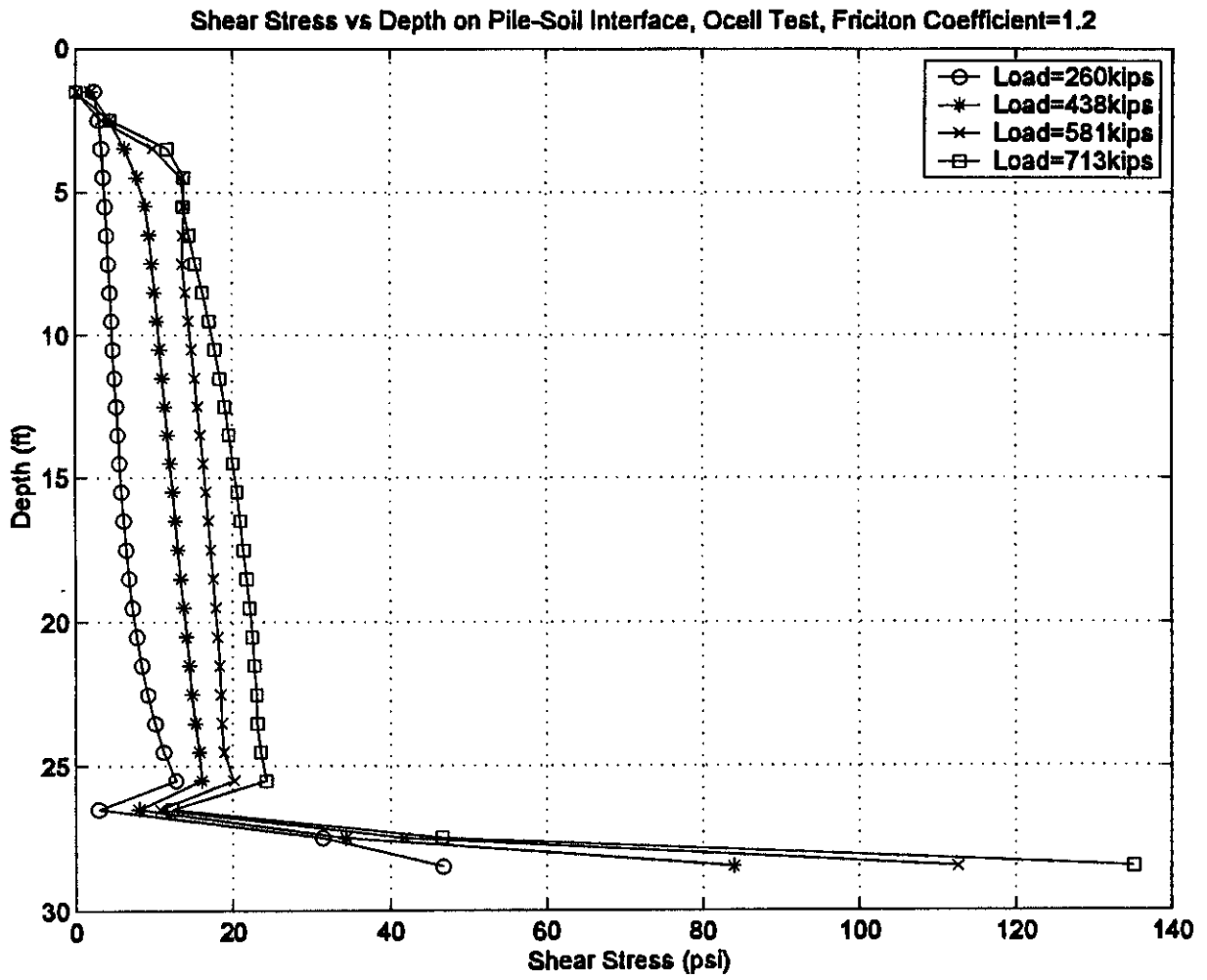


Figure A-51 Shear Stress vs Depth Curve, O-cell Test, $\mu=1.2$

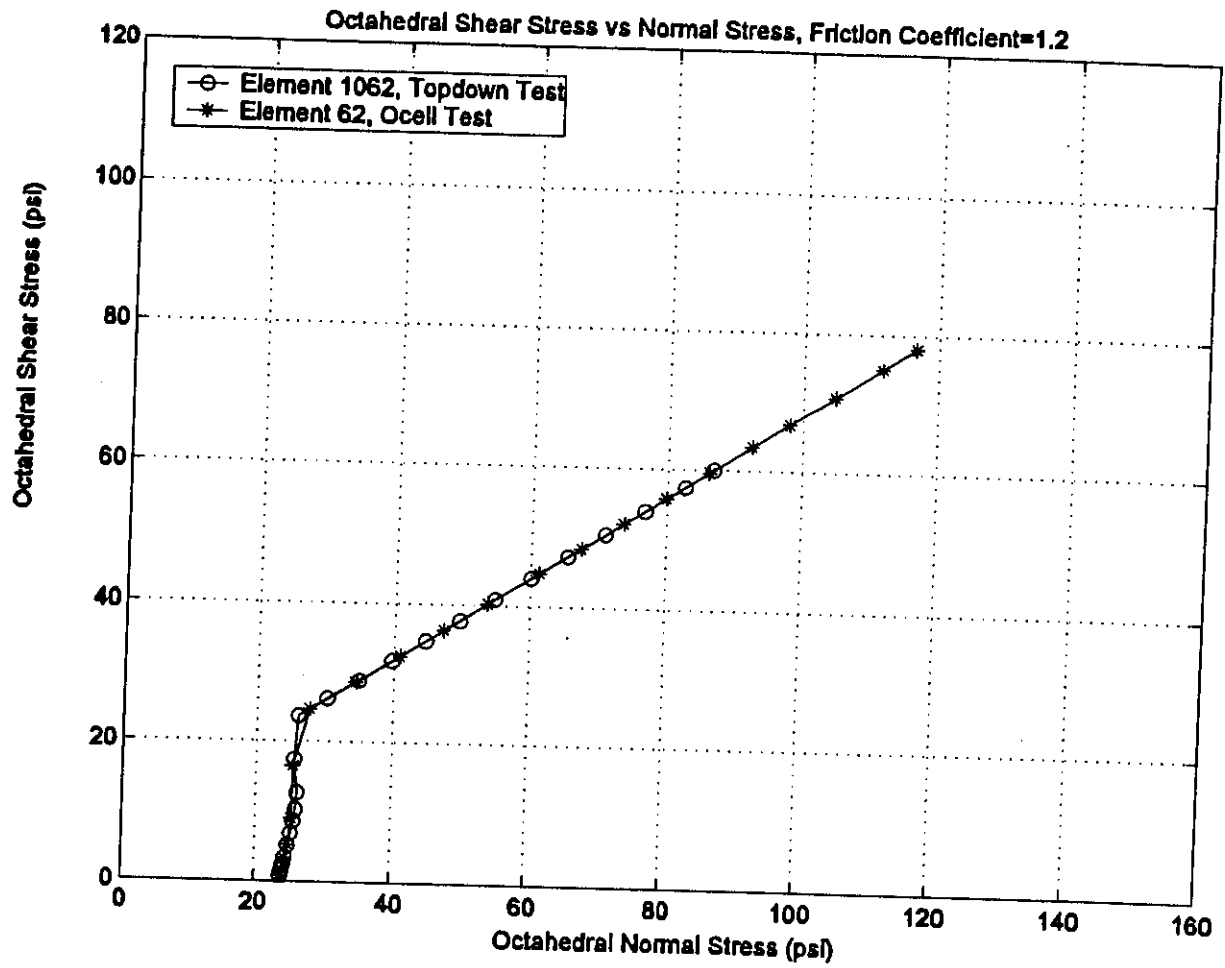


Figure A-52 Stress Path of Soil Element, $\mu=1.2$

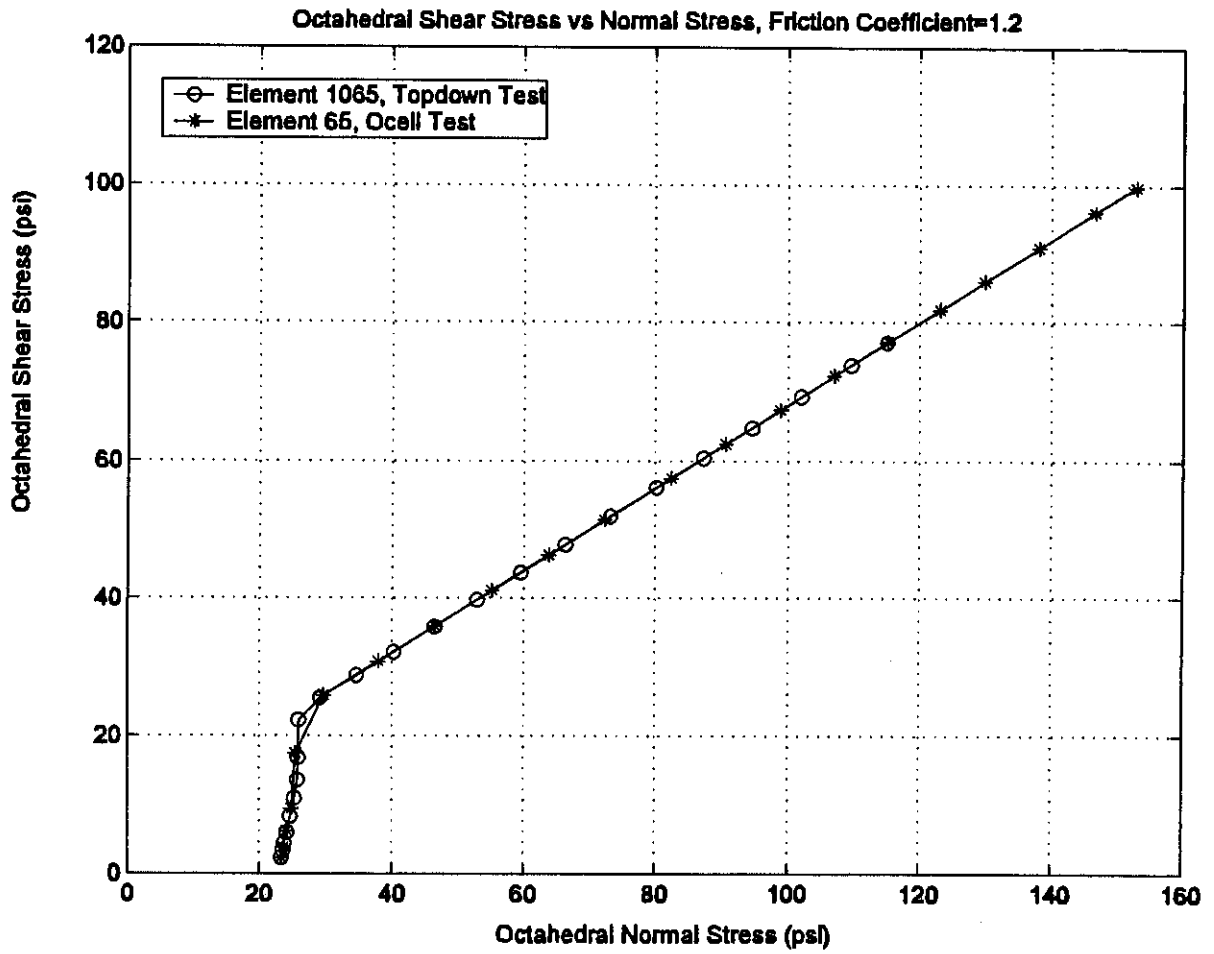


Figure A-53 Stress Path of Soil Element, $\mu=1.2$

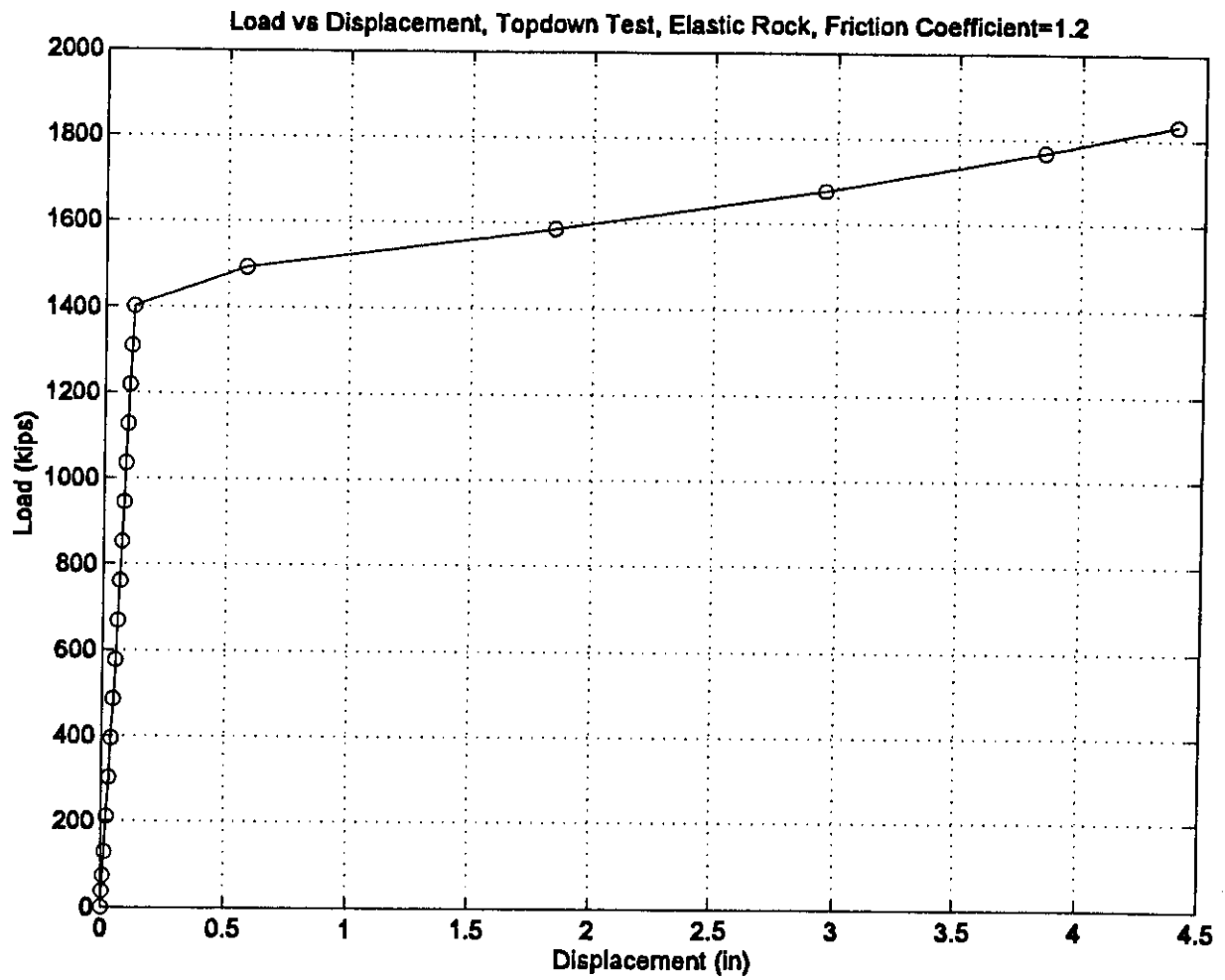
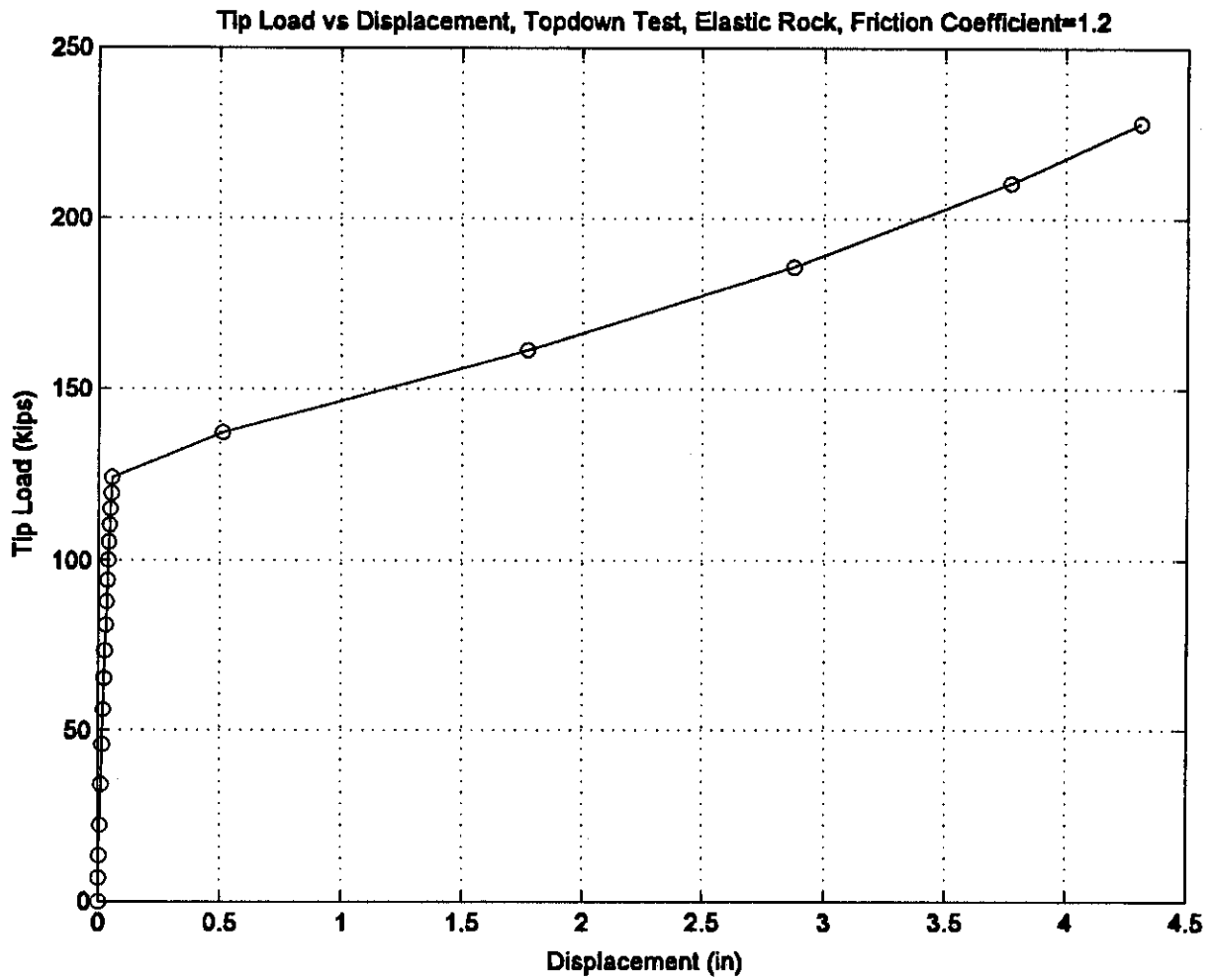


Figure A-54 Load-Displacement Curve, Topdown Test, Elastic Rock, $\mu=1.2$



*Figure A-55 Tip Load vs Displacement Curve, Topdown Test,
Elastic Rock, $\mu=1.2$*

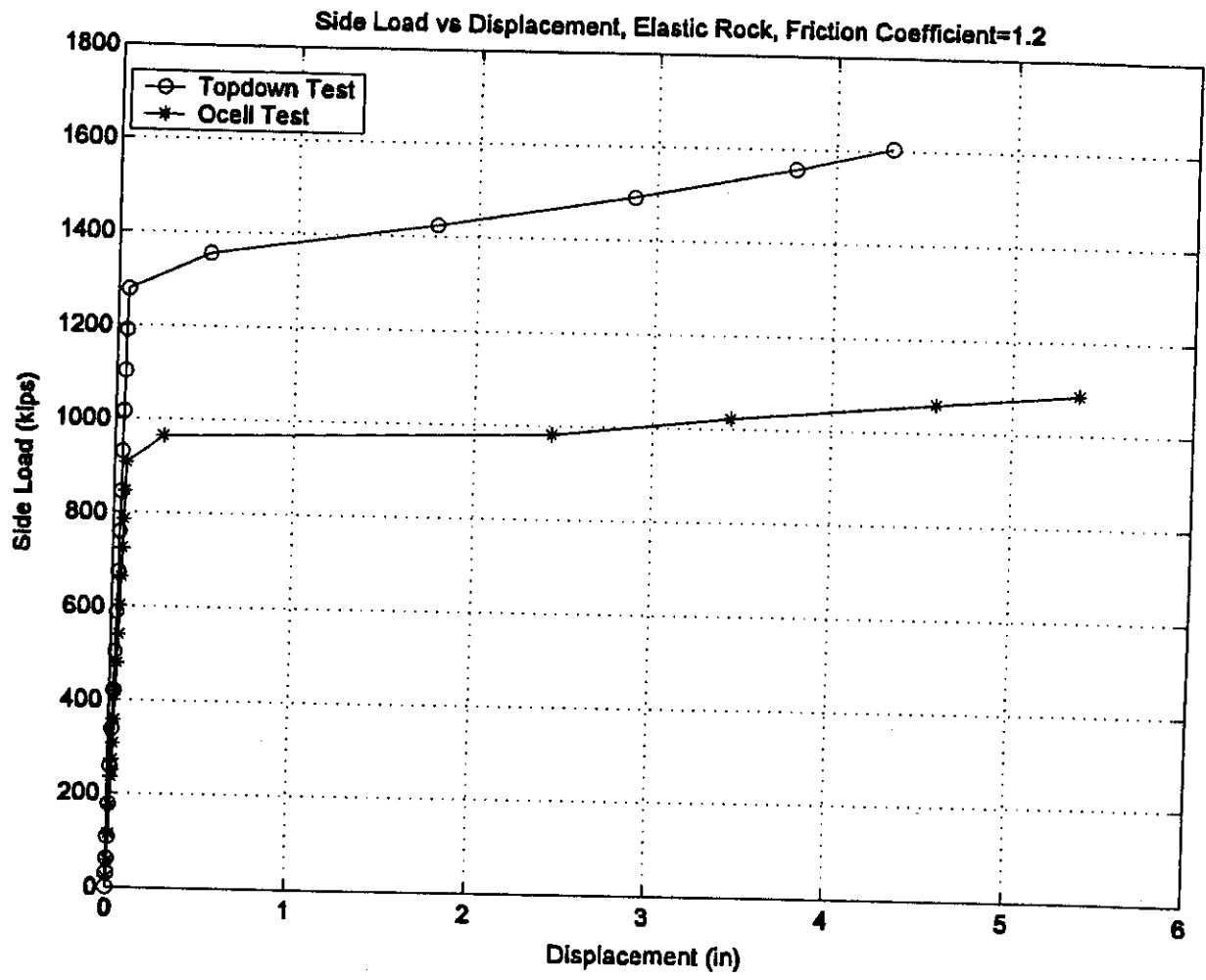


Figure A-56 Side Load vs Displacement Curve, Elastic Rock, $\mu=1.2$

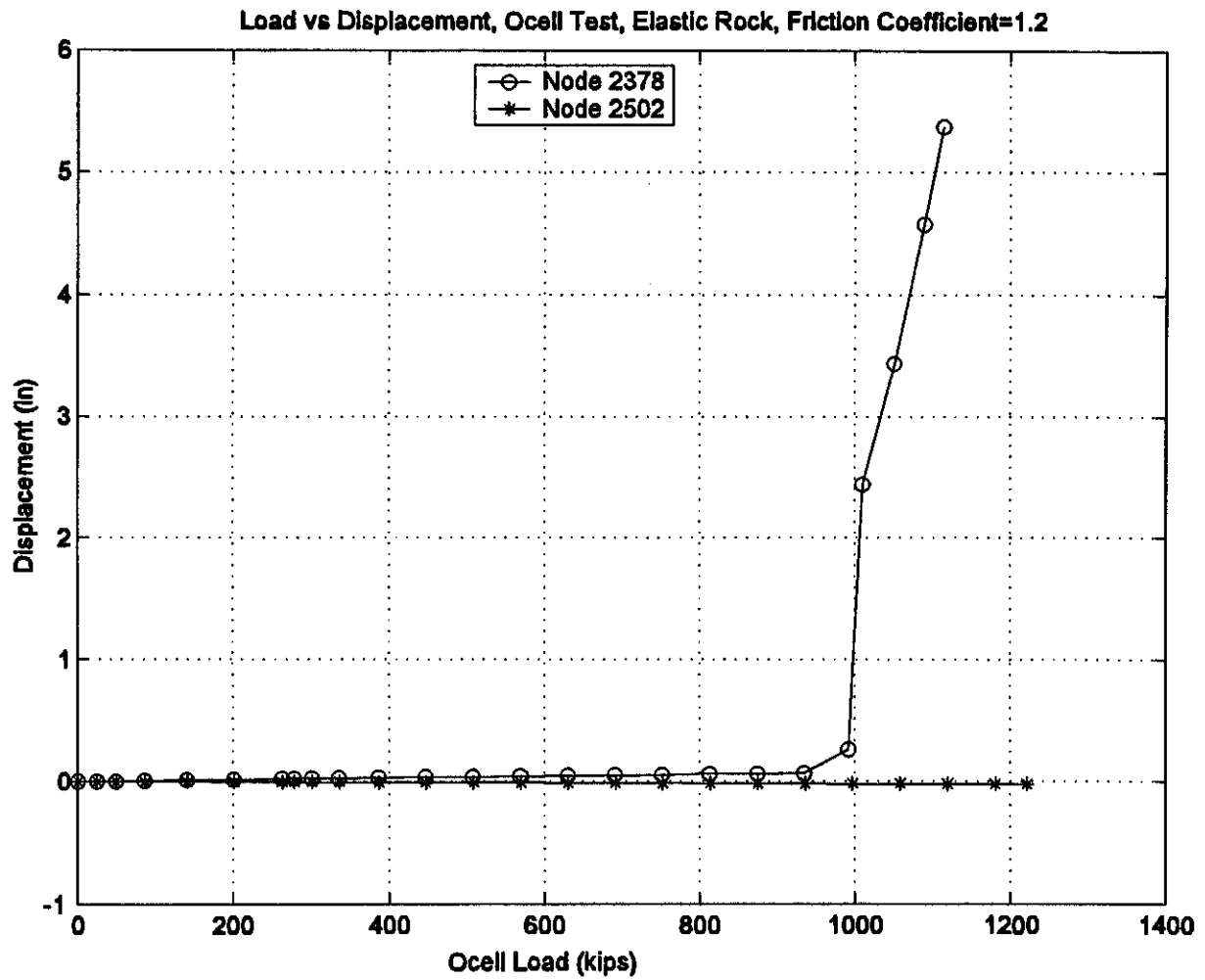
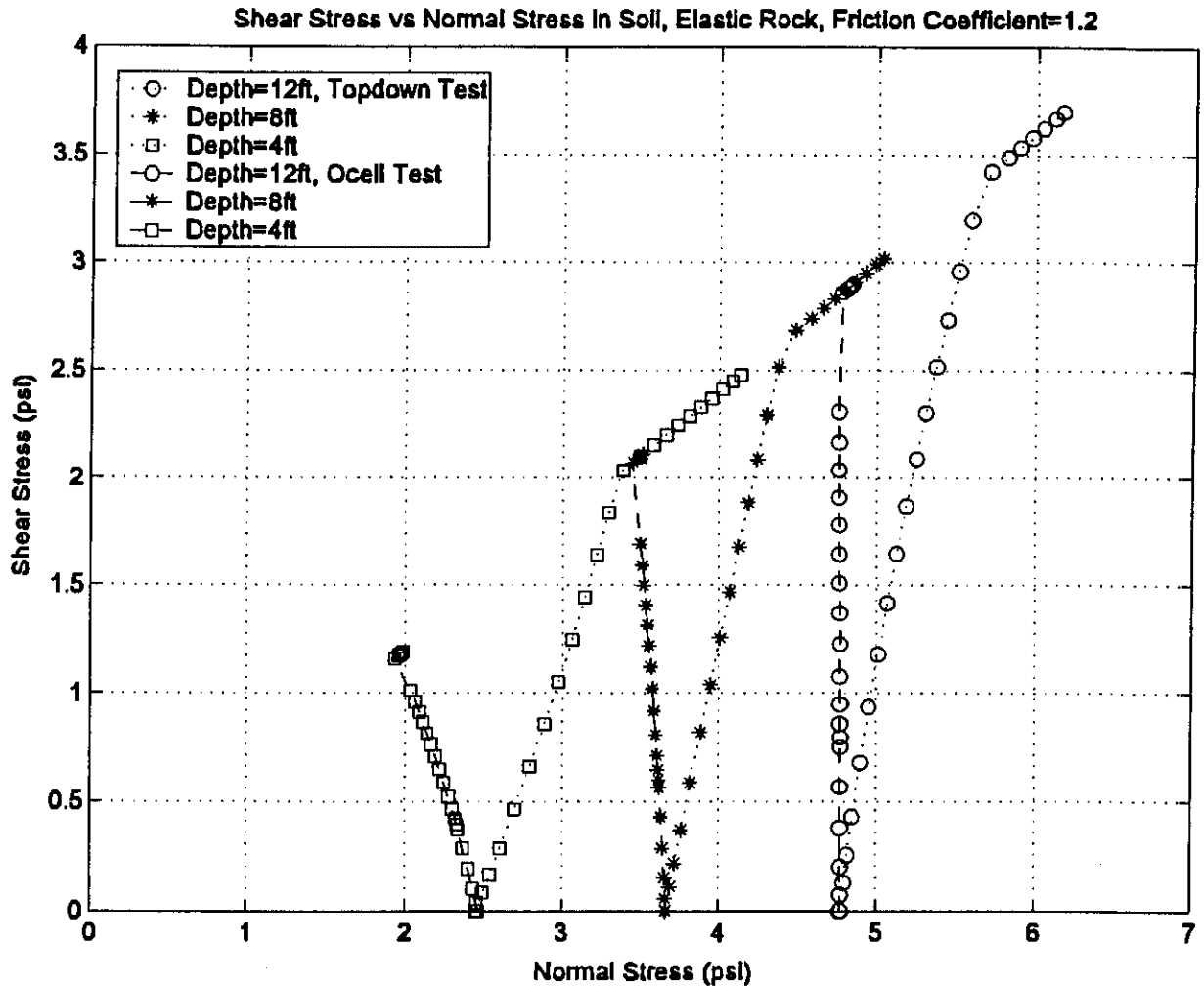
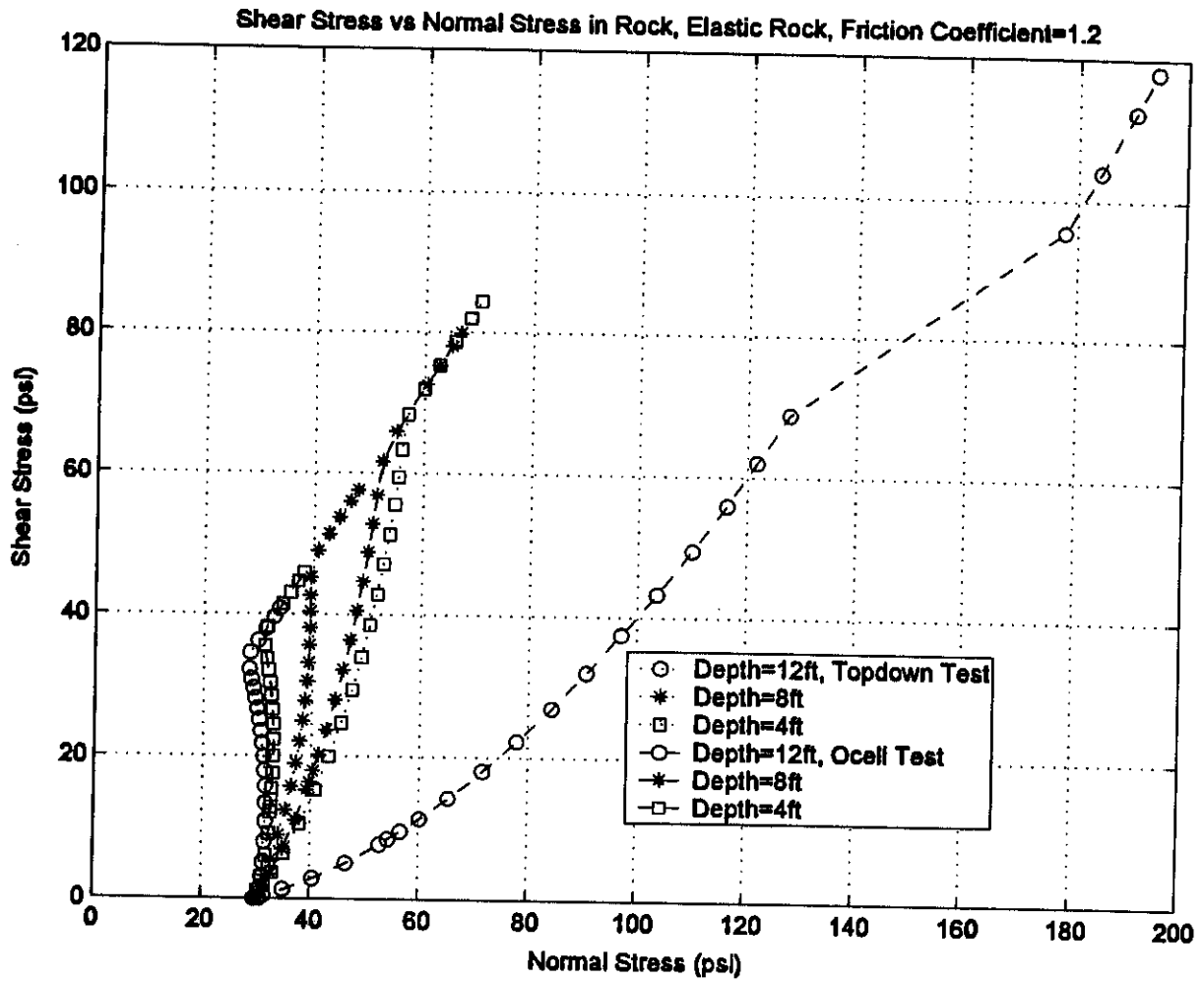


Figure A-57 Load-Displacement Curve, O-cell Test, Elastic Rock, $\mu=1.2$



*Figure A-58 Stress Path at Different Nodes on Soil-Pile Interface in Soil,
Elastic Rock, $\mu=1.2$*



*Figure A-59 Stress Path at Different Nodes on Soil-Pile Interface in Rock,
Elastic Rock, $\mu=1.2$*

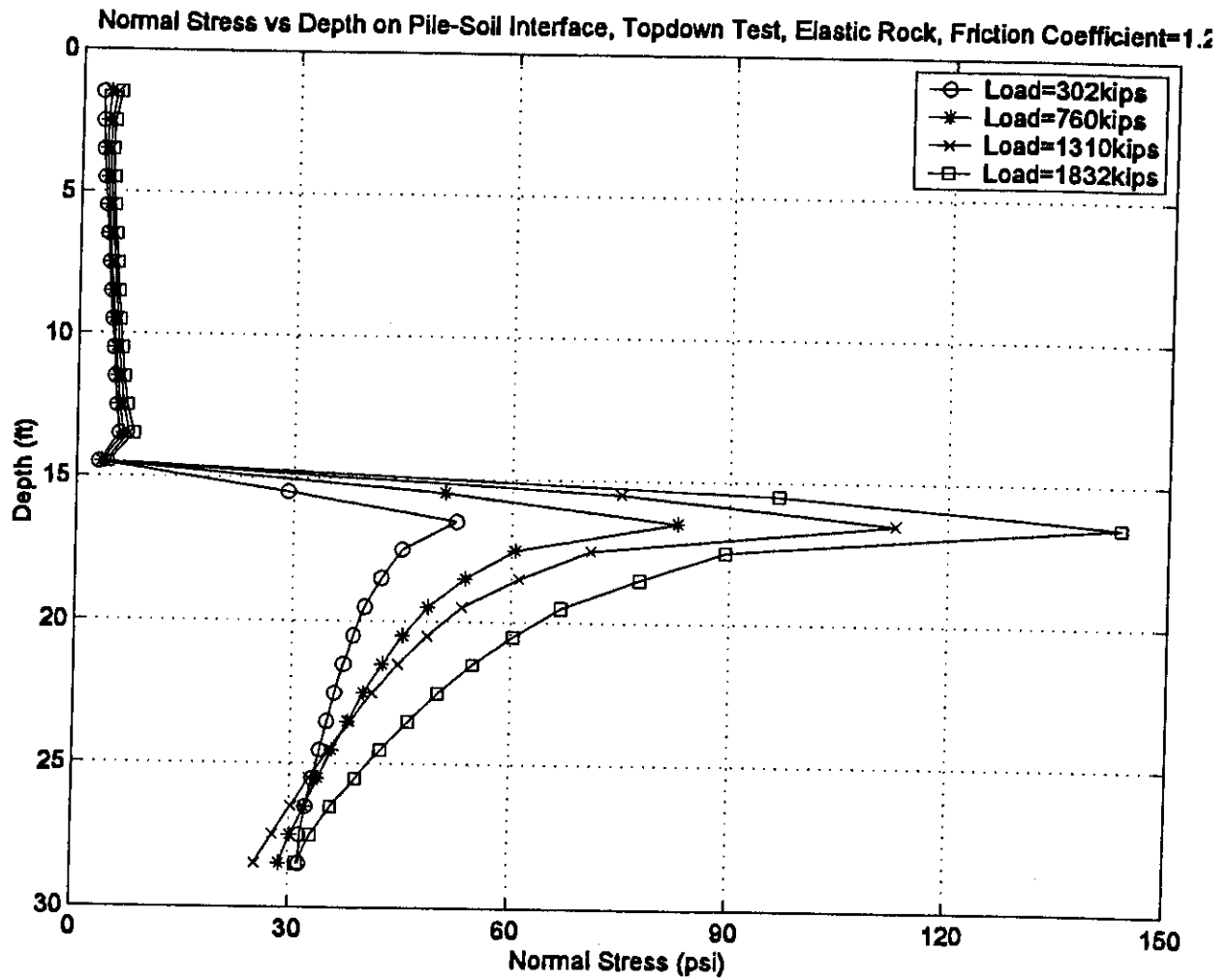
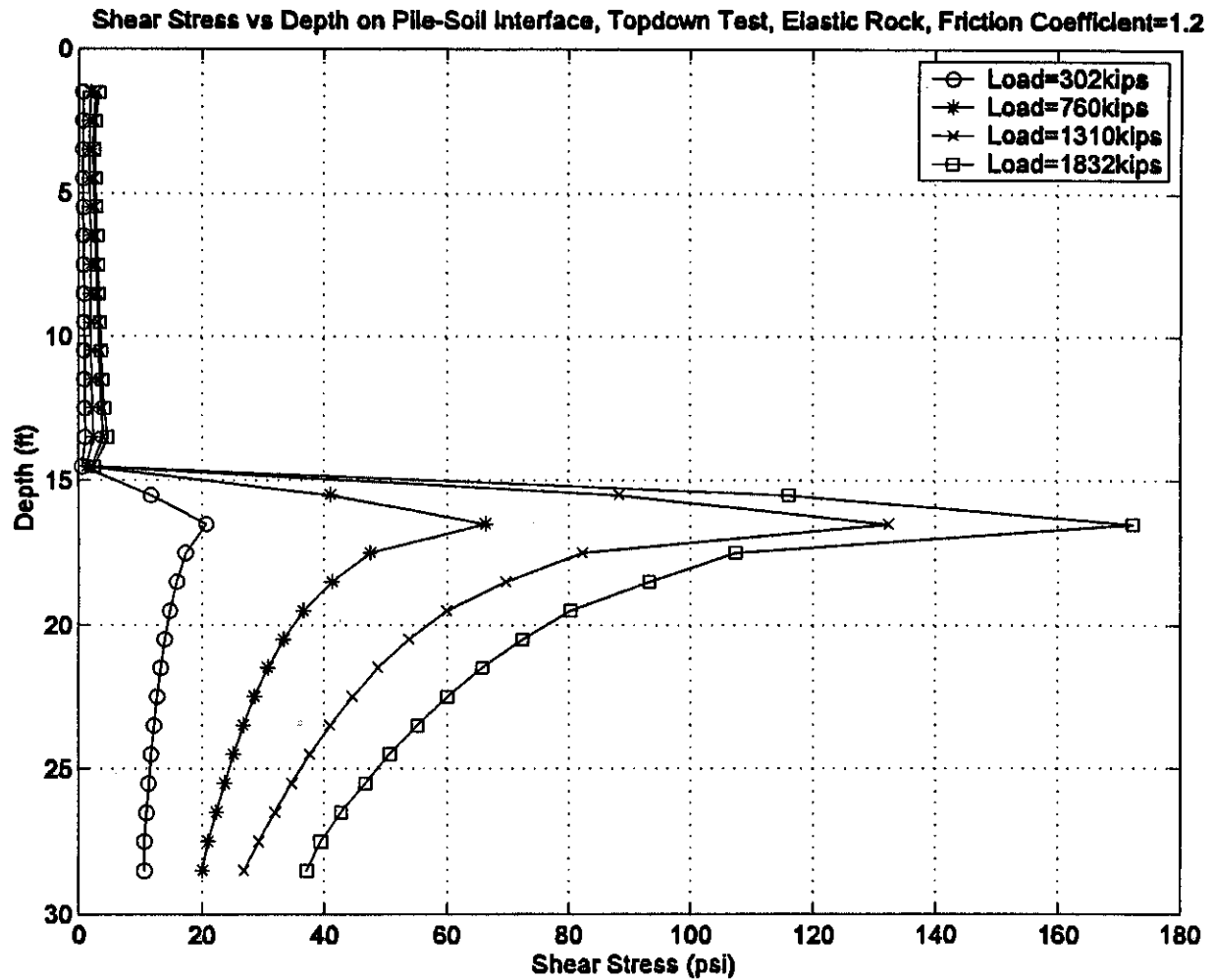
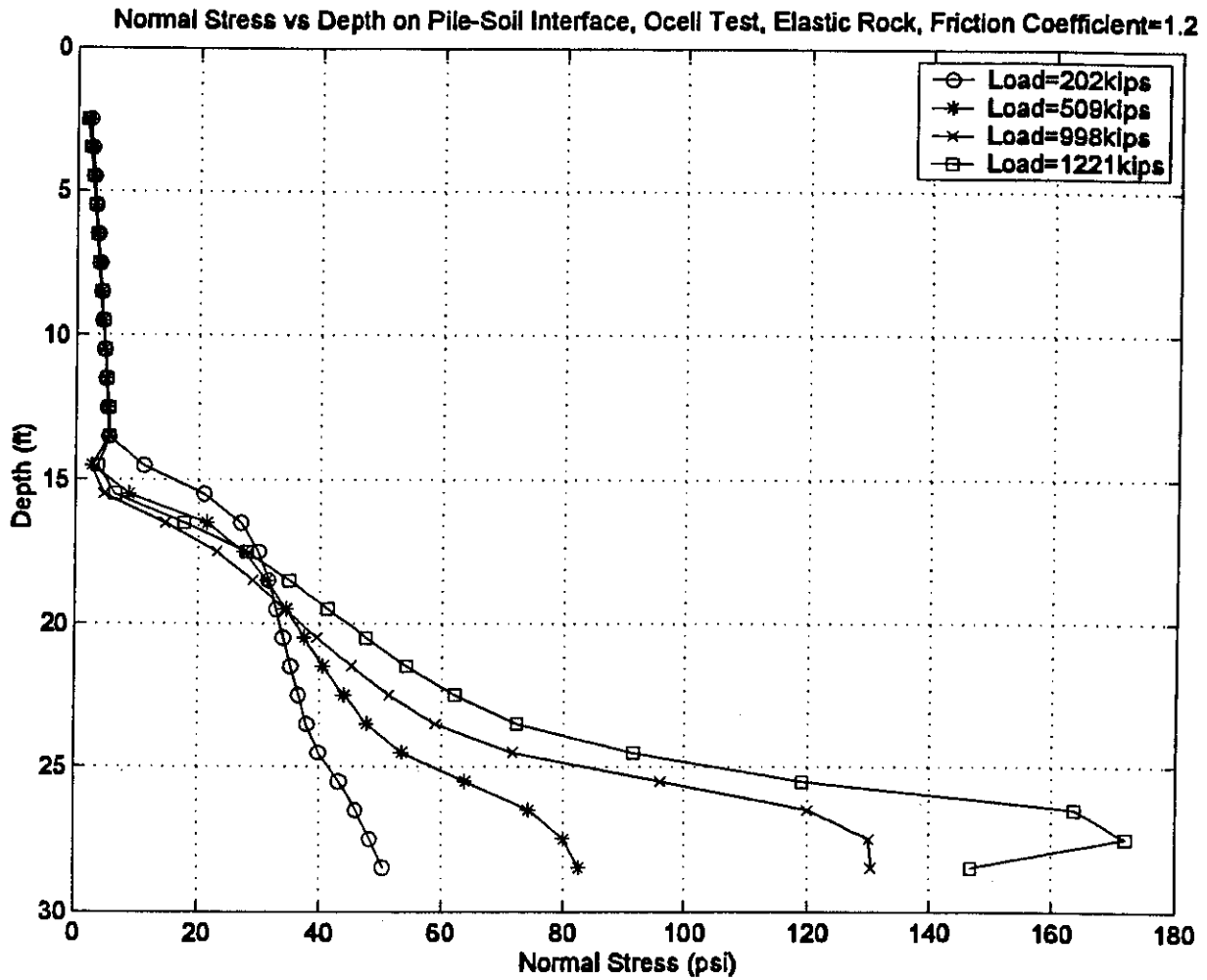


Figure A-60 Normal Stress vs Depth Curve, Topdown Test,
Elastic Rock, $\mu = 1.2$



*Figure A-61 Shear Stress vs Depth Curve, Topdown Test,
Elastic Rock, $\mu=1.2$*



*Figure A-62 Normal Stress vs Depth Curve, O-cell Test,
Elastic Rock, $\mu=1.2$*

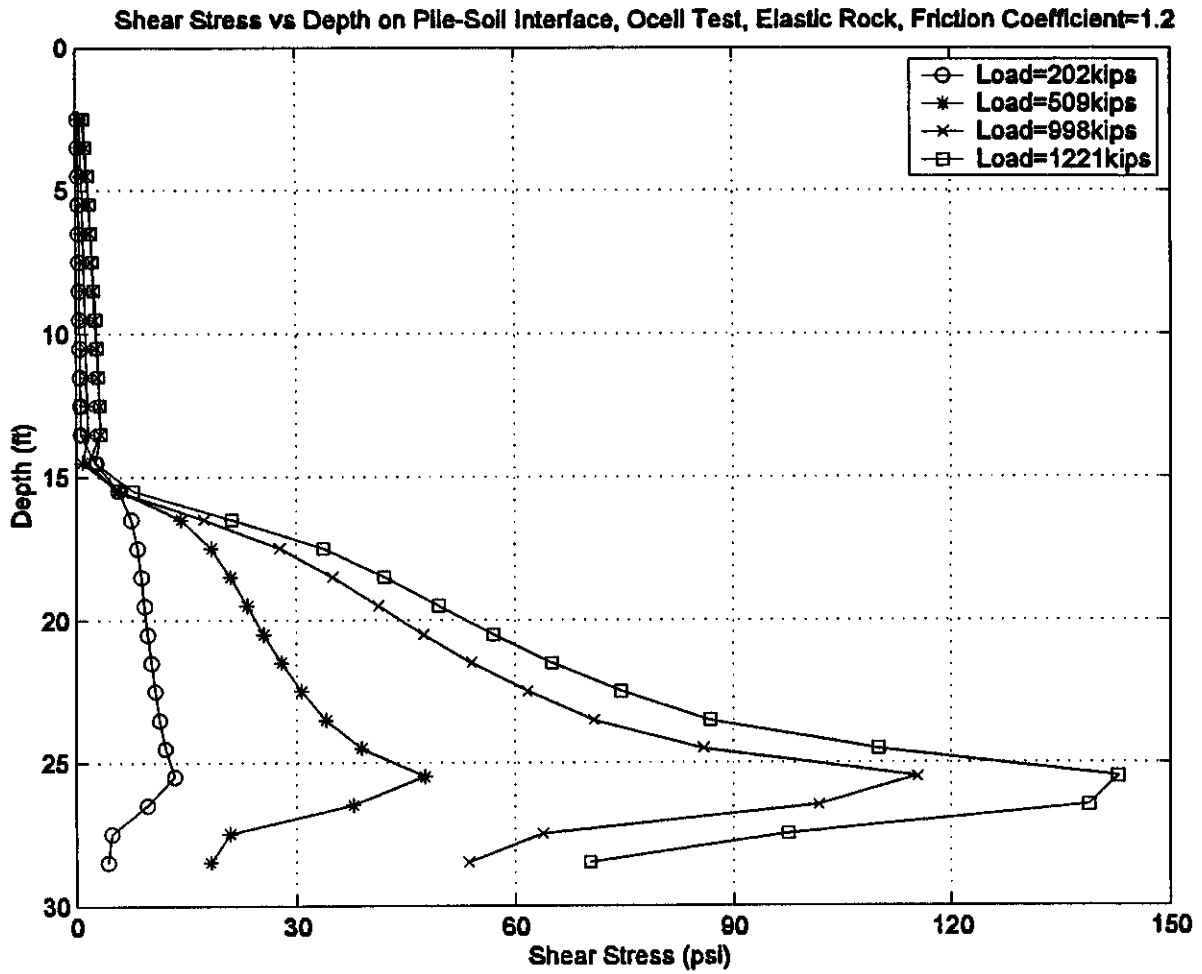


*Figure A-63 Shear Stress vs Depth Curve, O-cell Test,
Elastic Rock, $\mu=1.2$*

Part B

PARAMETRIC STUDY OF ROCK SOCKETED PILE

INTRODUCTION

The research was then focus on the behavior the rock socketed pile. This is the most popular condition of the application of drilled shaft foundation. This portion describes the finite element model used in the analysis and the detailed parametric study regarding several factors which are believed to have significant influence on the pile behavior. The ratio of the average mobilized side shear of the top down test and the O-cell test was defined to evaluate the difference between the two testing methods. The effect of different parameters on this ratio has been examined. The results will give a picture about the circumstances under which the two load test results match well or more effect need to done with regard to the interpretation of the O-cell test results.

MODEL DESCRIPTION

The whole model was similar to the soil model, but with a rock layer underlying a 15ft thick dense sand layer. Sand properties were the same as the soil model, $E_{soil} = 14ksi$, $c_{soil} = 8psi$ and $\phi_{soil} = 30^\circ$. Rock was also modeled using Drucker-Prager model, with much higher strength parameters than soil. In the analysis, the rock properties used are correspondent to the Melbourne mudstone, which is relatively soft rock. If not specified, soil properties are $E_{rock} = 70ksi$, $c_{rock} = 200psi$ and $\phi_{rock} = 20^\circ$.

One aspect that needs to be paid attention to is the pile-rock interface properties. It's quite difficult to model the exact pile-rock interface behavior since there are many

uncertainties. Similar to the soil model, the interface between pile and sand was modeled using Coulomb frictional model, in which the maximum shear stress depends on the frictional coefficient and the contact pressure. The friction angle used was $\phi_i = 31^\circ$, corresponding to a frictional coefficient of 0.6. However, the interface between pile and rock much rougher than the interface between pile and sand. It may also show some resistance to the shear force when the contact pressure is zero. Based on this, a modified frictional model with a cohesion, shown in Figure B-1, was applied to the interface between the pile and the rock. The maximum shear stress can be written as $\tau_{max} = c_i + \sigma_{contact} \tan \phi_i$. A FORTRAN program was written to interact with ABAQUS. Two factors c_i and ϕ_i were used to define the interface behavior. If not specified, the interface properties are $c_i = 20psi$ and $\phi_i = 31^\circ$.

For better comparison, the O-cell was placed at the tip of the pile to make sure the side loads for top down test and O-cell test are consistent.

Figure B-2 shows the finite element mesh used in the analysis. The mesh dimensions are 60ft \times 45ft. It extends a pile length deep below the pile tip and 15 times of pile diameter in width. A total of 3016 nodes and 2850 elements were generated. This mesh was used for most of the analysis except when the pile length was changed.

ROCK SOCKETED PILE BEHAVIOR

A typical rock socketed pile was analyzed from both the top down load test and O-cell load test. In the model, the concrete pile was considered as elastic as before, with a Young's modulus of 5000ksi, which was actually used through the analysis. The rock below the sand layer was typical mudstone with a Young's modulus of 70ksi. The

strength parameters are $c_{rock} = 200\text{psi}$ and $\phi_{rock} = 20^\circ$. The pile-sand interface was modeled using Coulomb friction model with a friction coefficient of 0.6, corresponding to a friction angle of 31° . The modified Coulomb friction model with a cohesion was employed to represent pile-rock interface, with a cohesion of 20psi and a friction angle of 31° .

Top Down Compressive Test

Figure B-3 shows the applied load vs pile top displacement curve. The maximum applied vertical stress is 2000psi and the maximum mobilized vertical displacement is about 0.88in. The side load vs displacement curve and the tip load vs displacement curve are shown in Figure B-4 and Figure B-5 respectively. The tip load was calculated from the vertical stress of the row of nodes at the pile tip, and the side load was calculated by subtracting the tip load from the total load applied to the pile top. In order of consistence, the displacement of the pile tip was picked for tip load vs displacement curve, and the displacement of the top of the socket (at the middle of the pile) was picked to generate the side load vs displacement curve.

Figure B-4 presents a strain-softening behavior of the side resistance. The maximum mobilized side force occurs at a displacement of about 0.2in, which is 1014kips. The average side shear can be calculated as 24.9psi for the whole interface including both soil and rock. The tip load vs displacement displays a two-stage behavior. Only a small value of end bearing is mobilized at the beginning of loading. For example, when the applied load is half of the maximum applied load, which is about 1018kips, the mobilized end bearing is only 120kips. Almost 88% of the applied load is carried by the side resistance. However, the portion of the end bearing increases with the mobilization

of the side resistance. At the load level where the maximum side force is reached, 29% of the applied load is carried by the end bearing. After this, the increased applied load all goes to end bearing, resulting in the increase of the B/P ratio, where B is the mobilized end bearing and P is the applied load. At the maximum applied load, this ratio has increase to 53%. However large end bearing will mobilize large displacement, indicating the failure of the side shear, which is not expected at the working load.

Further study of the pile-soil or pile-rock interface behavior is available from the shear stress and normal stress distribution. Figure B-6 presents the distribution of the normal stress at pile-soil (rock) interface along the pile length at different load level. It showed how normal stress develops with the applied load and along the pile length. Obviously, the normal stress at pile-soil interface is smaller than that at pile-rock interface. This is attributed to the different interface models and overburden pressure. As observed from the soil model, the normal stress is much larger at the top of the socket, and it decreases with the depth. With the increase of the applied load, the maximum normal stress (occurs at the top of the socket) increases, but no significant increase can be found at other depths. It is also shown that the nodes close to pile tip tend to be open with the increase of the applied load, and it develops upward. The appearance of the open contact nodes somewhat indicates the failure of the side shear.

Similar plots for shear stress are shown in Figure B-7. Like normal stress, shear stress is much larger at the top of the socket. And it also increases with the increase of the applied load, particularly at the top portion of the socket. For the bottom part, more contact nodes are open with the increase of the applied load.

Closer observation of the pile-rock interface behavior is available through the plot of the shear stress vs normal stress curve at each node. Figure B-8 illustrates the development of the shear stress as a function of normal stress at three nodes along the socket length. Node 217, 613 and 937 are located at a depth of 13ft, 8ft and 3ft below the top of the socket (or 28ft, 23ft and 18ft below the top of the pile) respectively. It is noticed that the shear stress vs normal stress curves for all three nodes follow the same straight line after yielding. The straight line has a slope of 0.6 and an intercept of 20 with shear stress axis if extrapolated. It is correspondent to the interface properties defined in the model, so Figure B-8 also verifies the modified Coulomb friction model. It is also shown that all three curves start from similar normal stress around 30psi, which is induced by the overburden pressure. However, for Node 613 and 937, normal stress increases with the increase of the applied load, resulting in the increase of the shear stress. While for Node 217, the normal stress increases first and then decreases suggesting that this contact node tends to be open at large load level. This result is consistent with the normal stress and shear stress versus depth curves.

O-cell Test

A soft spring was placed at the top of the pile to prevent the rigid body motion when modeling the O-cell test. An appropriate O-cell load was applied just enough to mobilize the side shear. This was indicated by dramatic increase of the upward movement. This is the moment when a real O-cell test is stopped. Figure B-9 gives the applied O-cell load vs displacement curve. The O-cell load used is the gross load including self weight of the pile above the O-cell level and the spring force. The spring force is usually very small before the failure of the side shear, and increases a lot after

that. Figure B-9 illustrates that the upward movement is very small before the failure of the side shear. This is because the dilation of the pile-soil interface was not considered in the analysis. The downward movement curves displays a non-linear behavior. It is suggested that side shear fails before the failure of the end bearing for this case.

Similar to the top down test, normal stress and shear stress are plotted versus depth at different load levels, as shown in Figure B-10 and Figure B-11. A different pattern of normal stress and shear stress distribution along the pile length was observed. Both normal stress and shear stress have a maximum value near the O-cell level. At the top of the socket, both normal stress and shear stress have a large value, which is believed to be the result of the numerical problems since the interface properties are not continuous at this point. It's also shown that the normal stress at both ends of the socket decrease with the increase of the applied O-cell load suggesting that the contact nodes tend to be open at large load level. At an O-cell load of 692kips and 865kips, several nodes at the pile tip are open, and both normal stress and shear stress are reduced to zero. However, same as the top down test, the shear stress at pile-soil interface is much smaller than that at pile-rock interface.

The development of the shear stress as a function of the normal stress at different depth is shown in Figure B-12. Same as the top down test, node 217, 613 and 937 are located at a depth of 13ft, 8ft and 3ft below the top of the socket (or 28ft, 23ft and 18ft below the top of the pile) respectively. It is indicated that the three nodes follow the same function after yielding as defined for the pile-rock interface properties. But at a deep depth (node 217), the normal stress tends to decrease before yielding.

Comparison Between Top Down Test and O-cell Test

The comparison between the two testing methods is focused on the mobilized side shear, of which the interface between pile and rock is more important. So it is necessary to compare the side load vs displacement curve of both testing methods. The side load from a top down test can be obtained using the method described in the results of the top down test. It should be noticed that the side load (upward load) includes the self weight of the pile above the Osterberg cell and the spring force at the top of the pile. Therefore, it is necessary to adjust this load when comparing the two testing methods.

Figure B-13 shows the comparison between the two testing methods where the side load is the pure side load. The top down test curve exhibits a strain-softening behavior with a maximum side load at a displacement of 0.2-0.3in. However, the O-cell test curve presents a little strain-hardening because of the existence of the spring at the top of the pile. The side shear is failed at a side load of around 800kips with the mobilization of the spring force and the upward displacement. It is obvious that the O-cell load testing methods gives a weaker response than the top down load testing method, which is actually observed throughout the analysis. This result is consistent with the soil model, which means the side shear derived from an O-cell test is conservative compared with the top down test.

However, it is also necessary to quantify this difference. For the rock socketed pile case, it's appropriate to compare the side shear from the pile-rock interface, which can be calculated following the procedure described below.

- a) Estimate the side load at yielding;

For top down test where a peak value can be found, the failure side load is taken from the maximum side load. For O-cell test, the failure side load can be taken at the moment when large upward displacement is mobilized. It's always the last time step since the applied load was tried to be just enough to fail the side shear.

For this case, $(Q_s)_{td} = 1013.5kips$, $(Q_s)_{oc} = 826.9kips$, where the subscript td and oc means top down test and O-cell test respectively.

- b) Estimate the side shear at pile-soil interface;

The side shear at pile-soil interface can be estimated from the shear stress versus depth curve. Since the mesh in soil is uniform in vertical direction, the side shear can be simply averaged through the pile length in soil.

For this case, $(f_{soil})_{td} = 7.09psi$, and $(f_{soil})_{oc} = 3.31psi$.

- c) Calculate the side load carried by pile-soil interface;

This can be done by multiplying side shear and surface area of pile-soil interface.

For this case, $(Q_{soil})_{td} = 144.3kips$, and $(Q_{soil})_{oc} = 67.4kips$.

- d) Calculate the side load carried by pile-rock interface;

The side load carried by pile-rock interface can be calculated by subtracting the side load carried by pile-soil interface from the total side load. For this case, $(Q_{rock})_{td} = 869.2kips$, and $(Q_{rock})_{oc} = 759.5kips$.

- e) Calculated the average side shear at pile-rock interface;

For this case, $(f_{rock})_{td} = 42.70psi$, and $(f_{rock})_{oc} = 37.31psi$.

- f) Calculate the ratio of the side shear at pile-rock interface from both testing methods.

For this case, $(f_{rock})_{td} / (f_{rock})_{oc} = 1.14$.

This procedure will be used throughout the parametric study from which the effect of different parameters can be determined.

PARAMETRIC STUDY

In order to study the two load testing methods in detail, some parameters were examined closely with regard to how they affect testing results and the difference between the two load testing methods. These parameters are believed to have significant influence on the pile response. As before, load vs displacement curve, side load vs displacement curve, and tip load vs displacement curve were compared for different cases. Side load vs displacement curve was compared between top down load test and O-cell load test.

Several significant parameters were believed to have great influence on pile response, including

1. Embedded ratio L_{socket}/D , where L_{socket} is the part of pile length in the rock and D is the pile diameter,
2. Young's modulus of the rock E_{rock} ,
3. Cohesion of the rock c_{rock} ,
4. Cohesion of pile-rock interface c_i ,
5. Friction angle of pile-rock interface ϕ_i , and
6. In-situ horizontal stress ratio K_0 .

Since many people believe that the dilation angle of the rock ψ_{rock} has effect on pile response, different models regarding it were also examined. In most analyses,

associate flow rule was employed, in which the dilation angle equaled to the internal friction angle.

A total of 25 different cases were performed. For each case, both top down load testing method and O-cell testing method were analyzed, and a comparison between these two methods was studied. The following is a list of these 25 cases.

Case 1. Base case, $L_{socket}/D = 5$, $E_{rock} = 70ksi$, $c_{rock} = 200psi$, $\phi_{rock} = 20^\circ$,

$c_i = 20psi$, $\phi_i = 31^\circ$ (friction coefficient=0.6), and $K_0 = 1$ with an associate flow rule for rock. For other cases, if not specified, these parameters were kept the same.

Case 2. Non-associate flow rule was applied, $\psi_{rock} = 0$, and $\phi_i = 50^\circ$ (friction coefficient=1.2).

Case 3. $\phi_i = 50^\circ$

Case 4. $\phi_i = 14^\circ$ (friction coefficient=0.25)

Case 5. $E_{rock} = 700ksi$

Case 6. $E_{rock} = 7000ksi$

Case 7. $\phi_i = 50^\circ$ and $E_{rock} = 700ksi$

Case 8. $\phi_i = 50^\circ$ and $E_{rock} = 7000ksi$

Case 9. $\phi_i = 14^\circ$ and $E_{rock} = 700ksi$

Case 10. $\phi_i = 14^\circ$ and $E_{rock} = 7000ksi$

Case 11. Normally consolidated, $K_0 = 0.43$

Case 12. $L_{socket}/D = 1.5$

Case 13. $L_{socket} / D = 3$

Case 14. $L_{socket} / D = 10$

Case 15. $L_{socket} / D = 1.5$ and $\phi_i = 50^\circ$

Case 16. $L_{socket} / D = 3$ and $\phi_i = 50^\circ$

Case 17. $L_{socket} / D = 10$ and $\phi_i = 50^\circ$

Case 18. $c_i = 0 \text{ psi}$

Case 19. $c_i = 10 \text{ psi}$

Case 20. $c_i = 0 \text{ psi}$ and $\phi_i = 50^\circ$

Case 21. $c_i = 10 \text{ psi}$ and $\phi_i = 50^\circ$

Case 22. $c_i = 0 \text{ psi}$ and $\phi_i = 14^\circ$

Case 23. $c_i = 10 \text{ psi}$ and $\phi_i = 14^\circ$

Case 24. Elastic rock

Case 25. $c_{rock} = 50 \text{ psi}$

Case 6 and Case 8 are not realistic because the compressive stress in the pile is so large that the concrete can be damaged before reaching the pile capacity. Therefore, these two cases were not considered in the following study.

Dilation Angle ψ_{rock}

Figure B-14 shows the comparison of the load vs displacement curve from the top down testing between a non-associate flow rule and a fully associate flow rule. It is shown that the two curves match well at the beginning. However, the associate flow rule shows a little stronger response than the non-associate flow rule after the applied load

reaches about 1800kips. This is due to the mobilization of the end bearing which depends on the rock behavior.

The calculated side load vs displacement curve is plotted in Figure B-15. The two cases display similar response especially at the first part of the curve. It's also indicated that the maximum mobilized side force for the two cases is almost same, which is about 1472kips. It may be concluded that the dilation angle has little effect on the side load response. However, dilation angle has more significant influence on the end bearing. This can be seen from the tip load vs displacement curve presented in Figure B-16. Rock with dilation shows stronger response although the two curves match well at low load levels.

The comparison of load vs displacement curve from the O-cell testing is shown in Figure B-17, from which the same conclusions can be drawn. The O-cell load vs the upward movement curves are consistent for both cases and both cases fail the side shear at the same O-cell load level. But for the O-cell load vs downward movement curve, the case without dilation is weaker and it's consistent with the results from the top down test.

Although there's some difference in the end bearing response between two plastic flow models, the side resistance is almost same for two cases, especially when the difference between the two testing methods. The $(f_{rock})_{td} / (f_{rock})_{oc}$ ratio was calculated to be 1.30 and 1.29 for $\psi_{rock} = 20^\circ$ case and $\psi_{rock} = 0$ case respectively. For most cases, side shear is mobilized before the yield of the end bearing, therefore the differences between associate and non-associate flow rules are small compared with other factors. So dilation angle won't be considered as a significant factor, and no further analyses will be conducted regarding its influence on the two testing methods and their difference.

Rock Interface Friction Angle ϕ_i

The internal friction angle plays an important role in side resistance and the axial capacity since the maximum shear stress is proportional to $\tan \phi_i$. Different cases have been performed with different interface friction angle. Case 1, 3 and 4 were picked to examine the effect of ϕ_i on both of the testing methods and their difference.

Shown in Figure B-18 is the comparison of the load-displacement curves from top down test. It is obvious that larger friction angle results in stronger pile-rock system. For instance, at 1500kips applied load level, the displacement for $\phi_i = 50^\circ$ case is about 0.18in, and the displacement is 0.3in and 0.5in respectively for $\phi_i = 31^\circ$ case and $\phi_i = 14^\circ$ case. More insight into the effect of the frictional on the top down testing method can be found from side load vs displacement curve (Figure B-19) and tip load vs displacement curve (Figure B-20). Figure B-20 indicates that there's little difference in tip load vs displacement curve, but the difference in side load vs displacement curve is significant as shown in Figure B-19. The maximum side forces are 1472kips, 1014kips, and 740kips for $\phi_i = 50^\circ$, $\phi_i = 31^\circ$ and $\phi_i = 14^\circ$ respectively. But the three cases show the same pattern of side shear response. A maximum side force is obtained at a displacement of between 0.2-0.3in, after which the side force decreases somewhat to a residual value showing a strain-softening behavior. It can be concluded that the friction angle of the pile-rock interface has little influence on end bearing, but rougher interface (larger friction angle) will improve side resistance significantly. Any difference from a top down test because of it is contributed by the difference of the side resistance.

The comparison of the load vs displacement curve from O-cell test is shown in Figure B-21. Similar to the top down test, there's almost no difference in O-cell load vs downward displacement curve. However the difference in O-cell vs upward displacement curve is significant. Note in Figure B-21, the O-cell load is the gross applied load including self weight of the pile and the spring force. The maximum applied O-cell pressure for three cases is 1100psi, 850psi and 680psi respectively. It is again indicated that the friction angle at pile-rock interface has almost no influence on end bearing, but has substantial effect on side resistance.

Figure B-22 presents the comparison of side load vs displacement curve for three cases. All three cases show the similar behavior, with O-cell testing results conservative comparing with the top down testing results. But before failure, the O-cell test gives a stronger behavior than the top down test. The comparison of the difference between the top down testing and the O-cell testing can be illustrated by the side shear ratio at pile-rock interface using the procedure described before. The ratio turns out to be 1.30, 1.14 and 1.05 respectively. This result leads to the conclusion that the difference between the two load testing methods decreases when the interface friction angle decrease.

More results can be calculated from other cases regarding the side shear ratio for different interface friction angle. Table 1 is a summary of results from different cases. For both $E_{rock} = 700ksi$ and $E_{rock} = 7000ksi$, $(f_{rock})_{td} / (f_{rock})_{oc}$ increases with the increase of the friction angle, indicating the difference between the two load testing methods is more significant when the interface is rougher. The data in Table 1 can be plotted as shown in Figure B-23. The effect of ϕ_i can be easily observed, and it is also shown that the effect of ϕ_i is more considerable if Young's modulus of rock is larger. For example, the ratio

increases about 83% when ϕ_i increases from 14° to 50° for $E_{rock} = 70ksi$ case. However, for $E_{rock} = 700ksi$ case, the increase is only 24%.

More details of the shear stress distribution at failure in rock can be found from Figure B-24. For each plot, shear stress distribution curves from the top down test and the O-cell test are shown. The shear stress distribution can be represented by the ratio of the shear stress at any depth to the average shear stress which was calculated from the procedure described before. It should be noticed that z is the depth below the top of the socket (15ft deep) and L_{socket} is the socket length which is 15ft. The plots show that the shear stress has a larger value at the top of the socket for top down test, but for O-cell test, the shear stress has a larger value close to the O-cell. The contact nodes at the bottom tend to be open for both tests. The comparison of the three sets of curves indicates that for a lower interface friction angle case, the shear stress distribution is more uniform for both top down test and O-cell test. However, for larger interface friction angle case, for example $\phi_i = 50^\circ$, the distribution is more diverse. The ratio of the shear stress at the top of the socket to the average shear stress is about 4.0, which is only about 1.7 for $\phi_i = 14^\circ$ case.

Young's Modulus of Rock E_{rock}

Several cases with different Young's modulus of rock were performed to study its effect on pile response. However, for some cases (for example, $E_{rock} = 7000ksi$ case with an interface friction angle of 31° or 50°), the pile capacity was calculated to be so large that the concrete pile tends to be damaged before the mobilization of the capacity.

Therefore, the comparison of different rock modulus was focused on the cases with an interface friction of 14° .

Figure B-25 illustrates the comparison of the load vs displacement behavior from the top down test. It is shown that the increase of rock modulus can greatly improve the pile response. For instance, to mobilize 0.3in displacement, the required load for $E_{rock} = 70ksi$ case is about 1300kips, while for $E_{rock} = 700ksi$ and $E_{rock} = 7000ksi$ case, it is up to 2400kips and 4500kips respectively. Although $E_{rock} = 7000ksi$ case is not very realistic since the rock modulus is even greater than the modulus of the concrete causing some dramatic behavior, it still can explain the influence of the rock modulus. It is also indicated that the mobilized displacement for $E_{rock} = 7000ksi$ case is very small, part of which is induced by the compression of the concrete pile.

Presented in Figure B-26 and Figure B-27 is the comparison of side load vs displacement curve and tip load vs displacement curve respectively. For $E_{rock} = 700ksi$ and $E_{rock} = 7000ksi$ case, the side load vs displacement curve does not show a peak value like $E_{rock} = 70ksi$ case, but it exhibits a strain-hardening behavior. Therefore, it's quite difficult to estimate the side load at yielding or failure. But it was found that the maximum side load occurs at a displacement of 0.2-0.3in for most of the cases performed in which the peak side load exists, so it's reasonable to choose the side load at which a 0.2-0.3in displacement is mobilized as the failure side load, which will be discussed later. Figure B-27 shows that the rock modulus has a significant effect on the tip load vs displacement curve. Much stronger end bearing behavior was observed for $E_{rock} = 7000ksi$ case. The maximum tip load was found about 2300kips with a mobilized

displacement of only less than 0.15in. Comparing Figure B-25 and Figure B-27 indicates that for $E_{rock} = 7000ksi$ case, most of the displacement at the pile top is induced by the compression of the concrete pile.

Results from the top down test lead to the conclusion that the rock modulus not only has influence on the end bearing response, but it also affects the side resistance considerably. Same conclusion can also be drawn from the O-cell testing results, as shown in Figure B-28. Both side resistance and end bearing resistance can be improved a lot with the increase of the rock modulus, especially when the rock modulus increases from $700ksi$ to $7000ksi$. The maximum applied O-cell pressure for three cases is 680psi, 700psi and 950psi respectively. But this pressure didn't mobilize much downward movement except for $E_{rock} = 70ksi$ case.

The comparison of the side load vs displacement curve between two testing methods for three cases is shown in Figure B-29. The $E_{rock} = 700ksi$ case and $E_{rock} = 7000ksi$ case are very similar in the side load vs displacement curves from both tests except that less displacement has been mobilized for $E_{rock} = 7000ksi$ case. For these two cases, the two curves match well before yielding, but the O-cell test gives a much lower side resistance as observed before. While for $E_{rock} = 70ksi$ case, the O-cell test appears stiffer before failure, but it still results in a lower side resistance. The average side shear mobilized at the pile-rock interface can be calculated then. For $E_{rock} = 700ksi$ case and $E_{rock} = 7000ksi$ case in which there is no obvious peak side load from the top down test, the side load at failure can be estimated using 0.2-0.3in displacement criteria. For example, the side load at yielding was estimated as 942.8kips, and the average side

shear at the pile-rock interface was then calculated as 42.31psi. While for the O-cell test, the average side shear at pile-rock interface was computed as 30.92psi.

The detailed results of side shear and $(f_{rock})_{td} / (f_{rock})_{oc}$ for different cases were already presented in Table 1. The increase of the rock modulus has a great influence on the mobilized side shear for both the top down test and the O-cell test. When the rock modulus increases from 700ksi to 7000ksi, the side shear increases twice for the top down test and 40% for the O-cell test. The ratio $(f_{rock})_{td} / (f_{rock})_{oc}$ can be plotted against E_{rock} shown in Figure B-30. The difference between the top down test and the O-cell test becomes larger when the Young's modulus of the rock increases. When $E_{rock} = 70ksi$, the ratio is 1.05, which may be omitted with an error within 5%. However, for $E_{rock} = 7000ksi$ case, the ratio is up to 3.2. Figure B-30 also shows that the effect of E_{rock} is greater for larger interface friction angle case. But it should be realized that $E_{rock} = 7000ksi$ is not very realistic because the rock modulus is greater than the modulus of the concrete pile.

More detailed shear stress distribution characteristic along the pile length in rock can be found in Figure B-31 for $E_{rock} = 70ksi$ and $E_{rock} = 700ksi$. It appears that the shear stress distribution is more uniform with a lower rock modulus especially for the top down test. The result from the top down test for $E_{rock} = 70ksi$ case shows that the ratio of the shear stress to the average shear stress is very close to 1.0 at the depth with a z/L_{rock} of 0.2 to 0.9. While for $E_{rock} = 700ksi$ case, the distribution is more varied. It is shown again the difference of shear stress distribution between the two testing methods. For the

top down test, the maximum shear stress occurs at the top of the socket, but for the O-cell test, the maximum side shear occurs close to the O-cell.

Interface Cohesion c_i

Interface cohesion can affect side resistance significantly because it is related to the maximum shear stress as shown in the pile-rock interface model. Therefore, different values of interface cohesion at c_i were used to model the pile-rock interface. The three different values are 0 (corresponding to Coulomb friction model), 10psi, and 20psi respectively. And each combination of interface friction angle and interface cohesion results in a reasonable value of mobilized side shear. The study of the effect of c_i will be focused on the $\phi_i = 31^\circ$ case (Case 1, 18 and 19).

The comparison of the load versus displacement curve from the top down test is shown in Figure B-32. The three cases exhibit similar pile response. The three curves agree well when the mobilized displacement is less than 0.1in, but larger interface cohesion case displays a stronger behavior. At an applied load of 1500kips, the mobilized displacement for $c_i = 0$ case is about 0.63in, but this value for $c_i = 10psi$ case and $c_i = 20psi$ case is only 0.43in and 0.30in respectively. It also appears that the influence of c_i is fairly uniform since c_i is a constant in the modified Coulomb friction model.

Figure B-33 and Figure B-34 present the comparison of the derived side load vs displacement curve and tip load vs displacement curve from the top down test respectively. Similar to the interface friction angle, it can be found from Figure B-34 that c_i almost has no effect on the end bearing since the three curves match very well. As a result of it, the difference of the top down test with different interface cohesion is induced

by the side resistance. As shown in Figure B-33, the large c_i case exhibits a stronger response. However, all the three curves have strain-softening characteristics. The maximum side load occurs at a displacement of 0.2-0.3in. The peak value is 1013.5kips, 806.8kips and 596.1kips respectively. The difference is 206.7kips between $c_i = 20psi$ case and $c_i = 10psi$ case, and 210.7kips between $c_i = 10psi$ case and $c_i = 0$ case. These two values are very close to the side load carried by a uniform side shear of 10psi, which is 203.6kips.

It can be concluded from the top down test results that c_i has a uniform effect on the side resistance, but has almost no influence on the end bearing. This conclusion is very similar to the effect of the interface friction angle. Same trend can be observed from the comparison of the load-displacement curve from the O-cell test, as shown in Figure B-35. Almost no difference can be found from downward displacement curves. But the side load response is stronger for the larger c_i case. The maximum applied O-cell pressure for these cases is 850psi, 700psi and 540psi respectively. Although the difference between each two adjacent cases seems to be uniform, its value does not conform to the side force with a 10psi shear stress.

Like before, the comparison of the two testing methods for three cases is shown in Figure B-36. The three plots exhibits similar features, but with different mobilized side load. The average side shear at the pile-rock interface was calculated. For the top down test, the average side shear for three cases is 42.70psi, 32.92psi, and 23.05psi respectively. For the O-cell test, the corresponding values are 37.31psi, 29.67psi and 21.50psi. The resultant $(f_{rock})_{td} / (f_{rock})_{oc}$ ratio for three case is 1.14, 1.17 and 1.07 respectively.

More results from other cases are available in Table 2. It is shown that the increase of c_i can result in larger differences between the top down test and the O-cell test. For the combination of $c_i = 0$ and $\phi_i = 14^\circ$, there's almost no difference between the results from the two testing methods. However, it should be noticed that for this case, the side resistance is too small for rock to be realistic. And in the model, it is even weaker than the pile-soil interface. It can also be found that the difference of the side shear between two adjacent cases for the top down test is about 10psi, which is the difference of the interface cohesion. But for the O-cell test, this difference is smaller than 10psi. The $(f_{rock})_{td} / (f_{rock})_{oc}$ ratio was plotted against c_i in Figure B-37, showing that the influence of c_i is quite uniform.

Shear distribution comparison is show in Figure B-38. The three cases exhibit similar behavior. However, for $c_i = 20psi$ case, more contact nodes are open, while no contact node is open for $c_i = 0$. It can also be found that $c_i = 20psi$ case has more uniform shear stress distribution for the top down test, but not for the O-cell test.

Cohesion of Rock c_{rock}

In order to study the influence of the cohesion of rock, three cases were performed (Case 1, Case 24 and Case25), one of which involved the use of the elastic model for rock. The elastic rock case is equivalent to the case with an infinite rock cohesion. The effect of c_{rock} on the load vs displacement curve from the top down test is shown in Figure B-39. The elastic rock model is much stronger than the other two cases. Its load-displacement curve exhibits a two-straight-line behavior. The change of the slope of the straight line indicates the mobilization of the end bearing. Since the rock won't

fail, the load-displacement curve doesn't show the yielding and the applied load can be theoretically increased infinitely with more displacement mobilized. For cases where Drucker-Prager model was used, larger c_{rock} case has a stronger response. It is shown in Figure B-39 that for $c_{rock} = 50\text{psi}$ case, the curve becomes flat rapidly after the yielding of the side shear because the rock is too weak to provide high capacity.

Figure B-40 and Figure B-41 present the side load vs displacement and tip load vs displacement results from the top down test respectively. It can be seen from Figure B-40 that $c_{rock} = 200\text{psi}$ case and $c_{rock} = 50\text{psi}$ case both display a strain-softening behavior as some other cases. While for the elastic rock case, a strain-hardening behavior was observed. It is because the rock will not fail after the mobilization of the end bearing, which will result in the increase of the interface contact pressure and thus the side resistance when the applied load is increase. It is also indicated that the displacement at which the maximum side load occurs decreases with a reduction of the rock cohesion. For the tip load vs displacement plots as shown in Figure B-41, the elastic rock model case has the similar characteristic to the side resistance behavior except that the initial slope is smaller. It is due to the fact that the end bearing is mobilized after the failure of the side resistance. Also can be found from Figure B-40 is that higher c_{rock} case shows a stronger end bearing response.

It may be concluded from the top down test results that c_{rock} has significant influence on both side resistance and end bearing. Larger c_{rock} value, especially elastic rock case, shows a stronger response for both side resistance and end bearing. Similarly, the results from the O-cell test are plotted in Figure B-42. Again, it is shown that the

larger c_{rock} case is stronger in both side resistance and end bearing. It should be also notice that for $c_{rock} = 50\text{psi}$ case, the rock is so weak that the end bearing tends to be fail before the failure of the side shear. While the downward movement curve for elastic case appears to be the straight line indicating the elastic behavior. The maximum applied O-cell pressure for elastic rock case, $c_{rock} = 200\text{psi}$ case and $c_{rock} = 50\text{psi}$ case is 1003psi, 850psi and 680psi respectively.

The comparison between the top down test and the O-cell test is plotted in Figure B-43. The elastic rock case does not show an obvious peak side load value for the top down test, but it can be estimated as 1080.3kips using the displacement criteria. The average side shear at pile-rock interface can be then calculated as 45.97psi. The corresponding vale for the O-cell test was computed as 44.69psi, resulting in a $(f_{rock})_{td} / (f_{rock})_{oc}$ ratio of 1.03. The details are shown in Table 3.

It may be concluded that the difference between the top down test and the O-cell test decreases with the increase of the rock cohesion. For elastic rock case, the $(f_{rock})_{td} / (f_{rock})_{oc}$ ratio is only 1.03, so there's no significant difference between the two load testing methods. But this case is corresponding to the very high strength rock which is impossible to fail. It is also illustrated that the c_{rock} can affect the mobilized side shear for both testing methods. However, this influence is becoming smaller when the value of c_{rock} is large. For instance, the average side shear for the top down test increases about 10% when c_{rock} increases from 50psi to 200psi. But no more than 5% increase was found when c_{rock} increases from 200psi to infinity.

The shear stress distribution for three cases is presented in Figure B-44. Beside the findings about difference of the location of the maximum shear stress, it is also shown that for the elastic rock case, no contact node was open for both top down test and O-cell test. The lower c_{rock} case displays a strange behavior at a depth of 0.7-0.9 of the socket length. This may be caused by the numerical problems since the rock is too low, and the rock around the pile failed before the failure of the side shear.

Embedded Ratio L_{socket}/D

The pile length embedded in the rock is also believed to be an important factor. The following section will discuss its effect, which is represented by the embedded ratio L_{socket}/D . Several cases with different L_{socket}/D values have been analyzed. Four different L_{socket}/D values involved are 1.5, 3.0, 5.0 and 10.0. The finite element mesh was changed accordingly. For case $L_{socket}/D = 10$, there are a total of 5248 nodes and 5035 elements generated. The load vs displacement results from the top down test are shown in Figure B-45. As expected, the longer socket case exhibits a stronger pile response although the four curves are very similar. When 1500kips load is applied, the $L_{socket}/D = 10$ case is still in the elastic range, but $L_{socket}/D = 1.5$ case already mobilizes a large displacement of 0.8in and this load has reached the pile capacity. Figure B-45 also shows that the initial slopes for the four curves are very different.

Figure B-46 and Figure B-47 are the plots of the derived side load vs displacement and tip load vs displacement from the top down test respectively. Figure B-46 shows that the L_{socket}/D ratio has a significant influence on the side resistance, and side resistance can be improved greatly by increasing the socket length because the side

load capacity is proportional to the socket length. It also appears that larger L_{socket}/D case has less side load reduction after yielding and the strain-softening behavior is not very obvious. Less difference was found in the tip load vs displacement curves, as shown in Figure B-47. The case with larger L_{socket}/D ratio shows a little weaker behavior in end bearing. This is because less end bearing is mobilized for larger L_{socket}/D case due to the large side resistance.

The load-displacement curves from the O-cell test are plotted in Figure B-48. The findings are consistent with those from the top down test. Larger L_{socket}/D case results in a higher side resistance. But there's almost no difference for the downward movement curves. It's also noticed that for $L_{socket}/D = 10$ case, large downward displacement has been mobilized and the end bearing almost reached the failure.

The difference between the two testing methods for these four cases can be found in Figure B-49. All the cases show the similar behavior. As before, the O-cell test results exhibit a little stronger response before the failure of the side shear, but it gives a lower side resistance capacity. It is also indicated that for the larger L_{socket}/D case, the strain-softening behavior is not obvious. The $(f_{rock})_{td}/(f_{rock})_{oc}$ ratio for each case can be then calculated. The detailed mobilized side shear from both testing methods and $(f_{rock})_{td}/(f_{rock})_{oc}$ ratio for some cases can be found from Table 4.

Table 4 shows that L_{socket}/D ratio has little effect on the mobilized side shear for both top down testing and O-cell testing except for case where L_{socket}/D is very large ($L_{socket}/D = 10$). Therefore, the influence of L_{socket}/D on the difference of the two

testing methods is not very significant. However, when L_{socket}/D ratio is large enough, the difference is becoming larger. For example, for $L_{socket}/D = 10$ with $\phi_i = 50^\circ$, the $(f_{rock})_{td}/(f_{rock})_{oc}$ ratio is 1.54, and the difference need to be considered. The data in Table 4 can be plotted in Figure B-50. It can be concluded that there is no significant influence of L_{socket}/D on the difference of the two load testing methods if L_{socket}/D is not very large. But the increase of L_{socket}/D tends to enlarge the difference as shown in Figure B-50.

Figure B-51 shows the shear stress distribution for all four cases. For lower L_{socket}/D case, the shear stress distribution for both the top down test and the O-cell test is more varied, and no contact nodes are open at failure although some nodes tend to. But with the increase of the L_{socket}/D ratio, more nodes tend to or turn out to be open at failure especially for the O-cell test. And the distribution becomes more uniform although no significant different is found for the maximum f_x/f_{avg} value. For all four cases, no open contact nodes appear at the top of the socket when failure occurs.

In-situ Horizontal Stress Ratio K_0

The following section will focus on the influence of the overconsolidation ratio. Different cases were conducted by changing the horizontal pressure applied on the far side edge of the finite element mesh. Both normal consolidated case ($K_0 = 0.43$) and $K_0 = 1.0$ case were performed.

Figure B-52 shows the load vs displacement curves from the top down test. It can be seen that the $K_0 = 1.0$ case has a stronger behavior because the larger radial stress will

increase the contact pressure at the interface between pile and soil, which will then increase the side resistance. This result can also be observed from the derived side load vs displacement results from the top down test, as shown in Figure B-53. The two curves are similar, but the $K_0 = 1.0$ case shows a larger maximum side load, which is 1013.5kips. The corresponding value for normal consolidated case is only 658.8kips. However, the tip load vs displacement results, shown in Figure B-54, indicate that there's almost no difference in end bearing between two cases.

The results from the O-cell test are plotted in Figure B-55. It confirms the results obtained from the top down test. K_0 has a significant influence on the side resistance, but has no effect on the end bearing.

The difference between the two testing methods for both cases is shown in Figure B-56. It seems that the maximum side load of the normal consolidated case occurs at a smaller displacement than $K_0 = 1.0$. The $(f_{rock})_{td} / (f_{rock})_{oc}$ ratio for $K_0 = 1.0$ case and normal consolidated case can be calculated as 1.10 and 1.33 respectively. The detailed results can be found in Table 5.

From Table 5, one can find that the increase of K_0 can improve side resistance for both top down test and O-cell test greatly. For $\phi_i = 31^\circ$ case, the side shear increases 47% for the top down test and 71% for the O-cell test respectively. And for $\phi_i = 50^\circ$ case, the increase is 75% and 89% respectively. So with a larger ϕ_i , the influence of K_0 can be more significant. It is also shown that the $(f_{rock})_{td} / (f_{rock})_{oc}$ ratio for $K_0 = 1.0$ case is smaller than the normal consolidated case. Therefore there's smaller difference

between two testing methods for larger radial stress case. This result seems different from the soil model.

Figure B-57 shows the shear stress distribution characteristic for both cases. As can be seen from the plots, the shear distribution from the top test for both cases is very similar. But for the O-cell test, the normal consolidated case appears dramatic. Many contact nodes at the top of the socket are open at failure. The nodes near the pile tip tend to be open, but not open yet. This behavior is different from the $K_0 = 1.0$ case, where contact nodes near the pile tip are open while no open nodes appear at the top of the socket. It may be due to the less contact pressure developed at the pile-soil interface.

SUMMARY

A rock socketed pile model was analyzed using finite element method, and a detailed parametric study was performed to determine the influence of each factor on the difference between the top down test and the O-cell test. For the cases examined, it is always true that the O-cell load test is conservative to estimate the pile capacity compared with the conventional compressive top down load test. Some results regarding the pile response behavior and the parametric study can be summarized as following.

1. Strain-softening behavior of the side load response

For the top down load test, the pile response suggests that side resistance is mobilized before the end bearing. As can be seen from most of the cases analyzed, the side load vs displacement exhibits a strain-softening behavior with a peak value occurring at a displacement of 0.2-0.3in. The end bearing is mobilized after the failure of the side shear. But for some strong cases, such as large rock modulus case, the side load response

shows a strain-hardening behavior, which is due to the larger contact pressure developed at the pile-soil interface.

2. Influence of each parameter

It has been shown the six factors, which are pile-rock interface friction angle ϕ_i and cohesion c_i , Young's modulus of rock E_{rock} , cohesion of rock c_{rock} , embedded ratio L_{socket}/D , and the stress ratio K_0 , have significant influence on the pile response in both top down test and O-cell test. However, little difference was found for cases with different dilation angle of the rock ψ_{rock} .

The study of ϕ_i and c_i suggests that the interface roughness has great influence on the pile response, because they are related directly to the maximum side shear mobilized. The increase of the interface roughness can improve the side resistance greatly, and the influence of c_i seems uniform. However, both factors have no influence on the end bearing behavior. It was also found that the rougher of the interface, the more difference between the top down test and the O-cell test. Another finding is related to the shear stress distribution. It is observed that the shear stress distribution tends to be more uniform for cases with a lower ϕ_i . On the contrary, larger c_i case shows more uniform shear stress distribution.

The rock properties, i.e. E_{rock} and c_{rock} , have considerable influence on both side resistance and end bearing. The increase of these two factors will increase the pile capacity in both side resistance and end bearing. However, their influence on the difference between the top down test and the O-cell test is in the opposite direction. Larger rock modulus will result in more difference between the two testing methods. But

the increase of the cohesion of the rock will give less difference. As to the shear stress distribution, larger c_{rock} or lower E_{rock} will result in more uniform distribution.

The increase of the embedded ratio L_{socket}/D will give larger pile capacity, but the average mobilized unit side shear doesn't have much difference except if L_{socket}/D is large enough. This holds true for the difference between the two testing methods. Larger L_{socket}/D ratio tends to induce more difference.

The overconsolidation ratio also has significant influence since it can improve the contact pressure developed at the interface which will then result in greater side resistance. But it has almost no effect on the end bearing. The results suggest that larger difference between the two testing methods will be induced by a smaller K_0 .

Table 1 Effect of ϕ_i and E_{rock} on Pile Response and Difference

Between Top Down Test and O-cell Test

E_{rock} (ksi)	$\phi_i = 14^\circ$			$\phi_i = 31^\circ$			$\phi_i = 50^\circ$		
	$(f_{rock})_{td}$ (psi)	$(f_{rock})_{oo}$ (psi)	$\frac{(f_{rock})_{td}}{(f_{rock})_{oo}}$	$(f_{rock})_{td}$ (psi)	$(f_{rock})_{oo}$ (psi)	$\frac{(f_{rock})_{td}}{(f_{rock})_{oo}}$	$(f_{rock})_{td}$ (psi)	$(f_{rock})_{oo}$ (psi)	$\frac{(f_{rock})_{td}}{(f_{rock})_{oo}}$
70	29.83	28.43	1.05	42.70	37.31	1.14	64.80	49.76	1.30
700	42.31	30.92	1.37	72.82	44.00	1.66	152.20	60.68	2.51
7000	139.63	43.70	3.20	/	/	/	/	/	/

Table 2 Effect of c_i on Pile Response and Difference

Between Top Down Test and O-cell Test

ϕ_i ($^\circ$)	$c_i = 0$			$c_i = 10 \text{ psi}$			$c_i = 20 \text{ psi}$		
	$(f_{rock})_{td}$ (psi)	$(f_{rock})_{oo}$ (psi)	$\frac{(f_{rock})_{td}}{(f_{rock})_{oo}}$	$(f_{rock})_{td}$ (psi)	$(f_{rock})_{oo}$ (psi)	$\frac{(f_{rock})_{td}}{(f_{rock})_{oo}}$	$(f_{rock})_{td}$ (psi)	$(f_{rock})_{oo}$ (psi)	$\frac{(f_{rock})_{td}}{(f_{rock})_{oo}}$
14	10.30	10.27	1.00	20.05	19.44	1.03	29.83	28.43	1.05
31	23.05	21.50	1.07	32.92	29.67	1.11	42.70	37.31	1.14
50	44.65	37.57	1.19	54.81	43.83	1.25	64.80	49.76	1.30

Table 3 Effect of c_{rock} on Pile Response and Difference

Between Top Down Test and O-cell Test

Elastic Rock			$c_{rock} = 200 \text{ psi}$			$c_{rock} = 50 \text{ psi}$		
$(f_{rock})_{td}$ (psi)	$(f_{rock})_{oo}$ (psi)	$\frac{(f_{rock})_{td}}{(f_{rock})_{oo}}$	$(f_{rock})_{td}$ (psi)	$(f_{rock})_{oo}$ (psi)	$\frac{(f_{rock})_{td}}{(f_{rock})_{oo}}$	$(f_{rock})_{td}$ (psi)	$(f_{rock})_{oo}$ (psi)	$\frac{(f_{rock})_{td}}{(f_{rock})_{oo}}$
45.97	44.69	1.03	42.70	37.31	1.14	38.76	29.12	1.33

Table 4 Effect of L_{socket} / D on Pile Response and Difference

Between Top Down Test and O-cell Test

L_{socket} / D	$\phi_i = 31^\circ$			$\phi_i = 50^\circ$		
	$(f_{rock})_{td}$ (psi)	$(f_{rock})_{oo}$ (psi)	$\frac{(f_{rock})_{td}}{(f_{rock})_{oo}}$	$(f_{rock})_{td}$ (psi)	$(f_{rock})_{oo}$ (psi)	$\frac{(f_{rock})_{td}}{(f_{rock})_{oo}}$
1.5	42.74	37.37	1.14	61.47	51.02	1.20
3.0	41.70	38.07	1.10	61.85	51.08	1.21
5.0	42.70	37.31	1.14	64.80	49.76	1.30
10.0	46.78	37.97	1.23	74.47	48.44	1.54

Table 5 Effect of K_0 on Pile Response and Difference

Between Top Down Test and O-cell Test

K_0	$\phi_i = 31^\circ$			$\phi_i = 50^\circ$		
	$(f_{rock})_{td}$ (psi)	$(f_{rock})_{oo}$ (psi)	$\frac{(f_{rock})_{td}}{(f_{rock})_{oo}}$	$(f_{rock})_{td}$ (psi)	$(f_{rock})_{oo}$ (psi)	$\frac{(f_{rock})_{td}}{(f_{rock})_{oo}}$
0.43	28.97	21.77	1.33	37.07	26.39	1.40
1.0	42.70	37.31	1.14	64.80	49.76	1.30

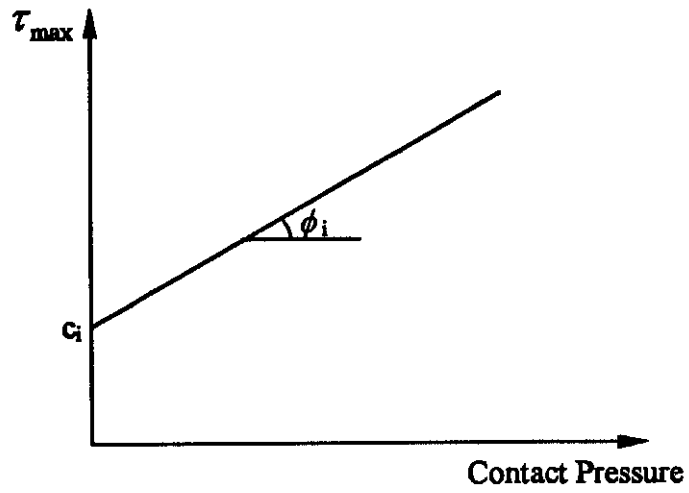


Figure B-1 Constitutive Model for Pile-Rock Interface

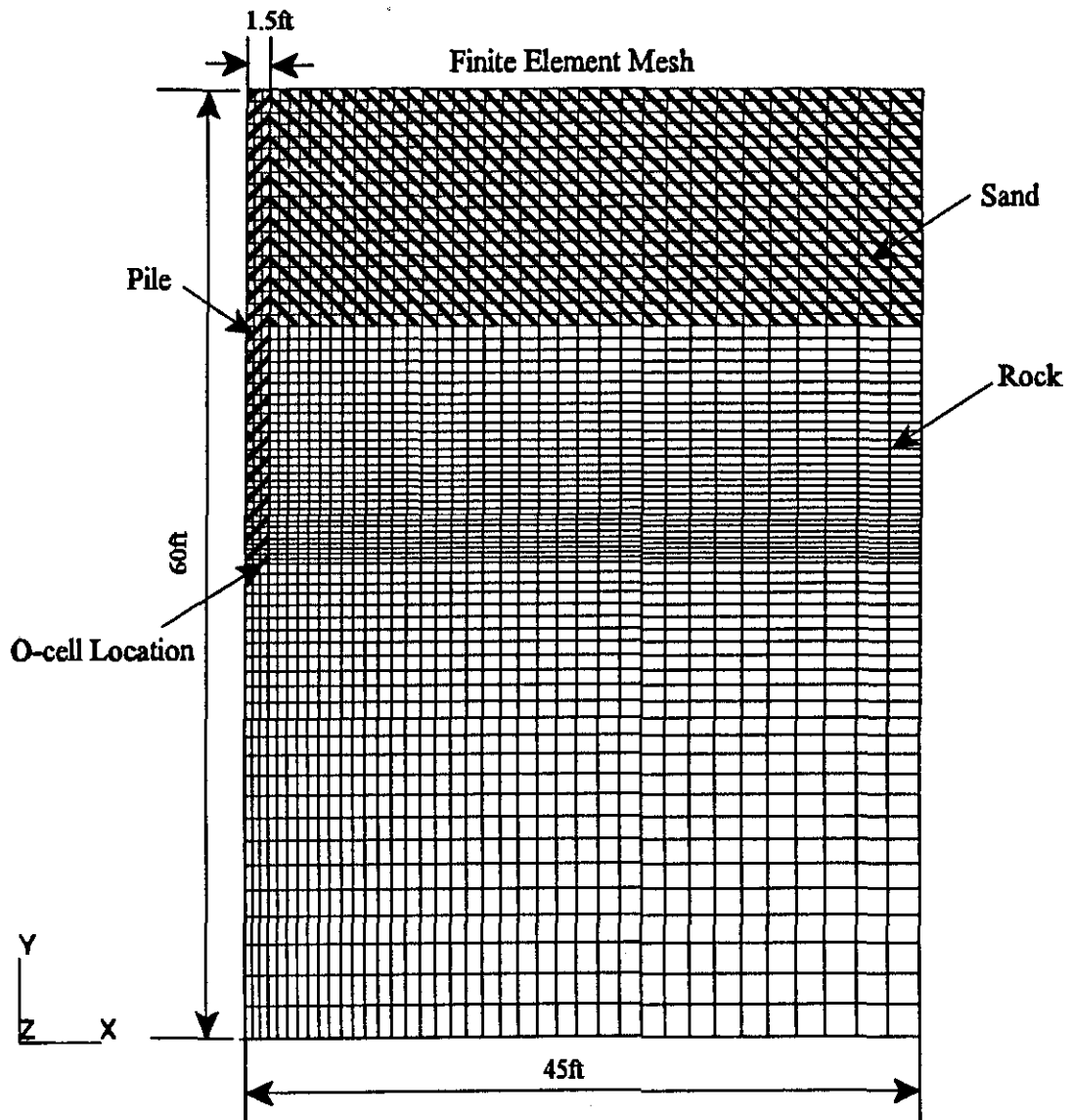


Figure B-2 Finite Element Mesh for Rock Socket Model

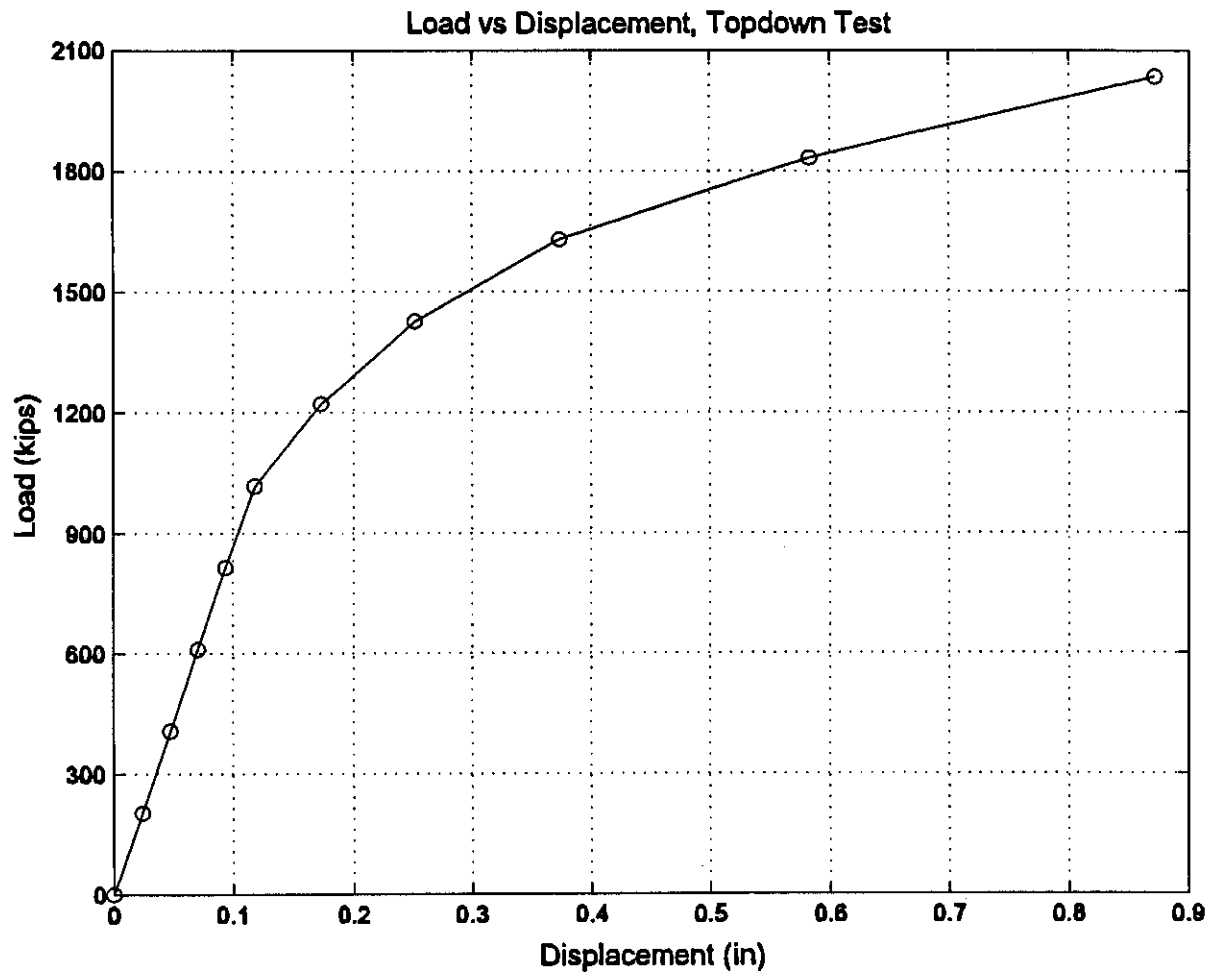


Figure B-3 Load vs Displacement Curve, Top Down Test

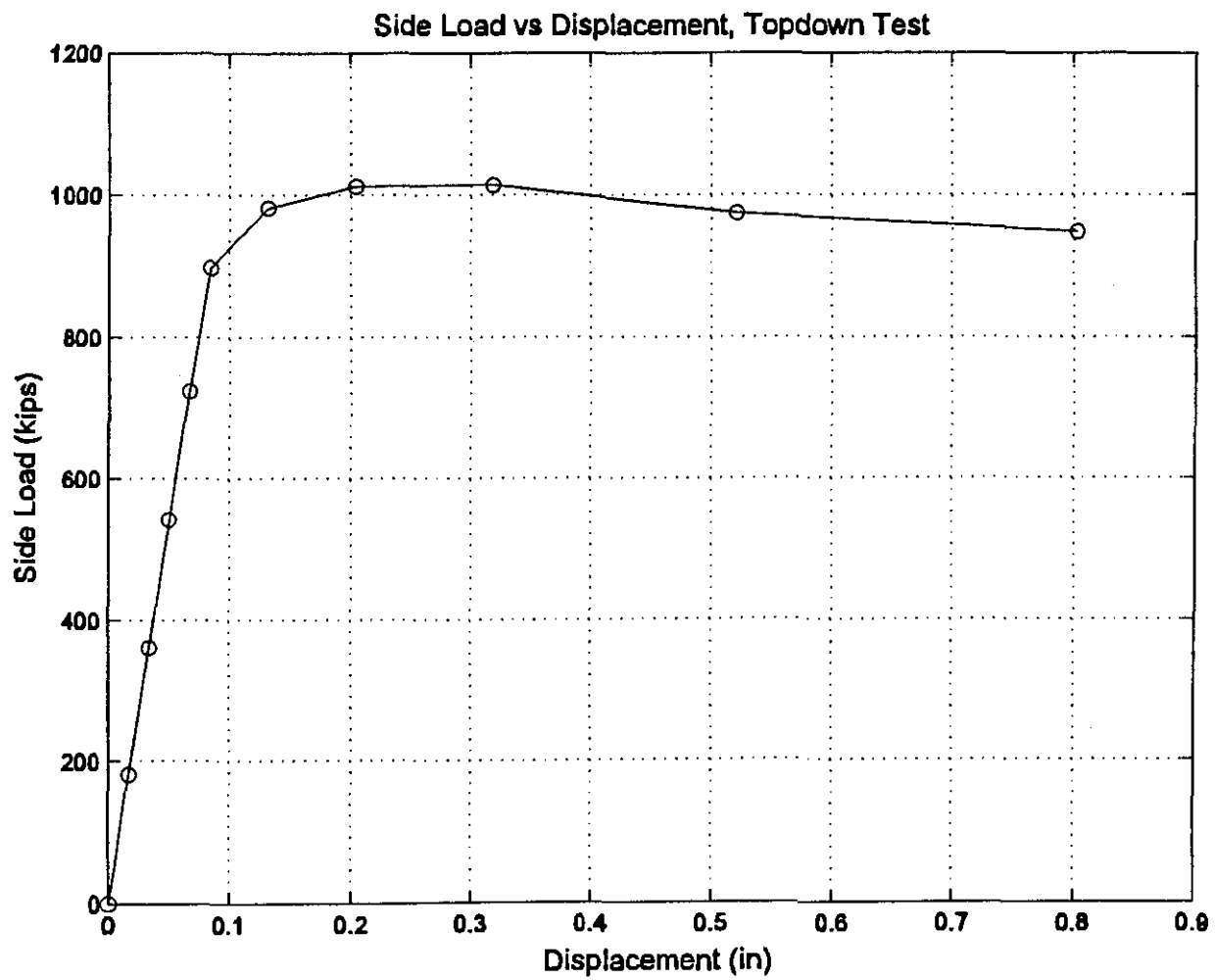


Figure B-4 Side Load vs Displacement Curve, Top Down Test

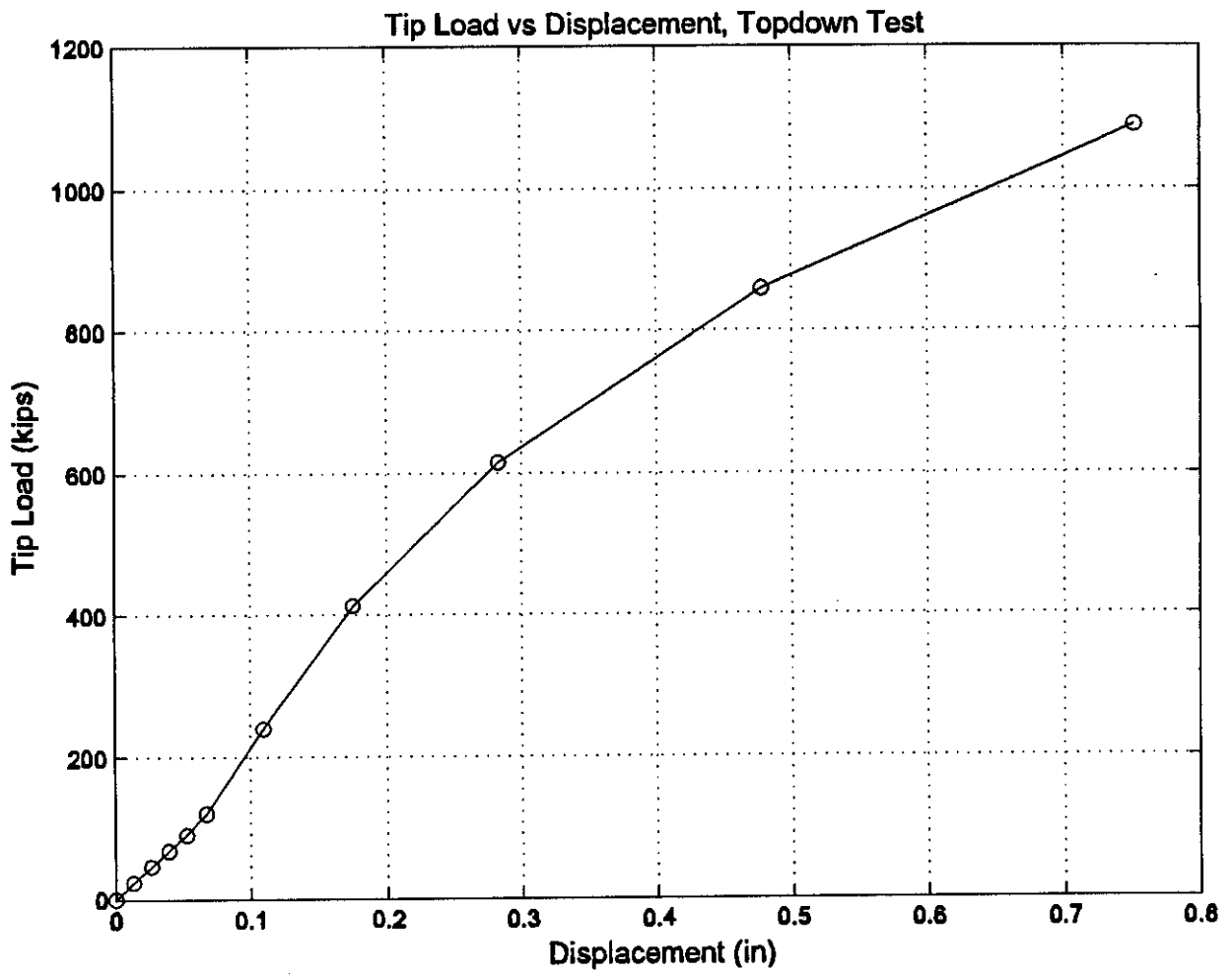


Figure B-5 Tip Load vs Displacement Curve, Top Down Test

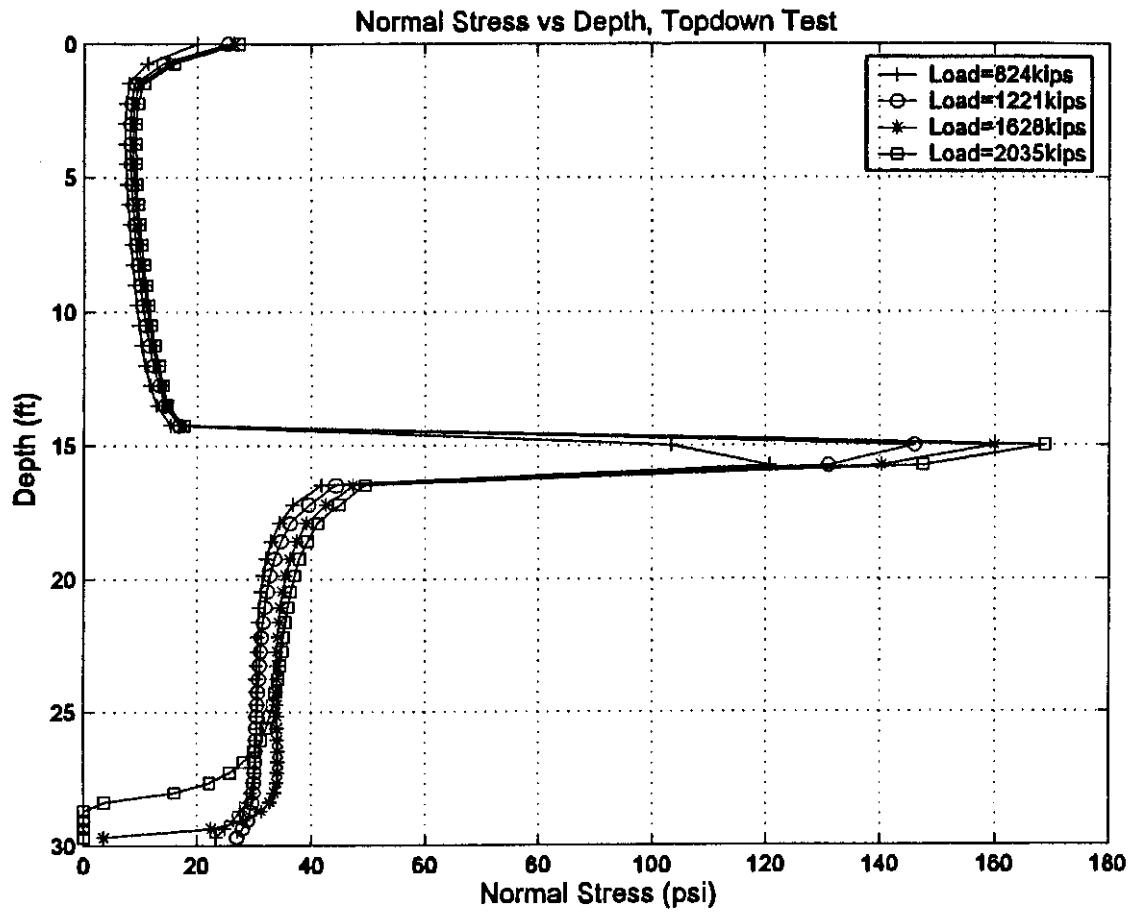


Figure B-6 Normal Stress vs Depth, Top Down Test

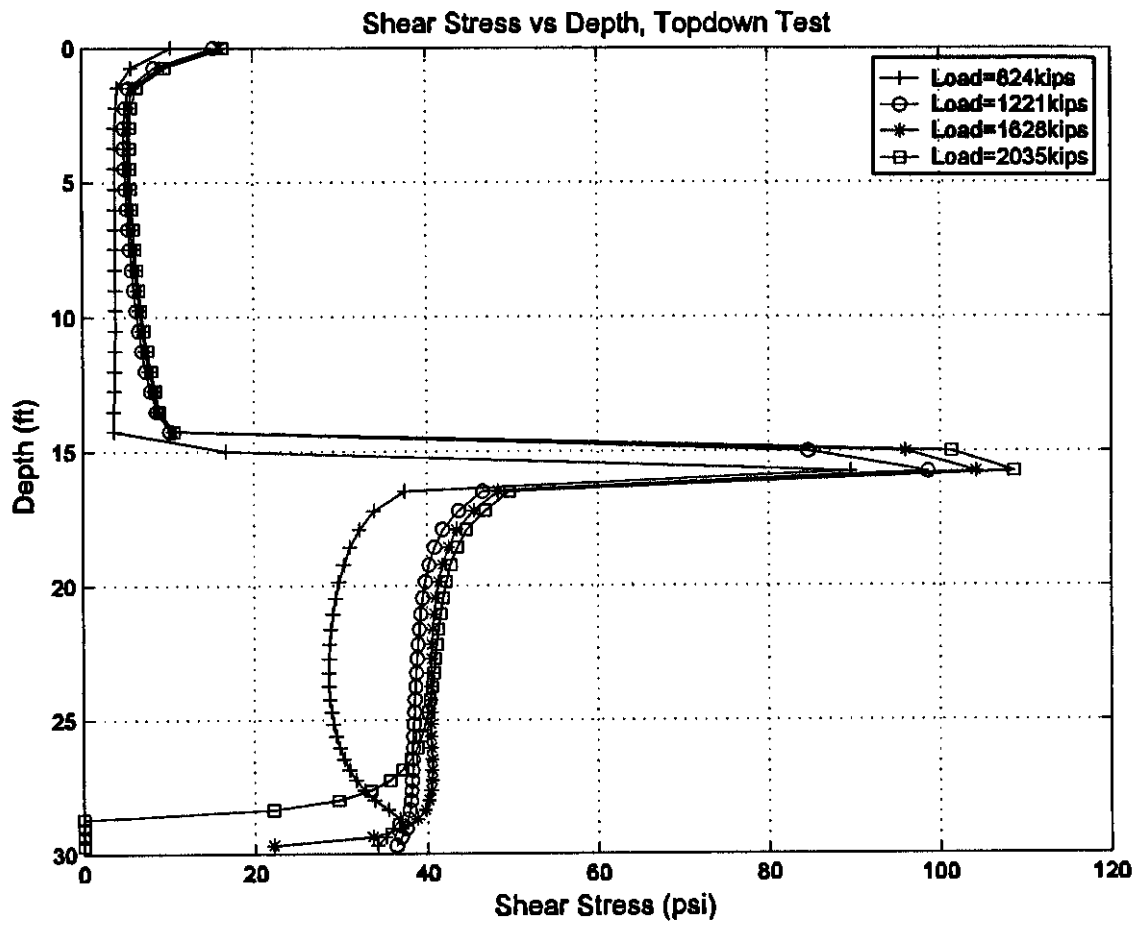


Figure B-7 Shear Stress vs Depth, Top Down Test

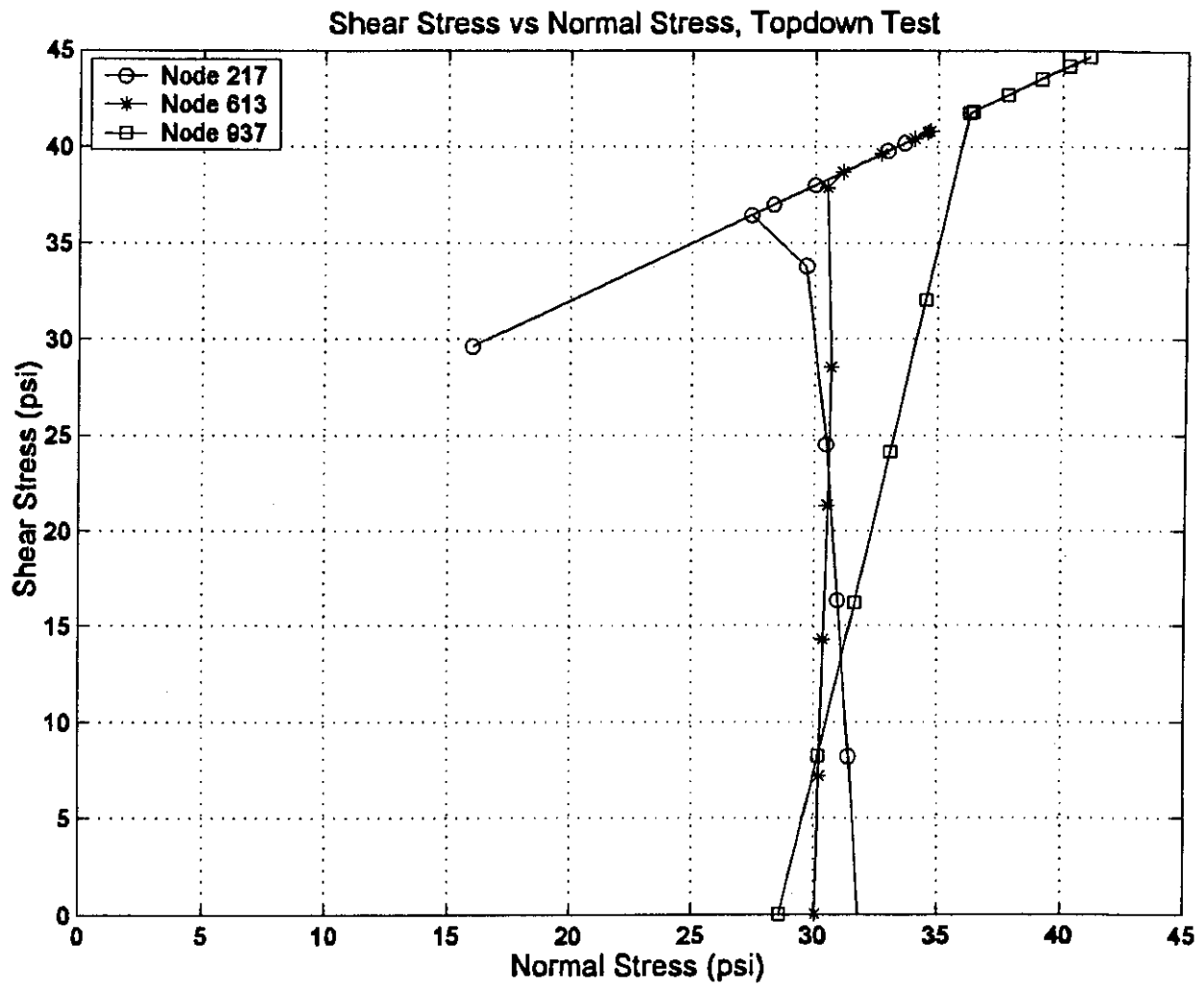


Figure B-8 Shear Stress vs Normal Stress, Top Down Test

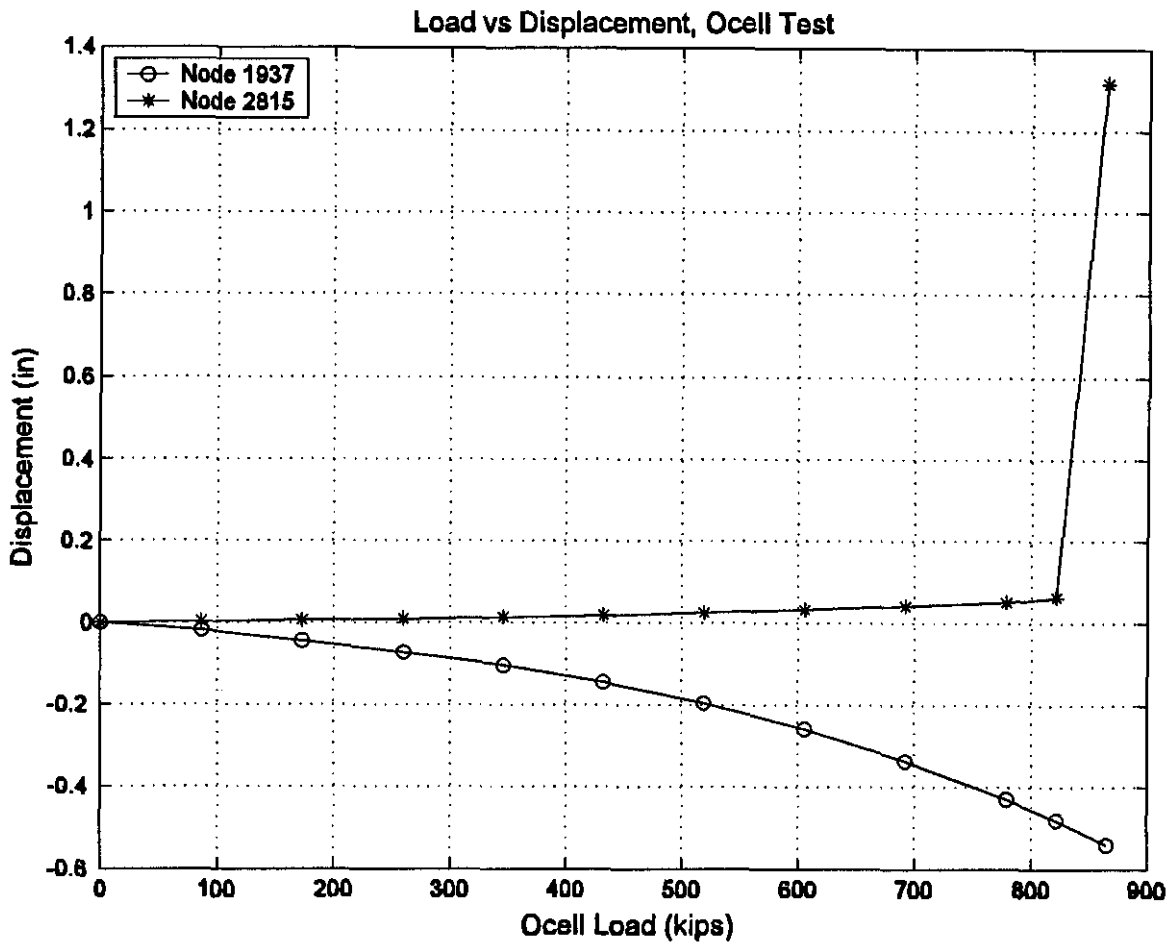


Figure B-9 Load vs Displacement Curve, O-cell Test

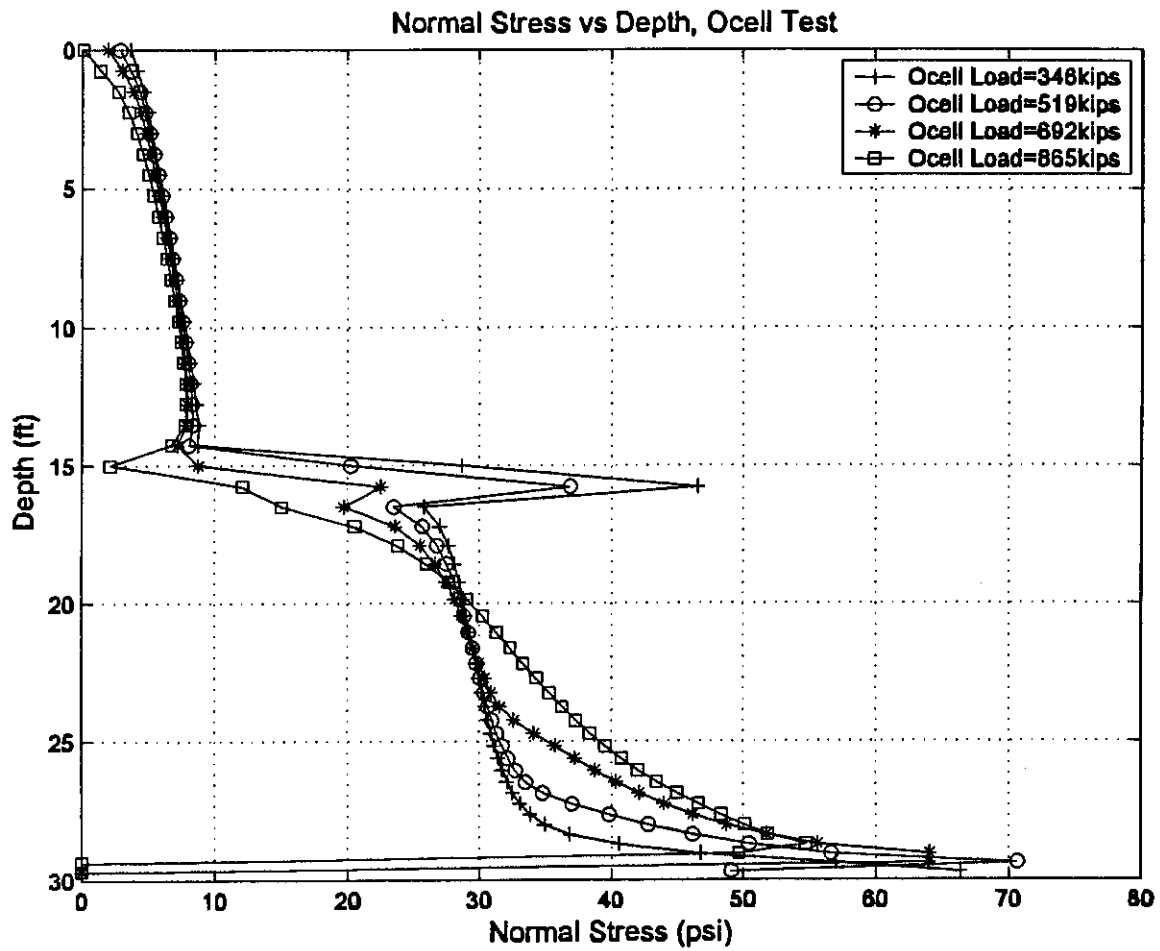


Figure B-10 Normal Stress vs Depth, O-cell Test

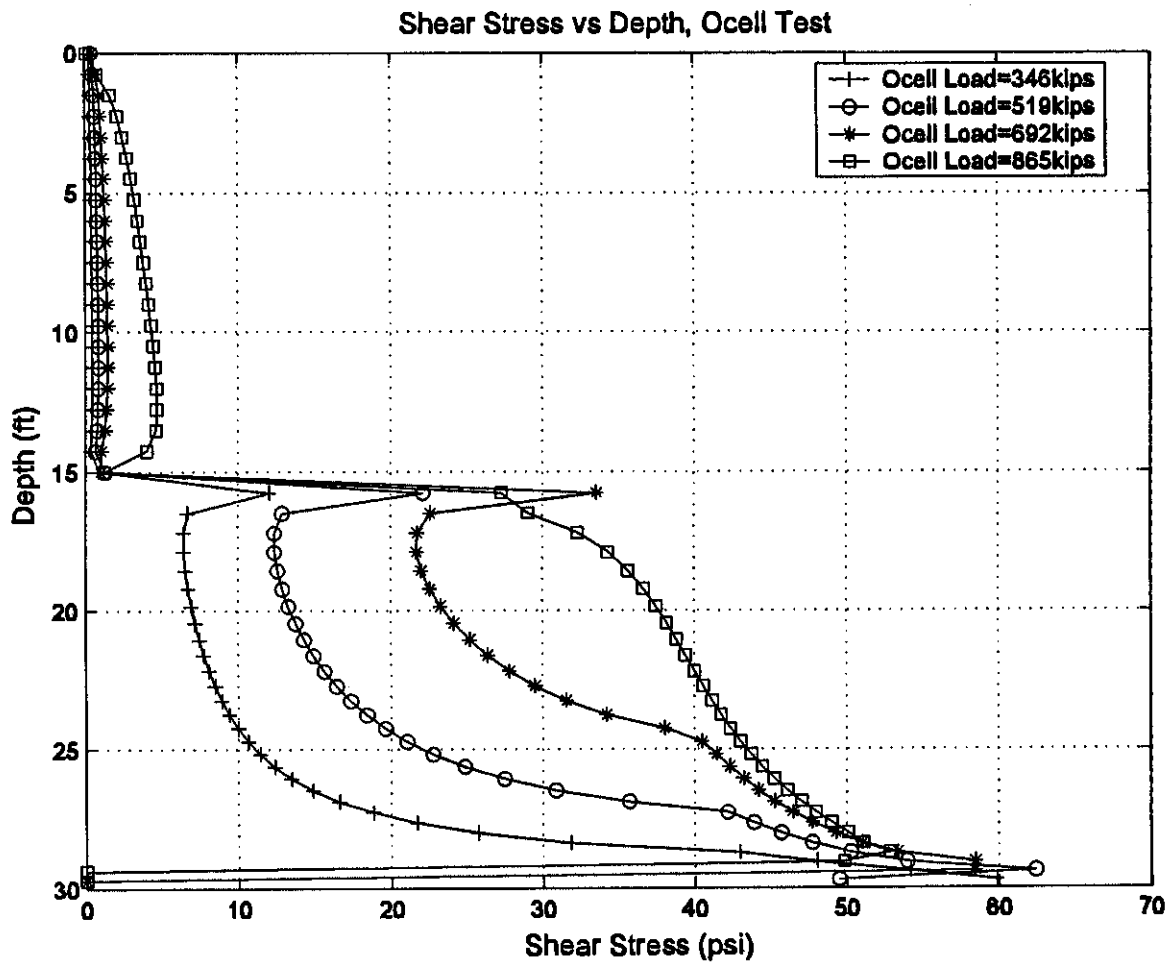


Figure B-11 Shear Stress vs Depth, O-cell Test

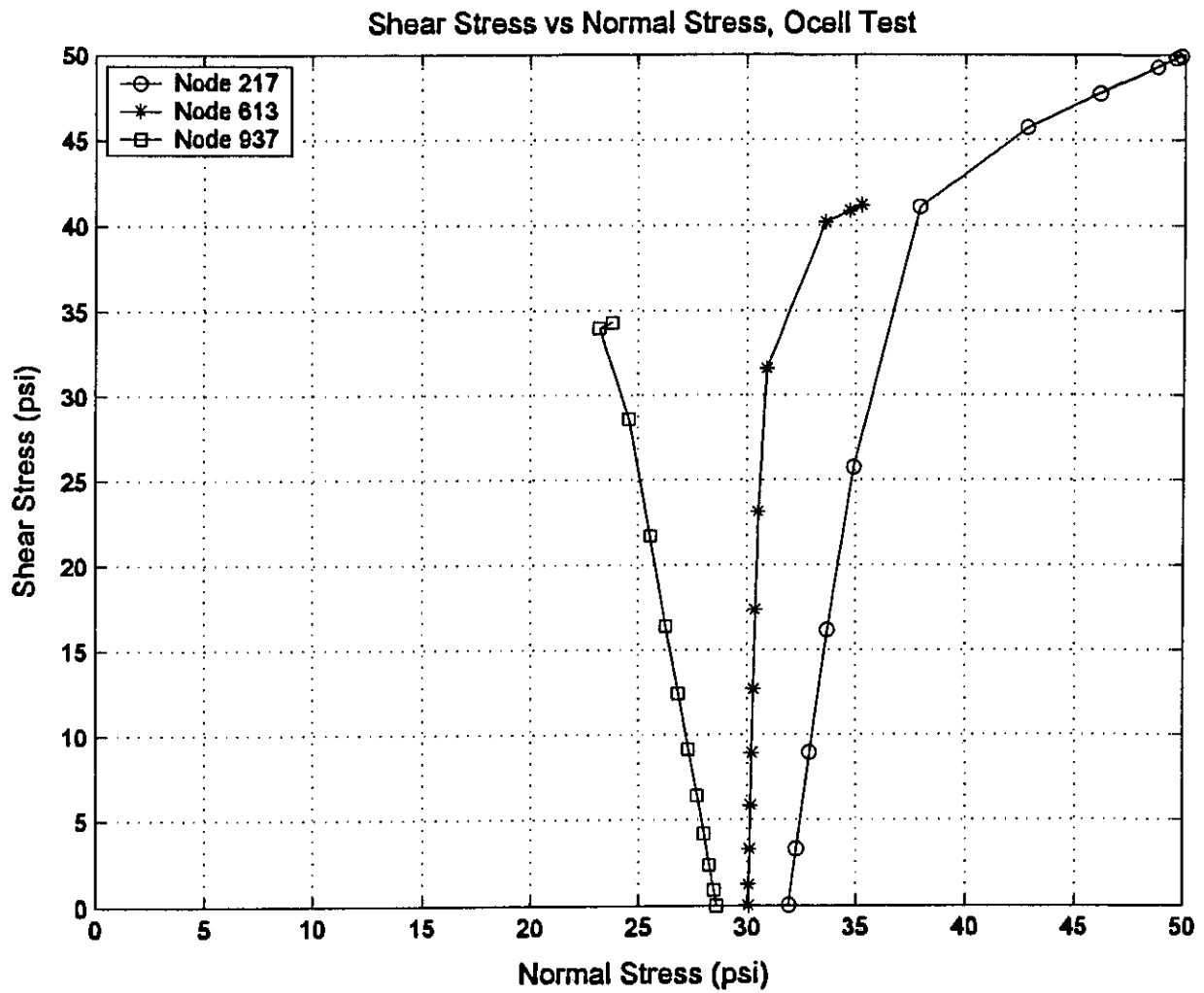
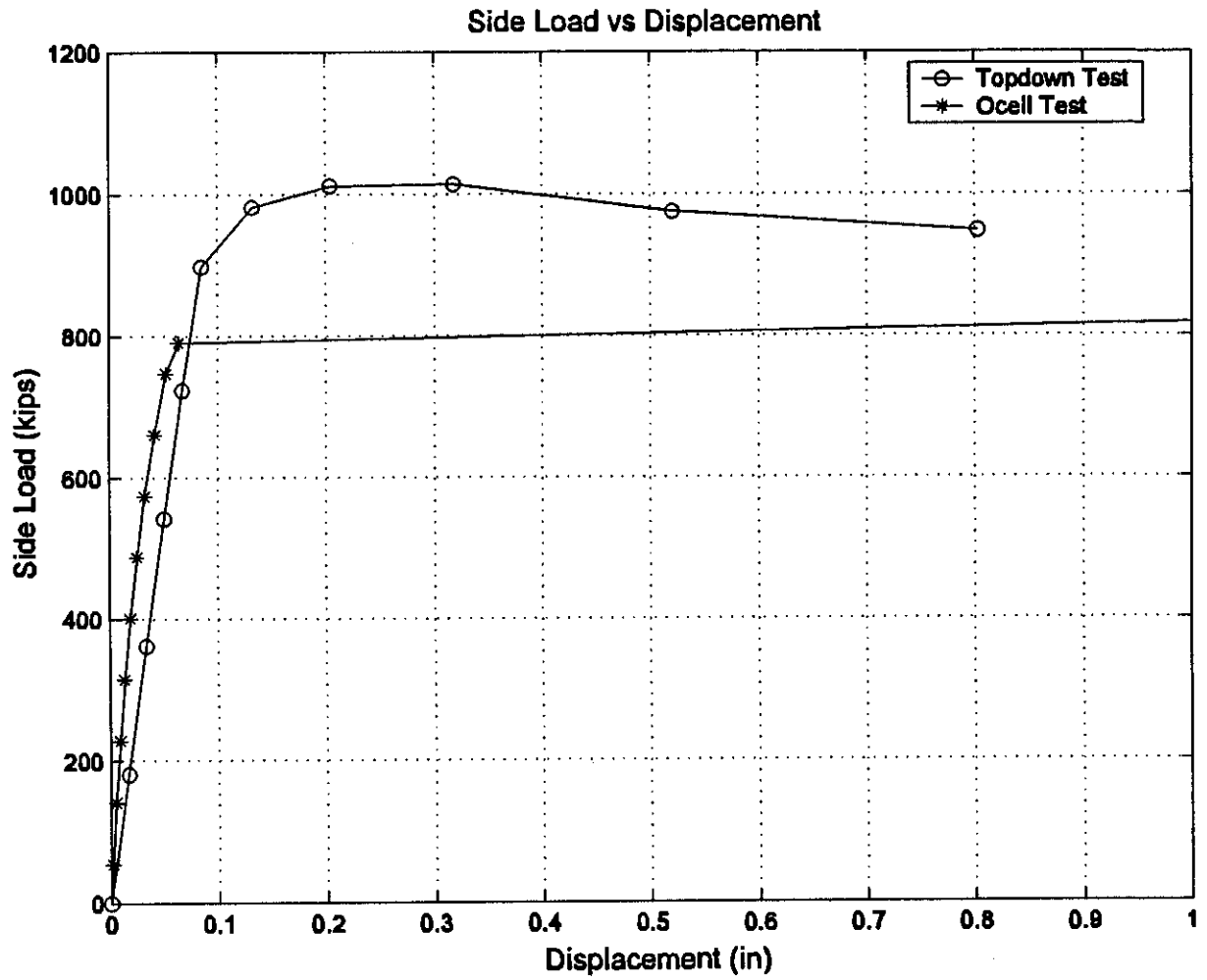


Figure B-12 Shear Stress vs Normal Stress, O-cell Test



*Figure B-13 Comparison of Side Load vs Displacement Curve
Between Top Down Test and O-cell Test*

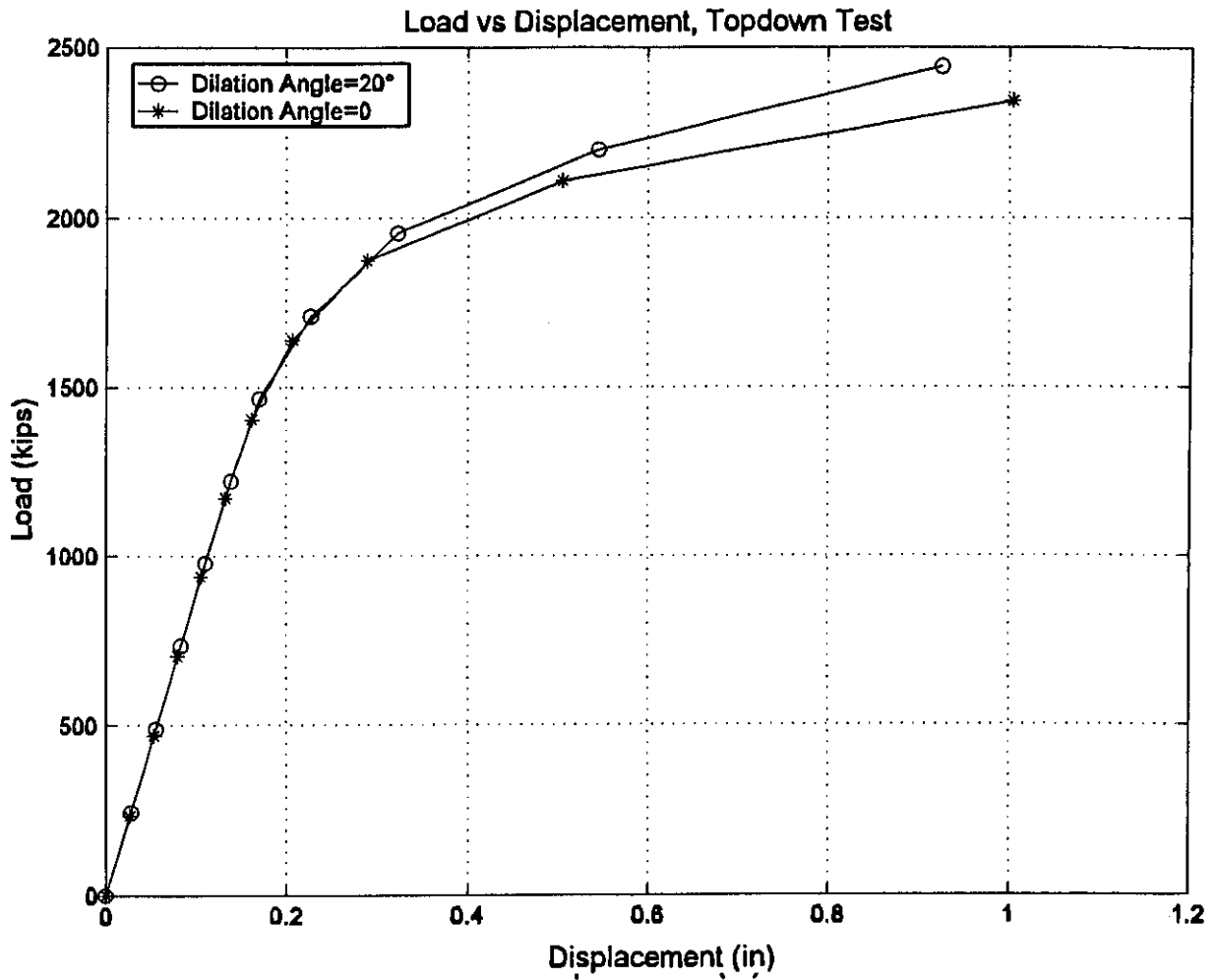


Figure B-14 Effect of ψ_{rock} on Load vs Displacement Curve, Top Down Test

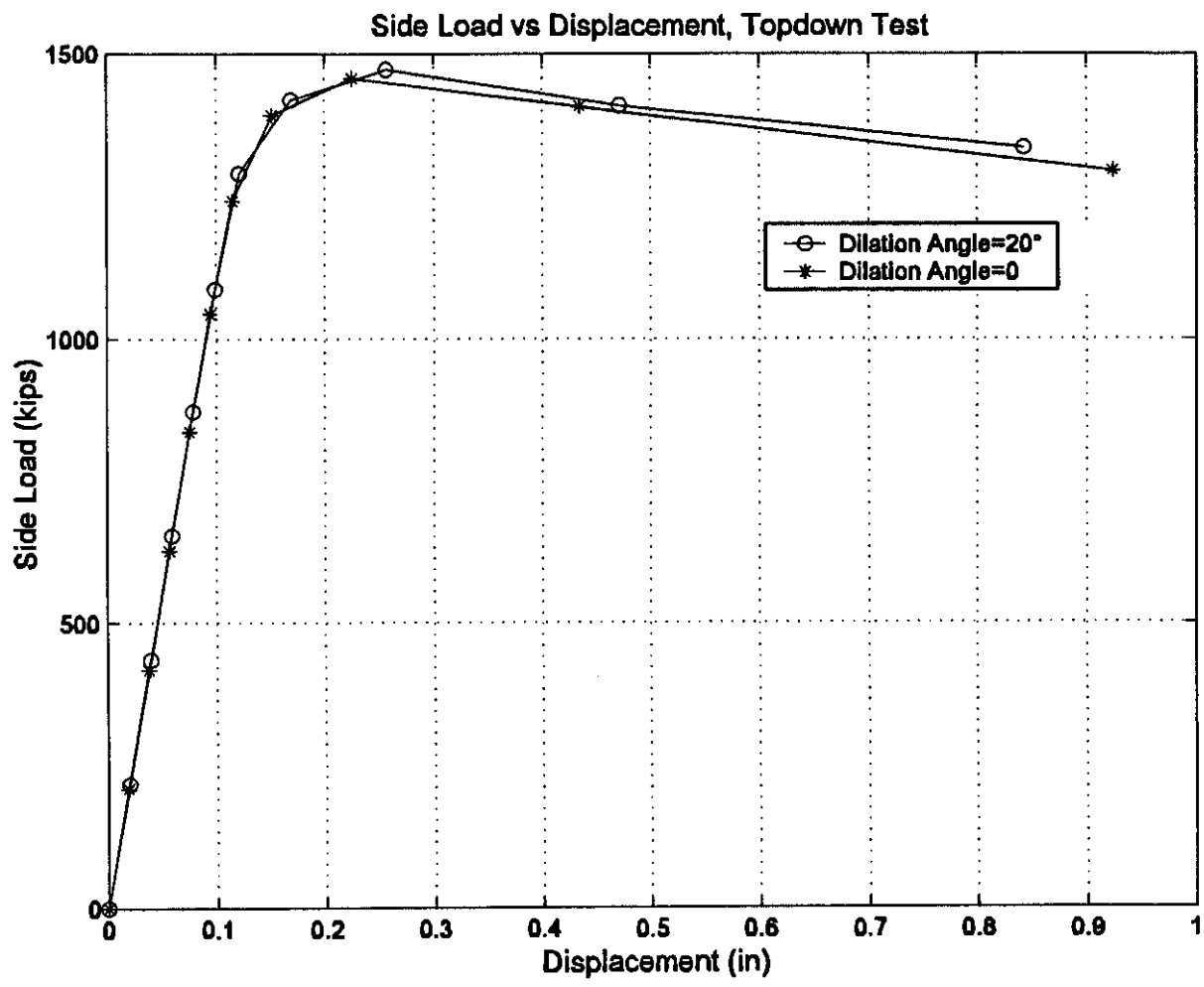


Figure B-15 Effect of ψ_{rock} on Side Load vs Displacement, Top Down Test

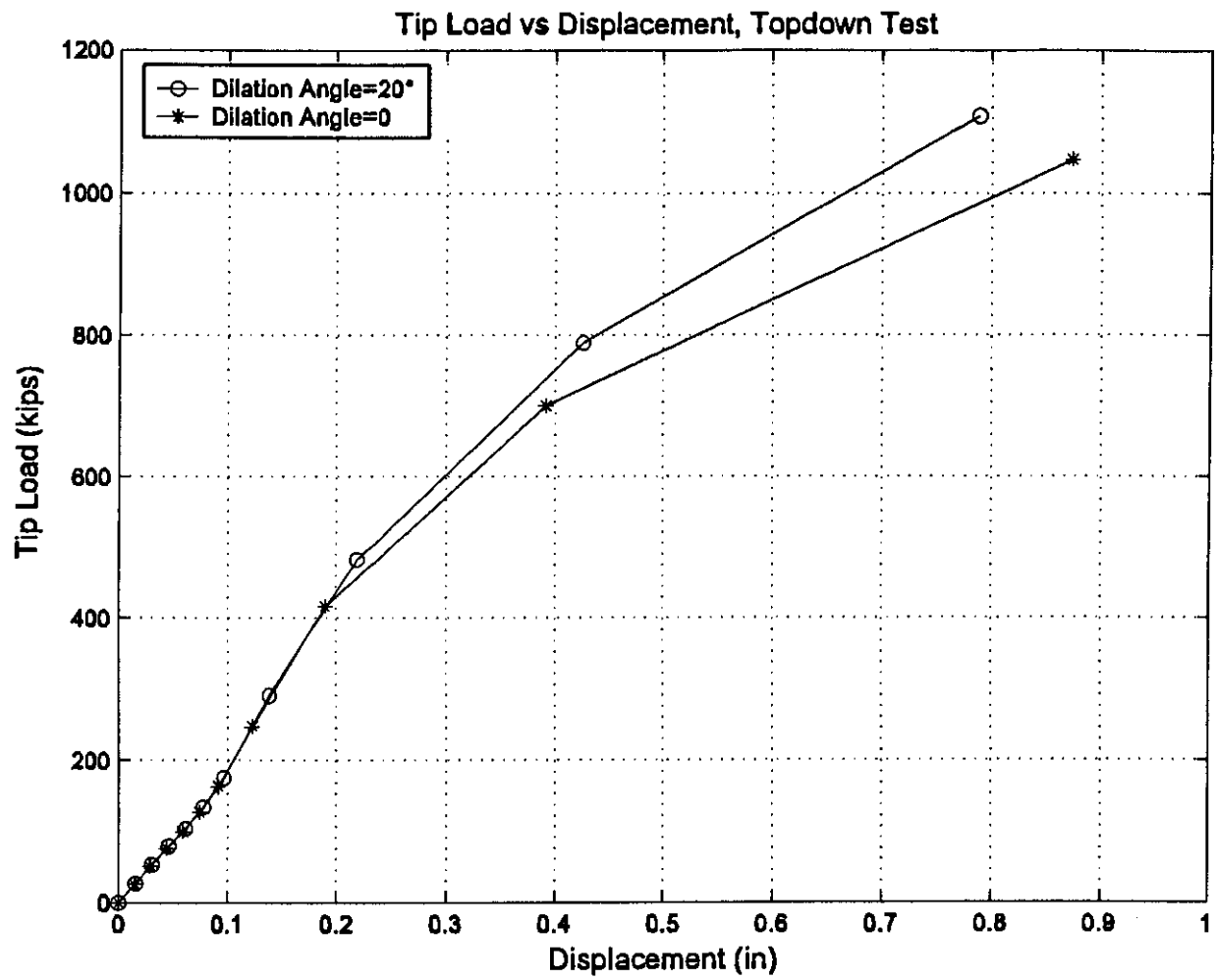


Figure B-16 Effect of ψ_{rock} on Tip Load vs Displacement, Top Down Test

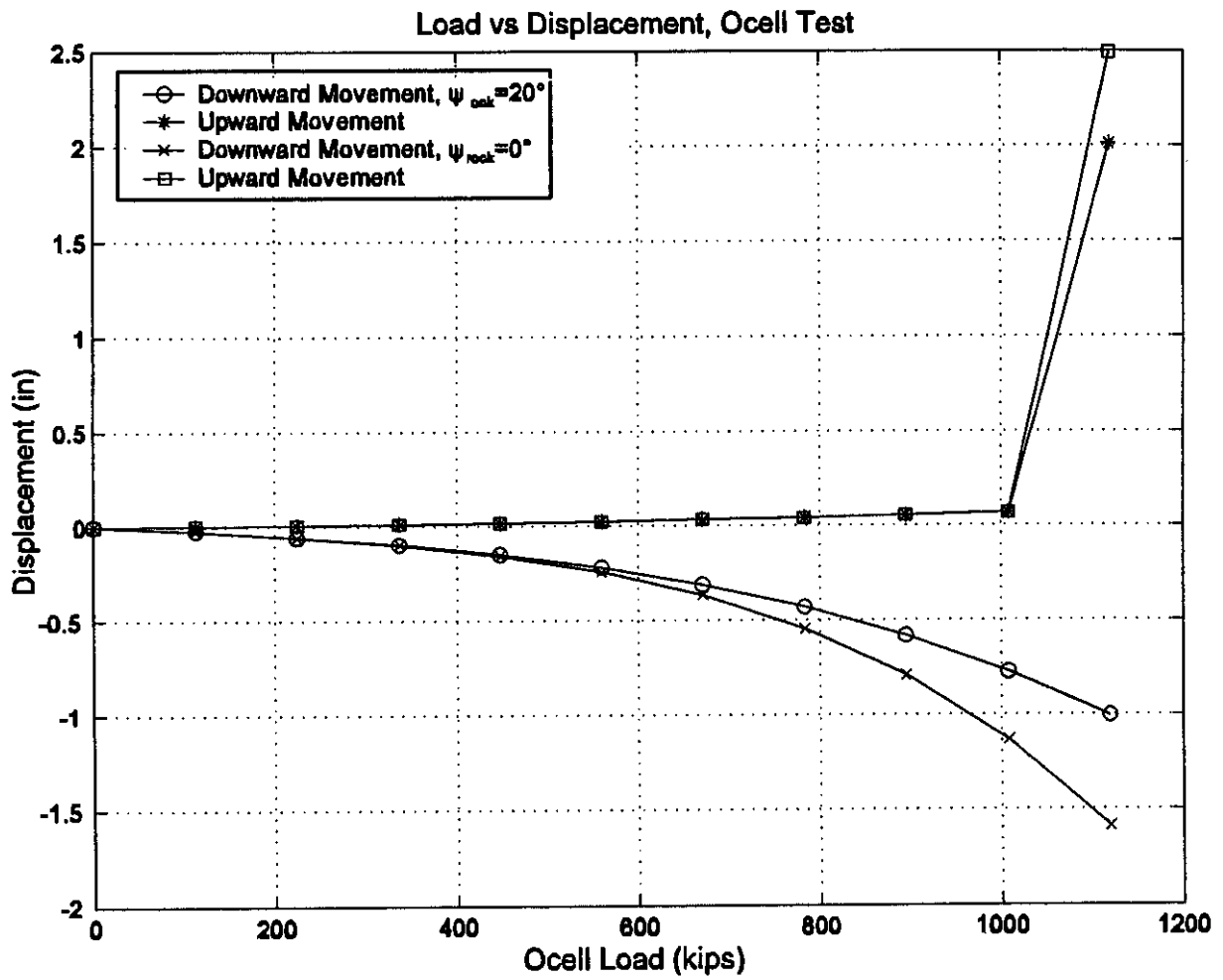


Figure B-17 Effect of ψ_{rock} on Load vs Displacement Curve, O-cell Test

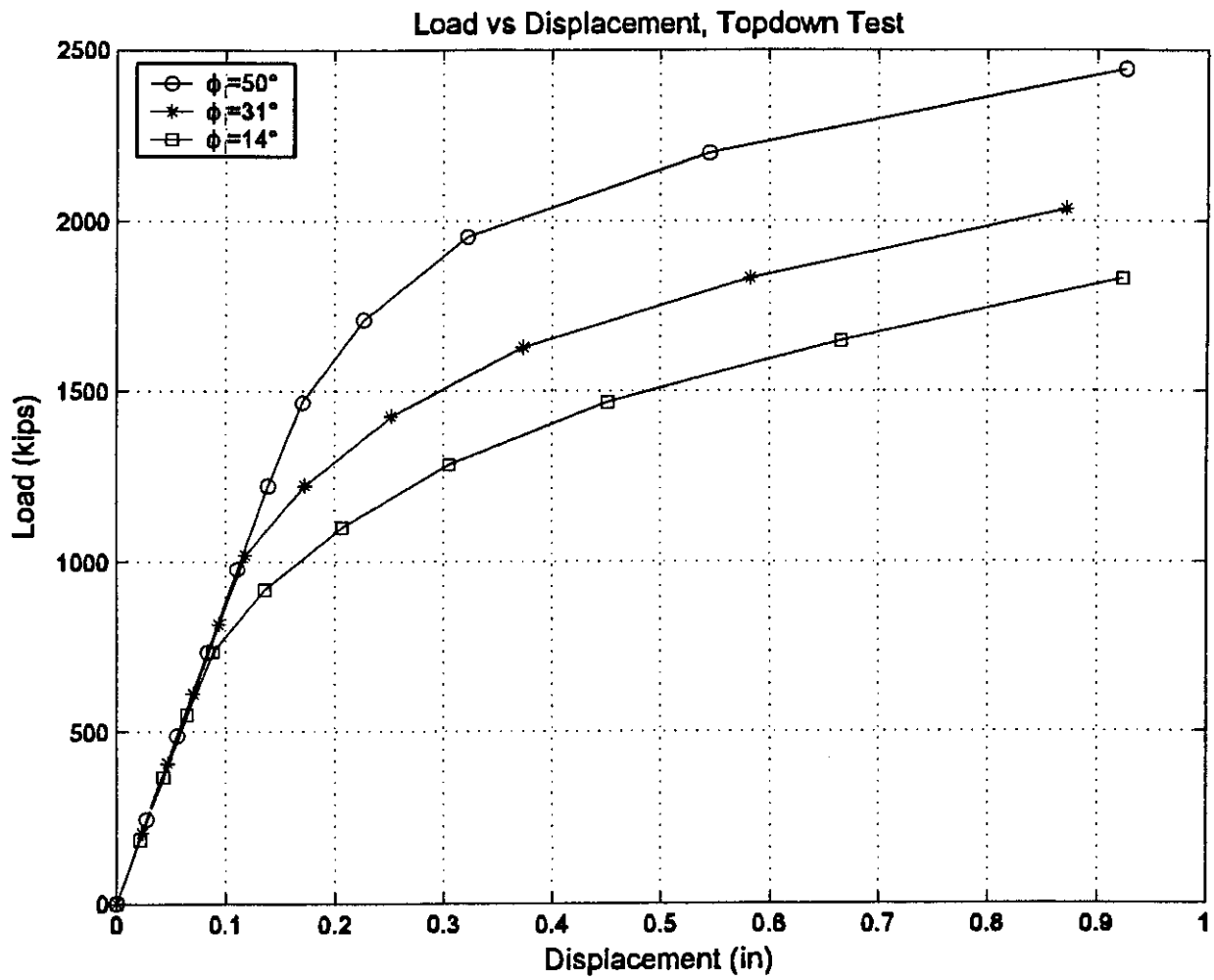


Figure B-18 Effect of ϕ , on Load vs Displacement Curve, Top Down Test

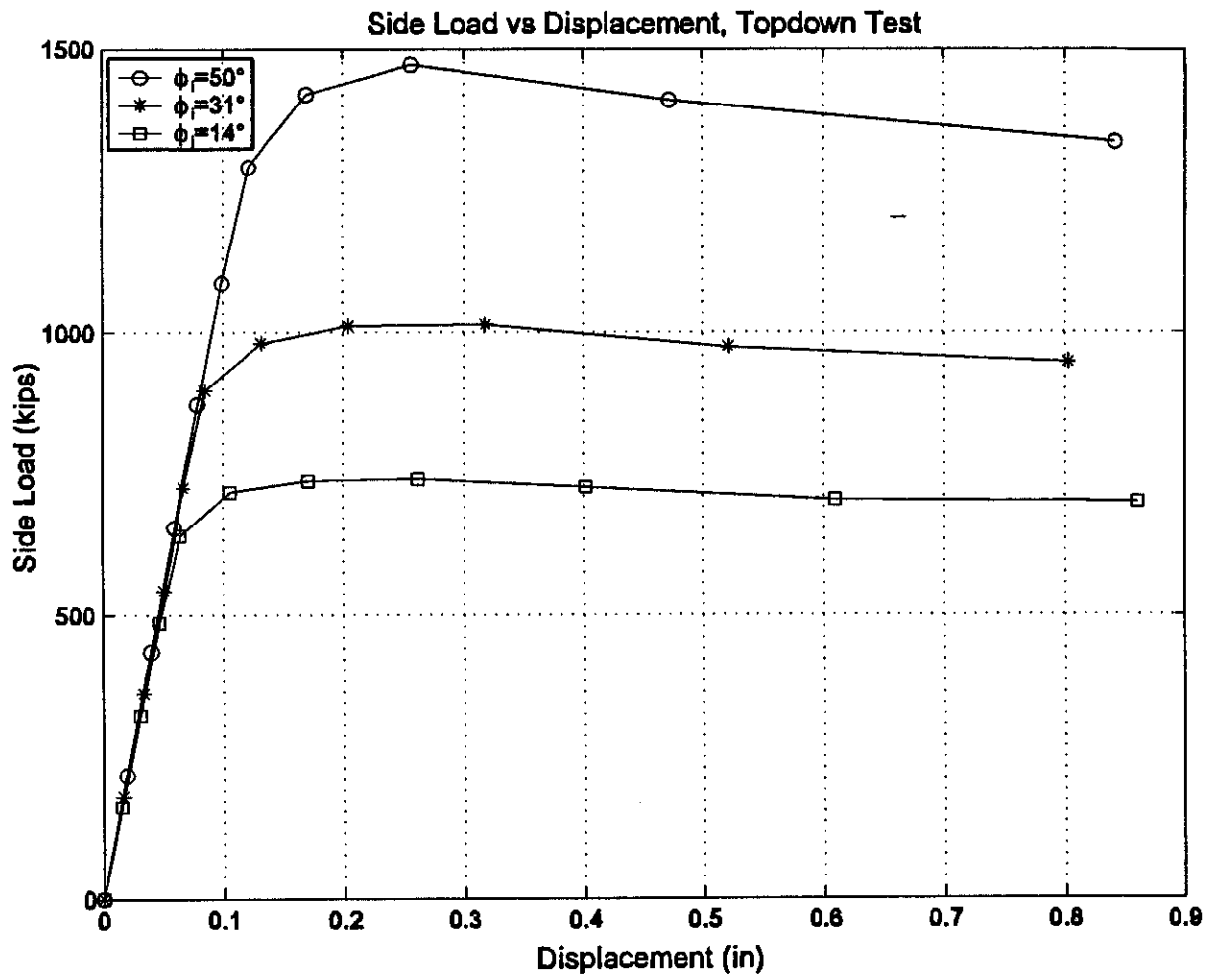


Figure B-19 Effect of ϕ_1 on Side Load vs Displacement Curve, Top Down Test

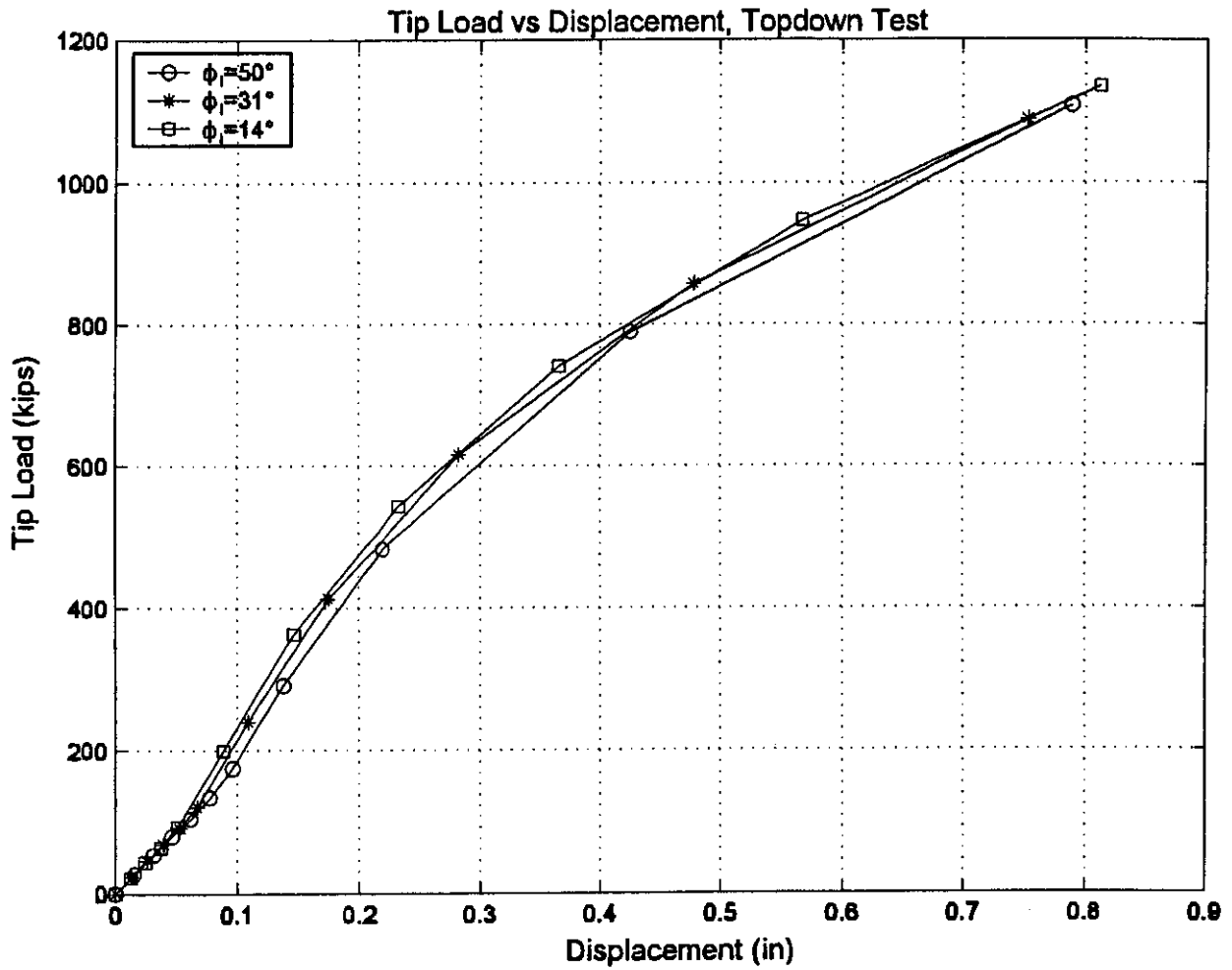


Figure B-20 Effect of ϕ_i on Tip Load vs Displacement Curve, Top Down Test

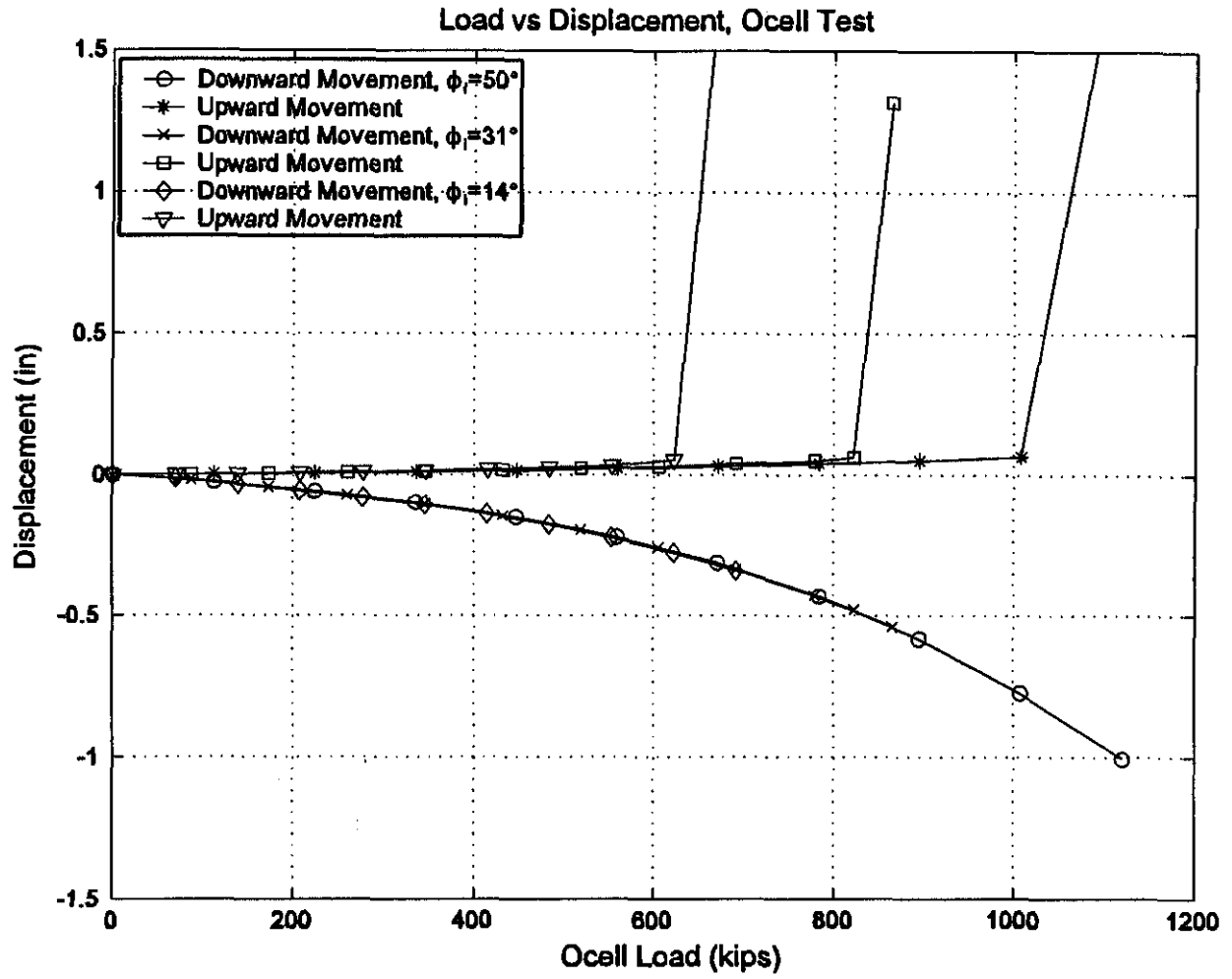


Figure B-21 Effect of ϕ_i on Load vs Displacement Curve, O-cell Test

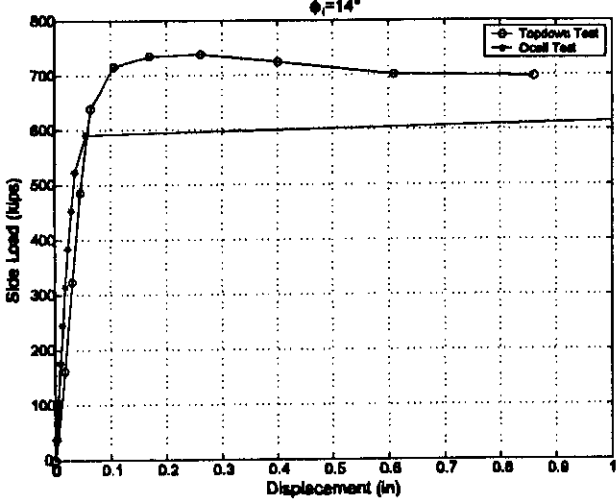
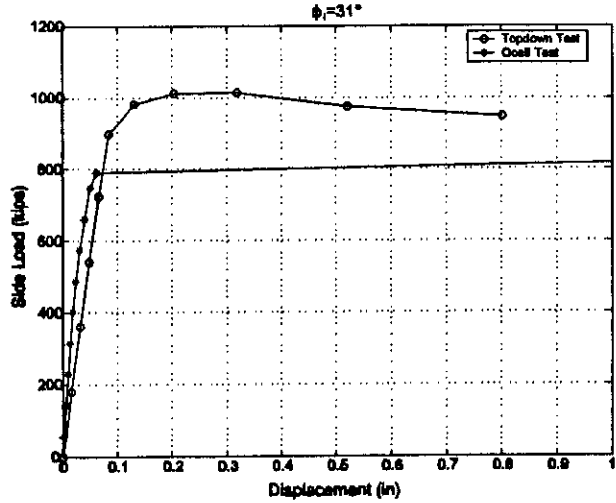
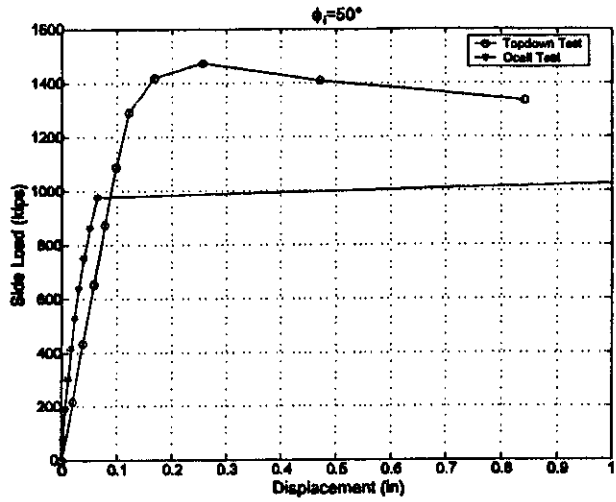


Figure B-22 Side Load vs Displacement Comparison for Different ϕ_i Values

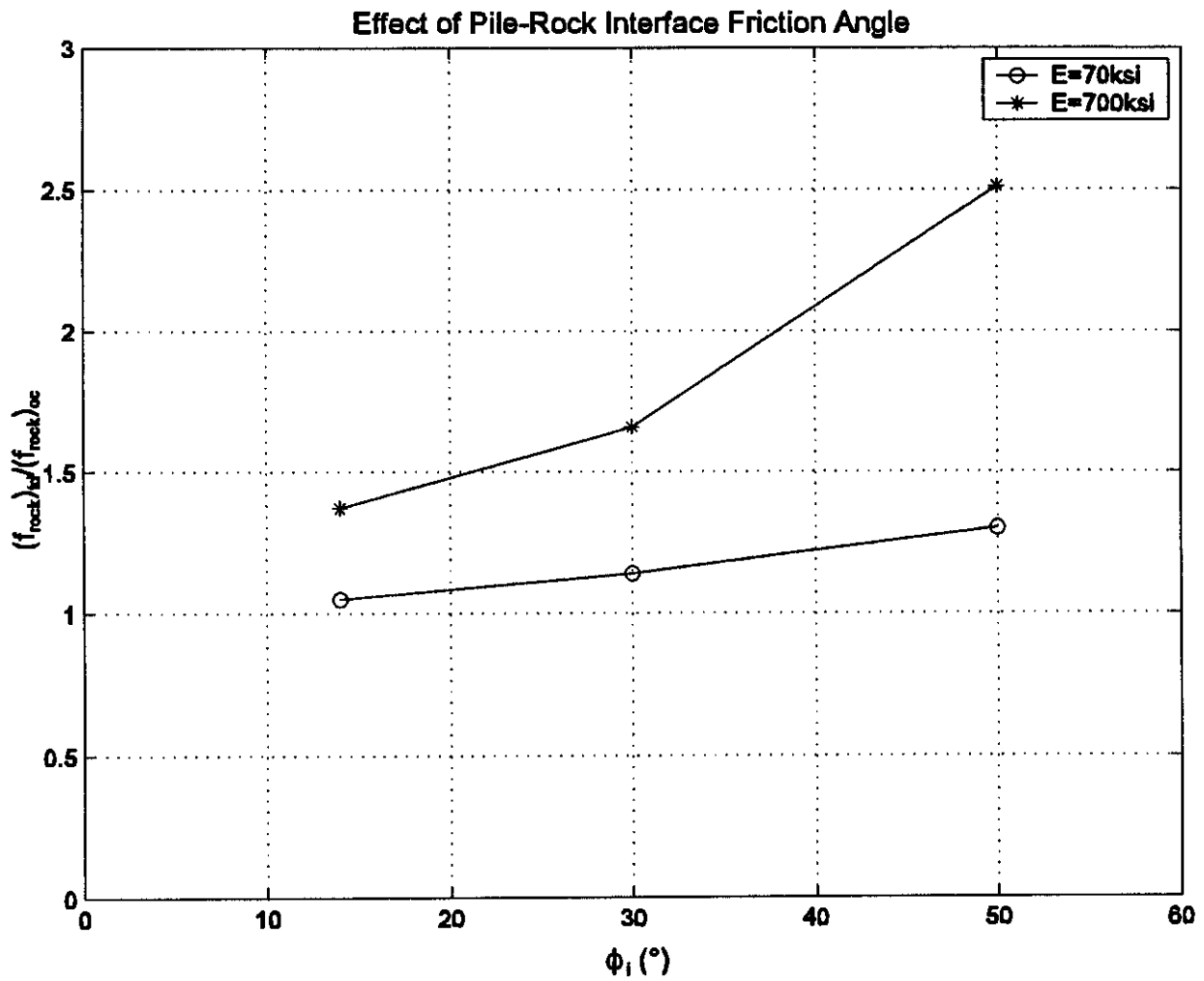


Figure B-23 Effect of ϕ_i on the Difference Between Top Down Test and O-cell Test

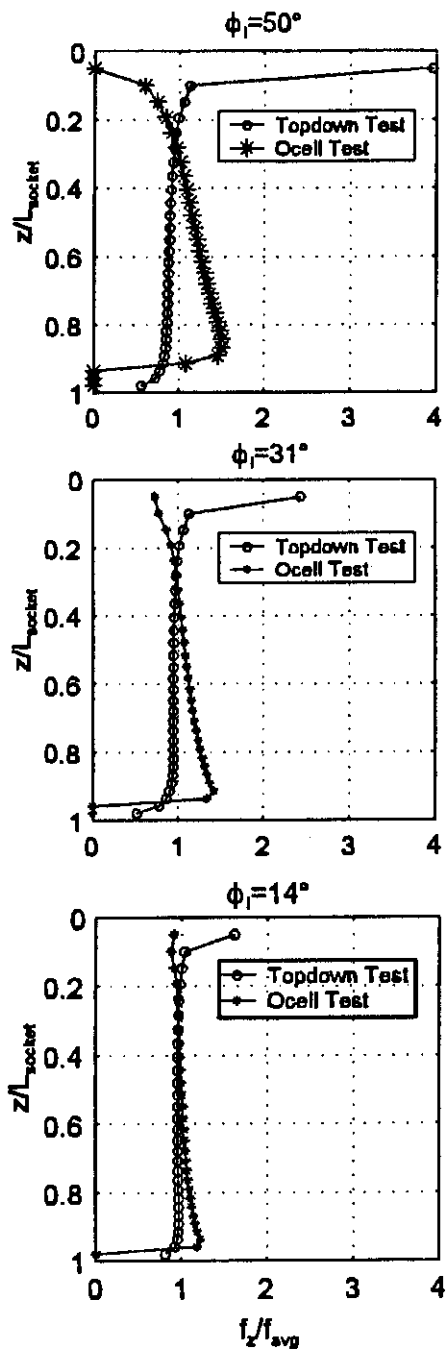


Figure B-24 Shear Distribution Comparison for Different ϕ_i Values

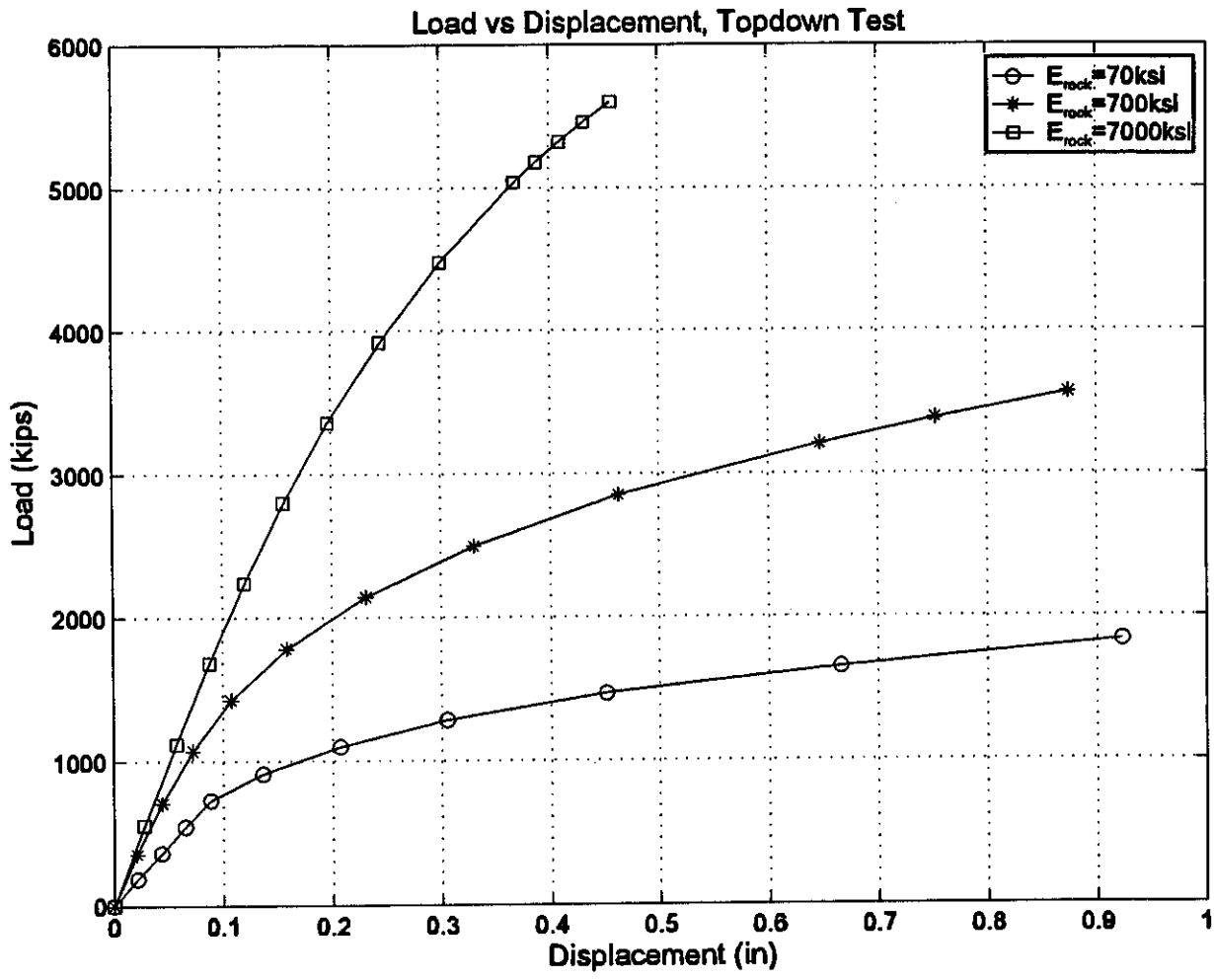


Figure B-25 Effect of E_{rock} on Load vs Displacement Curve, Top Down Test

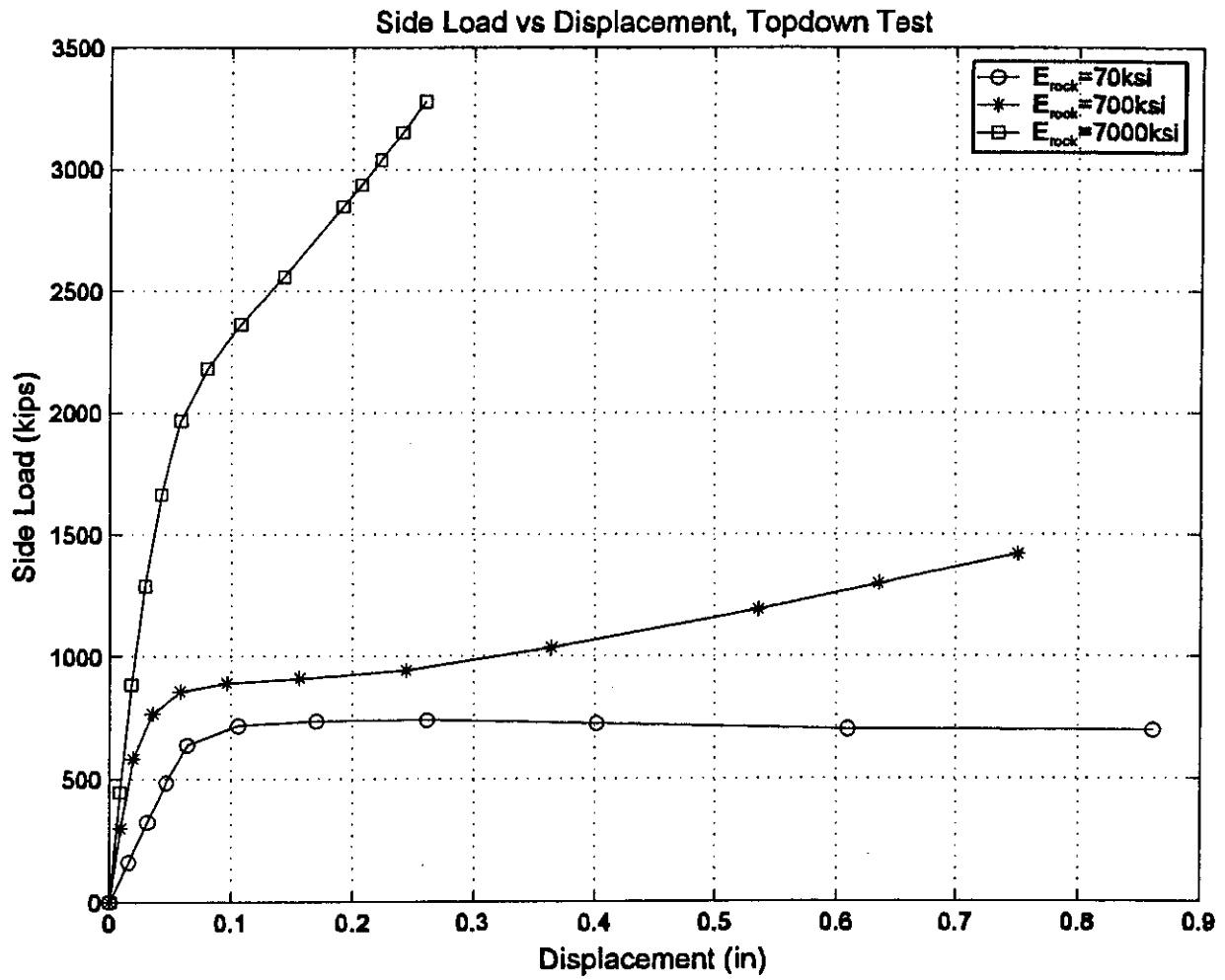


Figure B-26 Effect of E_{rock} on Side Load vs Displacement Curve, Top Down Test

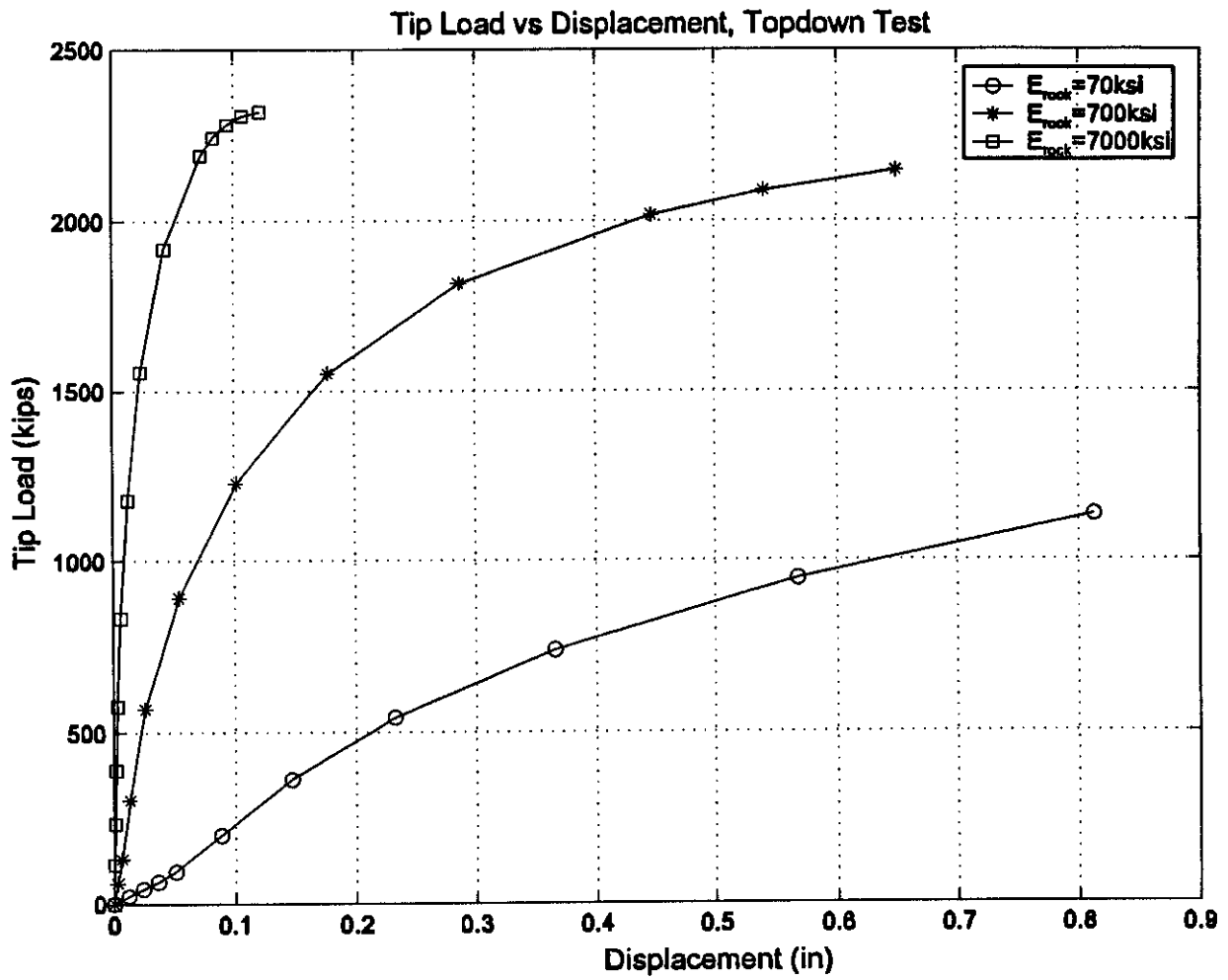


Figure B-27 Effect of E_{rock} on Tip Load vs Displacement Curve, Top Down Test

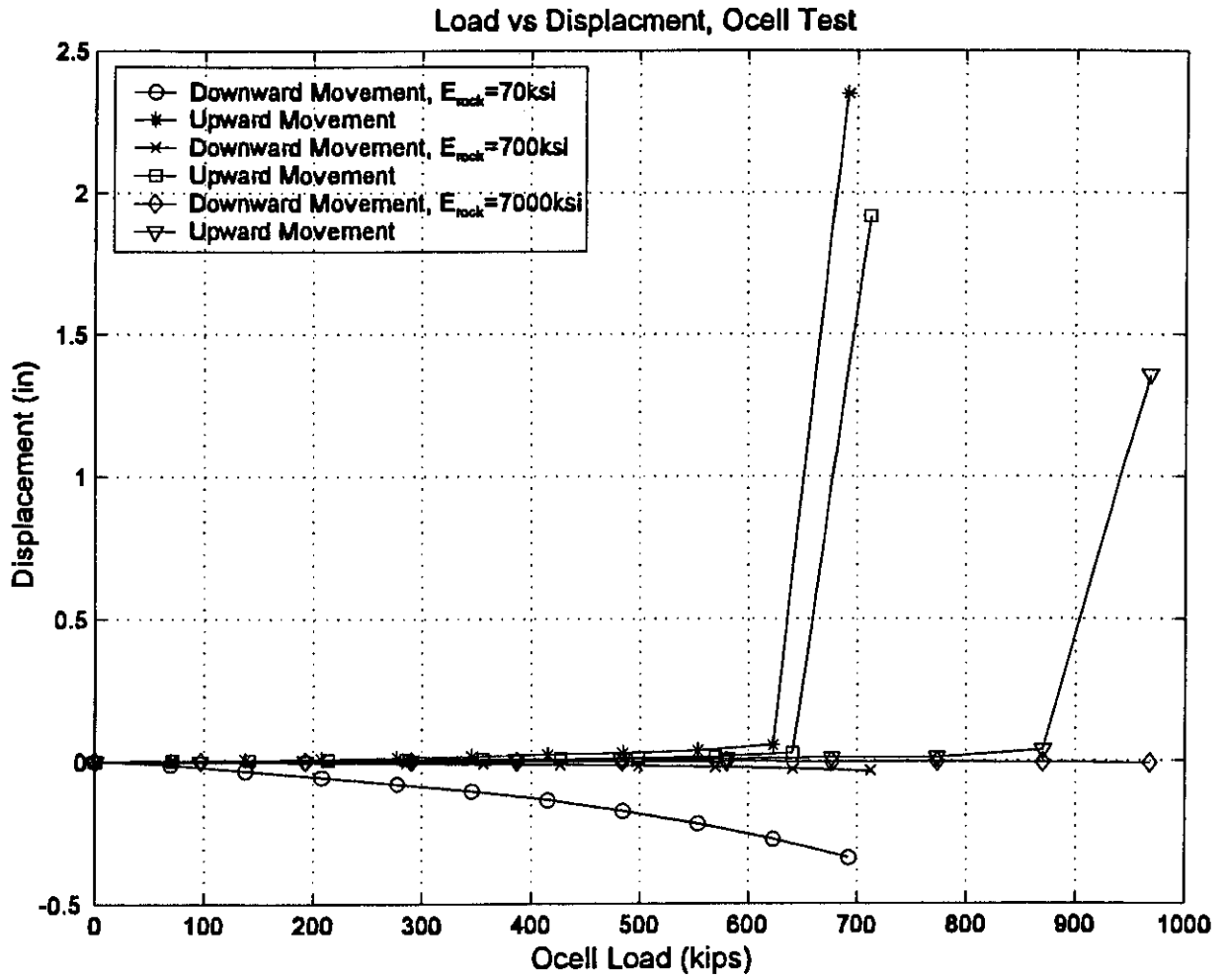


Figure B-28 Effect of E_{rock} on Load vs Displacement Curve, O-cell Test

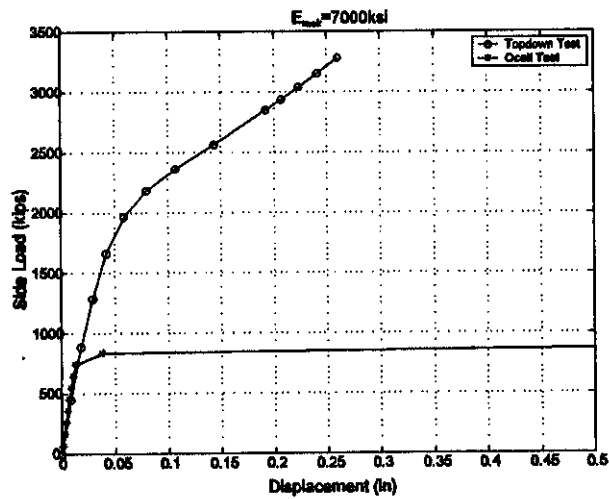
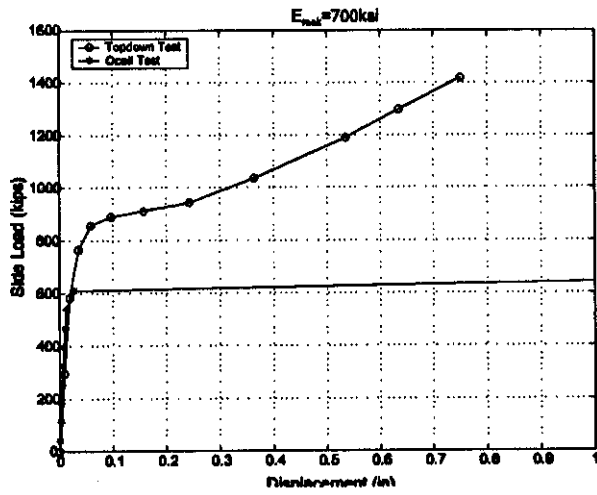
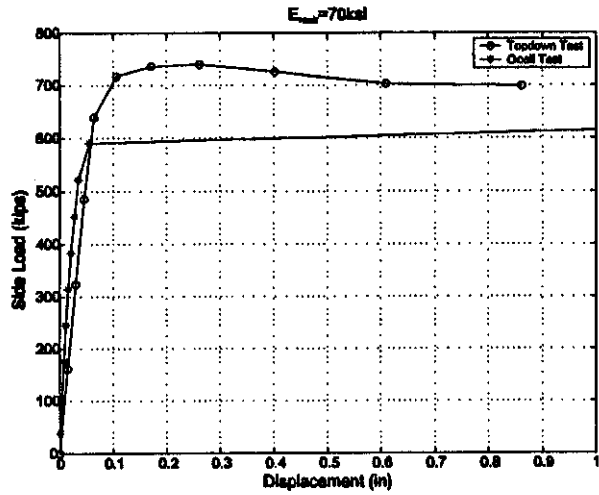


Figure B-29 Side Load vs Displacement Comparison for Different E_{rock} Values

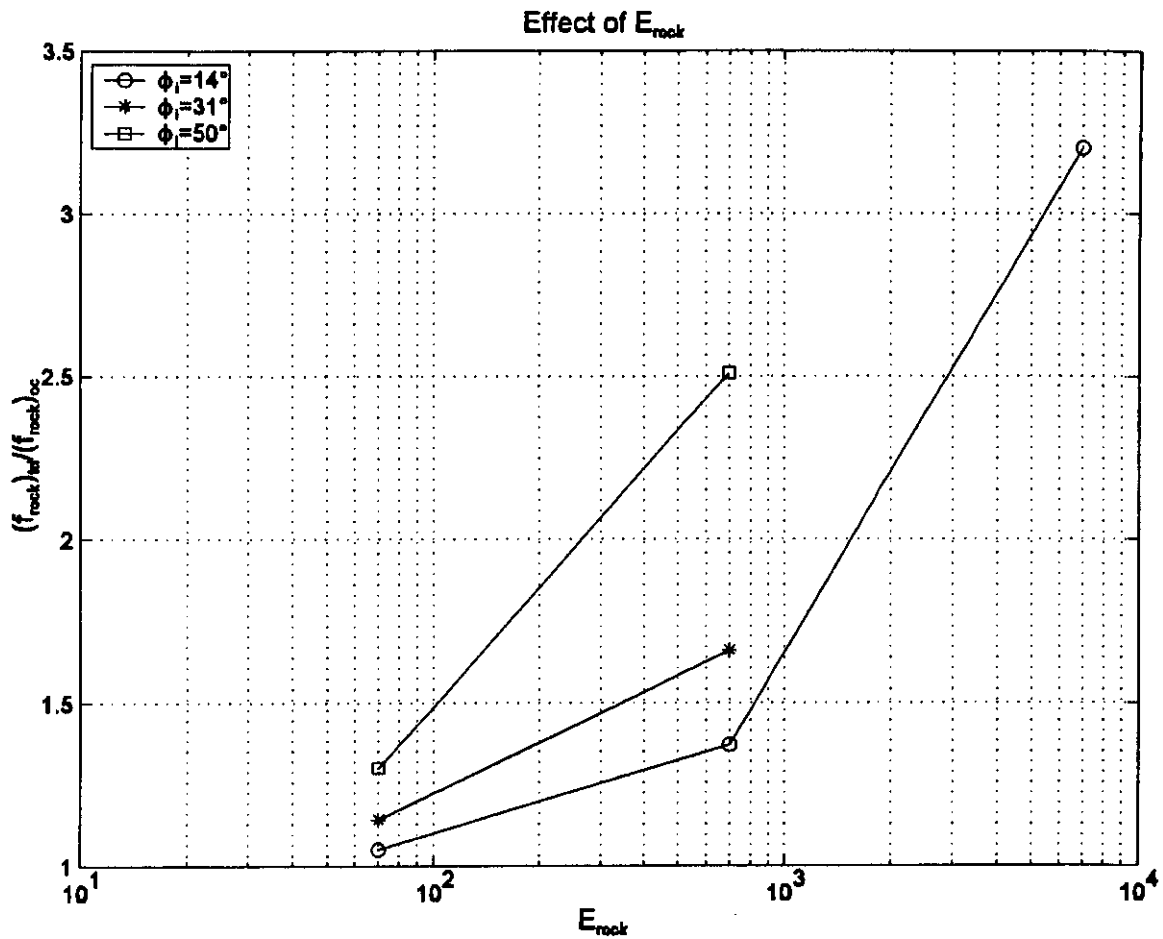


Figure B-30 Effect of E_{rock} on the Difference Between Top Down Test and O-cell Test

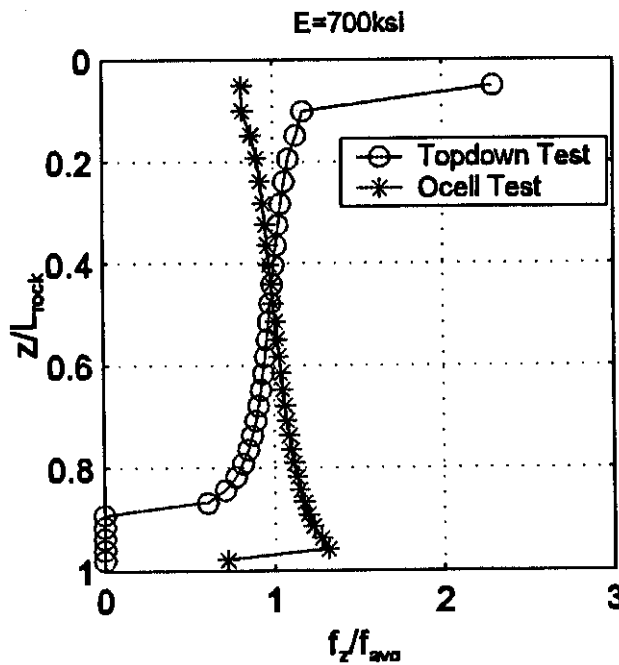
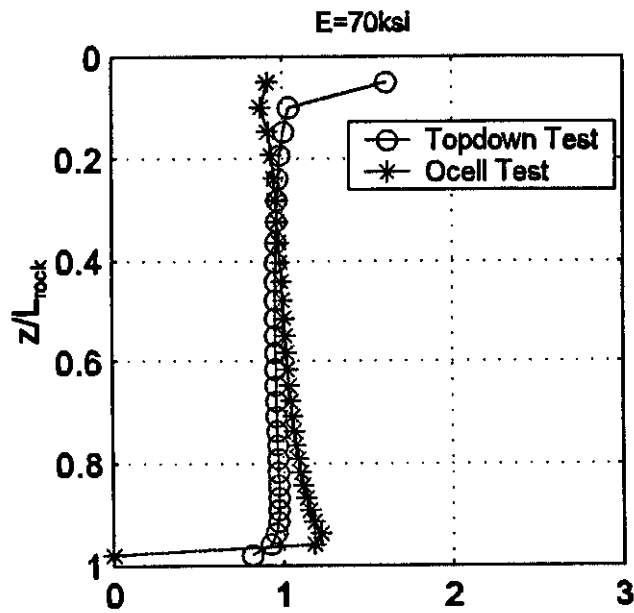


Figure B-31 Shear Stress Distribution Comparison for Different E_{rock} Values

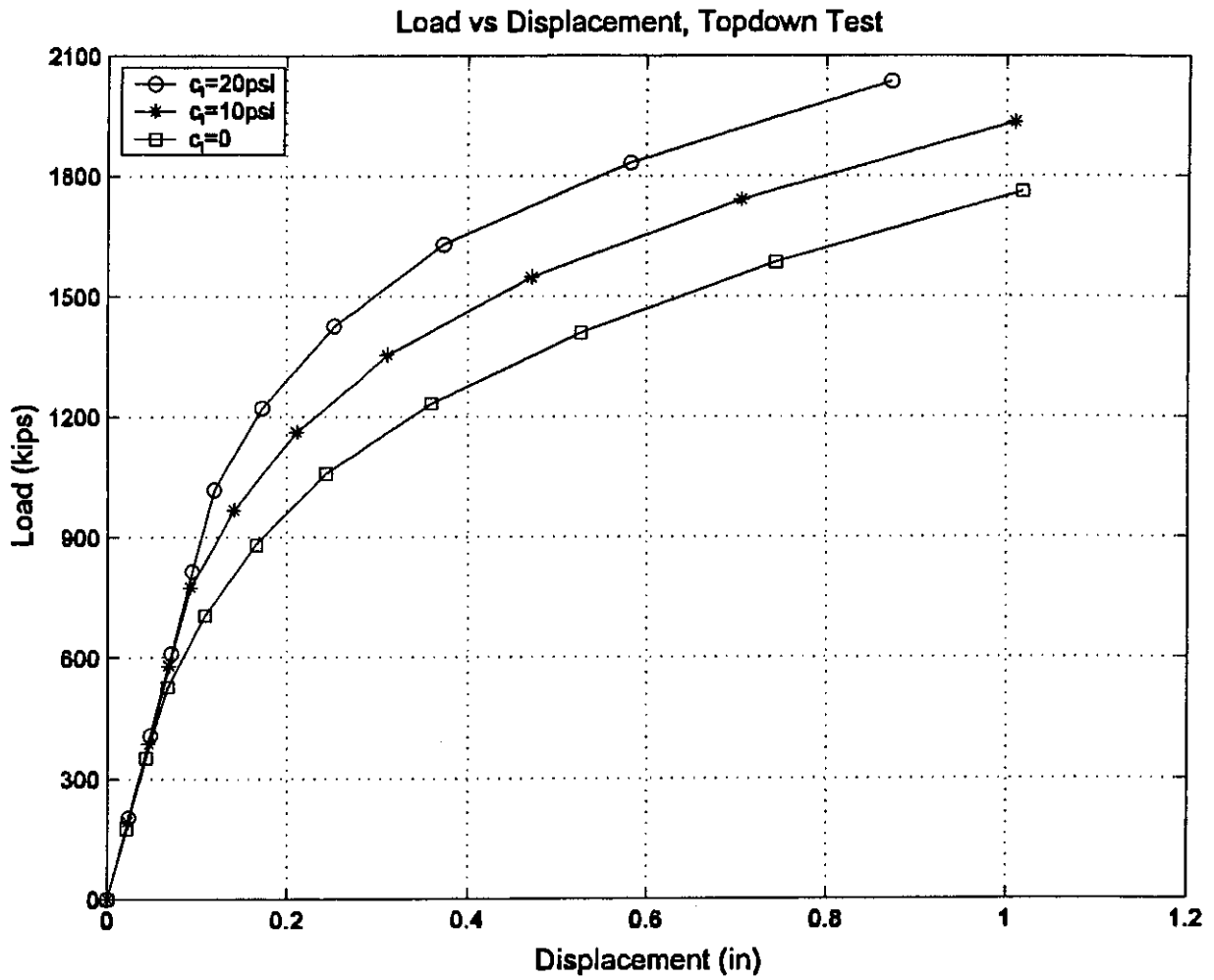


Figure B-32 Effect of c_1 on Load vs Displacement Curve, Top Down Test

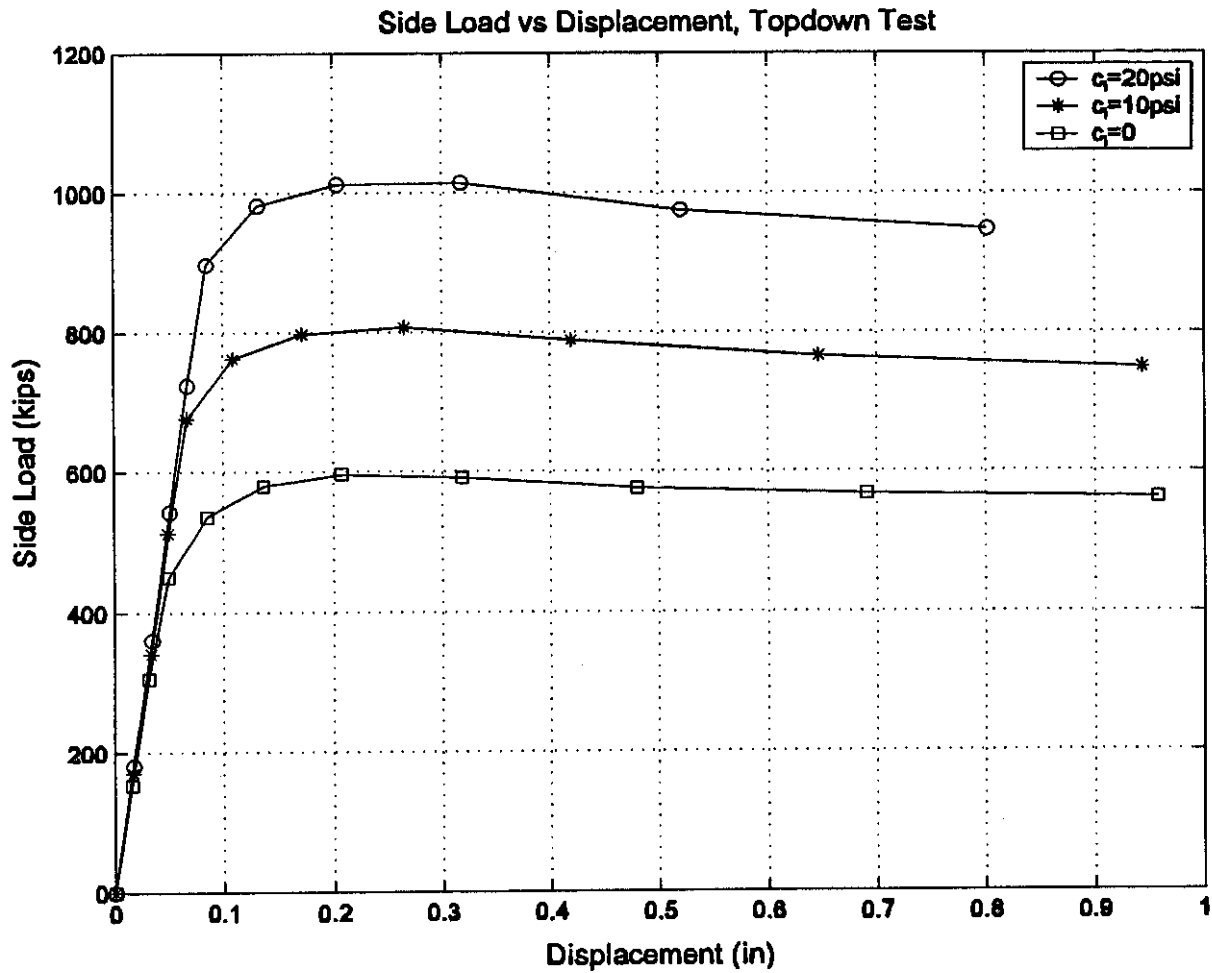


Figure B-33 Effect of c_1 on Side Load vs Displacement Curve, Top Down Test

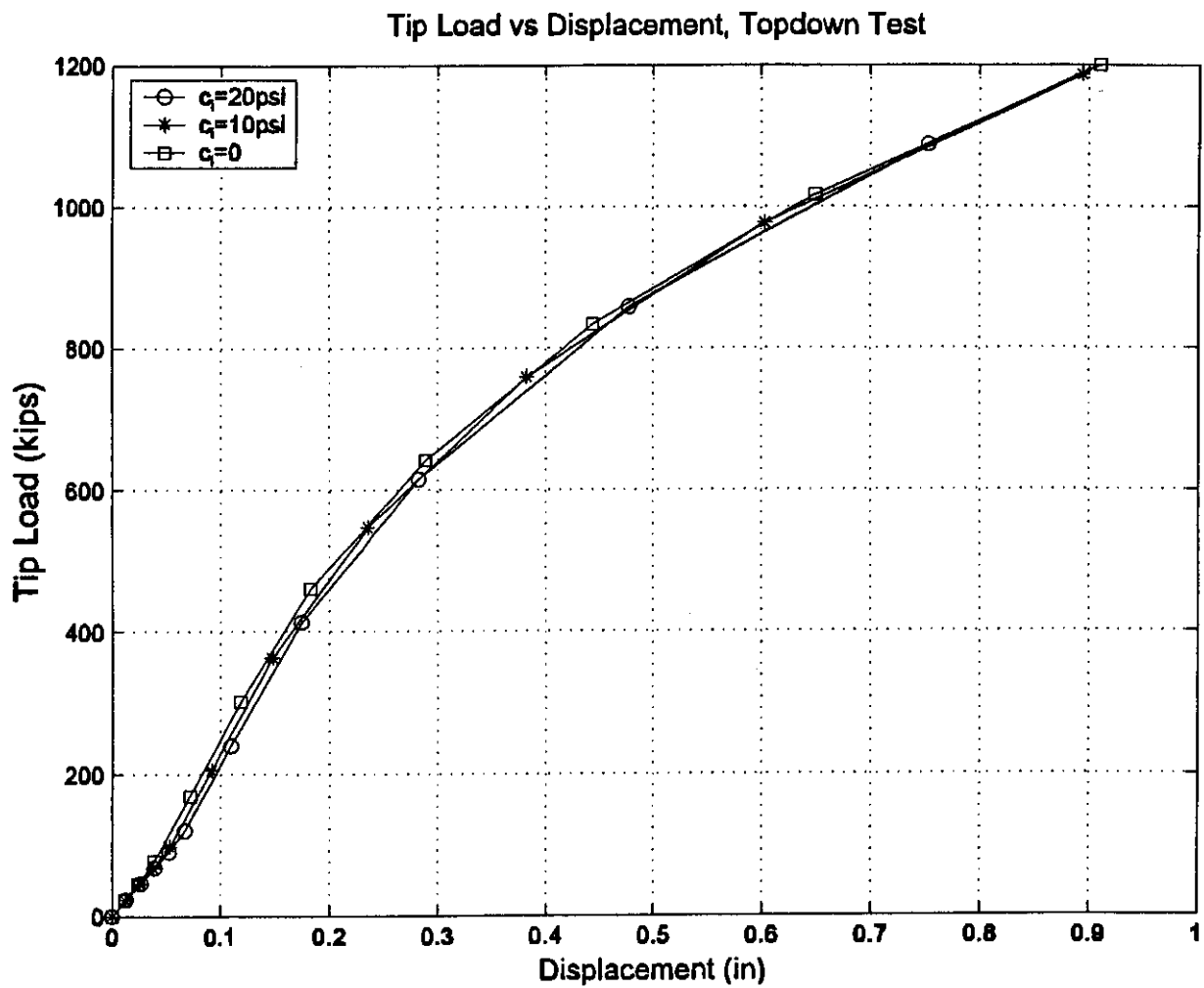


Figure B-34 Effect of c_i on Tip Load vs Displacement Curve, Top Down Test

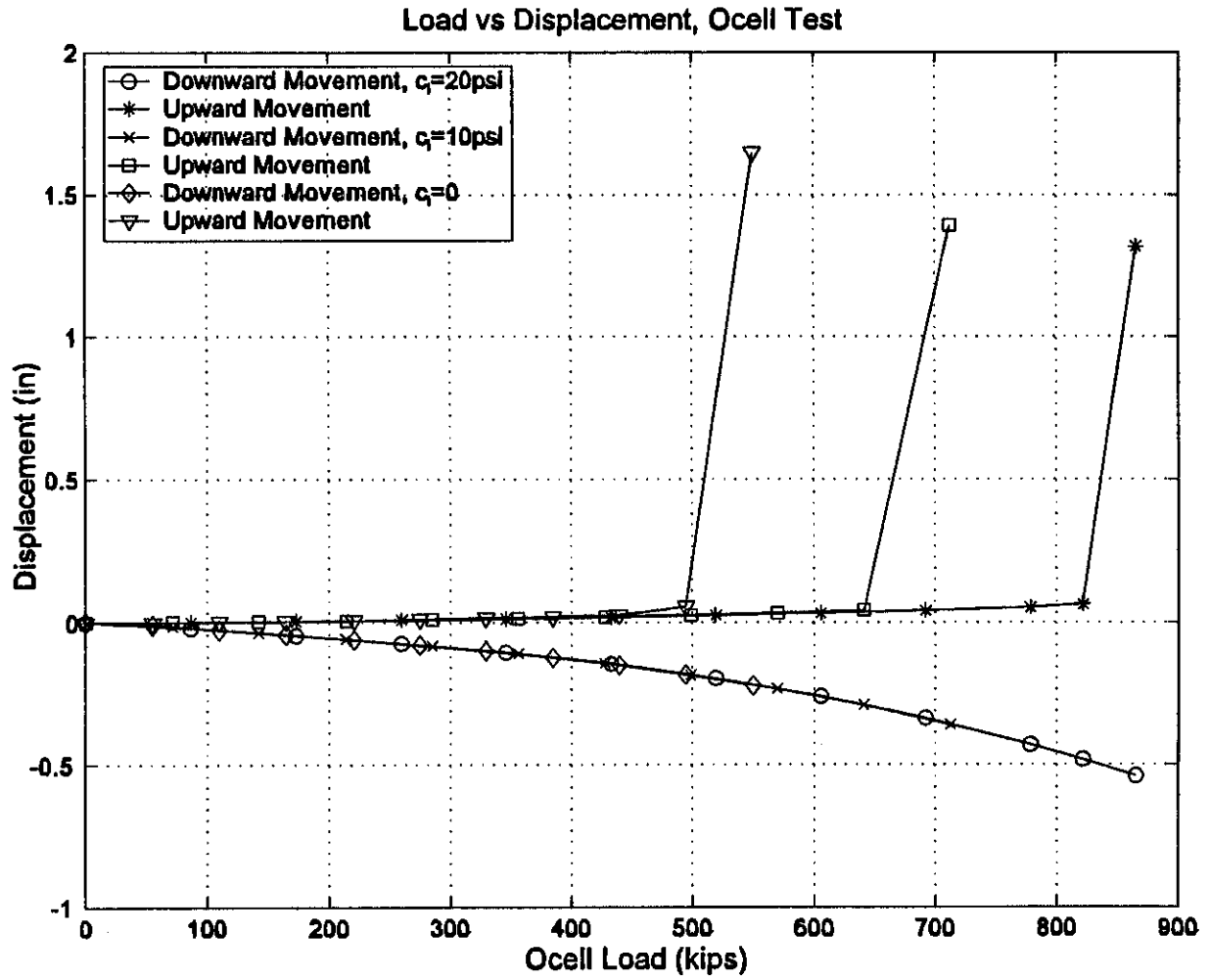


Figure B-35 Effect of c_i on Load vs Displacement Curve, O-cell Test

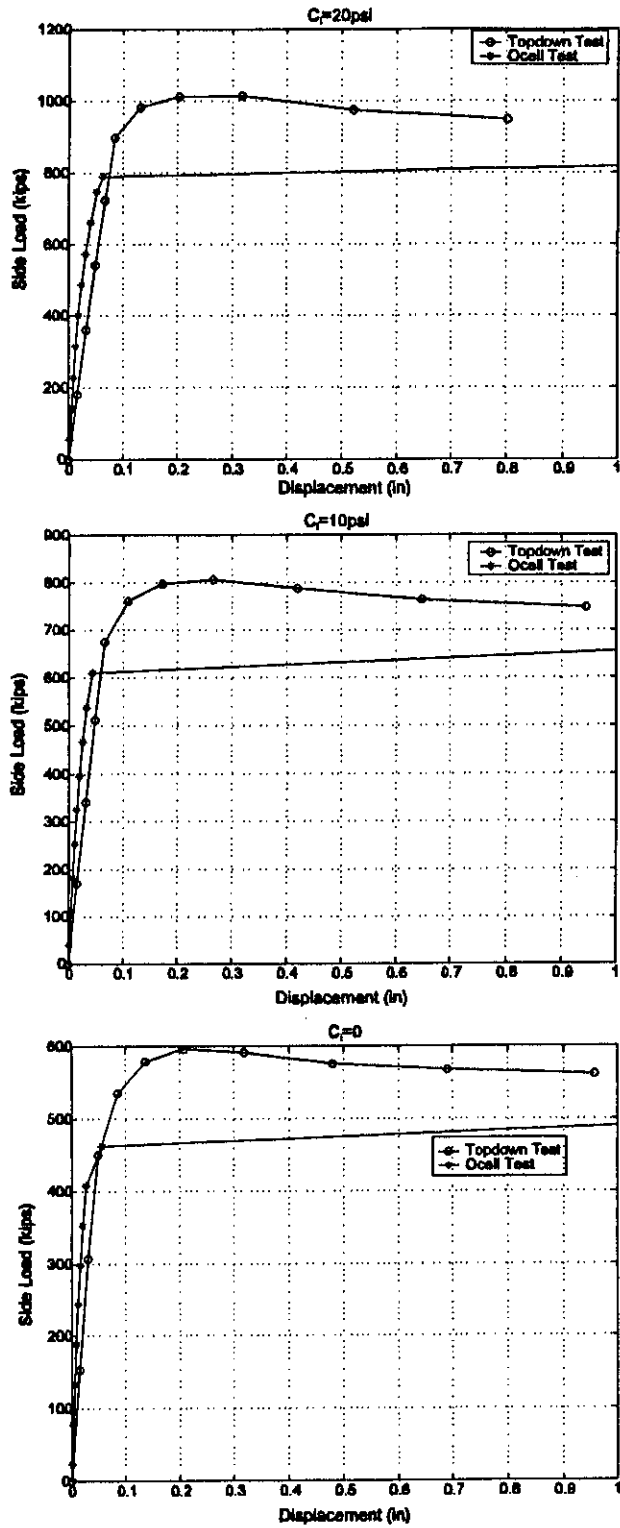


Figure B-36 Side Load vs Displacement Comparison for Different c_i Values

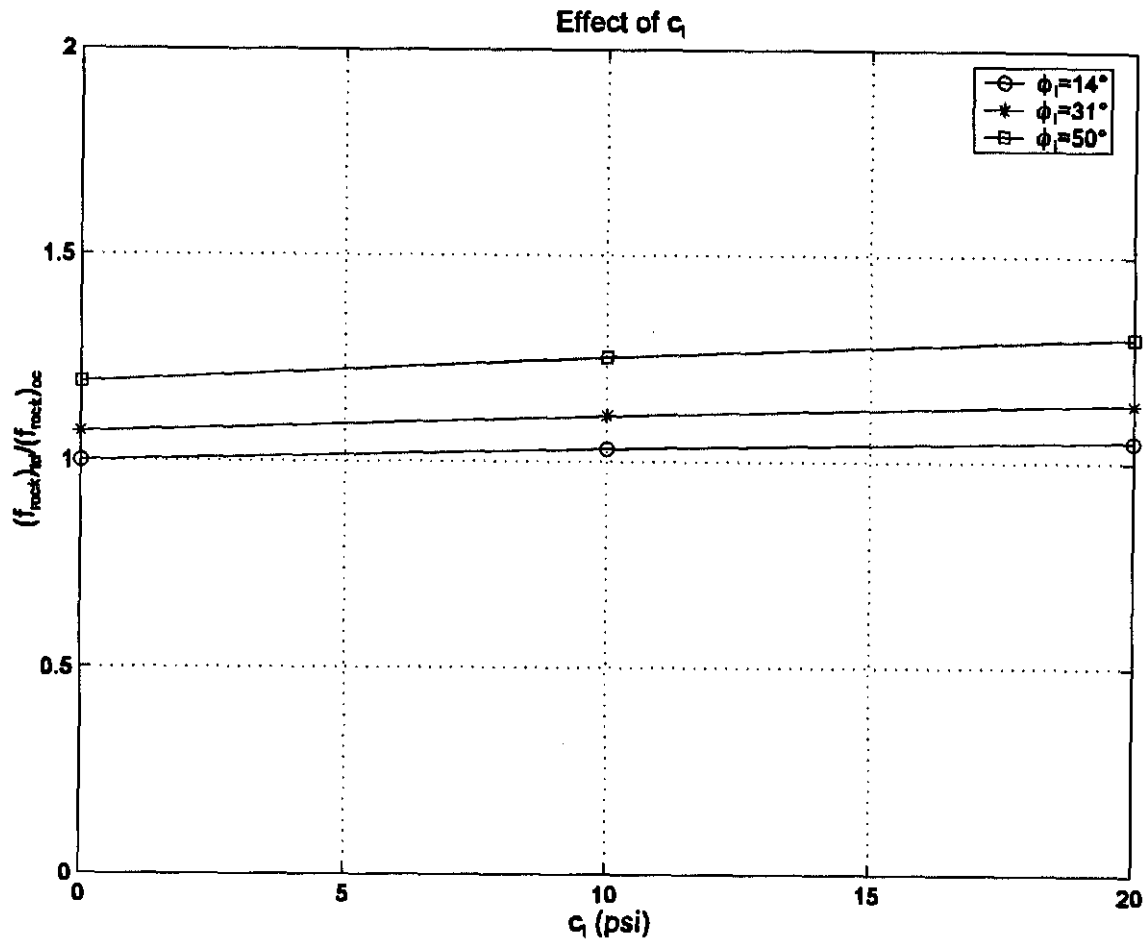


Figure B-37 Effect of c_1 on the Difference Between Top Down Test and O-cell Test

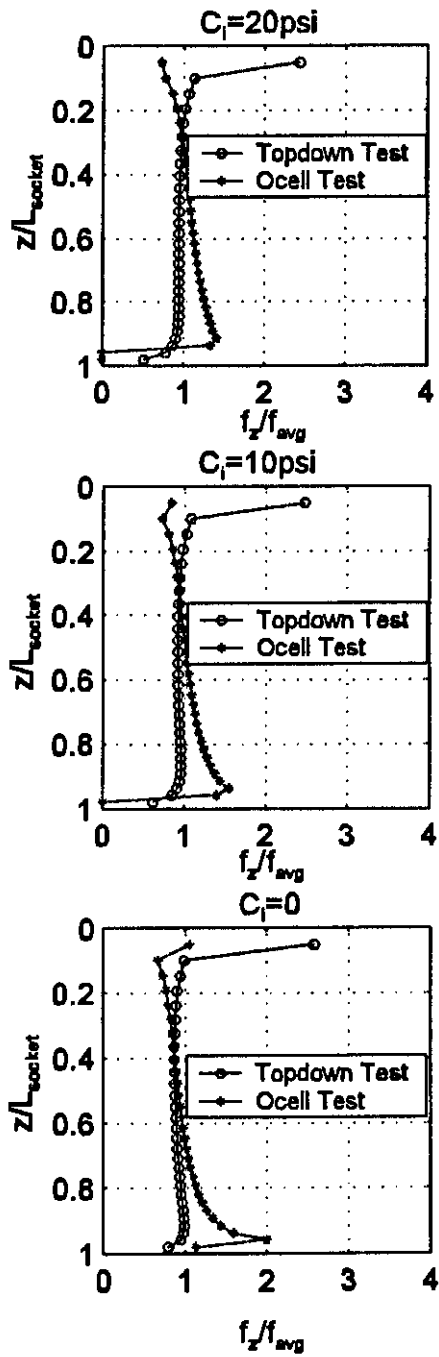


Figure B-38 Shear Stress Distribution Comparison for Different c_1 Values

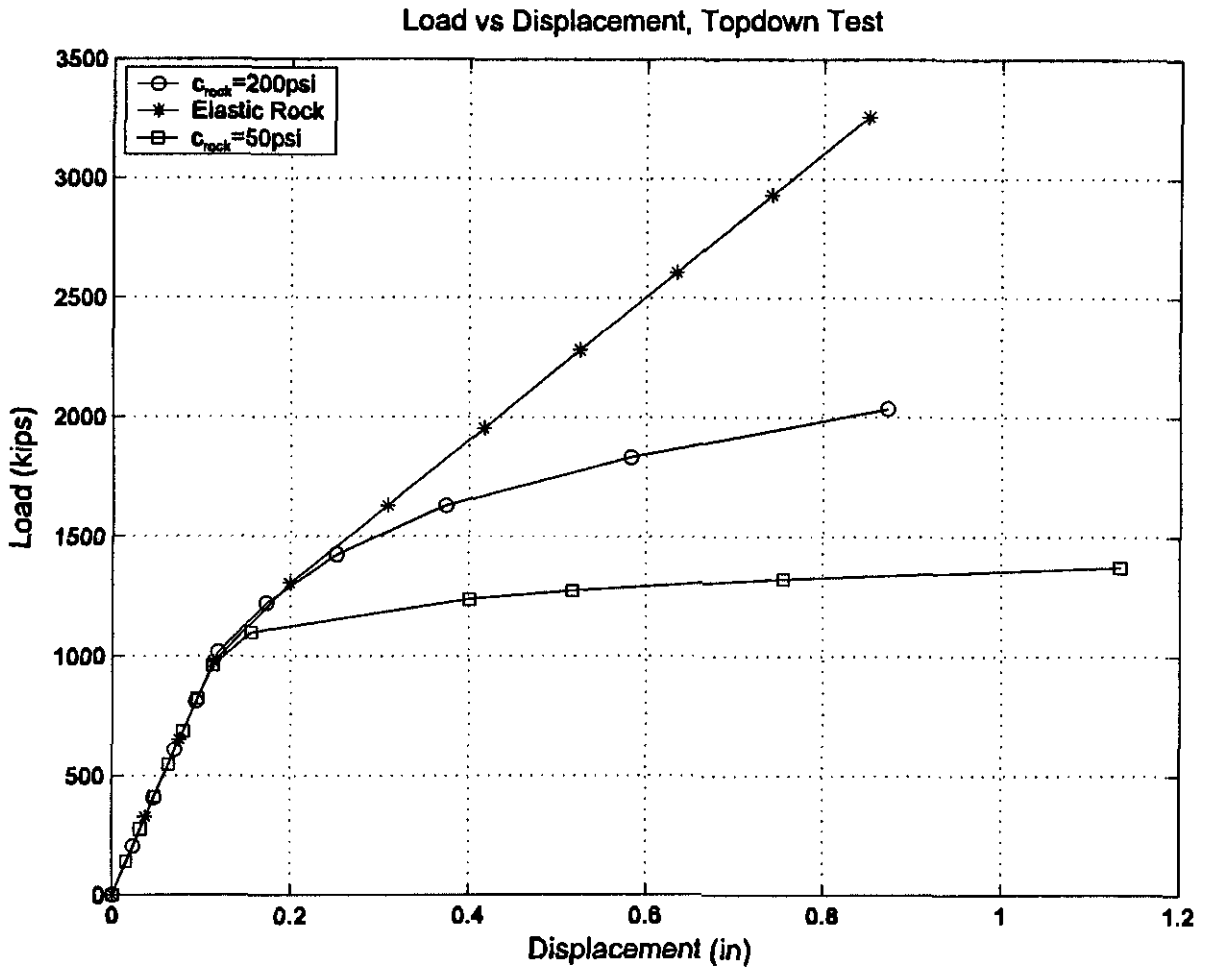


Figure B-39 Effect of c_{rock} on Load vs Displacement Curve, Top Down Test

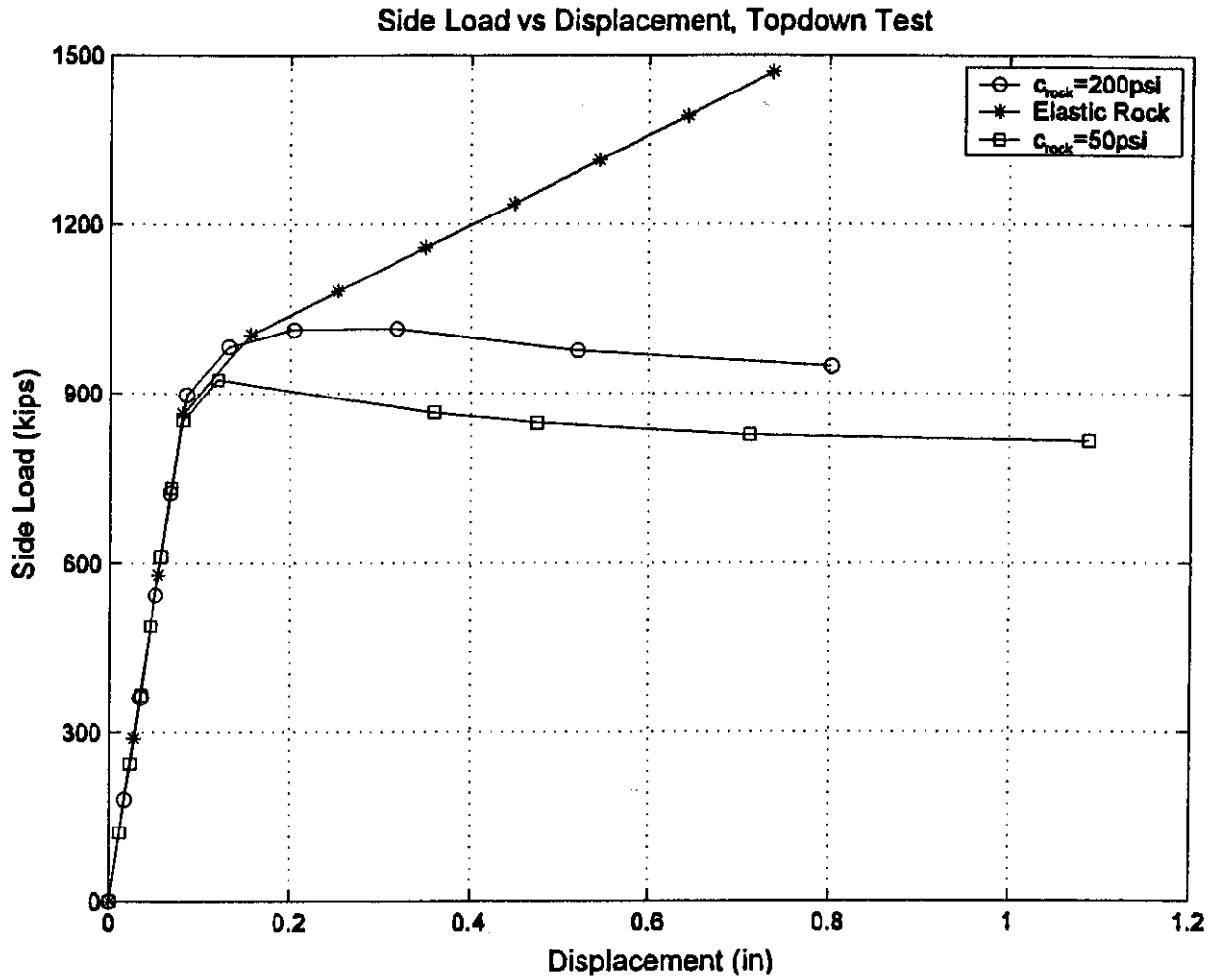


Figure B-40 Effect of c_{rock} on Side Load vs Displacement Curve, Top Down Test

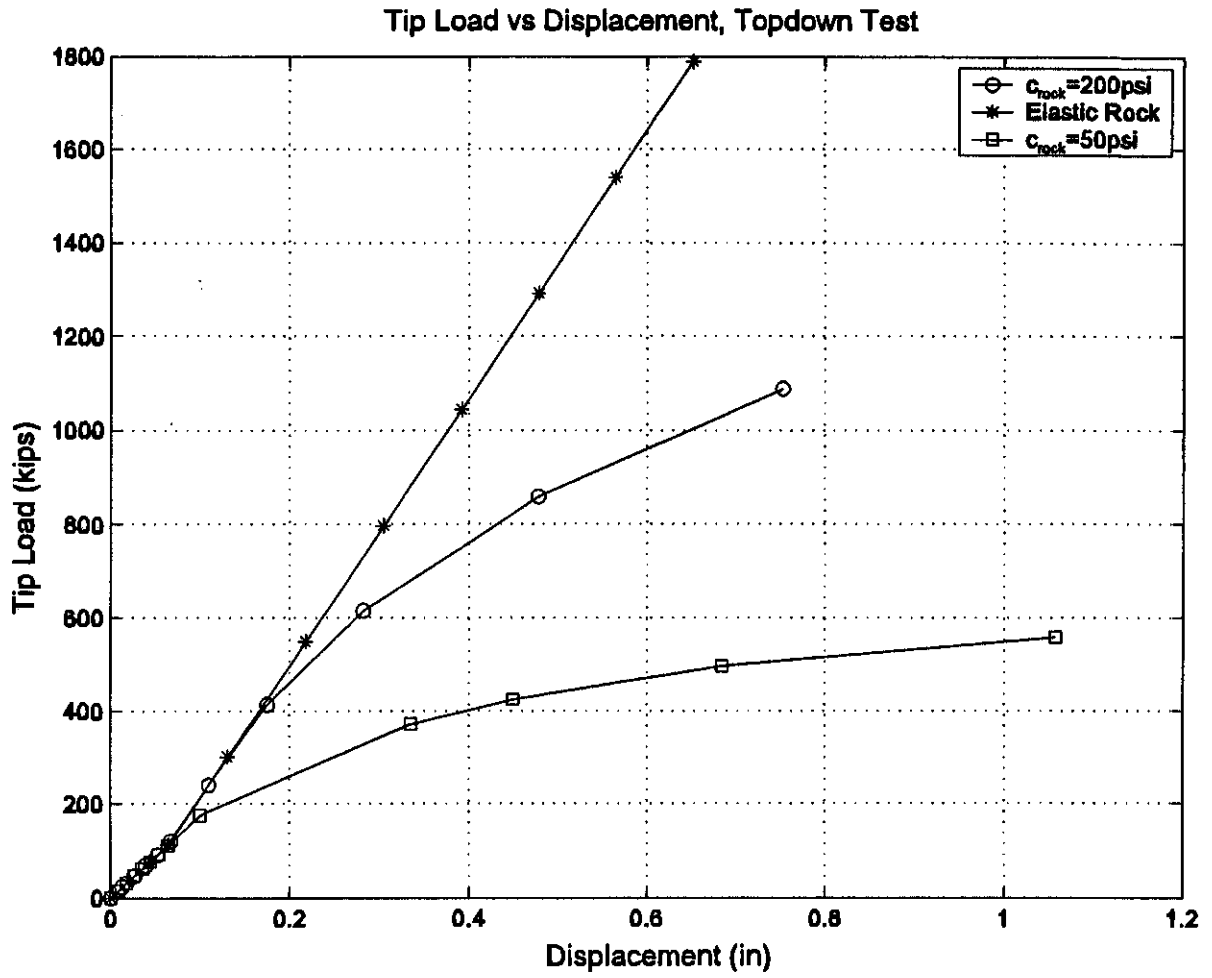


Figure B-41 Effect of c_{rock} on Tip Load vs Displacement Curve, Top Down Test

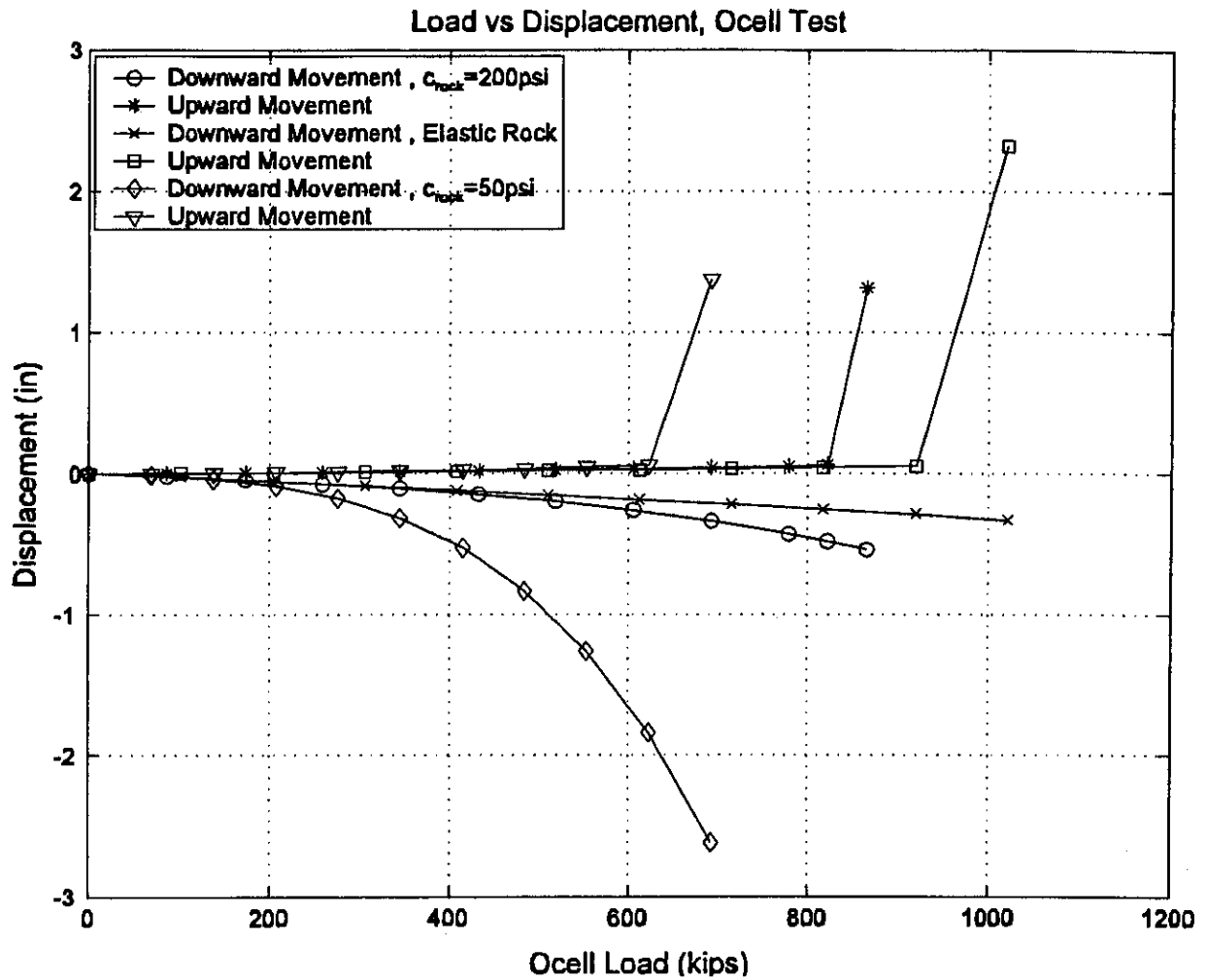


Figure B-42 Effect of c_{rock} on Load vs Displacement Curve, O-cell Test

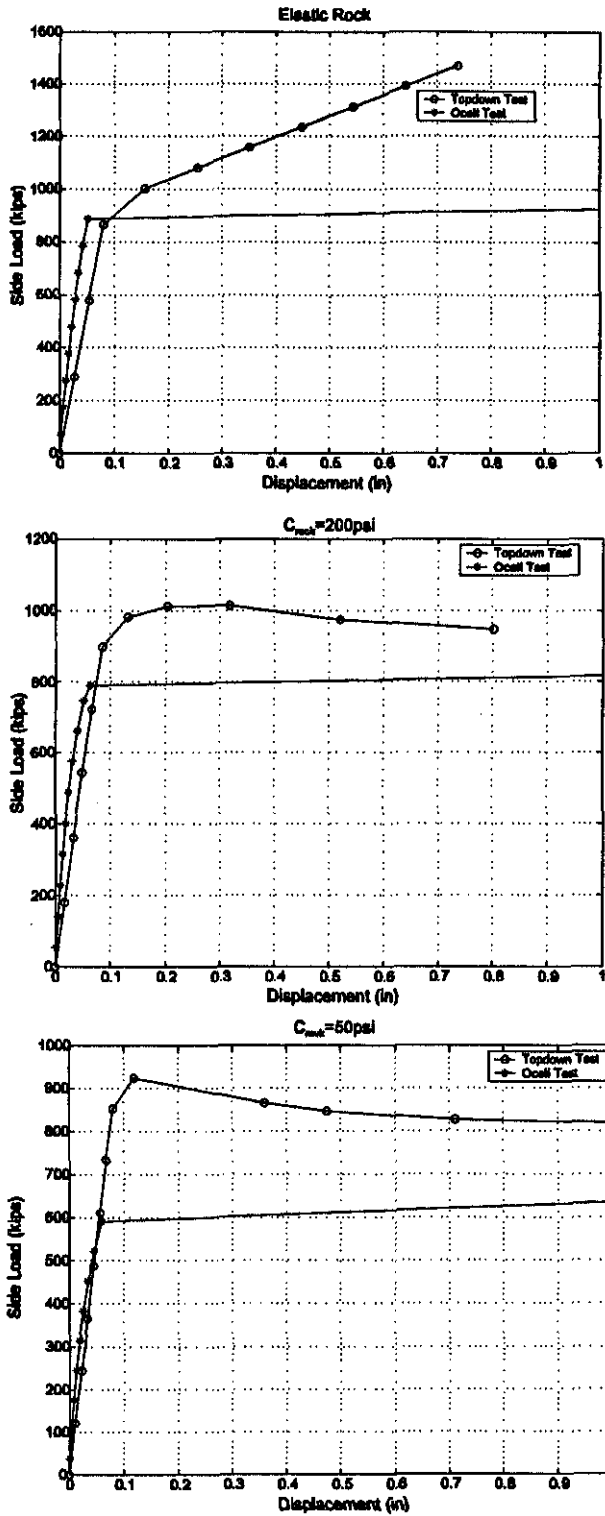


Figure B-43 Side Load vs Displacement Comparison for Different c_{rock} Values

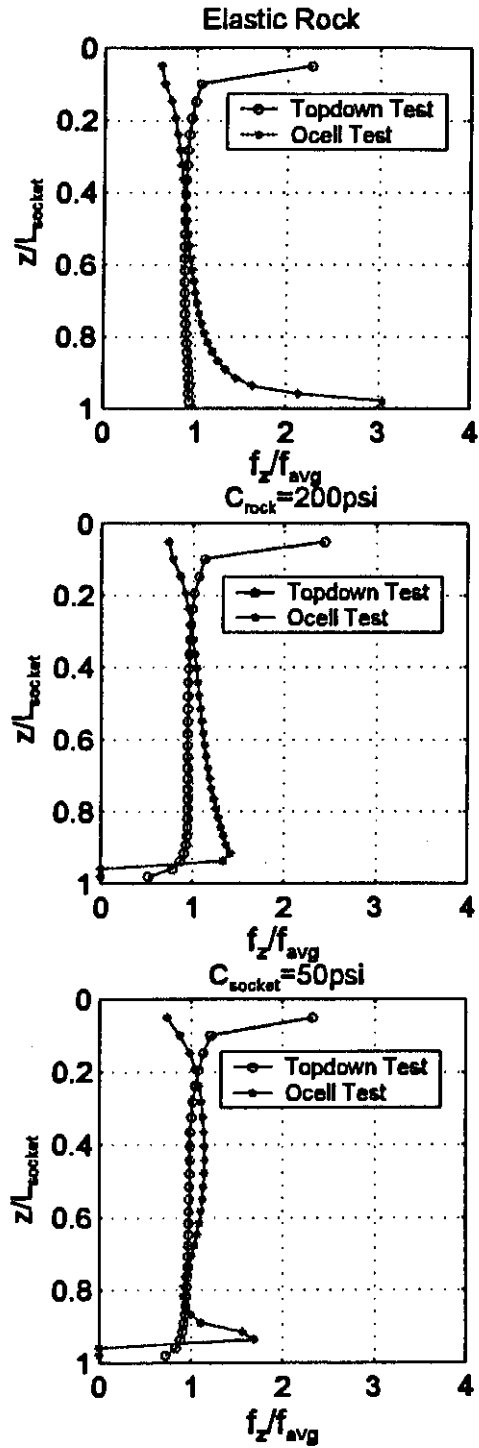


Figure B-44 Shear Stress Distribution Comparison for Different c_{rock} Values

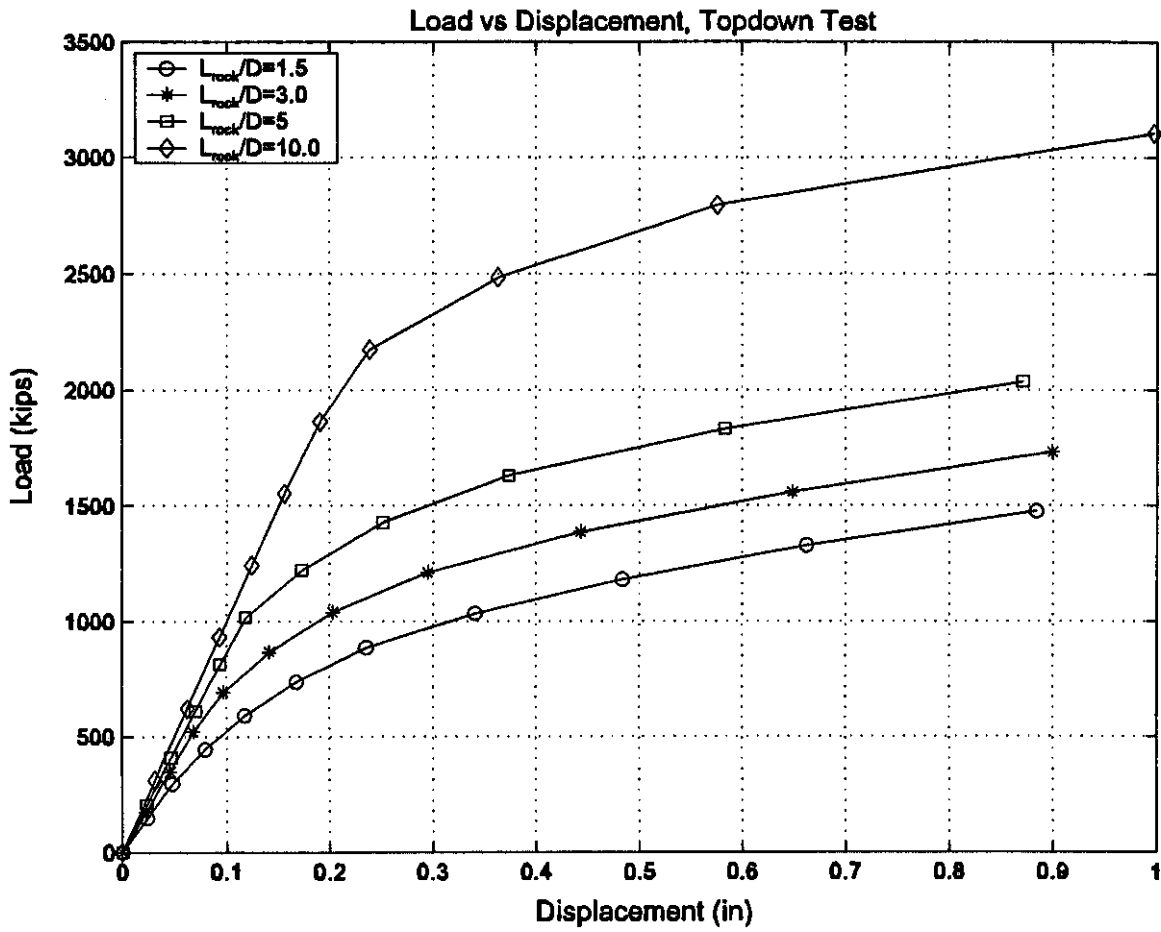


Figure B-45 Effect of L_{rock}/D on Load vs Displacement, Top Down Test

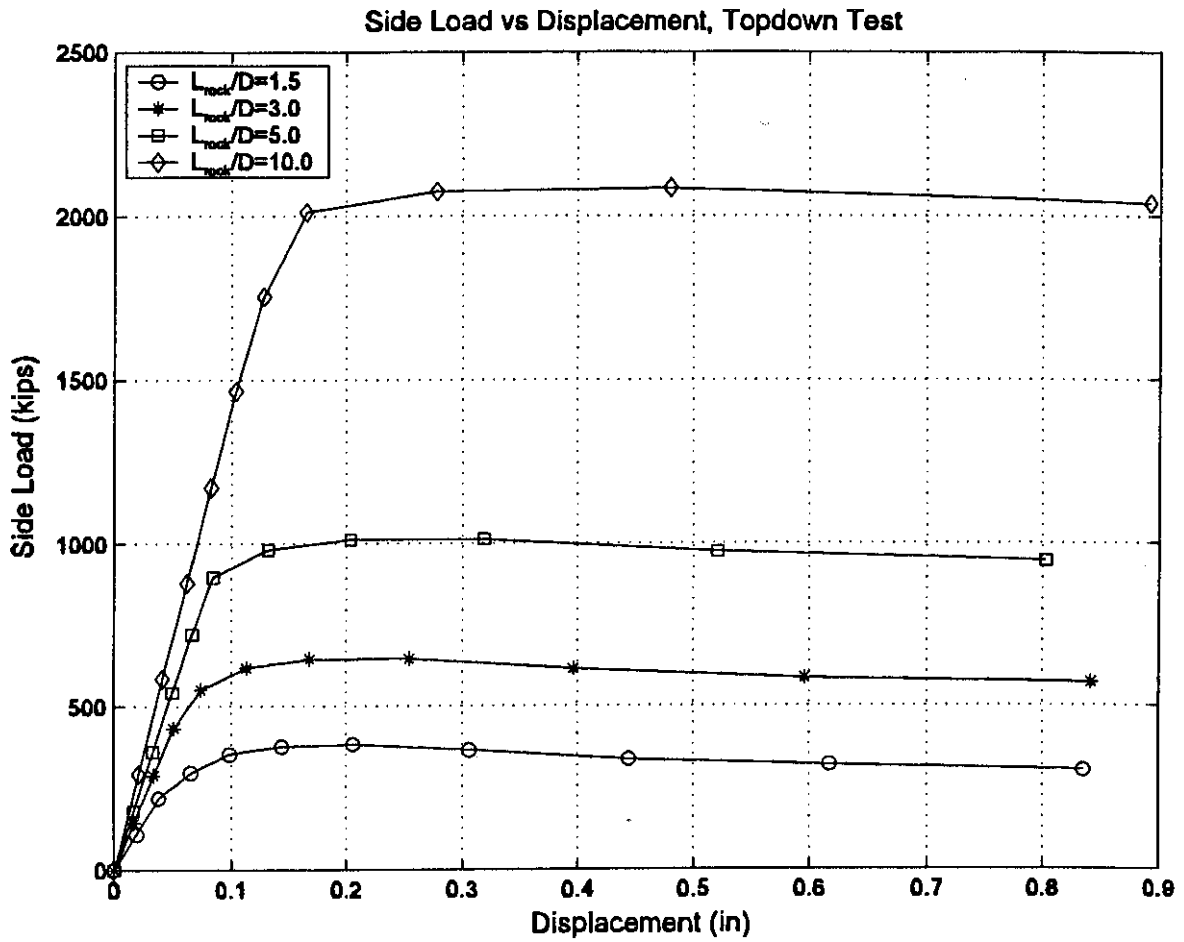


Figure B-46 Effect of L_{rock}/D on Side Load vs Displacement, Top Down Test

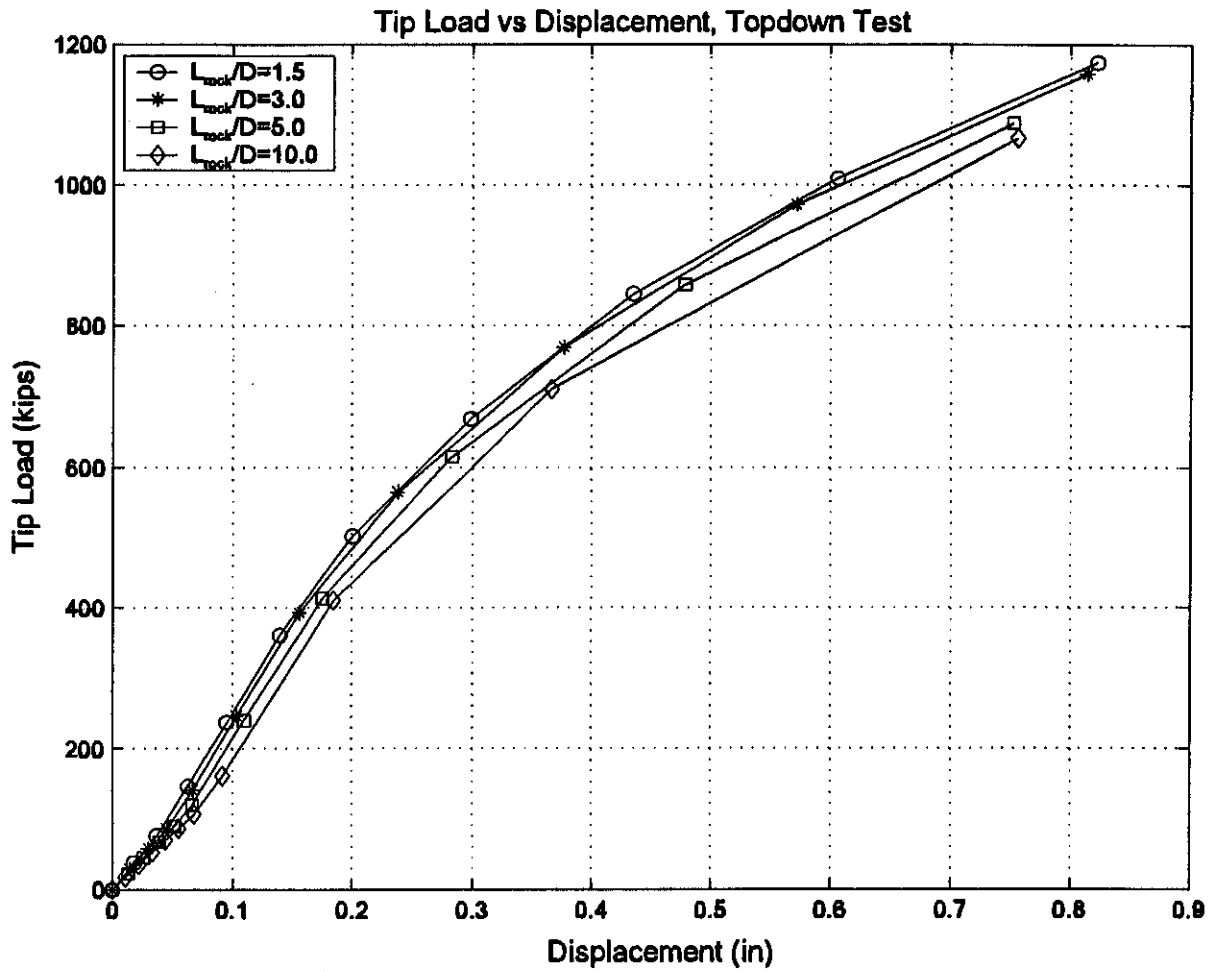


Figure B-47 Effect of L_{socket}/D on Tip Load vs Displacement, Top Down Test

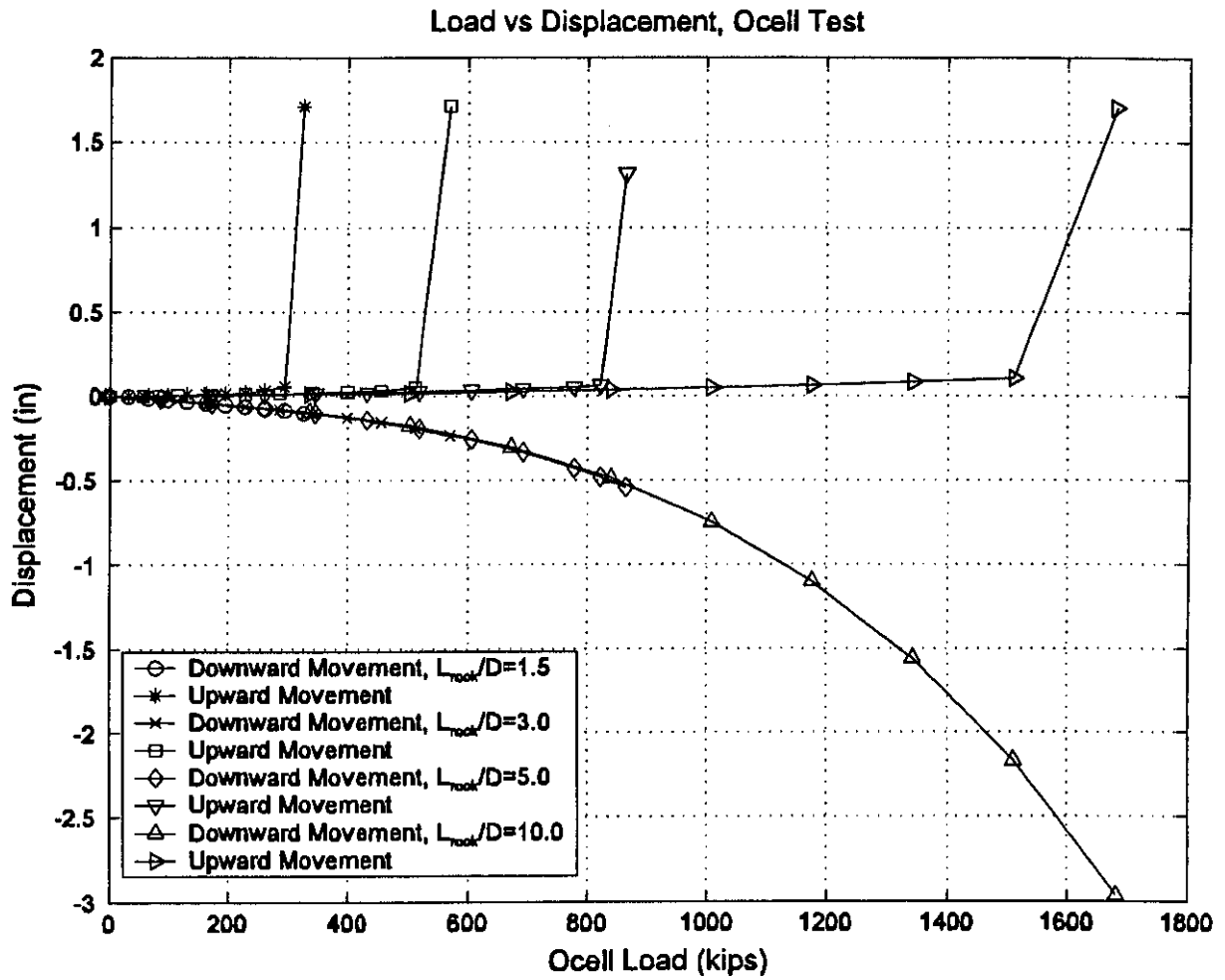


Figure B-48 Effect of L_{socket}/D on Load vs Displacement Curve, O-cell Test

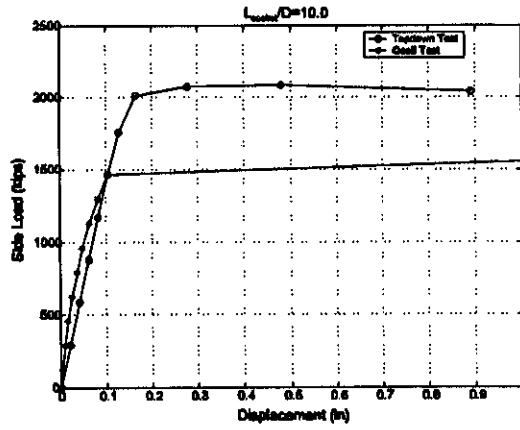
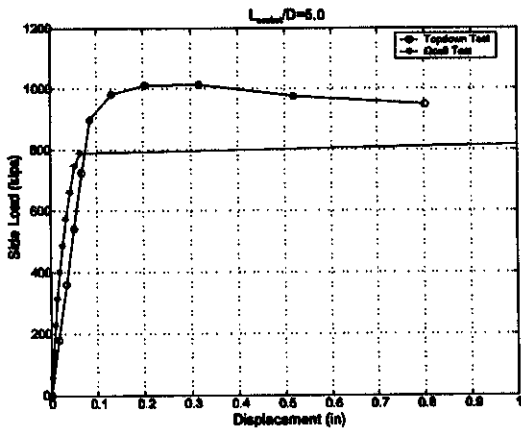
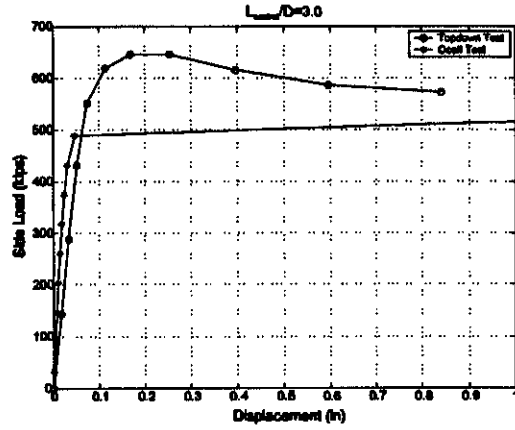
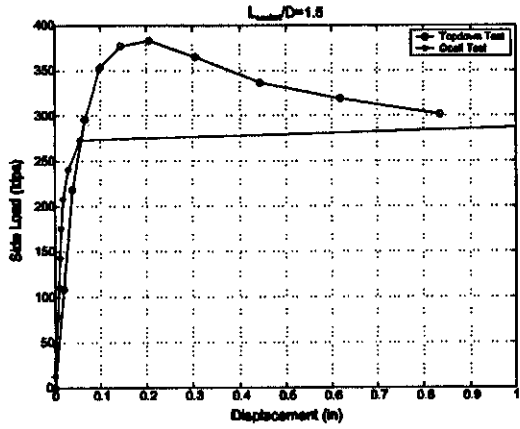


Figure B-49 Side Load vs Displacement Curve Comparison for Different L_{rocket}/D Values

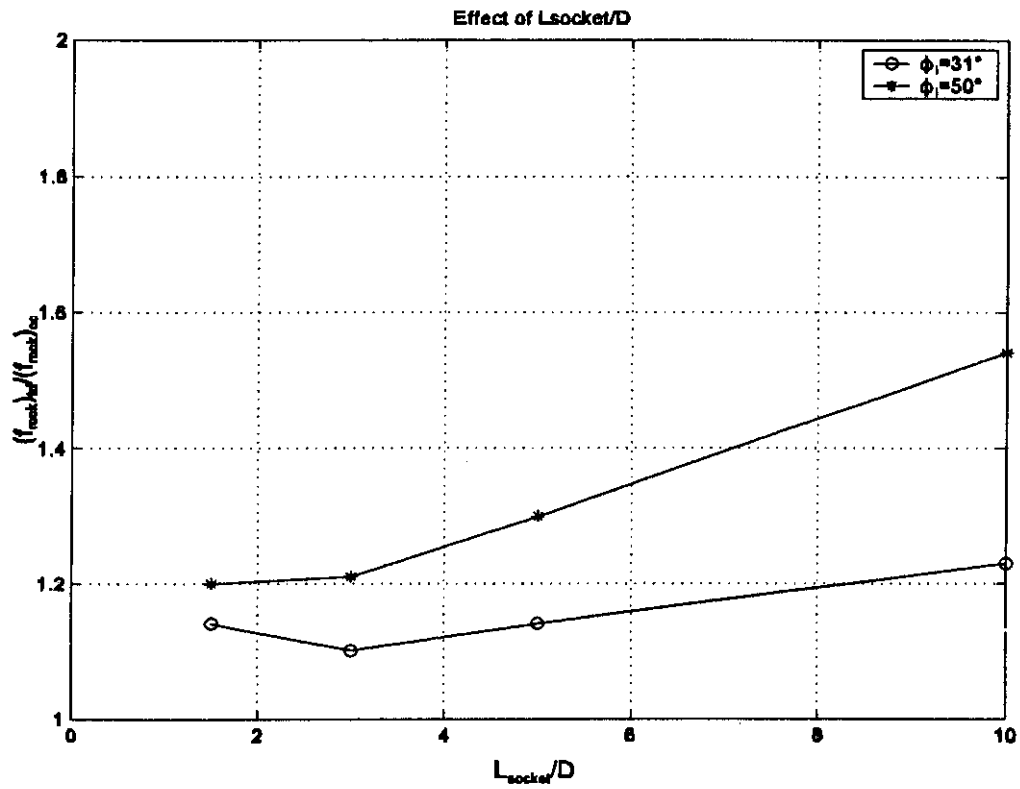


Figure B-50 Effect of L_{socket}/D on the Difference Between Top Down Test and O-cell Test

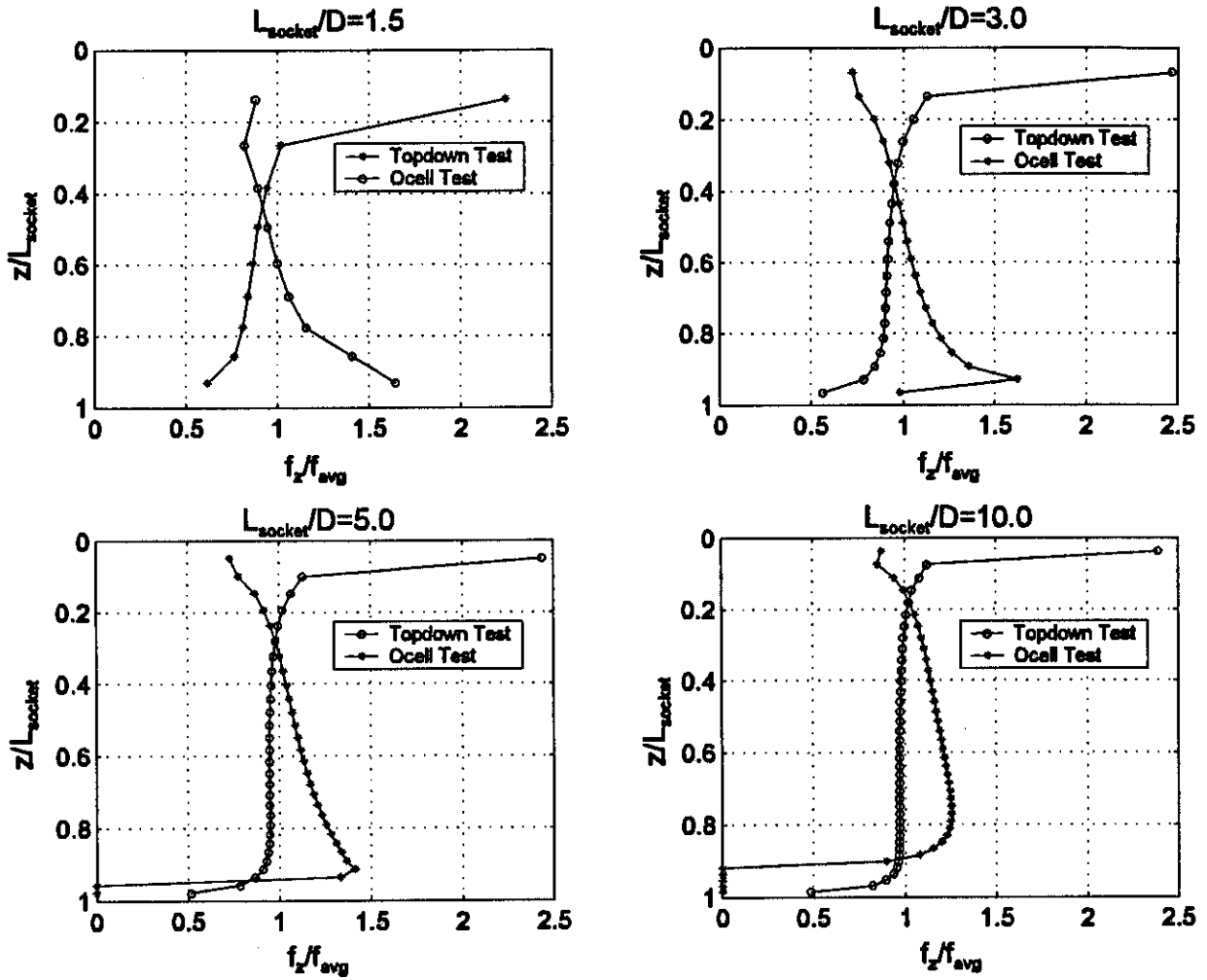


Figure B-51 Shear Stress Distribution Comparison for Different L_{socket}/D Values

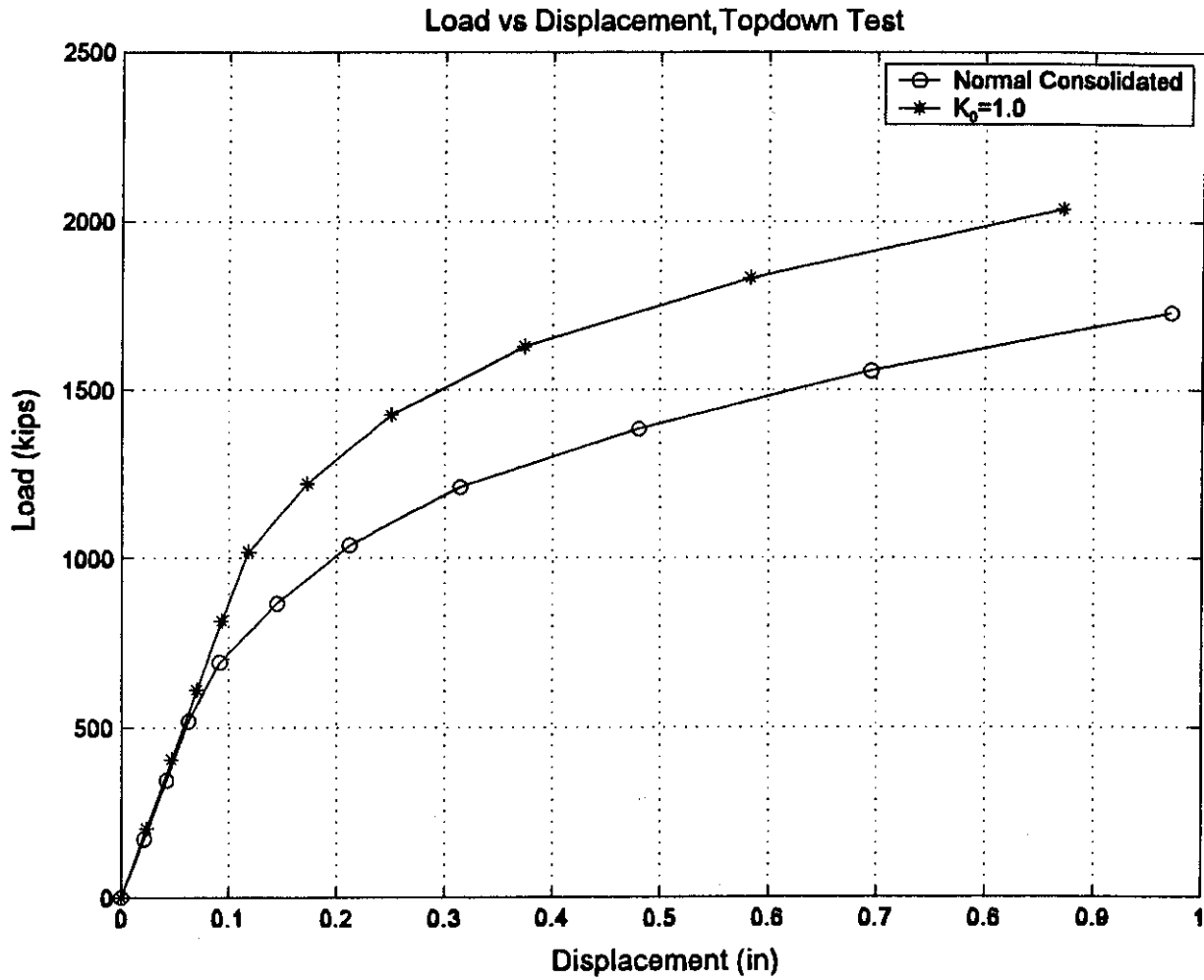


Figure B-52 Effect of K_0 on Load vs Displacement Curve, Top Down Test

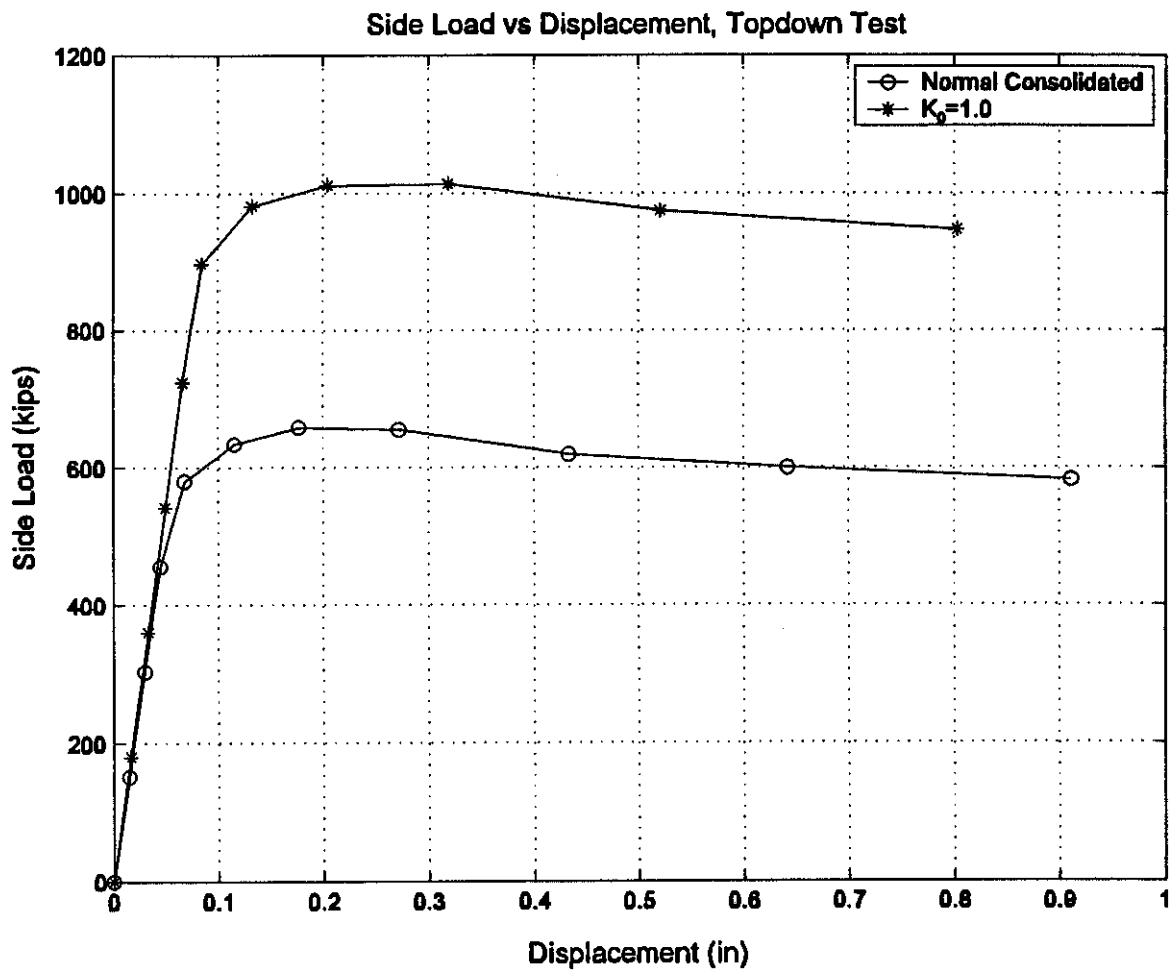


Figure B-53 Effect of K_0 on Side Load vs Displacement Curve, Top Down Test

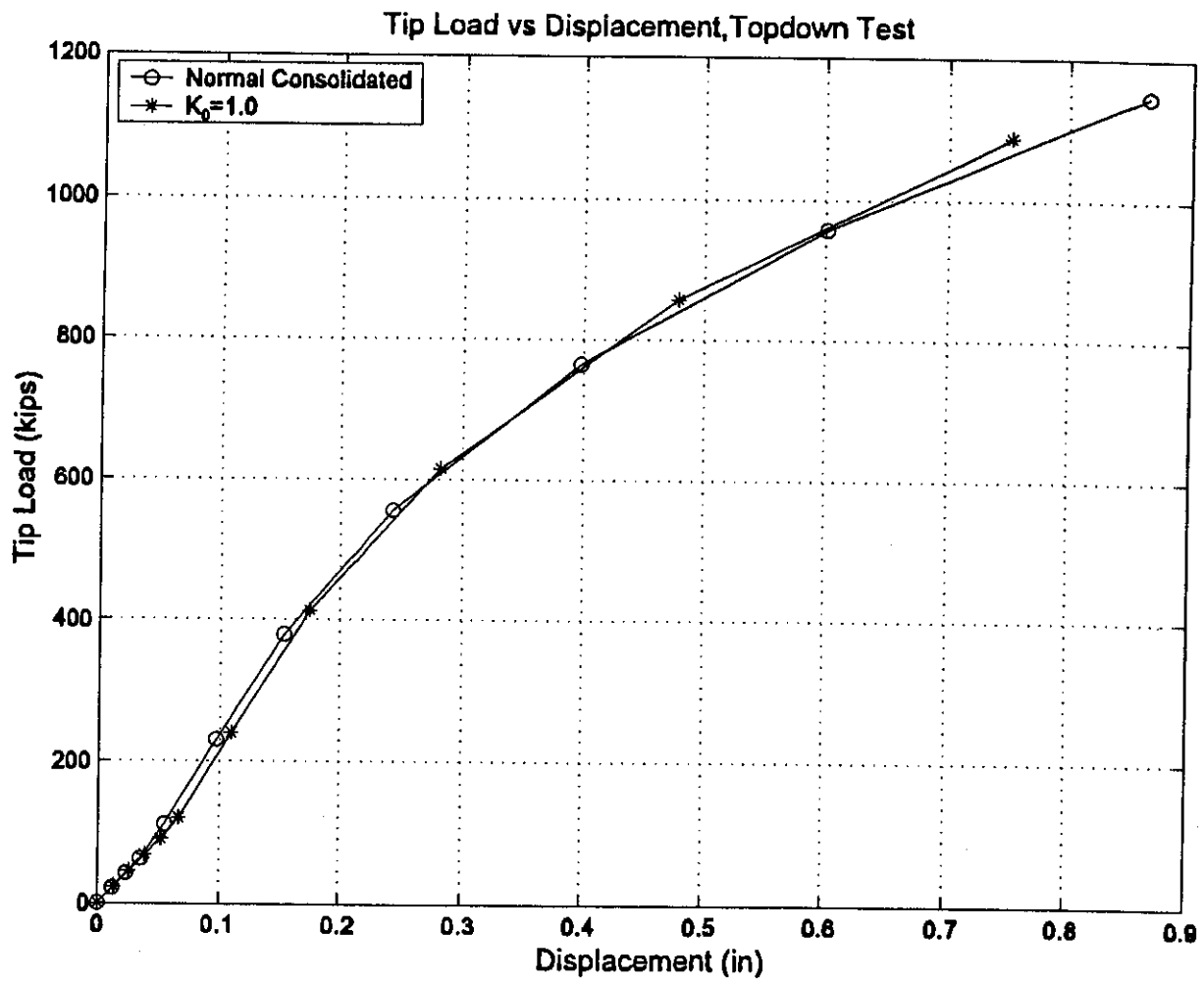


Figure B-54 Effect of K_0 on Tip load vs Displacement Curve, Top Down Test

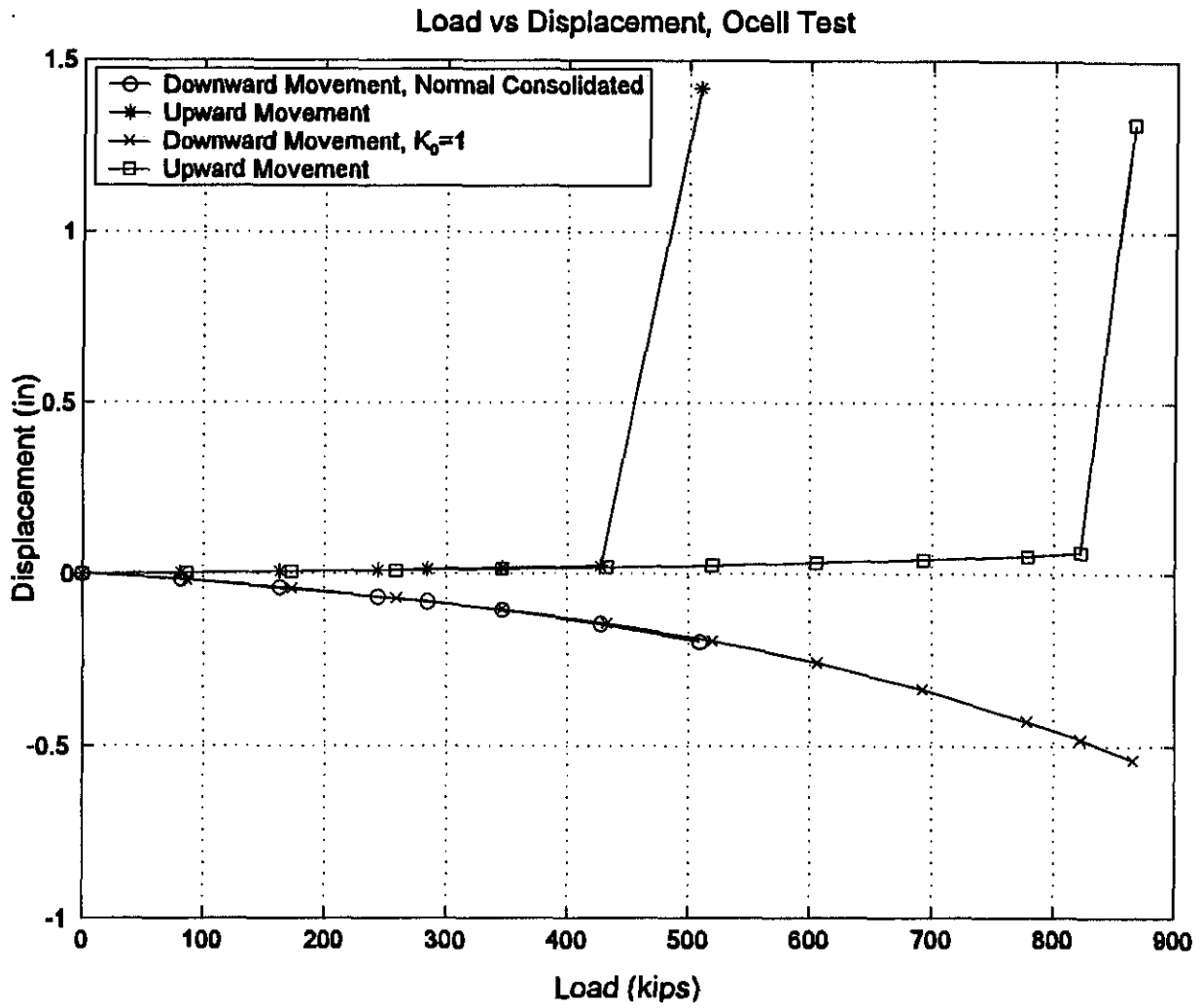


Figure B-55 Effect of K_0 on Load vs Displacement Curve, O-cell Test

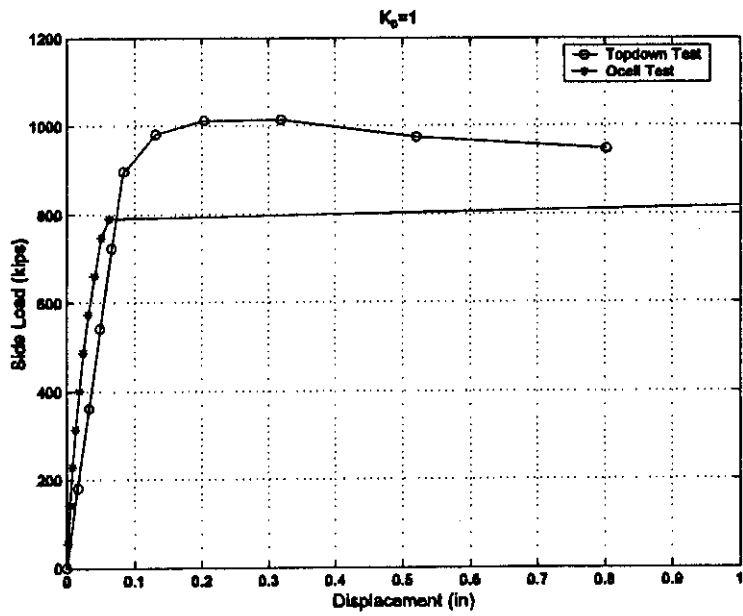
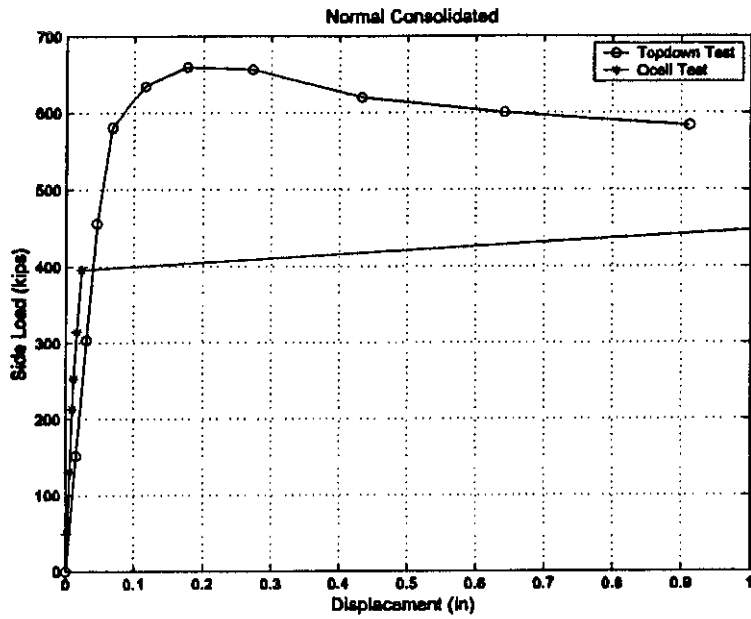


Figure B-56 Side Load vs Displacement Comparison for Different K_0 Values

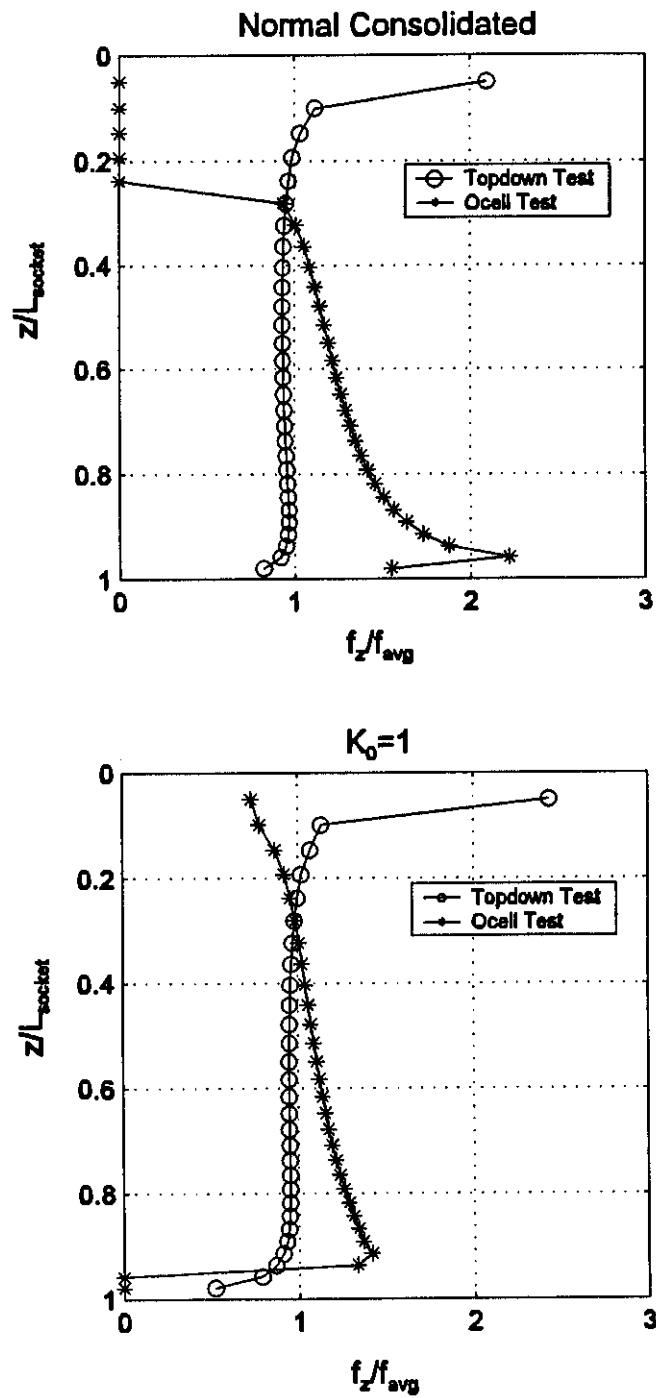


Figure B-57 Shear Stress Distribution Comparison for Different K_0 Values

Part C

COMPARISON WITH FIELD TESTS

INTRODUCTION

In order to verify the finite element model, several well-documented case histories were modeled and compared with the field test results. Both the O-cell test and the top down test were performed on the same mesh. The focus was the comparison of the load vs displacement curve and the load transfer curve. The unit mobilized side shears calculated from the strain gage readings were also compared with the model results. It should be noticed that it is quite difficult to estimate the deposit properties with the limited information. Therefore, some parameters were adjusted to achieve better results.

HENDERSON, NV CASE

General Information

This project included an Osterberg load test performed by Ladtest, Inc at I-215/I-515 interchange, Henderson, NV.

The test site mainly consists of very stiff sandy lean clay with gravel, with several silty sand layers. The test shaft was 60in in diameter and 40ft long, and the top of the shaft was 45ft below the ground surface. A detailed dimension and shaft instrumentation was shown in Figure C-1. The O-cell was placed at 25.2ft below the top of the shaft, with the other 14.8ft shaft carrying the downward load. Three strain gages were placed along the shaft to estimate the load transfer information, one of which was installed in the shaft segment below the base of the O-cell. Three LVWDTs were positioned between the lower and upper plates to measure O-cell expansion. Two pipe piles were also attached to

the test shaft to measure compression of the shaft between the cell and the top of the shaft with two telltales.

During the test, each load increment was held constant for four minutes. The data logger automatically recorded the instrument readings every 30 seconds. The maximum applied O-cell pressure was 7600psi, resulting a load of 1980kips. The maximum mobilized upward and downward displacement was 0.in and 4.9in respectively. The unit shaft resistance could be derived from the strain gage data, which was calculated as 1.08ksf from the top of the shaft to strain gage level 3, 2.72ksf from strain gage level 3 to strain gage level 2, 8.83ksf from strain gage level 2 to O-cell, and 6.02ksf from O-cell to strain gage level 1.

Finite Element Model

A finite element model was built up to simulate the field test. The 45ft sand and clay layer above the top of the shaft was omitted in the modeling, but the overburden pressure was applied on the top of the mesh. A total of 3471 nodes and 3300 elements were generated. The top down was also performed on the same mesh. Two different sets of interface properties were employed to the pile-soil interface.

The following is a list of parameters used in the model.

Soil properties:

Young's modulus $E = 10ksi$

Cohesion $c = 80psi$

Friction angle $\phi = 0$

Pile-Soil interface properties:

Upper part shaft: Cohesion $c_i = 0psi$

Friction angle $\phi_i = 27^\circ$

Lower part shaft: Cohesion $c_i = 0 \text{ psi}$

Friction angle $\phi_i = 18.5^\circ$

Comparison of Results

The comparison of the load vs displacement curve from measurement and model is shown in Figure C-2. For the downward movement curve, the finite element model shows a stronger behavior, while for the upward movement curve, the finite element model exhibits a weak behavior. But both finite element model and measurement have a same average side resistance.

The load transfer curve can be calculated from the strain gage data. Table C-1 presents the calculated vertical load at different load levels for all 3 gages from both measured results and the finite element results. The corresponding mobilized side shear is shown in Table C-2. The data in Table C-1 was also plotted in Figure C-3. Note in Table C-1, the numbers in the parenthesis are the loads from the finite element model, which are not exactly same as the measured load. At the lower load level, the load transfer curve from both results match fairly well. However, it is show that more loads are carried by the middle of the shaft at large load levels.

The top down test was then conducted with the same parameters. Figure C-4 shows the load vs displacement curves from finite element model and the derived from the field test results. The finite element model exhibits a weaker behavior at when the load was first applied. However, it has a larger pile capacity as can be seen from Figure C-4.

The maximum mobilized side shear at different depth intervals can be calculated from the vertical strain information. Table C-3 summarizes strain, load and side shear results, showing that the side shear is smaller at a lower depth.

With both measured results and model results, a comparison can be made regarding the maximum mobilized side shear at different depth intervals, as shown in Table C-4. At the interval from gage 1 to O-cell and O-cell to gage 2, measured results have the largest value, which is 6.02ksf and 8.83ksf respectively. While at the interval from gage 2 to gage 3 and gage 3 to the pile top, the top down test exhibit the largest value, 5.03ksf and 6.49ksf respectively.

WILSONVILLE, AL CASE

General Information

This project involved an Osterberg load test on a test shaft for the Department of Energy's Power Systems Development Facility, Wilsonville, Alabama. The test was performed by Loadtest, Inc. The purpose of this load test was to assess and verify the drilled shaft design capacity.

The site stratigraphy consists of the approximately 1ft of fill, underlain by shale which has a maximum compressive strength of 1300psi. Groundwater was not encountered in the shaft. The test shaft was 32in in diameter and 18.5ft long. The detailed dimension and instrumentation is shown in Figure C-5. Two telltales were attached to the vertical hydraulic pressure pipe to measure the upward and downward movement. Four strain gages were installed to measure the axial strain in order to obtain the side shear distribution information.

The load test was conducted on Feb. 9, 1994, about 26 hours after the placement of the concrete. The concrete was test to have an average compressive strength of 4500psi. Based on this information and the contribution of the reinforcing steel, the modulus of the shaft was estimated as 4.16E6psi. The load was applied in increments of approximately 60tons for loading and 120tons for unloading. Pressure was held for 4 minutes, with the maximum load held for 10 minutes, and 2 minutes for unloading. The maximum applied O-cell load was 534tons with an upward displacement of 0.660in and a downward displacement of 2.384in. The maximum mobilized side shear was 7.8tsf from O-cell to gage 1, 4.3tsf from gage 1 to gage2, 3.8tsf from gage 2 to gage 3, and 1.3tsf from gage3 to gage 4 respectively.

Finite Element Model

The shaft was modeled using finite element method to perform the O-cell test. The finite element mesh involves a total of 3129 nodes and 2967 elements. Since there are some uncertainties about the properties of shale, different properties were tried to match the test results. The Young's modulus of the rock may be reduced because it was considered as intact in the model while there may be some seams and joints. The corresponding top down test was also performed on the same finite element model with the same parameters.

The following is a summary of the all parameter used in the model.

Rock properties:

Young's modulus $E_{rock} = 60ksi$

Cohesion $c_{rock} = 200psi$

Friction angle $\phi_{rock} = 14^\circ$

Pile-rock interface properties:

Cohesion $c_i = 30 \text{ psi}$

Friction angle $\phi_i = 50^\circ$

Comparison of Results

Figure C-6 shows the load-displacement curve from both field test and model calculation. The downward displacement match fairly well, but for the upward displacement, the finite element model exhibits a stronger response because the dilatancy was not considered at the pile-rock interface. However, the failure load is about the same at which the side resistance was failed.

The shear stress and normal stress distribution along the pile length at different load levels are shown in Figure C-7 and Figure C-8 respectively. As can be seen, the contact nodes at both ends tend to be open with the increase of the applied load. Therefore, both shear stress and normal stress decrease at both ends and increase in the middle with the increase of the applied load.

Side shear information can also be obtained from the strain gage reading. Similar to the field test, the vertical strain at gage levels was picket out and the corresponding load and side shear was calculated. Table C-5 shows the calculated vertical load at different load levels for all 4gages from both measured results and the finite element results. The corresponding mobilized side shear is shown in Table C-6. The data in Table C-5 was also plotted in Figure C-9. In Table C-5 and Table C-6, the numbers in the parenthesis are the loads from the finite element model, which are not exactly same as the measured load.

It is shown that the unit shaft resistance from the finite element model exhibits a large value in the middle of the shaft when the applied load is large. This is because the contact nodes at both ends tend to be open, but in the real test, the shaft resistance increases with the depth and the maximum side shear always occurs close to the O-cell.

The top down test was then conducted with the same parameters. Figure C-10 shows the load vs displacement curves from finite element model and the derived from the field test results. It can be seen that the finite element model is stronger, which is due to the interface model used in the calculation. As mentioned above, dilatancy was not considered at the pile-rock interface, so the slip between the pile and the rock was calculated smaller.

The shear stress vs depth curve and normal stress vs depth curve at different load levels are presented in Figure C-11 and Figure C-12 respectively. Different from the O-cell test, the maximum shear stress occurs at the top of the shaft. Below a depth of 4ft, the shear stress distribution becomes uniform. The mobilized side shear near yielding at different depth intervals can be calculated from the vertical strain information. Table C-7 summarizes strain, load and side shear results at failure of the side resistance. The mobilized side shear decreases with the depth.

With both measured results and model results, a comparison can be made regarding the maximum mobilized side shear at different depth intervals, as shown in Table C-8. At the interval from the O-cell to gage 1, measured results have the largest value, which is 7.8tsf. While at the interval from gage 1 to gage 2 and gage 2 to gage 3, there is no much difference among three results, with an approximate value of 4.0tsf.

However, at the interval of gage 3 to gage 4 (the top part of the shaft), the top down test exhibit the largest value (4.5tsf) as expected.

DENVER, CO CASE

General Information

This project also involved an Osterberg load test preformed by Loadtest, Inc for Southeast Corridor Construction. The test shaft was located at the I-25/I-225 interchange, Denver, Colorado.

The test site consists of a layer of 10ft sandy lean clay, overlying weathered claystone with silty sand and fined grained seams. The claystone has different blow count at different depth although it was treated as the same in the finite element model. The detailed shaft information and instrumentation is show in Figure C-13. The nominal shaft diameter was 42in. The top 4.5ft of the test shaft was in the clay layer, and the socket length was 17.25ft. Two strain gages were installed along the shaft length to assess the side shear load transfer of the shaft above the Osterberg cell. The test shaft assembly also included two telltales in two steel pipes in order to monitor the upward and downward movement.

The test was carried out on Jan 14, 2002. The load was applied incrementally and each successive load increment was hold for four minutes. The maximum load was reached at the sixth increment with a value of 559kips. The corresponding maximum upward net load applied to the side shear was 527kips, calculated by subtracting the self weight of the shaft above the O-cell from the gross load. At this load level, the total upward movement was 1.58in, and the downward movement was 2.30in. At the time of testing, the concrete unconfined compressive strength was reported to be 3423psi. Based

on the strain gage readings, the unit side shear was calculated as 1.08ksf from the top of the shaft to strain gage 2, 2.63ksf from strain gage 2 to strain gage 1, and 3.51ksf from strain gage 1 to the O-cell level.

Finite Element Model

The finite element model was built to model the Denver test shaft. It should be noticed that 4.5ft of the test shaft was in the clay soil layer. Therefore, the interface properties used for at the pile-clay interface are different from those at the pile-rock interface, which is much weaker. The 6ft deep clay above the top of the shaft was neglected in the finite element mesh, but its influence on the overburden pressure was considered. In the finite element model, 4.375psi vertical pressure was applied on the top of mesh. Different interface properties were used to define pile-clay interface and pile-rock interface. The pile-clay interface was assumed to have 5psi resistance. The following is a list of the parameters used in the analysis.

Rock properties:

Young's modulus $E_{rock} = 40ksi$

Cohesion $c_{rock} = 50psi$

Friction angle $\phi_{rock} = 10^\circ$

Pile-rock interface properties:

Cohesion $c_i = 9.6psi$

Friction angle $\phi_i = 31^\circ$

Pile-clay interface properties:

Cohesion $c_i = 5.0psi$

Friction angle $\phi_i = 0$

Comparison of Results

The comparison of the load vs displacement curved from both field test and finite element model is shown in Figure C-14. The two downward movement curves fit very well, but the finite element model seems much stronger than the field test although the failure load is about the same for both cases. Same as before, it is because the interface model doesn't include dilatancy. Figure C-15 and Figure C-16 present the shear stress vs depth curve and normal stress vs depth at different levels. As can be seen from Figure C-15, the maximum mobilized side shear for the top 4.5ft is 5psi as defined in the interface properties. The shear stress in the rock is much larger with a maximum value close to the O-cell level. However, with the increase of the applied load, both shear stress and normal stress at the bottom tend to be zero indicating that the contact nodes are open. This results in the reduction of the shear stress at node near O-cell. It was also found that the shear stress close to the clay-rock interface is larger, which is believed to be due to the numerical problem since the interface properties are not continuous at that depth.

Similar to the real test, the strain information can be used to calculate the side load transfer and then estimate the unit shaft resistance. Table C-9 summarizes the side load calculated at gage levels from both field test results and model results. The derived side shear results were shown in Table C-10. The number in the parenthesis is the applied load in the finite element model which is not equal to the applied load in test for some cases. The data in Table C-9 were also plotted in Figure C-17. It was shown that at lower applied load, the two side load transfer curves match well. However, when the applied load increases, the difference between field test and finite element model is becoming

larger. For the finite element model, the side shear distribution is more uniform. It is because the contact nodes near O-cell become open and more side force is carried at the middle of the shaft.

The top down test was also performed using the same model. Figure C-18 presents the load vs displacement curve from the finite element model and derived from the O-cell field test results. The finite element model again exhibits stronger response before the failure of the side resistance, which is because dilatancy at pile-rock interface was not considered in the finite element model.

Shear stress vs depth curve and normal stress vs depth curve are presented in Figure C-19 and Figure C-20 accordingly. It is shown that larger shear stress and normal stress occurs at the top of the socket. The maximum mobilized side shear in the clay layer is 5psi as defined in the interface properties. Similarly, the unit shaft resistance can be calculated from the strain information, as shown in Table C-11.

Table C-12 compares the mobilized side shear from the measurement, finite element top down test and O-cell test model. For the O-cell test, the maximum mobilized side shear occurs at the bottom of the shaft from both measurement and model results. But for the finite element model, more loads are carried by the middle of the pile since the interface becomes open at the bottom. For the top down test, the maximum side shear occurs at the middle since the overlying clay layer has weaker interface properties.

SUMMARY

Two field tests were model using the finite element method. Both tests involve an Osterberg load test of a rock socketed pile. In the model, the interface properties can be adjusted to match the measured load-displacement curve. The same model was then used

to perform the top down test. The comparison between the measured results and the model results can be summarized as follows.

1. The downward displacement curves for the O-cell test from both measurement and model results can fit well. However, for the upward displacement, the finite element model shows a stronger behavior. This is due to the negligence of the dilatancy at the pile-soil interface in the finite element model.
2. At lower load levels, the load transfer curves from both measurement and model results match closely, so do the side shear results. While at larger load levels, the side shear has larger value at the middle from the model results, but the bottom of the pile shows larger side shear from the measurement. In the finite element model, the contact nodes at the interface tend to be open when the side resistance is about to fail.
3. The top down test and the O-cell test exhibit different side shear distribution characteristic. For the top down test, the maximum shear stress appears at the top of the pile or socket. But for the O-cell test, the maximum side shear occurs close to the O-cell.

*Table C-1 Comparison of the Load at Gage Intervals
Between Field Test Results and Model Results, Henderson Case*

Applied Load (kips)	Gage 1		Gage 2		Gage 3	
	From Test (kips)	From Model (kips)	From Test (kips)	From Model (kips)	From Test (kips)	From Model (kips)
789 (790)	192.2	247.2	131.9	204.3	21.5	2.7
944 (988)	295.4	350.7	168.6	293.8	23.4	23.3
1408 (1383)	615.5	650.8	305.8	488.6	40.8	79.7
1718 (1704)	872.4	948.8	422.6	692.3	60.7	133.8
1976 (1976)	1120.9	1206.7	556.6	899.0	102.2	177.2

Table C-2 Side Shear at Gage Intervals From Model Results, Henderson Case

Applied Load (kips)	Gage 1 to O-cell (ksf)	O-cell to Gage 1 (ksf)	Gage 1 to Gage 2 (ksf)	Gage 2 to Gage 3 (ksf)
790	4.03	3.54	1.10	0
988	4.70	4.23	1.53	0.05
1383	5.37	5.50	2.42	0.71
1704	5.53	6.26	3.37	1.31
1976	5.62	6.67	4.41	1.57
1976 (Measured)	6.02	8.83	2.72	1.08

*Table C-3 Mobilized Side Shear at Gage Intervals, Top Down Test,
Henderson Case*

Strain Gage	Strain ($\mu\epsilon$)	Load (kips)	Unit Side Shear (ksf)
Gage 1	84.1	768.2	4.06 (Gage 1 to O-cell)
Gage 2	231.9	2118.0	5.30 (O-cell to Gage 2)
Gage 3	315.5	2878.0	5.03 (Gage 2 to Gage 3)
			6.49 (Gage 3 to Pile Top)

*Table C-4 Comparison of the Maximum Mobilized Unit Shaft Resistance,
Henderson Case*

Depth Interval	Measured (O-cell Test) (ksf)	FE Model (O-cell Test) (ksf)	FE Model (Top Down Test) (ksf)
Gage 1 to O-cell	6.02	5.62	4.06
O-cell to Gage 2	8.83	6.67	5.30
Gage 2 to Gage 3	2.72	4.41	5.03
Gage 3 to Pile Top	1.08	1.57	6.49

Table C-5 Comparison of the Load at Gage Intervals

Between Field Test Results and Model Results, Wilsonville Case

Applied Load (tons)	Gage 1		Gage 2		Gage 3		Gage 4	
	From Test (tons)	From Model (tons)	From Test (tons)	From Model (tons)	From Test (tons)	From Model (tons)	From Test (tons)	From Model (tons)
183 (198)	173.8	118.4	117.0	75.0	41.9	38.0	8.1	0.9
246 (248)	180.2	157.1	139.1	99.8	55.6	50.6	7.1	2.1
308 (298)	253.7	202.2	168.8	129.0	65.3	65.2	7.4	2.5
434 (446)	327.6	379.4	227.2	258.5	89.2	119.7	10.0	1.0
496 (496)	366.8	432.3	258.2	309.8	99.6	135.8	15.8	4.0

Table C-6 Comparison of the Unit Shaft Resistance

Between Field Test Results and Model Results, Wilsonville Case

Applied Load (tons)	O-cell to Gage 1		Gage 1 to Gage 2		Gage 2 to Gage 3		Gage 3 to Gage 4	
	From Test (tsf)	From Model (tsf)	From Test (tsf)	From Model (tsf)	From Test (tsf)	From Model (tsf)	From Test (tsf)	From Model (tsf)
183 (198)	0.5	4.7	2.3	1.7	1.8	0.8	0.5	0.5
246 (248)	3.9	5.4	1.6	2.2	2.0	1.1	0.7	0.7
308 (298)	3.2	5.6	3.4	2.8	2.5	1.5	0.9	0.9
434 (446)	4.7	4.0	4.0	4.8	3.3	3.3	1.2	1.7
496 (496)	6.3	3.8	4.3	4.8	3.8	4.1	1.3	1.5

Table C-7 Mobilized Side Shear at Gage Intervals, Top Down Test,

Wilsonville Case

Strain Gage	Strain ($\mu\epsilon$)	Load (tons)	Unit Side Shear (tsf)
Gage 1	99.2	166.0	3.6 (O-cell to Gage 1)
Gage 2	160.5	268.5	4.1 (Gage 1 to Gage 2)
Gage 3	264.6	442.6	4.2 (Gage 2 to Gage 3)
Gage 4	442.6	740.5	4.5 (Gage 3 to Gage 4)

Table C-8 Comparison of the Maximum Mobilized Unit Shaft Resistance,

Wilsonville Case

Depth Interval	Measured (O-cell Test) (tsf)	FE Model (O-cell Test) (tsf)	FE Model (Top Down Test) (tsf)
O-cell to Gage 1	7.8	5.6	3.6
Gage 1 to Gage 2	4.3	4.8	4.1
Gage 2 to Gage 3	3.8	4.1	4.2
Gage 3 to Gage 4	1.3	1.7	4.5

*Table C-9 Comparison of the Load at Gage Intervals
Between Field Test Results and Model Results, Denver Case*

Applied Load (kips)	Gage 1		Gage 2	
	From Test (kips)	From Model (kips)	From Test (kips)	From Model (kips)
273 (279)	129.2	118.3	59.6	56.0
351 (355)	181.0	155.0	81.2	74.6
429 (449)	230.7	251.6	102.1	122.2
507 (505)	284.0	314.6	124.5	151.0
559 (559)	312.0	380.0	129.9	186.4

*Table C-10 Comparison of Side Shear at Gage Intervals
Between Field Test Results and Model Results, Denver Case*

Applied Load (kips)	O-cell to Gage 1		Gage 1 to Gage 2		Gage 2 to Pile Top	
	From Test (ksf)	From Model (ksf)	From Test (ksf)	From Model (ksf)	From Test (ksf)	From Model (ksf)
273 (279)	2.05	2.31	0.76	0.81	0.42	0.39
351 (355)	2.44	2.91	1.38	1.09	0.63	0.56
429 (449)	2.87	2.86	1.82	1.83	0.82	1.09
507 (505)	3.25	2.75	2.28	2.35	1.03	1.28
559 (559)	3.61	2.58	2.63	2.80	1.03	1.61

Table C-11 Mobilized Side Shear at Gage Intervals, Top Down Test,

Denver Case

Strain Gage	Strain ($\mu\epsilon$)	Load (kips)	Unit Side Shear (ksf)
Gage 1	93.0	476.6	2.73 (O-cell to Gage 1)
Gage 2	130.7	670.1	3.06 (Gage 1 to Gage 2)
			2.25 (Gage 2 to Pile Top)

Table C-12 Comparison of the Maximum Mobilized Unit Shaft Resistance,

Denver Case

Depth Interval	Measured (O-cell Test) (ksf)	FE Model (O-cell Test) (ksf)	FE Model (Top Down Test) (ksf)
O-cell to Gage 1	3.61	2.91	2.73
Gage 1 to Gage 2	2.63	2.80	3.06
Gage 2 to Pile Top	1.03	1.61	2.25

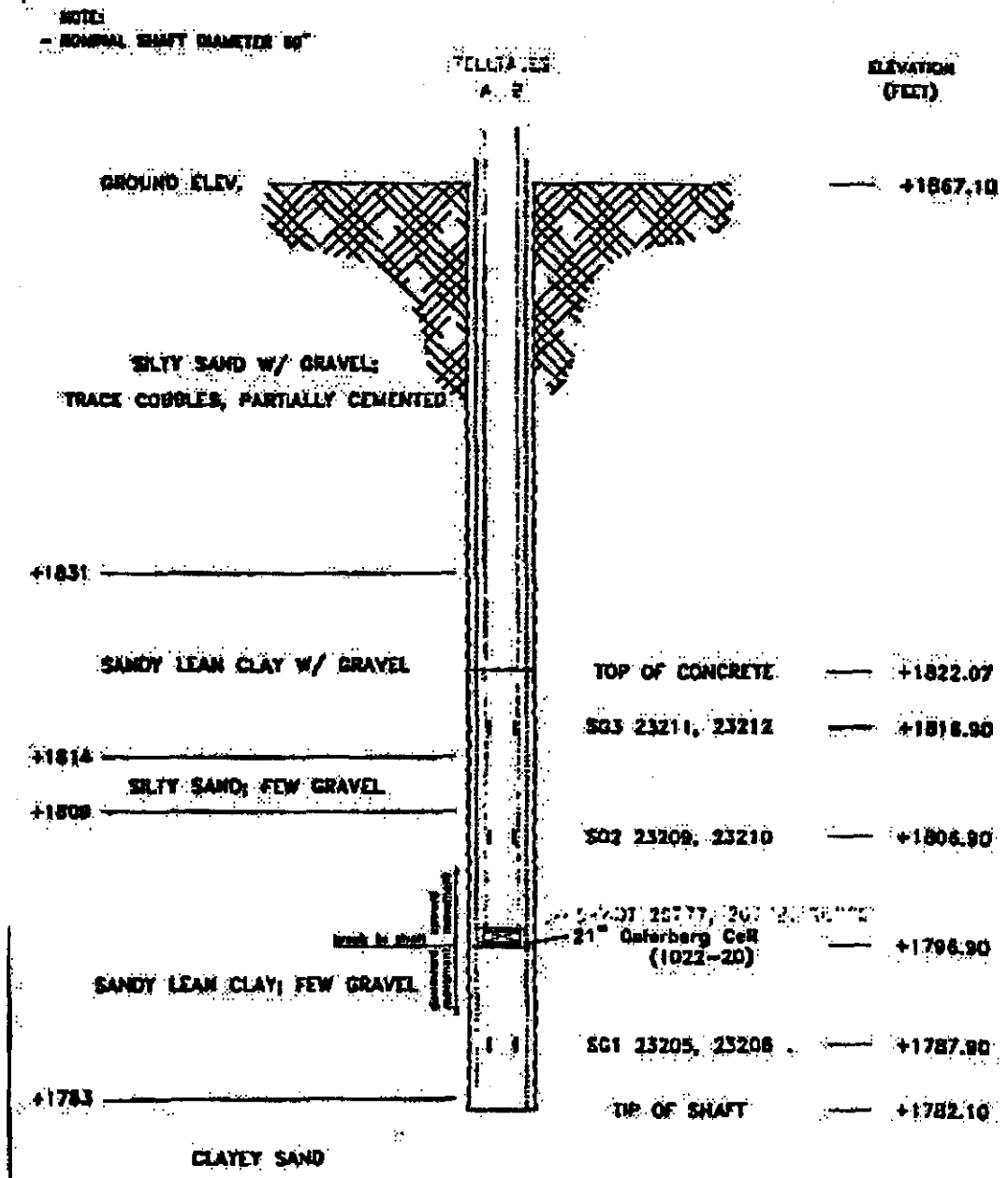


Figure C-1 Dimensions and Instrumentation of Test Shaft, Henderson Case

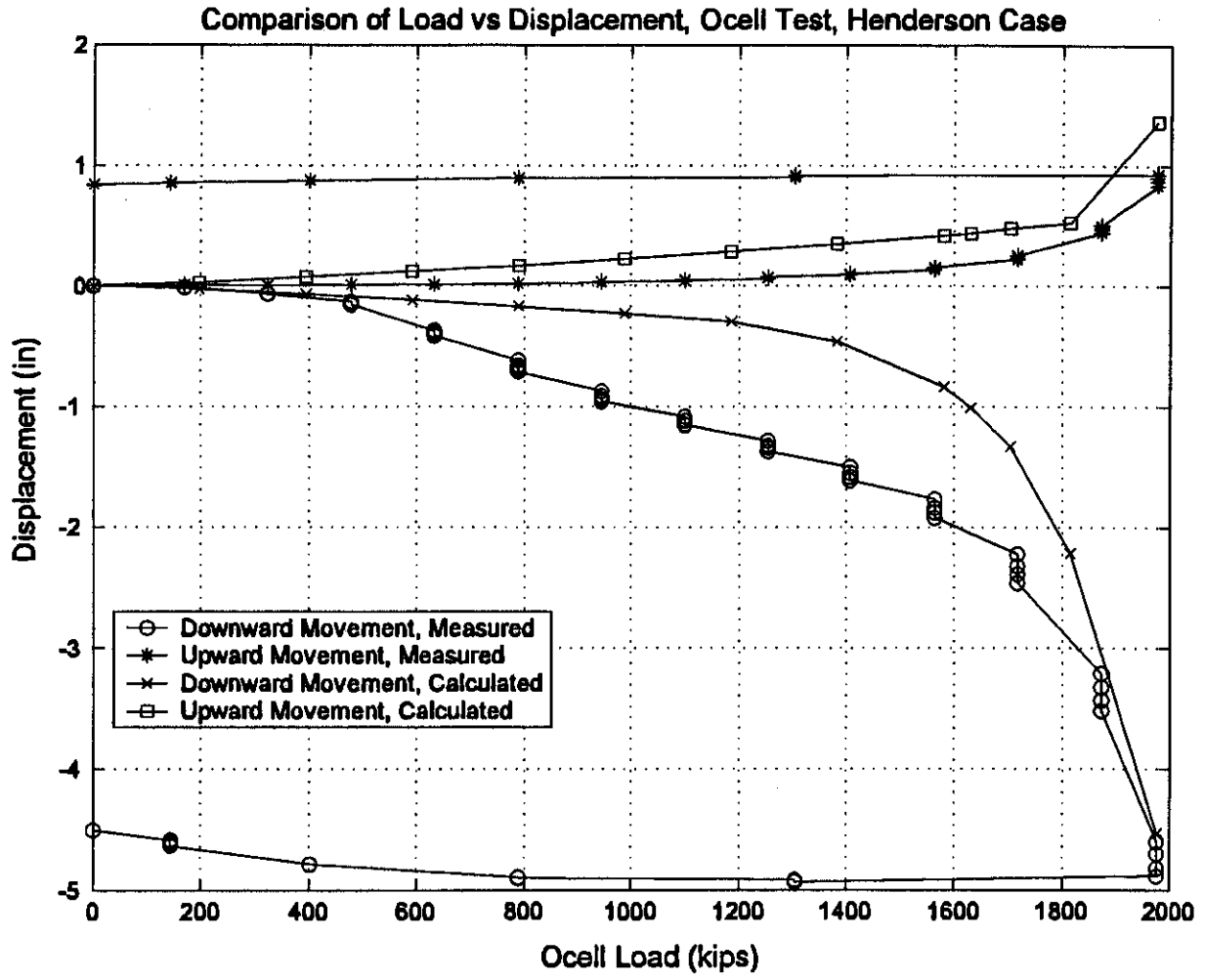


Figure C-2 Comparison of Load vs Displacement Curve, O-cell Test, Henderson Case

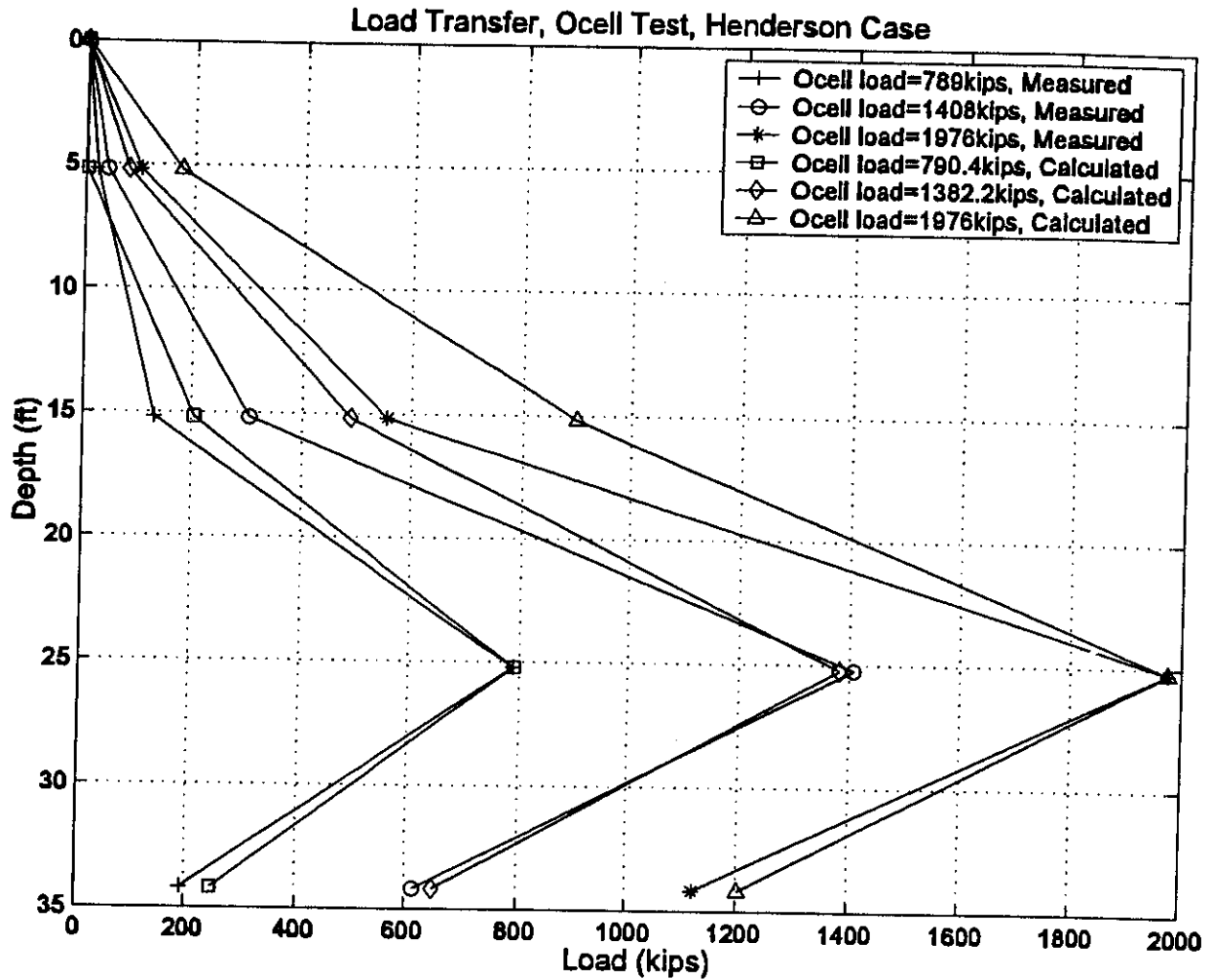


Figure C-3 Comparison of Load Transfer Curve Between Measurement and Model Results, Henderson Case

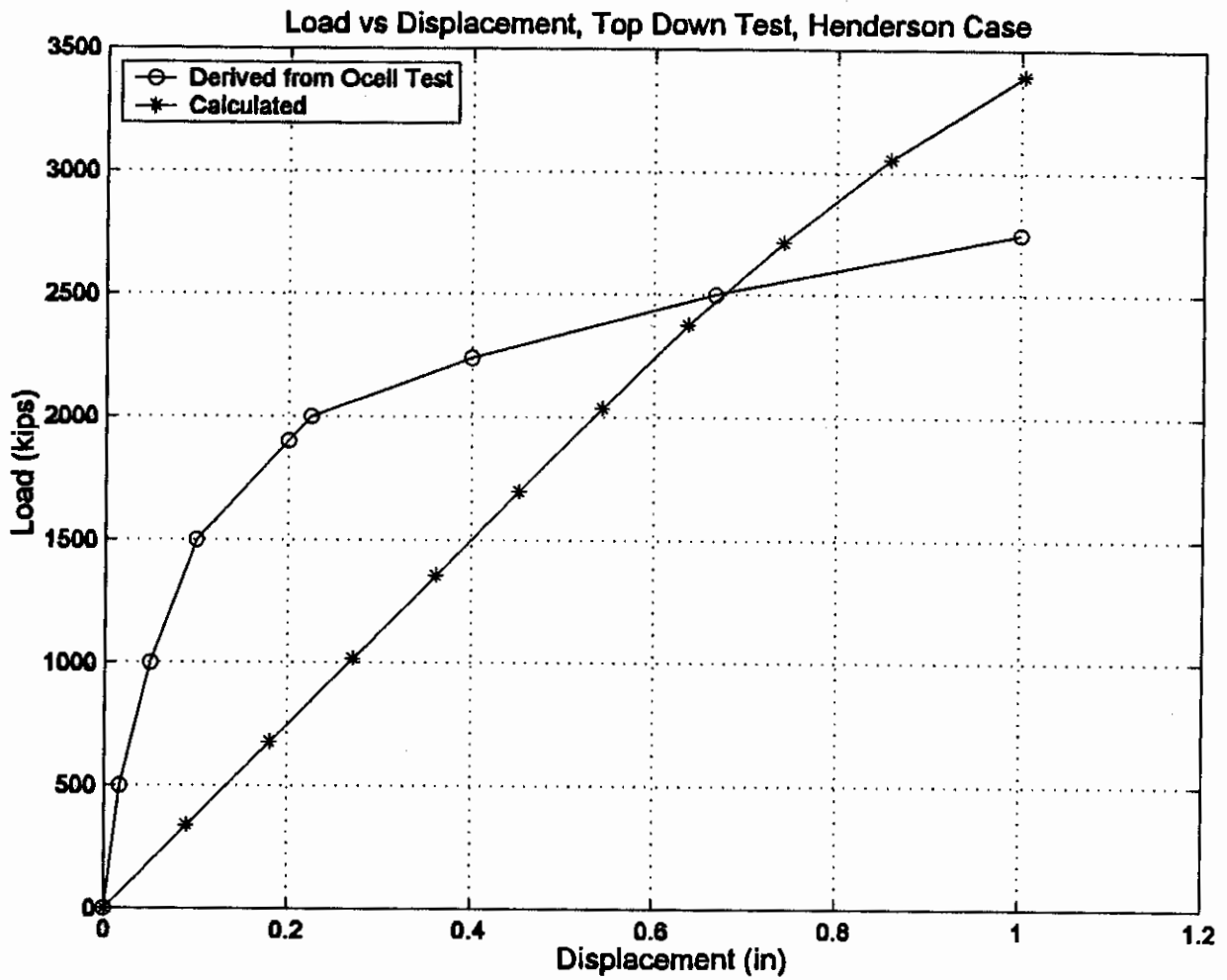


Figure C-4 Comparison of Load vs Displacement Curve, Top Down Test, Henderson Case

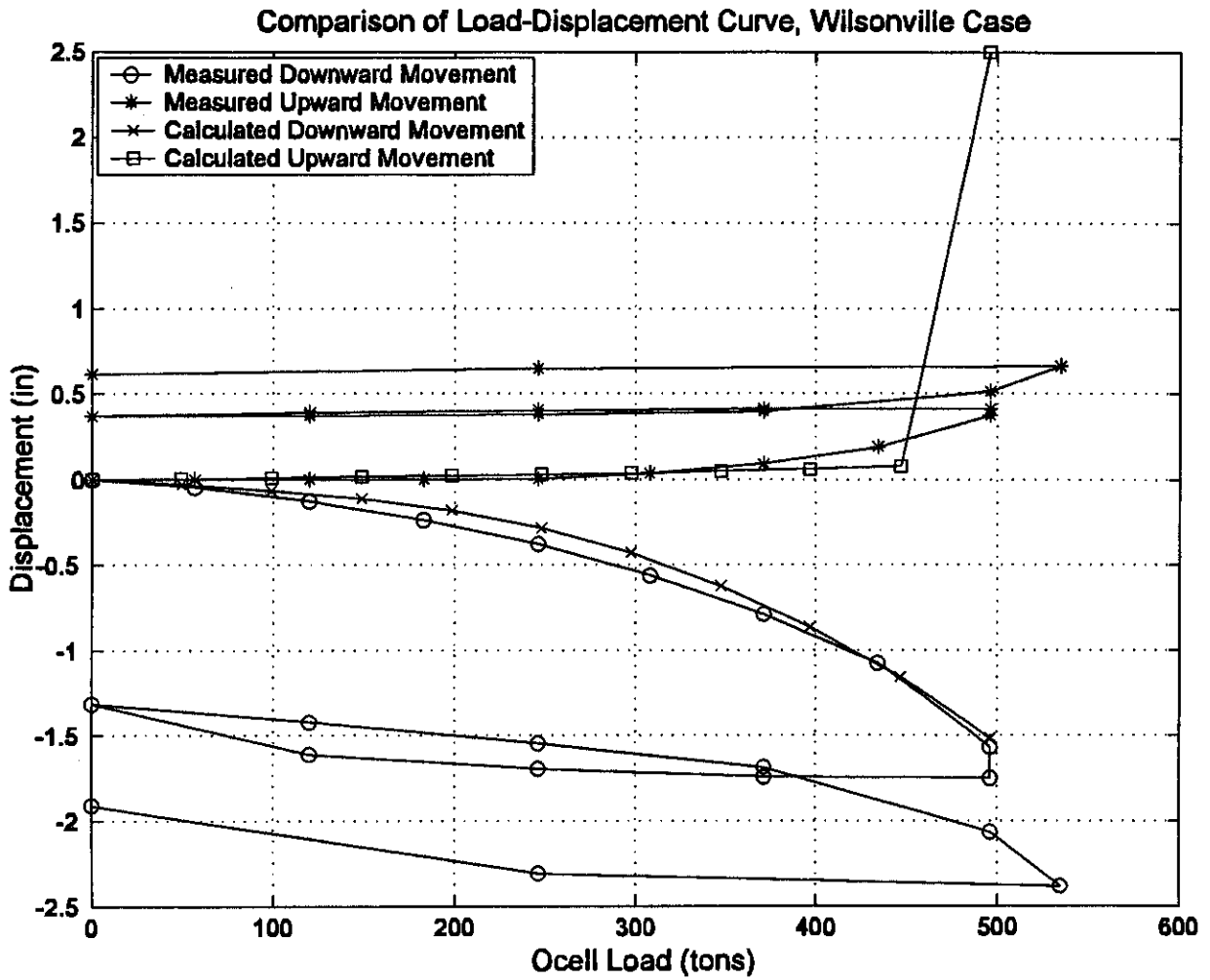


Figure C-6 Comparison of Load vs Displacement Curve, O-cell Test, Wilsonville Case

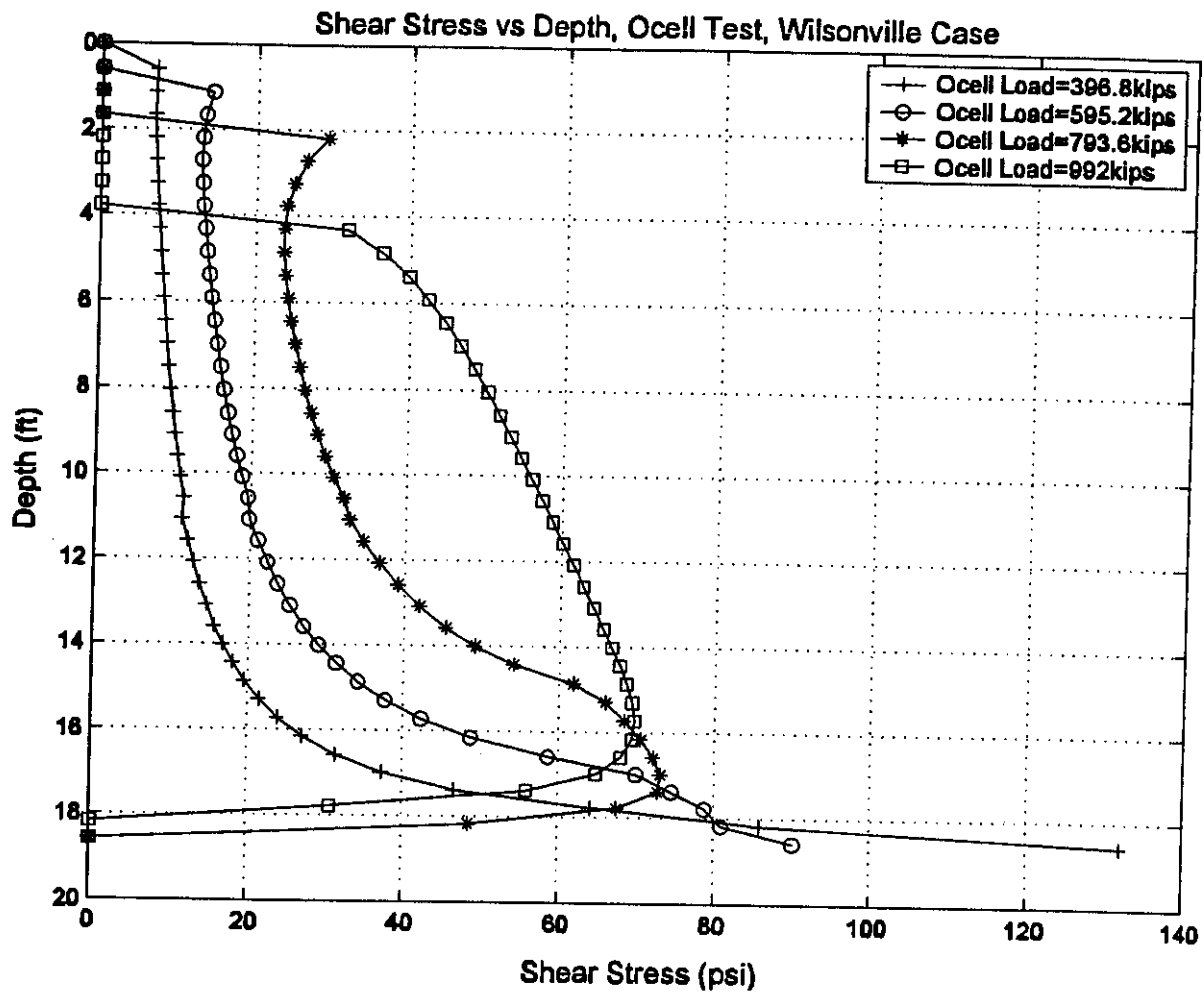


Figure C-7 Shear Stress vs Depth, O-cell Test, Wilsonville Case

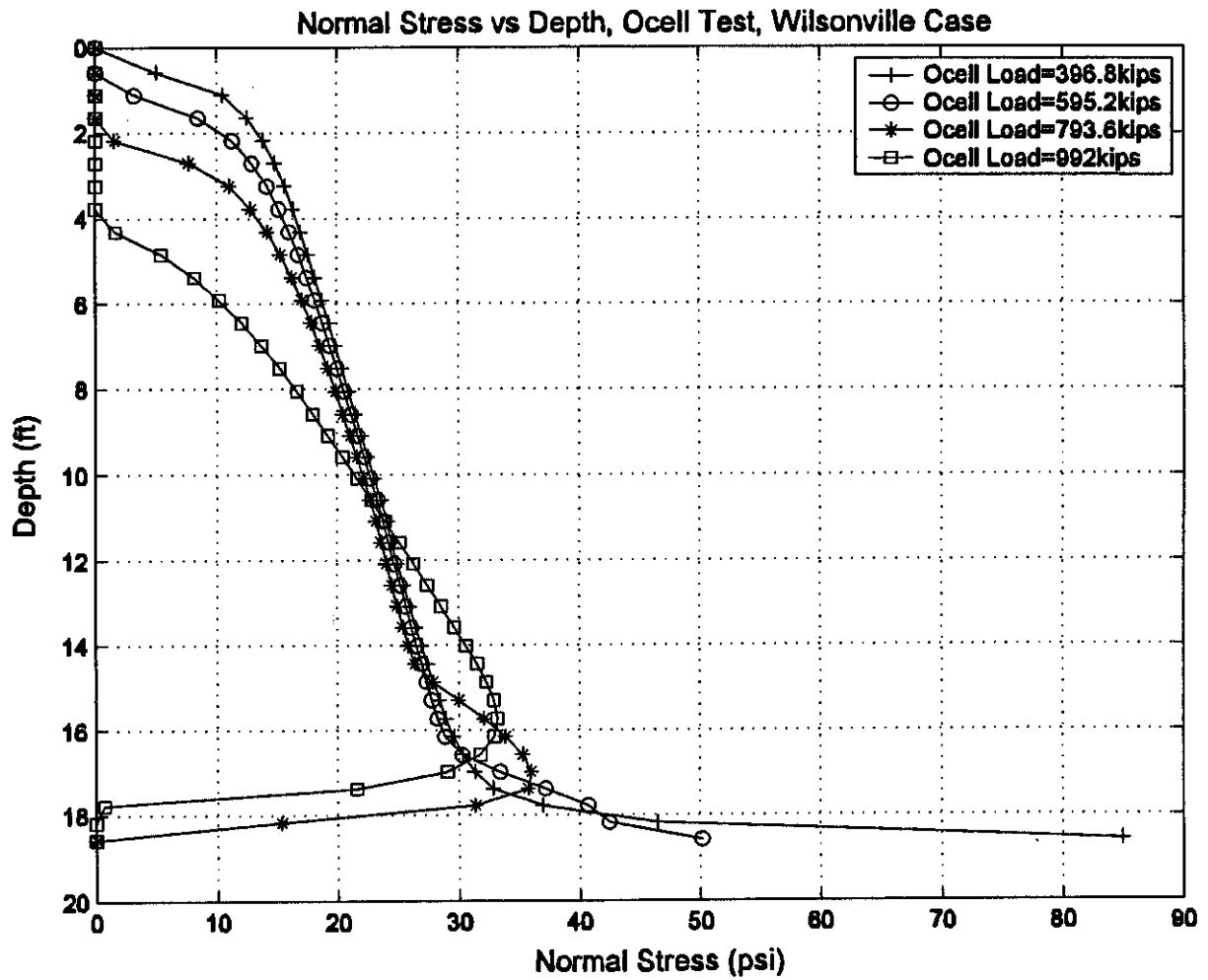


Figure C-8 Normal Stress vs Depth, O-cell Test, Wilsonville Case

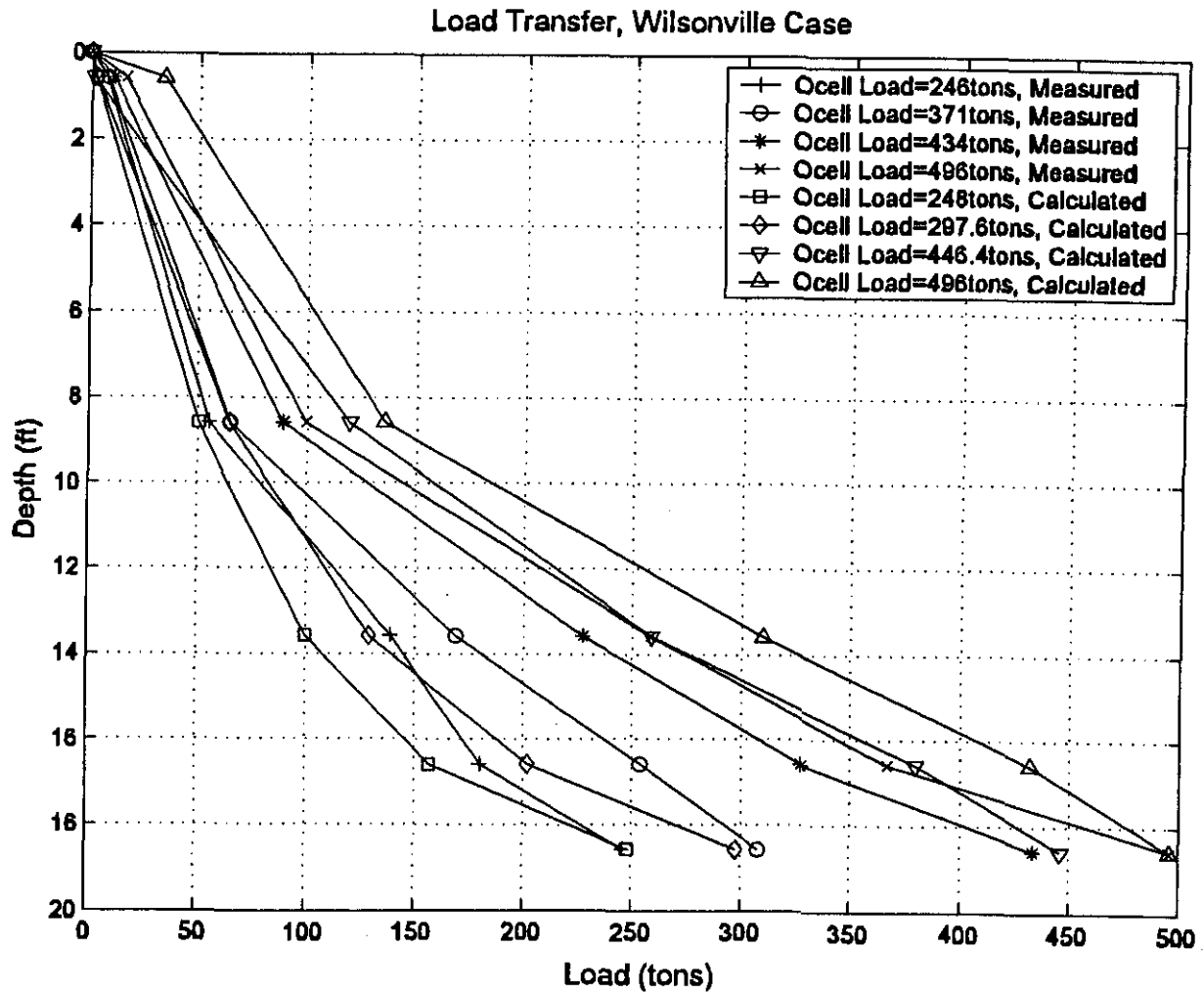


Figure C-9 Load Transfer Comparison Between Measurement and Model Results, Wilsonville Case

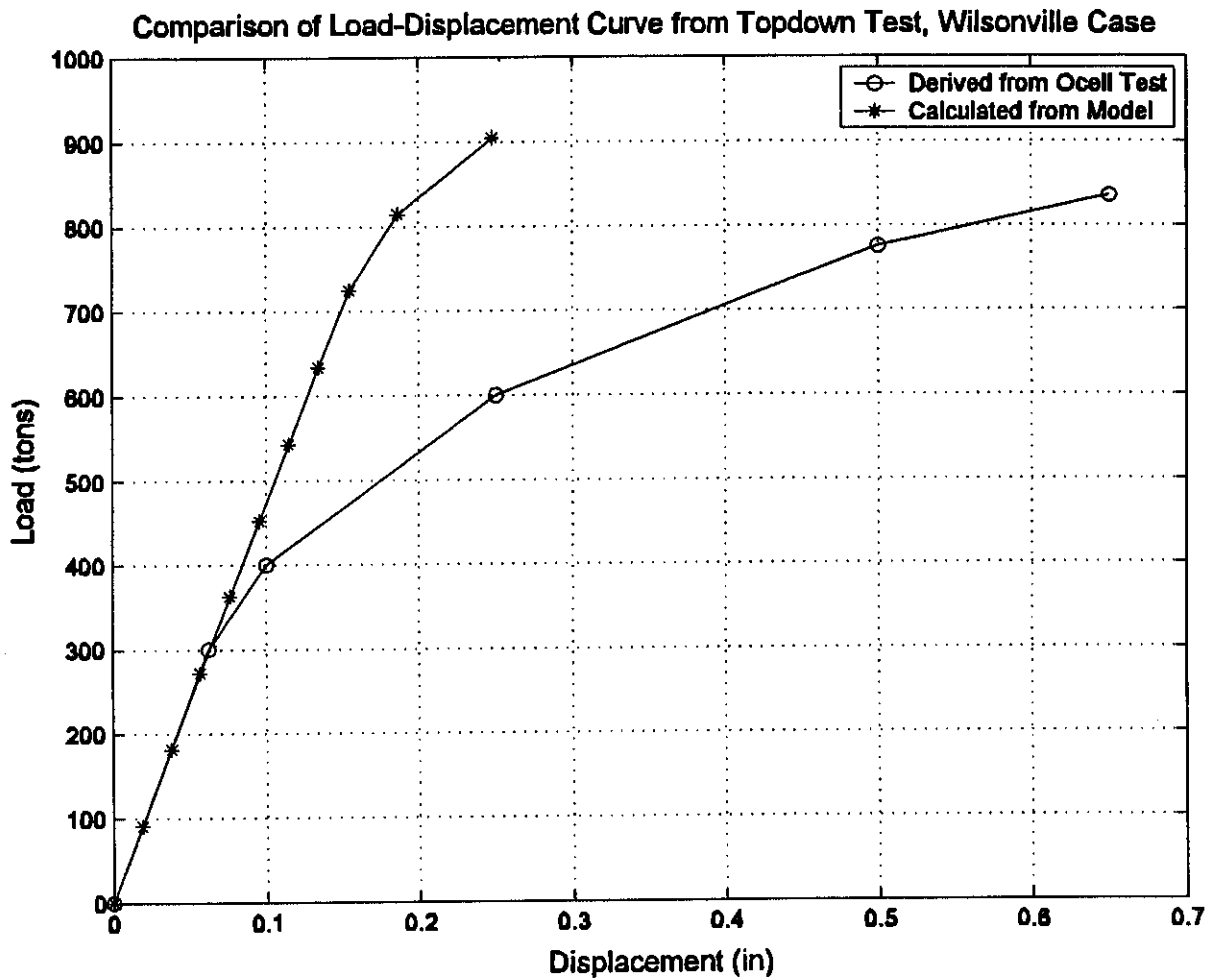


Figure C-10 Comparison of Load vs Displacement Curve, Top Down Test, Wilsonville Case

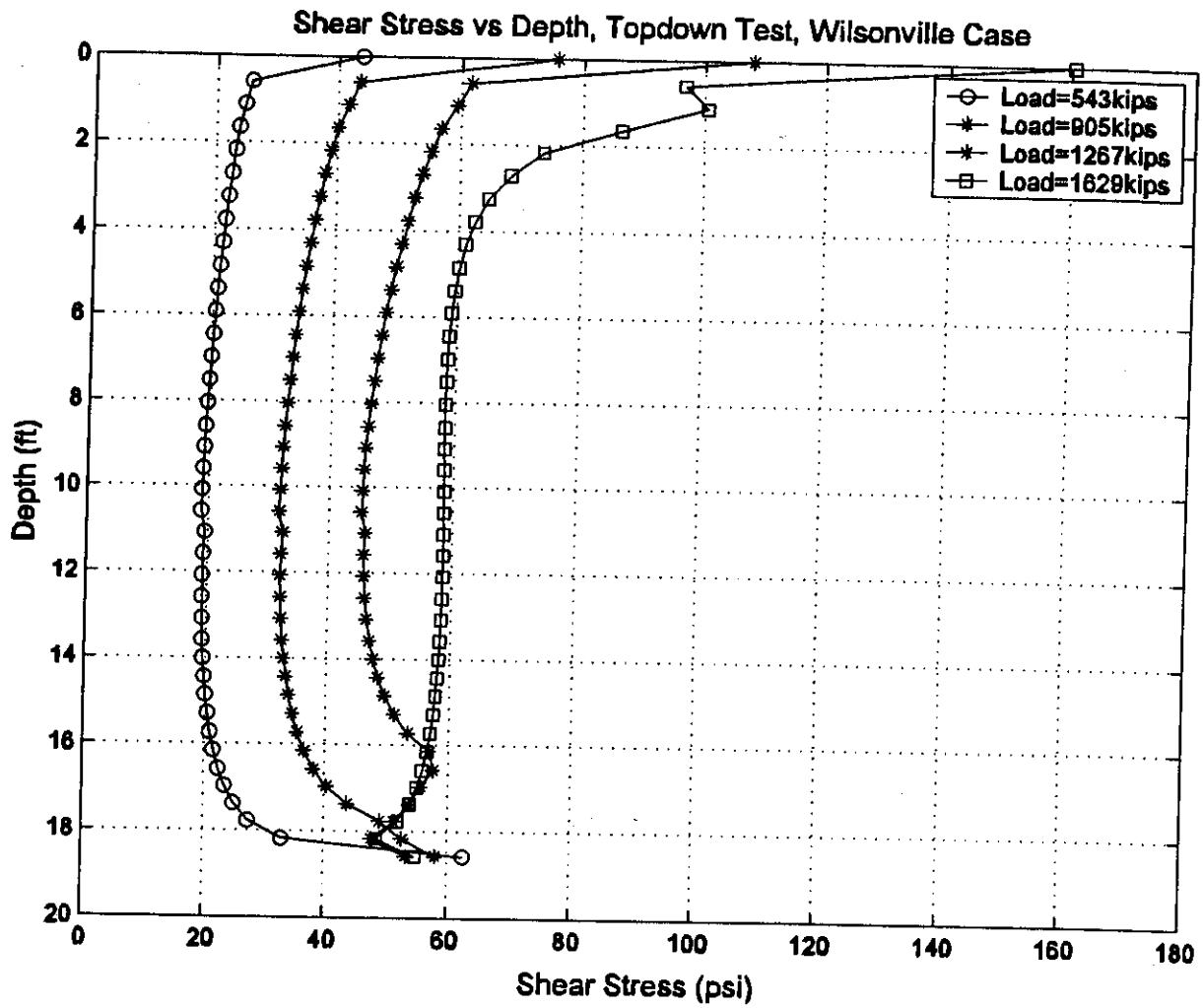


Figure C-11 Shear Stress Distribution, Top Down Test, Wilsonville Case

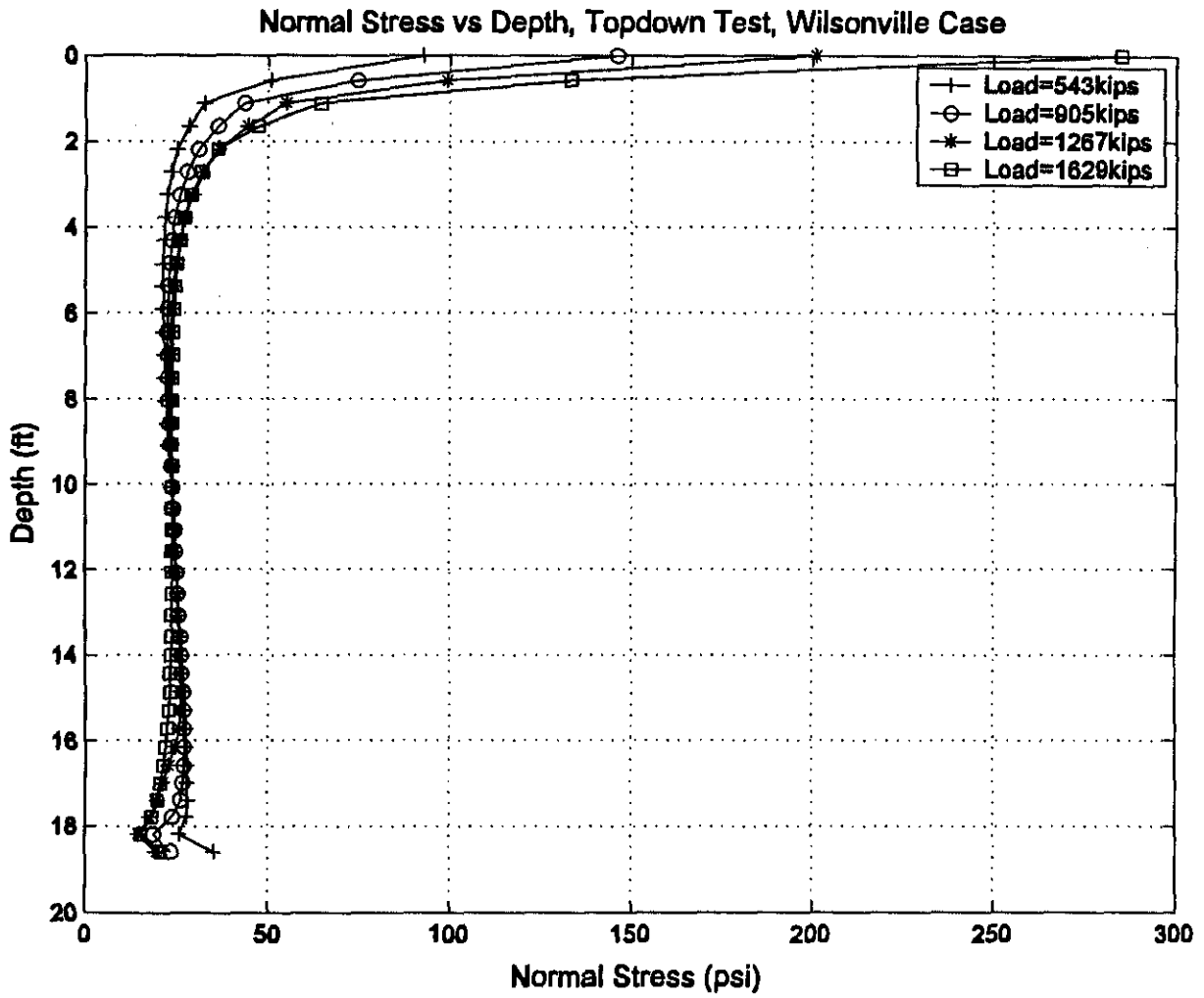


Figure C-12 Normal Stress Distribution, Top Down Test, Wilsonville Case

NOTE:
 - NOMINAL SHAFT DIAMETER 42"

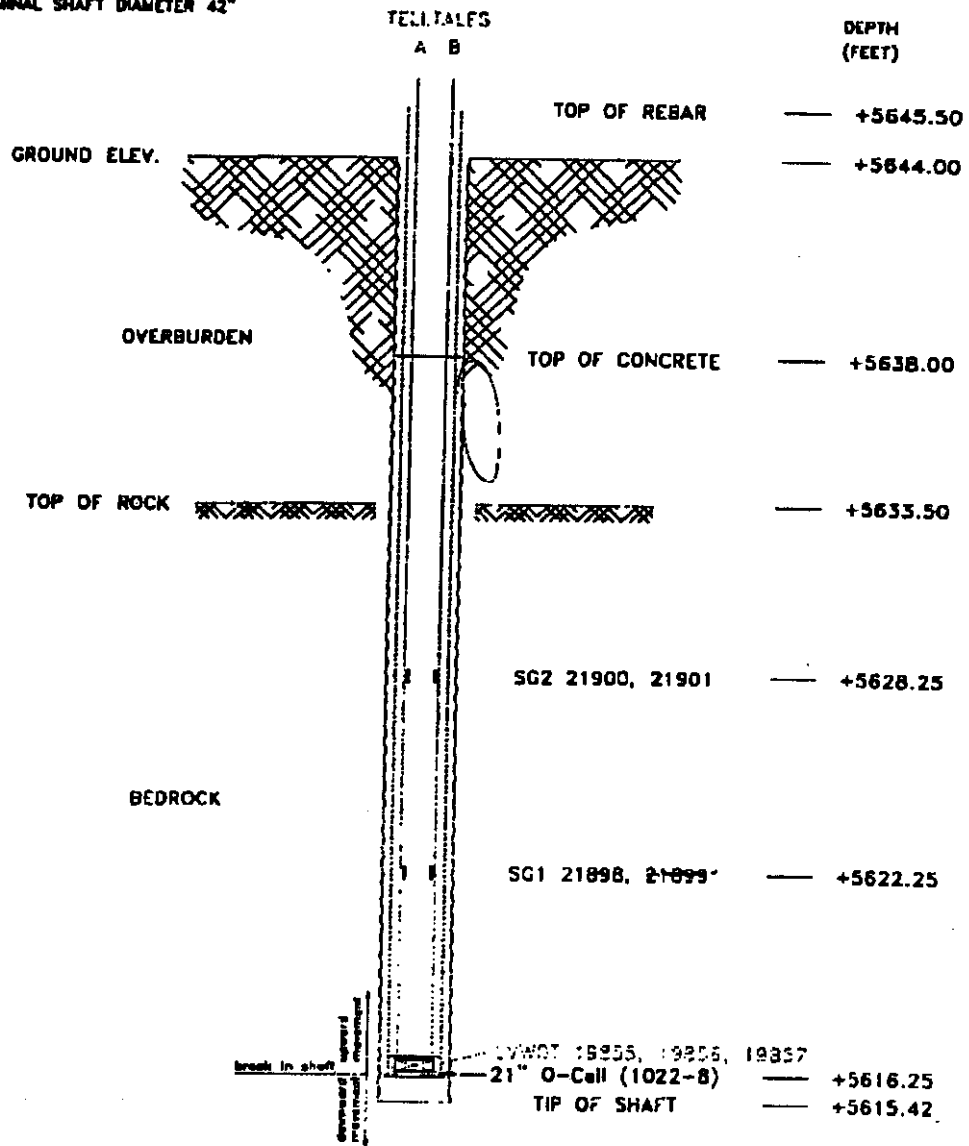


Figure C-13 Dimensions and Instrumentation of Test Shaft, Denver Case

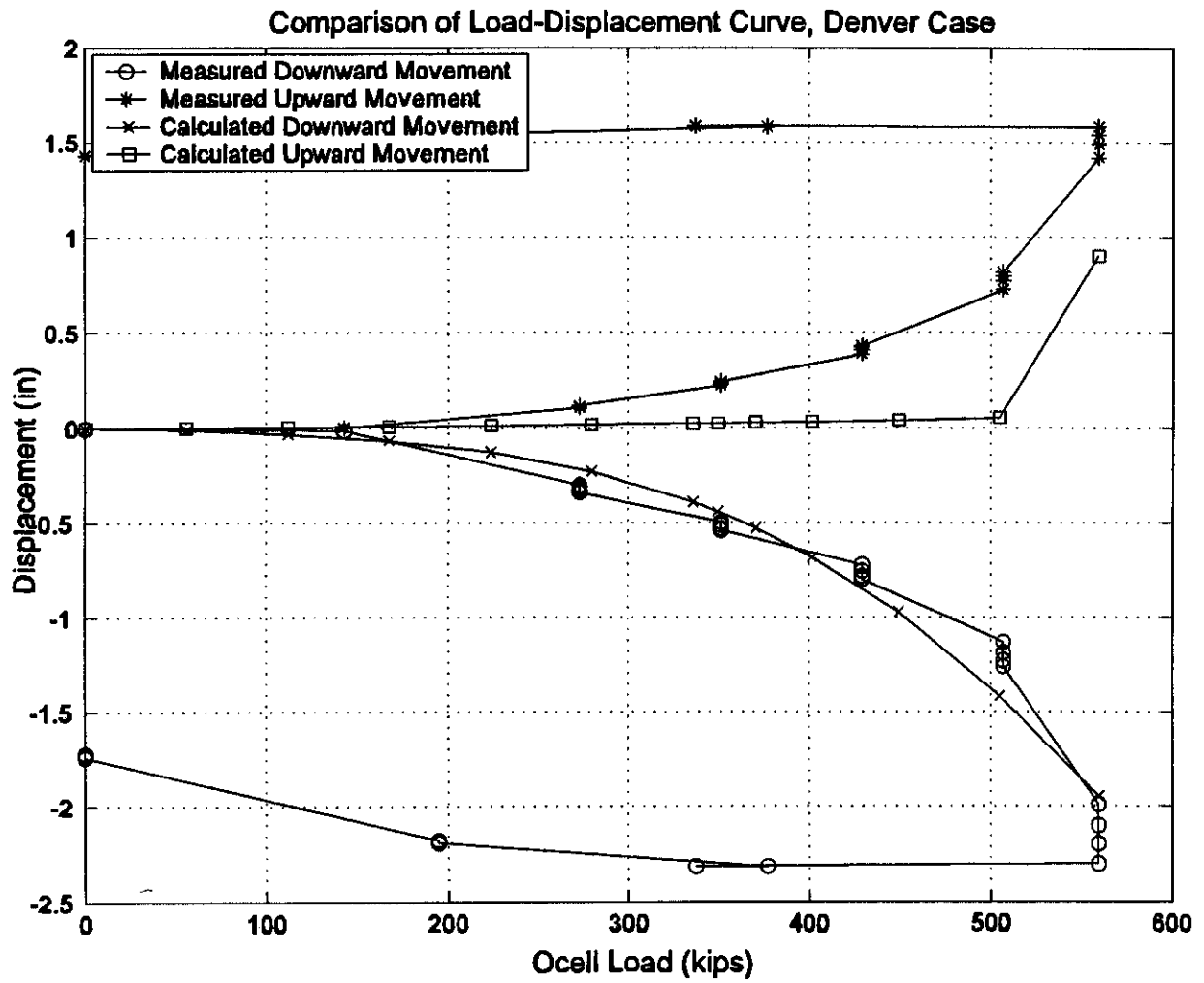


Figure C-14 Comparison of Load vs Displacement Curve, O-cell Test, Denver Case

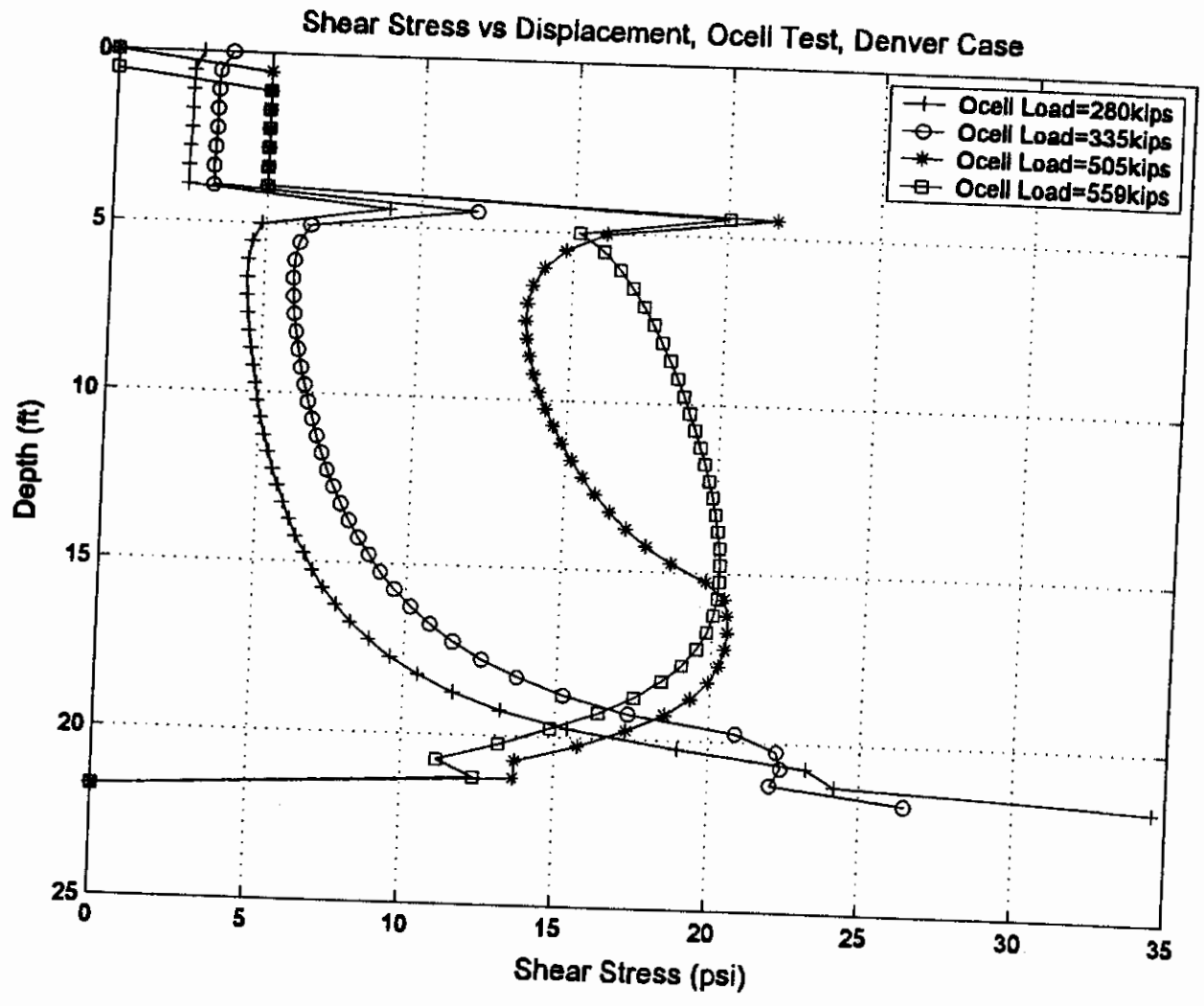


Figure C-15 Shear Stress vs Depth, O-cell Test, Denver Case

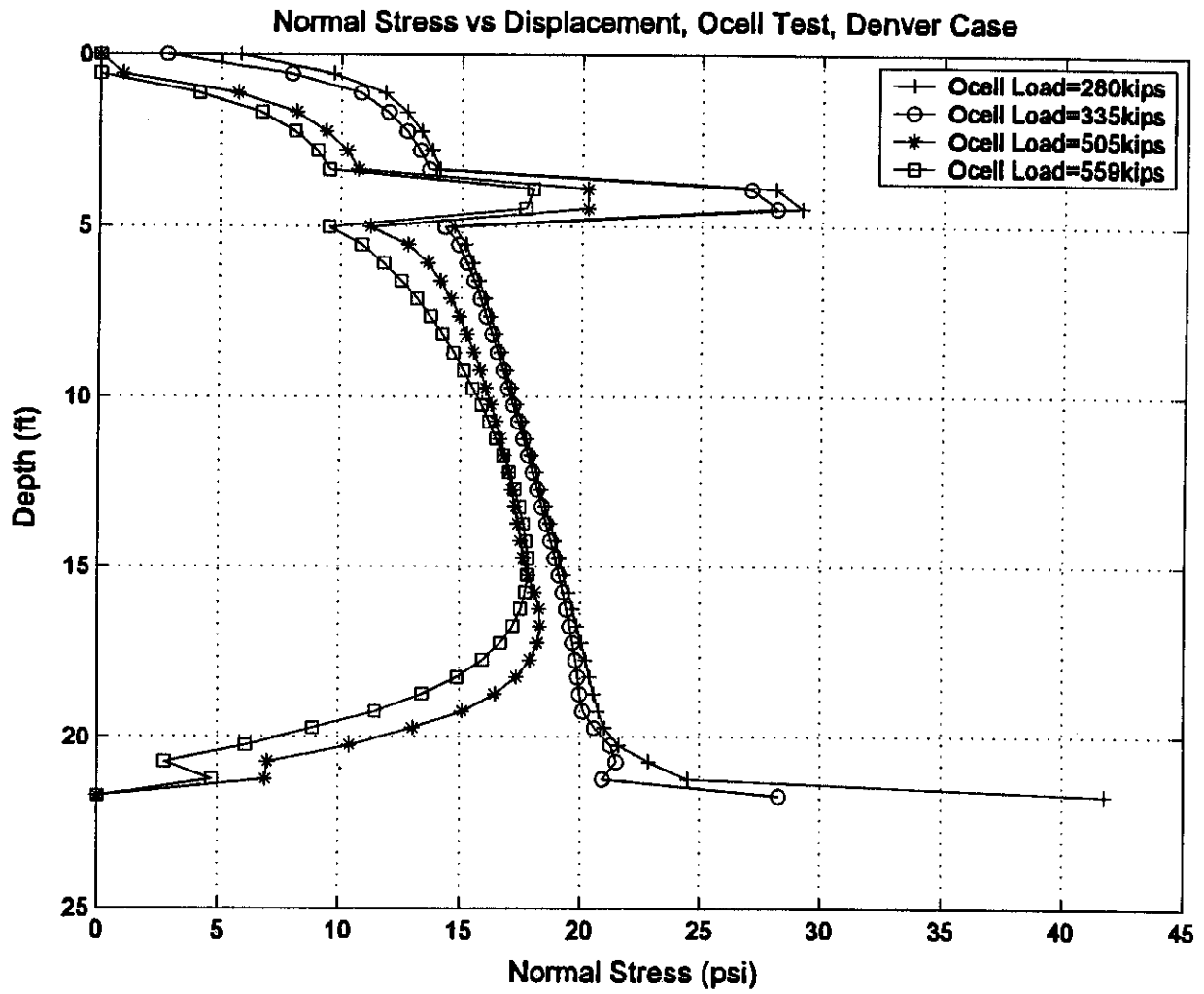


Figure C-16 Normal Stress vs Depth, O-cell Test, Denver Case

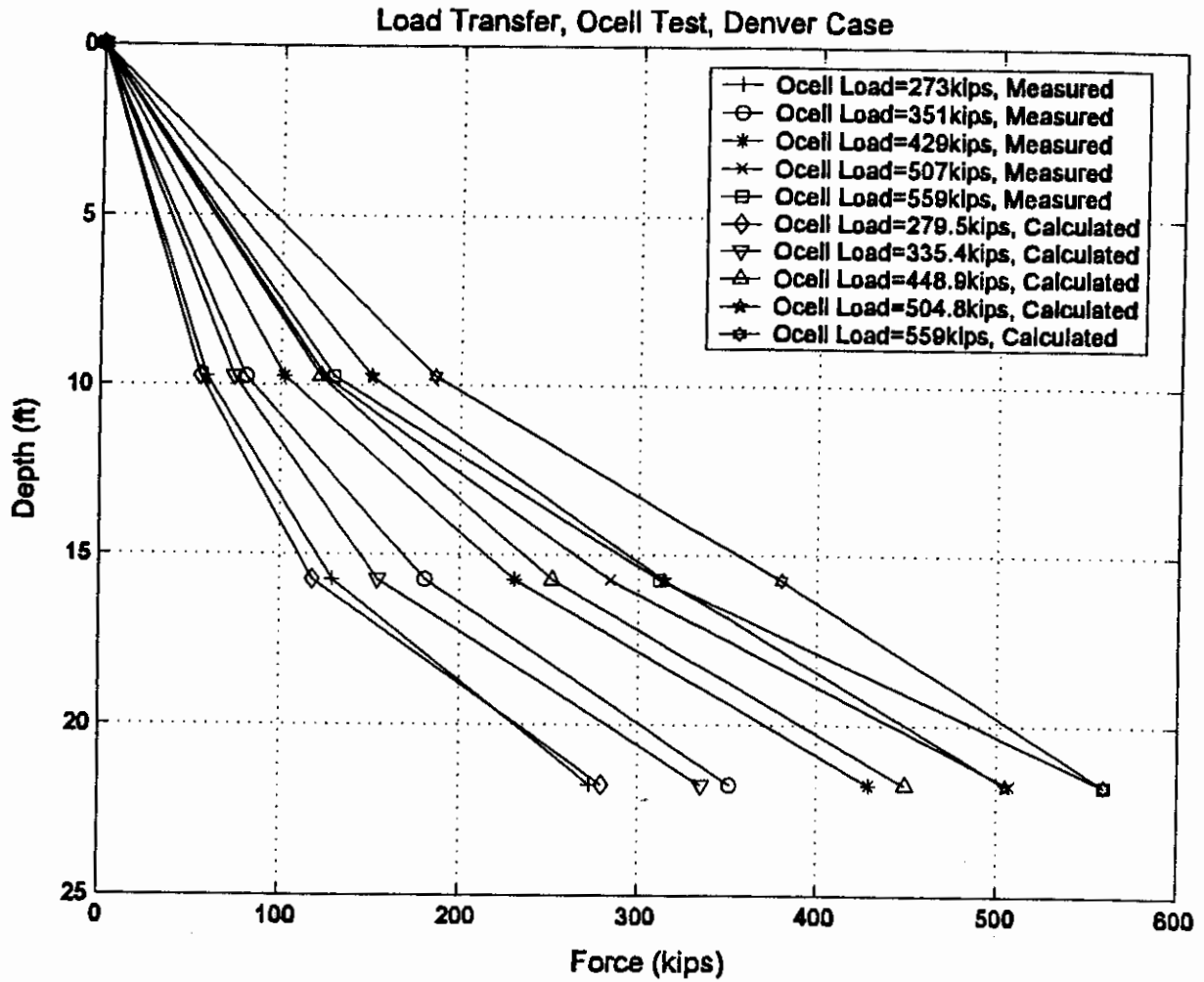


Figure C-17 Load Transfer Comparison Between Measurement and Model Results, Denver Case

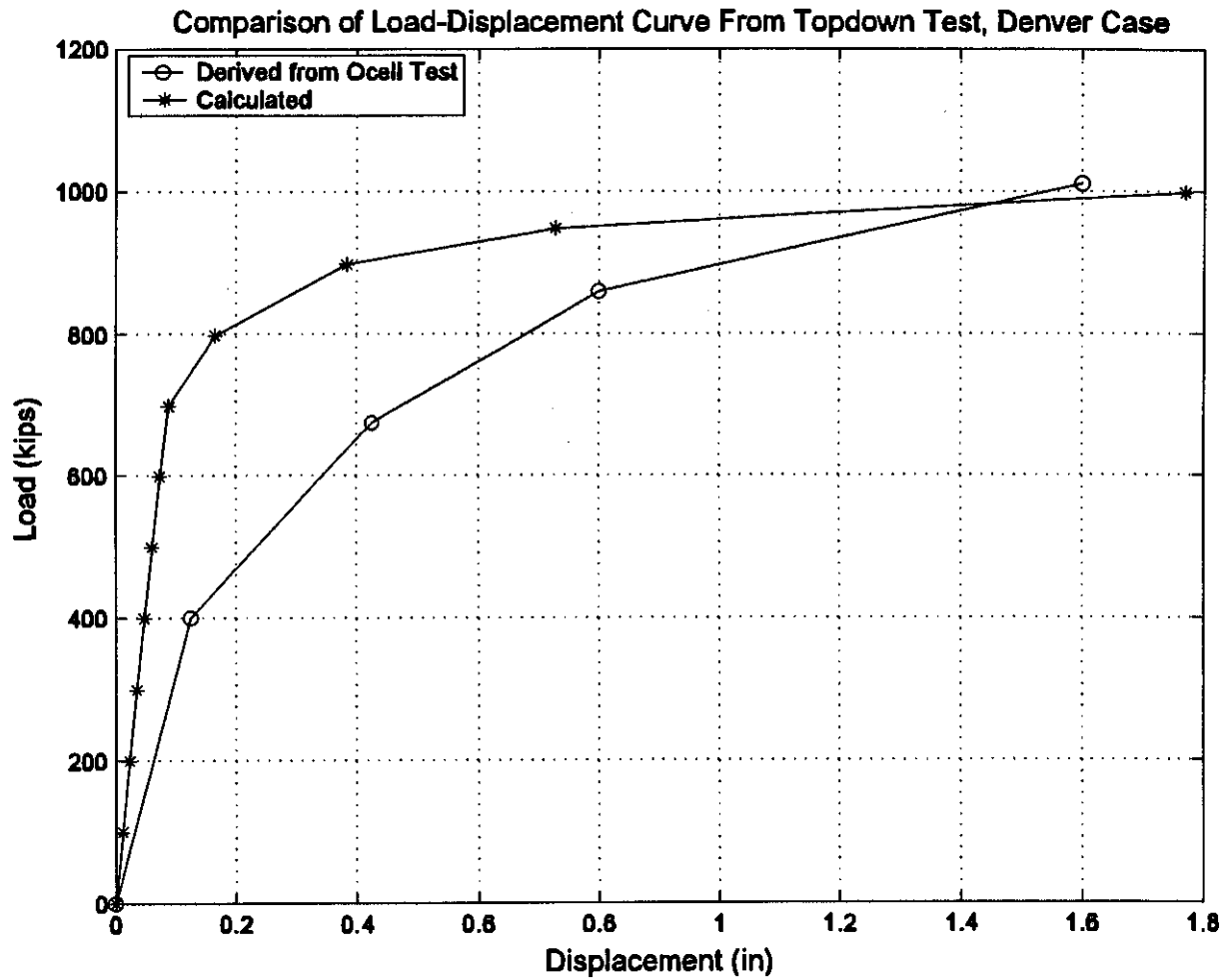


Figure C-18 Comparison of Load vs Displacement Curve, Top Down Test, Denver Case

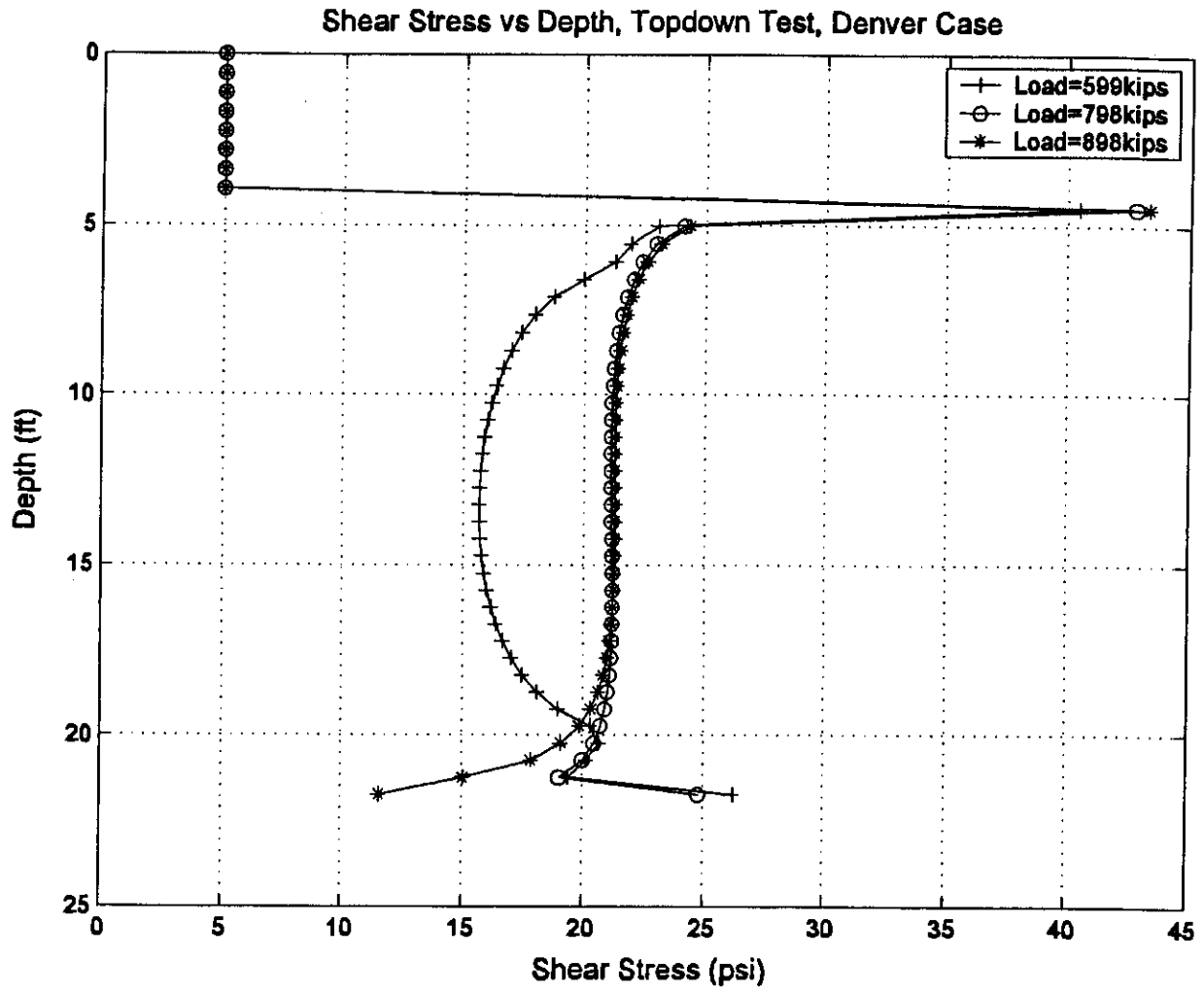


Figure C-19 Shear Stress vs Depth, Top Down Test, Denver Case

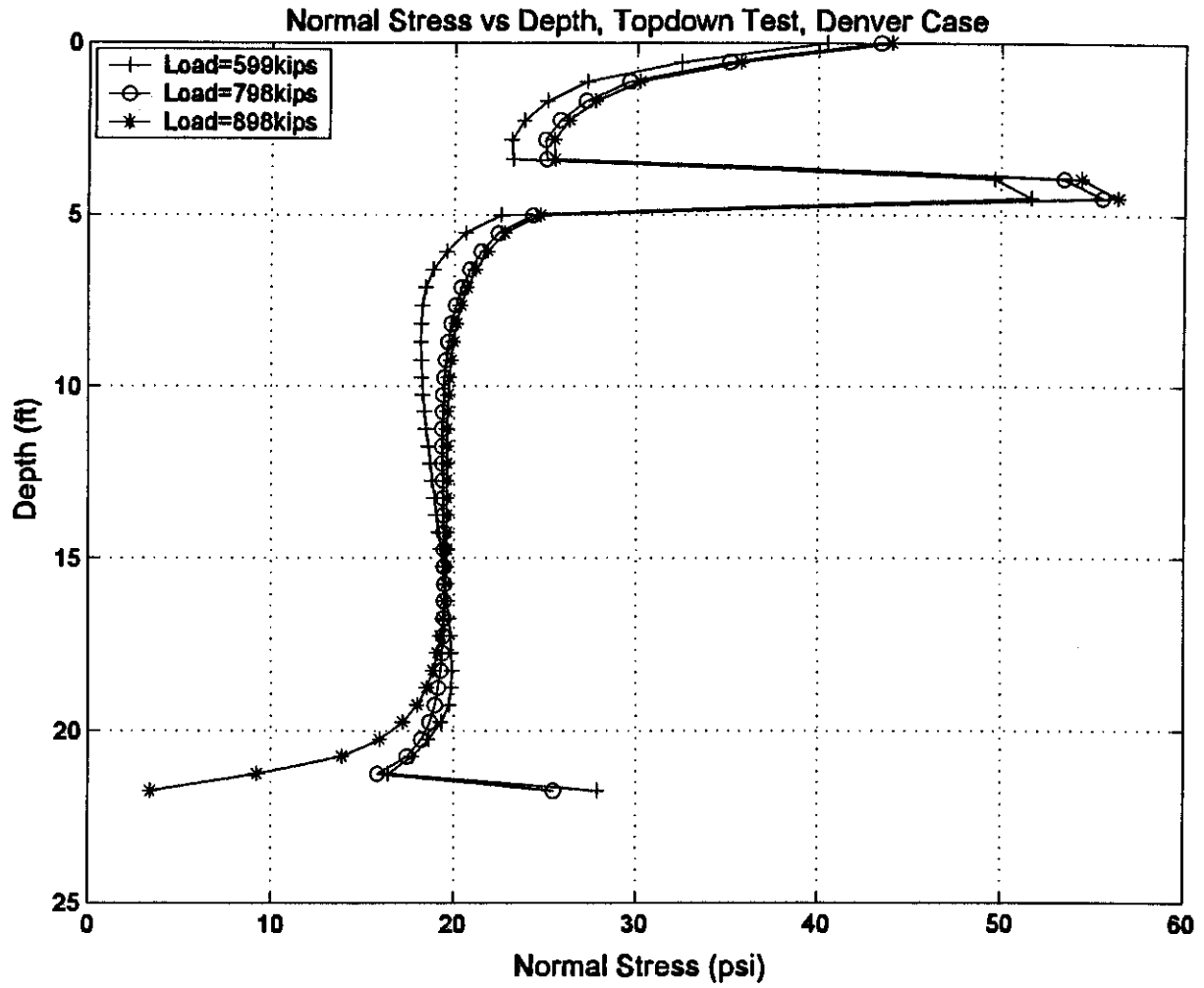


Figure C-20 Normal Stress vs Depth, Top Down Test, Denver Case

22-2/1 COPY NO.

NCHRP 21-08

INNOVATIVE LOAD TESTING SYSTEMS

APPENDIX B

Details of Databases

Prepared for
National Cooperative Highway Research Program
Transportation Research Board
National Research Council

By

Samuel G. Paikowsky
Geosciences Testing and Research Inc. (GTR)
55 Middlesex St., Suite 225
N. Chelmsford, MA. 01863

Gray A. Mullins
Department of Civil and Environmental. Engineering
University. of South Florida
Tampa FL 33620

Zenxuan (Frank) Li
Geotechnical Engineering Research Laboratory
Department. of Civil and Environmental Engineering
University of Massachusetts
Lowell, MA 01854

August 2002

TABLE OF CONTENTS

Part A – Database DW/LT2000	A-1, A-81
Part B – Case Histories of Statnamic and Static Load Tests	B-1, B-35
Part C – Simbat Analyses (Long, 2001)	C-1, C-10

PART A

Database of Drop Weight Testing On Drilled Shafts

DATABASE DW/LT2000-Details of Drilled shafts and Static Load Test Results

UML Case No.	Reference	Pile	Drilled Shaft					Static Load Test Results (kN)						Comments
			Diameter	Length	Soil Type		Construction	Load _{max}	Davission	DeBeer	Shape of Curve	FHWA 0.05D	Representative Capacity	
			<i>m</i>	<i>m</i>	Side	Tip	Method							
1	Briaud J. L. Ballouz M. and George N. (2000)	2	0.9	12.0	sand	sand	W	1350	1068	700	1200	700	1255	Same Pile. One Dynamic Test. Two Static Tests.
2	Briaud J. L. Ballouz M. and George N. (2000)	2	0.9	12.0	sand	sand	W	1650	1602	1600	1500	1450	1951	
3	Briaud J. L. Ballouz M. and George N. (2000)	4	0.9	11.5	stiff clay	stiff clay	W	4150	4004	4000	4000	3500	4914	
4	Briaud J. L. Ballouz M. and George N. (2000)	7	0.9	11.0	stiff clay	stiff clay	W	3050	3025	3000	3000	2800	3719	
5*	Mukaddam M.A. and Iskandarani M.W. (1996)	211	0.8	10.0	silty ansd	sand stone	W	3600	5600	6000	5600	6000	5700	Same site, Dynamic and Static not on the same pile.
6*	Mukaddam M.A. and Iskandarani M.W. (1996)	56	0.5	15.0	silty sand	silty sand	W	1400	2450	3000	3000	2900	2800	Same site, Dynamic and Static not on the same pile.
7*	Kanhere D.K. and Ravikiran V. (2000)	14L	1.2	22.5	N/A	soft rock	W	5150	10200	10000	11000	12000	10400	
8*	Nayak N.V. Kanhere D.K. and Ravikiran V. (2000)	JJUV	1.2	7.0	N/A	rock	W	13750	20500	20000	20000	23000	21000	
9	Walter G.B. (2000)	DSG1	1.0	13.7	sand	sand	W	6226	5900	5500	5500	N/A	5782	
10	Walter G.B. (2000)	DSG3	1.3	17.5	sand	sand	W	8895	9000	5500	6900	9200	10865	

(*Load tests are not to failure

DATABASE DW/LT2000-Details of Drilled shafts and Static Load Test Results

UML Case No.	Reference	Pile	Drilled Shaft					Static Load Test Results (kN)						Comments
			Diameter	Length	Soil Type		Construction Method	Load _{max}	Davission	DeBeer	Shape of Curve	FHWA 0.05D	Representative Capacity	
			m	m	Side	Tip								
11	Jianren D. and Shihong Z. (1992)	T3	0.8	30.0	silty clay	silty sand	W	3000	2650	2650	2750	2830	2760	
12	Jianren D. and Shihong Z. (1992)	T4	0.8	30.0	silty clay	silty sand	W	4000	3020	3030	3300	4400	4438	
13*	Keisar I. (1998)		0.6	10.0	N/A	N/A	W	6000	8200	9500	9000	9000	8900	
14	Townsend F.C. Theos J.F. and Sheilds M.D. (1991)	TP	0.7	13.2	silty clay	sand	W	3550	3250	3200	3300	3800	4275	
15*	Keisar I. (2000)	D1 D2 A	0.6	11.0	N/A	N/A	W	5500	16500	12000	N/A	17700	14250	Same site, 2 dynamic 1 static
16	Liang X. (2000)	DH	0.6	30.0	N/A	N/A	W	6100	4700	5000	N/A	5500	5325	
17	Guoxi Z. Zhuchang C. and Jinli L. (1995)	BJ2	0.3	10.0	N/A	sand	W	1120	1060	1120	1120	1120	1120	
18*	Guoxi Z. Zhuchang C. and Jinli L. (1995)	BJ1	1.0	14.5	N/A	sand	D	8400	9700	10000	N/A	12500	9800	
19	Guoxi Z. Zhuchang C. and Jinli L. (1995)	AY	0.8	20.6	N/A	loan	W	3600	3400	3500	3400	N/A	3475	
20*	Keisar I. (2001)	D1 D2 TPA	0.4	6.5	N/A	N/A	W	1900	2700	3000	N/A	3050	2900	Same site 2 dynamic 1 static

(*Load tests are not to failure

DATABASE DW/LT2000-Details of Drilled shafts and Static Load Test Results

UML Case No.	Reference	Pile	Drilled Shaft					Static Load Test Results (kN)						Comments
			Diameter	Length	Soil Type		Construction Method	Load _{max}	Davission	DeBeer	Shape of Curve	FHWA 0.05D	Representative Capacity	
			m	m	Side	Tip								
21	Cannon J.G. (2000)	68B	0.6	10.0	sand	stiff clay	w	2000	1500	2000	N/A	N/A	1800	
22	Prebaharan N. Broms B. and Richard Y. (1990)	1	1.0	39.0	marine clay	stiff clay	w	14500	14500	N/A	15000	14500	14500	
23	Prebaharan N. Broms B. and Richard Y. (1990)	2	1.0	53.0	marine clay	stiff clay	w	14500	14500	N/A	15000	14500	14500	
24	Baker C.N. Drumright E.E. and Briaud J.L. (1992)	TP2	1.0	9.0	dense clay	dense clay	w	8000	6700	7000	N/A	N/A	7200	
25	Baker C.N. Drumright E.E. and Briaud J.L. (1992)	TP4	1.0	9.0	dense clay	dense clay	w	6400	6600	N/A	N/A	N/A	6500	
26	Frank R. (1984)	3385-1	1.5	38.6	silty clay	dense clay	w	16500	17500	17000	20000	22000	18600	
27*	Frank R. (1984)	2121-2	1.5	42.0	silty clay	dense clay	w	15500	23000	27000	N/A	27500	23250	
28	Frank R. (1984)	426-2E	1.5	40.2	silty clay	dense sand	w	20000	21000	20000	20000	N/A	20000	
29*	Frank R. (1984)	428-41	1.5	62.4	silty clay	dense sand	w	20000	21000	32000	N/A	33000	30000	
30*	Frank R. (1984)	428-3	1.1	39.5	silty clay	dense sand	w	13500	17700	20000	N/A	20000	17800	

(*Load tests are not to failure

DATABASE DW/LT2000-Details of Drilled shafts and Static Load Test Results

UML Case No.	Reference	Pile	Drilled Shaft					Static Load Test Results (kN)						Comments
			Diameter	Length	Soil Type		Construction	Load _{max}	Davission	DeBeer	Shape of Curve	FHWA 0.05D	Representative Capacity	
			m	m	Side	Tip	Method							
31*	Frank R. (1984)	3385-1	1.1	36.4	silty clay	dense sand	w	15000	33000	N/A	N/A	35000	34000	
32	Frank R. (1984)	2121-2	1.2	17.1	silty clay	sense sand	w	14100	14000	14000	14000	14100	14000	
33	Frank R. (1984)	426-2C	0.8	706.0	silty clay	silty clay	w	10500	9900	11000	11000	10500	10500	
34*	Frank R. (1984)	428-3	1.3	18.8	silty clay	dense sand	w	12000	28500	25000	N/A	24500	25000	
35	Frank R. (1984)	TP4	1.5	15.6	N/A	N/A	w	16500	8000	12000	12000	17500	13000	
36*	Qingyang C. (2001)	SSH	1.0	38.6	clay	decayed rock	w	8000	16500	16000	N/A	19500	15000	
37	Qingyang C. (2001)	NJ1	0.8	30.4	N/A	sand	w	3000	2600	2600	2700	2950	2770	
38	Qingyang C. (2001)	NJ2	0.8	30.4	N/A	sand	w	4000	3500	3500	3600	4000	4000	
39	Qingyang C. (2001)	YZ3	1.0	58.5	sand	decayed rock	w	11800	N/A	N/A	N/A	N/A	11800	
40	Qingyang C. (2001)	YZ13	1.0	55.0	sand	decayed rock	w	11000	N/A	N/A	N/A	N/A	11000	

(*Load tests are not to failure

DATABASE DW/LT2000-Details of Drilled shafts and Static Load Test Results

UML Case No.	Reference	Pile	Drilled Shaft					Static Load Test Results (kN)						Comments
			Diameter	Length	Soil Type		Construction	Load _{max}	Davission	DeBeer	Shape of Curve	FHWA 0.05D	Representative Capacity	
			m	m	Side	Tip	Method							
41	Qingyang C. (2001)	YZ18	1.0	55.0	sand	decayed rock	w	11800	N/A	N/A	N/A	N/A	11800	
42*	Kirsch F. (2001)	1	0.5	32.0	silty clay	silty clay	w	6300	11000	N/A	N/A	8400	9700	
43	Xuefeng W. Shiming W. (2001)	ZH1	1.2	6.8	silty clay	silty clay	D	3400	2500	3000	3000	3400	3250	
44	Xuefeng W. Shiming W. (2001)	ZH2	1.2	7.1	silty clay	sand	D	3800	3700	3500	3600	3800	3600	
45	Xuefeng W. Shiming W. (2001)	ZH3	1.2	7.1	silty clay	sand	D	2500	2300	2000	2300	2500	2400	
46	Xuefeng W. Shiming W. (2001)	ZH4	1.4	11.6	silty clay	silty clay	D	7600	7100	7000	7000	7600	7200	
47	Xuefeng W. Shiming W. (2001)	ZH5	1.4	5.3	silty clay	sand	D	3600	3300	3300	3400	3600	3400	
48	Xuefeng W. Shiming W. (2001)	ZH6	1.4	6.7	silty clay	sand	D	2800	2600	2500	2600	2800	2600	
49	Xuefeng W. Shiming W. (2001)	ZH7	1.2	10.7	silty clay	sand	D	4800	4400	4400	4400	5000	4500	
50	Xuefeng W. Shiming W. (2001)	ZH8	1.2	13.2	silty clay	sand	D	6600	6150	5500	6200	6800	6300	

(*Load tests are not to failure)

DATABASE DW/LT2000-Details of Drilled shafts and Static Load Test Results

UMI Case No.	Reference	Pile	Drilled Shaft					Static Load Test Results (kN)						Comments
			Diameter	Length	Soil Type		Construction	Load _{max}	Davission	DeBeer	Shape of Curve	FHWA 0.05D	Representative Capacity	
			m	m	Side	Tip	Method							
51	Xuefeng W. Shiming W. (2001)	ZH9	1.2	12.6	silty clay	sand	D	6500	6000	6000	6000	6600	6000	
52	Hanwu Z. (2995)	W-1	0.8	48.4	sand	rock	W	8100	5600	7000	7100	7200	7200	
53	Hanwu Z. (2995)	W-2	0.8	48.7	sand	rock	W	8600	6500	8000	8100	8100	8100	
54	Hanwu Z. (2995)	W-3	1.0	46.7	sand	rock	W	13000	11500	10000	N/A	14000	13000	
55	Hanwu Z. (2995)	W-4	1.0	49.5	sand	rock	W	13500	11300	10500	13000	14000	13500	
56	Guang Z. (2000)	S3	0.8	18.7	N/A	rock	W	9200	9100	9000	9000	9100	9000	
57	Zhangliang L. (2001)	XTZ1	0.4	15.0	N/A	N/A	W	1000	720	950	940	960	950	
58	Zhangliang L. (2001)	XTZ2	0.5	16.3	N/A	N/A	W	850	640	800	810	830	850	
59	Yong Q. (2000)	HC1	1.5	11.0	N/A	N/A	D	8710	4700	9000	N/A	9000	9020	
60	Yong Q. (2000)	HC2	1.2	11.0	N/A	N/A	D	9020	5200	8000	8200	N/A	8710	

(*)Load tests are not to failure

DATABASE DW/LT2000-Details of Drilled shafts and Static Load Test Results

UML Case No.	Reference	Pile	Drilled Shaft					Static Load Test Results (kN)						Comments
			Diameter	Length	Soil Type		Construction Method	Load _{max}	Davission	DeBeer	Shape of Curve	FHWA 0.05D	Representative Capacity	
			<i>m</i>	<i>m</i>	Side	Tip								
61	Yong Q. (2000)	HC3	0.9	11.0	N/A	N/A	D	5340	1800	N/A	N/A	5000	5340	
62	Chenghua L. (2001)	MS1	1.0	19.8	sand	rock	W	7200	4700	N/A	N/A	6300	6300	
63	Chenghua L. (2001)	MS2	1.0	19.7	sand	rock	W	6000	4900	N/A	N/A	8300	8100	
64	Chenghua L. (2001)	MS3	1.0	19.7	sand	rock	W	7200	4300	N/A	N/A	6400	6300	
65*	Jianping Y. (2001)	CH1	1.2	21.0	sand	rock	W	14200	23400	20000	N/A	N/A	21700	
66	Jianping Y. (2001)	CH2	0.6	16.0	sand	rock	W	5640	5400	5100	5200	5600	5170	
67	Iskander M. Kelley S. and Carl E. (2001)	TP2	0.9	14.3	clay	clay	W	1250	1030	1000	1000	1210	1100	
68	Iskander M. Kelley S. and Carl E. (2001)	TP4	0.9	14.3	clay	clay	W	1080	920	920	1020	1080	980	
69														
70														

(*Load tests are not to failure

DATABASE DW/LT2000-Details of Drop Weight, Dynamic Anlysis and Prediction Ratio

UMI Case No.	Reference	Pile	Drilled Shaft		Drop Weight		Dynamic Test				Predictive Ratio				Comments
			Diameter	Length	Weight	Stroke	Fmax	ZVmax	Energy	CAPWAP	Static/ Dynamic				
			m	m	kN	m	kN	kN	kN*m	kN	Davission	DeBeer	FHWA	Representative	
1	Briaud J. L. Ballouz M. and George N. (2000)	2	0.9	12	90	N/A	N/A	N/A	N/A	1300	0.82	0.54	0.54	0.97	Same Pile. One Dynamic Test. Two Static Tests.
2	Briaud J. L. Ballouz M. and George N. (2000)	2	0.9	12	90	N/A	N/A	N/A	N/A	1300	1.23	1.23	1.23	1.50	
3	Briaud J. L. Ballouz M. and George N. (2000)	4	0.9	11.5	90	N/A	N/A	N/A	N/A	2900	1.38	1.38	1.38	1.69	
4	Briaud J. L. Ballouz M. and George N. (2000)	7	0.9	11	90	N/A	N/A	N/A	N/A	4250	0.71	0.71	0.71	0.88	
5*	Mukaddam M.A. and Iskandarani M.W. (1996)	211	0.8	10	65	1.5	N/A	N/A	N/A	3480	1.61	1.72	1.72	1.64	Same site, Dynamic and Static not on the same pile.
6*	Mukaddam M.A. and Iskandarani M.W. (1996)	56	0.5	15	30	N/A	N/A	N/A	N/A	1520	1.61	1.97	1.91	1.84	Same site, Dynamic and Static not on the same pile.
7*	Kanhere D.K. and Ravikiran V. (2000)	14L	1.2	22.5	60	2	N/A	N/A	N/A	5150	1.98	1.94	2.33	2.02	
8*	Nayak N.V. Kanhere D.K. and Ravikiran V. (2000)	JJUV	1.2	7	140	N/A	N/A	N/A	N/A	14000	1.46	1.43	1.64	1.50	
9	Walter G.B. (2000)	DSG1	1.0	13.7	N/A	N/A	N/A	N/A	N/A	6871	0.86	0.8	N/A	0.84	
10	Walter G.B. (2000)	DSG3	1.3	17.5	N/A	N/A	N/A	N/A	N/A	8900	1.01	0.62	1.03	1.22	

(*Load tests are not to failure

DATABASE DW/LT2000-Details of Drop Weight, Dynamic Analysis and Prediction Ratio

UML Case No.	Reference	File	Drilled Shaft		Drop Weight		Dynamic Test				Predictive Ratio				Comments
			Diameter	Length	Weight	Stroke	Fmax	ZVmax	Energy	CAPWAP	Static/ Dynamic				
			m	m	kN	m	kN	kN	kN*m	kN	Davission	DeBeer	FHWA	Representative	
11	Jianren D. and Shihong Z. (1992)	T3	0.8	30	120	>2.5	N/A	N/A	N/A	2882	0.92	0.92	0.98	0.96	
12	Jianren D. and Shihong Z. (1992)	T4	0.8	30	120	>2.5	N/A	N/A	N/A	3290	0.92	0.92	1.34	1.35	
13*	Keisar I. (1998)	TP1	0.6	10	100	N/A	N/A	N/A	N/A	6350	1.29	1.5	1.42	1.40	
14	Townsend F.C. Theos J.F. and Sheilds M.D. (1991)	TP	0.7	13.2	N/A	N/A	3818	3478	28	3190	1.02	1	1.19	1.34	
15*	Keisar I. (2000)	D1 D2 A	0.6	11	N/A	N/A	N/A	N/A	N/A	3845	4.29	3.12	4.6	3.71	Same site, 2 dynamic (Ave.) 1 static
16	Liang X. (2000)	DH	0.6	30	N/A	N/A	N/A	N/A	N/A	6400	0.73	0.78	0.86	0.83	
17	Guoxi Z. Zhuchang C. and Jinli L. (1995)	BJ2	0.3	10	N/A	N/A	N/A	N/A	N/A	1040	1.02	1.08	1.08	1.08	
18*	Guoxi Z. Zhuchang C. and Jinli L. (1995)	BJ1	1	14.5	120	N/A	N/A	N/A	N/A	9000	1.08	1.11	1.39	1.09	
19	Guoxi Z. Zhuchang C. and Jinli L. (1995)	AY	0.8	20.6	N/A	N/A	N/A	N/A	N/A	3400	1	1.03	N/A	1.02	
20*	Keisar I. (2001)	D1 D2 TPA	0.4	6.5	40	N/A	N/A	N/A	N/A	3075	0.88	0.98	0.99	0.94	Same site 2 dynamic(Ave.) 1 static

(*Load tests are not to failure

DATABASE DW/LT2000-Details of Drop Weight, Dynamic Anlysis and Prediction Ratio

UML Case No.	Reference	Pile	Drilled Shaft		Drop Weight		Dynamic Test				Predictive Ratio				Comments
			Diameter <i>m</i>	Length <i>m</i>	Weight <i>kN</i>	Stroke <i>m</i>	Fmax <i>kN</i>	ZVmax <i>kN</i>	Energy <i>kN*m</i>	CAPWAP <i>kN</i>	Static/ Dynamic				
											Davission	DeBeer	FHWA	Representative	
21	Cannon J.G. (2000)	68B	0.6	10	N/A	N/A	N/A	N/A	N/A	2200	0.68	0.91	N/A	0.82	
22	Prebaharan N. Broms B. and Richard Y. (1990)	1	1	39	77	3	N/A	N/A	N/A	9300	1.56	N/A	1.56	1.56	
23	Prebaharan N. Broms B. and Richard Y. (1990)	2	1	53	77	3	N/A	N/A	N/A	13000	1.12	N/A	1.12	1.12	
24	Baker C.N. Drumright E.E. and Briaud J.L. (1992)	TP2	1	9	87	3	11787	N/A	264	6900	0.97	1.01	N/A	1.04	
25	Baker C.N. Drumright E.E. and Briaud J.L. (1992)	TP4	1	9	87	2	13522	N/A	79	6000	1.1	N/A	N/A	1.08	
26	Frank R. (1984)	3385-1	1.5	38.6	200	N/A	42660	35937	225	20000	0.88	0.85	1.1	0.93	
27*	Frank R. (1984)	2121-2	1.5	42	200	N/A	50680	40838	229	27000	0.85	1	1.02	0.86	
28	Frank R. (1984)	426-2E	1.5	40.2	200	N/A	42560	35211	183	21000	1	0.95	N/A	0.95	
29*	Frank R. (1984)	428-417	1.5	62.4	200	N/A	49250	41563	178	32000	0.66	1	1.03	0.94	
30*	Frank R. (1984)	428-3	1.1	39.5	200	N/A	24420	27684	141	14000	1.26	1.43	1.43	1.27	

(*)Load tests are not to failure

DATABASE DW/LT2000-Details of Drop Weight, Dynamic Analysis and Prediction Ratio

UML Case No.	Reference	Pile	Drilled Shaft		Drop Weight		Dynamic Test				Predictive Ratio				Comments
			Diameter	Length	Weight	Stroke	Fmax	ZVmax	Energy	CAPWAP	Static/ Dynamic				
			m	m	kN	m	kN	kN	kN*m	kN	Davission	DeBeer	FHWA	Representative	
31*	Frank R. (1984)	3385-1	1.1	36.4	200	N/A	23260	27152	144	18000	1.83	N/A	1.94	1.89	
32	Frank R. (1984)	2121-2	1.2	17.1	200	N/A	36850	25903	196	15500	0.9	0.9	0.91	0.90	
33	Frank R. (1984)	426-2C	0.8	706.0	200	N/A	16200	12132	164	10000	0.99	1.1	1.05	1.05	
34*	Frank R. (1984)	428-3	1.3	18.8	200	N/A	17300	15814	61	21000	1.36	1.19	1.64	0.19	
35	Frank R. (1984)	TP4	1.5	15.6	N/A	N/A	N/A	N/A	N/A	15800	0.5	0.76	1.11	0.82	
36*	Qingyang C. (2001)	SSH	1.0	38.6	80	N/A	N/A	N/A	N/A	7500	2.2	2.13	2.6	2.00	
37	Qingyang C. (2001)	NJ1	0.8	30.4	120	N/A	N/A	N/A	N/A	2774	0.9	0.94	1.06	1.00	
38	Qingyang C. (2001)	NJ2	0.8	30.4	120	N/A	N/A	N/A	N/A	3716	0.9	0.94	1.08	1.08	
39	Qingyang C. (2001)	YZ3	1.0	58.5	120	N/A	N/A	N/A	N/A	12316	N/A	N/A	N/A	0.96	
40	Qingyang C. (2001)	YZ13	1.0	55.0	120	N/A	N/A	N/A	N/A	10921	N/A	N/A	N/A	1.01	

(*)Load tests are not to failure

DATABASE DW/LT2000-Details of Drop Weight, Dynamic Analysis and Prediction Ratio

UML Case No.	Reference	Pile	Drilled Shaft		Drop Weight		Dynamic Test				Predictive Ratio				Comments
			Diameter <i>m</i>	Length <i>m</i>	Weight <i>kN</i>	Stroke <i>m</i>	Fmax <i>kN</i>	ZVmax <i>kN</i>	Energy <i>kN*m</i>	CAPWAP <i>kN</i>	Static/ Dynamic				
											Davission	DeBeer	FHWA	Representative	
41	Qingyang C. (2001)	YZ18	1.0	55.0	120	N/A	N/A	N/A	N/A	8950	N/A	N/A	N/A	1.32	
42*	Kirsch F. (2001)	1	0.5	32.0	N/A	N/A	N/A	N/A	N/A	6000	1.83	N/A	1.4	1.62	
43	Xuefeng W. Shiming W. (2001)	ZH1	1.2	6.8	70	1~1.5	N/A	N/A	N/A	3634	0.69	0.83	0.94	0.89	
44	Xuefeng W. Shiming W. (2001)	ZH2	1.2	7.1	70	1~1.5	N/A	N/A	N/A	3526	1.05	0.99	1.08	1.02	
45	Xuefeng W. Shiming W. (2001)	ZH3	1.2	7.1	70	1~1.5	N/A	N/A	N/A	2298	1	0.87	1.09	1.04	
46	Xuefeng W. Shiming W. (2001)	ZH4	1.4	11.6	70	1~1.5	N/A	N/A	N/A	7006	1.01	1	1.08	1.03	
47	Xuefeng W. Shiming W. (2001)	ZH5	1.4	5.3	70	1~1.5	N/A	N/A	N/A	3125	1.06	1.06	1.15	1.09	
48	Xuefeng W. Shiming W. (2001)	ZH6	1.4	6.7	70	1~1.5	N/A	N/A	N/A	2897	0.9	0.86	0.97	0.90	
49	Xuefeng W. Shiming W. (2001)	ZH7	1.2	10.7	70	1~1.5	N/A	N/A	N/A	5003	0.88	0.88	1	0.90	
50	Xuefeng W. Shiming W. (2001)	ZH8	1.2	13.2	70	1~1.5	N/A	N/A	N/A	7008	0.88	0.78	0.97	0.90	

(*Load tests are not to failure

DATABASE DW/LT2000-Details of Drop Weight, Dynamic Analysis and Prediction Ratio

UML Case No.	Reference	Pile	Drilled Shaft		Drop Weight		Dynamic Test				Predictive Ratio				Comments
			Diameter	Length	Weight	Stroke	Fmax	ZVmax	Energy	CAPWAP	Static/ Dynamic				
			m	m	kN	m	kN	kN	kN*m	kN	Davission	DeBeer	FHWA	Representative	
51	Xuefeng W. Shiming W. (2001)	ZH9	1.2	12.6	70	1~1.5	N/A	N/A	N/A	6845	0.88	0.88	0.96	0.88	
52	Hanwu Z. (2995)	w-1	0.8	48.4	80	1	N/A	N/A	N/A	6879	0.81	1.02	1.05	1.05	
53	Hanwu Z. (2995)	w-2	0.8	48.7	80	1	N/A	N/A	N/A	7921	0.82	1.01	1.02	1.02	
54	Hanwu Z. (2995)	w-3	1.0	46.7	80	1.4	N/A	N/A	N/A	13547	0.85	0.74	1.03	0.96	
55	Hanwu Z. (2995)	w-4	1.0	49.5	80	1.6	N/A	N/A	N/A	13394	0.84	0.78	1.05	1.01	
56	Guang Z. (2000)	s3	0.8	18.7	N/A	N/A	N/A	N/A	N/A	9594	0.94	0.94	0.95	0.94	
57	Zhangliang L. (2001)	XTZ1	0.4	15.0	N/A	N/A	N/A	N/A	N/A	972	0.74	0.98	0.99	0.98	
58	Zhangliang L. (2001)	XTZ2	0.5	16.3	N/A	N/A	N/A	N/A	N/A	900	0.71	0.89	0.92	0.94	
59	Yong Q. (2000)	HC1	1.5	11.0	N/A	N/A	N/A	N/A	N/A	8078	0.58	1.11	1.11	1.12	
60	Yong Q. (2000)	HC2	1.2	11.0	N/A	N/A	N/A	N/A	N/A	8020	0.65	1	N/A	1.09	

(*)Load tests are not to failure

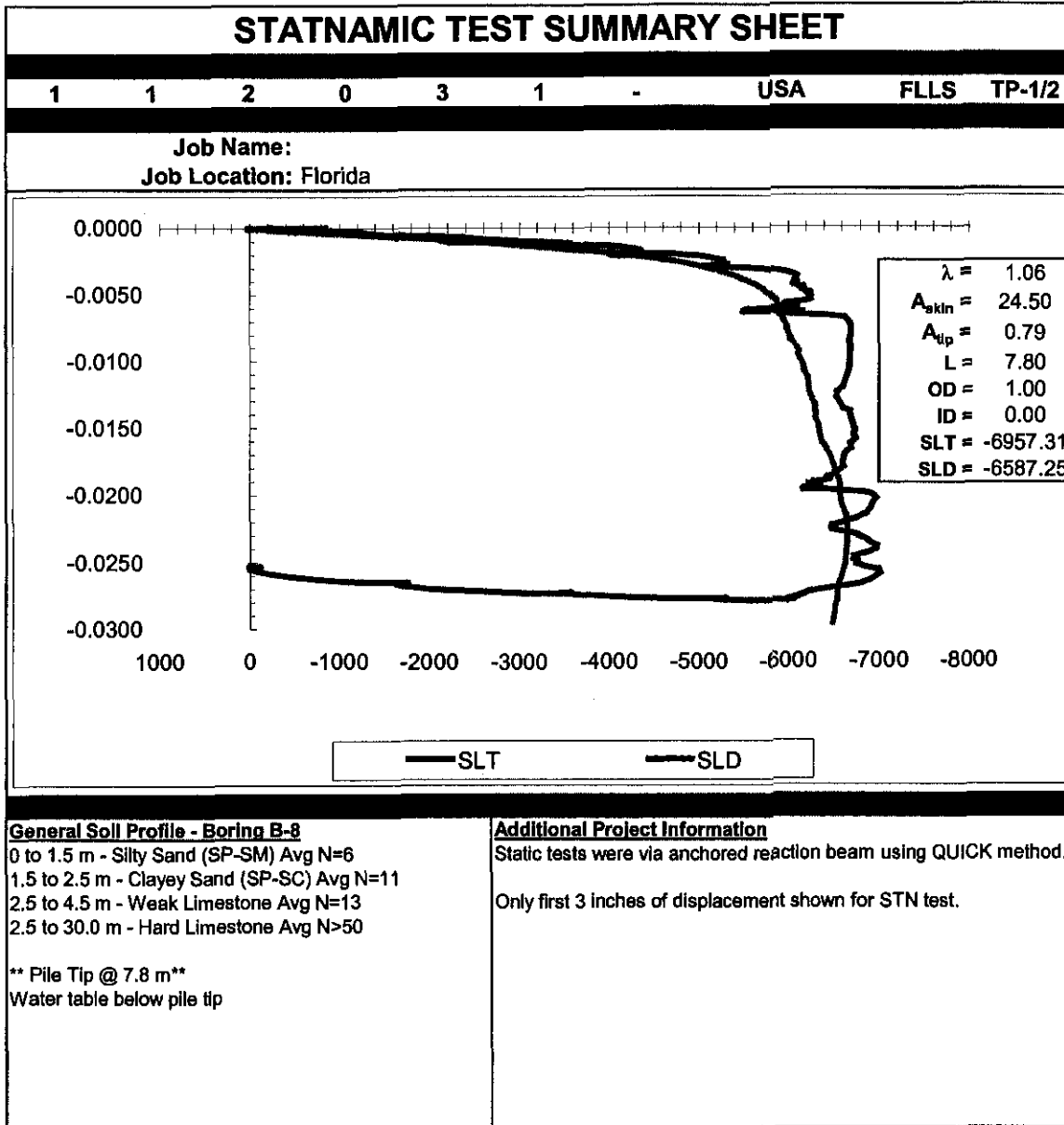
DATABASE DW/LT2000-Details of Drop Weight, Dynamic Analysis and Prediction Ratio

UML Case No.	Reference	Pile	Drilled Shaft		Drop Weight		Dynamic Test				Predictive Ratio				Comments
			Diameter <i>m</i>	Length <i>m</i>	Weight <i>kN</i>	Stroke <i>m</i>	Fmax <i>kN</i>	ZVmax <i>kN</i>	Energy <i>kN*m</i>	CAPWAP <i>kN</i>	Static/ Dynamic				
											Davission	DeBeer	FHWA	Representative	
61	Yong Q. (2000)	HC3	0.9	11.0	N/A	N/A	N/A	N/A	N/A	5904	0.3	N/A	0.85	0.90	
62	Chenghua L. (2001)	MS1	1.0	19.8	N/A	N/A	14033	N/A	N/A	6951	0.68	N/A	0.91	0.91	
63	Chenghua L. (2001)	MS2	1.0	19.7	N/A	N/A	12168	N/A	N/A	9010	0.54	N/A	0.92	0.90	
64	Chenghua L. (2001)	MS3	1.0	19.7	N/A	N/A	8183	N/A	N/A	6459	0.67	N/A	0.99	0.98	
65*	Jianping Y. (2001)	CH1	1.2	21.0	N/A	N/A	19619	N/A	N/A	13585	1.72	1.47	N/A	1.60	
66	Jianping Y. (2001)	CH2	0.6	16.0	N/A	N/A	9688	N/A	N/A	4783	1.13	1.07	1.17	1.08	
67	Iskander M. Kelley S. and Carl E. (2001)	TP2	0.9	14.3	75	0.53	5560	N/A	10.83	930	1.11	1.08	1.3	1.18	
68	Iskander M. Kelley S. and Carl E. (2001)	TP4	0.9	14.3	75	0.9	6983	N/A	17.62	1156	0.8	0.8	0.93	0.85	
69															
70															

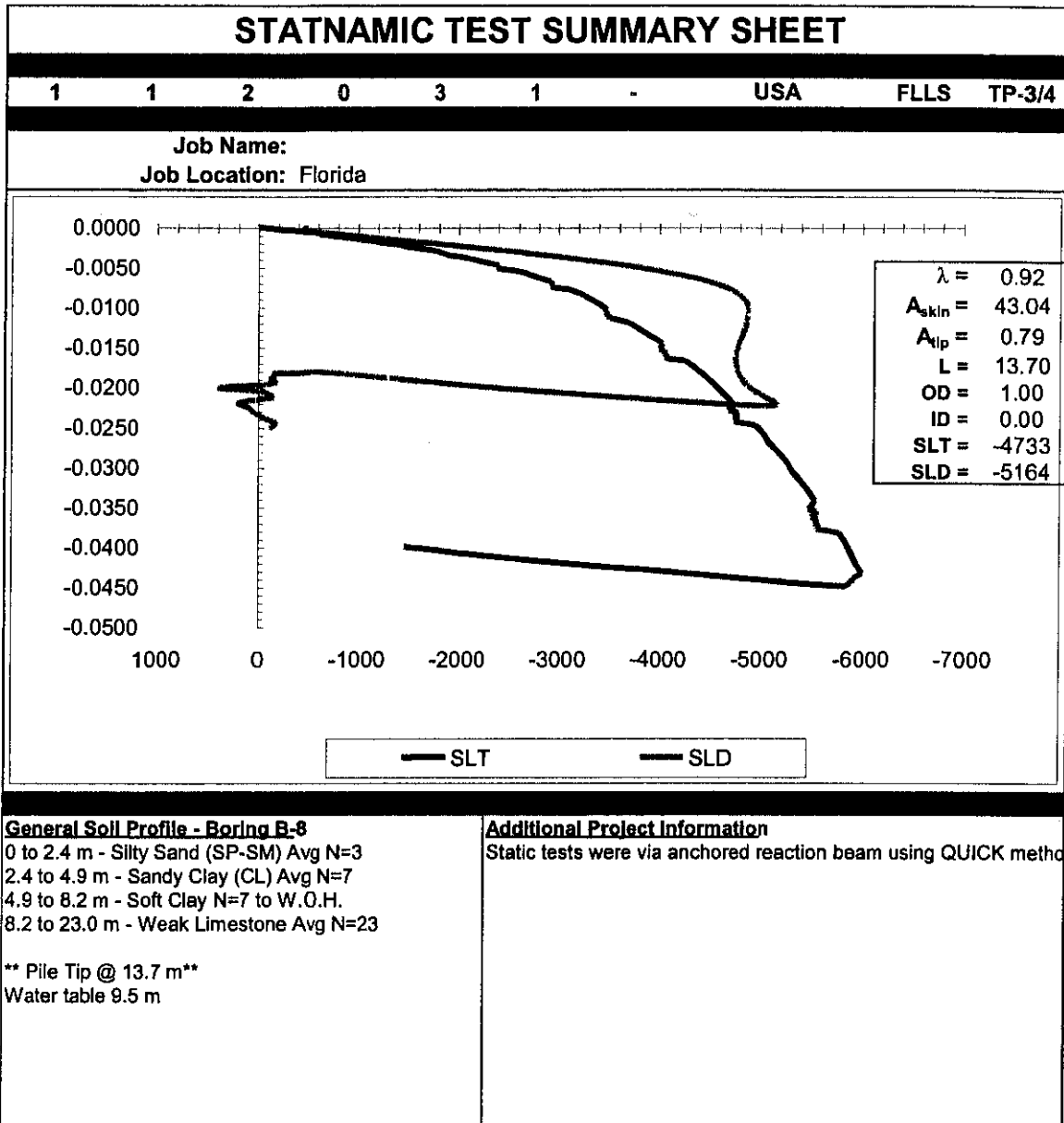
(*Load tests are not to failure)

PART B
Case Histories of Statnamic and Static Load Tests

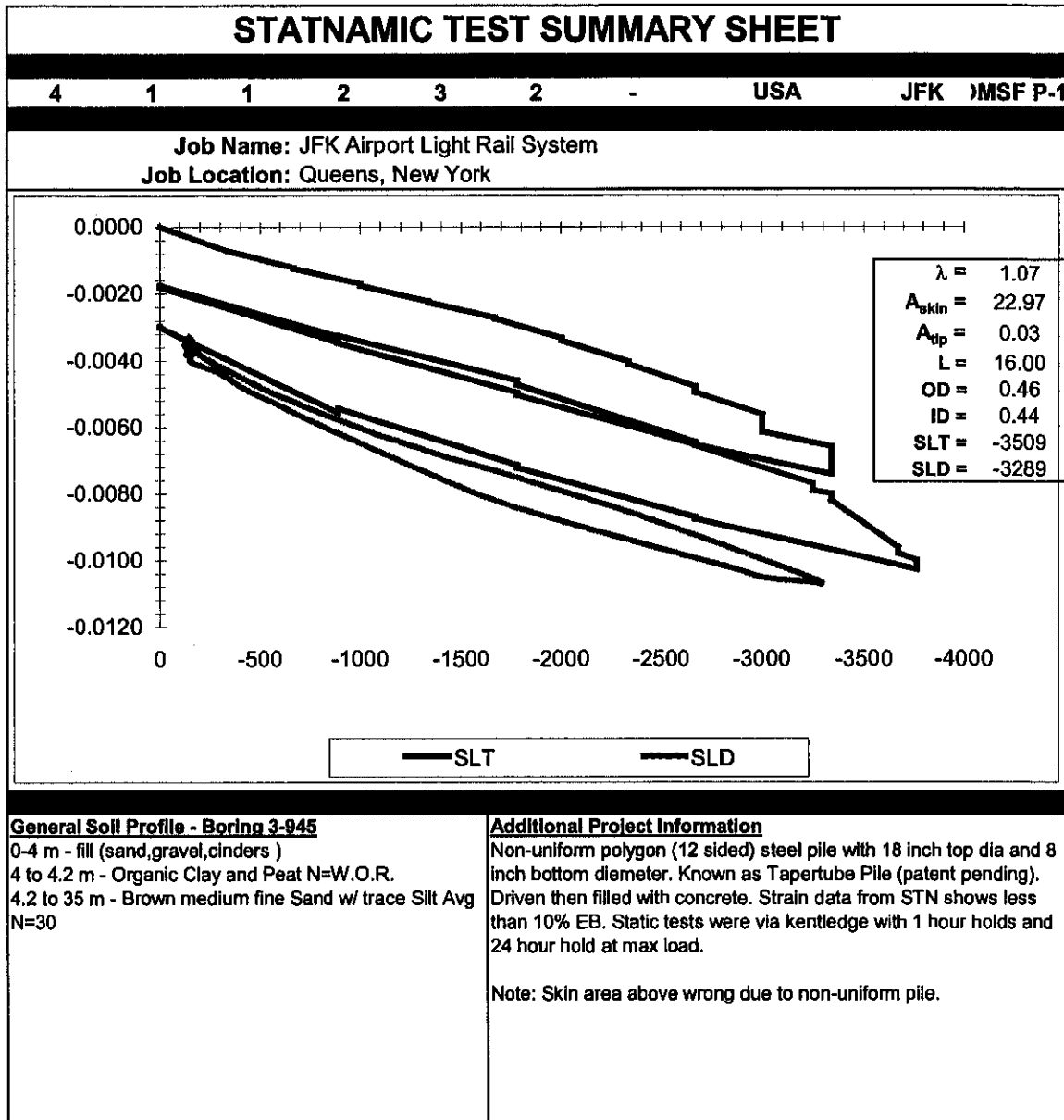
Appendix B Part B



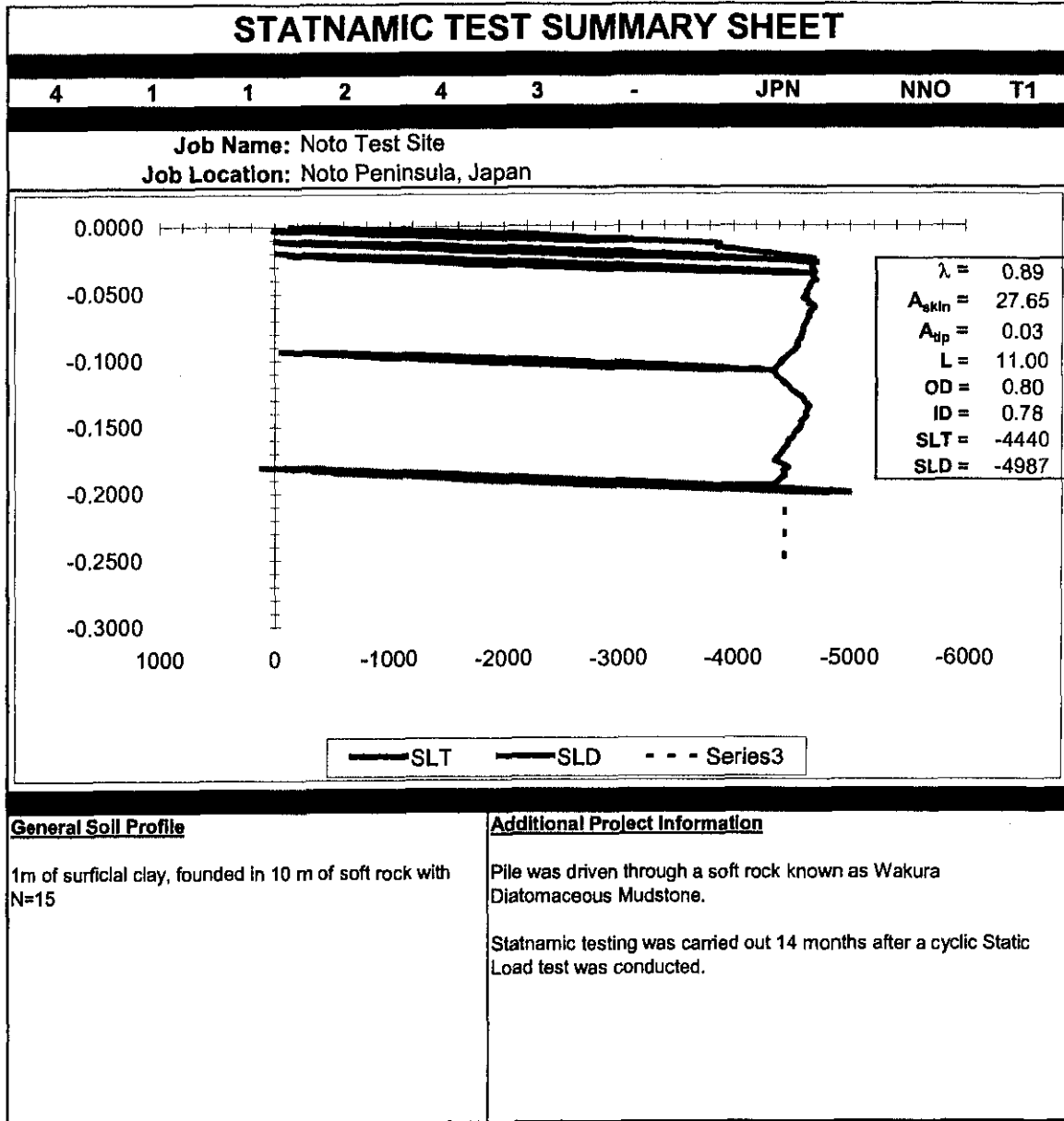
Appendix B Part B



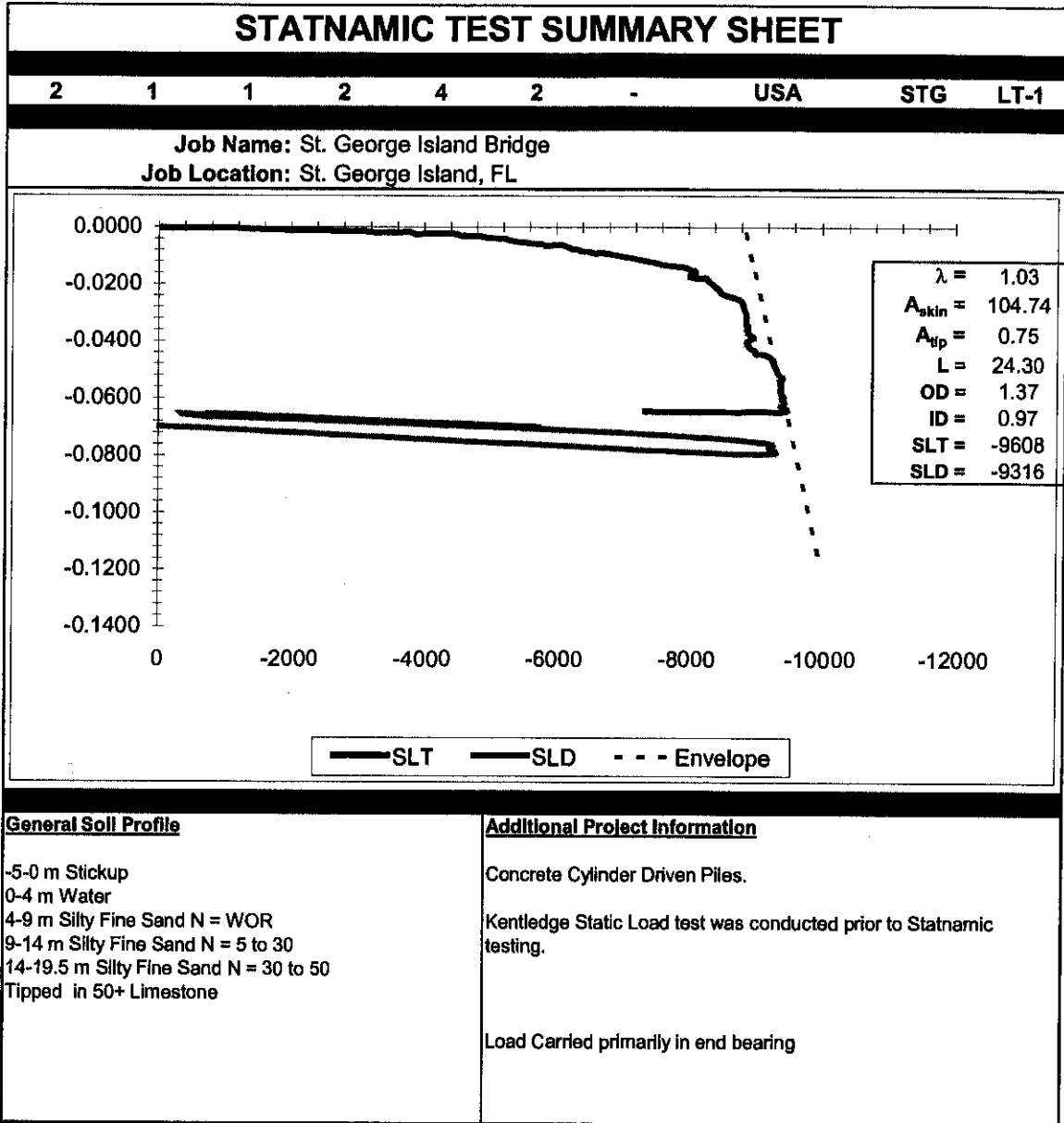
Appendix B Part B



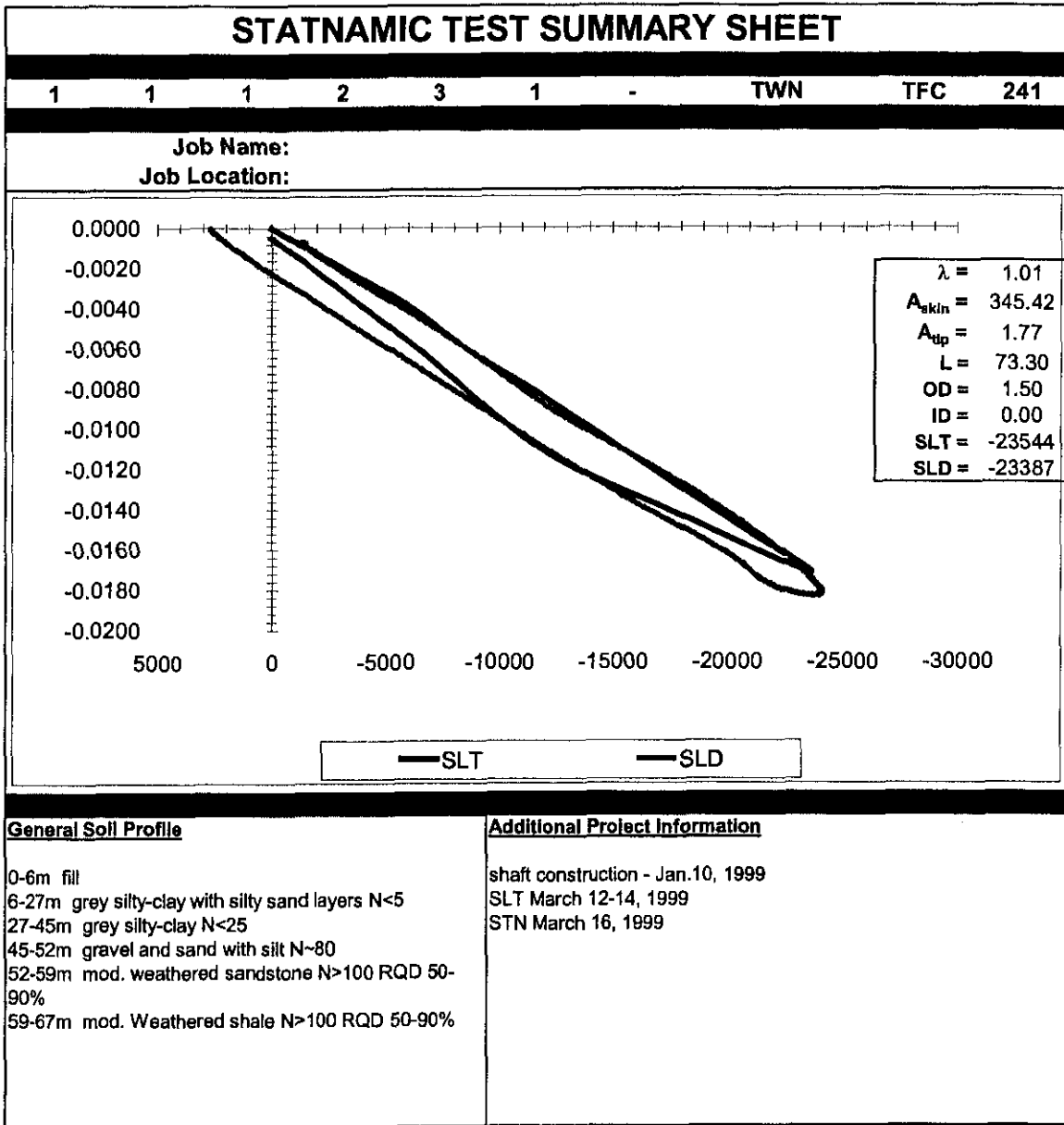
Appendix B Part B



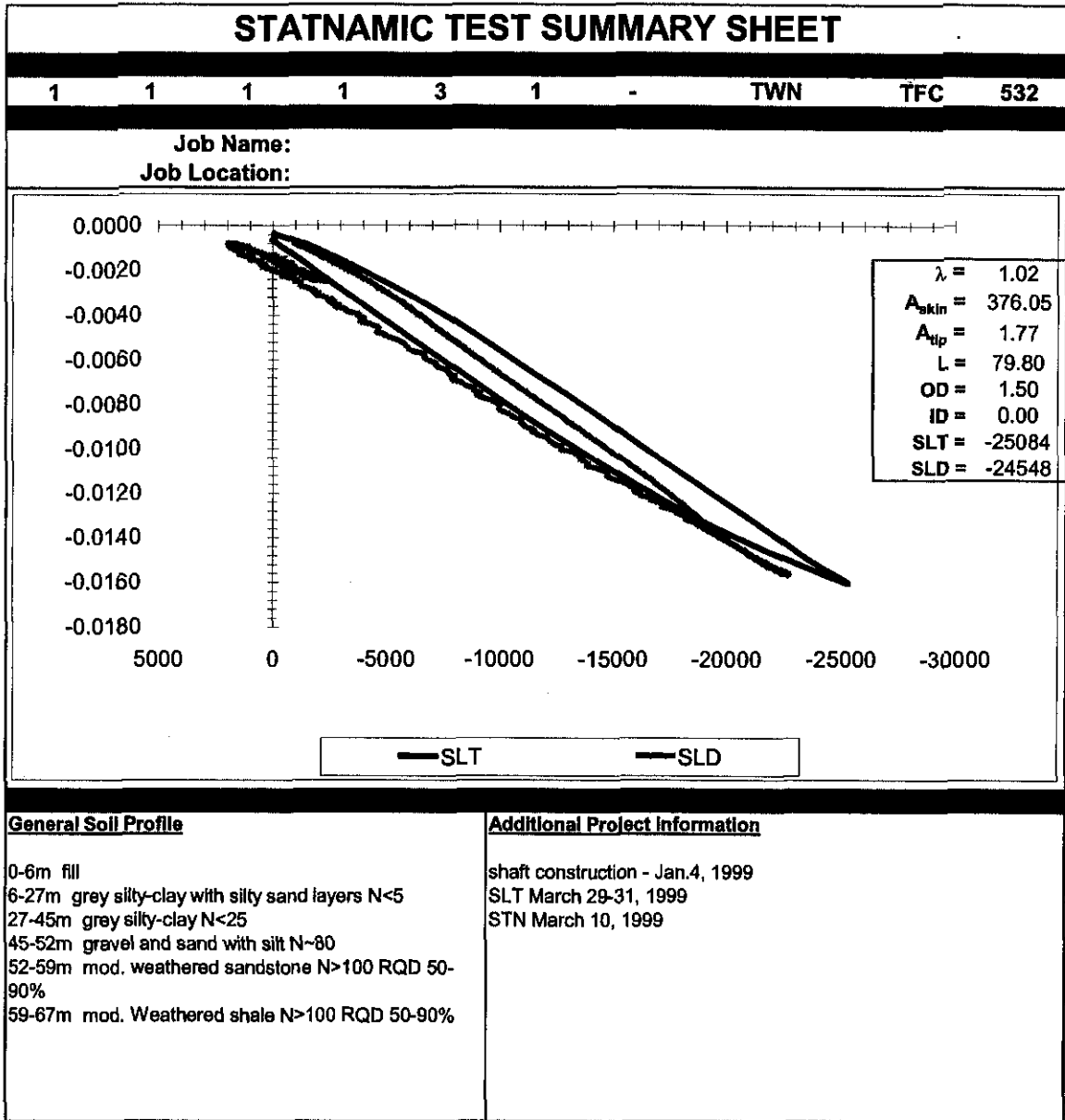
Appendix B Part B



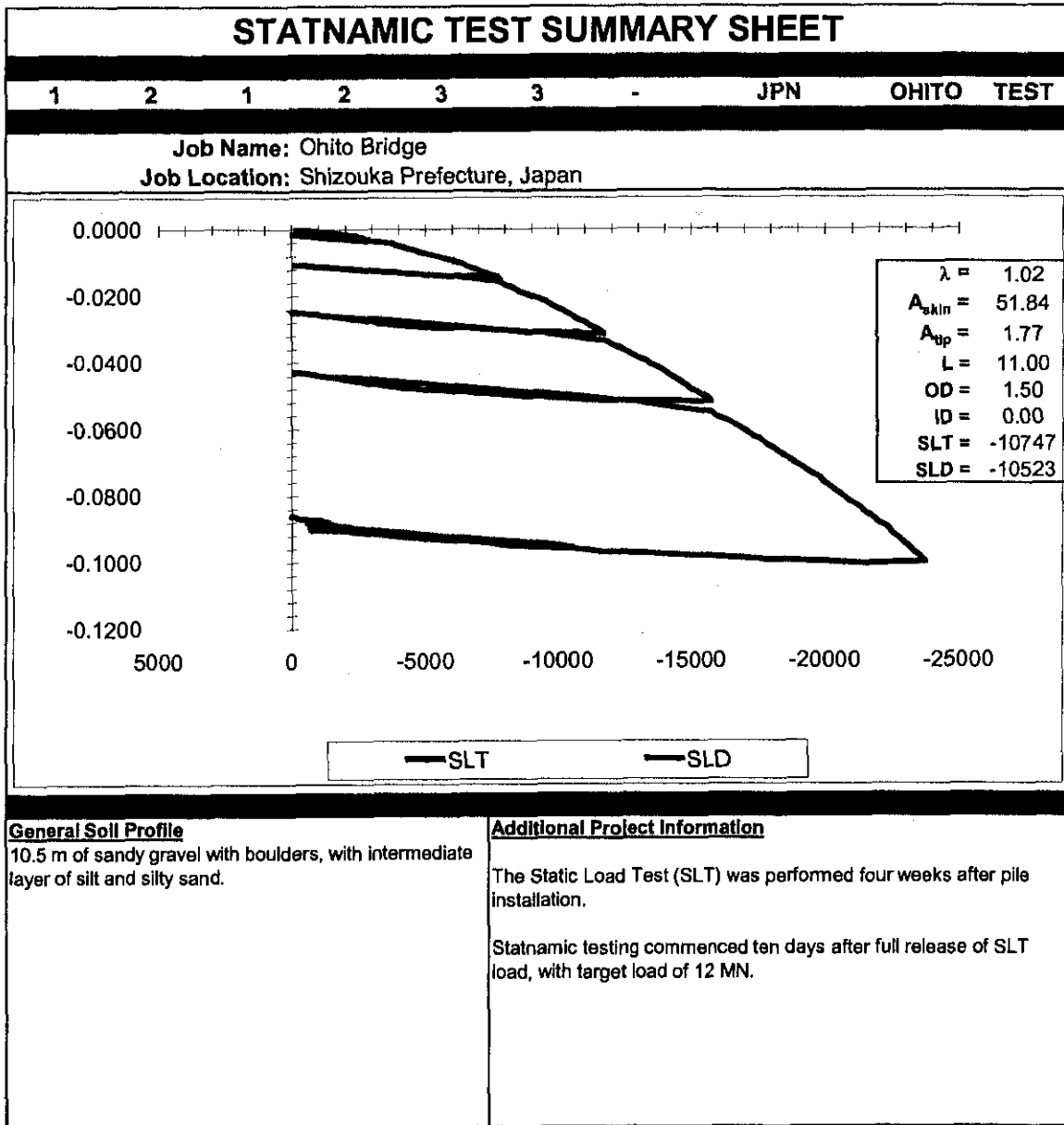
Appendix B Part B



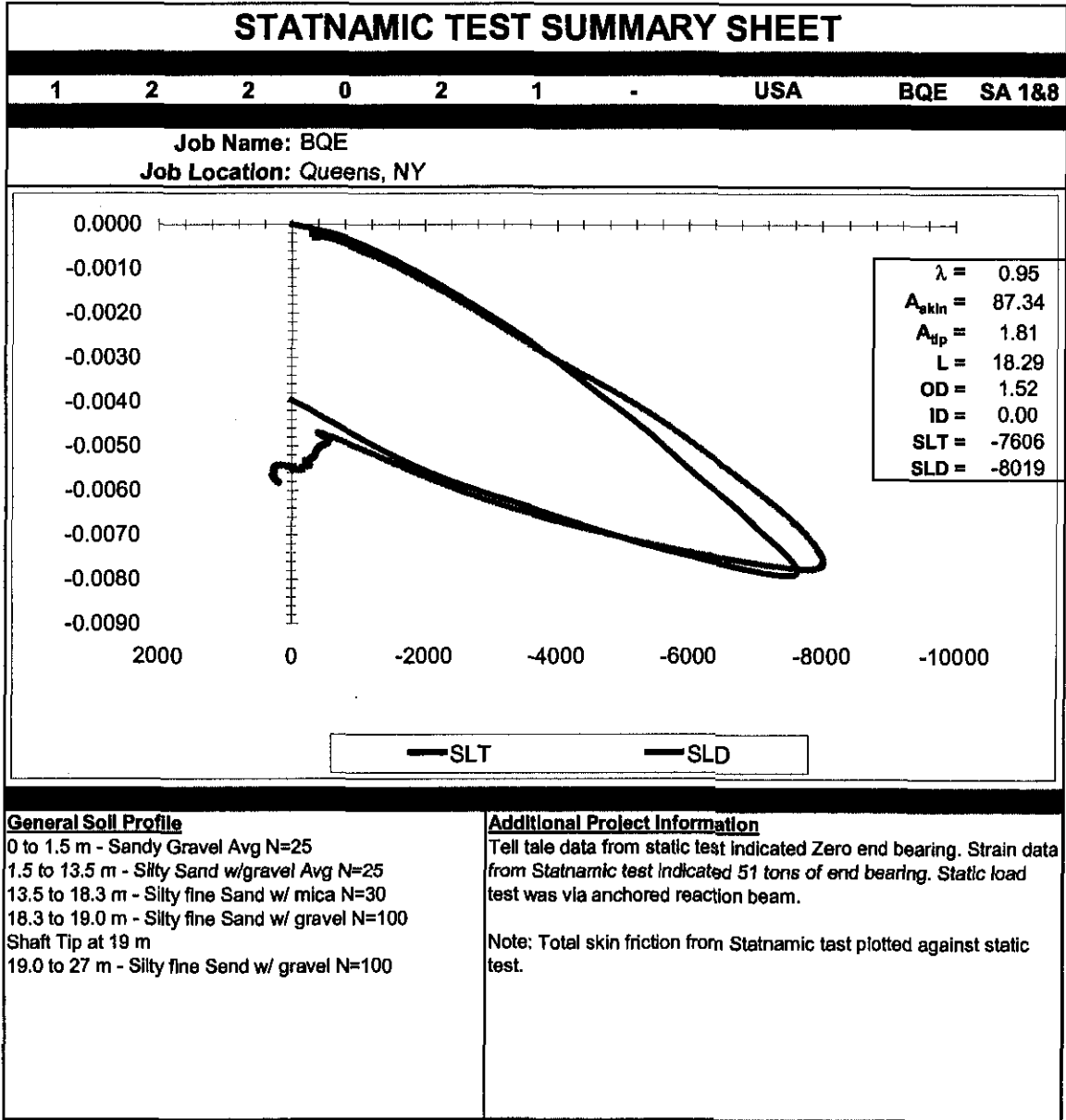
Appendix B Part B



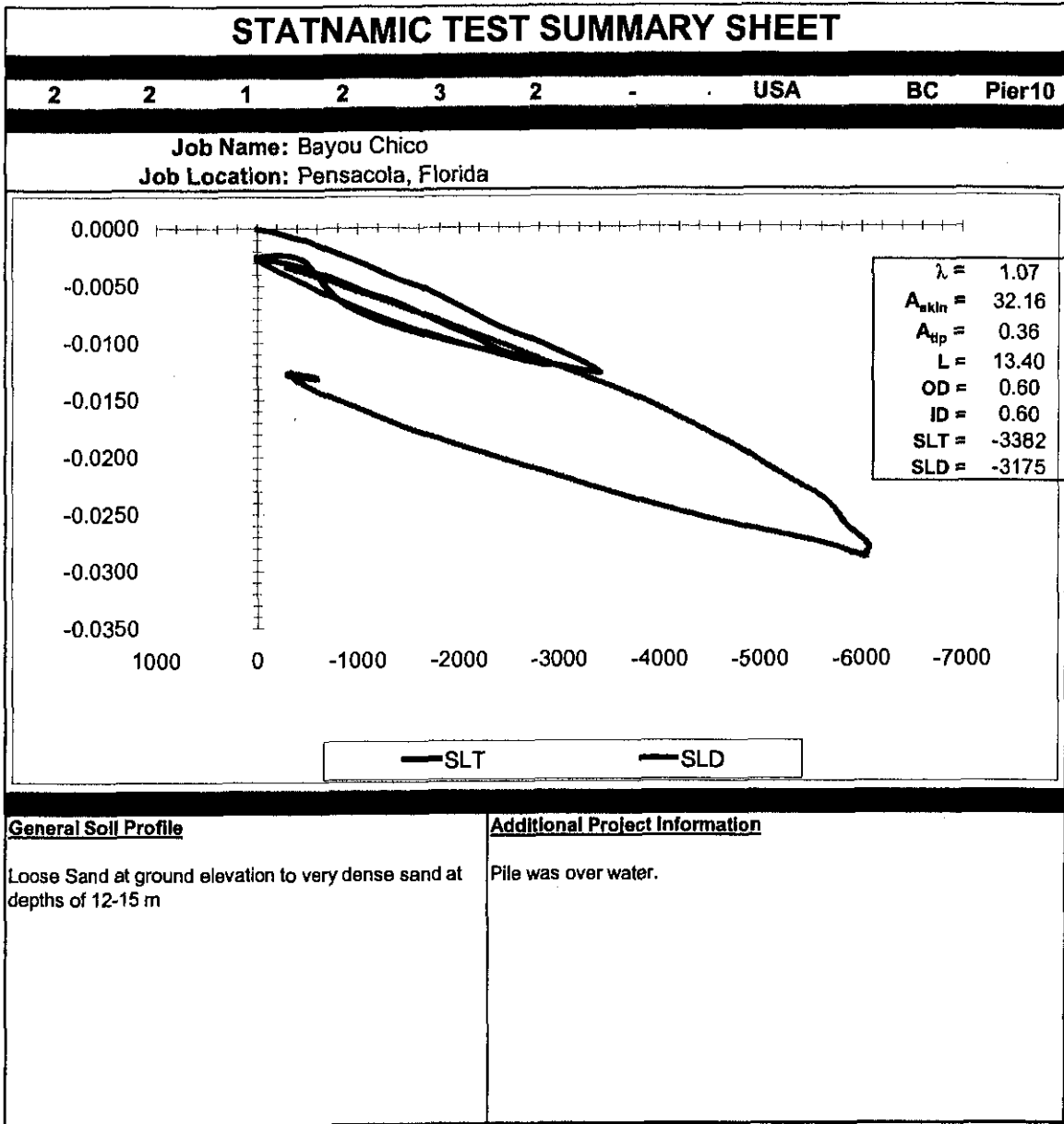
Appendix B Part B



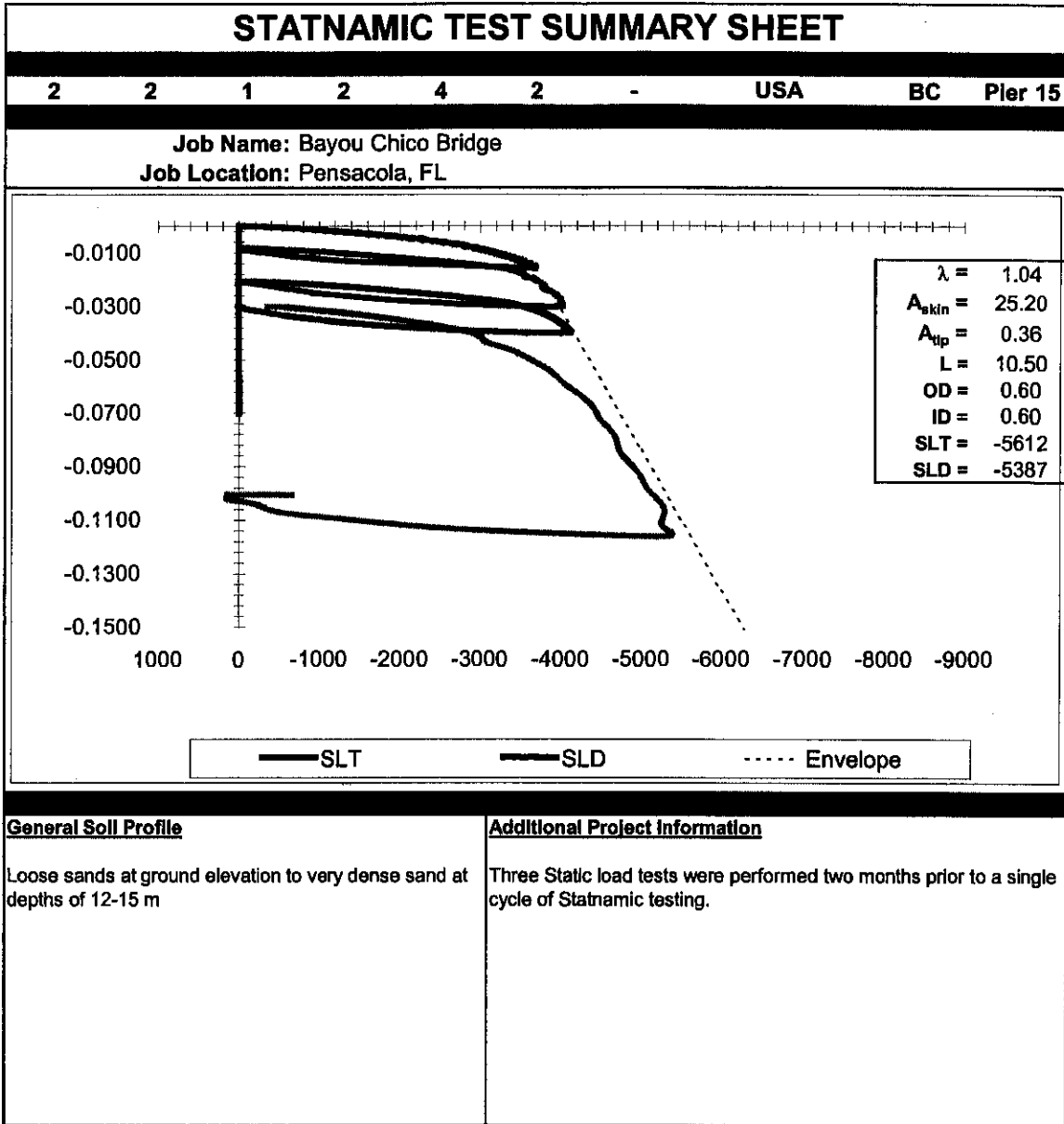
Appendix B Part B



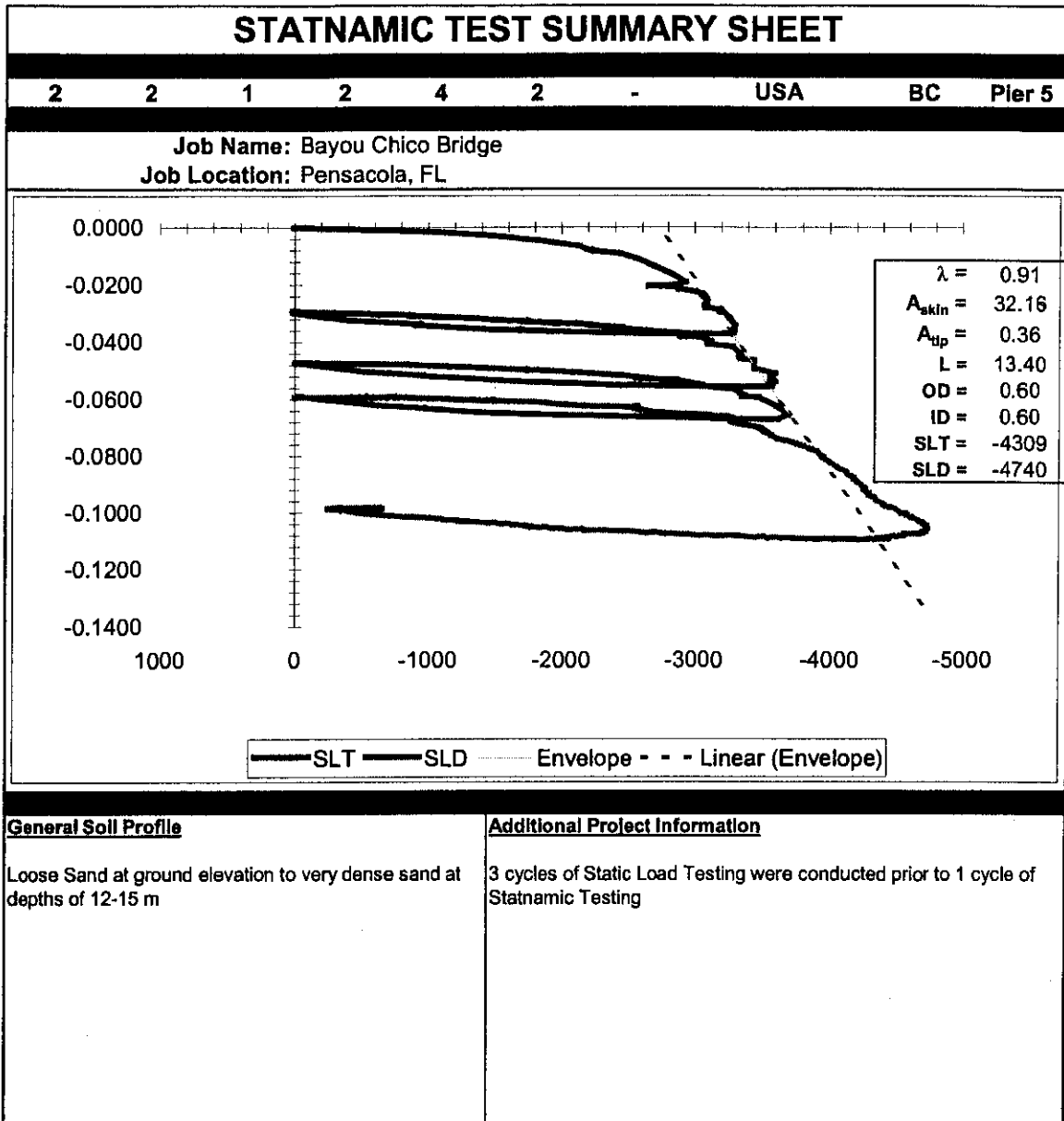
Appendix B Part B



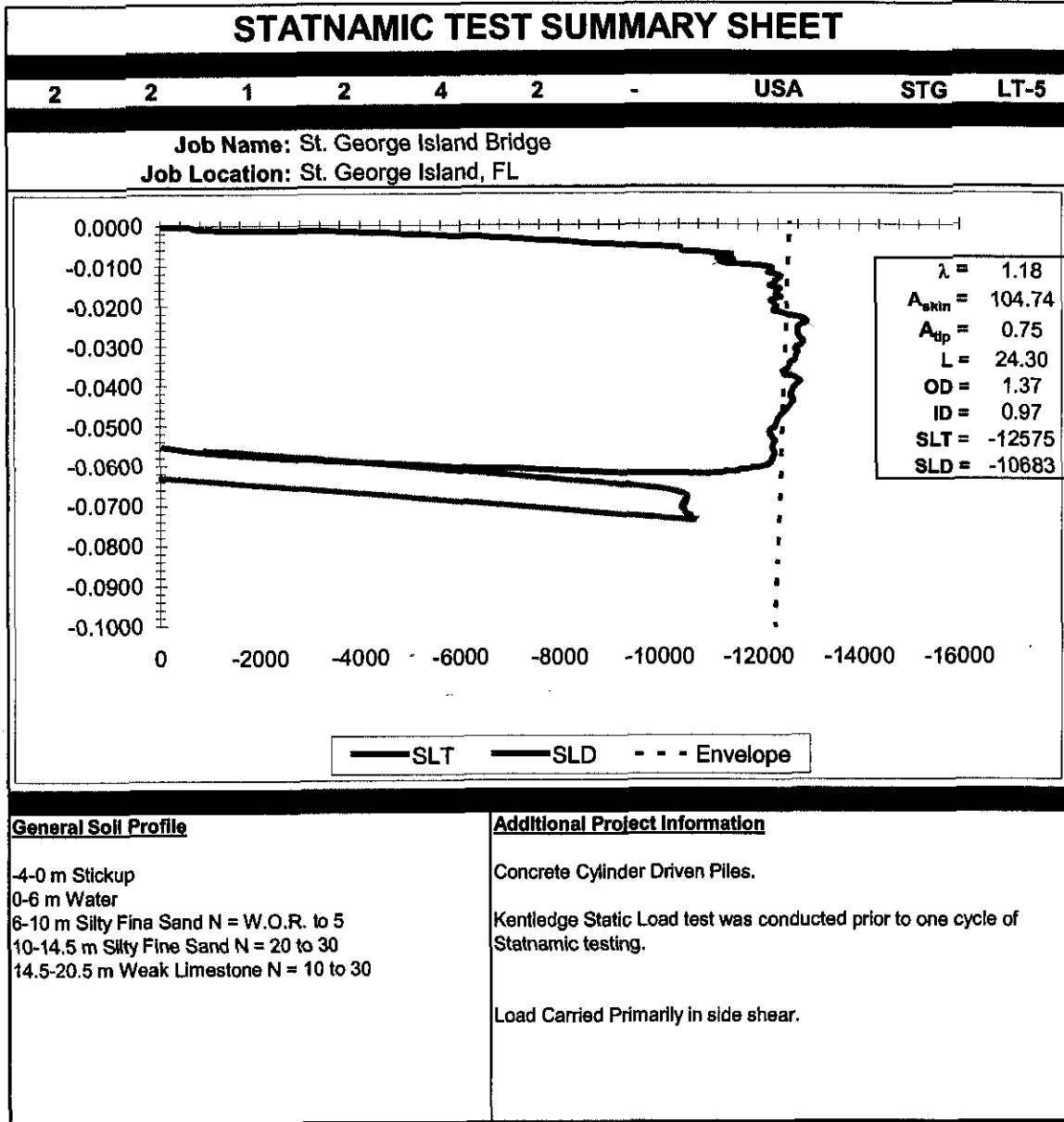
Appendix B Part B



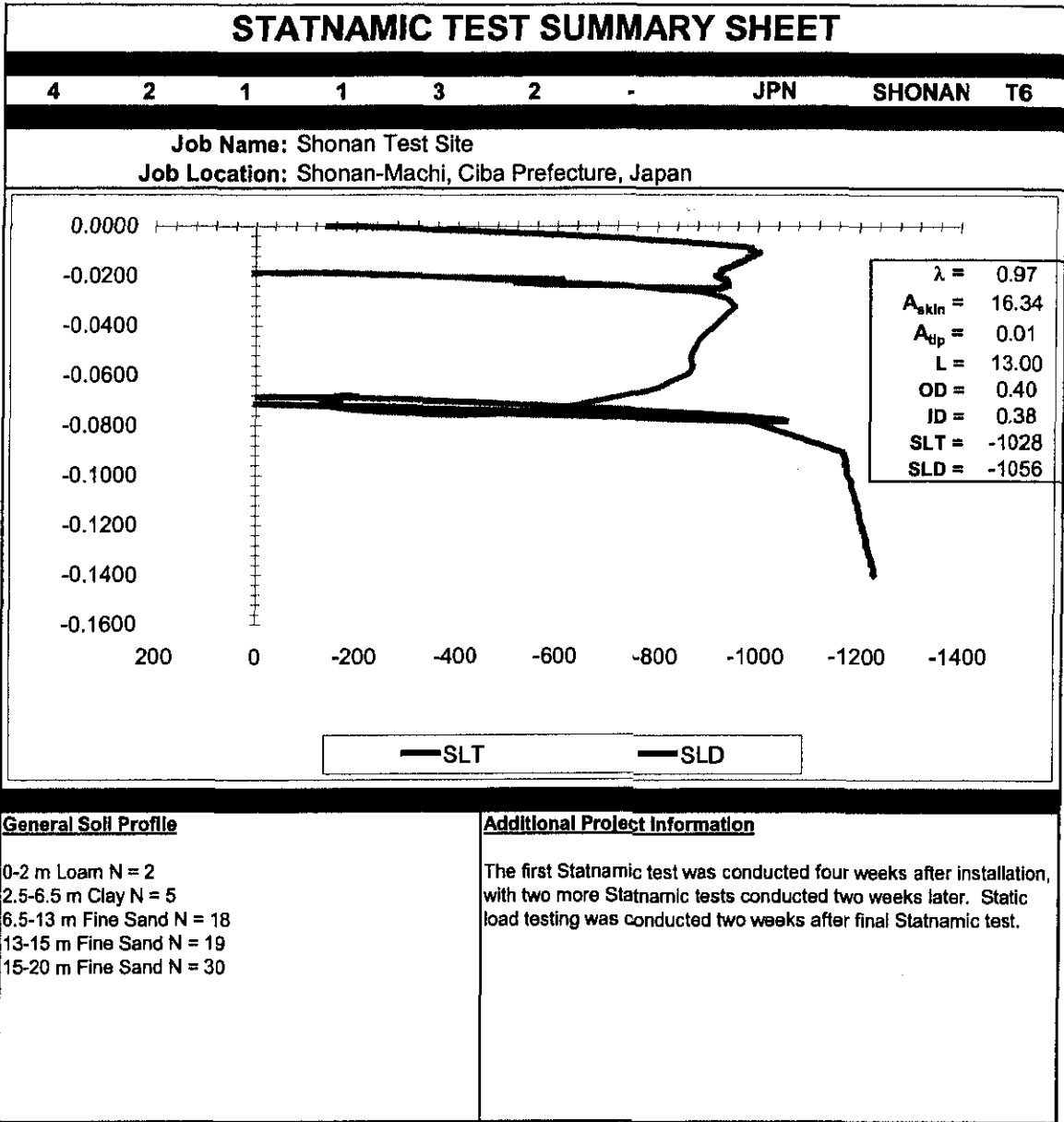
Appendix B Part B



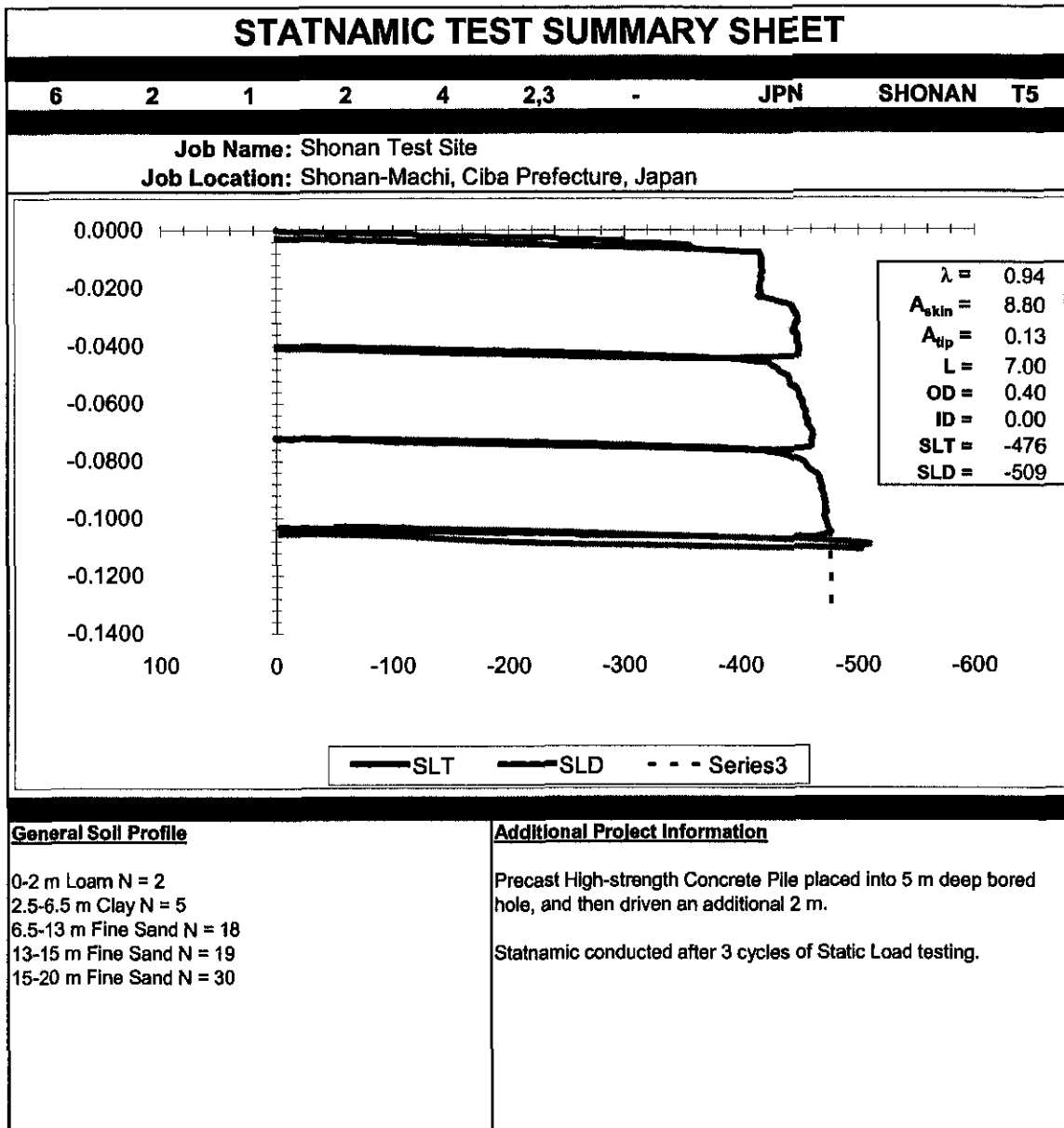
Appendix B Part B



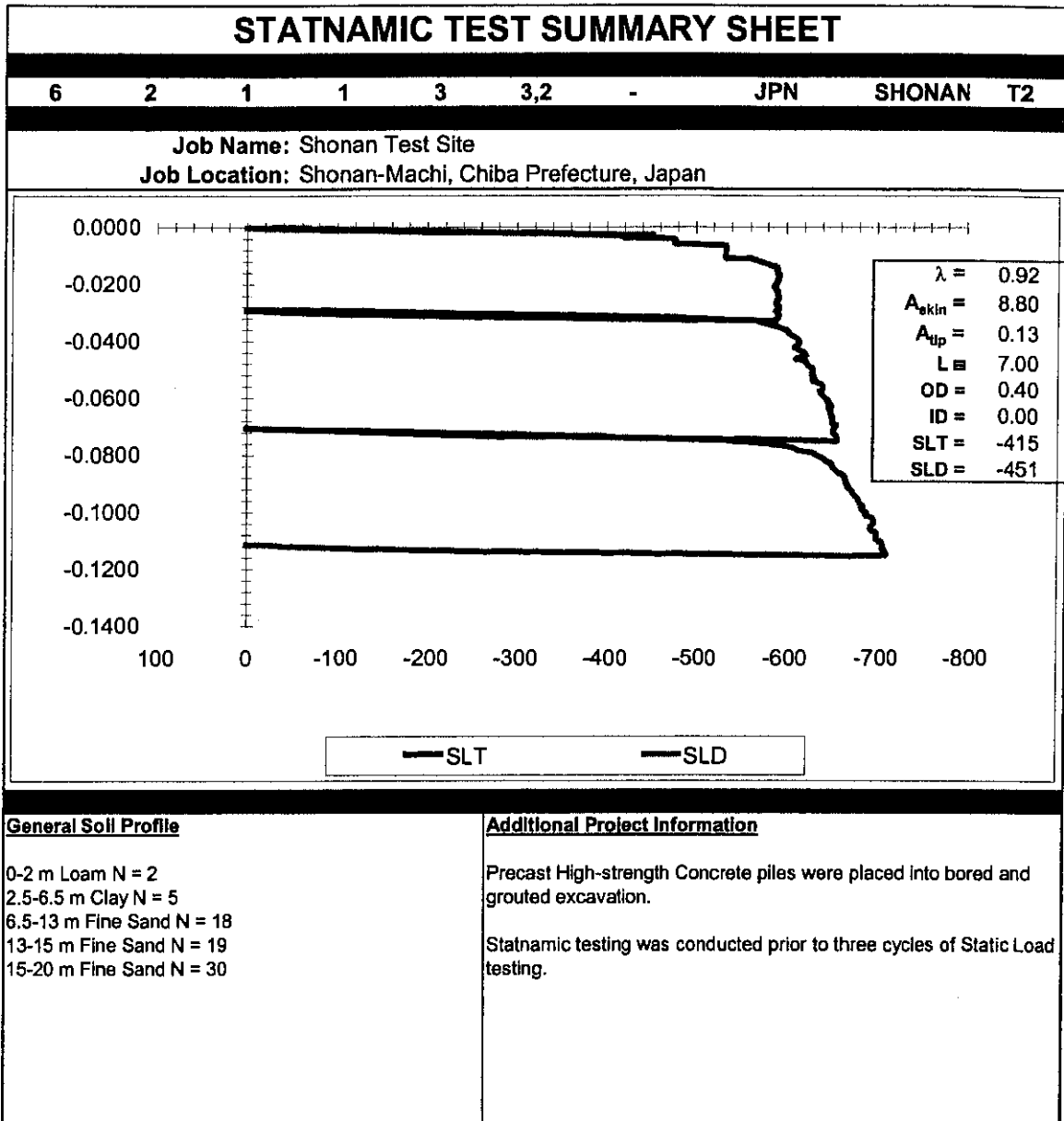
Appendix B Part B



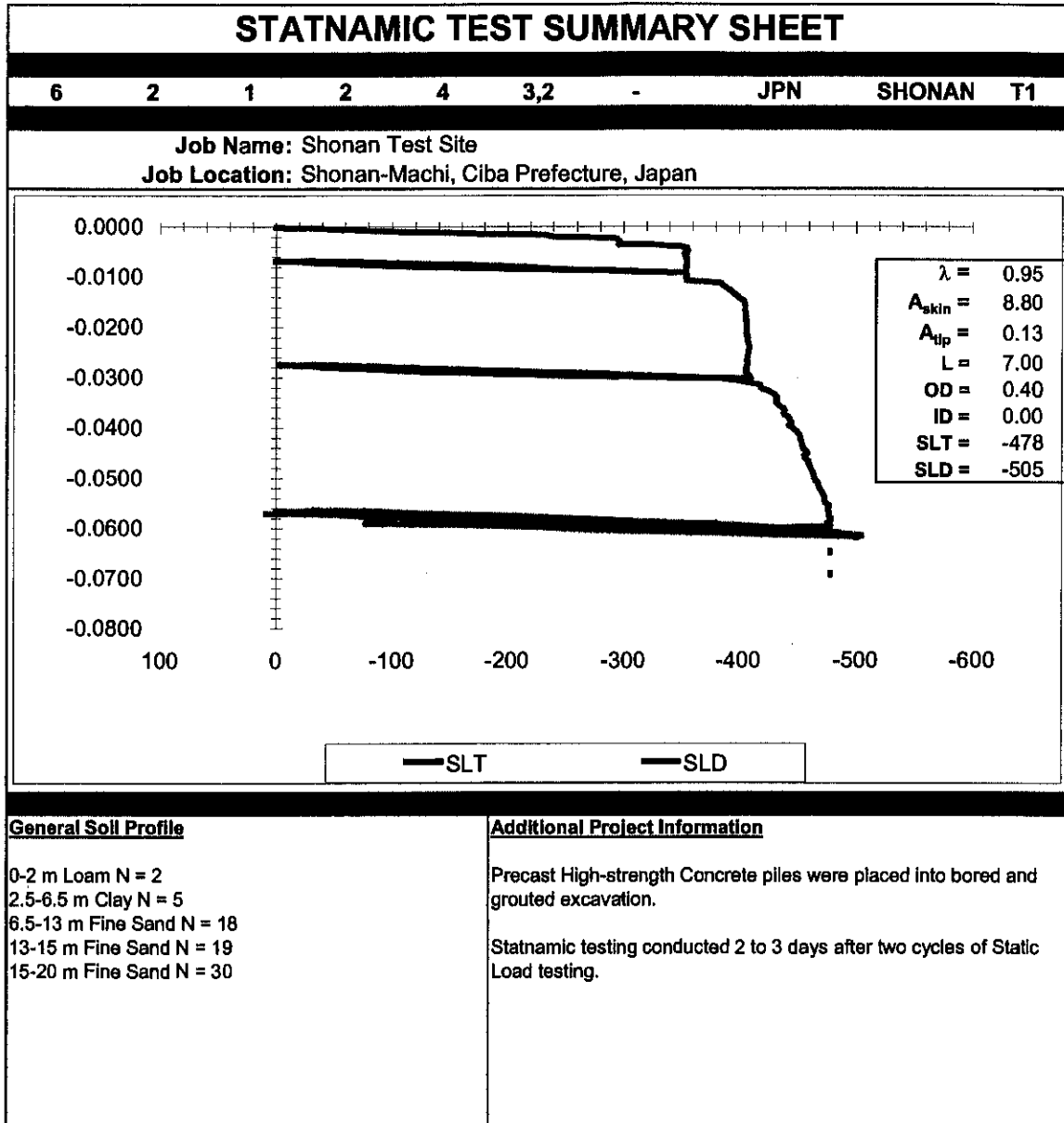
Appendix B Part B



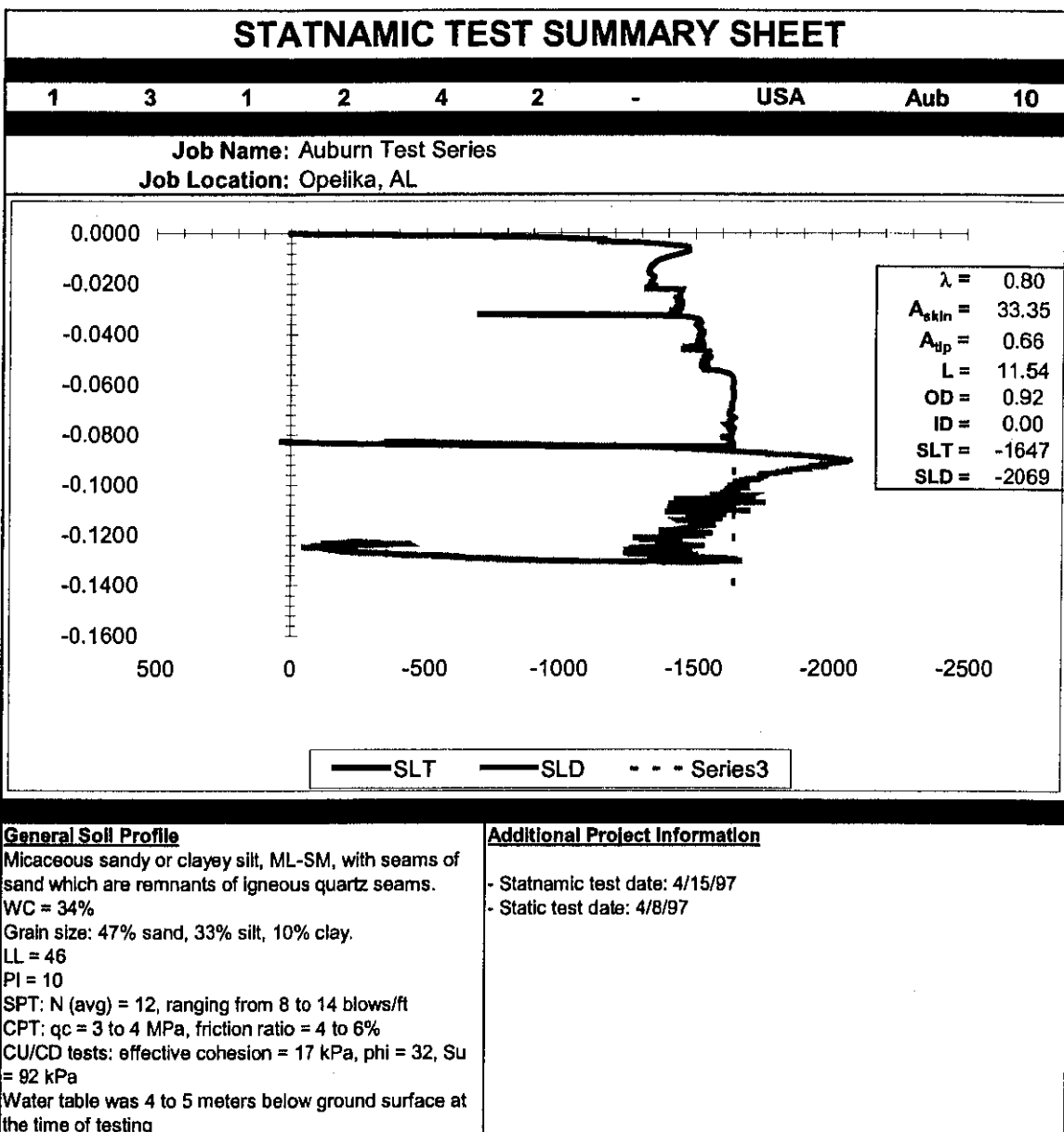
Appendix B Part B



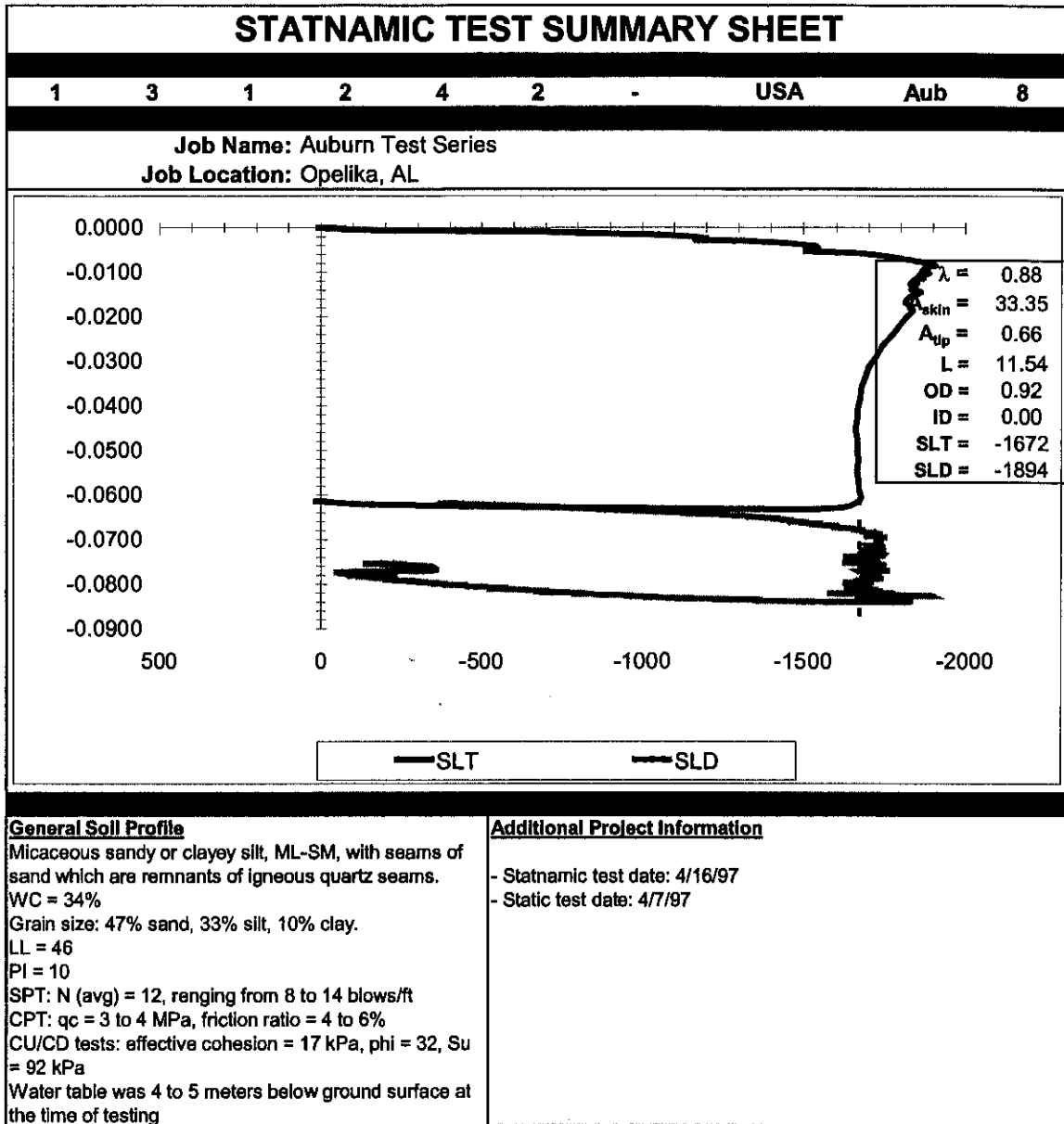
Appendix B Part B



Appendix B Part B



Appendix B Part B

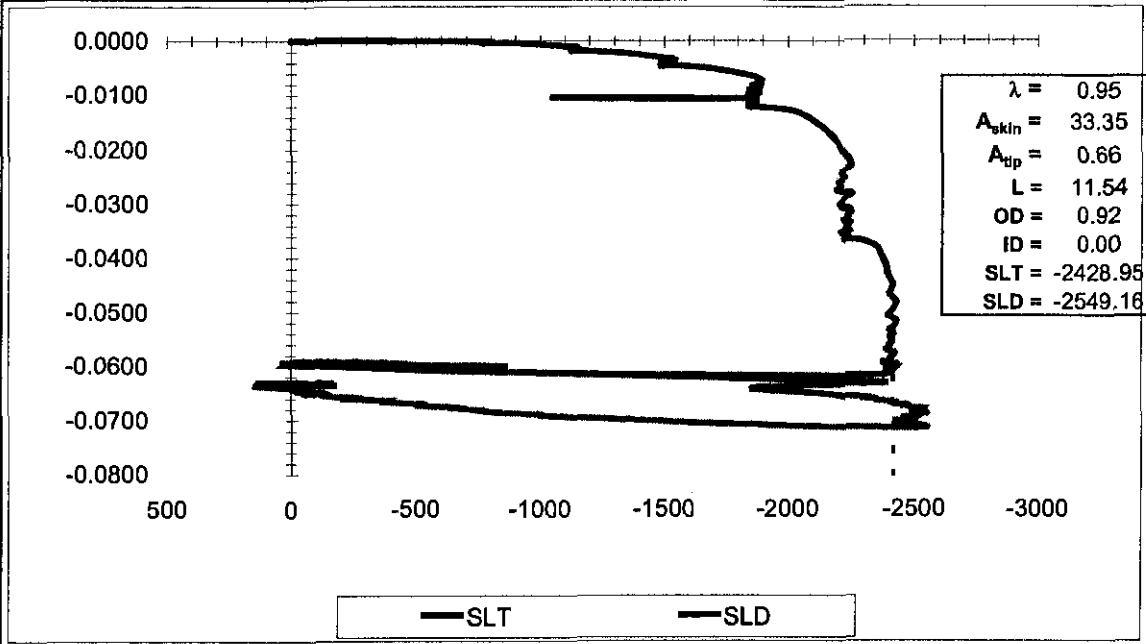


Appendix B Part B

STATNAMIC TEST SUMMARY SHEET

1 3 1 2 4 2 - USA Aub 7

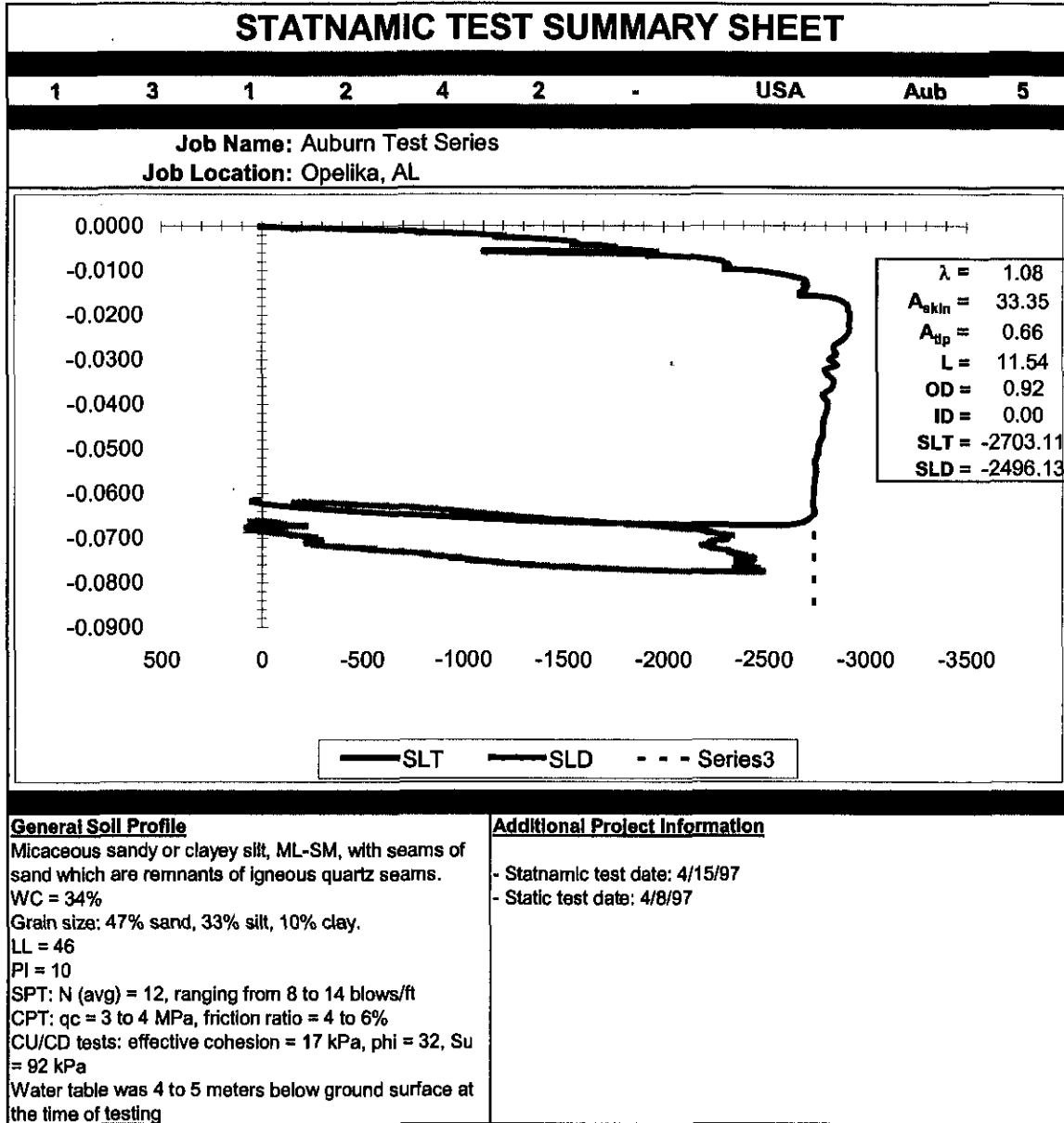
Job Name: Auburn Test Series
Job Location: Opelika, AL



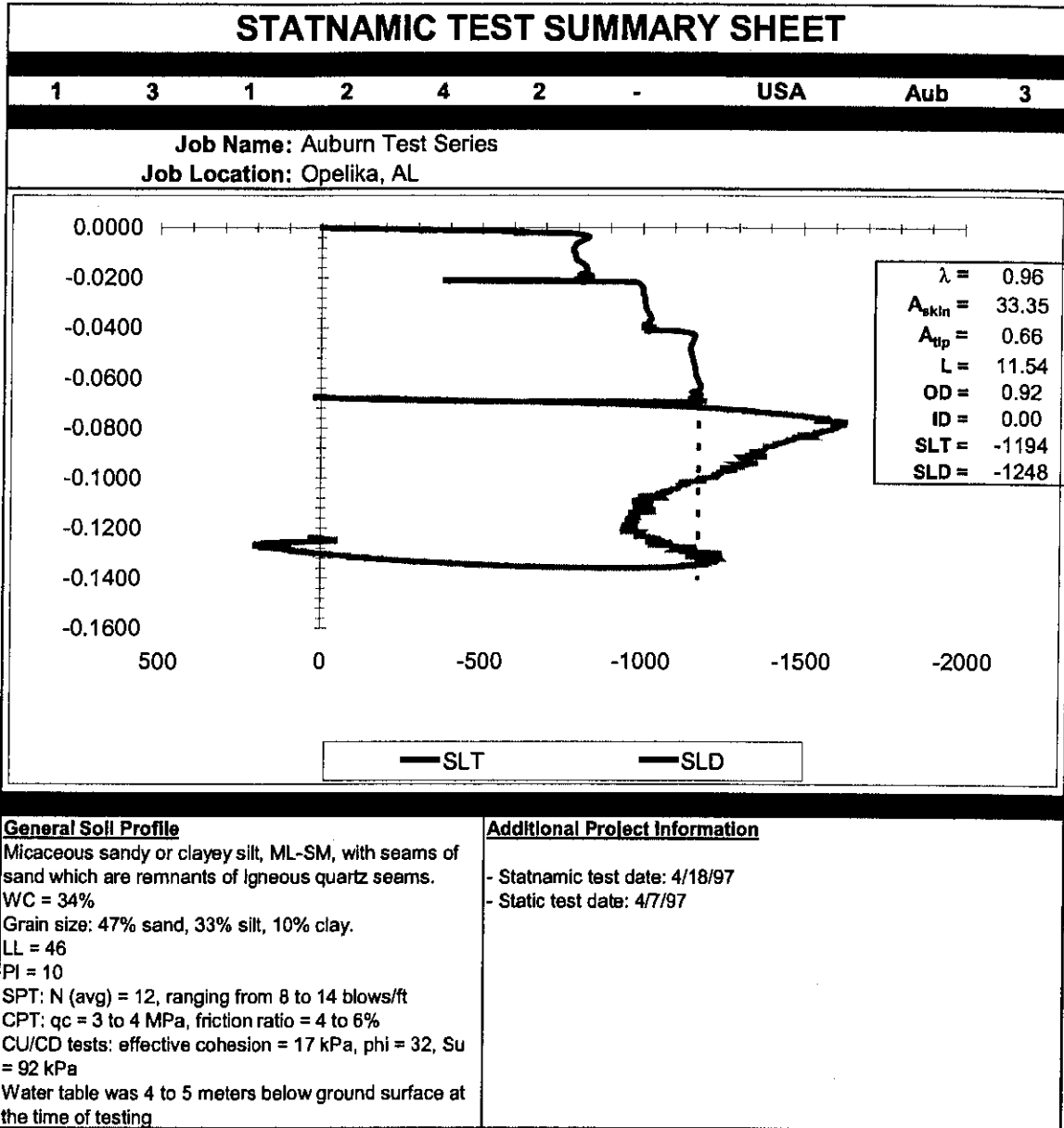
General Soil Profile
 Micaceous sandy or clayey silt, ML-SM, with seams of sand which are remnants of igneous quartz seams.
 WC = 34%
 Grain size: 47% sand, 33% silt, 10% clay.
 LL = 46
 PI = 10
 SPT: N (avg) = 12, ranging from 8 to 14 blows/ft
 CPT: q_c = 3 to 4 MPa, friction ratio = 4 to 6%
 CU/CD tests: effective cohesion = 17 kPa, ϕ = 32, S_u = 92 kPa
 Water table was 4 to 5 meters below ground surface at the time of testing

Additional Project Information
 - Statnamic test date: 4/25/97
 - Static test date: 4/4/97

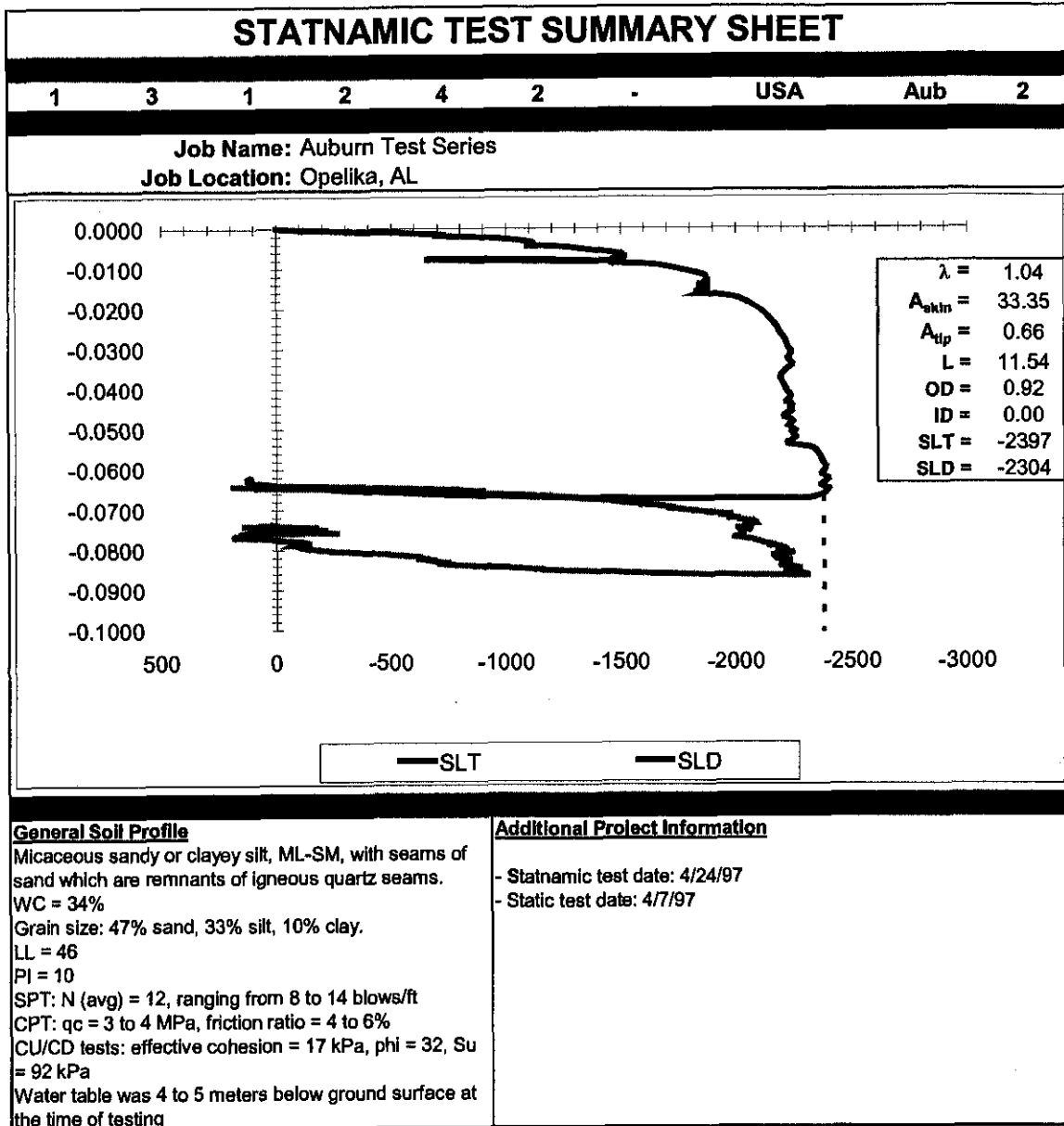
Appendix B Part B



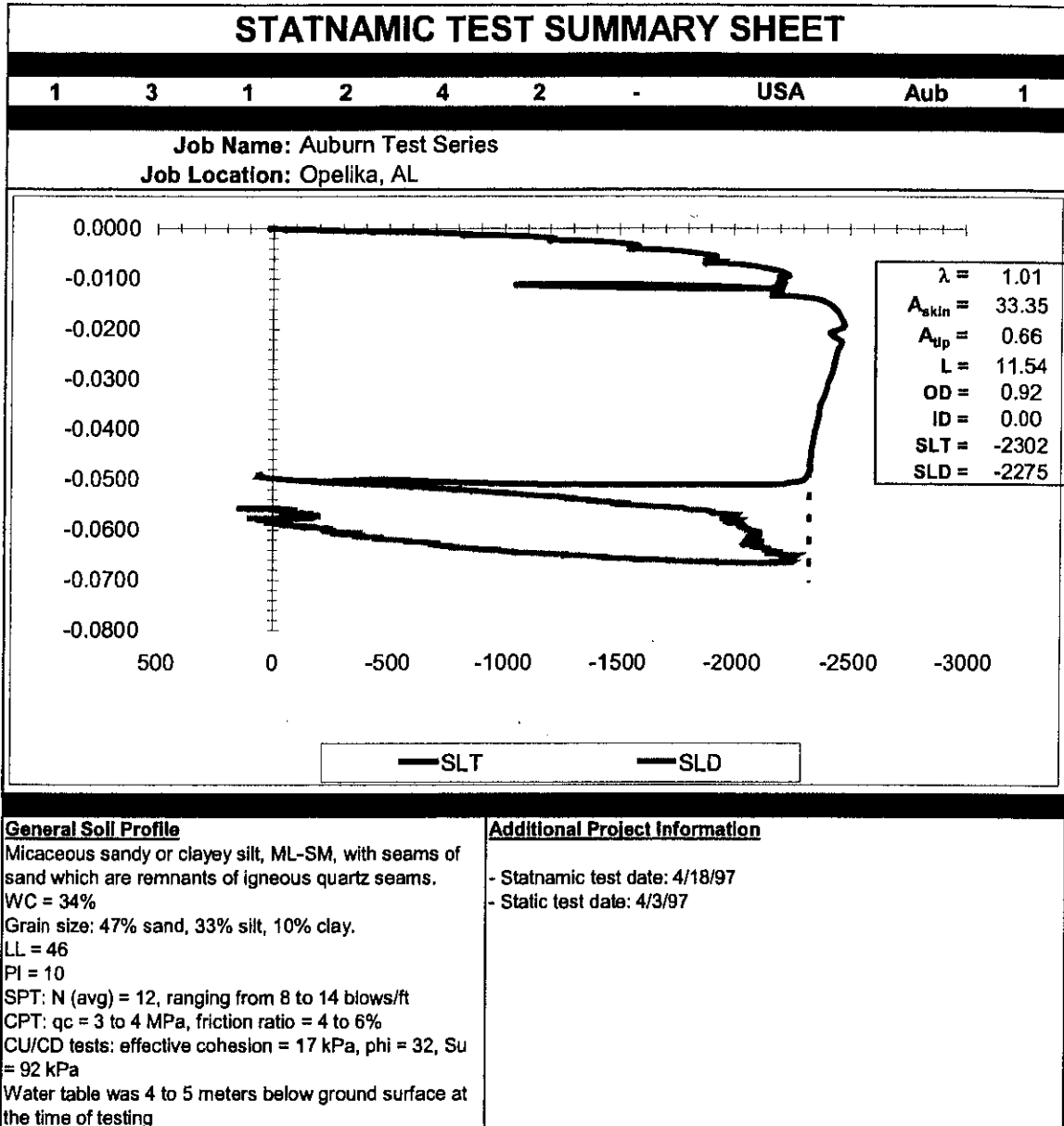
Appendix B Part B



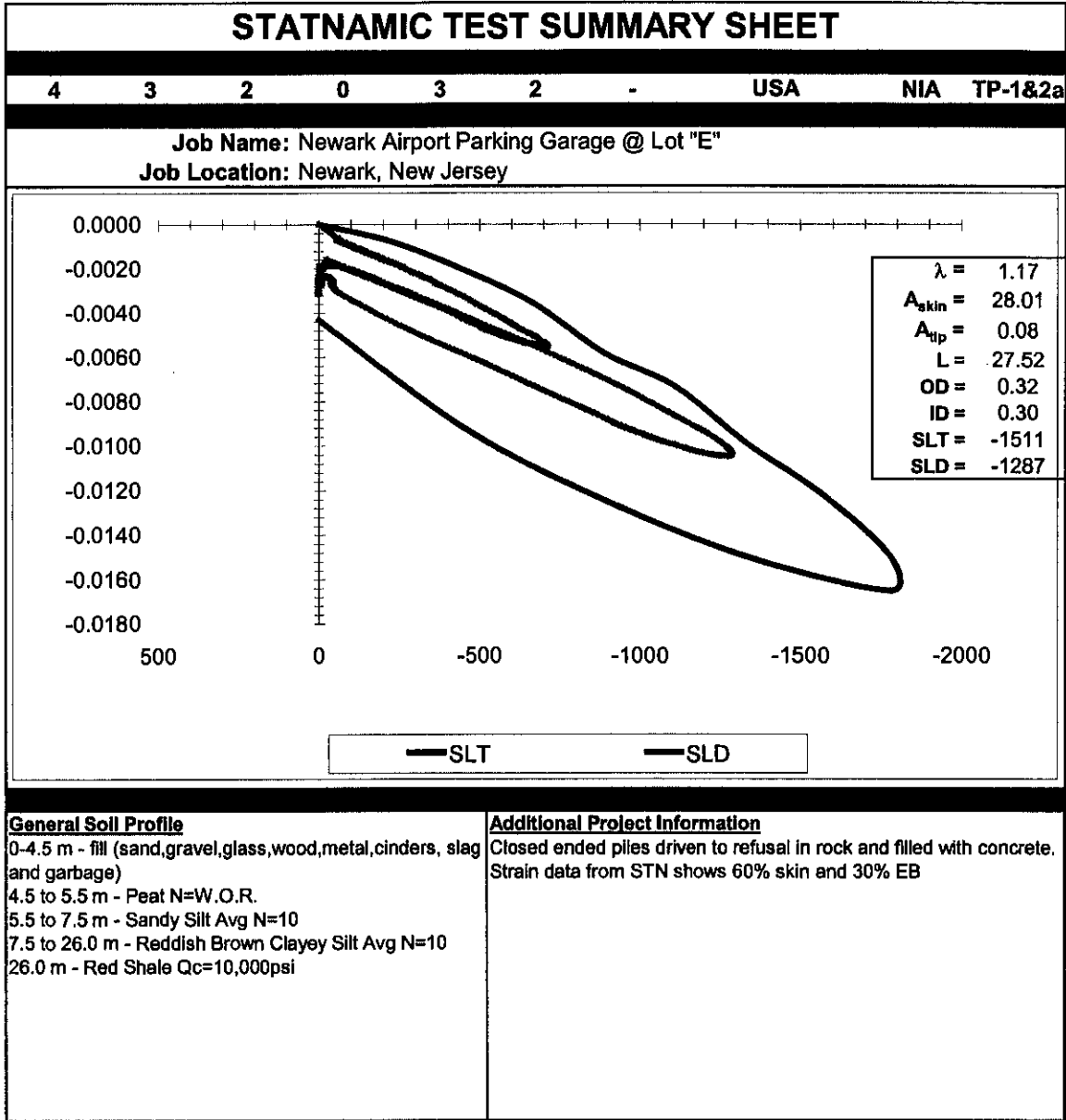
Appendix B Part B



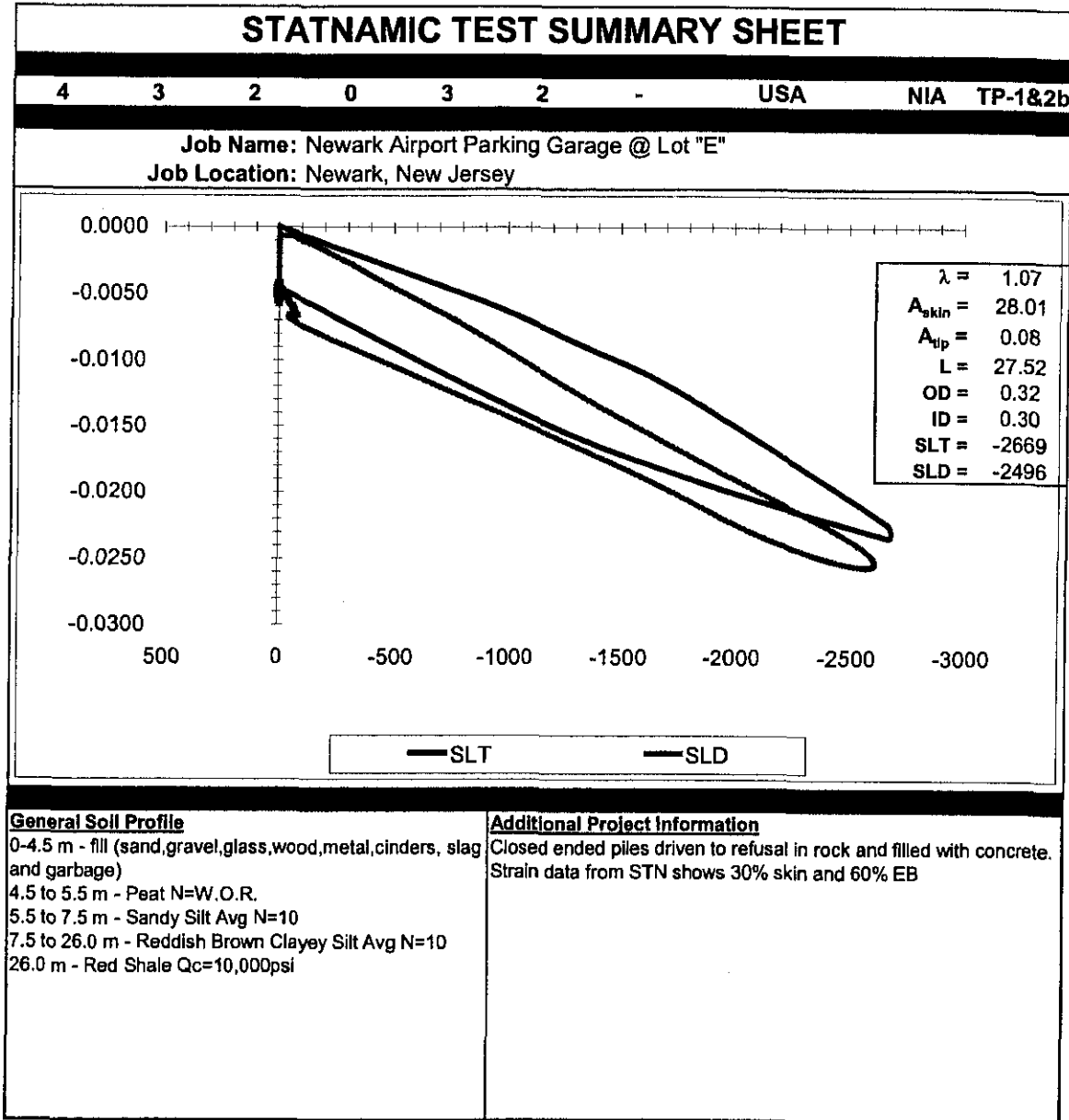
Appendix B Part B



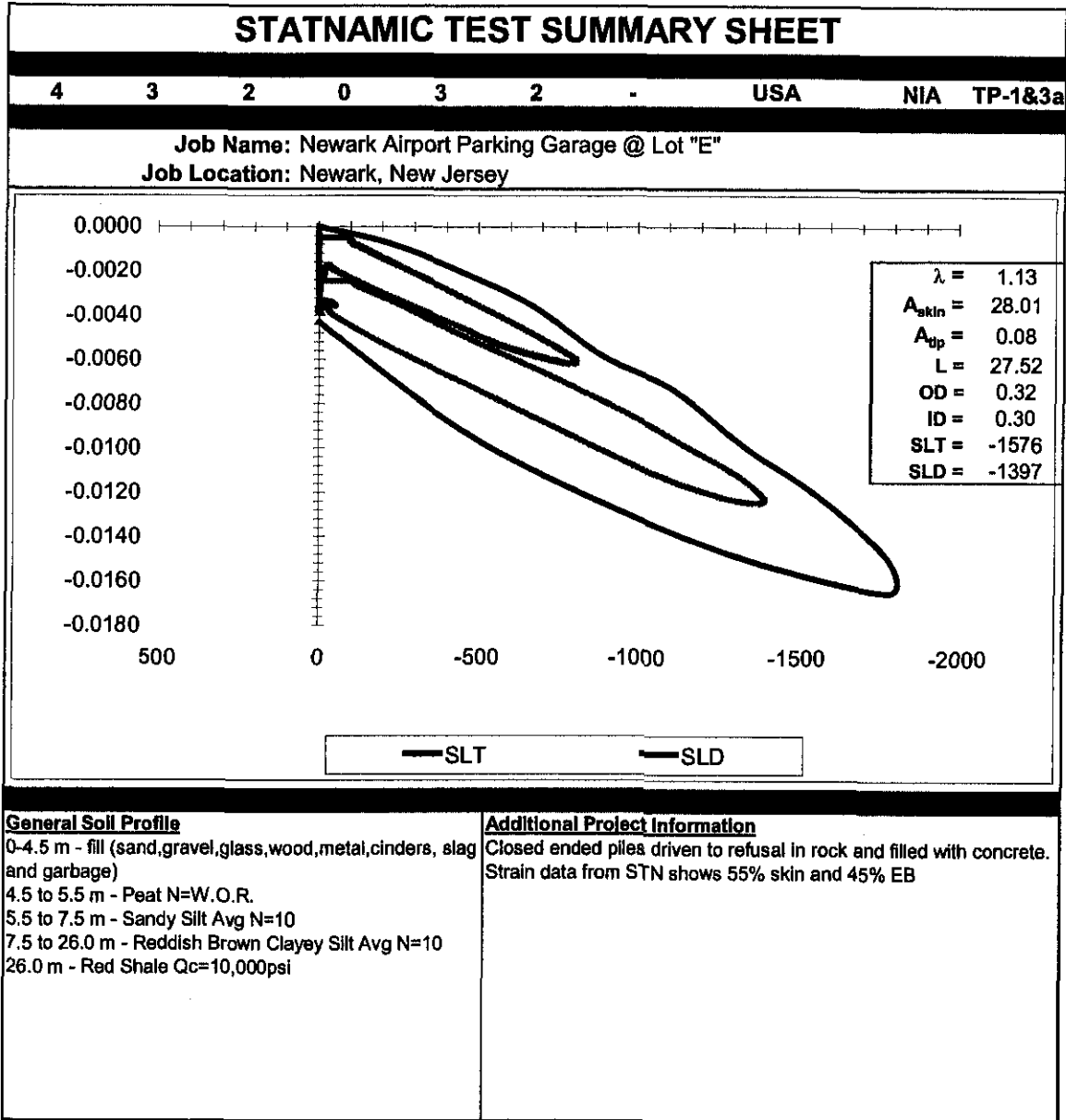
Appendix B Part B



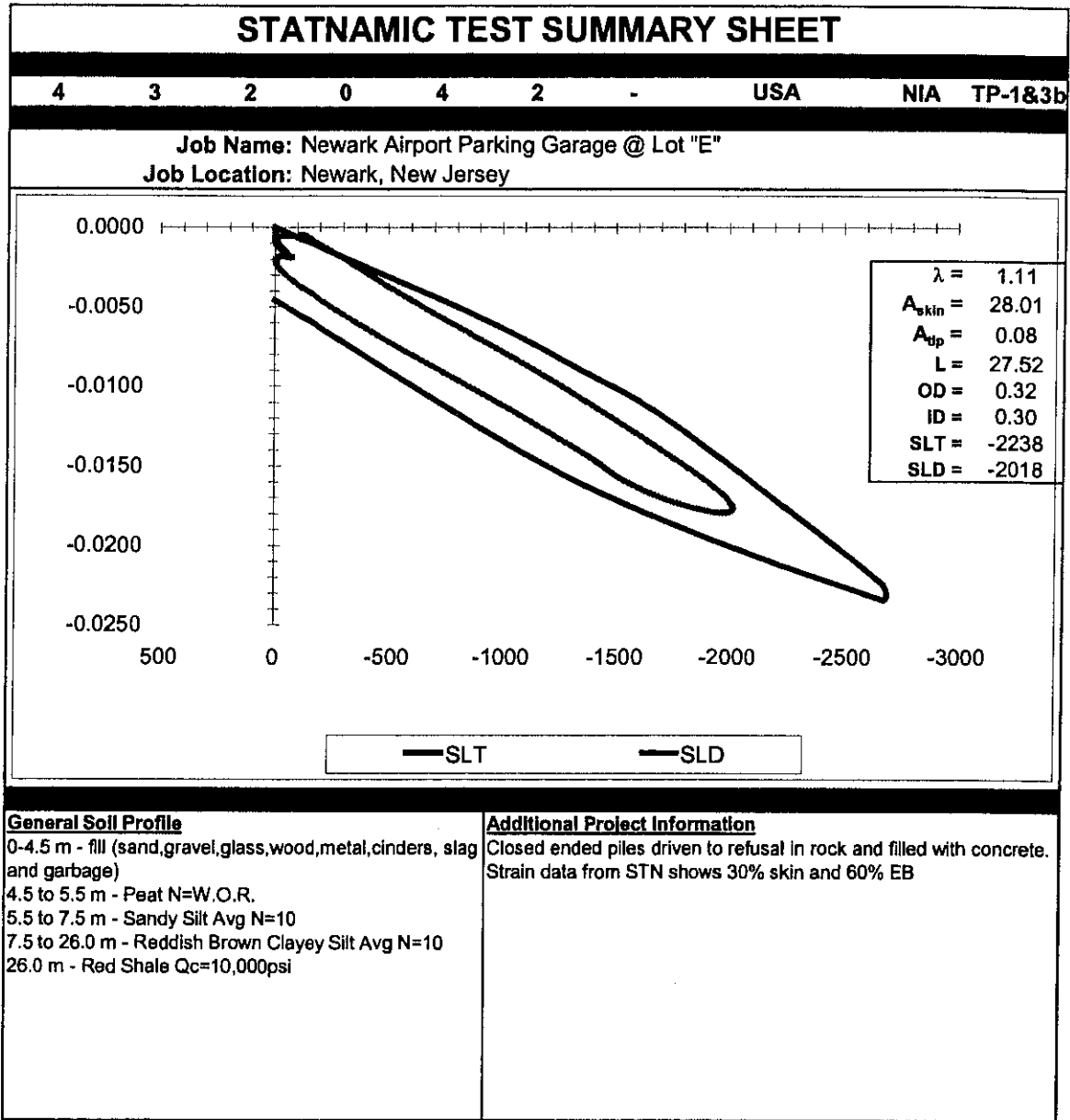
Appendix B Part B



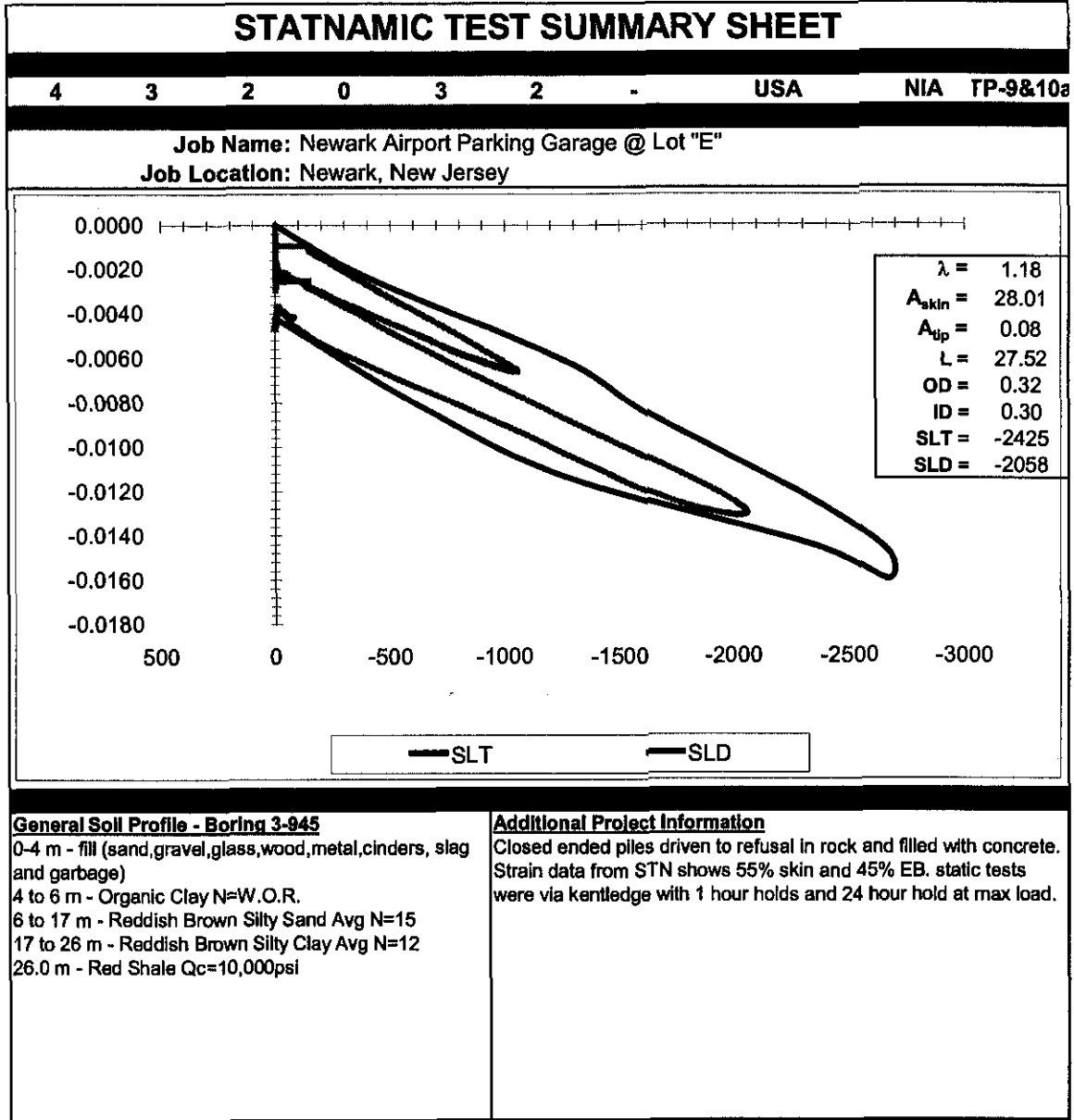
Appendix B Part B



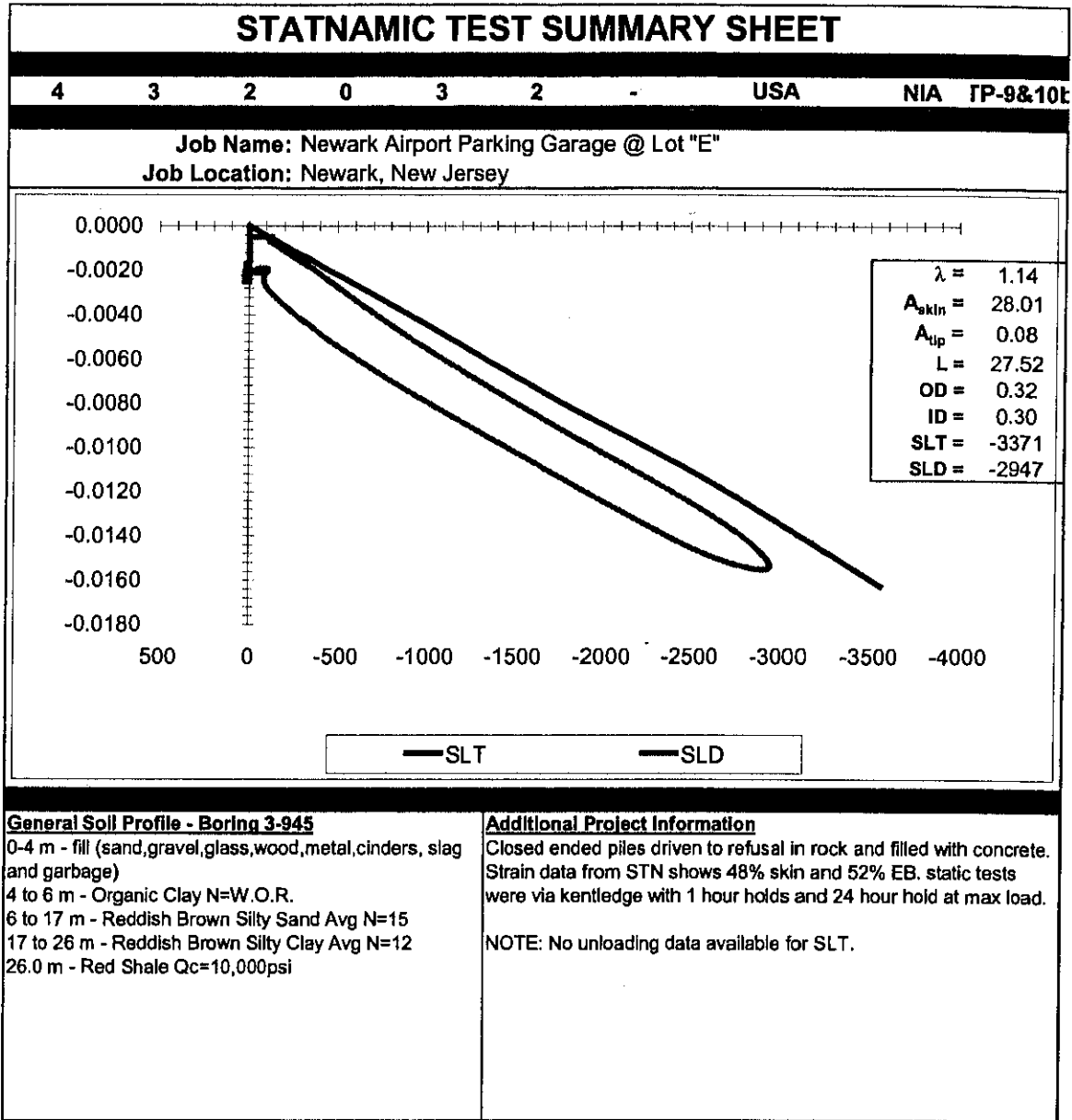
Appendix B Part B



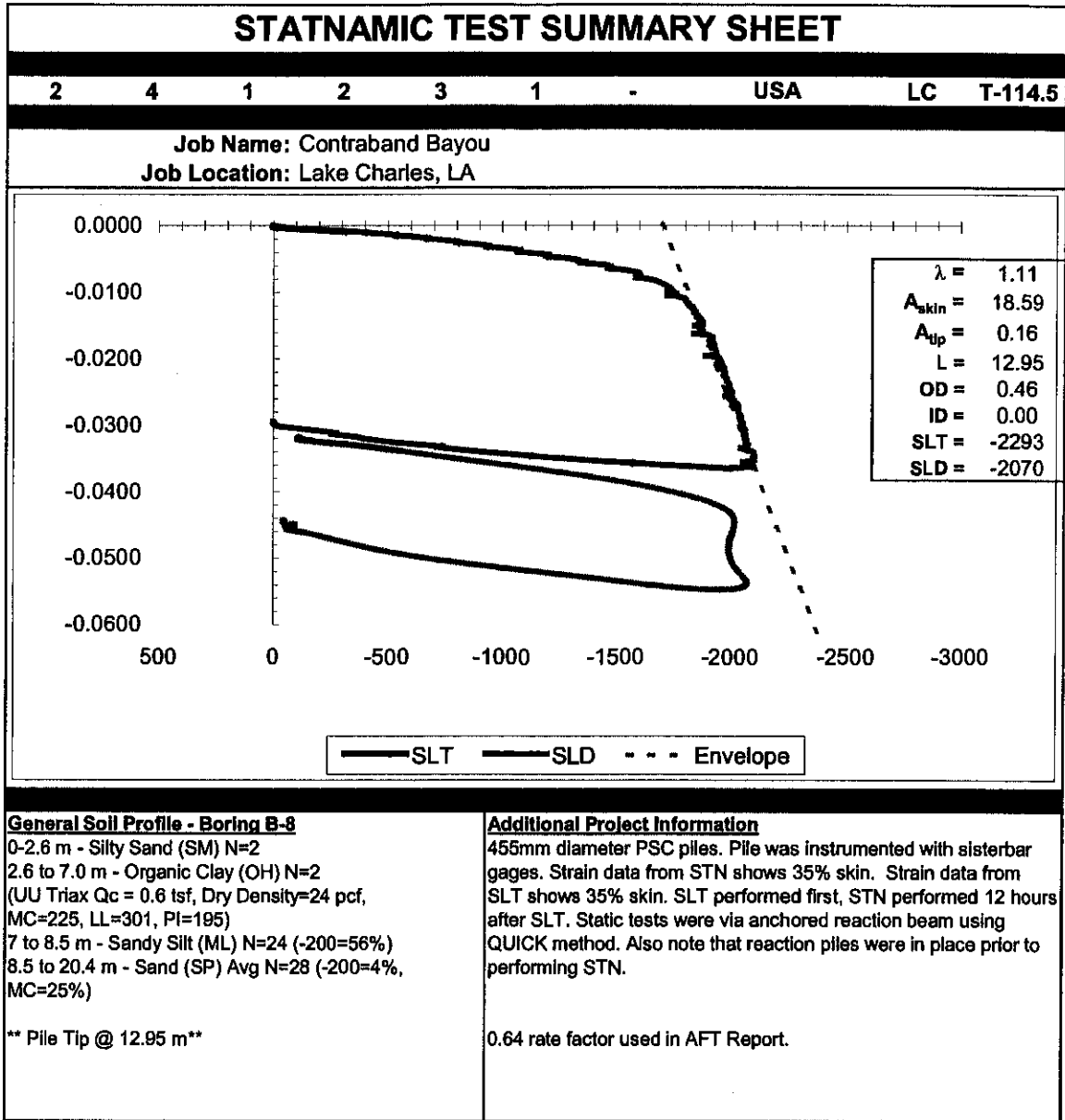
Appendix B Part B



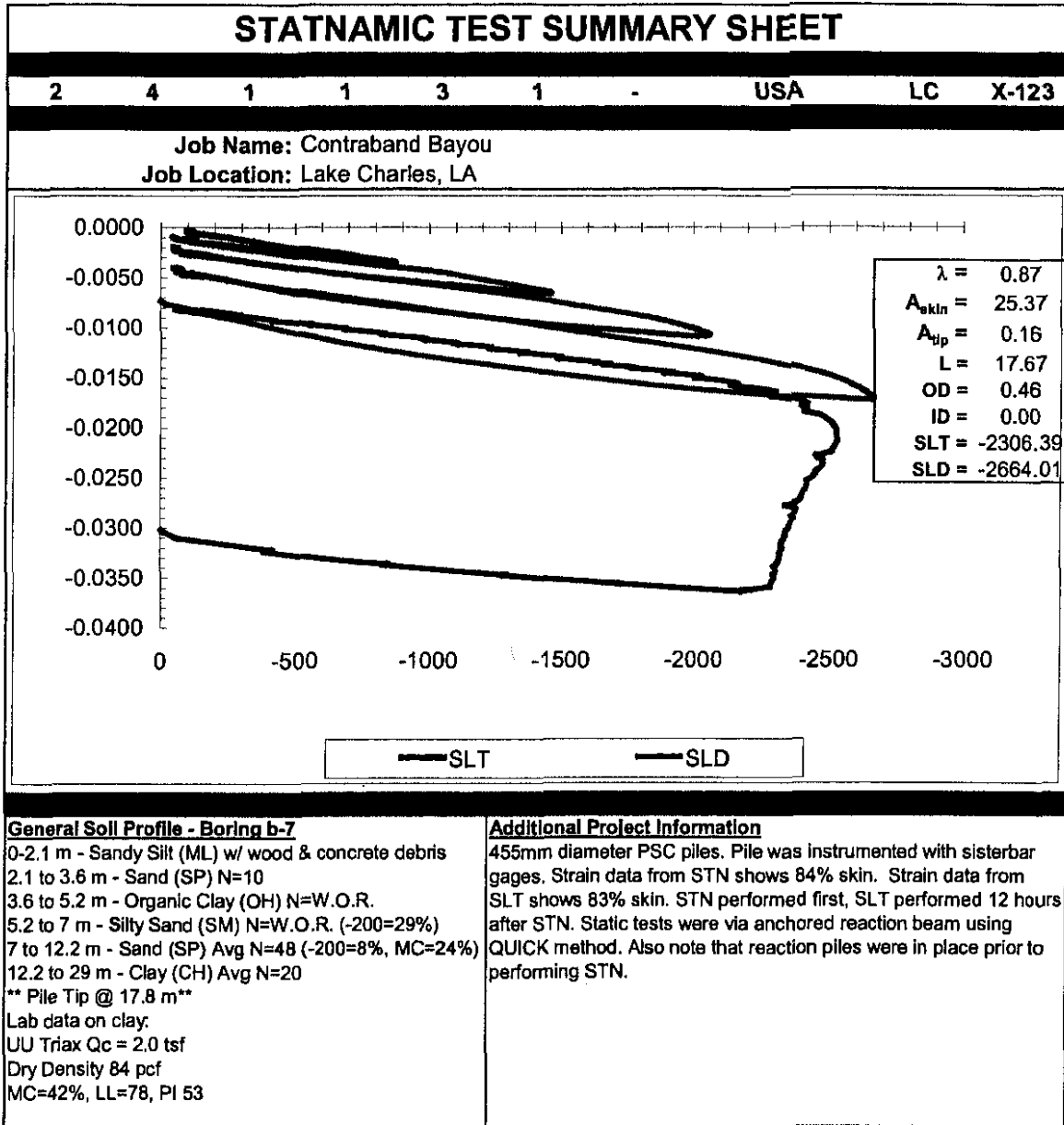
Appendix B Part B



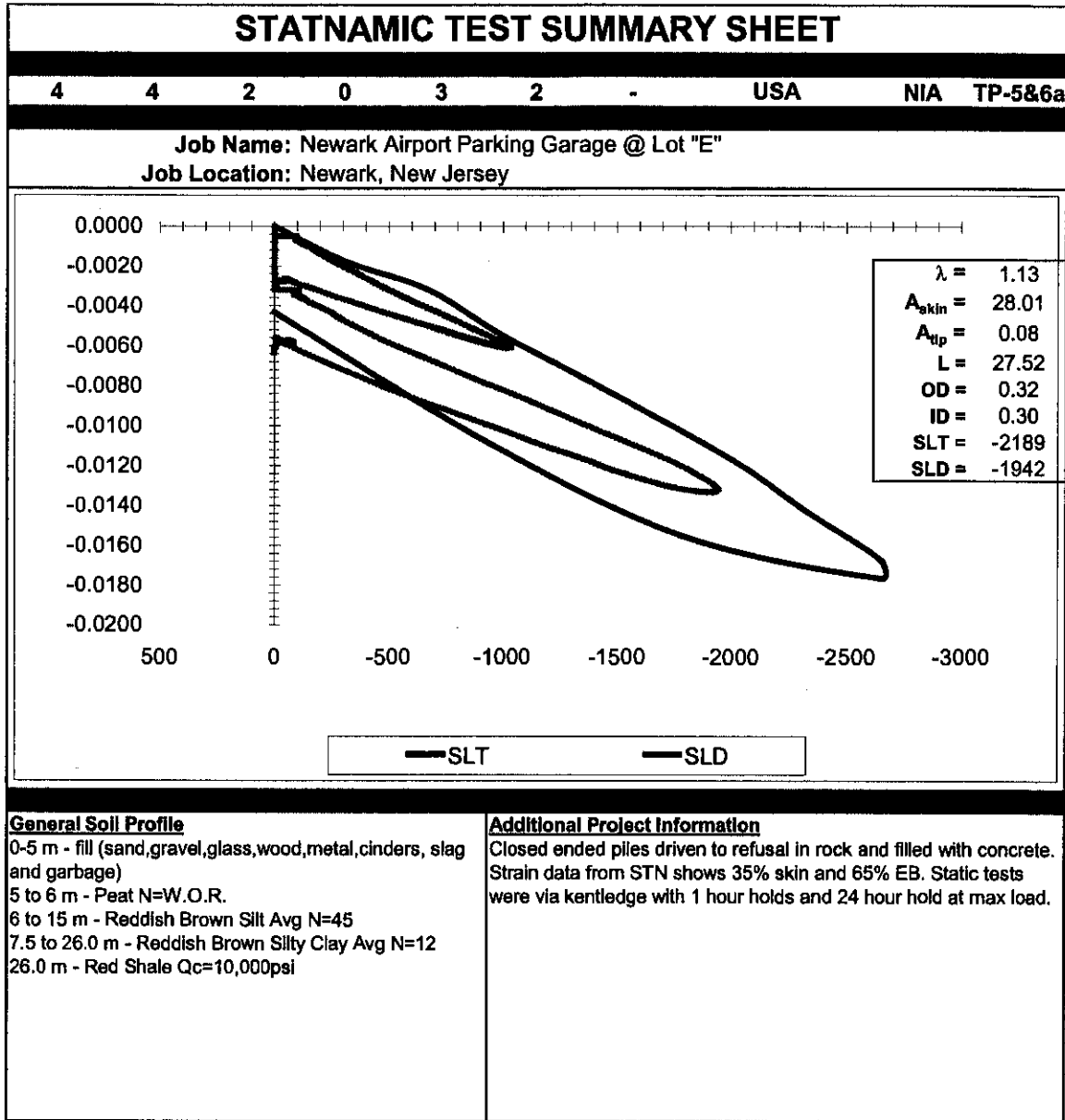
Appendix B Part B



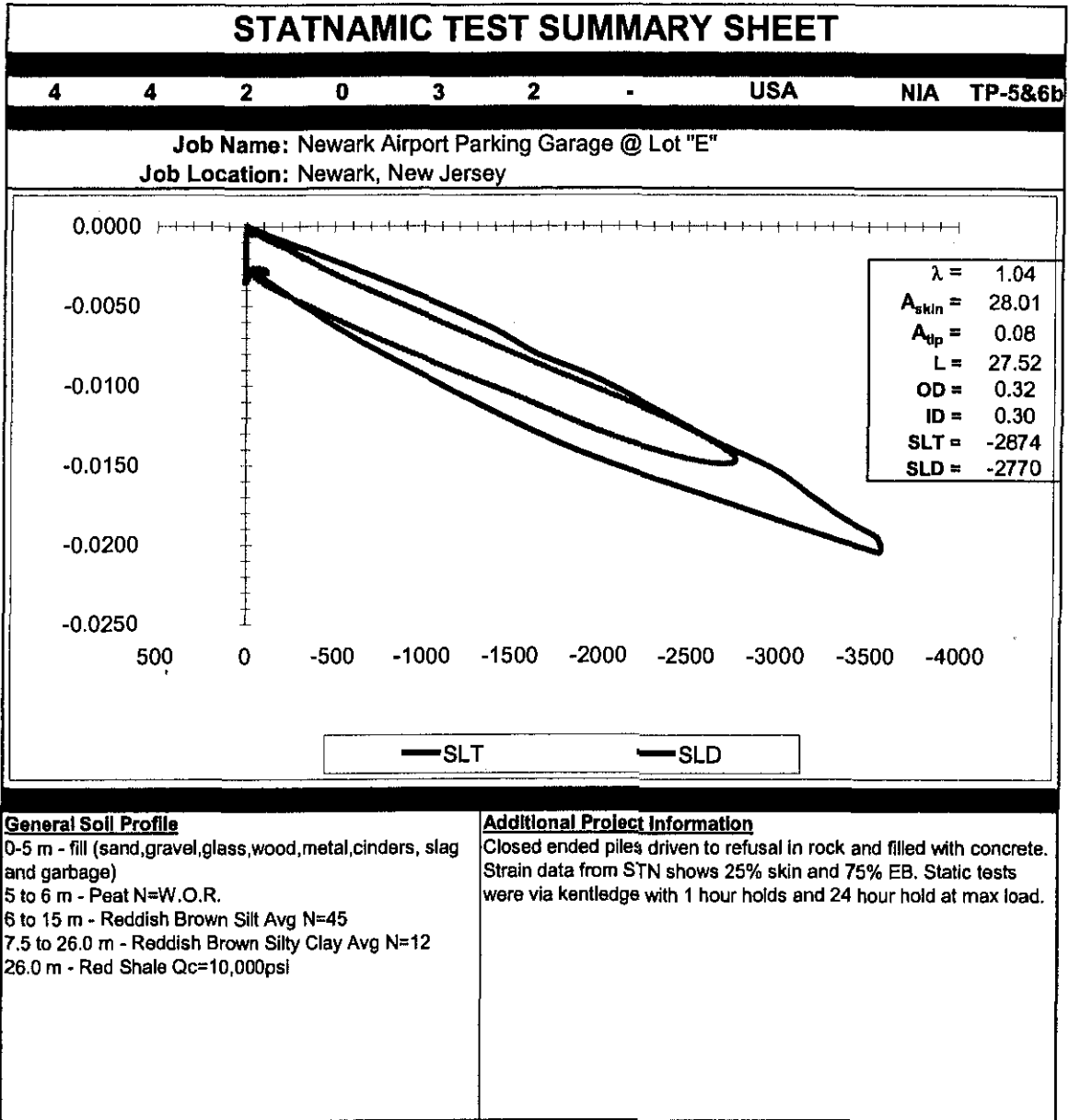
Appendix B Part B



Appendix B Part B



Appendix B Part B



PART C

Database of Simbat Analyses (Long, 2001)

Table 1. SIMBAT Database-Pile in Rock-1

Location	Pile No.	Ave. Diameter mm	Rock Socket m	Length m	SWL kN	Settlement at SWL mm	Settlement at 1.5SWL kN	Max R _{dynamic} kN	Comments
Heatherfield Carrigaline Co. Cork						Dynamic			Clay with boulders and silty gravel over pressured bedrock at pile toe.
	14	250		6.0	400	2.10	3.51		
	8/C	250		5.5	400	2.80	4.61		
	5/A	250		7.0	400	2.35	4.18		
	6 3/4	250		2.5	400	2.40	4.21		
	14 3/4	250		2.5	400	2.15	3.66		
	14 3/4	250		6.0	400	2.30	3.81		
	TP1 3/4	250		5.0	400	2.15	3.68		
						Static			
8/C	250		5.5	400	2.52	6.13			
Chlef State Solicitors office Ship St. Dublin						Dynamic			Limestone with mudstone bands same pile static first
	8	300	2	11.0	1000	3.76	6.18		
	11	300	2	12.0	1000	4.01	6.43		
	34	300	2	9.0	1000	4.41	6.83		
	TP A	300	2	8.2	1000	4.37	6.64	2357	
	TP B	300	2	8.2	1000	4.24	6.96	2279	
						Static			
TP A	300	2	8.2	1000	3.76	5.81			
Heuston Strn. Dublin						Dynamic			Gravel over shattered Limestone rock
	6a	305	0	10.0	750	3.49	5.91		
	6b	305	0.7	11.7	750	4.35	7.37		
	B7	168	0.5	11.5	500	4.91	8.08	872	
	N9	168	0.5	11.5	500	4.96	7.53	802	
	6e	168	0.5	11.5	500	4.36	7.08		
						Static			
6h	168	0	11.0	500	3.45	5.81			
RCSI St. Stephen's Green Dublin						Dynamic			Nainly strong Limestone with weak bances
	7a	171	1.17	7.5	400	2.65	4.18	708	
	7b	171	1.17	7.5	400	2.74	4.55	680	
						Static			
7c	171	5.67	12.0	400	2.50	4.60			

SWL=Specified Working Load

Table 1. SIMBAT Database-Pile in Rock-2

Location	Pile No.	Ave. Diameter mm	Rock Socket m	Length m	SWL kN	Settlement at SWL mm	Settlement at 1.5SWL kN	Max R _{dynamic} kN	Comments
Geomes Hill Dublin						Dynamic			Boulders from 4.2-6.8m
	12a	375		7.0	1000	3.85	6.19		
	12b	375		7.0	1000	5.13	8.30		
						Static			
	12c	375		7.0	1000	3.88	7.12		
Earisfort Tce. Dublin						Dynamic			Limestone and weak mudstone
	18a	300	1.00	10.5	700	3.74	5.86		
	18b	300	1.00	10.0	700	3.89	6.01		
						Static			
	18c	275	1.00	9.3	700	2.68	4.25		
Oliver Bond Street NCAD						Dynamic			Strong Limestone and moderate mudstone
	1a	375	1.53	8.0	1000	5.78	9.11	1868	
	1b	375	1.53	8.0	1000	6.03	8.9	1660	
	1c	375	1.53	8.0	1000	5.23	8.4	1711	
	1d	375	1.53	8.0	1000	5.41	9.18	1909	
	1e	375	1.53	8.0	1000	6.43	9.3	1790	
					Static				
	1f	375	2.73	9.2	1000	3.45	5.8		
Shannon Airport Co. Clara						Dynamic			Slightly to highly weathered Limestone
	13a	305	2.09	6.7	600	2.2	3.86		
	13i	305	0.09	4.7	600	2.3	3.66		
	13n	305	0.00	4.6	600	1.71	3.06		
	13o	305	0.19	4.8	600	1.9	3.26	926	
						Static			
	13p	305	1.69	6.3	600	1.85	2.85		
	13q	305	0.39	5.0	600	1.44	2.20		
Georges Quay Dublin						Dynamic			Moderately strong limestone with mudstone banks
	16a	375	5.30	11.0	1000	3.33	5.34		
	16b	375	5.30	11.0	1000	3.43	5.24		
	16c	375	5.30	11.0	1000	3.92	6.13		
						Static			
	16d	375	5.30	11.0	1000	2.05	3.55		

Table 1. SIMBAT Database-Pile in Rock-3

Location	Pile No.	Ave. Diameter <i>mm</i>	Rock Socket <i>m</i>	Length <i>m</i>	SWL <i>kN</i>	Settlement at SWL <i>mm</i>	Settlement at 1.5SWL <i>kN</i>	Max R _{dynamic} <i>kN</i>	Comments
Fitz's Boreen Cork						Dynamic			Very strong sandstone shale 5.5-8.1m
	17a	280	1.00	7.6	600	3.05	4.56		
	17b	280	1.00	7.6	600	2.97	4.93		
						Static			
	17c	280	1.00	7.5	600	2.39	4.26		
Castle St. Dublin						Dynamic			Limestone
	20a	375	1.00	10.0	1000	8.14	12.2		
	20b	375	0.50	9.4	1000	8.52	12.8		
	20c	375	2.50	11.4	1000	8.81	13.1		
						Static			
	20d	375	0.50	9.6	1000	3.13	5.04		
	20e	375	0.50	9.6	1000	5.98	13.85		
Xerox Dunduk mini-piles						Dynamic			Moderately strong to strong sandstone with siltstone bands same pile static first
		192		3.9	350	2.40			
		192		4.1	350	2.50			
		192		5.8	350	3.05			
		192		5.0	350	3.20			
		192		5.0	350	2.95			
		192		3.3	350	2.98			
		192		5.3	350	2.23			
		192		4.9	350	2.83			
		192		3.8	350	2.52			
						Static			
		192		4.6	350	2.20			
		192		4.7	350	3.18			
						Dynamic			
		305		5.0	550	2.05			
		305		3.8	550	2.55			
	305		5.0	550	2.70				
	305		7.0	550	2.58				
	305		4.2	550	2.82				
	305		5.0	550	2.42				

Table 1. SIMBAT Database-Pile in Rock-4

Location	Pile No.	Ave. Diameter <i>mm</i>	Rock Socket <i>m</i>	Length <i>m</i>	SWL <i>kN</i>	Settlement at SWL <i>mm</i>	Settlement at 1.5SWL <i>kN</i>	Max $R_{dynamic}$ <i>kN</i>	Comments
Xerox Dunduk mini-piles		305		5.8	550	2.46			Moderately strong to strong sandstone with siltstone bands
		305		5.5	550	2.34			
		305		4.3	550	1.74			
		305		4.3	550	2.88			
		305		5.0	550	2.64			
		305		4.4	550	1.96			
		305		5.0	550	1.75			
		305		5.9	550	2.45			
		305		6.0	550	2.46			
		305		6.0	550	2.28			
		305		6.0	550	2.82			same pile static first
		305		6.0	550	2.24			
		305		3.9	550	2.36			
		305		5.0	550	2.49			
		305		5.0	550	2.10			
						Static			
		305		7.5	550	3.64			
	305		4.3	550	4.00				

Table 2. SIMBAT-Datrabase-Piles in Clay-1

Location	Pile No.	Ave. Diameter mm	Length m	SWL kN	Settlement at SWL mm	Settlement at 1.5SWL kN	Max Rdynamic kN	Comments
Marrowbone lane Dublin					Dynamic			Borehole shows a stiff black silty, gravelly clay with frequent cobbles and boulders
	54	300	11	600	3.74	5.4	1056	
	72	300	8	600	3.49	5.31		
	75	300	8	600	4.48	6.9		
					Static			
	TP1	300	7.5	500	3.88	6.62		
Custon House Dublin					Dynamic			Borehole shows a black Dublin boulder clay
	75A	178	13	300	2.71	4.12		
	77	178	13	300	3.19	4.4		
					Static			
	TP1	178	13	300	1.2	2.12		
Dublin Airport					Dynamic			Borehole shows a very stiff gravelly clay with cobbles and boulders pile dailure at 450kN
	TP1	200	7	250	2.31	3.57		
	TP2	150	7	250	1.83	2.96		
	TP3	150	7	250	1.91	2.81		
					Static			
	TP5	150	7	250	6.8	10.38		
	TP6	150	7	250	1.35	2.78		
TP7	150	7	250	1.95	3.01			
Fish Auction Hall Howth					Dynamic			Boulder clay
	5a	210	11.5	600	9.55	14.4		
	5b	210	11.3	600	9.64	14.7		
	5c	210	11	600	8.77	13.4		
					Static			
	5d	210	9.5	300	2.4	3.95		
	5e	210	9	300	4.3	7.6		
	5f	210	11.5	300	3.9	6.95		
5g	210	11	300	4.8	7.97			

Table 3. SIMBAT-Database-Pile in Sand and Gravel-1

Location	Pile No.	Ave. Diameter mm	Length m	SWL kN	Settlement at SWL mm	Settlement at 1.5SWL kN	Max Rdynamic kN	Comments
Smithwicks Brewerv Klikennv					Dynamic			
	3a	375	11.0	1200	5.4	8.73	2011	
	3b	375	11.0	1200	5.66	9.13	1967	
	3c	375	13.8	1200	Static 3.58	8.02		
Athlone					Dynamic			Gravels at varicos deoths
	4d	192	6.0	350	2.7	4.38	584	
	4m	192	6.0	350	2.5	3.91	584	
	4n	192	6.0	350	2.54	4.05	541	
	4t	192	6.0	350	Static 1.4	4.85		
Blenerville Bridone Tralee					Dynamic			
	A19	200	10.5	300	2.17	3.58	554	
	J1	200	10.5	300	2.24	3.45	516	
	J5	200	8.5	300	2.45	4.06	469	
	8i	200	9.0	300	Static 1.79	3.52		
Beechwood Middleton Co. Cork					Dynamic			
	plot 7/8	250	6.0	450	3.26	5.67		
	polt 5/6	250	7.0	450	2.66	4.32		
	plot3/4	250	8.0	450	2.81	4.93		
	plot 13/14	250	8.5	450	3.31	5.43		
	plot 25/26	250	8.0	450	3.36	5.33		
	plot 27/28	250	8.0	450	2.96	5.07		
	plot 21/22	250	8.0	450	2.96	4.47		
	plot 29/30	250	8.0	450	3.06	4.88		
	plot 37/38	250	8.0	450	2.81	4.47		
	plot 35/36	250	7.7	450	3.06	4.72		
	plot 33/34	250	7.2	450	2.91	4.42		
	plot 31/32	250	7.2	450	3.16	4.97		
plot 2	250	8.4	450	2.96	4.63			
plot1	250	8.2	450	2.86	4.37			

Table 3. SIMBAT-Database-Pile in Sand and Gravel-2

Location	Pile No.	Ave. Diameter mm	Length m	SWL kN	Settlement at SWL mm	Settlement at 1.5SWL kN	Max Rdynamic kN	Comments
Beechwood Middleton Co. Cork					Static			
	TP1	250	7.5	450	3.05	4.39		
	TP2	250	8.0	450	5.34	8.08		
Douglas Cr. Cork					Dynamic			Very dense fine to coarse oravel
	45A	300	8.0	300	1.30	2.56		
	36	300	7.0	300	1.50	2.51		
	30B	300	8.0	300	1.35	2.36		
					Static			
	41	300	8.0	300	1.21	1.94		
Abbev St. Kilkenny					Dynamic			Sand Oravel and cobbels
	2a	192	9.0	350	2.64	3.85		
	2b	192	9.0	350	2.73	4.09		
					Static			
	2c	192	9.0	350	1.4	2.05		
Duaciss Adartments cork					Dynamic			Dense anoutar limestone oravel with cobbels
	46	350	12.0	600	2.61	4.62		
	91	350	13.0	600	2.66	4.27		
	74	350	13.0	600	2.48	3.84		
	5	350	11.0	600	2.36	3.77		
	103	350	13.0	600	2.91	4.52		
					Static			
	59	350	9.0	600	1.61	2.63		
Caash and Co. Carcline Street Cork					Dynamic			Medium-dense to dense reddisk sandy fine to coarse oravel
	TP	300	14.0	550	2.96	3.82		
	11	300	14.0	550	3.36	4.97		
	40	300	14.0	550	3.42	5.13		
					Static			
	TPA	350	14.0	500	1.37	2.46		
Bow Lane Cleansing Dept.					Dynamic			Very dense crevel from 7-8m
	14a	160	8.0	250	2.31	3.72		
	14b	160	8.0	250	2.35	3.96		
					Static			
	14c	160	8.5	250	1.74	3.38		

Table 3. SIMBAT Database-Pile in Sand and Gravel-3

Location	Pile No.	Ave. Diameter mm	Length m	SWL kN	Settlement at SWL mm	Settlement at 1.5SWL kN	Max Rdynamic kN	Comments	
Mary Street Limnck					Dynamic			Dense gravel with hard brown boulder clay	
	TP1	300	7.0	450	2.11	3.32			
	TP2	300	7.0	450	2.34	3.70			
	TP3	300	7.0	450	2.19	3.40			
	TP4	300	7.0	450	1.96	3.12			
						Static			
Grand Canal Cuav Dublin					Dynamic				
	10a	800	8.0	1700	3.16	5.88			
	11a	800	8.5	1700	3.1	6.12			
	11b	800	8.5	1700	3.06	5.33			
	11c	800	8.0	1700	2.96	5.23			
	11d	800	8.6	1700	3.41	6.12			
	11e	800	10.5	1700	3.16	5.72			
						Static			
	11f	800	10.5	1700	1.95	3.56			
11g	800	8.0	1700	5.11	7.52				
Sean Mc Dermot St. Dubin					Dynamic			Gravel with sand and cobbles from 5.5m to bottom Above is clay	
	15a	285	7.0	700	3.25	5.37			
	15b	285	7.0	700	3.64	6.56			
	15c	285	7.0	700	3.52	5.44			
	15d	285	7.0	700	4.50	9.13			
						Static			
Teoca Cork					Dynamic			Silt to 10.6m with gravel this 19e failed between 800kN to 1030kN	
	19a	280	14	750	5.93	8.95			
	19b	280	14	750	5.56	8.8			
	19c	280	14	750	5.00	7.62			
	19d	280	14	750	5.49	8.31			
						Static			
	19e	280	14	750	4.86				
19f	280	14	750	4.91	7.92				

Table 3. SIMBAT-Database-Pile in Sand and Gravel-4

Location	Pile No.	Ave. Diameter mm	Length m	SWL kN	Settlement at SWL mm	Settlement at 1.5SWL kN	Max Rdynamic kN	Comments	
Excise St. Quay Athione					Dynamic			Dynamic to failure Sandy gravel on bottom	
	TP1	323	7.5	600	7.5	13.60			
	22b	323	8.0	600	7.2	12.30			
	22c	323	9.1	600	6.6	9.91			
	22d	323	11.5	600	5.4	8.24			
						Static			
	TP1	323	7.5	600	9.2	17.40		test to failure	
Grand Parade Cork					Dynamic			Medium dense small gravel with fine sand	
	TP1	350	14	600	3.52	5.33			
	TP2	350	14	600	3.02	4.83			
						Static			
	TPA	350	14	600	1.84	3.15			
Tibali Dock Cork					Dynamic			12m of soft alluvial silt over medium dense gravels	
	122	450	21	1000	4.11	6.68			
	143	450	21	1000	4.36	6.77			
	72	450	21	1000	3.82	6.08			
	73	450	21	1000	3.77	6.03			
	178	450	21	1000	4.21	6.63			
	109	450	21	1000	3.77	6.03			
						Static			
		PP1	450	21	1000	7.48	10.63		
	85	450	21	1000	8.36	13.52			

22-2/1 COPY NO.

NCHRP 21-08

INNOVATIVE LOAD TESTING SYSTEMS

APPENDIX C

Codes

Prepared for
National Cooperative Highway Research Program
Transportation Research Board
National Research Council

By

Samuel G. Paikowsky
Geosciences Testing and Research Inc. (GTR)
55 Middlesex St., Suite 225
N. Chelmsford, MA. 01863

Zenxuan (Frank) Li
Geotechnical Engineering Research Laboratory
Department. of Civil and Environmental Engineering
University of Massachusetts
Lowell, MA 01854

August 2002

TABLE OF CONTENTS

Part A – Chinese Code for High Strain Testing of Piles	A-1, A-15
Part B – Draft of Japanese Code for Rapid Load Test	B-1, B-5

PART A

Chinese Code for High Strain Testing of Piles



**Chinese Code JGJ 106-97 Specification for
High Strain Dynamic Testing of Piles (1997)
(Driven Piles and Drop Weight Systems)**

Translated by: Frank Li, April 2001

Reviewed by: Samuel G. Paikowsky

**Geotechnical Engineering Research Laboratory
Department of Civil and Environmental Engineering
University of Massachusetts Lowell, MA 01854**

1. General Principles

- 1.0.1 This specification unites the methods of high-strain dynamic testing and ensures the high quality of pile testing.
- 1.0.2 According to the code for pile foundation technique (JGJ94-94) that are used now, this principle is suitable for the determination of the ultimate bearing capacity and the evaluation of the integrity of the pile foundation.
- 1.0.3 When the high strain dynamic testing method is used, the comparison between dynamic and static testing which is reliable and under the same condition should be available.
- 1.0.4 In addition to this code, the high strain dynamic testing should also comply with other relevant codes currently in use.

2. Symbols

2.0.1 Material Properties

- c Speed of stress wave propagation
- E Young's modulus of the pile
- R_c Ultimate static bearing capacity obtained by the Case method
- R_u Ultimate soil static resistance force
- Z Pile's impedance
- ρ Mass density of the pile's material

2.0.2 Impact Parameters

- a Particle acceleration
- E_n Energy transferred from hammer to pile
- F Force on the pile head caused by hammer
- S_q Maximum elastic soil displacement
- t_l The time of maximum velocity

- t_r The period extends from t_0 to the time of maximum force
- t_x The time corresponding to the location of change in the pile's impedance changed
- V Particle velocity
- σ_p Maximum compression stress in the pile
- σ_t Maximum tension stress in the pile
- 2.0.3 Geometry Parameters
 - A Cross sectional area of the pile
 - L Pile length below the sensors
 - M Pile mass
- 2.0.4 Calculation Parameters
 - J_c Case damping coefficient
 - β Parameter of pile integrity

3. Basic Requirements

- 3.0.1 The results of the high strain dynamic testing can be used for the following purposes:
 - 3.0.1.1 Monitor the strain in the pre-cast pile and efficiency of the hammer. Select the equipment and the parameters.
 - 3.0.1.2 Select the reasonable pile type and the length of the pile.
 - 3.0.1.3 Estimate the soil resistance distribution around the pile and at the bottom of the pile. Simulate Q-s curve in the static load test.
- 3.0.2 The following material should be offered when the high strain dynamic test is required.
 - 3.0.2.1 The name of the project and the companies who design and construct the structure.
 - 3.0.2.2 The report of soil investigation in the field.
 - 3.0.2.3 The design of the pile foundation.
 - 3.0.2.4 The construction report for the pile foundation.
 - 3.0.2.5 The report for the concrete strength in the pile.
 - 3.0.2.6 The elevation of the top of the pile before and after the consolidation.
- 3.0.3 The amount of the tested pile should not be less 2% of the total piles and at least 5 piles should be tested when the geological condition, the pile type, and the equipment are same in one project which is constructed by one company.
- 3.0.4 The high strain dynamic testing is a kind of non-destructive testing.

4. Equipments for the Testing

- 4.0.1 The equipment used should have the ability to display, record, save the

tested force and acceleration, and analyze the data and print the results. The properties of the equipment should satisfy the following conditions:

- 4.0.1.1 The precision of the analog to digital conversion of the equipment for data acquisition should not be less than 10 digits. The difference between different channels should not be less than 50 μ S.
- 4.0.1.2 The sensor for measuring the force should be strain gauge. The frequency of harmonic vibration of the sensor should be larger than 2kHz. The nonlinear deviation should be less than +1% in the range of 1000 μ ε. The reduction of the sensitivity resulted by the resistance of the conductive wire should be less than 1%.
- 4.0.1.3 The change of the sensitivity of the installed accelerometer should be less than +5% in the range of 2~3000Hz. The nonlinear deviation of the amplitude should be less than +5% in the range of 10000m*s-2.
- 4.0.2 The sensor should be calibrated once every year.
- 4.0.3 The hammer used should have homogeneous mass and symmetric shape. The bottom of the hammer should be smooth. It is better that the hammer is made of steel. When a free falling hammer is used, the weight of it should be larger than 1% of the estimated ultimate bearing capacity of the pile.
- 4.0.4 The set of the pile can be measured using a level or a laser displacement measuring device.

5. Set of Parameters for the Field Testing

5.1 Determination of the parameters of the pile

- 5.1.1 The cross-section area of the pile, wave velocity in the pile, the density and the elastic modulus of the pile at the tested position should be determined according to the real condition.
- 5.1.2 The length and the cross-section area of the pile below the testing point should be determined according to the following specification:
 - 5.1.2.1 The length below the testing point is the distance between the testing point and the bottom of the pile.
 - 5.1.2.2 For a pre-cast pile, the length and the cross-section area of the pile can be offered by the construction company.
 - 5.1.2.3 For a cast-in-situ pile, the length and the cross-section area of the pile can be obtained from the construction record.
- 5.1.3 The wave velocity in the pile can be determined as follows:
 - 5.1.3.1 For a steel pile, the wave velocity can be taken as 5120m/s.
 - 5.1.3.2 For a pre-cast concrete pile, the average wave velocity measured before the pile is driven can be taken as the wave velocity in the pile.

5.1.3.3 For a cast-in-situ pile, when the length of the pile is known, the average velocity can be determined by stress wave refraction method. If the refraction signal from the bottom of the pile is not clear, the velocity can be determined based on the strength of the concrete and other parameters.

5.1.4 The density of the pile should satisfy the following conditions:

5.1.4.1 For a steel pile, the density should be 7.85t/m³.

5.1.4.2 For a pre-cast concrete pile, the density should be between 2.45 and 2.55t/m³.

5.1.4.3 For a cast-in-situ concrete pile, the density should be 2.40t/m³.

5.1.5 The elastic modulus of the pile can be calculated by the following equation,

$$E = \rho \cdot c^2$$

Here,

E Elastic modulus of the pile (M Pa);

C The velocity of the stress wave in the pile (m/s);

ρ The density of the pile (t/m³).

5.2 Sampling frequency and the length of the data record:

5.2.1 The sampling frequency should be between 5 and 10kHz.

5.2.2 The sample length for every signal should not be less than 1024.

5.3 Calibration coefficient for the stress gauge and accelerometer:

5.3.1 The calibration coefficient of the stress gauge and the accelerometer should be set according to the value offered by the manufacturer.

6. Testing Technique

6.1 General principle

6.1.1 When the bearing capacity is tested, the duration between the testing and the end of the driving should satisfy the following requirements:

6.1.1.1 The duration after the end of driving should not be less than the time listed in Table 6.1.1 for a pre-cast pile.

Table 6.1.1 Duration after the end of driving

Type of Soil		Duration (Days)
Sand		7
Silt		10
Clay	Unsaturation	15
	Saturated	25

- 6.1.1.2 For a cast-in-situ concrete pile, the test time should be after the concrete reached the designed strength and the duration after installation should not be less than that listed in Table 6.1.1.
- 6.1.2 The time effect of bearing capacity of the pre-cast concrete pile can be determined by a re-strike.
- 6.1.3 The end of the test should be determined according to the set and the signal quality.
- 6.1.4 When a free hammer is used, the hammer should be heavy and the height of the hammer should be low. The stroke should be less than 2.50m.

6.2 Preparation

- 6.2.1 To make sure that the force can be transferred correctly, the top of a cast-in-situ concrete pile, a pre-cast concrete pile with severely damaged pile top and a steel pile with deformation on the top should be repaired or reinforced before the test. The repair or reinforcement can be carried out according to Appendix A.
- 6.2.2 A cushion should be put on the top of the pile and it should be changed frequently. The cushion should be made up of homogeneous material such as plywood, wood and fiber plate.

6.3 The installation of the sensor

- 6.3.1 To monitor and reduce the effect of eccentric impact, two strain gages and two accelerometers should be installed. The installation of the sensors should satisfy the following conditions:
 - 6.3.1.1 The sensor should be installed symmetrically on both sides of the pile some distance under the top of the pile (shown in Fig. 6.3.1). The distance between the sensor and the top of the pile, for a general pile type, should not be less than two times the diameter or the side of the pile. For a pile with large diameter, it should not be less than 1 times the diameter or the side of the pile.
 - 6.3.1.2 The surface of the pile where the sensor is installed should be flat and there is no deficiency or fractured area around the sensors location. The material and the cross-section area at the position where the sensor is installed should be the same as that of the original pile.
 - 6.3.1.3 The center of the strain gage and the accelerometer should be at the same horizontal line. The distance between them should not be larger than 10cm.
- 6.3.2 When an anchor is used to attach the sensor, the installation should satisfy the following conditions:
 - 6.3.2.1 The bolt hole should be vertical along the axis of the pile. The diameter of the hole should be suitable to the bolt.

6.3.2.2 The fixing surface of the sensor should be in tight contact with the surface of the pile after installation. The preliminary deformation should be less than the specified value. There should not be a relative slippage during the testing.

6.3.3 When continuous hammering test is used, the conductive wire of the sensor should be fixed on the pile in case it is damaged by the vibration.

6.4 Requirement for the testing technique

6.4.1 Make sure that the testing system is under the normal condition before testing. Check the set parameters according to 5.1 to 5.3. After the checking, the test can be started.

6.4.2 The set under every hammer blow should be measured. To generate plastic deformation in the soil around the pile, the set every time should not be less than 2.5mm and not larger than 10mm.

6.4.3 The data should be checked during the testing. When there is some problem in the testing system or there is distinct deficiency or the degree of the deficiency is increased, the testing should be stopped and checked.

6.4.4 When the testing is to measure the integrity of the pile, the weight of the hammer and the stroke can be reduced, the thickness of the mat can also be reduced if the clear refraction signal from the bottom of the pile can be measured.

7. Determination of the Bearing Capacity of the Pile and the Evaluation of the Pile Integrity

7.1 Selection of the signal

7.1.1 The signal can not be used for calculation if any of the following conditions happen:

1. The curve of the force in the time domain does not go to zero at the end.
2. An eccentric impact results in a tensile stress on one side.
3. The sensor does not work properly.
4. There is crack or plastic deformation at the position where the sensor is installed.

7.1.2 When the bearing capacity is tested, the selection of the signal should satisfy the following conditions:

7.1.2.1 During the driving of the pre-cast concrete pile, the one with the higher energy in the last blow should be selected.

7.1.2.2 In the re-striking of the pre-cast pile and testing of the cast-in-situ pile, the blow with higher energy should be selected.

7.1.3 Before analyzing the data, the average wave velocity in the pile can be

obtained from the tested signal according to the following methods:

7.1.3.1 When the refraction signal from the bottom of the pile can be clearly detected, the velocity can be calculated from the length of the pile and the time difference between the starting point of the downward wave and that of the upward wave.

7.1.3.2 When the refraction signal from the bottom of the pile is not clear, the velocity can be selected according to the length of the pile, the reasonable value of the wave velocity in the concrete and the velocity in adjacent piles.

7.2 Determination of the pile bearing capacity according to the signal matching techniques

7.2.1 The mechanical model used in signal matching techniques should satisfy the following requirements:

7.2.1.1 Mechanical model of the soil should reflect the real stress-strain property.

7.2.1.2 The mechanical model of the pile should reflect the real properties. One dimension elastic rod model can be used.

7.2.2 The calculation in signal matching techniques should follow the following requirements:

7.2.2.1 The measured wave of velocity, force or upward wave can be used as a boundary condition for signal matching.

7.2.2.2 The time for signal matching should not be less than $5L/c$ and the duration after $2L/c$ should not be less than 20ms.

7.2.2.3 The selected parameters in signal matching should be reasonable in geotechnical engineering. The maximum elastic displacement (S_q) of the soil in every unit of the model should not be larger than the maximum calculated displacement of the pile unit.

7.2.2.4 The calculated curve and the measured curve should be matched at the end of the signal.

7.2.2.5 The calculated set and the measured set should match.

7.3 Determination of the bearing capacity of the pile using CASE method

7.3.1 The following condition should be satisfied when the CASE method is used to determine the bearing capacity of the single pile:

7.3.1.1 It is only suitable for a pile with medium or small diameter.

7.3.1.2 Without static load test, J_c should be determined using signal matching method. The number of tested piles with signal matching should not be less than 30% of the total number of the piles and also should not be less than 3 piles.

7.3.1.3 When it is used for cast-in-situ concrete piles, the material of

the pile should be homogeneous and the cross-section area of the pile should be uniform. A reliable experience is also required.

7.3.1.4 At the same site, for the same pile type and size, the difference between the ultimate value and the average value of the damping coefficient should not be greater than 0.1.

7.3.2 Using the Case method, the ultimate bearing capacity of a single pile can be calculated using the following equation:

$$R_c = (1 - J_c) [F(t_1) + Z \cdot V(t_1)]/2 + (1 + J_c) \cdot [F(t_1 + 2L/c) - Z \cdot V(t_1 + 2L/c)]/2$$

$$Z = A \cdot E/c$$

R_c	Ultimate static bearing capacity using CASE method (kN)
J_c	Case damping coefficient
t_1	The time of maximum velocity (ms)
$F(t_1)$	Force at the time t_1 (kN)
$V(t_1)$	Velocity at time t_1 (m/s)
Z	Pile's impedance (kN · s/m)
A	Cross sectional area of the pile (m ²)
L	Pile length below the sensors (m)

7.4 The integrity evaluation of the pile

7.4.1 While determining the integrity of the pile, the signal should be qualitatively checked first.

1. The wave of force and velocity (or upward wave) should be qualitatively analyzed to investigate the position and the condition of the deficiency.
2. Under continuous hammering, the expansion and the closure of the deficiency should be observed.

7.4.2 The integrity of the pile can be evaluated using signal matching techniques. The following conditions should be satisfied:

7.4.2.1 The selected parameters of the pile and soil in the signal matching should be within a reasonable range in geotechnical engineering.

7.4.2.2 According to the different types of piles, different parameters should be used in the matching analysis, using pile's impedance matching for cast-in-place pile or using connection matching for precast concrete pile.

7.4.3 For the pile with the same cross-area, β method can be used to evaluate the first defect below the top of the pile, which is described in Table 7.4.3.

7.4.3.1 The integrity coefficient (β) of the first defect can be

calculated using the following equation:

$$\beta = \frac{\{[F(t_1) + Z \cdot V(t_1)]/2 - \Delta R + [F(t_x) - Z \cdot V(t_x)]/2\}}{\{[F(t_1) + Z \cdot V(t_1)]/2 - [F(t_x) - Z \cdot V(t_x)]/2\}}$$

- β Parameter of pile integrity
 t_1 The time of maximum velocity (ms)
 t_x The time corresponding the location of change in the pile's impedance (ms)
 ΔR Estimated value of soil resistance force from the pile head to the location where the pile's impedance changes. Refer to figure 7.4.3

Table 7.4.3 Pile Integrity Evaluation

β	Evaluation
$\beta = 1.0$	Without deficiency
$0.8 \leq \beta < 1.0$	Slight deficiency
$0.6 \leq \beta < 0.8$	Clear deficiency
$\beta < 0.6$	Seriously damaged or broken pile

7.4.3.2 The position of the defect in the pile can be calculated using the following equation:

$$X = c \cdot (t_x - t_1)/2$$

Where, X is the distance between the position of the defect and the sensor.

7.4.4 When any of the following condition happens, the integrity of the pile can be evaluated according to the geological condition, construction method and signal matching techniques:

1. The diameter of the pile is enlarged in some position.
2. The cross-section area of the cast-in-situ concrete pile is not regular.
3. There is abnormality near the peak of the wave of force and velocity, and there is defect near the top of the pile.
4. The force wave is rising very slowly and the ratio between the force signal and the velocity signal is not reasonable.

7.4.5 When any one of the following condition happens, the integrity of the pile should be evaluated combined with other measuring method:

1. The refraction signal from the bottom of the pile is not clear although there is no abnormal refraction signal.
2. The cross-section area of the pile changes gradually or at many positions, and the change is relatively large.

8. Selecting Driving Equipment and the Pile Driving Monitoring Process

8.1 Driving equipment selection

8.1.1 For the selection of the pile type and length under a certain soil condition, the test pile should satisfy the following conditions:

8.1.1.1 The engineering geological condition at the position of the indicator pile should be representative of the site.

8.1.1.2 The indicator pile should be tested when the pile's tip penetrated into different soil layers. When the bearing stratum is thick, more than one test should be carried in any soil layer.

8.1.2 The bearing layer should be selected according to the relationship between the load and the set and geological investigation of the field.

8.1.3 The following conditions should be satisfied when the test pile is used to determine the bearing capacity:

8.1.3.1 The design load should be equal or smaller than the product of the total calculated static resistance (friction and tip) multiplied by a coefficient (1 over factor of safety) that is a function of the pile type, size, soil type and time of driving. (The code does not specify the actual factor of safety to be used.)

8.1.3.2 The duration between the re-strike and the end of the driving is shown in Table 6.1.1.

8.2 Monitoring the stresses in the pile during driving

8.2.1 The monitoring of the stress in the pile should satisfy the following condition:

8.2.1.1 The pile type and material should be identical to that of the piles used in construction. The hammer type, stroke and the hammer cushion should also be identical to those in the construction.

8.2.1.2 The tensile and compression stresses in the pile should be monitored during driving.

8.2.2 To measure the extreme stresses in the pile under impact, the monitoring should be carried out under the following conditions:

8.2.2.1 The tensile stress in the pile should be tested when it is estimated that the pile's tip penetrates a soft soil layer or it penetrates into a hard soil layer or into a soft soil layer between hard soil layers.

8.2.2.2 The tension stress should be measured when the pile's tip penetrates a hard soil layer or the soil resistance around the pile is relatively large.

8.2.3 The maximum compression stress in the pile should be calculated using the following equation:

$$\sigma_t = \{Z \cdot V(t_1 + 2L/c) - F(t_1 + 2L/c) - Z \cdot V[t_1 + (2L - 2X)/c] - F[t_1 + (2L - 2X)/c]\} / 2A$$

- σ_t Maximum tension stresses in the pile
- X Distance from the point of measurement (location of sensor) to the point of analysis

8.2.4 The maximum compression stress in the pile should be calculated using the following equation:

$$\sigma_p = F_{\max} / A$$

8.2.5 The controlled value of the maximum stress in the pile during driving should follow the section 5.5 in the code of pile foundation technique.

8.3 Monitoring the hammer's energy

8.3.1 The energy transferred from the hammer to the pile can be calculated by the following equation:

$$E_n = \int_0^T F \cdot V \cdot dt$$

- E_n Transferred energy (from hammer to pile)
- T The time length of the end of recorded signal

8.3.2 The hammer efficiency is monitored, the ratio between the transferred energy from the hammer to the pile and the hammer rating should be checked. It should satisfy the condition in Table 8.3.2.

Table 8.3.2 Hammer efficiency

Pile Type	Real Transferred Energy /Energy Rating
Single-Acting Diesel Pile Hammer	0.20~0.30
Steam Hammer	0.45~0.55
Free Falling Hammer	0.42~0.50

Shanghai (Foundation Design Code) DGJ-11-1999

Time Interval Before Restrike

Pile Type	Soil Type	Duration (days)
Driven Pile	Sand	> 14
	Clay	> 28
Drilled Shaft		> 28

中华人民共和国行业标准

基桩高应变动力检测规程

Specification for High Strain Dynamic Testing of Piles

JGJ 106—97

1997 北京



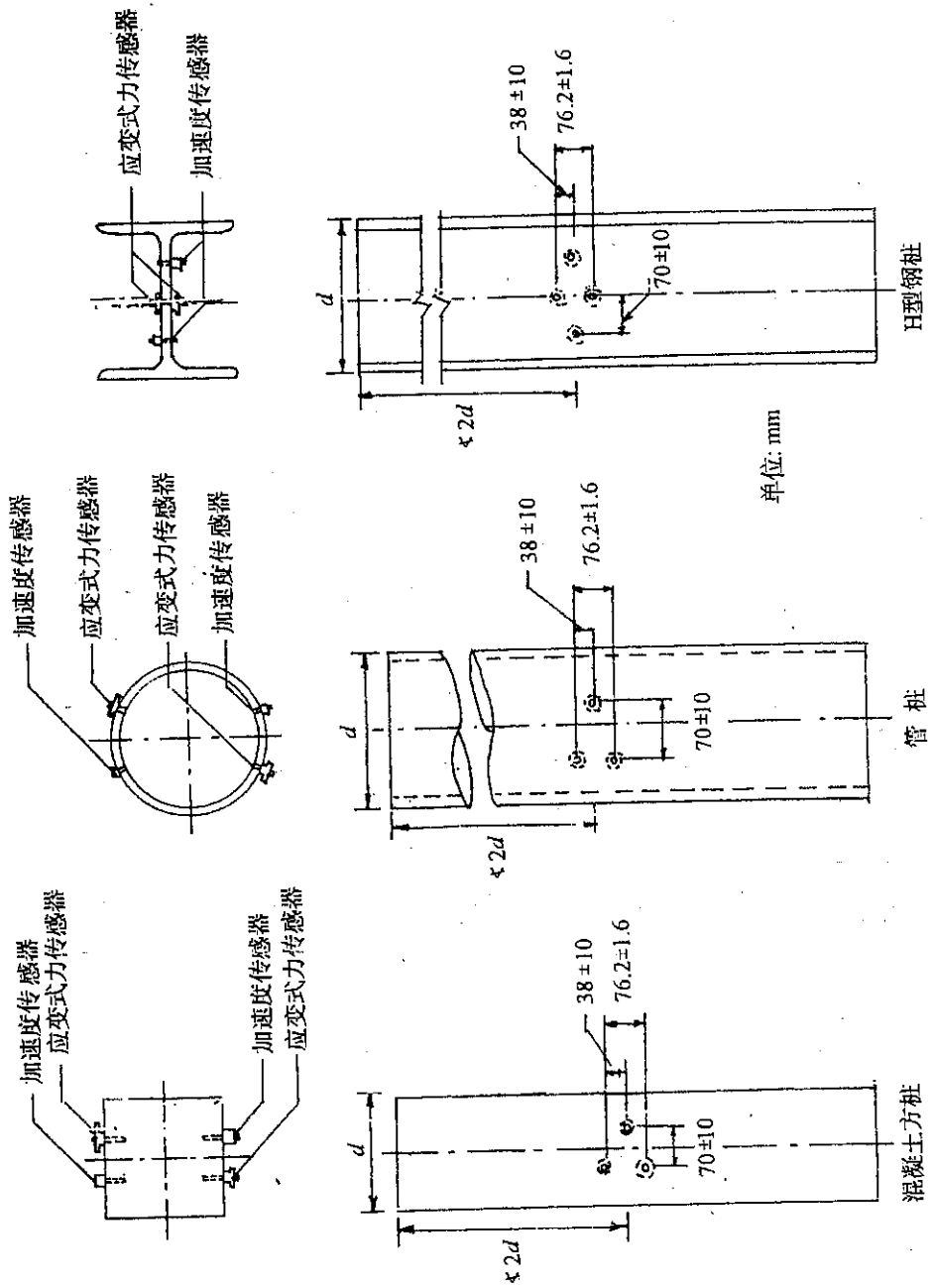


图 6.3.1 测点处传感器安装

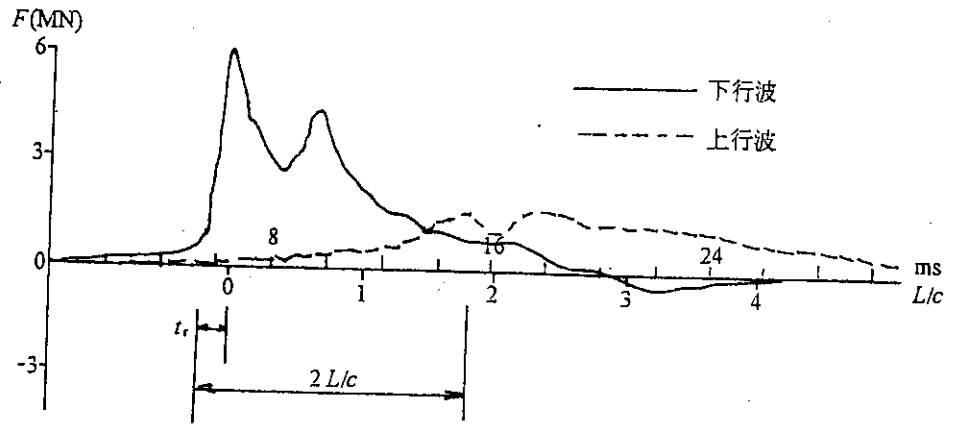


图 7.1.3 桩身波速的确定

F —锤击力； L —测点下桩长； c —桩身波速

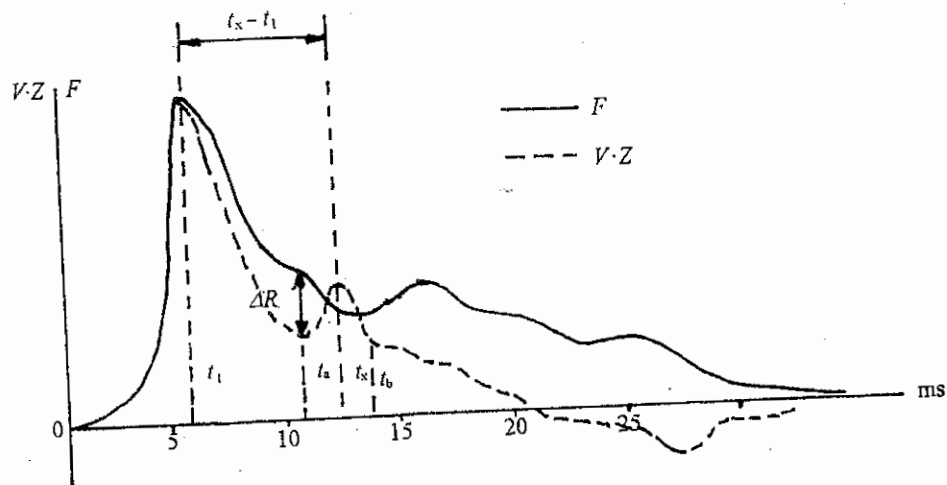


图 7.4.3 桩身结构完整性系数计算

接检测方法进行：

- (1) 虽无异常信号反射，但并未测得桩底反射的桩；
- (2) 桩截面渐变或多变，且变化幅度较大的混凝土灌注桩。

PART B

Draft of Japanese Code for Rapid Load Test

1. GENERAL

1.1 Scope

This standard shall be applied to rapid load tests (hereafter referred to as "test(s)") in which a single pile is subjected to a rapid axial compressive load. For reaction devices, if any, the standard set in the specification "Method of pile loading test (JGS 1811 – 200X)" should be used.

1.2 Objectives of test

The objectives of the test are to obtain the load displacement relation up to the ultimate capacity of a pile and/or to ensure the predetermined design capacity of a pile.

1.3 Terminology

Descriptions of terms specific to this standard:

Rapid load : A load that is rapidly applied but is of sufficient duration to result in the full pile length being in compression during loading. The load shall be applied in a continuously increasing and continuously decreasing manner. The duration of the rapid load would typically lie in the range of $5 < T_r < 500$, where T_r is defined as relative loading duration (see the definition below).

Planned maximum load : The pre-specified maximum applied load which is estimated to be adequate for achieving the test objectives

Loading duration (t_L): The duration from the start of loading to the end of unloading

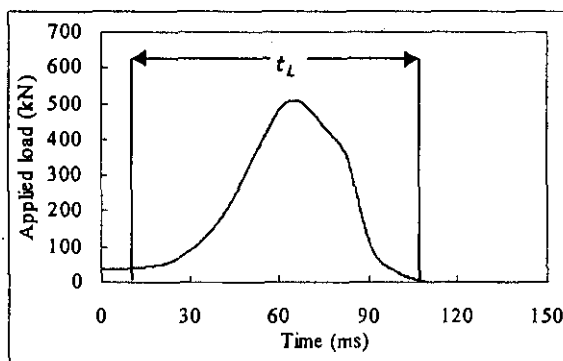


Figure 1. Definition of loading duration

Working pile: Pile(s) installed as a part of a structure

Test pile: Pile(s) to be tested

Strain rate dependency: The dependency of soil resistance on the strain rate

Bar wave : Axial strain wave traveling in the axial direction of a pile.

Bar wave velocity (c) is given by the following equation:

$$c = \sqrt{E/\rho}$$

where E and ρ are Young's modulus and density of pile material respectively.

Relative loading duration (T_r): Ratio of loading duration (t_L) to the time necessary for the wave to travel once around the pile length. Relative loading duration is defined as:

$$T_r = t_L / (2L/c)$$

where, L is pile length.

Single mass model analysis: An analytical method of a rapid load test in which the pile is modeled as a single lumped mass connected to spring(s) and dashpot(s) which represent the soil resistance.

2. BASIC PLANNING

2.1 Basic items

In planning the test, basic items such as the planned maximum load, the test pile specifications, the number and locations of test piles, and the test method need to be determined by taking into account the following points: the objectives of the test, the ground conditions, the loading conditions, the required period and costs, installation methods, pile dimensions, pile number, pile head level, and arrangement of working piles, etc.

2.2 Planned maximum load

- 1) Based on the test objectives, the planned maximum load shall be not less than either the estimated ultimate bearing capacity for a working pile, or the design capacity times a factor of safety. In addition, inertia force effects of the pile and soil shall be added to the above load.
- 2) For a pile installed in clayey soils, the planned maximum load shall be determined with consideration of increase in soil resistance due to strain rate effects.
- 3) When conditions of the test pile are different from those of a working pile, these effects on the bearing capacity of the test pile shall be considered.

2.3 Planned loading duration

Loading duration shall be long enough to avoid wave propagation effects in the pile. Generally a relative loading duration, T_r , of more than 5 will satisfy this condition.

2.4 Specifications, number and location of test piles

- 1) A test pile shall have the same properties as the representative working piles, and shall be planned separately.
- 2) A working pile may be used as a test pile, provided that the pile conditions after the test do not affect its performance after the test.
- 3) An appropriate number of test piles and their locations shall be selected based on the objectives of the test.

2.5 Method of loading and measurements

- 1) Loading devices shall have enough capability of satisfactorily meeting the planned maximum load and loading duration.
- 2) Loading pattern shall be chosen to achieve the required test objectives.
- 3) Items to be measured and transducers shall be arranged, according to the objectives of the test.

3. TEST PREPARATION

3.1 Preparation of execution plan

In advance of a test, an execution plan shall be made and documented based on the basic plan and the field inspections. The plan shall include the following items:

- (1) test objectives,
- (2) ground conditions,
- (3) planned maximum load,
- (4) planned loading duration,
- (5) specifications, location, and installation method of the test pile,
- (6) assembly drawing, specifications and operating method of the test equipment,
- (7) items to be measured,
- (8) composition, specifications and positions of sensors,
- (9) data sampling period and frequency,
- (10) composition of testing personnel,
- (11) items to be recorded,
- (12) processing of test results,
- (13) schedule, and
- (14) items to be considered during test.

3.2 Design of test piles

- 1) A test pile shall have strength with a sufficient margin of safety against the planned maximum load.
- 2) A test pile shall be long enough for setting the loading devices and sensors above the ground surface.
- 3) The pile head shall be reinforced adequately to avoid failure during testing as a result of unpredicted or accidental eccentric loads.

3.3 Installation and curing of test piles

- 1) A test pile shall be installed in the same manner as the working piles.
- 2) The installation process of the test pile shall be recorded in detail.
- 3) The test pile shall be cured for a period long enough to allow for the recovery of soil strength, hardening of pile materials such as concrete and cement mix, etc.
- 4) During the curing period, care shall be taken not to apply any loads, impacts and vibrations onto the test pile that might influence the test results.

3.4 Set up of test equipment and site

- 1) The test equipment shall be precisely positioned according to the execution plan.
- 2) Adequate countermeasures shall be taken to avoid harmful effects of sunshine, wind and rain, on the test results.
- 3) The effects of the construction work, machine and vehicle operations nearby shall be examined and adequate measures shall be taken to minimize their effects.

4. TEST EQUIPMENT

4.1 Composition of test equipment

- 1) The test equipment consists of loading devices and a measuring system.
- 2) The loading devices consist of a load application system and a base plate between the pile head and the load application system. A base plate may be used to ensure the even application of load to the pile head.
- 3) The measuring system consists of measuring devices and their reference points. The measuring devices consist of sensors such as load cells, displacement transducers, accelerometers, strain gages, and data acquisition and display equipment.

4.2 Loading devices

- 1) The loading devices shall have a sufficient margin of safety against the planned maximum load.
- 2) The loading devices shall have a sufficient capacity for the planned maximum load and loading duration.
- 3) The loading devices shall be positioned on the center of the test pile to avoid eccentricity in the load.
- 4) The base plate shall be sufficiently rigid for the planned maximum load.

4.3 Measurement devices

- 1) All measurement devices shall be inspected and shall have adequate accuracy and dynamic responses to achieve the test objectives.
- 2) The sensors shall be firmly set in their appropriate positions and proper directions.
- 3) Care shall be taken to prevent any influences of the displacement and/or the vibrations of the test pile and loading devices on the measurement devices.

4.4 Reference points

- 1) All reference points shall be established on the stationary points.
- 2) The reference points shall be set at a sufficient distance so as to avoid test-induced disturbances such as vibration or/and displacement (Generally at a distance of at least 10 m away from the test pile).
- 3) When vibration is expected during the loading, the reference point shall have enough rigidity so as not to be influenced by the vibration.

5. METHOD OF LOADINGS AND MEASUREMENTS

5.1 Loading pattern

An appropriate number of cycles shall be selected as the loading pattern according to the objectives of the test.

5.2 Items to be measured

The following items shall be measured depending on the test objectives:

- (1) time,
- (2) load applied,
- (3) displacement at pile head,

- (4) acceleration at pile head,
- (5) accelerations at pile tip and middle part of pile shaft,
- (6) axial strains along pile, and
- (7) others.

5.3 Sampling periods and intervals

- 1) Data shall be acquired from the initial condition before the loading to the condition when vibration of the pile are sufficiently small that they can be ignored after the loading.
- 2) The sampling intervals shall be less than 1 ms.

6. EXECUTION OF TEST

6.1 Testing personnel

Testing personnel shall consist of a test supervisor, a loading operator, a record keeper and a safety manager.

6.2 Tasks of testing personnel

- 1) The test supervisor shall, in accordance with the execution plan, arrange appropriate personnel to share the tasks and shall be in charge of overall management of the test to achieve the test objectives safely and properly.
- 2) The testing personnel shall ensure the safety of the loading systems prior to the commencement of the test and shall ensure the normal functioning of the equipment.
- 3) The loading operator shall operate the loading devices accurately.
- 4) Before the commencement of test, the test recorder shall inspect and check the measuring devices and ensure their normal operation during the loading.
- 5) The safety manager shall pay sufficient attention to the safety of the test equipment and surrounding site.

6.3 Commencement and completion of test

- 1) The test shall be commenced only after ensuring the surrounding site conditions, preparations of each equipment, and the suitability of the weather conditions.
- 2) If any abnormal condition(s) is/are noticed before the test, the load shall not be applied to the pile. The test can only be resumed when the cause for the abnormal condition is detected and removed so that the load can be applied.
- 3) The test shall be terminated when the objectives of the test have been achieved.

6.4 Items to be recorded at the site

The following items shall be recorded at the site:

- (1) dates and times of commencement, interruption and completion of the test,
- (2) names of the testing personnel,
- (3) weather conditions,
- (4) arrangement and dimensions of test equipment and test pile,
- (5) photographs showing test equipment and test conditions, and
- (6) special items such as site situations, reasons for and measures taken when the actual execution differs from the initial plan, and others.

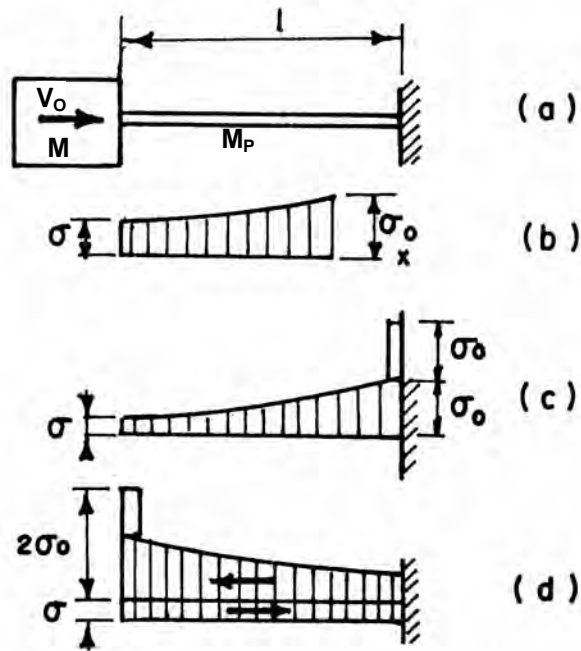


Figure 1. Stress Propagation in a Fixed End Bar Struck by a Moving Mass (after Timoshenko and Goodier, 1934).

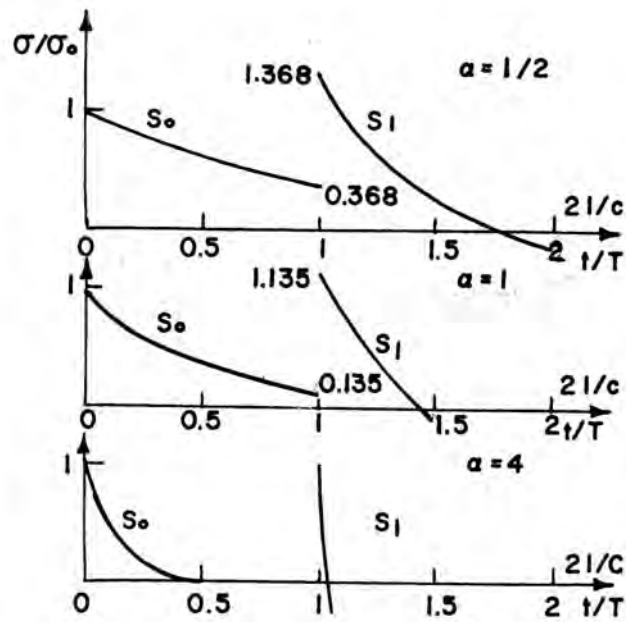


Figure 2. Stress Wave Magnitude and Duration (Graphical Representation of Functions S_0 and S_1) as a Function of the Ratio Between the Mass of the Pile to the Mass of the Striking Body.

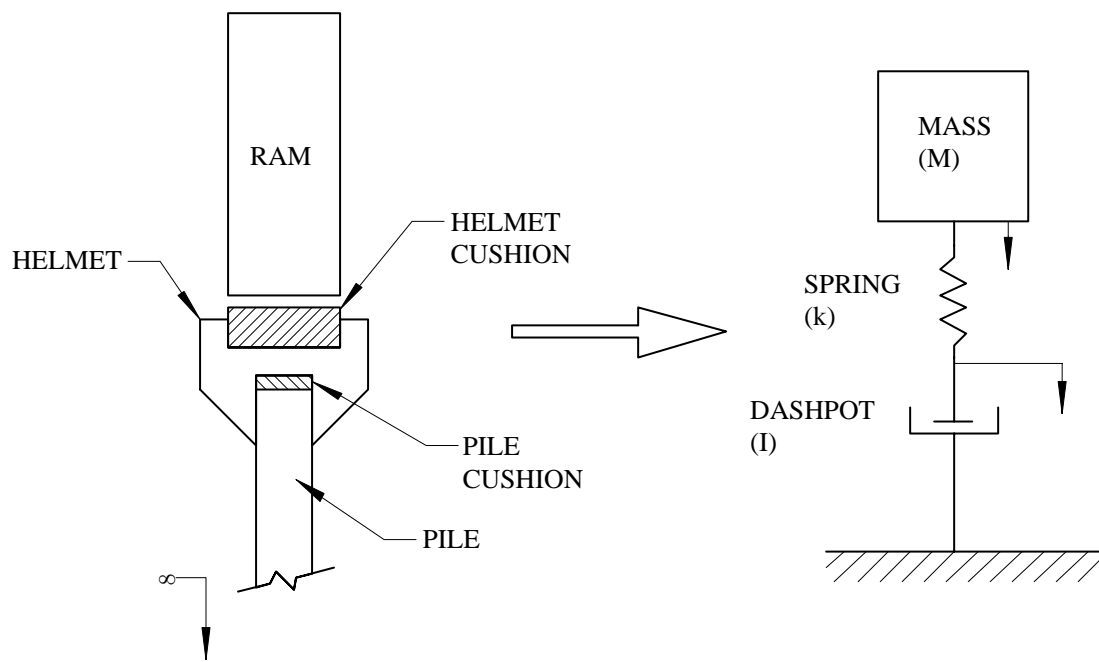


Figure 3. Physical and Mechanical Representation of a Mass Impacting Infinite Long Pile.

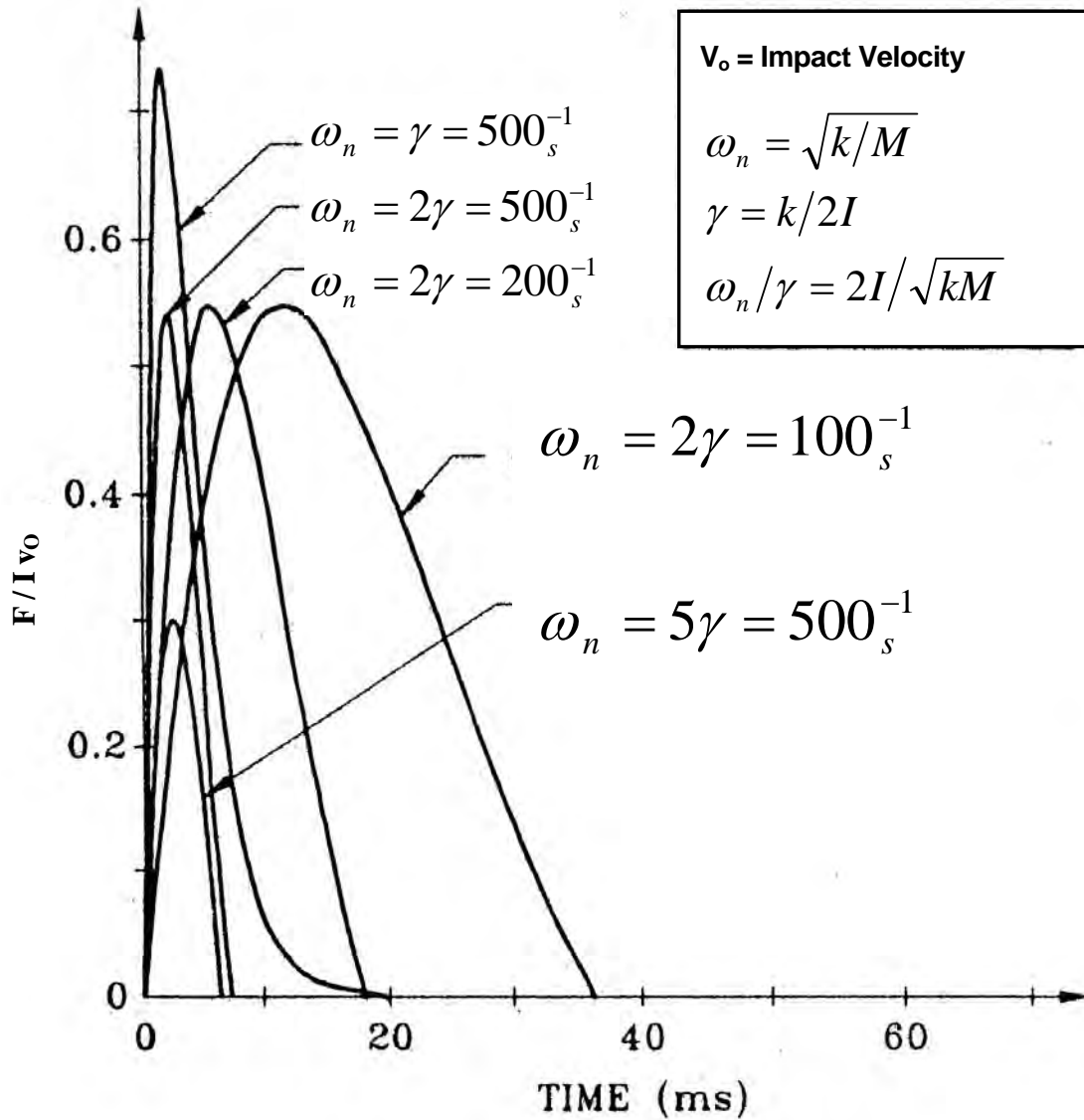


Figure 4. Non-Dimensional Force Pulses in a Pile as a Function of Time and the Ratio of Cushioning Element to Pile Stiffness (Holeyman 1992, see also Parola, 1970).

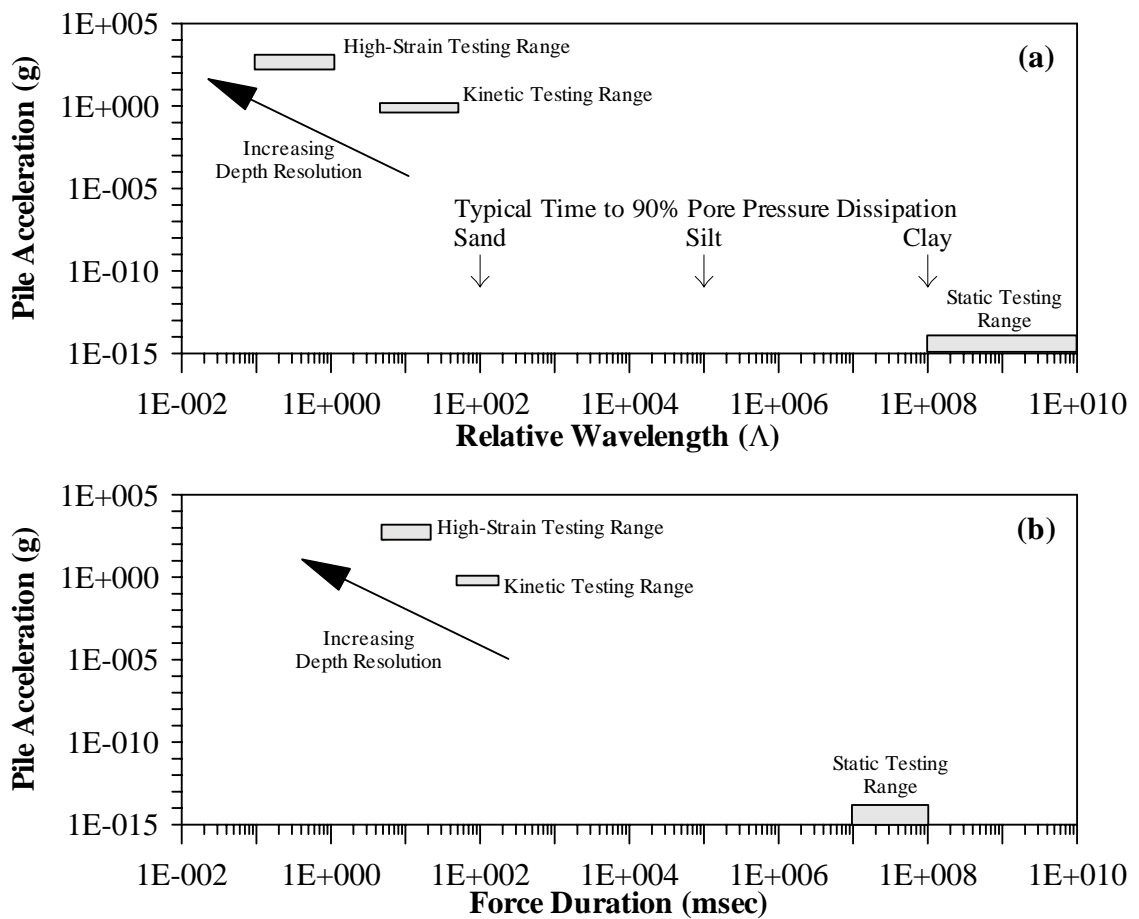


Figure 5. Typical Load Testing Values for Pile Acceleration vs. (a) Relative Wavelength and (b) Force Duration (after Holeyman, 1992).

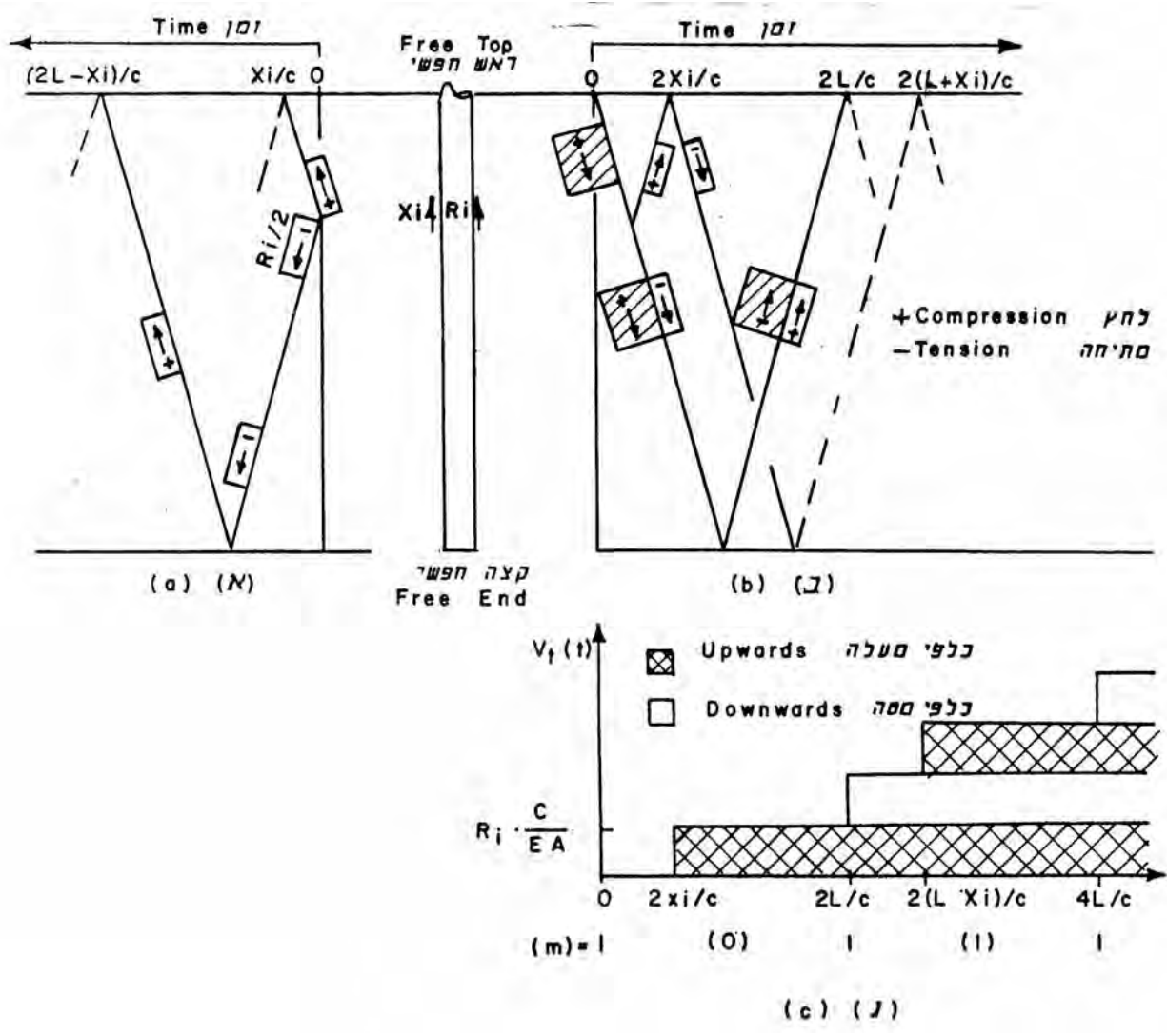


Figure 6. Wave Propagation through a Pile with Free Ends;
 (a) As a Result of a Sudden Applied Force R_i Located at X_i
 (b) As a Result of Activation of R_i by a Traveling Compression Wave
 (c) Velocity Effect at Pile Top Caused by a Resistance Step Force R_i at Location X_i

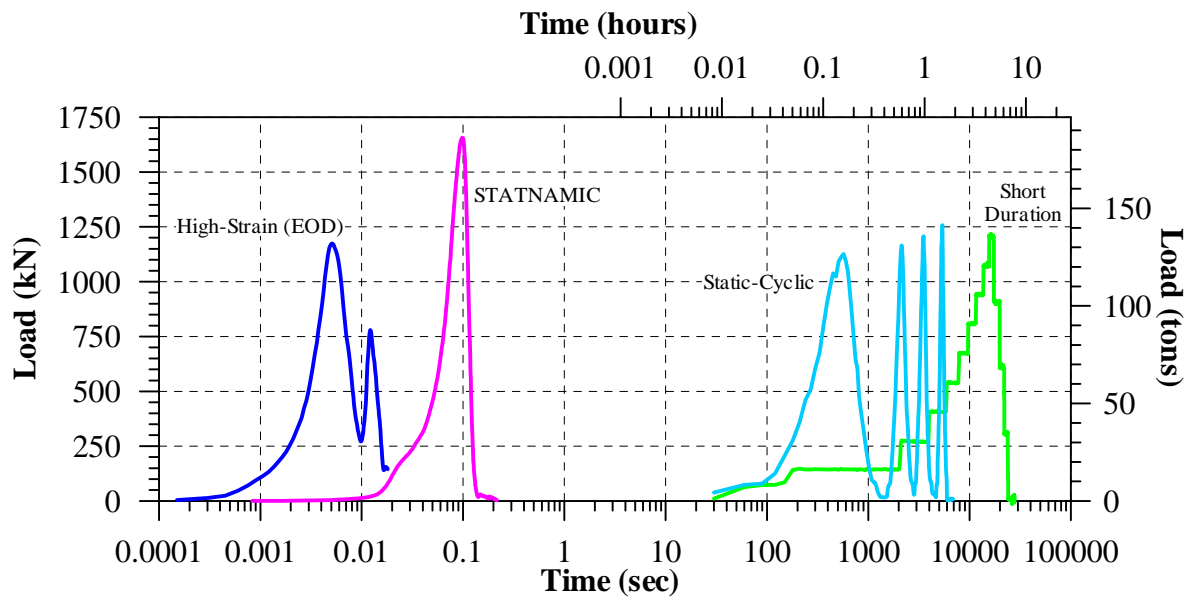


Figure 7. Typical Loading Durations for Various Tests Performed on Test Pile #3 by the Geotechnical Engineering Research Laboratory of the University of Massachusetts Lowell, at the Newbury Test Site

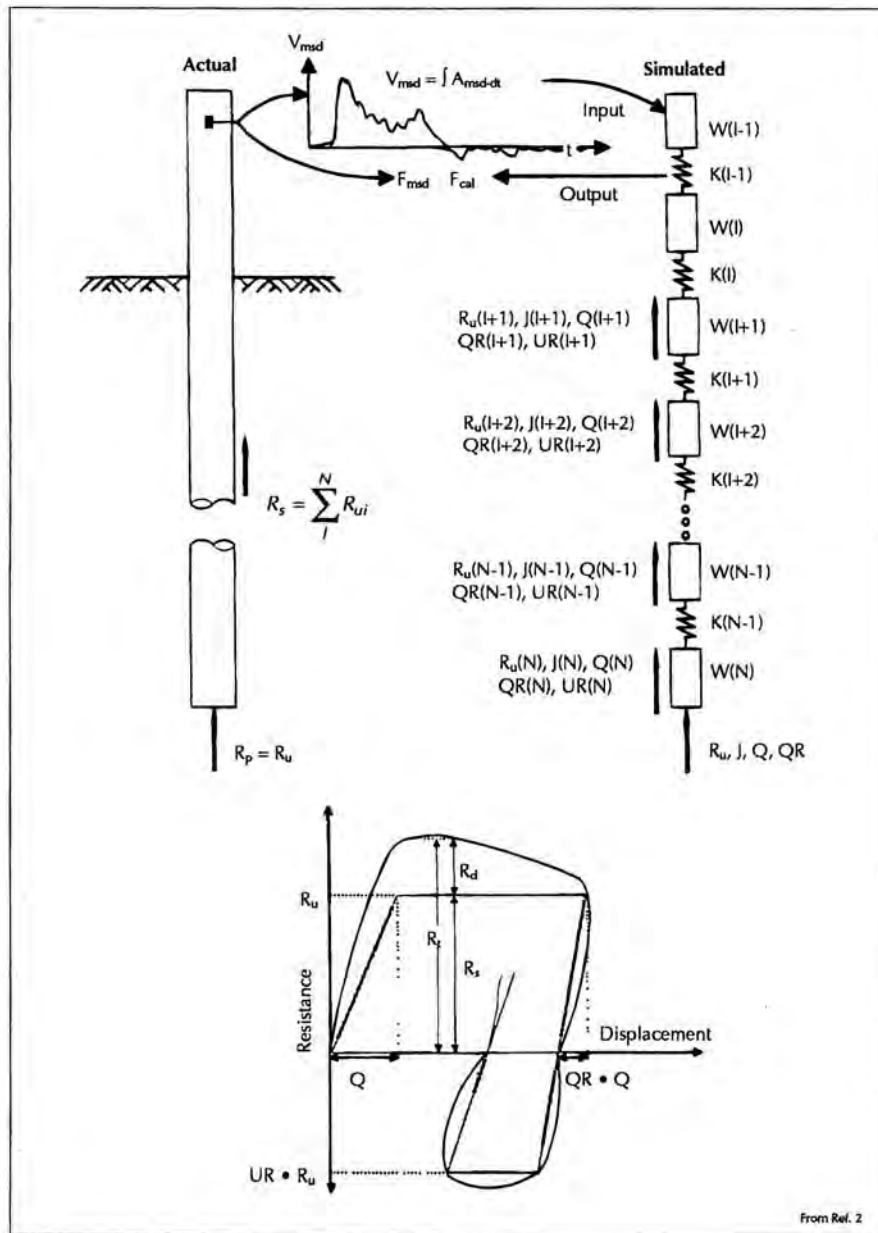


Figure 8. Notations used for model of pile and soil in TEPWAP analysis (Paikowsky, 1982).

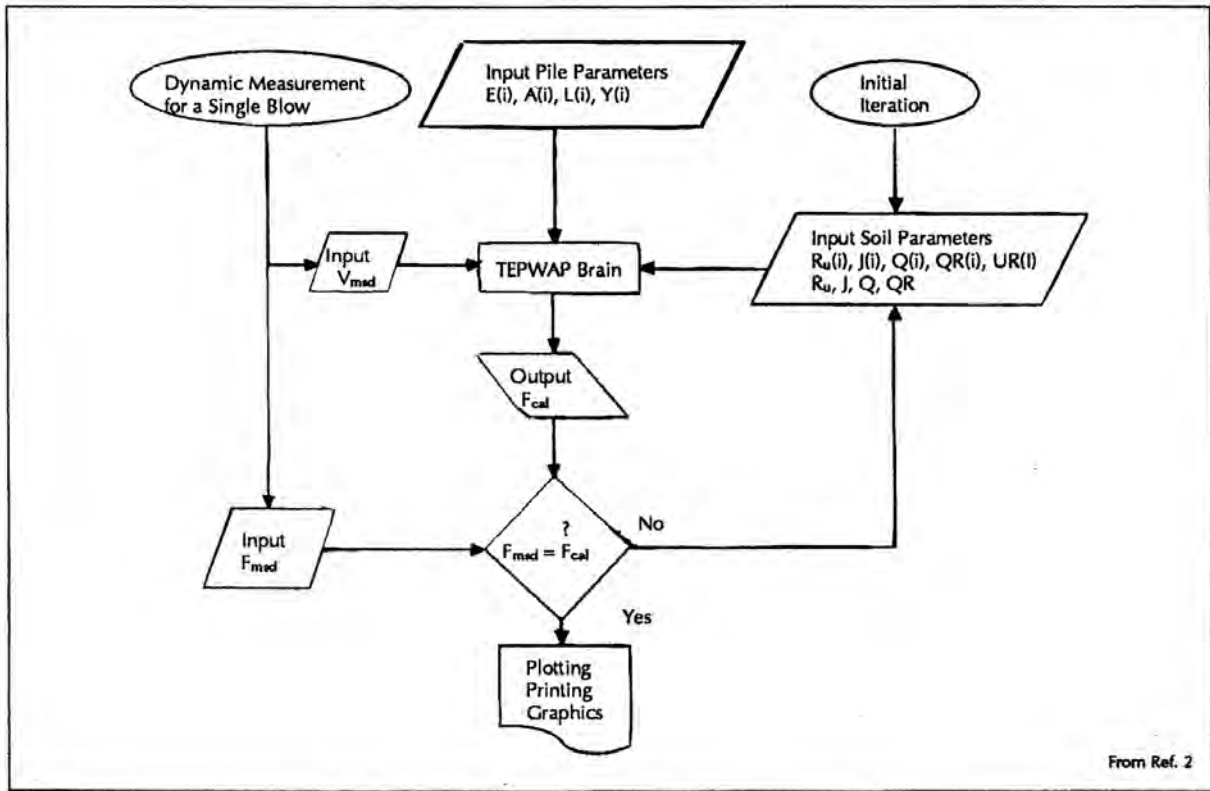


Figure 9. Flow chart describing the analysis process using TEPWAP (Paikowsky, 1982)



(a)



(b)

Figure 10. Drop Weight System DW-A (Li, 1993): (a) General view, and (b) Lowering the system in an excavation above a drilled shaft



Figure 11. Drop Weight System DW-B (Li, 2000): (a) General View, and (b) Close view with dynamic measurements taken by Zengxuan (Frank) Li

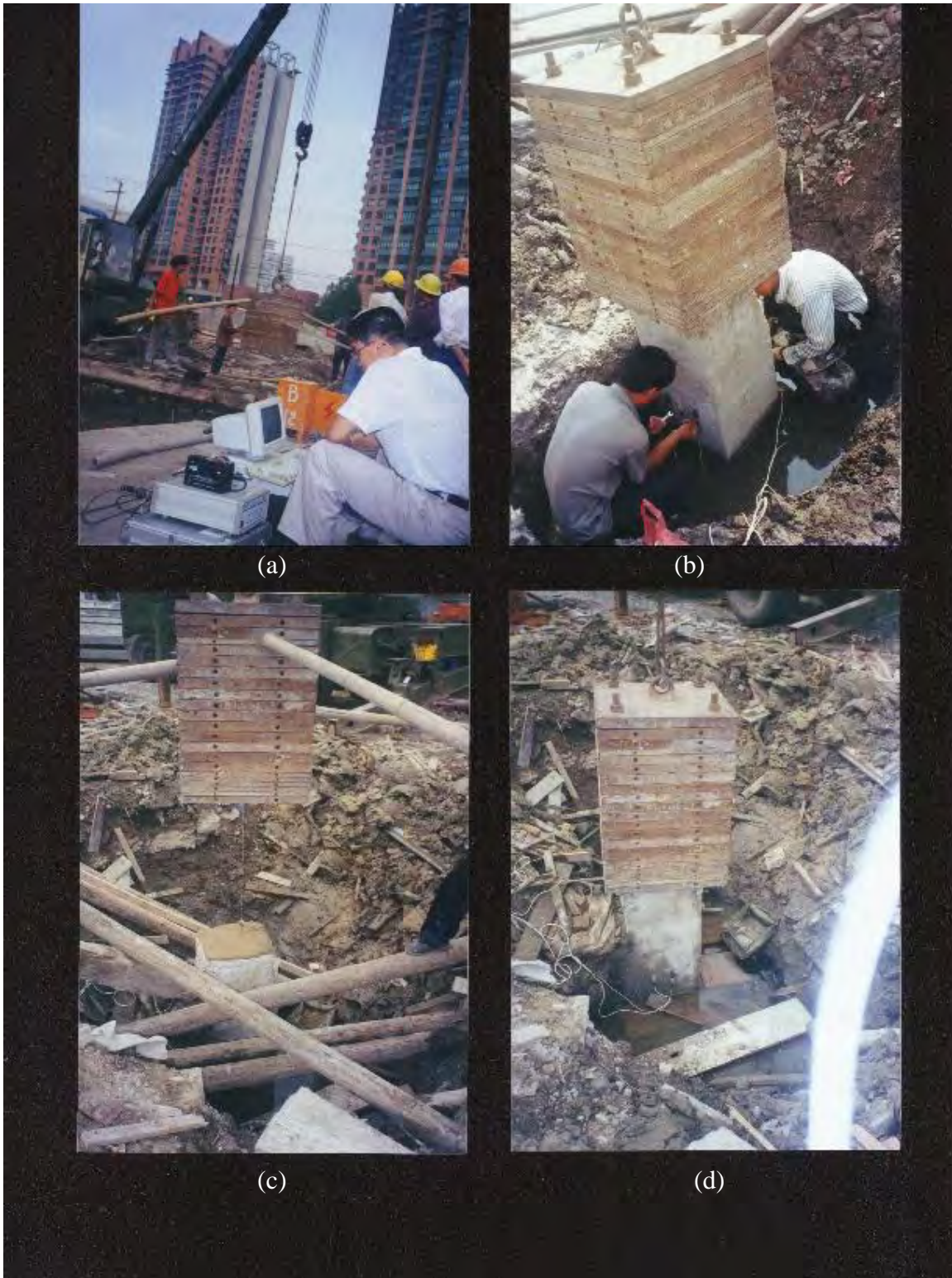
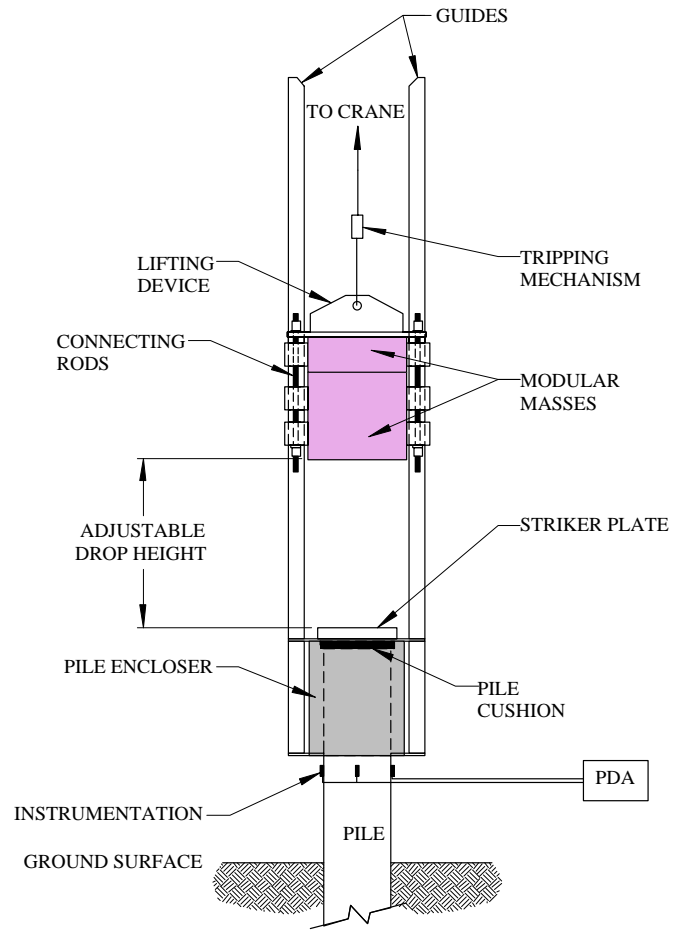


Figure 12. Drop Weight System – DW-C (Weibing, 2000). From TL to BR:
(a) General view, hanging ram without a guiding system and the data acquisition system
(b) transducer attachment under the hanging ram
(c) ram and cushion, close up view with pipes keeping the ram above the pile
(d) impact



(a)



(b)

Figure 13. Israeli Drop Weight System DW-D (GTR, 1997): (a) photograph, and (b) schematic.

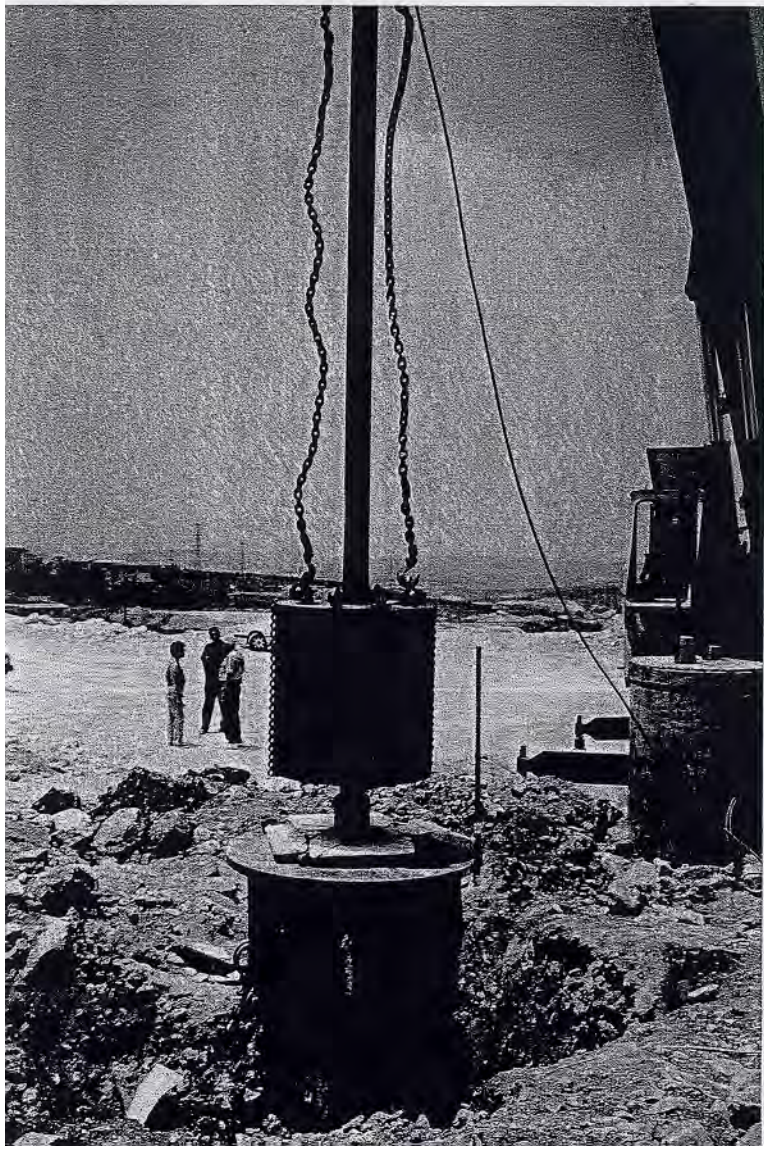
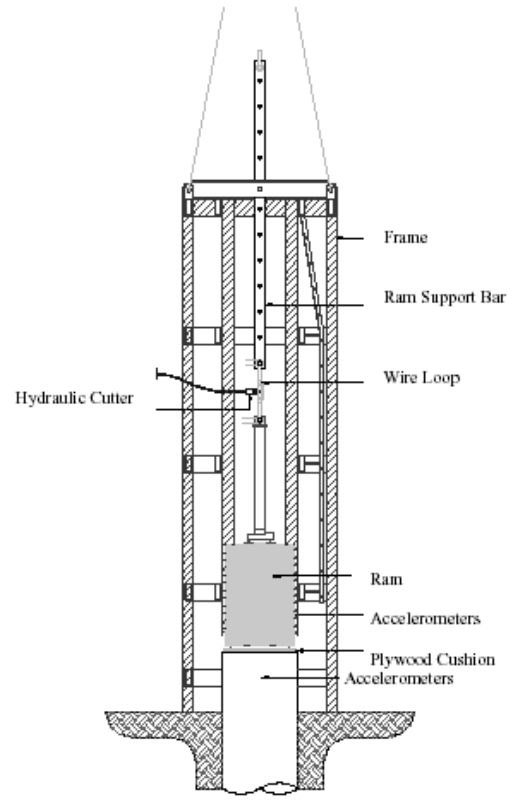


Figure 14. Isotop Drop Weight Device DW-E (Sokolovsky et al., 1998)



(a)



(b)

Figure 15. GRL Newton's Apple System DW-F; (a) General view, (b) Details of instrumented ram impacting a drilled shaft (Robinson and Rausche, 2000)

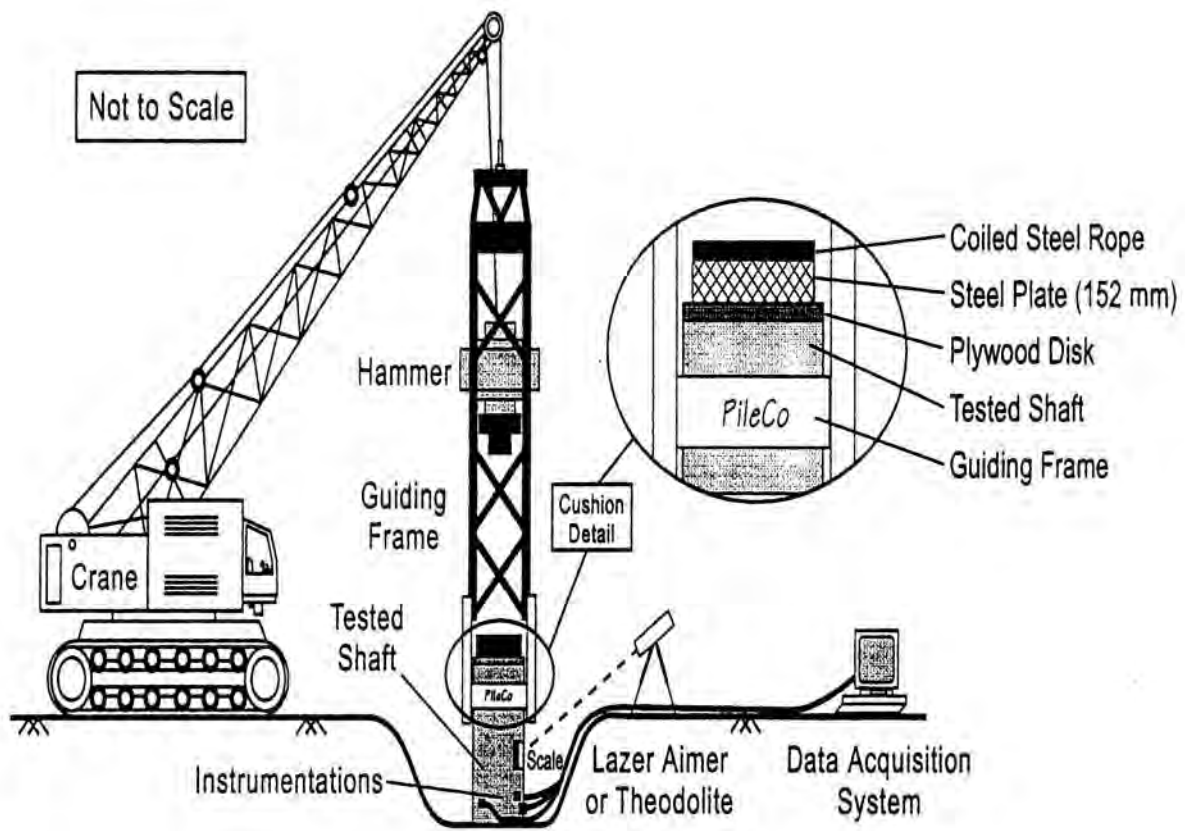
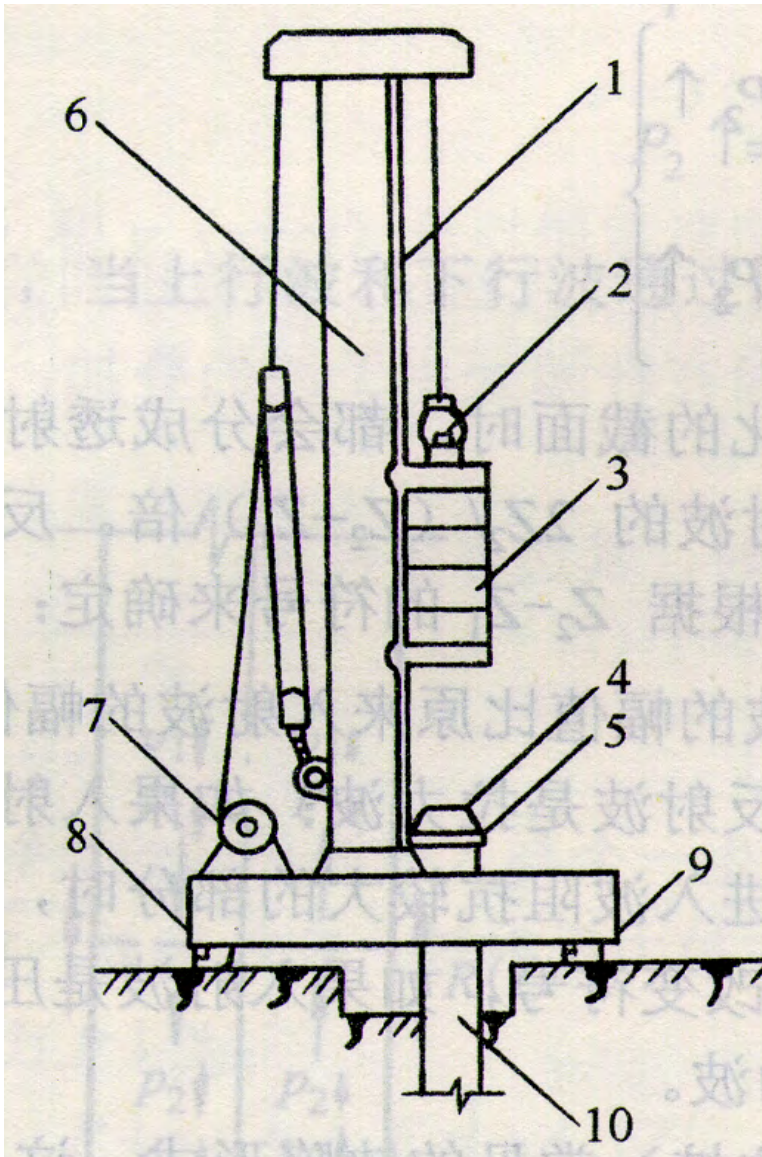


Figure 16. Drop Weight System DW-G (Briaud et al. 2000)



Figure 17. Drop Weight System DW-H (Townsend et al., 1991)



1. Frame/Guide
2. Manual Trigger (hook)
3. Modular steel hammer
4. Anvil/Striking Plate
5. Plywood Cushion
6. Reaction Frame
7. Electric Motor
8. Platform
9. Wood Blocking
10. Tested Pile

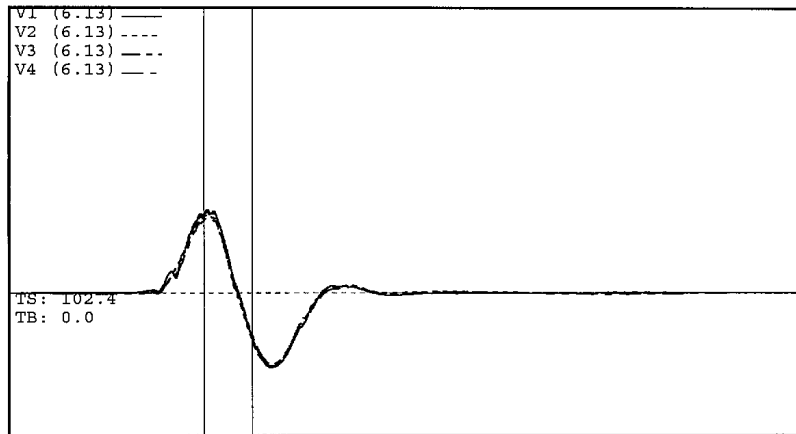
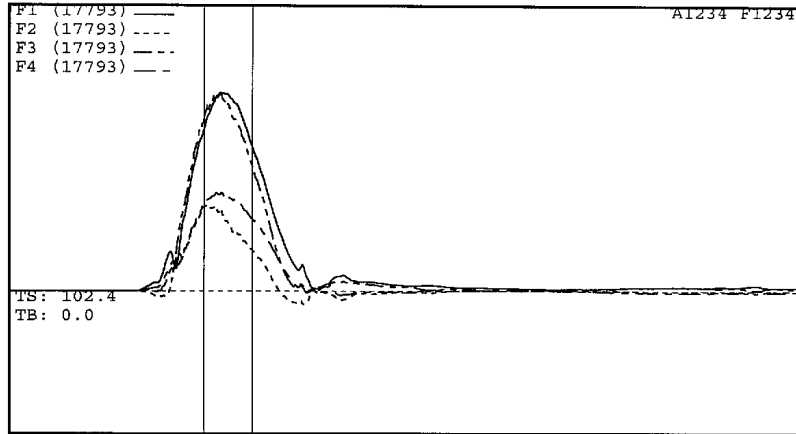
Figure 18. Drop Weight System DW-I (Longgen et al. 1999)

GTR

Pile Driving Analyzer ®

Electric Co

SHAFTA



Project Information

PROJECT: Electric Co
 PILE NAME: SHAFTA
 DESCR: CIP60cm
 OPERATOR:
 FILE: Shafta.x01
 10/20/97 6:46:04 PM
 Blow Number 3

Pile Properties

LE 13.0 m
 AR 2827.00 cm²
 EM 43156 MPa
 SP 24.0 kN/m³
 WS 4200.0 m/s
 EA/C 2905 kN-s/m
 2L/C 6.20 ms
 JC 0.50 []
 LP 13.0 m

Quantity Results

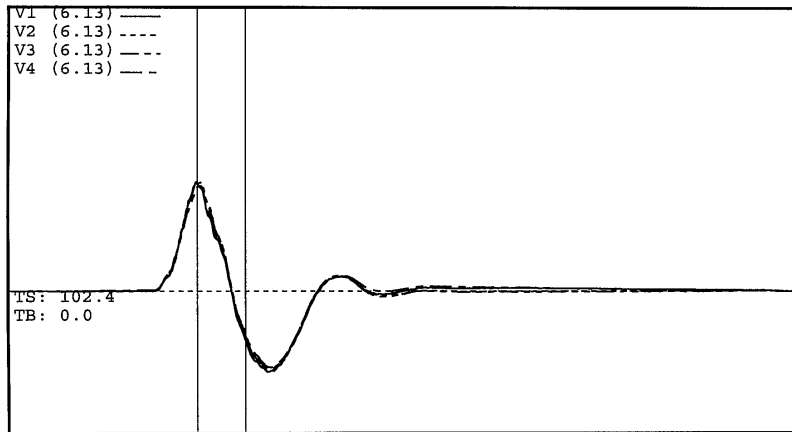
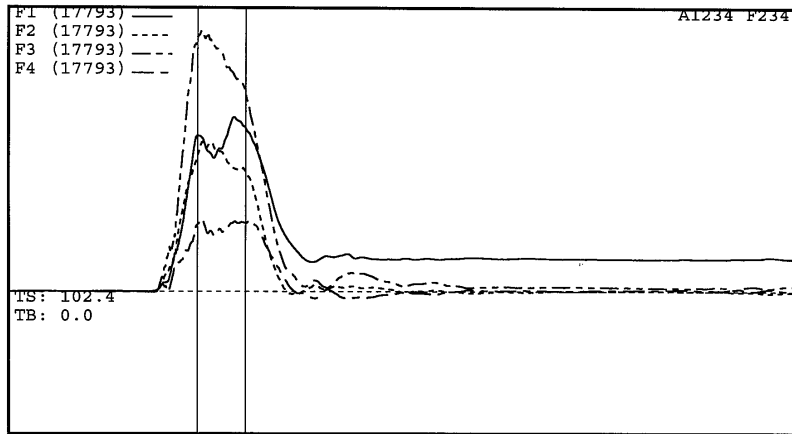
EMX 64.8 kN-m
 DMX 9 mm
 DFN -0 mm
 CSX 31.6 MPa
 TSX 4.8 MPa
 FMX 8942 kN
 RMX 9978 kN
 QUT 13946 kN
 RX5 9978 kN

Sensors

F1: 111.1 (1)
 F2: 112 (1)
 F3: 120.5 (1)
 F4: 115.6 (1)
 A1: 965 g's/v (1)
 A2: 955 g's/v (1)
 A3: 290 mv/5000g's (1)
 A4: 345 mv/5000g's (1)
 CLIP: OK
 F1/F2: HIGH 1.96
 V3/V4: OK 1.07

Version 2001.085

Figure 19. Individual Force and Velocity Records of Four Strain and Acceleration Gauges Used During Impact No. 3 on Shaft-A (GTR, 1997)



Project Information

PROJECT: Electric Co
 PILE NAME: SHAFTA
 DESCR: CIP60cm
 OPERATOR:
 FILE: Shafta.x01
 10/20/97 7:04:12 PM
 Blow Number 4

Quantity Results

EMX 90.6 kN-m
 DMX 11 mm
 DFN 2 mm
 CSX 35.7 MPa
 TSX 5.8 MPa
 FMX 10080 kN
 RMX 12544 kN
 QUT 14011 kN
 RX5 12544 kN

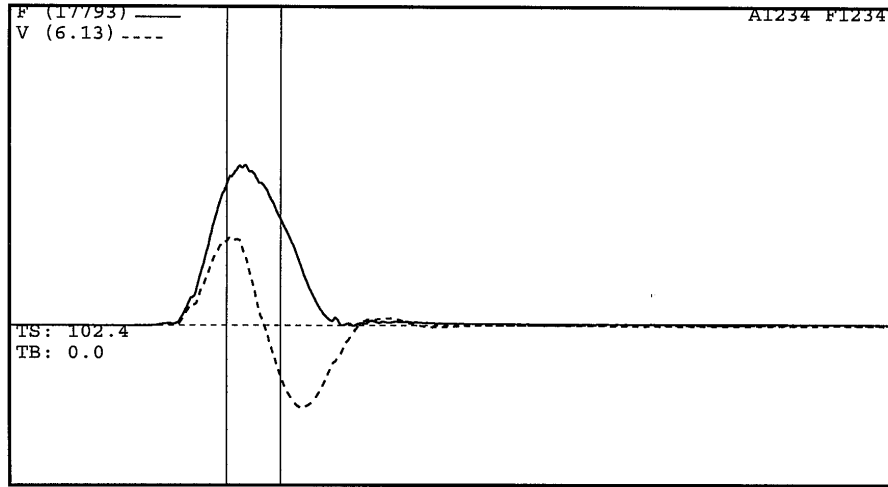
Pile Properties

LE 13.0 m
 AR 2827.00 cm²
 EM 43156 MPa
 SP 24.0 kN/m³
 WS 4200.0 m/s
 EA/C 2905 kN-s/m
 2L/C 6.20 ms
 JC 0.50 []
 LP 13.0 m

Sensors

F2: 112 (1)
 F3: 120.5 (1)
 F4: 115.6 (1)
 A1: 965 g's/v (1)
 A2: 955 g's/v (1)
 A3: 290 mv/5000g's (1)
 A4: 345 mv/5000g's (1)
 CLIP: OK
 F3/F4: HIGH 3.76
 V3/V4: OK 1.03

Figure 20. Individual Force and Velocity Records of Four Strain and Acceleration Gauges Used During Impact No. 4 on Shaft-A (GTR, 1997)



Project Information

PROJECT: Electric Co
 PILE NAME: SHAFTA
 DESCR: CIP60cm
 OPERATOR:
 FILE: Shafta.x01
 10/20/97 6:46:04 PM
 Blow Number 3

Pile Properties

LE 13.0 m
 AR 2827.00 cm²
 EM 43156 MPa
 SP 24.0 kN/m³
 WS 4200.0 m/s
 EA/C 2905 kN-s/m
 2L/C 6.20 ms
 JC 0.50 []
 LP 13.0 m

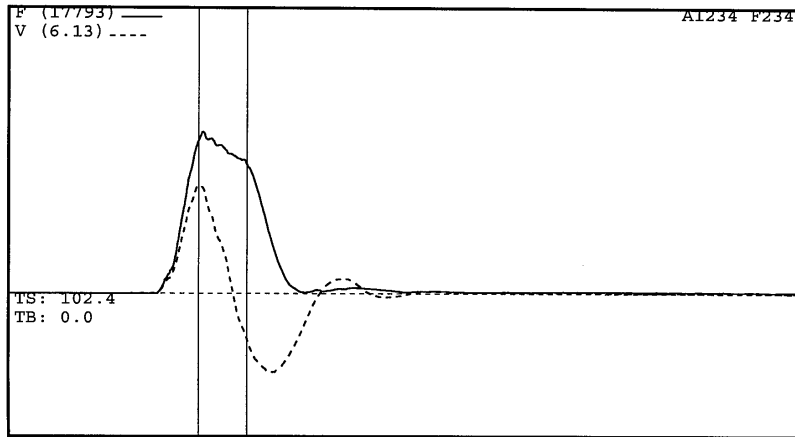
Quantity Results

EMX 64.8 kN-m
 DMX 9 mm
 DFN -0 mm
 CSX 31.6 MPa
 TSX 4.8 MPa
 FMX 8942 kN
 RMX 9978 kN
 QUT 13946 kN
 RX5 9978 kN

Sensors

F1: 111.1 (1)
 F2: 112 (1)
 F3: 120.5 (1)
 F4: 115.6 (1)
 A1: 965 g's/v (1)
 A2: 955 g's/v (1)
 A3: 290 mv/5000g's (1)
 A4: 345 mv/5000g's (1)
 CLIP: OK
 F1/F2: HIGH 1.96
 V3/V4: OK 1.07

Figure 21. Average Force and Velocity Measurements for Impact No. 3 on Shaft-A (GTR, 1997)



Project Information

PROJECT: Electric Co
 PILE NAME: SHAFTA
 DESCR: CIP60cm
 OPERATOR:
 FILE: Shafta.x01
 10/20/97 7:04:12 PM
 Blow Number 4

Quantity Results

EMX 90.6 kN-m
 DMX 11 mm
 DFN 2 mm
 CSX 35.7 MPa
 TSX 5.8 MPa
 FMX 10080 kN
 RMX 12544 kN
 QUT 14011 kN
 RX5 12544 kN

Pile Properties

LE 13.0 m
 AR 2827.00 cm²
 EM 43156 MPa
 SP 24.0 kN/m³
 WS 4200.0 m/s
 EA/C 2905 kN-s/m
 2L/C 6.20 ms
 JC 0.50 []
 LP 13.0 m

Sensors

F2: 112 (1)
 F3: 120.5 (1)
 F4: 115.6 (1)
 A1: 965 g's/v (1)
 A2: 955 g's/v (1)
 A3: 290 mv/5000g's (1)
 A4: 345 mv/5000g's (1)
 CLIP: OK
 F3/F4: HIGH 3.76
 V3/V4: OK 1.03

Figure 22. Average Force and Velocity Measurements for Impact No. 4 on Shaft-A (GTR, 1997)

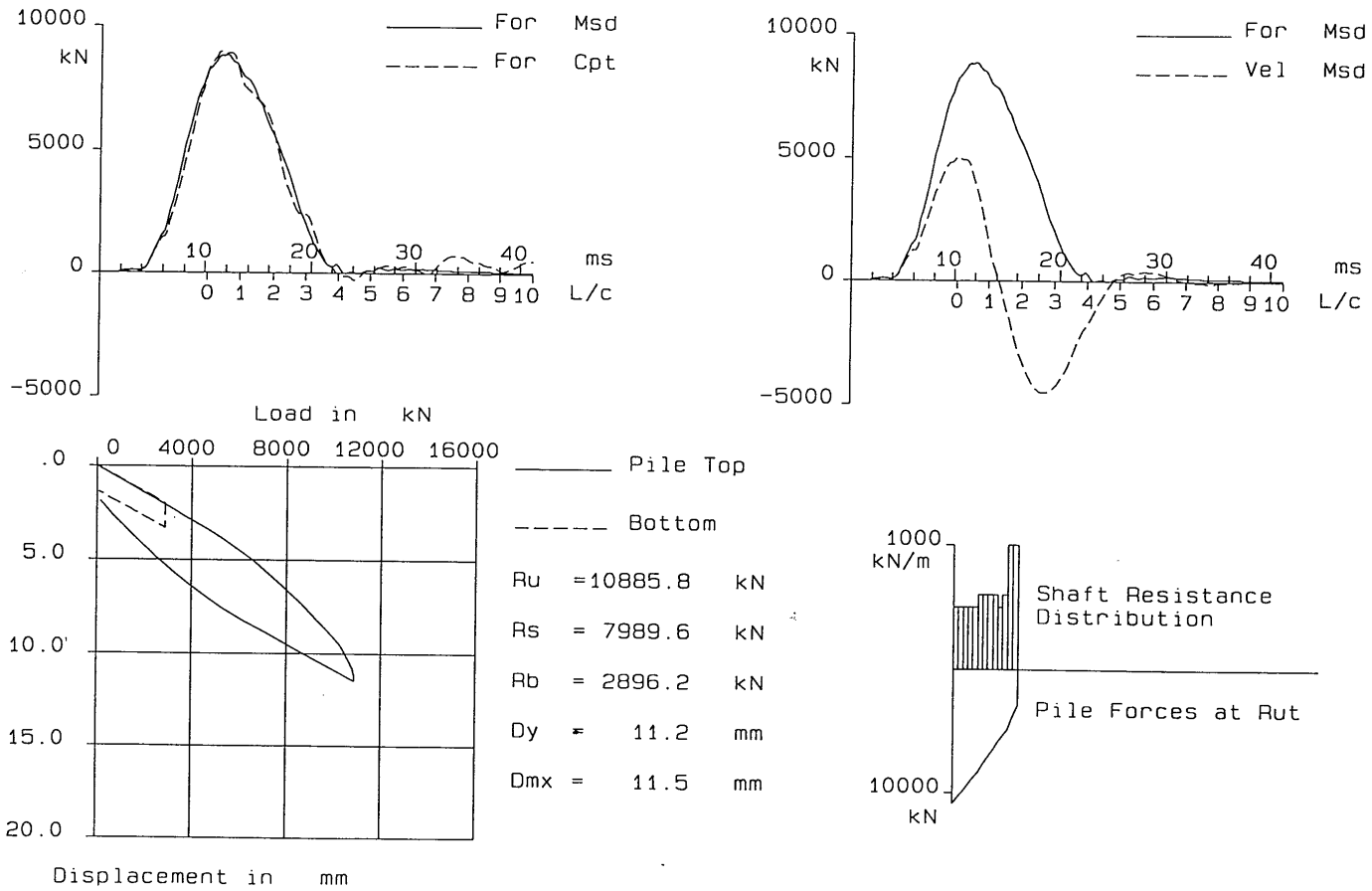


Figure 23. Signal Match Analysis (CAPWAP) Results for Impact No. 3 on Shaft-A (GTR, 1997)

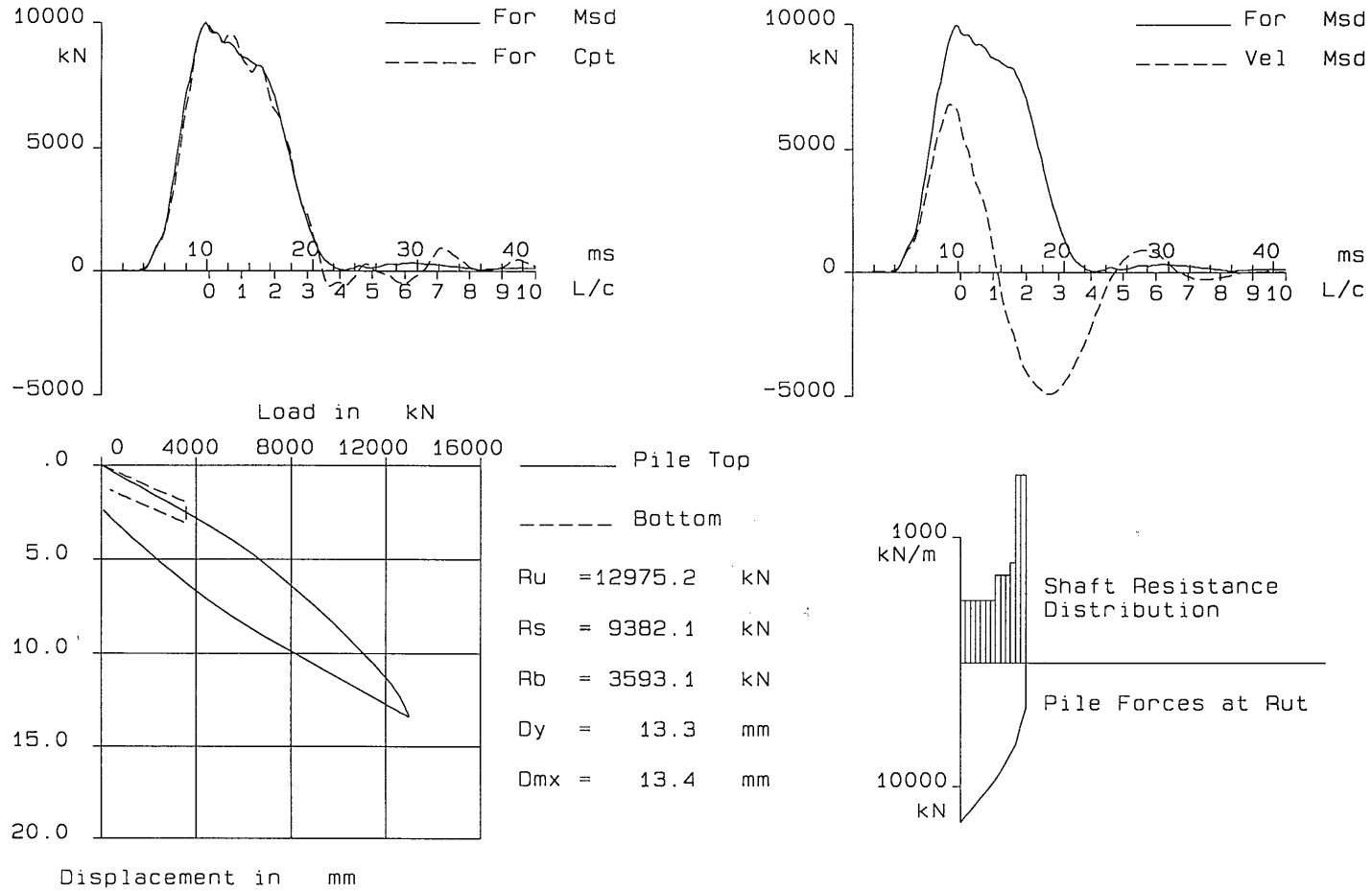


Figure 24. Signal Match Analysis (CAPWAP) Results for Impact No. 4 on Shaft-A (GTR, 1997)

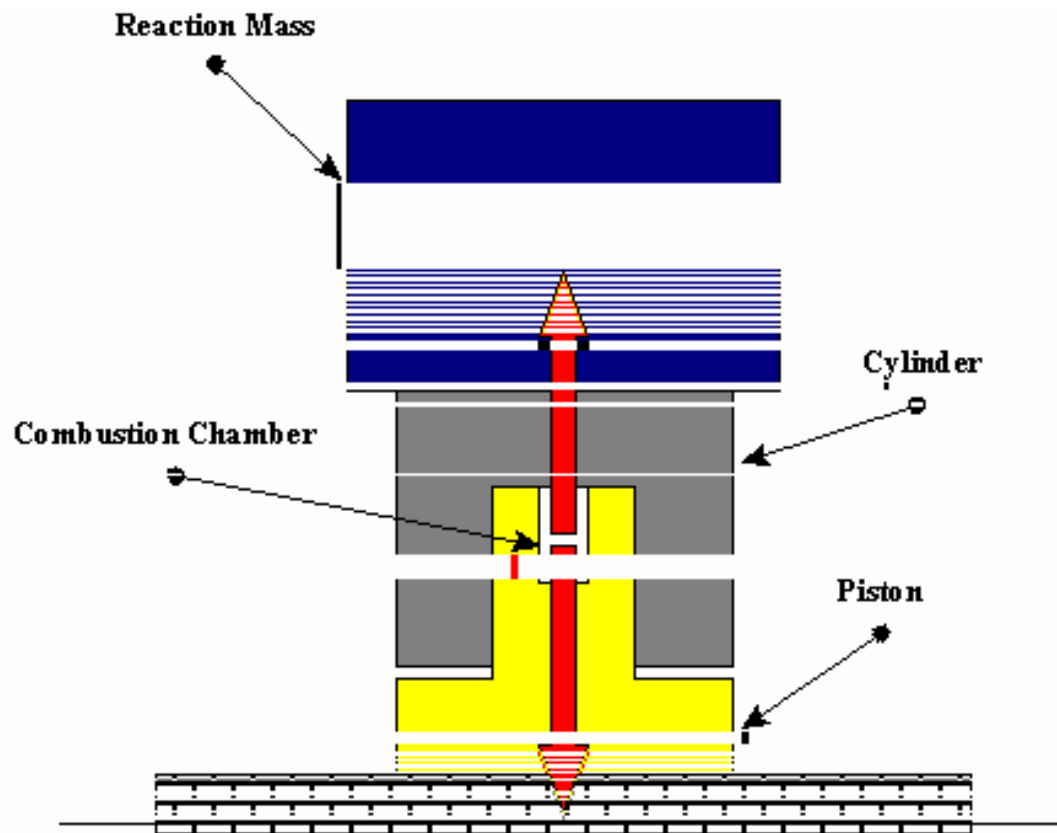


Figure 25. Schematic of the Statnamic Testing Device



Figure 26. Statnamic Piston (16 MN)



Figure 27. Statnamic Cylinder (4 MN)



(a)



(b)

Figure 28. (a) 4 MN reaction mass utilizing gravel and water in a rectangular steel shell, (b) 16 MN reaction masses utilizing concrete in a steel shell



(a)



(b)

Figure 29. (a) 30 MN gravel catch system, (b) Mechanical catch system utilizing submerged, water-filled reaction masses



Figure 30. (a) 0.6 MN device, and (b) 4 MN device utilizing mechanical and hydraulic catch mechanisms respectively

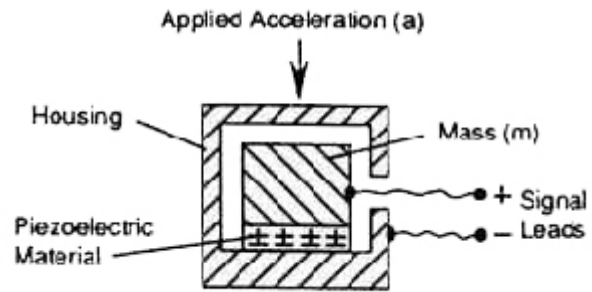


Figure 31. Piezoelectric accelerometer diagram (Courtesy of PCB Piezotronics)

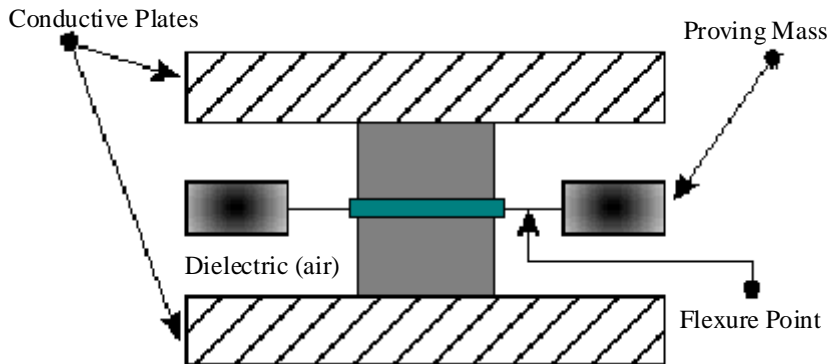


Figure 32. Capacitive accelerometer diagram

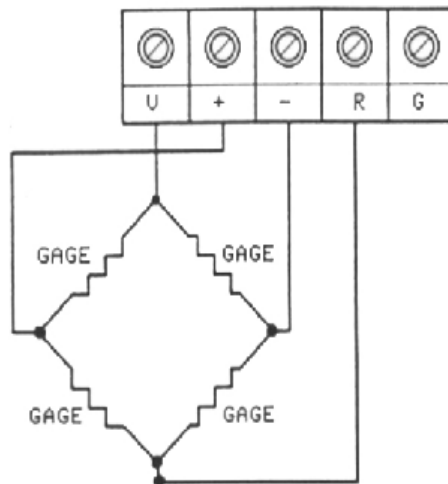


Figure 33. Wheatstone Bridge (Courtesy of Optim Electronics)



Figure 34. MEGADAC computer system (Courtesy of Optim Electronics).



Figure 35. MEGADAC daisy-chain

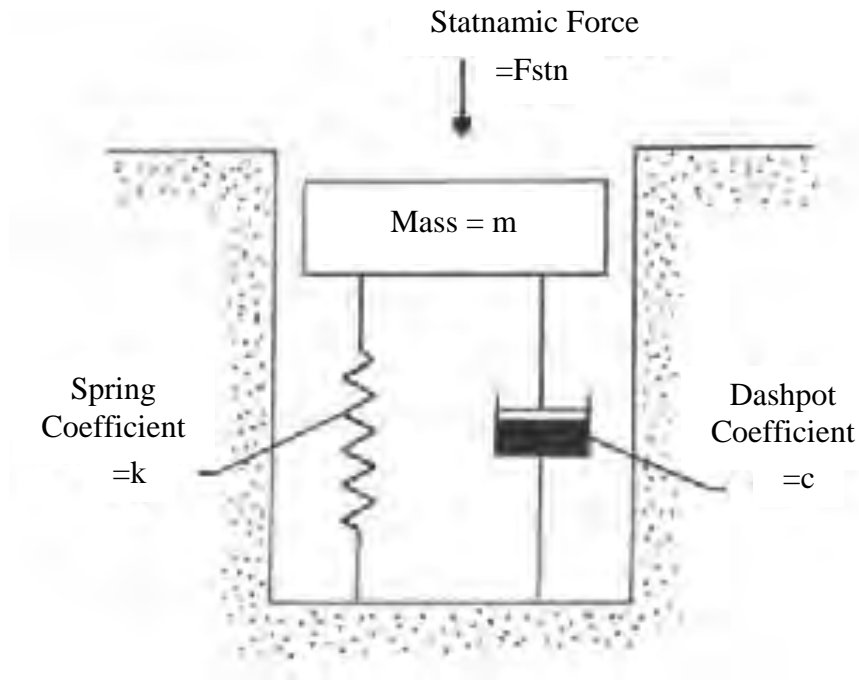


Figure 36. K-V Model (After Das 1994)

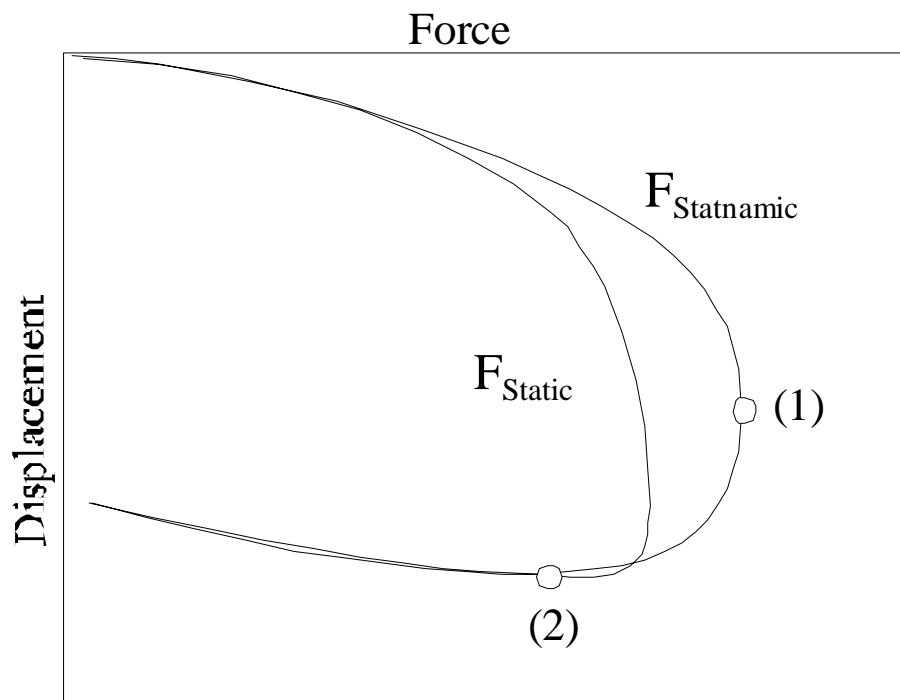


Figure 37. UPM time window for C determination

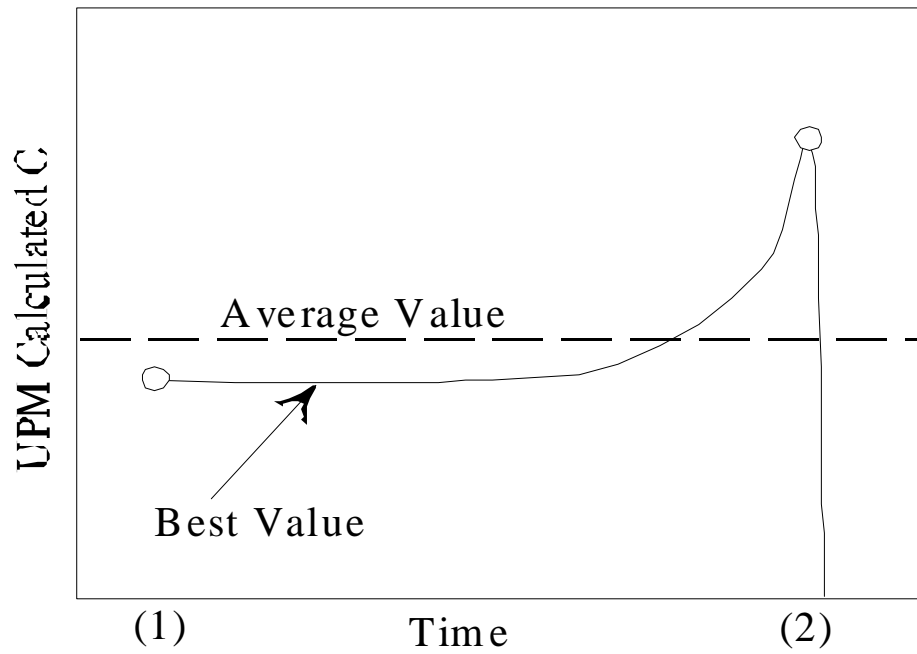


Figure 38. Variation in C between times (1) and (2)

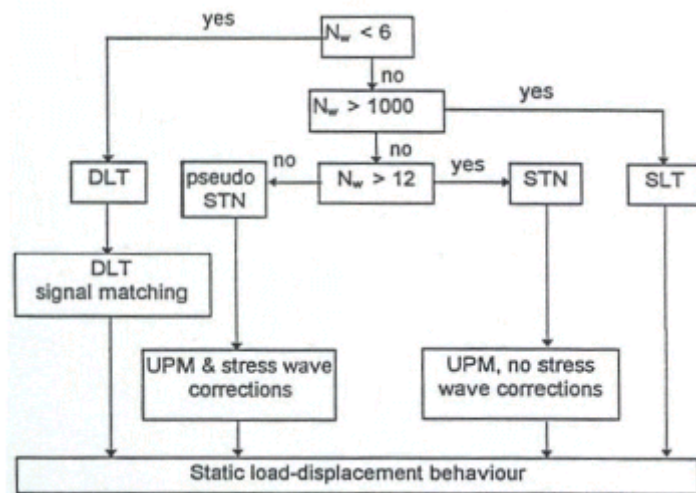


Figure 39. Selection Criteria (After Middendorp 1998)

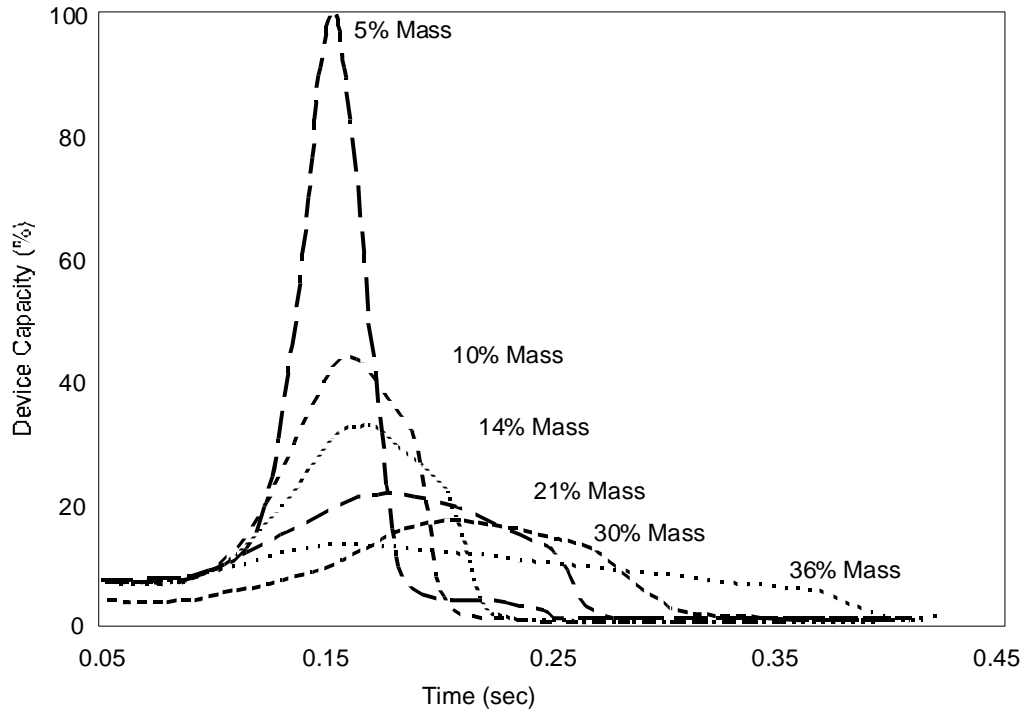


Figure 40. The effects of mass ratio on Statnamic load duration

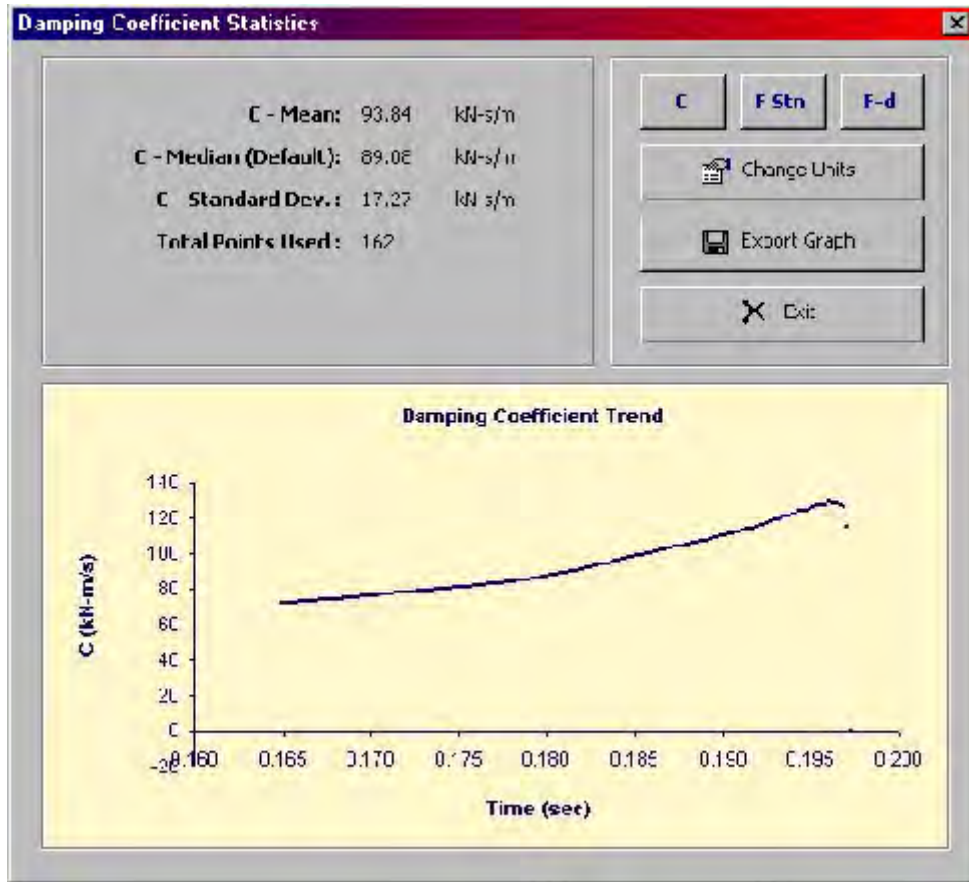


Figure 41. Statistics screen available in Statnamic analysis software

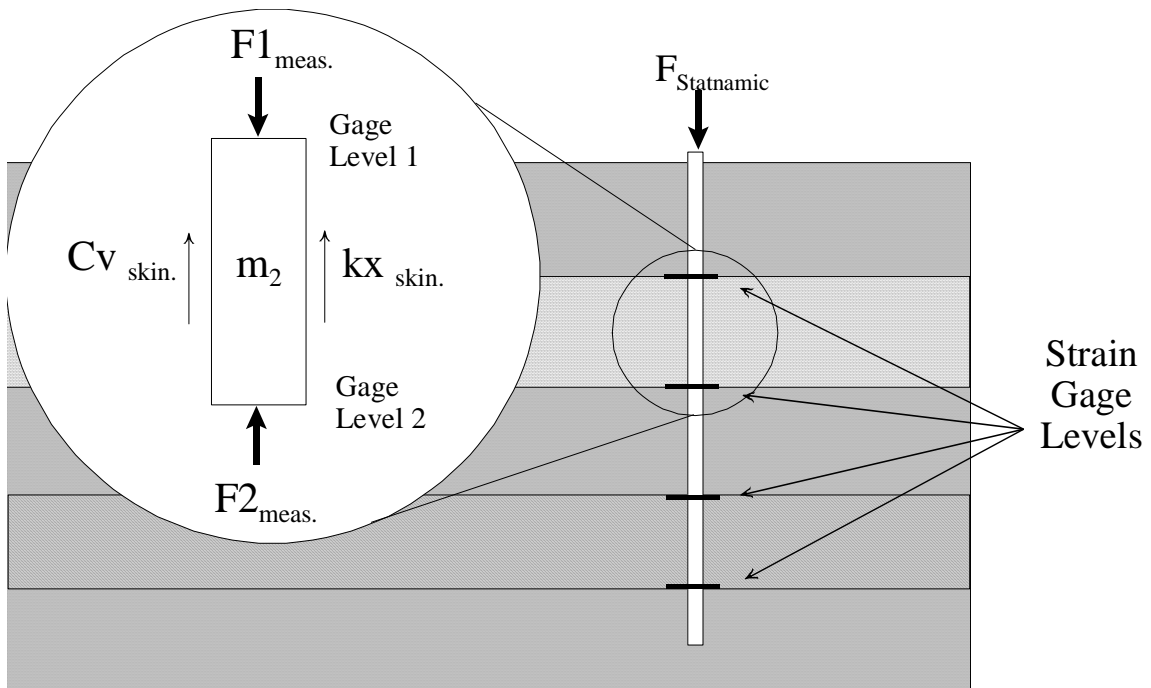


Figure 42. Schematic of segments and strain gage levels

Gage Level Information

Gage Level 1

Select Input Units

SI Units Note: All data will be exported as SI units. Selecting English units will convert input data to SI units
 English Units

Cross Section:

Concrete Diameter: m Pipe Pile Thickness: mm
 Void Diameter: m Pipe Pile Inner Diameter: m

Elevation: m H-Piles:

Number of Gages: Area: mm²

Number of Re-Bar:

Bar Number:

Update Level

Next Level

Exit

Gage Locations

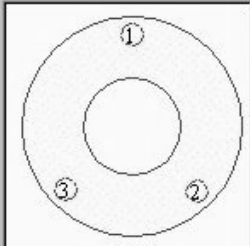


Figure 43. SUP Software Screen Capture (Gage Level Information Input Screen)

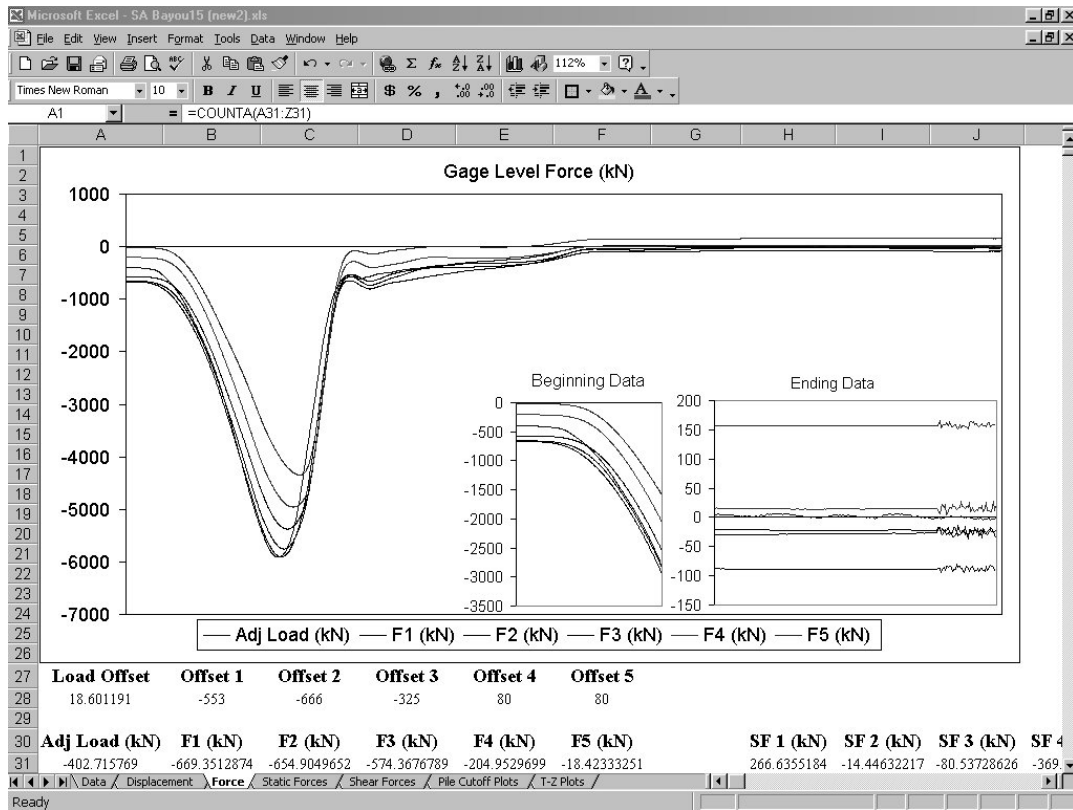


Figure 44. SUP Segmental Analyzer Module

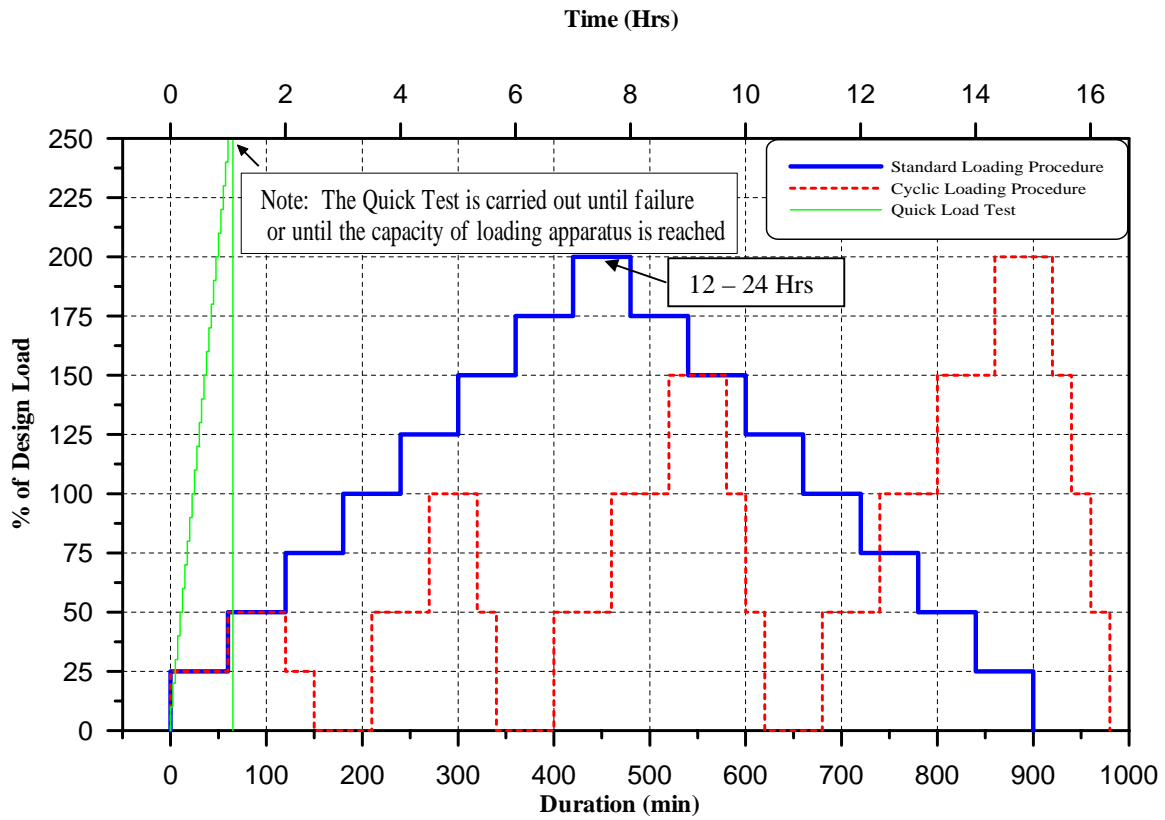


Figure 45. Static Pile Load Testing Procedures According to ASTM in Comparison with the Static-Cyclic Loading Procedure (Paikowsky et al., 1999).

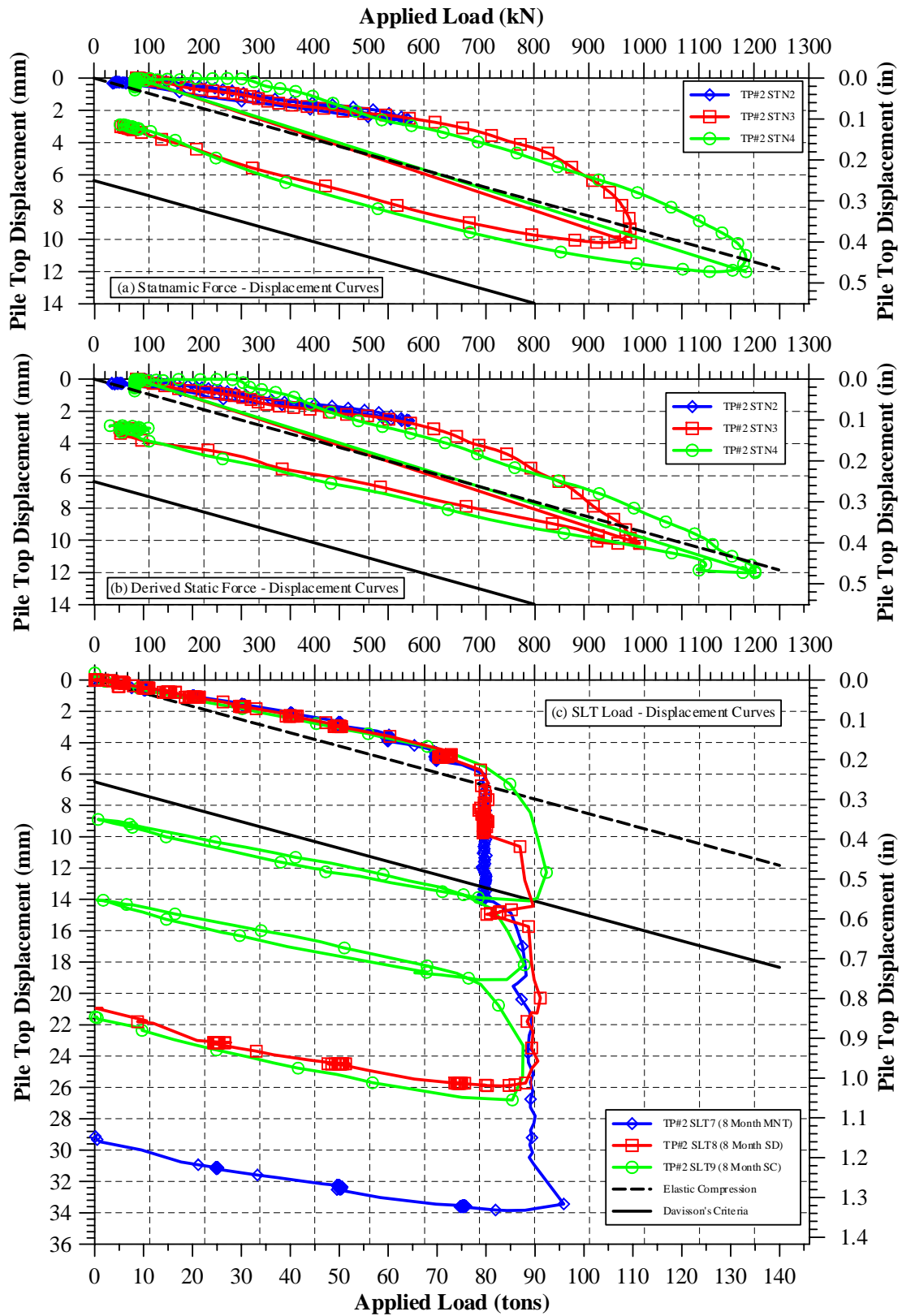


Figure 46. Various Static and Statnamic Test Results, Test Pile #2 in Newbury MA (Hajduk et al., 1998)

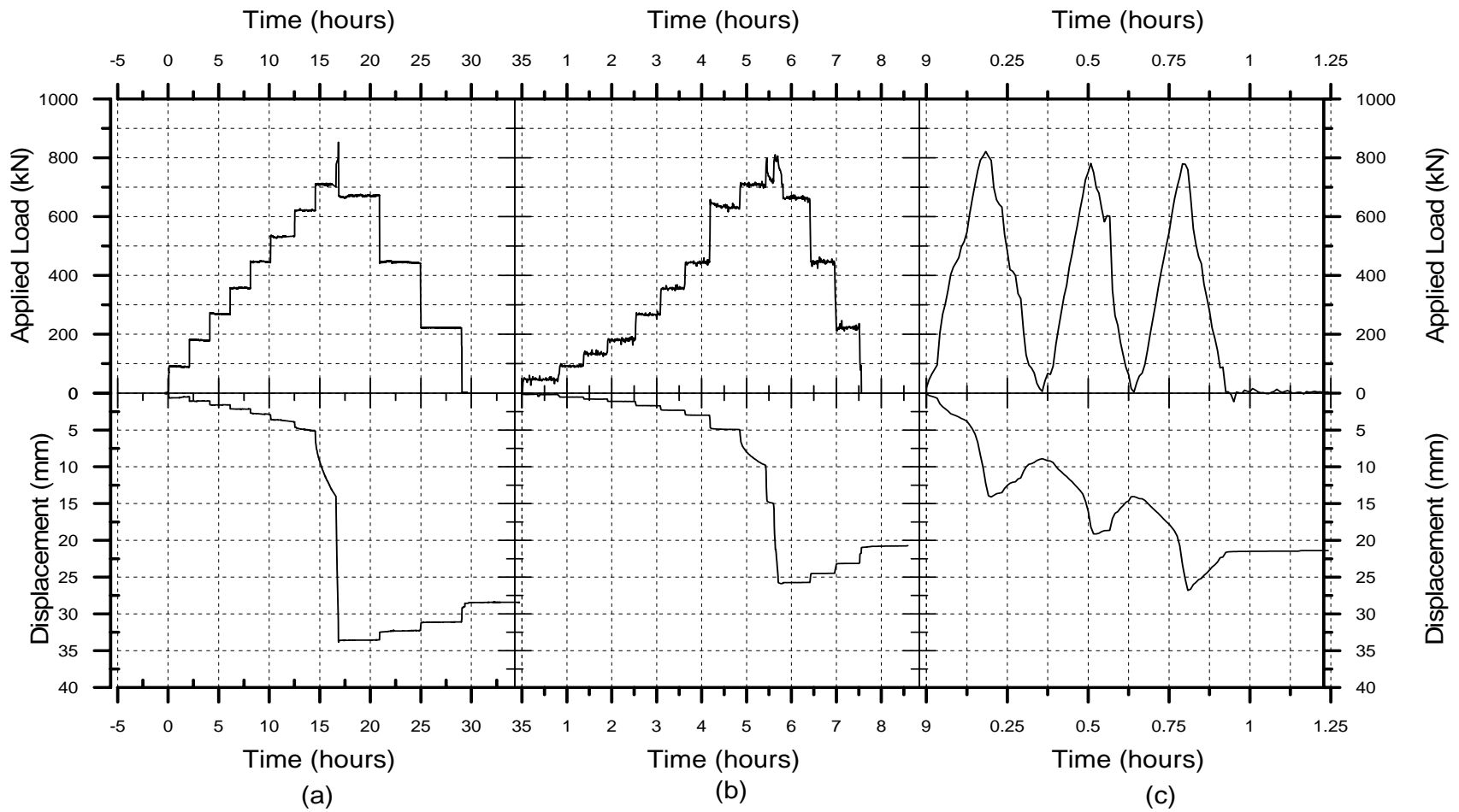


Figure 47. Static-Cyclic Test plots of Displacement vs. time and Load vs. displacement
 (a) Slow maintained (b) short Duration (c) Static-Cyclic

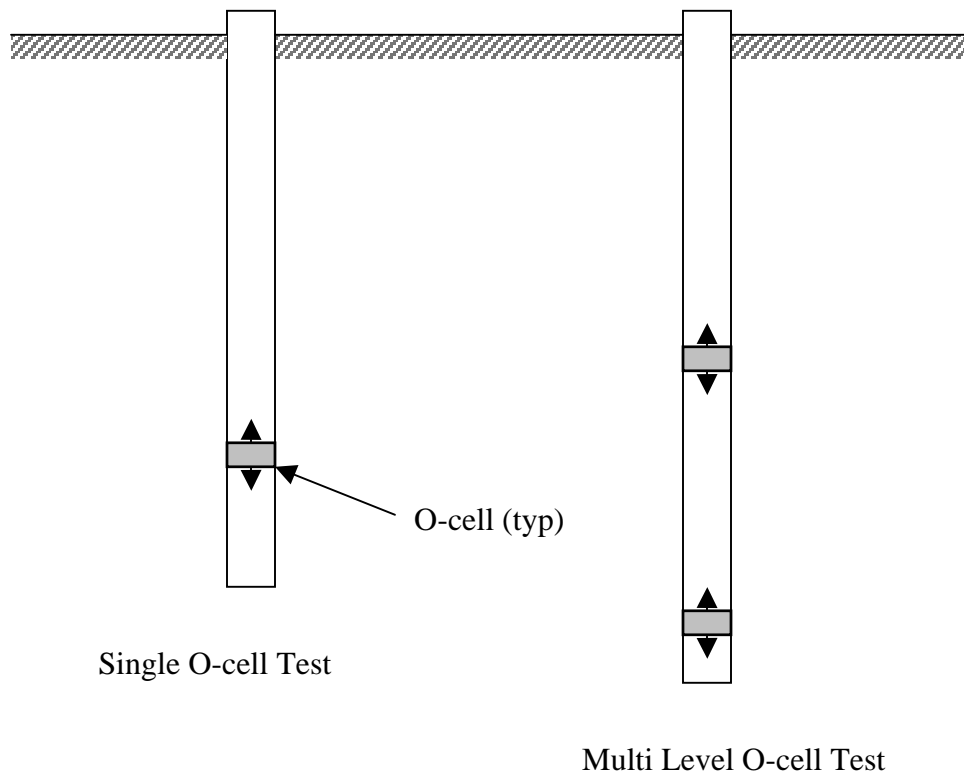


Figure 48 Schematic Diagram of O-cell Testing

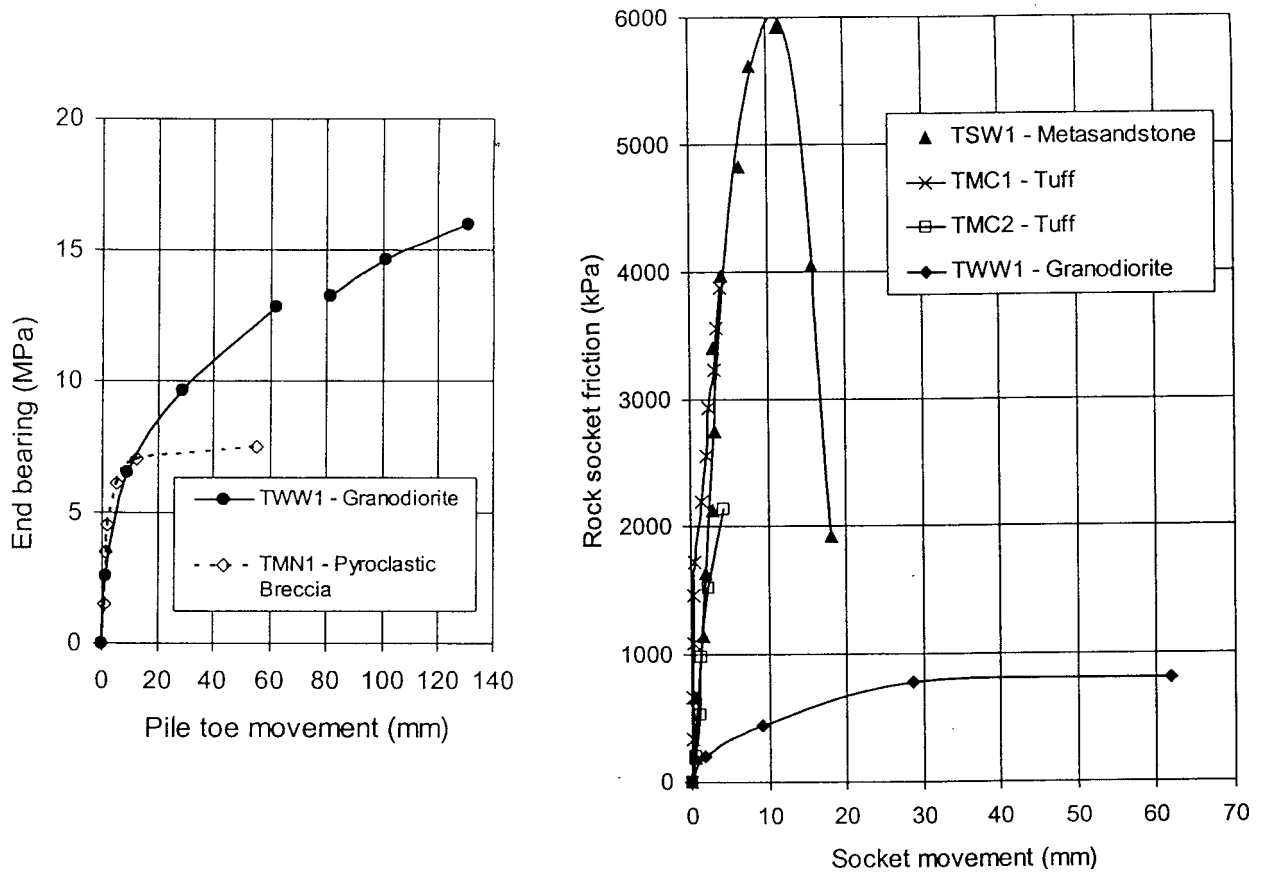
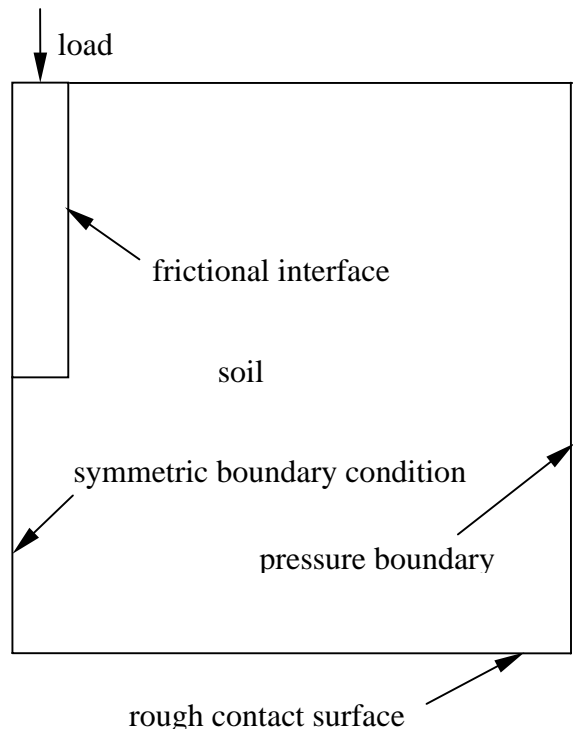
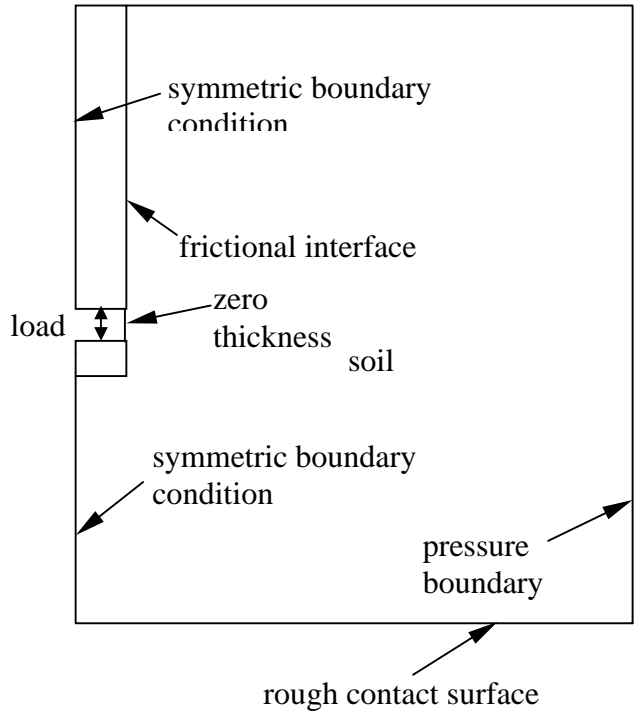


Figure 49. O-cell Testing Results for the Kowloon-Canton Railway, Hong Kong (Littlechild, et al., 2000)



(a) Top Down Test



(b) O-cell Test

Figure 50. Schematic Diagram of Axi-symmetric FE Model

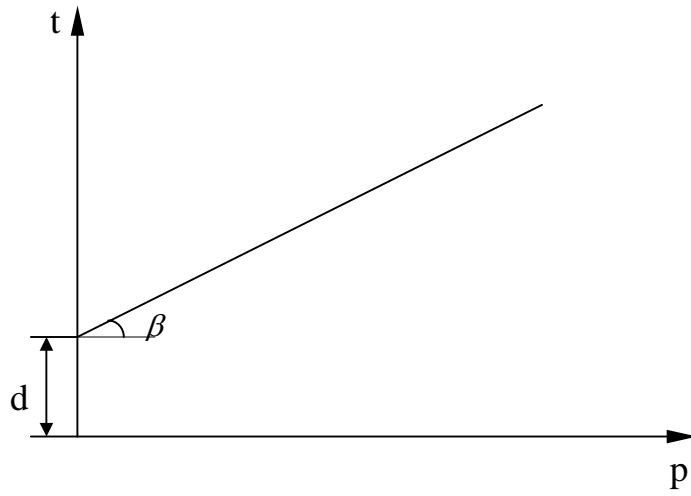


Figure 51. Drucker-Prager Model Yield Surface in Meridian Plane

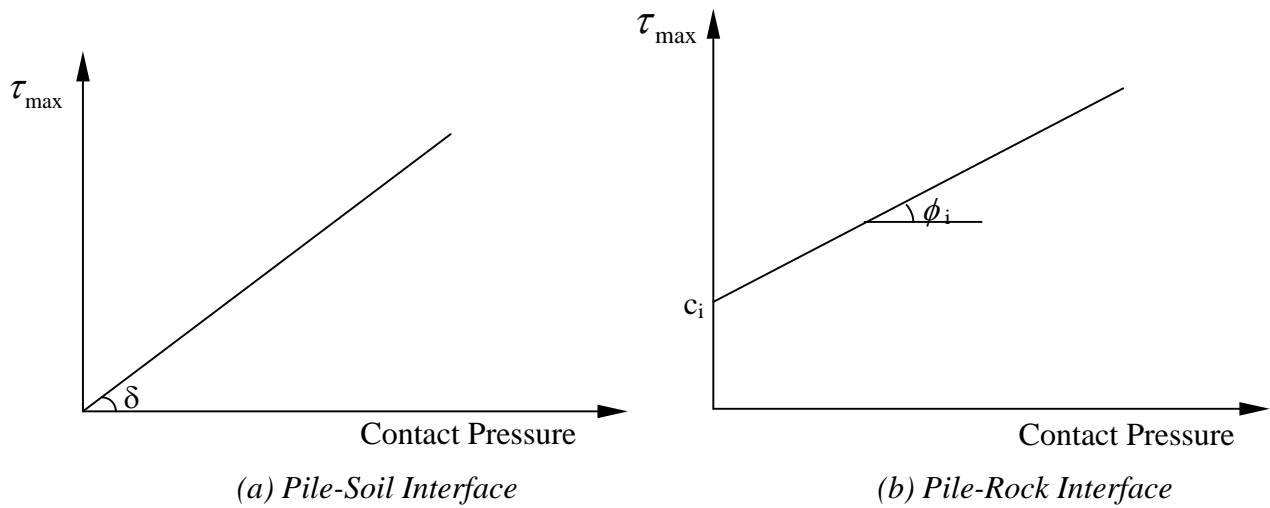


Figure 52. Pile-Soil and Pile-Rock Interface Model

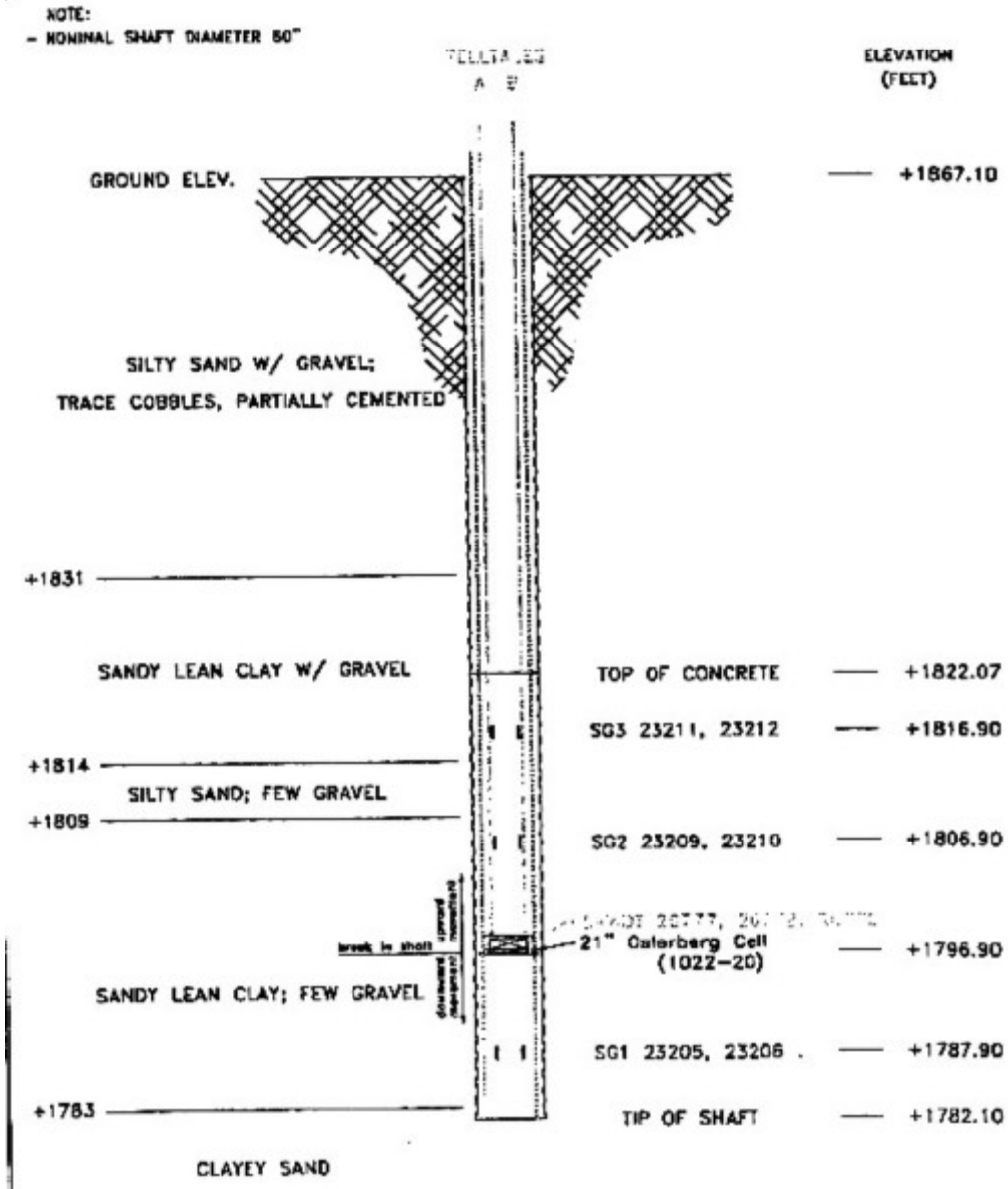


Figure 53. Dimensions and Instrumentation of Test Shaft6, Henderson Case

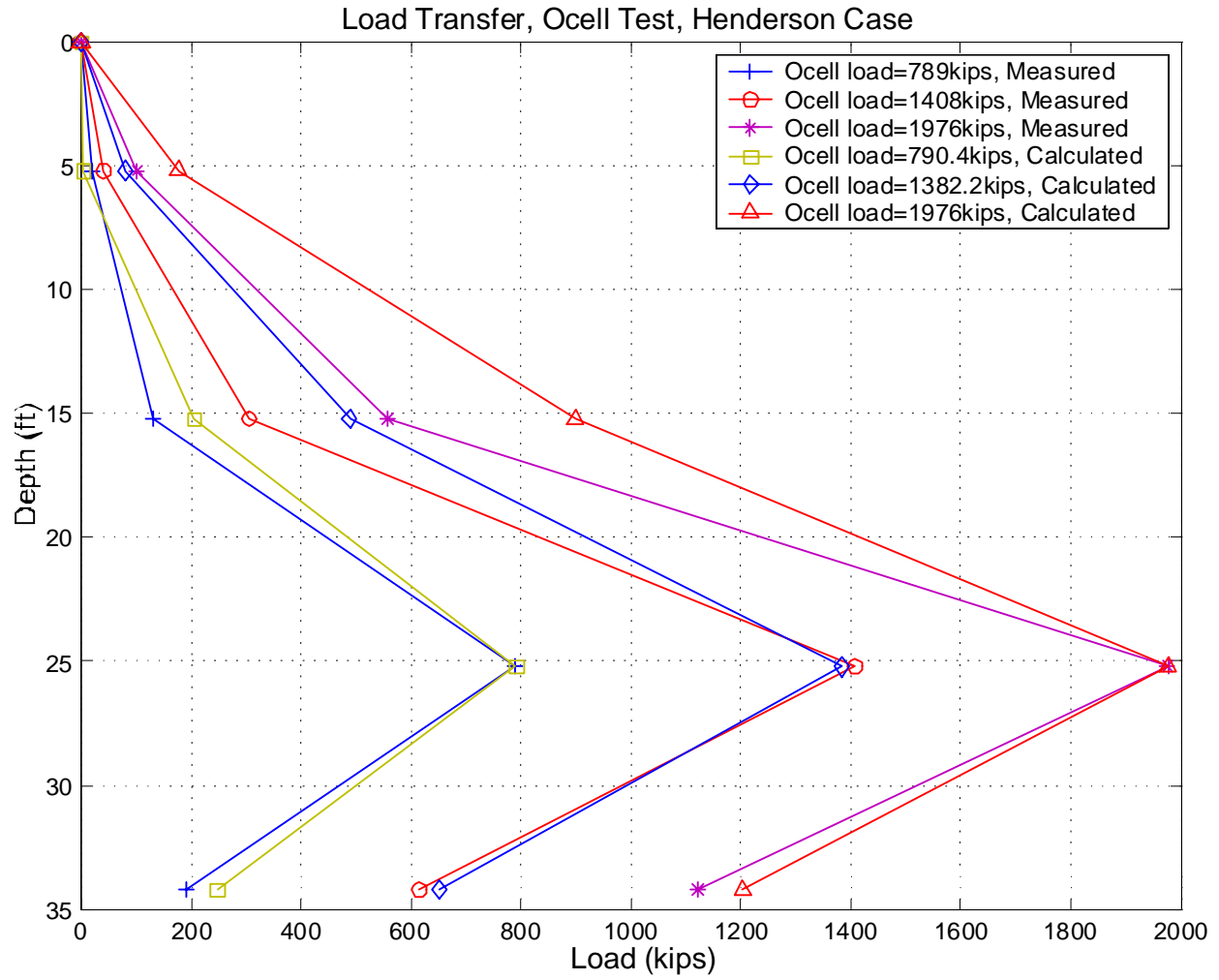


Figure 55. Comparison of Load Transfer Curve, O-cell Test, Henderson Case

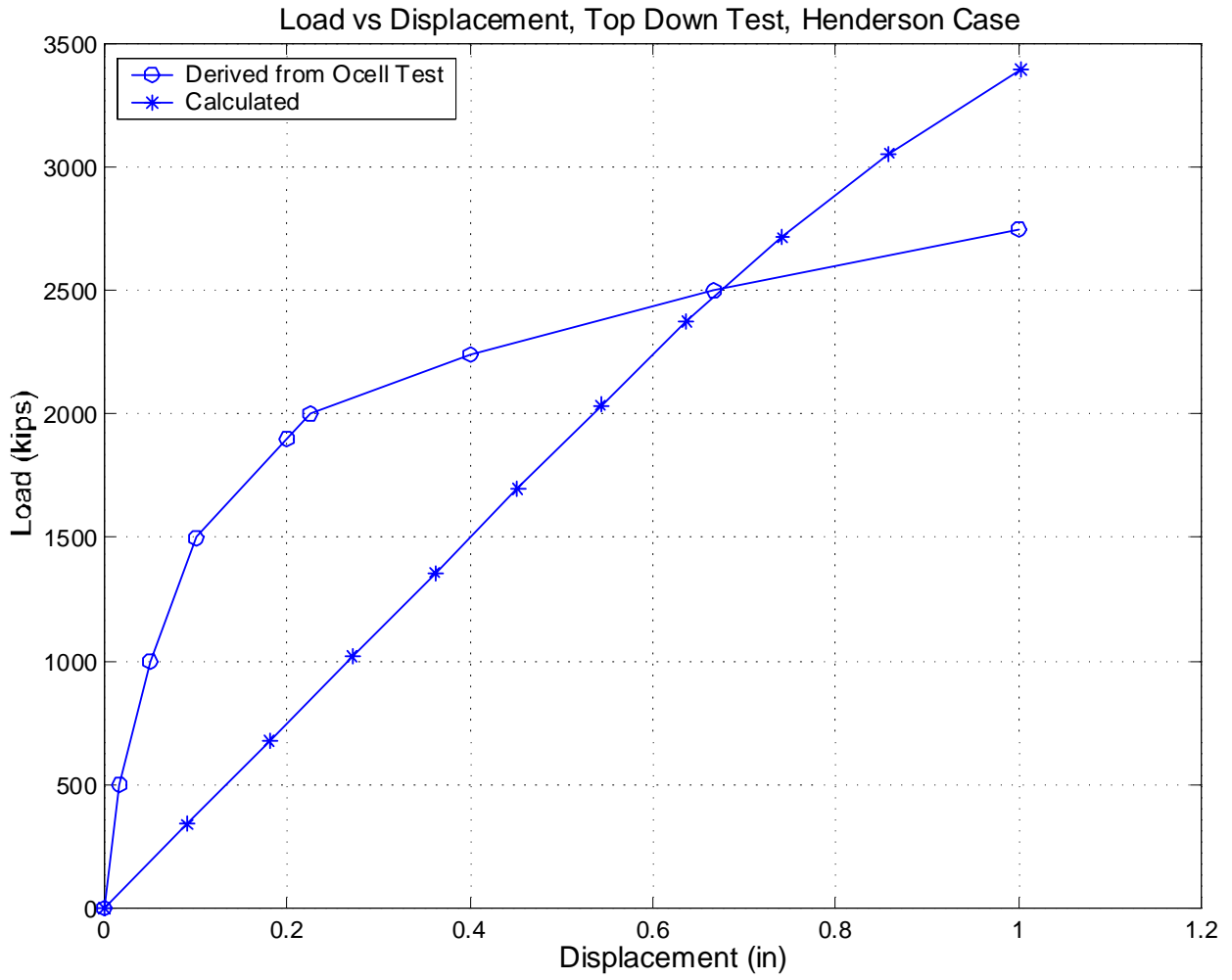
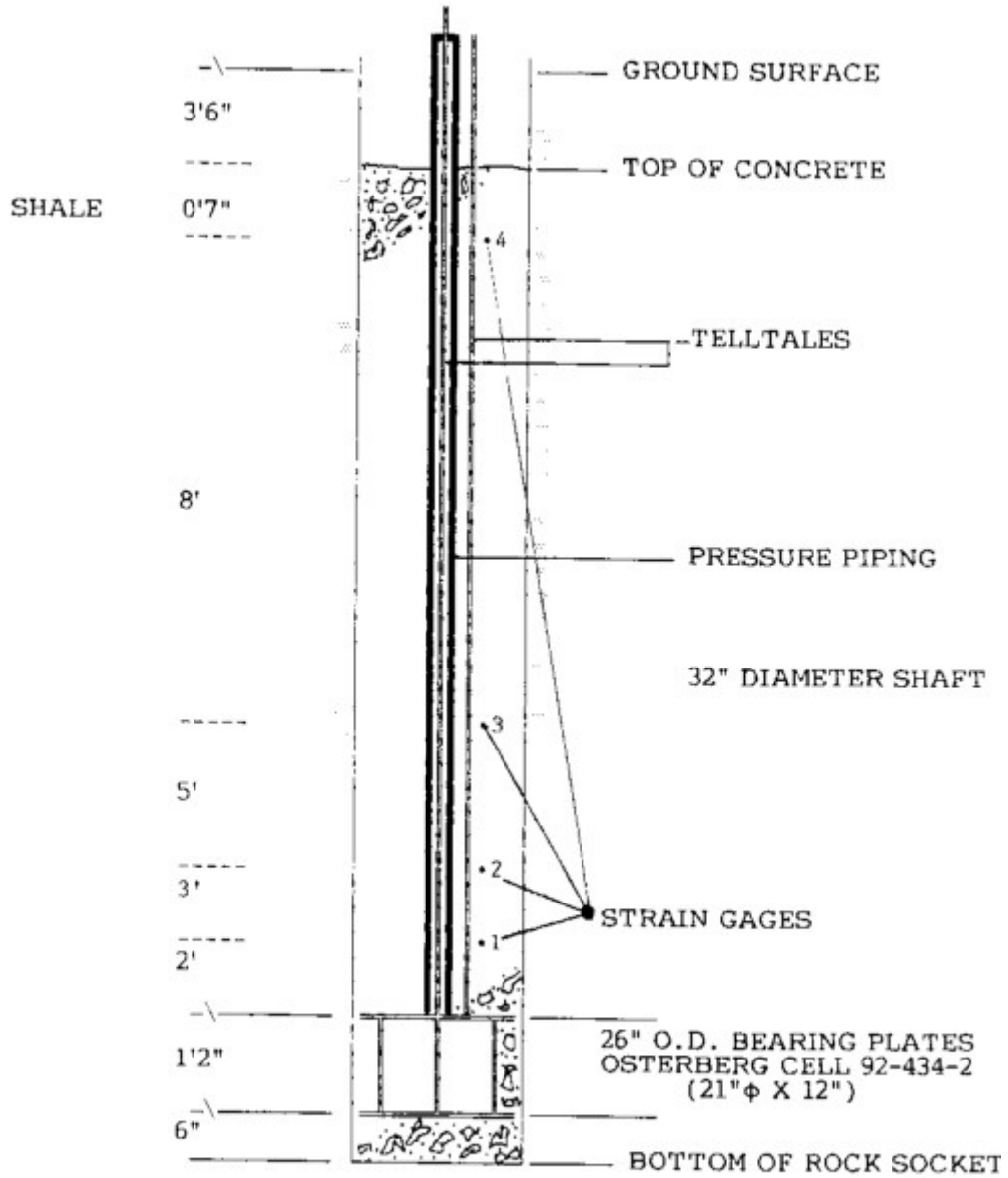


Figure 56. Comparison of Load vs. Displacement Curve, Top Down Test, Henderson Case

**TEST SHAFT INSTALLATION SCHEMATIC
(NOT TO SCALE)**



**POWER SYSTEMS DEVELOPMENT FACILITY
WILSONVILLE, ALABAMA
LOADTEST PROJECT No. LT-163**

Figure 57. Dimensions and Instrumentation of Test Shaft, Wilsonville Case

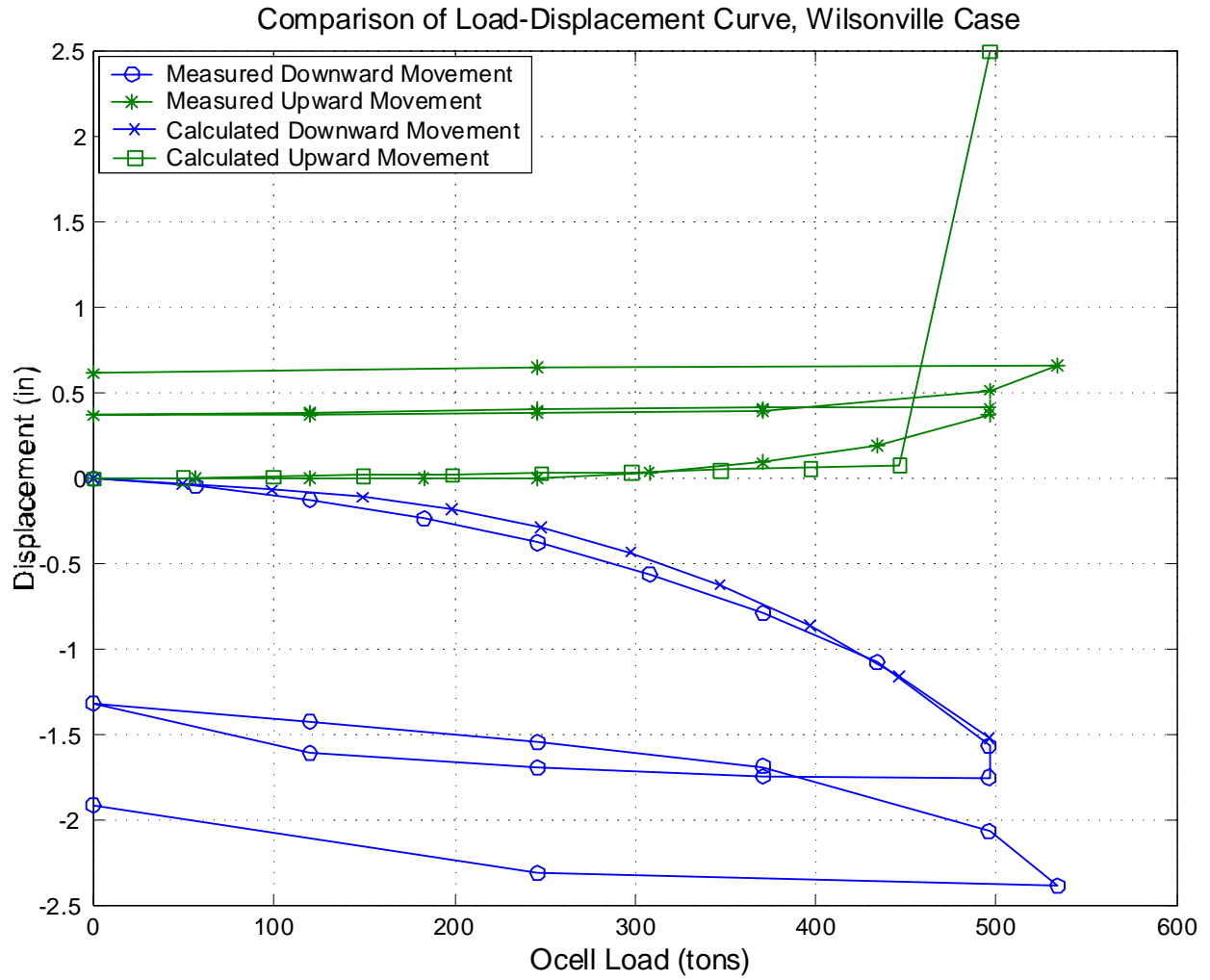


Figure 58. Comparison of Load vs. Displacement Curve, O-cell Test, Wilsonville Case

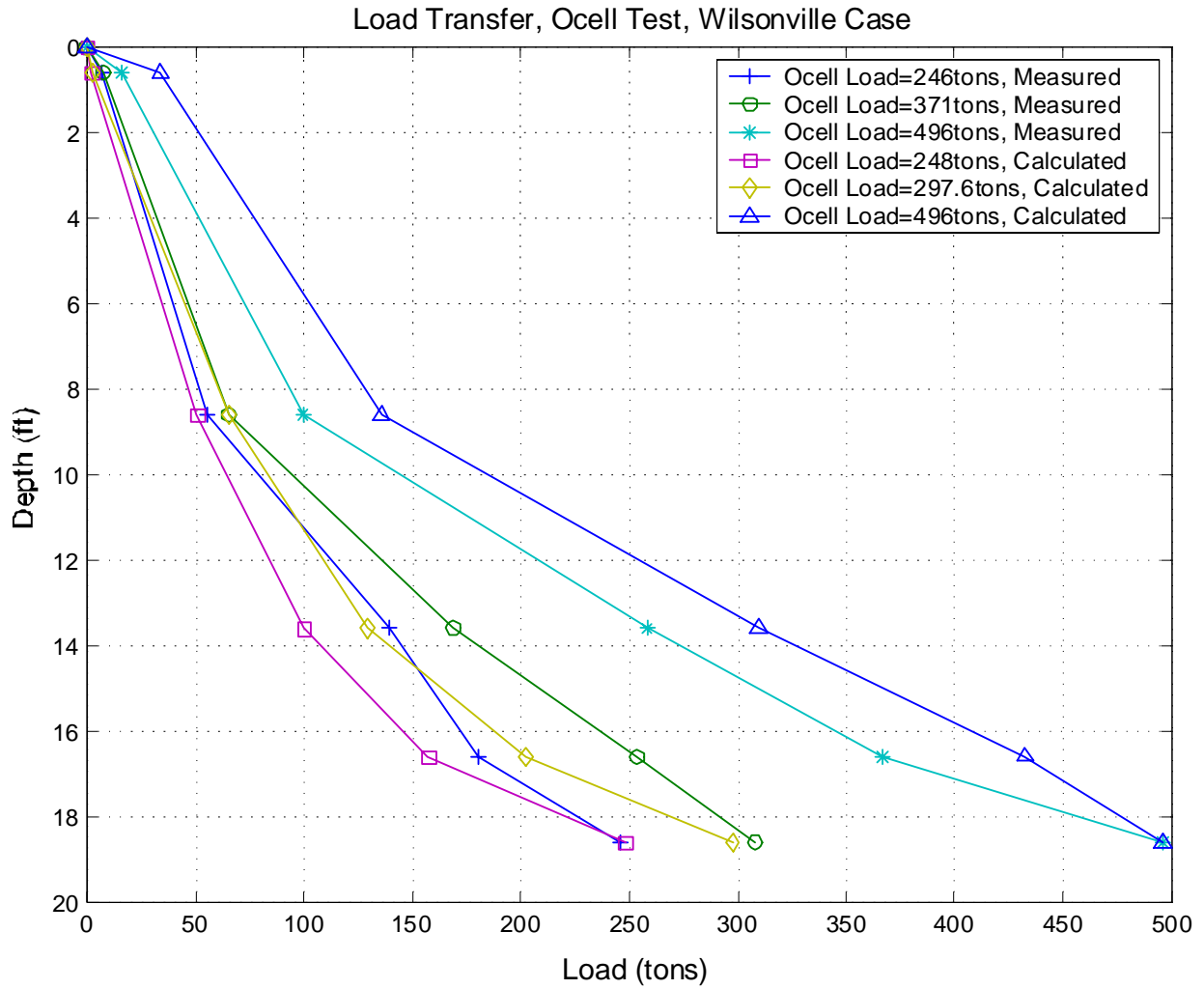


Figure 59. Comparison of Load Transfer Curves, O-cell Test, Wilsonville Case

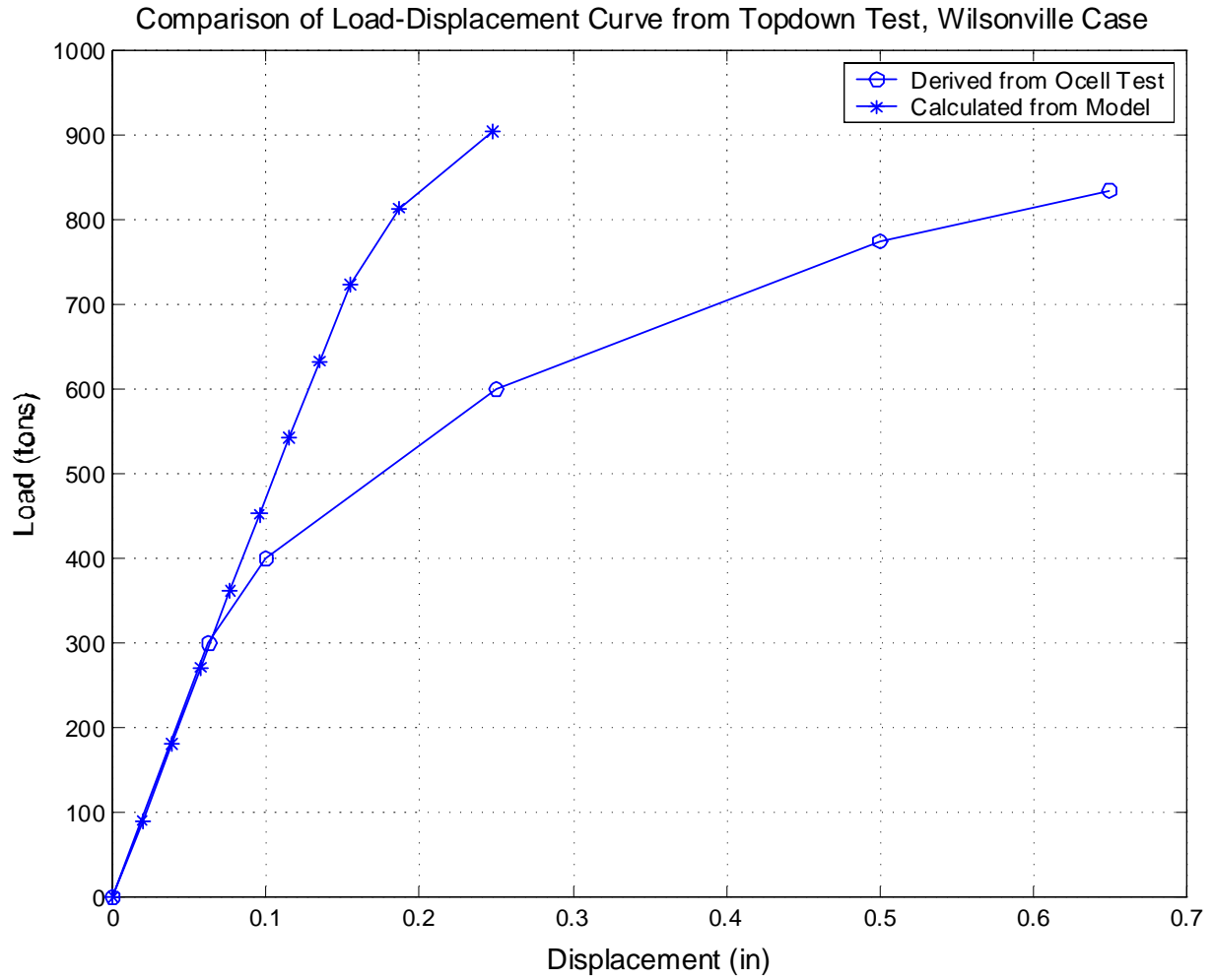


Figure 60. Comparison of Load vs. Displacement Curve, Top Down Test, Wilsonville Case

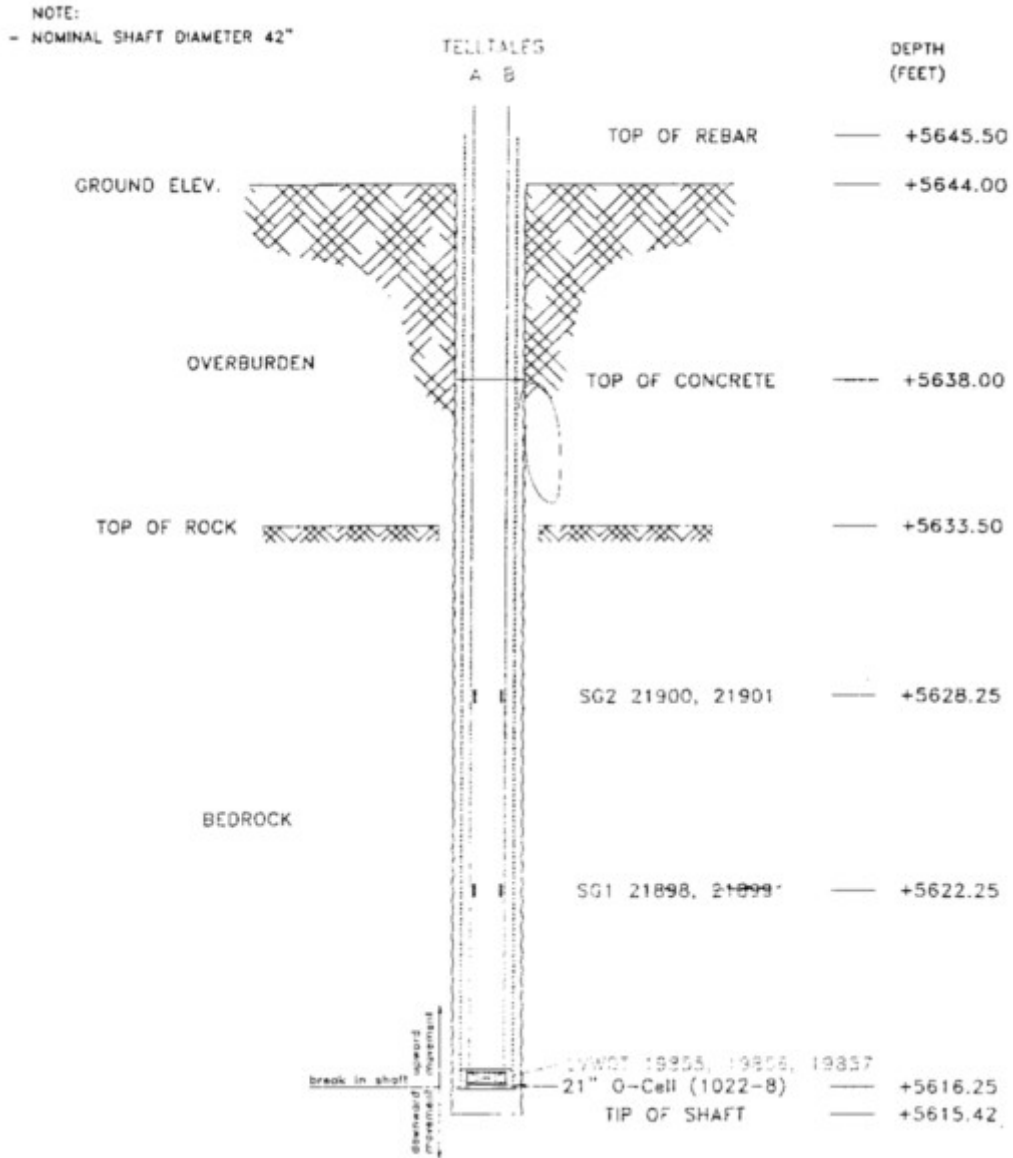


Figure 61. Dimensions and Instrumentation of Test Shaft, Denver Case

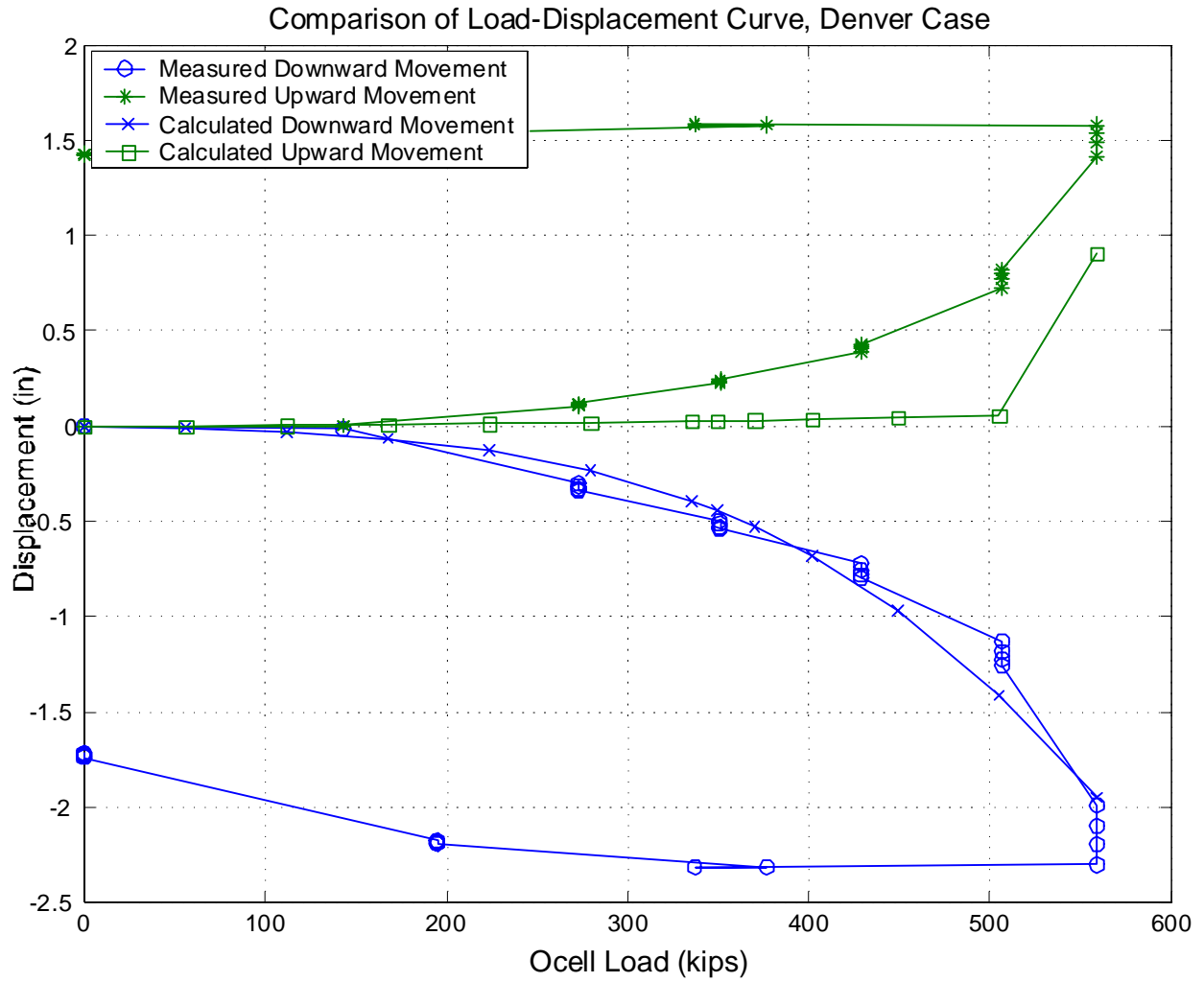


Figure 62. Comparison of Load vs Displacement curve, O-cell Test, Denver Case

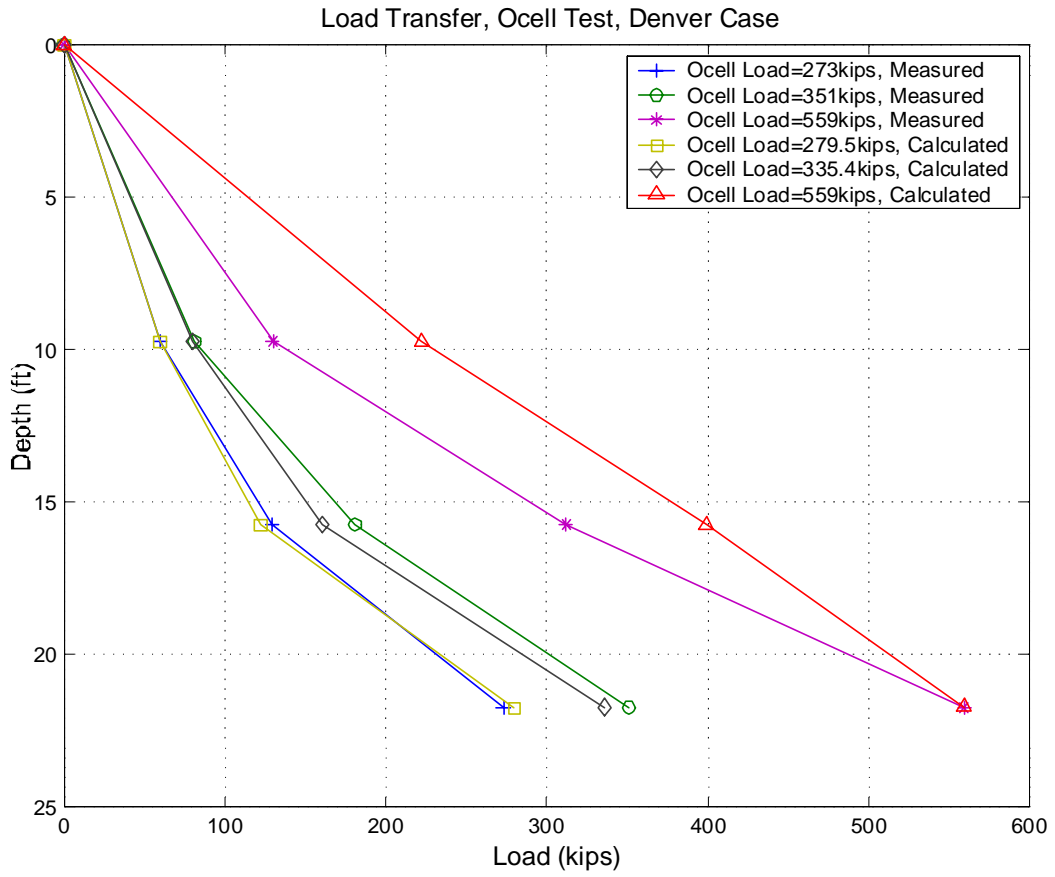


Figure 63. Comparison of Load Transfer Curves, O-cell Test, Denver Case

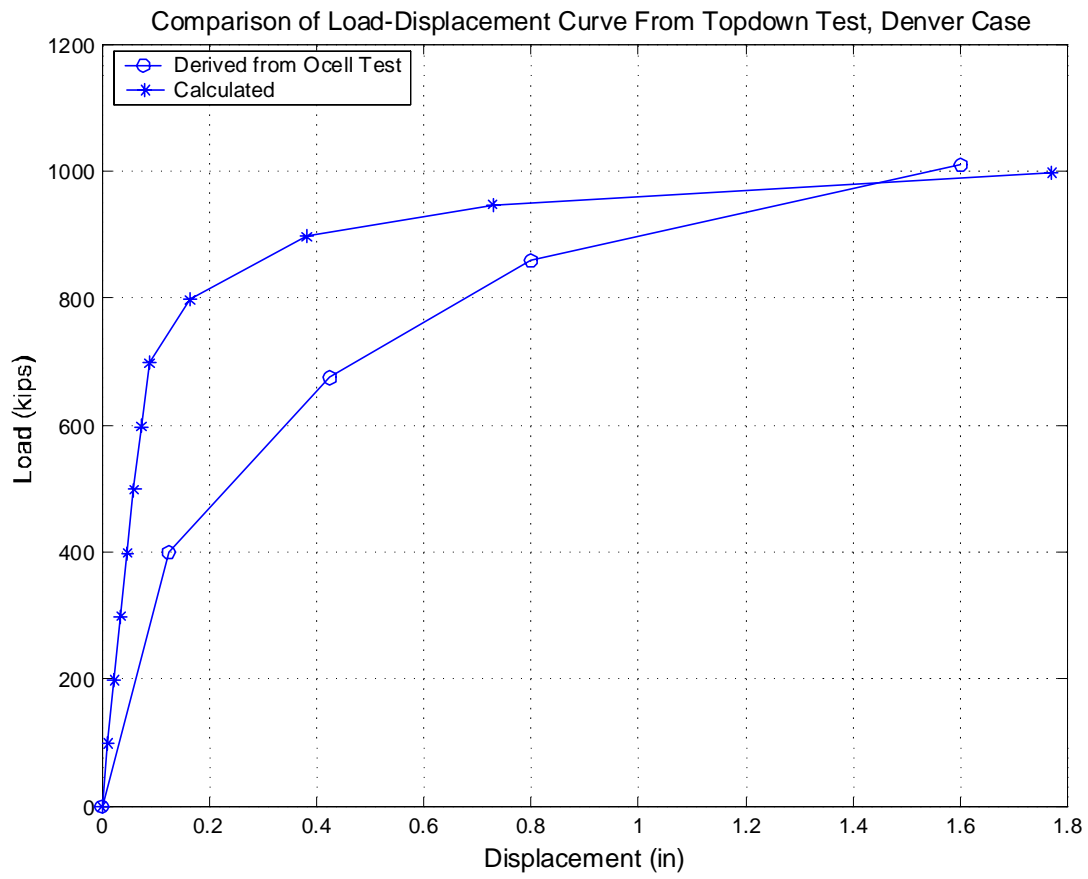
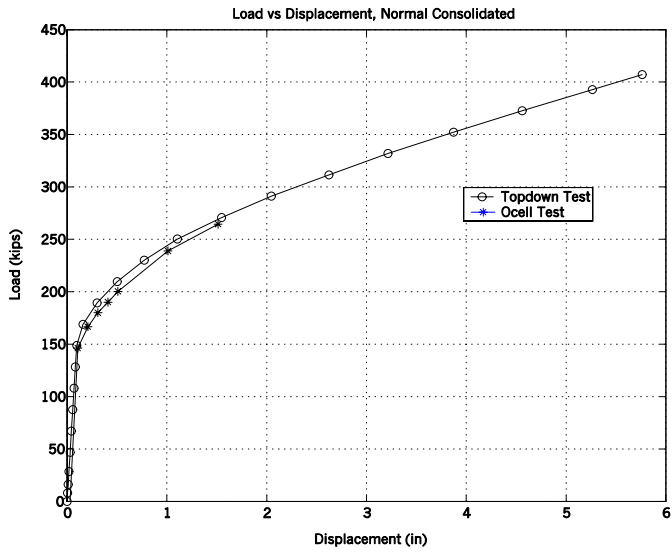
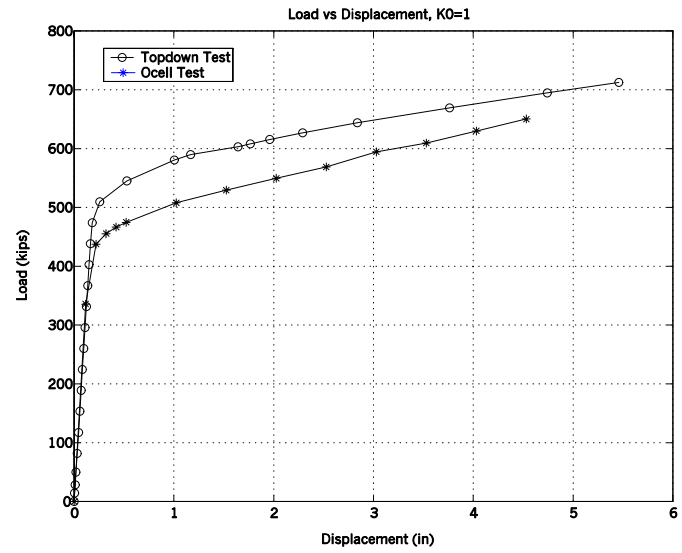


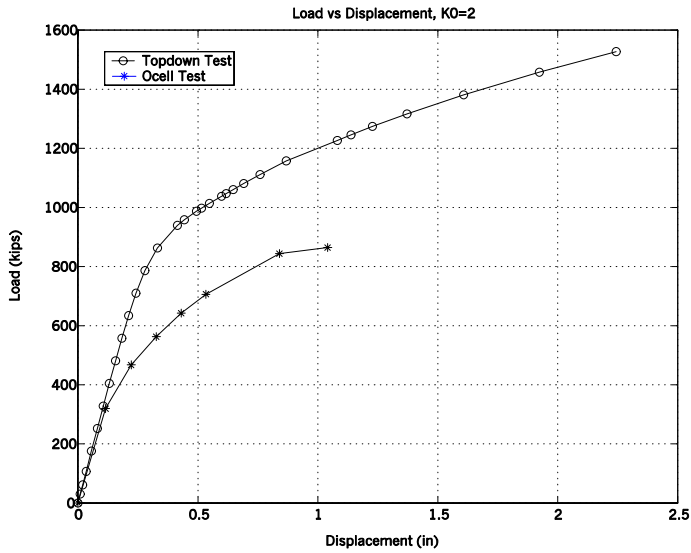
Figure 64. Comparison of Load vs. Displacement Curve, Top Down Test, Denver Case



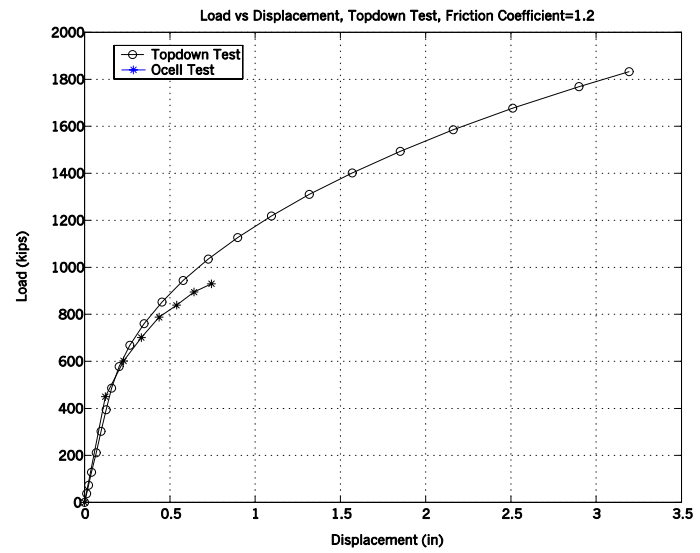
a) $K_o = 0.43$, Shaft/Soil friction $\delta = 31^\circ$



b) $K_o = 1$, Shaft/Soil friction $\delta = 31^\circ$

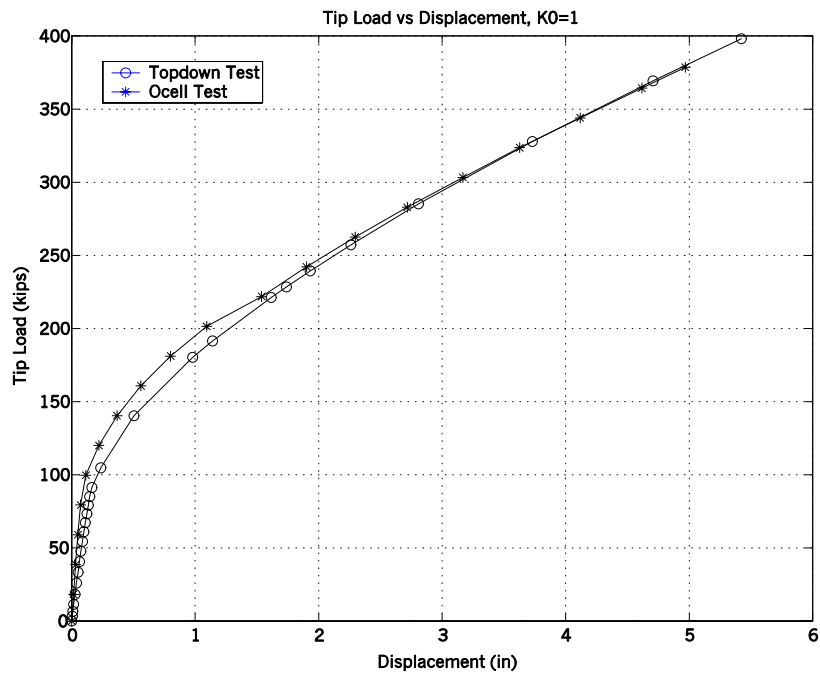


c) $K_o = 2$, Shaft/Soil friction $\delta = 31^\circ$

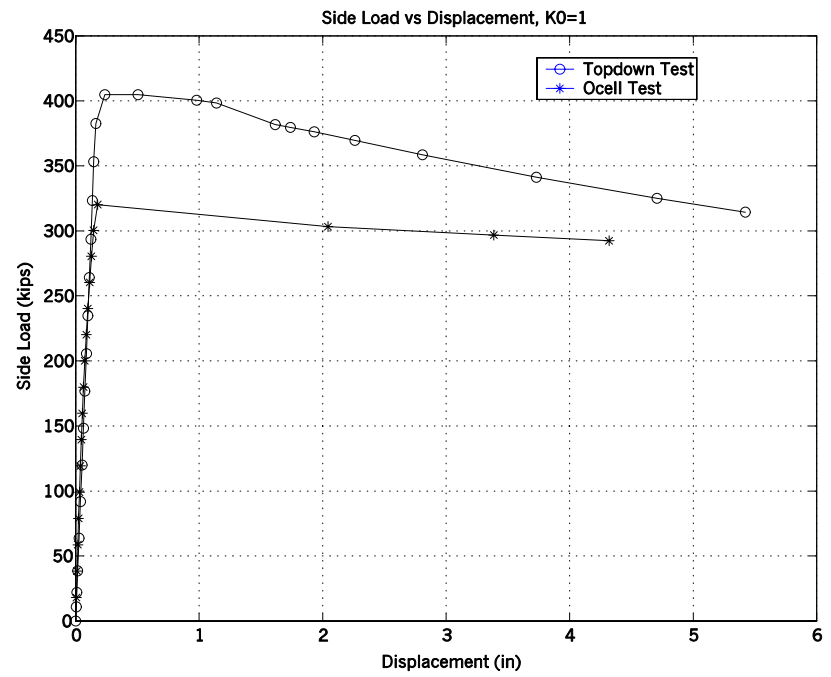


d) $K_o = 1$, Shaft/Soil friction $\delta = 50^\circ$

Figure 65. Top Down vs O-cell Computed Load-Deflection for Soils

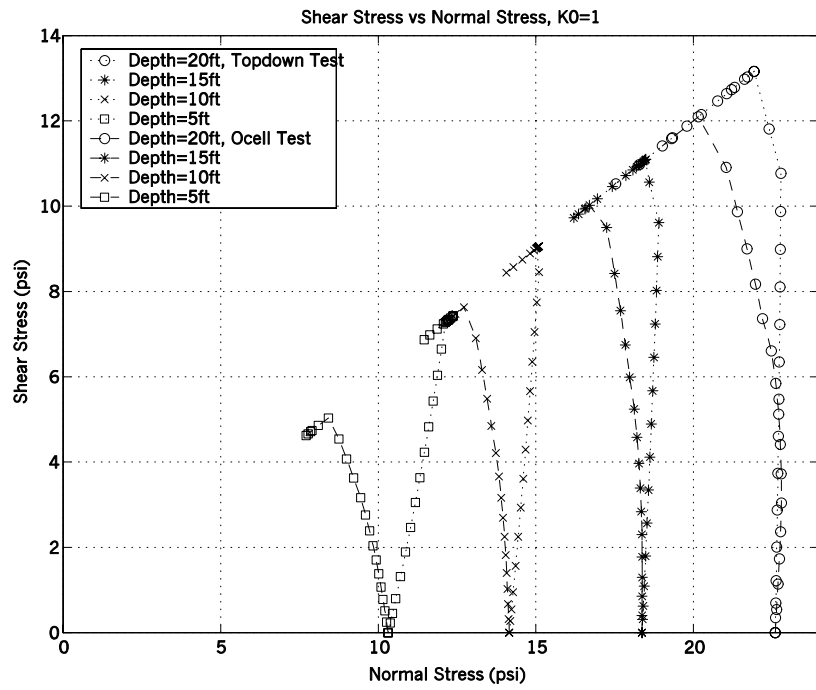


(a) tip resistance

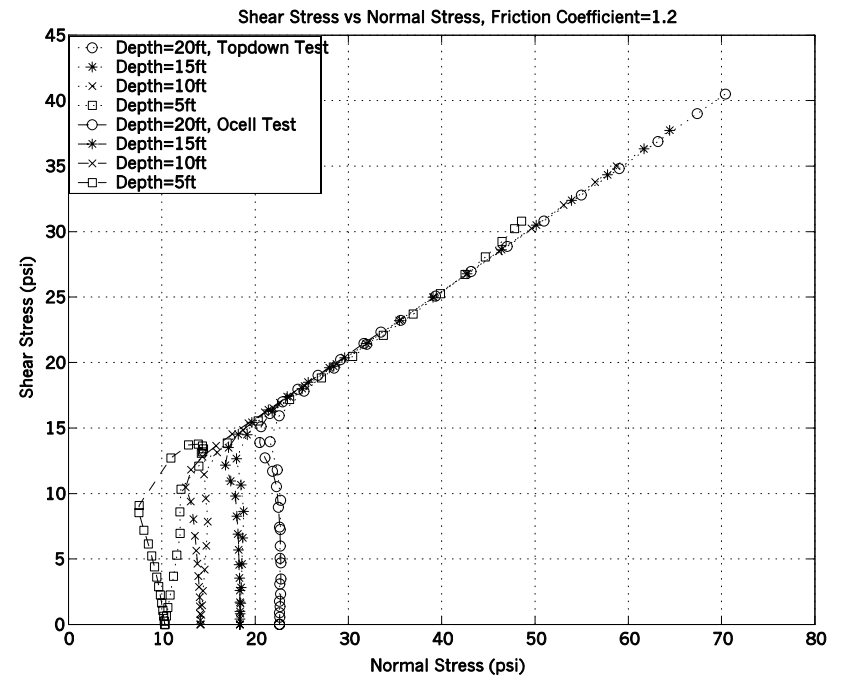


(b) side shear

Figure 66. Computed Tip Resistance and Side Shear for $K_0 = 1$, $\delta = 31^\circ$



(a) $K_0 = 1, \delta = 31^\circ$



(b) $K_0 = 1, \delta = 50^\circ$

Figure 67. Stress Path at Points Along the Shaft/Soil Interface

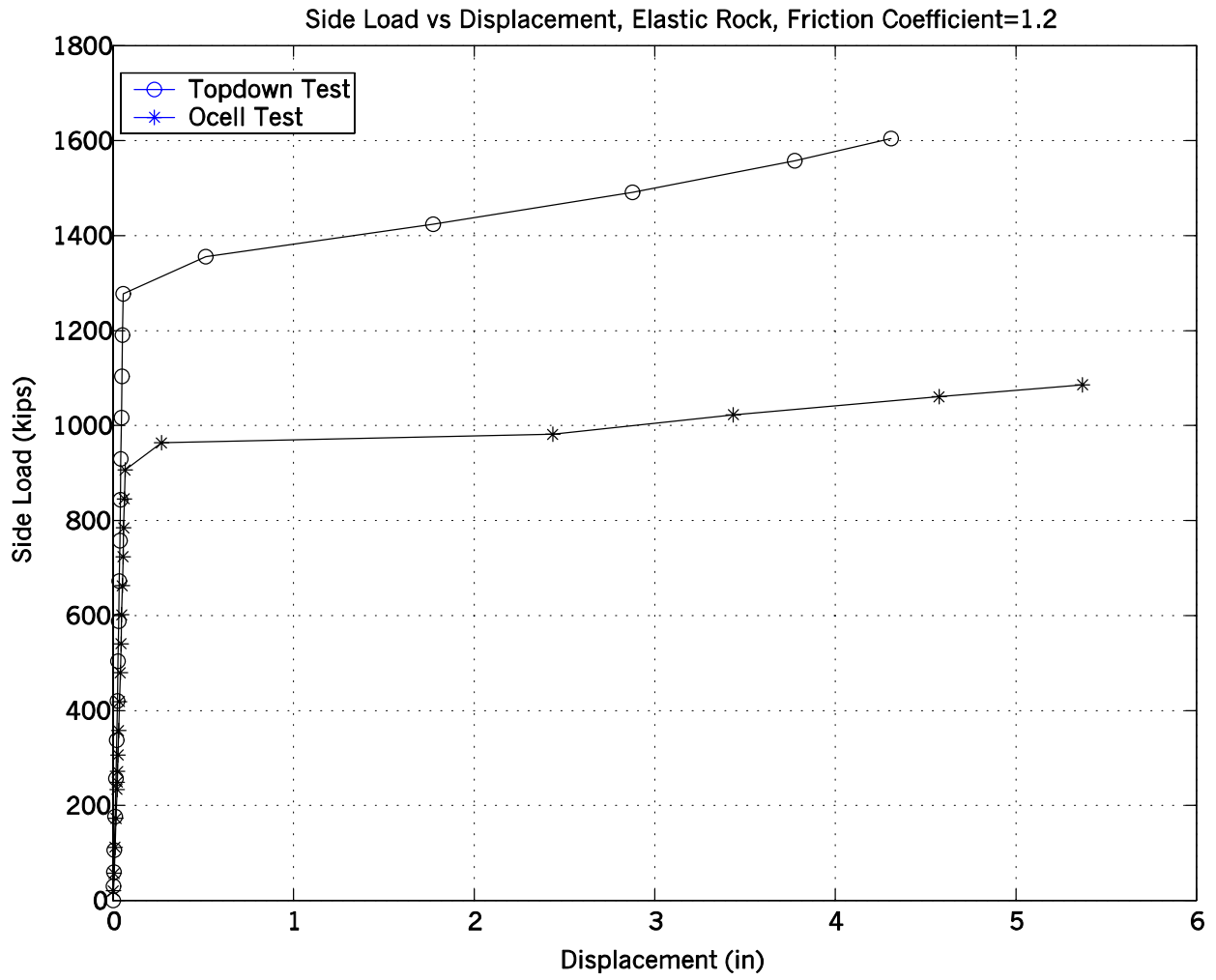
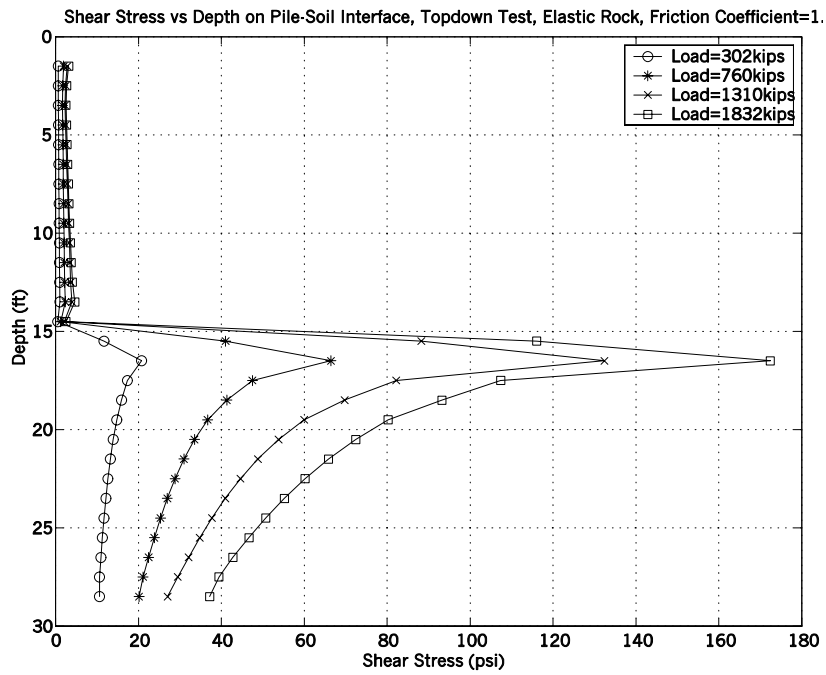
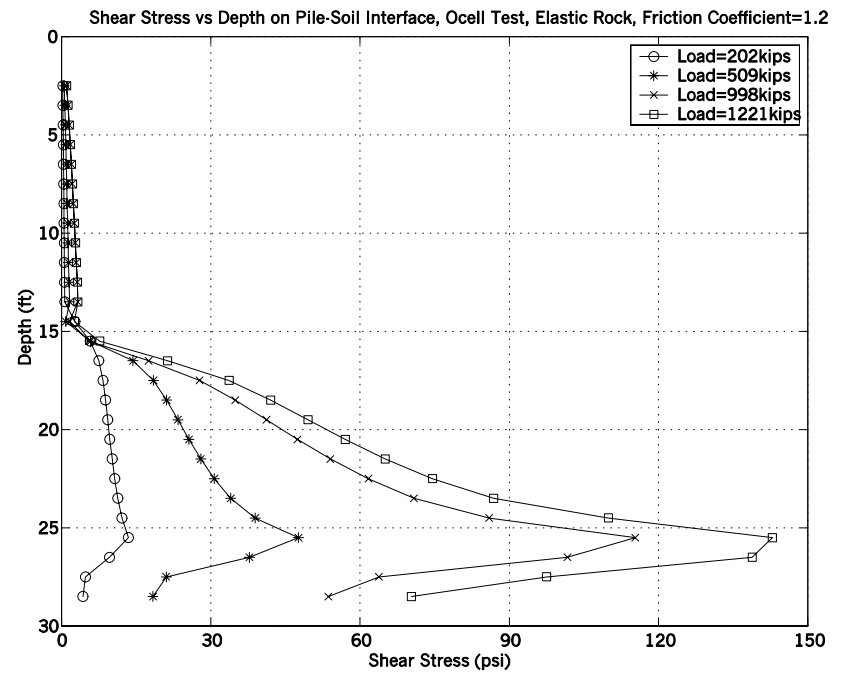


Figure 68. Comparison of Side Shear vs. Displacement for Rock Models



(a) Top Down Model



(b) O-cell Model

Figure 69. Computed Rock Socket Shear Stresses

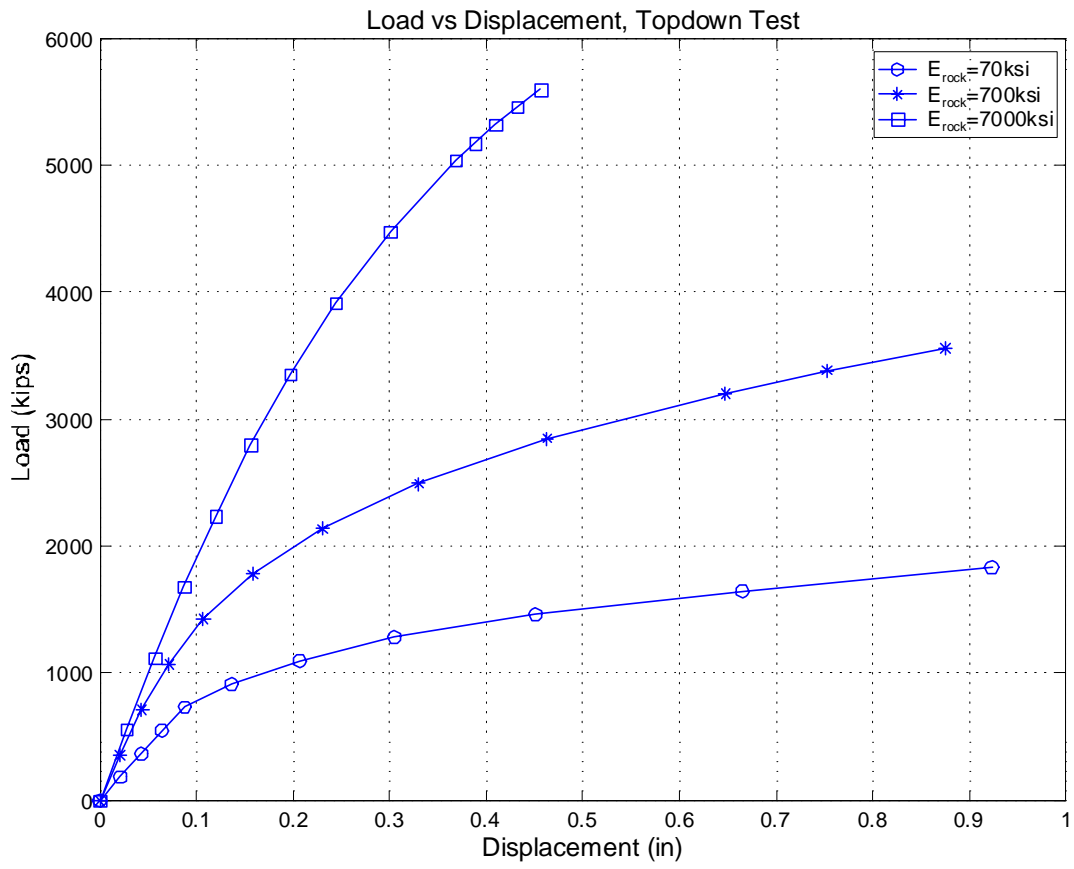
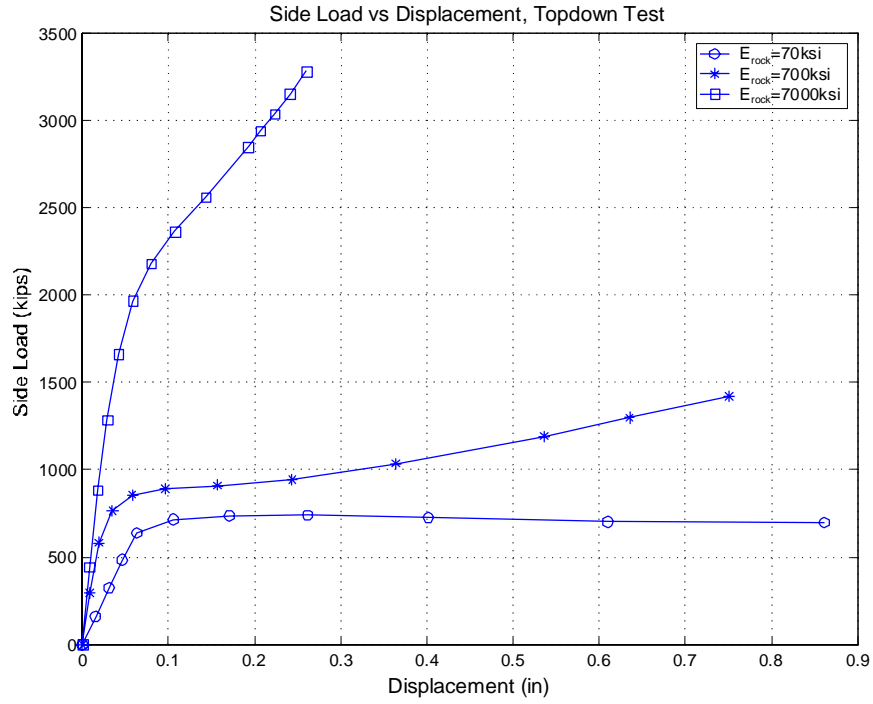
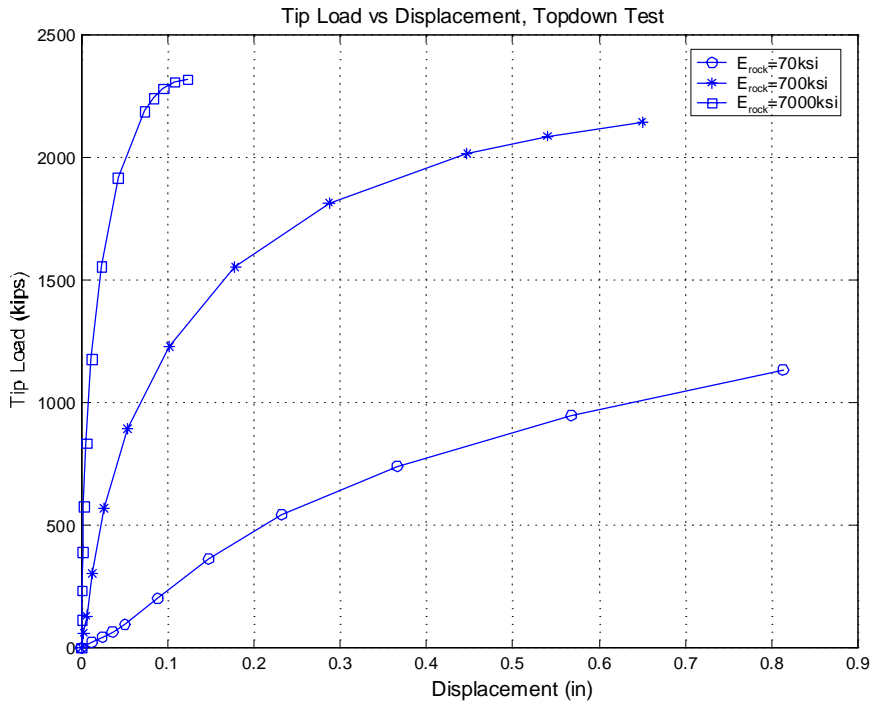


Figure 70. Effect of E_{rock} on Load vs. Displacement Curve, Top Down Test



(a) Side Load vs. Displacement



(b) Tip Load vs. Displacement

Figure 71. Effect of E_{rock} on Side Load vs. Displacement and Tip Load vs. Displacement Curve, Top Down Test

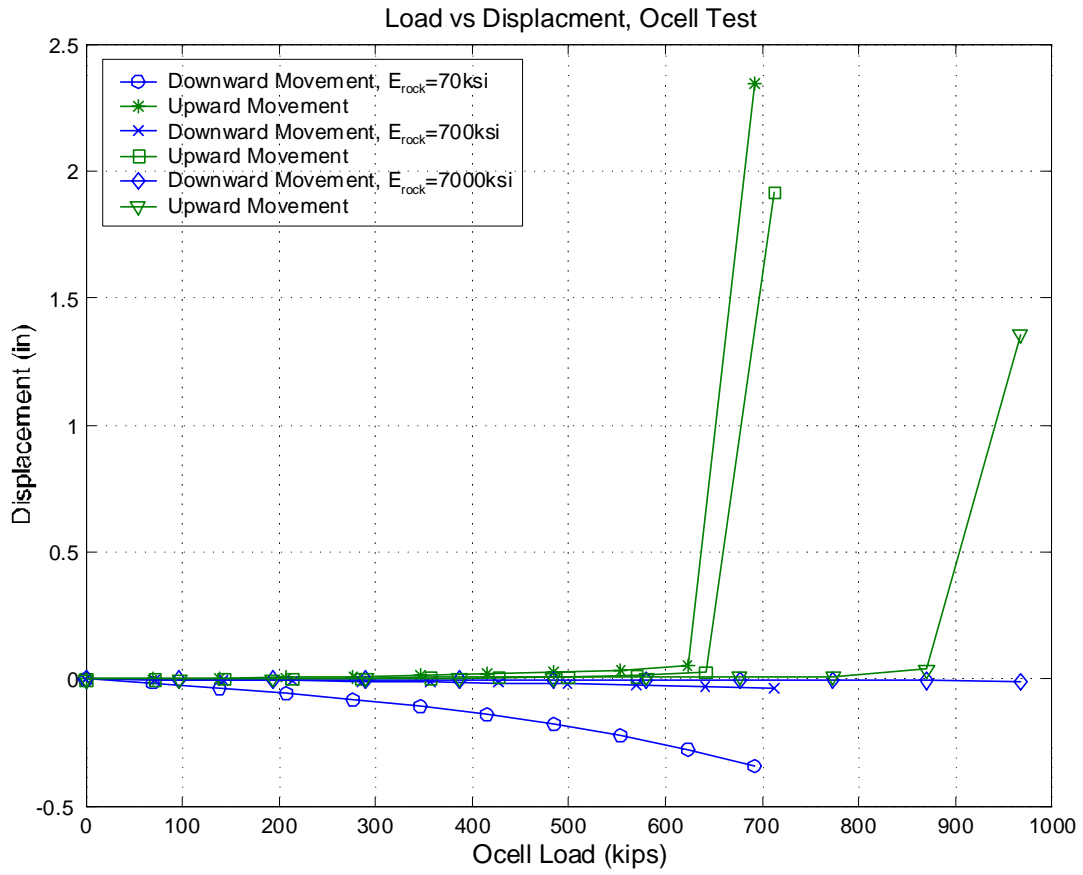


Figure 72. Effect of E_{rock} on Load vs. Displacement Curve, O-cell Test

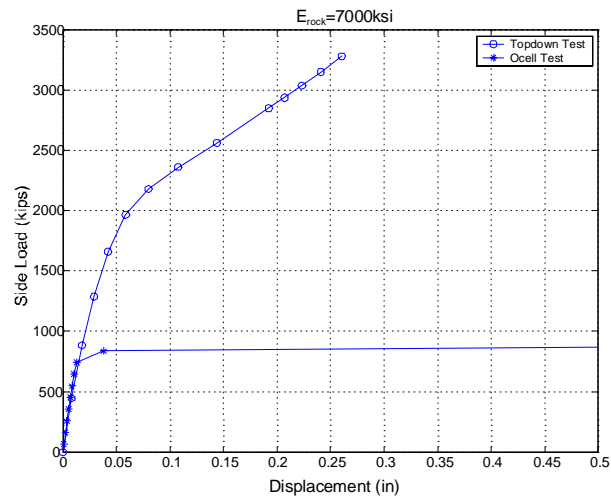
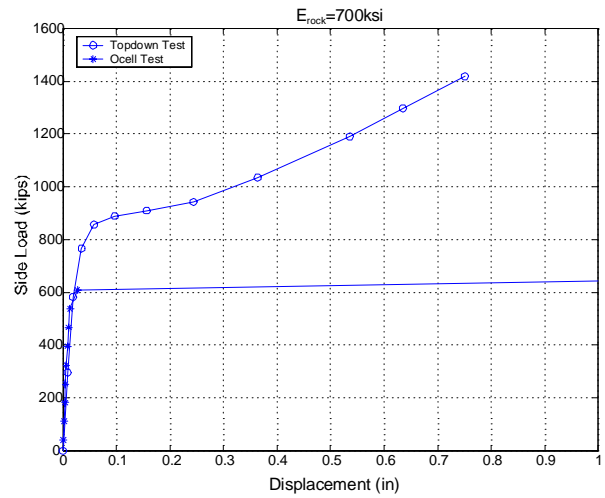
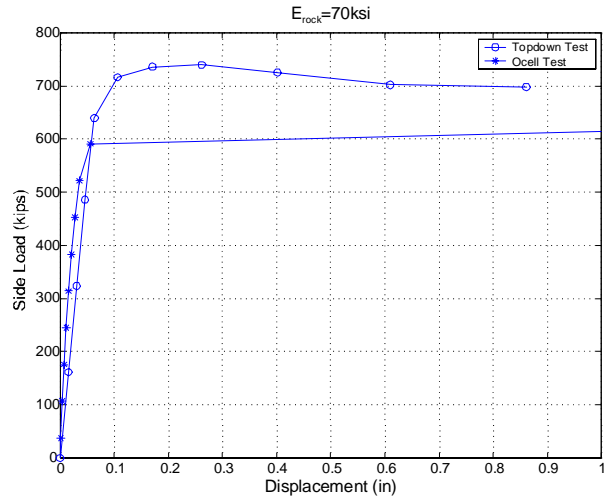


Figure 73. Side Load vs. Displacement Comparison for Different E_{rock} Values

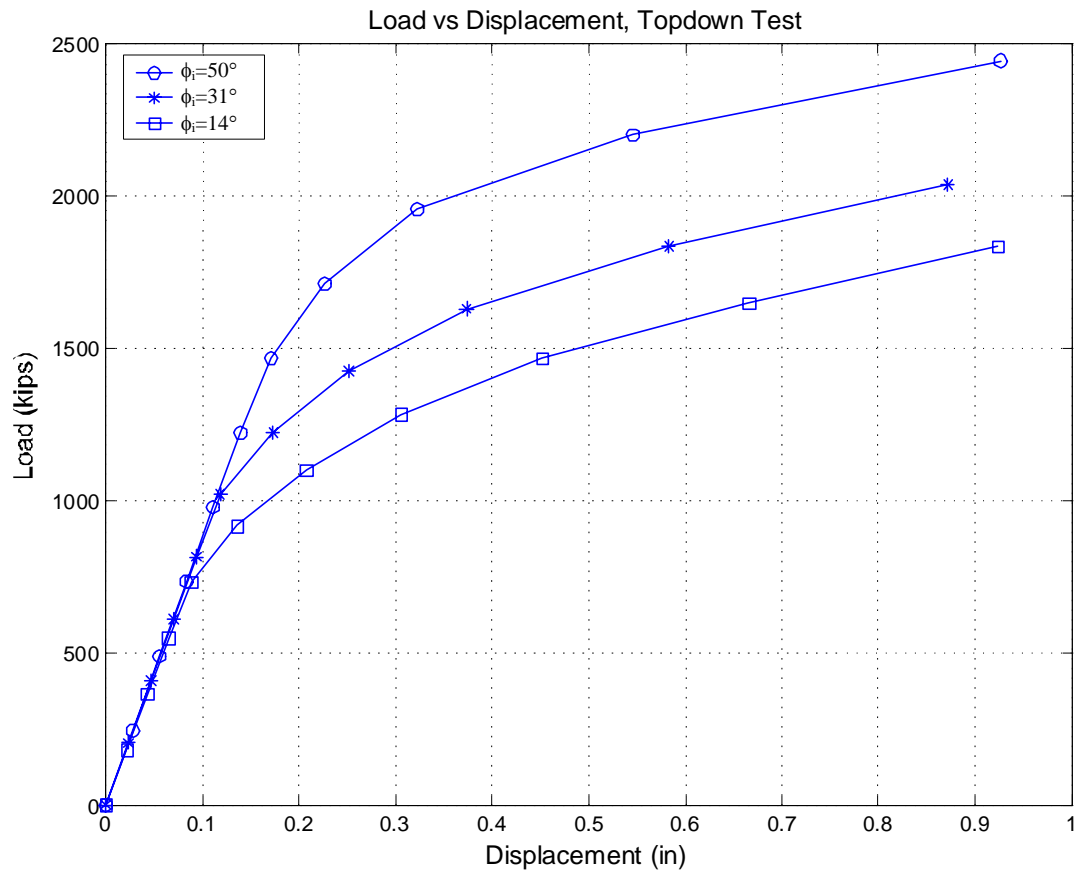
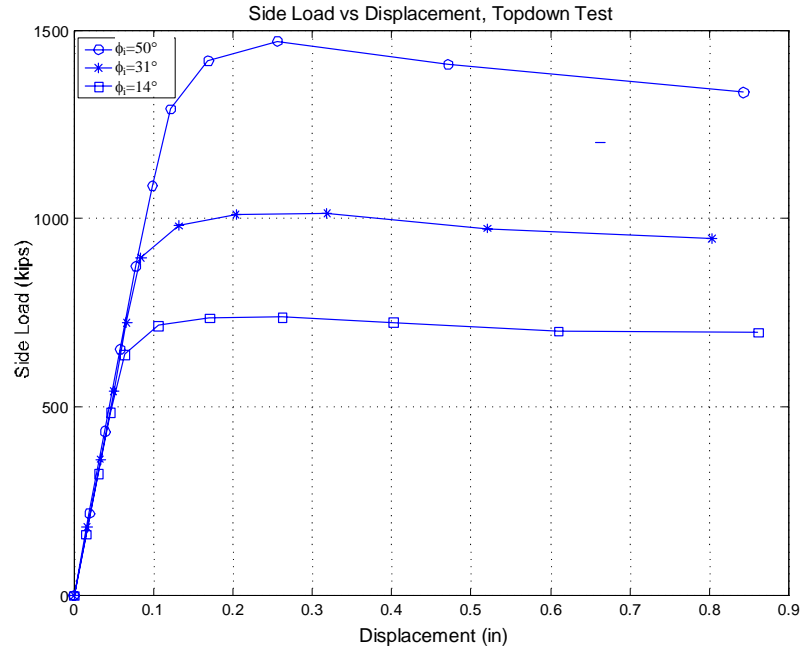
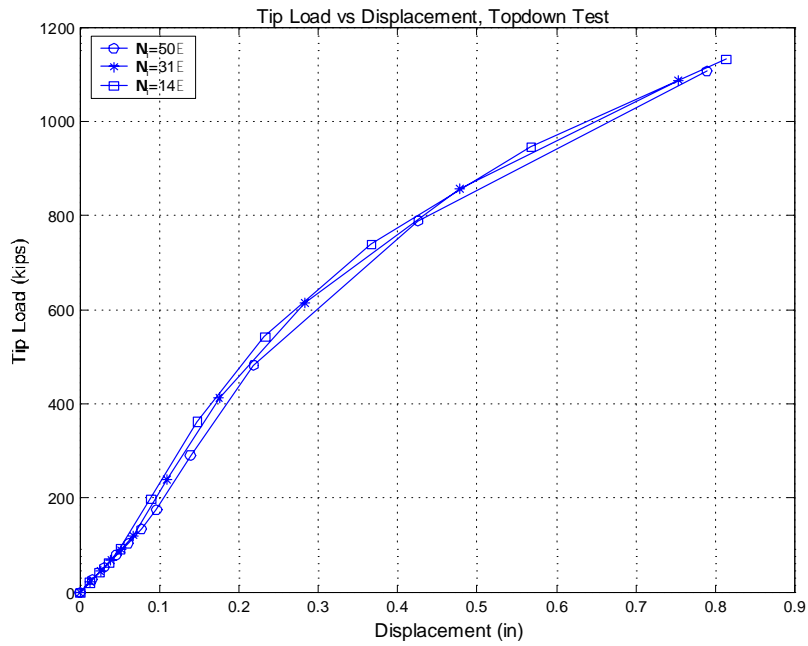


Figure 74. Effect of ϕ_i on Load vs. Displacement Curve, Top Down Test



(a) Side Load vs. Displacement



(b) Side Load vs. Displacement

Figure 75. Effect of ϕ_i on Side Load vs. Displacement and Tip Load vs. Displacement Curve, Top Down Test

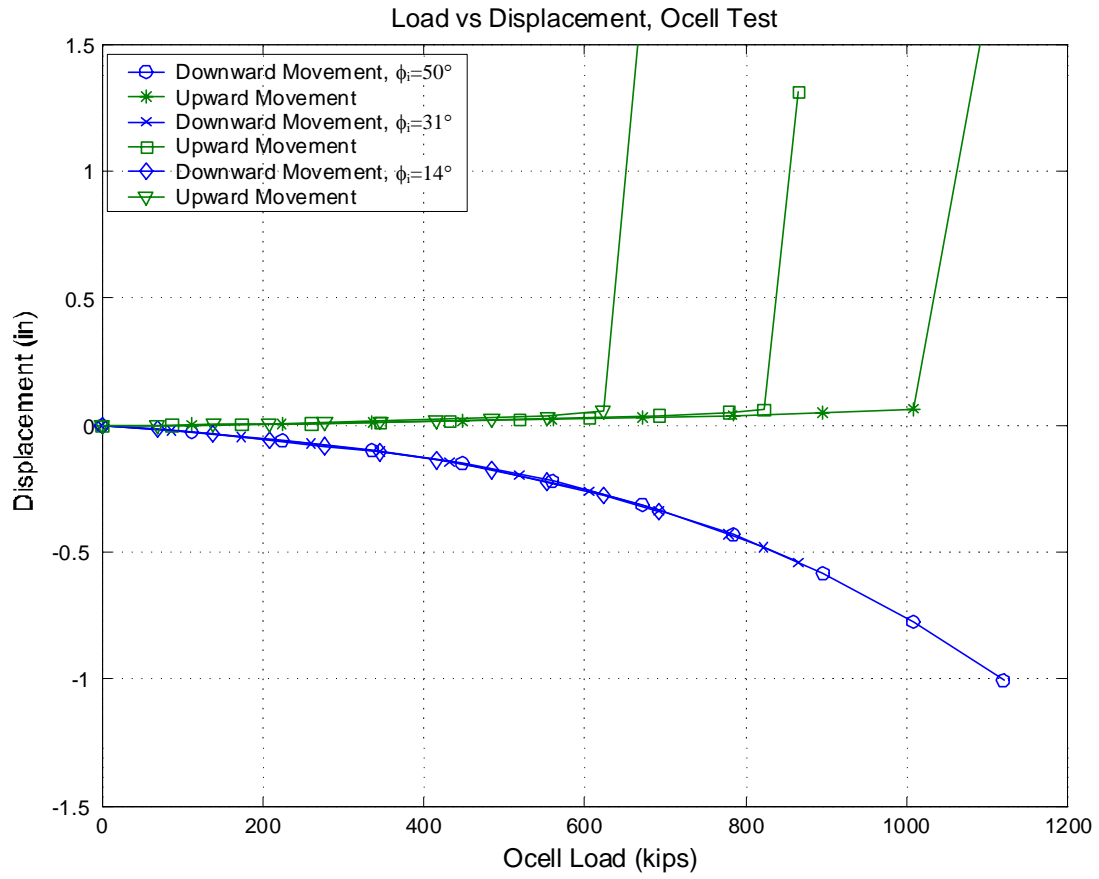


Figure 76. Effect of ϕ_i on Load vs. Displacement Curve, O-cell Test

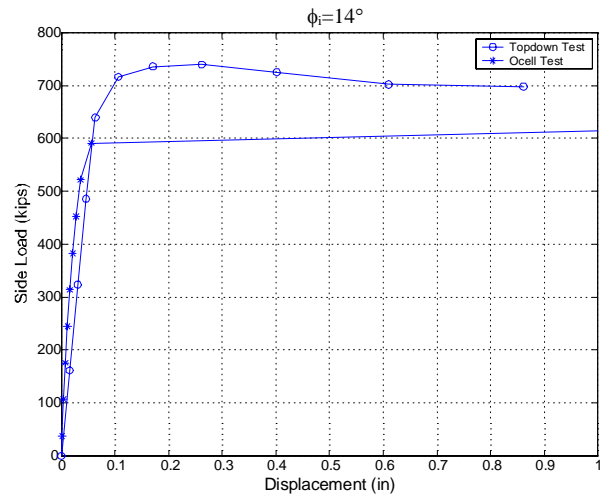
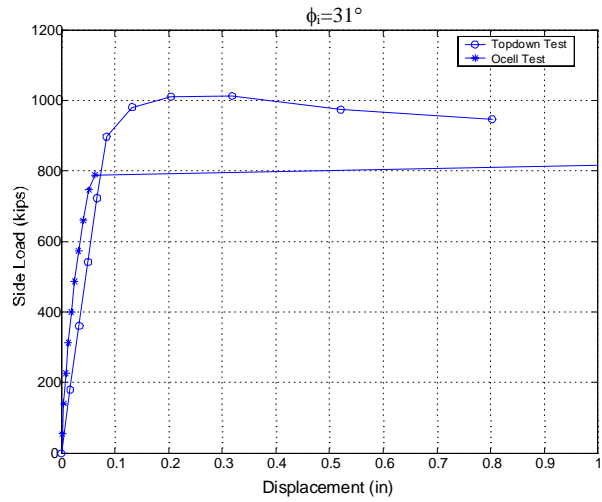
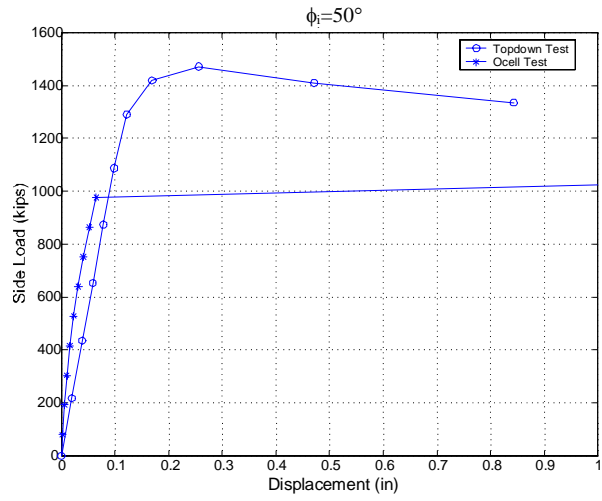
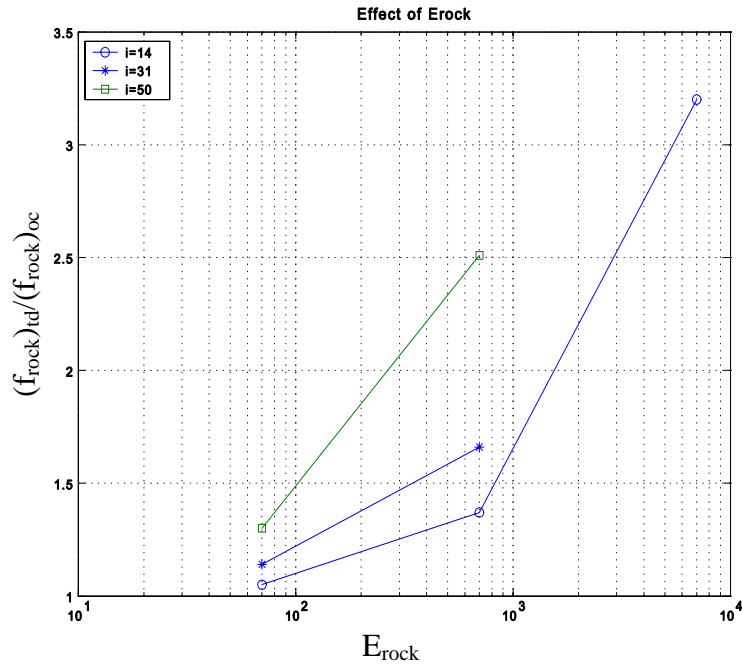
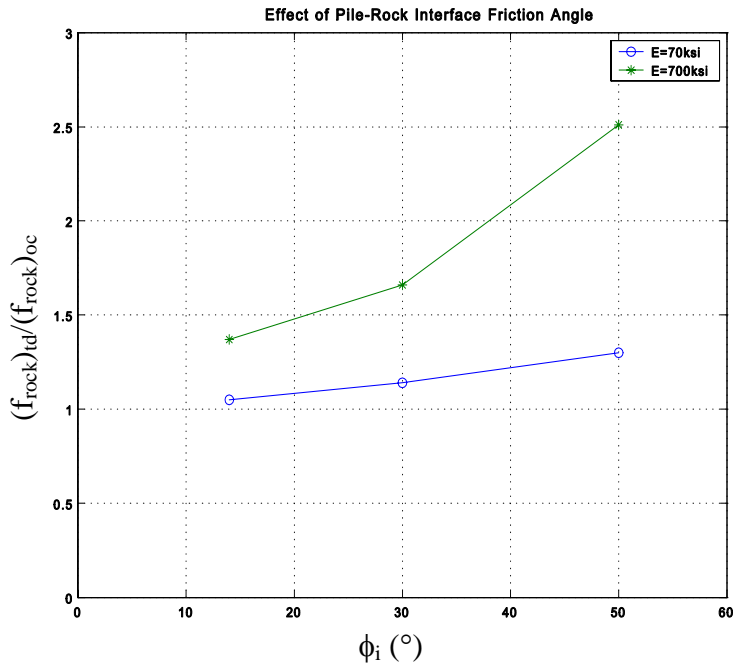


Figure 77. Side Load vs. Displacement Comparison for Different ϕ_i Values



(a) Effect of E_{rock}



(b) Effect of ϕ_i

Figure 78. Effect of E_{rock} and ϕ_i on the Difference Between Two Testing Methods (top down vs. O-cell).

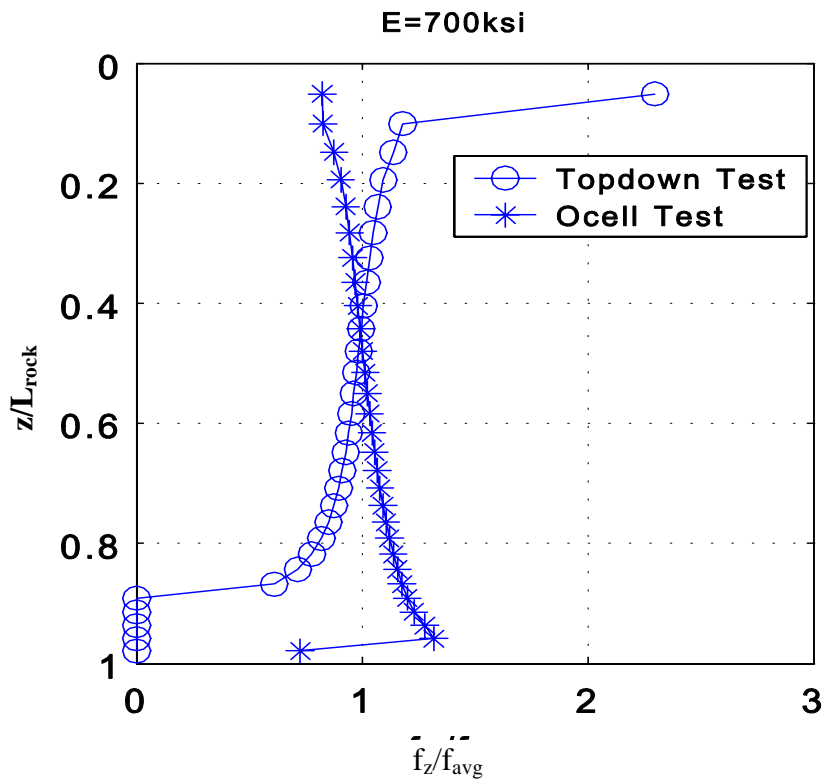
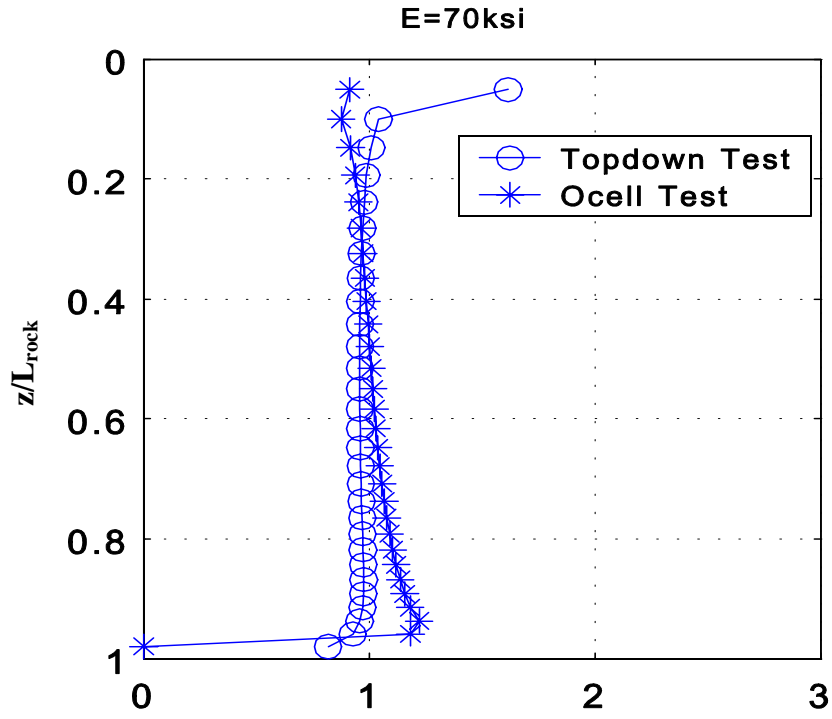


Figure 79. Shear Stress Distribution Comparison for Different E_{rock} Values

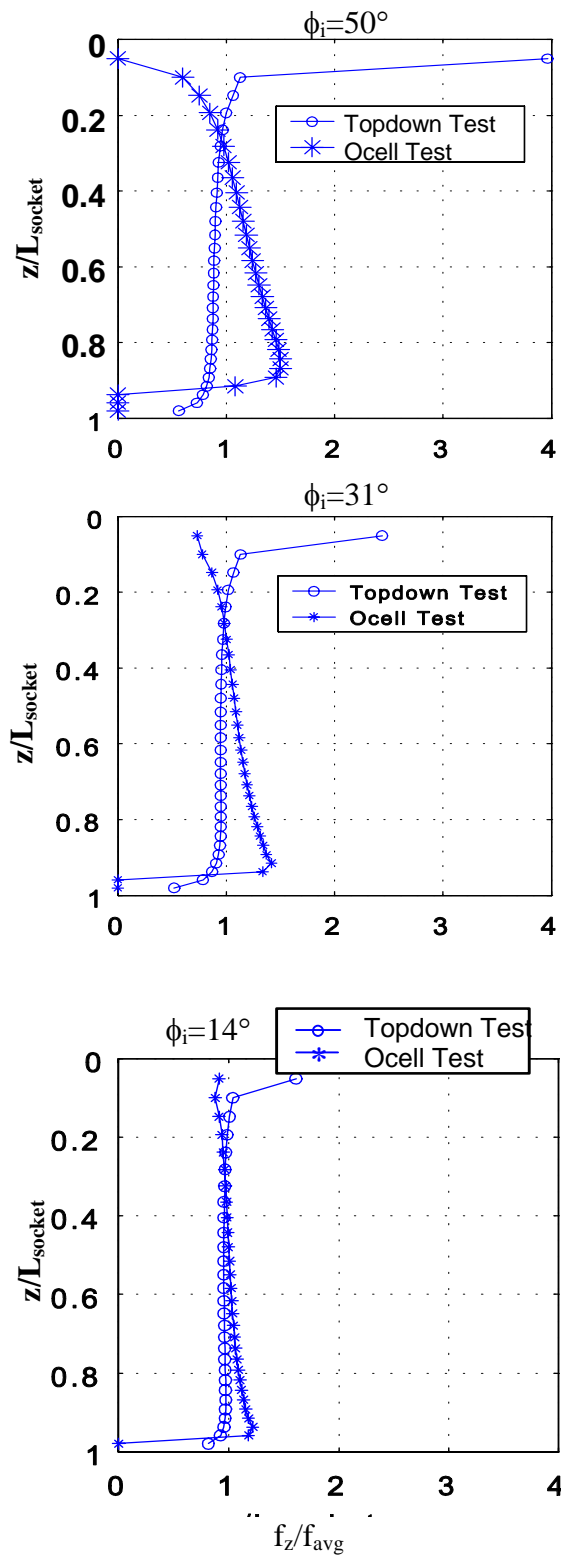


Figure 80. Shear Stress Distribution Comparison for Different ϕ_i Values (z = depth below rock, L_{socket} = socket length)

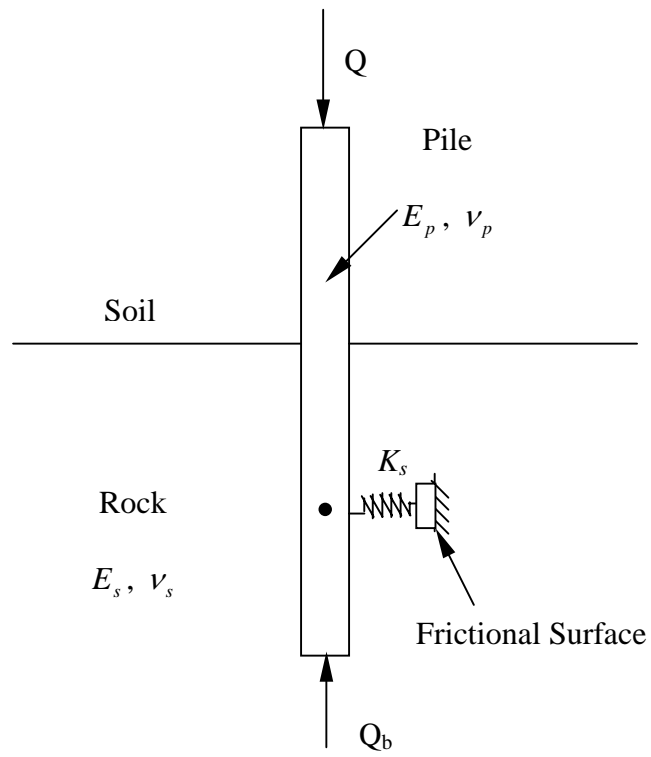


Figure 81. Simplified Model of Rock-Socketed Pile

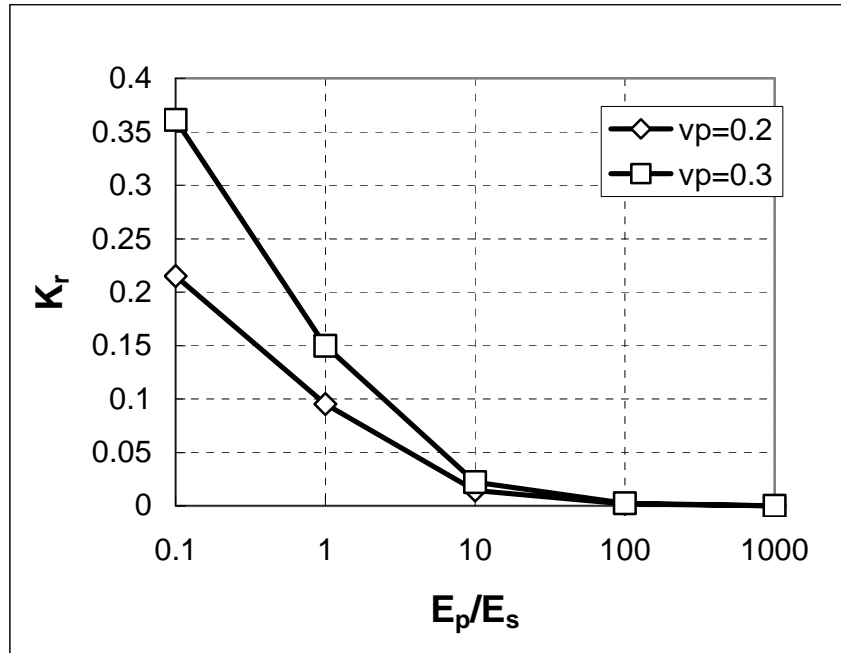


Figure 82. The Effect of E_p / E_s and ν_p on Stress Coefficient K_r

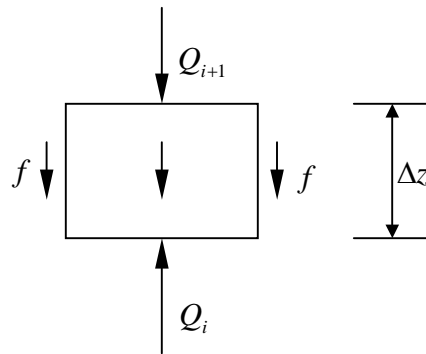


Figure 83. Free Body Diagram for a Segment of Pile

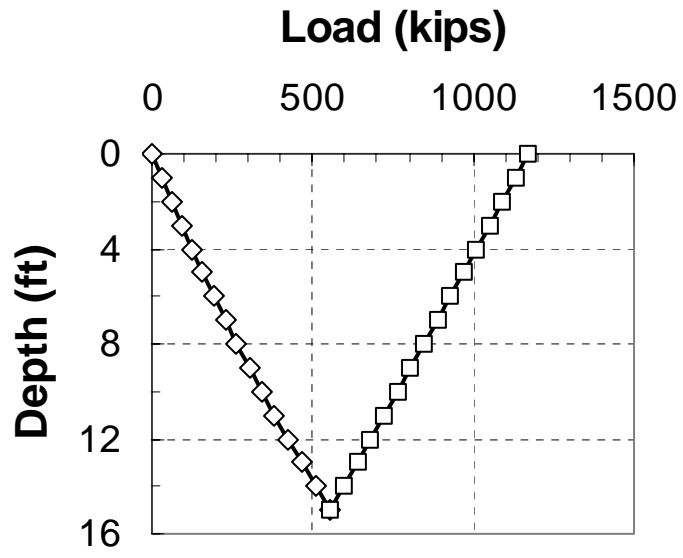


Figure 84. Load Distribution, Example

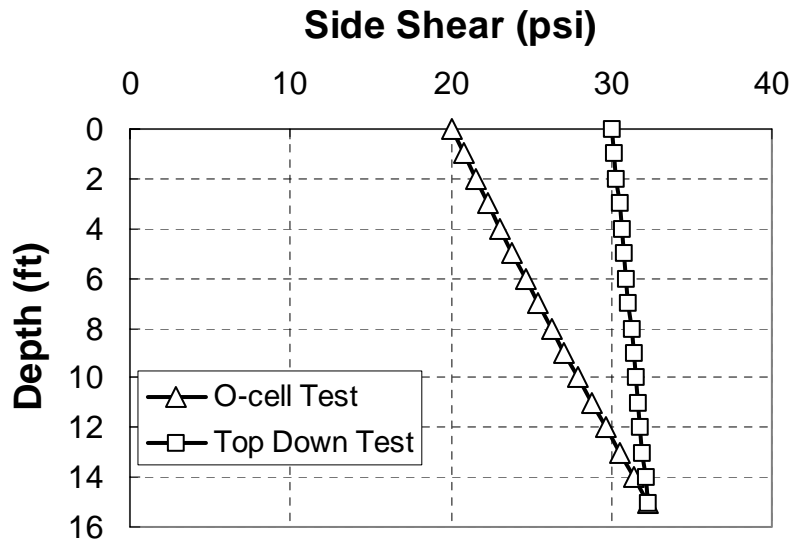
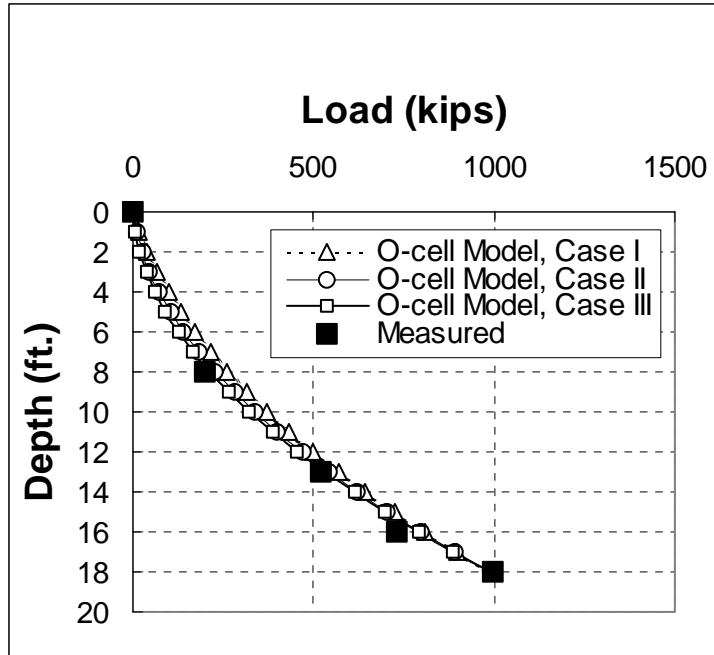
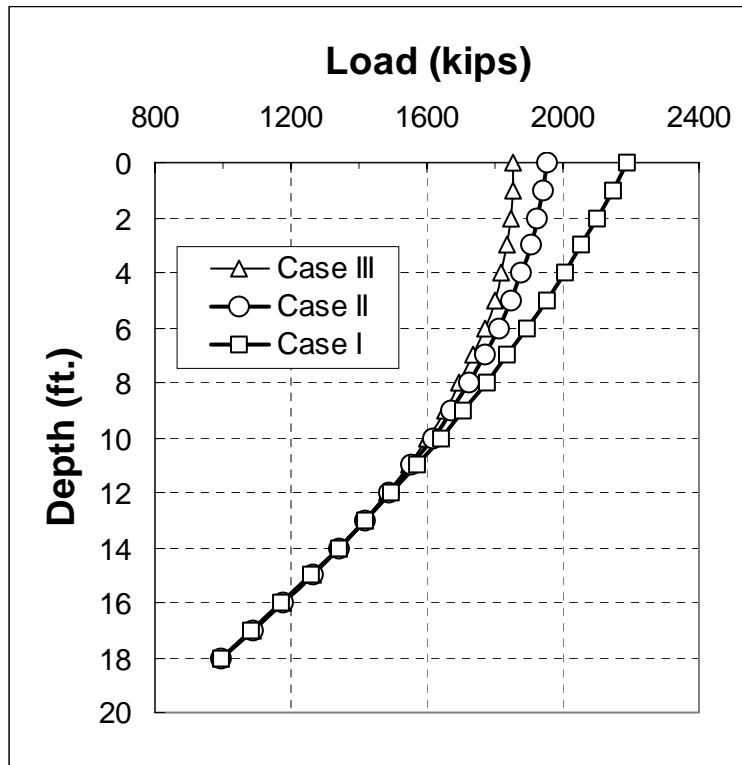


Figure 85. Comparison of Side Shear Distribution

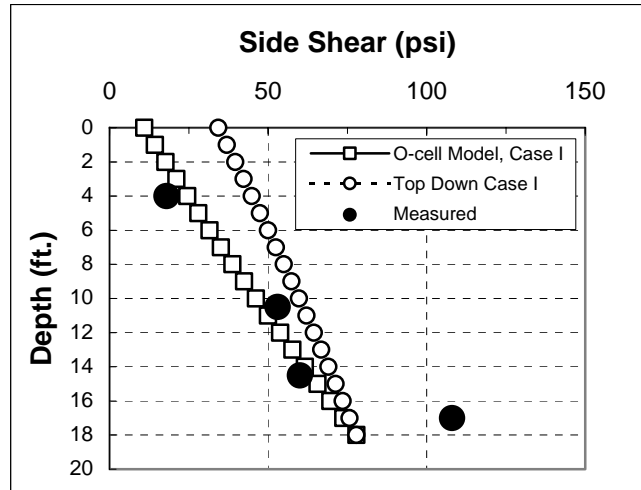


(a) O-cell Test

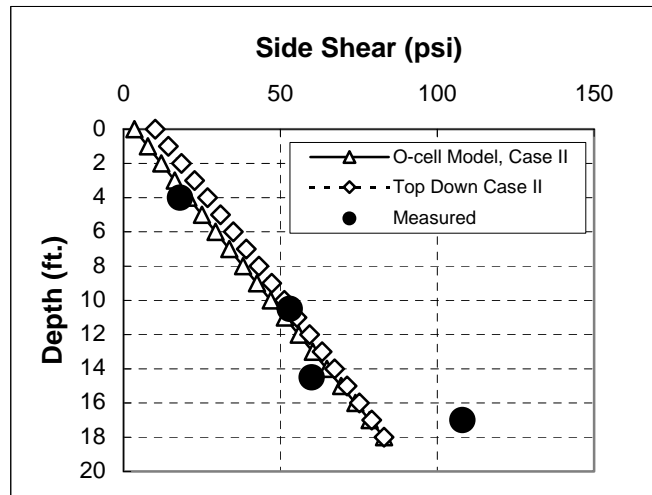


(b) Top Down Loading

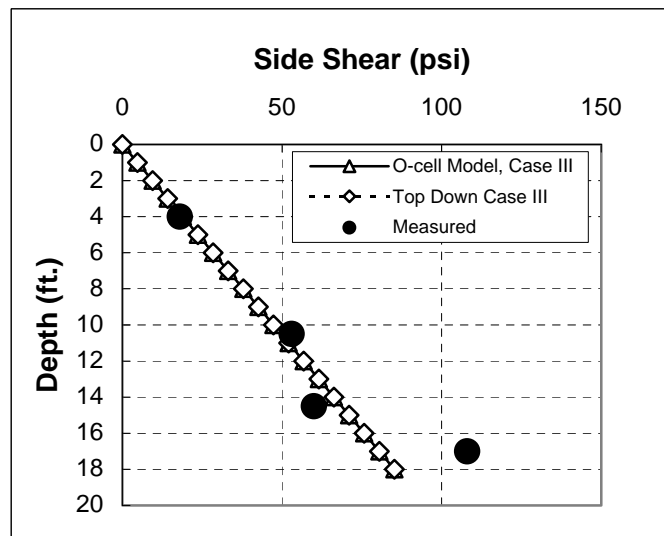
Figure 86. Load Distribution using the simplified model for the Wilsonville, AL case (a) O-Cell Test, (b) Top Down Loading



(a) Case I



(b) Case II



(c) Case III

Figure 87. Side Shear Distribution for Wilsonville (a) Case I, (b) Case II, and (c) Case III

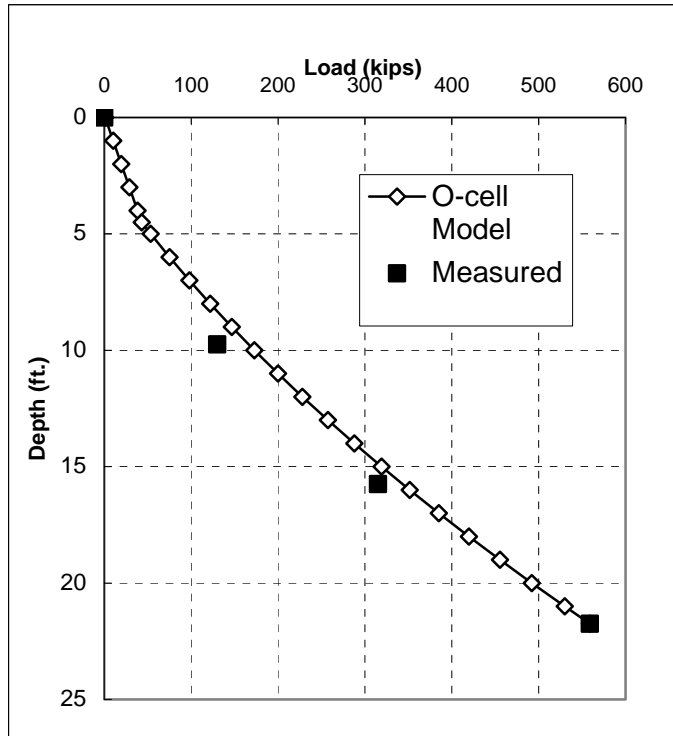


Figure 88. Load Distribution, O-cell Test, Denver Case

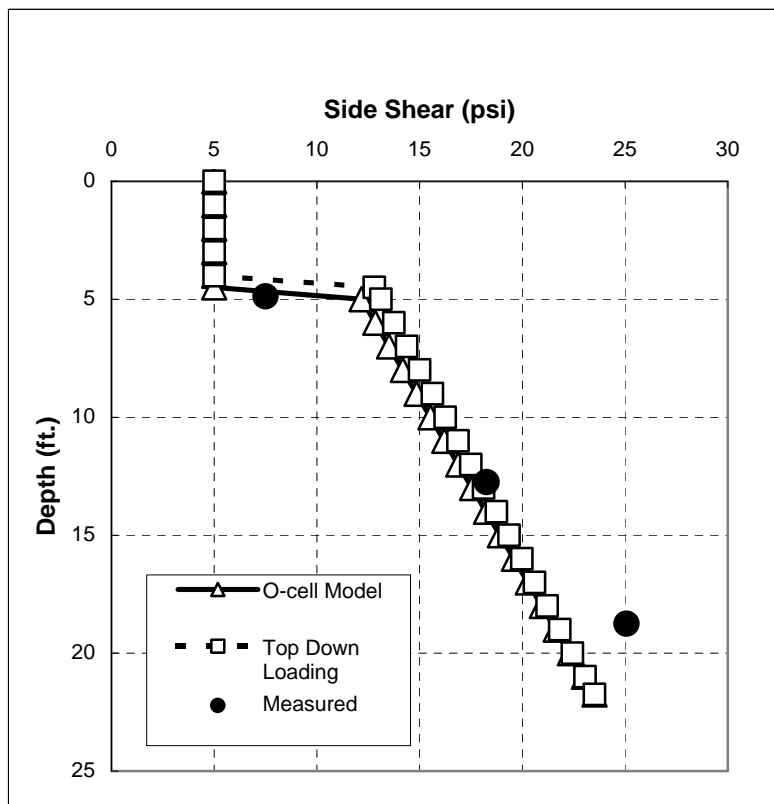


Figure 89. Side Shear Distribution, Denver Case

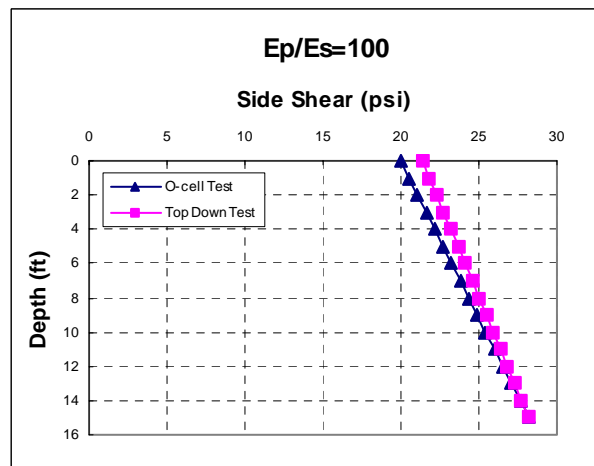
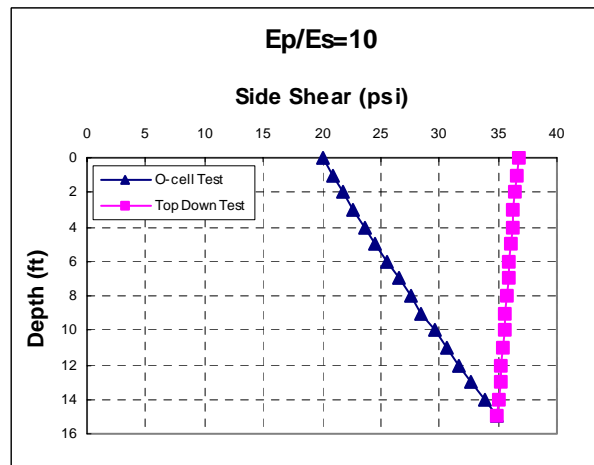
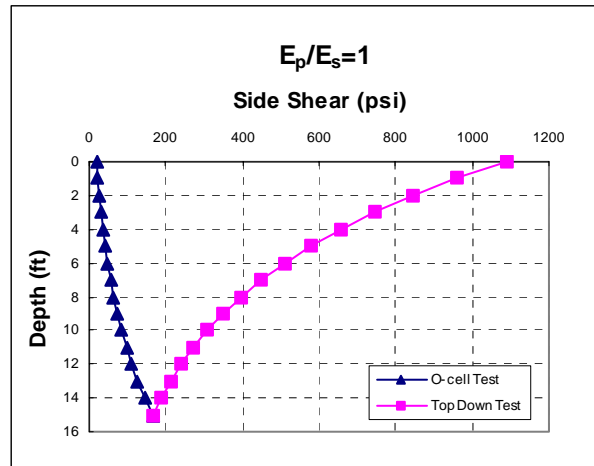


Figure 90. Side Shear Distribution for Different E_p / E_s

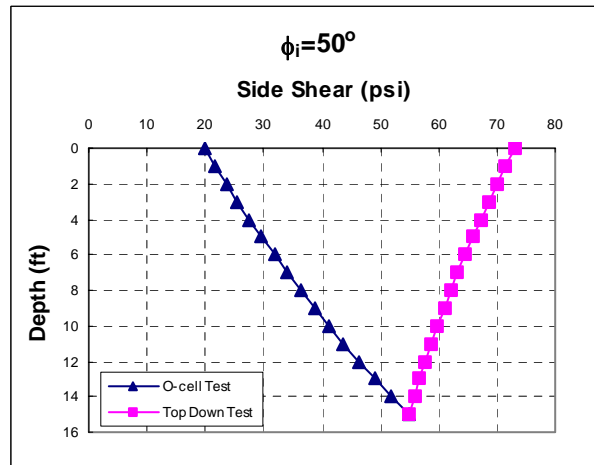
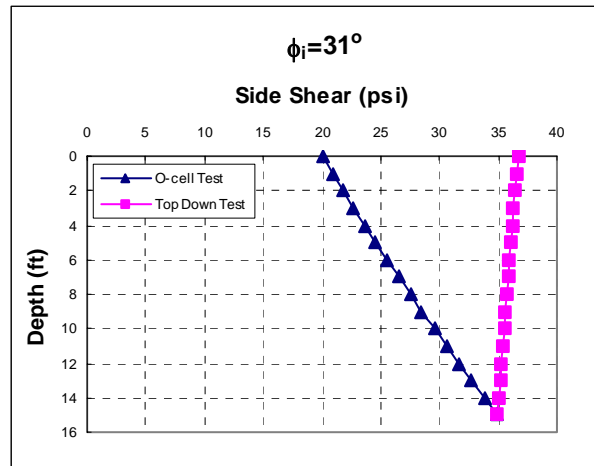
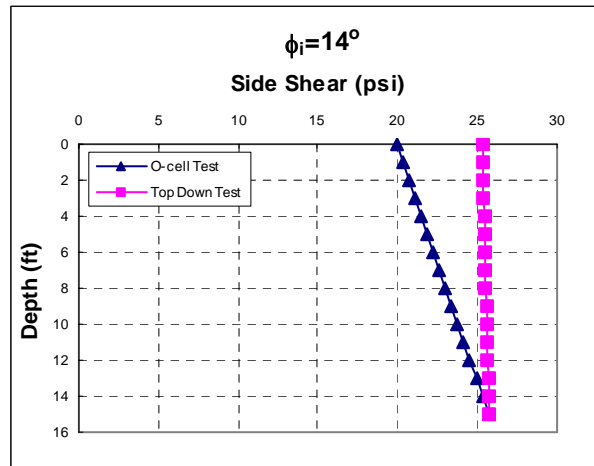


Figure 91. Side Shear Distribution for Different ϕ_i

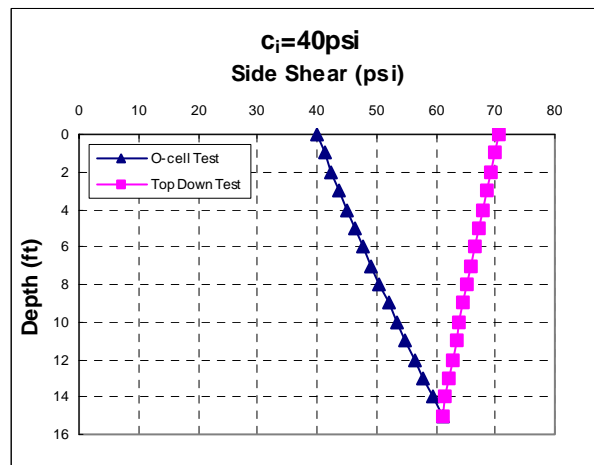
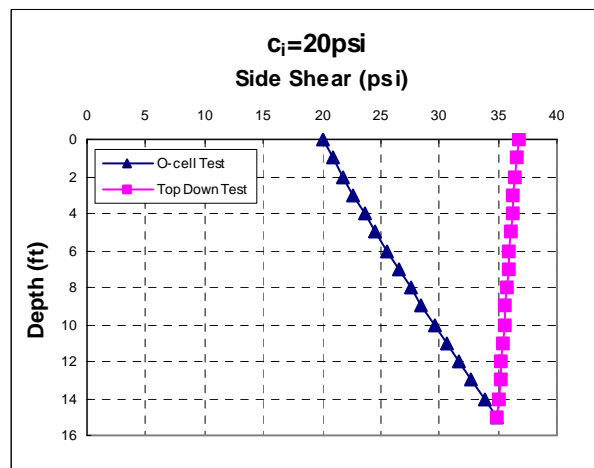
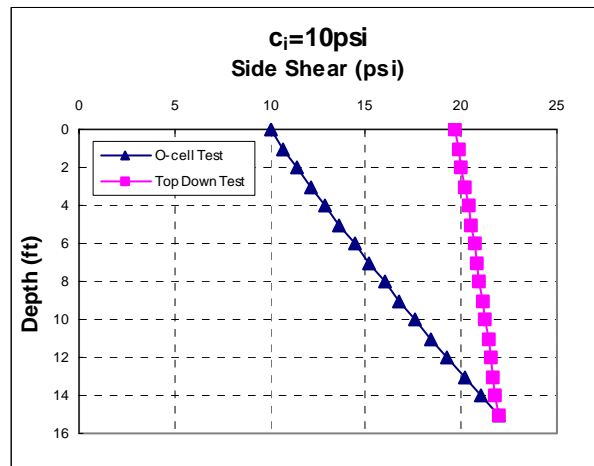


Figure 92. Side Shear Distribution for Different c_i

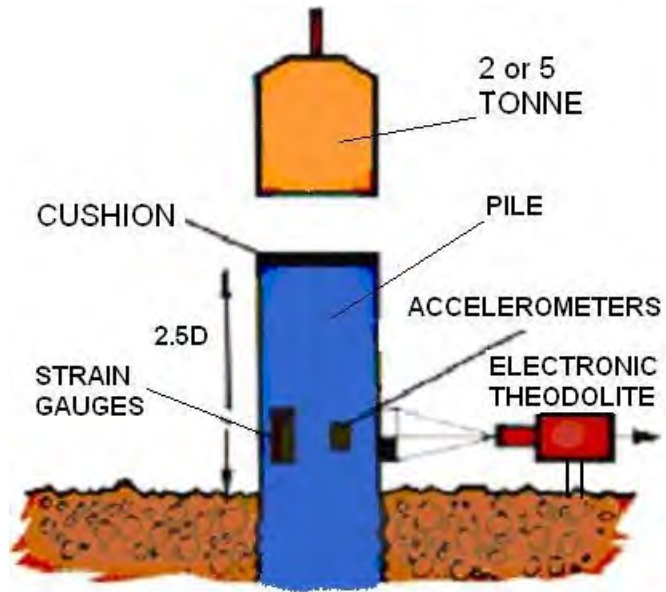


Figure 93. General Arrangement of the SIMBAT system (Testconsult Website)



Figure 94. The Components of the SIMBAT System (Testconsult Website)

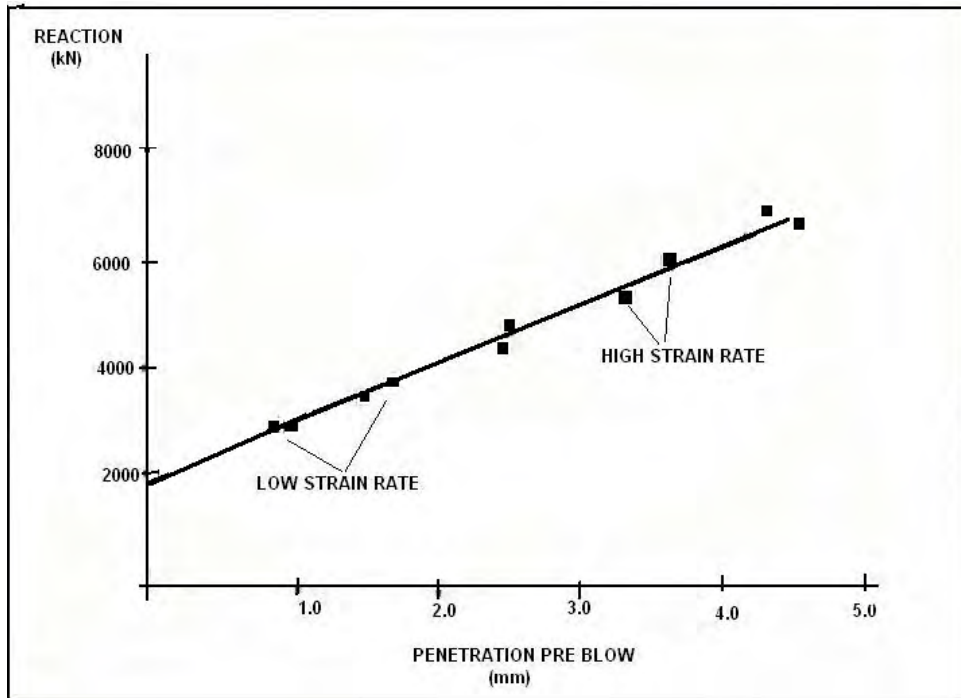


Figure 95. Dynamic Testing at Varying Strain Rates (Testconsult Website)

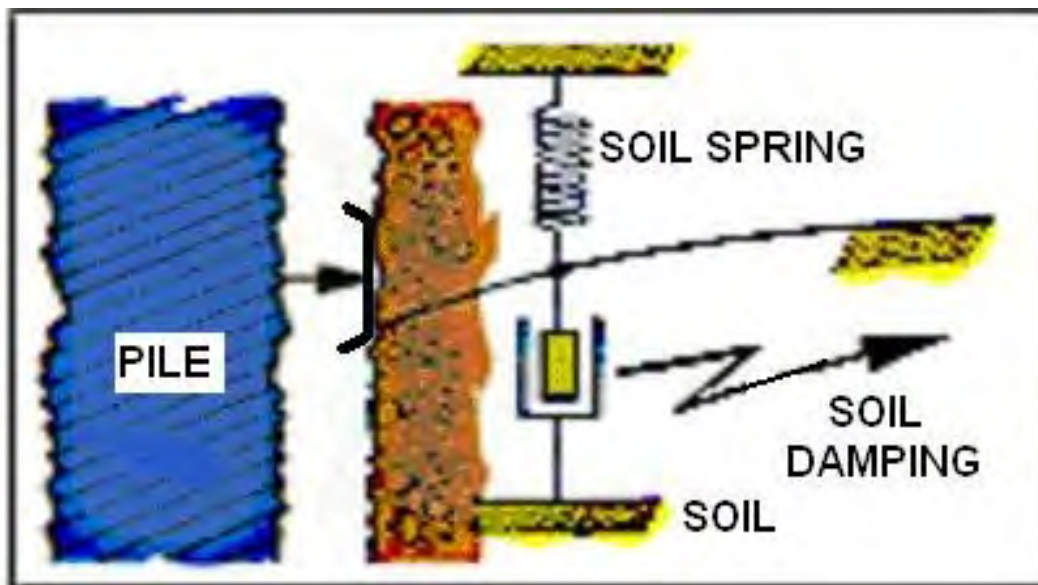


Figure 96. SIMBAT Pile/Soil Model (Testconsult Website)



Figure 97. Digital/Optical Theodolite used in the SIMBAT Test (Testconsult Website)

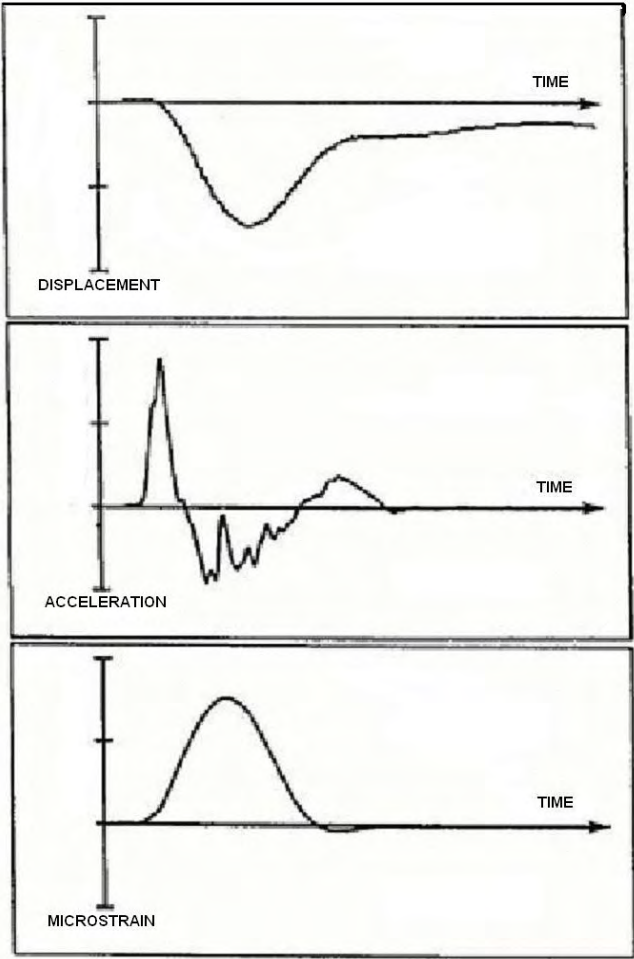


Figure 98. Raw Curves from a Single Impact (Testconsult Website)

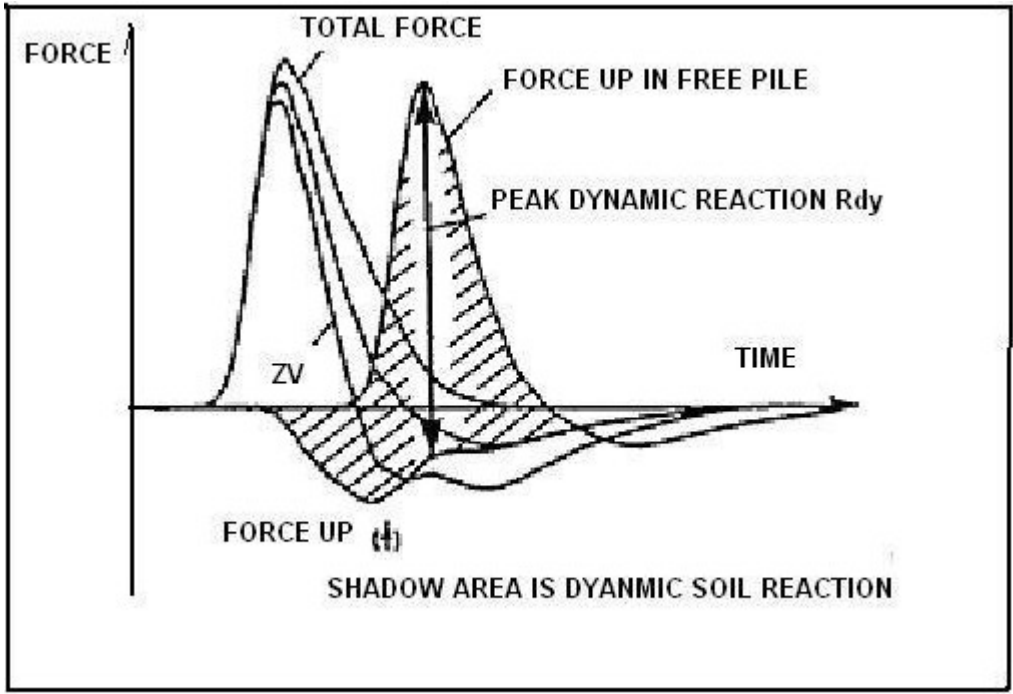


Figure 99. Separation of Forces, Calculated $R_{dynamic}$ (Testconsult Website)

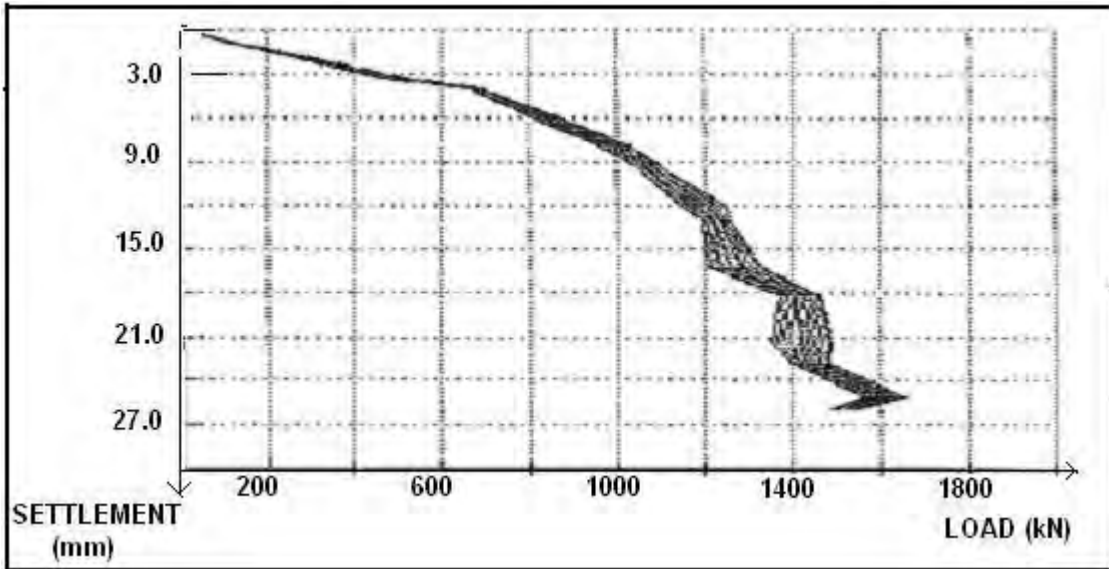


Figure 100. Predicted Load/Settlement Curves (Testconsult Website)

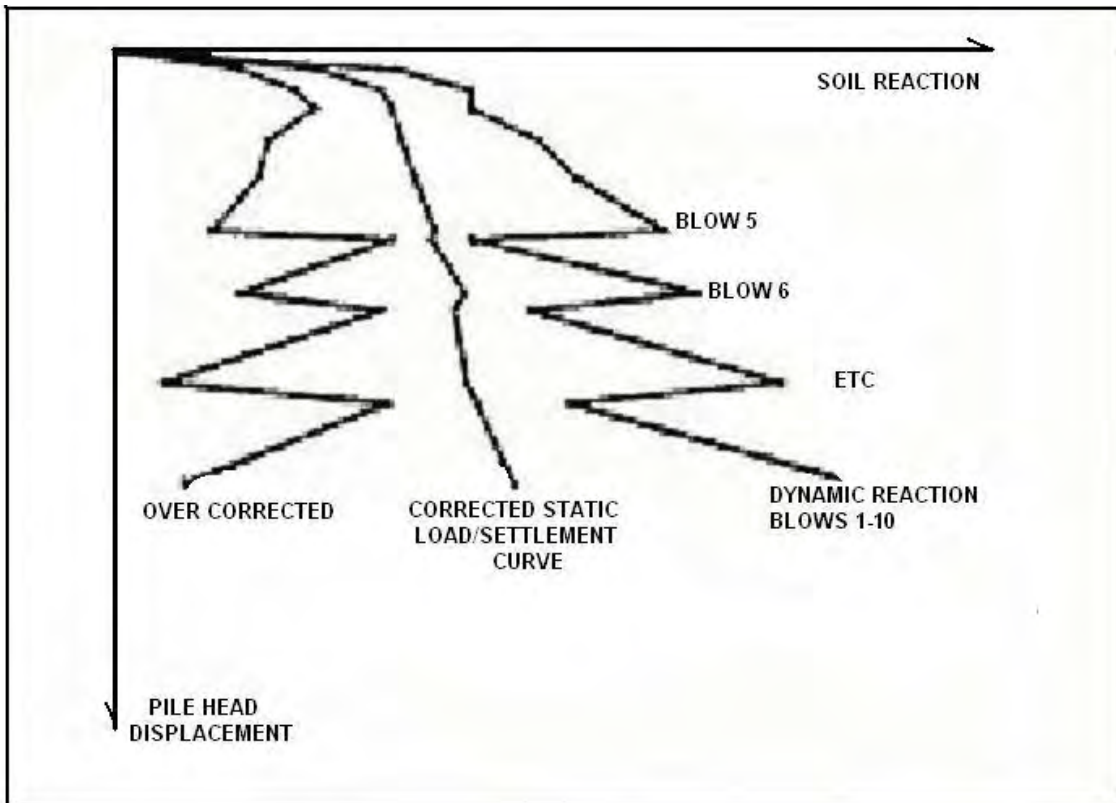


Figure 101. SIMBAT Dynamic to Static Correction Procedure (Testconsult Website)

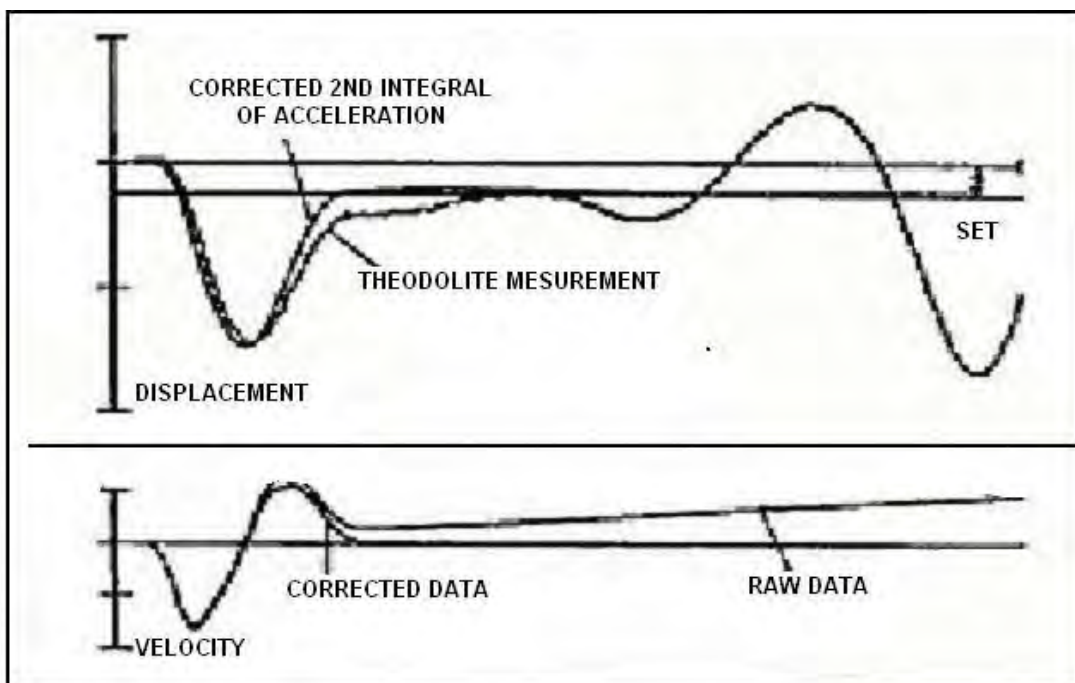


Figure 102. Correction of Velocity Using Theodolite Measurement (Testconsult Website)

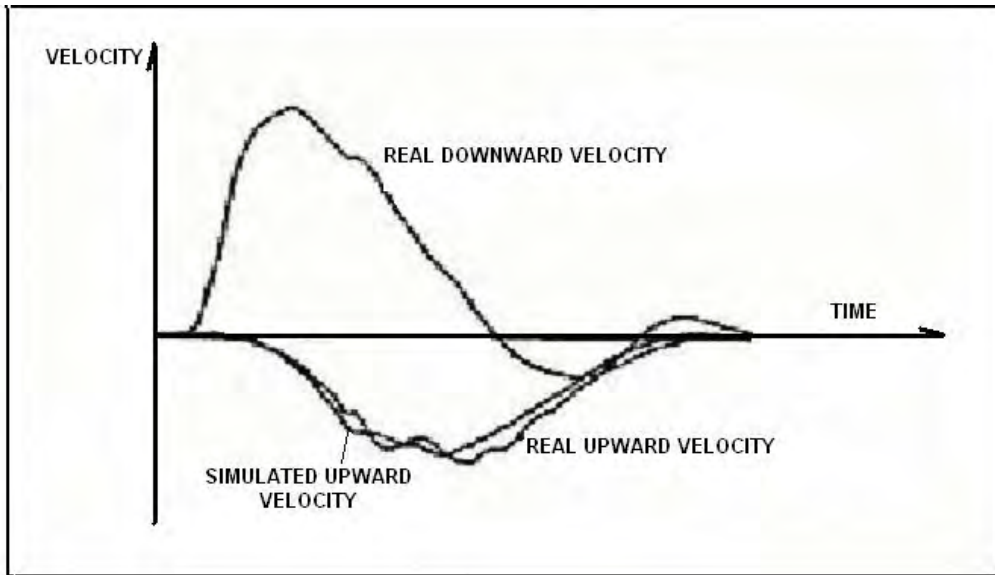


Figure 103. Computer Matching of Velocity (Testconsult Website)

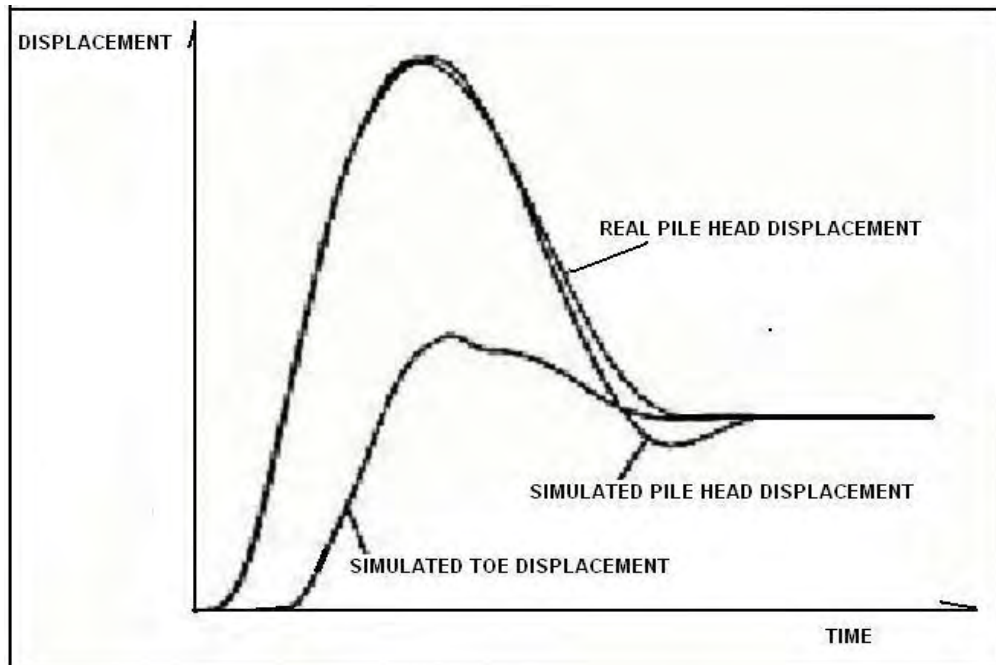


Figure 104. Computer Matching of Displacement. (Testconsult Website)

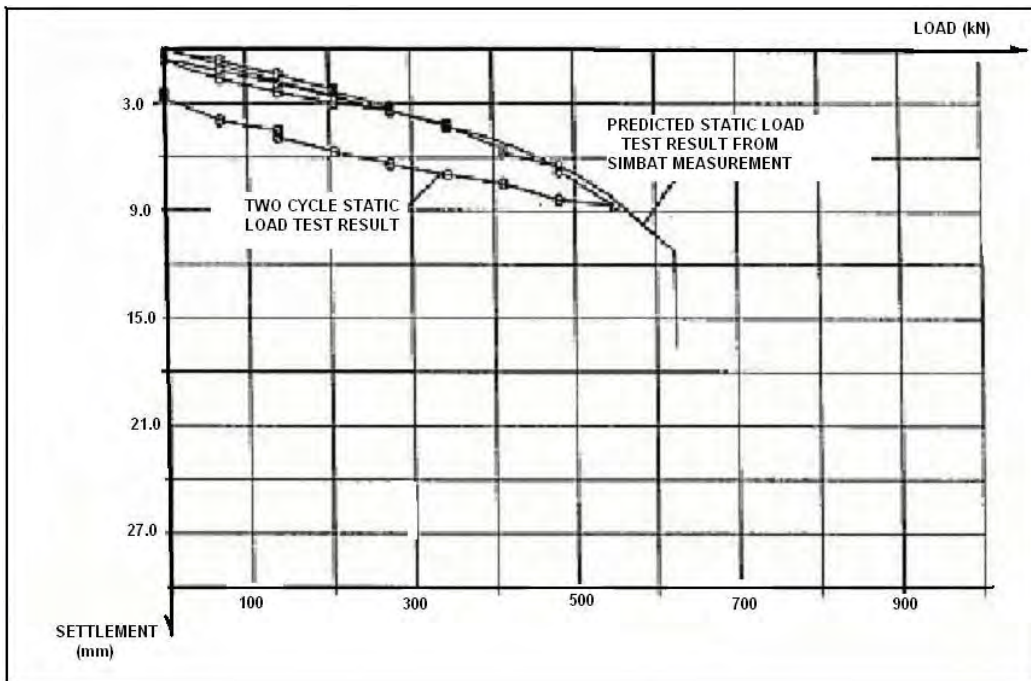


Figure 105. Comparison between Static and Dynamic Load Tests (Testconsult Website)

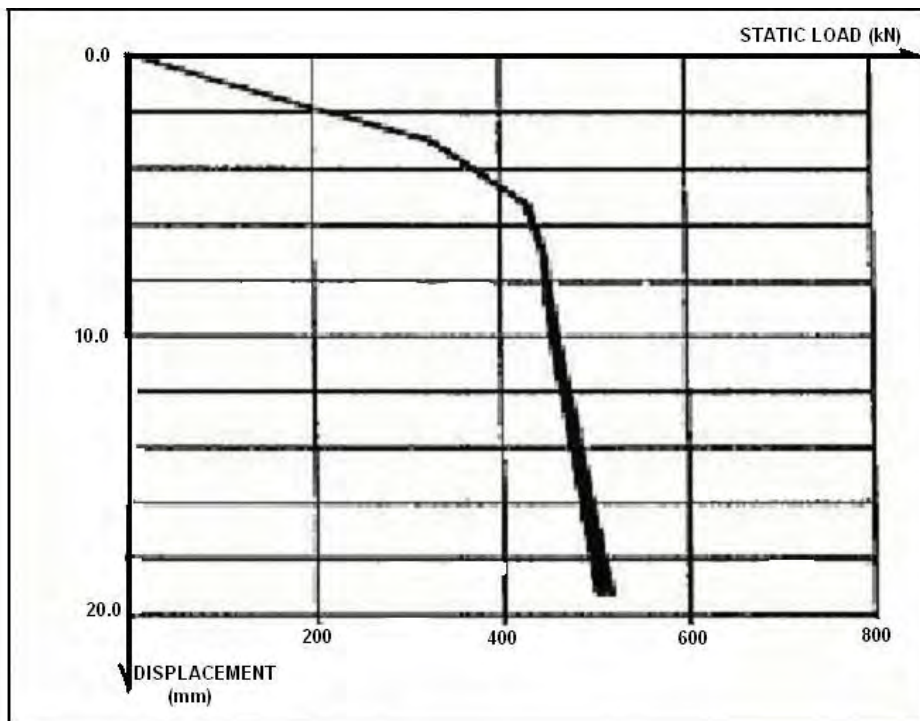


Figure 106. Final Static Load Settlement Plot from SIMBAT (Testconsult Website)

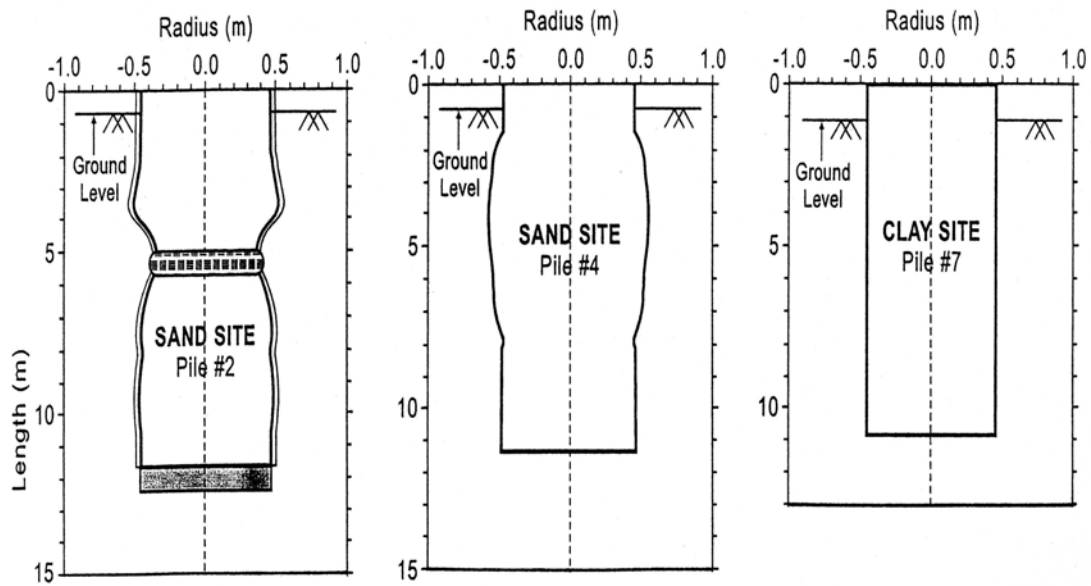


Figure 107. Bored Piles at NGES-TASU Sites (Briaud et al. 2000)

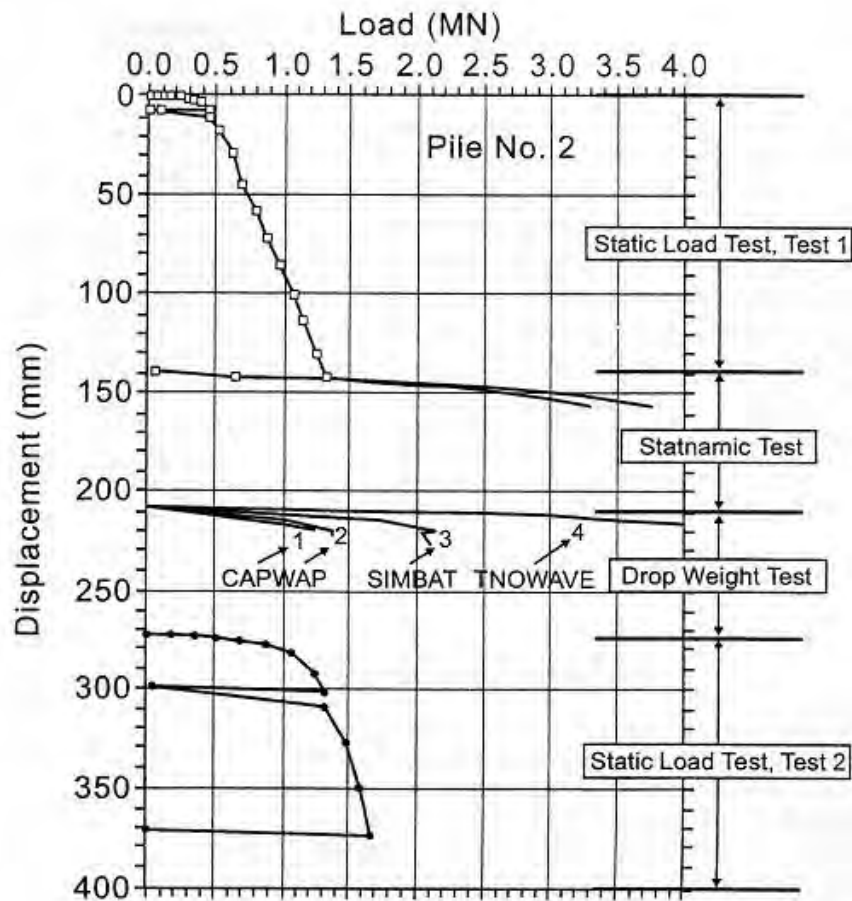


Figure 108. Complete Load-Settlement History for All Test on Pile No.2 (Briaud et al. 2000)

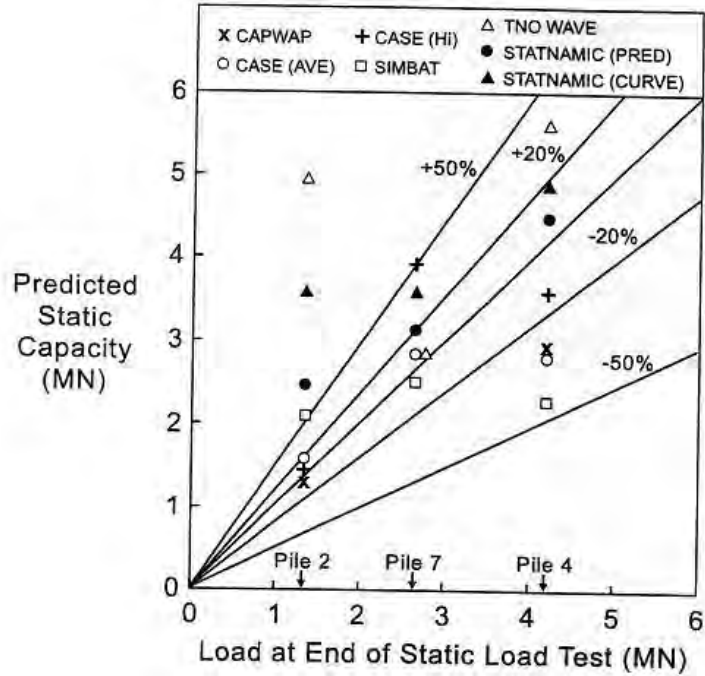


Figure 109. Comparison between Predicted and Measured Static Capacities (Briaud et al. 2000)

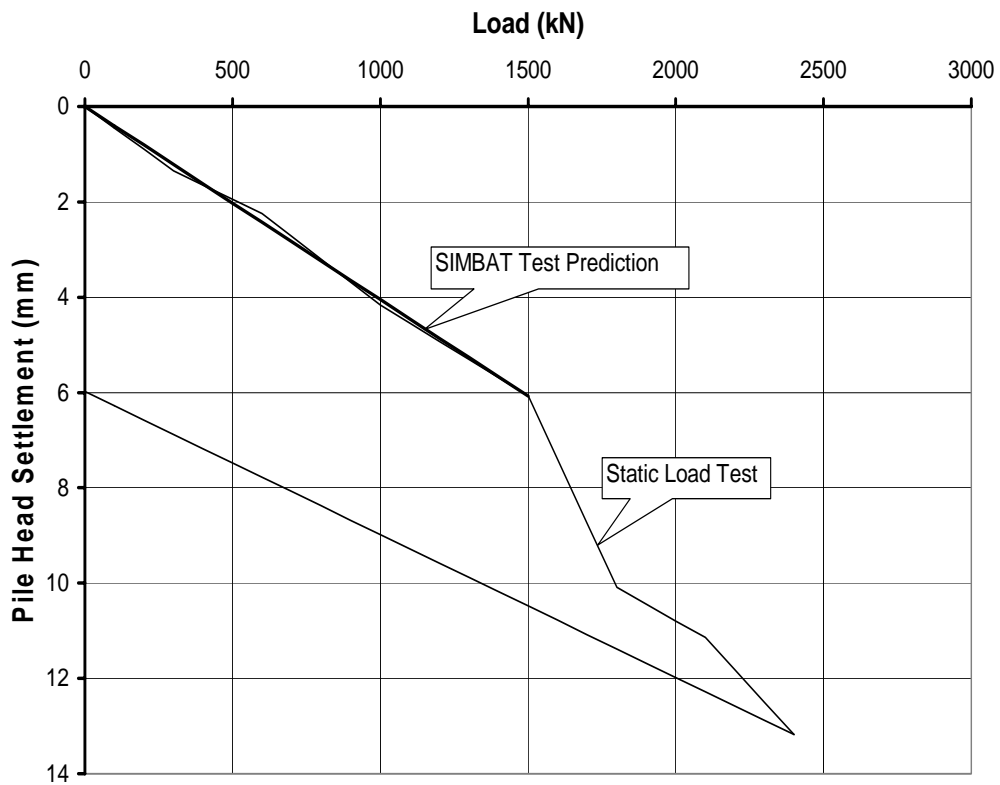


Figure 110. Comparison of SIMBAT and Static Testing Results (Long, 2001)

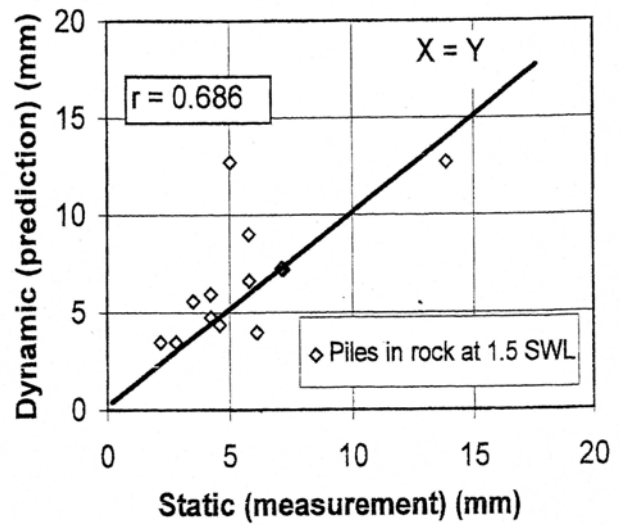
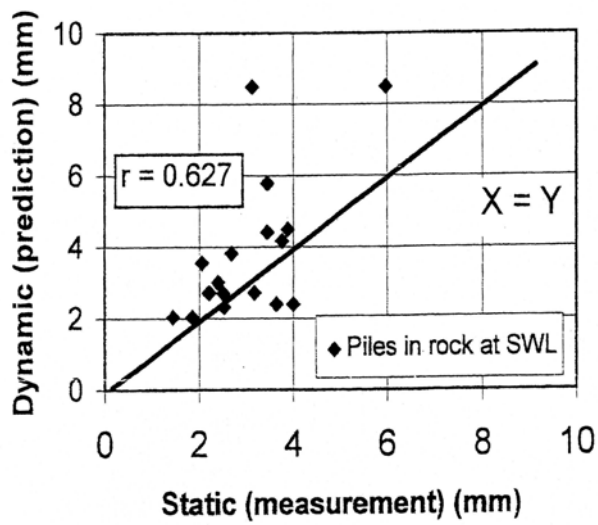


Figure 111. Piles in Rock – Loading to SWL / 1.5SWL (Long, 2001)

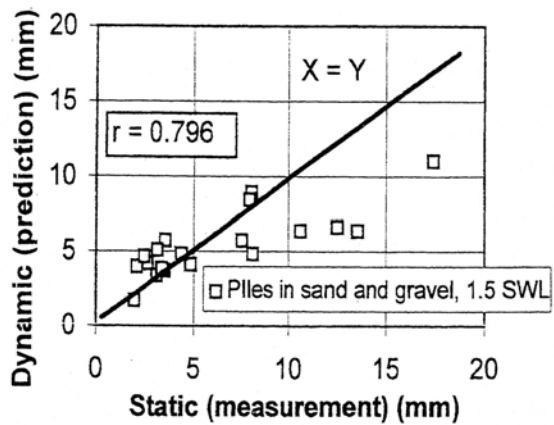
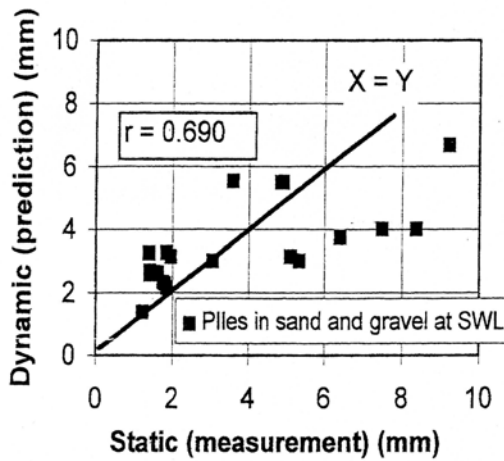


Figure 112. Piles in Sand and Gravel Loading to SWL TO 1.5SWL (Long, 2001)

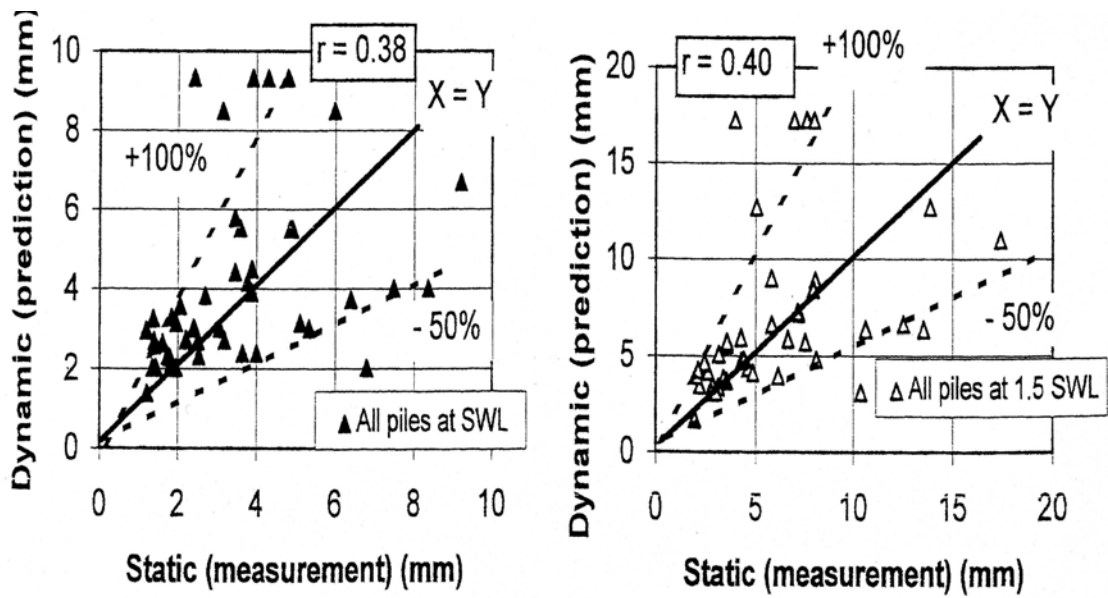


Figure 113. All piles Loading to SWL / 1.5SWL (Long, 2001)

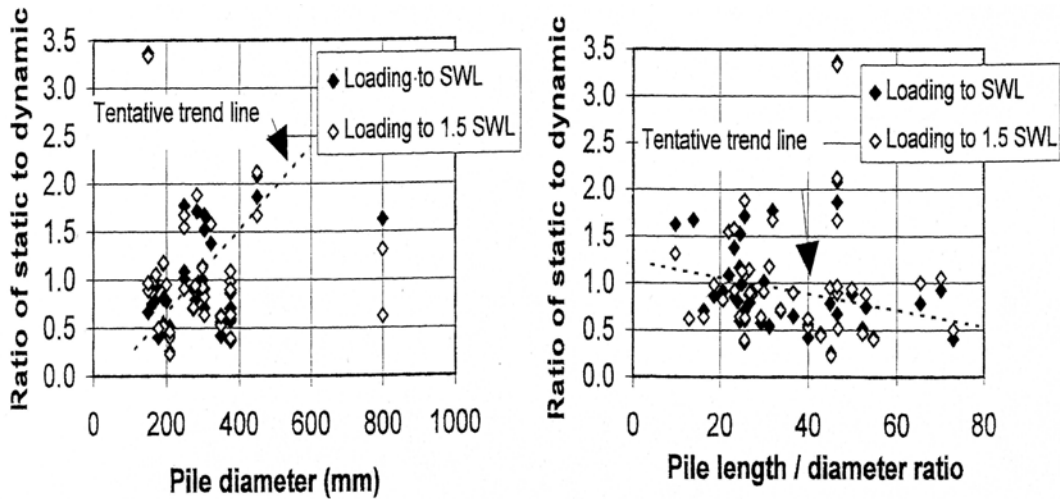


Figure 114. Influence of Pile Diameter/Length to Diameter Ratio (Long, 2001)

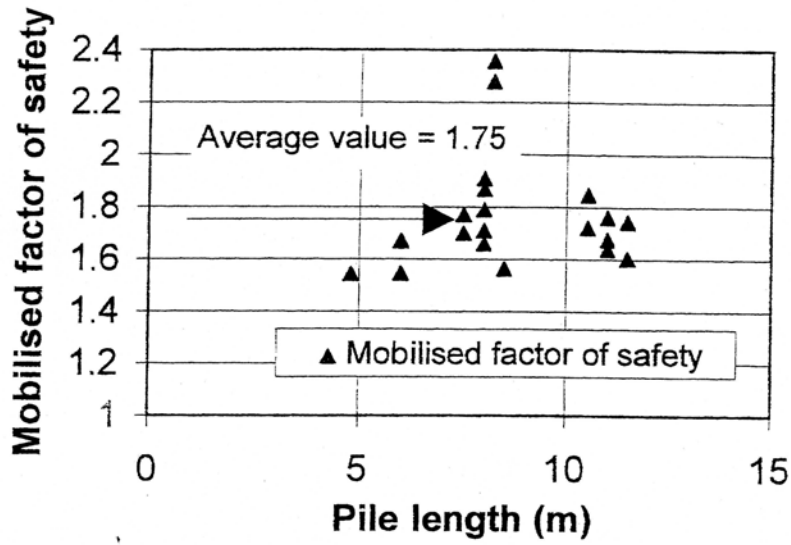


Figure 115. Mobilized Safety Factor (Long, 2001)

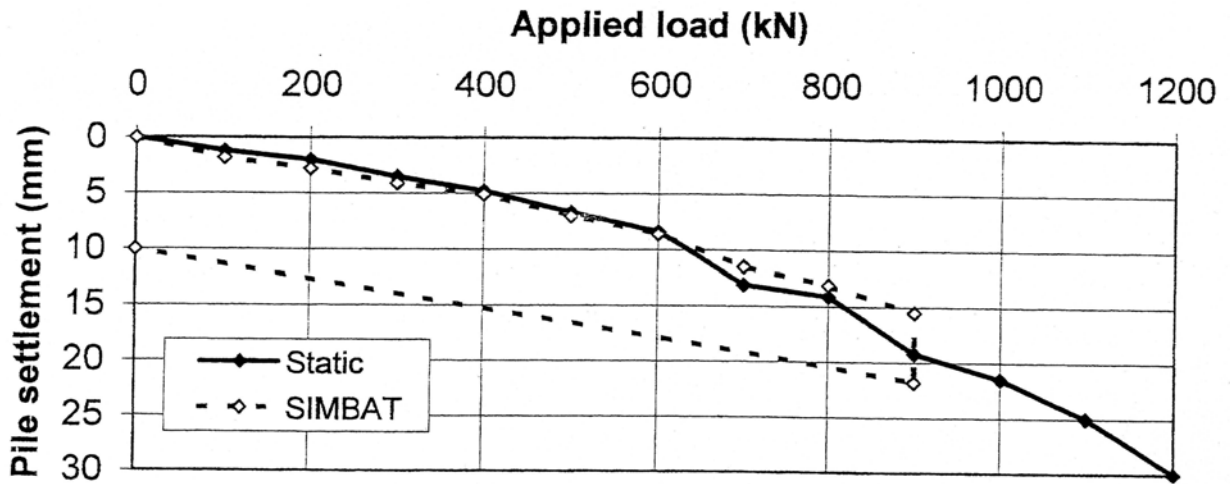


Figure 116. Case History of Identification of Failed Pile (Long, 2001)



Figure 117. The FUNDEX Field Testing System (Americanpiledriving Website)

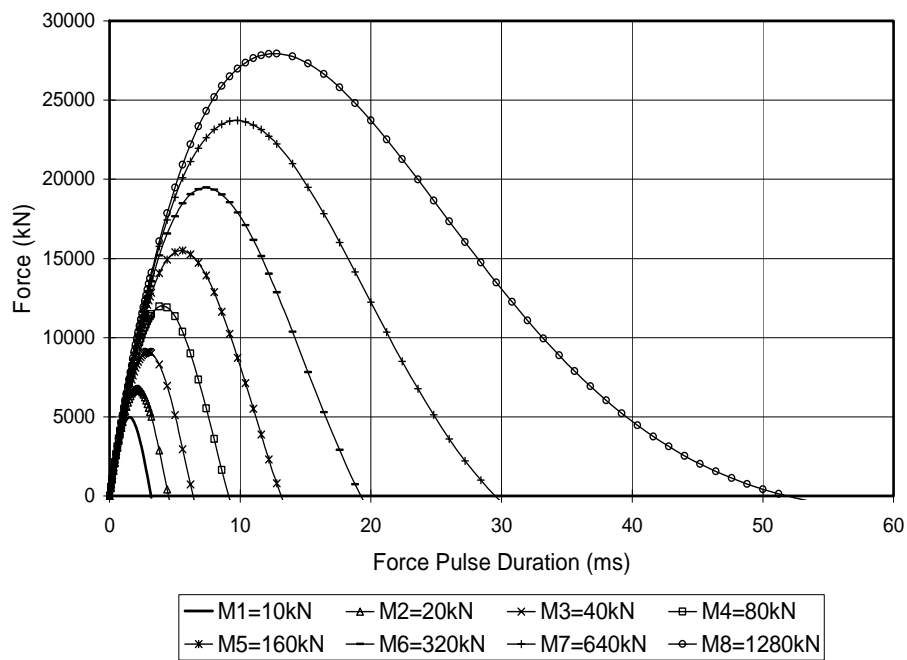


Figure 118. Force Pulses Acting on a Given Pile's Head under Different Size Impacting Mass and a constant Stroke Height of 1.5m

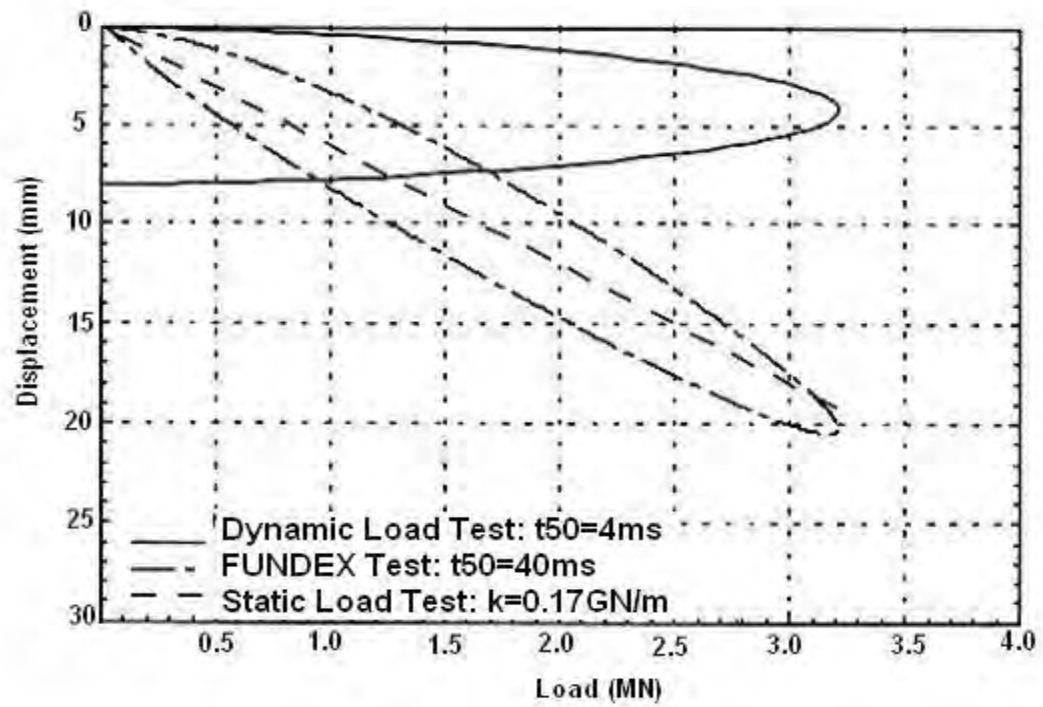


Figure 119. The Load Settlement Curves Calculated for a Dynamic, a FUNDEX and a Static Load Test. (Schellingerhort, 1996)

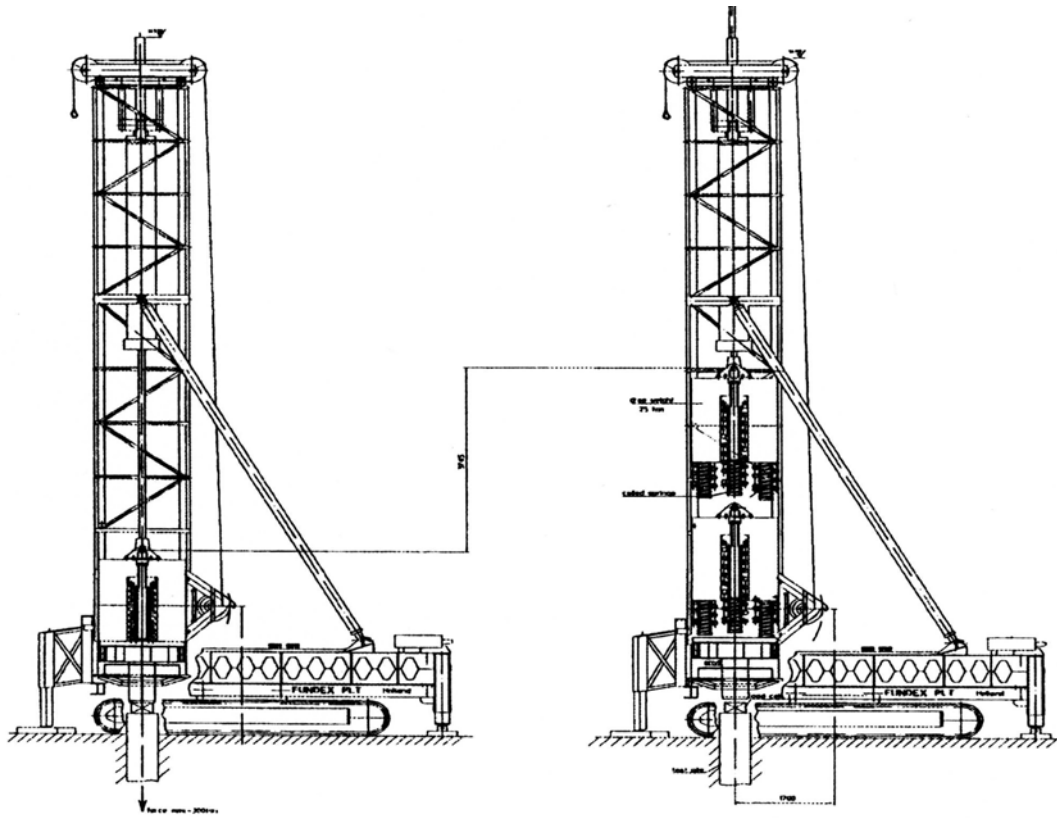


Figure 120. Illustration of the Pseudo Static Pile Load Tester (Schellinghort, 1996, Coe.Berkeley Website)

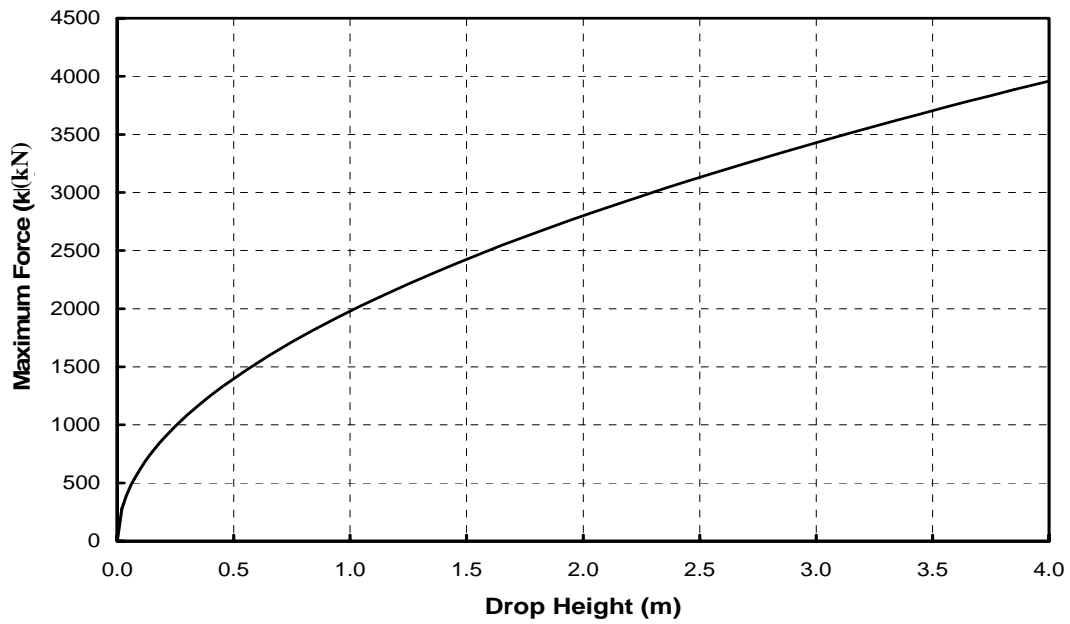


Figure 121. Maximum Force as a Function of Drop Height (Schellinghort, 1996)

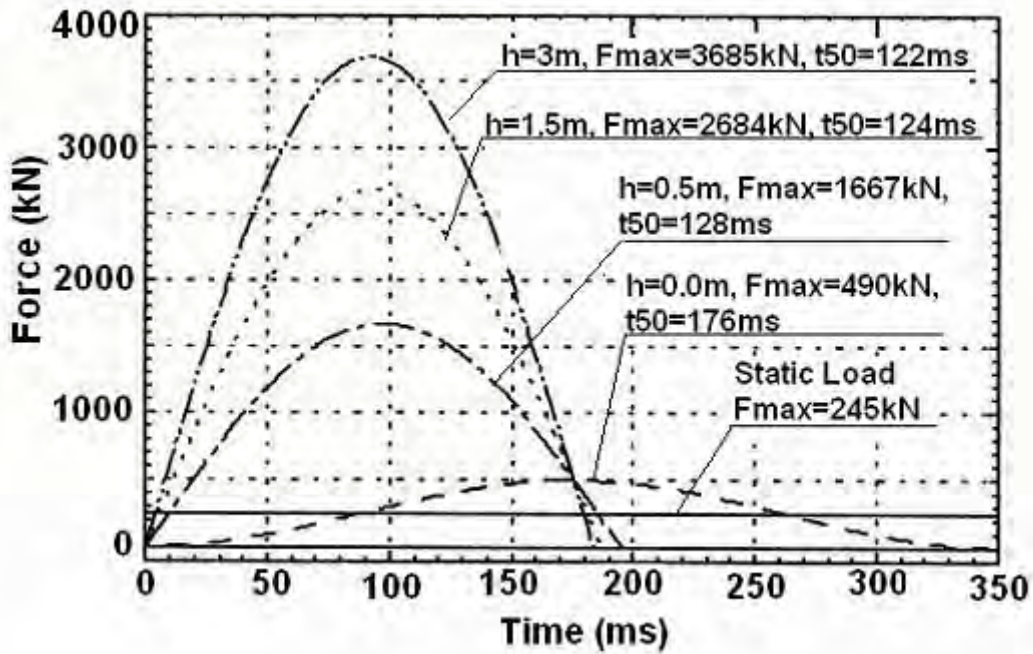


Figure 122. The Force at the Pile Top as a Function of Time for Different Drop Heights (Schellinghort, 1996)

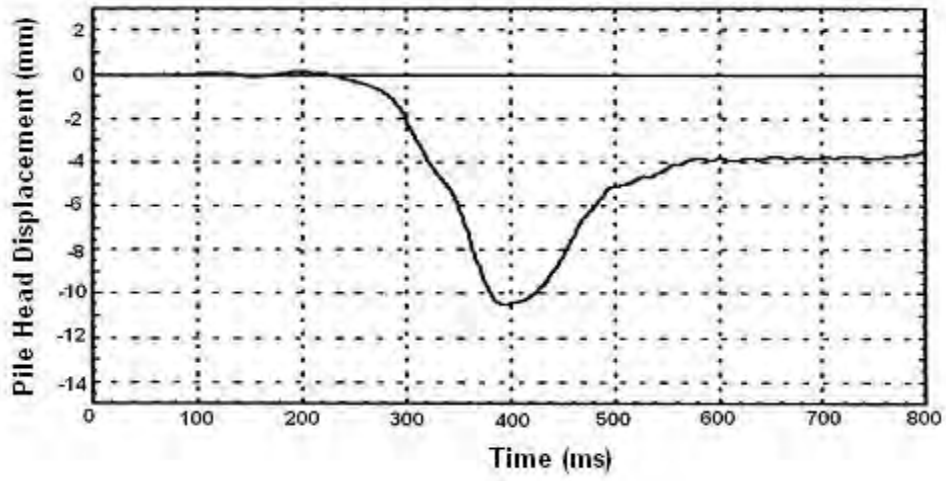
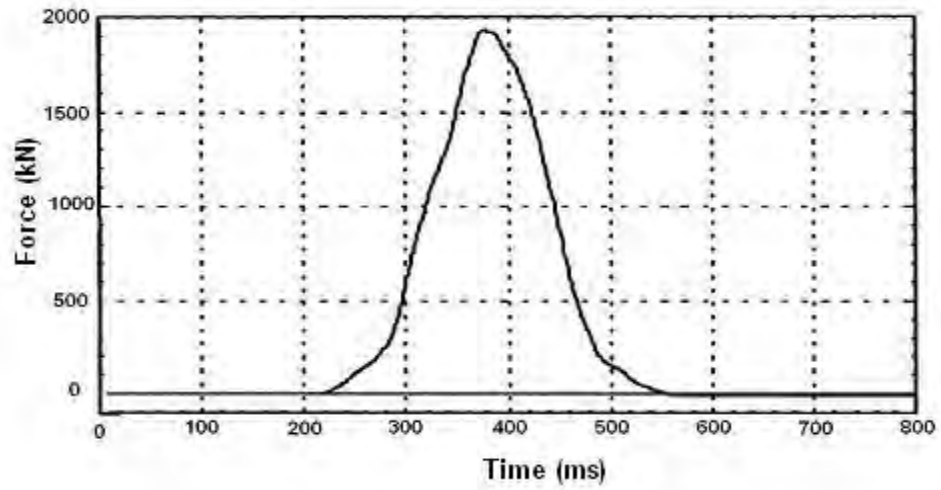


Figure 123. The Measured Force and Displacement Under a Single Impact by PSPLT (Schellingerhort, 1996)

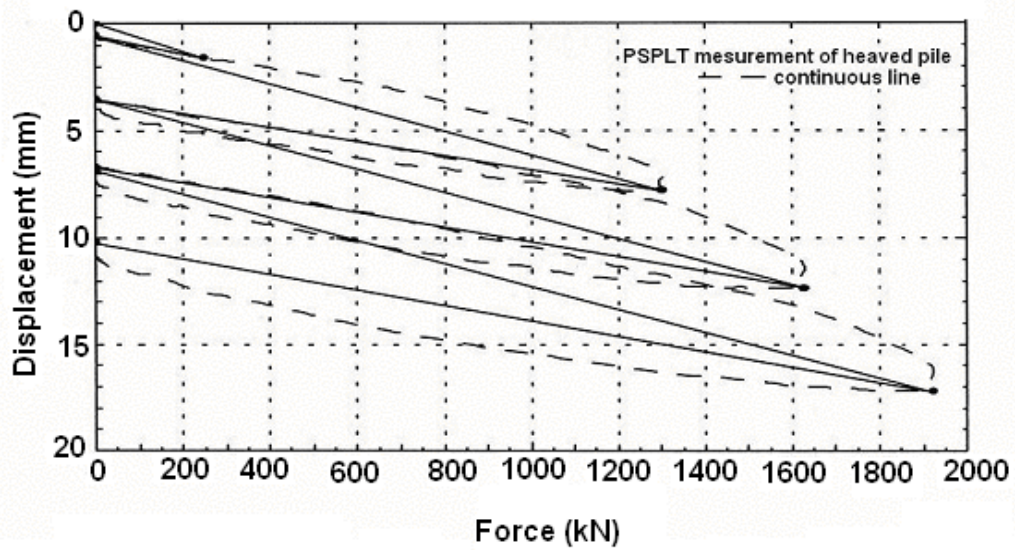


Figure 124. Load Displacement Curve Generated by Four Consecutive Drop Heights (Schellingerhort, 1996)

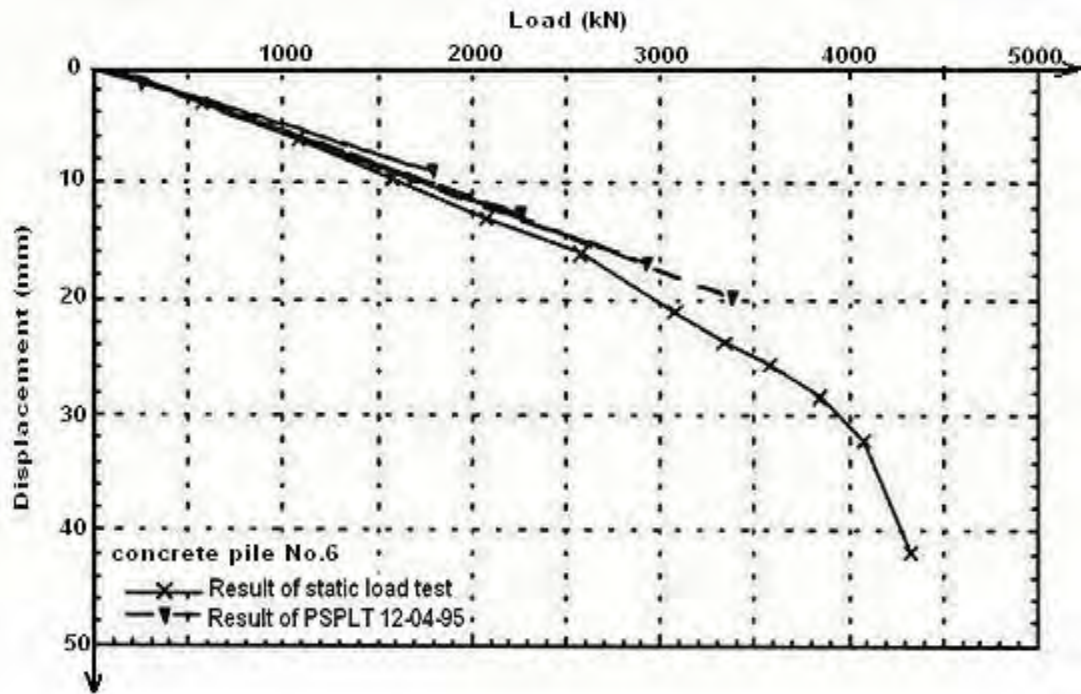


Figure 125. Case 1, Comparison of a Static Load Test and FUNDEX Measurements. (Schellingerhort, 1996)

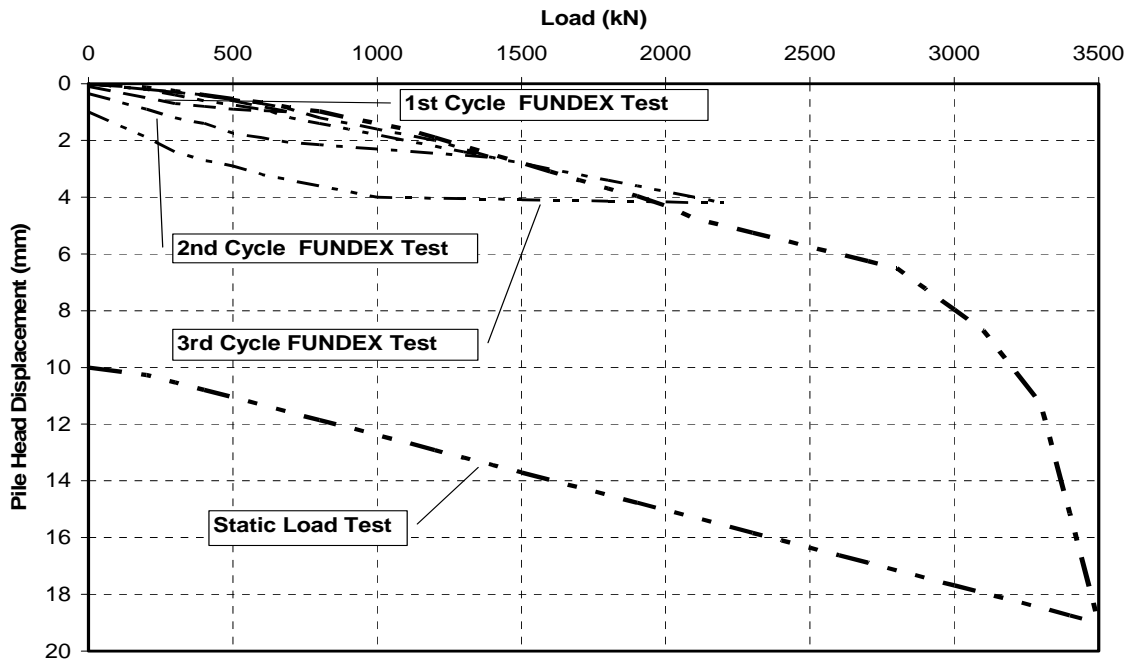


Figure 126. Case 2, Comparison of a Static Load Test and FUNDEX Measurements. (Americanpiledriving Website)

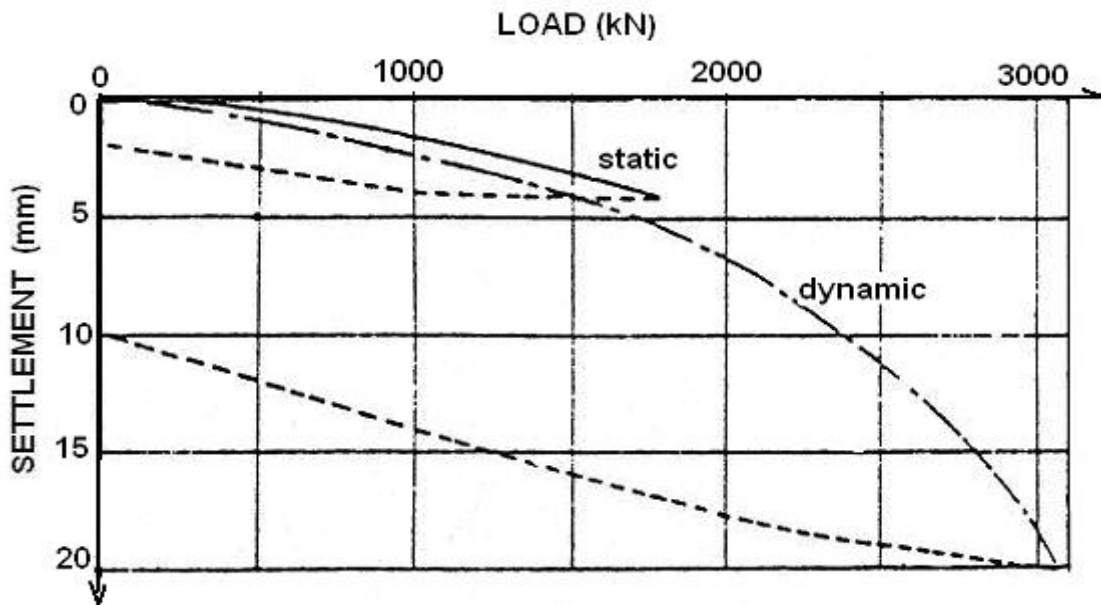


Figure 127. Case 3, Comparison of a Static Load Test and FUNDEX Measurements. (Iwanowski et al. 1984)

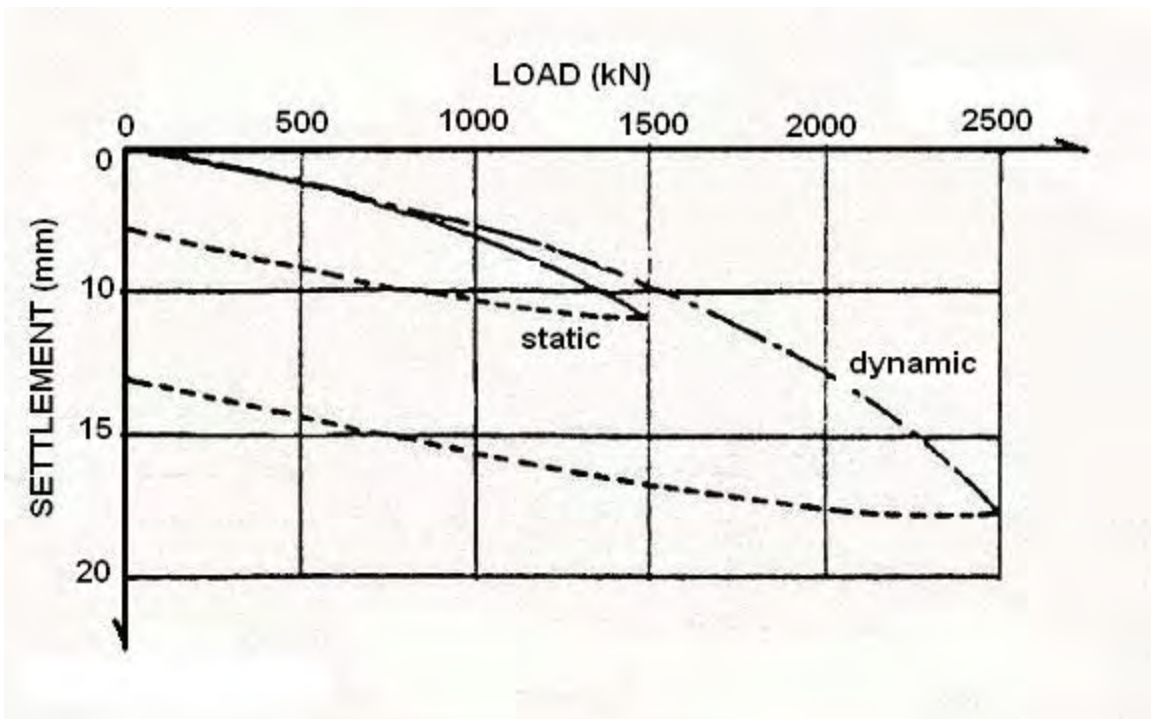


Figure 128. Case 4, Comparison of a Static Load Test and FUNDEX Measurements.
(Iwanowski et al. 1984)

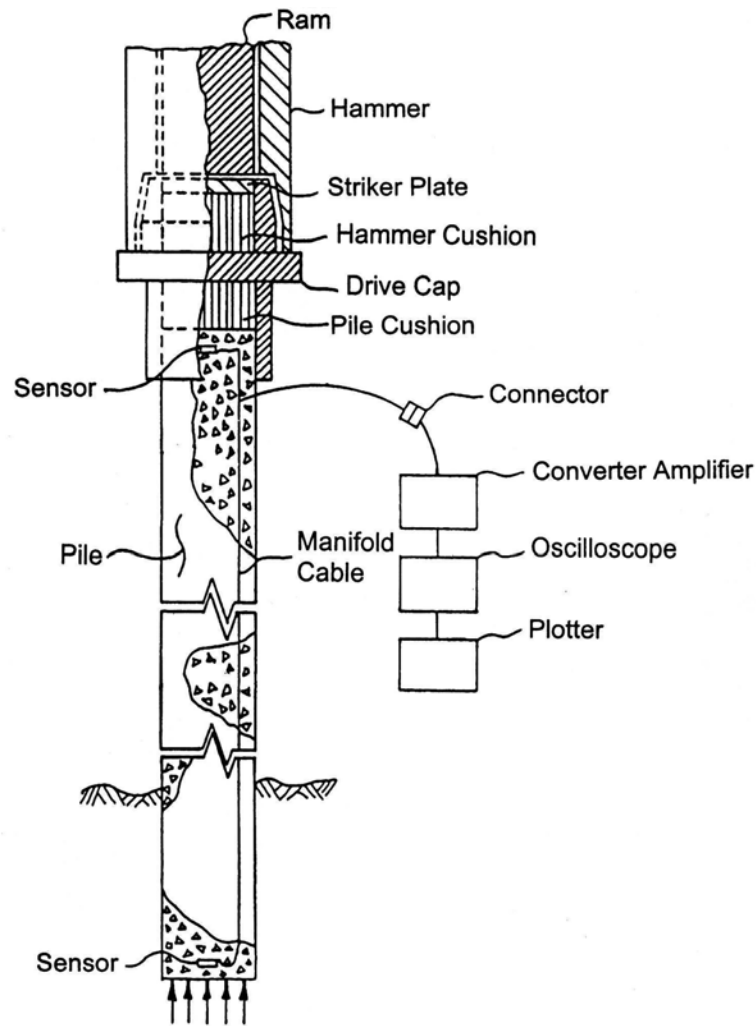


Figure 129. Smartpile Test Set-up
(Ooi and Frederick, 2003)

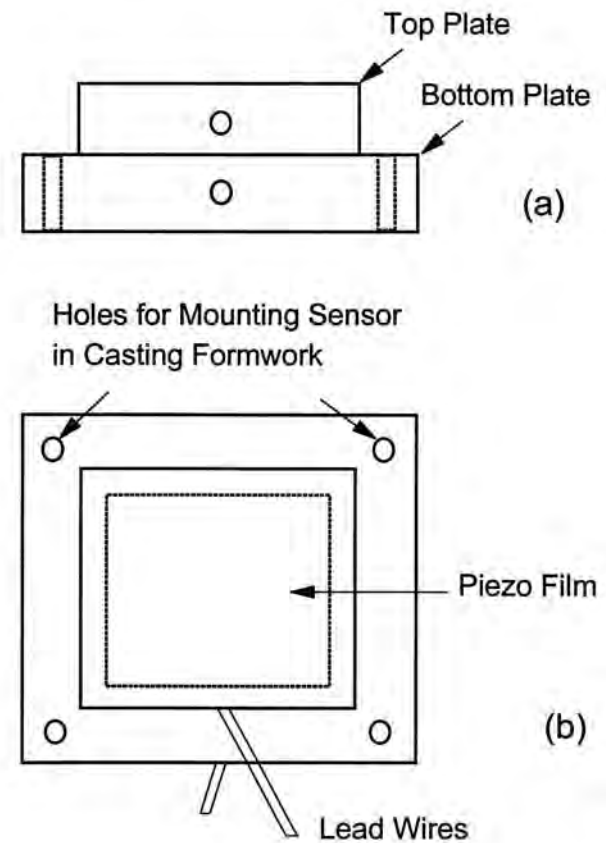
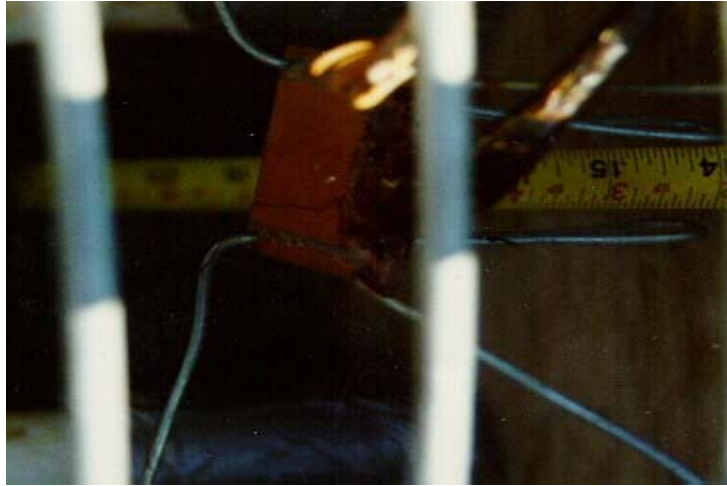


Figure 130. Force Sensor (a) Elevation View (b) Plan View
(Ooi and Frederick, 2003)



(a) Typical Sensor Installation



(b) The Smartpile Sensor

Figure 131. Smartpile Sensor Installation Photographs. (Geotechnical Engineering Research Laboratory, University of Massachusetts Lowell, Newbury Site TP#3)

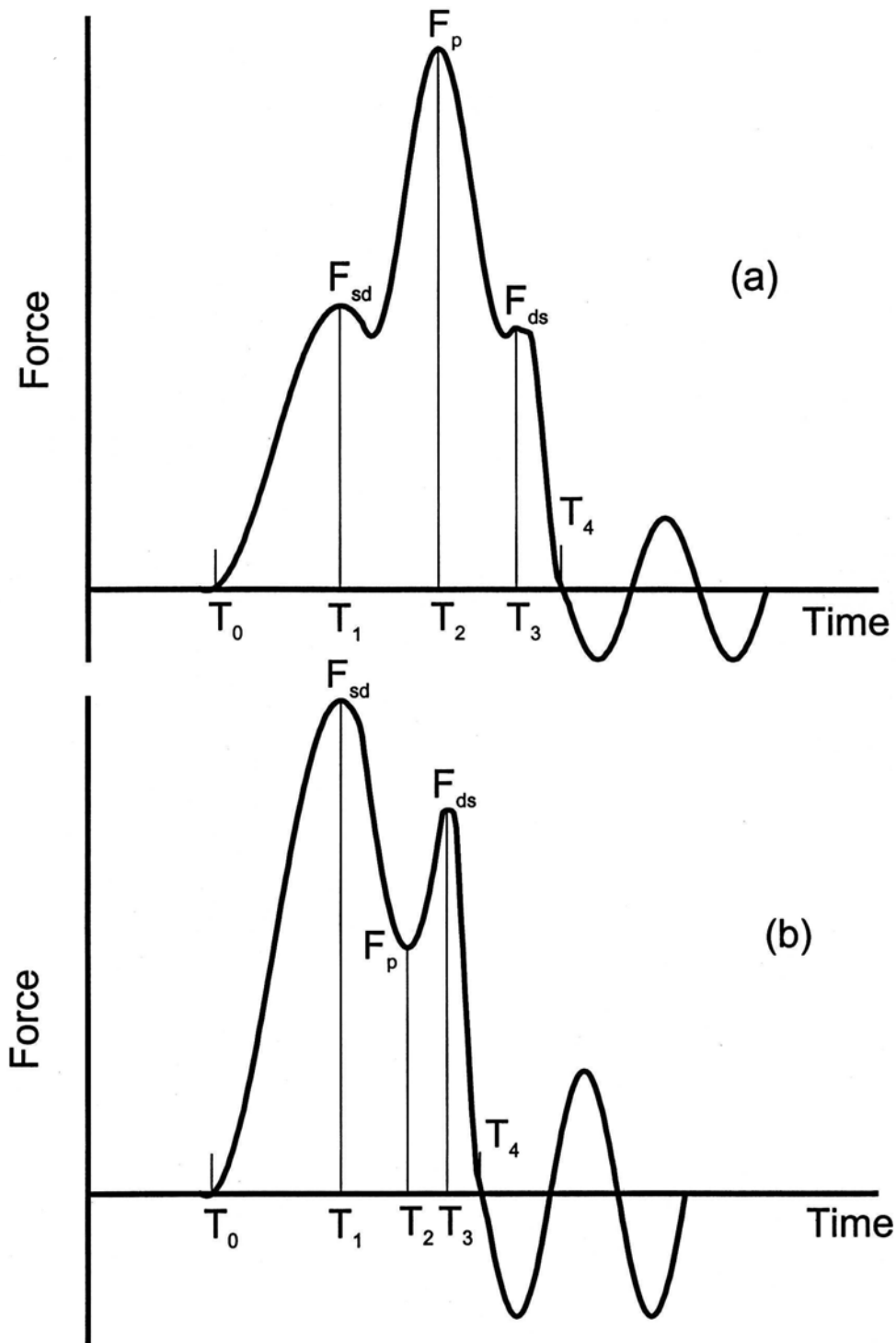


Figure 132. Typical Force Versus Time Plots from Smartpile Test: (a) with a Peak between F_{sd} and F_{ds} , and (b) with a Trough between F_{sd} and F_{ds} .
(Ooi and Frederick, 2003)

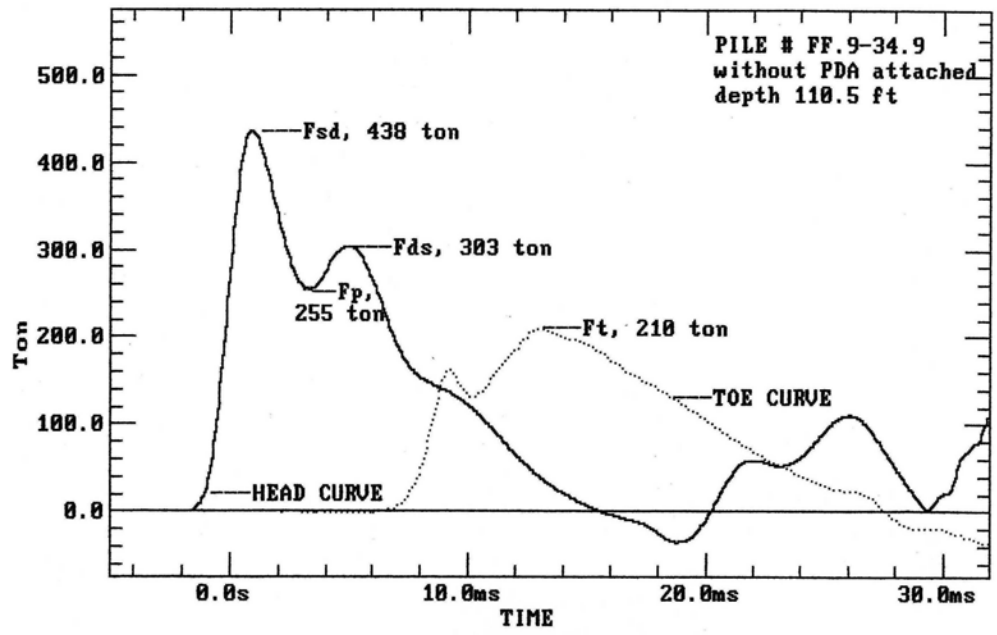


Figure 133. The Smartpile Testing Field Measurements using Top and Tip Sensors (Haley & Aldrich, 1995)

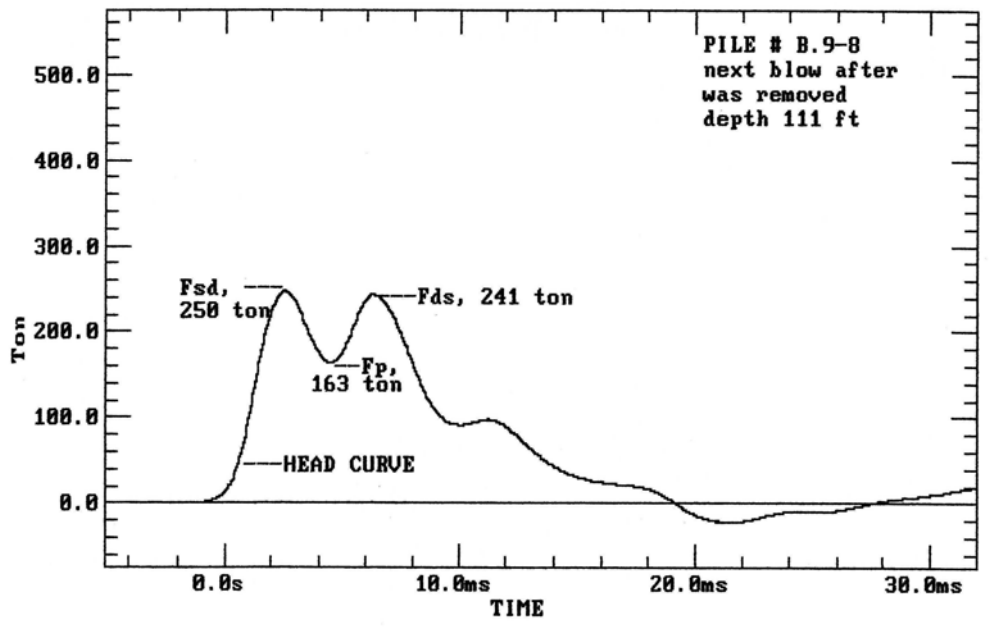


Figure 134. The Smartpile Testing Field Measurements using Top Measurements Alone (Haley & Aldrich, 1995)

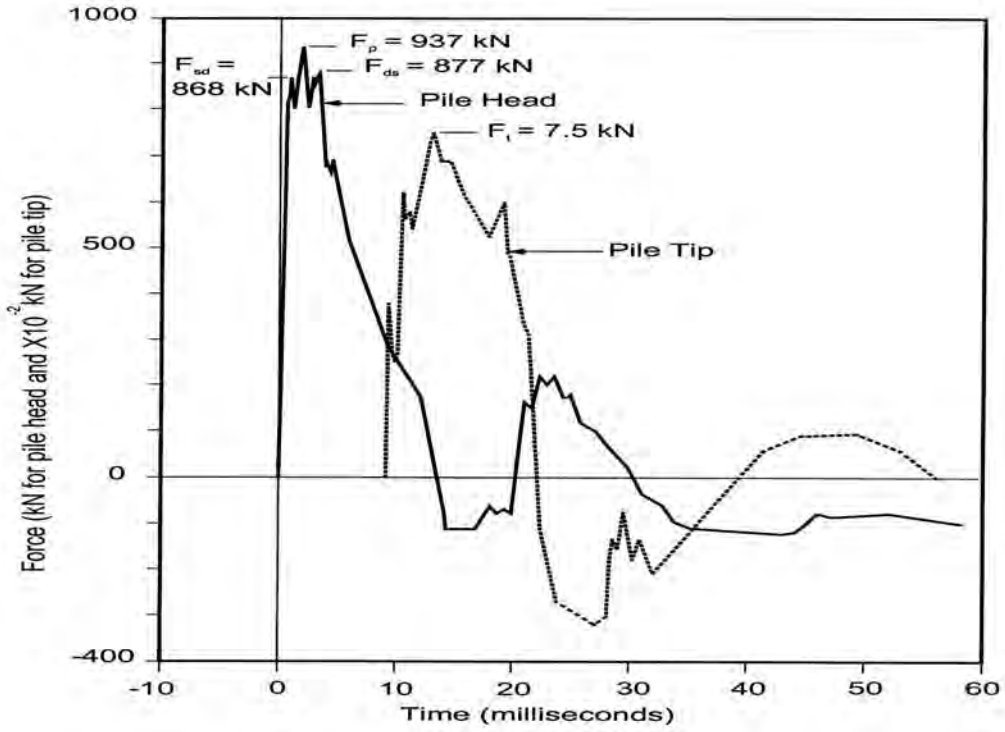


Figure 135. The Smartpile Measurements for TP#1(Ooi and Frederick, 2003)

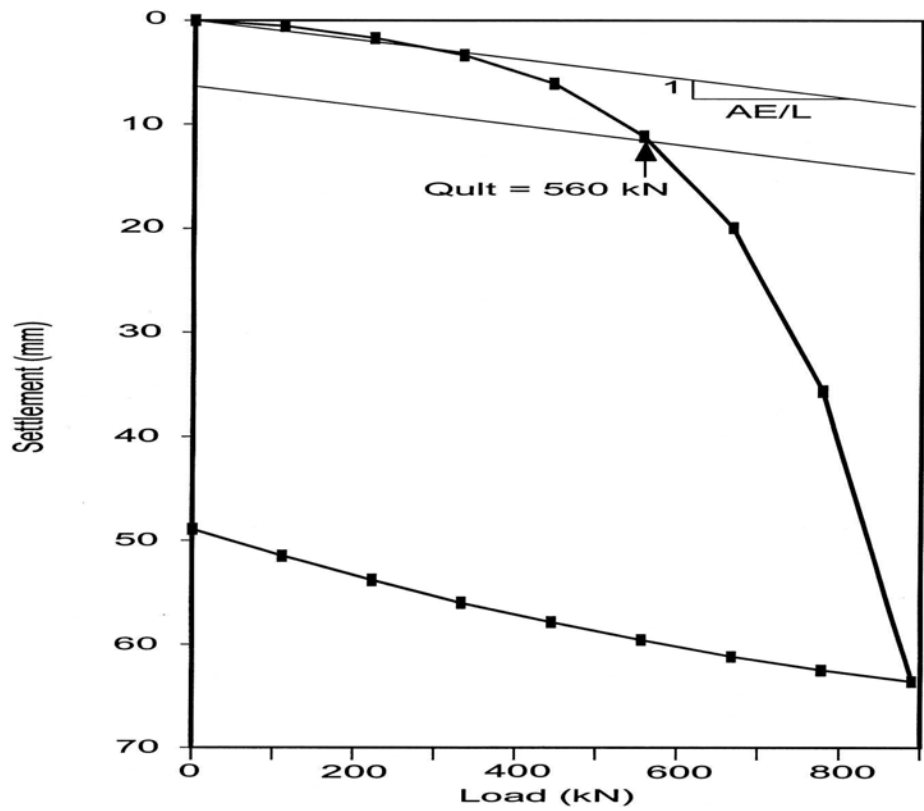


Figure 136. The Static Testing Result for TP#1 (Ooi and Frederick, 2003)

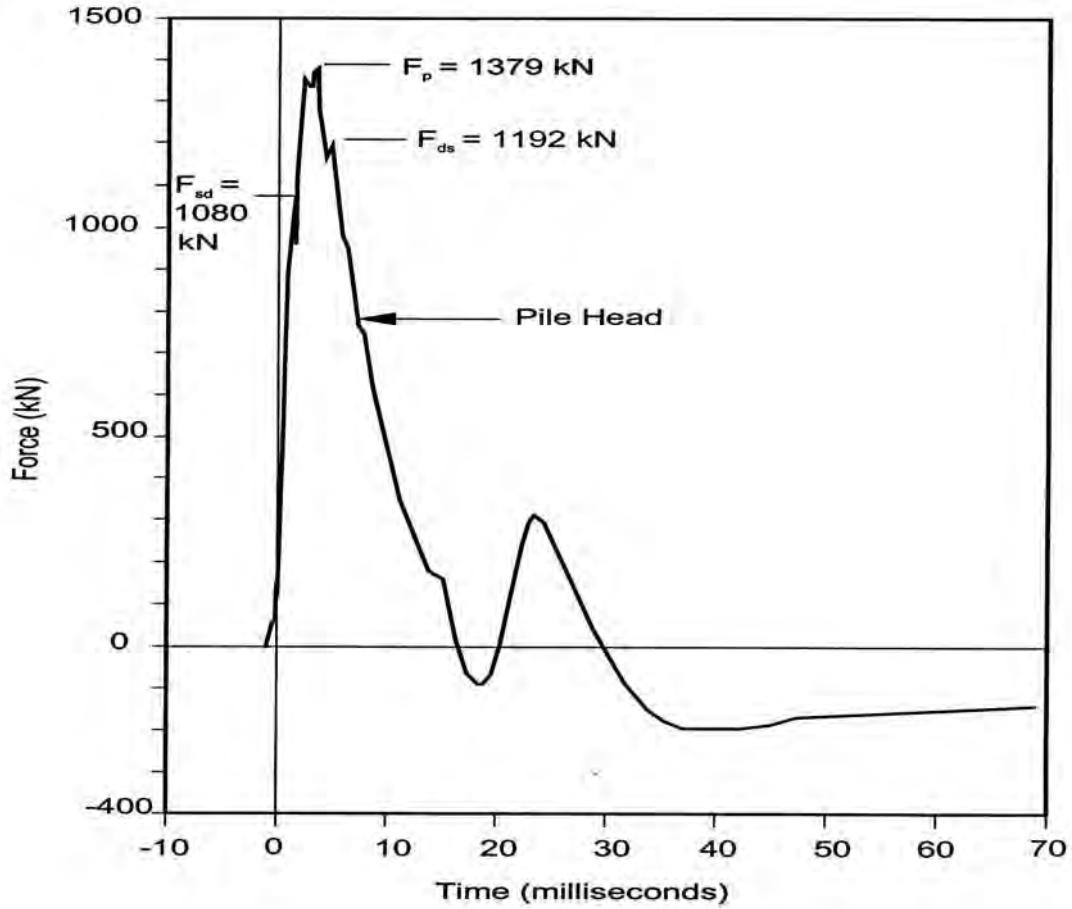


Figure 137. The Smartpile Measurements for TP#1 (Ooi and Frederick, 2003)

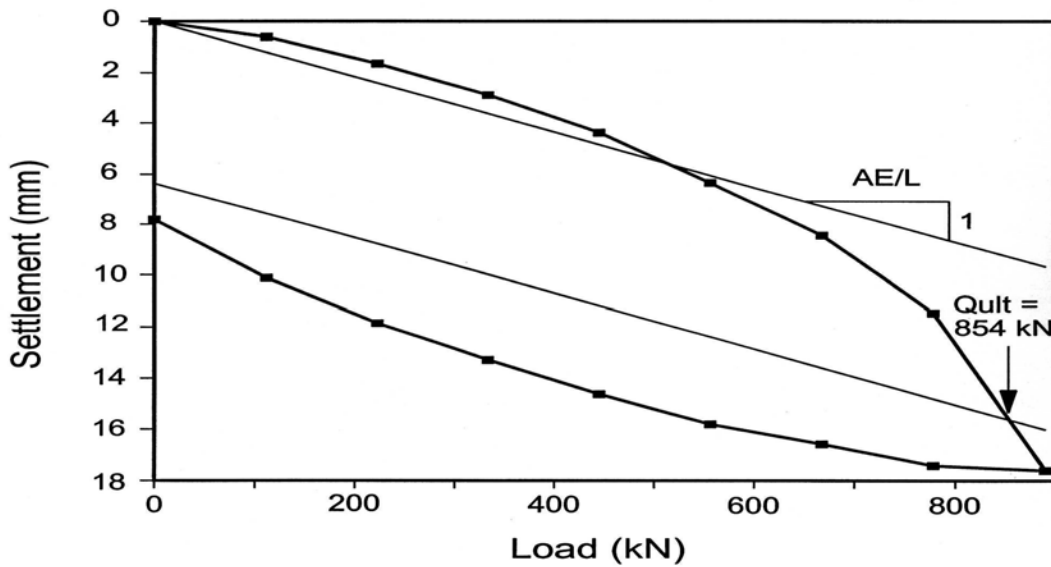


Figure 138. The Static Testing Result for TP#1 (Ooi and Frederick, 2003)

SMARTPILE SYSTEM FREDERICK ENGINEERING CO.
15 CRESTVIEW TER. WHIPPANY, NJ 07981 201-887-1256

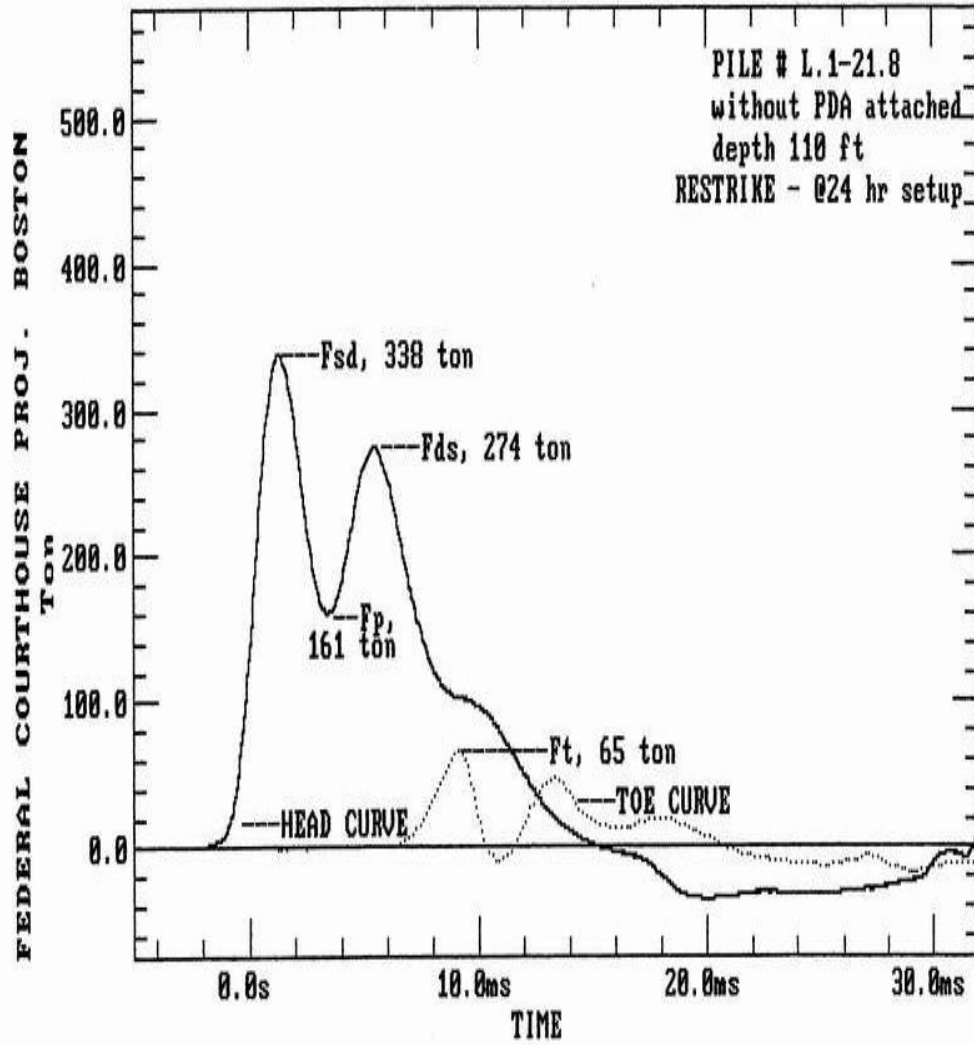


Figure 139. Illustration of Smartpile results for Courthouse Project Frederick Engineering Co. (Haley & Aldrich, 1995)

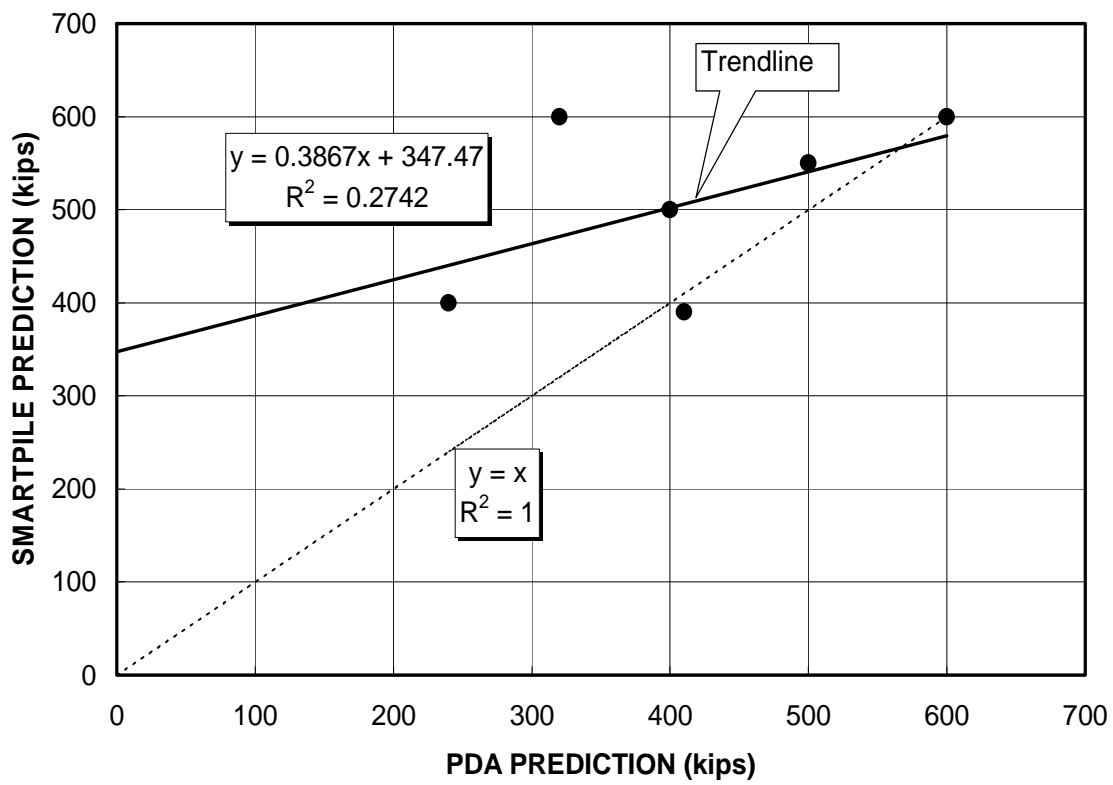


Figure 140. Comparison of PDA Prediction and Smartpile Measurements (Tests were done by Haley & Aldrich. Cambridge, MA. May 1995)

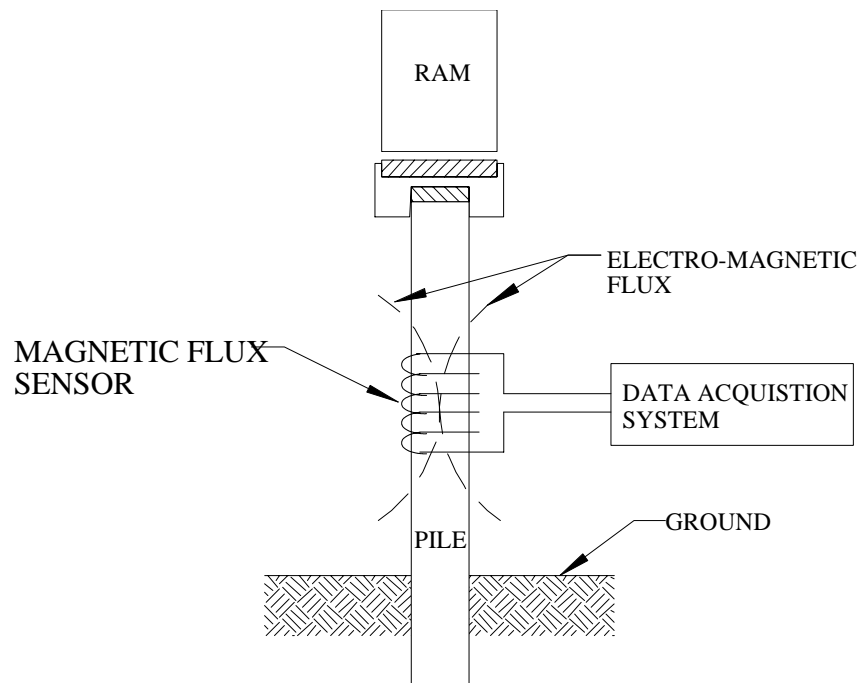


Figure 141. Typical Smart Coil System (SCS) Setup (after Frederick, 1999).

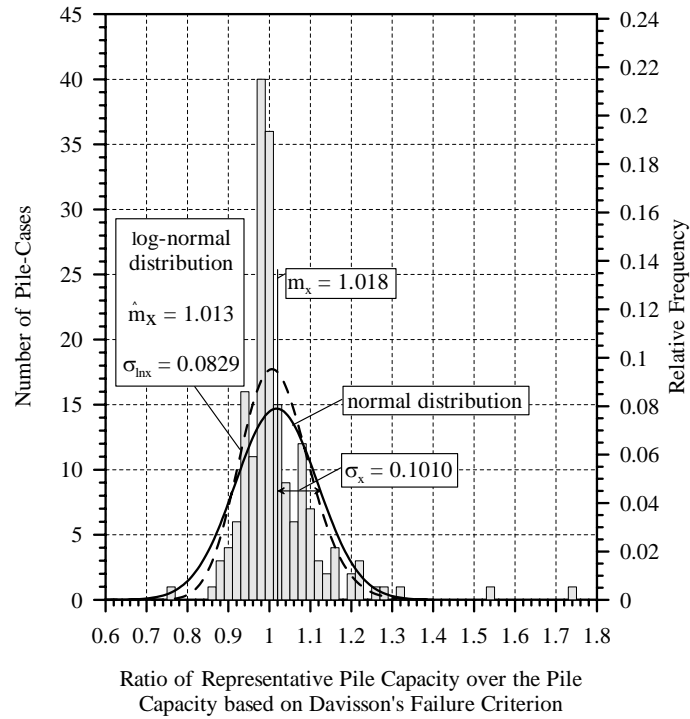


Figure 142. Histogram and frequency distributions of K_{SD} for 186 PD/LT2000 pile-cases in all types of soils. (Paikowsky and Stenerson 2000)

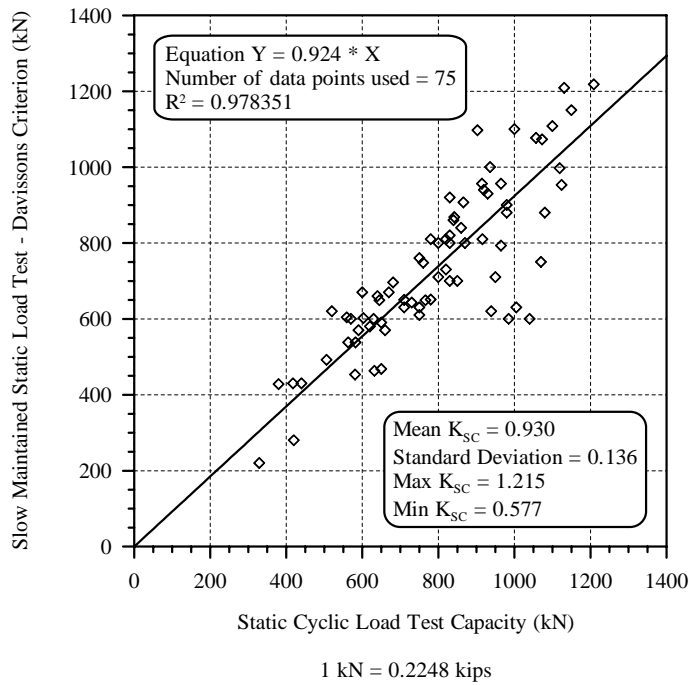


Figure 143. Comparison between pile capacity based on Davisson's criterion for slow maintained load tests and static cyclic load test capacity for 75 piles, (Paikowsky et al., 1999).

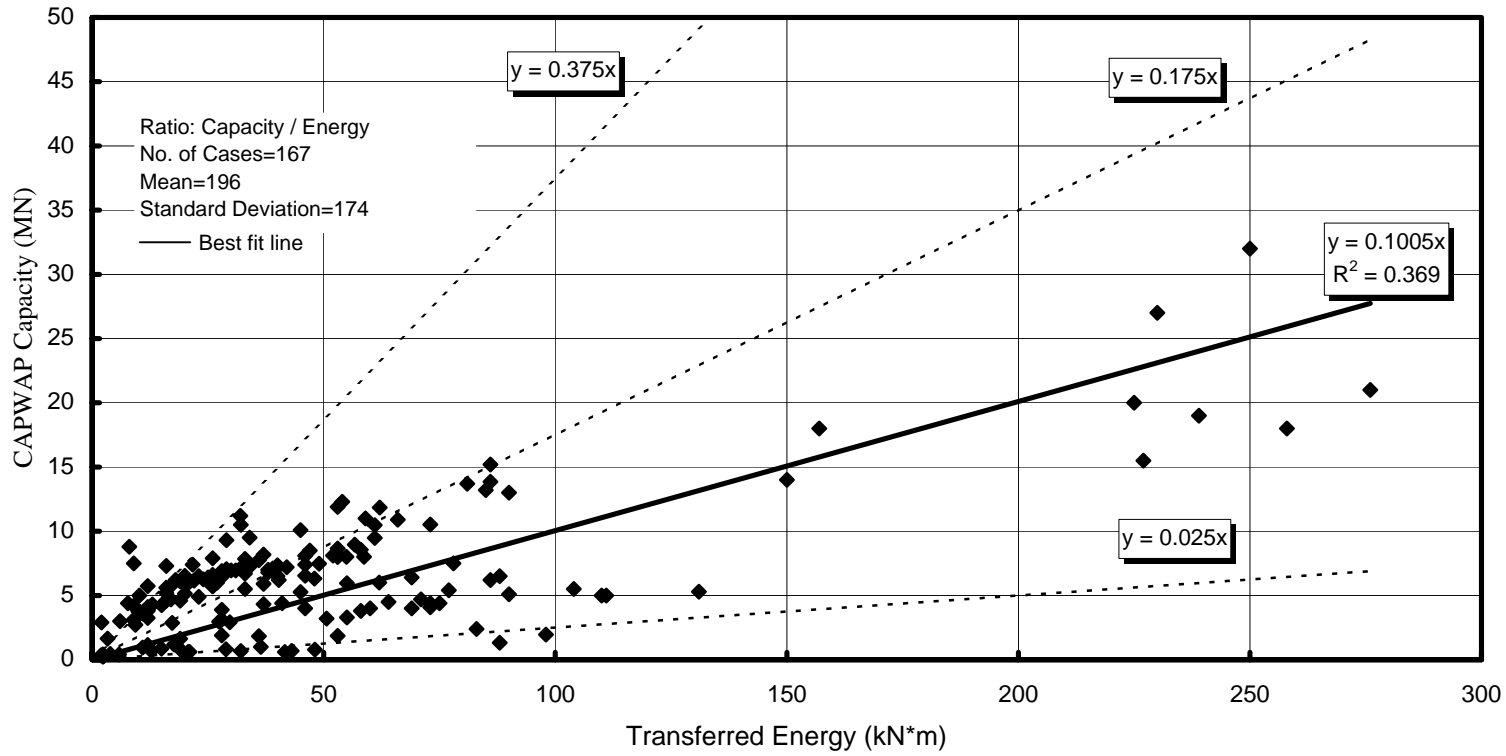


Figure 144. CAPWAP Drilled Shaft Capacity vs. Transferred Energy

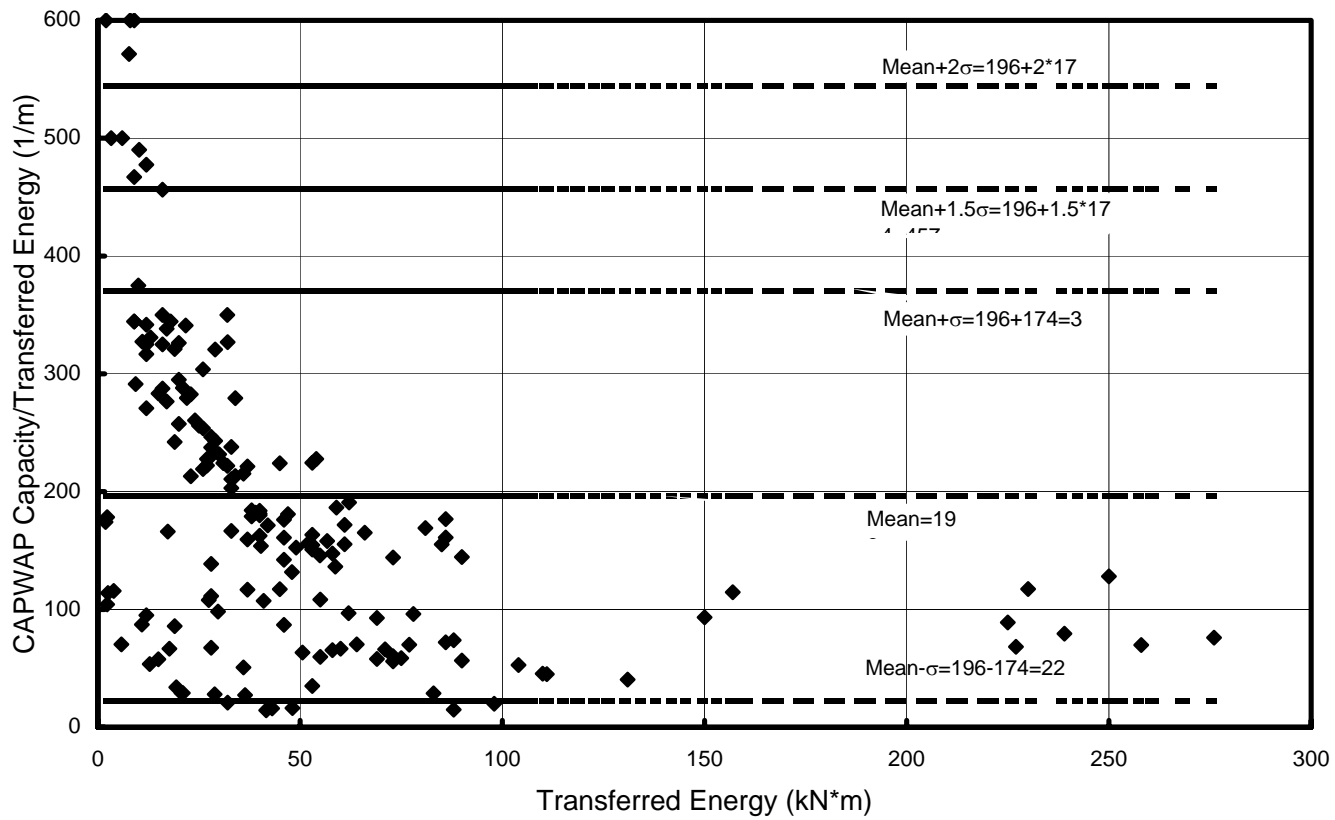


Figure 145. The Ratio of CAPWAP Drilled Shaft Capacity to Transferred Energy vs. Transferred Energy (No. of Cases=167, Mean=196, S.D. =174)

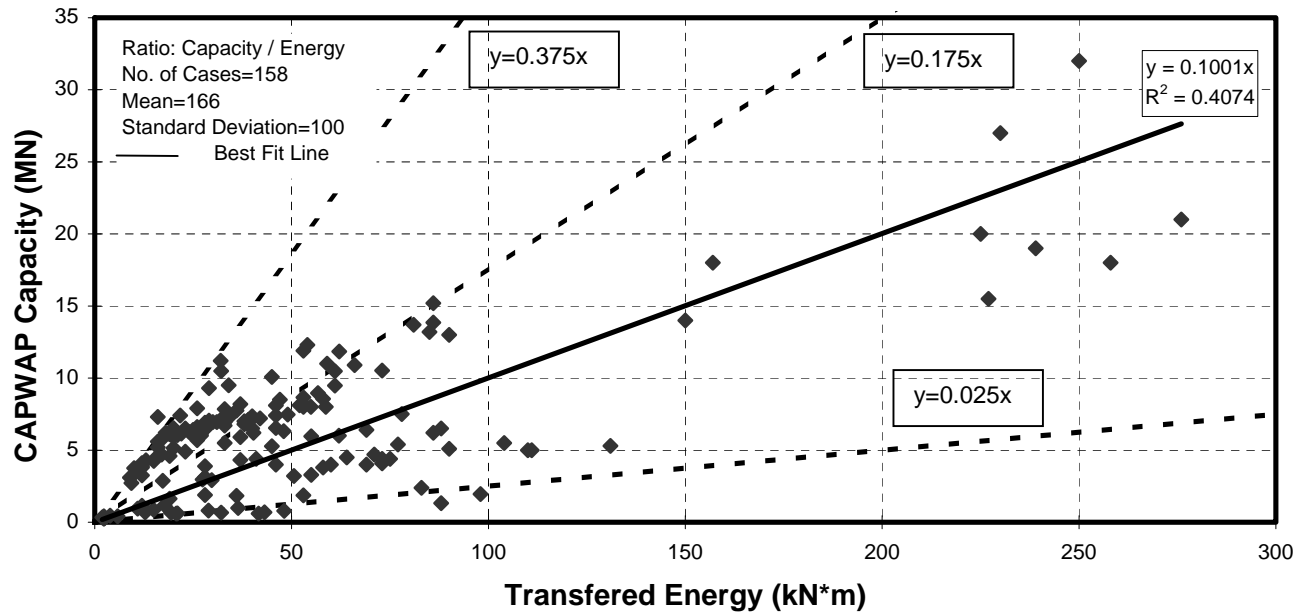


Figure 146. CAPWAP Drilled Shaft Capacity vs. Transferred Energy For Capacity to Energy Ratio < Mean+1.5(S.D)

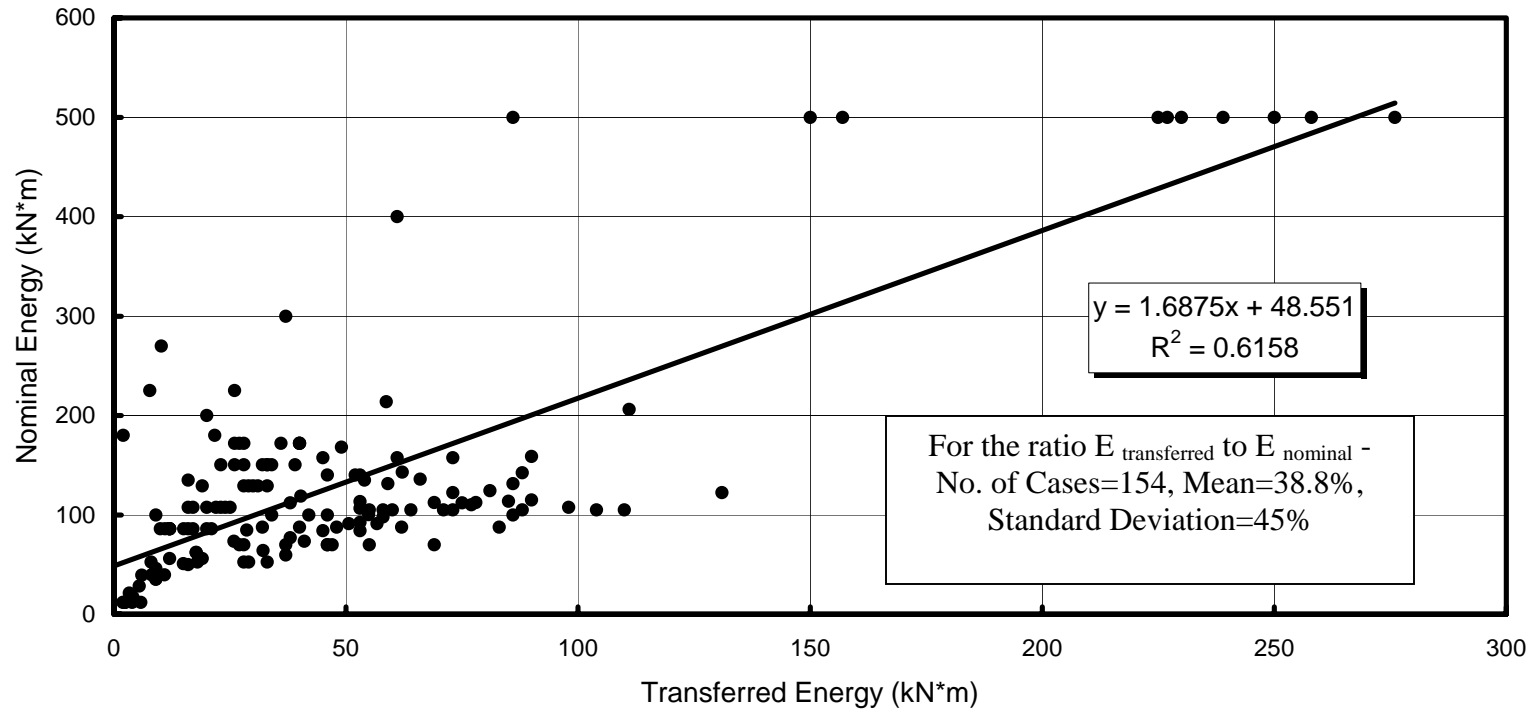


Figure 147. Transferred Energy vs. Nominal Energy

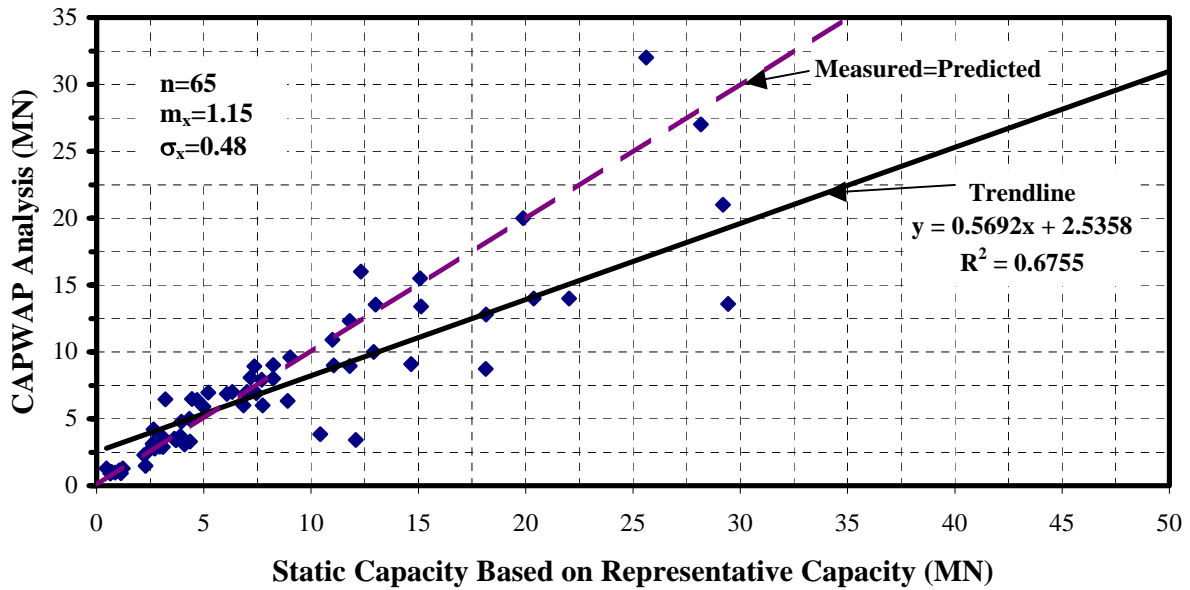


Figure 148. Drilled Shaft Static Load Test Results (Representative Capacity) vs. Drop Weight CAPWAP Analysis for All Cases

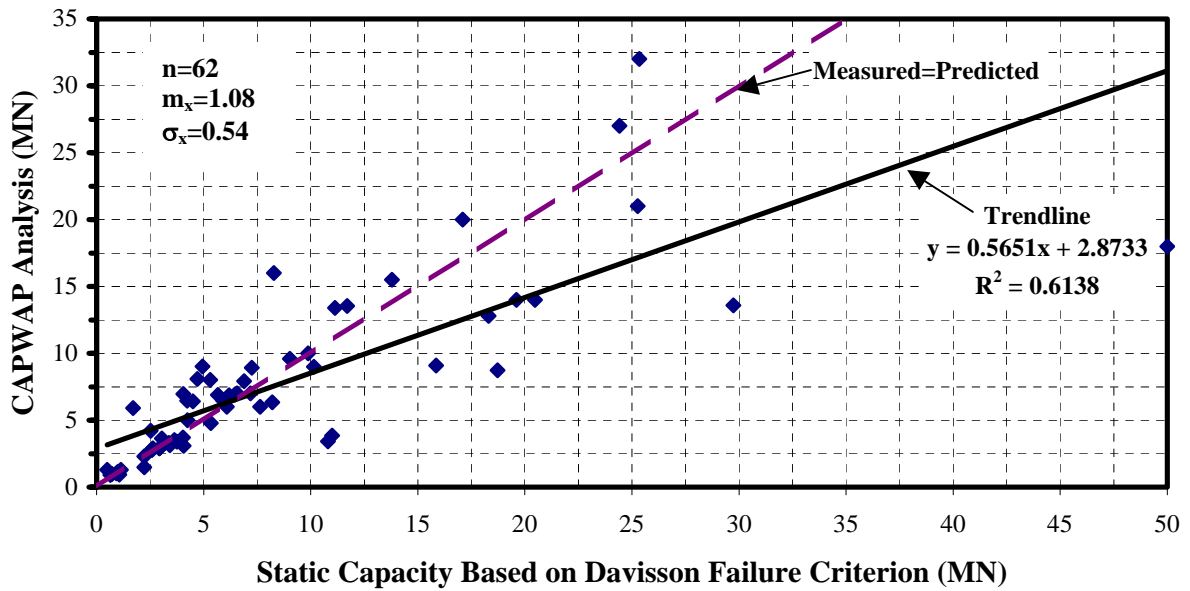


Figure 149. Drilled Shaft Static Load Test Results (Davisson's Failure Criterion) vs. Drop Weight CAPWAP Analysis for All Cases

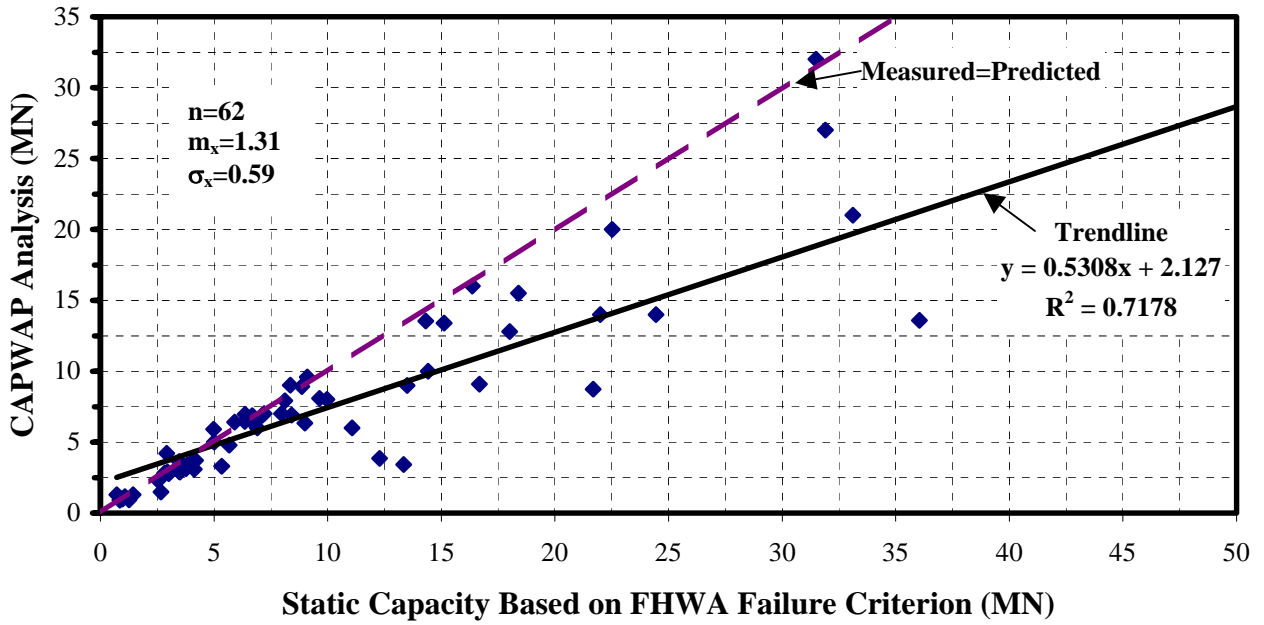


Figure 150. Drilled Shaft Static Load Test Results (FHWA Failure Criterion) vs. Drop Weight CAPWAP Analysis for All Cases

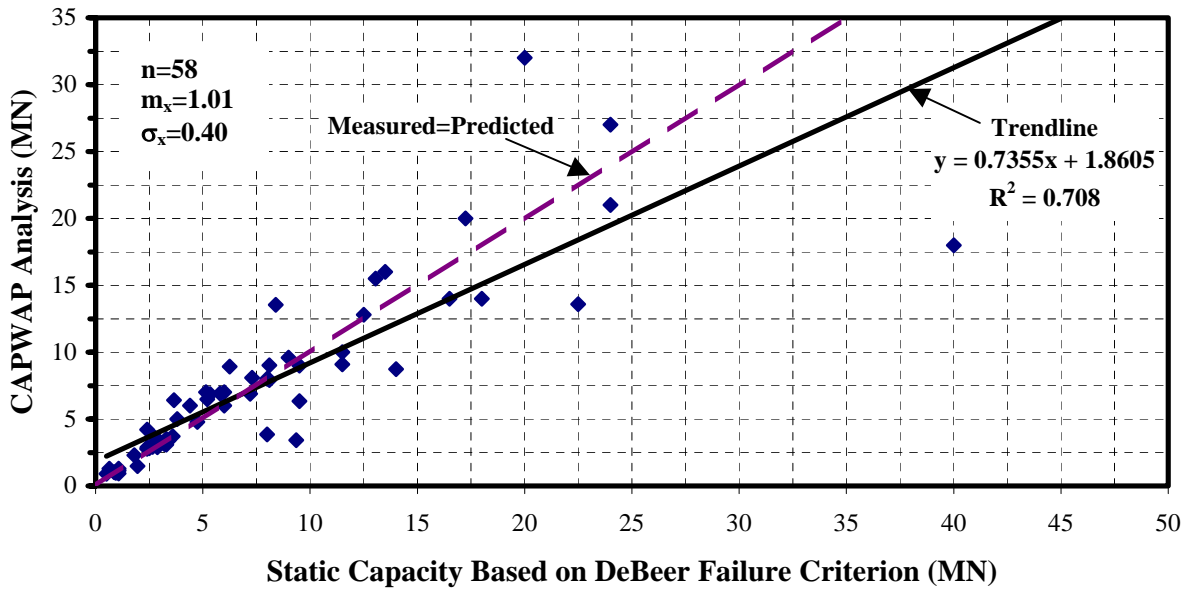


Figure 151. Drilled Shaft Static Load Test Results (DeBeer Failure Criterion) vs. Drop Weight CAPWAP Analysis for All Cases

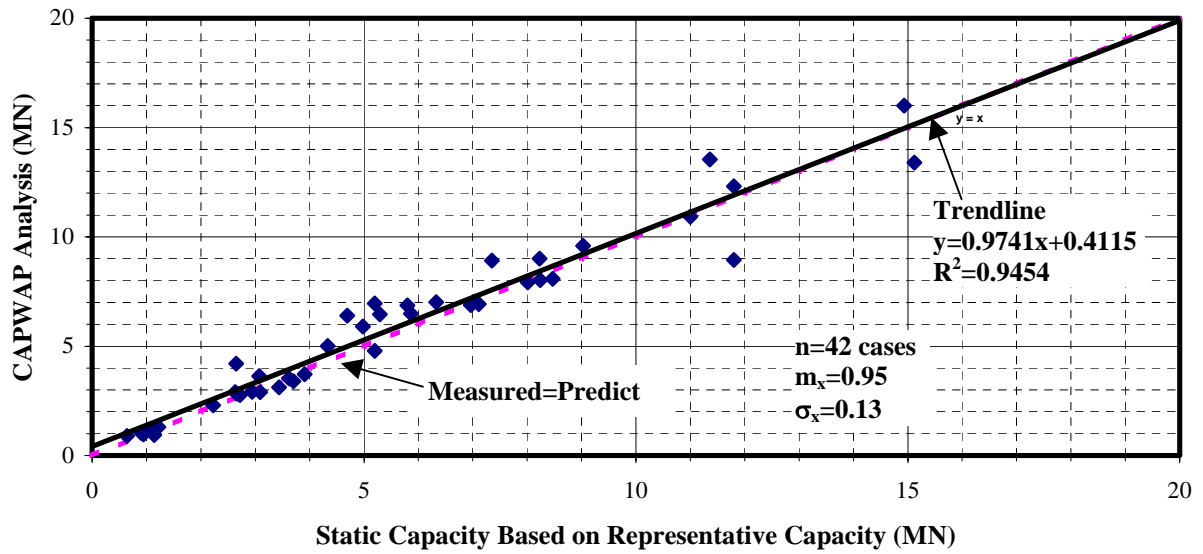


Figure 152. Drilled Shaft Static Load Test to Failure Results (Representative Capacity) vs. Drop Weight CAPWAP Analysis

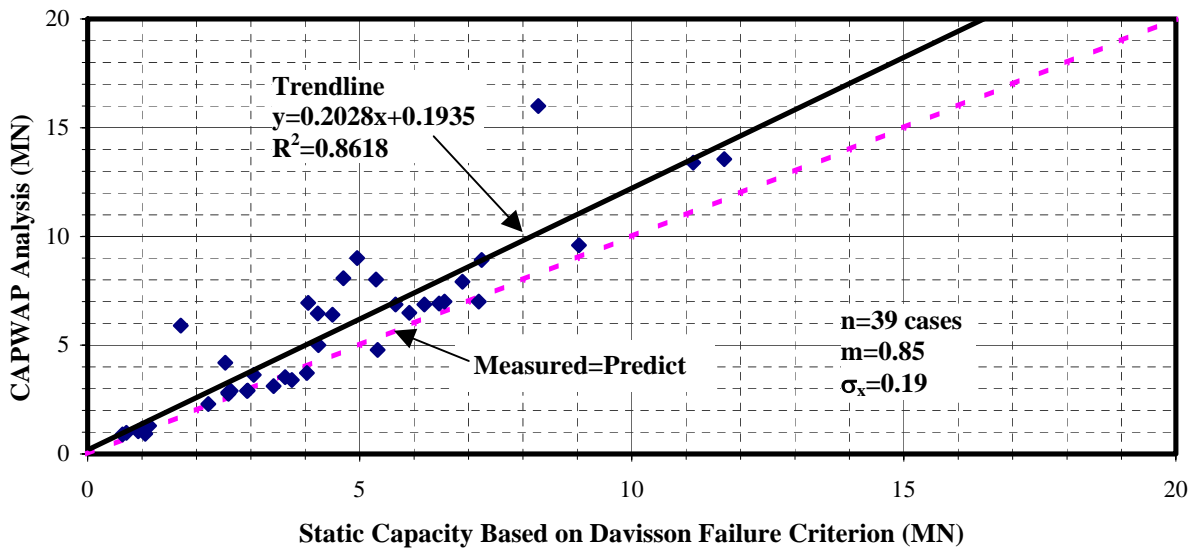


Figure 153. Drilled Shaft Static Load Test to Failure Results (Davisson's Failure Criterion) vs. Drop Weight CAPWAP Analysis

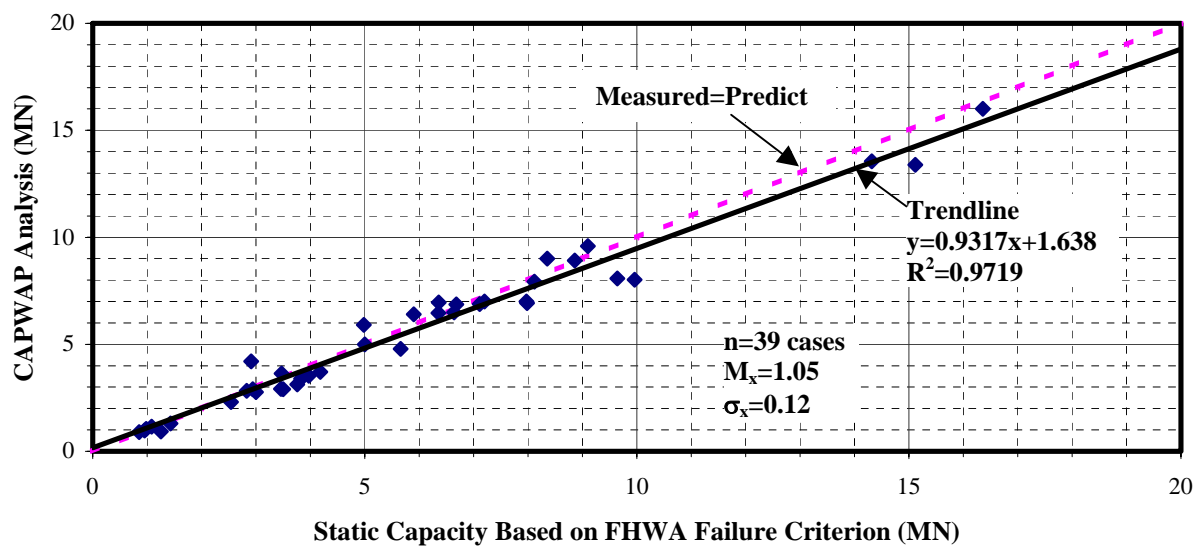


Figure 154. Drilled Shaft Static Load Test to Failure Results (FHWA Failure Criterion) vs. Drop Weight CAPWAP Analysis

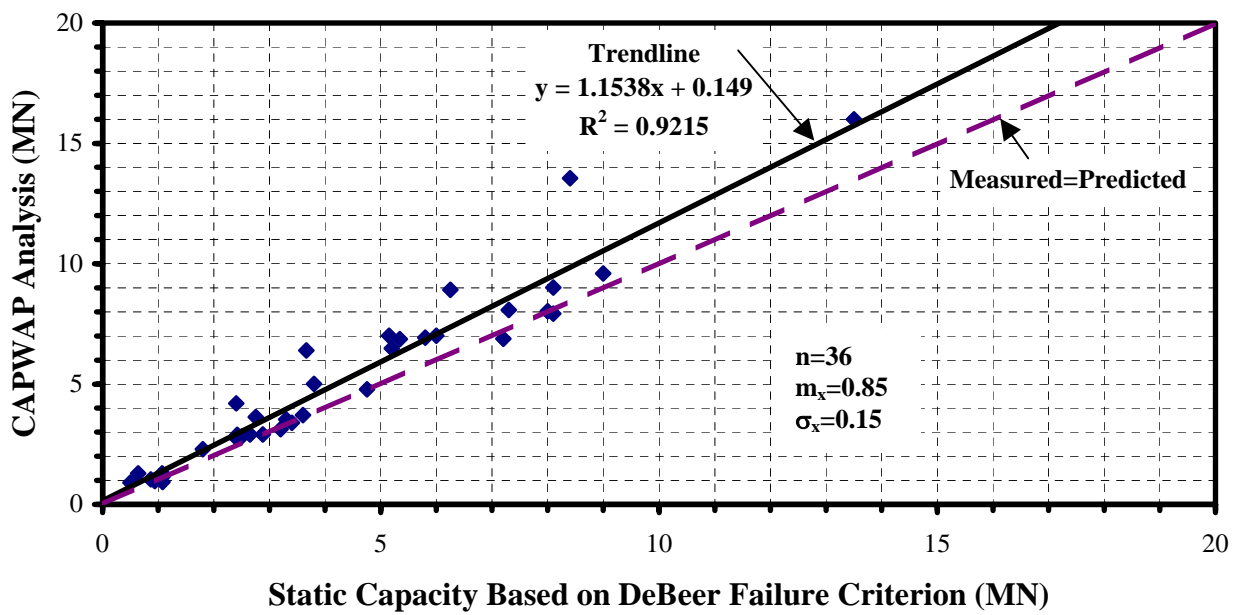


Figure 155. Drilled Shaft Static Load Test to Failure Results (DeBeer Failure Criterion) vs. Drop Weight CAPWAP Analysis

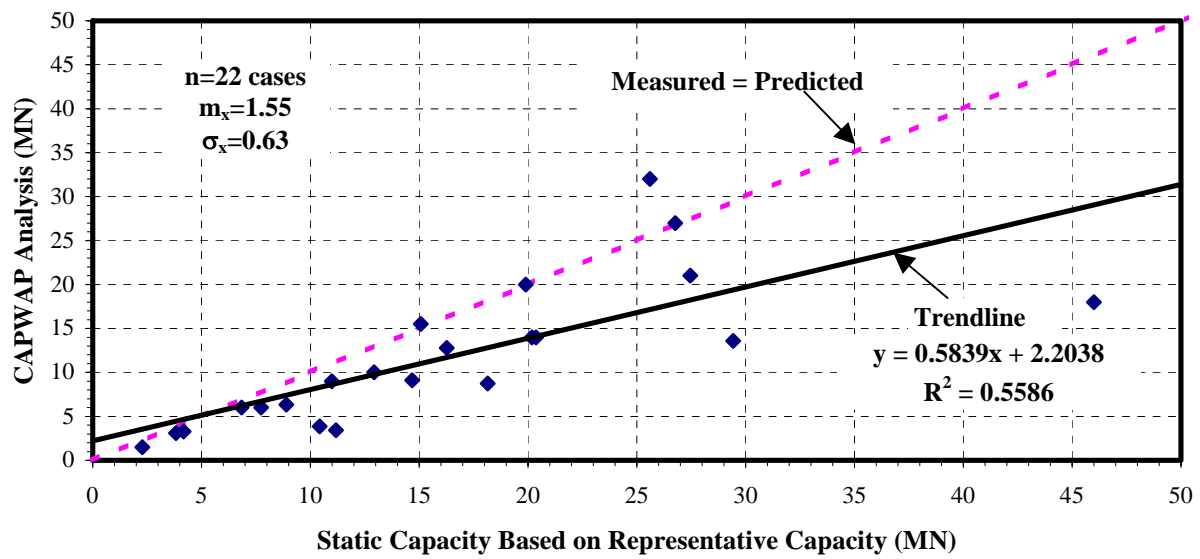


Figure 156. Drilled Shaft Static Extrapolated Load Test Results (Representative Capacity) vs. Drop Weight CAPWAP Analysis

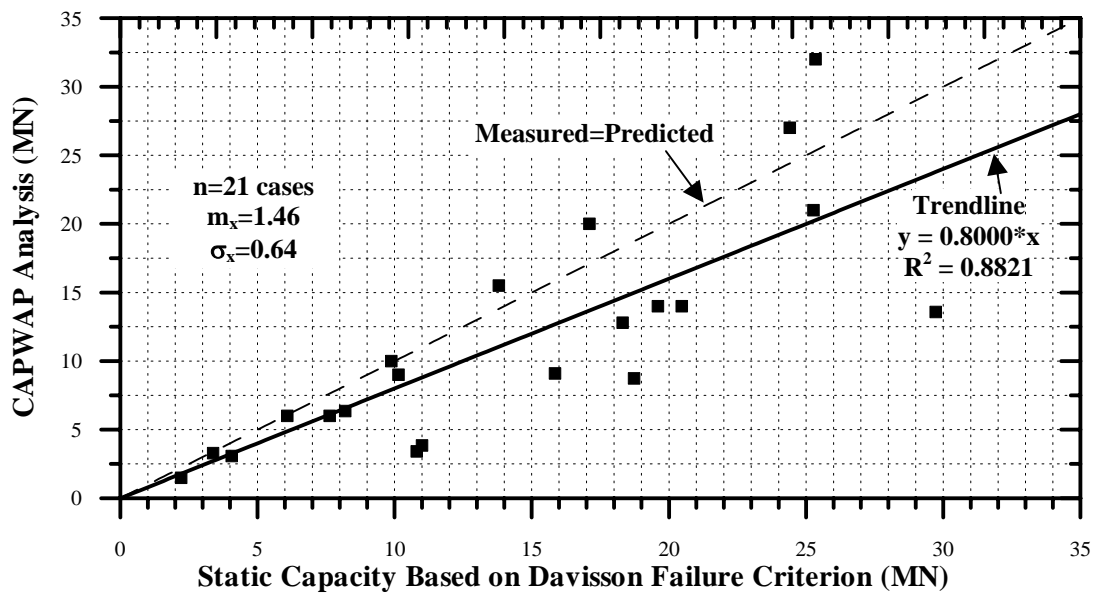


Figure 157. Drilled Shaft Extrapolated Static Load Test Results (Davisson Failure Criterion) vs. Drop Weight CAPWAP Analysis

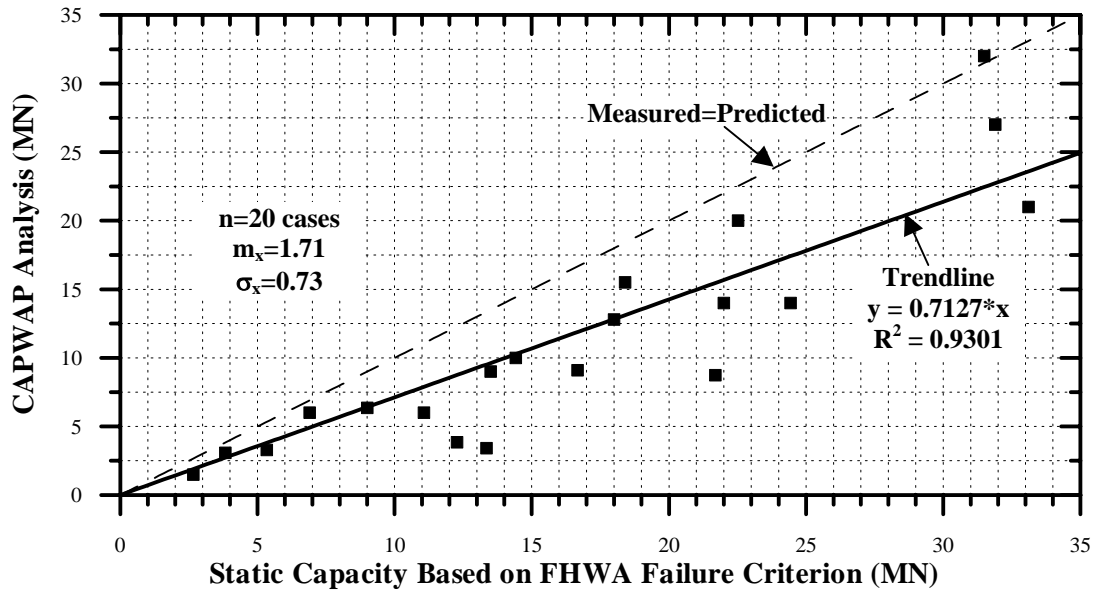


Figure 158. Drilled Shaft Extrapolated Static Load Test Results (FHWA Failure Criterion) vs. Drop Weight CAPWAP Analysis

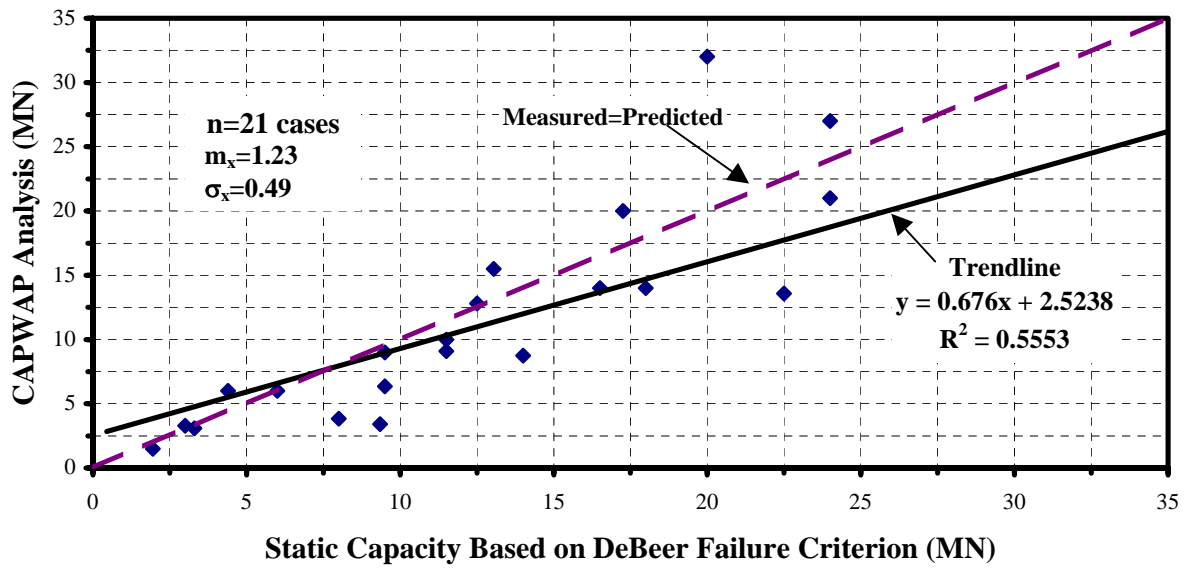
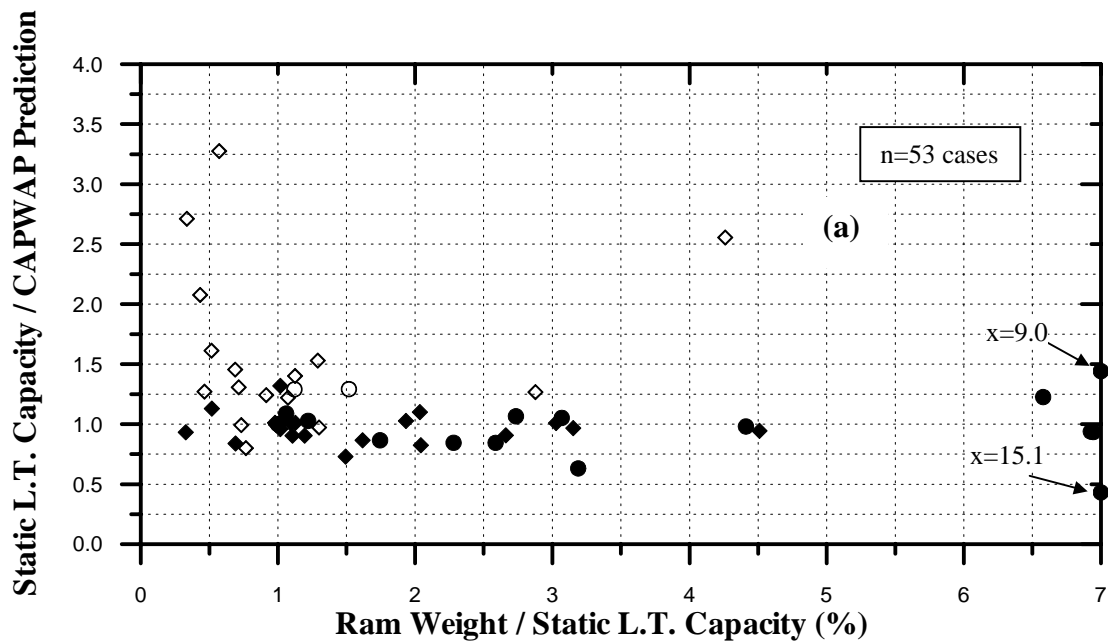


Figure 159. Drilled Shaft Extrapolated Static Load Test Results (DeBeer Failure Criterion) vs. Drop Weight CAPWAP Analysis



	Load Test	Failure	Extrapolated
Major Resistance	Friction	●	○
	End Bearing	◆	◇

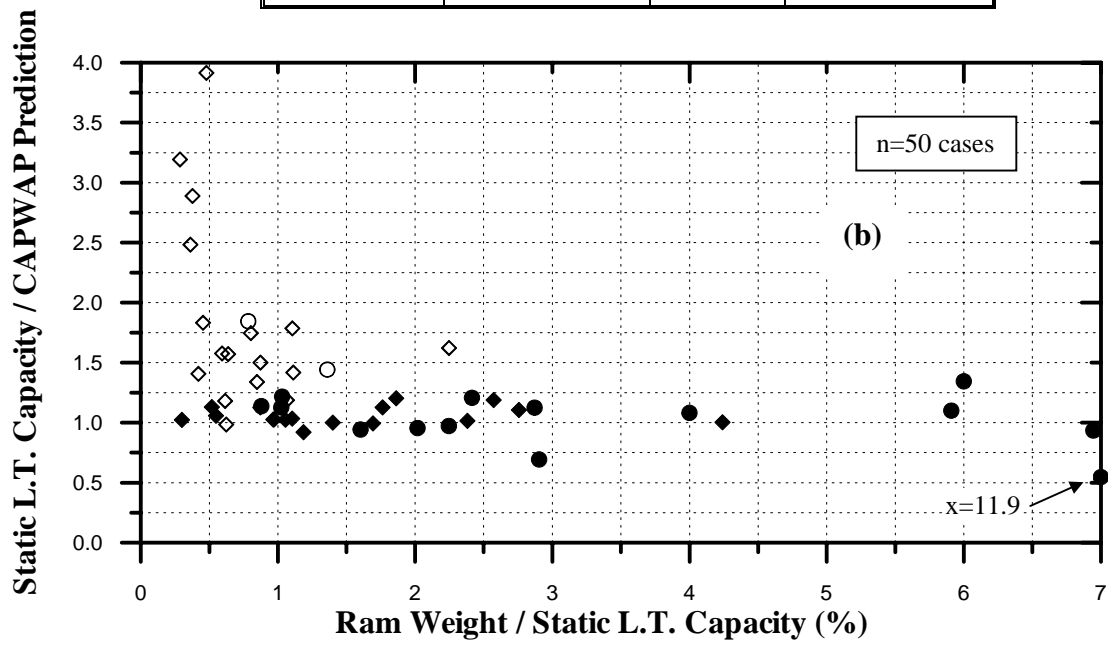


Figure 160. Static L.T. Capacity Over CAPWAP Prediction vs. Ram Weight Over Static L.T. Capacity; (a) Using the Representative Static Capacity, (b) Using the FHWA Failure Criterion.

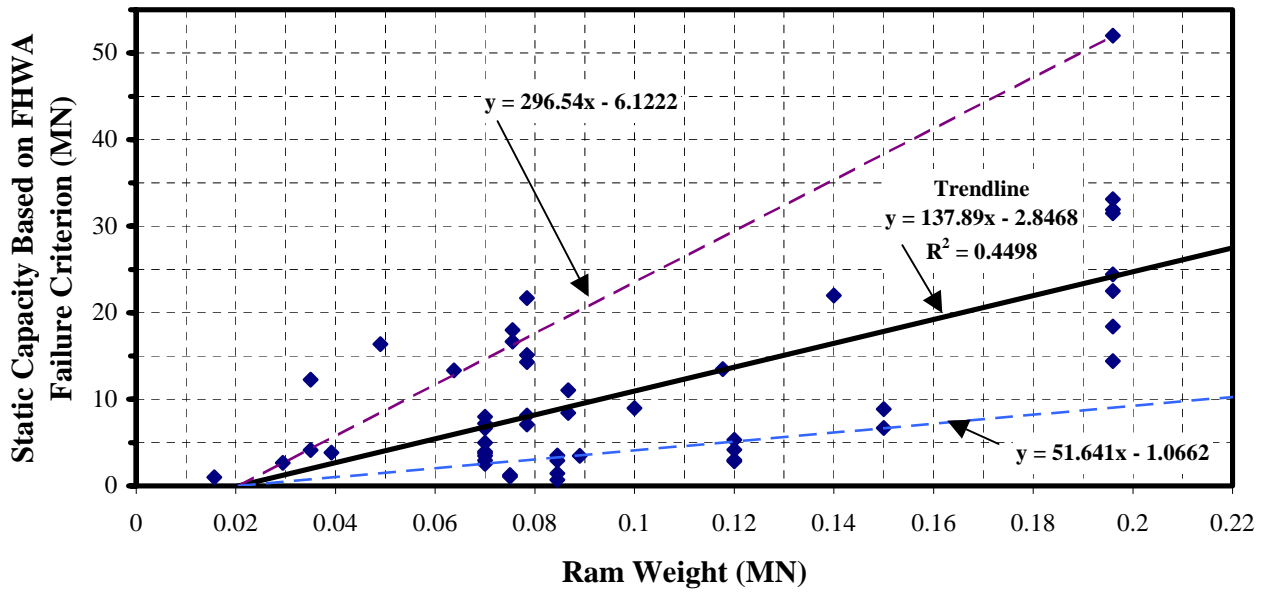


Figure 161. Measured Static Capacity (FHWA Failure Criterion) vs. Ram Weight Using Database DW/LT 2000 for All Load Test Cases

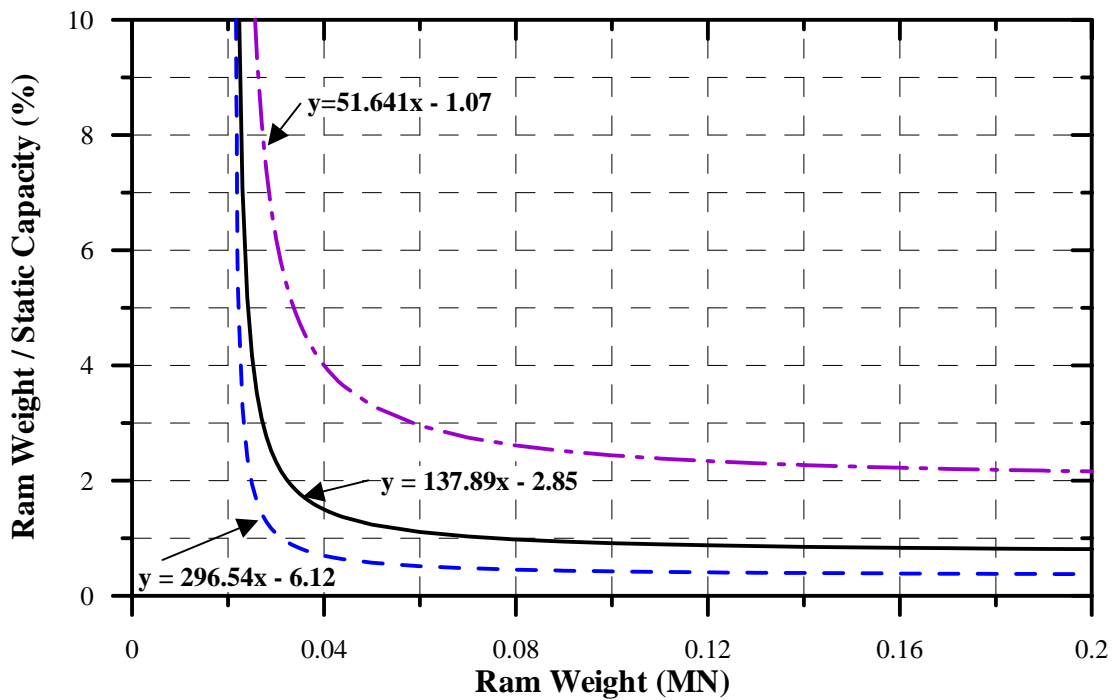


Figure 162. Relationship Between the Ratio of Ram Weight to Drop Weight Capacity (FHWA Failure Criterion) vs. Ram Weight Based on Database DW/LT 2000

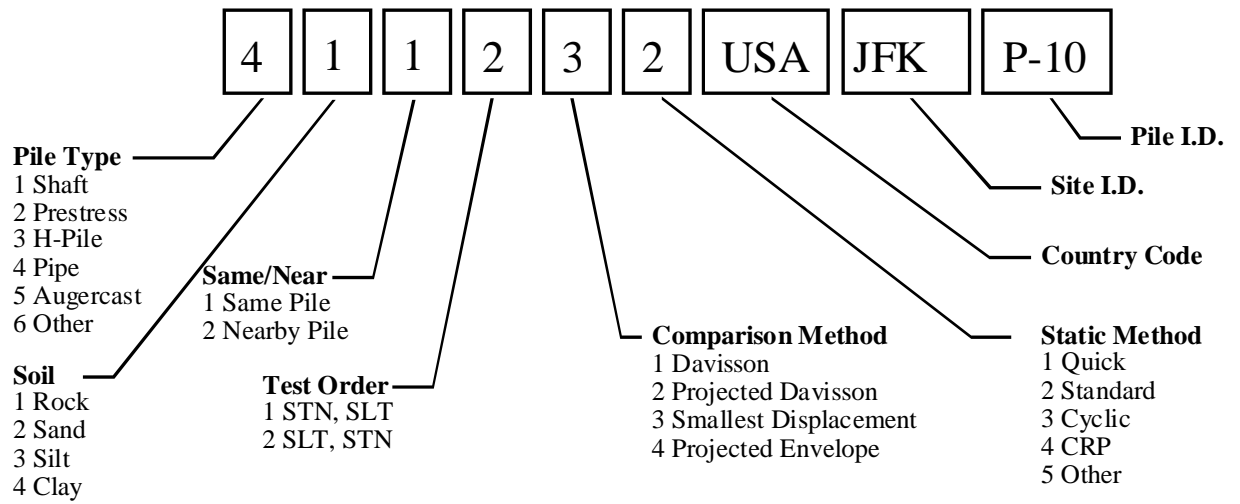


Figure 163. Load test program parameters used to uniquely define comparisons

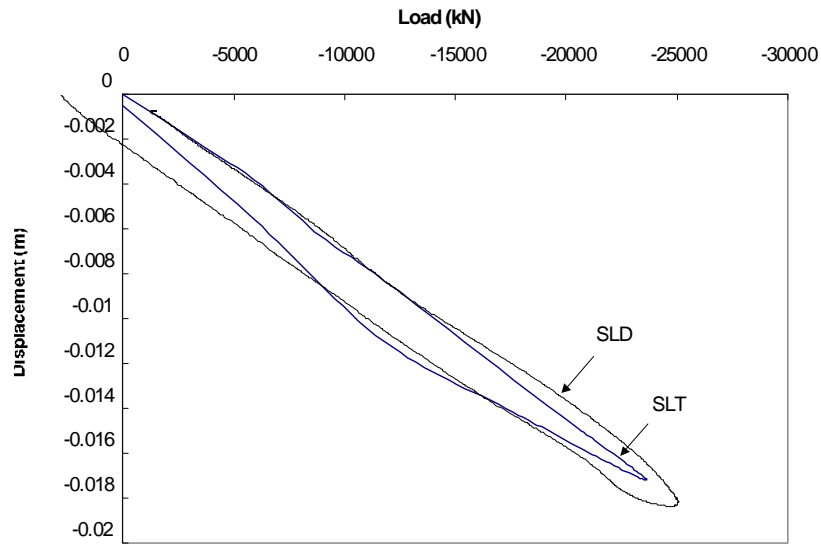


Figure 164. TFC-241 Pre

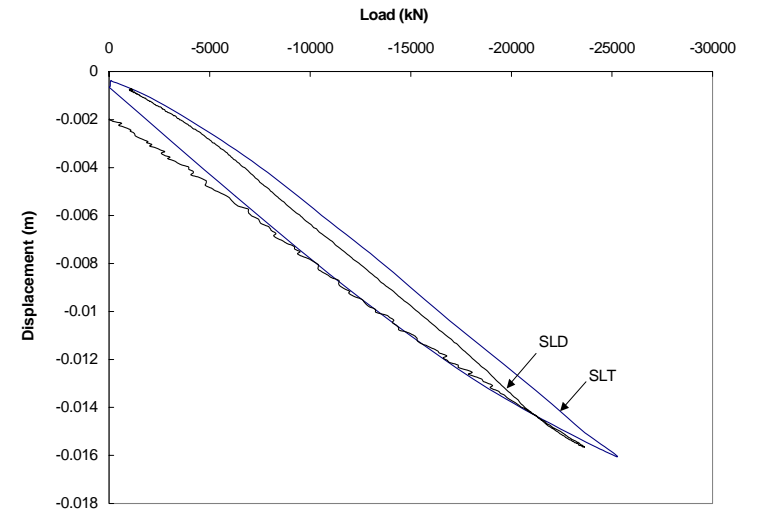


Figure 165. TFC-241 Post

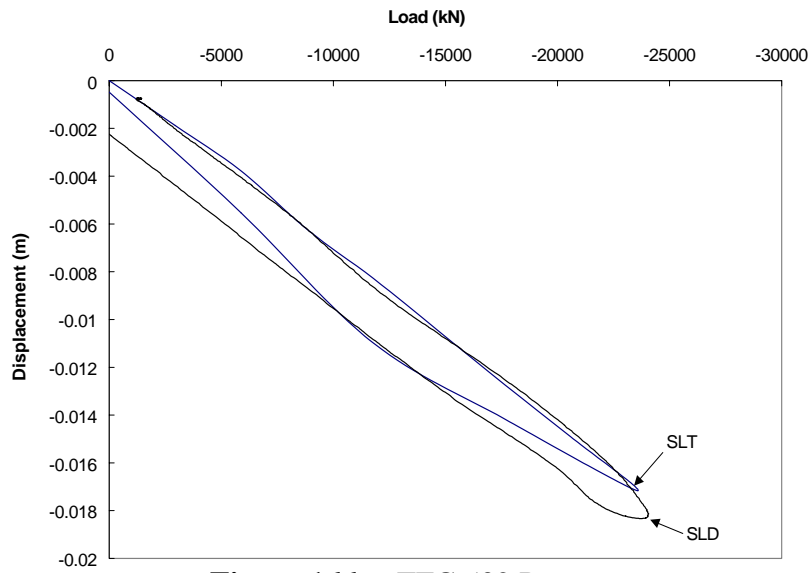


Figure 166. TFC 532 Pre

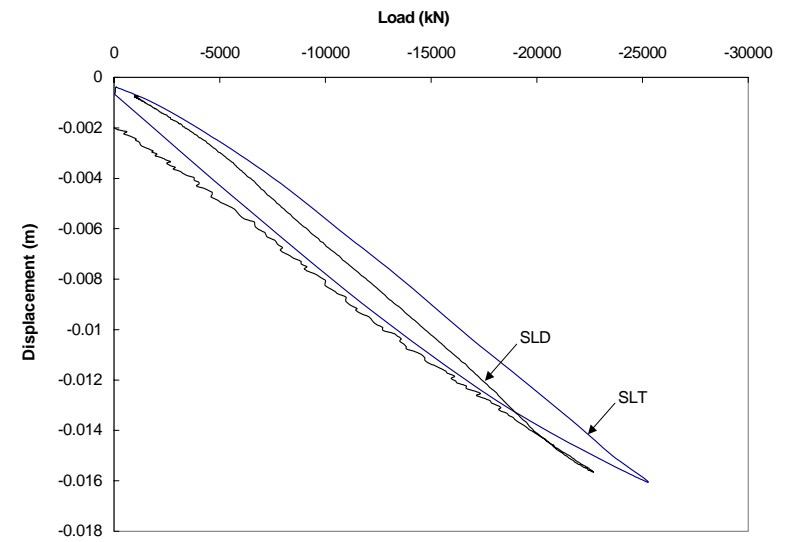


Figure 167. TFC 532 Post

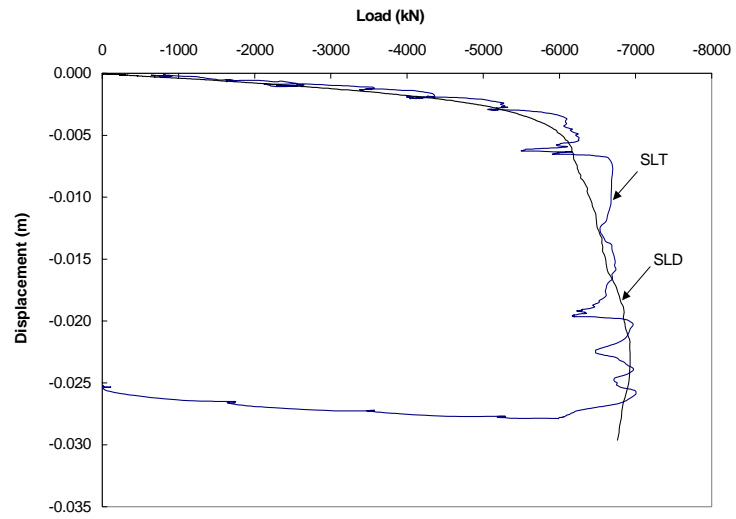


Figure 168. FLLS TP-1/2 Pre

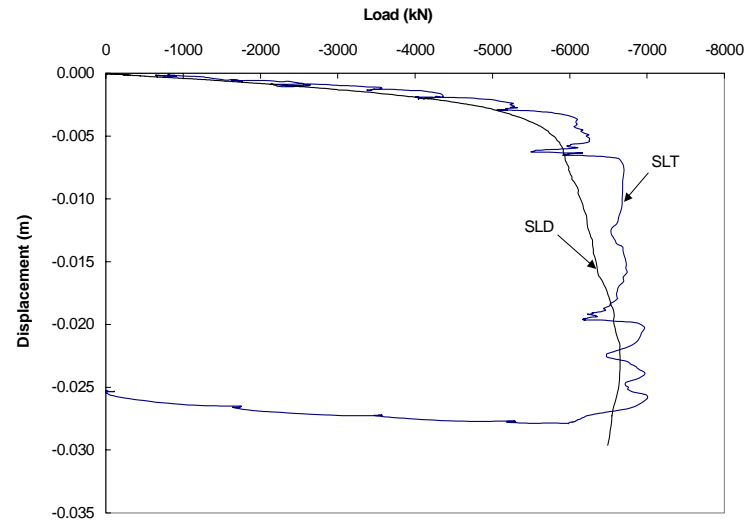


Figure 169. FLLS TP-1/2 Post

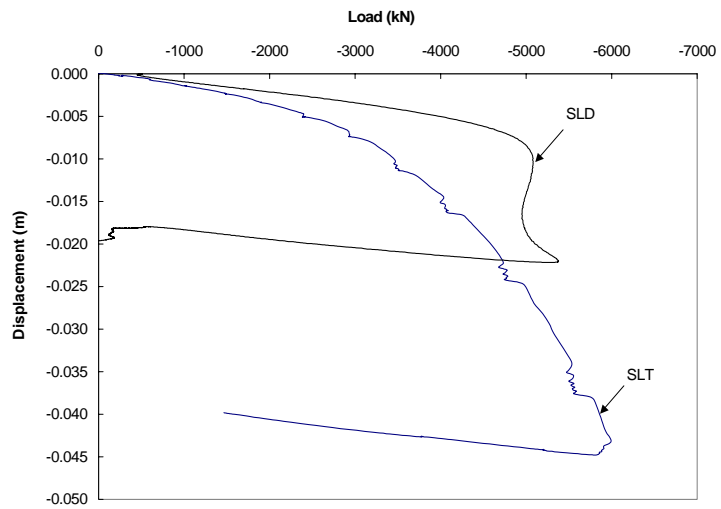


Figure 170. FLLS TP-3/4 Pre

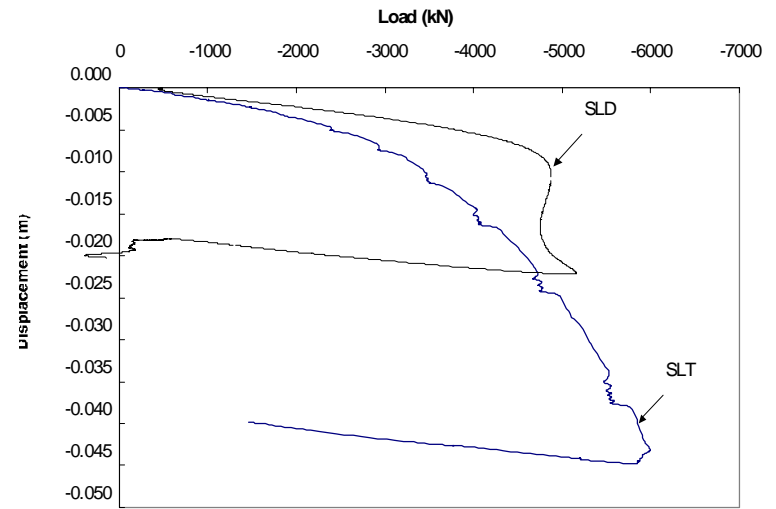


Figure 171. FLLS TP-3/4 Pre

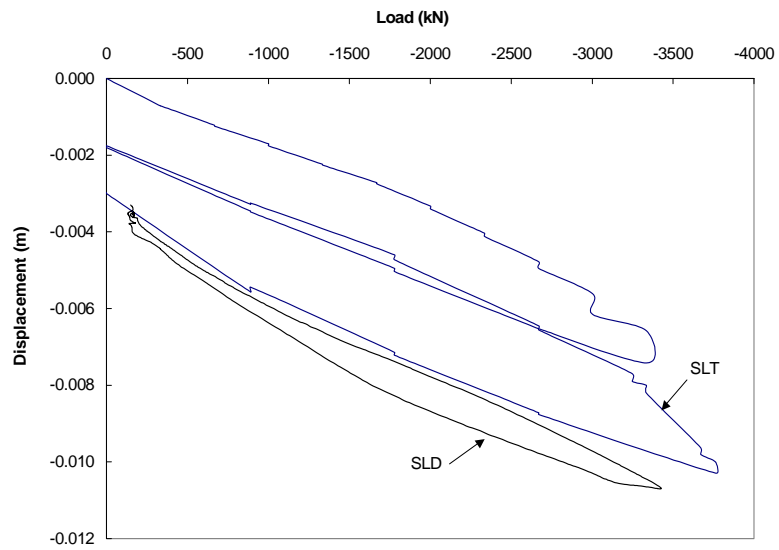


Figure 172. JFK OMSF P-10 Pre

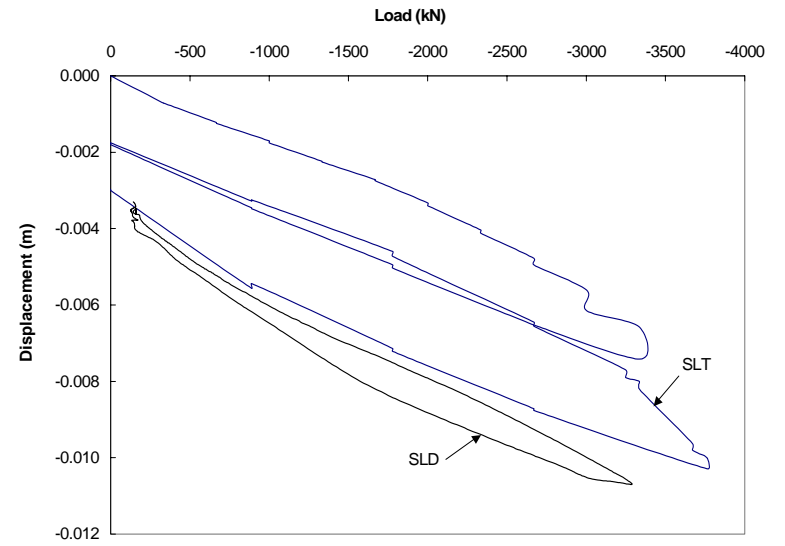


Figure 173. JFK OMSF P-10 Post

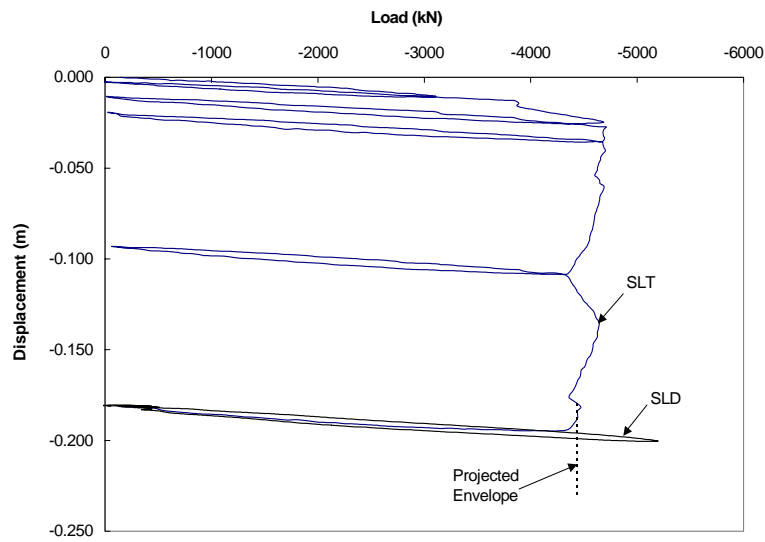


Figure 174. NNO T1 Pre

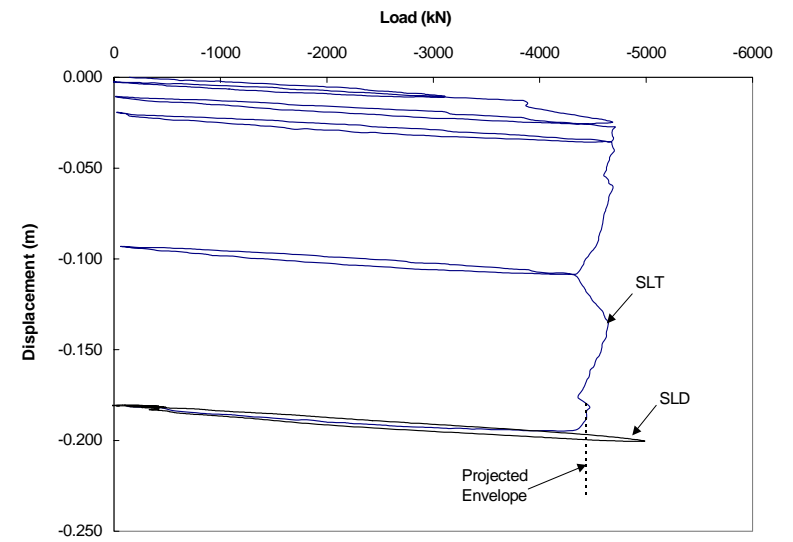


Figure 175. NNO T1 Post

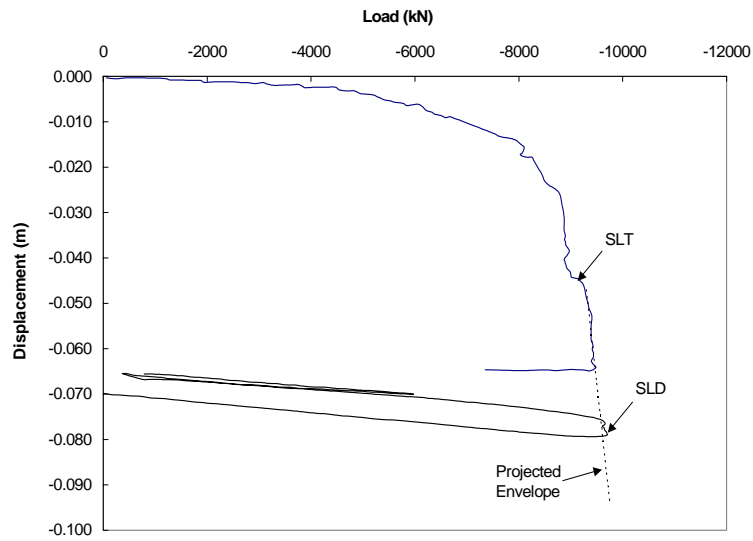


Figure 176. STG LT-1 Pre

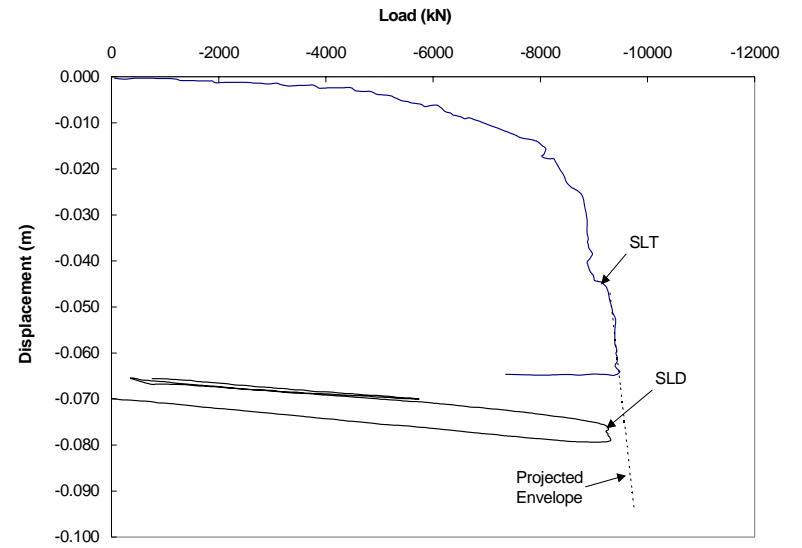


Figure 177. STG LT-1 Post

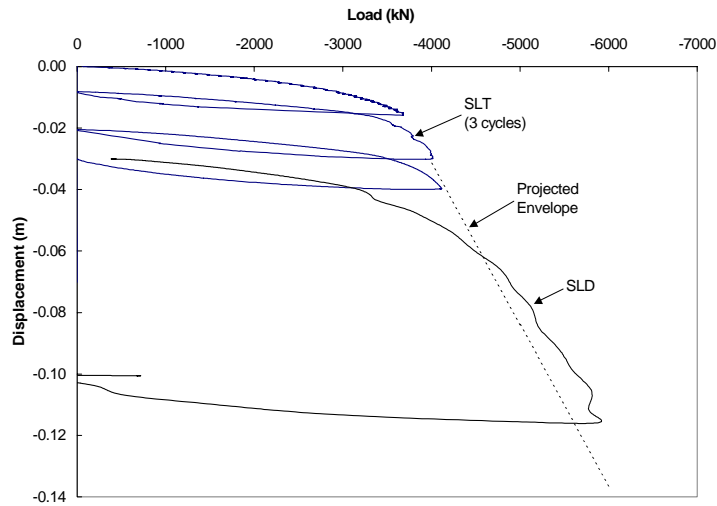


Figure 178. BC Pier 15 Pre

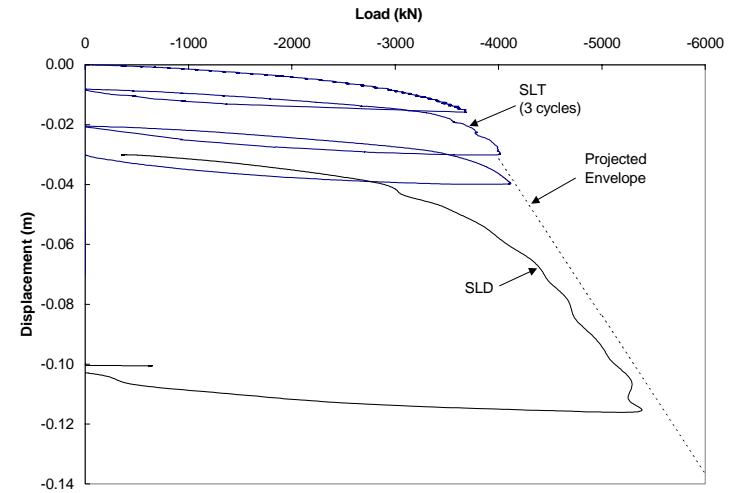


Figure 179. BC Pier 15 Post

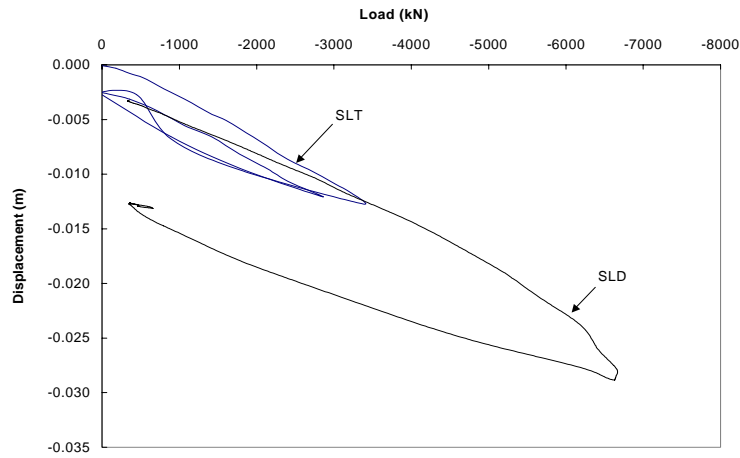


Figure 180. BC Pier 10 Pre

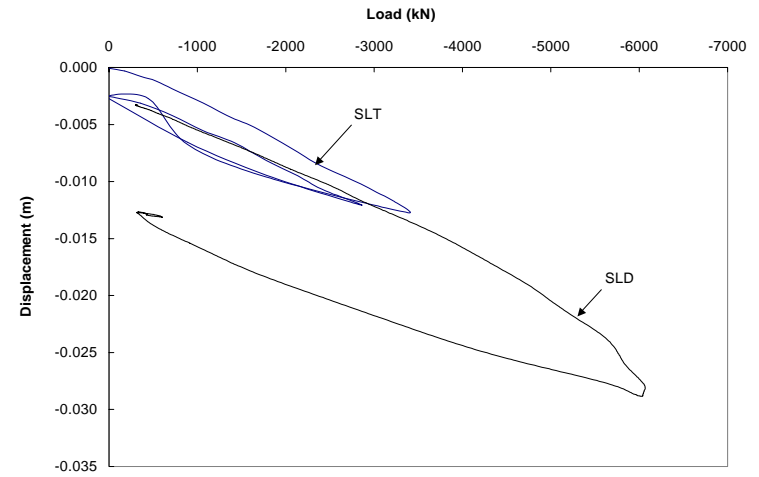


Figure 181. BC Pier 10 Post

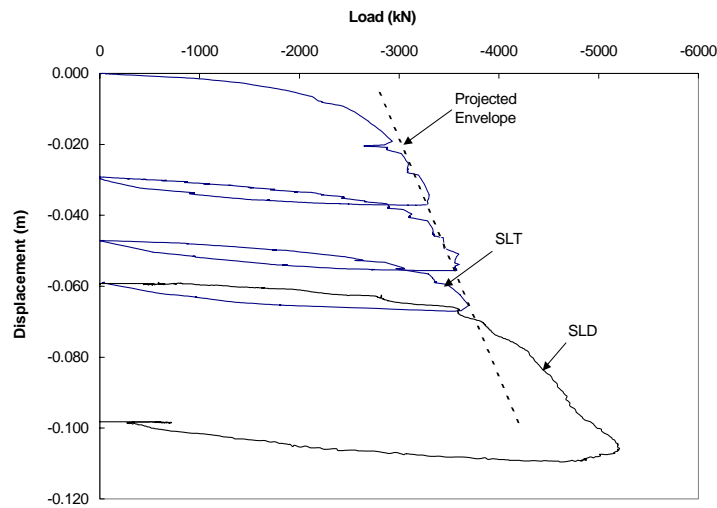


Figure 182. BC Pier 5 Pre

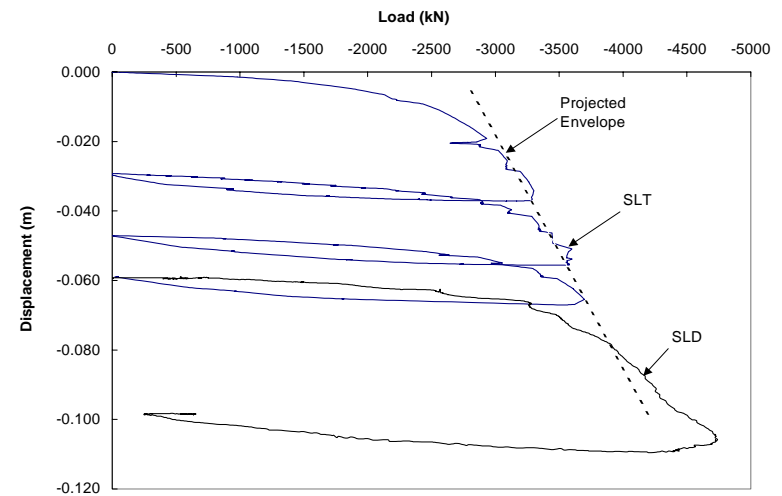


Figure 183. BC Pier 5 Post

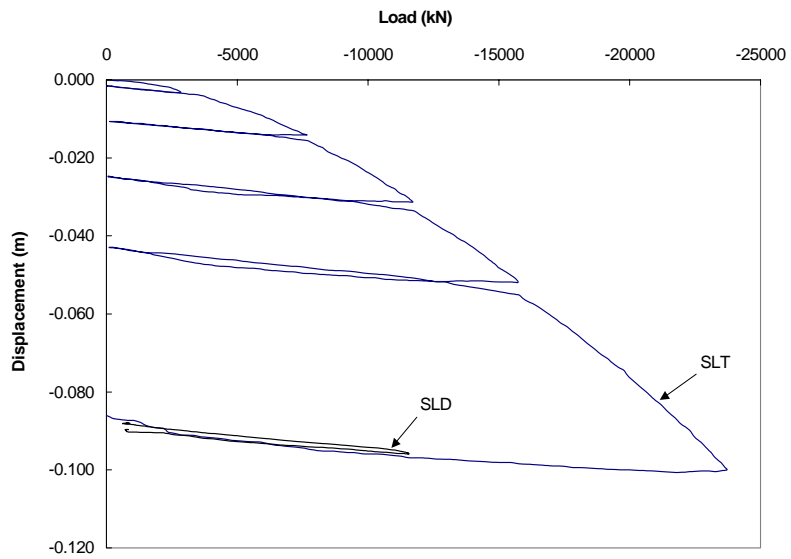


Figure 184. Ohito TEST Pre

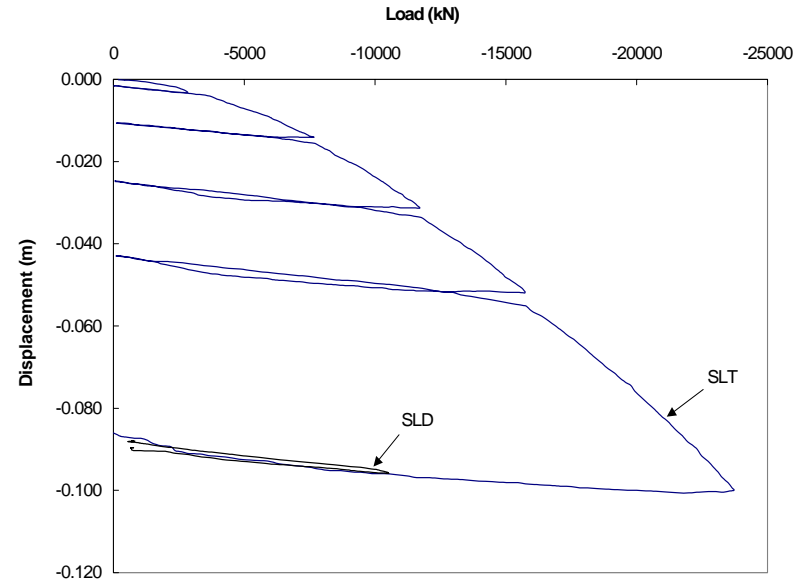


Figure 185. Ohito TEST Post

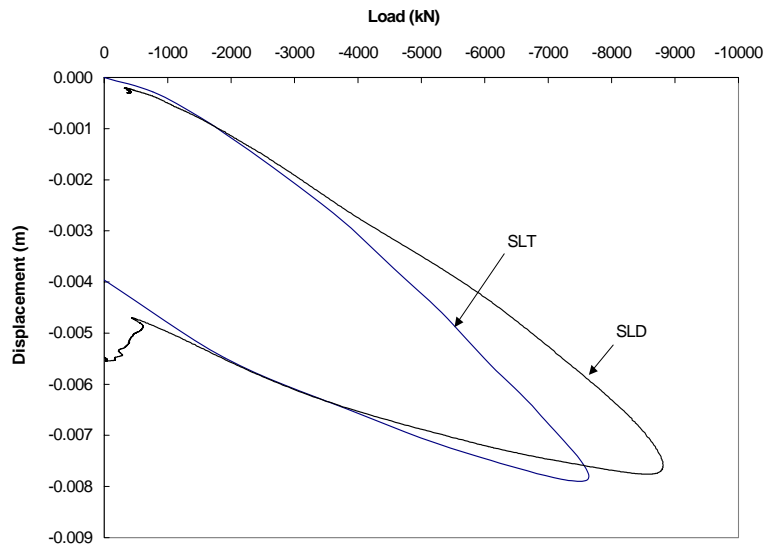


Figure 186. BQE SA 1&8 Pre

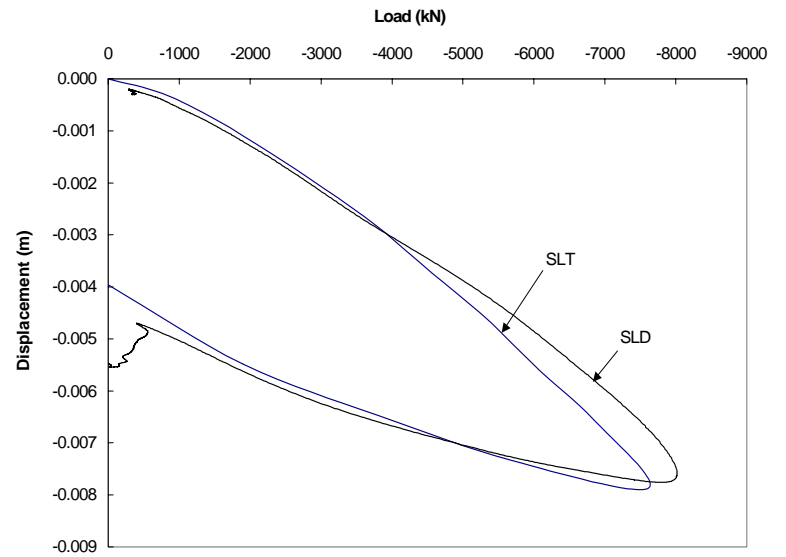


Figure 187. BQE SA 1&* Post

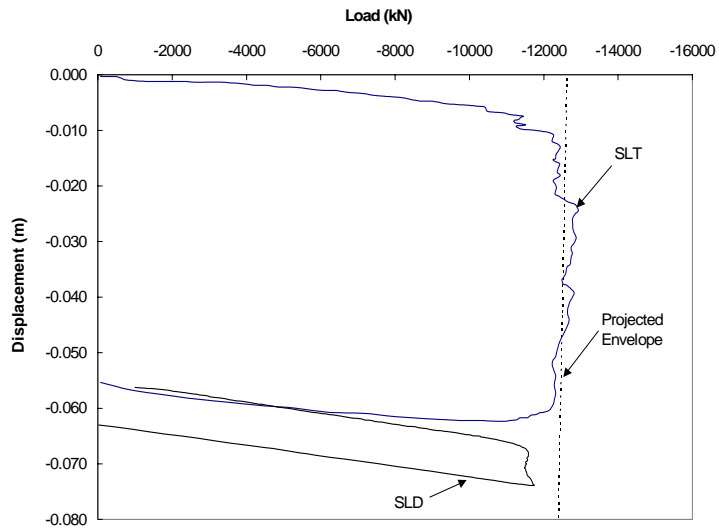


Figure 188. STG LT-5 Pre

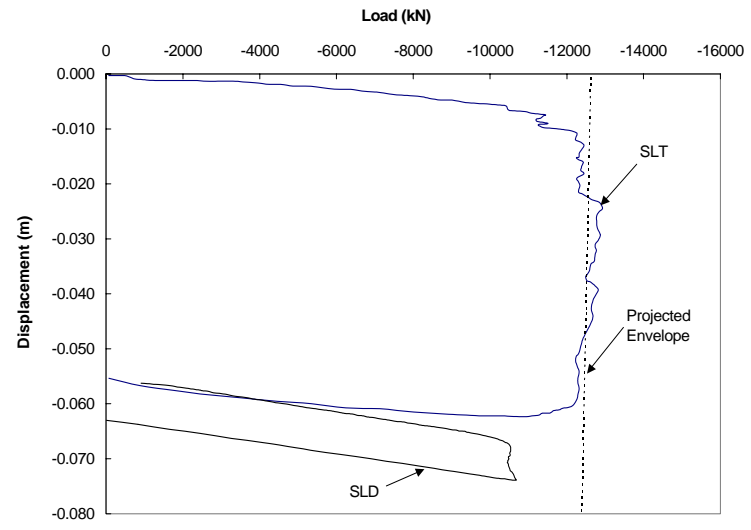


Figure 189. STG LT-5 Post

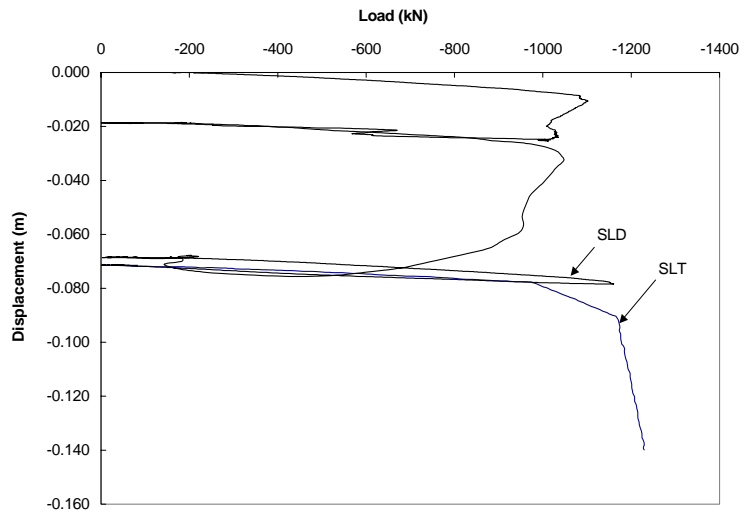


Figure 190. SHONAN T6 Pre

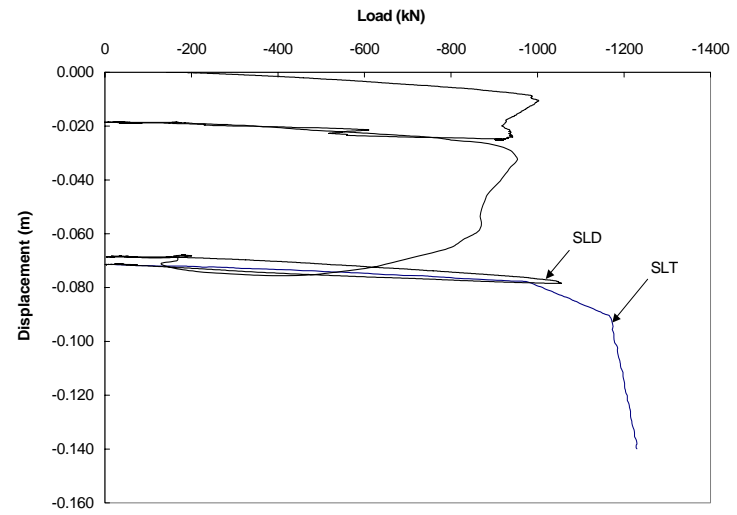


Figure 191. SHONAN T6 Post

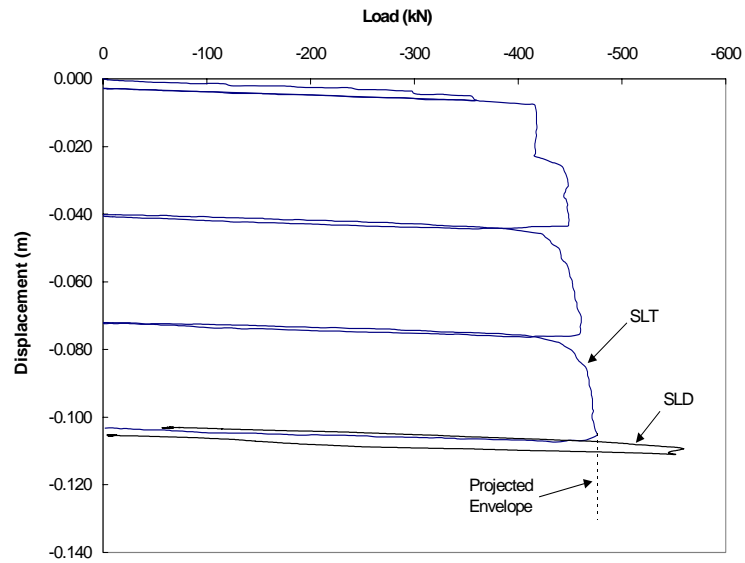


Figure 192. SHONAN T5 Pre

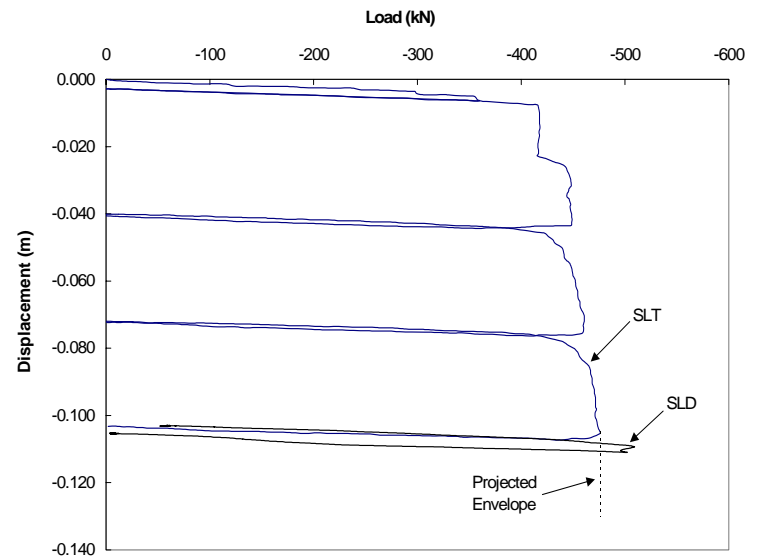


Figure 193. SHONAN T5 Post

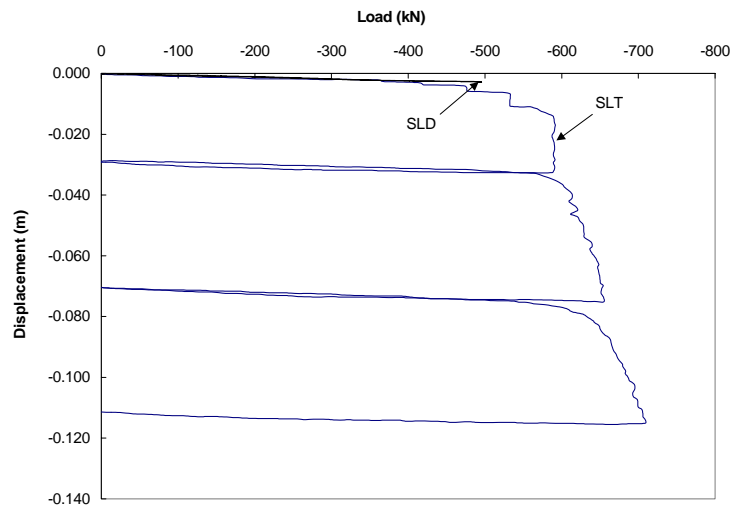


Figure 194. SHONAN T2 Pre

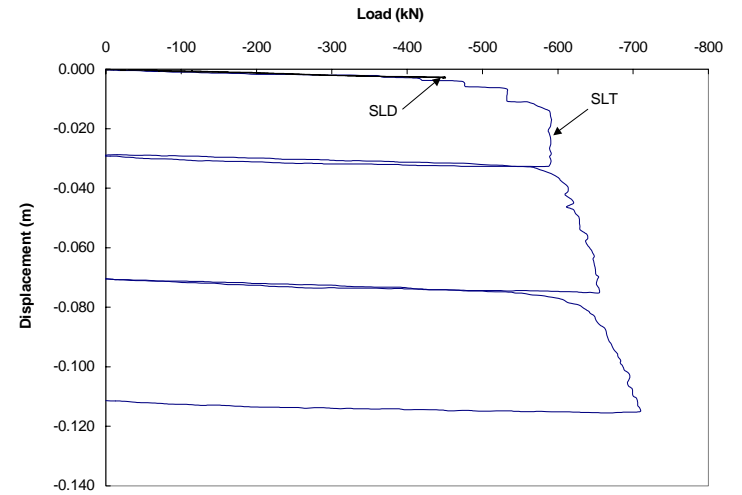


Figure 195. SHONAN T2 Post

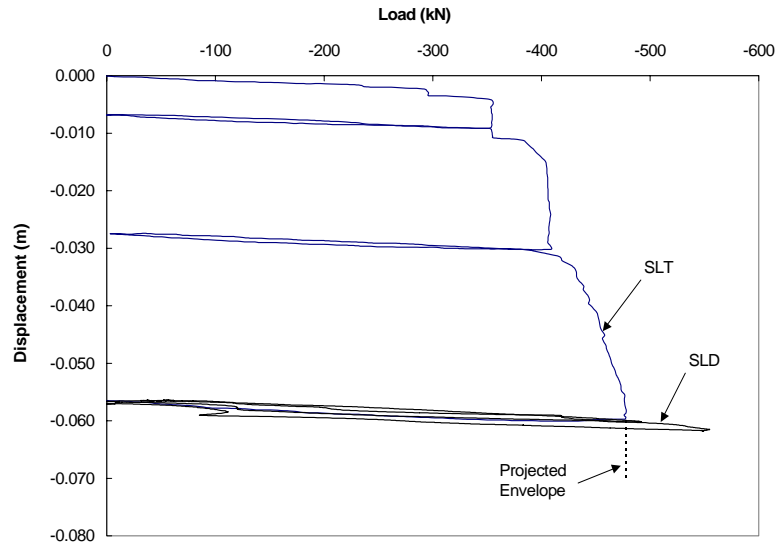


Figure 196. SHONAN T2 Post

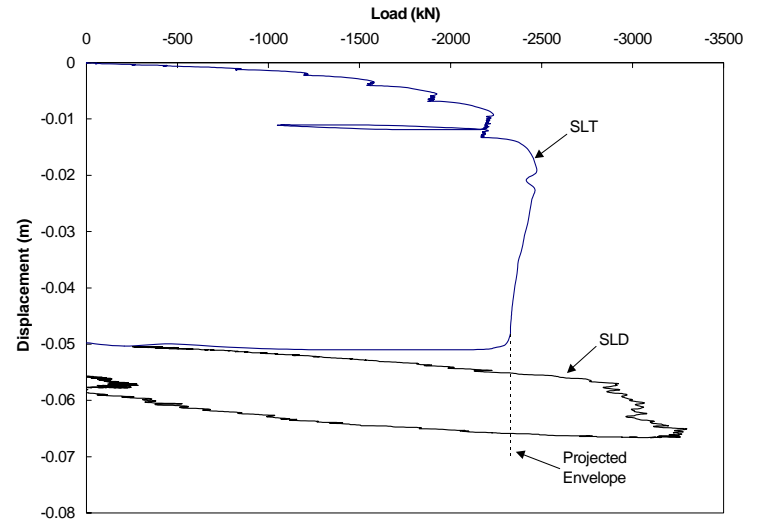


Figure 197. SHONAN T1 Post

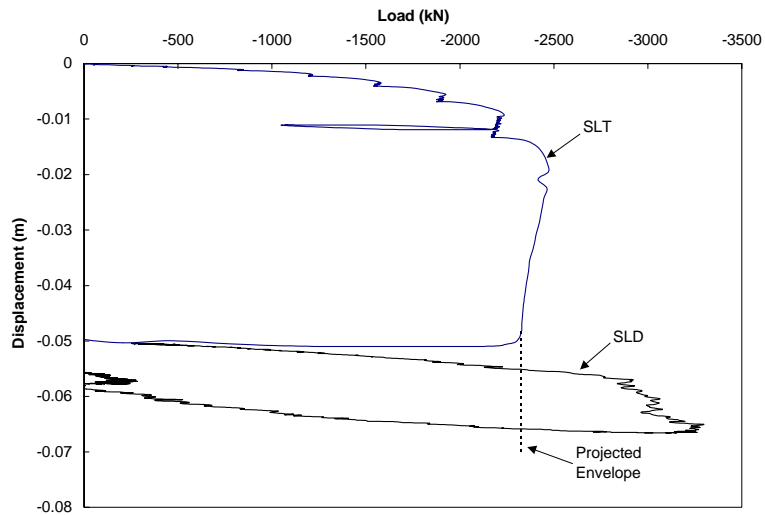


Figure 198. Aub 1 Pre

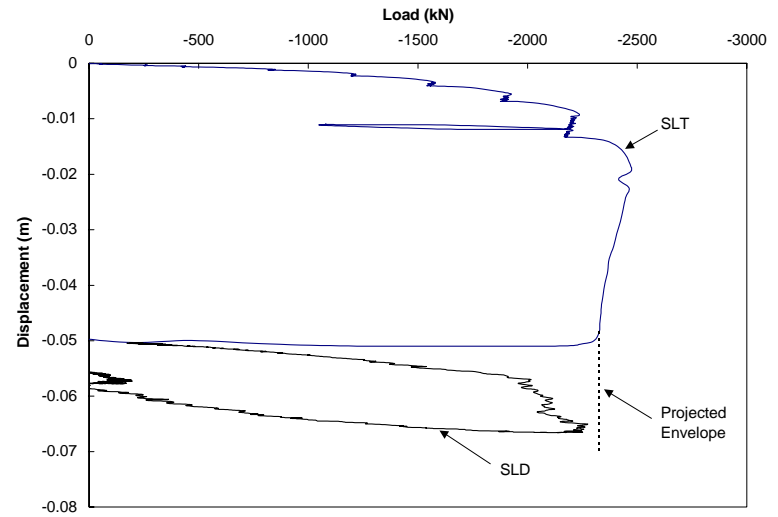


Figure 199. Aub 1 Post

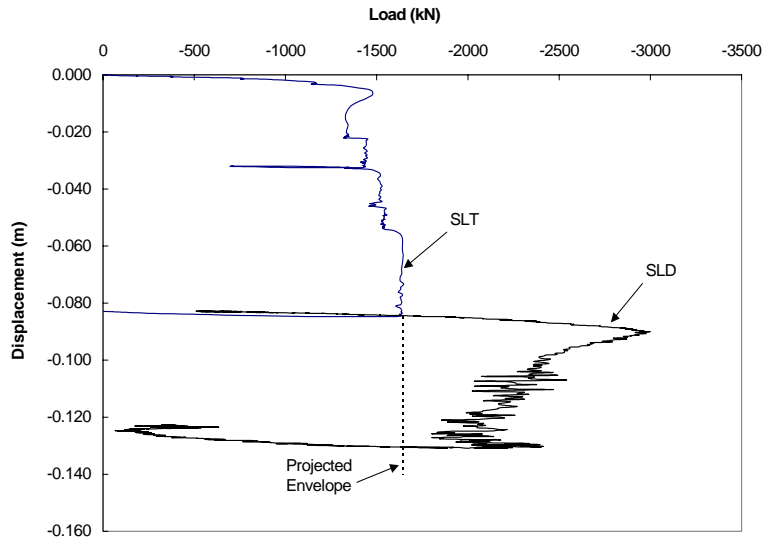


Figure 200. Aub 10 Pre

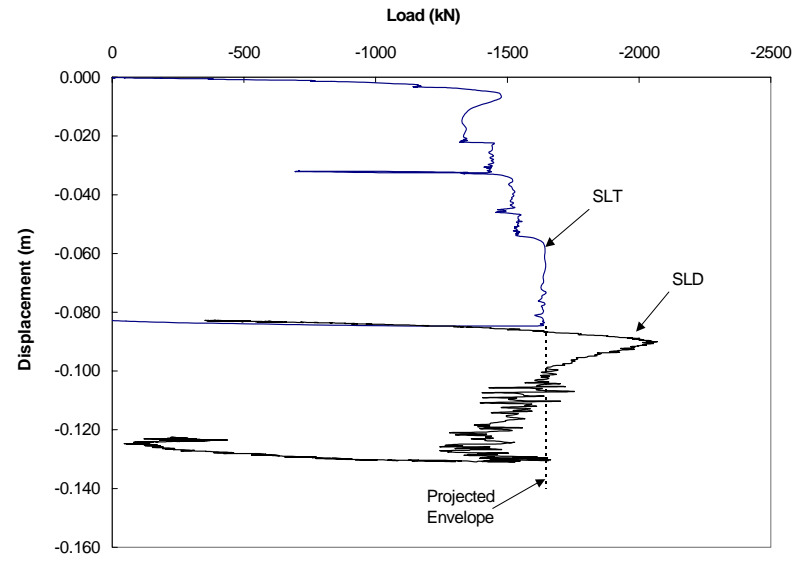


Figure 201. Aub 10 {pst}

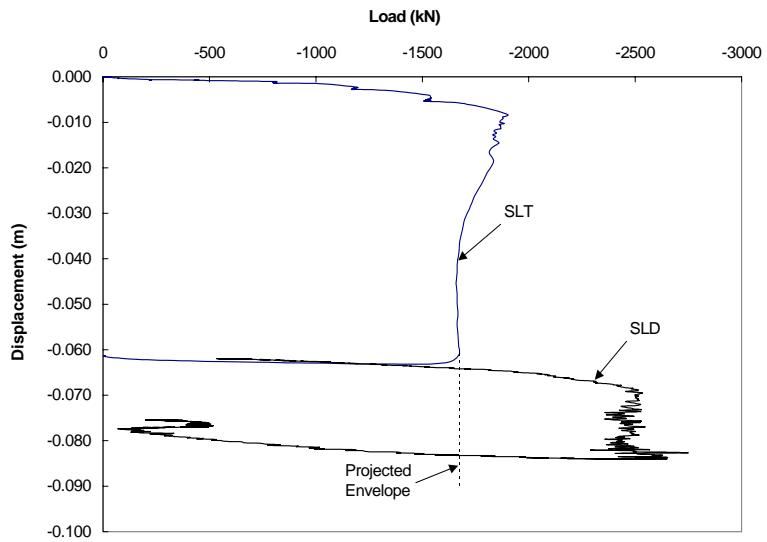


Figure 202. Aub 8 Pre

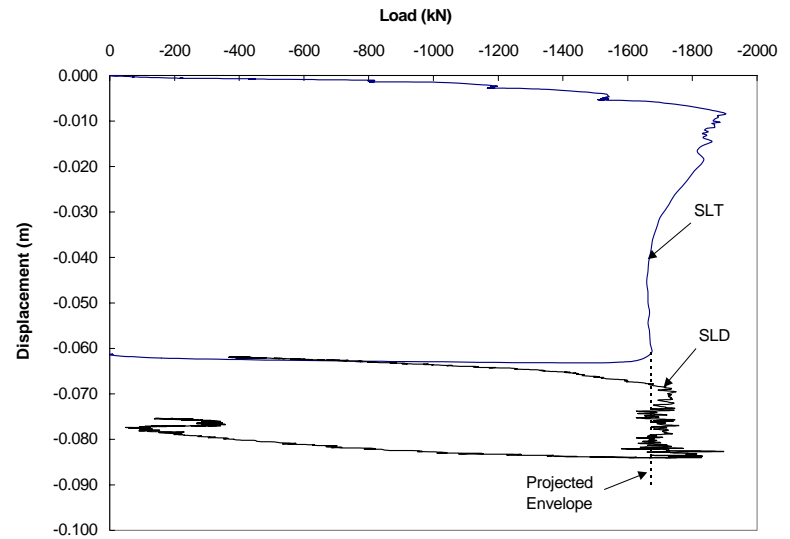


Figure 203. Aub 8 Post

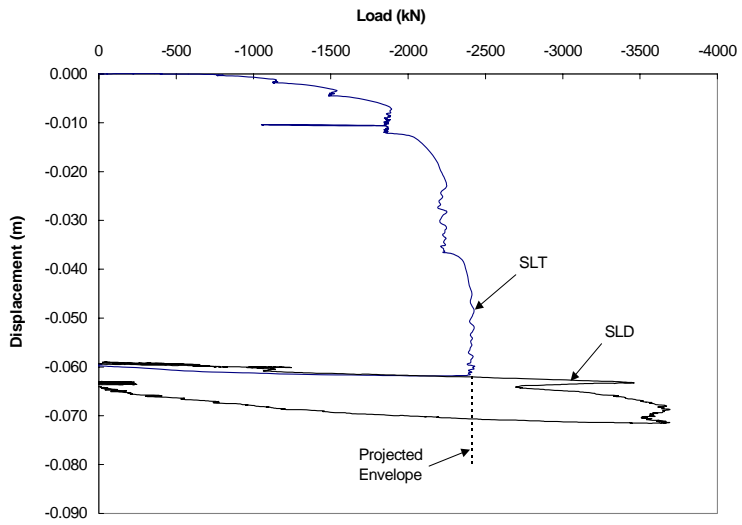


Figure 204. Aub 7 Pre

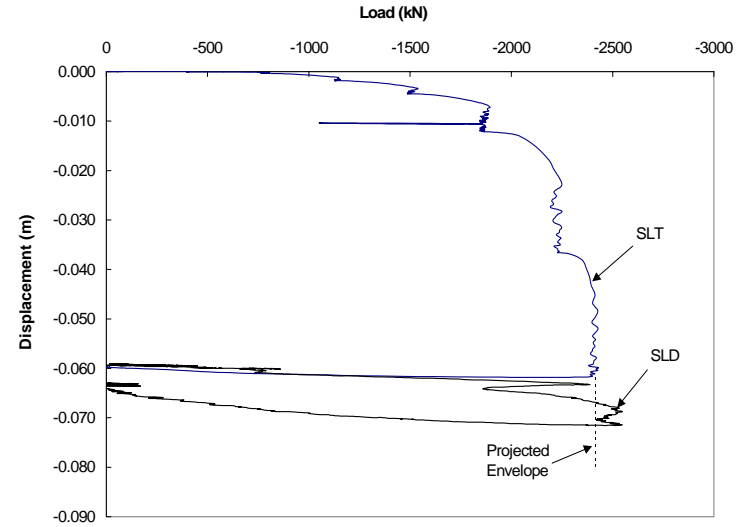


Figure 205. Aub 7 Post

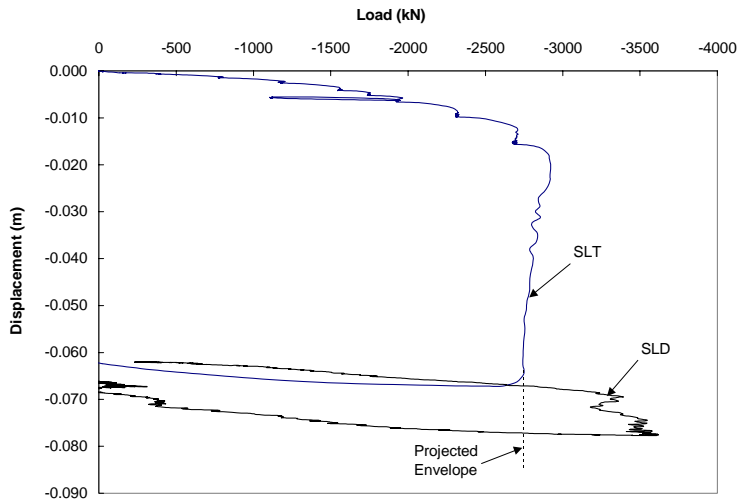


Figure 206. Aub 5 Pre

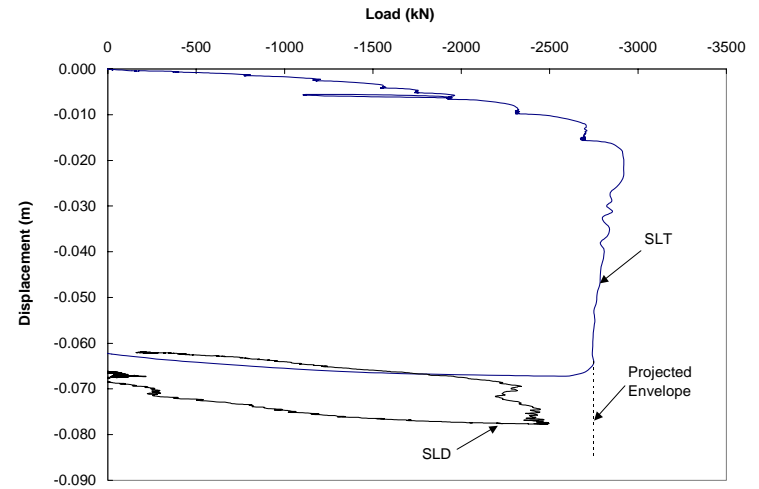


Figure 207. Aub 5 Post

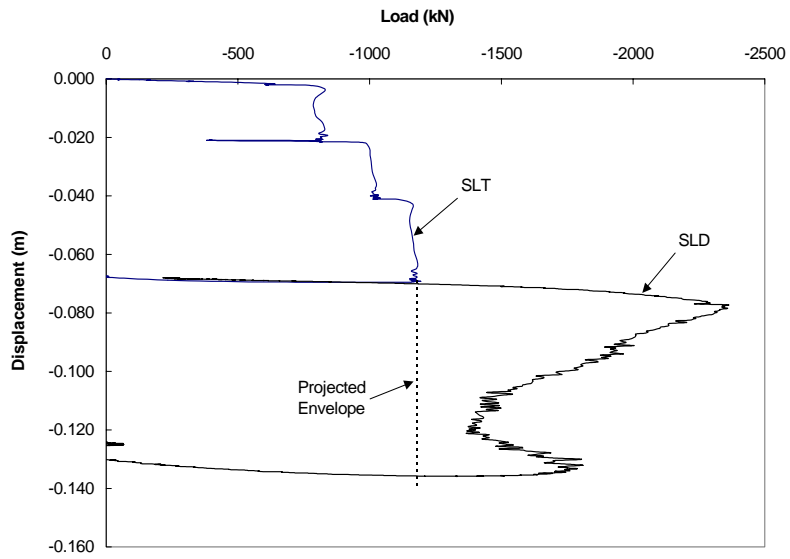


Figure 208. Aub 3 Pre

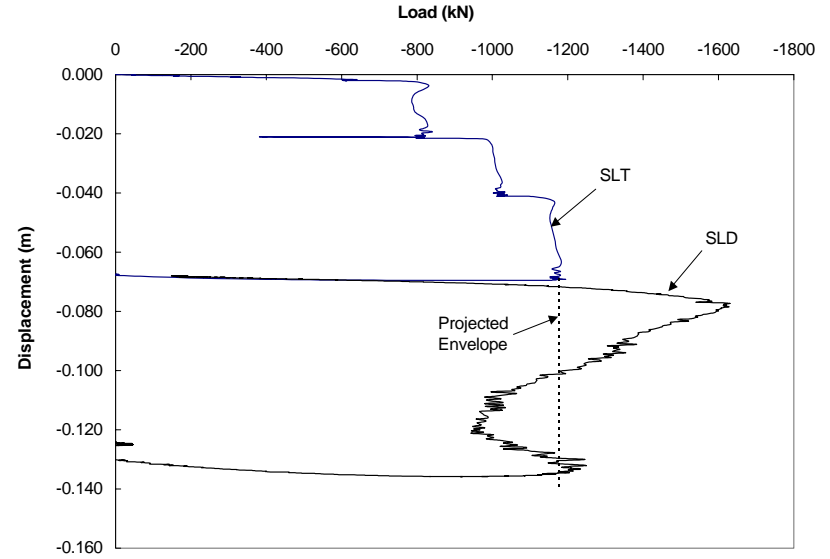


Figure 209. Aub 3 Post

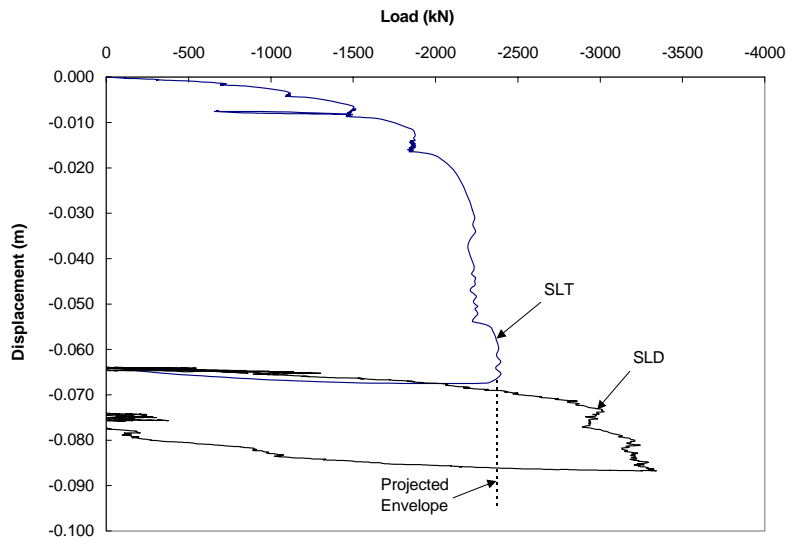


Figure 210. Aub 2 Pre

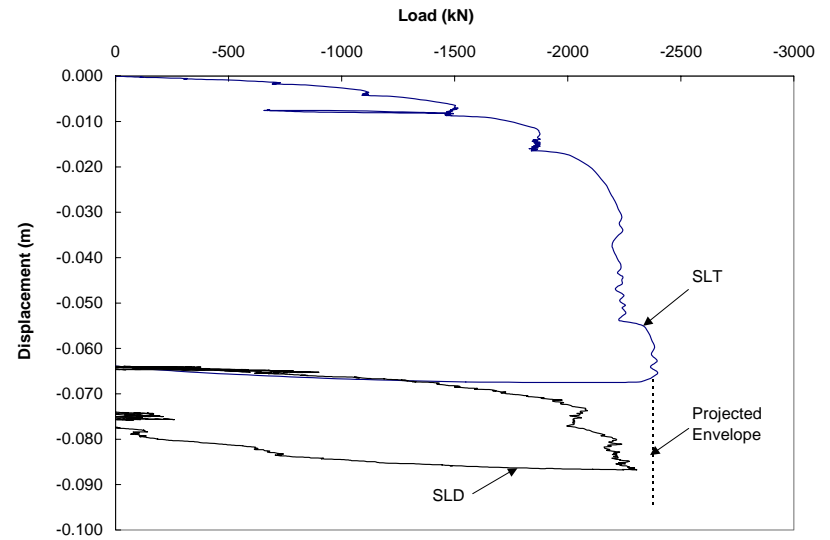


Figure 211. Aub 2 Post

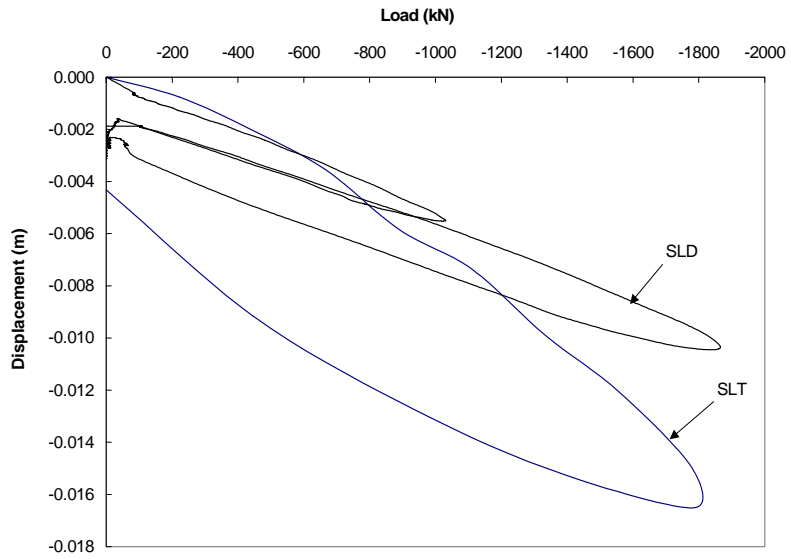


Figure 212. NIA TP-1&2a Pre

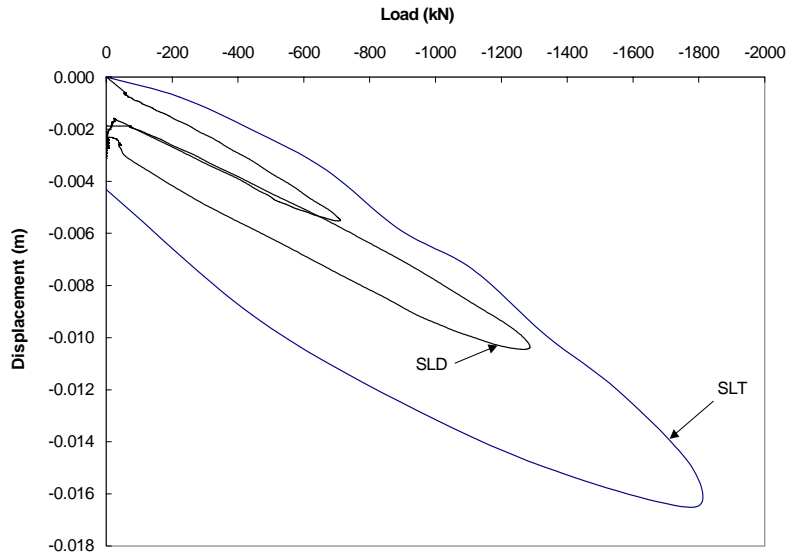


Figure 213. NIA TP-1&2a Post

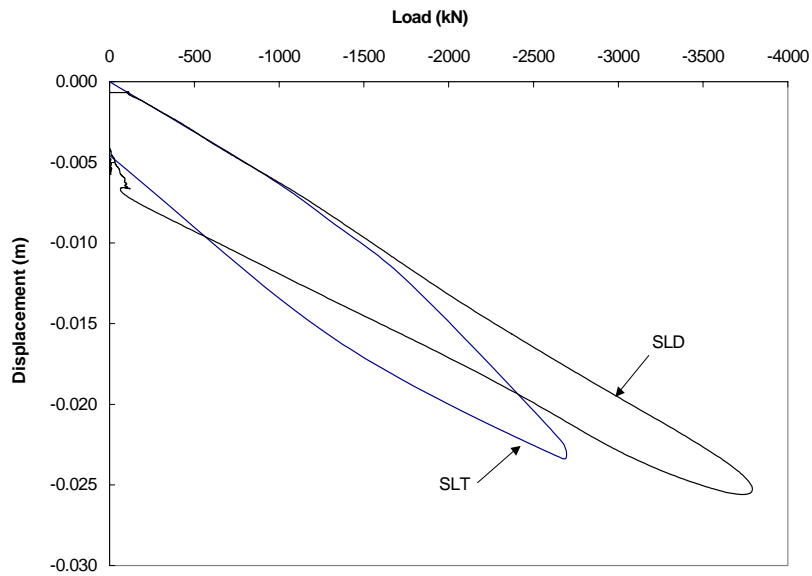


Figure 214. NIA TP-1&2b Pre

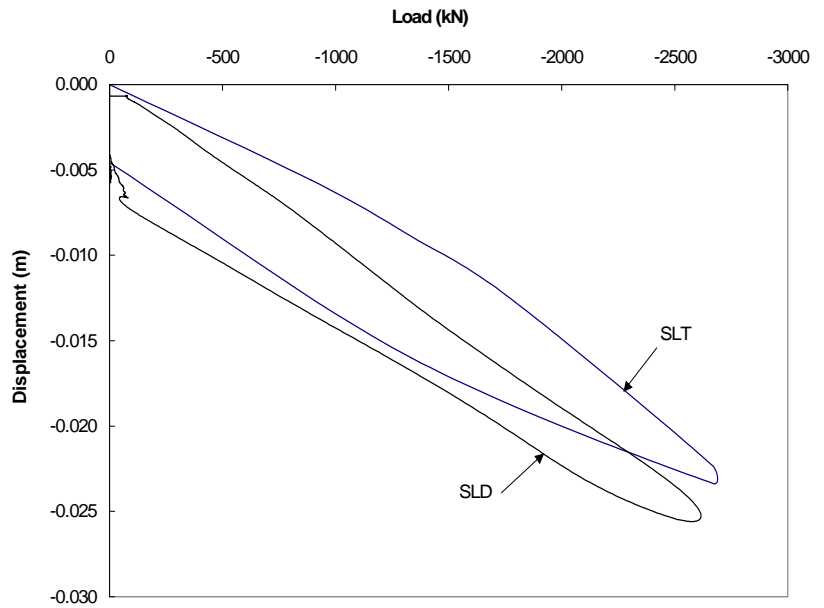


Figure 215. NIA TP-1&2b Post

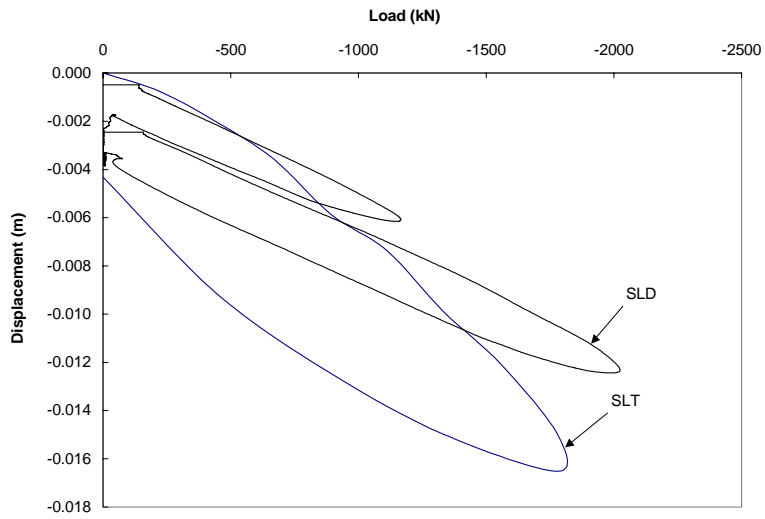


Figure 216. NIA TP -1&3a Pre

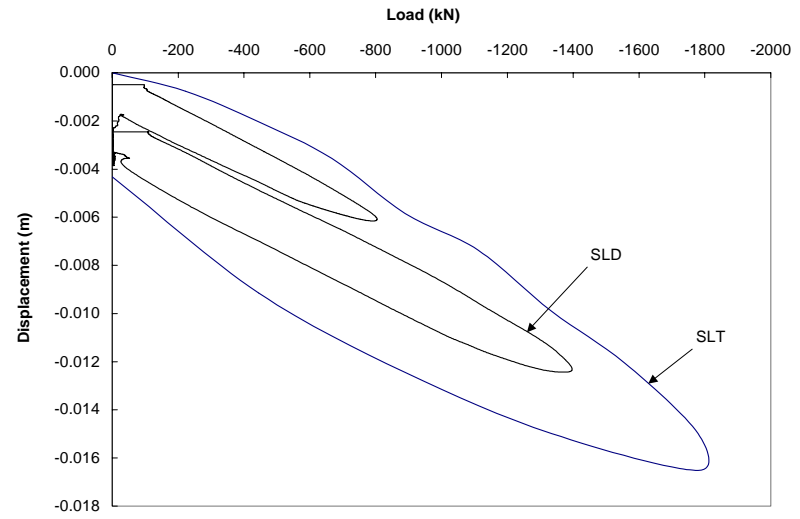


Figure 217. NIA TP-1&3a Post

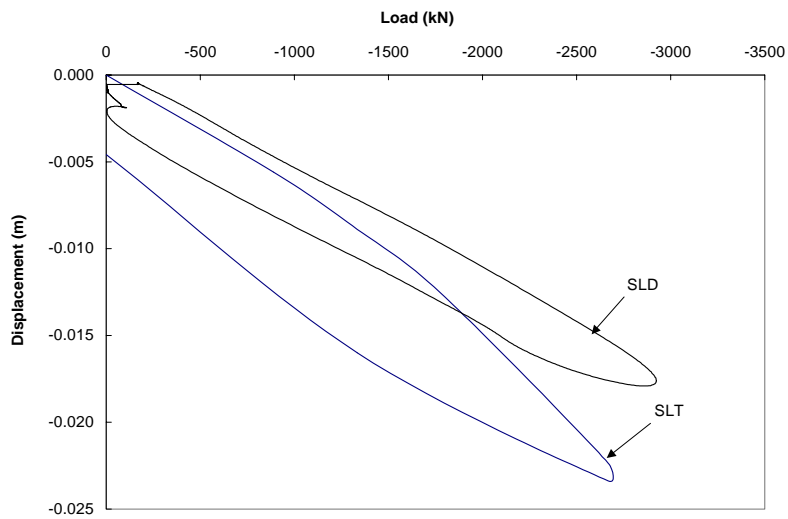


Figure 218. NIA TP -1&3b Pre

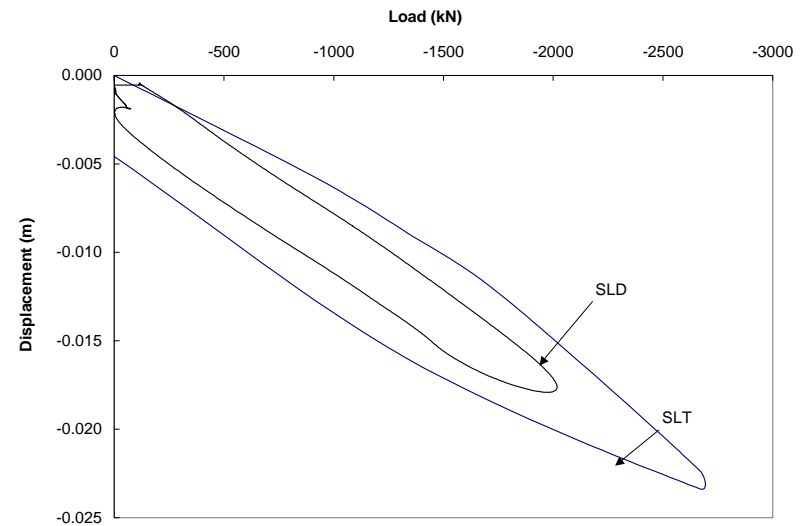


Figure 219. NIA TP-1&3b Post

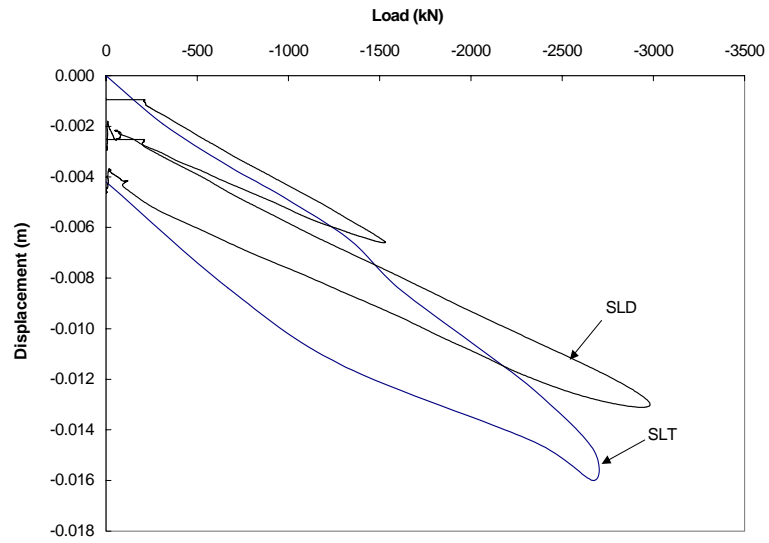


Figure 220. NIA TP-9&10a Pre

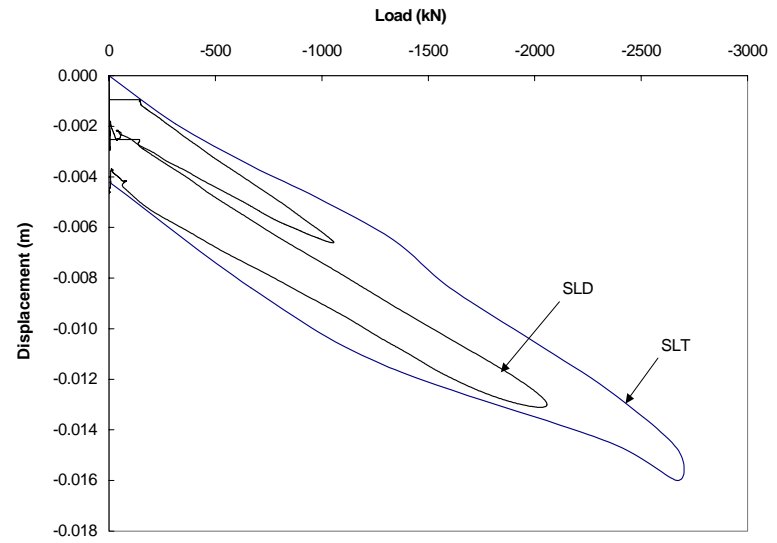


Figure 221. NIA TP-9&10a Post

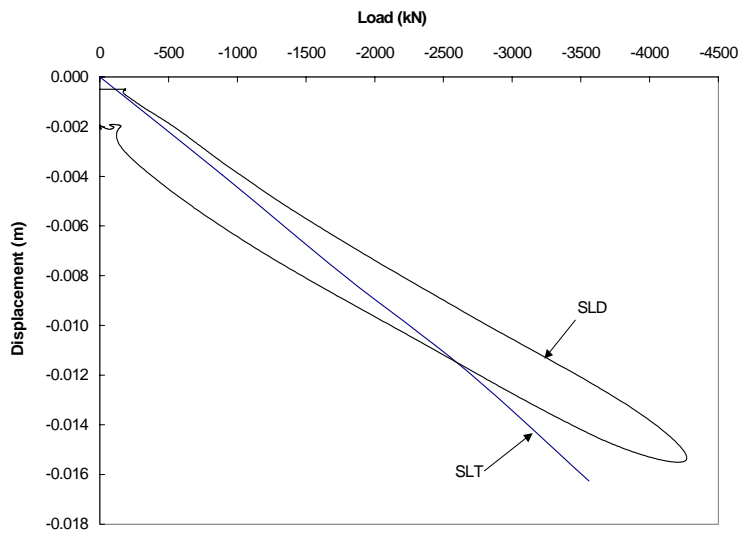


Figure 222. NIA TP-9&10b Pre

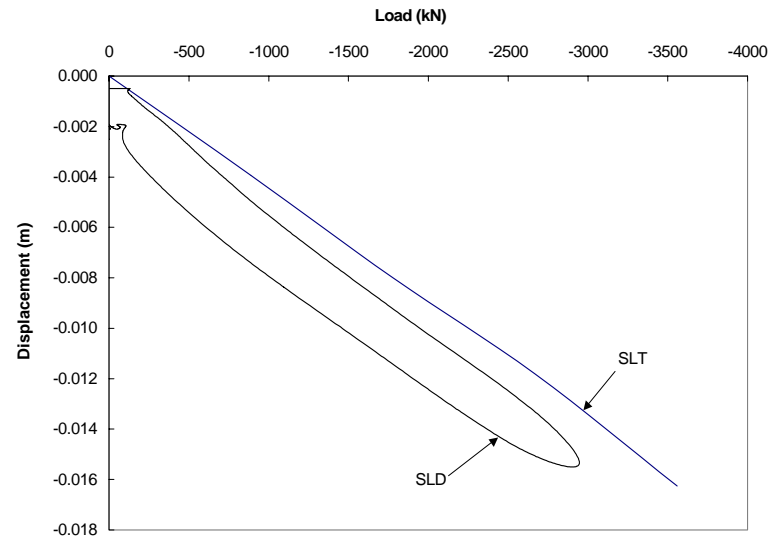


Figure 223. NIA TP-9&10a Post

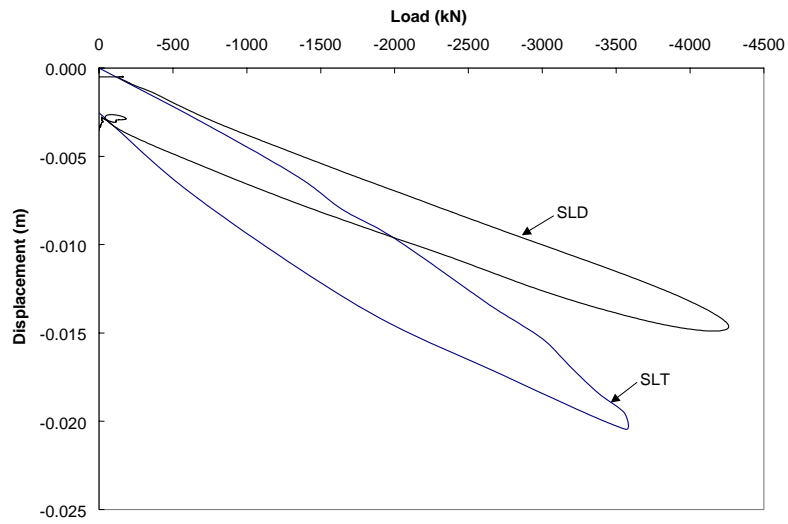


Figure 224. NIA TP-5&6b Pre

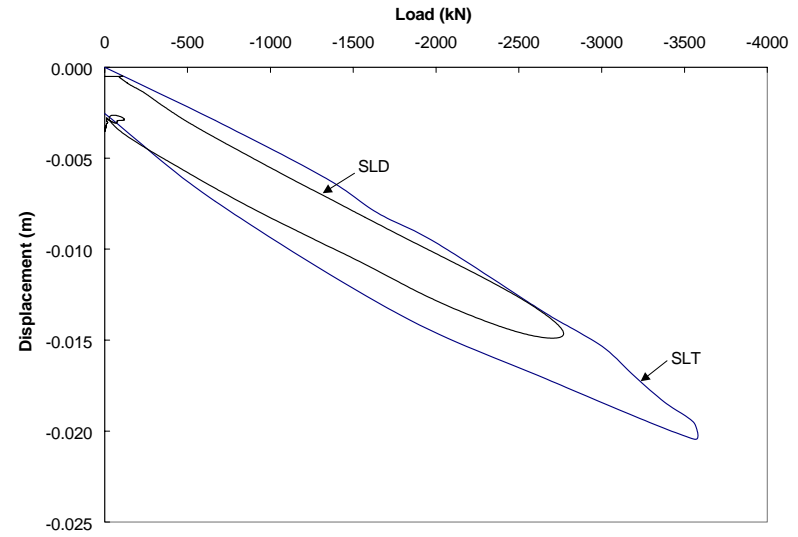


Figure 225. NIA TP 5&6b Post

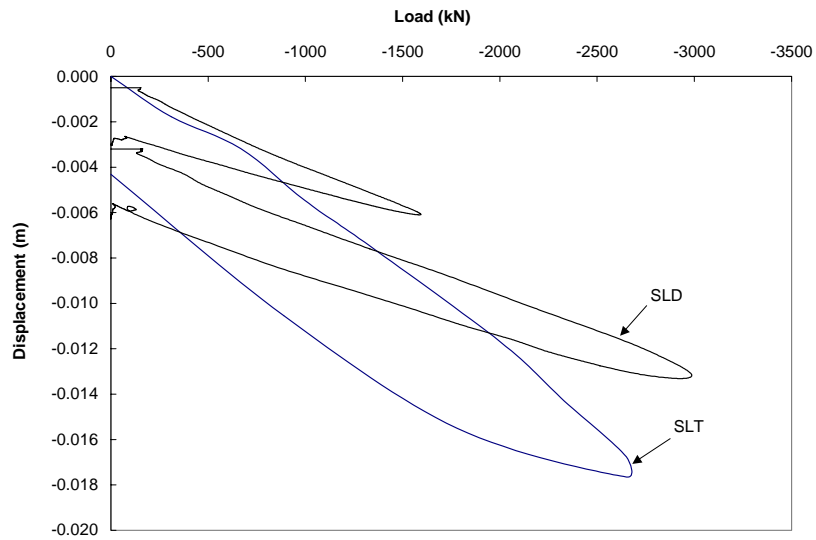


Figure 226. NIA TP-5&6a Pre

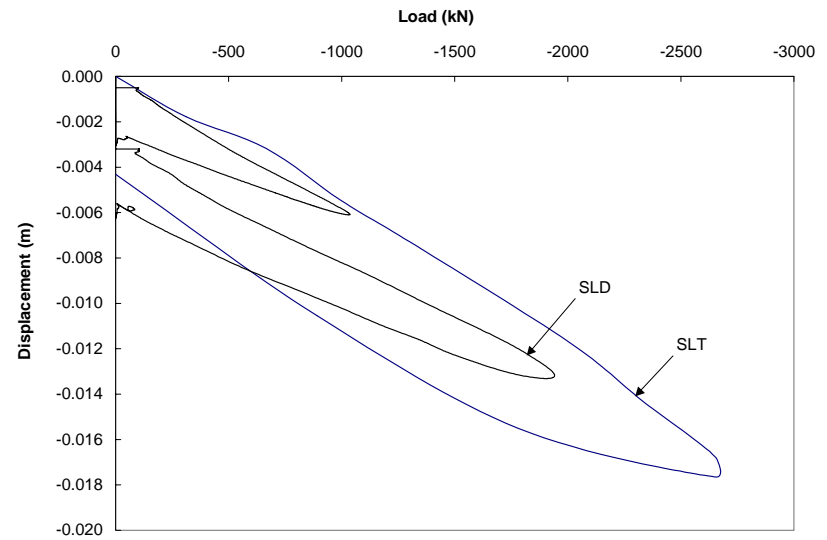


Figure 227. NIA TP 5&6a Post

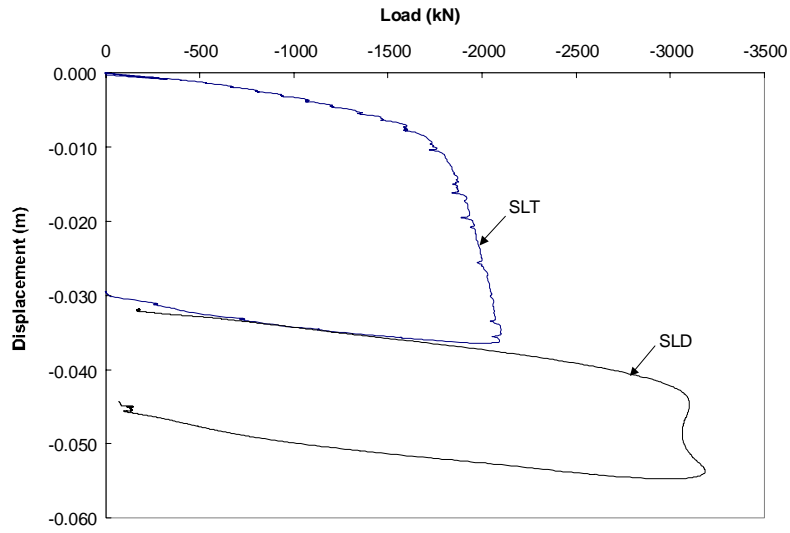


Figure 228. LC T-114.5 Pre

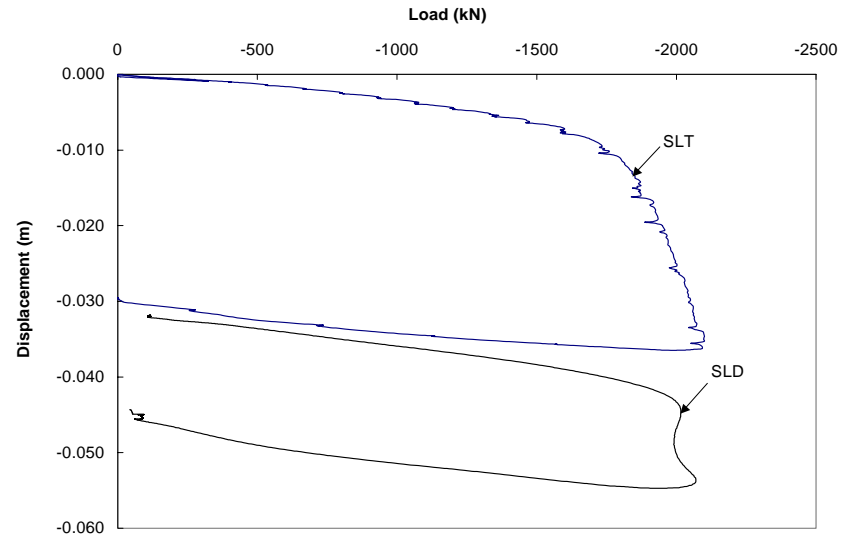


Figure 229. LC T-114.5 Post

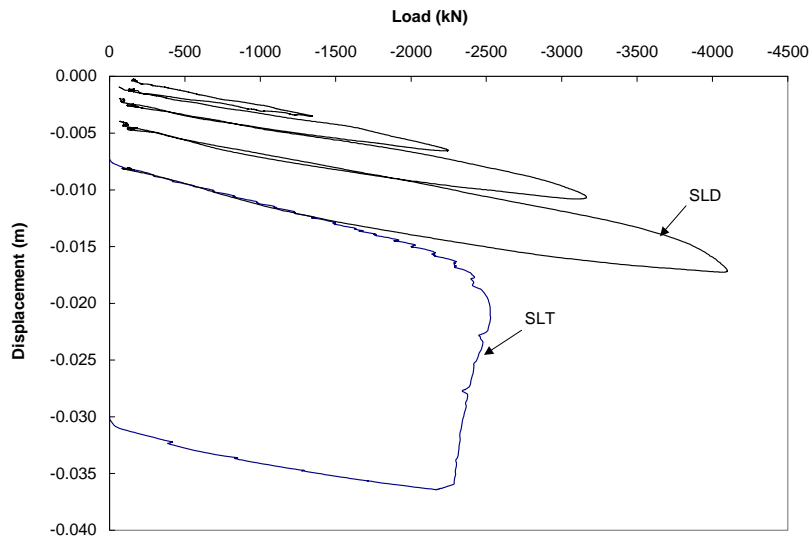


Figure 230. LC X-123 Pre

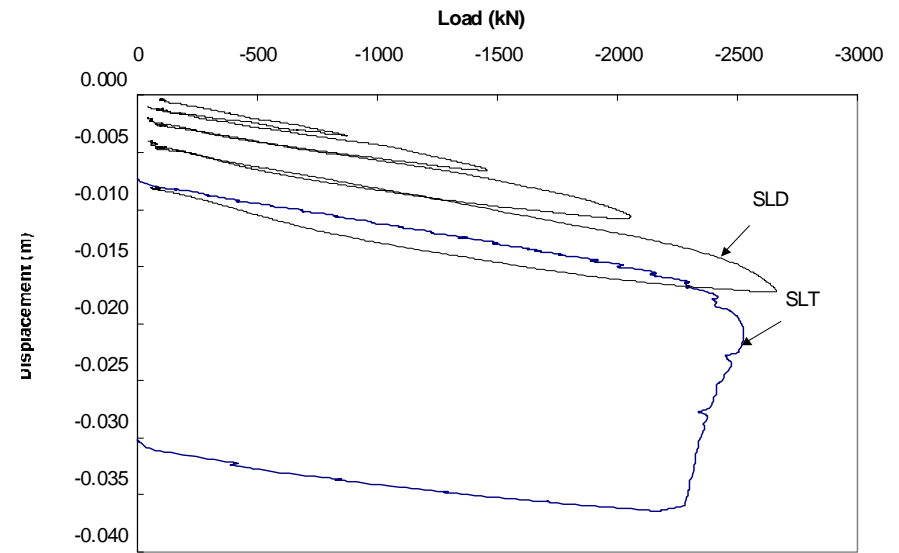


Figure 231. LC X-11123 Post

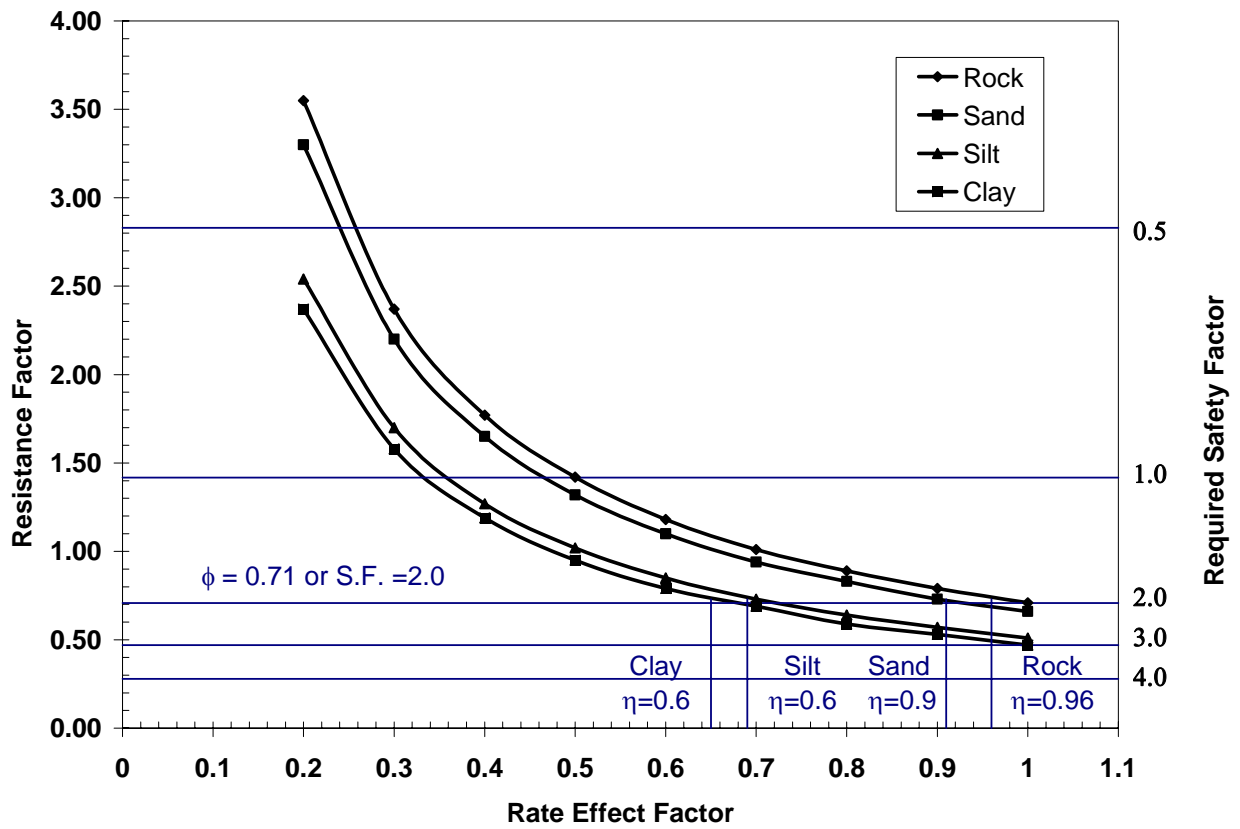


Figure 232. Safety and Resistance Factors vs. Rate Effect Factor

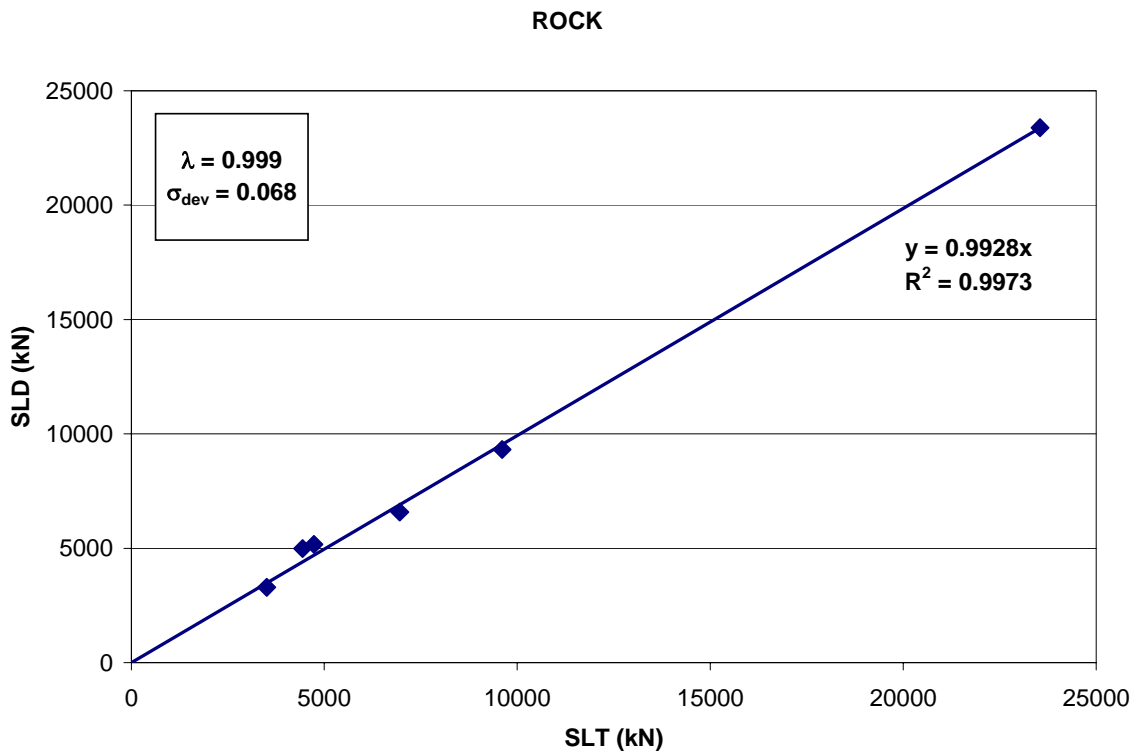


Figure 233. Predicted (SLD) vs. actual (SLT) for rock

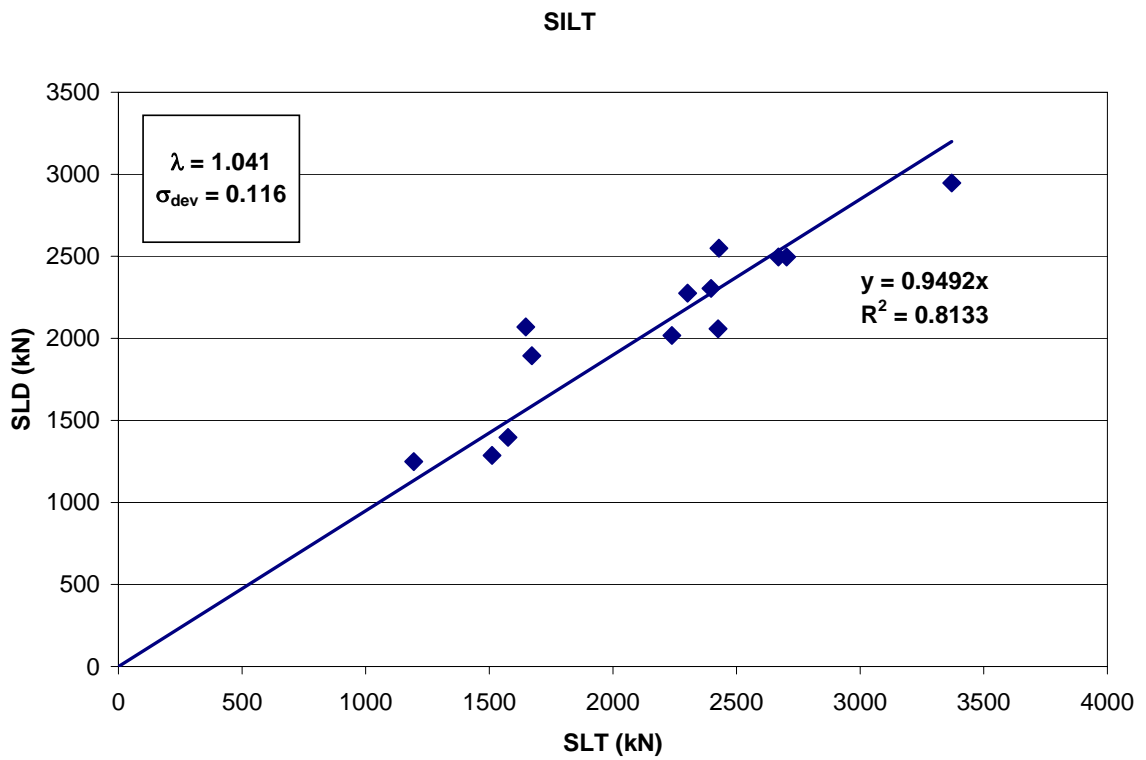


Figure 234 Predicted (SLD) vs. Actual (SLT) for Silt

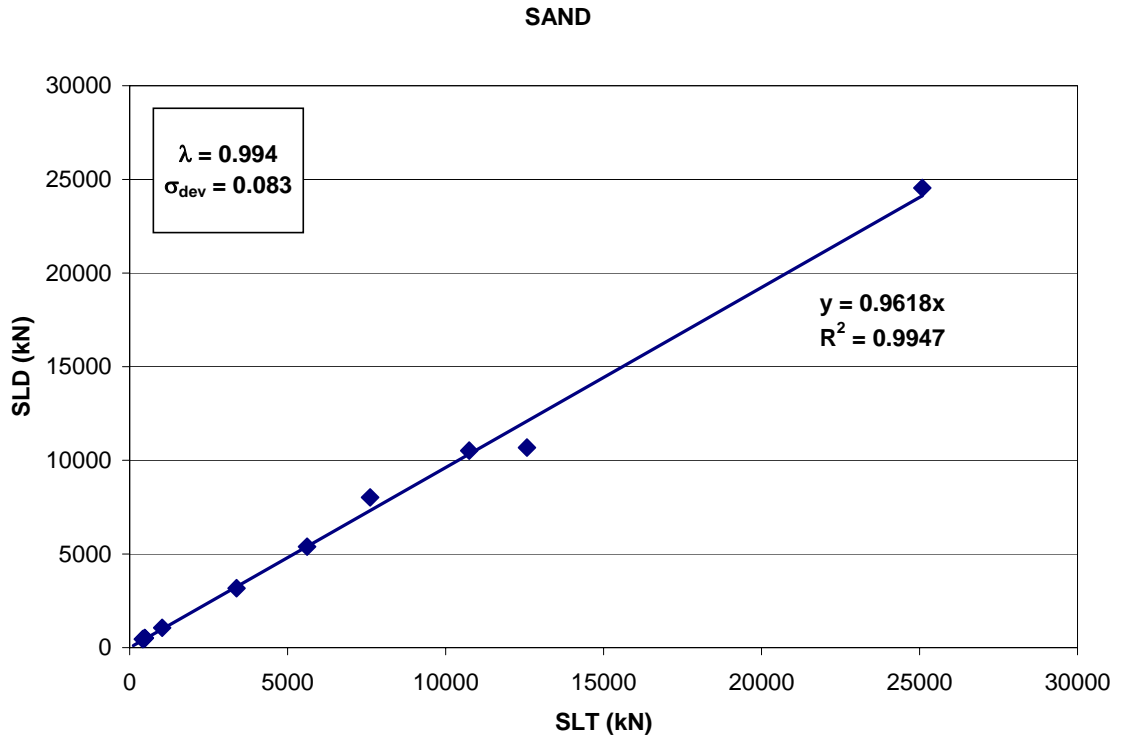


Figure 235. Predicted (SLD) vs. Actual (SLT) for Sand

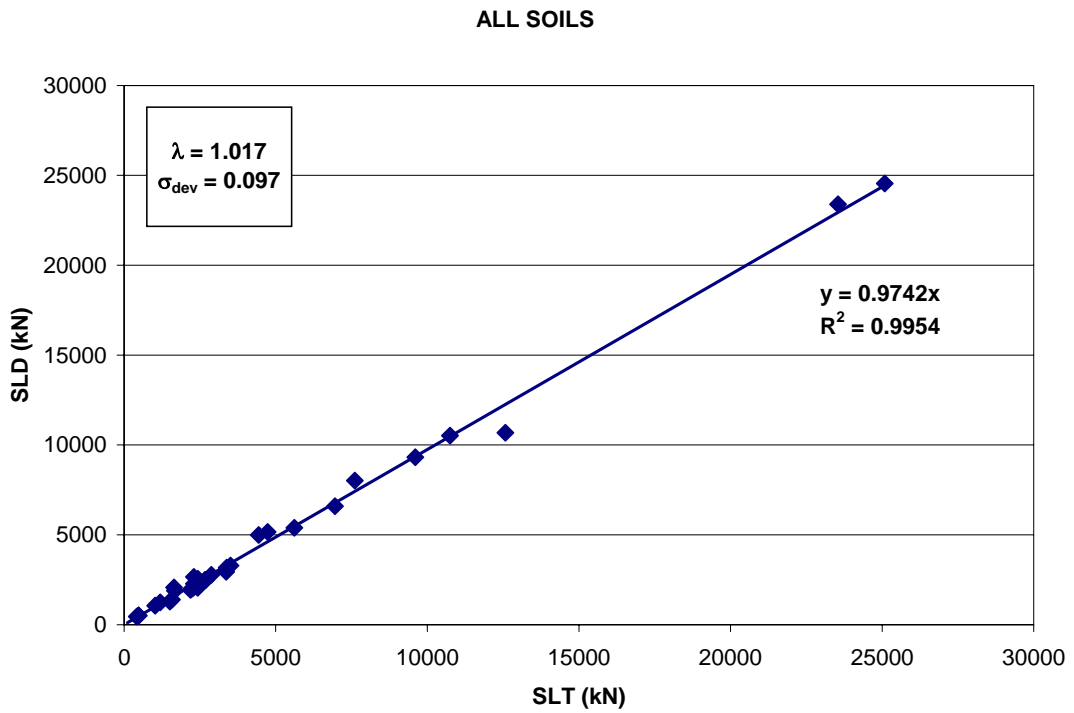


Figure 236. Predicted (SLD) vs Actual (SLT) for All Soils

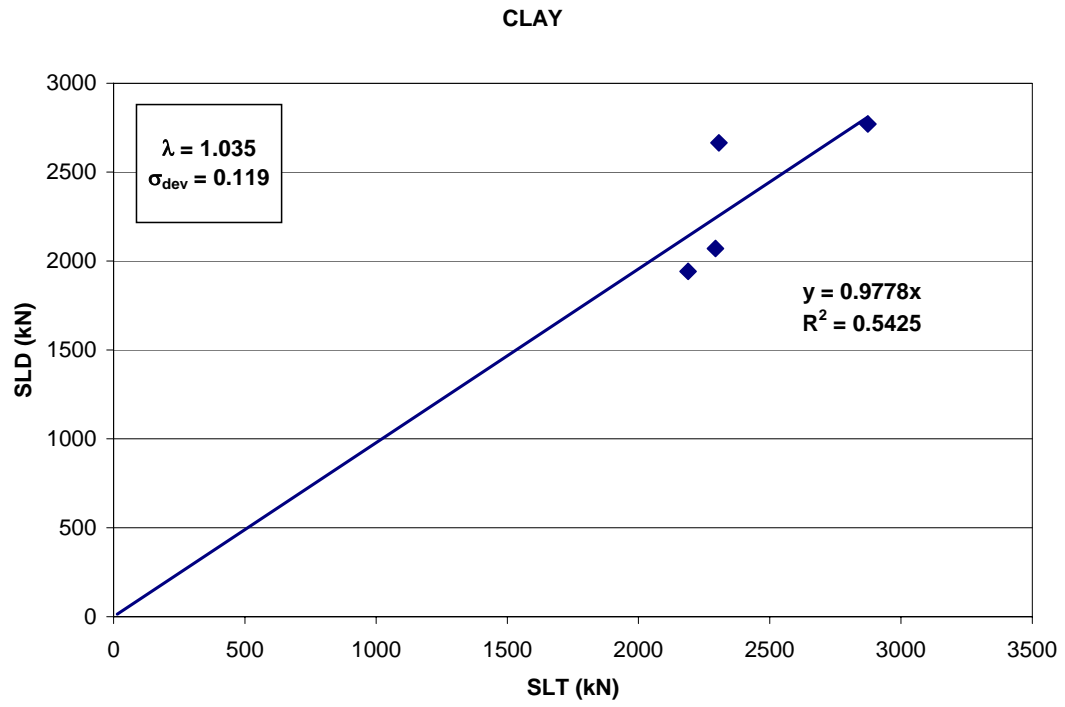


Figure 237. Predicted (SLD) vs. Actual (SLT)

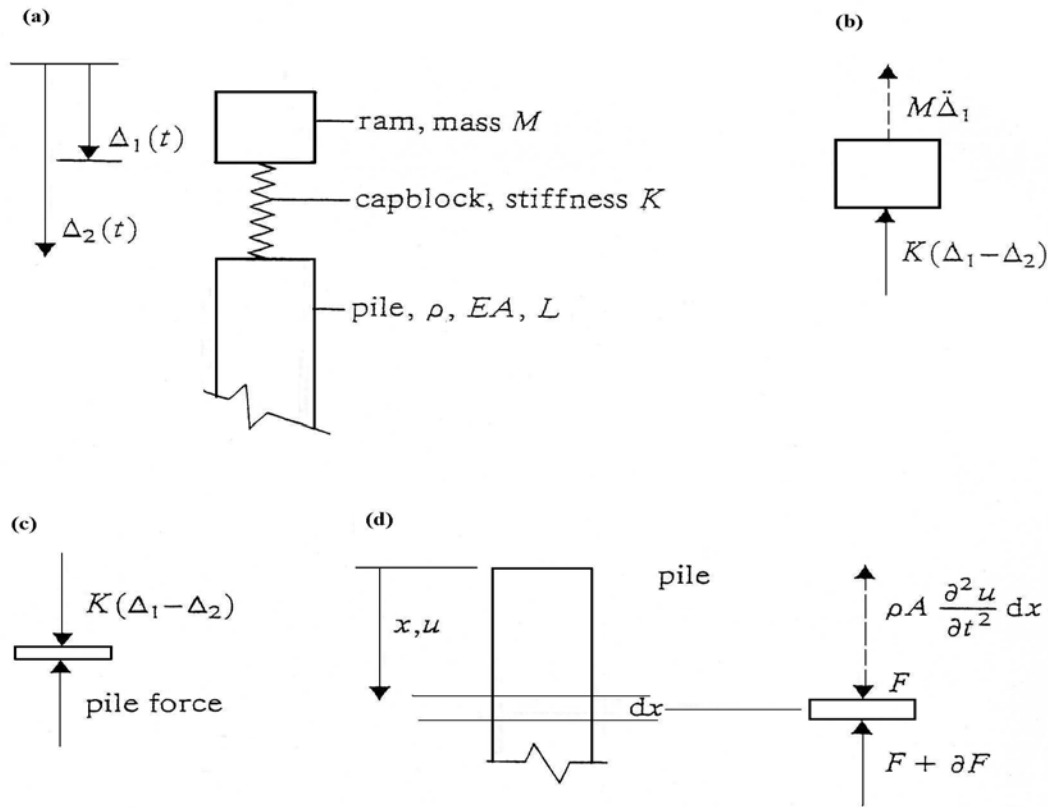


Figure 238. (a) Definition Diagram for Pile-driving Equations, (b) Equilibrium of Ram, (c) Equilibrium at Capblock-pile Interface, (d) Definition diagrams for pile force. (Irvine, 1986)

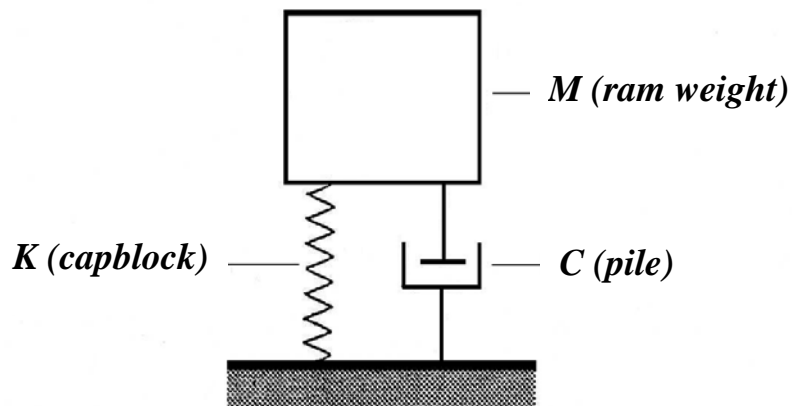


Figure 239. Equivalent Model for Pile System (Irvine, 1986)

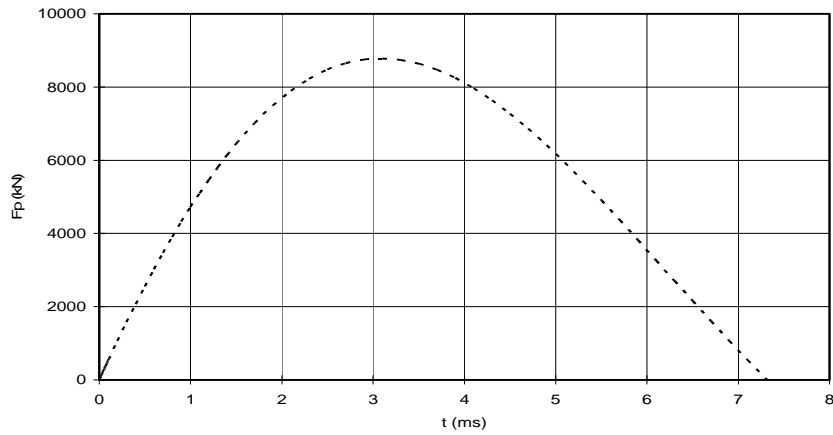


Figure 240. Force Pulse on Pile Head ($\zeta < 1$)

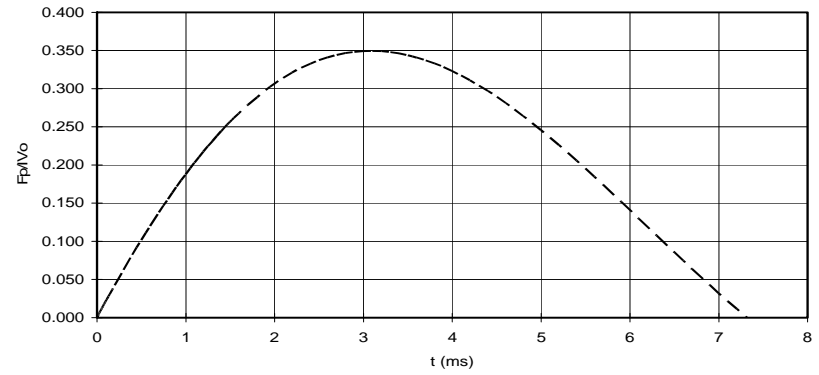


Figure 241. Non-dimensional Force Pulse on Pile Head ($\zeta < 1$)

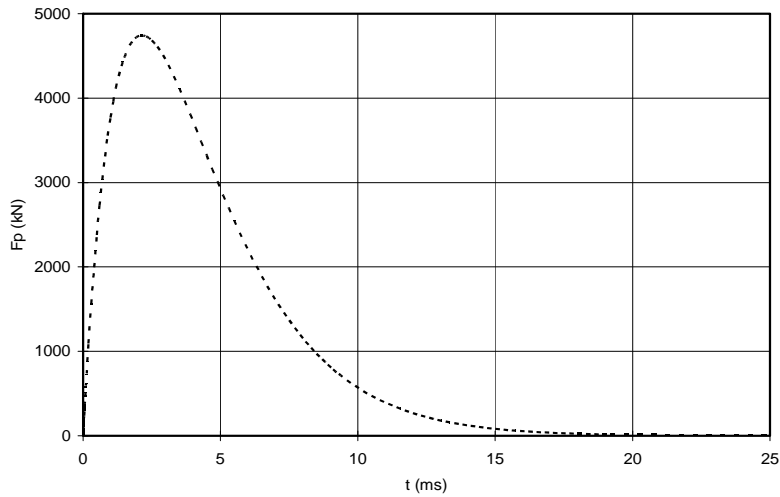


Figure 242. Force Pulse on Pile Head ($\zeta = 1$)

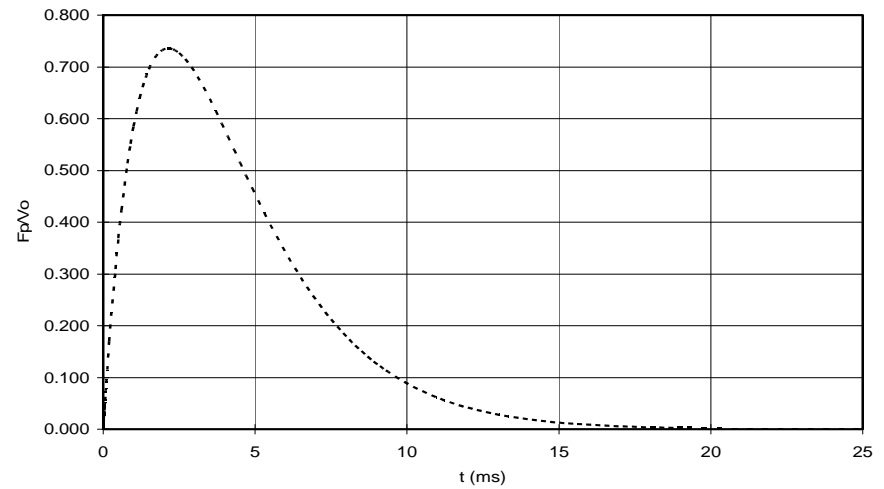


Figure 243. Non-dimensional Force Pulse on Pile Head ($\zeta = 1$)

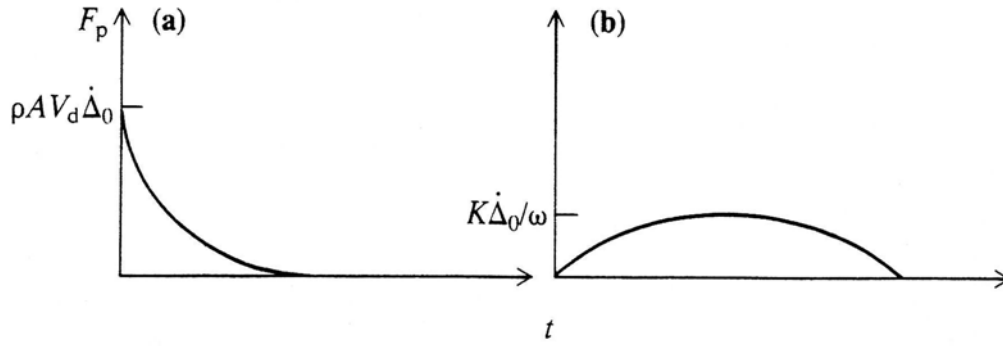


Figure 244. Limiting Cases for Dynamics Loads in Piles (a) Rigid Capblock; and (b) Rigid Pile (Irvine, 1986)

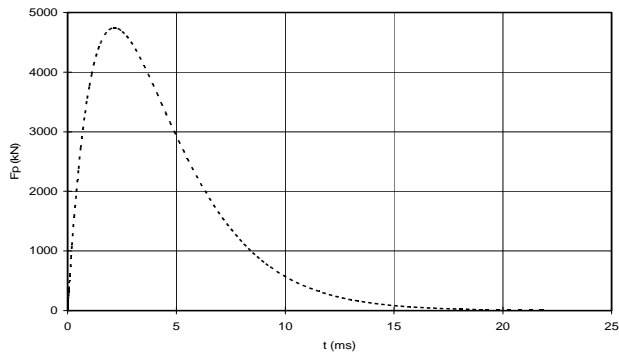


Figure 245. Dimensional Force Pulse on Pile Head ($\zeta > 1$)

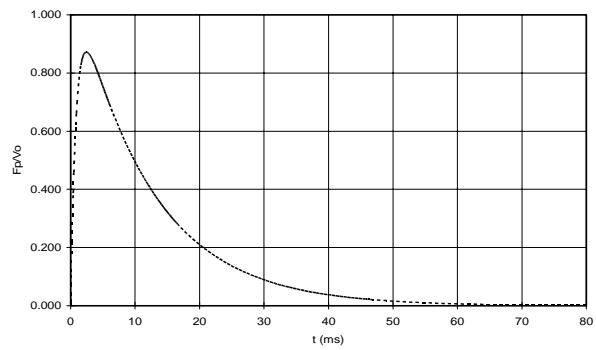


Figure 246. Non-dimensional Force Pulse on Pile Head ($\zeta > 1$)

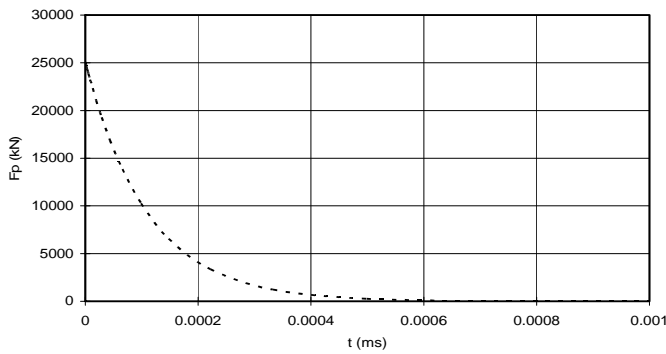


Figure 247. Force Pulse on Pile Head

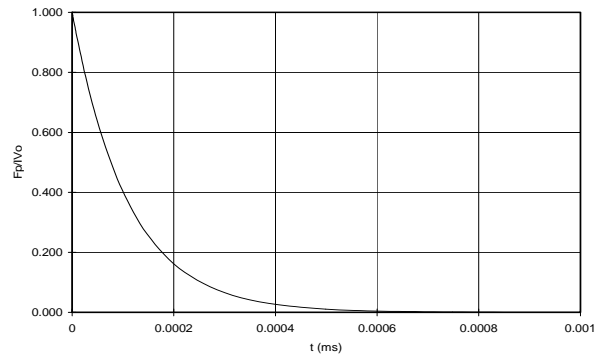


Figure 248. Non-dimensional Force Pulse on Pile Head

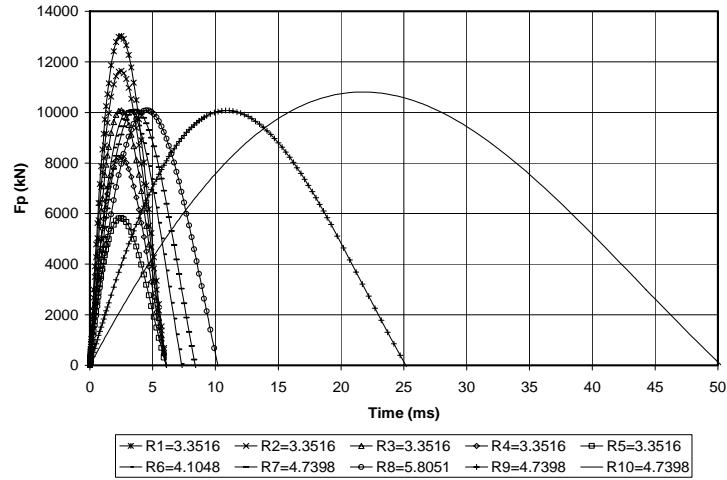


Figure 249. Force Pulses on Pile Head ($\zeta < 1$)

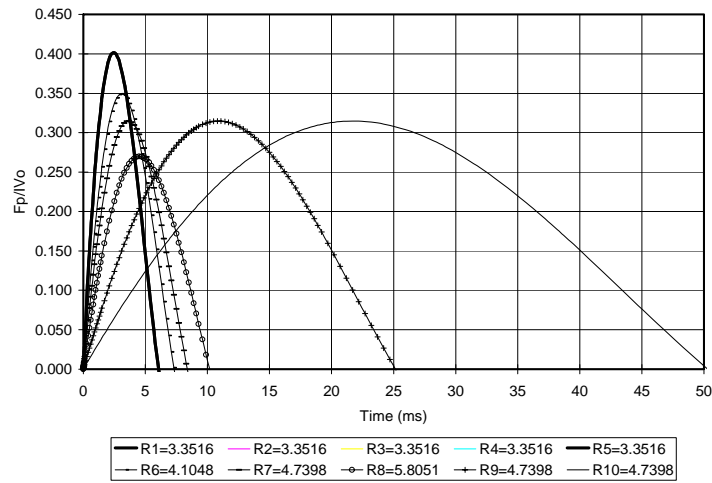


Figure 250. Non-dimensional Force Pulses on Pile Head ($\zeta < 1$)

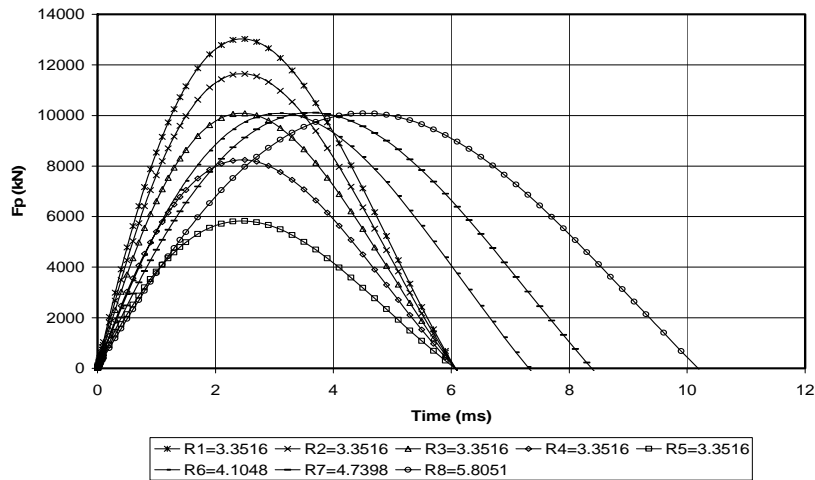


Figure 251. Force Pulse on Pile Head ($\zeta < 1$)

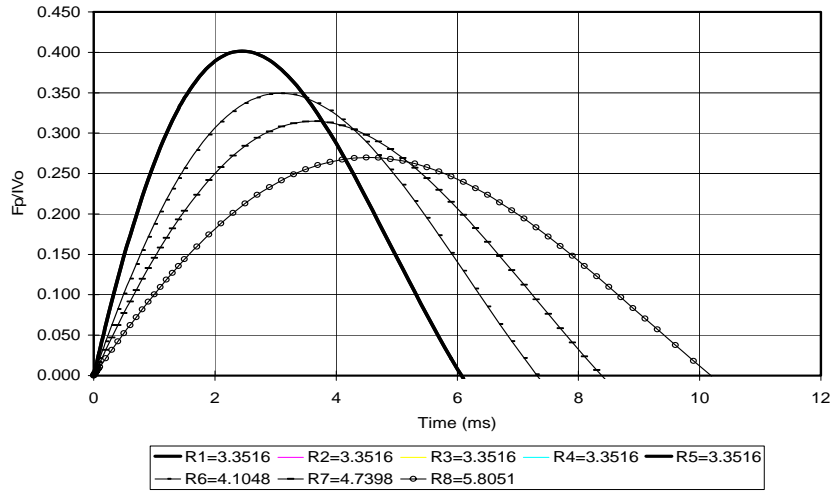


Figure 252. Non-dimensional Force Pulse on Pile Head ($\zeta < 1$)

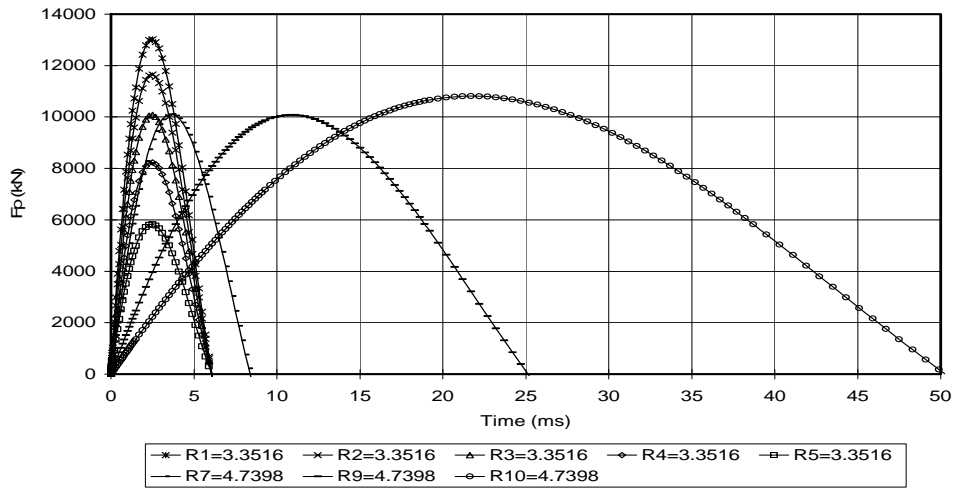


Figure 253. Force Pulses on Pile Head ($\zeta < 1$)

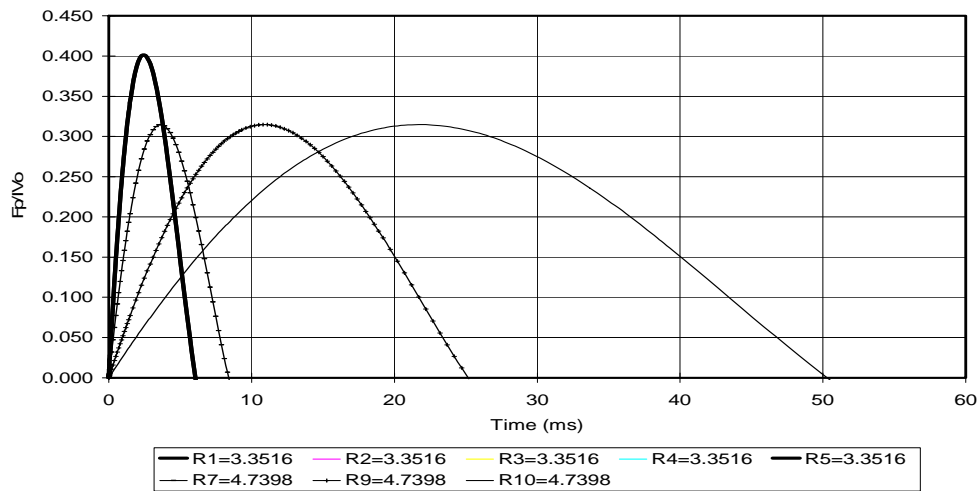


Figure 254. Non-dimensional Force Pulses on Pile Head ($\zeta < 1$)

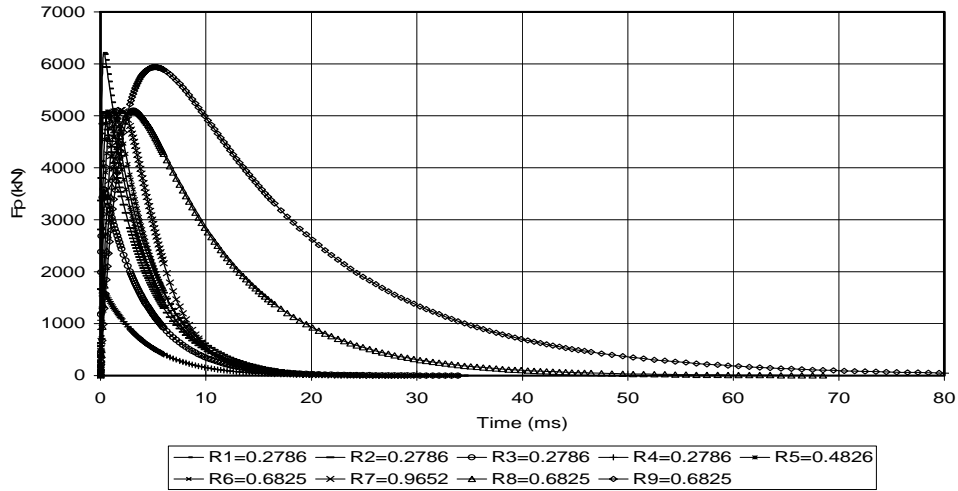


Figure 255. Force Pulses on Pile Head ($\zeta > 1$)

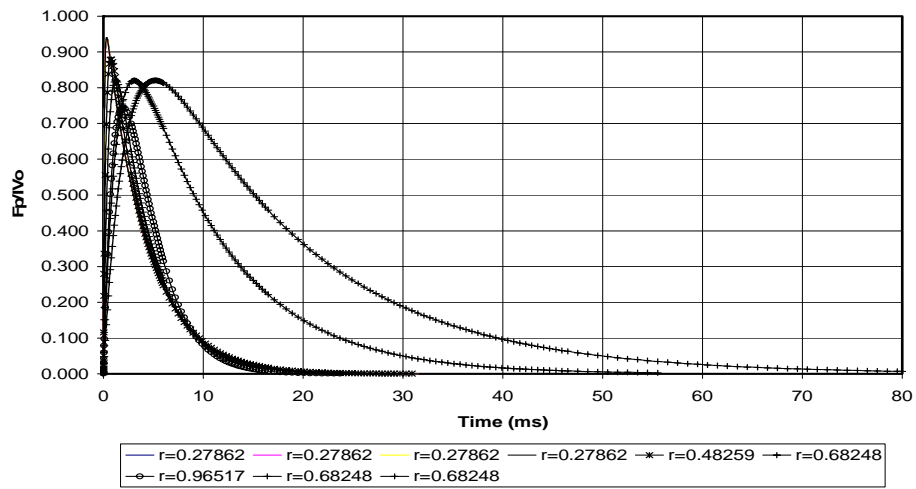


Figure 256. Non-dimensional Force Pulses on Pile Head ($\zeta > 1$)

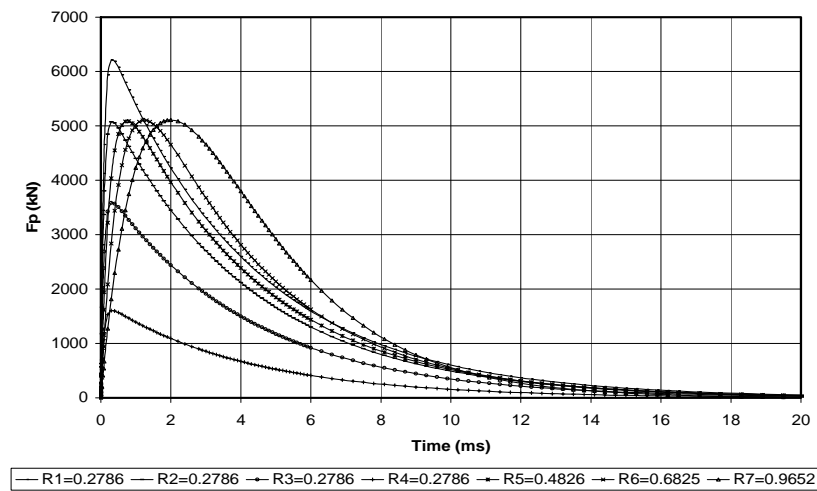


Figure 257. Force Pulses on Pile Head ($\zeta > 1$)

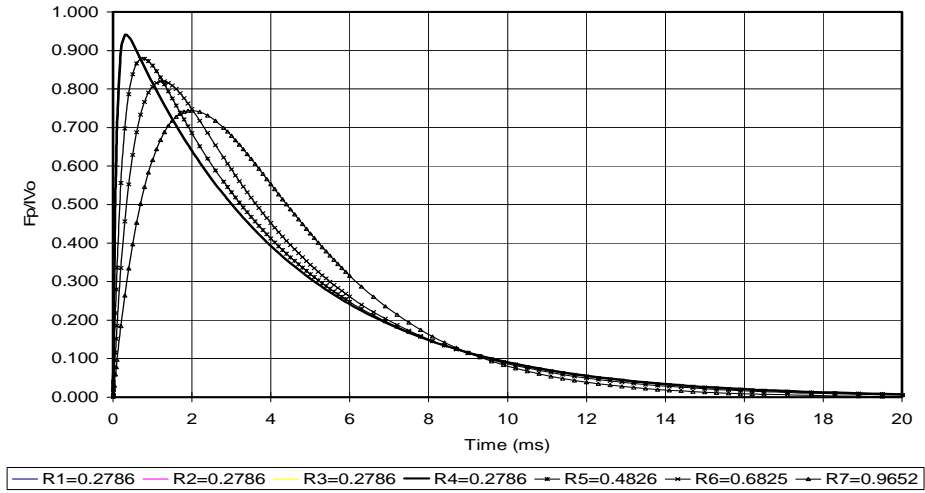


Figure 258. Non-dimensional Force Pulses on Pile Head ($\zeta > 1$)

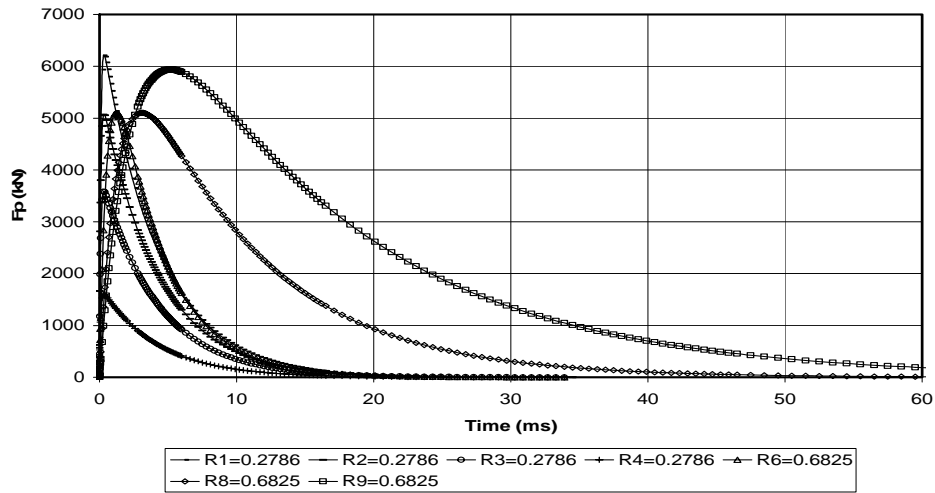


Figure 259. Force Pulses on Pile Head ($\zeta > 1$)

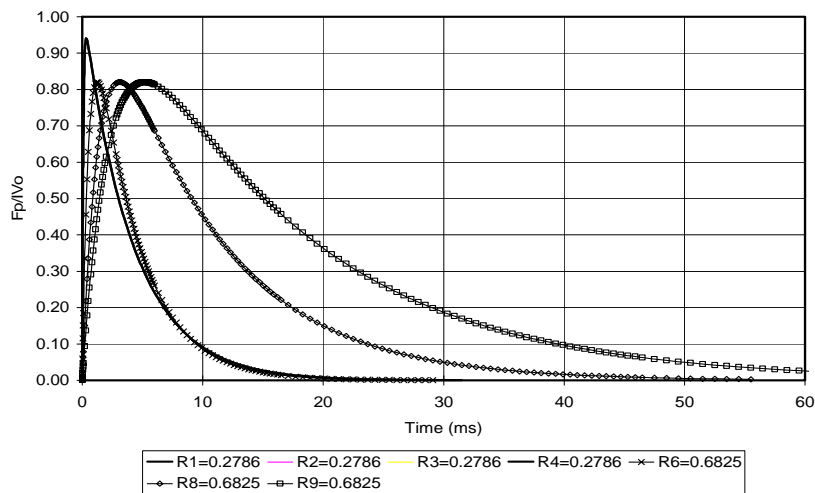


Figure 260. Non-dimensional Force Pulses on Pile Head ($\zeta > 1$)

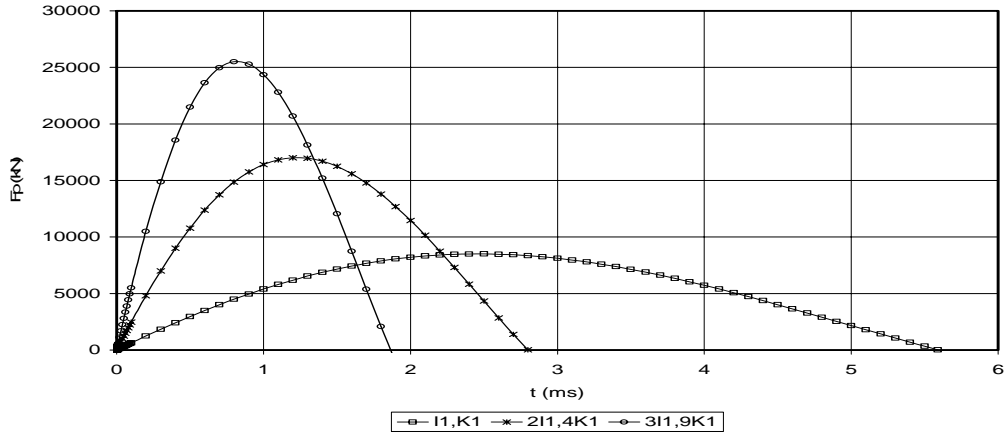


Figure 261. Force Pulses on the Pile Head With Same R Value

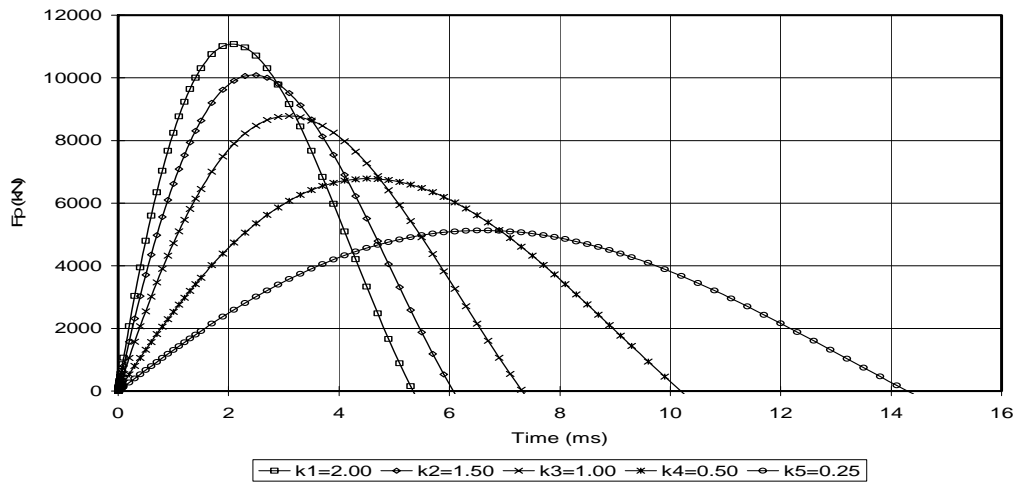


Figure 262. Force Pulses on Pile Head ($\zeta < 1$), $M=50\text{kN}$, $H=1.5\text{m}$, $K=(2.0, 1.5, 1.0, 0.5, 0.25) * 1000\text{kN/mm}$

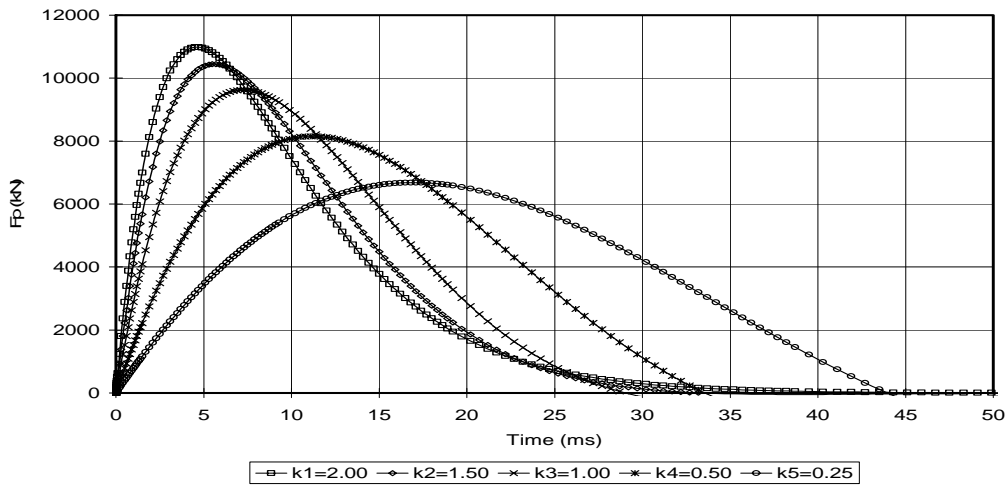


Figure 263. Force Pulses on Pile Head ($\zeta < 1$), $M=420\text{kN}$, $H=0.5\text{m}$, $K=(2.0, 1.5, 1.0, 0.5, 0.25) * 1000\text{kN/mm}$

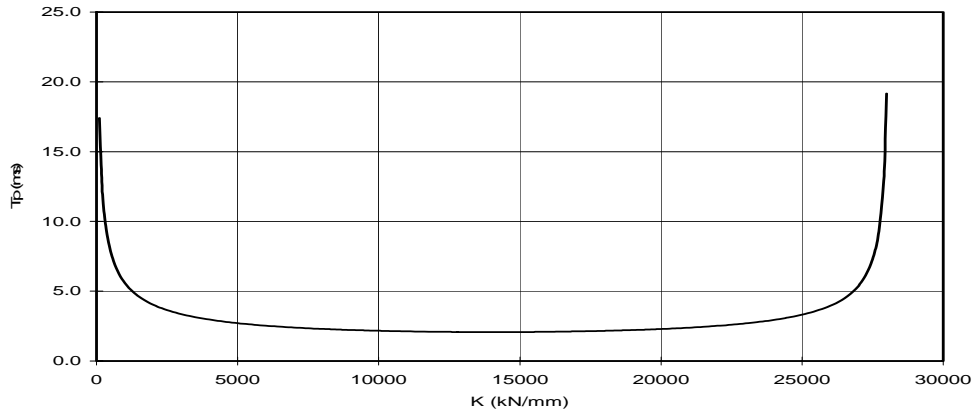


Figure 264. Capblock Stiffness K vs. Force Pulse Duration T_p ($0.0596 < \zeta < 0.9985$)

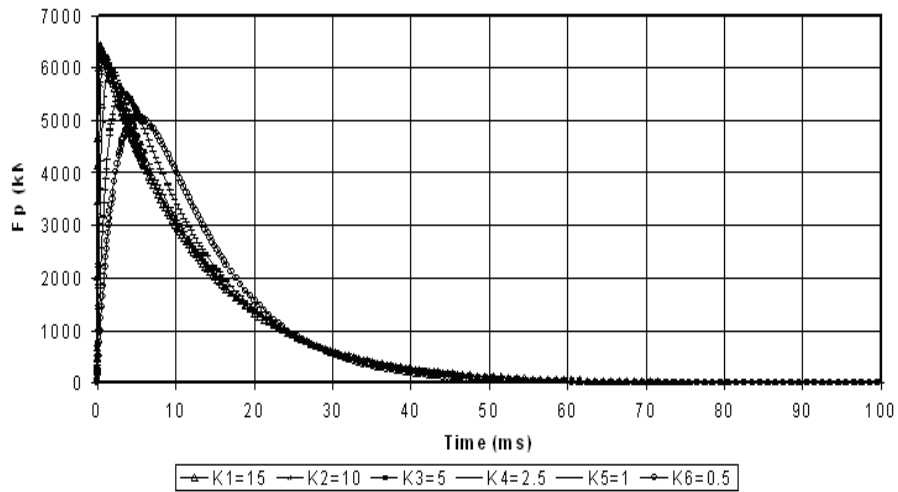


Figure 265. Force Pulses on Pile Head ($\zeta > 1$), $M=150\text{kN}$, $H=1.5\text{m}$, $K=(15,10,5,2.5,1,0.5 * 1000\text{kN/mm})$

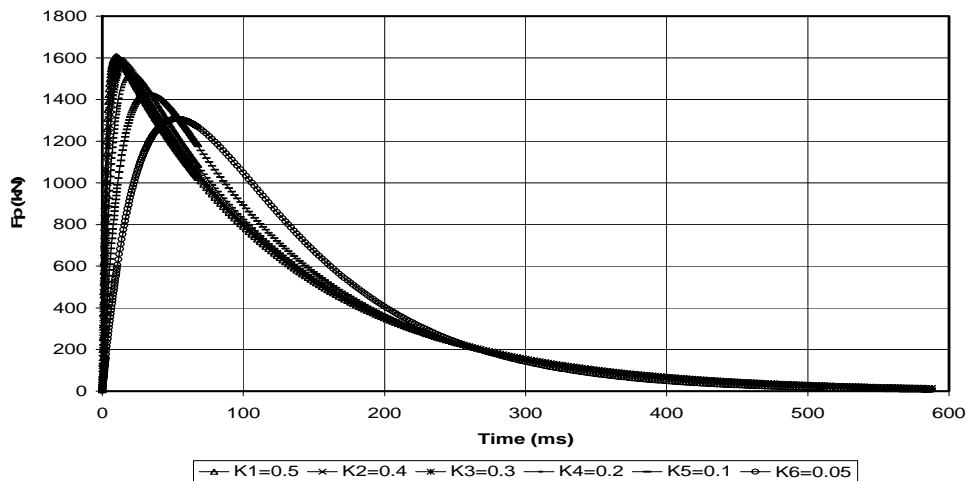


Figure 266. Force Pulses on Pile Head ($\zeta > 1$), $M=1500\text{kN}$, $H=0.1\text{m}$, $K=(0.5,0.4,0.3,0.2,0.1,0.05 * 1000\text{kN/mm})$

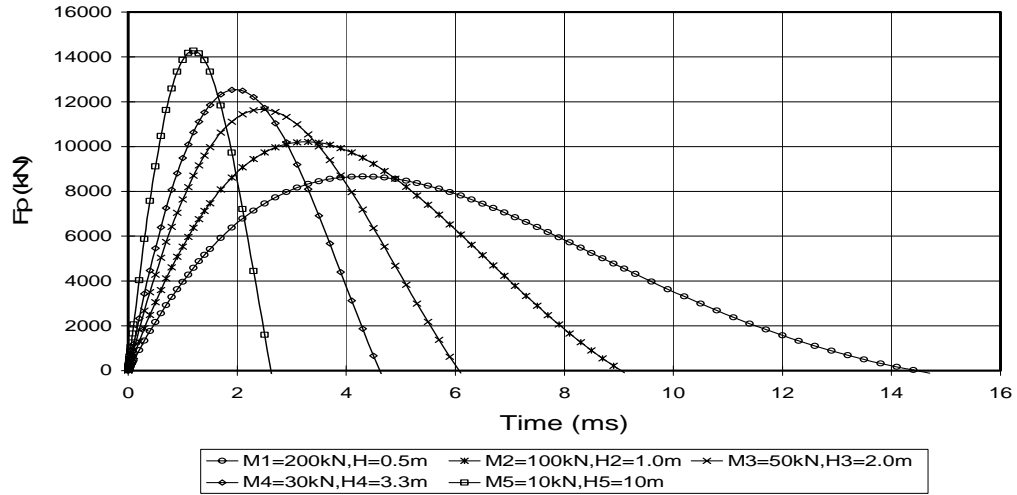


Figure 267. Time Histories of Force Pulse on Pile Head ($\zeta < 1$) (Same Energy)

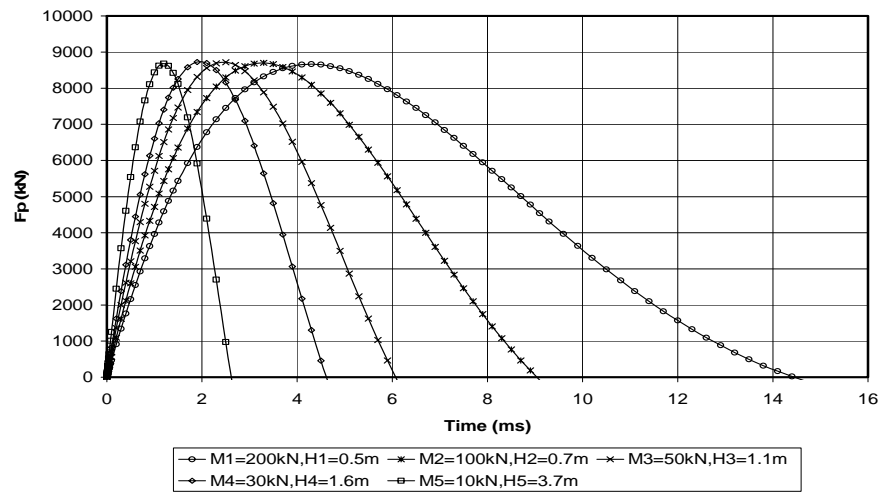


Figure 268. Force Pulses on Pile Head ($\zeta < 1$)

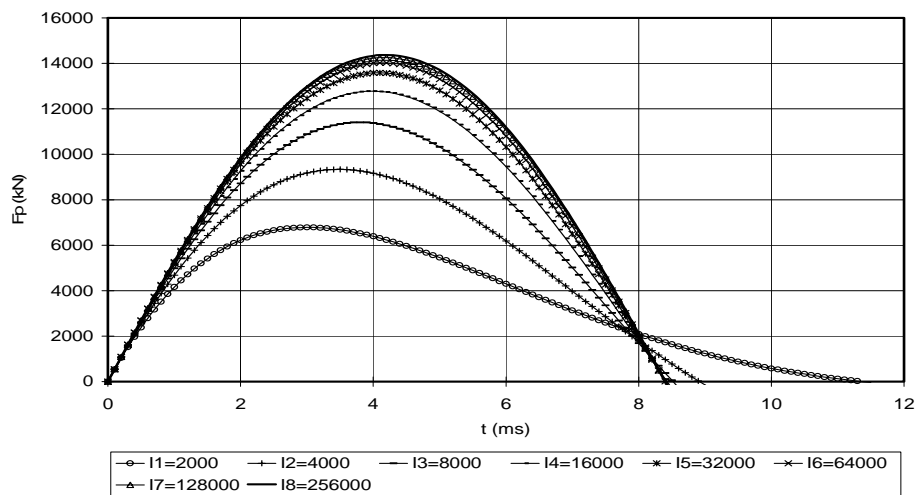


Figure 269. Force Pulse on Pile Head; Same M and H, Different I

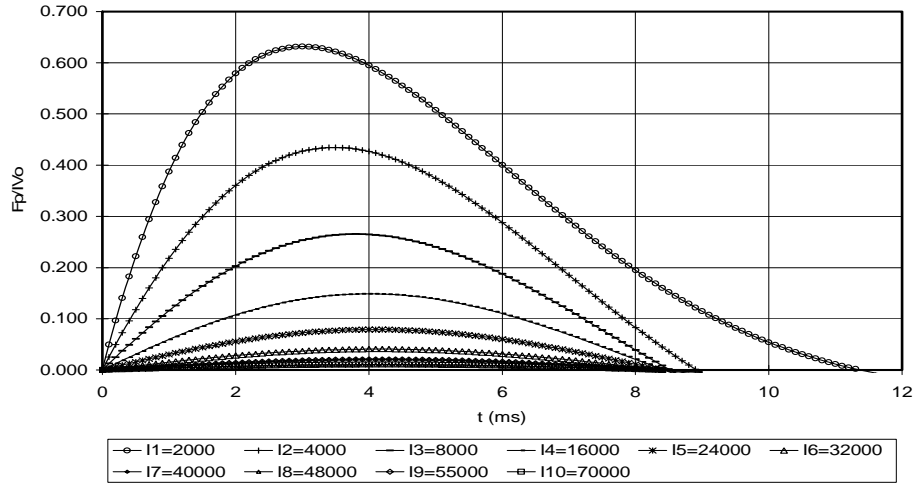


Figure 270. Non-dimensional Force Pulse on Pile Head; Same M and H, Different I

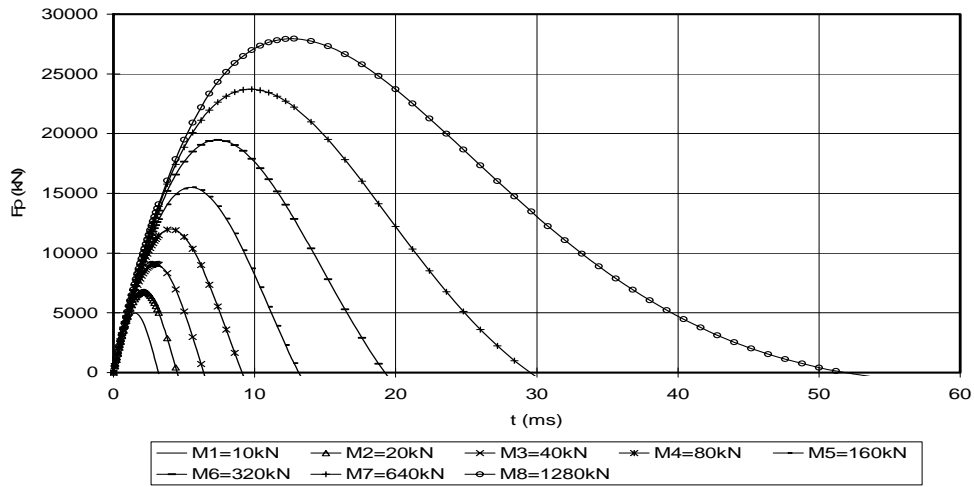


Figure 271. Force Pulse on Pile Head; Same K, H and I, Different M

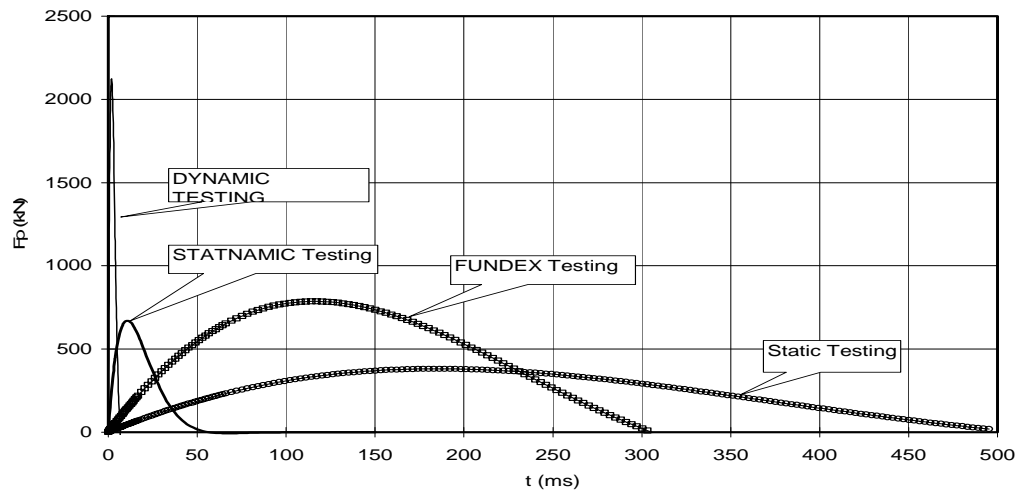
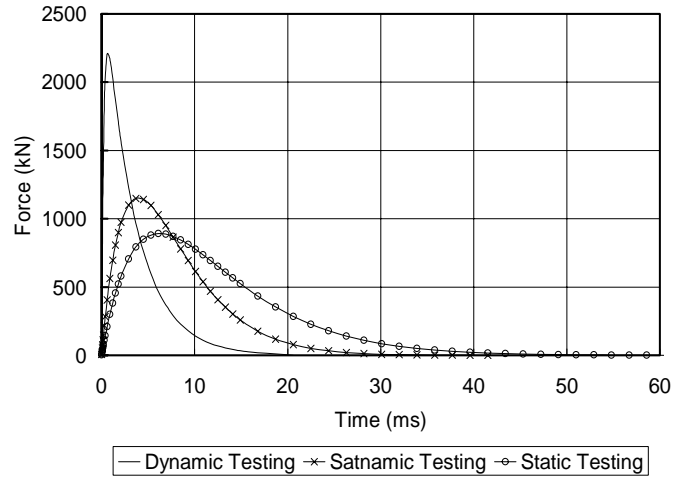
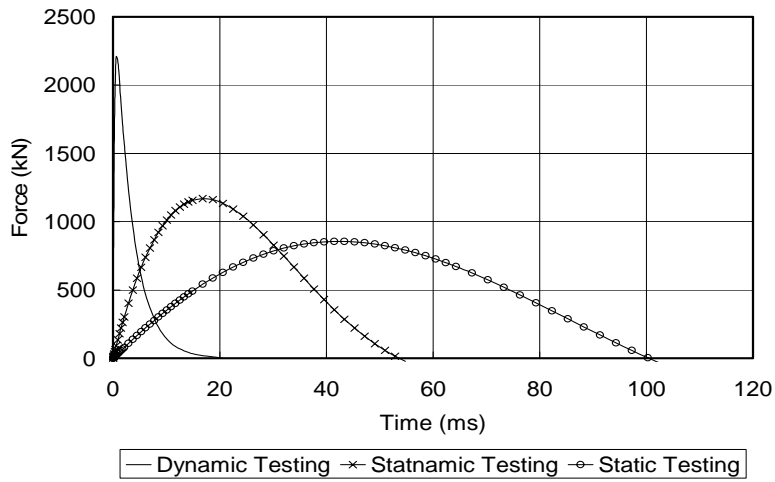


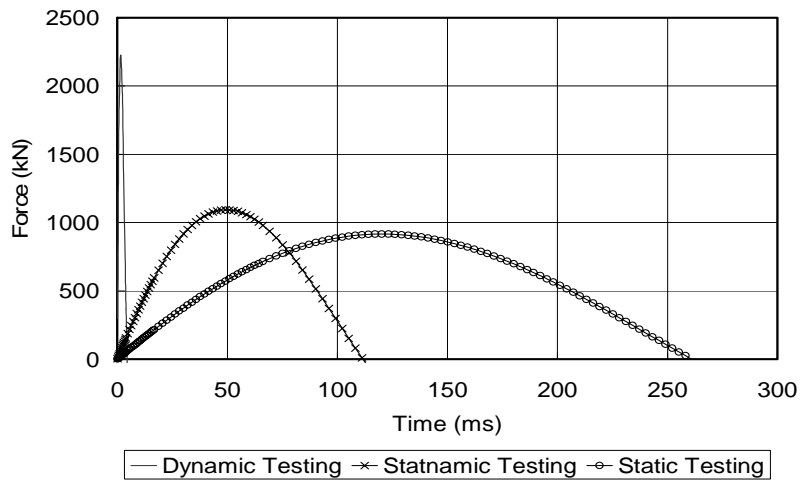
Figure 272. The Influence of a Load Testing System



(a)

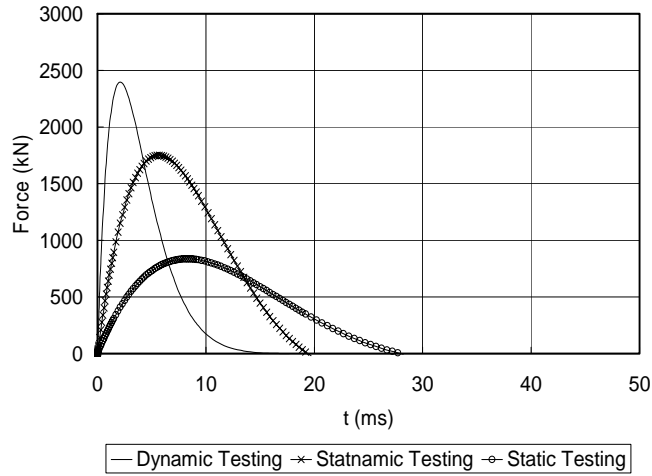


(b)

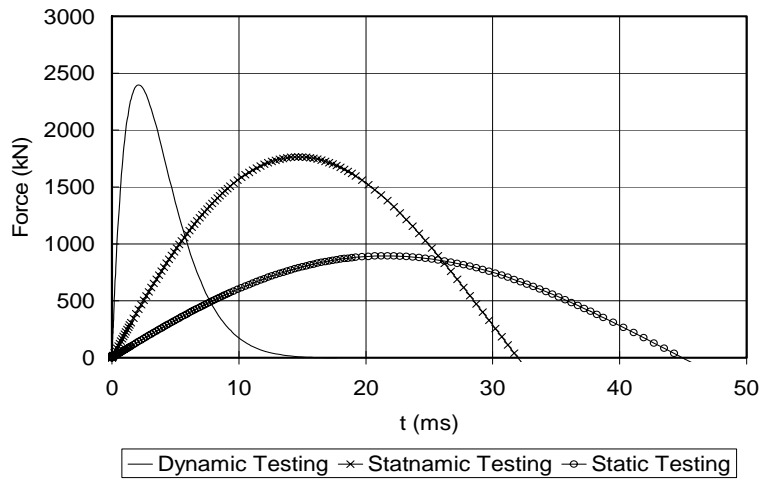


(c)

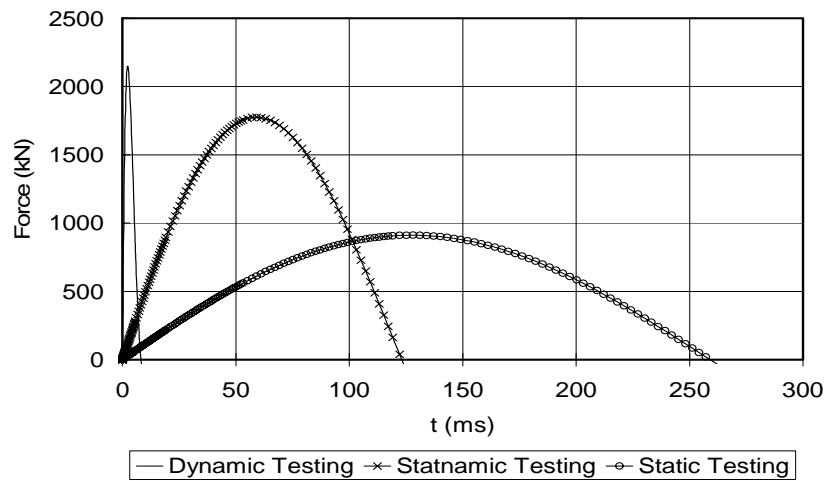
Figure 273. Force Pulse on pile Head (Newbury Test Pile No.2)



(a)



(b)



(c)

Figure 274. Force Pulse on pile Head (Newbury Test Pile No.3)

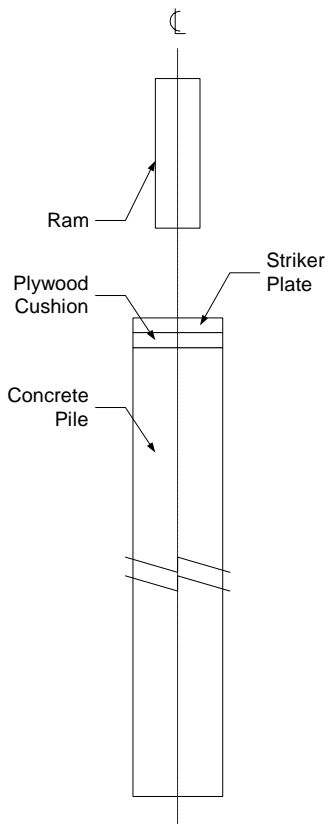


Figure 275. Schematic of Pile and Impact System in LSDYNA Modeling.

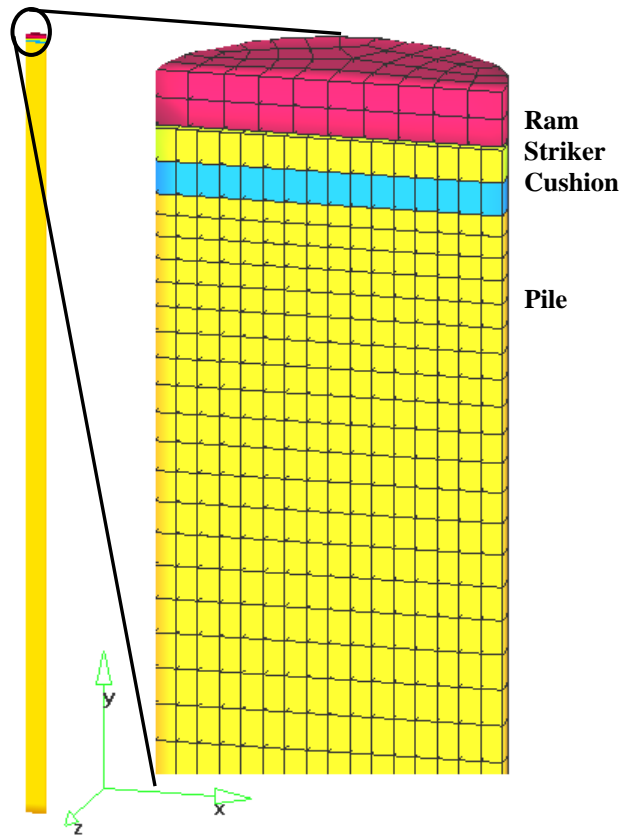


Figure 276. Isometric View of Pile and Ram.

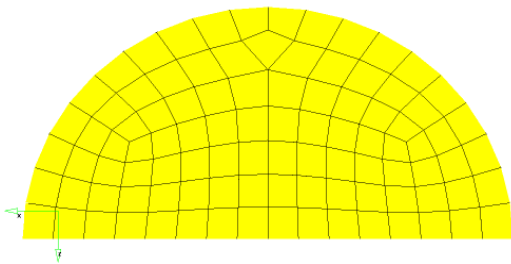


Figure 277. Top View of Pile.

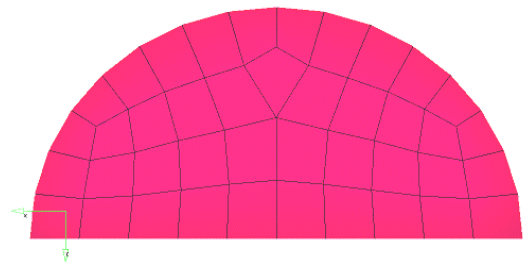


Figure 278. Top View of Ram.

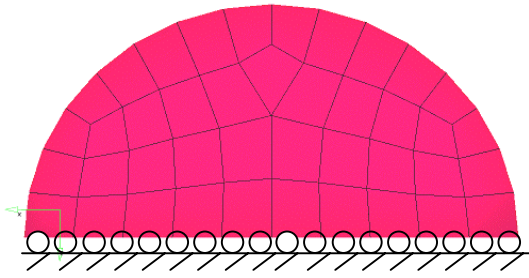


Figure 279. Half-Symmetry Constraint Schematic for Ram and Pile.



Figure 280. Constraint Schematic for the Pile's Tip.

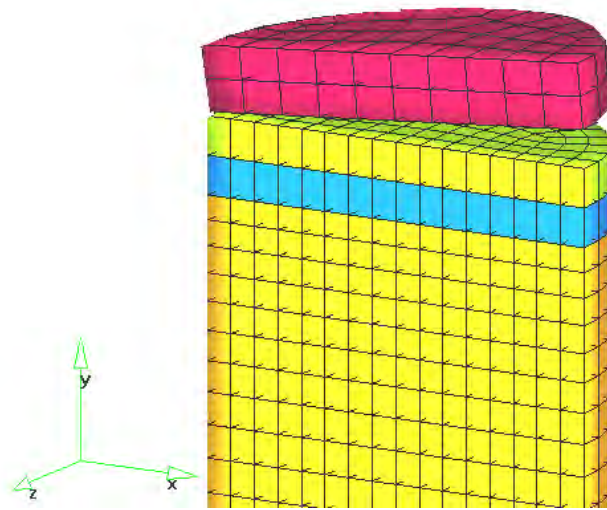


Figure 281. Isometric View of System with a Rotated Ram for an Offset (Uneven) Impact.

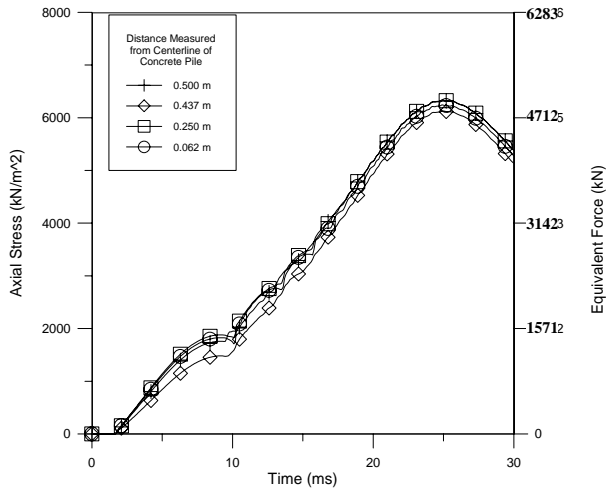


Figure 283. Calculated Normal Stress for Elements on Concrete Surface in Baseline FE Model

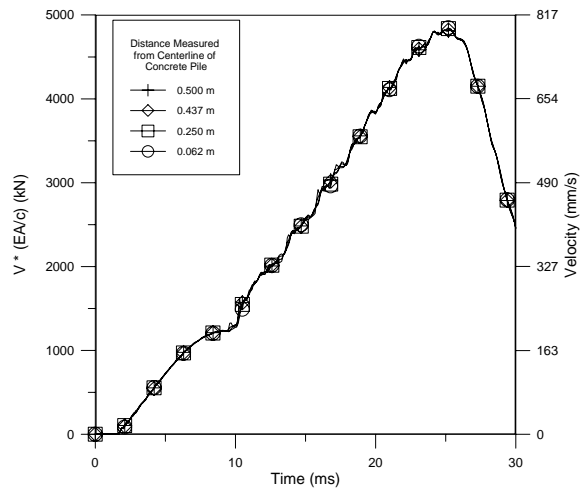


Figure 284. Calculated Velocity (V*I) for Nodes on Concrete Surface in Baseline FE Model

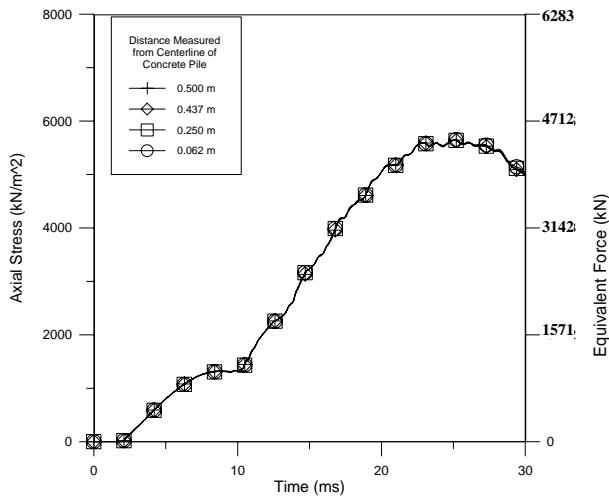


Figure 285. Calculated Normal Stress for Elements ~1m Below Surface in Baseline FE Model

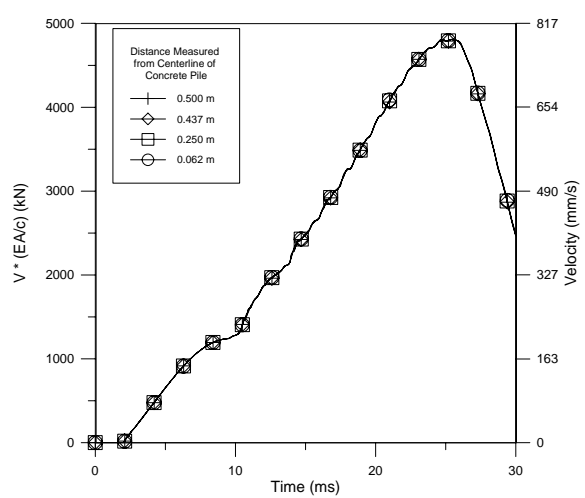


Figure 286. Calculated Velocity (V*I) for Nodes ~1m Below Surface in Baseline FE Model

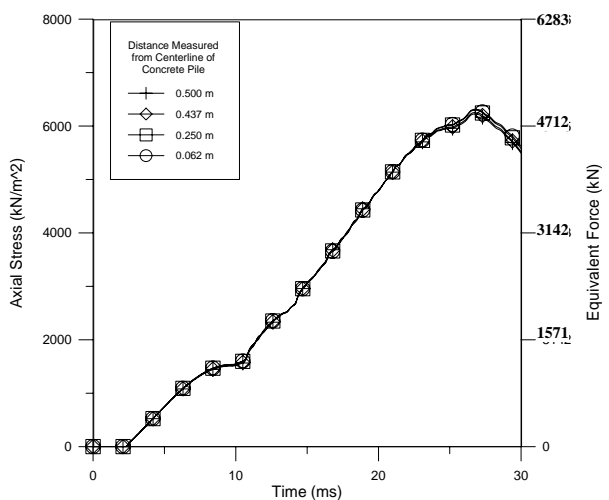


Figure 287. Calculated Normal Stress for Elements ~2m Below Surface in Baseline Model.

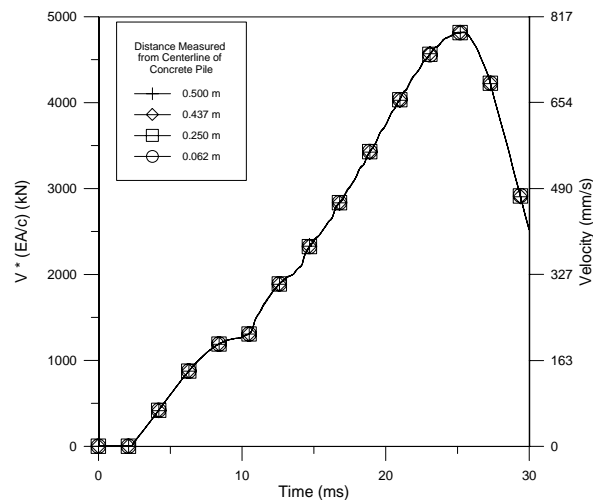


Figure 288. Calculated Velocity (V*I) for Nodes ~2m Below Surface in Baseline FE Model.

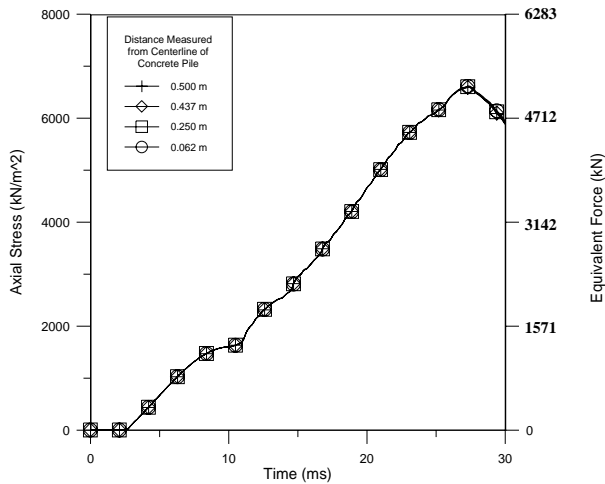


Figure 289. Calculated Normal Stress for Elements ~3m Below Surface in Baseline Model.

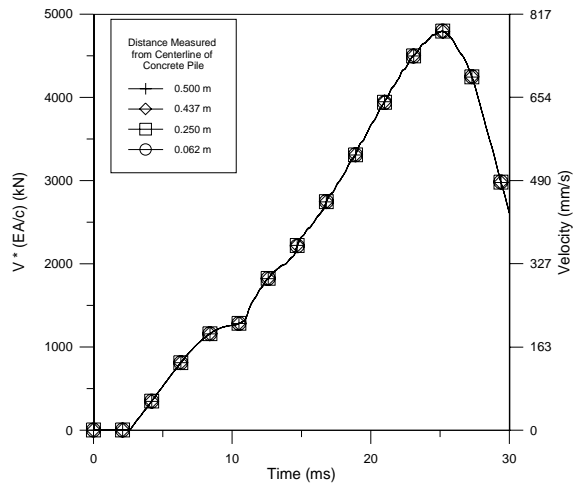


Figure 290. Calculated Velocity (V*I) for Nodes ~3m Below Surface in Baseline FE Model.

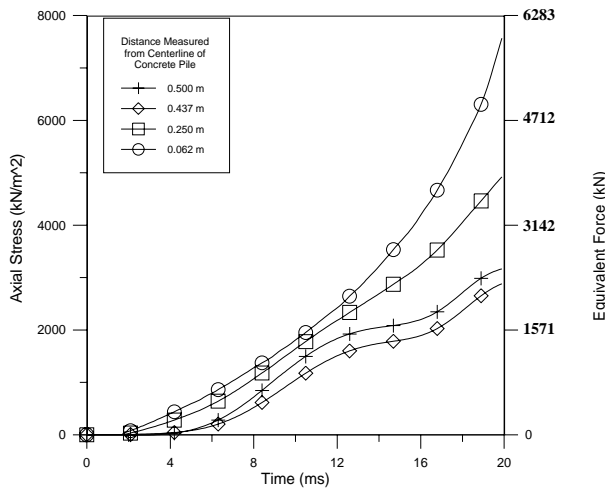


Figure 291. Calculated Normal Stress for Elements on Concrete Surface in FE Model with Ram Diameter = 0.2m for 0ms - 20ms.

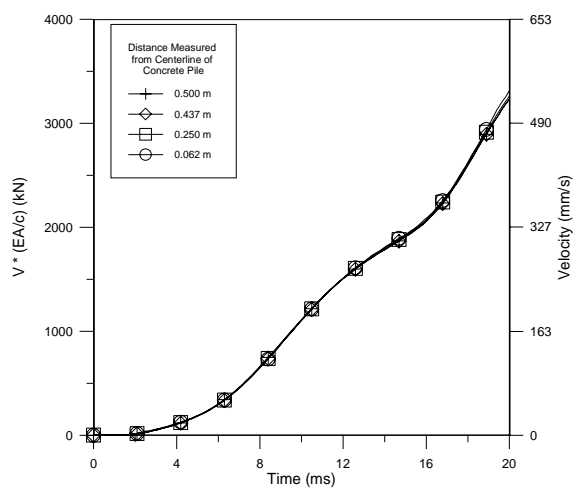


Figure 292. Calculated Velocity (V*I) for Nodes on Concrete Surface in FE Model with Ram Diameter = 0.2m for 0ms - 20ms.

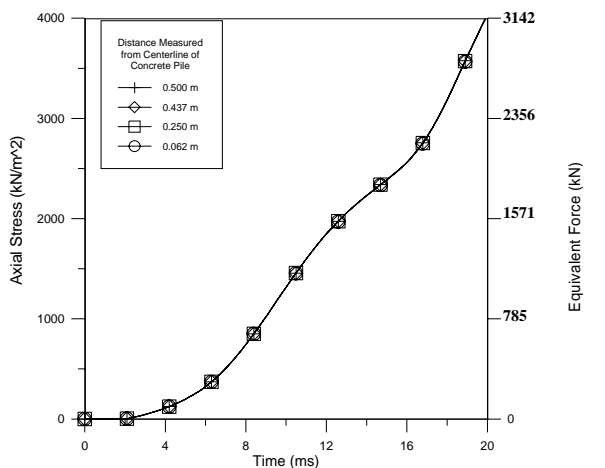


Figure 293. Calculated Normal Stress for Elements ~1m Below Surface in FE Model with Ram Diameter = 0.2m for 0ms - 20ms.

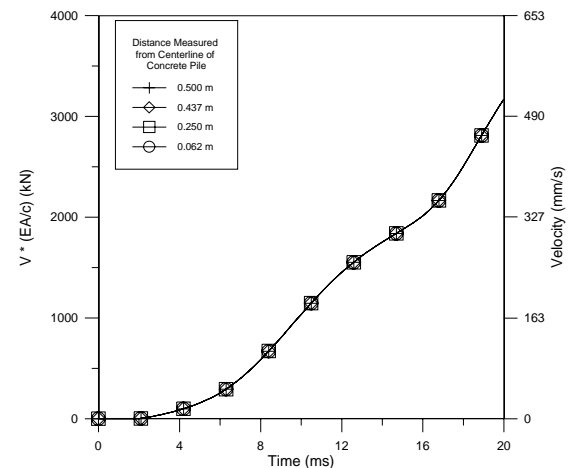


Figure 294. Calculated Velocity (V*I) for Nodes ~1m Below Surface in FE Model with Ram Diameter = 0.2m for 0ms - 20ms.

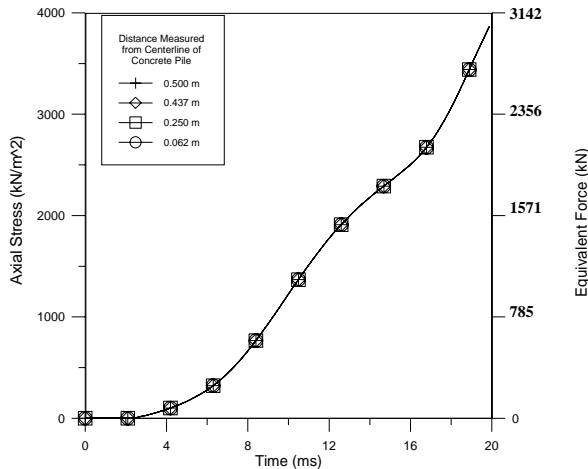


Figure 295. Calculated Normal Stress for Elements ~2m Below Surface in FE Model with Ram Diameter = 0.2m for 0ms - 20ms.

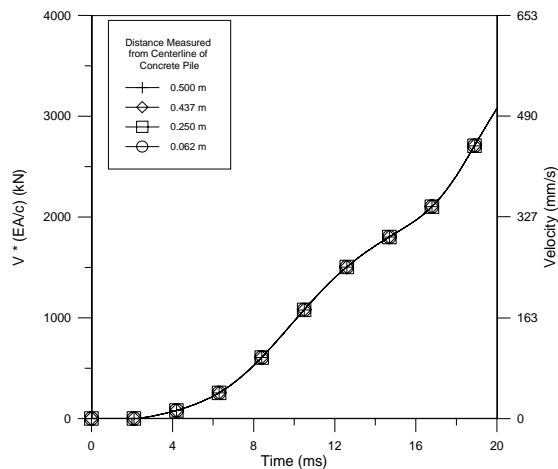


Figure 296. Calculated Velocity ($V \cdot I$) for Nodes ~2m Below Surface in FE Model with Ram Diameter = 0.2m for 0ms - 20ms.

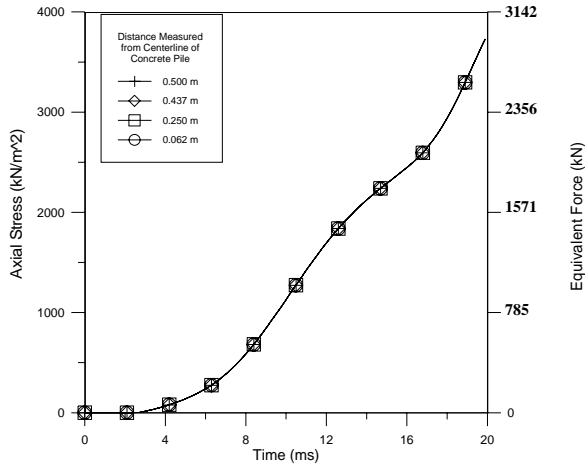


Figure 297. Calculated Normal Stress for Elements ~3m Below Surface in FE Model with Ram Diameter = 0.2m for 0ms - 20ms.

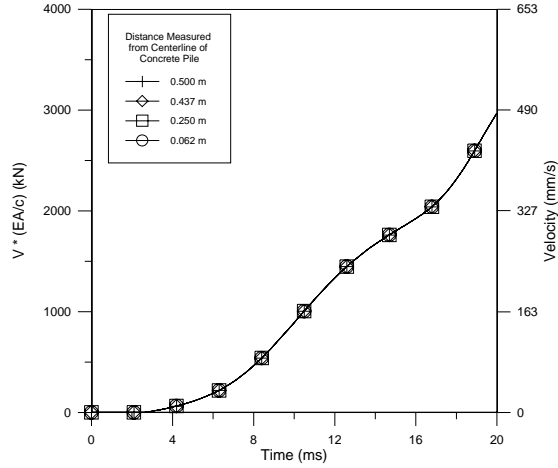


Figure 298. Calculated Velocity ($V \cdot I$) for Nodes ~3m Below Surface in FE Model with Ram Diameter = 0.2m for 0ms - 20ms.

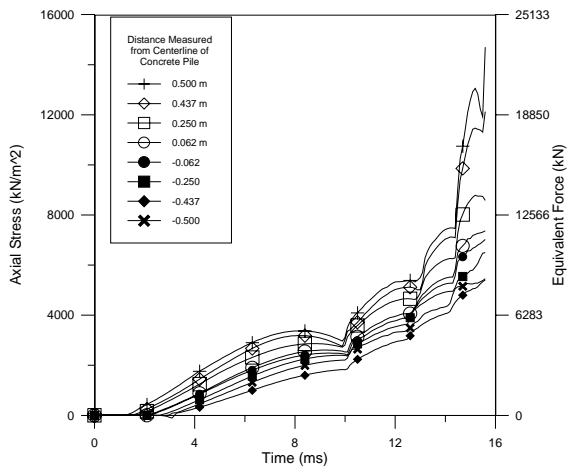


Figure 299. Calculated Normal Stress for Elements on Concrete Surface in FE Model with Ram Diameter = 1.0m and Tilt Angle = 1° for 0ms - 16ms.

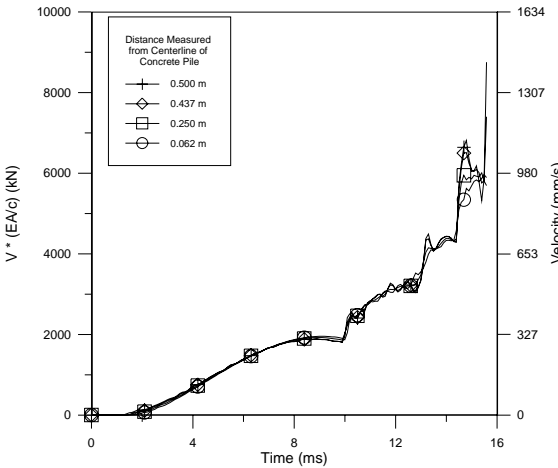


Figure 300. Calculated Velocity ($V \cdot I$) for Nodes on Concrete Surface in FE Model with Ram Diameter = 1.0m and Tilt Angle = 1° for 0ms - 16ms.

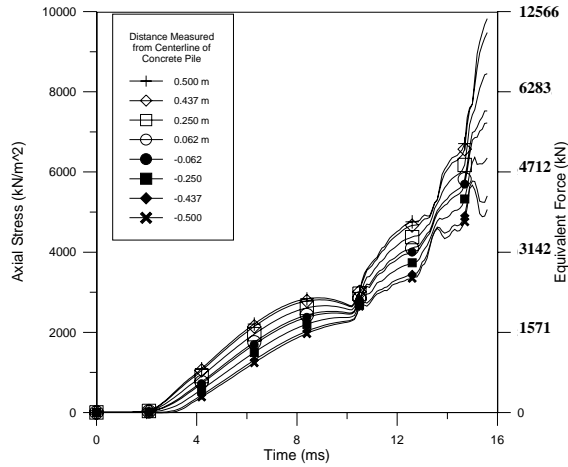


Figure 301. Calculated Normal Stress for Elements ~1 m Below Surface in FE Model with Ram Diameter = 1.0m and Tilt Angle = 1° for 0ms - 16ms.

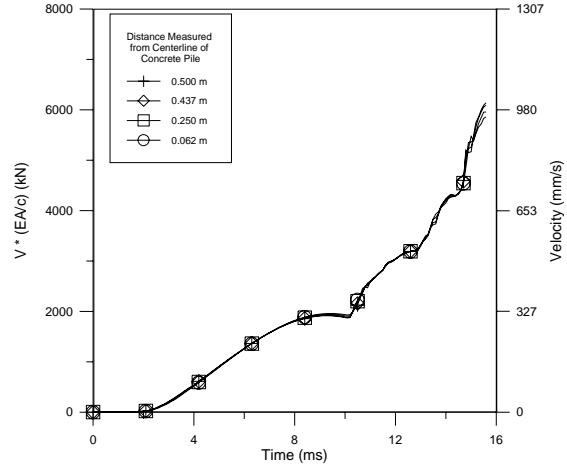


Figure 302. Calculated Velocity ($V*I$) for Nodes ~1m Below Surface in FE Model with Ram Diameter = 1.0m and Tilt Angle = 1° for 0ms - 16ms.

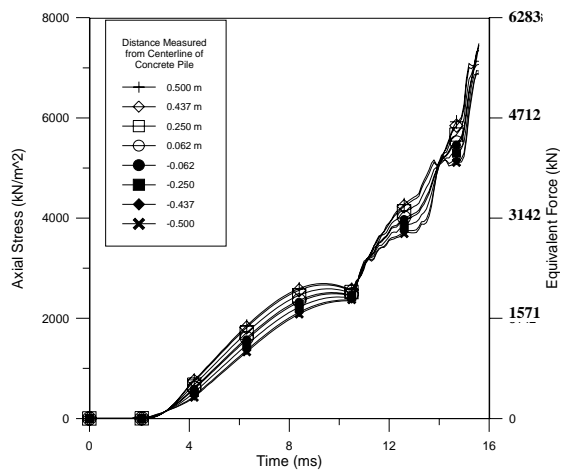


Figure 303. Calculated Normal Stress for Elements ~2 m Below Surface in FE Model with Ram Diameter = 1.0m and Tilt Angle = 1° for 0ms - 16ms.

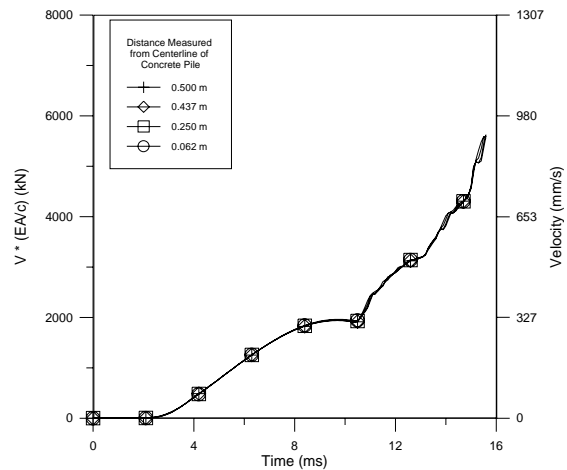


Figure 304. Calculated Velocity ($V*I$) for Nodes ~2 m Below Surface in FE Model with Ram Diameter = 1.0m and Tilt Angle = 1° for 0ms - 16ms.

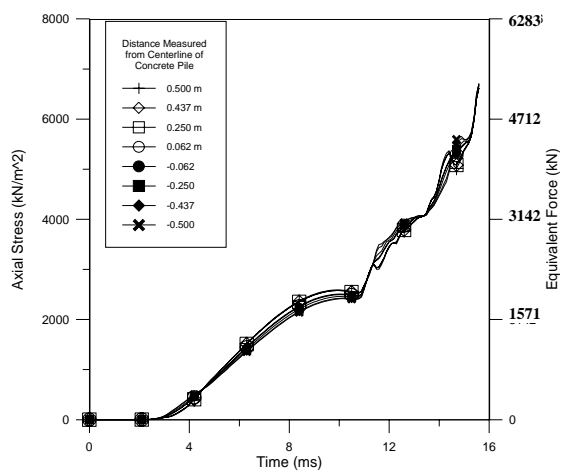


Figure 305. Calculated Normal Stress for Elements ~3m Below Surface in FE Model with Ram Diameter = 1.0m and Tilt Angle = 1° for 0ms - 16ms.

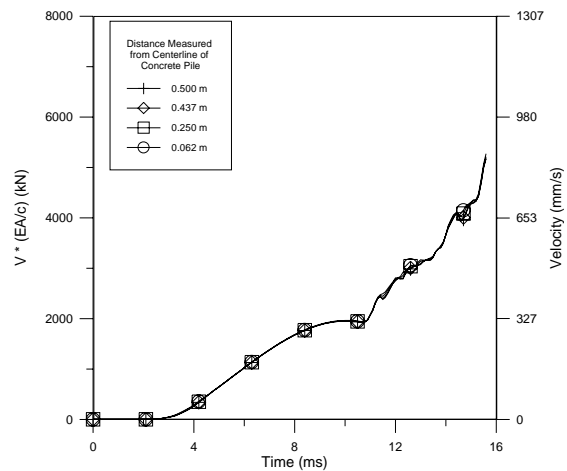


Figure 306. Calculated Velocity ($V*I$) for Nodes ~3m Below Surface in FE Model with Ram Diameter = 1.0m and Tilt Angle = 1° for 0ms - 16ms.

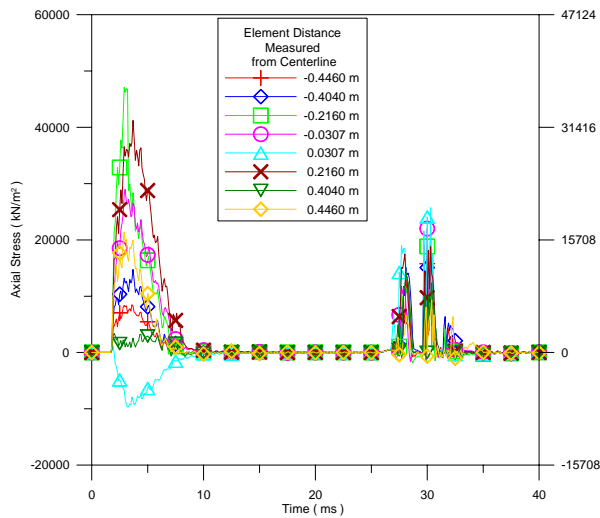


Figure 307. Calculated Normal Stress for Elements on Concrete Surface in FE Model with Ram Diameter = 1.0m and Tilt angle = 0° for Time = 0ms – 40ms.

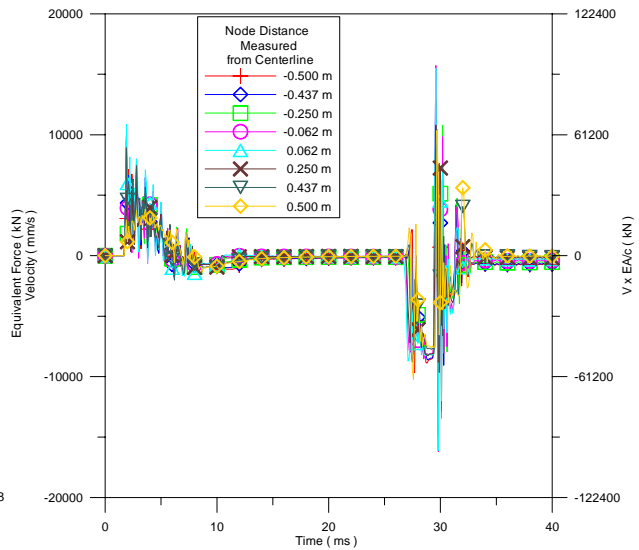


Figure 308. Calculated Velocity for Nodes on Concrete Surface in FE Model with Ram Diameter = 1.0m and Tilt Angle = 0° for Time = 0ms – 40ms.

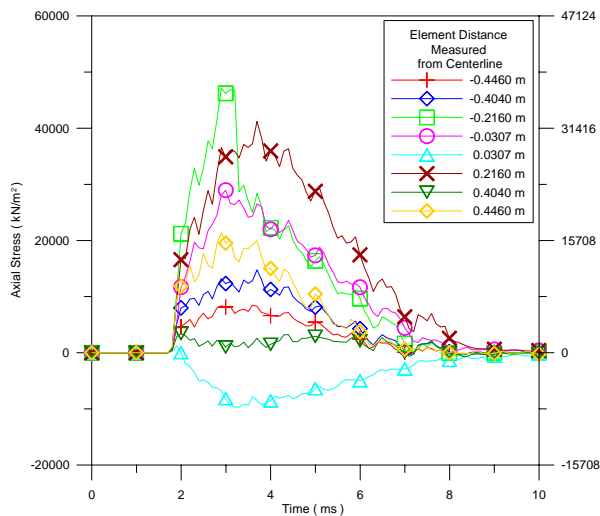


Figure 309. Calculated Normal Stress for Elements on Concrete Surface in FE Model with Ram Diameter = 1.0m and Tilt Angle = 0° for Time = 0ms – 10ms.

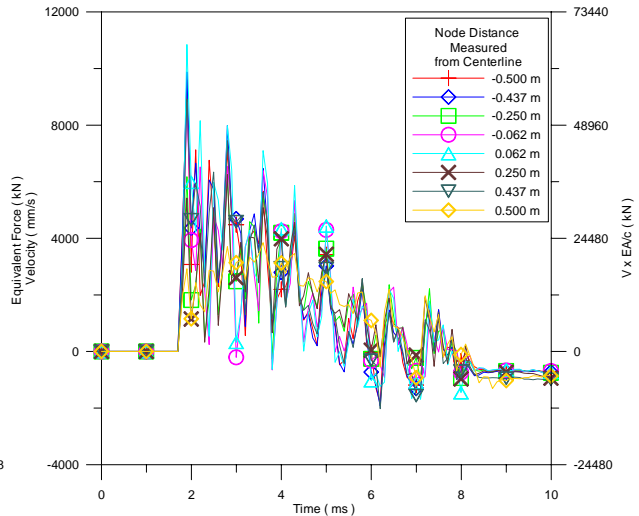


Figure 310. Calculated Velocity for Nodes on Concrete Surface in FE Model with Ram Diameter = 1.0m and Tilt Angle = 0° for Time = 0ms – 10ms.

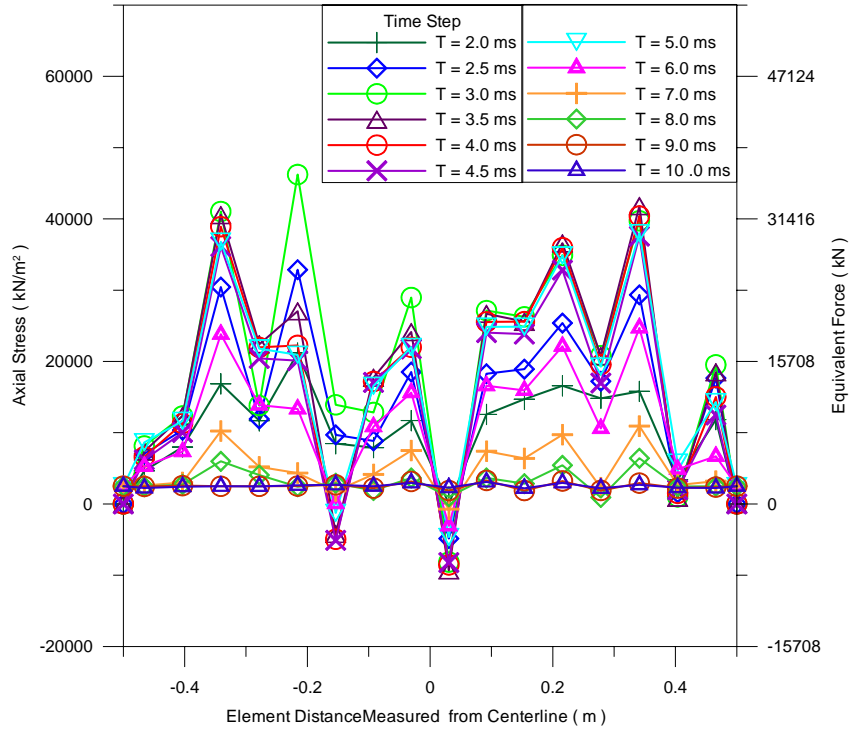


Figure 311. Calculated Normal Stress for Elements on Concrete Surface in FE Model with Ram Diameter = 1.0m and Tilt Angle = 0° for d = -0.5 to 0.5m.

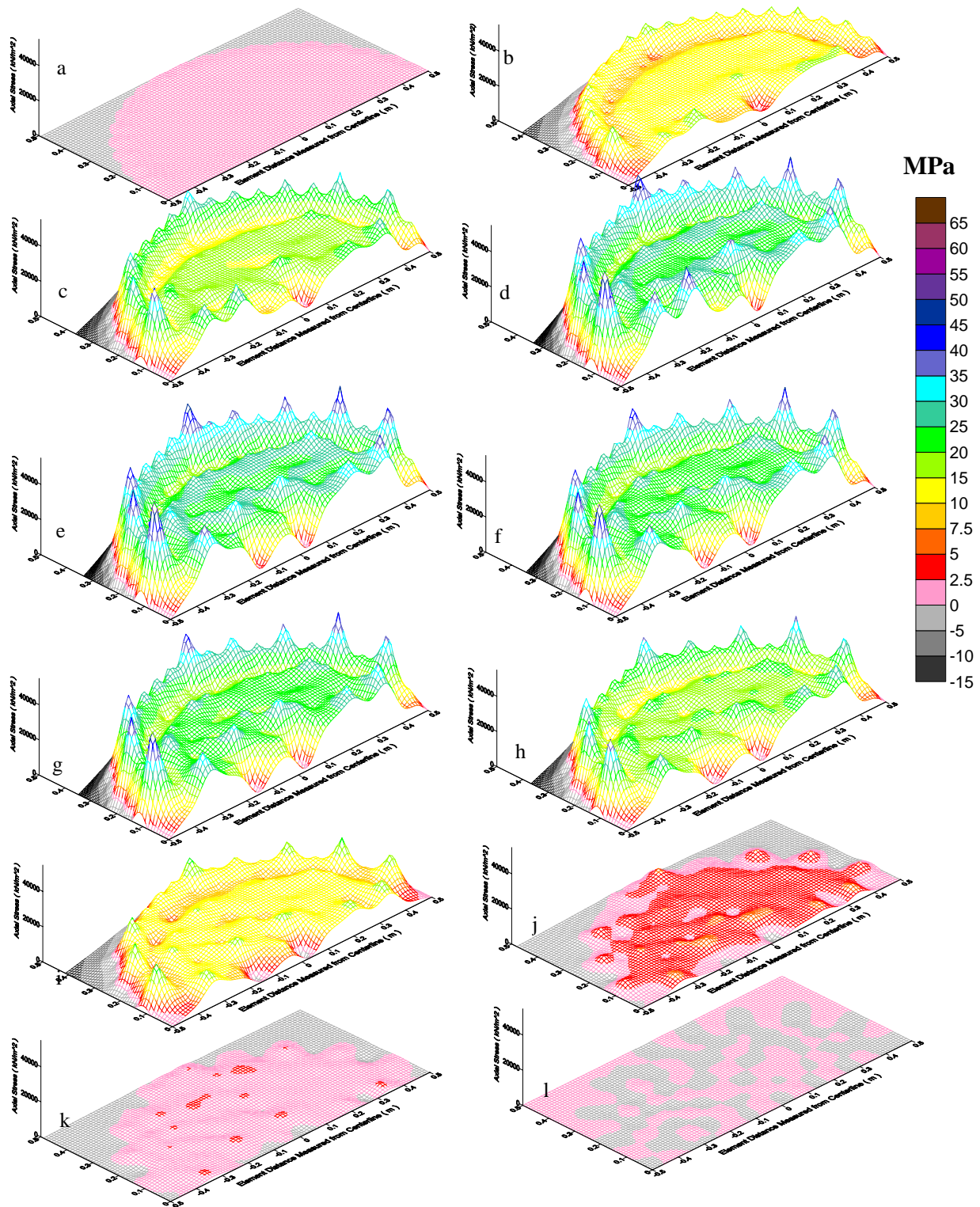


Figure 312. Calculated Normal Stress for Elements on the Concrete Surface in the FE Model with Ram Diameter = 1.0m and Tilt Angle = 0° for Time Equal to; (a) 1.8ms, (b) 2.0ms, (c) 2.5ms, (d) 3.0ms, (e) 3.5ms, (f) 4.0ms, (g) 4.5ms, (h) 5.0ms, (i) 6.0ms, (j) 7.0ms, (k) 8.0ms, and (l) 9.0ms.

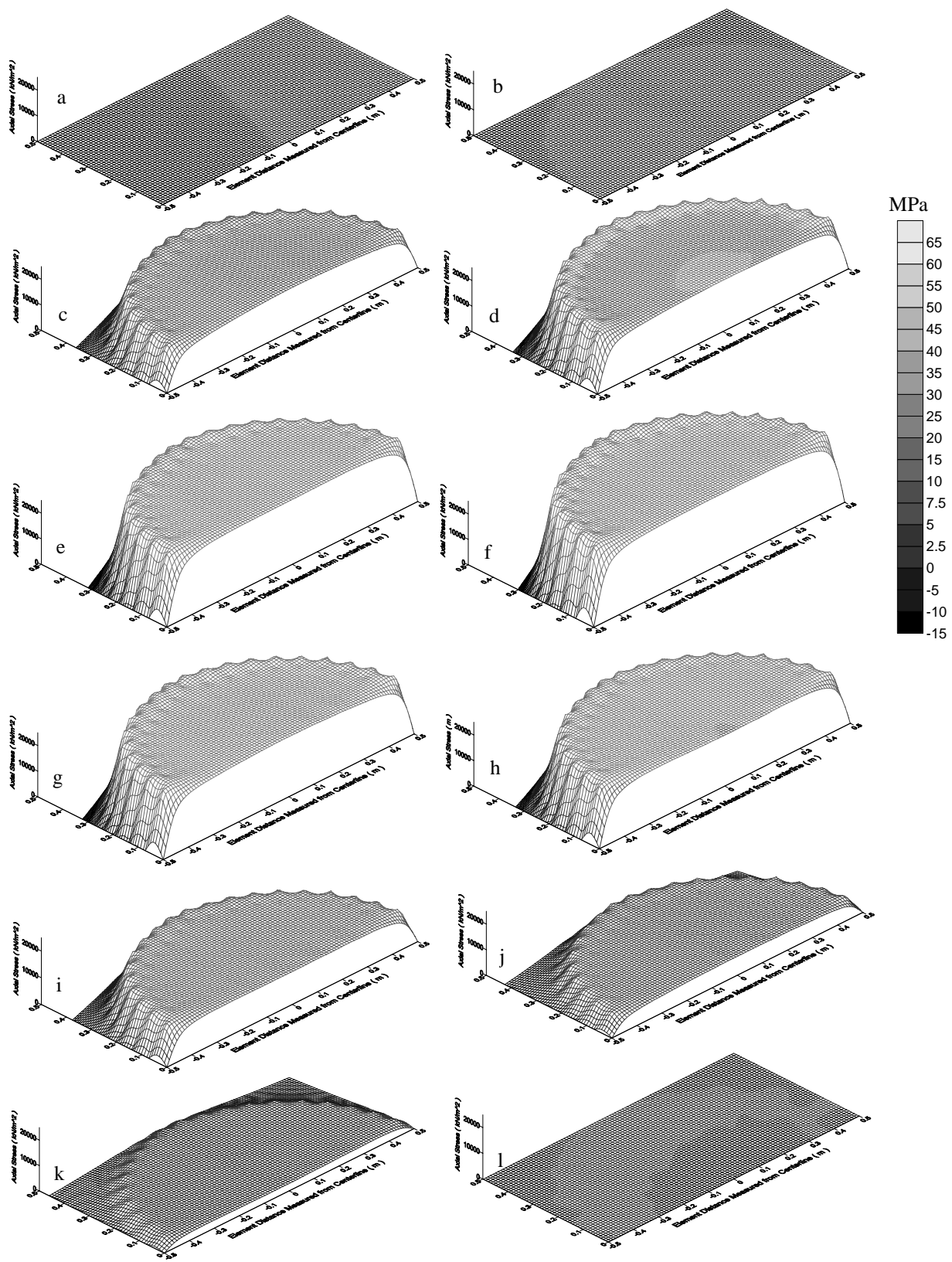


Figure 313. Calculated Normal Stress for Elements 1m Below the Concrete Surface in the FE Model with Ram Diameter = 1.0m and Tilt Angle = 0° for Time equal to; (a) 1.8ms, (b) 2.0ms, (c) 2.5ms, (d) 3.0ms, (e) 3.5ms, (f) 4.0ms (g) 4.5ms, (h) 5.0ms, (i) 6.0ms, (j) 7.0ms, (k) 8.0ms, and (l) 9.0ms.

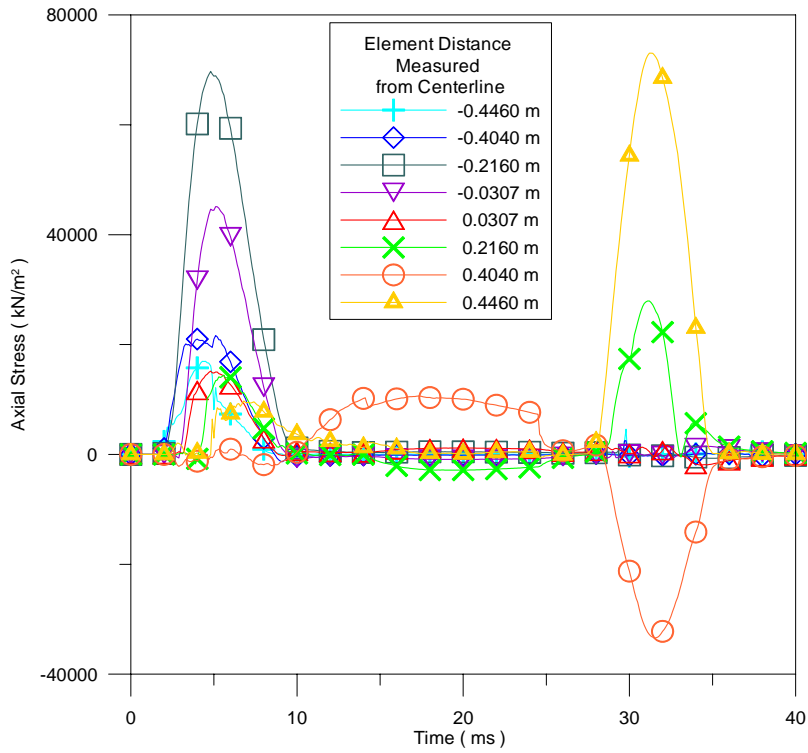


Figure 314. Calculated Normal Stress for Elements on the Concrete Surface in the FE Model with Ram Diameter = 1.0m and Tilt Angle = 1° for Time = 0ms – 40ms.

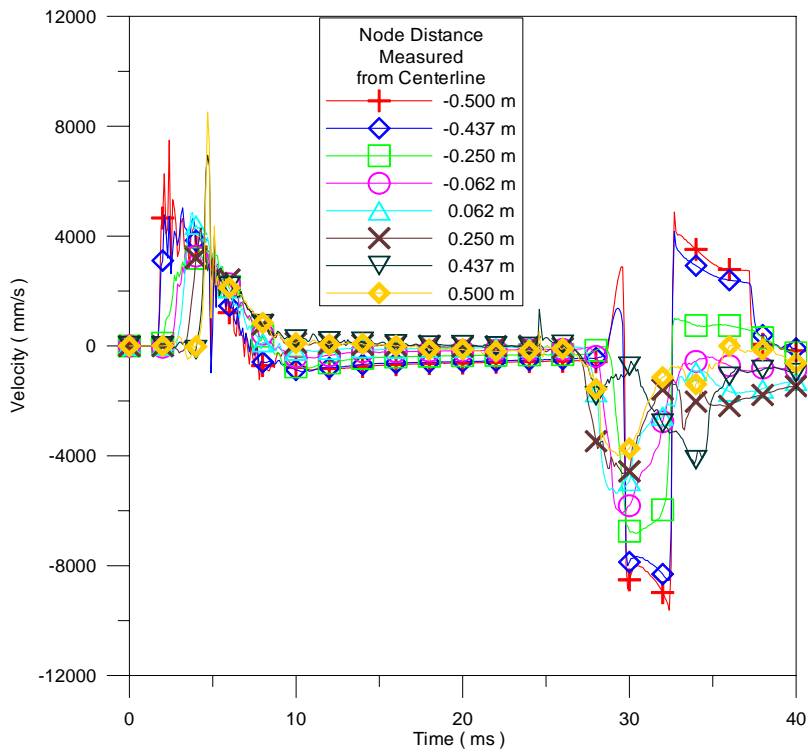


Figure 315. Calculated Velocity for Nodes on the Concrete Surface in the FE Model with Ram Diameter = 1.0m and Tilt Angle = 1° for Time = 0ms – 40ms.

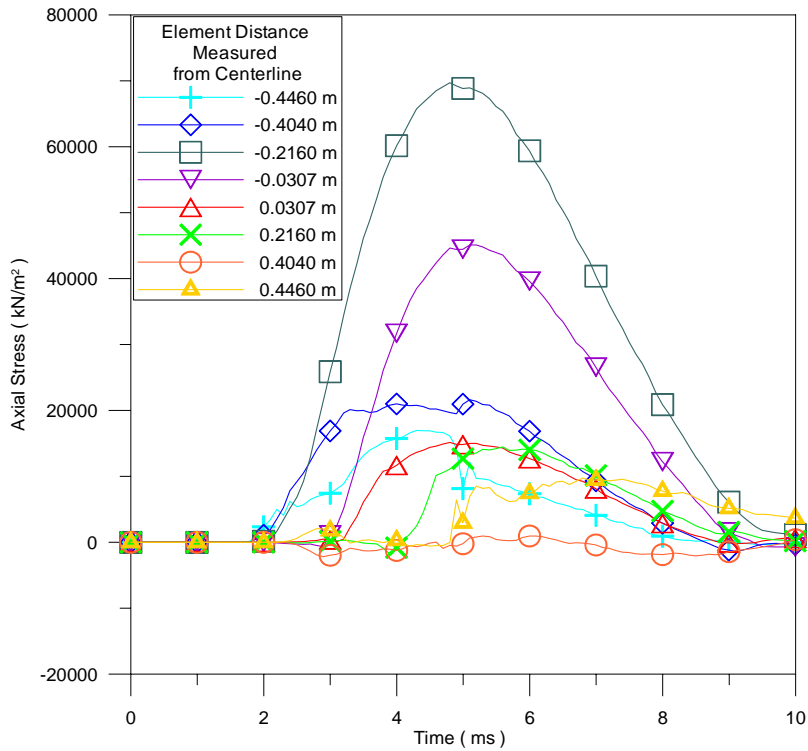


Figure 316. Calculated Normal Stress for Elements on the Concrete Surface in the FE Model with Ram Diameter = 1.0m and Tilt Angle = 1° for Time = 0ms – 10ms.

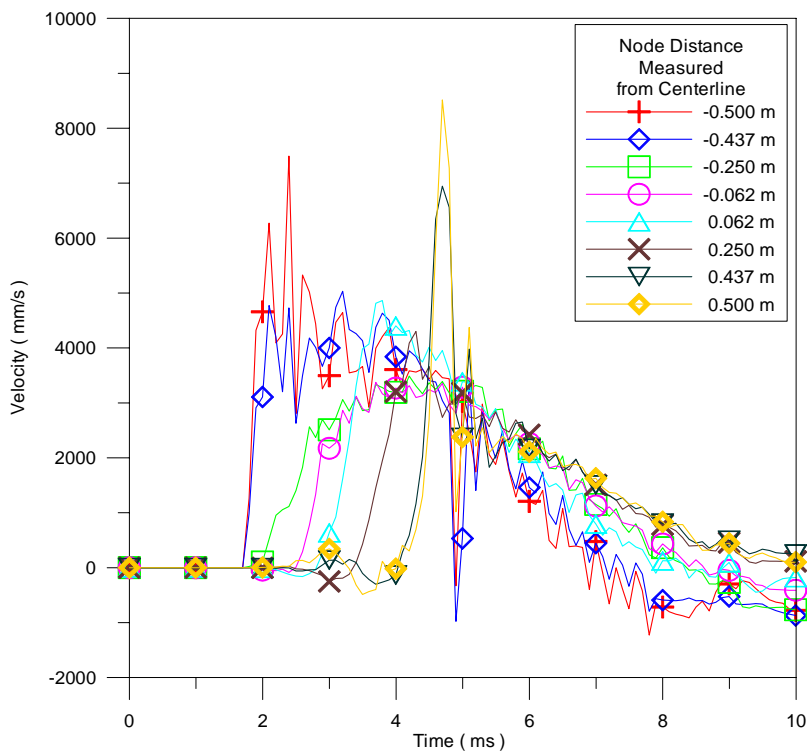


Figure 317. Calculated Velocity for Nodes on the Concrete Surface in the FE Model with Ram Diameter = 1.0m and Tilt Angle = 1° for Time = 0ms – 10ms.

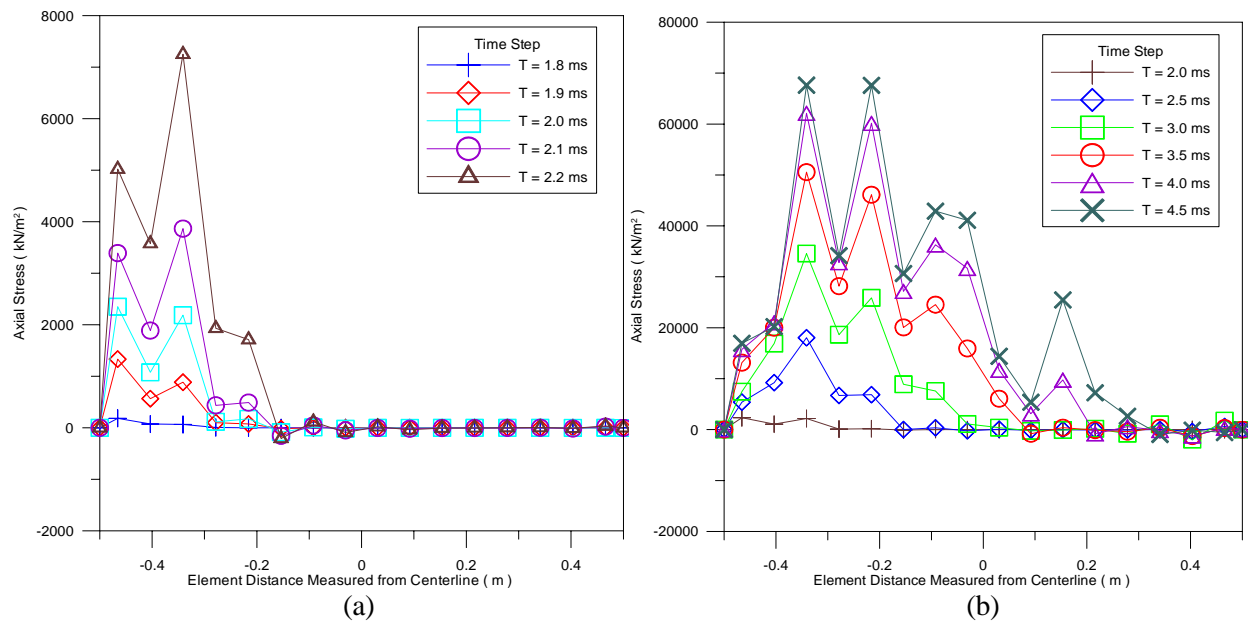


Figure 318. Calculated Normal Stress for Elements on the Concrete Surface in the FE Model with Ram Diameter = 1.0m and Tilt Angle = 1° for d = -0.5 to 0.5m and time equal to (a) 1.8 to 2.2ms, and (b) 2.0 to 4.5ms.

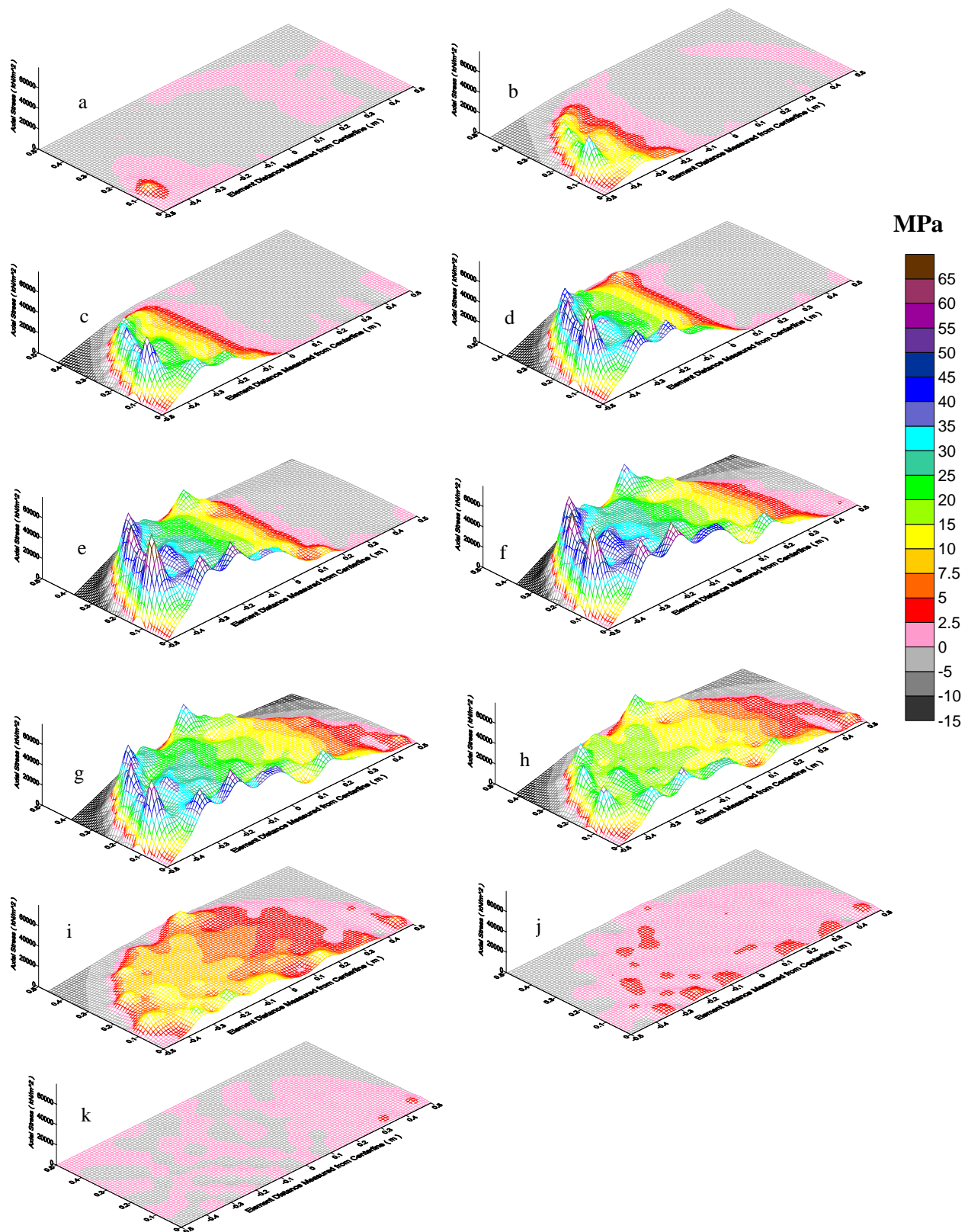


Figure 319. Calculated Normal Stress for Elements on the Concrete Surface in the FE Model with Ram Diameter = 1.0m and Tilt Angle = 1° for Time Equal to; (a) 2.0ms, (b) 2.5ms, (c) 3.0ms, (d) 3.5ms, (e) 4.0ms, (f) 5.0ms, (g) 6.0ms, (h) 7.0ms, (i) 8.0ms, (j) 9.0ms, and (k) 10.0ms.

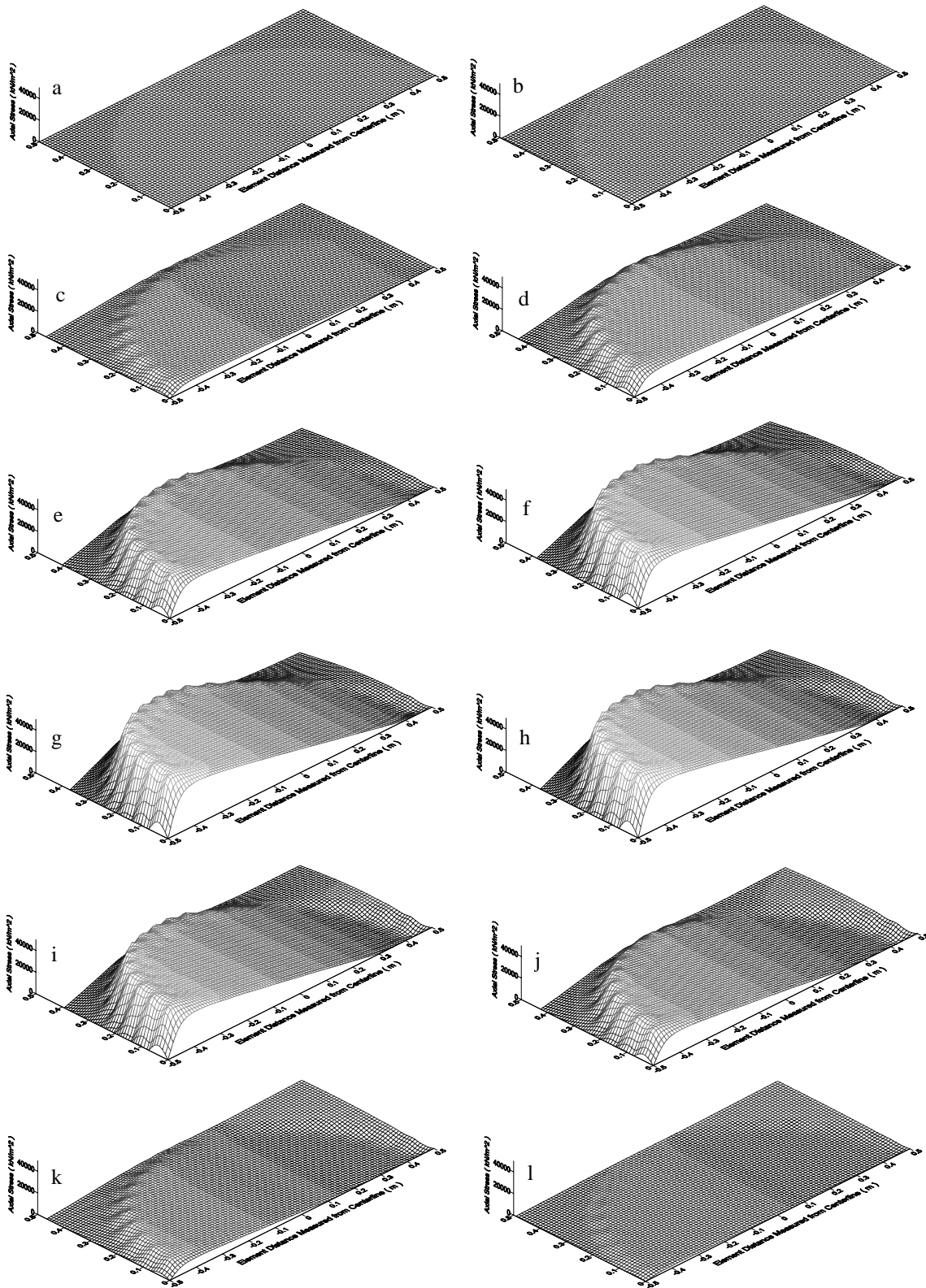


Figure 320. Calculated Normal Stress for Elements 1m Below Concrete Surface in FE Model with Ram Diameter = 1.0m and Tilt Angle = 1° for Time equal to; (a) 2.0ms, (b) 2.5ms, (c) 3.0ms, (d) 3.5ms, (e) 4.0ms, (f) 4.5ms, (g) 5.0ms (h) 6.0ms, (i) 7.0ms, (j) 8.0ms, (k) 9.0ms, and (l) 10.0ms.

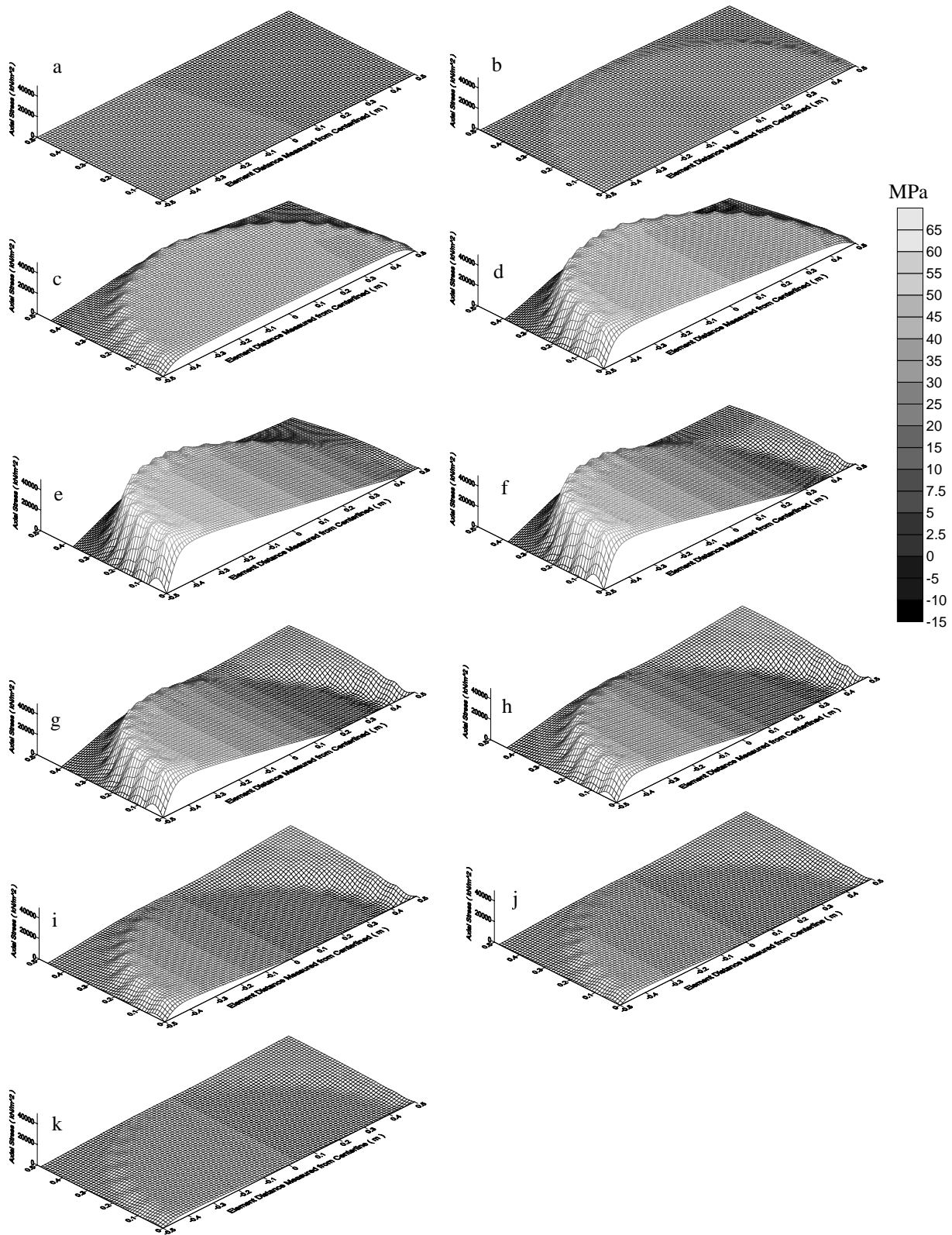


Figure 321. Calculated Normal Stress for Elements 2m Below the Concrete Surface in the FE Model with Ram Diameter = 1.0m and Tilt Angle = 1° for Time equal to; (a) 2.0ms, (b) 3.0ms, (c) 4.0ms, (d) 5.0ms, (e) 6.0ms, (f) 7.0ms, (g) 8.0ms, (h) 9.0ms, (i) 10.0ms, (j) 11.0ms, and (k) 12.0ms.

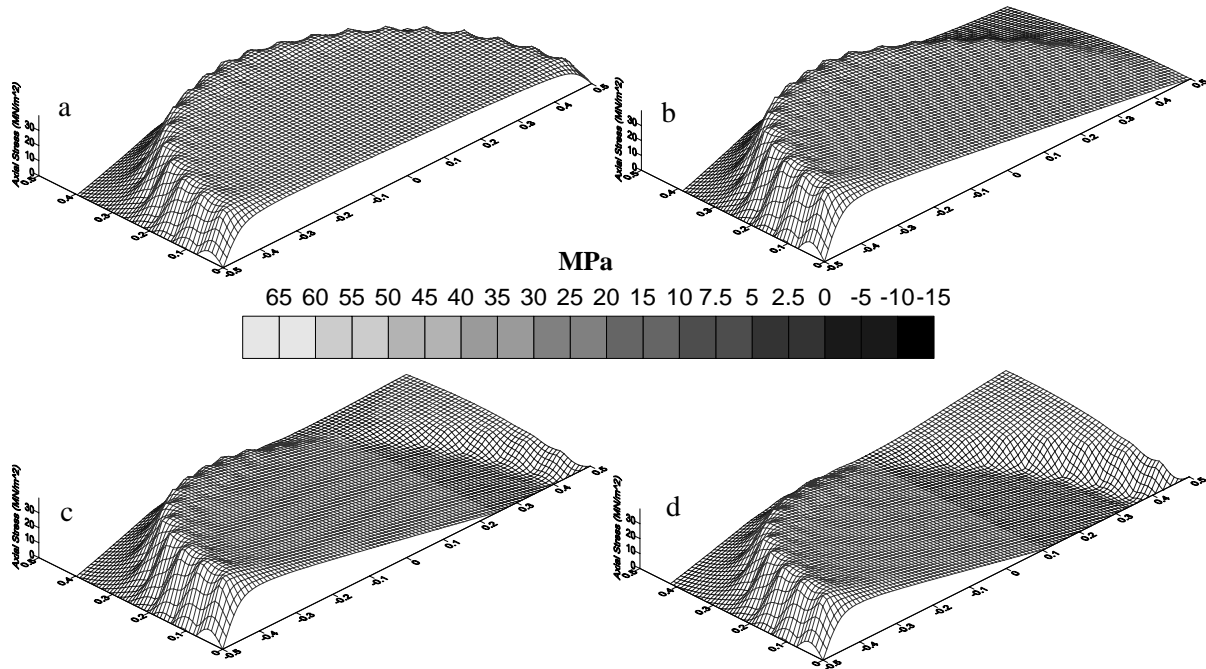


Figure 322. Calculated Normal Stress for Elements 3m Below the Concrete Surface in the FE Model with Ram Diameter = 1.0m and Tilt Angle = 1° for Time Equal to (a) 6.0ms, (b) 7.0ms, (c) 8.0ms, and (d) 9.0ms.

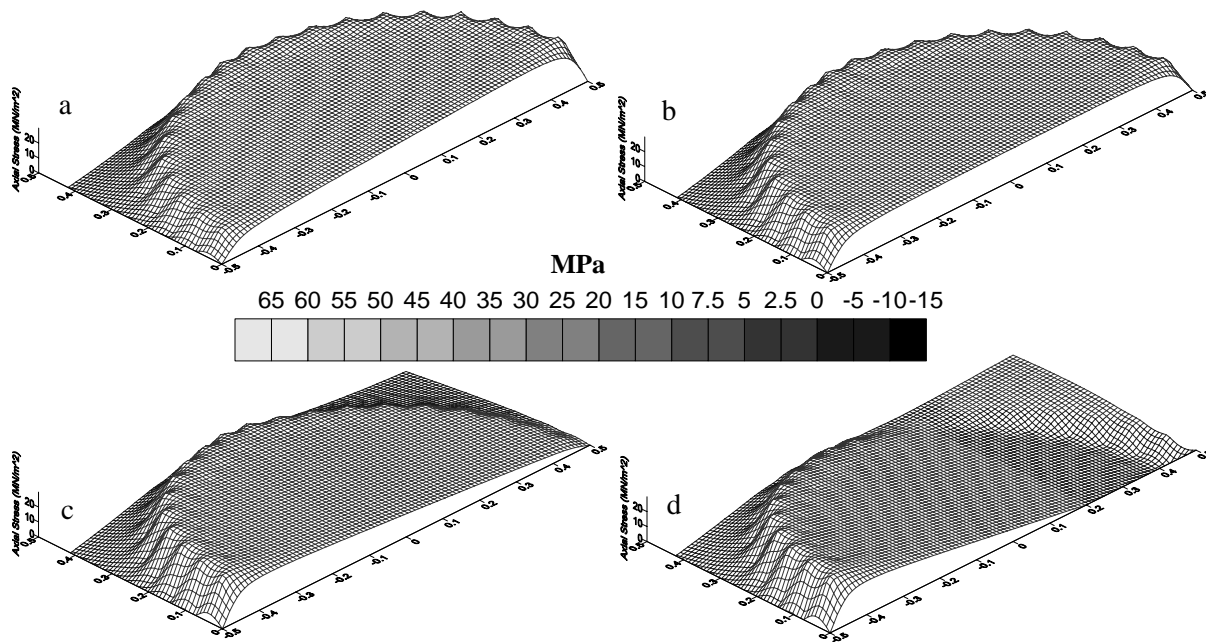


Figure 323. Calculated Normal Stress for Elements 4m Below the Concrete Surface in the FE Model with Ram Diameter = 1.0m and Tilt Angle = 1° for Time Equal to (a) 6.0ms, (b) 7.0ms, (c) 8.0ms and (d) 9.0ms.

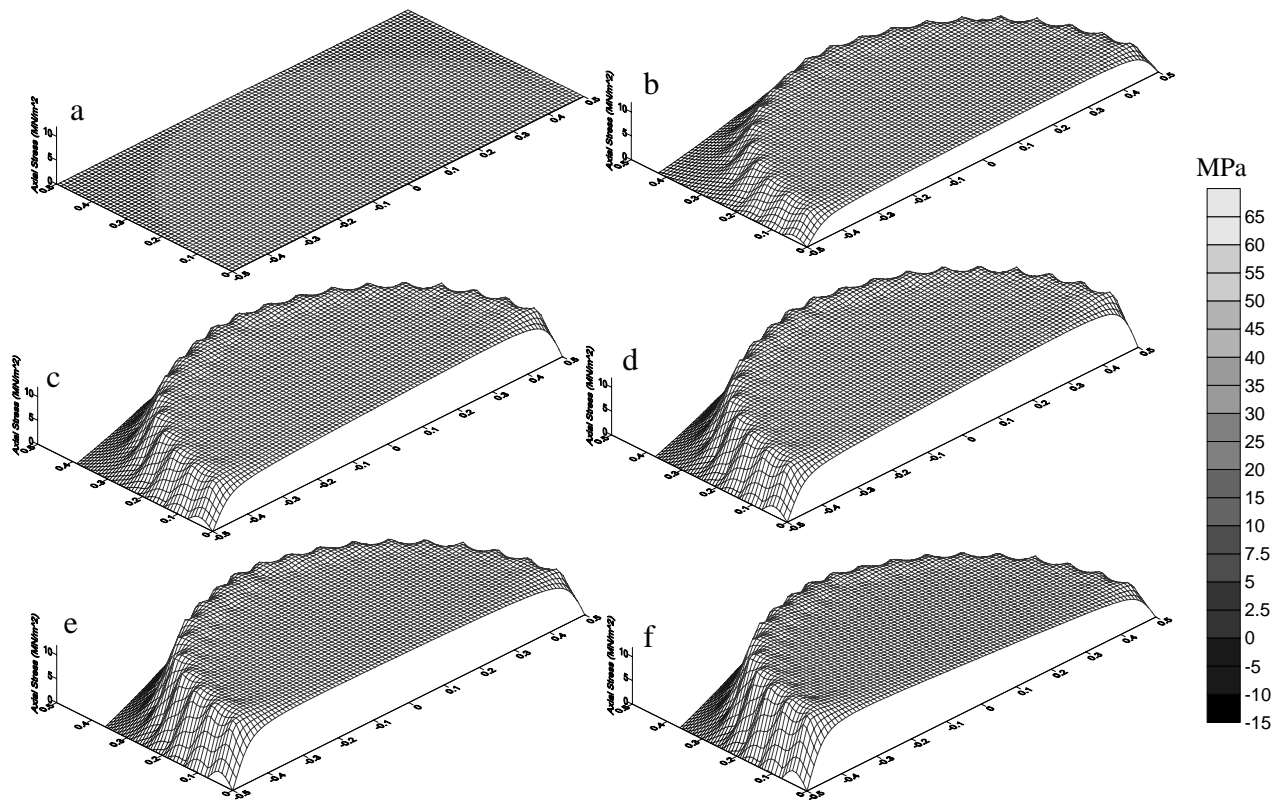


Figure 324. Calculated Normal Stress for Elements 2m Below the concrete Surface in the FE Model with Ram Diameter = 1.0m and Tilt Angle = 1° with a Soft Cushion for Time Equal to (a) 3ms, (b) 6ms, (c) 8ms, (d) 10ms, (e) 12ms, and (f) 14ms.

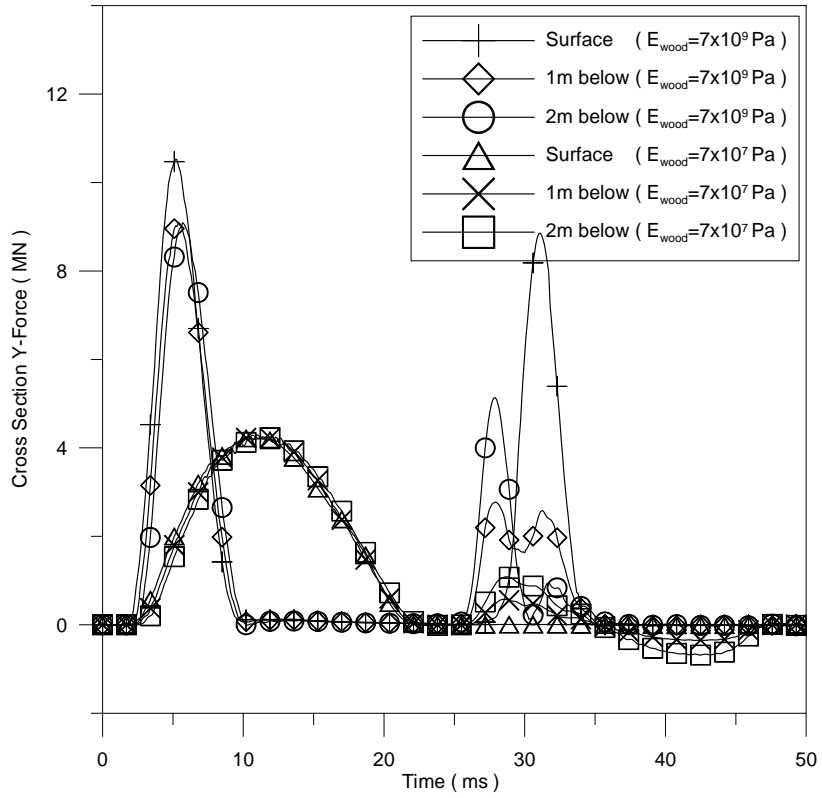


Figure 325. Average Forces with Time Across the Shaft at the Top (Surface) and One and Two Diameters Below the Surface (1m, 2m Respectively) for Representative and “Soft” Wood Cushions.

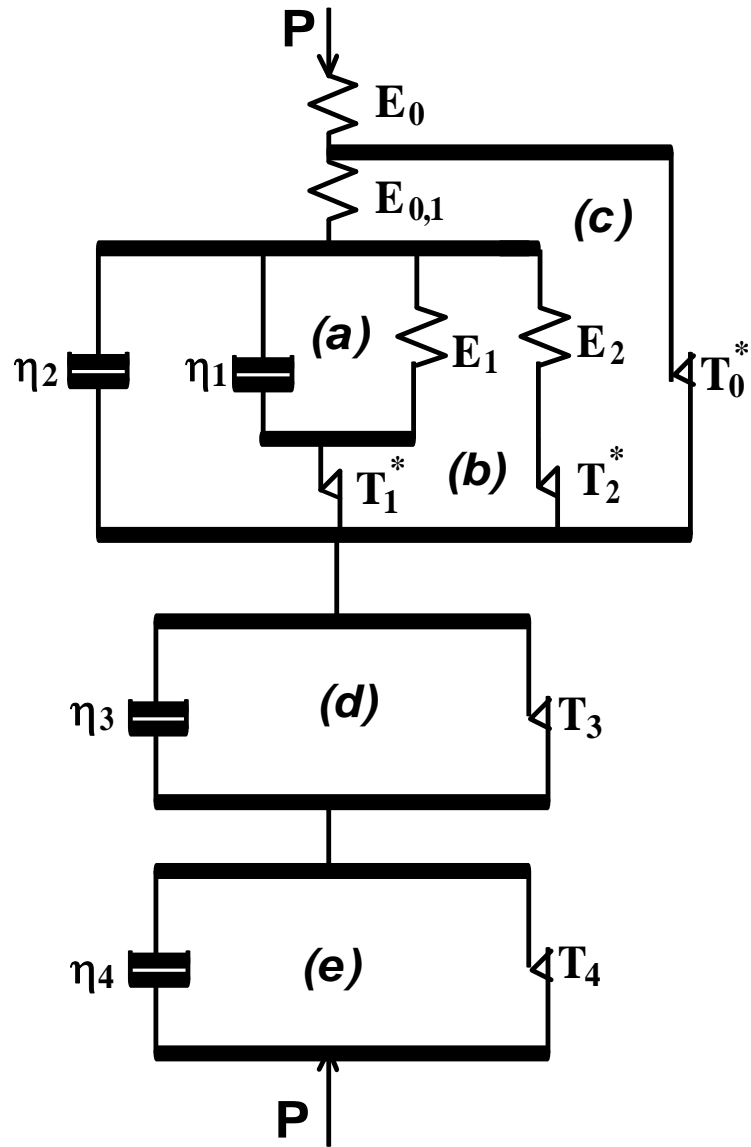


Figure 326. The Rheological Model Component for the Description of Pile-Soil Interaction

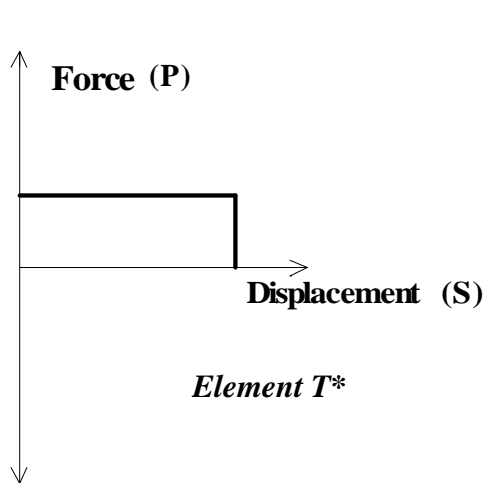


Figure 327. Load Displacement Relations for Element T

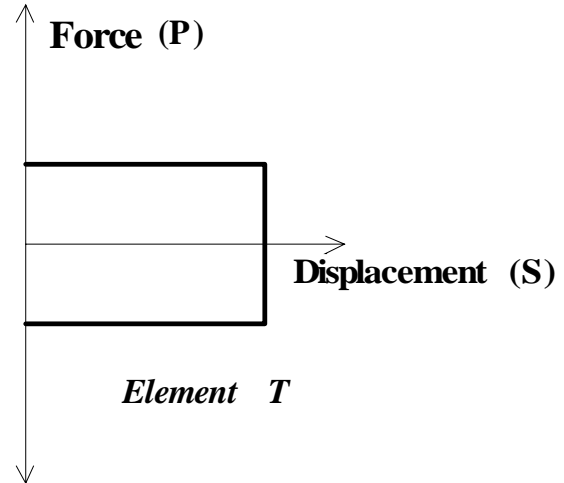


Figure 328. Load Displacement Relations for Element T*

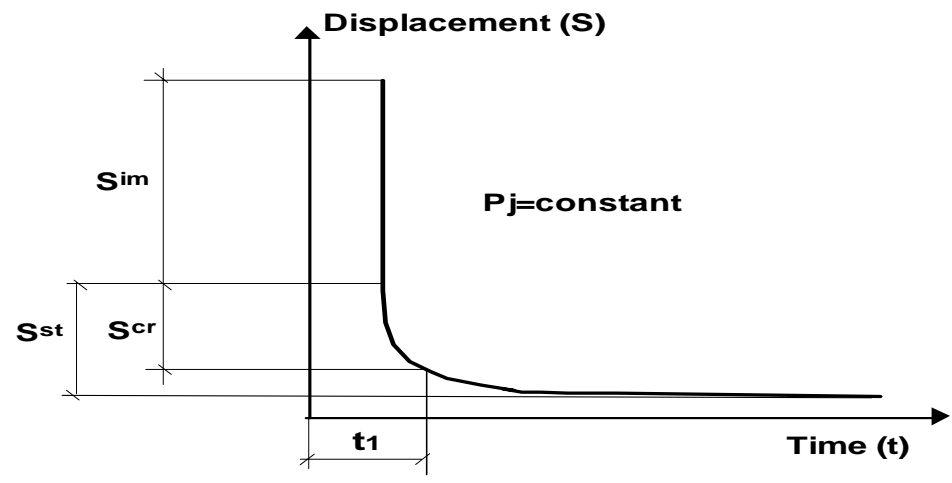


Figure 329. Time-Settlement Relations Under a Constant Load Step P_j

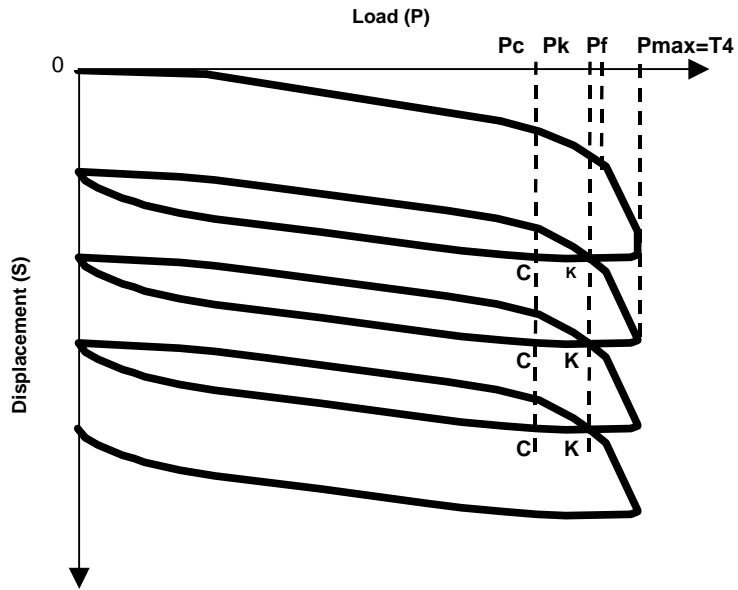


Figure 330. Load-Displacement Relations for a Compression Express static-Cyclic Test with Defined Controlling Loads, the Maximum Elastic Load (P_c), the Bearing Capacity (P_k), the Failure Load (P_f) and the Maximum Applied Load (P_{max}).

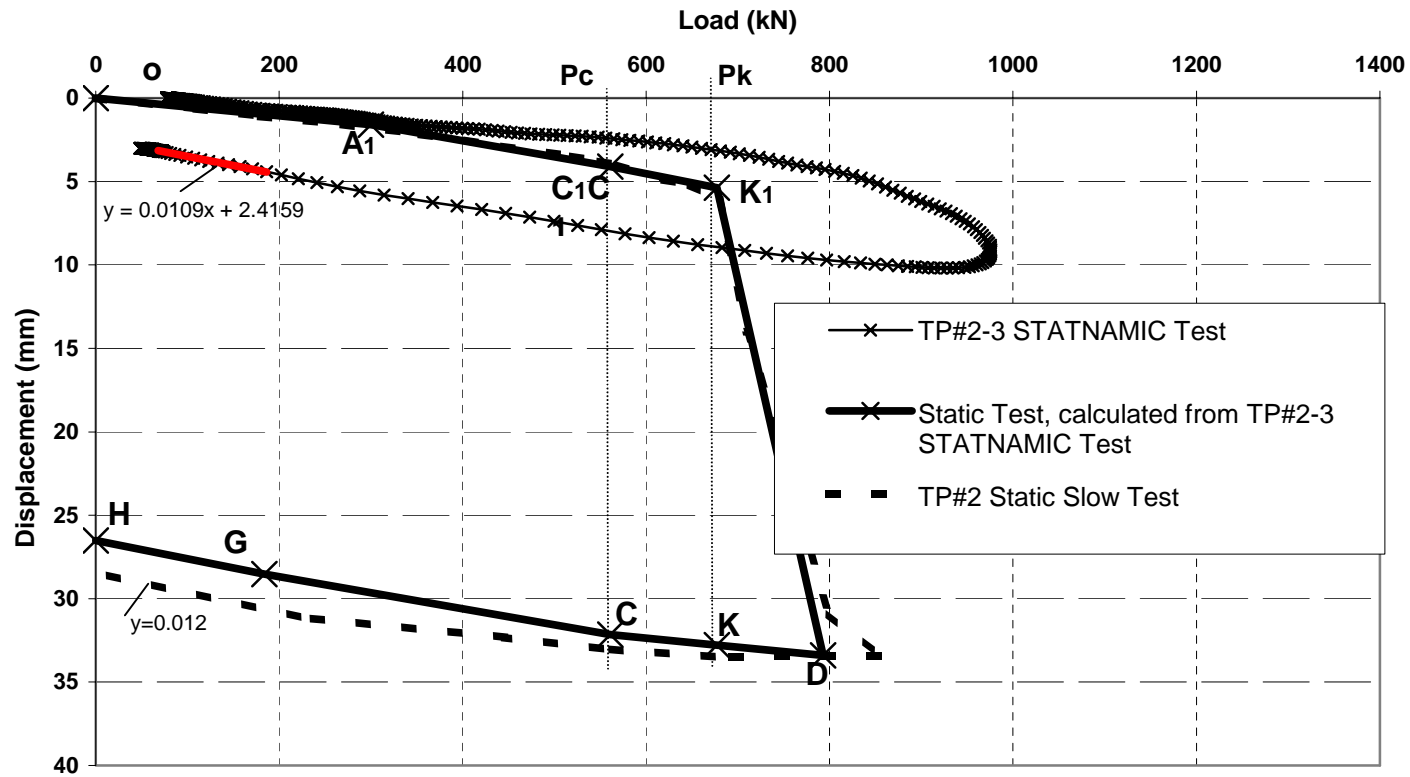


Figure 331. Comparison of Load-Displacement Relations for a Static Slow Maintained Load Test Measured and Calculated by the Rheological Model Based on a Statnamic Test No. 3 on Newbury Test Pile No. 2 (TP#2-3)

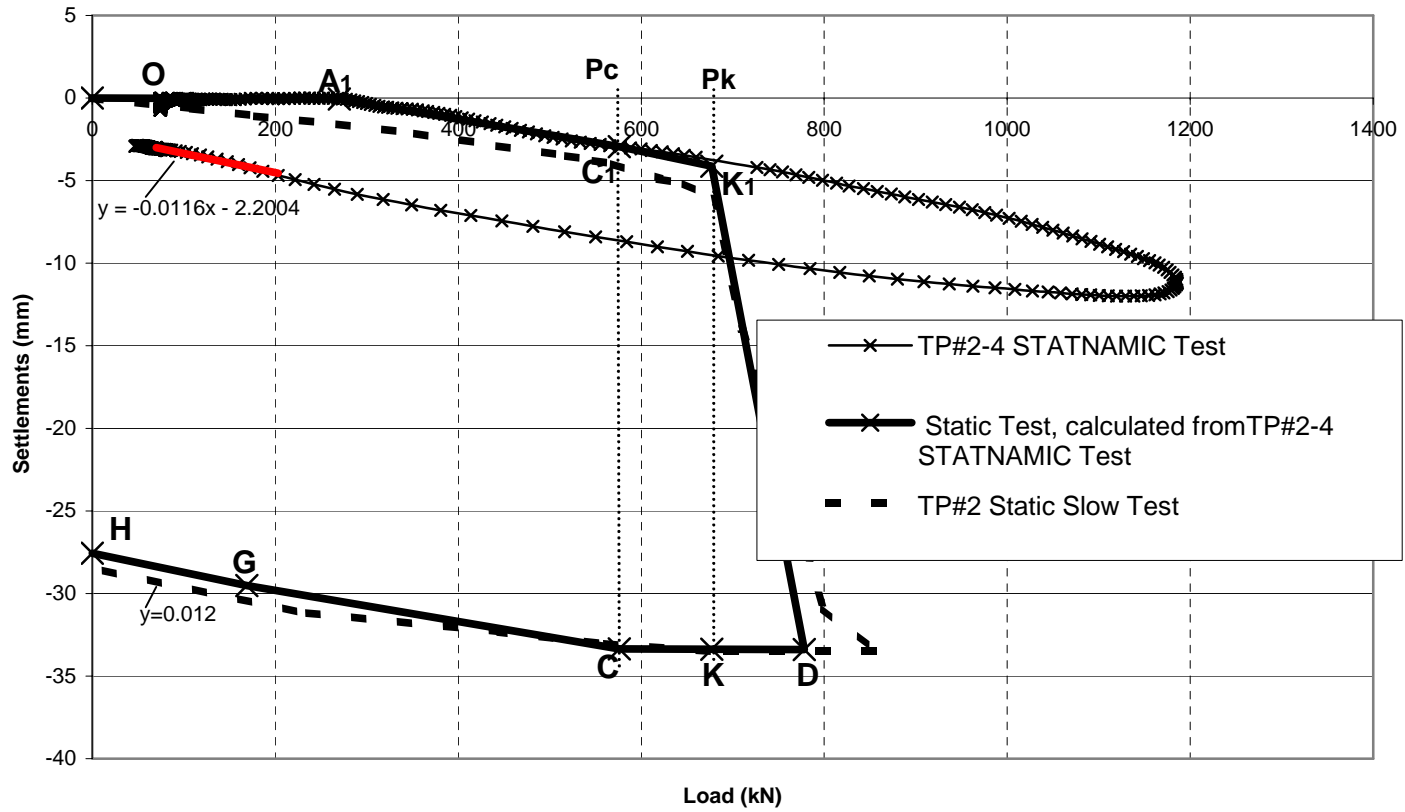


Figure 332. Comparison of Load-Displacement Relations for a Static Slow Maintained Load Test Measured and Calculated by the Rheological Model Based on a Statnamic Test No. 4 on Newbury Test Pile No. 2 (TP#2-4)

Table 1. Typical Key Attributes of Different Types of Pile Tests (Holeyman, 1992).

Attributes \ Test Type	Integrity Testing	High-Strain Dynamic Testing	Kinetic Testing	Static Testing
Mass of Hammer	0.5 - 5kg	2,000 - 10,000 kg	2,000 - 5,000 kg	N/A
Pile Peak Strain	2 - 10 μ str	500 - 1,000 μ str	1,000 μ str	1,000 μ str
Pile Peak Velocity	10 - 40 mm/s	2,000 - 4,000 mm/s	500 mm/s	10^{-3} mm/s
Peak Force	2 - 20 kN	2,000 - 10,000 kN	2,000 - 10,000 kN	2,000 - 10,000 kN
Force Duration	0.5 - 2 ms	5 - 20 ms	50 - 200ms	10^7 ms
Pile Acceleration	50 g	500 g	0.5 - 1 g	10^{-14} g
Pile Displacement	0.01 mm	10 - 30 mm	50 mm	>20 mm
Relative Wave Length	0.1	<1.0	>10	10^8

Table 2. Summary of Innovative Load Testing Methods and Analyses

Test Type	Test Principle	Testing Method	Manufacturer Developer	Available Analysis Method										Usage	
				Wave Analysis			Dynamic			Static			Other		
				Case	WM	SPS	UP	EA	PS	OC	SC	RM		Type	Extent
DYNAMIC	Dynamic - Wave Action	Drop Weight	Varied	Y	Y			Y						Rep.	WW
		SIMBAT	CEBTP France	Y	Y			Y						Rep.	L
		SmartPile (SPS)	Frederick Engineering			Y		P						Ex./Rep.	L
		Smart Coil (SCS)	Frederick Engineering									Y		Rep.	L
	Dynamic - Fast Penetration	STATNAMIC	Berming-hammer	P	P		Y							Rep.	WW
		Dynatest	France Atlas	P	P		Y							Rep.	L
		PSPLT	Fundex				P		Y					Rep.	L
		Pile Load Tester	American Pile Driving				P		Y					Rep.	L
STATIC	New Static	Osterberg Load Cell	Load Test							Y	P	P		Ex.	WW
		Static-Cyclic	UML								Y	Y		Rep.	L

Legend:

Dynamic Fast Penetration: PSPLT = Pseudo Static Load Tester

Available Analysis Methods: (Y = Yes, P = Possible)

Wave Analysis: Case: Case Method

Dynamic: UP: Unloading Point Method

Static: OC: Osterberg Load Cell

WM: Wave Matching (e.g. CAPWAP)

EA: Energy Approach Method

SC: Static-Cyclic

SPS: SmartPile System

PS: Pseudo-Static

RM: Rheological Modeling

Usage Type: (Rep. = Repetitive, Ex. = Expendable), L = Limited, WW = Worldwide

Table 3. Summary of Drop Weight Systems

System Designation	Geographic Location	Ram Weight (kN)	Stroke (m)	Max Energy (kN•m)	Comments	Reference	Figure
DW-A	China Zhanjing	30, 50, 80	4	320	Requires a crane and includes a guidance system	Li, 1993	10
DW-B	China Shanghai	60	2.5	150	Does not require a crane, has a limited guiding system	Li, 2000	11
DW-C	China Shanghai	20-90	4	360	Requires a crane, does not have a guiding system	Weibirg, 2000	12
DW-D	Israel	20-90	4	360	Requires a crane, guided system with a modular ram and strokes	GTR, 1997	13
DW-E	Israel	35	1.5(?)	53	Requires a crane, effectiveness of guiding system is questionable	Sokolovski et al., 1998	14
DW-F	USA	50-200	2.7	540	Part of the Newton system with instrumented ram	Robinson & Rausche, 2000	15
DW-G	USA Texas A&M	90	5	450	Requires a crane, includes a guidance system, available pile-driving hammer	Briaud et al., 2000	16
DW-H	USA UOF	100	3	300	Requires a crane, includes a guidance system, available pile-driving hammer	Townsend et al., 1991	17
DW-I	China Shanghai	20-80	4	320	Includes a self lifting winch and guidance system, does not require a crane	Longgen, et. al, 1999	18

Table 4. Sources for Possible Difficulties of Dynamic Measurements on In-place Constructed Deep Foundations

Case	Description	Comment	Figure	Effect	Possible Remedy
1	Non-uniform Cross-section	Mostly dry or slurry construction		<ul style="list-style-type: none"> • Unknown area for force calculations • Wave reflections and analysis of unknown geometry 	<ul style="list-style-type: none"> • Use of a caissing at the top part of the shaft
2	Uneven shaft surface	All type of construction		<ul style="list-style-type: none"> • Uneven impact results with uneven stress distribution and hence misleading force calculations 	<ul style="list-style-type: none"> • Careful leveling of the shaft top with above ground extension • Multiple gauges (4) located 2-3 diameters below impact • Additional acceleration measurements on the ram
3	Poor quality concrete in the exterior sections	Mostly slurry construction		<ul style="list-style-type: none"> • Inaccurate force measurements as force calculations based on typical modulus do not reflect actual gauge location conditions 	<ul style="list-style-type: none"> • Use of caissing and concrete quality control at the end of construction (e.g. placing concrete until clear concrete appears at the top)
4	Uneven ram impact	<ul style="list-style-type: none"> • Poor or no guiding system • Uneven shaft surface 		<ul style="list-style-type: none"> • Uneven stress distribution 	<ul style="list-style-type: none"> • Use of a cushion • Use of a guiding system for the ram • Placing gauges as suggested in 2
5	Small section ram	<ul style="list-style-type: none"> • Shaft area larger than ram's 		<ul style="list-style-type: none"> • Uneven stress distribution to a limited distance below impact 	<ul style="list-style-type: none"> • Use of a cushion • Use of a striking plate • Placing gauges as suggested in 2
6	High friction at the top of the shaft	Placement of concrete against rock or granular dense soil		<ul style="list-style-type: none"> • Non proportionality between force and velocity due to early reflections does not allow verification of data quality and difficulties in analysis 	<ul style="list-style-type: none"> • Placing gauges as suggested in 2 • Careful signal matching analysis

Table 5. Listing of Statnamic Devices and Capacities

Manufacturer Rated Capacity	Practical Load Application Range
30 MN	7.5 - 33 MN
20 MN	5 - 22 MN
16 MN	4 - 17.6 MN
14 MN	3.5 - 15.4 MN
8 MN	2 - 8.8 MN
5 MN	1.25 - 5.5 MN
4 MN	1 - 4.4 MN
3 MN	0.75 - 3.3 MN
0.6 MN	0.15 - 0.66 MN
98.9 kN	2.2 - 9.8 kN

Table 6. Summary of Static Load Test Procedures (after Paikowsky et al. 1999)

Code	Test Name	Loading		Hold Time at Max. Load	Unloading		Hold time at Zero Load
		Increments	Hold Time		Increments	Hold Time	
ASTM	<i>Standard Loading Procedure</i>	25%	.01"/Hr	12-24 Hr	25%	1 hr and .01"/Hr	1 Hr
	<i>Cyclic Loading</i>	50%	1 Hr	0 Hr	50%	.33 Hr	1 Hr
		50%	.33 Hr	12-24 Hr	25%	1 Hr	0 Hr
	<i>Quick Load Test</i>	10-15%	2.5 Min	5 min	1 step	Instantaneous	0 Hr
<i>Constant Rate of Penetration</i>	0.25-2.5 mm/min (.01-.1 in/min)	0 Hr	-	-	-	-	
MHD	<i>Short Duration</i>	25%	.5 Hr	1 Hr	25%	.25 Hr	1 Hr
	<i>Maintained Load Test</i>	50%	2 Hr	12-24 Hr	25%	4 Hr	4 Hr
	<i>Quick Load Test</i>	50-100 kN	2.5 min	5 min	25% of Max.	2.5 min	15 min
MBC	<i>Loading Procedure</i>	25%	.5 Hr	1 Hr	25%	.25 Hr	1 Hr
TQT	<i>Quick Load Method</i>	10-15%	2.5 min	2.5 min	1 step	Instantaneous	2.5 min
S USSR	<i>Standard STest</i>	1/10 Max	Varies	-	2 x loading	.25 Hr	-
Recent Research	<i>Static-cyclic loading</i>	3 cycles to failure at 150kN/min (15t/min)	0	0	Rate of 300kN/min (30t/min)	0	0

Notes:

1. ASTM American Standard for Testing and Materials
2. MHD Massachusetts Highway Department
3. MBC Massachusetts Building Code
4. TQT Texas Quick Test
5. S USSR Standard USSR State Code
6. All percentages are in percent of total design load of the pile.
7. The loading increment for the standard test is based on the assumed bearing capacity of the pile.

Table 7. Comparison of the Maximum Mobilized Unit Shaft Resistance, Henderson Case

Depth Interval	Measured (O-cell Test) (ksf)	FE Model (O-cell Test) (ksf)	FE Model (Top Down Test) (ksf)
Gage 1 to O-cell	6.02	5.62	4.06
O-cell to Gage 2	8.83	6.67	5.30
Gage 2 to Gage 3	2.72	4.41	5.03
Gage 3 to Pile Top	1.08	1.57	6.49

Table 8. Comparison of the Unit Shaft Resistance Between Field Test Results and Model Results, Wilsonville Case

Applied Load (tons)	O-cell to Gage 1		Gage 1 to Gage 2		Gage 2 to Gage 3		Gage 3 to Gage 4	
	From Test (tsf)	From Model (tsf)	From Test (tsf)	From Model (tsf)	From Test (tsf)	From Model (tsf)	From Test (tsf)	From Model (tsf)
183 (198)	0.5	4.7	2.3	1.7	1.8	0.8	0.5	0.5
246 (248)	3.9	5.4	1.6	2.2	2.0	1.1	0.7	0.7
308 (298)	3.2	5.6	3.4	2.8	2.5	1.5	0.9	0.9
434 (446)	4.7	4.0	4.0	4.8	3.3	3.3	1.2	1.7
496 (496)	6.3	3.8	4.3	4.8	3.8	4.1	1.3	1.5

Table 9. Comparison of the Maximum Mobilized Unit Shaft Resistance, Wilsonville Case

Depth Interval	Measured (O-cell Test) (tsf)	FE Model (O-cell Test) (tsf)	FE Model (Top Down Test) (tsf)
O-cell to Gage 1	7.8	5.6	3.6
Gage 1 to Gage 2	4.3	4.8	4.1
Gage 2 to Gage 3	3.8	4.1	4.2
Gage 3 to Gage 4	1.3	1.7	4.5

Table 10. Comparison of Side Shear at Gage Intervals Between Field Test Results and Model Results, Denver Case

Applied Load (kips)	O-cell to Gage 1		Gage 1 to Gage 2		Gage 2 to Pile Top	
	From Test (ksf)	From Model (ksf)	From Test (ksf)	From Model (ksf)	From Test (ksf)	From Model (ksf)
273 (279)	2.05	2.31	0.76	0.81	0.42	0.39
351 (355)	2.44	2.91	1.38	1.09	0.63	0.56
429 (449)	2.87	2.86	1.82	1.83	0.82	1.09
507 (505)	3.25	2.75	2.28	2.35	1.03	1.28
559 (559)	3.61	2.58	2.63	2.80	1.03	1.61

Table 11. Comparison of the Maximum Mobilized Unit Shaft Resistance, Denver Case

Depth Interval	Measured (O-cell Test) (ksf)	FE Model (O-cell Test) (ksf)	FE Model (Top Down Test) (ksf)
O-cell to Gage 1	3.61	2.91	2.73
Gage 1 to Gage 2	2.63	2.80	3.06
Gage 2 to Pile Top	1.03	1.61	2.25

Table 12. Effect of Different Factors on Pile Response and Difference Between Two Testing Methods

E_{rock} (ksi)	$\phi_i = 14^\circ$			$\phi_i = 31^\circ$			$\phi_i = 50^\circ$		
	$(f_{rock})_{td}$ (psi)	$(f_{rock})_{oc}$ (psi)	$\frac{(f_{rock})_{td}}{(f_{rock})_{oc}}$	$(f_{rock})_{td}$ (psi)	$(f_{rock})_{oc}$ (psi)	$\frac{(f_{rock})_{td}}{(f_{rock})_{oc}}$	$(f_{rock})_{td}$ (psi)	$(f_{rock})_{oc}$ (psi)	$\frac{(f_{rock})_{td}}{(f_{rock})_{oc}}$
70	29.83	28.43	1.05	42.70	37.31	1.14	64.80	49.76	1.30
700	42.31	30.92	1.37	72.82	44.00	1.66	152.20	60.68	2.51
7000	139.63	43.70	3.20	/	/	/	/	/	/

(a) Effect of ϕ_i and E_{rock}

ϕ_i ($^\circ$)	$c_i = 0$			$c_i = 10\text{ psi}$			$c_i = 20\text{ psi}$		
	$(f_{rock})_{td}$ (psi)	$(f_{rock})_{oc}$ (psi)	$\frac{(f_{rock})_{td}}{(f_{rock})_{oc}}$	$(f_{rock})_{td}$ (psi)	$(f_{rock})_{oc}$ (psi)	$\frac{(f_{rock})_{td}}{(f_{rock})_{oc}}$	$(f_{rock})_{td}$ (psi)	$(f_{rock})_{oc}$ (psi)	$\frac{(f_{rock})_{td}}{(f_{rock})_{oc}}$
14	10.30	10.27	1.00	20.05	19.44	1.03	29.83	28.43	1.05
31	23.05	21.50	1.07	32.92	29.67	1.11	42.70	37.31	1.14
50	44.65	37.57	1.19	54.81	43.83	1.25	64.80	49.76	1.30

(b) Effect of c_i

Elastic Rock			$c_{rock} = 200\text{ psi}$			$c_{rock} = 50\text{ psi}$		
$(f_{rock})_{td}$ (psi)	$(f_{rock})_{oc}$ (psi)	$\frac{(f_{rock})_{td}}{(f_{rock})_{oc}}$	$(f_{rock})_{td}$ (psi)	$(f_{rock})_{oc}$ (psi)	$\frac{(f_{rock})_{td}}{(f_{rock})_{oc}}$	$(f_{rock})_{td}$ (psi)	$(f_{rock})_{oc}$ (psi)	$\frac{(f_{rock})_{td}}{(f_{rock})_{oc}}$
45.97	44.69	1.03	42.70	37.31	1.14	38.76	29.12	1.33

(c) Effect of c_{rock}

L_{socket} / D	$\phi_i = 31^\circ$			$\phi_i = 50^\circ$		
	$(f_{rock})_{td}$ (psi)	$(f_{rock})_{oc}$ (psi)	$\frac{(f_{rock})_{td}}{(f_{rock})_{oc}}$	$(f_{rock})_{td}$ (psi)	$(f_{rock})_{oc}$ (psi)	$\frac{(f_{rock})_{td}}{(f_{rock})_{oc}}$
1.5	42.74	37.37	1.14	61.47	51.02	1.20
3.0	41.70	38.07	1.10	61.85	51.08	1.21
5.0	42.70	37.31	1.14	64.80	49.76	1.30
10.0	46.78	37.97	1.23	74.47	48.44	1.54

(d) Effect of L_{socket} / D

K_0	$\phi_i = 31^\circ$			$\phi_i = 50^\circ$		
	$(f_{rock})_{td}$ (psi)	$(f_{rock})_{oc}$ (psi)	$\frac{(f_{rock})_{td}}{(f_{rock})_{oc}}$	$(f_{rock})_{td}$ (psi)	$(f_{rock})_{oc}$ (psi)	$\frac{(f_{rock})_{td}}{(f_{rock})_{oc}}$
0.43	28.97	21.77	1.33	37.07	26.39	1.40
1.0	42.70	37.31	1.14	64.80	49.76	1.30

(e) Effect of K_0

Table 13. Detailed Results for Different E_p / E_s

E_p / E_s	O-cell Test		Top Down Test		f_{td} / f_{oc}
	Bottom Load (kips)	Average Side Shear (psi)	Top Load (kips)	Average Side Shear (psi)	
1	1550	72	12100	500	6.9
10	580	27	1300	36	1.3
100	510	24	1000	25	1.04

Table 14. Detailed Results for Different ϕ_i

ϕ_i	O-cell Test		Top Down Test		f_{td} / f_{oc}
	Bottom Load (kips)	Average Side Shear (psi)	Top Load (kips)	Average Side Shear (psi)	
14°	480	23	990	25.5	1.1
31°	580	27	1290	36	1.3
50°	770	36	2050	63	1.7

Table 15. Detailed Results for Different c_i

c_i (psi)	O-cell Test		Top Down Test		f_{td} / f_{oc}
	Bottom Load (kips)	Average Side Shear (psi)	Top Load (kips)	Average Side Shear (psi)	
10	340	16	750	21	1.3
20	580	27	1290	36	1.3
40	1050	50	2380	64	1.3

Table 16. Comparison of Pile Capacities from Smartpile and Static Load Test (Ooi and Frederick, 2003)

Test Pile Number	Method of Defining Ultimate Failure	Ultimate Pile Capacity kN (tons)	SMARTPILE Capacity Ultimate Pile Capacity
Test Pile 1	Davisson (1972)	560 (63)	155%
	DeBeer (1972)	543 (61)	160%
	Brinch Hansen's 80% Criterion (1963)	920 (103)	94%
	Chin (1970, 1971)	1050 (103)	83%
	SMARTPILE	868 (98)	100%
Test Pile 2	Davisson (1972)	854 (96)	126%
	DeBeer (1972)	712 (80)	152%
	Brinch Hansen's 80% Criterion (1963)	1070 (120)	101%
	Chin (1970, 1971)	1210 (136)	89%
	SMARTPILE	1080 (121)	100%

Table 17 Testing Result Summary For US Courthouse Pile Foundation (Ooi and Frederick, 2003)

Location	Date	Boring	Top of Glacial El. (Ft)	Top of Till El (Ft)	Pile of Rock El. (Ft)	Pile Tip El. (Ft)	Driving Criteria (BPI)	PDA Capacity (Kips)	Smartpile Capacity (Kips)	Hammer Type	Hammer Energy Kip-Ft	Comments
B.9/19.8	5/2/95	B208	-	-97.7	-115.7	-114.2	9,8,8,9,8,9	320	600	CON160	28	
EC/70	5/2/95	RC-2	-	101.0	-112.0	-113.4	10,11,10,11,12,12	500	550	CON160	30	
EC/70	5/3/95		-									Redrive
L1/21.8	5/3/95	B101	-	-95.3	-116.5	-111.1	9,10,11,12,11,12	240	400	CON160	31	
B.9/8	5/3/95 5/4/95	B207	-	-90.4	-120.4	-111.3	8,8,7,9,8,8 9,7,8,7,7,7	400	500	CON160	28	Redrive
L.1/9	5/4/95 5/5/95	RC-1	-	-86.2	-114.2	-107.8	7,7,7,8,7,8	410 600	390 600	CON160	30 26	Restrike
JJ.9/26.1	5/5/95	B113	-	-92.2	-112.2	-111.4	14,15,14,15,15,17	490*	1060*	CON140	25	
FF.9/34.9	5/5/95	B203	-86.4	-97.9	-110.4	-110.5	13,15,18,16,16,16	500-550*	876*	CON140	25	
V.1/PY	5/9/95	B105	-	-92.7	-127.2	-108.3	9,9,9,8,9,9	330	N/A	CON140	29	
D.4/PX/E.9	5/10/95 5/11/95	B206	-	-87.4	-117.4	-100.7	7,8,7,8,8,9	360 460	N/A	CON140 CON140	26 23	Restrike
G.7/PX/2.5	5/11/95	B206	-	-87.4	-117.4	-105.1	8,8,8,8,7,8	N/A	N/A	CON160	34	
TEST PILE 1	5/9/95 5/10/95	B203	-86.4	-97.9	-110.4	-100.6	7,8,8,8,8,10	700 740	N/A N/A	CON140	29 24	Restrike
TEST PILE 2	5/11/95 5/12/95	B208	-	-97.7	-115.7	-109.1	4,4,4,4,4,4	630	N/A	CON160 CON160	36 32	Restrike
TEST PILE 3	5/12/95	B208	-	-97.7	-115.7	-108.6	8,8,8,9,9,9			CON160	26	Backup

Notes:

1. Test pile 3 was driven with a 12-in thickness of plywood pile cushion;
2. * PDA removed their instruments approx. 2 in about ground level. SMARTPILE reading taken after 2 in furtherdriving.

Table 18. Evaluation of Failure Criteria for Statically Loaded Drilled Shafts

Statistics for the Ratio between Drilled Shaft Capacity of different Interpretation Methods and the Representative Capacity											
Davisson			DeBeer			Shape of Curve			FHWA		
<i>#</i>	<i>m_x</i>	<i>σ_x</i>	<i>#</i>	<i>m_x</i>	<i>σ_x</i>	<i>#</i>	<i>m_x</i>	<i>σ_x</i>	<i>#</i>	<i>m_x</i>	<i>σ_x</i>
47	0.862	0.17	39	0.908	0.11	36	0.956	0.09	40	0.999	0.13

- no. of cases

m_x=mean

σ_x=standard deviation

loads 0.85 to 20 MN

diameter 0.3 to 1.5m

length 5.3 to 58.5m

Table 19. Recommended Relations Between Tested Shaft Capacity and Drop Weight System Requirements for 0.5m<H<2.5m

Capacity (kN)	Height (m) for Ram Weight (G)					
	G=50kN	G=70kN	G=90kN	G=120kN	G=150kN	G=200kN
1000	0.5					
2000	1.0	0.7	0.5			
3000	1.5	1.0	0.8	0.6	0.5	
4000	2.0	1.4	1.1	0.8	0.7	0.5
5000	2.5	1.8	1.4	1.0	0.8	0.6
6000		2.1	1.6	1.2	1.0	0.7
7000		2.5	1.9	1.4	1.2	0.9
8000			2.2	1.6	1.3	1.0
9000			2.5	1.9	1.5	1.1
11000				2.3	1.8	1.4
12000				2.5	2.0	1.5
13000					2.2	1.6
14000					2.3	1.7
15000					2.5	1.9
16000						2.0
17000						2.1
18000						2.2
19000						2.4
20000						2.5

Using $\eta=40\%$ for simplicity: $G \bullet H = (C - 100)/40$

where H(m)=Stroke height, G(kN)=weight of ram, C(kN)=drilled shaft capacity (estimated or required)

Table 20. Statistical Summary of Drop-Weight Dynamic Analysis Predictions For Drilled Shafts

Data Type	Static Failure Criterion															
	Representative				Davisson				FHWA				DeBeer			
	#	m_x	σ_x	Figure	#	m_x	σ_x	Figure	#	m_x	σ_x	Figure.	#	m_x	σ_x	Figure
All Tests	65	1.15	0.48	148	62	1.08	0.54	149	62	1.31	0.59	150	58	1.01	0.40	151
Tests to Failure	42	0.95	0.13	152	39	0.85	0.19	153	39	1.05	0.12	154	36	0.85	0.15	155
Failure from L.T.Extrapolation	22	1.55	0.63	156	21	1.46	0.64	157	20	1.71	0.73	158	21	1.23	0.49	159

- no. of analyzed cases m_x – Mean (bias) of the static capacity over the dynamic predictions σ_x – Standard deviation

Table 21. Statistical Summary of the Dynamic Methods for Capacity Prediction of Driven Piles (Paikowsky and Stenersen, 2000)

Method		Time of Driving	No. of Cases	Mean λ	Standard Deviation	COV
Dynamic Measurements	CAPWAP	General	377	1.368	0.620	0.453
		EOD	125	1.626	0.797	0.490
		EOD - AR < 350 & Bl. Ct. < 16 BP10cm	37	2.589	2.385	0.921
		BOR	162	1.158	0.393	0.339
	Energy Approach	General	371	0.894	0.367	0.411
		EOD	128	1.084	0.431	0.398
		EOD - AR < 350 & Bl. Ct. < 16 BP10cm	39	1.431	0.727	0.508
		BOR	153	0.785	0.290	0.369

Notes: EOD = End of Driving BOR = Beginning of Restrike AR = Area Ratio
 Bl. Ct. = Blow Count BP10cm = Blows per 10cm COV = Coefficient of Variation
 Mean = of the Ratio between Static Load Test Results (Davisson) to the predicted capacity (Bias)

Table 22. A Statistical Summary of the Performance of the FHWA Drilled Shaft Static Analysis Method (Based on Paikowsky, 2004).

Soil Type	No. of Cases	Mean m_x	COV
Sand	32	1.71	0.60
Clay	53	0.90	0.47
Mixed	44	1.19	0.30
Rock*	46	1.23	0.41

Table 23. Statnamic Database Summary

Identification Code														
Sheet	File	Pile Type	Soil Type	Same/Near	Order	Comp. Method	Static Method	Country Code	Site ID	Pile ID	λ	SLD	SLT	
1	Florida LS1	1	1	2	0	3	1	USA	FLLS	TP-1/2	1.056	6587	6957	
2	Florida LS2	1	1	2	0	3	1	USA	FLLS	TP-3/4	0.916	5164	4733	
3	JFK P10a	4	1	1	2	3	2	USA	JFK	OMSF P-10	1.067	3289	3509	
4	NNO	4	1	1	2	4	3	JPN	NNO	T1	0.890	4987	4440	
0	STGLT1	2	1	1	2	4	2	USA	STG	LT-1	1.031			
5	TFC-241	1	1	1	2	3	1	TWN	TFC	241	1.007	9316	9608	
6	TFC-532	1	1	1	1	3	1	TWN	TFC	532	1.022	23387	23544	
7	Ohito	1	2	1	2	3	3	JPN	OHITO	TEST	1.021	24548	25084	
8	BQE	1	2	2	0	2	1	USA	BQE	SA 1&8	0.949	10523	10747	
9	BCPier10	2	2	1	2	3	2	USA	BC	Pier10	1.065	8019	7606	
10	BCPier15	2	2	1	2	4	2	USA	BC	Pier 15	1.042	3175	3382	
11	BCPier5	2	2	1	2	4	2	USA	BC	Pier 5	0.909	5387	5612	
13	STGLT5	2	2	1	2	4	2	USA	STG	LT-5	1.177	10683	12575	
14	ShonanT6	4	2	1	1	3	2	JPN	SHONAN	T6	0.974	1056	1028	
15	ShonanT5	6	2	1	2	4	2,3	JPN	SHONAN	T5	0.935	509	476	
16	ShonanT2	6	2	1	1	3	3,2	JPN	SHONAN	T2	0.920	451	415	
17	ShonanT1	6	2	1	2	4	3,2	JPN	SHONAN	T1	0.947	505	478	
18	ashaft10	1	3	1	2	4	2	USA	Aub	10	0.796	2069	1647	
19	ashaft8	1	3	1	2	4	2	USA	Aub	8	0.883	1894	1672	
20	ashaft7	1	3	1	2	4	2	USA	Aub	7	0.953	2549	2429	
21	ashaft5	1	3	1	2	4	2	USA	Aub	5	1.083	2496	2703	
22	ashaft3	1	3	1	2	4	2	USA	Aub	3	0.957	1248	1194	
23	ashaft2	1	3	1	2	4	2	USA	Aub	2	1.040	2304	2397	
24	ashaft1	1	3	1	2	4	2	USA	Aub	1	1.012	2275	2302	
25	NIA TP 12a	4	3	2	0	3	2	USA	NIA	TP-1&2a	1.174	1287	1511	
26	NIA TP 12b	4	3	2	0	3	2	USA	NIA	TP-1&2b	1.069	2496	2669	
27	NIA TP 13a	4	3	2	0	3	2	USA	NIA	TP-1&3a	1.128	1397	1576	
28	NIA TP 13b	4	3	2	0	4	2	USA	NIA	TP-1&3b	1.109	2018	2238	
29	NIA TP 910a	4	3	2	0	3	2	USA	NIA	TP-9&10a	1.179	2058	2425	
30	NIA TP 910b	4	3	2	0	3	2	USA	NIA	TP-9&10b	1.144	2947	3371	
31	Contraband T114	2	4	1	2	3	1	USA	LC	T-114.5	1.108	2070	2293	
32	Contraband X123	2	4	1	1	3	1	USA	LC	X-123	0.866	2664	2306	
33	NIA TP 56a	4	4	2	0	3	2	USA	NIA	TP-5&6a	1.127	1942	2189	
34	NIA TP 56b	4	4	2	0	3	2	USA	NIA	TP-5&6b	1.037	2770	2874	

Table 24. Pile Specific Bias (λ) Values.

Site ID	Pile ID	Soil Type	λ
FLLS	TP-1/2	1	1.06
FLLS	TP-3/4	1	0.92
JFK	OMSF P-10	1	1.07
NNO	T1	1	0.89
STG	LT-1	1	1.03
TFC	241	1	1.01
TFC	532	1	1.02
OHITO	TEST	2	1.02
BQE	SA 1&8	2	0.95
BC	Pier10	2	1.07
BC	Pier 15	2	1.04
BC	Pier 5	2	0.91
STG	LT-5	2	1.18
SHONAN	T6	2	0.97
SHONAN	T5	2	0.94
SHONAN	T2	2	0.92
SHONAN	T1	2	0.95
Aub	10	3	0.80
Aub	8	3	0.88
Aub	7	3	0.95
Aub	5	3	1.08
Aub	3	3	0.96
Aub	2	3	1.04
Aub	1	3	1.01
NIA	TP-1&2a	3	1.17
NIA	TP-1&2b	3	1.07
NIA	TP-1&3a	3	1.13
NIA	TP-1&3b	3	1.11
NIA	TP-9&10a	3	1.18
NIA	TP-9&10b	3	1.14
LC	T-114.5	4	1.11
LC	X-123	4	0.87
NIA	TP-5&6a	4	1.13
NIA	TP-5&6b	4	1.04

1-rock, 2-sand, 3-silt, 4-clay

Table 25. Summary of Safety Factors Without Using Rate Effect Corrections

Soil Type	Bias Factor λ	Standard Deviation σ_{dev}	Required Safety Factor	Resistance Factor ϕ	Number of Observations
Rock	0.959	0.066	2.0	0.71	7
Sand	0.904	0.076	2.1	0.66	10
Silt	0.718	0.080	2.8	0.51	13
Clay	0.672	0.077	3.0	0.47	4
All Soils	0.817	0.135	2.6	0.54	34

Table 26. Summary of Rate Effect Factors and Associated Values

Soil Type	Rate Effect Factor	Bias Factor λ	Standard Deviation σ_{dev}	Required Safety Factor	Resistance Factor ϕ	Number of Observations
Rock	0.96	0.999	0.068	1.92	0.739	7
Sand	0.91	0.994	0.083	1.95	0.726	10
Silt	0.69	1.041	0.116	1.92	0.737	13
Clay	0.65	1.035	0.119	1.94	0.730	4
All Soils	N/A	1.017	0.097	1.93	0.734	34

Table 27 Summary of Rate Effect Factors and Design Values.

Soil Type	Rate Effect Factor η	Recommended Safety Factor without η	Recommended Resistance Factor without η	Recommended Safety Factor with η	Recommended Resistance Factor with η
Rock	0.96	2.0	0.7	2.0	0.7
Sand	0.91	2.1	0.65	2.0	0.7
Silt	0.69	2.8	0.5	2.0	0.7
Clay	0.65	3.0	0.45	2.0	0.7
All Soils	N/A	2.6	0.5	2.0	0.7

Table 28. Data Details for an Under-Damped System ($\zeta < 1$)

Case	G (kN)	H (m)	K (10^9 N/m)	I (10^3 N/m/s)	ζ	ω_n (s^{-1})	α (s^{-1})	$R = \omega_n/\alpha$
1	50	2.50	1.500	4636	0.2984	542.22	161.78	3.352
2	50	2.00	1.500	4636	0.2984	542.22	161.78	3.352
3	50	1.50	1.500	4636	0.2984	542.22	161.78	3.352
4	50	1.00	1.500	4636	0.2984	542.22	161.78	3.352
5	50	0.50	1.500	4636	0.2984	542.22	161.78	3.352
6	50	1.98	1.000	4636	0.2436	442.72	107.85	4.105
7	50	2.45	0.750	4636	0.2110	333.41	80.89	4.740
8	50	3.32	0.500	4636	0.1723	313.05	53.93	5.805
9	50	2.43	0.250	4636	0.2110	127.80	26.96	4.740
10	50	2.80	0.125	4636	0.2110	63.90	13.48	4.740

Table 29. Data Details for an Over-Damped System ($\zeta > 1$)

Case	G (kN)	H (m)	K (10^9 N/m)	I (10^3 N/m/s)	ζ	ω_n (s^{-1})	α (s^{-1})	$R = \omega_n/\alpha$
1	50	1.50	15	1219	3.5891	1714.64	6154.04	0.279
2	50	1.00	15	1219	3.5891	1714.64	6154.04	0.279
3	50	0.50	15	1219	3.5891	1714.64	6154.04	0.279
4	50	0.10	15	1219	3.5891	1714.64	6154.04	0.279
5	50	1.15	5	1219	2.0722	989.95	2051.35	0.483
6	50	1.33	2.5	1219	1.4652	700.00	1025.67	0.683
7	50	1.62	1.25	1219	1.0361	494.97	512.84	0.965
8	125	1.33	1	1219	1.4652	280.00	410.27	0.683
9	208	1.80	0.6	1219	1.4652	168.00	246.16	0.683

Table 30. Secant Modulus of Elasticity for Common Capblock and Pile-Cushion Materials.

Material	E (ksi)	E (MPa)
Micarta	450	3100
Hardwood, oak	45	310
Asbestos disks	45	310
Plywood, fir	35	240
Pine	25	170
Softwood, gum	30	205

(Approximate A=12 in. or 20 cm square and L=A unless other data are available to compute spring constant of AE/L.)

Table 31. Data Details for the Analyses with the Same M, H and K, and a Different I

Case	G (kN)	H (m)	K (10^9 N/m)	I (10^3 N/m/s)	ζ	ω_n (s^{-1})	α (s^{-1})	R= ω_n/α
1	70	1.5	1.0	2000	0.6745	374.17	252.38	1.483
2	70	1.5	1.0	4000	0.3373	374.17	126.19	2.965
3	70	1.5	1.0	8000	0.1686	374.17	63.094	5.930
4	70	1.5	1.0	16000	0.0843	374.17	31.547	11.861
5	70	1.5	1.0	32000	0.0422	374.17	15.774	23.721
6	70	1.5	1.0	64000	0.0211	374.17	7.887	47.442
7	70	1.5	1.0	128000	0.0105	374.17	3.943	94.884
8	70	1.5	1.0	256000	0.0053	374.17	1.972	189.768

Table 32. The Influence of a Load Testing System (Data Details for Figure 272)

Testing Method	G (kN)	H (m)	K (10^9 N/m)	I (10^3 N/m/s)	ζ	ω_n (s^{-1})	α (s^{-1})	R= ω_n/α
Dynamic	25	0.4	1	1219	0.6553	626.10	410.27	1.526
STATNAMIC	50	0.2	0.5	1219	0.6553	31.30	20.51	1.526
FUNDEX	800	0.04	0.1	1219	0.3707	11.07	4.10	2.698
Static	1500	0.02	0.07	1219	0.4247	6.76	2.87	2.355

Table 33. Details of Newbury Test Pile No.2, Figure 273 (a, b, c)

<i>Fig. No.</i>	<i>Testing Method</i>	<i>G (kN)</i>	<i>H (m)</i>	<i>K (10⁹ N/m)</i>	<i>I (10³ N/m/s)</i>	ζ	ω_n (s ⁻¹)	α (s ⁻¹)	$R=\omega_n/\alpha$
a	Dynamic	17.6	1.3	2.224	503	1.9858	1112.82	2209.79	0.504
	STATNAMIC	38.0	0.5	0.250	503	0.9783	253.92	248.40	1.022
	Static	60.0	0.3	0.159	503	0.9803	161.15	157.98	1.020
b	Dynamic	17.6	1.3	2.224	503	1.9858	1112.82	2209.79	0.504
	STATNAMIC	500	0.02	0.250	3265	0.5469	70.00	38.29	1.828
	Static	1500	0.003	0.159	10064	0.2450	32.23	7.90	4.080
c	Dynamic	17.6	0.4	1.107	1510	0.4669	785.11	366.64	2.141
	STATNAMIC	600	0.08	0.05	5032	0.1738	28.58	4.97	5.752
	Static	1000	0.04	0.015	5032	0.1229	12.12	1.49	8.135

Table 34. Details of Newbury Test Pile No.3, Figure 274 (a, b, c)

<i>Fig. No.</i>	<i>Method</i>	<i>G (kN)</i>	<i>H (m)</i>	<i>K (10⁹ N/m)</i>	<i>I (10³ N/m/s)</i>	ζ	ω_n (s ⁻¹)	α (s ⁻¹)	$R=\omega_n/\alpha$
a	Dynamic	44.5	0.4	1.080	119	0.9273	487.80	452.34	1.087
	STATNAMIC	70.0	0.3	0.300	119	0.6131	204.94	125.65	1.631
	Static	100.0	0.07	0.200	119	0.5983	140.00	83.77	1.671
b	Dynamic	44.5	0.4	1.080	119	0.9273	487.80	452.34	1.078
	STATNAMIC	300.0	0.025	0.300	1194	0.1269	98.99	12.56	7.879
	Static	400.0	0.006	0.200	2388	0.0598	70.00	4.19	16.713
c	Dynamic	44.5	0.20	1.080	178	0.6198	487.80	302.35	1.613
	STATNAMIC	600	0.08	0.040	1193	0.0655	25.56	1.68	15.257
	Static	1000	0.04	0.015	2387	0.0260	12.12	0.31	38.597

Table 35. Summary of Attributes for Modeled Ram

Ram Diameter	Ram Length	Ram Drop Height	Ram Mass	Energy	Impact Angle
1.0m	1.6667m	2.0m	1.0276 E+04 kg	2.016 E+5 J	0°

Table 36. Model Statistics

3-D Half-Symmetry Model	
Number of Nodes	9,500
Number of Elements	7,728
Type of Element	8-node solid

Table 37. Material Properties

Component	Density (kg/m³)	Elastic Modulus (Pa)	Poisson's Ratio
Striker Plate (steel)	7.850 E+03	2.00 E+11	0.30
Pile (concrete)	2.380 E+03	2.55 E+10	0.15
Cushion (plywood)	4.830 E+02	2.00 E+06	0.30
Ram (steel)	7.850 E+03	2.00 E+11	0.30

Table 38. Component Geometry for Baseline Model

Component	Diameter (m)	Length (m)
Striker Plate	1.00	0.100
Pile	1.00	40.000
Cushion	1.00	0.100
Ram	1.00	0.167

Table 39. Drop Height and Corresponding Impact Velocity

Drop Height (m)	Impact Velocity (m/s)
0.5	3.1006
1.0	4.4072
1.5	5.4068
2.0 (baseline)	6.2485
2.5	6.9895

Table 40. Ram Diameter and Corresponding Density

Ram Diameter (m)	Density (kg/m³)
0.2	1.9430 E+07
0.6	2.1588 E+05
1.0 (baseline)	7.850 E+03
1.5	3.4541 E+04

Table 41. Summary of Attributes for Modeled Ram.

Ram Diameter	Ram Length	Ram Drop Height	Ram Mass	Energy	Impact Angle
1.0m	1.6667m	2.0m	1.0276 E+04 kg	2.016 E+5 J	0°
1.0m	1.6667m	2.0m	1.0276 E+04 kg	2.016 E+5 J	1°

Table 42. Summary of Model Parameters Obtained from the Statnamic and Static Tests of TP#2

Analyzed Test	Based on Statnamic Tests		Based on Static Test
	TP # 2-3	TP # 2-4	
T_0^* (kN)	542	202	250
$T_4 = P_{max}$ (kN)	764	770	806
E_0 (kN/mm)	194	5,000	300
$E_{0,1}$ (kN/mm)	259	108	187
$\eta_4 = (\text{kN}\cdot\text{hr}/\text{mm}) * 10^{-3}$.34	1.03	---
$\eta_1 = (\text{kN}\cdot\text{hr}/\text{mm}) * 10^{-3}$	---	---	878
$\eta_2 = (\text{kN}\cdot\text{hr}/\text{mm}) * 10^{-3}$	---	---	35
$\eta_3 = (\text{kN}\cdot\text{hr}/\text{mm}) * 10^{-3}$	---	---	1
E_1 (kN/mm)	---	---	610
E_2 (kN/mm)	---	---	36
T_1^* (kN)	---	---	283
T_2^* (kN)	---	---	127
T_3 (kN)	---	---	710

Table 43. Summary Table for the Attributes, Status and Future Work of the Primary Investigated Load Testing Systems

Test Type	Loading Method	Wave Length Λ	Application	Capacity Range MN (tons)	Advantages	Limitations	Principle of Analysis	Current Status	Guidelines	Future Work
Drop Weight	High stress dynamic – fast loading	<1	<ul style="list-style-type: none"> • IPCDF • Old DF (IPCDF/DP) 	<15 (1500)	<ul style="list-style-type: none"> • High mobility • Local development of simple impact device • Low cost • Proven wave mechanics analysis • Soil structure interaction from analysis • High strain integrity testing 	<ul style="list-style-type: none"> • Loading system capacity • Careful preparation and testing needed for good quality data • High quality, independent displacement measurements not used routinely 	1-D W.E. signal matching	Mature proven requires clear identification of problems and solutions	Needs a comprehensive development of guidelines	<ol style="list-style-type: none"> 1. Complete study of ram/DF impact; identifying problems, limits and solutions 2. Detailed evaluation of foundation structure (shape and quality) influence on measurements and analyses 3. Benchmark testing for comparison with static load tests 4. Assessment of accuracy for soil-structure interaction
Statnamic	High stress – kinetic	>10	<ul style="list-style-type: none"> • IPCDF • Old DF (IPCDF/DP) 	<30 (3000)	<ul style="list-style-type: none"> • High mobility • Medium cost • High capacity in difficult to reach places • Reliable and consistent measurement 	<ul style="list-style-type: none"> • Low reliability in cohesive soils • Soil structure interaction is difficult to obtain • Proprietary 	UPM (Unloading Point Method) using Kalvin-Voigt model and its modification (MUP) with multipoint measurements	Proven for granular soils, needs reliable analysis tools for all subsurface conditions	Existing guidelines for testing procedures and measurements Needs a clear distinction between reliable and unreliable conditions for application	<ol style="list-style-type: none"> 1. Reliable analysis tool to address the mechanics of the problem in all subsurface conditions 2. Comparison testing between Statnamic and static 3. Continued evaluation of the current/new analyses methods
O-Cell	Static	10^8	<ul style="list-style-type: none"> • IPCDF • DP (rarely) 	Single cell <50 (5000) multi-cell <150 (15000)	<ul style="list-style-type: none"> • High capacity • Static loading • Soil-structure interaction plausible with additional instrumentation 	<ul style="list-style-type: none"> • Preselected foundations • Upward loading and its interpretation • Questionable O-cell selection location • Possible soft end reaction • Proprietary • High cost/ unrecoverable equipment 	Top-down equivalent curves from bi-direction testing	In use though limited knowledge of limitations and proof for accuracy	Needs a comprehensive development of guidelines for use, design, and interpretation;	<ol style="list-style-type: none"> 1. In-depth study of factors affecting top-down and down-up interfacial shear and force-displacement curves 2. Reliability and improvements of the equivalent curves 3. Possible development of alternative non-proprietary testing methods 4. Careful comparison and testing subjected to the above and in cooperation with industry

IPCDF – In Place Constructed Deep Foundations

DF – Deep Foundations

DP – Driven Piles

1-D W.E. – One Dimensional Wave Equation

Table 44. Summary Table for the Attributes, Status and Future Work of the Secondary Investigated Load Testing Systems

Test Type	Loading Method	Wave Length Λ	Application	Capacity Range MN (tons)	Advantages	Limitations	Principle of Analysis	Current Status	Guidelines	Future Work
Simbat	High stress dynamic – fast loading	<1	<ul style="list-style-type: none"> • IPCDF • Old DF (IPCDF/DP) 	<15 (1500)	<ul style="list-style-type: none"> • High mobility (have the potential for all drop weight advantages) • Sophisticated and reliable measuring system 	<ul style="list-style-type: none"> • Unproven reliability of interpretation method for ultimate capacity 	Seperation of measured dynamic force signal for up and down forces and a simplified evaluation of the synamic effects	In use locally in Europe, France and England	None	<ol style="list-style-type: none"> 1. Examine the possible use of the advantages of typical drop weight system and Simbat for improvements in both 2. Combine drop weight future study with Simbat
Findex	High stress – kinetic	>10	<ul style="list-style-type: none"> • IPCDF • Old DF (IPCDF/DP) 	<10 (1000)	<ul style="list-style-type: none"> • Complete system mobilized with a rig 	<ul style="list-style-type: none"> • Long stress waves with no proven benefit • Model does not seem to effectively address the conditions created during the loading 	Basic mechanics and simple model	Limited use	None	No future work is proposed
Smartpile	High stress dynamic – fast loading	<1	<ul style="list-style-type: none"> • DP 	Dependin g on the impacting hammer	<ul style="list-style-type: none"> • Possible improvements of measurement (direct force) for dynamic and drop weight testing 	<ul style="list-style-type: none"> • Unproven interpretation method • Unrecoverable instrumentation at the tip 	Interpretation of recorded force response curve	Limited use	None	<ol style="list-style-type: none"> 1. Examine to use the advantages of drop weight/dynamic testing and Smartpile for improvements of all 2. Combine drop weight future study with Smartpile
Smart Coil	High stress dynamic – fast loading	<1	<ul style="list-style-type: none"> • DP 	Dependin g on the impacting hammer	<ul style="list-style-type: none"> • Potentially a promising system 	<ul style="list-style-type: none"> • Untested, unknown 	N/A	No sufficient information is available	N/A	Cannot be evaluated at this stage

IPCDF – In Place Constructed Deep Foundations

DF – Deep Foundations

DP – Driven Piles